Natural Resources Canada | Ressources naturelles Canada

GEOLOGICAL SURVEY OF CANADA
OPEN FILE 8712

Targeted Geoscience Initiative 5: Contributions to the Understanding of Canadian Gold Systems

Edited by
P. Mercier-Langevin, C.J.M. Lawley, and S. Castonguay

2020

Canada

GEOLOGICAL SURVEY OF CANADA
OPEN FILE 8712

Targeted Geoscience Initiative 5: Contributions to the Understanding of Canadian Gold Systems

Edited by
P. Mercier-Langevin[1], C.J.M. Lawley[2], and S. Castonguay[1]

[1]Geological Survey of Canada, 490, rue de la Couronne, Québec, Quebec G1K 9A9
[2]Geological Survey of Canada, 601 Booth Street, Ottawa, Ontario K1A 0E8

2020

© Her Majesty the Queen in Right of Canada, as represented by the Minister of Natural Resources, 2020

Information contained in this publication or product may be reproduced, in part or in whole, and by any means, for personal or public non-commercial purposes, without charge or further permission, unless otherwise specified.
You are asked to:
- exercise due diligence in ensuring the accuracy of the materials reproduced;
- indicate the complete title of the materials reproduced, and the name of the author organization; and
- indicate that the reproduction is a copy of an official work that is published by Natural Resources Canada (NRCan) and that the reproduction has not been produced in affiliation with, or with the endorsement of, NRCan.

Commercial reproduction and distribution is prohibited except with written permission from NRCan. For more information, contact NRCan at nrcan.copyrightdroitdauteur.rncan@canada.ca.

Permanent link: https://doi.org/10.4095/323661

This publication is available for free download through GEOSCAN (https://geoscan.nrcan.gc.ca/).

Recommended citation
Mercier-Langevin, P., Lawley, C.J.M., and Castonguay, S., (ed.), 2020. Targeted Geoscience Initiative 5: Contributions to the Understanding of Canadian Gold Systems; Geological Survey of Canada, Open File 8712, 328 p. https://doi.org/10.4095/323661

Publications in this series have not been edited; they are released as submitted by the author

Contribution to the Geological Survey of Canada's Targeted Geoscience Initiative 5 (TGI-5) Program (2015-2020)

TABLE OF CONTENTS

Targeted Geoscience Initiative 5, Gold Project: A summary of contributions to the understanding of Canadian gold systems

Patrick Mercier-Langevin, Christopher J.M. Lawley, Sébastien Castonguay, Benoît Dubé, Wouter Bleeker, Nicolas Pinet, Valérie Bécu, Jean-Luc Pilote, Simon E. Jackson, Natasha Wodicka, Ian W. Honsberger, William J. Davis, Duane C. Petts, Zhaoping Yang, Josué Jautzy, and Kathleen Lauzière 1

Geology and gold enrichment at the Horne 5 Archean volcanogenic massive sulphide deposit, Abitibi greenstone belt, Quebec: A synthesis

Alexandre Krushnisky, Patrick Mercier-Langevin, Pierre-Simon Ross, Jean Goutier, Claude Pilote, and Claude Bernier 31

Sulphide clast-bearing felsic volcaniclastic units of the Rouyn-Pelletier Formation: Comparison with similar units of the Horne Block, Rouyn-Noranda, Abitibi greenstone belt, Quebec

Catherine Boudreau, Patrick Mercier-Langevin, Alexandre Krushnisky, and Jean Goutier 45

Stratigraphic setting of the LZ5 and Ellison mineralized zones, LaRonde Zone 5 project, Doyon-Bousquet-LaRonde mining camp, Abitibi, Quebec

Émile Boily-Auclair, Patrick Mercier-Langevin, Pierre-Simon Ross, and David Pitre 57

Interrogating the composition and genesis of argillite-hosted pyrite nodules at the LaRonde Penna gold-rich volcanogenic massive sulphide deposit, Abitibi, Quebec: Insights into metallogenic implications

Jean-Luc Pilote, Patrick Mercier-Langevin, Simon E. Jackson, Benoît Dubé, Zhaoping Yang, Christopher J.M. Lawley, Duane C. Petts, Graham D. Layne, and Stephen J. Piercey 75

The B26 Cu-Zn-Ag-Au project, Brouillan volcanic complex, Abitibi greenstone belt, part 1: Geological setting and geochronology

Quentin Fayard, Patrick Mercier-Langevin, Natasha Wodicka, Réal Daigneault, and Serge Perreault 93

The B26 Cu-Zn-Ag-Au project, Brouillan volcanic complex, Abitibi greenstone belt, part 2: Hydrothermal alteration and mineralization

Quentin Fayard, Patrick Mercier-Langevin, Réal Daigneault, Serge Perreault, and Natasha Wodicka 109

Geological setting and gold mineralization associated with the Sunday Lake and Lower Detour deformation zones, northwestern Abitibi greenstone belt, Ontario and Quebec

Sébastien Castonguay, Benoît Dubé, Natasha Wodicka, and Patrick Mercier-Langevin 127

Geology, structural evolution, and hydrothermal alteration of the Island gold deposit, Michipicoten greenstone belt, Ontario

Tyler J. Ciufo, Katia Jellicoe, Chris Yakymchuk, Shoufa Lin, Patrick Mercier-Langevin, and Natasha Wodicka 143

Bottom-up mineral exploration: Ore-element upgrading in the upper mantle and tools for its discovery

Christopher J.M. Lawley and Bruce A. Kjarsgaard 157

Fingerprinting ore processes in orogenic auriferous systems: Insights into metallogenic and exploration implications from argillite-hosted iron sulphide nodules from the Timmins-Matheson gold corridor

Jean-Luc Pilote, Simon E. Jackson, Patrick Mercier-Langevin, Benoît Dubé, Christopher J.M. Lawley, Duane C. Petts, Zhaoping Yang, Ed van Hees, and Dave Rhys 165

Vein-hosted gold mineralization in the Wilding Lake area, central Newfoundland: Structural geology and vein evolution

Ian W. Honsberger, Wouter Bleeker, Hamish A.I. Sandeman, Dave T.W. Evans, and Sandra L. Kamo 179

The emerging Paleozoic gold district of central Newfoundland: New insights on structural controls and tectonic drivers of gold mineralization and preservation

Ian W. Honsberger, Wouter Bleeker, Sandra L. Kamo, Hamish A.I. Sandeman, and Dave T.W. Evans 193

Paleoproterozoic gold and its tectonic triggers and traps: Implications from Re-Os sulphide and U-Pb detrital zircon geochronology, Lynn Lake, Manitoba

Christopher J.M. Lawley, David Selby, William J. Davis, Eric Yang, Shuangquan Zhang, Simon E. Jackson, Duane C. Petts, A. Rhys O'Connor, and David A. Schneider 211

Superimposed Late Cretaceous and earliest Eocene gold mineralization and deformation events along the Llewellyn-Tally Ho deformation corridor in northwest British Columbia and southern Yukon

Sébastien Castonguay, Luke Ootes, Fionnuala Devine, and Richard Friedman 223

Structural controls and relative timing of gold mineralization of the banded iron formation-associated Tiriganiaq deposit, Meliadine district, Rankin Inlet greenstone belt, Nunavut

Brayden St.Pierre, Patrick Mercier-Langevin, Jean-Claude Blais, Guilhem Servelle, Marjorie Simard, Olivier Côté-Mantha, and Michel Malo 237

Lithological and tectonic controls on banded iron formation-associated gold at the Amaruq deposit, Churchill Province, Nunavut, and implications for exploration

Manon Valette, Stéphane De Souza, Patrick Mercier-Langevin, Olivier Côté-Mantha, Marjorie Simard, Natasha Wodicka, Vicki J. McNicoll, and Patrice Barbe 251

Ore mineralogy and mineral chemistry of the Whale Tail zone, Amaruq gold deposit, Nunavut

Marie-Christine Lauzon, Patrick Mercier-Langevin, Manon Valette, Georges Beaudoin, Stéphane De Souza, Olivier Côté-Mantha, and Marjorie Simard 267

Neoproterozoic-hosted Carlin-type mineralization in central Yukon, part 1: Regional- to prospect-scale geological controls

Nicolas Pinet, Patrick Sack, Patrick Mercier-Langevin, Maurice Colpron, Denis Lavoie, Benoît Dubé, and Virginia I. Brake 281

Neoproterozoic-hosted Carlin-type mineralization in central Yukon, part 2: Mineralization

Nicolas Pinet, Patrick Sack, Patrick Mercier-Langevin, William J. Davis, Denis Lavoie, Omid Haeri-Ardakani, Bram A. Komaromi, Benoît Dubé, Jean S. Cline, Duane C. Petts, Josué Jautzy, Simon E. Jackson, Jeanne B. Percival, Martine M. Savard, and Virginia I. Brake 299

APPENDICES

Appendix 1: Peer-reviewed journal publications related to the TGI-4/TGI-5 gold projects (2015–2020) 315

Appendix 2: Government publications related to the TGI-4/TGI-5 gold projects (2015-2020) 317

Appendix 3: Theses related to the TGI-5 Gold Project (2015–2020) and legacies of the TGI-4 Lode Gold Project (2010–2015) 327

Targeted Geoscience Initiative 5, Gold Project: A summary of contributions to the understanding of Canadian gold systems

Patrick Mercier-Langevin[1*], Christopher J.M. Lawley[2], Sébastien Castonguay[1], Benoît Dubé[1], Wouter Bleeker[2], Nicolas Pinet[1], Valérie Bécu[1], Jean-Luc Pilote[1], Simon E. Jackson[2], Natasha Wodicka[2], Ian W. Honsberger[2], William J. Davis[2], Duane C. Petts[2], Zhaoping Yang[2], Josué Jautzy[1], and Kathleen Lauzière[1]

[1]Geological Survey of Canada, 490 rue de la Couronne, Québec, Quebec G1K 9A9
[2]Geological Survey of Canada, 601 Booth Street, Ottawa, Ontario K1A 0E8
[*]Corresponding author's e-mail: patrick.mercier-langevin@canada.ca

ABSTRACT

The discovery of new mineral deposits is essential to maintain a stable supply of mineral commodities, however, new mineral discoveries are in ever more remote, deeper, and/or covered geological environments, which presents significant challenges. The fifth phase of the Targeted Geoscience Initiative (TGI-5) was developed to address these challenges and to advance our understanding of ore-forming processes at various spatial scales and across geological time. Here we present a selection of highlights from research activities comprising the Gold Project. These research activities, all of which included significant field components, focused on different aspects of the gold mineral systems and included gold districts with variable metal endowment (e.g. southern and northern Neoarchean Abitibi greenstone belt), geological setting (e.g. pre-, syn-, and post-orogenic processes), and geological age (e.g. Paleoproterozoic Trans-Hudson, and Phanerozoic Appalachian orogenic belts).

The southern Abitibi is host to many different types of giant gold deposits (e.g. synvolcanic and orogenic gold ore systems), although the sources of ore-components for these mineral systems remained unclear. New TGI research addressed this knowledge gap and demonstrate that (1) diagenetic sulphides (pyrite nodules) and their host sedimentary sequences within the Superior Province are pre-enriched in gold; (2) Archean calc-alkaline felsic volcanic centres associated with large synvolcanic gold deposits further suggest that igneous differentiation in the lower crust may be associated with the generation of synvolcanic gold-rich magmatic-hydrothermal systems; and (3) undocumented upper mantle pathways existed, which were revealed by anomalous ore-forming element concentrations within cratonic mantle samples from the southern Superior Province. Together these research activities provide new insights into the upgrading of ore components from the mantle to the upper crust, although the role of these pre-enriched source rocks to gold ore systems remains unclear.

Other research activities focused on the complete source-to-ore pathways of gold-bearing fluids for multiple gold districts across Canada. The similar pacing of events and timing of auriferous vein development within the overall tectonic evolution for several of these gold districts likely reflects a common driver (e.g. upwelling asthenosphere) and/or tectonic triggers (e.g. crustal extension and associated magmatism). However, the contrasting metal endowment of areas with otherwise similar histories (e.g. southern versus northern Abitibi belt) suggests that the prospectivity of gold districts is not entirely related to the large-scale drivers and triggers of ore-forming fluids. Moreover, long-term preservation is another critical factor in gold ore systems, which is promoted by rapid burial; limited post-ore remobilization during hydrothermal and metamorphic overprinting; and long-term craton stability. Indications of preferential preservation, such as the occurrence of synorogenic polymict conglomerate, constitute key exploration criteria.

New analytical methods that were developed as part of TGI-5 are also providing new tools (e.g. rapid in situ element mapping and data interrogation approaches; new geochronological methods; clumped isotope thermometers) for recognizing ore-proximal depositional controls from the rock record. An improved understanding of these controls and efficient vectoring tools are increasingly important for mineral exploration targeting.

Mercier-Langevin, P., Lawley, C.J.M., Castonguay, S., Dubé, B., Bleeker, W., Pinet, N., Bécu, V., Pilote, J.-L., Jackson, S.E., Wodicka, N., Honsberger, I.W., Davis, W.J., Petts, D.C., Yang, Z., Jautzy, J., and Lauzière, K., 2020. Targeted Geoscience Initiative 5, Gold Project: A summary of contributions to the understanding of Canadian gold systems; *in* Targeted Geoscience Initiative 5: Contributions to the Understanding of Canadian Gold Systems, (ed.) P. Mercier-Langevin, C.J.M. Lawley, and S. Castonguay; Geological Survey of Canada, Open File 8712, p. 1–30. https://doi.org/10.4095/323662

INTRODUCTION

This volume summarizes the research conducted between April 2015 and March 2020 by the Geological Survey of Canada (GSC) and its collaborators as part of the Gold Project of Natural Resources Canada's Targeted Geoscience Initiative Program (Phase 5). This synthesis volume contains 20 individual papers, including this contribution, that discuss regional- to deposit-scale characteristics of auriferous deposits across Canada.

The primary goal of Phase 5 of the TGI program ("Source-to-ore geoscience for effective exploration") was to generate new knowledge, models, and methodologies to enhance the exploration industry's ability to detect mineral deposits. Each of these research activities is integrated into a source-to-ore processes-based framework. Other important objectives of the Gold Project were to adopt collaborative approaches in research activities, to publicly disseminate the results in a timely manner, and to contribute to replenishing the pool of highly qualified personnel (HQP) in geosciences. Progress on each of the Gold Project objectives is discussed below.

A general introduction to the Gold Project synthesis volume and background information about the project are given here. We also summarize a subset of the main contributions to the understanding of Canadian gold mineral systems made through the various activities of the project. Readers are referred to the original contributions for further details on the scientific highlights specific to each research activity. It is important to note that this synthesis volume can only provide a snapshot of the state of research and data analysis at the end of March, 2020; however, product delivery will continue for some time, with longer term outcomes in preparation or planned for the future.

The Targeted Geoscience Initiative

The *Resources and Technical Surveys Act* of 1985 mandates that the Minister of Natural Resources "shall make detailed investigations of mining camps and areas containing economic minerals or deposits of other economic substances, for the purpose of determining the mode of occurrence and the extent and character of ore-bodies and deposits" (R.S., 1985, c. R-7, s. 31994, c. 41, s. 3b). In the late 1990s, following various phases of restructuring at Natural Resources Canada, the GSC asked the Canadian Geoscience Council (CGC) to provide advice on the Minerals Geoscience Program. The CGC recommended that scientific leadership should be fostered at the national level and that regional, field-based metallogenic studies should represent important components of future mineral programs (Cathro et al., 2000). The GSC responded with a revised strategy built around newly funded, integrated, multidisciplinary and partnered national programs of thematic research (Duke, 2000). In 2000, this led to the development and implementation of the TGI Program, comprising a budget of $15 million over three years (2000–2002) to fund deposit- to district-scale mineral research projects throughout Canada. TGI was renewed for two years (Phase 2: 2003–2004) and comprised research projects focused on energy resources. A third phase followed, with a total budget of $25 million over five years (2005–2010), primarily for research promoting exploration for Cu resources in and around major base metal mining camps with operational smelters. A fourth phase was announced in mid-2010 with an initial budget of $10 million for two years, which was extended to $25 million for five years (2010–2015) in late 2010. Phase 4 marked a change from site-specific to ore system-based thematic research. TGI was renewed in 2015 for 5 years (Phase 5: 2015–2020) with a total budget of $22 million.

TGI-5 used a thematic, ore-system approach to define research projects (Fig. 1) that was guided by an internal review of the TGI-4 program and recommendations for future thematic research (Bleeker et al., 2014), while building on the research conducted on key Canadian ore systems during Phase 4 (2010–2015) of the program. In this context, an "ore system" can be defined as "*a mineralized system, across a range of scales, which culminated in one, or more typically a group of related deposits that share common genetic and geologic characteristics. At the large scale, the ore system is defined by the geodynamic and tectonic setting that created the set of conditions which, at the smaller scale, resulted in ore deposition. Ore deposits comprising an ore system can differ in style and position in the crust, and in timing, but share common causative ore-forming processes and controlling parameters*." This definition is a slight modification of the original definition of "mineral systems" proposed by Wyborn et al. (1994), which followed the perspective of "petroleum systems" used by the hydrocarbon exploration industry. The revised definition adopted here considers the entire process chain (Fig. 1) and resembles the definition of metallogeny, as initially proposed by De Launay (1913), and which is a largely overlapping concept: "*the study of the genesis of mineral deposits, with emphasis on their relationship in space and time to regional petrographic and tectonic features of the Earth's crust*" (American Geosciences Institute's Glossary of Geology: Neuendorf et al., 2005).

The Gold Project – Rationale, Objectives, and Approaches

Exploration for gold has historically represented a significant part of global and Canadian mineral exploration expenditures with an increasingly important proportion

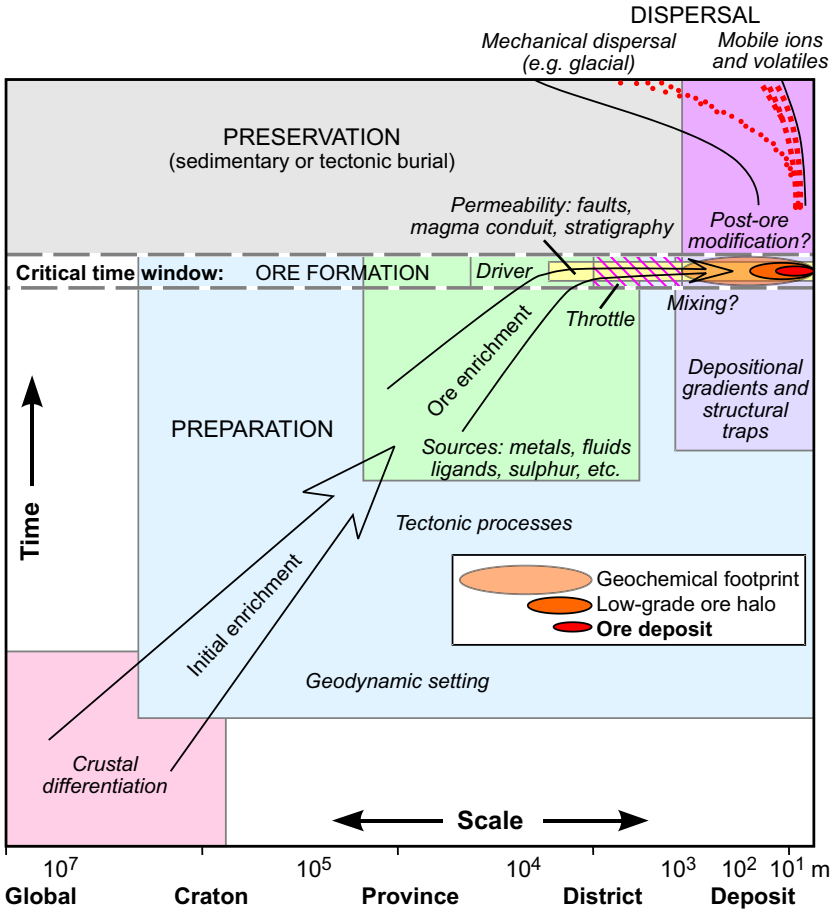

Figure 1. Schematic diagram of time versus scale illustrating the concept of complex mineral systems culminating in an economic ore deposit (small red ellipse). Ore deposits typically require an initial preparatory processes ("ground preparation") that pre-dates ore formation, several critically linked ore-forming processes that overlap in space and time, preservation of orebodies, and dispersion of spent fluids and/or metals. These processes typically operate across a vast range of scales. Initially, large-scale geodynamic and tectonic processes concentrate elements of interest into a regional- to district-scale source region, from which they are stripped by hydrothermal fluids or magmas. Faults or other permeable zones then focus ore-forming fluids or magmas into depositional environments where chemical, physical, or thermal gradients cause ore deposition. After passing through the depositional environment, spent fluids disperse into the environment. Many of these processes leave forensic evidence, such as hydrothermal alteration, that can be used to locate mineral deposits and their larger geochemical "footprints". Post-depositional dispersal of ore constituents or "pathfinder" elements, whether by chemical or mechanical means (e.g. erosion), may increase the scale of the exploration target. *From* Bleeker et al. (2014) as *adapted from* Huston et al. (2012).

in the last decade (Fig. 2a,b). Since 2017, between 55% and 65% of the total exploration expenditures in Canada were spent on gold (Fig. 2b,c). The increasing proportion of exploration budgets being spent on gold exploration is not only due to the higher costs associated with exploring for more remote or deeper deposits but is also due to the increased interest in gold due to its favourable market price, which is, in turn, largely influenced by global events (Fig. 2d,e). To mitigate increasing costs and risks, exploration efforts and spending in Canada are focused on the most favourable geological settings, including the southern parts of the Archean Superior Province in Quebec and Ontario (i.e. over half of exploration expenditures), the Cordillera (British Columbia and Yukon) and emerging districts in Nunavut (Natural Resources Canada, Canadian Mineral Exploration Information Bulletin, 2019).

Many gaps remain in our knowledge of gold mineral systems, including the source(s) of gold, transportation mechanisms, and final concentration processes (source-to-ore framework) result in significant limitations to developing improved exploration and genetic models. National databases that map the overall distribution of deposits, even within historical Canadian gold districts, are outdated and are missing some significant new discoveries. The objective of the Gold Project, as defined in 2015, was to improve our understanding of the mechanisms that control or influence the heterogeneous distribution of gold resources through space and time, to study fundamental aspects of ore genesis and optimize exploration models by improving our knowledge of their predictive features (Mercier-Langevin et al., 2017). The Gold Project took a multi-scale (craton/orogen to ore zone), multi-disciplinary, and collaborative approach to tackle these gaps in our understanding of ore-forming processes.

Two complementary research themes defined the Gold Project: 1) system controls on gold through space and time (source, concentrating mechanisms, and depositional controls); and 2) tectonic influences on gold (tectonic drivers and conduits). These two subprojects are complementary and comprised a series of thematic and/or regional to site-specific activities (Fig. 3) in many of the gold-bearing Canadian geological provinces (Fig. 4). Importantly, most components of the Gold Project were field-based with scientists and students carrying out significant field work and data acquisition in areas of interest across Canada.

Subproject G-1: System Controls on Gold through Space and Time (Source to Ore)

The formation and localization of major gold deposits and districts are linked to the secular evolution of the Earth through time, including the periods of continen-

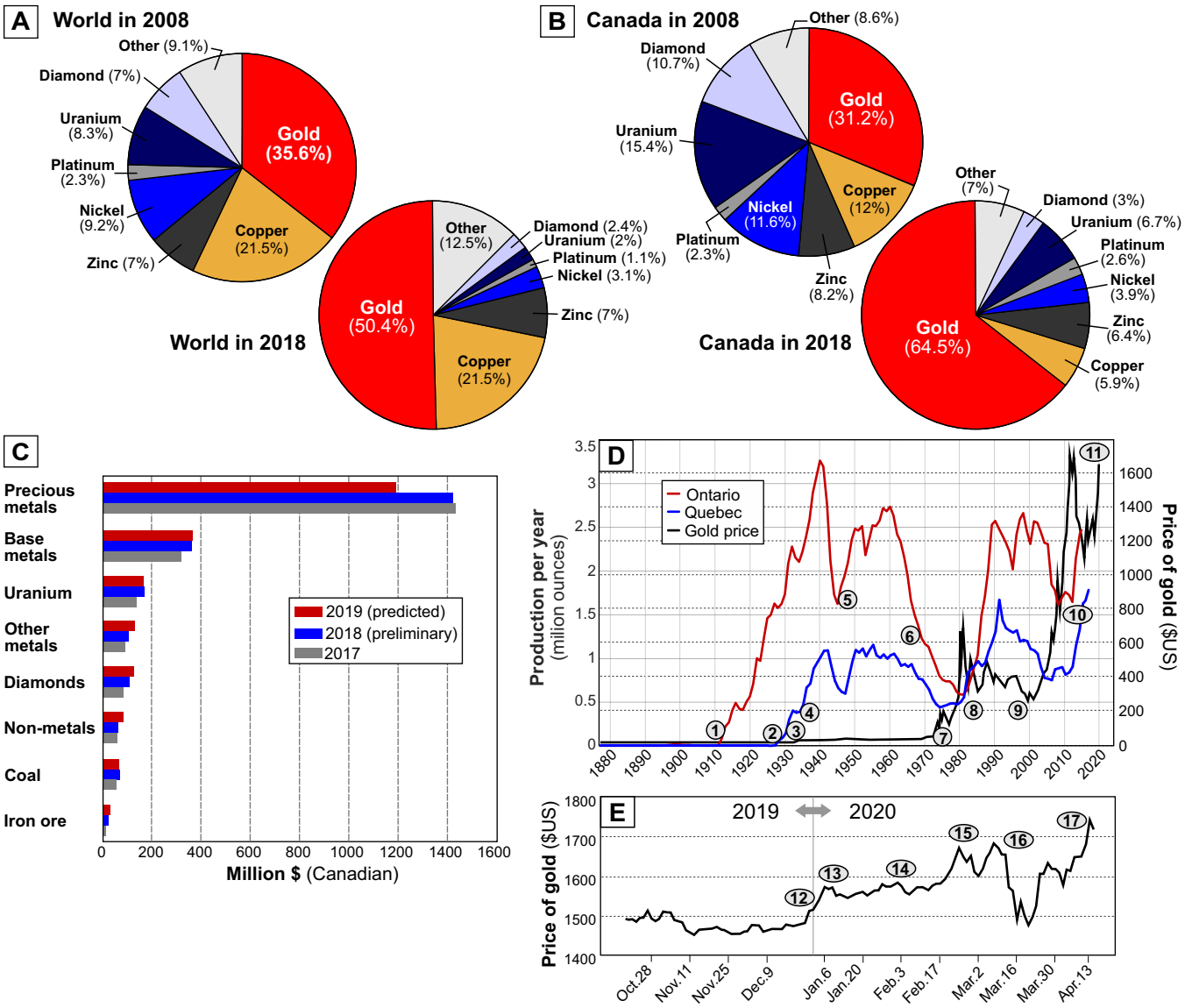

Figure 2. a, b) Global (a) and in Canada (b) exploration expenditures in 2008 and 2018. *From* Prospectors and Developers Association of Canada, State of Mineral Finance 2019: At the Crossroads online report. **c)** Exploration and deposit appraisal expenditures in Canada by mineral commodity for the years 2017 to 2019. Data for 2018 are preliminary, whereas data for 2019 are predicted. Precious metals, which includes gold, maintains a sizeable lead over all other commodity groups throughout the entire period. From Natural Resources Canada, Canadian mineral exploration information bulletin 2019. **d)** Historical gold production in Quebec and Ontario and gold price evolution from 1877 to 2017, *from* Dubé and Mercier-Langevin (2019, 2020). Numbers refer to specific events: 1 = onset of production from large gold deposits in Ontario (Dome, Hollinger, and McIntyre mines; onset of major gold production in Canada coincides with the major decline of gold production in the United States in the first few decades of the twentieth century (Lindgren, 1933)); 2 = onset of production from large gold deposits in Quebec (Horne mine); 3 = gold price raised from US$ 20.74 to US$ 35 per troy ounce by the Roosevelt administration in 1934 following the passage of the Gold Reserve Act; 4 = Sigma and Lamaque mine enters production in Quebec; 5 = World War II; 6 = closure of several major gold-producing mines (e.g. Hollinger, Wright-Hargreaves, Teck-Hughes, and Horne); 7 = price of gold decoupled from the United States dollar under President Nixon's administration; 8 = Large gold producers enter production (e.g. Hemlo, Doyon, and Bousquet mines); 9 = Bre-X scandal; 10 = large tonnage open pit mining starts at the Canadian Malartic and Detour Lake mines; 11 = surge in gold price due to geopolitical risks and economic uncertainty. **e)** Variations in the price of gold between October 2019 and April 2020 due to the coronavirus disease 2019 (COVID-19) pandemic: 12 = China's authorities report cases of a severe pneumonia in Wuhan; 13 = Word Health Organization (WHO) announces identification of a new coronavirus with the first deaths reported in China and the first cases reported outside of China in mid-January. WHO declares global public health emergency on March 30th, 2020; 14 = first deaths due to the new virus outside of China, WHO names new coronavirus COVID-19; 15 = global stock market volatility and major plunge on February 24, 2020 due to heightened coronavirus fears, first major measures (lockdowns and travel bans); 16 = WHO confirms COVID-19 as a pandemic, lockdowns and quarantines become global, stock markets plunge causing trading to be halted on a few occasions, massive gold reserves are liquidated to raise cash, and supply chains are disrupted; 17 = Rise in the price of gold in response to continued stock markets instability.

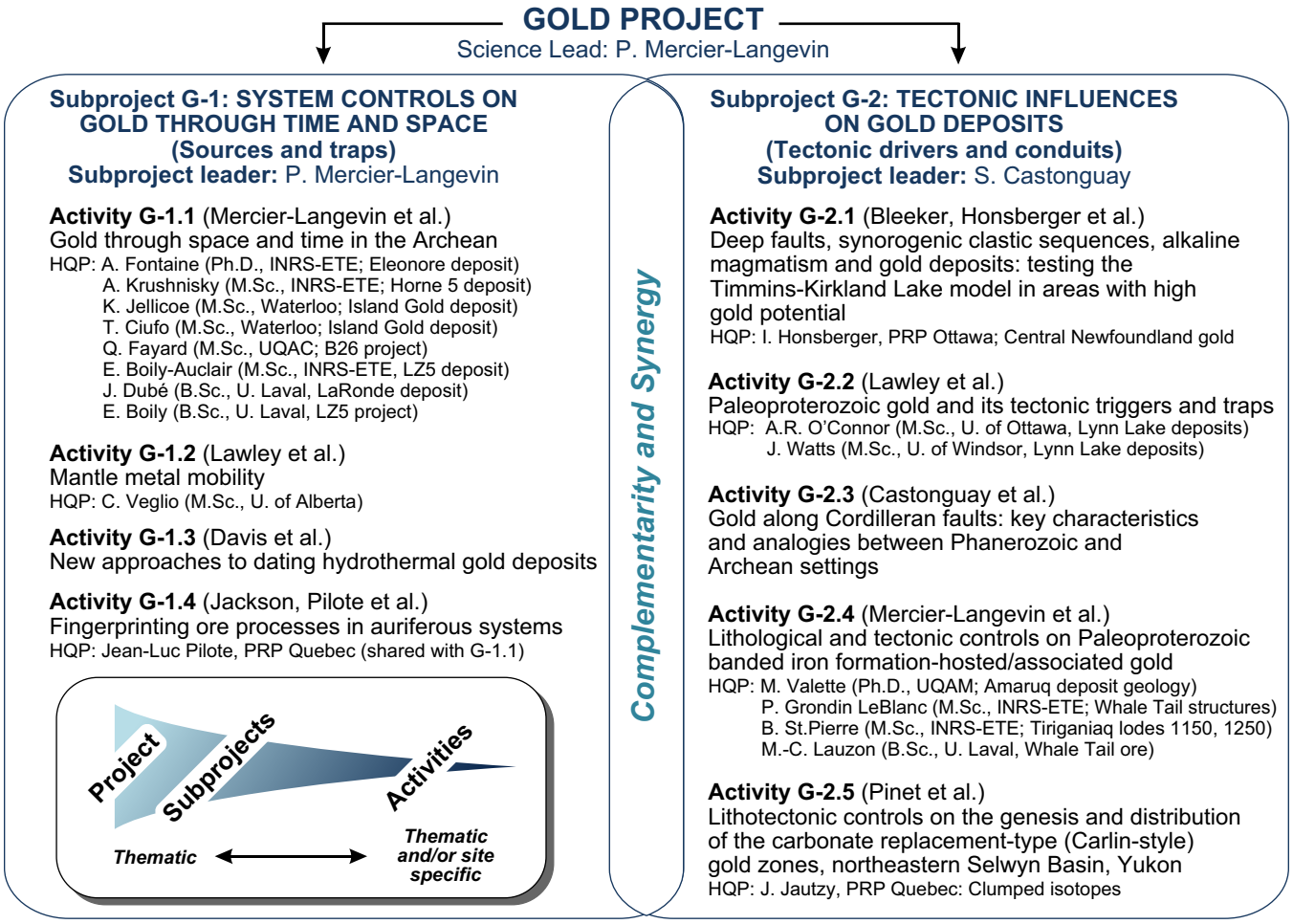

Figure 3. Schematic diagram showing the structure of the Gold Project with its two subprojects and nine activities. *See* Figure 4 for a map of the location of the pojects. *Modified from* Mercier-Langevin et al. (2017). Abbreviations: HQP = highly qualified personnel, PRP = postdoctoral research program.

tal amalgamation and breakup that occur during supercontinent cycles (Barley and Groves, 1992). Archean cratons, particularly Neoarchean parts, are amongst the best gold-endowed regions of the world. Numerous world-class orogenic gold deposits were formed during that era, in addition to several major gold deposits of other types, with some containing polyphase mineralization (e.g. Dubé et al., 2015, and references therein). The precise reasons for such a major "temporal" peak in gold endowment are still not completely understood. Among the proposed controls of gold deposition in the Neoarchean are fertile upper mantle to lower crustal source(s), enriched upper crustal units and peak felsic crust formation, onset of plate tectonics, terrane collisions, the presence of large-scale fault systems that were able to channel large-scale fluid flow and repeated tapping of the same enriched source regions, and/or particularly efficient depositional mechanisms (e.g. Barley and Groves, 1992; Sillitoe, 2008; Dubé et al., 2015, and references therein).

Activities comprising this subproject aimed at defining controls of ore formation by examining the following: 1) the characterization of unusual, important, and/or newly discovered mineralization styles, with the goal to contribute new information that will be critical for finding new deposits, or extensions of known orebodies, and that will continuously improve exploration models at various scales; 2) the review of the geological characteristics of gold mineralization at multiple scales in well endowed regions and/or areas that represent exceptional opportunities to study processes relevant to gold deposit genesis, such as in emerging districts and "poorly endowed" terranes; and 3) the synthesis of the available data/knowledge on established and emerging districts to provide basic but critical information on the geological setting and evolution of the most prolific periods/areas for gold mineralization. Many of these research activities emphasized district- to deposit-scale features because they represent key exploration vectors for the mineral industry. Subproject G-1 comprised four activities (Fig. 3) and numerous subactivities, the main results of which are summarized in Boily-Auclair et al. (2020), Boudreau et al. (2020), Castonguay et al. (2020a), Ciufo et al. (2020), Fayard

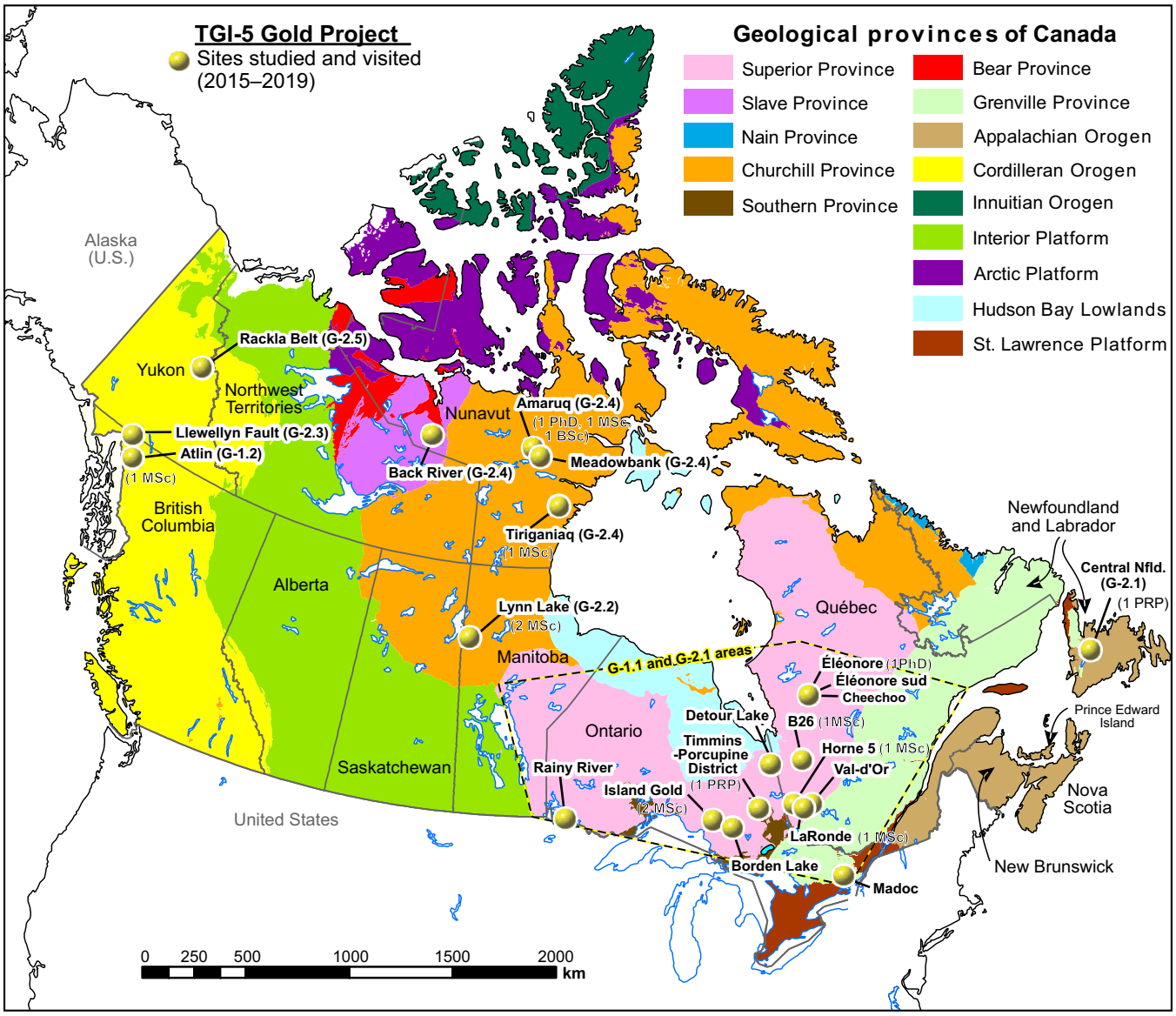

Figure 4. Location map of the principal study sites of the Gold Project (2015–2019). Geology *modified from* Wheeler et al. (1996). *See* Figure 3 for an explanation of the individual gold projects (G-x.x) and the theses. Abbreviation: PRP = postdoctoral research program.

et al. (2020a,b), Krushnisky et al. (2020), Lawley and Kjarsgaard (2020), and Pilote et al. (2020b,c).

Subproject G-2: Tectonic Influences on Gold (Tectonic Drivers and Conduits)

The incomplete understanding of the major fault zones, terrane boundaries, and tectonometamorphic discontinuities in the best endowed regions or metallogenic provinces of Canada hinders efficient regional- to district-scale mineral deposit targeting. Several ore-associated, long-lived structures have been studied in detail, but many still need to be investigated to better establish their extent, kinematic history, and critical role(s) in the formation (and preservation) of gold ore systems. Subproject G-2 focused on the known tectonic controls on gold transport, deposition, and preservation, including an analysis of the nature and evolution of major ore-associated structures in selected gold districts. Many of the research activities of this subproject were based on the results of previous phases of TGI projects. For example, previous research in the Abitibi greenstone belt defined the apparent predictable relationships between deep-reaching (first-order or lithospheric-scale) faults characterized by a synorogenic phase of extensional faulting, preserved panels of clastic sequences, (alkaline) magmatism, and orogenic gold deposits (Bleeker, 2015). New research conducted as part of TGI-5 tested whether these relationships also occur in other gold districts of different ages and variable metal endowment (e.g. Trans-Hudson, Appalachians, Cordillera, etc.). Some key auriferous faults and/or terrane boundaries were specif-

ically targeted by documenting their evolution and significance in the genesis and preservation of gold deposits. Several of these research activities included a significant geochronology component to refine the geological and temporal evolution of each gold district. Subproject G-2 comprised five activities (Fig. 3) and a number of subactivities, which are summarized in Castonguay et al. (2020b), Honsberger et al. (2020a,b), Lauzon et al. (2020), Lawley et al. (2020c), Pinet et al. (2020a,b), St.Pierre et al. (2020), and Valette et al. (2020).

The Gold Project Synthesis Volume

The Open File format

This synthesis volume is published as a GSC Open File report comprising external peer-reviewed and professional copy-edited contributions. The rationale behind using this format was to make the results of the project available to our stakeholders in a timely manner without compromising scientific rigour.

Short- versus long-term outputs and outcomes

Phase 5 of the Targeted Geoscience Initiative ended March 31st, 2020, and the contributions contained in this synthesis volume represent the state of knowledge at the end of 2019. This knowledge had to be summarized in very concise individual reports, which forced authors to limit discussion to key aspects of their research and prevented them from incorporating large data sets and extensive analyses and interpretations. Many of the activities and subactivities described below will be completed after the program has ended and after this synthesis volume is published. Additional reports, scientific papers, data releases, theses, and presentations will stem from the Gold Project.

Throughout the evolution of the project, new results, data, and information from most of the activities have been made available to the public through numerous scientific publications and presentations. Over 170 publications (e.g. peer-reviewed scientific papers, GSC current research and open file reports, theses, etc.) have been published; the reader will find a detailed list of these contributions in the appendices. Participants of the Gold Project have also presented over 200 oral and poster presentations at national and international venues between 2015 and March 2020, a reflection of the commitment of the scientists to disseminate their results in a timely manner.

Selected Research Highlights from the Gold Project Synthesis Volume

System controls on gold through space and time (Subproject G-1)

The study by Krushnisky et al. (2020) of the Horne 5 volcanogenic massive sulphide (VMS) deposit (Rouyn-Noranda, Quebec) shows that the gold is synvolcanic and hosted in some of the oldest volcanic rocks of the Blake River Group, which are predominantly intermediate to felsic in composition and transitional to calc-alkaline in affinity. The Blake River Group is the youngest of the seven volcanic-dominated assemblages of the Abitibi greenstone belt and hosts the largest and best gold-rich VMS deposits of the belt. The Horne system (~15 Moz or 467 t Au), which is found in association with calc-alkaline volcanism, represents a key example of a large synvolcanic gold system formed late in the volcanic construction of the Abitibi greenstone belt.

The Horne deposit host sequence is truncated by the Andesite fault, south of which occur sulphide clast-bearing felsic volcaniclastic units that share similarities with the Horne stratigraphy. However, Boudreau et al. (2020) demonstrate that sulphide clasts in the felsic volcanic units south of the Andesite fault are devoid of metals, which is unlike the Horne West zone and Horne 5 deposit. The presence of barren sulphide clasts south of the fault nevertheless provides further evidence of early (ca. 2701 Ma) hydrothermal activity on the seafloor in different areas during the construction of the Blake River Group.

The association between synvolcanic gold and transitional to calc-alkaline intermediate to felsic rocks has been demonstrated in the Doyon-Bousquet-LaRonde mining camp (e.g. Mercier-Langevin et al., 2007a,b). Boily-Auclair et al. (2020) reinforce this relationship by showing that the LZ5 ore zones (LaRonde Zone 5 deposit, Quebec) are directly associated, in both time and space, with the onset of transitional to calc-alkaline magmatism. The LZ5 ore zones were previously considered to occur lower in the volcanic stratigraphy and were therefore considered to be slightly older than the prospective calc-alkaline felsic rocks.

Pilote et al. (2020c) have studied pyrite nodules hosted in argillite lenses located in the main massive sulphide lens of the LaRonde Penna gold-rich VMS deposit in Quebec. Pyrite textures and geochemistry suggest that the nodules are diagenetic and that their Sn-Cu-Zn-Pb-Bi budget primarily reflects the composition of the host argillite. Trace metals in the argillite are interpreted to come from the exhalative and/or alteration product of the VMS-forming fluids. This implies that interflow argillite with pyrite nodules enriched in the above elements may be good markers of fertile volcanic centres and serve as vectors pointing towards VMS mineralization.

Fayard et al. (2020a,b) describe a ca. 2728 Ma calc-alkaline magmatic centre located in the northwestern Abitibi belt in Quebec, which hosts the B26 precious metal-rich VMS system. They compare the B26 deposit Ag-rich mineralization to the neighbouring

Selbaie mine, which has previously been interpreted as an Archean epithermal system. Geological, geochemical, and mineralogical similarities between both deposits suggest that B26 may have been formed at shallow depths. This setting may have played a role in the geometry, precious metal distribution, and Ag content at B26.

The southern Abitibi greenstone belt is well known as the best endowed part of the Superior Province (e.g. Dubé and Mercier-Langevin, 2019, 2020, in press). However, except for a few major deposits, portions of the northern Abitibi greenstone belt and the Wawa segment of the Abitibi-Wawa Subprovince contain less gold. The factors controlling this variable gold endowment within otherwise similar geological settings remains a knowledge gap in our understanding of the Abitibi belt metallogeny (cf. Robert et al., 2005). Castonguay et al. (2020a) report new results from the Sunday Lake and Lower Detour deformation zones and their associated orogenic gold deposits and showings in the northwestern Abitibi greenstone belt. These regional-scale auriferous deformation zones are spatially associated with bands of polymict conglomerate and intermediate to felsic, typically sub-alkaline to alkaline dykes and small plutons that likely represent polyphase deep-reaching structures. Similarly, Ciufo et al. (2020) describe the Island Gold orogenic deposit in the Michipicoten greenstone belt (Wawa segment, Abitibi-Wawa Subprovince) to be predominantly hosted in intermediate volcanic rocks and associated with the Goudreau Lake deformation zone, which has been interpreted by Leclair et al. (1993) as the extension of the Larder Lake-Cadillac fault west of the Kapuskasing structure. Results show similar controls on the formation and location of the gold-bearing veins and relative timing between host-rock formation, deformation, metamorphism, and ore-forming hydrothermal activity to those of orogenic gold deposits of the southern Abitibi greenstone belt. Comparing and contrasting the geological settings of these lesser known gold deposits with the better studied Destor-Porcupine and Larder Lake-Cadillac deformation zones and gold deposits of the southern Abitibi belt provide new insights into the geological evolution and variable metal endowment across the southern Superior Province.

Determining the ultimate sources of the ore components represents one of the other fundamental knowledge gaps in understanding gold ore systems. The scale of the gold-bearing structures (100s of km), coupled with isotopic tracer studies that point to long transport distances, tend to suggest that some ore components were sourced from the lower crust and/or upper mantle (e.g. McInnes et al., 1999; Sillitoe, 2008; Tassara et al., 2017). Lawley and Kjarsgaard (2020) tested the possibility of gold-enrichment processes in the upper mantle by analyzing upper mantle rocks directly (ophiolites and mantle xenoliths and xenocrysts; British Columbia, Yukon, Ontario, and Nunavut). Their results suggest that previously melt-depleted mantle domains that reacted with upwelling asthenospheric melts are enriched in gold. Re-melting of these pre-enriched domains (i.e. re-fertilized domains of the previously melt-depleted lithospheric mantle) represent one of the possible source regions for melts and/or hydrothermal fluids that transported ore components to orogenic gold deposits in the mid to upper crust.

Sedimentary rocks in the upper crust have also been considered as a potential source of metals through the liberation of gold from diagenetic pyrite (including pyrite nodule-bearing argillite) during high-grade metamorphism (e.g. Kribek, 1991; Large et al., 2009). Pilote et al. (2020b) thoroughly document the textural and geochemical nature of argillite-hosted pyrite and discuss the origin of these distinctive nodules using the Timmins-Porcupine district (Ontario) as a study case. Research results highlight the ability of pyrite nodules to sequester highly anomalous levels of gold, which appears to be controlled by the provenance of the host sedimentary rocks.

Tectonic influences on gold (Subproject G-2)

Notwithstanding the uncertain source(s) of gold, the tectonic drivers and favourable pathways for gold-bearing fluids are well known to exhibit important controls on the genesis of orogenic gold deposits (e.g. Robert et al., 2005; Dubé and Gosselin, 2007; Bleeker, 2015). Documenting the multi-phase history of large-scale, gold-bearing structures is another important contribution of the Gold Project. Honsberger et al. (2020a,b) demonstrate that Paleozoic orogenic gold mineralization in the footwall of the Victoria Lake shear zone (central Newfoundland) is related to approximately 20 to 30 million years of tectonism that spanned Late Silurian and Early Devonian. This phase of tectonism (ca. 430–405 Ma) involved extension-related synorogenic bimodal magmatism followed by crustal-scale thrust imbrication, regional metamorphism, and vein-hosted gold mineralization in the upper crust. The sequence and temporal pacing of events in central Newfoundland appear to be similar to those of the southern Abitibi belt. Lawley et al. (2020c), in their study of the Lynn Lake belt in northern Manitoba, indicate a similar context and timeframe for the formation of orogenic gold deposits within the Paleoproterozoic Trans-Hudson Orogen, with an early gold event associated with the shift from accretionary to collisional tectonics.

Although the broad evolution of some major crustal-scale deformation zones can be similar in different oro-

gens, the metallogenesis can vary in detail and through geological time. The study of the Llewellyn-Tally Ho deformation corridor in the Cordillera (British Columbia and Yukon) by Castonguay et al. (2020b) documents an example of superimposed, polyphase gold mineralization events. There, early gold associated with Late Cretaceous ductile deformation and plutonism is overprinted by early Eocene, dextral, transpressive, brittle faulting and volcanism associated with low-sulphidation epithermal gold. Except for Neoproterozoic high-sulphidation-type mineralization at Hope Brook in central Newfoundland (Dubé et al., 1995), which is older than the orogenic gold deposits studied by Honsberger et al. (2020a,b), late-stage and shallow epithermal-style gold mineralization is notably absent in the other gold districts studied as part of the Gold Project. This may reflect a distinct metallogenic evolution for certain Cordilleran fault zones or some unique preservation control (e.g. shallower erosion?).

St.Pierre et al. (2020) document the structural controls of the 1150 and 1250 "lodes", or ore zones, at the Tiriganiaq gold deposit in the Meliadine district (Nunavut). The 1150 and 1250 lodes are controlled by protracted folding and shearing of the host sedimentary succession in the hanging wall of the Lower Fault, a subsidiary reverse fault of the district-scale Pyke fault. At the Tiriganiaq deposit, moderately north-dipping, late D_2 shears host mineralized quartz and carbonate veins, and are locally associated with bonanza-grade, shallowly south-dipping extension veins that are preferentially developed in tightly folded, metres-thick banded iron formation units. In contrast, the main ore zone (1000 lode), which is also associated with D_2 deformation along the Lower Fault, consists of a large (up to 5 metres thick), continuous laminated shear vein that is predominantly hosted in siltstone. This shows that ore zone geometry and grade distribution can vary significantly within one ore system depending on the local conditions.

The Amaruq deposit, located about 50 kilometres north of the Meadowbank mine in the Kivalliq region of Nunavut, consists of replacement- and vein-style gold hosted in Archean chert, argillite, silicate-facies iron formation and to a lesser extent in mafic-ultramafic volcanic rocks and greywacke (Valette et al., 2020). The deposit was deformed and metamorphosed during the Trans-Hudson orogenesis at approximately 1.85 Ga. New field observations, textural evidence, and preliminary Re-Os and $^{40}Ar/^{39}Ar$ ages suggest that an early stage of veining may pre-date Trans-Hudsonian peak metamorphism and is potentially much older than 1.85 Ga (Lauzon et al., 2020). These new results agree with the complex and multi-phase metallogenic history proposed by recent work elsewhere in the region (Lawley et al., 2015).

Pinet et al. (2020a,b) review the regional to nanoscale characteristics of the Rackla belt Carlin-type gold zones in the Selwyn Basin (Yukon) and show that the mineralized zones exhibit the main characteristics of sediment-hosted micron-gold Carlin-type deposits of Nevada. Several early deformation events led to the development of favourable traps (structural ground preparation). These structures control the location of mineralized zones at the regional scale (juxtaposition of two crustal blocks), prospect scale (generation of complexly shaped fold-fault traps), and mineralized-zone to sample scale (formation of several fracture and vein sets). Sedimentary processes also influenced the development of favourable traps. The primary sediment properties (e.g. silty layers and impermeable barriers, reactive carbonates) and post-depositional processes (e.g. slope facies and sedimentary breccia) helped create and preserve porosity and permeability. New results further suggest that the gold mineralizing event in the eastern Rackla belt is associated with minor (in terms of bulk strain) reactivation of early structures and is significantly younger than the main intrusion-related gold mineralizing events in the Selwyn Basin.

Updated Compilation of Gold Deposits of the Superior Province

Based on the premise that gold is a major economic target for many exploration and mining companies in Canada, the GSC developed, with the help of sponsors from industry, the World Minerals Geoscience Database Project (WMGDP: 1998–2004). The aim of this joint initiative was to produce geoscience data sets to be used in conjunction with GIS (Geographic Information Systems) and database software to help understand the broad relationships between global tectonics and the regional geological settings of mineral deposits. This endeavour led to the Canadian Gold Database (Gosselin and Dubé, 2005b, 2015), which collated lode gold deposit information from all of Canada's geological provinces.

The Canadian Gold Database was updated to include the location, metal content (reported data from industry at the end of 2018), and relevant geological information for new and previously reported gold deposits (≥100,000 oz or 3.2 metric t Au, including production, reserves, and measured and indicated resources) in the Superior Province. The revised database (Bécu et al., in progress, 2020) will be released separately, following the publication of this synthesis volume.

The revised database comprises 181 entries. Deposits with 1 Moz (31.1 t) gold or less represent 61% of those deposits (110/181; Fig. 5a). Seventy-one deposits contain more than 1 Moz gold, with more than half of these containing less than 3 Moz (93.3 t gold).

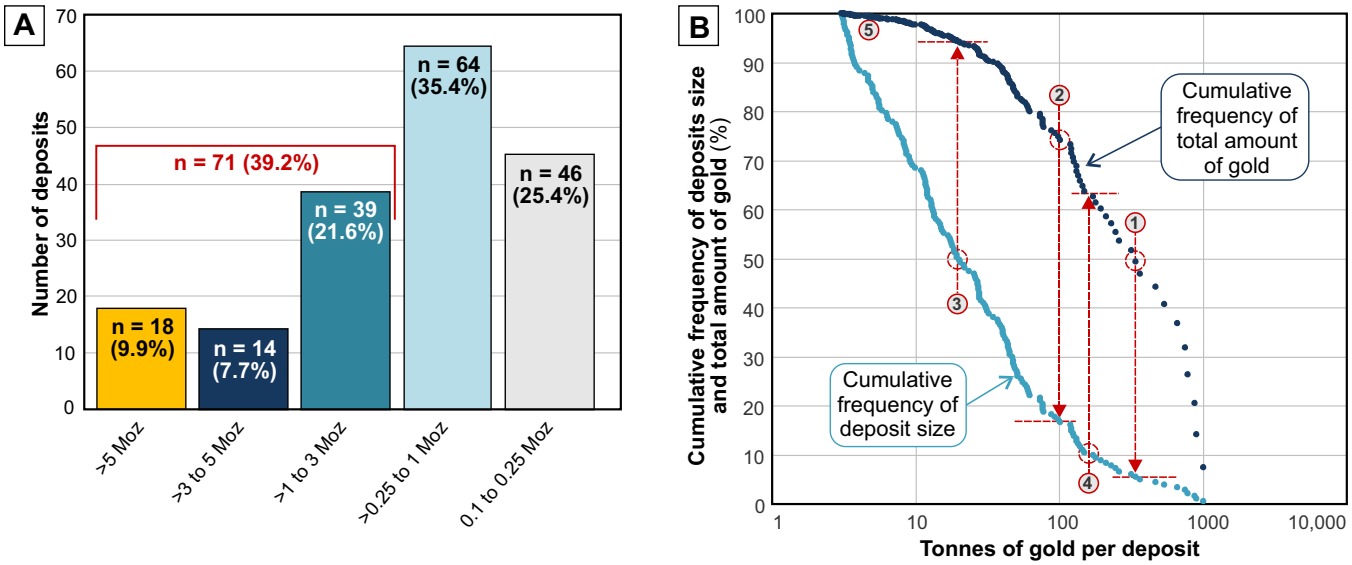

Figure 5. Gold deposits (≥100,000 ounces, or 3.1 metric t Au) of the Superior Province. The data includes production, reserves, and resources (measured and indicated). Inferred resources are excluded. **a)** The number of deposits versus the deposit size (n = 181). Only 10% of the deposits (18/181) contain 5 million ounces (Moz), or 155.5 t, of gold or more. Seventy-one deposits contain 1 Moz (31.1 t) gold or more, which amounts to about two-fifths of the total number of gold deposits in the Superior Province with over 0.1 Moz gold. **b)** Plot of the cumulative frequency of deposit size (light blue) and the total contained gold (dark blue) among gold deposits of the Superior Province. 1 = the 10 largest deposits, which account for 5.5% of the total number of deposits, which contain almost 50% of the total gold; 2 = deposits with 100 t (3.2 Moz) gold or more and account for approximately 75% of the total gold; 3 = 50% of the deposits included in the database that have less than 20 t (0.64 Moz) gold and account for only about 6% of the total gold; 4 = the top 10% of the deposits in terms of size, which each have 171 t (5.5 Moz) gold or more and account for approximately 63% of the total gold, indicating that a large proportion of the gold in the Superior Province is contained in only a few deposits; 5 = flattening of the cumulative gold tonnage curve despite a large number of deposits with less than 10 t gold (0.32 Moz), indicating that the use of a ≥0.10 Moz (3.1 t) gold cut-off in our compilation allows for a representative image of gold distribution across the Superior Province.

Thirty-two world-class deposits (i.e. with >3 Moz Au) are present in the Superior Province (32/181; Fig. 5a). These world-class deposits, however, account for over 75% of the total gold of the Superior Province (Fig. 5b). Figure 5b shows that the 10 largest deposits of the Superior Province, accounting for 5.5% of the total number of deposits, contain almost 50% of the total gold. The top 10% of the deposits in terms of size, which each have 171 t (5.5 Moz) of gold or more, account for approximately 63% of the total gold. Interestingly, although the largest deposits are dominantly orogenic, five of the 18 deposits with more than 5 Moz (155.5 t) of gold can be classified as intrusion-associated (n = 2), and synvolcanic (n = 3: Table 1), indicating some diversity in the types of very large deposits. At district scale, orogenic gold also dominates, but two of the 10 largest gold districts of the Superior Province consist predominantly of synvolcanic gold (Table 2). Approximately half of the deposits included in the database have less than 20 t (0.64 Moz) of gold and account for only about 6% of the total gold. These data indicate that a large proportion of the gold in the Superior Province is contained in just a few deposits. Similar figures have been previously reported (e.g. Hodgson and MacGeehan, 1982) and our data further highlight the importance of world-class deposits to global gold production, emphasizing that ore system research should focus on identifying the geological settings that are most prospective for giant to world-class deposits. Almost 80% of the gold of the Superior Province is in the Abitibi-Wawa terrane, with a significant proportion of these deposits in the Abitibi belt (Fig. 6). Smaller deposits are also more abundant in the Abitibi greenstone belt than in the rest of the Superior Province (Fig. 6). Since 2005, 49 new entries were added to the Superior Province gold database (Fig. 7). These additional entries consist of five past producers, nine past producers with significant new reserves and/or resources (e.g. Akasaba, Buffalo), and 35 new discoveries or recently discovered deposits that were put into production since 2005, or for which significant gold ounces were added since 2005 (Fig. 7, 8). Despite increased exploration in greenfield areas, more than 60% of the new (2005–2018) entries, and almost 70% of the associated gold, are from the Abitibi greenstone belt (Fig. 8, 9), specifically along the Destor-Porcupine and Cadillac-Larder Lake fault zones in well established districts (e.g. Timmins West in Timmins, and Westwood in the Doyon-Bousquet-LaRonde camp). Emerging areas that were previously considered less prospective (e.g. Kapuskasing structural zone: Borden mine, and the Swayze greenstone

Table 1. Gold deposits of the Superior Province containing more than 5 Moz (155.5 t) of gold.

Deposit[2]	Terrane	Location	Main deposit type	Total gold (production, reserves, and measured and indicated resources)[1] Tonnage (Mt)[3]	Au grade (g/t)	Au (metric t)	Au (Moz)	Rank
Hollinger-McIntyre-Coniaurum	Abitibi	Ontario	Orogenic	120.3	8.43	1,013.6	32.6	1
Kirkland Lake (Main camp)	Abitibi	Ontario	Orogenic	63.5	14.25	904.7	29.1	2
Red Lake[4]	Uchi	Ontario	Orogenic	53.0	16.60	879.8	28.3	3
Hemlo	Wawa	Ontario	Orogenic	176.9	4.49	794.1	25.5	4
Detour Lake	Abitibi	Ontario	Orogenic	738.2	1.03	759.6	24.4	5
Dome	Abitibi	Ontario	Orogenic	276.4	2.40	664.5	21.4	6
Canadian Malartic[5]	Abitibi	Quebec	Orogenic	361.7	1.45	523.1	16.8	7
Horne	Abitibi	Quebec	Synvolcanic	144.9	3.22	466.6	15.0	8
Kerr Addison	Abitibi	Ontario	Orogenic	40.3	8.42	339.1	10.9	9
Sigma-Lamaque-Triangle	Abitibi	Quebec	Orogenic	61.0	5.54	337.6	10.8	10
Côté Gold	Abitibi	Ontario	Intrusion-associated	326.2	0.95	310.1	10.0	11
LaRonde Penna	Abitibi	Quebec	Synvolcanic	64.6	3.85	248.6	8.0	12
Musselwhite	North Caribou	Ontario	Orogenic (BIF-hosted)	40.9	5.87	239.6	7.7	13
Pamour	Abitibi	Ontario	Orogenic	120.5	1.90	229.2	7.4	14
Rainy River	Wabigoon	Ontario	Synvolcanic	200.7	1.02	205.0	6.6	15
Young-Davidson	Abitibi	Ontario	Orogenic	73.5	2.65	194.5	6.3	16
Casa Berardi	Abitibi	Quebec	Orogenic	46.8	3.69	172.6	5.6	17
Doyon	Abitibi	Quebec	Intrusion-associated	32.6	5.26	171.7	5.5	18

Notes: [1]inferred resources are not included; [2]In many cases, deposits consist of more than one mine; [3]Million tonnes (metric); [4]Includes Red Lake, Campbell, New Dickinson, and Young mines. [5] Includes Canadian Malartic, Barnat, Sladen, and East Malartic mines. Abbreviation: BIF = banded iron formation.

Table 2. Gold deposits of the Superior Province containing more than 25 Moz (755.5 t) of gold.

Camp	Subprovince	Location	Main deposit type	Total gold (production, reserves, and measured and indicated resources) Tonnage (Mt)	Au grade (g/t)	Au (metric t)	Au (Moz)	Rank
Timmins	Abitibi	Ontario	Orogenic	649.8	4.03	2619.5	84.2	1
Val d'Or-Malartic	Abitibi	Quebec	Orogenic	620.3	2.40	1487.8	47.8	2
Kirkland Lake-Larder Lake	Abitibi	Ontario	Orogenic	132.6	10.49	1391.9	44.8	3
Red Lake	Uchi	Ontario	Orogenic	145.6	8.18	1190.0	38.3	4
Hemlo	Wawa	Ontario	Orogenic	189.3	4.26	806.3	25.9	5
Bousquet (DBL)-Cadillac	Abitibi	Quebec	Synvolcanic and orogenic	158.3	4.99	790.1	25.4	6
Noranda	Abitibi	Quebec	Synvolcanic and orogenic	237.7	3.31	787.7	25.3	7
Detour	Abitibi	Ontario	Orogenic	741.1	1.05	776.2	25.0	8

Abbreviation: DBL = Doyon-Bousquet-LaRonde camp.

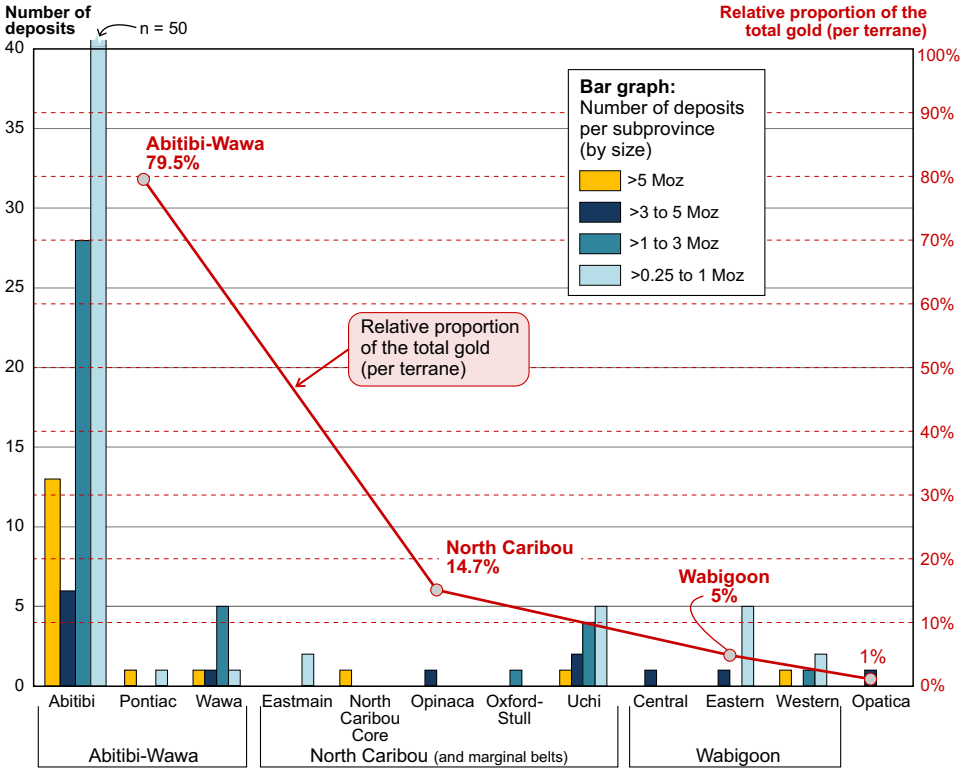

Figure 6. Distribution of gold deposits within individual terranes of the Superior Province based upon their total gold content. From a total of 181 deposits, 135 contain more than 0.25 million ounces (Moz), or 7.8 metric t of gold (total production, reserves, and measured and indicated resources). Almost four out of five deposits in the Superior Province with more than 0.25 Moz (7.8 t) of gold are in the Abitibi-Wawa Subprovince (79.3%: 107/135). The Abitibi greenstone belt is especially well endowed, with a total of 98 deposits (72.6%: 98/135), the Uchi terrane ranks second, with a total of 12 deposits with more than 0.25 Moz (7.8 t) gold. The Canadian Malartic deposit is included in the Pontiac in this diagram, but a significant part of the ore is hosted in the Piché Group of the Abitibi belt.

belt: Coté Gold deposit) clearly indicate significant potential outside of the well established districts. In recent years, there has also been a renewed interest in the western Superior Province. This follows the commercial production at the Island Gold (Wawa) and Rainy River (western Wabigoon) mines and the delineation of considerable resources at the Hammond Reef and Goliath deposits, for example (Fig. 8, 9b,c). The database also includes updated reserve and/or resource estimations for more than half of all producing and indexed deposits (n = 132).

Although the revision and updating of the compilation of gold deposits in the Superior Province is ongoing and contains the usual limitations and shortfalls associated with large compilations and classifications of complex deposits (*see* Singer, 1995, Franklin et al., 2005, and Mercier-Langevin et al., 2011), some general observations can be made. Volcanic rocks represent the dominant host lithology for almost half of the deposits (49.7%: n = 90/181; Fig. 10a), whereas intrusive and sedimentary rocks represent the dominant host for about one-third (34.3%: n = 62/181), and less than one-sixth of the cases (16.0%: n = 29/181), respectively. The favourable prospectivity of volcanic rocks is further highlighted by their total gold content. Volcanic rocks are the main (but not necessarily the only) host lithology for deposits totalling 240.6 million ounces (7485 t), which represents approximately 55% of the total contained gold in the Superior Province (Fig. 10b). Such a figure is expected considering that orogenic gold is preferentially found in greenstone belts

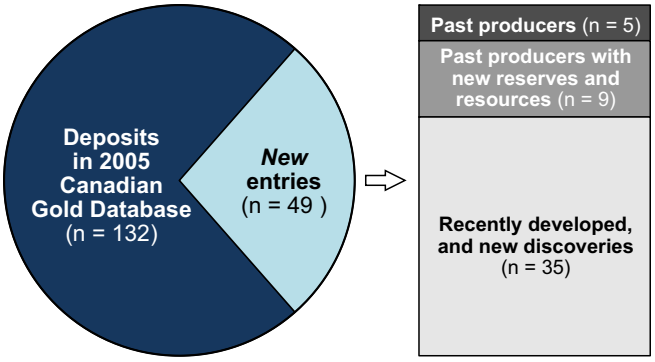

Figure 7. Compilation of 181 gold deposits of the Superior Province with ≥0.1 Moz (3.1 metric t) gold (total production, reserves, and measured and indicated resources), including the 49 new entries since the GSC's previous compilation in 2005 (Canadian Gold Database: *see* Gosselin and Dubé, 2005a,b). These 49 new entries consist of 5 past producers that were not included in the 2005 gold database (mainly from the Chibougamau area; e.g. Cedar Bay, Portage-Henderson); 9 past producers with significant new reserves and/or resources (e.g. Akasaba, Buffalo); and 35 deposits that were recently discovered and put into production since 2005, deposits for which significant gold ounces were added since 2005, and new discoveries that were made after 2005 (e.g. Lapa, Borden, Rainy River, and Windfall Lake).

(Fig. 8). A similar observation can be made in other Archean cratons (e.g. western Churchill Province: Lawley et al., 2015; Mercier-Langevin et al., 2018). Of note, our compilation includes gold-rich VMS deposits that are hosted in volcanic rocks. Volcanic rocks with mafic to intermediate bulk compositions (74 deposits and 191.5 Moz, or 5960 t Au; Fig. 10b) are the most

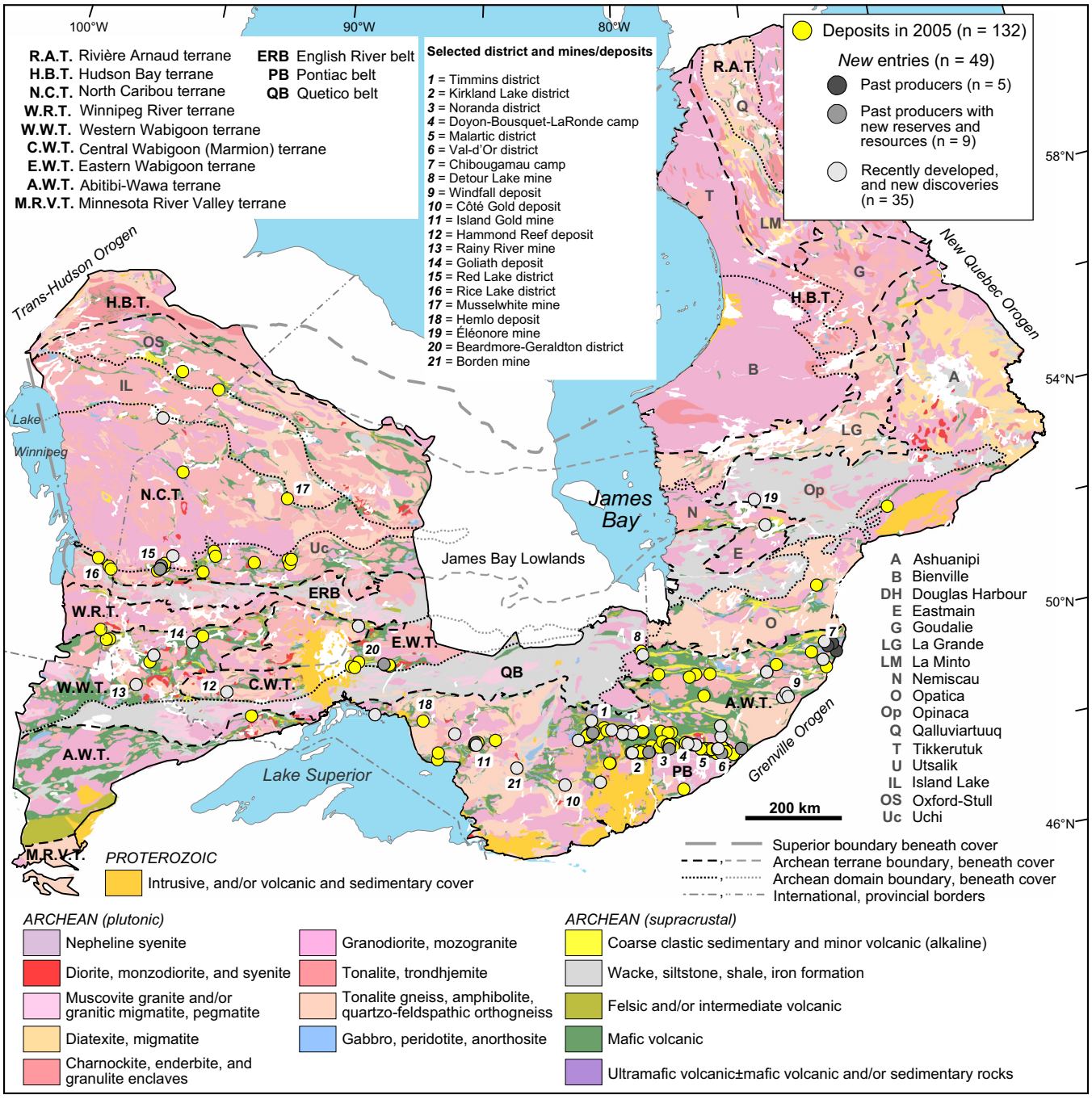

Figure 8. Bedrock geology compilation of the Superior Province (*from* Percival et al., 2012) showing the location of the gold deposits with ≥100,000 ounces. Yellow dots are the deposits that were included in Gosselin and Dubé (2005b, 2015) compilation. Grey dots are the 49 new entries (dark grey = past producers that were not included in the 2005 gold database; medium grey = past producers with significant new reserves and/or resources; pale grey = recently discovered deposits that were put into production since 2005, or for which significant gold ounces were added since 2005, and new discoveries made after 2005) (*see* Fig. 7 for details about the new entries).

prospective, in agreement with previously reported data (e.g. Hodgson and MacGeehan, 1982; Robert et al., 2005; Dubé and Gosselin, 2007). Intrusive and sedimentary rocks are associated with 113.6 million ounces (3533 t: 26% of the total gold) and 84.8 million ounces (2638 t: 19% of the total gold), respectively (Fig. 10b). The importance of volcanic rock-dominated, and to some extent sedimentary rock-dominated successions as the main hosts to gold becomes even greater when data are "normalized" relative to rock-type abundance, using the surficial area as a proxy. The best gold-bearing terranes all have a greater ratio of volcanic and sedimentary rocks to intrusive (and gneiss) rocks than the entire Superior Province (Fig. 10c). The Abitibi-Wawa terrane is the best endowed in terms of total gold and total number of deposits (Fig.

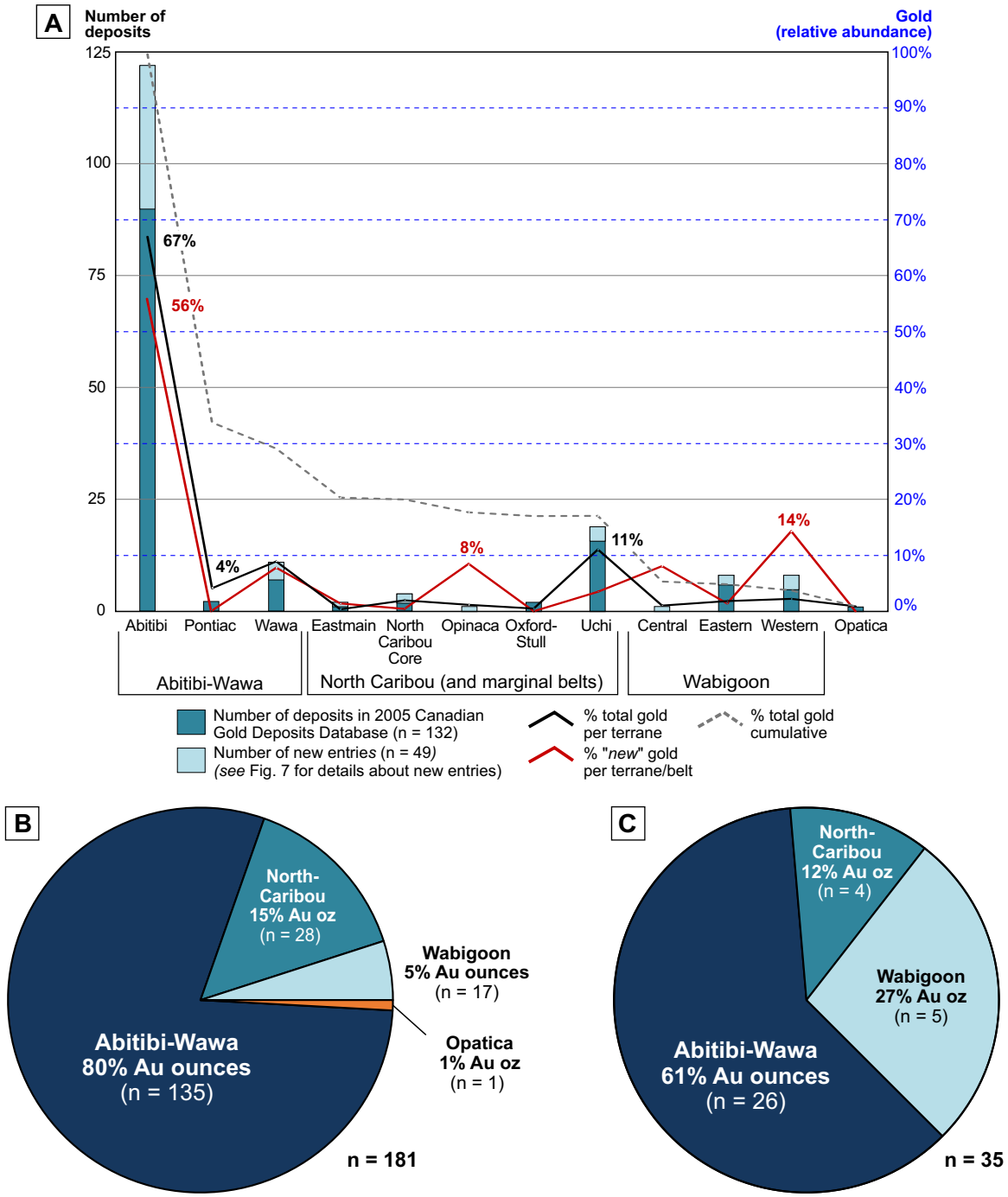

Figure 9. Location and gold content of the deposits of the Superior Province. **a)** Total number and total gold proportion per terrane for deposits with ≥0.1 million ounces (3.1 metric t) gold (n = 132; production, reserves, and measured and indicated resources) that were included in the Canadian Gold Database in 2005 (*see* Gosselin and Dubé, 2005b), which have since been revised and updated, and for new entries made in this compilation (n = 49 new entries, *see* Fig. 7). **b)** Total gold content and deposits per subprovince (n = 181). **c)** Total gold content and deposits per subprovince for the new entries (post-2005: n = 49).

8), but it is also recognized as the best preserved and largest Archean greenstone belt in the world. It contains approximately 50 kilograms of gold per square kilometre, which is six times more than the western part of the Wabigoon Subprovince and 10 times more than the North Caribou terrane that is largely dominated by intrusive and gneissic rocks (Fig. 8, 10c). Again, it must be noted that this analysis is preliminary and does not take into consideration that most gold deposits are not hosted in more than one lithology. Further work is under way to properly scale gold endowment against rock type and gold endowment versus regional tectonostratigraphic units. For example, many of the orogenic gold deposits in the Abitibi greenstone belt are spatially associated with panels of synorogenic conglomerate, which represent only a

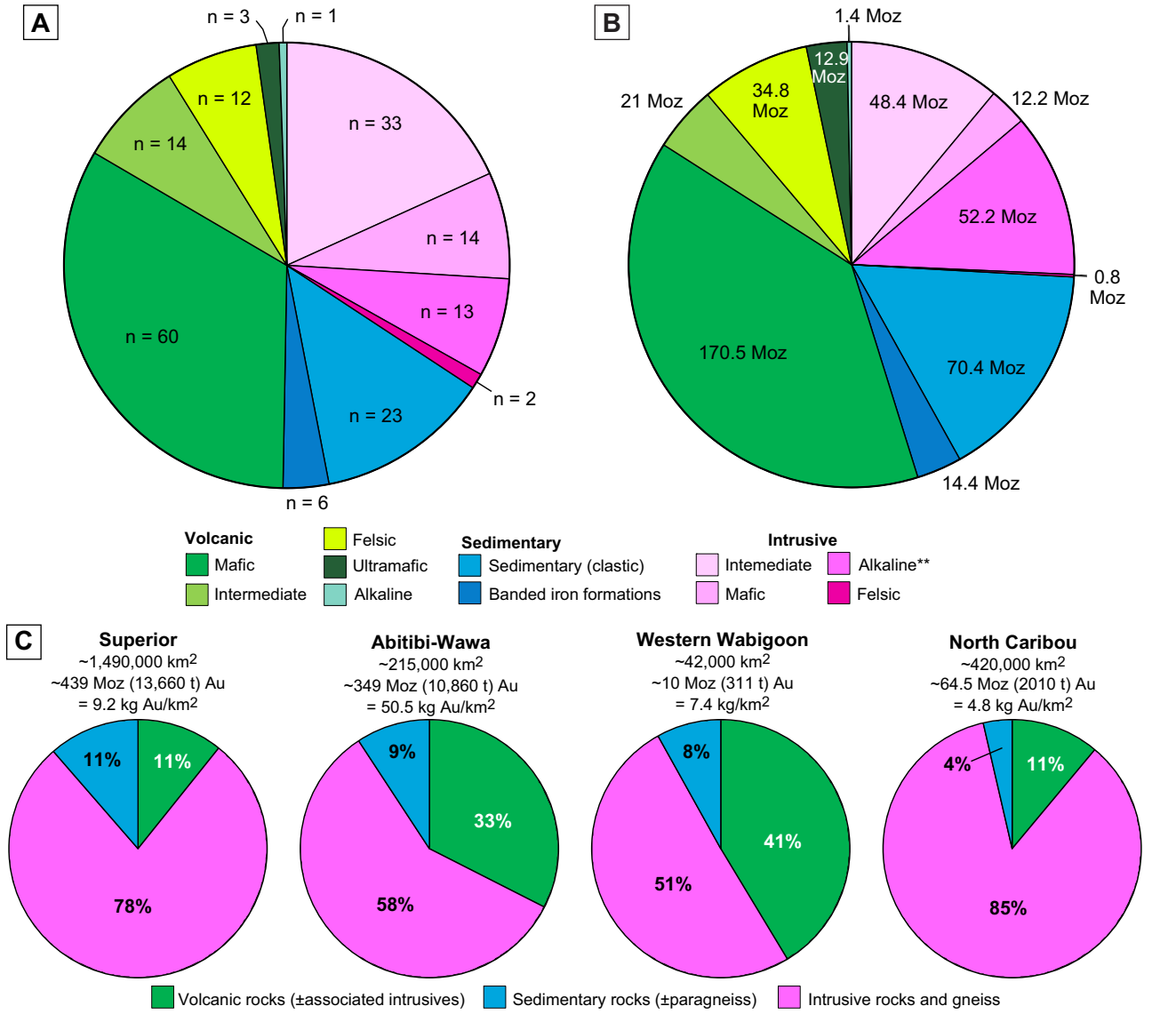

Figure 10. a) Total number of gold deposits in the Superior Province with ≥0.1 million ounces (3.1 metric t) gold (n = 181) versus the dominant host lithology. **b)** Total gold content is in million ounces (Moz) versus the deposit's dominant host lithology. The data in (a) and(b) include production, reserves, and resources (measured and indicated). Inferred resources are not included. **this also includes intrusive rocks that are subalkaline but which are often associated with the alkaline intrusive rocks (*see* Dubé and Mercier-Langevin, in press, for details about these intrusive rocks). **c)** Relative proportion of volcanic, sedimentary, and intrusive rock types in the Superior Province, Abitibi-Wawa terrane, Western Wabigoon Subprovince, and North Caribou terrane. Total surface estimated from the map of Wheeler et al. (1996). Values given here represent estimates and include only the Canadian part of the Superior Province. Gold "endowment" can be roughly estimated from these data, showing that the Abitibi-Wawa terrane favourably compares to other mineralized parts of the Superior Province. Except for the Western Wabigoon, volcanic and sedimentary rocks are not as abundant (based on surface exposure) as intrusive rocks but tend to be more commonly the main host lithologies for gold deposits.

minor proportion of all rock types in the belt. Similarly, Algoma-type banded iron formation generally represent a minor component of Archean sedimentary successions but appear to be associated with a significant number of large gold deposits.

The revised database of known deposits and the newly discovered deposits exemplify the broad range of auriferous ore styles and highlight the previously underestimated potential of certain areas of the Superior Province (Dubé et al., 2015). The updates to the gold database will provide key information about the distribution and gold content of known deposits and will be complemented, in specific cases, by recent geological knowledge. The classification of ore styles through common geological and genetic characteristics of individual deposits is on-going. The overall end-product will provide a useful framework for thematic studies investigating potential source(s), conduits, and processes at the depositional sites for gold mineralization in the Superior Province.

ADVANCING CANADIAN GOLD MINERAL SYSTEM MODELS

Context

Gold deposits are the final product of multiple processes that pre- to post-date the main stage(s) of ore formation and operate across a range of spatial scales (Fig. 1). Many aspects of the complete pathways from source to ore of these systems remain unanswered despite decades of research (*see* Boyle, 1988). For the Gold Project, the framing question was, what are the essential controls on the formation of gold mineralization? Or more specifically, by what cause and how did the most favourable conditions develop at specific times and locations? A large proportion of TGI-5 research activities focused on orogenic gold mineralization. However, several studies identified multiple overprinting styles of gold mineralization, even within a single deposit. The multi-phase character of gold deposits and districts that were identified as part of TGI-5 present a challenge for the ore system approach because the processes and critical time window for ore formation may vary during each evolutionary stage of an ore system (Fig. 1). As a result, a single deposit may represent the final product of multiple passes through the critical ore-forming window at different times (Fig. 1). Progress on these key questions and other gold ore system knowledge gaps that were addressed as part of TGI-5 are described below.

Sources and Transport Mechanisms

Two important questions remain largely unanswered for most gold ores systems: 1) what is/are the source(s); and 2) what are the different extraction and transport mechanisms. Some initial forms of gold enrichment, either at or below the seafloor have been clarified in the last few decades through the study of fossil and modern seafloor VMS deposits (e.g. Hannington et al., 1999; Huston et al., 2000; Dubé et al., 2007a). Modern examples have been particularly important because they demonstrated that gold-enrichment processes are clearly synvolcanic and therefore unequivocally not related to overprinting metamorphism and deformation during ocean basin closure. Results from past phases of TGI suggested that similar processes were also responsible for the precious metal endowment of some ancient gold-rich VMS deposits (e.g. LaRonde Penna: Dubé et al., 2007b; Mercier-Langevin et al., 2007a,b; Bousquet 2-Dumagami: Dubé et al., 2014; Lemoine: Mercier-Langevin et al., 2014b; Westwood: Yergeau et al., 2015; Lalor: Caté et al., 2015).

Multiple interpretations to explain synvolcanic gold enrichment at these early or syngenetic deposits have been proposed (e.g. inherently enriched source and fluids, direct magmatic input, efficient transport and capture, boiling, zone refining, etc.: Hannington et al., 1999; Huston, 2000; Dubé et al., 2007a; Mercier-Langevin et al., 2015; Gartman et al., 2018). As part of TGI-4 and -5, an empirical association has been established between Archean synvolcanic gold deposits (including many of the world's best examples of gold-rich VMS deposits) and transitional to calc-alkaline felsic magmatic centres (e.g. Mercier-Langevin et al., 2011, 2015). The temporal and spatial relationships between ore-forming fluids and shifting volcanic rock compositions (i.e. from tholeiitic, mid-ocean ridge basalt (MORB) to enriched mid-ocean ridge basalt (E-MORB) style to crustal-contaminated, mid-crustal calc-alkaline magmatism) suggest that the gold content of a VMS deposit might be related to, at least in part, underlying igneous petrogenetic processes. Krushnisky et al. (2020) added to the list of major gold-rich VMS deposits associated with transitional to calc-alkaline volcanic rocks by showing that the giant Horne and Horne 5 deposits are hosted in rocks of similar composition. Boily-Auclair et al. (2020) provide further evidence for a possible link between the magmatic evolution of Archean volcanic centres and the formation of synvolcanic gold deposits by showing that the onset of the gold-rich hydrothermal activity in the central part of the Doyon-Bousquet-LaRonde mining camp coincided with a transition from tholeiitic to transitional to calc-alkaline magmatism. This association between igneous petrogenesis and metal endowment may also be true for other precious metals such as silver, as indicated by the work of Fayard et al. (2020a,b) at the B26 project in the Brouillan calc-alkaline volcanic centre in the northern Abitibi belt. Ongoing work on the Archean synvolcanic gold deposits of the southern Superior Province (e.g. zircon geochronology and geochemistry) will help to improve our understanding of the potential genetic relationships between igneous petrogenesis and synvolcanic gold, at least in Archean settings.

Sedimentary rocks and their associated diagenetic sulphides represent another form of early gold enrichment in the upper crust. Pyrite nodules in carbonaceous to non-carbonaceous argillite units intercalated with volcanic flows of the Abitibi greenstone belt (e.g. Kidd-Munro, Tisdale, and Blake River assemblages) and deep basin-related settings (e.g. Porcupine) yield gold concentrations that range from a few ppb to 10s of ppm (Pilote et al., 2019a,c, 2020b,c). New TGI-5 research demonstrates that these gold-rich pyrite domains are genetically related to early pyrite crystallization rather than gold-upgrading during later hydrothermal and/or metamorphic overprinting. The factors controlling syn-sedimentary and/or diagenetic gold enrichment remains equivocal, but preliminary results suggest that sediment provenance (source)

could be one of the primary factors (Pilote et al., 2019a,b). The metal signature and budget of pyrite nodules, at least for those formed in interflow argillite, also appear to be controlled by syn-sedimentary enrichment from "distal" VMS vents. Pyrite nodules at the LaRonde VMS deposit (Blake River assemblage) provide such evidence, with a primary VMS-style trace metal enrichment (e.g. Au, Zn, Sn), which was likely inherited from the host sediments that were initially enriched in trace metals due to nearby synvolcanic hydrothermal activity (Pilote et al., 2020c).

The preliminary results and on-going TGI-5 research cited above demonstrate that parts of the greenstone belts that host orogenic gold deposits were pre-enriched in ore components. The large time gap between initial gold enrichment and the main phase of orogenic gold is one of the complicating factors that obscures the ultimate source of ore components for most orogenic gold districts and deposits. Orogenic gold deposits postdate their host rocks by 10s to 100s of millions of years, which indicates that the drivers of initial synvolcanic and/or syn-sedimentary gold-enrichment processes are unrelated (i.e. different geological setting) to late-stage orogenic gold systems.

The conventional view on the formation of orogenic gold deposits is that they are genetically related to metamorphic fluids that liberate gold from local volcanic and/or sedimentary rocks during the transition from greenschist- to amphibolite-facies metamorphism (e.g. Card et al., 1989; Colvine, 1989; Craw and Koons, 1989; Hagemann and Cassidy, 2000; Ridley and Diamond, 2000; Goldfarb et al., 2005; Goldfarb and Groves, 2015; Pitcairn et al., 2017, 2019). A growing number of studies further suggest that sedimentary sulphides and pyritic argillite act as one of the possible pre-enriched source rocks for gold and sulphur during metamorphism (e.g. Chang et al., 2008; Large et al., 2011; Tomkins, 2013; Steadman et al., 2015; Gregory et al., 2016; Selvaraja et al., 2017). If correct, the sedimentary source model would predict that the metal endowment of orogenic gold deposits is dependent, at least in part, on the distribution of these favourable sedimentary source rocks. Pilote et al. (2020a) address this question using field mapping, trace element chemistry, and multiple isotope tracers of sedimentary (e.g. nodules), ore vein-associated, and non ore-related metamorphic pyrite from the Timmins-Porcupine district. Complete isotope results are pending; however, preliminary results from triple sulphur isotopes indicate that ore vein-associated pyrite at the Bell Creek, Bradshaw, and Pamour orogenic gold deposits have non-zero mass independent fractionation values (negative and positive). These preliminary results suggest that atmospheric-derived sulphur (sequestered in sediments as S_8 or SO_2) was incorporated into the mineralizing fluids in addition to any possible magmatic input. Moreover, the restricted range of isotope compositions (in both $\delta^{34}S$ and $\Delta^{33}S$) from the ore vein-associated pyrite plots in the centre of the much broader isotopic signature field defined by pyrite nodules (negative $\delta^{34}S$ and $\Delta^{33}S$ array). In contrast, non ore-related metamorphic pyrite defines a broad positive $\delta^{34}S$ and $\Delta^{33}S$ array that is unlike the sedimentary or ore vein-associated pyrite types, and more akin to the "Archean reference array" (e.g. Thomassot et al., 2015). The restricted range of measured values in ore vein-associated pyrite and their overlap with the field defined by the pyrite nodules could be explained by mixing between the ore-forming fluid and the sedimentary rock S-isotope values at depth (cf. LaFlamme et al., 2018). If correct, this would imply that diagenetic (sedimentary) pyrite is likely to have contributed ligands (sulphur) to the ore-forming fluid through metamorphic recrystallization of sulphides at depth in the crust. This work and complementary isotopic analyses (e.g. Pb and Fe isotopes) will shed further light on the potential role of (or absence thereof) sedimentary pyrite in the genesis of orogenic gold deposits.

The southern Abitibi greenstone belt contains numerous orogenic and synvolcanic gold deposits, suggesting some sort of genetic relationship between these ore systems. If correct, this would provide a possible explanation for the exceptional prospectivity of this specific area (e.g. Hutchinson, 1993). For example, the corridor defined by the Larder Lake-Cadillac and Destor-Porcupine fault zones, often referred to as the southern Abitibi gold belt, hosts approximately 85% of the orogenic gold of the whole belt and also about 90% of the synvolcanic gold (e.g. Mercier-Langevin et al., 2014a; Dubé and Mercier-Langevin, in press). The spatial relationship between both ore systems has previously been used as evidence to suggest that gold in orogenic deposits was locally sourced (i.e. from pre-existing synvolcanic deposits) (e.g. Hutchinson, 1993). However, this is incompatible with the fact that synvolcanic gold deposits are gold-rich and that most mass balance estimates for sulphur and gold within pre-enriched volcanic rocks, where available (e.g. Detour deposit: Dubosq et al., 2018), typically conclude that an external source is required for some of the gold. Giant gold deposits also occur in the absence of significant synvolcanic/syngenetic gold deposits (e.g. Red Lake district, Ontario: MacGeehan and Hodgson, 1982; Pirie, 1982; and Homestake, Black Hills, South Dakota: Paterson et al., 1990), which casts additional doubt over the role of older synvolcanic deposits on the total metal endowment of orogenic gold districts. Even if the early synvolcanic mineralization or the pre-enriched volcanic rocks were the ultimate source of gold in later metamorphic fluids, it still would not

explain the exceptional endowment and provinciality of synvolcanic gold in the southern Abitibi belt and its preservation during later orogenesis.

Debate over gold transport mechanisms also contributes to uncertainty over the ultimate source of ore components in these systems. The conventional view is that metamorphic fluids that are released during the transition from greenschist- to amphibolite-facies metamorphism are the primary transport mechanism for gold (e.g. Hodgson and Hamilton, 1989; Hodgson, 1993; Goldfarb et al., 2005; Dubé and Gosselin, 2007; Phillips and Powell, 2009). This inference is fully consistent with the pressure and temperature conditions of most auriferous veins and the trace element and isotopic compositions of their fluid inclusions (Bodnar et al., 2014; Prokofiev et al., 2019). Bulk-rock gold concentrations that decrease systematically with increasing metamorphic grade provide additional support for gold mobility during metamorphism (Pitcairn et al., 2017). However, some gold deposits that are metamorphosed to mid-amphibolite facies, including examples from the Paleoproterozoic Lynn Lake greenstone belt (Lawley et al., 2020c), preserve auriferous veins that predate peak metamorphism. These early-stage veins suggest that syn-peak amphibolite-facies metamorphic fluids are, at least in some cases, ineffective at transporting gold from their original depositional site. The apparent limited mobility of gold during metamorphism is further evidenced by minor, small-scale (millimetre to metre scale) remobilization of gold in several Abitibi deposits metamorphosed up to upper greenschist facies (e.g. Horne 5: Krushnisky et al., 2020; B26: Fayard et al., 2020b; LZ5: Boily-Auclair et al., 2020; LaRonde Penna and Timmins auriferous pyrite nodules: Pilote et al., 2020b,c). Similarly, research on gold deposits in Nunavut further suggests that although metamorphic fluids and/or synmetamorphic polymetallic melts (Bi-Te-Au-Ag) may remobilize and/or upgrade gold from pre-peak metamorphic veins into high-grade and late-stage ore shoots (e.g. Lawley et al., 2017), precious metals do not appear to be transported over long distances during the greenschist- to amphibolite-facies transition (e.g. Janvier et al., 2015; Lawley et al., 2015; Mercier-Langevin et al., 2018; Lauzon et al., 2020; Valette et al., 2020). The rare examples of larger scale metamorphic remobilization (e.g. 10s of metres at the Lalor VMS deposit, Snow Lake: Caté et al., 2015; Caté, 2016; Lam, 2019) indicate that gold transport is limited to short distances during metamorphism, even at amphibolite grade in highly favourable conditions (e.g. H_2O and CO_2-rich rocks and gold- and trace metal-rich sulphides at the Lalor mine). Similar features were documented at the former Montauban mine in the Grenville Province (Jourdain et al., 1987; Tomkins, 2007). The Roberto deposit (Éléonore mine) has also been overprinted by upper greenschist-facies metamorphism and except for evidence of recrystallization, changes in the mineralogy, and local remobilization, gold does not appear to have been mobilized on a large scale (Fontaine et al., 2017; Fontaine, 2019). The Borden deposit is hosted in upper amphibolite- to granulite-facies rocks exposed along the Kapuskasing structural zone in Ontario. The deposit, located west of Timmins, is associated with a panel of Timiskaming-age metaconglomerate dated at ≤2667 ± 2 Ma (Krogh, 1993). Gold at the Borden mine is interpreted to have been introduced late during granulite- to amphibolite-facies retrogression and associated deformation based on its spatial association with late overprinting structures that are developed at the contact between preserved lenses of competent granulite-facies rocks and softer amphibolite-facies rocks after 2629 Ma (Lafontaine, 2016; Bouvier et al., 2017). Interestingly, Hf isotopes from Borden indicate that the protolith of the ore-associated biotite-garnet gneiss, host to recrystallized and deformed laminated auriferous veins, is probably a hydrothermally altered mafic rocks (Bouvier et al., 2017). This, combined with the presence of Timiskaming-age conglomerate and pelite in the host sequence, along the interpreted eastern extension of the Larder Lake-Cadillac fault zone (Leclair et al., 1993), may suggest that gold was present, at least in part, prior to peak metamorphism and has been locally remobilized during granulite-facies metamorphism and retrogression to amphibolite facies (Dubé and Mercier-Langevin, in press). This scenario, although in disagreement with the currently interpreted timing of gold introduction at Borden (*see* Bouvier et al., 2017), suggests that even at granulite facies, gold may not be remobilized over major distances. These examples of strongly metamorphosed gold deposits indicate that specific conditions, specific timing of events, or a combination of both are necessary to mobilize gold on a large-scale during metamorphism.

Magmatic fluids represent an alternate gold transport mechanism that is known to play an important role in some gold ore systems, including synvolcanic gold deposits in the southern Abitibi greenstone belt described above. The role of magmatic fluids in the genesis of orogenic gold deposits is less certain. New TGI-5 research highlights important differences between the timing of magmatic activity and the formation of most orogenic gold deposits (Castonguay et al., 2020a,b; Honsberger et al., 2020b; Lawley et al., 2020c; Pinet et al., 2020b; Dubé and Mercier-Langevin, in press). In fact, the timing of peak gold deposition in most accretionary settings is concomitant with a distinct lull in magmatic activity after the cessation of subduction (Bierlein and Crowe, 2000; Kerrich et al., 2000). Intrusive bodies that are interpreted to be

coeval with gold deposition tend to be smaller plutons, plugs, and/or dykes (e.g. Burrows and Spooner, 1989; Perring et al., 1989) that represent relatively minor parts of the gold deposits' host succession. They are unlikely to represent a major contributor to the total endowment of entire gold districts, but rather are a manifestation of larger magmatic systems at depth and part of important thermal/metamorphic perturbations (e.g. Fyon et al., 1989; Cameron, 1993; Bleeker, 2015). The evolution in the geochemical composition of pre-, syn-, and post-orogenic magmatism is thus likely an important proxy for the drivers and overall tectonic setting of orogenic gold deposits (Fyon et al., 1989; Kerrich et al., 2000). The tectonic evolution of the host successions is otherwise difficult to determine from the older host greenstone belts alone, and a subject of debate in itself (e.g. subduction versus subcretion tectonics in the Archean: Percival et al., 2012; Polat et al., 2015; Bédard, 2018). The isotopic signature and trace element composition of the alkalic rocks found in proximity to gold deposits suggest that the alkalic magma interacted with previously modified lithospheric mantle during ascent, which likely occurred during a phase of crustal extension. A similar setting is proposed for younger gold districts such as the Deseado Massif, an epithermal gold district in southern Argentina, where enriched domains of the upper mantle and/or lower crust are interpreted to have been a reservoir of gold that was tapped at different times throughout the tectonic evolution of the region (Tassara et al., 2017, 2018). New TGI-5 results demonstrate that some of these modified lithospheric mantle domains are up to 10x enriched in gold and other ore components relative to the primitive mantle (i.e. the expected composition of the mantle prior to crust extraction) and the continental crust (Lawley and Kjarsgaard, 2020 and references therein). The contribution of these pre-enriched lithospheric mantle domains to ascending alkalic melts is not fully understood, although oxidation of the ascending alkalic melts through interaction and surrounding mantle appears to enhance melt fertility by helping scavenge gold from previously modified areas of the sub-continental lithospheric mantle (Lawley et al., 2020a; Tassara et al., 2020). The degree of enrichment (10x continental crust) of those mantle domains is however modest relative to the exceptional gold grades observed at almost all orogenic gold deposits (1000x continental crust), suggesting that multiple gold concentrating mechanisms are likely involved during transport and/or deposition.

Drivers, Conduits, and Traps

The common occurrence of alkalic rocks, sanukitoids, and lamprophyres along major deformation zones that host orogenic gold deposits points to a specific orogenic stage that is critical in the development of auriferous systems (Dubé and Mercier-Langevin, in press, and references therein). Upwelling asthenosphere and interaction with lithospheric mantle is the most likely driver of alkalic magmatism, and the switch from crustal shortening to extension is likely responsible for transferring deep-seated melts and fluids into the mid- to upper-crust (e.g. Hodgson and Hamilton, 1989; Cameron, 1993; Robert et al., 2005; Bleeker, 2015). This extensional phase postdates the initial assembly and deformation of the host greenstone belts but predates the peak of crustal thickening, which, in some cases, ultimately led to late-stage crustal-derived melts (e.g. pegmatite and peralkaline granite). Upwelling asthenosphere is also likely important for transferring heat to the overlying crust, driving auriferous fluids along crustal-scale faults (e.g. Fyon et al., 1989; Perring et al., 1989), and may also provide a possible mechanism for the high-temperature and low-pressure metamorphism that is typically related to gold ore systems (e.g. Bleeker, 2015).

TGI-5 research has provided new multidisciplinary, field-based observations and data sets, including high-precision geochronology to better define the geological and metallogenic settings and sequencing of events in other prospective belts such as the central Newfoundland Appalachians, the northern Abitibi greenstone belt, and parts of the Canadian Cordillera. Gold in these study areas is related, at least spatially, to long-lived faults or deformation zones with a polyphase kinematic evolution.

In Newfoundland, Paleozoic gold mineralization and fluid-pressure cycling with associated devolatilization were coincident with crustal-scale re-imbrication and thickening between ca. 415 and 405 Ma, which occurred subsequent to a phase of extension-related synorogenic bimodal magmatism between ca. 430 and 418 Ma (Honsberger et al., 2020b). The authors compare this evolution with that of the Archean Abitibi greenstone belt and consider both districts to have undergone a very similar history in terms of sequential key events and pacing, reinforcing the notion that crustal/lithospheric thinning, synorogenic magmatism, and structural re-imbrication are critical for generating and preserving orogenic gold systems in the footwall of crustal-scale fault zones. The timespan between the onset of extension, uplift, thrust imbrication, and the main phase of mineralization is approximately between 20 and 30 million years in the Abitibi belt and in Newfoundland, as well as in Proterozoic rocks of the Lynn Lake belt in Manitoba, and is followed by late granitic magmatism and possible late-stage mineralization that extends for a few 10s of million years (Honsberger et al, 2020a; Lawley et al., 2020c).

The development of the poorly exposed, but prospective northwestern part of the Abitibi greenstone belt is similar to the inferred evolution of its exceptionally well endowed southern part. There, major, long-lived deformation zones (Sunday Lake and Lower Detour) are spatially related to structurally controlled gold deposits, such as the giant Detour Lake gold mine (Castonguay et al., 2020a, and references therein). These deposits occur as disseminated gold, or gold-bearing veins, within highly strained mafic volcanic and intermediate to felsic, commonly alkaline, plutonic rocks. The deformation zones, which are locally delineated by bands of polimict conglomerate, juxtapose volcanic rock packages against younger sedimentary rocks, indicating a polyphase structural evolution (i.e. basin-bounding extensional faults inverted as reverse faults). Although these fault zones are steep to sub-vertical, gold mineralization mainly occurs in the apparent structural hanging walls (as opposed to footwalls in the southern Abitibi belt). The syn-thrusting geometry of these deposits was likely modified by steepening, overturning, and late-stage strike-slip faulting, which further complicated the structural setting of the mineralization.

Major fault zones represent one of the characteristic features of most gold districts, but not all auriferous faults have the same metallogenic history. The Canadian Cordillera represents another area to study the role of fault zones as conduits and traps of gold, especially in the lower metamorphic-grade (epizonal to mesozonal) parts of the orogen. The work of Castonguay et al. (2020b) and Pinet et al. (2020a,b) tackle different aspects of some of the various types of Cordilleran gold mineralization.

The Llewellyn-Tally Ho deformation corridor in northwestern British Columbia and southern Yukon is a long-lived deformation zone that is spatially associated with numerous gold deposits and prospects of various styles and ages (Castonguay et al., 2020b). As in the Abitibi belt, the Llewellyn-Tally Ho deformation zone has undergone a polyphase structural evolution, including early (Late Cretaceous and older) ductile reverse faulting that is associated with coeval plutonism and intrusion-related and shear-hosted gold mineralization. Eocene transpressional deformation subsequently reactivated parts of the deformation zone as brittle dextral strike-slip faults, which are associated with volcanic complexes and epithermal gold mineralization (Ootes et al., 2018, 2019). This setting differs from the Abitibi greenstone belt in that both the pre-metamorphic extensional faulting and the late brittle-ductile structural event are devoid of preserved epithermal-style gold mineralization, even for fault zones that demarcate conglomerate-filled synorogenic basin remnants with minor subsequent exhumation and erosion. Such first-order comparisons not only highlight similarities, but also differences (e.g. preservation control) in the structural and metallogenic evolution of these major structural corridors.

The shifting tectonic regime that is common to several ancient gold ore systems is also suggested by new TGI-5 research on younger gold mineralization of the Rackla belt (Yukon; Pinet et al., 2020a,b). These gold zones represent some of the best examples of Carlin-type, sediment-hosted micron gold mineralization outside of Nevada. Like Carlin-type deposits, gold mineralization in the Rackla belt is much younger than the Neoproterozoic to mid-Paleozoic host rocks. However, Carlin-type deposits in both Nevada and central Yukon represent the end-product of long-lived, tectonically mature systems in which the host-succession permeability and fluid focussing were locally enhanced through repeated sedimentary and tectonic processes (*see* Muntean, 2018, and references therein) that led to a favourable upper crustal architecture. In Nevada, mineralization is contemporaneous with a relatively short-lived geodynamic event that modified the thermal state and tectonic regime of the lithosphere (the "perfect storm of events" of Cline, 2018). In Yukon, only a few dykes have been documented in proximity to the gold zones, and the spatial and temporal link between mineralization and magmatism remains elusive at the district scale. Pending U-Pb age constraints on calcite from mineralized veins will address the potential association between mineralization processes and regional geological events such as magmatism and, consequently, further document the similarities and differences with the Carlin-type deposits of Nevada.

Gold Project's Contributions to Methodology Development

While understanding the complete source-to-ore pathways of auriferous fluids is the goal of the mineral system approach and is critically important for grassroots exploration, most of the mineral exploration activity occurs within established gold mining districts. The importance of near-mine exploration makes recognizing deposit-scale depositional controls from the rock record particularly important. As demonstrated by Grondin LeBlanc et al. (2017) and St.Pierre et al. (2020), these depositional controls also have the greatest influence on mine design and gold recovery. Wood (2018) wrote, "*once in operation, about 70% of mines perform below the prediction of their feasibility studies, with underperformance usually caused by deficiencies in the collection of primarily geology related data prior to designing the mine and planning its operation*", indicating that research at district- to deposit-scale is still required, especially at the early stages of exploration and mining. Such research, if timely, can

have a major impact. To address this, the TGI-5 Program not only generated the new geoscience as discussed above, but also is developing and testing new tools for the detection and delineation of ore system markers and vectors towards mineralized areas. These techniques (*see below*) have had a major impact on the research conducted as part of TGI-5 and have the potential to be further applied for mineral exploration targeting.

The Gold Project has stimulated and facilitated the development of new and improved methods for quantitative trace element mapping in the GSC's laser ablation-inductively coupled plasma-mass spectrometry (LA-ICP-MS) laboratory. Improvements in the efficiency and optimization of the mapping protocol have resulted in the acquisition of element maps at higher spatial resolution or in less time than previously produced in the laboratory. Notable examples of this improved capability include the acquisition of nearly 1,000,000 multi-element data points for pyrite nodule-bearing samples from the Timmins-Matheson gold corridor (Pilote et al., 2020b,c), resolving gold-enriched pyrite rims (<4 μm in thickness) associated with Carlin-type mineralization in the Rackla belt in Yukon (Sack et al., 2019), and mapping the distribution of suspected native gold nanoparticles within samples of metasomatized mantle lithosphere (Lawley et al., 2020a).

Furthermore, data analytics tools and open-source workflows have been developed to process LA-ICP-MS results (Lawley et al., 2020a) and expand the capability of interrogating element maps (e.g. Lawley et al., 2020c; Pilote et al., 2020b,c). Applications of these advanced data analytics tools include extracting element data from mineralogically distinct features of interest (Sack et al., 2019), quantifying elemental relationships across multiple mapping experiments (Lawley et al., 2020a; Pilote et al., 2020b,c), and semi-automating the process of feature extraction for trace metal deportment at the micron-scale (e.g. Lawley et al., 2020a).

New processing code was also written to produce the first large-area map results by hand-held laser-induced breakdown spectroscopy (LIBS). The code was used to rapidly map the spectral signature of hydrothermal alteration minerals, including gold, related to gold-bearing quartz veins. Maps were acquired directly on the sawed surface of drill core. This technology represents an emerging tool for mineral exploration vectoring when combined with conventional geochemical analyses. Because the LIBS device is handheld, the same mapping approach can also be used in the field. Machine learning tools were also applied to convert qualitative LIBS concentrations to feature-of-interest maps that can be used to quantify the distribution of mineral vectors at the microscale (Harmon et al., 2019). In a separate study, the same advanced data analytics tools were used to distinguish ore-related and metamorphic biotite based on qualitative LIBS concentrations. Rapid acquisition of mineral chemistry on smooth, but otherwise untreated rock surfaces will certainly become a key geochemical vectoring tool.

A new, nano-powder analytical method was also developed for whole-rock analyses. This innovative method is based on wet-milling whole-rock powders to a median grain size of 0.7 to 2 μm followed by direct analysis of pressed powder pellets by LA-ICP-MS. Powdered reference materials that were reprocessed following this wet-milling approach indicate that major, trace, and ultra-trace whole-rock concentrations were in excellent agreement with their accepted values for most elements. Replicate analyses of these reprocessed reference materials show that measurement repeatability is only 2x less precise than glass reference materials for some elements, which represents a significant improvement over LA-ICP-MS analysis of the original, coarser rock powders. The nano-powder method was used to investigate enrichment of ore-forming elements in the upper mantle, which is normally challenging because of their low concentrations and heterogeneous distribution within rare accessory phases (Lawley et al., 2020b). Because the wet-milling method was miniaturized, the approach is also suitable for analyzing small-volume mantle xenolith samples (Kroner, 2019). Improved trace element determination of ore-forming elements has the potential to be further applied for studying cryptic geochemical footprints in other poorly mineralized rocks.

The next scientific and technical advances in the understanding of gold systems will most probably involve obtaining better resolution on the timing of tectonic, magmatic, metamorphic, and hydrothermal events (at all scales) that lead to the formation of gold deposits. In the Rackla belt, resolving the timing of mineralization was hampered by a lack of traditionally suitable minerals to date (e.g. arsenopyrite, hydrothermal titanite, xenotime, or monazite). Instead, Pinet et al. (2020a,b) have chosen to use in situ U-Pb dating of calcite at Rackla, where mineralization is associated with abundant calcite veining. In situ LA-ICP-MS U-Pb dating of calcite is a relatively new method that holds much promise for determining the age of mineralization and associated geological events. Carefully selected samples were analyzed at different spot sizes (160 and 210 μm diameter) through several analytical sessions, with reproducible results. Notably, the results of this work have been used to establish a preliminary age for the timing of gold mineralization at Rackla. Some of the samples revealed a complex record, as

indicated by a large spread in isotope ratios. This variability has been explained by multiple generations of calcite growth, isotopic mixing, and/or partial resetting of U-Pb ratios (i.e. open system behaviour). Extracting meaningful ages from this complex data has been made possible through detailed petrographic characterization, before and after U-Pb analyses, and by carefully establishing each sample's geological setting. The following list of ideal conditions for successfully dating calcite have been identified through this work: 1) samples with distinguishable generations of calcite; 2) a closed isotopic system; and 3) calcite that inherited variable proportions of common Pb during formation (i.e. significant spread data along an isochron). Improved sample targeting, using imaging techniques such as cathodoluminescence microscopy and LA-ICP-MS element mapping, allow for the identification and targeting of a uniform growth zone in complex samples (i.e. areas with no evidence of vein re-opening, diagenetic/metamorphic overprint, or cement dissolution-reprecipitation). Current development at the GSC includes targeting calcite with smaller spot size (e.g. Petts et al., 2019), which may further reduce variations and limitations due to micro-scale heterogeneity of the targeted samples. U-Pb dating of calcite will become a valuable tool in studying ore deposits.

Calcite clumped-isotope thermometry was also applied to the Rackla belt mineralized samples (N. Pinet et al., unpub. isotopic data, 2020). This technique does not require the initial isotopic composition of the parent water to estimate the temperature of crystallization, which is a major advantage relative to classic stable isotopic studies. The technique had previously been applied to low-temperature systems and complex calibrations and protocols had to be established to obtain reliable experimental data up to 725ºC. Though clumped isotope results can be partially or fully reset at temperatures above 100ºC (i.e. via solid-state reordering), such as during diagenesis, the application of thermal history reordering models can provide insights on the extent (i.e. temperature and duration) of the re-equilibration that may have occurred after primary crystallization. This technique has excellent potential to further constrain the conditions of ore formation.

The Contribution of the Gold Project to the Training of Highly Qualified Personnel (HQP)

Training and mentoring of students and post-doctoral researchers (HQP) represents one of the core objectives of the TGI-5 program. As such, the Gold Project has directly supported three undergraduate thesis projects at Université Laval (Dubé, 2016; Boily-Auclair, 2017; Lauzon, 2017), ten M.Sc. research projects (three completed: Krushnisky, 2018 at Institut de la Recherche scientifique – Centre Eau Terre Environnement; Ciufo, 2019 and Jellicoe, 2019 at University of Western Ontario, and seven ongoing: Boily-Auclair, Grondin LeBlanc, and St.Pierre at Institut de la Recherche scientifique – Centre Eau Terre Environnement; Fayard at Université du Québec à Chicoutimi; O'Connor at University of Ottawa; Veglio at University of Alberta; and Watts at University of Windsor), and two Ph.D. research projects (Fontaine, 2019 at Institut de la Recherche scientifique – Centre Eau Terre Environnement; Valette, ongoing at Université du Québec à Montréal). Three post-doctoral fellows at the GSC in Ottawa and Québec (PRPs: J.-L. Pilote, I. Honsberger, and J. Jautzy) have been involved and were key in delivering three of the Gold Project's activities (Fig. 3). The Gold Project also supported TGI-4 Lode Gold students in completing the final stages of their M.Sc. and (Pelletier, 2016) and Ph.D. theses (Caté, 2016; Janvier, 2016; Oswald, 2018) at Institut de la Recherche scientifique – Centre Eau Terre Environnement. Numerous students and professionals were hired and trained as part-time support for many of the activities, among them are A. Abraham, E. Boily-Auclair, D. Diekrup, V. Janvier, A. Krushnsky, A. Laberge, and C. Gray.

CONCLUDING REMARKS

The stable supply of mineral commodities depends on the continued development of known resources (e.g. through optimized mining and recovery methods) and, critically, on the discovery of new mineral deposits. In the future, new mineral deposit discoveries will have to occur in established districts as well as in emerging camps and new areas, i.e., most likely in more remote, deeper, and/or buried geological settings. To address this demand, governments have invested in making pre-competitive geoscience data and improved ore-system models freely available to the public through programs like TGI-5. A subset of highlights from the TGI-5 Gold Project and its implications for advancing gold ore system models are described in this synthesis volume.

Our understanding of gold systems has evolved with time and with the exploration, discovery, and study of new or redeveloped gold deposits and districts. Our ability to establish the relative and absolute timing of events has also improved significantly. Very precise constraints are necessary to define the sequence of events that led to the formation of gold deposits. Therefore, properly establishing the key mechanisms and their interactions that ultimately resulted in forming and preserving a gold deposit depends on an in-depth understanding of the geological events and their evolution in both space and time. For example, fundamental questions such as the role of magmatism in some Archean gold deposits will only be answered

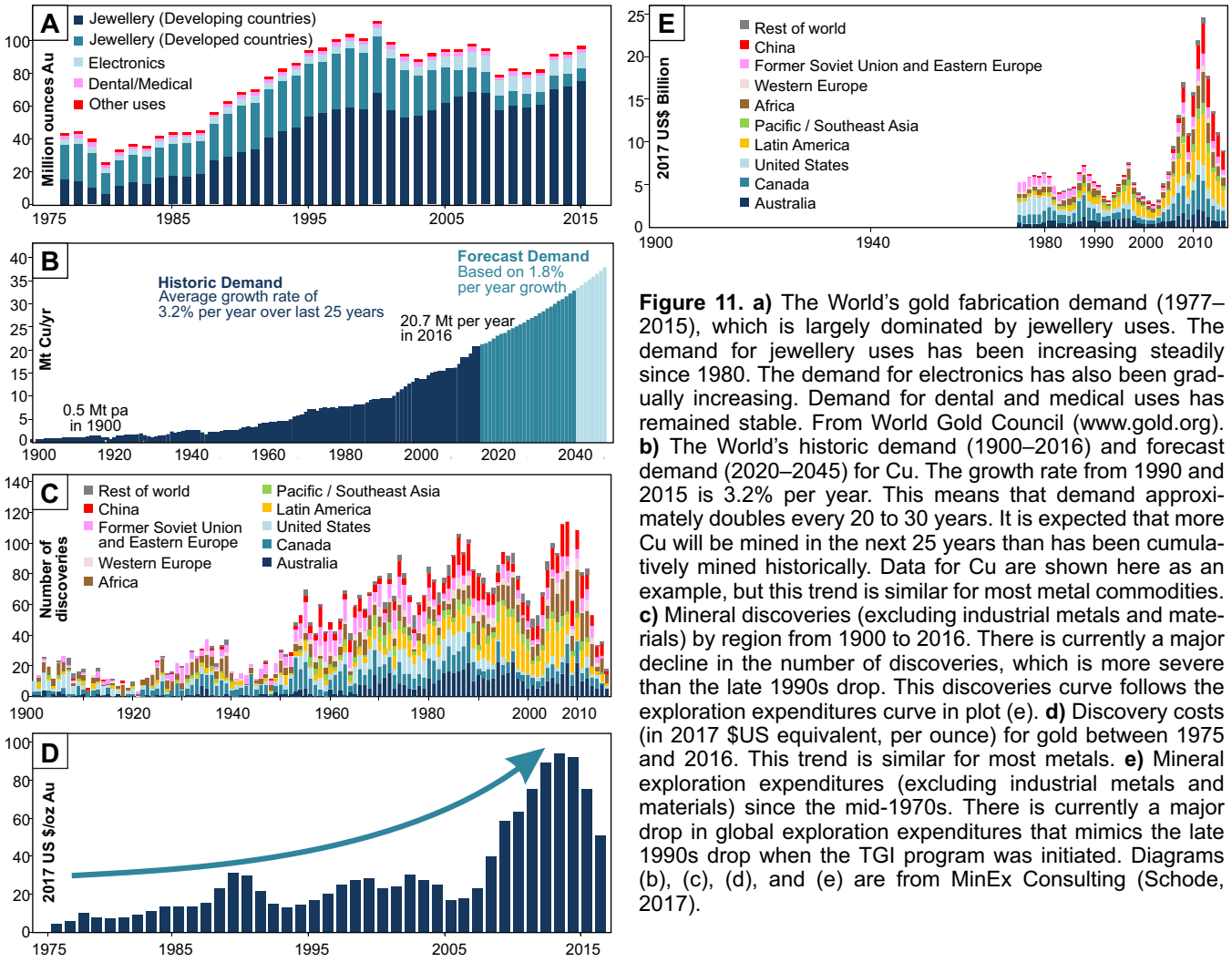

Figure 11. a) The World's gold fabrication demand (1977–2015), which is largely dominated by jewellery uses. The demand for jewellery uses has been increasing steadily since 1980. The demand for electronics has also been gradually increasing. Demand for dental and medical uses has remained stable. From World Gold Council (www.gold.org). **b)** The World's historic demand (1900–2016) and forecast demand (2020–2045) for Cu. The growth rate from 1990 and 2015 is 3.2% per year. This means that demand approximately doubles every 20 to 30 years. It is expected that more Cu will be mined in the next 25 years than has been cumulatively mined historically. Data for Cu are shown here as an example, but this trend is similar for most metal commodities. **c)** Mineral discoveries (excluding industrial metals and materials) by region from 1900 to 2016. There is currently a major decline in the number of discoveries, which is more severe than the late 1990s drop. This discoveries curve follows the exploration expenditures curve in plot (e). **d)** Discovery costs (in 2017 $US equivalent, per ounce) for gold between 1975 and 2016. This trend is similar for most metals. **e)** Mineral exploration expenditures (excluding industrial metals and materials) since the mid-1970s. There is currently a major drop in global exploration expenditures that mimics the late 1990s drop when the TGI program was initiated. Diagrams (b), (c), (d), and (e) are from MinEx Consulting (Schode, 2017).

once we have the necessary resolution in the timing of events, which is based on robust field observations and high-precision geochronological data. These field and laboratory data will translate into a series of parameters and diagnostic features that can be included in regional- to deposit-scale geological, genetic, and exploration models.

The TGI-5 Gold Project was successful in seeding and/or making significant improvement to a relatively large number of analytical methods. Advanced conceptual ore-system models, coupled with new or improved mineral-exploration methodologies, are essential for improving mineral-exploration targeting, particularly for deep deposits in remote areas with sparse geological data. This knowledge, and the improved skillsets associated with these scientific advancements, must however be transferred. Many of the students or early career researchers that participated in TGI-5 will go on to take leadership roles in the mining and mineral exploration industry. Field-based research activities play a critical role in the training of the next generation of highly qualified personnel (Gemmell, 2018). The long-term impact of the research continues, together with field-based training and mentoring opportunities since the beginning of the TGI Program in 2000, and represents the seminal impact of this government-led research.

At the time of writing, it is unclear whether the TGI program will be renewed or replaced. Nonetheless, geological surveys fulfil an essential role in providing objective and freely available pre-competitive geoscience information to inform land-use decisions, environmental management, and investments in mineral resources development (Duke, 2010). Government-funded research programs also complement new, collaborative, multidisciplinary, and industry-led mineral system research programs that tend to be shorter and, in some cases, comprise proprietary data sets. The global demand for metals keeps increasing (Fig. 11a,b), which will place additional pressure on governments to provide the mineral exploration and mining industry with these critical pre-competitive geoscience data sets. As discussed above, global demand is increasing at a time when new gold deposits are more difficult to find, as

demonstrated by the steep decline in the number of discoveries since 2010 (Fig. 11c; Kirwin, 2019) and higher discovery costs (Fig. 11d). The recent decline in exploration expenditures (Fig. 11e) is similar to that of the late 1990s when the TGI program was initially designed and launched, and suggests that governments must continue to invest in pre-competitive data sets. Innovative ways for meeting future resource demands are required, and geologists will need to become better explorers to find new deposits, requiring advanced knowledge, practical training, and tools (Kirwin, 2019). Similarly, sustainability in geoscientific research necessitates long-term investment to tackle major knowledge gaps and develop improved exploration models and tools. The Canadian Minerals and Metals Plan, a pan-Canadian collaborative (Federal, Provincial, and Territorial governments and industry) public geoscience strategy for mineral exploration should set the tone for future mineral resources-related research at the GSC.

ACKNOWLEDGMENTS

Most contributions to the TGI-5 Gold Project synthesis volume result from the collaborative research of the Geological Survey of Canada, the Geological Survey of Newfoundland-and-Labrador, the Ministère de l'Énergie et des Ressources naturelles du Québec, the Ontario Geological Survey, the Manitoba Geological Survey, the Yukon Geological Survey, and the British Columbia Geological Survey. Numerous colleagues from these organizations are thanked for their essential participation and scientific contributions. We acknowledge the numerous mining and exploration companies that generously gave access to their properties, drill core libraries and data, and provided logistical and technical support, as well as financial support to students. Support and direct involvement from the industry made the Gold Project and its various activities possible and more relevant to exploration and mining. The Gold Project would not have been possible without the major involvement of numerous colleagues from academia and we are grateful for their important contribution. We also want to highlight the amazing and indispensable work done by the students involved in the activities and sub-activities of the Gold Project. We acknowledge the TGI-5 management (C. Bjerkelund, C. Hutton, G. Marquis, Y. Michaud, and M. Villeneuve) for their support, and the members of the TGI-5 Scientific and Industry advisory groups for advice and guidance. Thanks to F. Aucoin for his help with GIS and some figures. We thank E. Ambrose for the technical editing and layout of the final version of this volume.

Each contribution of the Gold Project synthesis was peer-reviewed by geoscientists external to the GSC and the following individuals are thanked for kindly agreeing to critically review the manuscripts:

Name	Affiliation
Anderson, S.	1911 Gold Corp.
Casselman, S.	Yukon Geological Survey
de Souza, S.	Université du Québec à Montréal
Frieman, B.M.	Laurentian University
Gregory, D.	University of Toronto
Hinchey, J.	Geological Survey of Newfoundland and Labrador
Kuiper, Y.	Colorado School of Mines
Lafrance, B.	Laurentian University
Martin , A.J.	Memorial University
Moore, L.	Rio Tinto Mining and Exploration Limited
Muntean, J.	University of Nevada
Ootes, L.	British Columbia Geological Survey
Rhys, D.	Panterra Geoservices
Ross, P.-S.	Institut national de la recherche scientifique
Sack, P.	Yukon Geological Survey
Toth, Z.	Laurentian University
Yakymchuk, C.	University of Waterloo
Yergeau, D.	Agnico Eagle Mines Limited

REFERENCES

Barley, M.E. and Groves, D.I., 1992. Supercontinent cycles and the distribution of metal deposits through times; Geology, v. 20, p. 291–294.

Bédard, J.H., 2018. Stagnant lids and mantle overturns: Implications for Archaean tectonics, magma genesis, crustal growth, mantle evolution, and the start of plate tectonics; Geoscience Frontiers, v. 9, p. 19–49.

Bierlein, F.P. and Crowe, D.E., 2000. Phanerozoic orogenic lode gold deposits; *in* Gold in 2000, (ed.) S.G. Hagemann and P.E. Brown; Reviews in Economic Geology, v. 13, p. 103–139.

Bleeker, W., 2015. Synorogenic gold mineralization in granite-greenstone terranes: the deep connection between extension, major faults, synorogenic clastic basins, magmatism, thrust inversion, and long-term preservation; in Targeted Geoscience Initiative 4: Contributions to the understanding of Precambrian lode gold deposits and implications for exploration, (ed.) B. Dubé and P. Mercier-Langevin; Geological Survey of Canada, Open File 7852, p. 25–47.

Bleeker, W., Mercier-Langevin, P., and Ames, D., 2014. Science recommendations for future mineral research programs; unpublished internal report presented to Targeted Geoscience Initiative Management by the Mineral Exploration Science Advisory Group; Geological Survey of Canada, June 2014, 33 p.

Bodnar, R.J., Lecumberri-Sanchez, P., Moncada, D., and Steele-MacInnis, M., 2014. Fluid inclusions in hydrothermal ore deposits; *in* Treatise on Geochemistry (second edition), Volume

13: Geochemistry of Mineral Deposits, (ed.) S. Scott; Elsevier Science, Netherlands, p. 119–142.

Boily-Auclair, E., 2017. Nature et style de l'altération hydrothermale associée aux minéralisation aurifères du projet LaRonde Zone 5 (LZ-5), Abitibi, Québec; B.Sc. thesis, Université Laval, Québec, Quebec, 57 p.

Boily-Auclair, É., Mercier-Langevin, P., Ross, P.-S., and Pitre, D., 2020. Stratigraphic setting of the LZ5 and Ellison mineralized zones, LaRonde Zone 5 project, Doyon-Bousquet-LaRonde mining camp, Abitibi, Quebec; *in* Targeted Geoscience Initiative 5: Contributions to the Understanding of Canadian Gold Systems, (ed.) P. Mercier-Langevin, C.J.M. Lawley, and S. Castonguay; Geological Survey of Canada, Open File 8712, p. 57–73. doi:10.4095/323665

Boudreau, C., Mercier-Langevin, P., Krushnisky, A., and Goutier, J., 2020. Sulphide clast-bearing felsic volcaniclastic units of the Rouyn-Pelletier Formation: Comparison with similar units of the Horne Block, Rouyn-Noranda, Abitibi greenstone belt, Quebec; *in* Targeted Geoscience Initiative 5: Contributions to the Understanding of Canadian Gold Systems, (ed.) P. Mercier-Langevin, C.J.M. Lawley, and S. Castonguay; Geological Survey of Canada, Open File 8712, p. 45–56. doi:10.4095/323664

Bouvier, A., LaFontaine, D.J., and Hill, M-J., 2017. Lu-Hf chronometry and geothermometry of garnet from the gold-bearing sillimanite-garnet-biotite schist at the Borden gold deposit, Chapleau, Ontario; Society for Geology Applied to Mineral Deposits, Proceedings of the 14th SGA Biennial Meeting, p. 997–1000.

Boyle, R.W., 1988. Auriferous Archean greenstone-sedimentary belts; *in* Historical Perspectives of Genetic Concepts and Case Histories of Famous Discoveries, (ed.) R.W. Hutchinson and R.I Grauch; Society of Economic Geologists, Monograph 8, p. 164–191.

Burrows, D.R. and Spooner, E.T.C., 1989. Relationships between Archean gold quartz vein-shear zone mineralization and igneous intrusions in the Val d'Or and Timmins areas, Abitibi Subprovince, Canada; *in* The Geology of Gold Deposits: the Perspective in 1988, (ed.) R.R. Keays, W.R.H. Ramsay, and D.I. Groves; Society of Economic Geologists, Monograph 6, p. 424–444.

Cameron, E.M., 1993. Precambrian gold: Perspective from top to bottom of shear zones; The Canadian Mineralogist, v. 31, p. 917–944.

Card, K.D., Poulsen, H.K., and Robert, F., 1989. The Archean Superior Province of the Canadian Shield and its lode gold deposits; *in* The Geology of Gold Deposits: the Perspective in 1988, (ed.) R.R. Keays, W.R.H. Ramsay, and D.I. Groves; Society of Economic Geologists, Monograph 6, p. 19–36.

Castonguay, S., Dubé, B., Wodicka, N., and Mercier-Langevin, P., 2020. Geological setting and gold mineralization associated with the Sunday Lake and Lower Detour deformation zones, northwestern Abitibi greenstone belt, Ontario and Quebec; *in* Targeted Geoscience Initiative 5: Contributions to the Understanding of Canadian Gold Systems, (ed.) P. Mercier-Langevin, C.J.M. Lawley, and S. Castonguay; Geological Survey of Canada, Open File 8712, p. 127–142. doi:10.4095/323669

Castonguay, S., Ootes, L., Devine, F., and Friedman., R., 2020. Superimposed Late Cretaceous and earliest Eocene gold mineralization and deformation events along the Llewellyn-Tally Ho deformation corridor in northwest British Columbia and southern Yukon; *in* Targeted Geoscience Initiative 5: Contributions to the Understanding of Canadian Gold Systems, (ed.) P. Mercier-Langevin, C.J.M. Lawley, and S. Castonguay; Geological Survey of Canada, Open File 8712, p. 223–236. doi:10.4095/326670

Caté, A., 2016. Geology of the Paleoproterozoic Zn-Cu-Au Lalor volcanogenic massive sulphide deposit and its gold-rich lenses, Snow Lake, Manitoba; Ph.D. thesis, Institut national de la recherche scientifique – Centre Eau Terre Environnement, Québec, Quebec, 384 p.

Caté, A., Mercier-Langevin, P., Ross, P.-S., Duff, S., Hannington, M.D., Dubé, B., and Gagné, S., 2015. Geology and Au enrichment processes at the Paleoproterozoic Lalor auriferous volcanogenic massive sulphide deposit, Snow Lake, Manitoba; *in* Targeted Geoscience Initiative 4: Contributions to the Understanding of Volcanogenic Massive Sulphide Deposit Genesis and Exploration Methods Development, (ed.) J.M. Peter and P. Mercier-Langevin; Geological Survey of Canada, Open File 7853, p. 131–145.

Cathro, R.J., Jaques, A.L., Lesher, C.M., and Swinden, S.H., 2000. Summary report, Canadian Geoscience Council review committee on the Minerals Geoscience Program of the Geological Survey of Canada; Geoscience Canada, v. 27, p. 173–179.

Chang, Z., Large, R.R., and Maslennikov, V., 2008. Sulfur isotopes in sediment-hosted orogenic gold deposits: Evidence for an early timing and a seawater sulfur source: Geology, v. 36, p. 971–974.

Ciufo, T.J., 2019. Hydrothermal alteration and exploration vectors at the Island Gold deposit, Michipicoten greenstone belt, Wawa, Ontario; M.Sc. thesis, University of Waterloo, Waterloo, Ontario, 510 p.

Ciufo, T.J., Jellicoe, K., Yakymchuk, C., Lin, S., Mercier-Langevin, P., and Wodicka, N., 2020. Geology, structural evolution, and hydrothermal alteration of the Island Gold deposit, Michipicoten greenstone belt, Ontario; *in* Targeted Geoscience Initiative 5: Contributions to the Understanding of Canadian Gold Systems, (ed.) P. Mercier-Langevin, C.J.M. Lawley, and S. Castonguay; Geological Survey of Canada, Open File 8712, p. 143–156. doi:10.4095/323671

Cline, J.S., 2018. Nevada's Carlin-type gold deposits: what we've learned during the past 10 to 15 years; *in* Diversity of Carlin-style gold deposits, (ed.) J.L. Muntean; Reviews in Economic Geology, v. 20, p. 7–37.

Colvine, A.C., 1989. An empirical model for the formation of Archean gold deposits: products of final cratonization of the Superior Province, Canada; *in* The Geology of Gold Deposits: the Perspective in 1988, (ed.) R.R. Keays, W.R.H. Ramsay, and D.I. Groves; Society of Economic Geologists, Monograph 6, p. 37–53.

Craw, D. and Koons, P.O., 1989. Tectonically induced hydrothermal activity and gold mineralization adjacent to major fault zones; *in* The Geology of Gold Deposits: the Perspective in 1988, (ed.) R.R. Keays, W.R.H. Ramsay, and D.I. Groves; Society of Economic Geologists, Monograph 6, p. 471–478.

De Launay, L., 1913. Traité de Métallogénie: Gîtes minéraux et métallifères; Librairie Polytechnique Ch. Béranger, Paris et Liège, France, 2593 p.

Dubé, J., 2016. Caractérisation de la distribution de l'or à l'intérieur de la lentille 20 Nord dans le secteur LaRonde Extension à la mine LaRonde Penna, Abitibi, Québec; B.Sc. thesis, Université Laval, Québec, Quebec, 115 p.

Dubé, B. and Gosselin, P., 2007. Greenstone-hosted quartz-carbonate vein deposits; *in* Mineral Deposits of Canada – A Synthesis of Major Deposit-Types, District Metallogeny, the Evolution of Geological Provinces, and Exploration Methods, (ed.) W.D. Goodfellow; Geological Association of Canada, Mineral Deposits Division, Special Publication 5, p. 49–73.

Dubé, B. and Mercier-Langevin, P., 2019. L'or dans la ceinture de roches vertes de l'Abitibi, Québec et Ontario, Canada: un

aperçu géologique et historique; Ressources Mines et Industrie, v. 6, no. 2, p. 10–29.

Dubé, B. and Mercier-Langevin, P., 2020. Gold in the Abitibi greenstone belt, Canada: A geological and historical overview; Resources Mines and Industry, v. 1, p. 24–42.

Dubé, B. and Mercier-Langevin, P., in press. Gold deposits of the Archean Abitibi greenstone belt, Canada; *in* Global Gold Deposits, (ed.) R.H. Sillitoe, R.J. Goldfarb, F. Robert, and S.F. Simmons; Economic Geology Special Publication 23.

Dubé, B., Dunning, G., and Lauziére, K., 1995. Geology of the Hope Brook mine, Newfoundland, Canada: a preserved Late Proterozoic high-sulfidation epithermal gold deposit and its implications for exploration; Economic Geology, v. 93, p. 405–436.

Dubé, B., Gosselin, P., Mercier-Langevin, P., Hannington, M.D., and Galley, A., 2007a. Gold-rich volcanogenic massive sulphide deposits; *in* Mineral Deposits of Canada: A Synthesis of Major Deposit-Types, District Metallogeny, the Evolution of Geological Provinces, and Exploration Methods, (ed.) W.D. Goodfellow; Geological Association of Canada, Mineral Deposits Division, Special Publication 5, p. 75–94.

Dubé, B., Mercier-Langevin, P., Hannington, M.D., Lafrance, B., Gosselin, P., and Gosselin, G., 2007b. The LaRonde Penna giant gold-rich volcanogenic massive sulfide deposit, Abitibi, Quebec: alteration footprint, genesis and implications for exploration; Economic Geology, v. 102, p. 633–666.

Dubé, B, Mercier-Langevin, P., Kjarsgaard, I., Hannington, M., Bécu, V., Côté, J., Moorhead, J., Legault, M., and Bédard, N., 2014. The Bousquet 2-Dumagami world-class Archean Au-rich volcanogenic massive sulfide deposit, Abitibi, Quebec: a type example of submarine synvolcanic high-sulfidation style alteration and mineralization; Economic Geology, v. 109, p. 121–166.

Dubé, B., Mercier-Langevin, P., Castonguay, S., McNicoll, V.J., Bleeker, W., Lawley, C.J.M., De Souza, S., Jackson, S.E., Dupuis, C., Gao, J.-F., Bécu, V., Pilote, P., Goutier, J., Beakhouse, G.P., Yergeau, D., Oswald, W., Janvier, V., Fontaine, A., Pelletier, M., Beauchamp, A.-M., Katz, L.R., Kontak, D.J., Tóth, Z., Lafrance, B., Gourcerol, B., Thurston, P.C., Creaser, R.A., Enkin, R.J., El Goumi, N., Grunsky, E.C., Schneider, D.A., Kelly, C.J., and Lauzière, K., 2015. Precambrian lode gold deposits — a summary of TGI-4 contributions to the understanding of lode gold deposits, with an emphasis on implications for exploration; *in* Targeted Geoscience Initiative 4: Contributions to the understanding of Precambrian lode gold deposits and implications for exploration, (ed.) B. Dubé and P. Mercier-Langevin; Geological Survey of Canada, Open File 7852, p. 1–24.

Dubosq, R., Lawley, C.J.M., Rogowitz, A., Schneider, D., and Jackson, S.E., 2018. Pyrite deformation and connections to gold mobility: insight from micro-structural analysis and trace element mapping; Lithos, v. 310–311, p. 86–104.

Duke, N.M., 2000. Geological Survey of Canada response to the summary report of the review committee on GSC'S Minerals Geoscience Program; Geoscience Canada, v. 27, p. 180–182.

Duke, N.M., 2010. Government geosciences to support mineral exploration: public policy rationale and impact; unpublished report prepared for the Prospectors and Developers Association of Canada, March 2010, 64 p.

Fayard, Q., Mercier-Langevin, P., Wodicka, N., Daigneault, R., and Perreault, S., 2020. The B26 Cu-Zn-Ag-Au project, Brouillan volcanic complex, Abitibi greenstone belt, part 1: Geological setting and geochronology; *in* Targeted Geoscience Initiative 5: Contributions to the Understanding of Canadian Gold Systems, (ed.) P. Mercier-Langevin, C.J.M. Lawley, and S. Castonguay; Geological Survey of Canada, Open File 8712, p. 93–107. doi:10.4095/323668

Fayard, Q., Mercier-Langevin, P., Daigneault, R., Perreault, S., and Wodicka, N., 2020. The B26 Cu-Zn-Ag-Au project, Brouillan volcanic complex, Abitibi greenstone belt, part 2: Hydrothermal alteration and mineralization; *in* Targeted Geoscience Initiative 5: Contributions to the Understanding of Canadian Gold Systems, (ed.) P. Mercier-Langevin, C.J.M. Lawley, and S. Castonguay; Geological Survey of Canada, Open File 8712, p. 109–125. doi:10.4095/323669

Fontaine, A., Dubé, B., Malo, M., Ravenelle, J-F., Fournier, E., McNicoll, V.J., Beausoleil, C., Prud'homme, N., and Goutier, J., 2017. The Éléonore gold mine: Exploration, discovery and understanding of an emerging gold district in Eeyou Istchee James Bay, Superior Province, northern Québec, Canada; *in* Proceedings of Exploration 17, (ed.) V. Tschirhart and M.D. Thomas; Sixth Decennial International Conference on Mineral Exploration, 2017, p. 601–617.

Fontaine, A., 2019. Géologie des minéralisations aurifères de la mine Éléonore, Eeyou Istchee Baie-James, Province du Supérieur, Québec, Canada; Ph.D. thesis, Institut national de la recherche scientifique – Centre Eau Terre Environnement, Québec, Quebec, 526 p.

Franklin, J.M., Gibson, H.L., Jonasson, I.R., and Galley, A.G., 2005. Volcanogenic massive sulfide deposits; in Economic Geology 100th Anniversary Volume, (ed.) J.W. Hedenquist, J.F.H. Thompson, R.J. Goldfarb, and J.P Richards; Society of Economic Geologists, p. 523–560.

Fyon, J.A., Troop, D.G., Marmont, S., and MacDonald, A.J., 1989. Introduction of gold into Archean crust, Superior Province, Ontario: coupling between mantle-initiated magmatism and lower crustal thermal maturation; *in* The Geology of Gold Deposits: the Perspective in 1988, (ed.) R.R. Keays, W.R.H. Ramsay, and D.I. Groves; Society of Economic Geologists, Monograph 6, p. 424-444.

Gartman, A., Hannington, M., Jamieson, J.W., Peterkin, B., Garbe-Schönberg, D., Findlay, A.J., Fuchs, S., and Kwasnitschka, T., 2018. Boiling-induced formation of colloidal gold in black smoker hydrothermal fluids; Geology, v. 46, p. 39–42.

Gemmell, J.B., 2018. Presidential perspective – Don't forget your hand lens; SEG Newsletter, no. 115, p. 6.

Goldfarb, R.J. and Groves, D.I., 2015. Orogenic gold: common or evolving fluid and metal sources through time; Lithos, v. 233, p. 2–26.

Goldfarb, R.J., Baker, T., Dubé, B., Groves, D.I., Hart, C.J.R., and Gosselin, P., 2005. Distribution, character, and genesis of gold deposits in metamorphic terranes; *in* Economic Geology 100th Anniversary Volume, (ed.) J.W. Hedenquist, J.F.H. Thompson, R.J. Goldfarb, and J.P Richards; Society of Economic Geologists, p. 407–450.

Gosselin, P. and Dubé, B., 2005a. Gold deposits of the world: distribution, geological parameters and gold content; Geological Survey of Canada, Open File 4895, 271 p.

Gosselin, P. and Dubé, B., 2005b, Gold deposits of Canada: Distribution, geological parameters and gold content; Geological Survey of Canada, Open File 4896, 105 p.

Gosselin, P. and Dubé, B., 2015. Gold deposits of the world: distribution, geological parameters and gold content; Geological Survey of Canada, Open File 7930, 27 p.

Gregory, D.D., Large, R.R., Bath, A.B., Steadman, J.A., Wu, S., Danyushevsky, L., Bull, S.W., Holden, P., and Ireland, T.R., 2016. Trace element content of pyrite from the Kapai slate, St. Ives gold district, Western Australia: Economic Geology, v. 111, p. 1297–1320.

Grondin LeBlanc, P., Mercier-Langevin, P., Malo, M., Côté-Mantha, O., Simard, M., Barbe, P., Valette, M., and De Souza,

S., 2017. Structural controls on the nature and distribution of gold in polytectonized Precambrian volcano-sedimentary successions: an example from the Whale Tail zone, Amaruq project, Nunavut; Geological Survey of Canada, Scientific Presentation 63, 1 sheet.

Hagemann, S.G. and Cassidy, K.F., 2000. Archean orogenic lode gold deposits; *in* Gold in 2000, (ed.) S.G. Hagemann and P.E. Brown; Reviews in Economic Geology, v. 13, p. 9–68.

Hannington, M.D., Poulsen, K.H., Thompson, J.F.H., and Sillitoe, R.H., 1999. Volcanogenic gold in the massive sulfide environment; *in* Volcanic-associated Massive Sulfide Deposits: Processes and Examples in Modern and Ancient Settings, (ed.) C. Tucker Barrie and M.D. Hannington; Reviews in Economic Geology, v. 8, p. 325–356.

Harmon, R.S., Lawley, C.J.M., Watts, J., Harraden, C.L., Somers, A.M., and Hark, R.R., 2019. Laser-induced breakdown spectroscopy – an emerging analytical tool for mineral exploration; Minerals, v. 9, 45 p.

Hodgson, C.J., 1993. Mesothermal lode-gold deposits; *in* Mineral Deposits Modelling, (ed.) R.V. Kirkham, W.D. Sinclair, R.I. Thorpe, and J.M. Duke; Geological Association of Canada, Special Paper 40, p. 635-678.

Hodgson, C.J. and Hamilton, J.V., 1989. Gold mineralization in the Abitibi greenstone belt: end-stage result of Archean collisional tectonics?; *in* The Geology of Gold Deposits: the Perspective in 1988, (ed.) R.R. Keays, W.R.H. Ramsay, and D.I. Groves; Society of Economic Geologists, Monograph 6, p. 86–100.

Hodgson, C.J. and MacGeehan, P.J., 1982. A review of the geological characteristics of "gold-only" deposits in the Superior Province of the Canadian Shield; *in* Geology of Canadian Gold Deposits, (ed.) R.W. Hodder and W. Petruk; Canadian Institute of Mining and Metallurgy, Special Volume 24, p. 211–229.

Honsberger, I.W., Bleeker, W., Sandeman, H.A.I., Evans, D.T.W., and Kamo, S.L., 2020. Vein-hosted gold mineralization in the Wilding Lake area, central Newfoundland: Structural geology and vein evolution; in Targeted Geoscience Initiative 5: Contributions to the Understanding of Canadian Gold Systems, (ed.) P. Mercier-Langevin, C.J.M. Lawley, and S. Castonguay; Geological Survey of Canada, Open File 8712, p. 179–191. doi:10.4095/326020

Honsberger, I.W., Bleeker, W., Kamo, S.L., Sandeman, H.A.I., and Evans, D.T.W., 2020. The emerging Paleozoic gold distrct of central Newfoundland: New insights on structural controls and tectonic drivers of gold mineralization and preservation; *in* Targeted Geoscience Initiative 5: Contributions to the Understanding of Canadian Gold Systems, (ed.) P. Mercier-Langevin, C.J.M. Lawley, and S. Castonguay; Geological Survey of Canada, Open File 8712, p. 193–210. doi: 10.4095/326024

Huston, D.L., 2000. Gold in volcanic-hosted massive sulphide deposits: distribution, genesis, and exploration; *in* Gold in 2000, (ed.) S.G. Hagemann and P.E. Brown; Reviews in Economic Geology, v. 13, p. 400–426.

Huston, D.L., Blewett, R.S., Skirrow, R., McQueen, A., Wang, J., Jaques, L., Waters, D., Bierlein, F., 2012. Foundations of wealth—Australia's major mineral provinces; in Shaping a nation: a geology of Australia, (ed.) R.S. Blewett; Geoscience Australia and ANU E Press, Canberra, p. 381–431.

Hutchinson, R.W., 1993. A multi-stage, multi-process genetic hypothesis for greenstone-hosted gold lodes; Ore Geology Reviews, v. 7, p. 349–382.

Janvier, V., 2016. Géologie du gisement d'or Meadowbank encaissé dans des formations de fer rubanées, Nunavut, Canada; Ph.D. thesis, Institut national de la recherche scientifique – Centre Eau Terre Environnement, Québec, Quebec, 472 p.

Janvier, V., Castonguay, S., Mercier-Langevin, P., Dubé, B., Malo, M., McNicoll, V.J., Creaser, R.A., de Chavigny, B., and Pehrsson, S.J., 2015. Geology of the banded iron formation-hosted Meadowbank gold deposit, Churchill Province, Nunavut; *in* Targeted Geoscience Initiative 4: Contributions to the understanding of Precambrian lode gold deposits and implications for exploration, (ed.) B. Dubé and P. Mercier-Langevin; Geological Survey of Canada, Open File 7852, p. 255–269.

Jellicoe, K., 2019. Structural controls and deformation history of the orogenic Island Gold deposit, Michipicoten greenstone belt, Ontario; M.Sc. thesis, University of Waterloo, Waterloo, Ontario, 84 p.

Jourdain, V., Roy, D.W., and Simard, J-M., 1987. Stratigraphy and structural analysis of the North Gold Zone at Montauban-les-mines, Quebec; Canadian Institute of Mining and Metallurgy Bulletin, v. 80, p. 61–66.

Kerrich, R., Goldfarb, R., Groves, D., and Garwin, S., 2000. The geodynamics of world-class gold deposits: characteristics, space-time distribution, and origins; *in* Gold in 2000, (ed.) S.G. Hagemann and P.E. Brown; Reviews in Economic Geology, v. 13, p. 501–551.

Kirwin, D.J., 2019. Presidential perspective – The continuing decline in mineral discoveries and consequences for society; Society of Economic Geologists Newsletter, no. 116, p. 6.

Kribek, B., 1991. Metallogeny, structural, lithological and time controls of ore deposition in anoxic environments; Mineralium Deposita, v. 26, p. 122–131.

Krogh, T., 1993. High precision U-Pb ages for granulite metamorphism and deformation in the Archean Kapuskasing structural zone, Ontario: implications for structure and development of the lower crust; Earth and Planetary Science Letters, v. 119, p. 1–18.

Kroner, R.K., 2019. The Cordilleran lithosphere in south-central British Columbia: insights from two xenolith suites. M.Sc. thesis, University of British Columbia, Vancouver, British Columbia, 98 p.

Krushnisky, A., 2018. Controls of gold enrichment at the Horne 5 Archean VMS deposit, Abitibi greenstone belt, Québec; M.Sc. thesis, Institut national de la recherche scientifique – Centre Eau Terre Environnement, Québec, Quebec, 198 p.

Krushnisky, A., Mercier-Langevin, P., Ross, P.-S., Goutier, J., Pilote, C., and Bernier, C., 2020. Geology and gold enrichment at the Horne 5 Archean volcanogenic massive sulphide deposit, Abitibi greenstone belt, Quebec: A synthesis; *in* Targeted Geoscience Initiative 5: Contributions to the Understanding of Canadian Gold Systems, (ed.) P. Mercier-Langevin, C.J.M. Lawley, and S. Castonguay; Geological Survey of Canada, Open File 8712, p. 31–44. doi:10.4095/323663

LaFlamme, C., Sugiono, D., Thebaud, N., Caruso, S., Fiorentini, M., Selvaraja, V., Jeon, H., Voute, F., and Martin, L., 2018. Multiple sulfur isotopes monitor fluid evolution of an Archean orogenic gold deposit; Geochimica et Cosmochimica Acta, v. 222, p. 436–446.

Lafontaine, D., 2016. Structural and metamorphic control on the Borden Gold deposit, Chapleau, Ontario; M.Sc. thesis, Lakehead University, Thunder Bay, Ontario, 183 p.

Lam, J., 2019. Characterization of metamorphic assemblages and assessment of Cu-Pb-Ag-Au-Zn mobility at the Lalor deposit, Snow Lake, Manitoba; M.Sc. thesis, Laurentian University, Sudbury, Ontario, 137 p.

Large, R.R., Danyushevsky, L., Hollit, C., Maslennikov, V., Meffre, S., Gilbert, S., Bull, S., Scott, R., Emsbo, P., Thomas, H., Singh, B., and Foster, J., 2009. Gold and trace element zonation in pyrite using a laser imaging technique: Implications for the timing of gold in orogenic and Carlin-style sediment-hosted deposits; Economic Geology, v. 104, p. 635–668.

Large, R.R., Bull, S.W., and Maslennikov, V.V., 2011. A carbonaceous sedimentary source-rock model for Carlin-type and orogenic gold deposits; Economic Geology, v. 106, p. 331–358.

Lauzon, M.-C., 2017. Empreinte minéralogique et géochimique des minéralisations aurifères de la zone Whale Tail du projet Amaruq; B.Sc. thesis, Université Laval, Québec, Quebec, 48 p.

Lauzon, M.-C., Mercier-Langevin, P., Valette, M., Beaudoin, G., De Souza, S., Côté-Mantha, O., and Simard, M., 2020. Ore mineralogy and mineral chemistry of the Whale Tail zone, Amaruq gold deposit, Nunavut; *in* Targeted Geoscience Initiative 5: Contributions to the Understanding of Canadian Gold Systems, (ed.) P. Mercier-Langevin, C.J.M. Lawley, and S. Castonguay; Geological Survey of Canada, Open File 8712, p. 267–279. doi:10.4095/326044

Lawley, C.J.M. and Kjarsgaard, B.A., 2020. Bottom-up mineral exploration: Ore-element upgrading in the upper mantle and tools for its discovery; *in* Targeted Geoscience Initiative 5: Contributions to the Understanding of Canadian Gold Systems, (ed.) P. Mercier-Langevin, C.J.M. Lawley, and S. Castonguay; Geological Survey of Canada, Open File 8712, p. 157–164. doi:10.4095/323674

Lawley, C.J.M., Dubé, B., Mercier-Langevin, P., McNicoll, V.J., Creaser, R.A., Pehrsson, S.J., Castonguay, S., Blais, J.-C., Simard, M., Davis, W.J., and Jackson, S.E., 2015. Setting, age, and hydrothermal footprint of the emerging Meliadine gold district, Nunavut; *in* Targeted Geoscience Initiative 4: Contributions to the understanding of Precambrian lode gold deposits and implications for exploration, (ed.) B. Dubé and P. Mercier-Langevin; Geological Survey of Canada, Open File 7852, p. 99–111.

Lawley, C.J.M., Jackson, S.E., Yang, Z., Davis, W., and Eglington, B., 2017. Tracing the transition of gold from source to sponge to sink; Economic Geology, v. 112, p. 169–183.

Lawley, C.J.M., Petts, D.C., Jackson, S.E., Zagorevski, A., Pearson, D.G., Kjarsgaard, B.A., Savard, D., and Tschirhart, V., 2020a. Precious metal mobility during serpentinization and breakdown of base metal sulphide; Lithos, v. 354–355.

Lawley, C.J.M., Pearson, D.G., Waterton, P., Zagorevski, A., Bédard, J.H., Jackson, S.E., Petts, D.C., Kjarsgaard, B.S., Zhang, S., and Wright, D., 2020b. Element and isotopic signature of re-fertilized mantle peridotite as determined by nanopowder and olivine LA-ICPMS analyses; Chemical Geology, v. 536.

Lawley, C.J.M., Selby, D., Davis, W.J., Yang, E., Zhang, S., Jackson, S.E., Petts, D.C., O'Connor, A.R., and Schneider, D.A., 2020. Paleoproterozoic gold and its tectonic triggers and traps: Implications from Re-Os sulphide and U-Pb detrital zircon geochronology, Lynn Lake, Manitoba; *in* Targeted Geoscience Initiative 5: Contributions to the Understanding of Canadian Gold Systems, (ed.) P. Mercier-Langevin, C.J.M. Lawley, and S. Castonguay; Geological Survey of Canada, Open File 8712, p. 211–222. doi:10.4095/326033

Leclair, A.D., Ernst, R.E., and Hattori, K., 1993. Crustal-scale auriferous shear zones in the central Superior Province, Canada; Geology, v. 21, p. 399–402.

Lindgren, W., 1933. Mineral Deposits; McGraw-Hill Book Company, New York and London, Fourth Edition, 930 p.

MacGeehan, P.J. and Hodgson, C.J., 1982. Environments of gold mineralization in the Campbell Red Lake and Dickenson Mines, Red Lake district, Ontario; *in* Geology of Canadian gold deposits, (ed.) R.W. Hodder and W. Petruk; Canadian Institute of Mining and Metallurgy, Special Volume 24, p. 184–207.

McInnes, B.I.A., McBridge, J.S., Evans, N.J., Lambert, D.D., and Andre, A.S., 1999. Osmium isotope constraints on ore metal recycling in subduction zones; Science, v. 286, p. 512–516.

Mercier-Langevin, P., Dubé, B., Hannington, M.D., Richer-Laflèche, M., and Gosselin, G., 2007a. The LaRonde Penna Au-rich volcanogenic massive sulfide deposit, Abitibi greenstone belt, Quebec: Part II. Lithogeochemistry and paleotectonic setting; Economic Geology, v. 102, p. 611–631.

Mercier-Langevin, P., Dubé, B., Hannington, M.D., Davis, D., Lafrance, B., and Gosselin, G., 2007b. The LaRonde Penna Au-rich volcanogenic massive sulfide deposit, Abitibi greenstone belt, Quebec: Part I. Geology and geochronology; Economic Geology, v. 102, p. 585–609.

Mercier-Langevin, P., Hannington, M.D., Dubé, B., Bécu, V., 2011. The gold content of volcanogenic massive sulphide deposits; Mineralium Deposita, v. 46, p. 509–539.

Mercier-Langevin, P., Gibson, H.L., Hannington, M.D., Goutier, J., Monecke, T., Dubé, B., and Houlé, M.G., 2014a. A special issue on Archean magmatism, volcanism, and ore deposits: part 2. Volcanogenic massive sulfide deposits; Economic Geology, v. 109, p. 1–9.

Mercier-Langevin, P., Lafrance, B., Bécu, V., Dubé, B., Kjarsgaard, I., and Guha, J., 2014b. The Lemoine auriferous volcanogenic massive sulfide deposit, Chibougamau camp, Abitibi greenstone belt, Québec, Canada: geology and genesis; Economic Geology, v. 109, p. 231–269.

Mercier-Langevin, P., Hannington, M.D., Dubé, B., Piercey, S.J., Peter, J.M., and Pehrsson, S.J., 2015. Precious metal enrichment processes in volcanogenic massive sulphide deposits — A summary of key features, with an emphasis on TIGI-4 research contributions; *in* Targeted Geoscience Initiative 4: Contributions to the understanding of volcanogenic massive sulphide deposit genesis and exploration methods development, (ed.) J.M. Peter and P. Mercier-Langevin; Geological Survey of Canada, Open File 7853, p. 117–130.

Mercier-Langevin, P., Rogers, N., Dubé, B., Bleeker, W., Castonguay, S., McNicoll, V.J., Chapman, J.B., Lawley, C.J.M., Bellefleur, G., Houlé, M.G., Pinet, N., Jackson, S.E., Davis, W.J., Bécu, V., Peter, J.M., Paradis, S., Potter, E.G., Bjerkelund, C., Villeneuve, M.E., and Evans, R., 2017. Targeted Geoscience Initiative: 2016 Report of Activities – An Overview; *in* Targeted Geoscience Initiative – 2016 Report of Activities, (ed.) N. Rogers; Geological Survey of Canada, Open File 8199, p. 7–16.

Mercier-Langevin, P., Valette, M., De Souza, S., Creaser, R.A., McNicoll, V.J., Grondin LeBlanc, P., St.Pierre, B., Lauzon, M.-C., Malo, M., Côté-Mantha, O., and Simard, M., 2018. Lithologic controls on Paleoproterozoic BIF-hosted/associated gold: Overview of Re-Os geochronology and Pb isotopes preliminary results; *in* Targeted Geoscience Initiative: 2017 Report of Activities, Volume 1, (ed.) N. Rogers; Geological Survey of Canada, Open File 8358, p. 147–152.

Muntean, J.L., 2018. The Carlin gold system: applications to exploration in Nevada and beyond; in Diversity of Carlin-style gold deposits, (ed.) J.L. Muntean; Reviews in Economic Geology, v. 20, p. 39–88.

Natural Resources Canada, Canadian Mineral Exploration Bulletin, 2019. <https://www.nrcan.gc.ca/maps-tools-publications/publications/minerals-mining-publications/canadian-mineral-exploration-information-bulletin/17762#s4> [accessed March 13, 2020].

Neuendorf, K.K.E., Mehl, J.P.Jr., and Jackson, J.A., 2005. Glossary of Geology, Fifth Edition; American Geological Institute, Alexandria, Virginia, US, 779 p.

Ootes, L., Castonguay, S., Friedman, R., and Devine, F., 2018. Testing the relationship between the Llewellyn fault, Tally Ho shear zone, and gold mineralization in northwest British Columbia; in Geological Fieldwork 2017; British Columbia

Ministry of Energy, Mines and Petroleum Resources, British Columbia Geological Survey, Paper 2018-1, p. 67–81.

Ootes, L., Castonguay, S., Friedman, R., and Devine, F., 2019. Superimposed auriferous structural events along the Llewellyn-Tally Ho deformation corridor in southern Yukon and northwest British Columbia; *in* Targeted Geoscience Initiative: 2018 Report of Activities, (ed.) N. Rogers; Geological Survey of Canada, Open File 8549, p. 48–58.

Oswald, W., 2018. Geology of the banded iron formation-hosted Musselwhite gold deposit, Superior Province, Ontario, Canada; Ph.D. thesis, Institut national de la recherche scientifique – Centre Eau Terre Environnement, Québec, Quebec, 475 p.

Paterson, C.J., Lisenbee, Al., and Redden, J.A., 1990. Gold deposits in the Black Hills; *in* Metallogeny of gold in the Black Hills, South Dakota, (ed.) C.J. Paterson, and A.L Lisenbee; Society of Economic Geologists, Guidebook Series Volume 7, p. 10–19.

Pelletier, M., 2016. The Rainy River gold deposit, Wabigoon Subprovince, western Ontario: Style, geometry, timing and structural controls on ore distribution and grades; M.Sc. thesis, Institut national de la recherche scientifique – Centre Eau Terre Environnement, Québec, Quebec, 364 p.

Percival, J.A., Skulski, T., Sanborn-Barrie, M., Stott, G.M., Leclair, A.D., Corkery, M.T., and Boily, M., 2012. Geology and tectonic evolution of the Superior Province, Canada; *in* Tectonic Styles in Canada: the Lithoprobe perspective, (ed.) J.A. Percival, F.A. Cook, and R.M. Clowes; Geological Association of Canada, Special Paper 49, p. 321–378.

Perring, C.S., Barley, C.E., Cassidy, K.F., Groves, D.I., McNaughton, N.J., Rock, N.M.S., Bettenay, L.F., Golding, S.D., and Hallberg, J.A., 1989. The association of linear orogenic belts, mantle-crustal magmatism, and Archean gold mineralization in the eastern Yilgarn Block of western Australia; *in* The Geology of Gold Deposits: the Perspective in 1988, (ed.) R.R. Keays, W.R.H. Ramsay, and D.I. Groves; Society of Economic Geologists, Monograph 6, p. 571–584.

Petts, D.C., Davis, W.J., Jackson, S.E., and Girard, I., 2019. U-Pb dating of Paleoproterozoic travertine using LA-Q-ICP-MS and LA-SF-ICP-MS; North American Workshop on Laser Ablation, Jackson School of Geosciences, NAWLA19 Abstract Volume, p. 35.

Phillips, G.N. and Powell, R., 2009. Formation of gold deposits: Review and evaluation of the continuum model; Earth-Science Reviews, v. 94, p. 1–21.

Pilote, J.-L., Jackson, S.E., Mercier-Langevin, P., Dubé, B., Lawley, C.J.M, Petts, D.C., van Hees, E., and Rhys, D., 2019a. Caractérisation géochimique de pyrites nodulaires d'horizons d'argilites graphiteuses dans la région de Timmins, nord-est de l'Ontario; Ministère de l'Énergie et des Ressources naturelles du Québec, Résumés des Conférences et des Photoprésentations, DV 2019-01, p. 63.

Pilote, J.-L., Jackson, S., Mercier-Langevin, P., Dubé, B., Lawley, C.J.M., Rhys, D., Petts, D.C., and van Hees, E., 2019b. Gold endowment in iron sulphide nodules: insights on the enrichment controlling factors from the carbonaceous metasedimentary rocks of the Timmins-Matheson gold corridor, Ontario, Canada; Geological Association of Canada-Mineralogical Association of Canada, Volume of Abstracts, v. 42, p. 160.

Pilote, J.-L., Jackson, S.E., Mercier-Langevin, P., Dubé, B., and Rhys, D., 2019c. Characteristics of diagenetic and epigenetic sulphides in deformed and metamorphosed Archean carbonaceous metasedimentary rocks of the Timmins-Matheson corridor: establishing a framework for fingerprinting ore-forming processes in shear zone-hosted orogenic gold systems; *in* Targeted Geoscience Initiative: 2018 Report of Activities, (ed.) N. Rogers; Geological Survey of Canada, Open File 8549, p. 33–41.

Pilote, J.-L., Jackson, S.E., Mercier-Langevin, P., Dubé, B., Lawley, C.J.M., Petts, D.C., Yang, Z., Stern, R., van Hees, E., and Rhys, D., 2020a. Trace element and S and Fe isotope characteristics of argillite-hosted diagenetic and epigenetic pyrite from the Timmins-Matheson gold corridor, Abitibi; AME Roundup meeting, January 20-23, 2020, Vancouver, British Columbia, Canada.

Pilote, J.-L., Jackson, S.E., Mercier-Langevin, P., Dubé, B., Lawley, C.J.M., Petts, D.C., Yang, Z., van Hees, E., and Rhys, D., 2020b. Fingerprinting ore processes in orogenic auriferous systems: Insights into metallogenic and exploration implications from argillite-hosted iron sulphide nodules from the Timmins-Matheson gold corridor; *in* Targeted Geoscience Initiative 5: Contributions to the Understanding of Canadian Gold Systems, (ed.) P. Mercier-Langevin, C.J.M. Lawley, and S. Castonguay; Geological Survey of Canada, Open File 8712, p. 165–178. doi:10.4095/323675

Pilote, J.-L., Mercier-Langevin, P., Jackson, S.E., Dubé, B., Yang, Z., Lawley, C.J.M., Petts, D.C., Layne, G.D., and Piercey, S.J., 2020c. Interrogating the composition and genesis of argillite-hosted pyrite nodules at the LaRonde Penna gold-rich volcanogenic massive sulphide deposit, Abitibi, Quebec: Insights into metallogenic implications; *in* Targeted Geoscience Initiative 5: Contributions to the Understanding of Canadian Gold Systems, (ed.) P. Mercier-Langevin, C.J.M. Lawley, and S. Castonguay; Geological Survey of Canada, Open File 8712, p. 75–91. doi:10.4095/323666

Pinet, N., Sack, P., Mercier-Langevin, P., Colpron, M., Lavoie, D., Dubé, B., and Brake, V.I., 2020. Neoproterozoic-hosted Carlin-type mineralization in central Yukon, part 1: Regional- to prospect-scale geological controls; *in* Targeted Geoscience Initiative 5: Contributions to the Understanding of Canadian Gold Systems, (ed.) P. Mercier-Langevin, C.J.M. Lawley, and S. Castonguay; Geological Survey of Canada, Open File 8712, p. 281–297. doi:10.4095/326045

Pinet, N., Sack, P., Mercier-Langevin, P., Davis, W.J., Lavoie, D., Haeri-Ardakani, O., Komaromi, B.A., Dubé, B., Cline, J.S., Petts, D.C., Jautzy, J., Jackson, S.E., Percival. J.B., Savard, M.M., and Brake, V.I., 2020. Neoproterozoic-hosted Carlin-type mineralization in central Yukon part 2: Mineralization; *in* Targeted Geoscience Initiative 5: Contributions to the Understanding of Canadian Gold Systems, (ed.) P. Mercier-Langevin, C.J.M. Lawley, and S. Castonguay; Geological Survey of Canada, Open File 8712, p. 299–314. doi:10.4095/326047

Pirie, J., 1982. Regional geological setting of gold deposits, eastern Red Lake area, northwestern Ontario; *in* Geology of Canadian Gold Deposits, (ed.) R.W. Hodder and W. Petruk; Canadian Institute of Mining and Metallurgy, Special Volume 24, p. 171–183.

Pitcairn, I., Leventis, N.-G., Beaudoin, G., and Dubé, B., 2017. A metasedimentary source for orogenic gold in the Abitibi belt?; Society for Geology Applied to Mineral Deposits, Proceedings of the 14th SGA Biennial Meeting, p. 91–94.

Pitcairn, I., Peillod, A., Patten, C., Goutier, J., Guillemette, C., and Beaudoin, G., 2019. Metabasalts as sources of gold in Archean greenstone belts; Society for Geology Applied to Mineral Deposits, Proceedings of the 15th SGA Biennial Meeting, p. 651–654.

Polat, A., Wang, L., and Appel, P.W.U., 2015. A review of structural patterns and melting processes in the Archean craton of West Greenland: Evidence for crustal growth at convergent plate margins as opposed to non-uniformitarian models; Tectonophysics, v. 662, p. 67–94.

Prokofiev, V.Y., Banks, D.A., Lobanov, K.V., Slekto, S.L., Milichko, V.A., Akinfiev, N.N., Borovokov, A.A., Lüders, V., and Chicherov, M.V., 2019. Exceptionally Au-rich mid-crustal

fluids from the Kola super-deep borehole; Society for Geology Applied to Mineral Deposits, Proceedings of the 15th SGA Biennial Meeting, p. 748–751.

Prospectors and Developers Association of Canada, 2019. State of Mineral Finance 2019: At the Crossroads, 39 p. <https://www.pdac.ca/docs/default-source/priorities/access-to-capital/state-of-mineral-finance-reports/pdac-state-of-mineral-finance-2019.pdf?sfvrsn=96808a98_6> [accessed March 13, 2020].

Ridley, J.R. and Diamond, L.W., 2000. Fluid chemistry of orogenic lode gold deposits and implications for genetic models; *in* Gold in 2000, (ed.) S.G. Hagemann and P.E. Brown; Reviews in Economic Geology, v. 13, p. 141–162

Robert, F., Poulsen, H.K., Cassidy, K.F., and Hodgson, C.J., 2005. Gold metallogeny of the Superior and Yilgarn cratons; *in* Economic Geology 100th Anniversary Volume, (ed.) J.W. Hedenquist, J.F.H. Thompson, R.J. Goldfarb, and J.P. Richards; Society of Economic Geologists, p. 1001–1033.

Sack, P., Cline, J., Ren, M., Petts, D., and Pinet, N., 2019. Gold-bearing arsenian pyrite in Carlin-type gold prospects of the Nadaleen trend, Yukon; Geological Association of Canada-Mineralogical Association of Canada, Volume of Abstracts, v. 42, p. 169.

Selvaraja, V., Fiorentini, M.L., Jeon, H., Savard, D.D., LaFlamme, C., Guagliardo, P., Caruso, S., and Bui, T.H., 2017. Evidence of local sourcing of sulfur and gold in an Archaean sediment hosted gold deposit; Ore Geology Review, v. 89 p. 909–930.

Schodde, R., 2017. Long term trends in global exploration – are we finding enough metal?: 11th Fennoscandian Exploration and Mining Conference, October 31, 2017, Levi, Finland [accessed April 2019].

Sillitoe, R.H., 2008. Major gold deposits and belts of the North and South American Cordillera: distribution, tectonomagmatic settings, and metallogenic considerations; Economic Geology, v. 103, p. 663–687.

Singer, D.A., 1995. World class base and precious metal deposits – A quantitative analysis; Economic Geology, v. 90, p. 88–104.

St.Pierre, B., Mercier-Langevin, P., Blais, J.-C., Servelle, G., Simard, M., Côté-Mantha, O., and Malo, M., 2020. Structural controls and relative timing of gold mineralization of the banded iron formation-associated Tiriganiaq deposit, Meliadine district, Rankin Inlet greenstone belt, Nunavut; *in* Targeted Geoscience Initiative 5: Contributions to the Understanding of Canadian Gold Systems, (ed.) P. Mercier-Langevin, C.J.M. Lawley, and S. Castonguay; Geological Survey of Canada, Open File 8712, p. 237–250. doi:10.4095/326041

Steadman, J.A., Large, R.R., Meffre, S., Olin, P.H., Danyushevsky, L.V., Gregory, D.D., and Holden, P., 2015. Synsedimentary to early diagenetic gold in black shale-hosted pyrite nodules at the Golden Mile deposit, Kalgoorlie, Western Australia; Economic Geology, v. 110, p.1157–1191.

Tassara, S., Gonzáles-Jiménez, J.M., Reich, M., Schilling, M.E., Morata, D., Begg, G., Saunders, E., Griffin, W.L., O'Reilly, S.Y., Grégoire, M., Barra, F., and Corgne, A., 2017. Plume-subduction interaction forms large auriferous provinces; Nature Communications, v. 8, p. 1–7.

Tassara, S., Gonzáles-Jiménez, J.M., Reich, M., Saunders, E., Luguet, A., Morata, D., Grégoire, M., van Acken, D., Schilling, M.E., Barra, F., Nowell, G., and Corgne, A., 2018. Highly siderophile elements mobility in the subcontinental lithospheric mantle beneath southern Patagonia; Lithos, v. 314-315, p. 579–596.

Tassara, S., Reich, M., Konecke, B.A., Gonzáles-Jiménez, J.M., Simon, A.C., Morata, D., Barra, F., Fiege, A., Schilling, M.E., and Corgne, A., 2020. Unraveling the effects of melt-mantle interactions on the gold fertility of magmas; Frontiers of Earth Science. doi:10.3389/feart.2020.00029.

Thomassot, E., O'Neil, J., Francis, D., Cartigny, P., and Wing, B. A., 2015. Atmospheric record in the Hadean Eon from multiple sulfur isotope measurements in Nuvvuagittuq greenstone belt (Nunavik, Quebec); Proceedings of the National Academy of Sciences, v. 112, p. 707–712.

Tomkins, A.G., 2007. Three mechanisms of ore re-mobilisation during amphibolite facies metamorphism at the Montauban Zn-Pb-Au-Ag deposit; Mineralium Deposita, v. 42, p. 627–637.

Tomkins, A.G., 2013. On the source of orogenic gold; Geology, v. 41, p. 1255–1256.

Valette, M., De Souza. S., Mercier-Langevin, P., Côté-Mantha, O., Simard, M., Wodicka, N., McNicoll, V.J., and Barbe, P., 2020. Lithological and tectonic controls on banded iron formation-associated gold at the Amaruq deposit, Churchill Province, Nunavut, and implications for exploration; *in* Targeted Geoscience Initiative 5: Contributions to the Understanding of Canadian Gold Systems, (ed.) P. Mercier-Langevin, C.J.M. Lawley, and S. Castonguay; Geological Survey of Canada, Open File 8712, p. 251–266. doi:10.4095/326042

Wheeler, J.O., Hoffman, P.F., Card, K.D., Davidson, A., Sanford, B.V., Okulitch, A.V., and Roest, W.R., 1996. Geological map of Canada; Geological Survey of Canada, Map 1860A, 3 sheets, scale 1: 5 000 000.

Wood, D., 2018. Geology and mining: an introduction and overview; Soceity of Eeconomical Geologists Newsletter, no. 115, p. 1 and 10–21.

Wyborn, L.A.I., Heinrich C.A., and Jaques A.L., 1994. Australian Proterozoic mineral systems: essential ingredients and mappable criteria; Australian Institute of Mining and Metallurgy Annual Conference, Proceedings, p. 109–115.

Yergeau, D., Mercier-Langevin, P., Dubé, B., Malo, M., McNicoll, V.J., Jackson, S.E., Savoie, A., and La Rochelle, F., 2015. The Archean Westwood Au deposit, southern Abitibi: telescoped Au-rich VMS and intrusion-related Au systems; *in* Targeted Geoscience Initiative 4: Contributions to the understanding of Precambrian lode gold deposits and implications for exploration (ed.) B. Dubé and P. Mercier-Langevin; Geological Survey of Canada, Open File 7852, p. 177–191.

Geology and gold enrichment at the Horne 5 Archean volcanogenic massive sulphide deposit, Abitibi greenstone belt, Quebec: A synthesis

Alexandre Krushnisky[1]*, Patrick Mercier-Langevin[2], Pierre-Simon Ross[1], Jean Goutier[3], Claude Pilote[4], and Claude Bernier[4]

[1]Institut national de la Recherche scientifique – Centre Eau Terre Environnement, 490 rue de la Couronne, Québec, Quebec G1K 9A9
[2]Geological Survey of Canada, 490 rue de la Couronne, Québec, Quebec G1K 9A9
[3]Ministère de l'Énergie et des Ressources naturelles du Québec, 70 avenue Québec, Rouyn-Noranda, Quebec J9X 6R1
[4]Falco Resources Ltd., 161 avenue Murdoch, Rouyn-Noranda, Quebec J9X 1E3
*Corresponding author's e-mail: alex.krushnisky@gmail.com

ABSTRACT

The Archean Horne 5 volcanogenic massive sulphide deposit contains total resources of 172.6 t Au (5.6 Moz; 112.7 Mt at 1.53 g/t Au) with significant Ag, Cu, and Zn as by-products, one of the world's largest volcanogenic massive sulphide-associated gold resource. The deposit consists of stacked massive to semi-massive sulphide lenses that alternate with extensive zones of disseminated and stringer sulphides enclosed within steeply dipping felsic volcaniclastic and shallow synvolcanic intrusive units of transitional to calc-alkaline magmatic affinity. Massive sulphide clasts are locally abundant in the volcaniclastic rocks at several stratigraphic positions.

Gold is interpreted to be synvolcanic and is spatially associated with an assemblage primarily composed of pyrite, sphalerite, and chalcopyrite. Gold distribution in the Horne 5 deposit is largely controlled by the higher porosity and permeability of select host lithologies (fragmental felsic units), which facilitate hydrothermal fluid circulation in the subseafloor environment. The presence of felsic synvolcanic intrusions and fine-grained tuffs overlying auriferous zones also influences the distribution of the mineralization by acting as impermeable cap rocks to ascending fluids. Although part of the mineralization formed below the seafloor, the presence of massive sulphide clasts indicates that sulphide mounds also accumulated on or close to the seafloor. The architecture of the Horne 5 deposit is characterized by along-strike zonation of two dominant metal assemblages, i.e., Zn±Au and Cu-Au, with the Cu-Au assemblage likely representing higher temperature discharge sites. However, the original geometry of the deposit was modified when it was tilted and transposed along the east-west foliation during deformation and metamorphism. Remobilization of metals due to metamorphism and deformation likely occurred at the micro-scale and resulted primarily in the exsolution of gold and its associated trace elements from recrystallized pyrite.

This study provides further evidence for a major synvolcanic gold event in the southern Abitibi. It indicates that the Horne deposit is associated with calc-alkaline felsic volcanic rocks and is consistent with the preferential association between Archean synvolcanic gold and the early phases of rifting of a thickened arc crust towards the end of the southern Abitibi greenstone belt volcano-magmatic construction.

INTRODUCTION

The Horne 5 volcanogenic massive sulphide (VMS) deposit is currently one of the largest gold exploration targets in Canada. Resources are estimated at 112.7 Mt at 1.53 g/t Au (172.6 t or 5.6 Moz Au: www.falcores.com), with significant Ag, Cu, and Zn as by-products. The Horne 5 deposit is located in the Noranda camp in the southern part of the Archean Abitibi greenstone belt (Fig. 1), downdip of the historic Horne mine workings (Fig. 2). The Horne mine is the largest known example of gold-rich VMS mineralization, with a production history of 53.7 Mt of ore at 6.06 g/t Au (325.4 t or 10.5 Moz Au), 2.2% Cu, and 13.0 g/t Ag (Mercier-Langevin et al., 2011a), extracted largely from the Upper H and Lower H orebodies between 1927 and 1976 (Kerr and Mason, 1990; Cattalani et al., 1993).

Access to new material from the Horne 5 deposit following exploration drilling by Falco Resources provides an ideal opportunity to study gold-enrichment processes in a large Archean synvolcanic system (Krushnisky, 2018; Krushnisky et al., in prep). The results of this study are based on detailed drill core log-

Krushnisky, A., Mercier-Langevin, P., Ross, P.-S., Goutier, J., Pilote, C., and Bernier, C., 2020. Geology and gold enrichment at the Horne 5 Archean volcanogenic massive sulphide deposit, Abitibi greenstone belt, Quebec: A synthesis; *in* Targeted Geoscience Initiative 5: Contributions to the Understanding of Canadian Gold Systems, (ed.) P. Mercier-Langevin, C.J.M. Lawley, and S. Castonguay; Geological Survey of Canada, Open File 8712, p. 31–44. https://doi.org/10.4095/323663

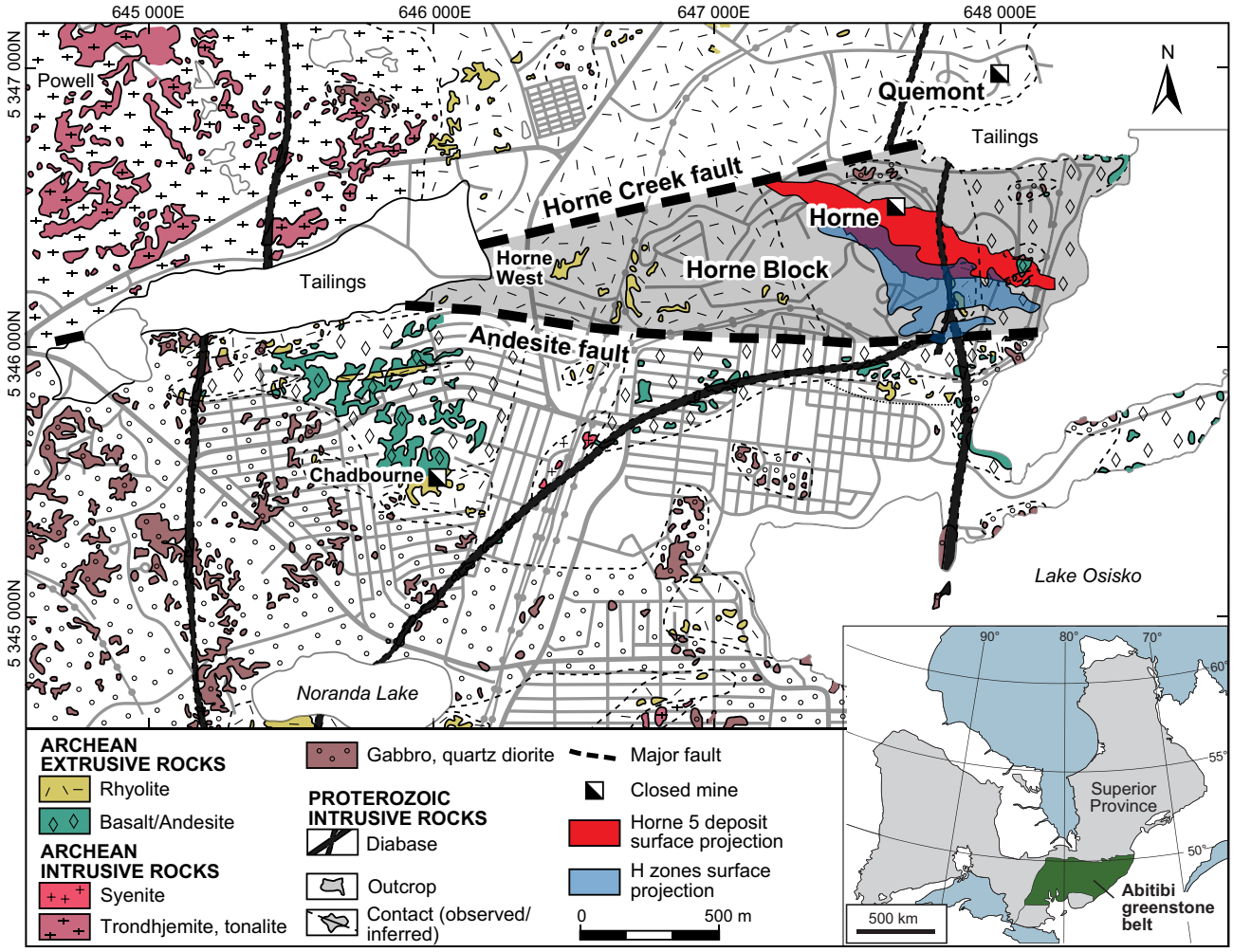

Figure 1. Geological map of the Horne Block (*modified from* Monecke et al., 2008). The trace of the Horne 5 lens (in red) and the Upper and Lower H zones (in blue; from Cattalani et al., 1993) are projected to the surface. Map coordinates are in UTM NAD83 Zone 17.

ging and sampling, whole-rock lithogeochemistry (Krushnisky et al., 2018), petrography, 3-D modeling, and micro-analyses of sulphide and alteration minerals. This project aims to provide a detailed documentation of the volcanic, hydrothermal, and structural context of the Horne 5 deposit to determine the principal controls on the timing and distribution of gold mineralization at various scales and to assess the effects of the deformation and metamorphism on gold remobilization.

This contribution presents a summary of the project that was conducted in collaboration between Natural Resources Canada, the Institut national de la Recherche scientifique, Falco Resources Limited, and the Ministère de l'Énergie et des Ressources naturelles du Québec. Readers are referred to Krushnisky (2018) and Krushnisky et al. (2018, in prep) for details.

GEOLOGICAL SETTING

The Horne 5 deposit is located in the Blake River Group within the southern Abitibi greenstone belt (Fig. 1). The 2704–2695 Ma Blake River Group consists of a sequence of subalkaline mafic to felsic volcanic rocks intruded by syn- to post-volcanic plutons and dykes (Dimroth et al., 1982; Piercey et al., 2008; Mueller et al., 2012; McNicoll et al., 2014). The geodynamic setting of the Blake River Group is interpreted to be analogous to modern island arc environments (e.g. the eastern Manus Basin of Papua New Guinea; Dimroth et al., 1983a,b; Mercier-Langevin et al., 2007; Monecke et al., 2017). The Blake River Group hosts a large number of VMS and Au-VMS deposits, which are mostly associated with rifting of the arc crust centred on the Noranda camp (Gibson, 1989; Gibson and Galley, 2007). An alternative to the rift model suggests that the Blake River Group is an ancient mega-caldera complex that hosts VMS mineralization along caldera structures (Mueller et al., 2009; Pearson and Daigneault, 2009; Moore et al., 2016).

Horne Block

The Horne 5 deposit lies in a structural wedge of felsic volcanic rocks referred to as the Horne Block, which is

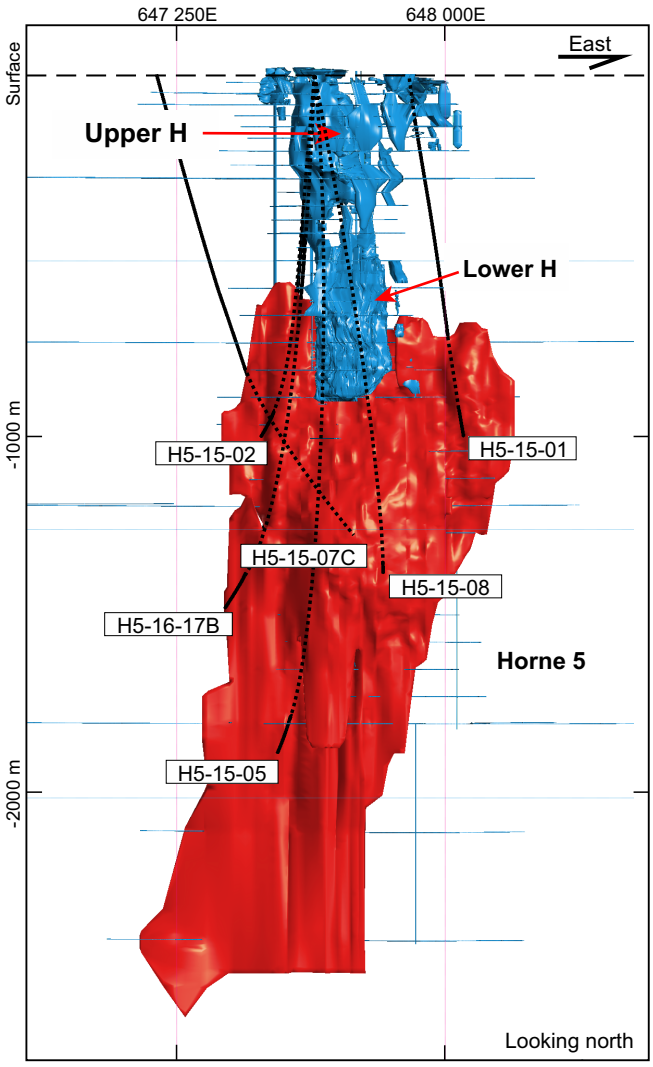

Figure 2. Three-dimensional model of the Horne 5 deposit (in red) showing the six drillholes that were relogged in detail and sampled during this project. The Horne mine workings are also shown in blue.

bound by the Horne Creek fault (north) and Andesite fault (south; Fig. 1). The volcanic rocks consist of dacitic to rhyolitic flows and domes with large volumes of associated volcaniclastic rocks, as well as minor pyroclastic rocks (Price, 1934; Sinclair, 1971; Kerr and Mason, 1990; Kerr and Gibson, 1993; Gibson et al., 2000). High-precision U-Pb dating of a coherent rhyolite in the lowermost part of the Horne sequence (2702.2 ± 0.9 Ma: McNicoll et al., 2014) indicates that the rocks in the block are amongst the oldest in the Blake River Group and predate the volcanic sequence of the Noranda Main camp and its archetypal Cu-Zn VMS deposits by approximately three to four million years.

Deformation within the Horne Block is considered moderate in intensity and is characterized by an east-west-oriented, subvertical foliation (Price, 1948; Barrett et al., 1991; Cattalani et al., 1993). The stretching lineation is vertical near the Andesite fault and inclined at 80°E near the Horne Creek fault (Cattalani et al., 1993). Regional metamorphism reached greenschist facies in the area (Dimroth et al., 1983b; Powell et al., 1995).

GEOLOGY OF THE HORNE 5 DEPOSIT

Volcanology and Lithogeochemistry of the Host Units

The Horne 5 deposit is hosted in a succession of felsic volcaniclastic rocks of transitional to calc-alkaline magmatic affinity (Krushnisky, 2018). This felsic package is steeply inclined, dips and faces north to north-northeast and is oriented west-northwest to east-southeast (Fig. 3; Price, 1934; Sinclair, 1971). Diagenesis, hydrothermal alteration, metamorphism, and deformation have affected these rocks to varying degrees, but in general, primary volcanic textures are relatively well preserved. The felsic succession is stratigraphically overlain by a number of calc-alkaline to tholeiitic basaltic intrusions that occupy the northern portion of the Horne Block up to the Horne Creek fault (Fig. 3).

Horne 5 footwall rhyolite

A series of coherent, felsic rocks and related in-situ breccia or pseudo-breccia are present locally in the footwall of the mineralized zones. These rocks are characterized by rhyolitic compositions (Fig. 4a,b: footwall rhyolite), with SiO_2 values generally above 73 wt% and by a transitional to calc-alkaline magmatic affinity (Fig. 4c).

Dacitic-rhyodacitic volcaniclastic and shallow intrusive unit

Volcaniclastic rocks of dacitic to rhyodacitic compositions (Fig. 4a,b: dacitic-rhyodacitic volcaniclastic rocks) are the principal hosts to the Horne 5 mineralized zones. Although felsic rocks in the Horne Block were mostly considered to be tholeiitic in past studies (Kerr and Mason, 1990; Barrett et al., 1991; Cattalani et al., 1993; Kerr and Gibson, 1993), this study demonstrates that the rocks hosting the Horne 5 deposit are in fact of calc-alkaline to transitional magmatic affinity (Fig. 4c; Krushnisky et al., 2018). This unit extends into the footwall and hanging wall of the deposit.

The volcaniclastic rocks are composed dominantly of aphanitic dacitic-rhyodacitic clasts, some of which exhibit flow-banding textures. Strongly vesicular sericite-rich clasts and massive sulphide fragments are also present throughout. Two principal fragmental facies are recognized: 1) moderately to poorly sorted lapilli tuff to tuff breccia, and 2) graded tuff occurs predominantly towards the stratigraphic upper portion of

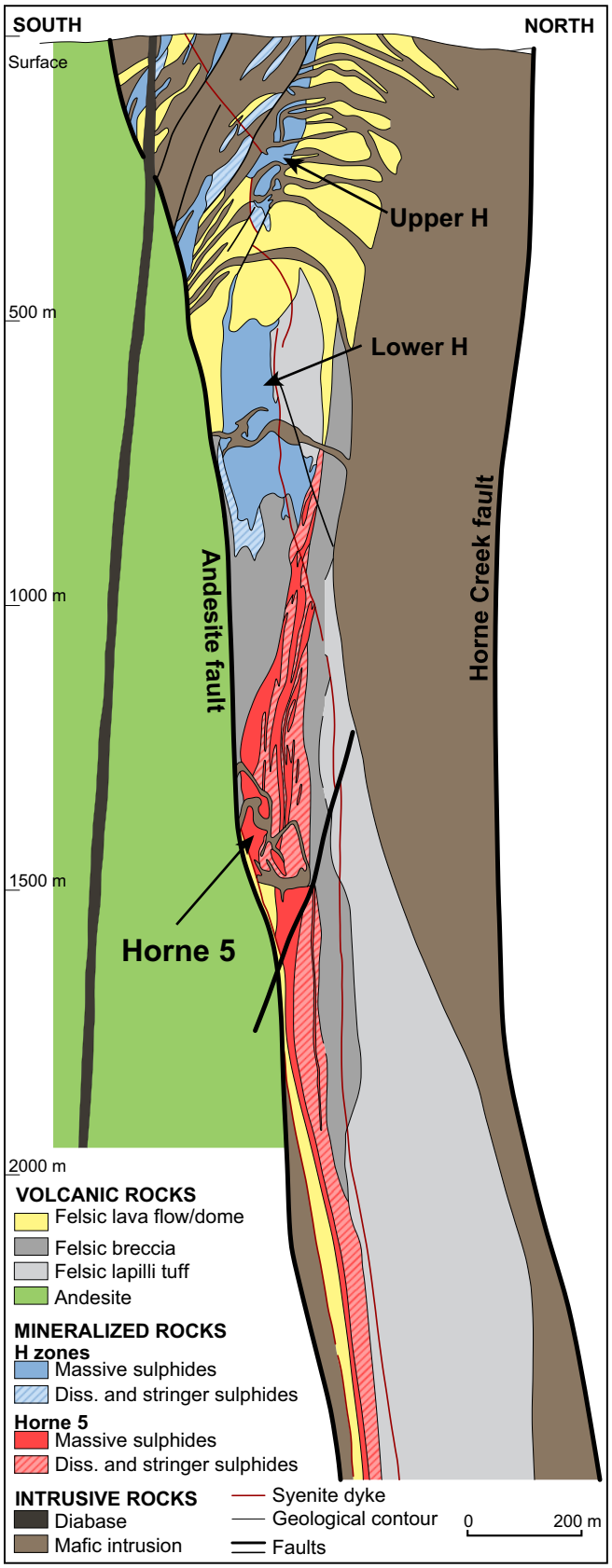

Figure 3. North-south composite section of the Horne Block at 647760 m E, showing the principal lenses of the Horne deposit (*modified from* Cattalani et al., 1993).

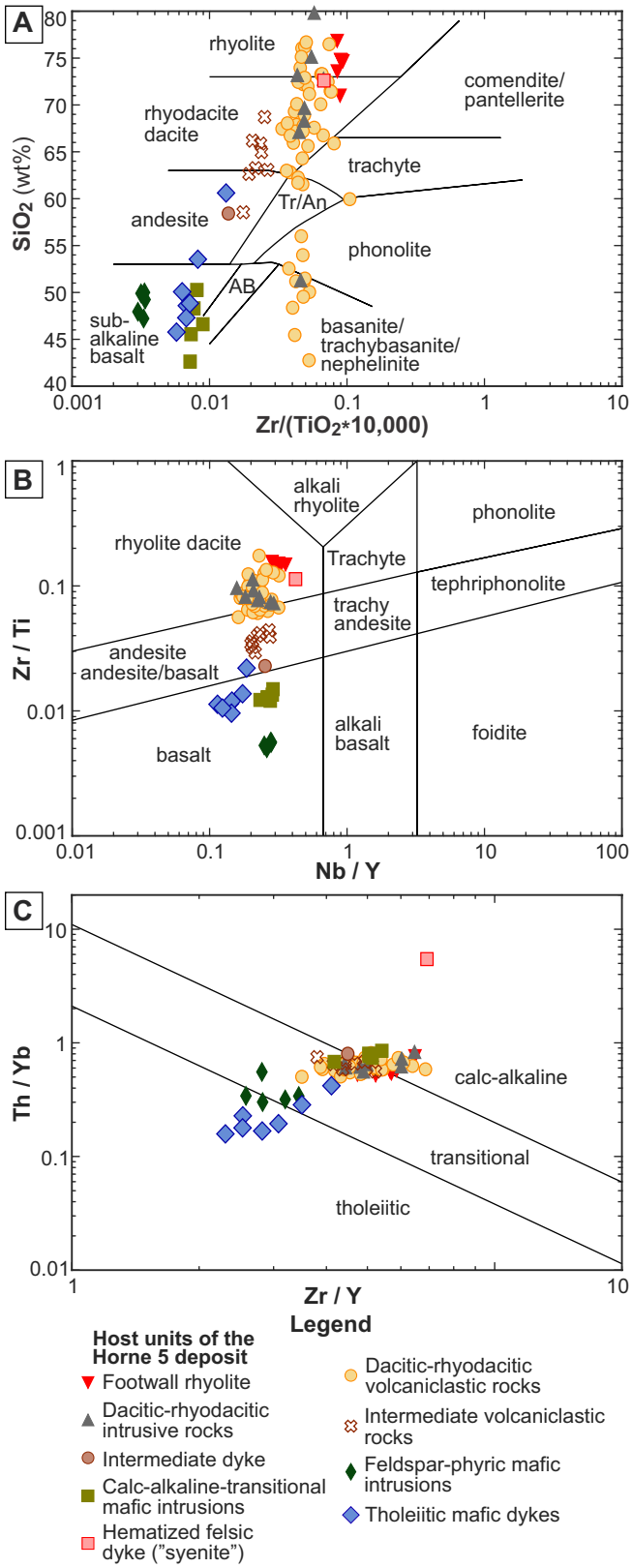

Figure 4. Major and trace element plots of the host units of the Horne 5 deposit. **a)** SiO_2 versus $Zr/(TiO_2*10{,}000)$ classification diagram of Winchester and Floyd (1977). **b)** Zr/Ti versus Nb/Y classification diagram of Pearce (1996). **c)** Th/Yb versus Zr/Y diagram for discrimination of magmatic affinities from Ross and Bédard (2009).

the mineralized zones and in the hanging wall. The volcaniclastic rocks are inferred to have formed from mass flows associated with fragmentation and mass wasting of felsic lava flows or domes upslope on a submarine volcanic edifice (Krushnisky, 2018).

A series of felsic coherent rocks intruding into the fragmental rocks are also part of this unit. The presence of peperite along the margins of some of the intrusions indicates that they were emplaced in water-saturated, non-consolidated fragmental rocks. They are interpreted as felsic synvolcanic sills that intruded the volcaniclastic rocks at relatively shallow depths below the seafloor. These intrusions closely resemble the felsic clasts of the volcaniclastic rocks in mineralogy, textures, and geochemistry (Fig. 4a–c: dacitic-rhyodacitic intrusive rocks), suggesting a petrogenetic link (Krushnisky, 2018; Krushnisky et al., in prep).

Intermediate volcaniclastic unit

Volcaniclastic rocks characterized by intermediate compositions (Fig. 4a,b: intermediate volcaniclastic rocks) and transitional magmatic affinities (Fig. 4c) are present along two horizons in the hanging wall of the mineralized zones, intercalated with the dacitic-rhyodacitic volcaniclastic rocks. In addition to felsic clasts, the intermediate volcaniclastic rocks contain a high proportion of intermediate to mafic clasts within a matrix composed of chlorite, sericite, and epidote-altered relict amphibole crystals, giving them a distinctly polymictic appearance.

Hanging-wall mafic intrusions

An intermediate dyke of transitional magmatic affinity (Fig. 4a–c: intermediate dyke) intrudes the felsic volcaniclastic rocks in the hanging wall of the mineralized zones. This feldspar and quartz-phyric intrusion contains abundant quartz-pyrite-epidote amygdules.

A unit of feldspar-phyric mafic intrusions overlies the dacitic-rhyodacitic volcaniclastic rocks and is characterized by a basaltic composition (Fig. 4a,b: feldspar-phyric mafic intrusions) and a transitional to tholeiitic magmatic affinity (Fig. 4c). This unit has a distinctive porphyritic texture with 5–20 vol.% feldspar and 5–15 vol.% amphibole and pyroxene phenocrysts.

Mafic intrusions of calc-alkaline to transitional magmatic affinities (Fig. 4c: calc-alkaline-transitional mafic intrusions) and subalkaline to alkaline basaltic compositions (Fig. 4a,b) occur between the feldspar-phyric intrusion and the Horne Creek fault. These intrusions are coarser grained and contain 10–40 vol.% amphibole and 5–20 vol.% feldspar in a heavily chloritized groundmass.

A series of dark green mafic dykes crosscut the Horne 5 stratigraphic succession. The dykes are characterized by a basaltic composition (Fig. 4a,b: tholeiitic mafic dykes) and a tholeiitic to transitional magmatic affinity (Fig. 4c). Their groundmass is very fine-grained (<0.1–0.2 mm) and strongly altered to chlorite and epidote, with minor sericite, magnetite, and pyrite.

Hematized felsic dykes ("syenites")

The volcanic and intrusive succession of the Horne Block is crosscut by a series of dark red to grey-red felsic dykes (Price, 1934; Barrett et al., 1991). Some of these dykes crosscut massive sulphide lenses in the Horne 5 mineralized zones. Although these felsic dykes are often referred to as syenites in the literature, Price (1934) noted important compositional variations that ranged from granitic to syenitic compositions throughout the Horne Block. Petrographic observations from this study agree with the more granitic to tonalitic compositions, with high quartz content (30 vol.%: Krushnisky, 2018). Whole-rock geochemistry for the relatively few samples available indicates a rhyolitic to dacitic composition (Fig. 4a,b) and a calc-alkaline magmatic affinity (Fig. 4c).

Hydrothermal Alteration

The Horne 5 mineralized zones are associated with a broad halo of sericite, which extends 100s of metres along strike and >1500 m along dip from the deposit and contains several higher intensity alteration zones. Although greenschist-facies metamorphism may have recrystallized some of the primary alteration phases to secondary minerals, metamorphic changes to the overall rock chemistry are considered minimal and local in scale, since no significant metasomatic textures are present (e.g. no large-scale veins indicating the passage of large quantities of metamorphic fluids, no coarse-grained altered volcanic rocks indicating high metamorphic grades; Krushnisky, 2018).

Moderate sericite-chlorite-epidote alteration

The sericite-chlorite-epidote alteration assemblage affects most of the dacitic-rhyodacitic unit, from the hanging wall to the footwall of the Horne 5 deposit. Partially preserved volcanic textures and Hashimoto alteration index (AI: Ishikawa et al., 1976; Fig. 5) values range from 20 to 55, indicating a moderate alteration intensity (Gifkins et al., 2005). Alteration phases are restricted to the matrix of volcaniclastic rocks, clast margins, fractures, and phenocrysts, and include foliated sericite (10–25 vol.%) and chlorite (5–15 vol.%), disseminated epidote (1–10 vol.%), and <5 vol.% pyrite, albite, carbonate, and hematite (Fig. 6a). This assemblage is associated with weak losses in Na_2O, very weak gains in MgO and CaO, and gains in FeO^T and SiO_2 (Krushnisky, 2018).

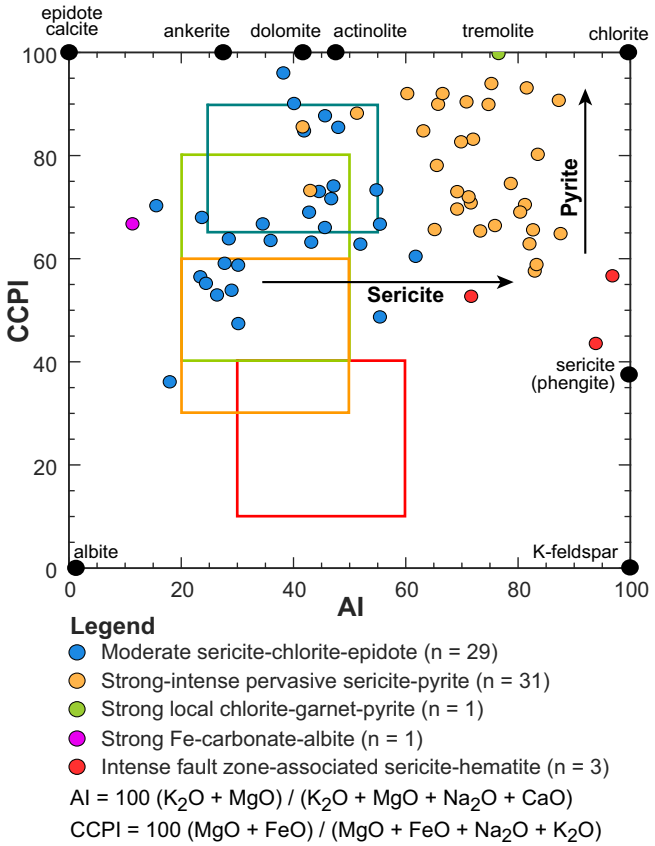

Figure 5. Alteration box plot of Large et al. (2001) for the principal alteration facies within the Horne 5 dacitic-rhyodacitic unit. Coloured rectangles in the alteration box plot represent least altered fields (*from* Gifkins et al., 2005): red = rhyolite least altered field, orange = dacite field, green = andesite field, blue = basalt field.

Strong to intense pervasive sericite-pyrite

Rocks within 10s of metres of massive sulphide lenses are characterized by strong gains in FeO^T and K_2O and leaching of MgO, CaO, and Na_2O. The abundance of strongly foliated sericite and disseminated to massive pyrite imparts a bleached appearance to the host rocks (Fig. 6b). Spessartine garnets occur locally in the footwall and contain 26.9 to 29.3 wt% MnO (Krushnisky, 2018).

The zonation from distal, moderately altered rocks to proximal, intensely altered zones at Horne 5 forms a trend of increasing AI and chlorite-carbonate-pyrite index (CCPI: Large et al., 2001) values that reflect the increasing relative abundance of sericite and pyrite towards the mineralized zones (Fig. 5). Variations in mineral chemistry are also present, with changes in white mica and epidote composition and increases in Mn content in chlorite and carbonate towards the mineralized zones (Krushnisky, 2018).

Strong local chlorite-garnet-pyrite

A few bands of strongly chloritized rocks (≤2 m in thickness) crosscut the moderate sericite-chlorite-epidote assemblage locally in the hanging wall of the mineralized zones. Foliated bands of chlorite (25–30 vol.%) associated with approximately 5 vol.% garnet and pyrite, and <5 vol.% carbonate and magnetite, overprint the felsic volcaniclastic rocks (Fig. 6c). Geochemically, this assemblage plots near the chlorite pole in the alteration box plot (Fig. 5) and is characterized by strong gains in FeO^T and MgO, and losses in CaO, Na_2O, and K_2O.

Strong local Fe-carbonate-albite

Local magnetite-chalcopyrite mineralization is associated with an alteration assemblage comprising siderite, ankerite, and albite, with minor quartz and chlorite. Carbonate generally occur interstitially within massive magnetite along with chalcopyrite and pyrite, and locally appear to be intergrown with magnetite grains. This assemblage is characterized by low AI values (Fig. 5) and important gains in FeO^T and Na_2O.

Intense fault zone-associated sericite-hematite

A fault zone crosscuts the felsic volcaniclastic rocks in the hanging wall of the mineralized zone in drill hole H5-15-05. Faulted rocks are intensely altered and lack any recognizable primary volcanic features. The associated alteration assemblage is characterized by pervasive sericite, fracture-controlled chlorite and carbonate, and disseminated hematite. This assemblage plots towards the sericite pole on the alteration box plot (Fig. 5) and shows strong overall mass losses with leaching of most elements, except for a strong gain in K_2O and a weaker gain in MgO.

Chlorite-epidote-sericite alteration of mafic intrusions

Most intermediate to mafic intrusions at Horne 5 are weakly altered, showing mostly an increase in CCPI. Alteration phases include weakly foliated chlorite and sericite, disseminated epidote and quartz-carbonate veinlets (Fig. 6d). Tholeiitic mafic dykes are the most strongly altered of the intrusions, with the intensity of alteration increasing for samples closer to or within the Horne 5 mineralized zones.

GOLD AND SULPHIDE MINERALIZATION

Geometry of the Mineralized Zones

The Horne 5 deposit consists of a low-grade mineralized envelope (Fig. 2), defined at a cut-off grade of 0.5 g/t Au, that encloses a number of high-grade Au (≥2.5 g/t), Cu (≥0.2 wt%), and Zn (≥0.75 wt%) zones. The mineralized envelope presently lies in a subvertical position that extends from 600 m below the surface to a depth of at least 2500 m and is oriented subparallel to the local felsic stratigraphy.

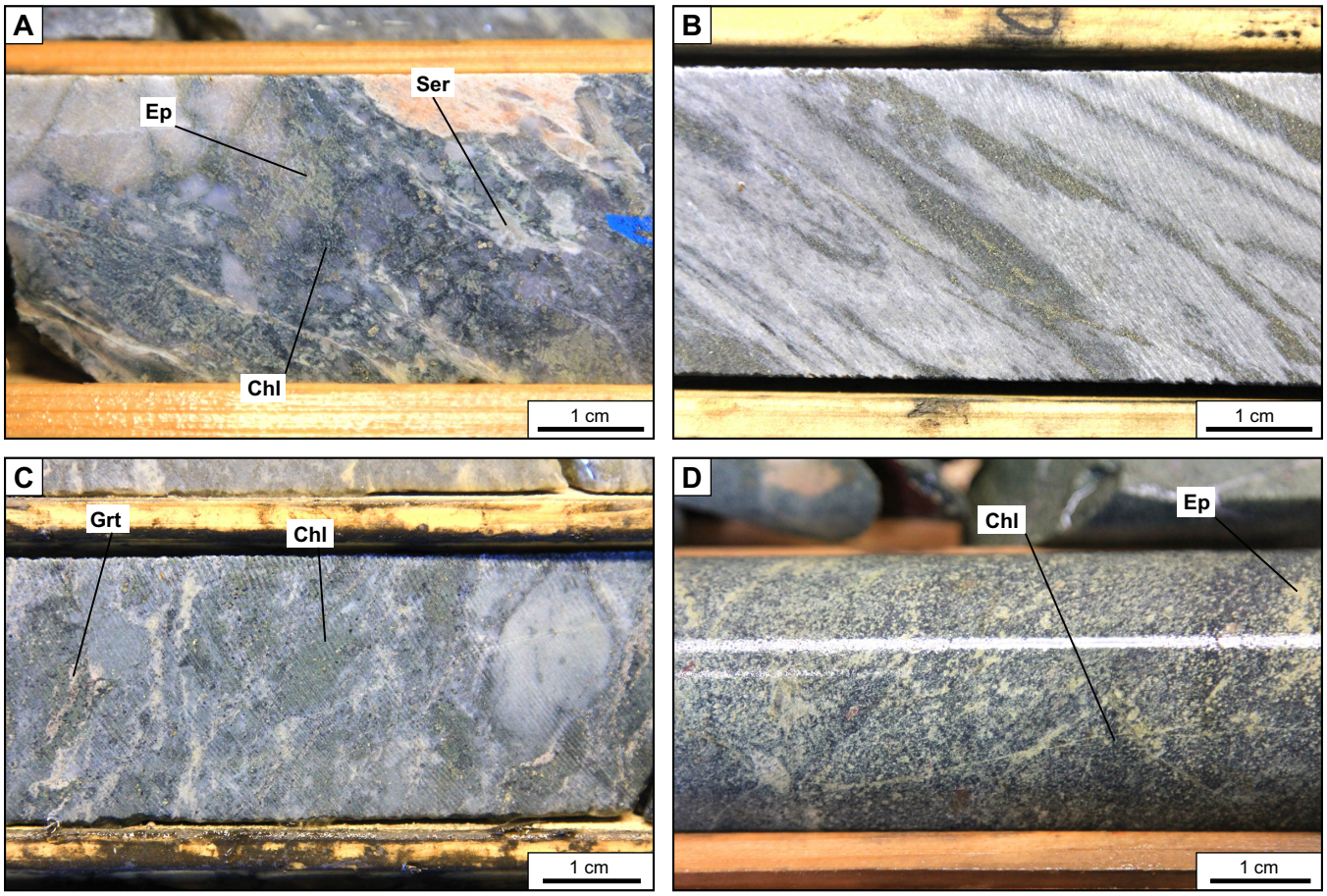

Figure 6. a) Moderate sericite-chlorite-epidote alteration assemblage in felsic volcaniclastic rocks (ddh H5-15-02, 975 m). **b)** Intense pervasive sericite-pyrite alteration assemblage typical of the mineralized intervals (ddh H5-15-02, 1067 m). **c)** Chlorite-garnet-pyrite alteration in a felsic volcaniclastic rock (ddh H5-15-02, 1140 m). **d)** Chlorite-sericite-epidote alteration assemblage in a mafic intrusive rock (ddh H5-15-02, 895 m). Abbreviations: Chl = chlorite, ddh = diamond drillhole, Ep = epidote, Grt = garnet, Ser = sericite.

The original geometry of the deposit was likely modified by deformation (Krushnisky, 2018). Effects of the deformation on the deposit include shearing and transposition along the east-west foliation, subvertical stretching, with the long axis of the deposit oriented subparallel to the local stretching lineation, and strong east-west shearing and fragmentation of individual massive sulphide lenses (Sinclair, 1971).

Styles of Mineralization

The Horne 5 mineralized zones are composed of extensive zones of disseminated and stringer sulphides containing a series of stacked semi-massive (>30 vol.% sulphides) to massive (>70 vol.% sulphides) lenses. Massive sulphide fragments are present at several stratigraphic levels within the mineralized zones. The structural upper eastern part of the deposit hosts semi-massive to massive magnetite-chalcopyrite mineralization.

Disseminated and stringer mineralization are hosted in a matrix of felsic volcaniclastic rocks, on felsic clast margins, and along fractures and flow bands in synvolcanic felsic intrusions. Locally, partial replacement of felsic clasts occurs where mineralization is more abundant (Fig. 7a). Pyrite is the predominant sulphide, but minor amounts of sphalerite and chalcopyrite are also present locally. Sulphides show evidence of recrystallization and remobilization due to deformation and metamorphism, and sulphide stringers are often partially transposed into the main foliation (Fig. 7b).

Semi-massive to massive sulphide mineralization consists of fine-grained to locally coarser grained pyrite (Fig. 7c), sphalerite, chalcopyrite, and trace pyrrhotite, galena, stannite, cassiterite, and a variety of Au, Ag, and Pb tellurides (Krushnisky, 2018). A gradual increase in sulphides is observed towards massive sulphide lenses and strongly altered felsic clasts are often preserved within massive mineralization. Pyrite grains occasionally exhibit relict primary hydrothermal textures, including spheroidal and nodular textures, colloform textures (Fig. 7d), and spongy textures, as documented in younger, less deformed massive sulphides and modern seafloor deposits (e.g. Eldridge et al., 1983; de Ronde et al., 2011). Cataclastic pyrite is

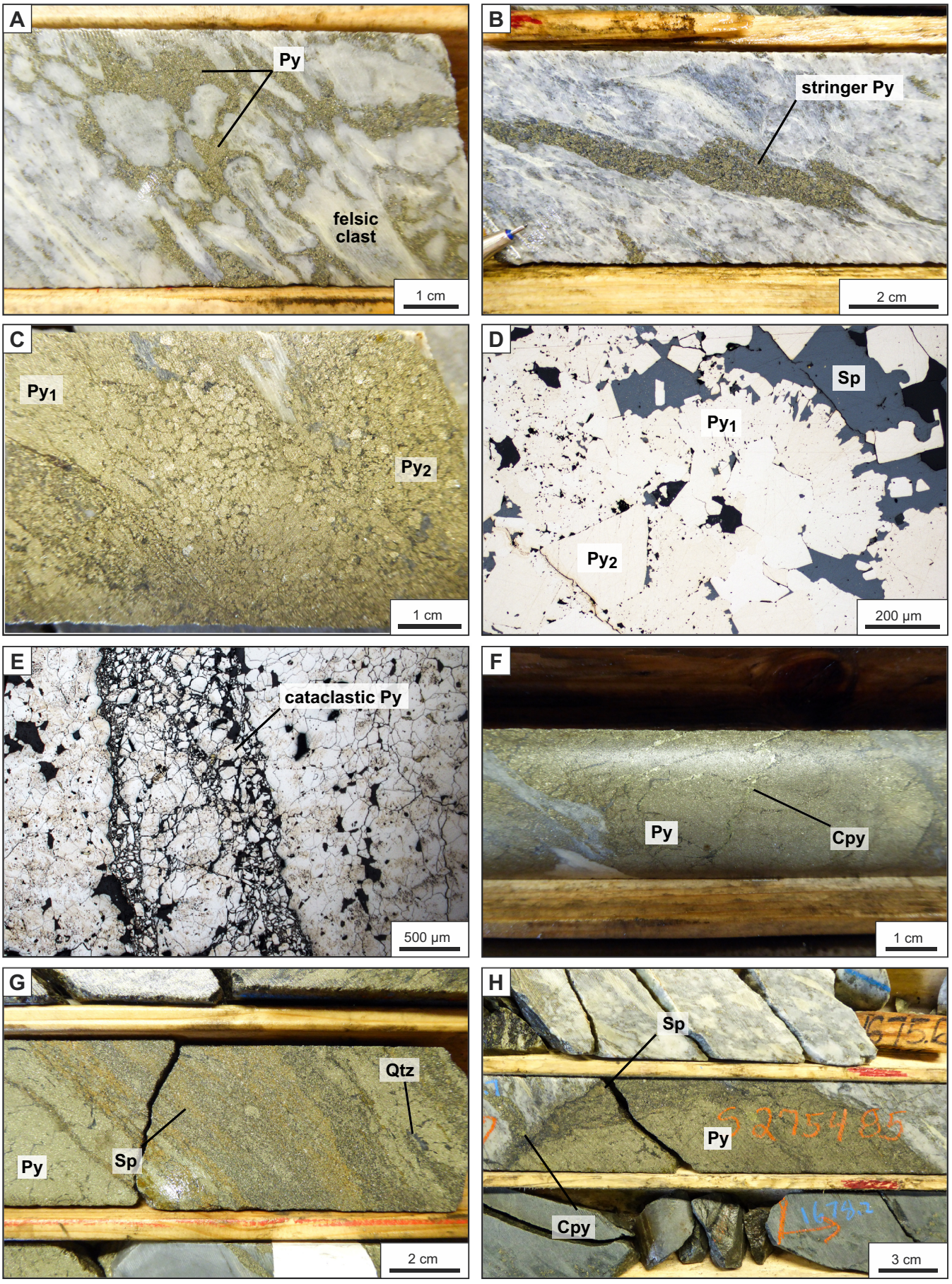
A
Py
felsic clast
1 cm
B
stringer Py
2 cm
C
Py1
Py2
1 cm
D
Sp
Py1
Py2
200 µm
E
cataclastic Py
500 µm
F
Py
Cpy
1 cm
G
Qtz
Sp
Py
2 cm
H
Sp
Py
Cpy
3 cm

also commonly present (Fig. 7e) and results from post-depositional brittle deformation. Three subtypes of semi-massive to massive mineralization are distinguished based on mineralogy and metal content: 1) Cu-Au-rich massive pyrite-chalcopyrite (Fig. 7f), located predominantly in the structural eastern portion of the Horne 5 deposit; 2) Zn±Au-rich massive pyrite-sphalerite (Fig. 7g), found in the structural upper-western part of the deposit; and 3) Au-poor massive pyrite lenses present locally along the stratigraphic base of the mineralized zones.

Massive sulphide fragments (Fig. 7h) within the mineralized zones are characterized by mineralogy and geochemistry that show close similarities with the semi-massive to massive mineralization. Gold content of the sulphide fragments is generally elevated, with a mean of 3.2 g/t Au (Krushnisky, 2018; Krushnisky et al., in prep). These fragments are rounded to sub-rounded with sharp contacts and their distribution is stratiform, suggesting a clastic origin. They were likely sourced from sulphide lenses exposed on or near the paleo-seafloor by felsic mass flows, which incorporated them in the volcaniclastic rocks.

Semi-massive to massive magnetite-chalcopyrite mineralization consists of fine-grained magnetite in the matrix of felsic volcaniclastic rocks. Magnetite grains locally overprint and replace granoblastic pyrite. Chalcopyrite occurs interstitially within massive magnetite and as stringers along fractures. Areas with abundant magnetite-chalcopyrite mineralization generally display relative Au and Ag depletion and higher Cu grades (Krushnisky, 2018). This mineralization style is possibly associated with the intrusion of the Proterozoic diabase dykes that crosscut this area of the Horne 5 deposit and may be due to contact metamorphism, as was similarly demonstrated by Mookherjee and Suffel (1968) in the Upper and Lower H zones.

Trace Element Geochemistry and Distribution

The Horne 5 mineralized zones contain anomalously elevated values of Pb, Te, Cd, Sn, Hg, and In in addition to significant Au, Ag, Cu, and Zn grades. Statistical analyses show two principal metal assemblages: 1) Cu-Au-Te±Ag±Pb assemblage and 2) Zn-Cd-Sn-Hg-In±Au±Ag±Pb assemblage (Fig. 8). In the pyrite-chalcopyrite mineralization, trace elements, such as Au, Te, Ag and Pb, are concentrated in pyrite, either within its crystal structure and/or as inclusions of tellurides and electrum. Sphalerite is an important host for Cd, Hg, and In in the pyrite-sphalerite mineralization, whereas Ag and Pb are mainly hosted in galena and tellurides (cf. Cook et al., 2009; George et al., 2016).

At the deposit scale, Au, Ag, Cu, and Zn concentrations correlate well with sulphide abundance. Moreover, metal-rich semi-massive to massive mineralization is generally distributed along beds of coarse-grained and permeable volcaniclastic rocks, such as coarse lapilli tuff to tuff breccia units.

The Au distribution correlates relatively well with Cu-rich zones in the structural eastern portion of the deposit, especially at depths below 1200 m (Fig. 9). However, a few high-grade Au zones are not associated with significant Cu grades, such as a subvertical linear zone of Au enrichment stratigraphically overlying the western Zn-rich zones (Krushnisky, 2018). Local Au remobilization during east-west shearing towards low-strain sites is inferred from cross-sections of Au distribution (Fig. 9).

A relatively strong Cu-Zn zonation is present along strike of the deposit. The western part of the deposit is characterized by Zn±Au-rich pyrite-sphalerite mineralization, whereas the eastern portion is composed predominantly of Cu-Au-rich pyrite-chalcopyrite mineralization. A subtle Cu-Zn zonation is also present upwards from the footwall to the hanging wall of the deposit, with higher Cu grades distributed towards the stratigraphic base of the deposit and higher Zn grades towards the top of the deposit.

At the mineral scale, Au is concentrated in relict primary pyrite textures, such as spheroidal pyrite (Fig. 10). In relict primary pyrite, Au often occurs as lattice substitutions or as nano-sized particles, as indicated by relatively homogeneous laser-ablation inductively-coupled plasma mass spectrometry analytical signals (cf. Huston et al., 1995; Deditius et al., 2011). Gold correlates well with Te within relict primary pyrite,

Figure 7 opposite page. a) Disseminated pyrite (Py) mineralization preferentially developing in the matrix of felsic volcaniclastic rocks and partially replacing clast margins (ddh H5-15-07C, 1690.6 m). **b)** Partially transposed pyrite stringer within strongly altered felsic volcaniclastic rock located directly below a massive sulphide lens (ddh H5-15-07C, 1627.6 m). **c)** Fine-grained massive pyrite (Py_1) texture intermingled with coarser grained granoblastic pyrite (Py_2; ddh H5-15-07C, 1729.3 m). **d)** Photomicrograph (reflected light) of relict colloform pyrite texture showing radiating blades (Py_1) partially filled with massive sphalerite (Sp) and partially growing on euhedral pyrite porphyroblasts (Py_2, ddh H5-15-02, 1047.4 m). **e)** Photomicrograph (reflected light) of cataclastic pyrite showing strong brittle fragmentation of grains (ddh H5-15-01, 1159.4 m). **f)** Remobilized chalcopyrite (Cpy) along fractures in massive pyrite-chalcopyrite mineralization (ddh H5-15-08, 1535.2 m). **g)** Banded pale orange sphalerite with minor quartz (Qtz) gangue in massive pyrite-sphalerite mineralization (ddh H5-15-02, 1083.4 m). **h)** Round massive pyrite block with abundant pale orange sphalerite along the edges. Chalcopyrite is remobilized along a fracture in the felsic host rock (ddh H5-15-07C, 1676.7 m).

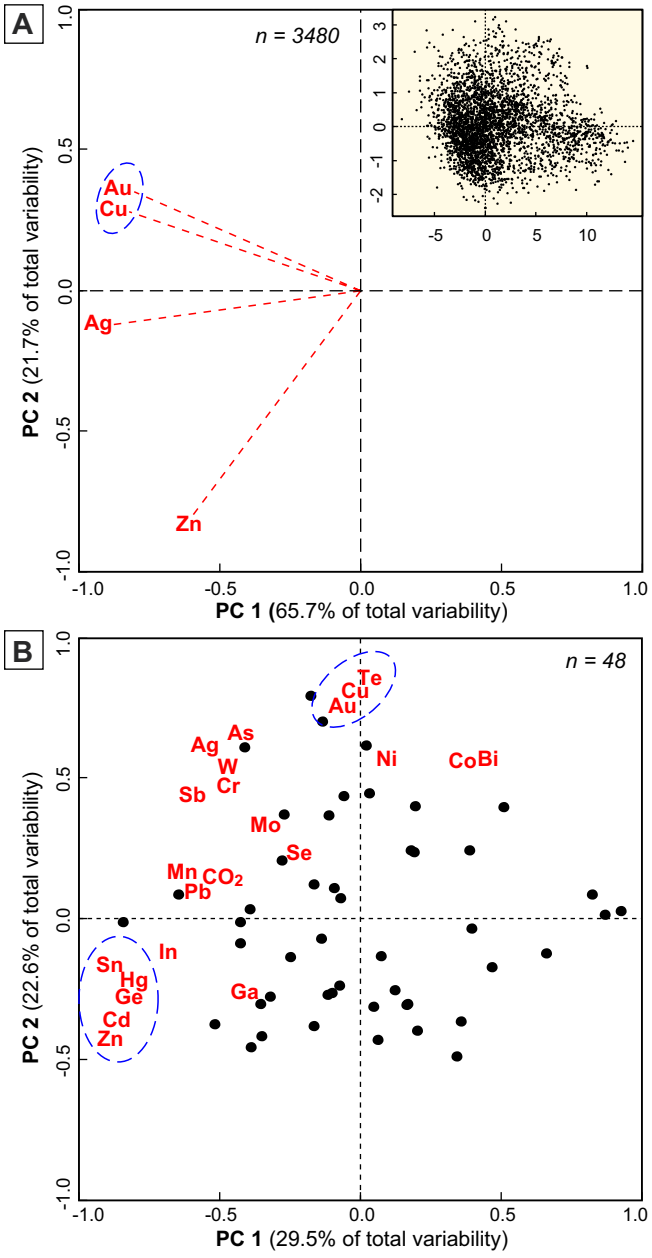

Figure 8. Principal component analyses performed in *R* programming language using the *rgr* package (Garrett, 2013). All data were standardized and transformed using a centred log ratio. **a)** Plot of the first and second principal components resulting from a robust principal components analysis (*gx.robmva.closed* function; minimum covariance determinant procedure) of Falco Resources Limited's historical database for Au, Ag, Cu, and Zn assays. Variables are shown in red and the individual data points are shown in the inset on a different scale. **b)** Plot of the first and second principal components (*gx.mva.closed* function) resulting from whole-rock geochemical analysis of most of the trace elements within the massive sulphide samples collected during this study. Variables (in red) and data points (black circles) are on the same scale and can be directly compared. Abbreviation: PC = principal component.

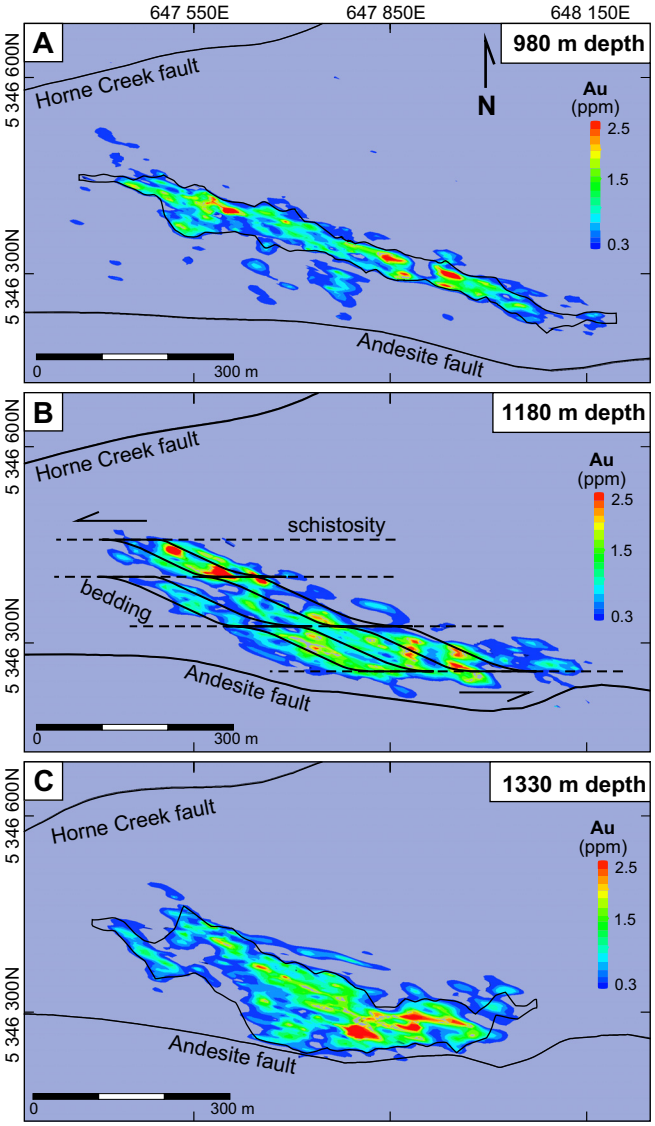

Figure 9. Sections of gold distribution in the Horne 5 deposit at **(a)** 980, **(b)** 1180, and **(c)** 1330 m depths. The outline of the Horne 5 mineralized envelope (≥0.5 g/t Au) is shown. Interpolations were performed in the *Leapfrog*™ software. Interpolation parameters can be found in Appendix E of Krushnisky (2018).

suggesting that these elements were transported in the same hydrothermal fluids that precipitated volcanogenic pyrite. In recrystallized pyrite, most trace elements occur as inclusions, such as galena, altaite, hessite, petzite and electrum, along grain boundaries, fractures, or in the surrounding silicates. Recrystallized pyrite contains very low trace element concentrations within its structure, except for elements such as As and Se (e.g. on the rim of spheroidal pyrite; Fig. 10).

DISCUSSION

This study provides several lines of evidence in favour of the synvolcanic nature of Au enrichment at the Horne 5 deposit. Gold deposition is interpreted to be contemporaneous to sulphide precipitation within a relatively large-scale VMS hydrothermal system. The presence of gold-enriched massive sulphide fragments in the mineralized zones indicates that early auriferous

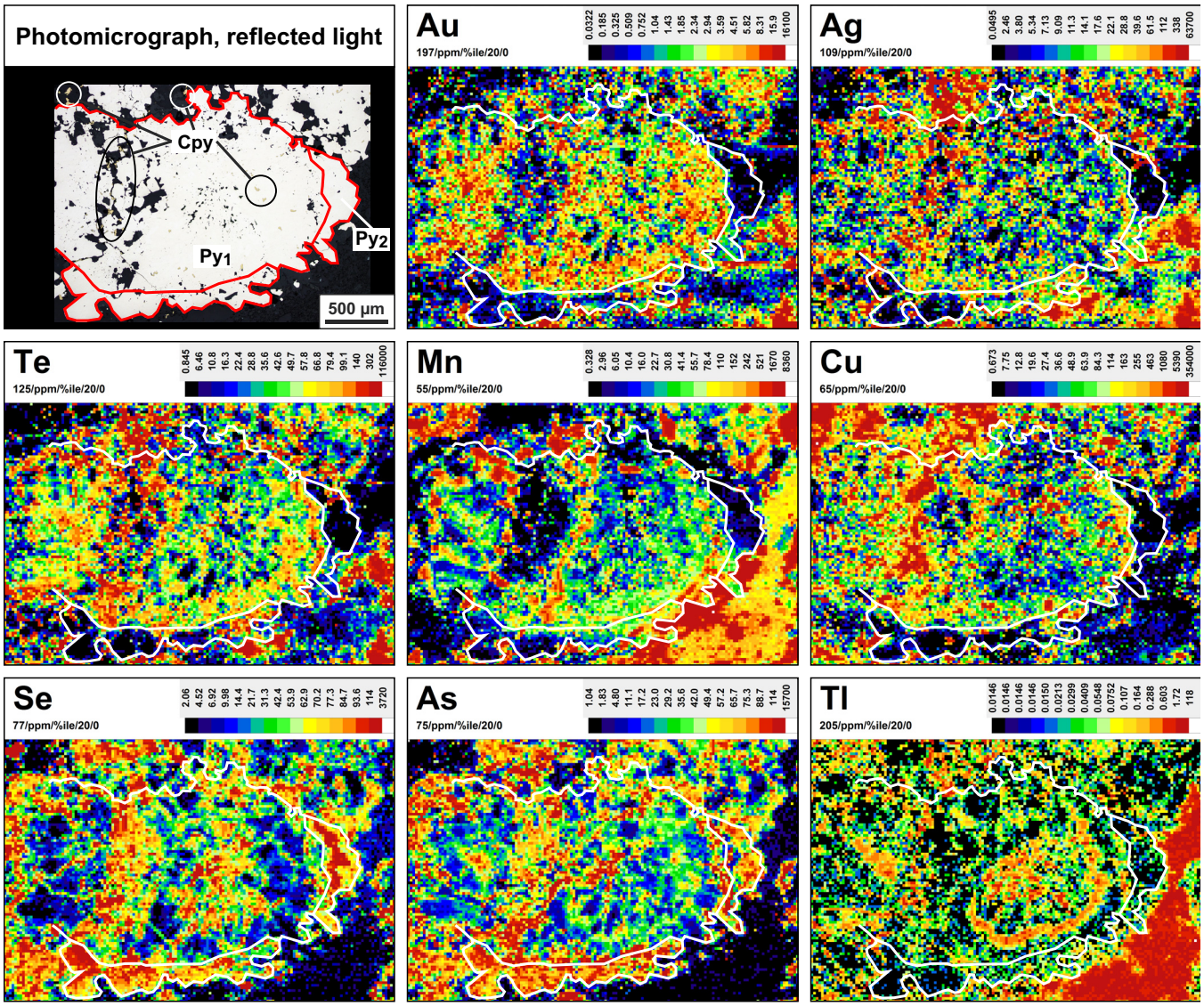

Figure 10. Laser ablation inductively-coupled plasma mass spectrometry compositional maps of spheroidal pyrite with a nodular texture (Py_1) rimmed by a metamorphic overgrowth (Py_2). Readers are referred to Lawley et al. (2015) for information on analytical methods.

sulphides were exposed at or near the seafloor and were eroded by mass flows during emplacement of the dacitic-rhyodacitic volcaniclastic rocks. Gold distribution at the deposit scale, which correlates well with the sulphide envelope, and its preferential association with partially preserved primary pyrite textures at the mineral scale also demonstrate that Au is synvolcanic. Furthermore, major fault zones in the immediate vicinity of the Horne 5 deposit contain no significant Au grades and are associated with alteration styles that contrast strongly with the synvolcanic alteration assemblages.

The distribution of Au and its associated trace elements (Te, Ag, Pb) is predominantly controlled by the variations in primary porosity and permeability of the host felsic volcaniclastic rocks. Gold and sulphide mineralization preferentially developed in the coarse-grained volcaniclastic rocks, which would have allowed for greater hydrothermal fluid circulation in the subseafloor environment. The presence of felsic syn-volcanic intrusions and fine-grained tuffs overlying some of the massive sulphide lenses suggests that they also controlled the distribution of the mineralization by acting as cap rocks to ascending hydrothermal fluids. Subseafloor precipitation of metals was likely an important process at Horne 5 by promoting fluid-rock interactions and reducing convective cooling as a result of the insulating effect of sulphide precipitation (Kerr and Gibson, 1993; Gibson et al., 1999; Doyle and Allen, 2003).

The Horne 5 deposit is characterized by a distinct metal zonation pattern. Zinc and its associated trace elements (Cd-Sn-Hg-In±Au±Ag±Pb) are distributed in the structural upper-western part of the deposit and a

Cu-Au-Te±Ag±Pb assemblage is concentrated in the eastern portion, at lower stratigraphic levels. Although modified by deformation and metamorphism, this zonation pattern reflects a primary architecture composed of distinct zones of Zn±Au and Cu-Au-rich mineralization, which likely formed under different physiochemical conditions. Zinc assemblages are typically associated with low-temperature hydrothermal fluids (100–200°C) which may have experienced extensive mixing with seawater, whereas the Cu-Au-rich zones likely represent higher temperature discharge sites (Large, 1977; Ohmoto, 1996).

Deformation and metamorphism at Horne 5 modified the geometry of the deposit, which was tilted, stretched, sheared, and transposed along the main schistosity. Gold remobilization appears to be very local in scale, with minimal redistribution along low-strain micro-structural sites. Similarly, ductile deformed minerals, such as chalcopyrite, are remobilized locally to fractures and pyrite grain boundaries. At the mineral scale, recrystallization of sulphide phases resulted in the expulsion of lattice-bound Au and its associated trace elements and local remobilization along fractures, inter-grain boundaries and the surrounding silicate gangue. Although Au-rich intervals are present along the margins of "syenite" dykes intruding into massive sulphide lenses of the Upper and Lower H zones, this is believed to be the result of deformation-induced Au remobilization (Kerr and Mason, 1990; Barrett et al., 1991; Gibson et al., 2000), as opposed to an orogenic gold overprint. This is further indicated by the absence of significant gold grades in the hematized felsic dykes (syenites) within the Horne 5 mineralized zones and the absence of Au-bearing deformation corridors.

The Horne 5 deposit presents both similarities and differences with the Upper and Lower H zones, in alteration styles, metal grades, mineralization styles, and sulphide mineralogy (Sinclair, 1971; Gibson et al., 2000). The similar host felsic volcaniclastic rocks and sericite-rich alteration styles suggest that the H zones and the Horne 5 deposit formed within the same broad hydrothermal system, which is also supported by a high Au to base metal ratio (2.6 for the H zones and 1.5 for Horne 5). Major differences in metal grades and mineralization styles, as well as the occurrence of strong chlorite alteration around the H orebodies, imply different physicochemical conditions of metal precipitation. Past studies suggested that the H orebodies and the Horne 5 deposit formed in different basins on the flank of a submarine volcanic complex (Kerr and Mason, 1990; Barrett et al., 1991; Cattalani et al., 1993; Kerr and Gibson, 1993; Gibson et al., 2000). The H orebodies presumably formed in a restricted basin that rapidly sealed itself from overlying seawater, facilitating the thermal evolution of the hydrothermal fluids and extensive zone refining of the sulphides which accounts for the pyrite-pyrrhotite-chalcopyrite assemblage and the very high Cu grades. The Horne 5 deposit likely formed in a larger, more open basin or depression, which allowed more seawater circulation in the permeable volcaniclastic rocks and thereby provided conditions that were favourable to the precipitation of a Au-rich pyrite-sphalerite-chalcopyrite assemblage. Additionally, since the Upper and Lower H zones appear to be separated by a fault (de Kemp et al., 2011), it is not unreasonable to assume that faulting brought the Lower H and Horne 5 zones in closer proximity during deformation.

In summary, this study indicates that the Au in the Horne 5 deposit is synvolcanic, making the Horne system (Upper and Lower H zones, plus Horne 5) one of the largest Au accumulations in the Abitibi greenstone belt, at approximately 16 Moz (~500 t) Au. It confirms the unique synvolcanic Au endowment of the southern Abitibi belt and strengthens previously proposed models inferring specific processes related to the early rifting of thickened arc - back-arc crust and formation of calc-alkaline felsic volcanic centres and Au-rich hydrothermal systems.

IMPLICATIONS FOR EXPLORATION

The Horne 5 deposit presents many interesting features that may be useful for exploration of synvolcanic Au in Archean terranes. Its stratigraphic setting, which is dominated by permeable felsic volcaniclastic rocks, demonstrates the potential of fragmental units to act as conduits for sulphide mineralization and hydrothermal fluid flow during VMS formation (Kerr and Gibson, 1993; Gibson et al., 1999; Doyle and Allen, 2003). The geochemical signature of the host felsic rocks constitutes another example of a large Au-VMS deposit associated with calc-alkaline felsic volcanic rocks. This highlights the importance of calc-alkaline felsic volcanic successions in volcano-sedimentary terranes such as the Abitibi greenstone belt when looking for VMS-Au mineralization (cf. Mercier-Langevin et al., 2011b).

The proximity of two major fault zones, the Horne Creek and the Andesite faults, to the Horne 5 deposit and textures attributed to deformation-induced Au remobilization share similarities with an orogenic Au overprint. The similarities between Au mineralization styles demonstrates the importance of conducting detailed mineralogical and geochemical studies of such deposits to accurately determine the principal controls on its distribution. This can strongly influence exploration models for deposit-scale exploration, as synvolcanic and orogenic Au deposits are characterized by different geometries, mineral assemblages, and Au

deportments; attributes that are critical in determining the feasibility of a potential mineral prospect.

Compositional variations in alteration phases from the footwall to the hanging-wall of the Horne 5 mineralized zones, especially for white mica and epidote, can be a useful exploration vector for district-scale exploration.

Similarly, the footwall of the mineralized zones is associated with Mn-rich spessartine garnet and increases in Mn content in chlorite, carbonate, and massive sulphides. These features can be interesting exploration vectors pointing towards hydrothermal discharge sites, as was similarly documented at the LaRonde Penna deposit (Dubé et al., 2007).

ACKNOWLEDGMENTS

We thank Falco Resources Ltd. for the opportunity to study the Horne 5 deposit and for their support throughout the project. This project was funded by the Geological Survey of Canada (GSC) through the Gold Project of the Targeted Geoscience Initiative 5 and by Falco Resources Ltd. Thanks to S.E. Jackson and Z. Yang at the GSC in Ottawa for help with pyrite analyses. L. Moore is thanked for her collaboration and constructive discussions throughout the project. Thanks to B. Dubé and D. Huston for their insights on Au-rich VMS systems. We also thank InnovExplo Inc. and their personnel for having shared the compilation of historical data from the Horne 5 deposit. Earlier versions of this contribution were reviewed by A.J. Martin and C.J.M. Lawley.

REFERENCES

Barrett, T.J., Cattalani, S., and MacLean, W.H., 1991. Massive sulfide deposits of the Noranda area, Quebec. I. The Horne mine; Canadian Journal of Earth Sciences, v. 28, p. 465–488.

Cattalani, S., Barrett, T.J., MacLean, W.H., Hoy, L., Hubert, C., and Fox, J.S., 1993. Métallogenèse des gisements Horne et Quemont (région de Rouyn-Noranda); Ministère de l'Énergie et des Ressources du Québec, ET 90-07, 132 p.

Cook, N.J., Ciobanu, C.L., Pring, A., Skinner, W., Shimizu, M., Danyushevsky, L., Saini-Eidukat, B. and Melcher, F., 2009. Trace and minor elements in sphalerite: A LA-ICPMS study; Geochimica et Cosmochimica Acta, v. 73, p. 4761–4791.

Deditius, A.P., Utsunomiya, S., Reich, M., Kesler, S.E., Ewing, R.C., Hough, R., and Walshe, J., 2011. Trace metal nanoparticles in pyrite; Ore Geology Reviews, v. 42, p. 32–46.

De Kemp, E.A., Monecke, T., Sheshpari, M., Girard, E., Lauzière, K., Grunsky, E.C., Schetselaar, E.M., Goutier, J.E., Perron, G., and Bellefleur, G., 2011. 3D GIS as a support for mineral discovery; Geochemistry: Exploration, Environment, Analysis, v. 11, p. 117–128.

De Ronde, C.E.J., Massoth, G.J., Butterfield, D.A., Christenson, B.W., Ishibashi, J., Ditchburn, R.G., Hannington, M.D., Brathwaite, R.L., Lupton, J.E., Kamenetsky, V.S., and Graham, I.J., 2011. Submarine hydrothermal activity and gold-rich mineralization at Brothers Volcano, Kermadec Arc, New Zealand; Mineralium Deposita, v. 46, p. 541–584.

Dimroth, E., Imreh, L., Rocheleau, M., and Goulet, N., 1982. Evolution of the south-central part of the Archean Abitibi belt, Quebec. Part I: Stratigraphy and paleogeographic model; Canadian Journal of Earth Sciences, v. 19, p. 1729–1758.

Dimroth, E., Imreh, L., Goulet, N., and Rocheleau, M., 1983a. Evolution of the south-central segment of the Archean Abitibi belt, Quebec. Part II: tectonic evolution and geomechanical model; Canadian Journal of Earth Sciences, v. 20, p. 1355–1373.

Dimroth, E., Imreh, L., Goulet, N., and Rocheleau, M., 1983b. Evolution of the south-central segment of the Archean Abitibi belt, Quebec. Part III: plutonic and metamorphic evolution and geotectonic model; Canadian Journal of Earth Sciences, v. 20, p. 1374–1388.

Doyle, M.G. and Allen, R.L., 2003. Subsea-floor replacement in volcanic-hosted massive sulfide deposits; Ore Geology Reviews, v. 23, p. 183–222.

Dubé, B., Mercier-Langevin, P., Hannington, M., Lafrance, B., Gosselin, G., and Gosselin, P., 2007. The LaRonde Penna world-class Au-rich volcanogenic massive sulfide deposit, Abitibi, Québec: mineralogy and geochemistry of alteration and implications for genesis and exploration; Economic Geology, v. 102, p. 633–666.

Eldridge, C.S., Barton Jr., P.B., and Ohmoto, H., 1983. Mineral textures and their bearing on formation of the Kuroko orebodies; *in* The Kuroko and Related Volcanogenic Massive Sulfide Deposits, (ed.) H. Ohmoto and B.J. Skinner; Society of Economic Geologists, Monograph 5, p. 241–281.

Garrett, R.G., 2013. The 'rgr' package for the R Open Source statistical computing and graphics environment - a tool to support geochemical data interpretation; Geochemistry: Exploration, Environment, Analysis, v. 13, p. 355–378.

George, L.L., Cook, N.J., and Ciobanu, C.L., 2016. Partitioning of trace elements in co-crystallized sphalerite–galena–chalcopyrite hydrothermal ores; Ore Geology Reviews, v. 77, p. 97–116.

Gibson, H.L., 1989. The Mine sequence of the Central Noranda Volcanic Complex: geology, alteration, massive sulphide deposits and volcanological reconstruction; Ph.D. thesis, Carleton University, Ottawa, Ontario, 800 p.

Gibson, H.L. and Galley, A.G., 2007. Volcanogenic massive sulphide deposits of the Archean, Noranda District, Quebec; *in* Mineral Deposits of Canada: A Synthesis of Major Deposit-Types, District Metallogeny, the Evolution of Geological Provinces, and Exploration Methods, (ed.) W.D. Goodfellow; Geological Association of Canada, Mineral Deposits Division, Special Publication No 5, p. 533–552.

Gibson, H.L., Morton, R.L., and Hudak, G.J., 1999. Submarine volcanic processes, deposits, and environments favourable for the location of volcanic-associated massive sulfide deposits; *in* Volcanic-Associated Massive Sulfide Deposits: Processes and Examples in Modern and Ancient Settings, (ed.) C.T. Barrie and M.D. Hannington; Reviews in Economic Geology, v. 8, p. 13–51.

Gibson, H.L., Kerr, D.J., and Cattalani, S., 2000. The Horne Mine: geology, history, influence on genetic models, and a comparison to the Kidd Creek Mine; Exploration and Mining Geology, v. 9, p. 91–111.

Gifkins, C., Herrmann, W., and Large, R., 2005. Altered volcanic rocks: A guide to description and interpretation; Centre for Ore Deposit Research, University of Tasmania, Australia, 275 p.

Huston, D.L., Sie, S.H., Suter, G.F., Cooke, D.R., and Both, R.A., 1995. Trace elements in sulfide minerals from eastern Australian volcanic-hosted massive sulfide deposits; Part I, Proton microprobe analyses of pyrite, chalcopyrite, and sphalerite, and Part II, Selenium levels in pyrite; comparison with delta ^{34}S values and implications for the source of sulfur in vol-

canogenic hydrothermal systems; Economic Geology, v. 90, p. 1167–1196.

Ishikawa, Y., Sawaguchi, T., Iwaya, S., and Horiuchi, M., 1976. Delineation of prospecting targets for Kuroko deposits based on modes of volcanism of underlying dacite and alteration halos; Mining Geology, v. 26, p. 105–117.

Kerr, D.J. and Mason, R., 1990. A re-appraisal of the geology and ore deposits of the Horne mine complex at Rouyn-Noranda, Quebec; Canadian Institute of Mining and Metallurgy, Special Volume 43, p. 153–165.

Kerr, D.J. and Gibson, H.L., 1993. A comparison of the Horne volcanogenic massive sulfide deposit and intracauldron deposits of the Mine Sequence, Noranda, Quebec; Economic Geology, v. 88, p. 1419–1442.

Krushnisky, A., 2018. Controls on gold enrichment at the Horne 5 Archean VMS deposit, Abitibi greenstone belt, Québec; M.Sc. thesis, Institut national de la recherche scientifique – Centre Eau Terre Environnement , Québec, Quebec, 198 p.

Krushnisky, A., Mercier-Langevin, P., Ross, P.-S., Bécu, V., Lauzière, K., and Goutier, J., 2018. Whole-rock lithogeochemistry of the gold-bearing mineralized zones of the Horne 5 deposit, Québec, Canada; Geological Survey of Canada, Open File 8501, 1 .zip file.

Krushnisky, A., Mercier-Langevin, P., Ross, P.-S., Goutier, J., Pilote, C., and Bernier, C., in prep The Archean Horne 5 volcanogenic massive sulfide deposit, Abitibi greenstone belt, Quebec: Geology, controls on gold enrichment, and implications for its genesis.

Large, R.R., 1977. Chemical evolution and zonation of massive sulfide deposits in volcanic terrains; Economic Geology, v. 72, p. 549–572.

Large, R.R., Gemmell, J.B., Paulick, H., and Huston, D.L., 2001. The alteration box plot: A simple approach to understanding the relationship between alteration mineralogy and lithogeochemistry associated with volcanic-hosted massive sulfide deposits; Economic Geology, v. 96, p. 957–971.

Lawley, C.J.M., Creaser, R.A., Jackson, S.E., Yang, Z., Davis, B.J., Pehrsson, S.J., Dubé, B., Mercier-Langevin, P., and Vaillancourt, D., 2015. Unraveling the Western Churchill Province Paleoproterozoic gold metallotect: Constraints from Re-Os arsenopyrite and U-Pb xenotime geochronology and LA-ICP-MS arsenopyrite trace element chemistry at the BIF-hosted Meliadine Gold District, Nunavut, Canada; Economic Geology, v. 110, p. 1425–1454.

McNicoll, V., Goutier, J., Dubé, B., Mercier-Langevin, P., Ross, P.-S., Dion, C., Monecke, T., Legault, M., Percival, J., and Gibson, H., 2014. U-Pb geochronology of the Blake River Group, Abitibi greenstone belt, Quebec, and implications for base metal exploration; Economic Geology, v. 109, p. 27–59.

Mercier-Langevin, P., Dubé, B., Hannington, M.D., Richer-Laflèche, M., and Gosselin, G., 2007. The LaRonde Penna Au-rich volcanogenic massive sulfide deposit, Abitibi greenstone belt, Quebec: Part II. Lithogeochemistry and paleotectonic setting; Economic Geology, v. 102, p. 611–631.

Mercier-Langevin, P., Goutier, J., Ross, P.-S., McNicoll, V., Monecke, T., Dion, C., Dubé, B., Thurston, P., Bécu, V., Gibson, H., Hannington, M., and Galley, A., 2011a. The Blake River Group of the Abitibi greenstone belt and its unique VMS and gold-rich VMS endowment: Field Trip 02B guidebook; Geological Survey of Canada, Open File 6869, 61 p.

Mercier-Langevin, P., Hannington, M.D., Dubé, B., and Bécu, V., 2011b. The gold content of volcanogenic massive sulfide deposits; Mineralium Deposita, v. 46, p. 509–539.

Monecke, T., Gibson, H.L., Dubé, B., Laurin, J., Hannington, M.D., and Martin, L., 2008. Geology and volcanic setting of the Horne deposit, Rouyn-Noranda, Quebec: initial results of a new research project; Geological Survey of Canada, Current Research 2008-9, 16 p.

Monecke, T., Gibson, H.L., and Goutier, J., 2017. Volcanogenic massive sulfide deposits of the Noranda camp; *in* Archean Base and Precious Metal Deposits, southern Abitibi Greenstone Belt, Canada, (ed.) T. Monecke, P. Mercier-Langevin, and B. Dubé; Reviews in Economic Geology, v. 19, p. 169–223.

Mookherjee, A. and Suffel, G.G., 1968. Massive sulfide-late diabase relationships, Home mine, Quebec: Genetic and chronological implications; Canadian Journal of Earth Sciences, v. 5, p. 421–432.

Moore, L.N., Daigneault, R., Aird, H.M., Banerjee, N.R., and Mueller, W.U., 2016. Reconstruction and evolution of Archean intracaldera facies: the Rouyn–Pelletier Caldera Complex of the Blake River Group, Abitibi greenstone belt, Canada; Canadian Journal of Earth Sciences, v. 53, p. 355–377.

Mueller, W.U., Stix, J., Corcoran, P.L., and Daigneault, R., 2009. Subaqueous calderas in the Archean Abitibi greenstone belt: An overview and new ideas; Ore Geology Reviews, v. 35, p. 4–46.

Mueller, W.U., Friedman, R., Daigneault, R., Moore, L., and Mortensen, J., 2012. Timing and characteristics of the Archean subaqueous Blake River Megacaldera Complex, Abitibi greenstone belt, Canada; Precambrian Research, v. 214–215, p. 1–27.

Ohmoto, H., 1996. Formation of volcanogenic massive sulfide deposits: the Kuroko perspective; Ore Geology Reviews, v. 10, p. 135–177.

Pearce, J.A., 1996. A user's guide to basalt discrimination diagrams; *in* Trace element geochemistry of volcanic rocks: applications for massive sulphide exploration, (ed.) D.A. Wyman; Geological Association of Canada, Short Course Notes, v. 12, p. 79–113.

Pearson, V. and Daigneault, R., 2009. An Archean megacaldera complex: The Blake River Group, Abitibi greenstone belt; Precambrian Research, v. 168, p. 66–82.

Piercey, S.J., Chaloux, E.C., Péloquin, A.S., Hamilton, M.A., and Creaser, R.A., 2008. Syn-volcanic and younger plutonic rocks from the Blake River Group: implications for regional metallogenesis; Economic Geology, v. 103, p. 1243–1268.

Powell, W.G., Carmichael, D.M., and Hodgson, C.J., 1995. Conditions and timing of metamorphism in the southern Abitibi greenstone belt, Quebec; Canadian Journal of Earth Sciences, v. 32, p. 787–805.

Price, P., 1934. The geology and ore deposits of the Horne Mine, Noranda, Quebec; The Transactions of the Canadian Institute of Mining and Metallurgy and of the Mining Society of Nova Scotia, v. 37, p. 108–140.

Price, P., 1948. Horne Mine; *in* Structural geology of Canadian Ore Deposits: A symposium; Geology Division, Canadian Institute of Mining and Metallurgy, p. 763–772.

Ross, P.-S. and Bédard, J.H., 2009. Magmatic affinity of modern and ancient subalkaline volcanic rocks determined from trace-element discriminant diagrams; Canadian Journal of Earth Sciences, v. 46, p. 823–839.

Sinclair, W.D., 1971. A volcanic origin for the No. 5 Zone of the Horne mine, Noranda, Quebec; Economic Geology, v. 66, p. 1225–1231.

Winchester, J.A. and Floyd, P.A., 1977. Geochemical discrimination of different magma series and their differentiation products using immobile elements; Chemical Geology, v. 20, p. 325–343.

Sulphide clast-bearing felsic volcaniclastic units of the Rouyn-Pelletier Formation: Comparison with similar units of the Horne Block, Rouyn-Noranda, Abitibi greenstone belt, Quebec

Catherine Boudreau[1,2], Patrick Mercier-Langevin[3*], Alexandre Krushnisky[4], and Jean Goutier[5]

[1]Université Laval, 1065 Avenue de la Médecine, Québec, Quebec G1V 0A6
[2]WSP, 1600 boulevard René-Lévesque Ouest, Montréal, Quebec H3H 1P9
[3]Geological Survey of Canada, 490 rue de la Couronne, Québec, Quebec G1K 9A9
[4]Institut national de la recherche scientifique, Centre Eau Terre Environnement, 490 rue de la Couronne, Québec, Quebec G1K 9A9
[5]Ministère de l'Énergie et des Ressources naturelles du Québec, 70 avenue Québec, Rouyn-Noranda, Quebec J9X 6R1
*Corresponding author's e-mail: patrick.mercier-langevin@canada.ca

ABSTRACT

Sulphide clast-bearing volcaniclastic units are a key exploration vector towards volcanogenic massive sulphide deposits. These marker units are commonly associated with base and precious metal-rich volcanogenic massive sulphide deposits of the Archean Abitibi greenstone belt. One such sulphide (pyrite ±sphalerite-chalcopyrite) clast-bearing felsic volcaniclastic unit is present in the uppermost part of the Rouyn-Pelletier Formation of the Blake River Group in Rouyn-Noranda. The Rouyn-Pelletier Formation is in faulted contact (Andesite fault) with the rocks of the Horne Formation, which are of the same age and style, are sulphide clast-bearing, and host to the giant Horne Au-rich volcanogenic massive sulphide deposit. This raises the question of a possible stratigraphic correlation between the Rouyn-Pelletier (upper part) and Horne formations, with the potential for major implications for exploration in the Rouyn-Pelletier Formation.

The study area is composed of broadly coeval extrusive felsic facies with mafic to intermediate extrusive and intrusive facies. Felsic units range from flows with lobate, flow banding and in situ brecciated textures to dominantly sulphide clast-bearing volcaniclastic units with tuff breccia, lapilli tuff and lesser tuff facies. Rocks of the upper portion of the Rouyn-Pelletier Formation and the Horne Block are of similar age and show similarities in volcanic facies. However, there are subtle but significant geochemical differences that suggest that it may not be possible to directly correlate their stratigraphy. The uppermost Rouyn-Pelletier Formation could represent a distal, poorly mineralized equivalent to the Horne West or Horne 5 zones, or it could be an unrelated succession.

INTRODUCTION

Context and Objectives

The Archean volcanic sequences of the Blake River Group in the Abitibi host one of the highest concentrations of volcanogenic massive sulphide (VMS) deposits and Au-rich VMS deposits ever found (Mercier-Langevin et al., 2011, and references therein). The Horne Formation, which is part of the Blake River Group, hosts the giant Horne VMS deposit (Goutier et al., 2009), which has a combined past production (Horne mine) and current resources estimate (Horne 5) of approximately 16 Moz Au (~500 metric t: Krushnisky et al., 2020). The host successions of the Horne deposit are characterized by felsic volcaniclastic rocks containing a high proportion of massive sulphide clasts, which were documented around the Upper and Lower H zones (Price, 1934; Kerr and Mason, 1990; Cattalani et al., 1993), the Horne 5 zone (Sinclair, 1971; Krushnisky, 2018; Krushnisky et al., 2020), and the Horne West zone (Monecke et al., 2008; Laurin, 2010; Goutier, 2017).

The Rouyn-Pelletier Formation is located immediately south of the Horne Formation and is separated from it by the Andesite fault (Goutier et al., 2009). Felsic volcaniclastic rocks of the upper portion of the Rouyn-Pelletier Formation also contain massive sulphide clasts and show obvious similarities with the volcaniclastic rocks of the Horne Formation. This study investigates the possible stratigraphic correlation between the upper portion of the Rouyn-Pelletier Formation and the felsic rocks of the Horne Formation by documenting volcanic facies, hydrothermal alteration, and the nature of the massive sulphide clasts in select localities within the Rouyn-Pelletier Formation (Boudreau, 2013) and comparing these with sulphide clasts from the Horne Formation. If correlation

Boudreau, C., Mercier-Langevin, P., Krushnisky, A., and Goutier, J., 2020. Sulphide clast-bearing felsic volcaniclastic units of the Rouyn-Pelletier Formation: Comparison with similar units of the Horne Block, Rouyn-Noranda, Abitibi greenstone belt, Quebec; *in* Targeted Geoscience Initiative 5: Contributions to the Understanding of Canadian Gold Systems, (ed.) P. Mercier-Langevin, C.J.M. Lawley, and S. Castonguay; Geological Survey of Canada, Open File 8712, p. 45–56. https://doi.org/10.4095/323664

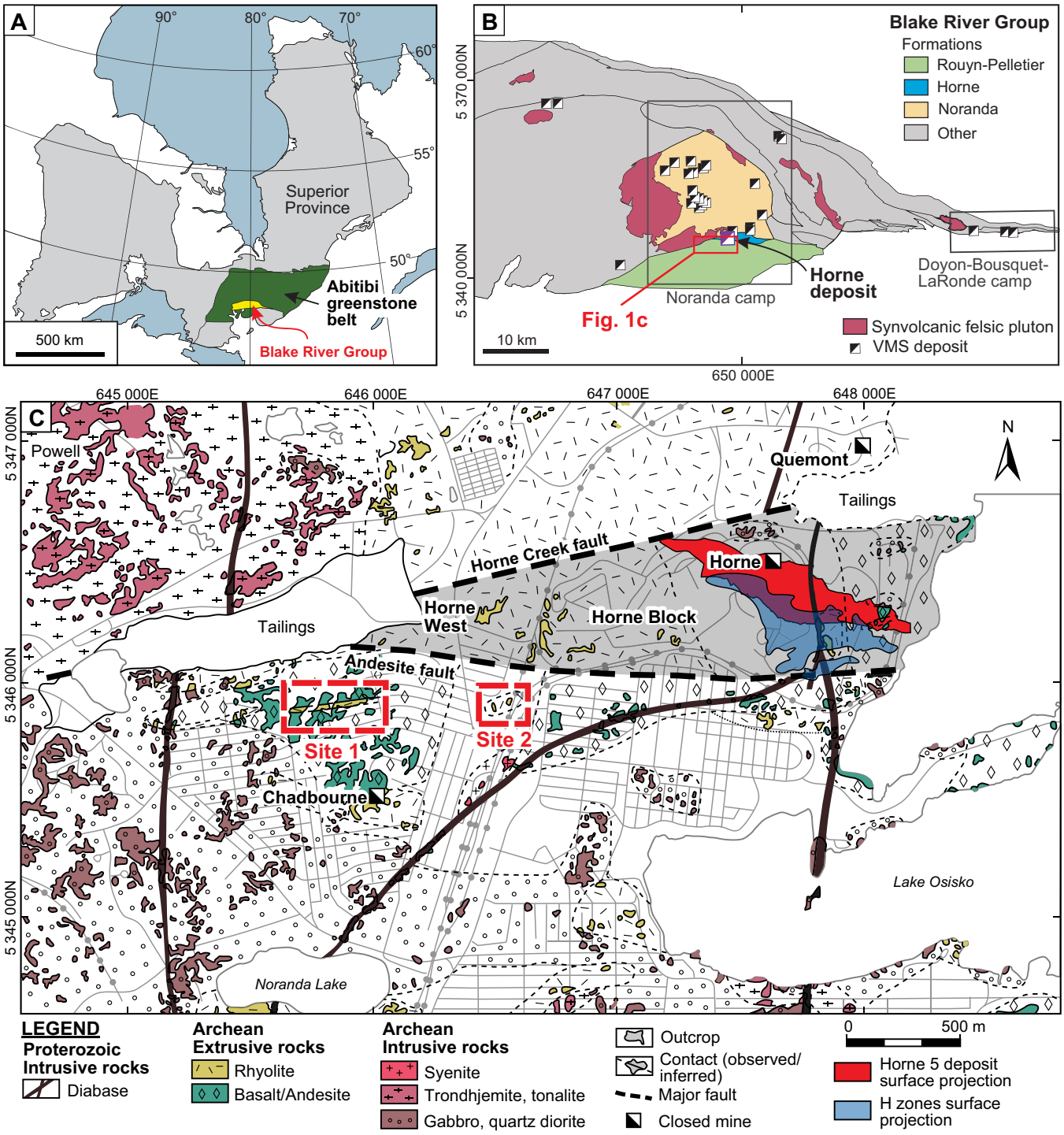

Figure 1. a) Location of Abitibi greenstone belt in the Superior Province of Canada. **b)** Simplified map of the Blake River Group and distribution of the Rouyn-Pelletier, Horne, and Noranda Formations (*modified from* Mercier-Langevin et al., 2011). **c)** Geological map of the Horne Block (*modified from* Monecke et al., 2008). The locations of study sites 1 and 2 are shown. Map coordinates are in UTM NAD83, zone 17.

between the two formations can be established, it would have positive implications for the mineral potential of the Rouyn-Pelletier Formation, which is currently viewed as being limited.

Geological Setting

The 2704 to 2695 Ma Blake River Group is located in the southern Abitibi greenstone belt (Fig. 1a; Monecke et al., 2017 and references therein). It consists of a sequence of subalkaline mafic to felsic volcanic rocks intruded by syn- to post-volcanic plutons and dykes (Dimroth et al., 1982; Piercey et al., 2008; Mueller et al., 2012; McNicoll et al., 2014). The Rouyn-Pelletier Formation (2703–2701 Ma: Mueller et al., 2012;

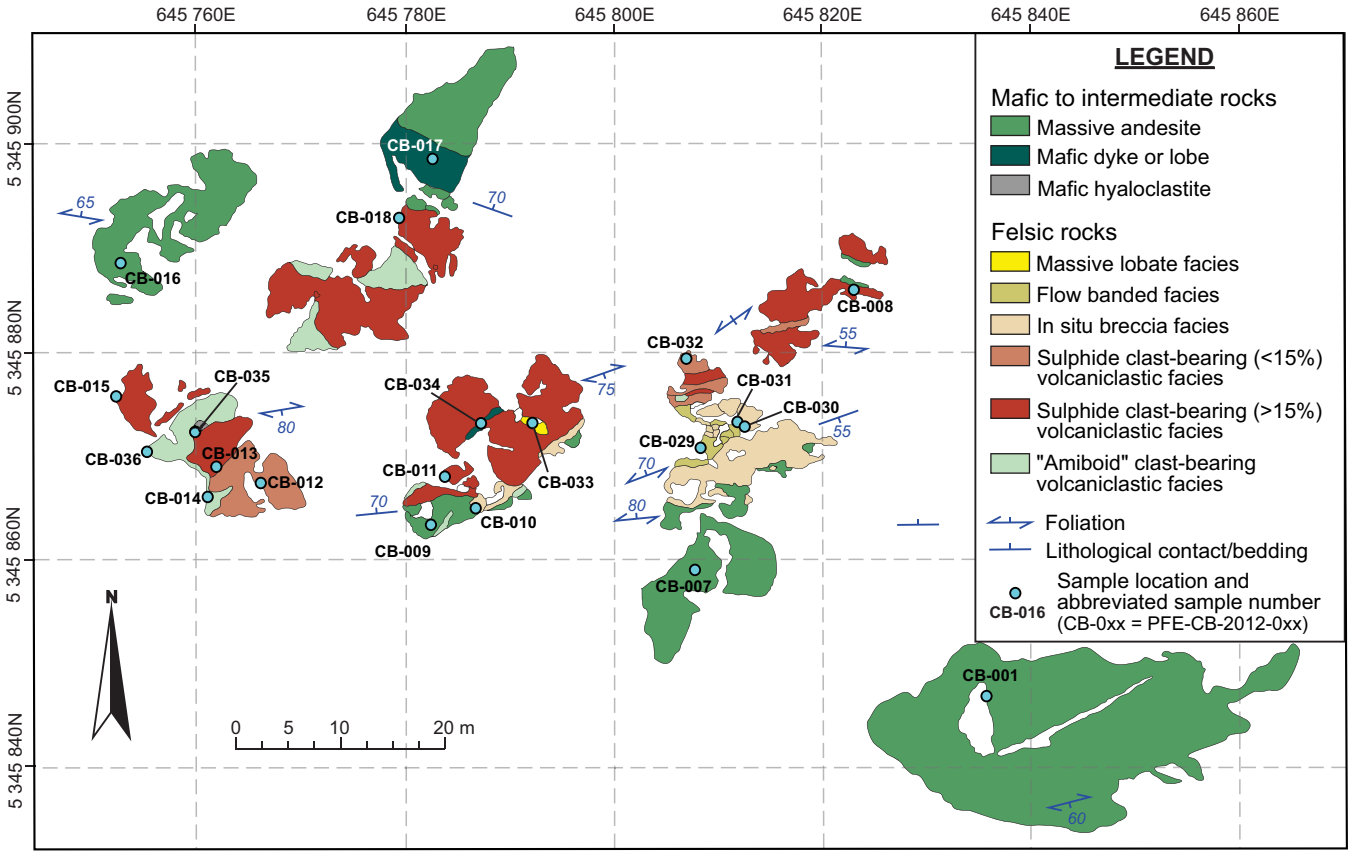

Figure 2. Geological map of site 1 of the study. *See* Figure 1 for a broader location of the study area (*from* Boudreau, 2013).

McNicoll et al., 2014) comprises the southernmost portion of the Blake River Group (Fig. 1b) and is dominated by andesitic to basaltic volcanic rocks with tholeiitic to transitional affinities and minor felsic lavas (Sterckx, 2018). The entire volcanic rock package generally faces north (Goutier et al., 2009; Moore et al., 2012). This area has also been referred to as the southern New Senator caldera (Moore et al., 2012) and the Rouyn-Pelletier caldera complex (Moore et al., 2016). The Andesite fault delineates the structural contact between the upper portion of the Rouyn-Pelletier Formation and the Horne Formation (Fig. 1c).

The Horne Formation (2702.2 ± 0.9 Ma: McNicoll et al., 2014), also referred to as the Horne Block, consists of a structural wedge of mafic to intermediate rocks and thick (100s of metres) felsic volcanic units. The volcanic rocks hosting the Horne deposit consist of dacitic to rhyolitic flows and domes and large volumes of associated volcaniclastic rocks that are interpreted as mass flow deposits (Price, 1934; Sinclair, 1971; Kerr and Mason, 1990; Kerr and Gibson, 1993). The Horne West zone is characterized by a similar volcanic succession composed of alternating felsic volcaniclastic rocks, felsic intrusions, and local extrusive rhyolite flows (Monecke et al., 2008; Laurin, 2010). Massive sulphide clasts, predominantly composed of pyrite with local traces of sphalerite and chalcopyrite, are ubiquitous within the felsic volcaniclastic rocks of the Horne Block.

RESULTS

Seven outcrops within the uppermost (northern) part of the Rouyn-Pelletier Formation (an area also referred to as the Chadbourne Block: Moore et al., 2016) were mapped in detail as part of this study. These outcrops are distributed in two separate areas, referred to as site 1 and site 2 (Fig. 1c). Representative samples of the principal volcanic facies were collected for petrographic study and whole rock lithogeochemical analyses. Two samples of massive sulphide clasts were also isolated to assess their metal content.

Description of Volcanic Facies

Site 1 is composed of steeply dipping bands of mafic rocks intercalated with massive to brecciated felsic rocks (Fig. 2). The rocks show very little deformation and exhibit a weak, steeply dipping foliation oriented N255º on average, which is consistent with the dominant east-west penetrative fabric. Site 2 consists mainly of layers of felsic volcaniclastic rocks hosting variable percentages of massive sulphide clasts, in addition to minor mafic rocks (Fig. 3). Strain is slightly stronger in this area and felsic fragments are aligned (flattened)

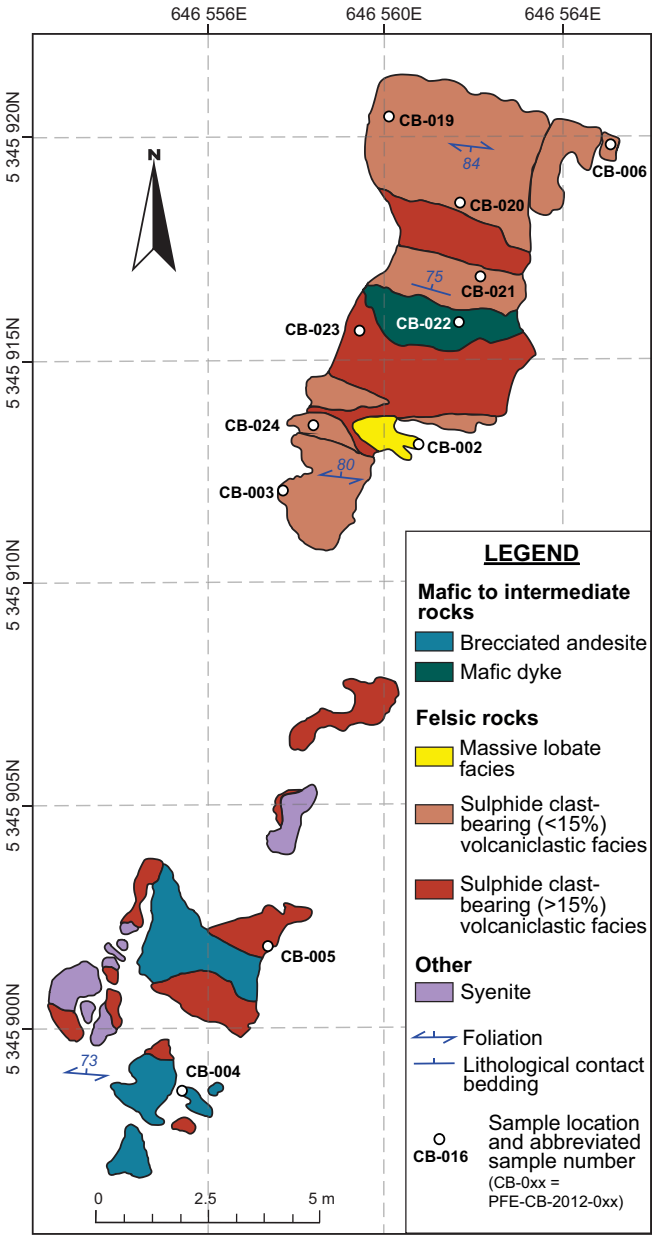

Figure 3. Geological map of site 2 of the study. *See* Figure 1 for a broader location of the study area (*after* Boudreau, 2013).

along a steeply dipping foliation oriented N277º on average.

Various facies of felsic volcanic rocks are present at the two sites: 1) lobate facies, which comprises lobes of rhyolite penetrating volcaniclastic rocks; 2) flow-banded facies; 3) in situ breccia facies (Fig. 4a); and 4) massive sulphide clast-bearing volcaniclastic facies (Fig. 4b,c). The felsic volcaniclastic rocks are grouped in two subfacies, based on the relative abundance of sulphide clasts. The first contains less than 15 vol.% sulphide clasts and is dominated by rhyolite fragments that range in size from 0.5 to 2 cm. The second is composed of more than 15 vol.% sulphide clasts with coherent rhyolite fragments, vesicular rhyolite fragments, and strongly silicified amoeboid fragments of mafic rocks measuring 0.1 to 1.5 m in size and exhibiting chilled margins. At site 2, massive sulphide clasts are mostly concentrated at the contacts between distinct layers of volcaniclastic rocks.

In the study area, the mafic to intermediate rocks predominantly consist of the following: 1) massive andesite flows and lobes that locally contain up to 1 vol.% disseminated pyrite (Fig. 4d); 2) mafic dykes and/or lobes that are up to 1 m thick and display irregular contacts with the surrounding felsic volcaniclastic rocks (Fig. 4e); and 3) oxidized, sericitized, and unmineralized volcaniclastic mafic rocks. Some of the clasts have a curvaceous, shard-like aspect, suggestive of hyaloclastites. Such rocks only appear very locally at site 1. Where present, mafic volcaniclastic rocks are completely enclosed by felsic volcaniclastic rocks. In the southern portion of site 2, massive andesite units are cut by a syenite intrusion. Angular fragments of andesite (10–40 cm in size) are enclosed within the syenite intrusion.

Felsic lobate, flow-banded, and in situ breccia facies

Felsic volcanic rocks from these facies are characterized by a weak foliation and a homogenous groundmass of microcrystalline quartz (65–80 vol.%), sericite (15–20 vol.%), locally up to 25 vol.% chlorite, and ≤3 vol.% garnet and Fe-Ti oxides. Sericite- and chlorite-altered plagioclase phenocrysts are rare (<3 vol.%). Relict perlite textures are present locally, as well as amygdules of quartz-calcite and quartz-calcite-epidote veins. Disseminated pyrite (1–5 vol.%) occurs throughout the groundmass, as well as local clusters of pyrite (2–3 vol.%) and trace amounts of sphalerite.

The flow-banded facies exhibit laminations measuring 0.1 to 1 cm in thickness. At site 1, in situ brecciated facies are in contact with the flow-banded facies, the sulphide clast-bearing volcaniclastic facies, and mafic to intermediate rocks. The felsic breccia is monomictic and consists mainly of fragments of rhyolite that measure 1 to 70 cm. The matrix represents 75 vol.% of the exposed surface and contains on average 3 vol.% pyrite fragments that measure between 0.5 and 5 cm. At site 1, the breccia is cut by thin andesite dykes and/or lobes near the contacts with the massive andesite.

Sulphide clast-bearing felsic volcaniclastic facies

Felsic volcaniclastic rocks comprise various layers of tuff, lapilli tuff, and tuff breccia. Although the variable alteration of the fragments gives the rock a polymictic appearance, it is largely dominated by rhyolite fragments (Fig. 4f). These rocks contain varying propor-

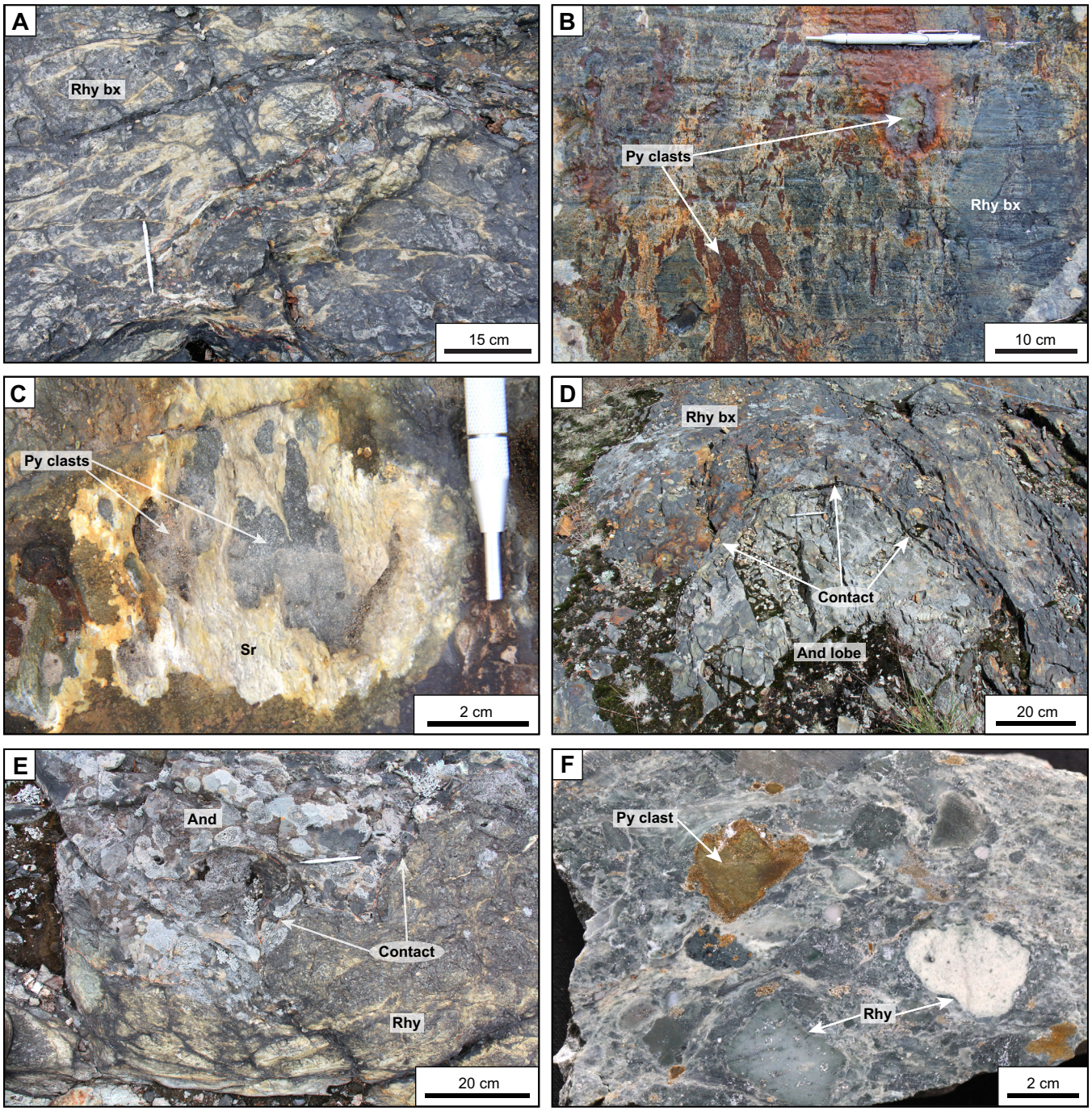

Figure 4. Photographs of representative outcrops at sites 1 and 2. **a)** Foliated and weakly sericite-altered rhyolite flow breccia in contact with in situ brecciated massive rhyolite (site 1). **b)** Polymictic rhyolitic tuff breccia with abundant, variably altered, angular to subangular rhyolitic clasts and flattened to amiboidal sulphide clasts (site 2). **c)** Amiboidal pyrite-rich sulphide clasts in a strongly sericite-altered matrix (felsic tuff to lapilli tuff; site 2). **d)** Andesite lobe intruding sulphide-rich clast-bearing fragmental rhyolite. The contact between the andesite and the rhyolite is sharp. The rhyolite is weakly to moderately sericite- and chlorite-altered, whereas the andesite is fresh (site 1). **e)** Andesitic dyke (or lobe) intruding rhyolite flow breccia deposits at site 1. The contact is highly irregular to peperitic, suggesting that the emplacement of the dyke was into the unconsolidated fragmental rhyolite unit (site 1). **f)** Rhyolitic lapilli tuff with angular sulphide clasts. The variably altered nature of the rhyolite clasts gives the impression that it is polymictic, although rhyolite clasts largely dominate (slab sample PFE-CB-2012-018, site 1). Abbreviations: And = andesite, Py = pyrite, Rhy = rhyolite, Rhy bx = fragmental rhyolite, Sr = sericite.

tions (15–65 vol.%) of four types of fragments, two of which are dominated by sulphides (Fig. 5a–c). The matrix is composed of foliated sericite, chlorite, and patches of fine-grained granoblastic pyrite, with local patches or irregular/discontinuous bands of coarse-grained (granoblastic) pyrite (Fig. 5d). The first type of fragment has a groundmass of microcrystalline quartz (50–65 vol.%), sericite (20–45 vol.%), chlorite (10–30

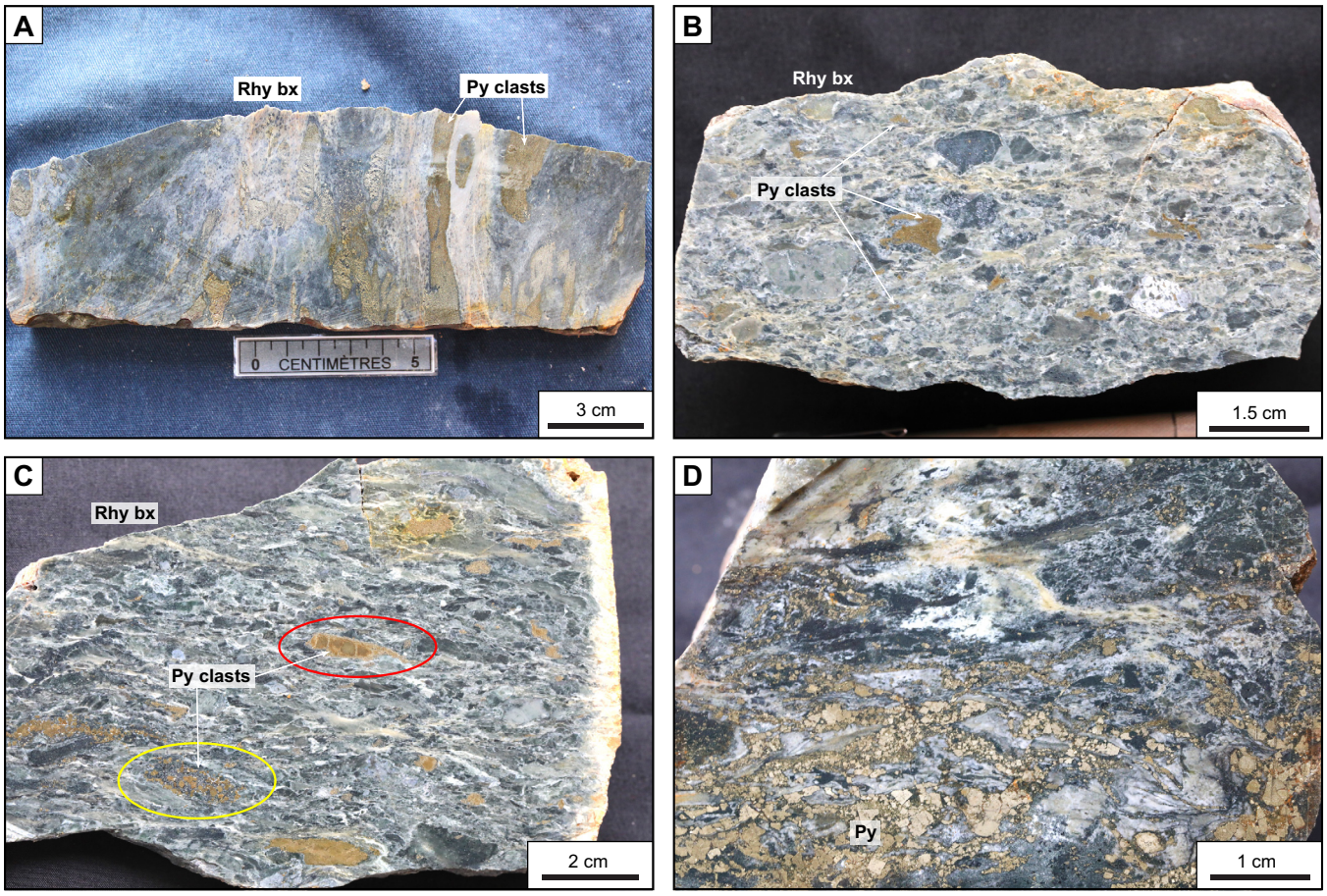

Figure 5. Photographs of representative slab samples from sites 1 and 2. **a)** Rhyolitic lapilli tuff to tuff breccia. The tuff is polymictic with abundant, variably altered rhyolitic clasts and flattened to amiboidal sulphide clasts. The matrix is sericite-±chlorite-altered with patches of fine granoblastic pyrite (slab sample from site 2). **b)** Rhyolitic lapilli tuff and tuff with abundant but very small sulphide clasts (slab sample PFE-CB-2012-012, site 1). **c)** Foliated rhyolitic lapilli tuff with abundant, flattened sulphide clasts. Some of the clasts consist of massive pyrite, whereas others consist of semi-massive pyrite (slab sample PFE-CB-2012-008, site 1). **d)** Granoblastic pyrite forming semi-massive bands in altered felsic lapilli tuff (sample PFE-CB-2012-005, site 2). Abbreviations: Py = pyrite, Rhy bx = fragmental rhyolite.

vol.%), disseminated pyrite (2–10 vol.%), and minor calcite (<5 vol.%), as well as sericitized plagioclase phenocrysts. These felsic fragments are mostly angular to subangular (Fig. 4b). The second type of fragment is darker in colour and contains plagioclase microlites within a strongly chlorite- and sericite-altered groundmass. The third type of fragment is composed of 30 to 40 vol.% sulphides (pyrite±trace sphalerite), quartz (40 vol.%), and chlorite (20–30 vol.%). The fourth type of fragment is very rich in sulphides (<80 vol.%) and contains mostly pyrite with traces of sphalerite±chalcopyrite, up to 15 vol.% epidote, up to 5 vol.% chlorite, and quartz-calcite-epidote-chlorite veins. The volcaniclastic rocks are cut by a silicified mafic dyke at site 1. In this area, sulphide mineralization is concentrated near the dyke contacts.

Mafic to intermediate rocks

Massive andesites are very weakly foliated and are characterized by a groundmass of 50 to 65 vol.% plagioclase and 10 to 20 vol.% quartz. Locally the rocks have a porphyritic texture with <5 vol.% relict plagioclase phenocrysts. Alteration phases include sericite (5–30 vol.%) and chlorite (15–30 vol.%), which replace plagioclase, as well as local epidote (3 vol.%) and calcite (≤5 vol.%). Up to 15 vol.% amygdules of quartz, chlorite, and calcite are present. Oxides and sulphides are disseminated throughout, including titanium oxide (≤5 vol.%), magnetite (≤5 vol.%), pyrite (1 vol.%), sphalerite (<1 vol.%), and chalcopyrite (<1 vol.%).

Mafic dykes are very weakly foliated and are composed of a groundmass of microcrystalline chlorite (35 vol.%), sericite (10–25 vol.%), and quartz (≤5 vol.%). Relict plagioclase phenocrysts (<5 vol.%), which are replaced by sericite and chlorite, are present locally. Veinlets of microcrystalline quartz and chlorite are common throughout, as well as local veins of calcite-chlorite-epidote.

Fine-grained volcaniclastic mafic rocks are characterized by angular clasts (shards?) of relict volcanic

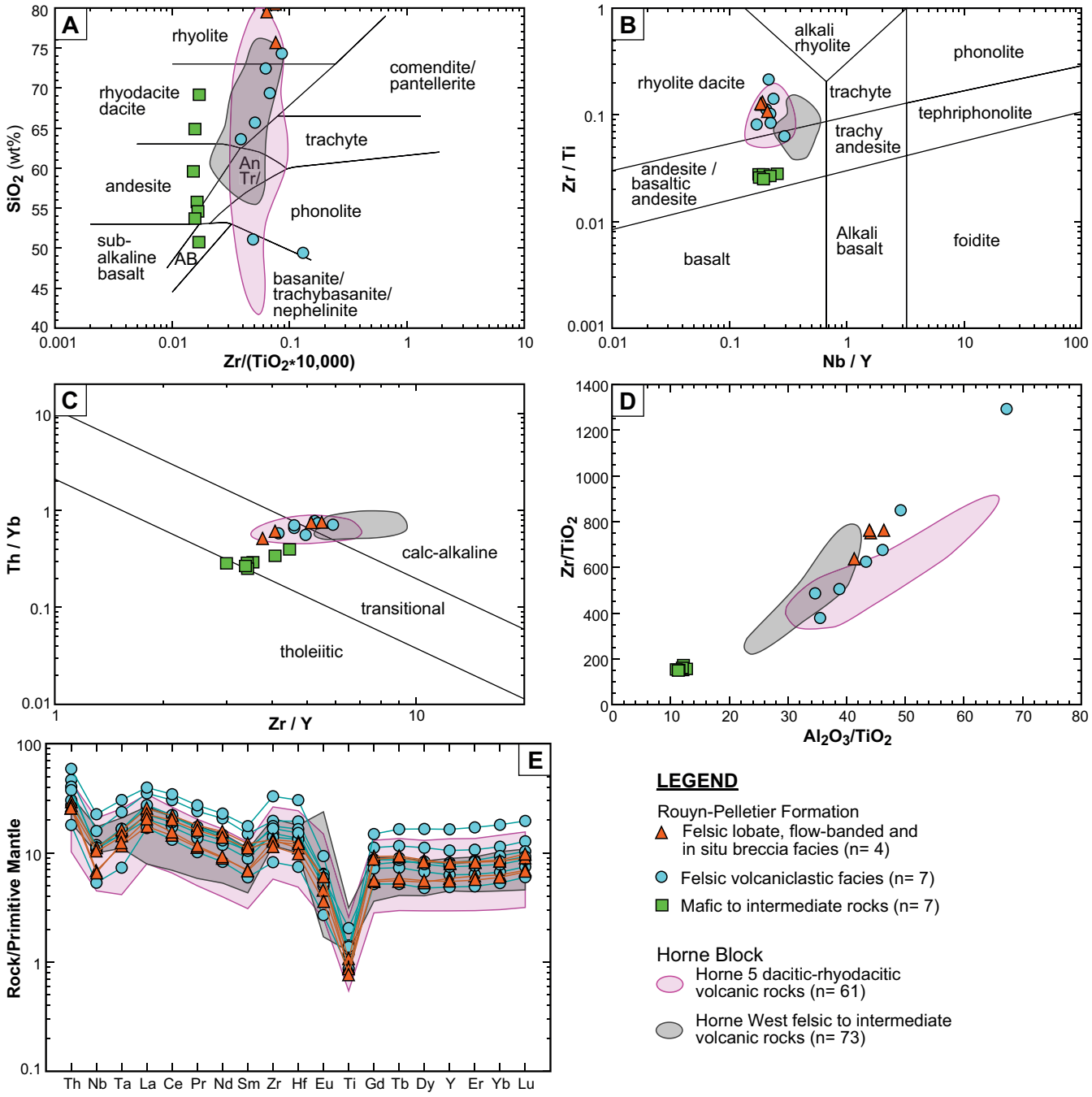

Figure 6. Major and trace element plots of the units mapped at sites 1 and 2, as well as a comparison with the Horne Block felsic volcanic units. **a)** SiO_2 versus $Zr/(TiO_2*10{,}000)$ classification diagram from Winchester and Floyd (1977). **b)** Zr/Ti versus Nb/Y classification diagram from Winchester and Floyd (1977). **c)** Th/Yb versus Zr/Y diagram for discrimination of magmatic affinities from Ross and Bédard (2009). **d)** Zr/TiO_2 versus Al_2O_3/TiO_2 discrimination diagram. **e)** Extended trace element profiles. Primitive mantle normalization values are from Sun and McDonough (1989). Data for the Rouyn-Pelletier Formation are from Mercier-Langevin et al. (2020), data for Horne 5 are from Krushnisky et al. (2018), and data for Horne West are from Laurin (2010).

glass (10–30 vol.%) arranged in a jigsaw pattern. These angular clasts are replaced by chlorite (20–60 vol.%), calcite (5–10 vol.%), and clusters of titanium oxide (10 vol.%). Locally, the rock has a groundmass of microcrystalline quartz (20–50 vol.%), chlorite (35 vol.%), and sericite (25 vol.%). Disseminated pyrite (<1 vol.%) containing traces of chalcopyrite inclusions is present locally.

Lithogeochemistry

To facilitate the geochemical characterization of the rocks, samples were grouped based on volcanic facies.

The first group consists of coherent felsic rocks (lobate and flow-banded facies) and related in situ breccia facies. These rocks are dacitic to rhyolitic in composition (Fig. 6a,b). Two samples have SiO_2 val-

ues exceeding 80 wt% (80.40 and 80.77 wt%: Mercier-Langevin et al., 2020). Rocks from this group have a transitional to calc-alkaline magmatic affinity (Fig. 6c). On a Zr/TiO_2 versus Al_2O_3/TiO_2 diagram (Fig. 6d), data points plot in a tight cluster at relatively elevated values of Zr/TiO_2 and Al_2O_3/TiO_2. Extended trace element profiles display a moderately steep light rare earth element (LREE) slope, flat heavy rare earth element (HREE) slope, a strong negative Ti anomaly, moderate negative Nb, Ta and Eu anomalies, and weak positive Zr and Hf anomalies (Fig. 6e).

The second group is composed of sulphide clast-bearing felsic volcaniclastic rocks. Rocks from this group are characterized by a dacitic to rhyolitic composition (Fig. 6a,b) and a transitional to calc-alkaline magmatic affinity (Fig. 6c). The spread of data along the y-axis in the SiO_2 versus $Zr/(TiO_2*10{,}000)$ diagram likely results from the variable but significant abundance of sulphide clasts and hydrothermal alteration, especially for samples displaying approximately 50 wt% SiO_2. Samples from this hydrothermally altered group plot in a linear trend on the Zr/TiO_2 versus Al_2O_3/TiO_2 immobile element diagram (Fig. 6d), supporting the interpretation of alteration-induced compositional variations rather than variations in the composition of the protolith. The extended trace element diagram shows profiles that are similar to the first group of felsic rocks, except for slightly weaker negative Ti anomalies and a pronounced vertical spread of profiles (Fig. 6e).

The third group consists of mafic to intermediate rocks that yield basaltic and andesitic compositions on the Zr/Ti versus Nb/Y diagram (Fig. 6b). Although the SiO_2 versus $Zr/(TiO_2*10{,}000)$ diagram (Fig. 6a) displays a strong spread of data along the y-axis (SiO_2), again likely due to hydrothermal alteration, clustering of data appears between the andesite and subalkaline basalt fields. These rocks have a tholeiitic to transitional magmatic affinity (Fig. 6c). Samples form a tight cluster of low Zr/TiO_2 and Al_2O_3/TiO_2 values (Fig. 6d), which is consistent with their more mafic trace element composition.

Hydrothermal Alteration and Sulphide Mineralization

Hydrothermal alteration of the felsic rocks in this area mainly consists of heterogeneous sericite and chlorite replacement of primary minerals in the matrix of the felsic volcaniclastic rocks. Coherent felsic units are generally weakly altered and are characterized by 15 to 20 vol.% foliated sericite in the groundmass, local chlorite, and plagioclase phenocrysts altered to sericite and chlorite. Vesicles present in these rocks are filled with calcite and quartz. Felsic volcaniclastic rocks are more strongly altered. Their matrix is composed of foliated chlorite and sericite that follow the contours of fragments, as well as disseminated sulphides and local calcite. Sulphide clasts are associated with strong halos of chlorite. All felsic rocks are crosscut by veins of quartz-calcite that locally contain chlorite, epidote, and sulphides. The sericite and chlorite alteration result in a significant increase in the Hashimoto alteration index (cf. Ishikawa et al., 1976) values and a moderate increase in the chlorite-carbonate-pyrite alteration index (cf. Large et al., 2001) values in the volcaniclastic rocks (not shown here; Boudreau 2013).

Mafic to intermediate rocks are weakly hydrothermally altered. The groundmass contains variable quantities of sericite (5–30 vol.%), and plagioclase phenocrysts are locally partially replaced by sericite and chlorite. Alteration phases, including quartz, calcite, chlorite, epidote, and sulphides, also appear as infillings of vesicles and veins. Fine-grained volcaniclastic mafic rocks are more strongly chlorite and sericite-altered than the massive rocks.

Mineralization in this area consists of disseminated granoblastic sulphides and sulphide clasts. Disseminated pyrite and traces of sphalerite and chalcopyrite are present in almost all rocks but rarely exceed 3 to 5 vol.%. These sulphides occur in the groundmass, in the matrix of volcaniclastic rocks (Fig. 5d), in fragments, in amygdules, and in veins. Semi-massive (>30 vol.% sulphides) to massive (>70 vol.% sulphides) sulphide clasts are subrounded to rounded and are often strongly elongated into the main foliation (Fig. 5a). Clasts are mostly composed of recrystallized pyrite (Fig. 7a,b), but also contain chlorite, quartz, calcite, and traces (<5 vol.%) of sphalerite, chalcopyrite, and pyrrhotite. Geochemical analyses of massive sulphide clasts indicate that they contain very low concentrations of Au, Ag, Cu, Zn, and Pb compared to sulphide clasts from the Horne West and Horne 5 zones (Fig. 8).

DISCUSSION

Depositional Setting

The study area is composed of extrusive felsic facies with mafic to intermediate extrusive and intrusive facies. Lithogeochemistry results are consistent with grouping all felsic rocks as part of the same unit with a dacitic to rhyolitic, transitional to calc-alkaline signature. Felsic units range from flows with lobate, flow banding and in situ brecciated textures to dominantly volcaniclastic with tuff breccia, lapilli tuff, and lesser tuff facies. The volcaniclastic rocks, which host the bulk of massive sulphide clasts and occur as multiple layers intercalated with the felsic coherent facies, are interpreted as flow breccia and debris flows that are associated with the emplacement of the felsic lava flows and lobes. Mafic to intermediate rocks also have

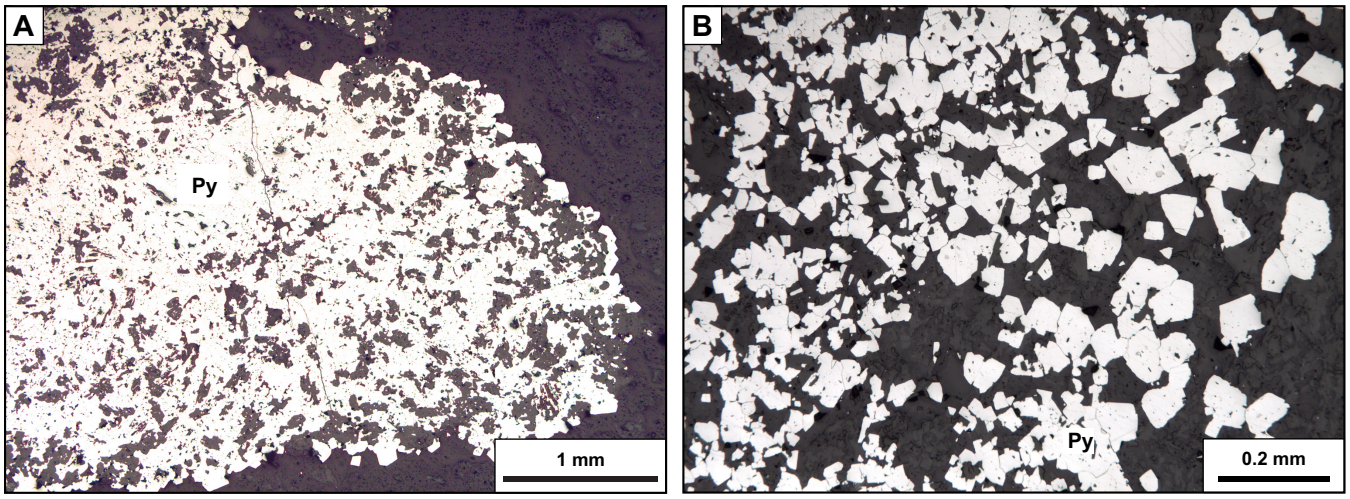

Figure 7. Photomicrographs (reflected light) of **(a)** massive and **(b)** semi-massive pyrite clasts. Abbreviation: Py = pyrite.

consistent geochemical signatures in this area, i.e., andesitic to basaltic andesitic, tholeiitic to transitional compositions. They occur as dykes, lava flows, and lobes, as well as local hyaloclastites that likely formed during quench fragmentation of subaqueous mafic flows (cf. Fisher and Schmincke, 1984).

Facies analysis of the felsic to mafic rocks reveals important crosscutting relationships. The contact between the massive andesite and the felsic in situ breccia at site 1, with bands of andesite intruding into the breccia, indicate that the mafic to intermediate rocks were emplaced after the felsic breccia. In addition, the presence of very irregular contacts between mafic dykes and felsic volcaniclastic rocks suggests that the dykes were emplaced in unconsolidated volcaniclastic debris. This is further confirmed by the

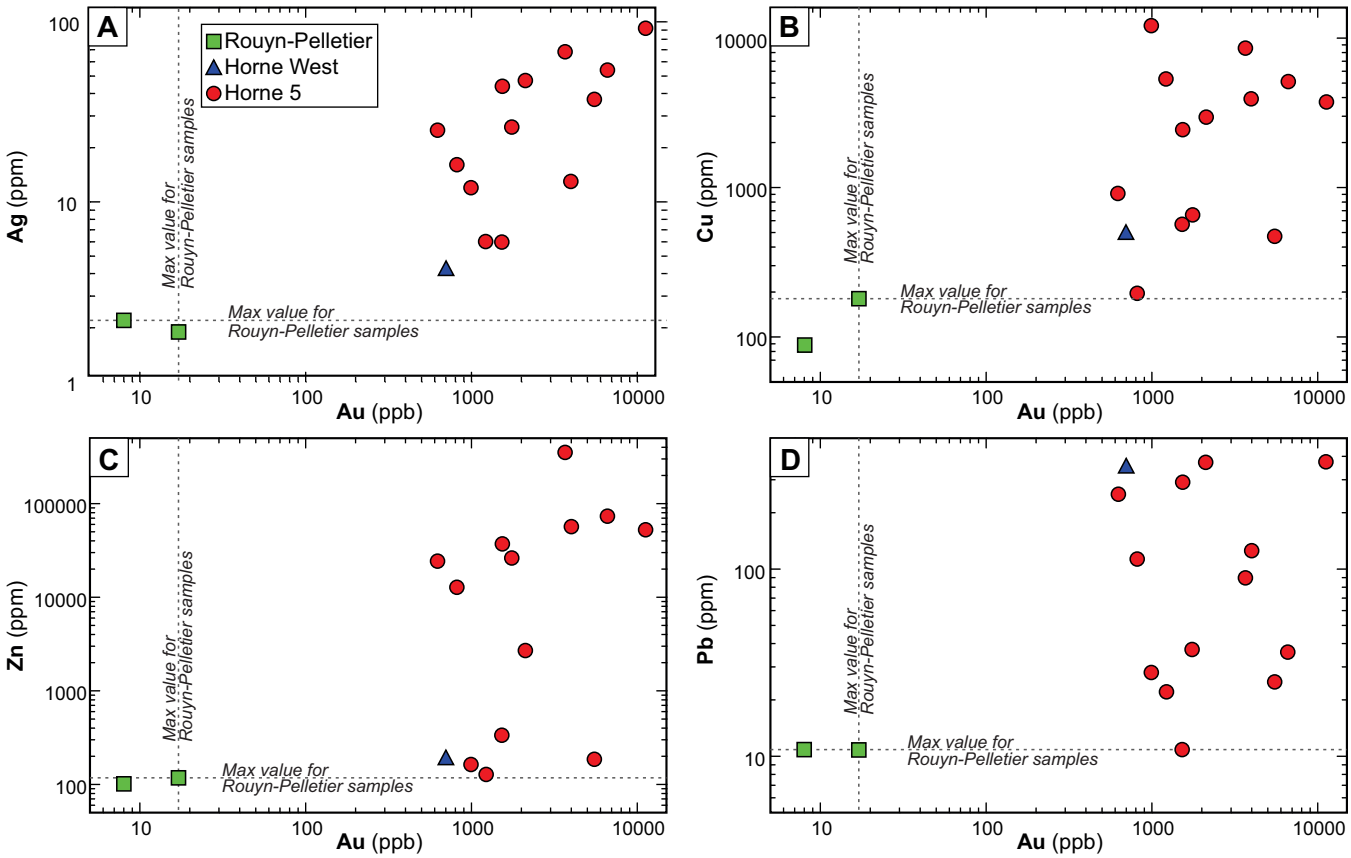

Figure 8. Metal biplots of massive sulphide fragments sampled in the Rouyn-Pelletier Formation, Horne West outcrops (Mercier-Langevin et al., 2020), and Horne 5 deposit (Krushnisky et al., 2018): **a)** Ag versus Au, **b)** Cu versus Au, **c)** Zn versus Au, and **d)** Pb versus Au.

presence of amoeboid andesite clasts in the felsic volcaniclastic rocks at site 1. These observations indicate that the mafic to intermediate rocks were emplaced shortly after formation of the felsic volcaniclastic rocks and the associated felsic lava flows, suggesting that felsic to mafic volcanism in this area was broadly coeval, as proposed by Moore et al. (2016).

Comparison with the Horne Block Felsic Rocks and Sulphide Clasts

The upper portion of the Rouyn-Pelletier Formation (*see* also Moore et al., 2016: stratigraphy of the Chadbourne Block) presents important similarities and differences with the rocks of the Horne Block. The felsic rocks in the study area and in the Horne Block share many textural similarities and the same facies are present in both areas, including lobate, flow-banded, and in situ breccia facies, as well as volcaniclastic rocks representing flow breccia and debris flows (Cattalani et al., 1993; Monecke et al., 2008; Laurin, 2010; Krushnisky et al., in prep). Both the upper portion of the Rouyn-Pelletier Formation and the Horne Block contain felsic volcaniclastic rocks that host massive sulphide clasts. Mafic to intermediate rocks are also present on both sides of the Andesite fault and were generally emplaced shortly after cessation of felsic volcanism (Kerr and Mason, 1990). Notable differences include, apart from the overall higher volume of felsic rocks in the Horne Block, the felsic facies that has been interpreted as pyroclastic flows in the Horne West zone (Monecke et al., 2008; Laurin, 2010) has not been correlated south of the Andesite fault in the study area. Additionally, the felsic volcaniclastic rocks at the Horne West zone span several dozen metres (Laurin, 2010), and up to 20 m and more in the Horne 5 zone (Krushnisky, 2018), however, beds of volcaniclastic rocks in the study area measure only a few metres thick. Hydrothermal alteration in the Rouyn-Pelletier rocks is similar to the alteration within the Horne Block (MacLean and Hoy, 1991), consisting primarily of sericite alteration with variable chlorite, epidote, and disseminated sulphides, but the alteration intensity is markedly lower.

The felsic rocks of the Rouyn-Pelletier Formation share certain compositional similarities with the host rocks of the Horne 5 deposit (e.g. Sterckx, 2018), as samples plot directly over the field of the Horne 5 felsic rocks in Figure 6a–c. Felsic rocks from Horne West have slightly higher Nb/Y ratios (Fig. 6b) and a more calc-alkaline character (Fig. 6c). On the Zr/TiO_2 versus Al_2O_3/TiO_2 diagram (Fig. 6d), felsic rocks from the Rouyn-Pelletier Formation form a trend that is intermediate between those from Horne 5 and Horne West, suggesting small compositional differences. Extended trace element profiles show similarities with the Horne 5 felsic rocks, whereas they vary quite significantly from the Horne West felsic rocks due to higher LREE values, stronger Ti and Nb negative anomalies, and weaker Zr and Hf positive anomalies (Fig. 6e). Rocks from the study area, therefore, share certain geochemical characteristics with rocks in the Horne Block, particularly those enclosing the Horne 5 deposit.

Sulphide mineralization in the upper portion of the Rouyn-Pelletier Formation does not appear to be associated with anomalous metal concentrations and instead are the result of sampling and transport of barren sulphide mineralization. Sulphide clasts in the Horne West and Horne 5 zones are significantly enriched in base and precious metals (Fig. 8); in comparison, sulphide clasts of the study area are extremely metal-depleted. Gold, Ag, Cu, Zn, and Pb grades in sulphide clasts of the Horne Block are often several orders of magnitude above those of the Rouyn-Pelletier clasts, which are completely barren.

Implications for Exploration

Rocks of the upper portion of the Rouyn-Pelletier Formation (or Chadbourne Block) and the Horne Block are of similar age (i.e. ca. 2702–2701 Ma: Mueller et al., 2012; McNicoll et al., 2014) and volcanic facies. However, there are subtle but significant geochemical differences that suggest their stratigraphy cannot be directly correlated. Moreover, the massive and volcaniclastic felsic rocks of the Horne Block form a much larger part of the stratigraphy than in the upper Rouyn-Pelletier Formation. The lower abundance of sulphide clasts, the absence of significant metal grades, the lower degree of hydrothermal alteration, and the limited thickness of the felsic volcaniclastic rocks in the uppermost Rouyn-Pelletier Formation suggest that the mapped area could represent a distal, poorly mineralized equivalent to the Horne West or Horne 5 zones, or an unrelated succession. Exploration in the uppermost part of the Rouyn-Pelletier Formation, therefore, should not be based solely on the premise that it is a direct continuity of the very prospective Horne Block stratigraphy.

The presence of sulphide clast-bearing felsic volcaniclastic units in the upper part of the Rouyn-Pelletier Formation indicates that there was hydrothermal activity before or during the emplacement of these rocks at ca. 2702 to 2701 Ma. Although the sulphide clasts at sites 1 and 2 do not carry significant base and precious metals, the hydrothermal activity responsible for the formation of sulphide zones from which they were sourced might have been fertile elsewhere along strike or similar time-stratigraphic intervals.

ACKNOWLEDGMENTS

This report results from a B.Sc. thesis (Université Laval) by the senior author as part of GSC's Targeted

Geoscience Program. The Rouyn-Pelletier project was conducted in collaboration with the Ministère de l'Énergie et des Ressources naturelles du Québec. Thanks to D. Yergeau and V. Bécu for their help with sample and data collection and analyses, and to G. Beaudoin, A. Caté, and E. Girard for scientific and technical support. We acknowledge C. Lawley, E. Ambrose, and V. Bécu for their editorial handling and reviews. An earlier version of this report benefited from a constructive review by L. Moore.

REFERENCES

Boudreau, C., 2013. Caractérisation des unités volcaniques à fragments de sulfures de la Formation Rouyn-Pelletier, Rouyn-Noranda, Québec; B.Sc. thesis, Université Laval, Québec, Quebec, 48 p.

Cattalani, S., Barrett, T.J., MacLean, W.H., Hoy, L., Hubert, C., and Fox, J.S., 1993. Métallogenèse des gisements Horne et Quemont (région de Rouyn-Noranda); Ministère de l'Énergie et des Ressources du Québec, ET 90-07, 132 p.

Dimroth, E., Imreh, L., Rocheleau, M., and Goulet, N., 1982. Evolution of the south-central part of the Archean Abitibi Belt, Quebec. Part I: Stratigraphy and paleogeographic model; Canadian Journal of Earth Sciences, v. 19, p. 1729–1758.

Fisher, R.V. and Schmincke, H.-U., 1984. Pyroclastic Rocks; Springer-Verlag, New York, 472 p.

Goutier, J., 2017. (Day 3 – Part I) Geology of the Blake River Group; Chapter 5 in Precious- and Base-Metal Deposits of the southern Abitibi Greenstone Belt, Superior Province, Canada: a field trip to the 14th Biennial Society for Geology Applied to Mineral Deposits meeting, (ed.) P. Mercier-Langevin, J. Goutier, and B. Dubé; Geological Survey of Canada, Open File 8317, 86 p.

Goutier, J., McNicoll, V.J., Dion, C., Lafrance, B., Legault, M., Ross, P.-S., Mercier-Langevin, P., Cheng, L.Z., de Kemp, E.A., and Ayer, J., 2009. L'impact du Plan cuivre et de l'IGC-3 sur la géologie de l'Abitibi et du Groupe de Blake River; Ministère des Ressources naturelles et de la Faune du Québec, GM 64195, p. 9–13.

Ishikawa, Y., Sawaguchi, T., Iwaya, S., and Horiuchi, M., 1976. Delineation of prospective targets for Kuroko deposits based on modes of volcanism of underlying dacites and alteration haloes; Mining Geology, v. 26, p. 105−117.

Kerr, D.J. and Gibson, H.L., 1993. A comparison of the Horne volcanogenic massive sulfide deposit and intracauldron deposits of the Mine Sequence, Noranda, Quebec; Economic Geology, v. 88, p. 1419–1442.

Kerr, D.L. and Mason, R., 1990, A re-appraisal of the geology and ore deposits of the Horne mine complex at Rouyn-Noranda, Quebec; *in* The Northwestern Quebec Polymetallic Belt, (ed.) M. Rive, P. Verpaelst, Y. Gagnon, J.M. Lulin, G., Riverin, and A. Simard; Canadian Institute of Mining and Metallurgy, Special Volume 43, p. 153–165.

Krushnisky, A., 2018. Controls on gold enrichment at the Horne 5 Archean VMS deposit, Abitibi greenstone belt, Québec; M.Sc. thesis, Institut national de la recherche scientifique – Centre Eau Terre Environnement, Québec, Quebec, 198 p.

Krushnisky, A., Mercier-Langevin, P., Ross, P.-S., Bécu, V., Lauzière, K., and Goutier, J., 2018. Whole-rock lithogeochemistry of the gold-bearing mineralized zones of the Horne 5 deposit, Québec, Canada; Geological Survey of Canada, Open File 8501, 1 .zip file.

Krushnisky, A., Mercier-Langevin, P., Ross, P.-S., Goutier, J., Pilote, C., and Bernier, C., 2020. Geology and gold enrichment at the Horne 5 Archean volcanogenic massive sulphide deposit, Abitibi greenstone belt, Quebec: A synthesis; *in* Targeted Geoscience Initiative 5: Contributions to the Understanding of Canadian Gold Systems, (ed.) P. Mercier-Langevin, C.J.M. Lawley, and S. Castonguay; Geological Survey of Canada, Open File 8712, p. 31–44. doi:10.4095/323663

Krushnisky, A., Mercier-Langevin, P., Ross, P.-S., Goutier, J., Pilote, C., and Bernier, C., in prep. The Archean Horne 5 volcanogenic massive sulfide deposit, Abitibi greenstone belt, Quebec: Geology, controls on gold enrichment, and implications for its genesis.

Large, R.R., Gemmell, J.B., Paulick, H., and Huston, D.L., 2001. The alteration box plot: A simple approach to understanding the relationship between alteration, mineralogy and lithogeochemistry associated with volcanic-hosted massive sulfide deposits; Economic Geology, v. 96, p. 957−971.

Laurin, J., 2010. Geology, gold mineralization and alteration of the Horne West Property Rouyn-Noranda; M.Sc. thesis, University of Ottawa, Ottawa, Ontario, 172 p.

MacLean, W.H. and Hoy, L.D., 1991. Geochemistry of hydrothermally altered rocks at the Horne Mine, Noranda, Quebec; Economic Geology, v. 86, p. 506–528.

McNicoll, V., Goutier, J., Dubé, B., Mercier-Langevin, P., Ross, P.-S., Dion, C., Monecke, T., Legault, M., Percival, J., and Gibson, H., 2014. U-Pb geochronology of the Blake River Group, Abitibi greenstone belt, Quebec, and implications for base metal exploration; Economic Geology, v. 109, p. 27–59.

Mercier-Langevin, P., Goutier, J., Ross, P.-S., McNicoll, V., Monecke, T., Dion, C., Dubé, B., Thurston, P., Bécu, V., Gibson, H., Hannington, M., and Galley, A., 2011. The Blake River Group of the Abitibi greenstone belt and its unique VMS and gold-rich VMS endowment: Field Trip 02B guidebook; Geological Survey of Canada, Open File 6869, 61 p.

Mercier-Langevin, P., Boudreau, C., Goutier, J., and Krushnisky, A., 2020. Whole-rock lithogeochemistry of the upper Rouyn-Pelletier Formation, Rouyn-Noranda, Quebec; Geological Survey of Canada, Open File 8709, 1 zip file.

Monecke, T., Gibson, H.L., Dubé, B., Laurin, J., Hannington, M.D., and Martin, L., 2008. Geology and volcanic setting of the Horne deposit, Rouyn-Noranda, Quebec: initial results of a new research project; Geological Survey of Canada, Current Research 2008-9, 16 p.

Monecke, T., Mercier-Langevin, P., Dubé, B., and Frieman, B.M., 2017. Geology of the Abitibi greenstone belt; *in* Archean Base and Precious Metal Deposits, Southern Abitibi Greenstone Belt, Canada, (ed.) T. Monecke, P. Mercier-Langevin, and B. Dubé; Society of Economic Geologists, Reviews in Economic Geology, v. 19, p. 7–49.

Moore, L.N., Mueller, W.U., and Daigneault, R., 2012. In situ hydroclastic fragmentation of subaqueous ponded lavas; New Senator caldera, Abitibi greenstone belt, Quebec, Canada; Precambrian Research, v. 214–215, p. 44–59.

Moore, L.N., Daigneault, R., Aird, H.M., Banerjee, N.R., and Mueller, W.U., 2016. Reconstruction and evolution of Archean intracaldera facies: the Rouyn–Pelletier Caldera Complex of the Blake River Group, Abitibi greenstone belt, Canada; Canadian Journal of Earth Sciences, v. 53, p. 355–377.

Mueller, W.U., Friedman, R., Daigneault, R., Moore, L., and Mortensen, J., 2012. Timing and characteristics of the Archean subaqueous Blake River Megacaldera Complex, Abitibi greenstone belt, Canada; Precambrian Research, v. 214–215, p. 1–27.

Piercey, S.J., Chaloux, E.C., Péloquin, A.S., Hamilton, M.A., and Creaser, R.A., 2008. Synvolcanic and younger plutonic rocks

from the Blake River Group: implications for regional metallogenesis; Economic Geology, v. 103, p. 1243–1268.

Price, P., 1934. The geology and ore deposits of the Horne Mine, Noranda, Quebec; Transactions of the Canadian Institute of Mining and Metallurgy and of the Mining Society of Nova Scotia, v. 37, p. 108–140.

Ross, P.-S. and Bédard, J.H., 2009. Magmatic affinity of modern and ancient subalkaline volcanic rocks determined from trace-element discriminant diagrams; Canadian Journal of Earth Sciences, v. 46, p. 823−839.

Sinclair, W.D., 1971. A volcanic origin for the No. 5 Zone of the Horne Mine, Noranda, Quebec; Economic Geology, v. 66, p. 1225–1231.

Sterckx, S., 2018. Géochimie des roches volcaniques archéennes du Groupe de Blake River, ceinture de roches vertes de l'Abitibi, Québec; M.Sc. thesis, Institut national de la recherche scientifique – Centre Eau Terre Environnement, Québec, Quebec, 209 p.

Sun, S.S. and McDonough, W.F., 1989. Chemical and isotopic systematics of oceanic basalts: implications for mantle composition and processes; *in* Magmatism in Ocean Basins, (ed.) A.D. Saunders and M.J. Norry; Geological Society of London, Special Publication 42, p. 313–345.

Winchester, J.A. and Floyd, P.A., 1977. Geochemical discrimination of different magma series and their differentiation products using immobile elements; Chemical Geology, v. 20, p. 325−343.

Stratigraphic setting of the LZ5 and Ellison mineralized zones, LaRonde Zone 5 project, Doyon-Bousquet-LaRonde mining camp, Abitibi, Quebec

Émile Boily-Auclair[1]*, Patrick Mercier-Langevin[2], Pierre-Simon Ross[1], and David Pitre[3]

[1]Institut national de la Recherche scientifique – Centre Eau Terre Environnement, 490 rue de la Couronne, Québec, Quebec G1K 9A9

[2]Geological Survey of Canada, 490 rue de la Couronne, Québec, Quebec G1K 9A9

[3]Agnico Eagle Mines Limited, LaRonde Division, 10200, route de Preissac, Rouyn-Noranda, Quebec J0Y 1C0

*Corresponding author's e-mail: emile.boily-auclair@ete.inrs.ca

ABSTRACT

The LaRonde Zone 5 (LZ5) project and the neighbouring mineralized zones of the Ellison property are part of the Doyon-Bousquet-LaRonde mining camp in the southern part of the Abitibi greenstone belt. The mineralized zones of the LZ5 (zones 4, 4.1, and 5) and the Ellison property (zones A and B) are hosted in the Bousquet Formation of the Blake River Group. The host rocks are steeply south-dipping (80–90°) and south-facing, mafic to felsic volcanic and volcaniclastic units. The synvolcanic gold mineralization consists of deformed discordant networks of millimetre to centimetre thick pyrite±pyrrhotite±chalcopyrite veinlets (10–20 vol.%) and, to a lesser extent, very finely disseminated pyrite (1 vol.%) in altered volcanic and volcaniclastic rocks. Prior to this study, the LZ5 and Ellison mineralized zones were interpreted to be hosted in the Bousquet heterogeneous unit (Unit 4.4) in the uppermost part of the lower member of the Bousquet Formation. The current study shows that the mineralized zones are located higher in the stratigraphic sequence, i.e., in highly deformed and altered mafic to felsic volcanic and volcaniclastic units (tuff and lapilli tuff) at the base of the upper member of the Bousquet Formation. Consequently, the LZ5 mineralization, which is considered one of the oldest in the camp, coincides in time and space with a shift in the magmatic evolution of the Bousquet Formation from dominantly tholeiitic-transitional mafic-intermediate (lower member) to dominantly transitional-calc-alkaline intermediate-felsic (upper member). The revised position of the LZ5 ore zones to slightly higher in the stratigraphic sequence substantiates the camp-wide association between Au (±Cu-Zn-Ag) mineralization and intermediate to felsic transitional to calc-alkaline magmatism and further indicates that hydrothermal and petrogenetic processes are linked in major synvolcanic Au deposits in the Archean.

INTRODUCTION

The Doyon-Bousquet-LaRonde mining camp in the southern Abitibi greenstone belt, Quebec, represents one of the richest Canadian gold districts. It hosts world-class Au-rich volcanogenic massive sulphide deposits as well as intrusion-associated Au±Cu vein systems (Mercier-Langevin et al., 2017). These contrasting deposit styles are considered to be mostly coeval, and part of an Archean synvolcanic magmatic-hydrothermal system (Yergeau et al., 2015; Mercier-Langevin et al., 2017, and references therein). Many of those deposits have been studied in detail over the past two decades, but the past-producing Bousquet 1 mine, and its lowermost ore zones (Zone 4.1, Zone 4, and Zone 5) remain poorly documented. These ore zones of the former Bouquet 1 mine are located in the central part of the camp and mark the transition between intrusion-related-style systems to the west, and volcanogenic massive sulphide (VMS)-style systems to the east. They thus represent a critical area for the understanding of the metallogenic evolution of the camp. Renewed mining activity in this area gave access to new material and exposures and provided an opportunity to study zones 4, 4.1, and 5, which define the LZ5 project. These zones were formerly part of the Bousquet 1 mine, which produced 42 t Au, or 1.36 Moz, from 1978 to 1996 (Mercier-Langevin et al., 2017). The LZ5 is currently mined underground by Agnico Eagle Mines Limited from the LaRonde mine complex and resources are estimated at 17.5 Mt of ore at 2.0 g/t Au for a total resource of 35.9 t Au (1.15 Moz) (Agnico Eagle Mines Ltd., 2019a).

Several models have been proposed for the timing and origin of the Au mineralization at Bousquet 1 (now LZ5 project), including a synvolcanic origin for both the gold and the sulphides (e.g. Valliant et al., 1982; Stone, 1990; Mercier-Langevin et al., 2007c), and a synvolcanic sulphide system overprinted by a syn-

Boily-Auclair, É., Mercier-Langevin, P., Ross, P.-S., and Pitre, D., 2020. Stratigraphic setting of the LZ5 and Ellison mineralized zones, LaRonde Zone 5 project, Doyon-Bousquet-LaRonde mining camp, Abitibi, Quebec; *in* Targeted Geoscience Initiative 5: Contributions to the Understanding of Canadian Gold Systems, (ed.) P. Mercier-Langevin, C.J.M. Lawley, and S. Castonguay; Geological Survey of Canada, Open File 8712, p. 57–73. https://doi:10.4095/323665

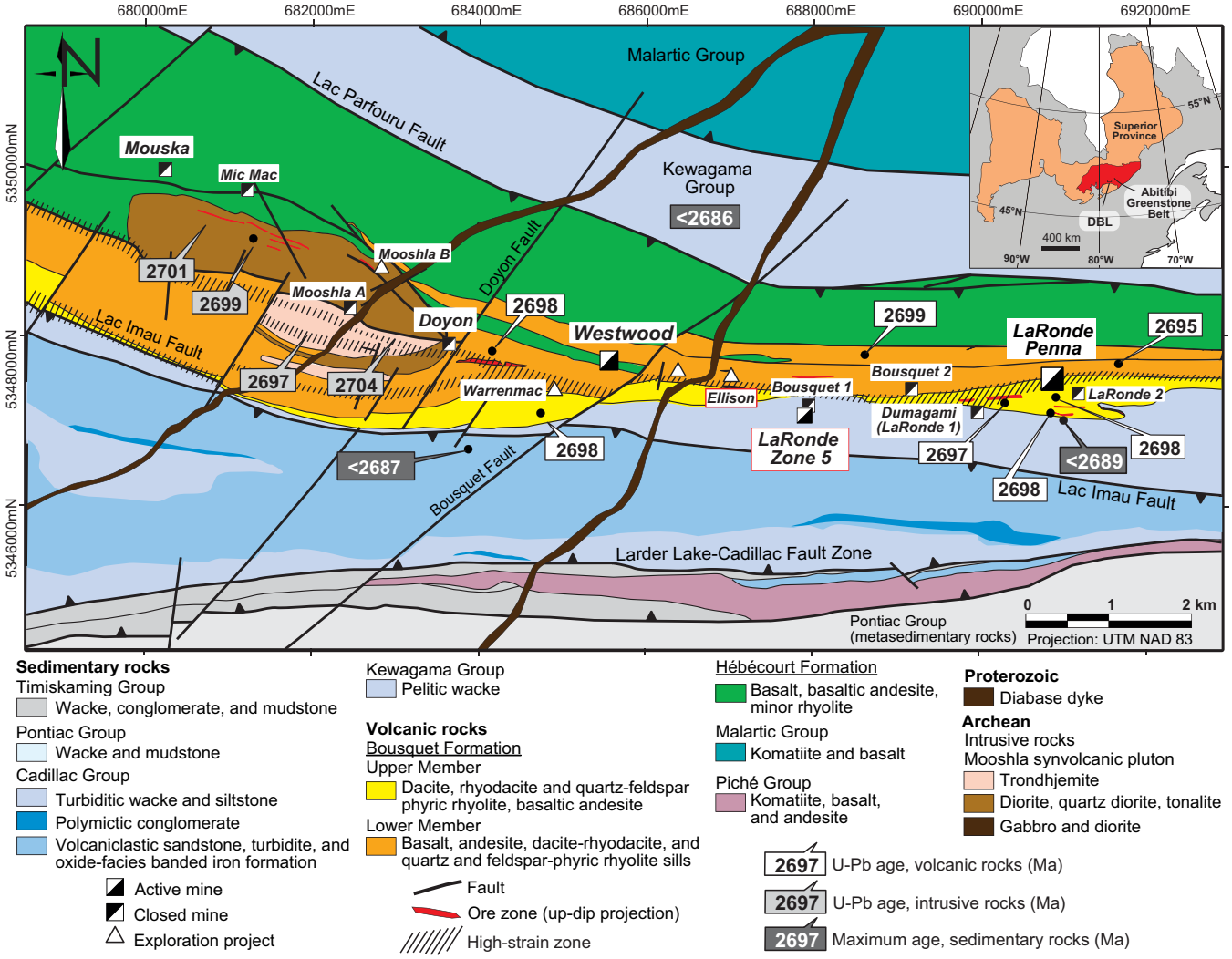

Figure 1. Geology of the Doyon-Bousquet-LaRonde mining camp (*from* Mercier-Langevin et al., 2017).

deformation gold episode (e.g. Tourigny et al., 1989). Even though recent work indicates a synvolcanic origin for the gold in the Doyon-Bousquet-Laronde (DBL) camp, doubts remain as to the exact timing of the auriferous mineralization at the LZ5 project, which shows characteristics that contrast with those of other deposits in the camp (Boily-Auclair et al., 2019). For example, the style of mineralization (pyrite±pyrrhotite±chalcopyrite±sphalerite veins and veinlets, and lesser disseminated and fragmental pyrite) strongly contrasts with the Au-rich massive and semi-massive sulphides, Au-rich sulphide vein stockworks and disseminations, intrusion-hosted sulphide-rich quartz veins, and orogenic sulphide-rich Au-Cu vein systems that have been documented in the DBL camp.

This report establishes the stratigraphic position of the mineralized zones at the LZ5 project and neighbouring Ellison property and examines the possible controls on ore style and distribution. Ongoing research at the LZ5 project and on the Ellison property aims to establish the relative timing of events, compare mineralization with the other ore styles of the camp, and contribute to the metallogenic models for Archean gold deposits in the southern Superior Province.

DOYON-BOUSQUET-LARONDE MINING CAMP

The Doyon-Bousquet-LaRonde mining camp represents one of the largest gold and base metal districts in Canada, with a total estimated gold budget of 865 t Au, (28.8 Moz; past production, estimated reserves, and resources: Mercier-Langevin et al., 2017). The stratigraphy of the DBL mining camp consists of a succession of volcanic and volcaniclastic rocks of the Hébécourt and Bousquet formations of the Blake River Group. The succession is homoclinal, dips steeply (~75–90º), and faces south (Fig. 1).

The Hébécourt Formation is the lowermost unit in the DBL camp and includes massive to pillowed mafic flows, including several variolitic layers of tholeiitic composition (Goutier, 1997; Fig. 1, 2). Conformably overlying the Hébécourt Formation is the Bousquet

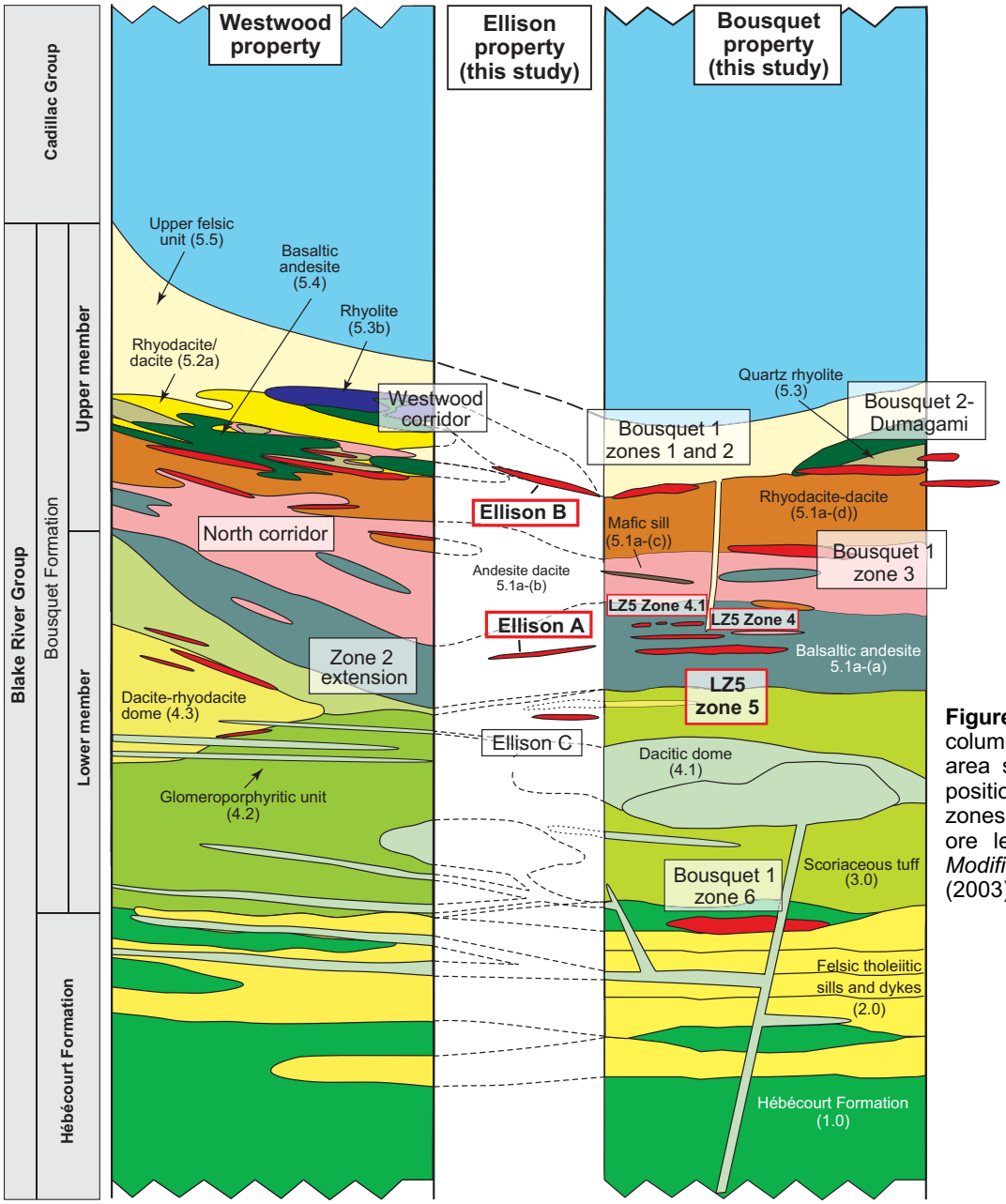

Figure 2. Simplified stratigraphic columns of the Bousquet-Ellison area showing the stratigraphic position of the main mineralized zones of the LZ5 project. The ore lenses are not to scale. *Modified from* Lafrance et al. (2003) and Yergeau (2015).

Formation (ca. 2699–2696 Ma), one of the youngest volcanic units of the Blake River Group (McNicoll et al., 2014). It is divided into two members: the lower member consists of volcanic to volcaniclastic, basaltic to andesitic rocks with minor felsic units; the upper member is andesitic to dacitic at the base and rhyolitic at the top (Fig. 2). The Bousquet Formation is tholeiitic at the base and calc-alkaline towards the top (Lafrance et al., 2003; Mercier-Langevin et al., 2007a).

The Hébécourt and Bousquet formations are structurally bounded to the north by the Kewagama Group sedimentary rocks (≤2684 ± 1 Ma: Davis, 2002) and to the south by the Cadillac Group sedimentary rocks (≤2687 ± 3 Ma: Davis, 2002; Lafrance et al., 2005). The contact between the Hébécourt Formation and the lower member of the Bousquet Formation is cut by the polyphase Mooshla intrusion (2698–2697 Ma: Lafrance et al., 2003; Galley and Lafrance, 2014; McNicoll et al., 2014; Fig. 1). The age of the Mooshla intrusion corroborates that it is temporally associated with the rocks of the Bousquet Formation, i.e., synvolcanic (Mercier-Langevin et al., 2007c; Galley and Lafrance, 2014). This intrusion is also thought to have contributed heat, hydrothermal fluids, and metals to the sulphide-quartz auriferous vein systems (Doyon and

Westwood Zone 2 Extension) and to the VMS deposits of the camp (Galley and Lafrance, 2014; Yergeau et al., 2015).

The rocks of the DBL mining camp were affected by at least three episodes of regional deformation (Mercier-Langevin et al., 2007c, and references therein). The geometry of the host rocks and ore zones is mainly controlled by the main phase of regional shortening (locally referred to as D_2). This is best defined by a steeply (~75–90º) south-dipping, east-trending foliation (S_2). This fabric corresponds to fabric S_3 at the regional scale (Monecke et al., 2017).

STRATIGRAPHY OF THE LZ5 PROJECT AND ELLISON PROPERTY

The LZ5 and Ellison mineralized zones are hosted in highly deformed, metamorphosed (greenschist facies) and altered volcanic and volcaniclastic units of the Bousquet Formation upper member. The effects of alteration, deformation, and metamorphism make it difficult to recognize primary textures and strongly hamper mapping solely based on macroscopic rock descriptions. Recent studies (e.g. Lafrance et al., 2003; Mercier-Langevin et al., 2007a,b, 2008, 2009; Yergeau et al., 2015) have shown that combining lithogeochemistry with careful surface, underground mapping, drill core descriptions, and microscopic observations make it possible to differentiate the units composing the upper and lower member of the Bousquet Formation with more confidence.

Since unaltered rocks are rare in the area, a protolith composition based on the average of samples considered the least altered has been used to estimate the primary composition of the host rock of the LZ5 and Ellison mineralized zones. The samples used were selected based on low loss of ignition values (LOI ≤6 wt%), and low S (<0.9 wt%) and CO_2 (<2.5 wt%) content, as well as specific ranges of alteration indices (i.e. Hashimoto alteration index (AI: Ishikawa et al., 1976) ≤60; advanced-argillic alteration index (AAAI: Williams and Davidson, 2004) ≤60; and chlorite-carbonate-pyrite index (CCPI: Large et al., 2001) ≤90). Results and observations presented in the following sections mostly come from the detailed study of core from 6 drillholes (S10-04, S11-44, BZ-1805136-1, 121-06-11, 121-06-16, and 121-06-20). These intersect the LZ5 and Ellison A and B ore zones and most of the footwall and hanging wall units.

LZ5 and Ellison Mineralized Zones

The LZ5 project is located halfway between two world-class Au deposits that are characterized by contrasting mineralization styles, i.e., the Bousquet 2-Dumagami Au-rich VMS deposit to the east, and the Westwood intrusion-related and Au-rich VMS deposit to the west (Fig. 1). The LZ5 and Ellison mineralized zones are hosted in a succession of mafic to felsic volcanic and volcaniclastic units (tuff and lapilli tuff±tuff breccia) forming part of the base of the upper member of the Bousquet Formation (*see* the following sections). The LZ5 consists of three distinct mineralized corridors, referred to as, from south to north, Zone 4.1, Zone 4, and Zone 5 (Fig. 2, 3). The Ellison zones are located a few hundred metres west of the LZ5 project and consist of three stacked mineralized corridors, referred to as zones A, B, and C (Fig. 2). The Ellison Zone B is located stratigraphically higher than the LZ5 mineralized corridors, whereas the Ellison Zone A is located approximately at the same stratigraphic position as the LZ5 mineralized corridors. The mineralized rocks at LZ5 and Ellison are generally moderately to intensely foliated, and locally sheared. The steeply south-dipping, east-trending regional S_2 schistosity (~80–90°) affects all rock units, which show evidence of flattening, stretching, boudinage, transposition, and folding (Boily-Auclair et al., 2019). The LZ5, as well as the Ellison Zone A mineralized corridors, were previously interpreted to be hosted within the heterogeneous Bousquet unit (unit 4.4) of the Bousquet Formation lower member. This unit consists of tuffs, lapilli tuffs, and massive, pillowed, and brecciated flows of mafic to intermediate composition (Yergeau, 2015).

Zone 5 is the main mineralized body at the LZ5 project. Gold grades are generally slightly higher and more consistent than in zones 4 and 4.1, which are considered as discontinuous satellite zones. Zone 5 is up to 30 m thick (Fig. 3) and extends over approximately 600 m along strike (east-west). Zone 5 extends from surface down to 1,100 m below surface (current resources envelope). The mineralized corridor gradually thins out both to the east and to the west to only a few metres thick, where it becomes subeconomic (Fig. 2). The mineralization consists of transposed discordant networks of millimetre to centimetre thick pyrite veinlets (10–20 vol.%; Fig. 4a) and, to a lesser extent, of very finely disseminated granoblastic pyrite, in clusters and/or as elongated/flattened centimetre to decimetre long fragments (≤10 vol.%; Fig. 4b–e). Pyrrhotite, chalcopyrite, and sphalerite are present in minor to trace amounts, in association with pyrite. Gold occurs as inclusions in granoblastic pyrite (Tourigny et al., 1989; Boily-Auclair et al., 2019). Zone 5 is hosted in massive mafic to intermediate rocks that are tentatively correlated to the Doyon dacite-rhyodacite unit (unit 5.1a) and possibly to the Westwood basaltic andesite unit (unit 5.4; Fig. 5a,b), as discussed below. The mineralization style of zones 4 and 4.1 is similar to that of Zone 5, although sulphides are slightly less abundant and gold grades are slightly lower on average than in Zone 5.The mineralized intervals of the Ellison zones

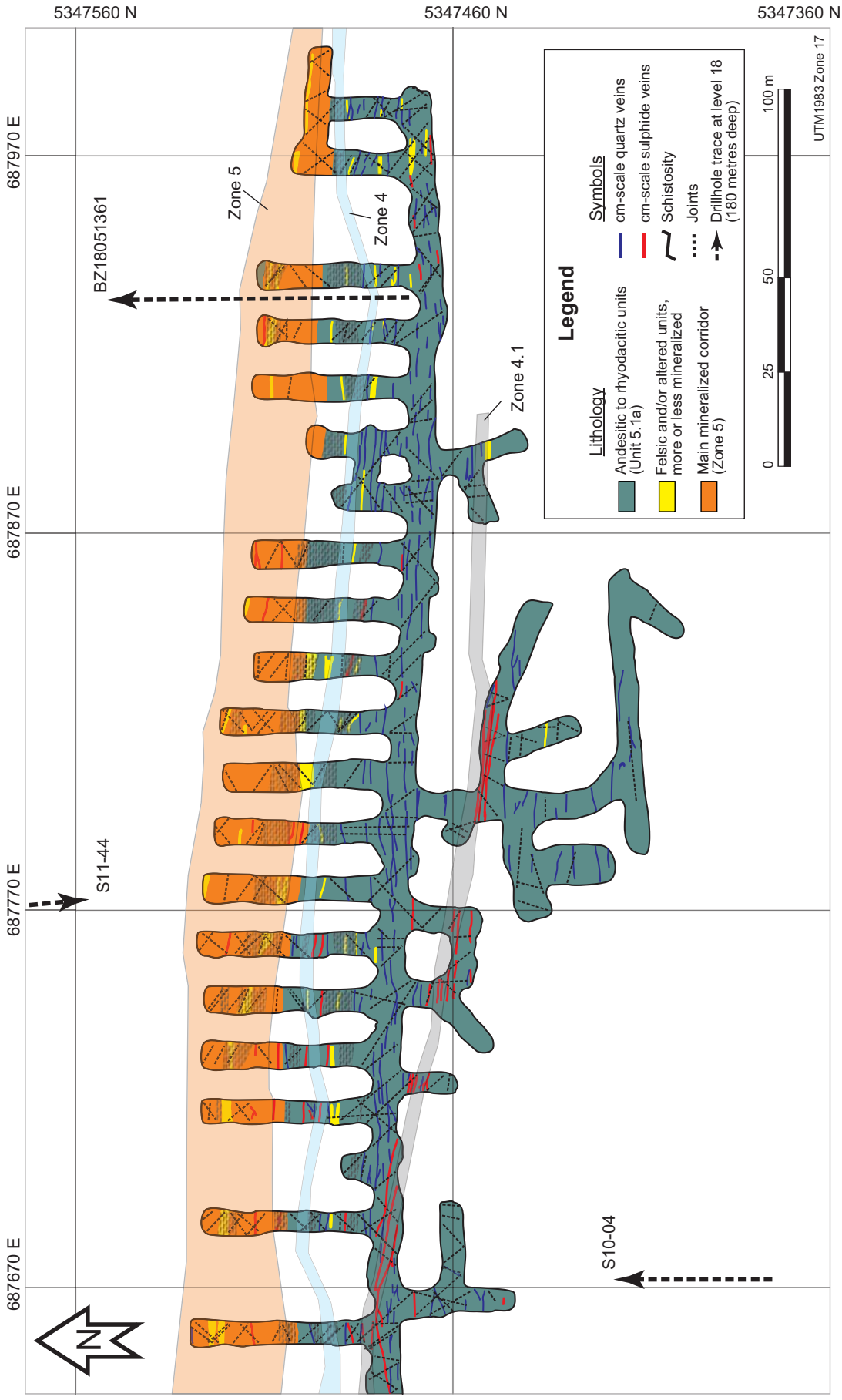

Figure 3. Plan view of mineralized zones 4, 4.1, and 5 on level 18 (180 m below surface) of the LZ5 project of the LaRonde complex. *Modified from* Agnico Eagle Mines Ltd (2019b).

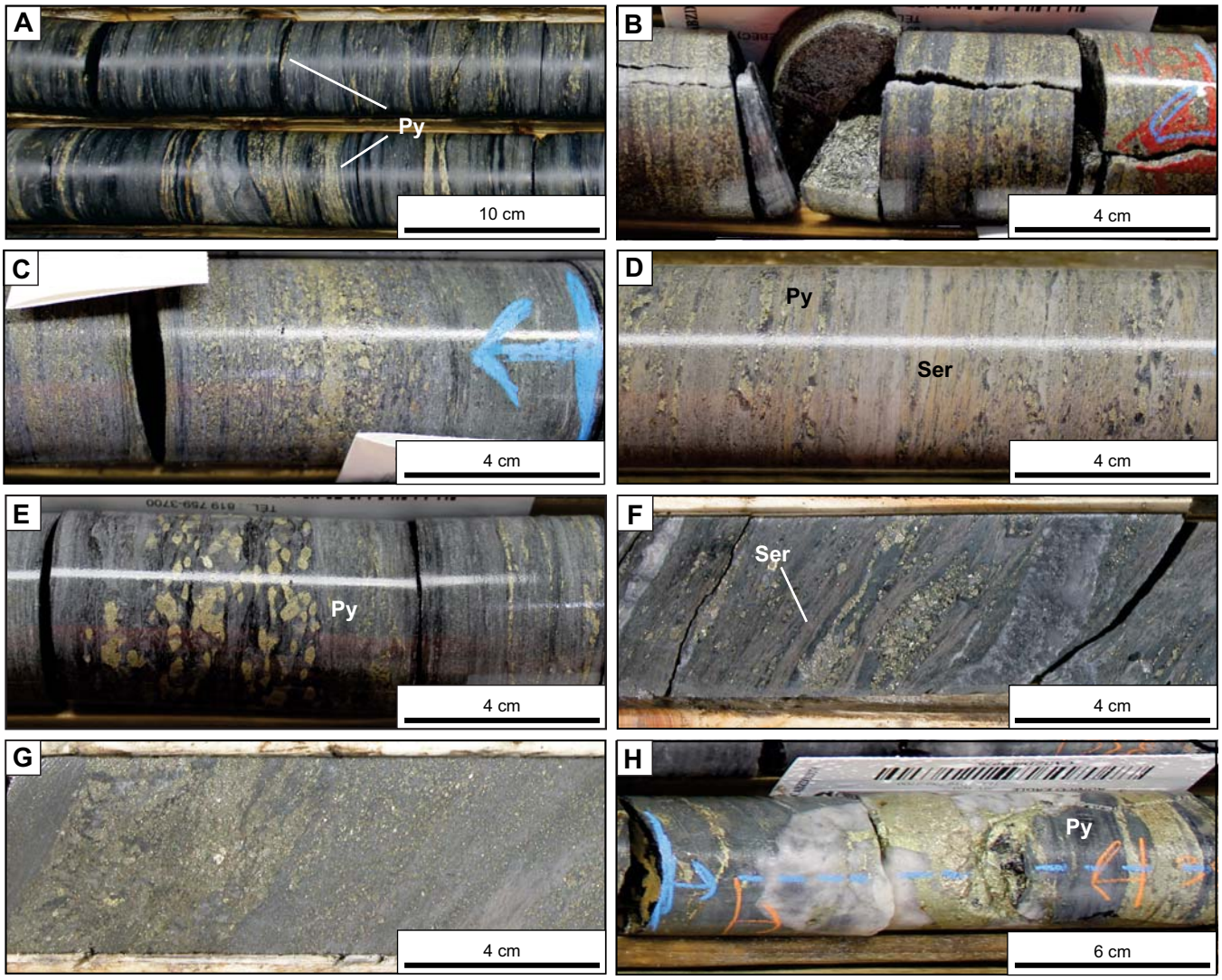

Figure 4. a) Massive and homogeneous andesitic rock (typical of Zone 5) with 10 to 12 vol.% millimetre-thick stringers of pyrite, subunit 5.1a-(b), drillhole BZ-0905119-1. **b)** Finely disseminated pyrite mineralization in an andesitic rock, north of Zone 5, unit 5.1a-(b), drillhole BZ-0905119-1. **c)** Banded andesitic unit located north of Zone 5. Finely disseminated sulphides and discontinuous millimetre-thick stringers, unit 5.1a-(a), drillhole BZ-0905116-1. **d)** Very fine-grained, strongly sericitized unit. The mineralization is finely disseminated in the matrix and in millimetre-thick fragments, Zone 4, unit 5.1a-(a), drillhole BZ-1805120-1. **e)** Millimetre-thick pyrite fragments in an intermediate rock, beginning of Zone 5, unit 5.1a-(b), drillhole BZ-0905119-1. **f)** Felsic lapilli tuff cut by centimetre-thick quartz veins as well as sulphide veinlets and fragments, Ellison Zone B, unit 5.3a-(b), drillhole 121-06-11. **g)** Disseminated to semi-massive granoblastic pyrite in an andesitic rock, Ellison Zone A, unit 5.1a-(a), drillhole 121-06-11. **h)** Quartz vein with a massive chalcopyrite cluster in a typical andesitic unit of Zone 5 (7.5 g/t Au), drillhole BZ-0905116-1. Abbreviations: Py = pyrite; Ser = sericite.

A and B consist of discordant networks of millimetre to centimetre thick pyrite veinlets (10–20 vol.%), disseminated pyrite, pyrite clusters, and elongated pyrite fragments (Fig. 4f). Whereas in zones 4, 4.1, and 5 of the LZ5, variable amounts of chalcopyrite, sphalerite, and pyrrhotite are present within the mineralized corridor of the Ellison property. Mineralized intervals of zones A and B show higher gold concentration (e.g. 6.4 g/t Au over 4 m, and 4.3 g/t Au over 8 m), but are thinner than those found at the LZ5 and are discontinuous. Silver grades are also higher at Ellison, which has Ag values as high as 80 g/t over short intervals (1.2 m long). In addition, semi-massive to massive bands of pyrite are present within the mineralized intervals (Fig. 4g). These bands have high gold grades (≤30 g/t over 1.5 m intervals), with relatively abundant chalcopyrite (Cu ≤0.1 wt%) and sphalerite (Zn ≤3.5 wt%). Ellison Zone A is hosted within Westwood basaltic andesite (subunit 5.1a-(a)) and Zone B is hosted within the Westwood porphyritic rhyolitic dome (subunit 5.3a-(b); Fig. 2).

Additionally, discordant, sulphide-rich, centimetre to decimetre thick quartz-carbonate veins are present within the LZ5 and Ellison mineralized zones, particularly in Zone 5 (Fig. 4h). Grades of up to 60 g/t are associated with some of these veins (Boily-Auclair et

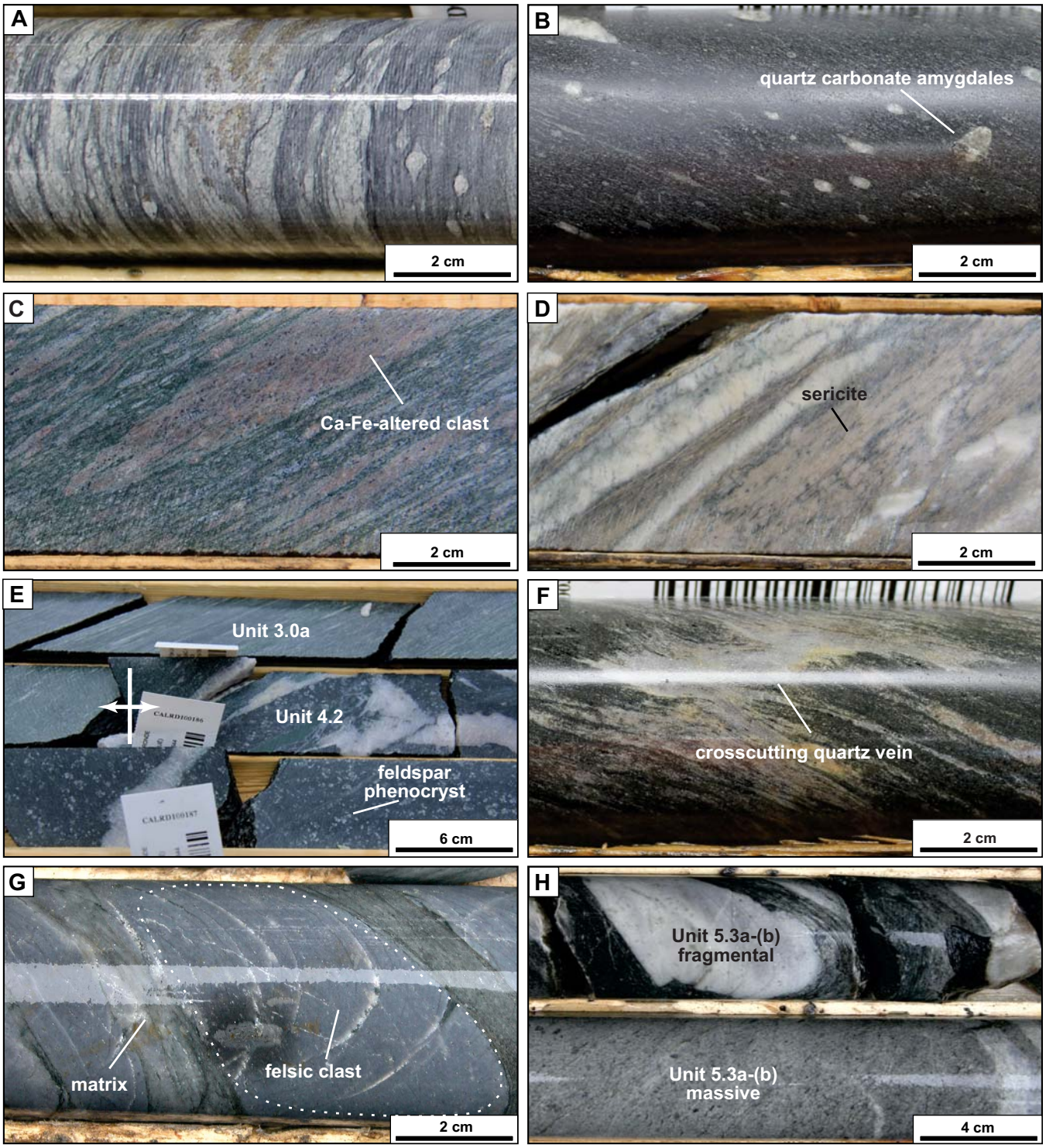

Figure 5. a) Typical fragmental intermediate rock of unit 5.1a-(a), drillhole BZ-18-05-136-1. **b)** Typical amygdaloidal massive rock of unit 5.1a-(b), drillhole S10-04. **c)** Lapilli tuff with altered chlorite matrix and altered Fe-carbonate fragments, unit 3.0a, drillhole S11-44. **d)** Altered rhyodacitic breccia with massive sericite and apparent flattened fragment, unit 4.1, drillhole S11-44. **e)** Crosscutting dyke or sill into a lapilli tuff unit. Note the presence of feldspar phenocrysts and thin quartz vein network, unit 4.2 and 3.0a, drillhole S11-44. **f)** Mafic sill or dyke cut by a quartz vein network in the footwall of Zone 5, unit 5.1a-(c), drillhole S10-04. **g)** Felsic block in a sericitized and chloritized matrix, unit 5.3a-(b), drillhole 121-06-16. **h)** Felsic lapilli tuff and quartz-feldspar porphyritic felsic rock, units 5.3a-(b) and 5.5, drillhole 121-06-11.

al., 2019). Silver and base metal grades are also low at LZ5 compared with the other deposits of the camp.

Footwall and Host Units of the LZ5 and Ellison Mineralized Zones

The LZ5 mineralized corridors are hosted in mafic to felsic rocks of transitional to calc-alkaline magmatic affinity (Fig. 6a,b,c). The base of the sequence consists of volcaniclastic subalkaline basalt and andesite of the Bousquet scoriaceous tuff (unit 3.0) intercalated with thin (≤10 m) but relatively continuous intermediate to felsic sills or dykes of the Bousquet dacitic dome (unit 4.1), the Doyon glomeroporphyritic unit (unit 4.2), and the Doyon felsic unit (unit 4.3).

The Bousquet scoriaceous tuff (unit 3.0) forms the base of the lower member of the Bousquet Formation (Fig. 2). It consists of mafic to intermediate lapilli tuff and/or tuff breccia that are commonly polymictic and locally sorted and normally graded (Yergeau, 2015; Fig. 5c). This unit has been divided into two subunits based on composition: 1) a mafic subunit (subunit 3.0a) and 2) an andesitic subunit (subunit 3.0b) (Yergeau, 2015). Both subunits are present at LZ5 (Fig. 6a,b). Subunit 3.0a also has a more tholeiitic magmatic affinity than subunit 3.0b (Fig. 6c). Samples of subunit 3.0a are the only ones to plot in the tholeiitic field of the Ross and Bédard (2009) diagram (Fig. 6c). The least altered samples of subunit 3.0a are characterized by low SiO_2 content (50.8 wt% on average), high TiO_2 content (1 wt% on average), and a very low $Zr/(TiO_2*10{,}000)$ ratio (0.003 on average: Fig. 6e, 7). The least altered samples also show low Zr (34.5 ppm on average) and low Y concentrations (11.6 ppm on average), which that contrasts with the other mafic units of the Bousquet Formation (Fig. 6d, 7). Subunit 3.0b is characterized by higher SiO_2 content (58.4 wt% on average), similar TiO_2 content (1.1 wt% on average). and higher $Zr/(TiO_2*10{,}000)$ ratio (0.0085 on average) with higher Zr and Y contents (94 ppm and 29.3 ppm on average, respectively: Fig. 6d,e, 7). Both subunits show similar chondrite-normalized multi-element patterns that are characterized by a small negative Nb-Ta anomaly, slightly negative light rare-earth elements (LREE), and flat to slightly U-shaped heavy rare-earth elements (HREE), although unit 3.0b shows a slight negative Ti anomaly (Fig. 8a).

The Bousquet dacitic dome (unit 4.1) was mapped north of the former Bousquet 1 mine (Lafrance et al., 2003; Fig. 2), but sills of similar composition are present a few kilometres to the west, at the Westwood mine (Mercier-Langevin et al., 2009). This unit is also present in the LZ5 footwall (Fig. 5d). The least altered rocks of the Bousquet dacitic dome have a high SiO_2 concentration of 69.5 wt% on average, a low TiO_2 concentration of 0.54 wt% on average, and a high $Zr/(TiO_2*10{,}000)$ ratio (0.05 on average; Fig. 6e, 7). Zirconium and Y values are high at 271 and 45.6 ppm (Fig. 6d, 7).

The Doyon glomeroporphyritic unit (unit 4.2) is compositionally similar to the Bousquet dacitic dome, but it contains abundant feldspar phenocrysts and glomerophenocrysts, whereas the Bousquet dacitic dome is generally very fine grained (Yergeau, 2015; Fig. 5e). This unit forms lobe-hyaloclastite deposits in the Doyon mine area but consists of thin sills and dykes in the Westwood mine area (Yergeau, 2015). Fresh samples from unit 4.2 are characterized by an average SiO_2 content of 61.7 wt%, an average TiO_2 content of 0.93 wt%, and an average $Zr/(TiO_2*10{,}000)$ ratio of 0.02 (Fig. 6e, 7). The Zr and Y contents of this unit are also relatively high at 200 and 41 ppm on average, respectively (Fig. 6d, 7).

The Doyon felsic unit (unit 4.3) is only very locally present in the LZ5 footwall succession. At Westwood, it comprises massive and coherent felsic rocks that do not show particular primary textures (Yergeau, 2015). At LZ5, this unit forms thin dacitic to rhyodacitic dykes or sills of calc-alkaline magmatic affinity (Fig. 6a,b,c). The only analyzed sample from this unit shows a high SiO_2 content (68.6 wt%), a low TiO_2 content (0.53 wt%), and a relatively high $Zr/(TiO_2*10{,}000)$ ratio (0.04: Fig. 6e, 7). Zirconium (236 ppm) and Y (25.7 ppm) are relatively high for this unit (Fig. 6d, 7).

The Bousquet dacitic dome, the Doyon glomeroporphyritic unit, and the Doyon felsic unit are also characterized by relatively pronounced Nb-Ta anomalies, steep LREE patterns and flat to slightly U-shaped HREE patterns with a strong negative Ti anomaly (Fig. 8b). These patterns are typical of transitional to calc-alkaline felsic units of the Bousquet Formation (cf. Mercier-Langevin et al., 2007b).

The upper part of the footwall sequence consists mainly of massive to fragmental felsic to mafic rocks of the Doyon dacite-rhyodacite unit (unit 5.1a) intercalated with thin discontinuous sills or breccia deposits of the Westwood basaltic sills (unit 5.4a). The Doyon dacite-rhyodacite has been divided into 4 subunits based on texture and composition: the Westwood basaltic andesite (subunit 5.1a-(a)), the Westwood andesite-dacite (subunit 5.1a-(b)), the Westwood mafic sills (subunit 5.1a-(c)), and the Westwood dacite-rhyodacite (subunit 5.1a-(d)) (Mercier-Langevin et al., 2009; Yergeau, 2015; Fig. 5a,b,f).

The Westwood basaltic andesite (subunit 5.1a-(a)) is composed of aphanitic to fine-grained, volcanic and volcaniclastic rocks of mafic composition that appear dark green to greyish green and contain between 5 and 15 vol.% feldspar phenocrysts (Yergeau, 2015) (Fig. 5a). Their composition varies between subalkaline

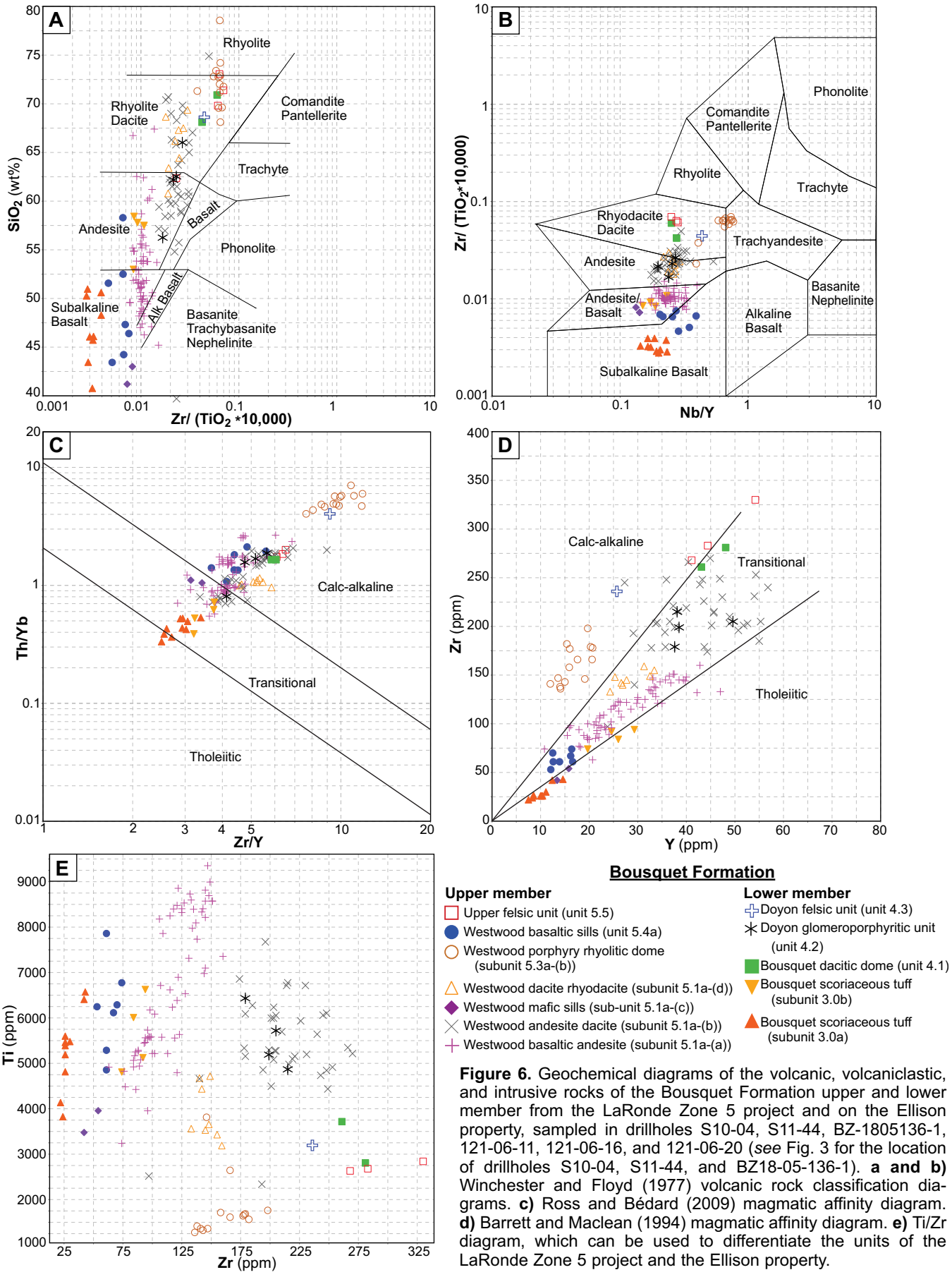

Bousquet Formation

Upper member

- Upper felsic unit (unit 5.5)
- Westwood basaltic sills (unit 5.4a)
- Westwood porphyry rhyolitic dome (subunit 5.3a-(b))
- Westwood dacite rhyodacite (subunit 5.1a-(d))
- Westwood mafic sills (sub-unit 5.1a-(c))
- Westwood andesite dacite (subunit 5.1a-(b))
- Westwood basaltic andesite (subunit 5.1a-(a))

Lower member

- Doyon felsic unit (unit 4.3)
- Doyon glomeroporphyritic unit (unit 4.2)
- Bousquet dacitic dome (unit 4.1)
- Bousquet scoriaceous tuff (subunit 3.0b)
- Bousquet scoriaceous tuff (subunit 3.0a)

Figure 6. Geochemical diagrams of the volcanic, volcaniclastic, and intrusive rocks of the Bousquet Formation upper and lower member from the LaRonde Zone 5 project and on the Ellison property, sampled in drillholes S10-04, S11-44, BZ-1805136-1, 121-06-11, 121-06-16, and 121-06-20 (*see* Fig. 3 for the location of drillholes S10-04, S11-44, and BZ18-05-136-1). **a and b)** Winchester and Floyd (1977) volcanic rock classification diagrams. **c)** Ross and Bédard (2009) magmatic affinity diagram. **d)** Barrett and Maclean (1994) magmatic affinity diagram. **e)** Ti/Zr diagram, which can be used to differentiate the units of the LaRonde Zone 5 project and the Ellison property.

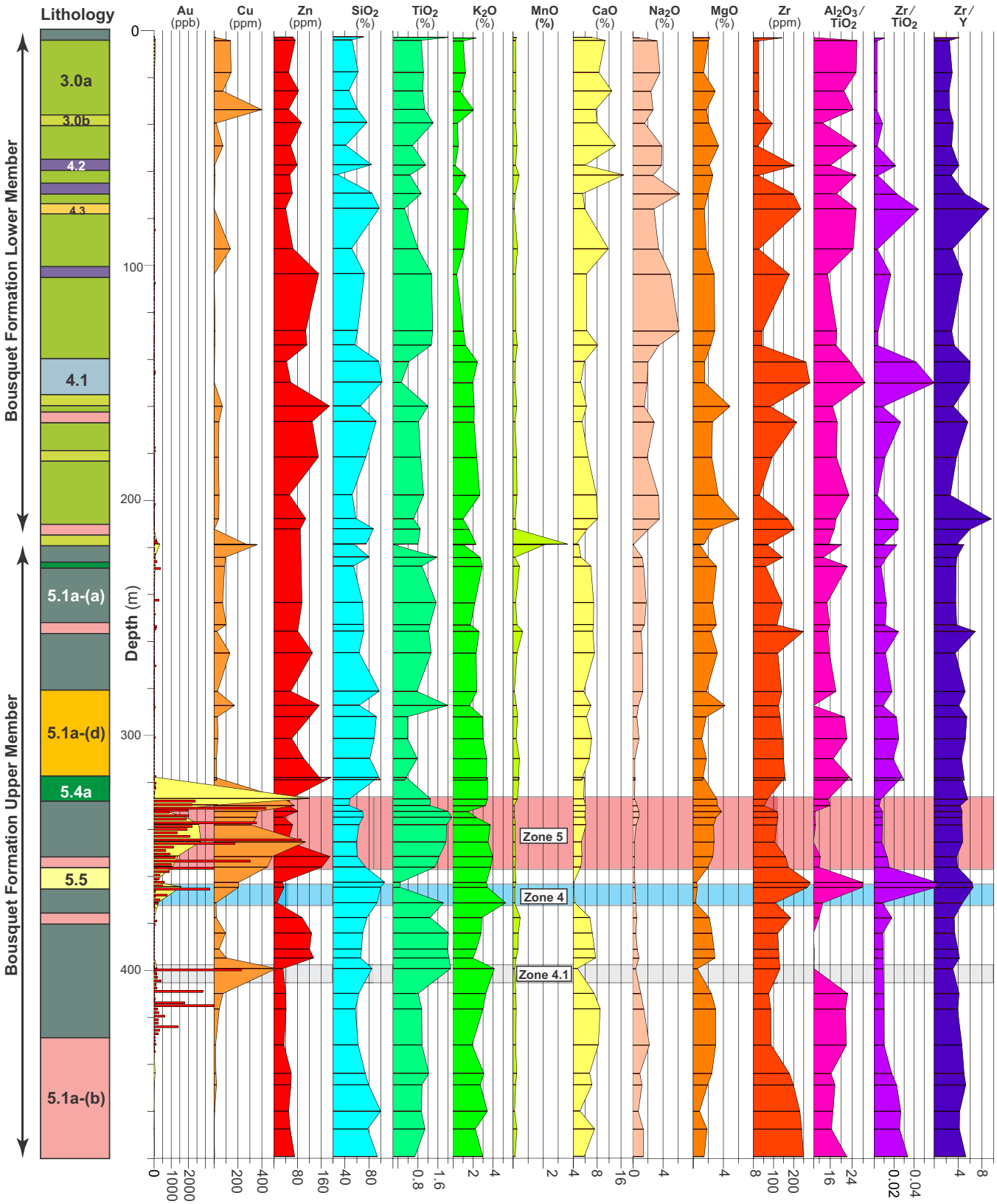

Figure 7. Geochemical profile of drillhole S11-44. Locations of samples and geochemical data are shown by short horizontal lines across each profile. Red bars in the Au column represent assays obtained from Agnico Eagle Mines Ltd.

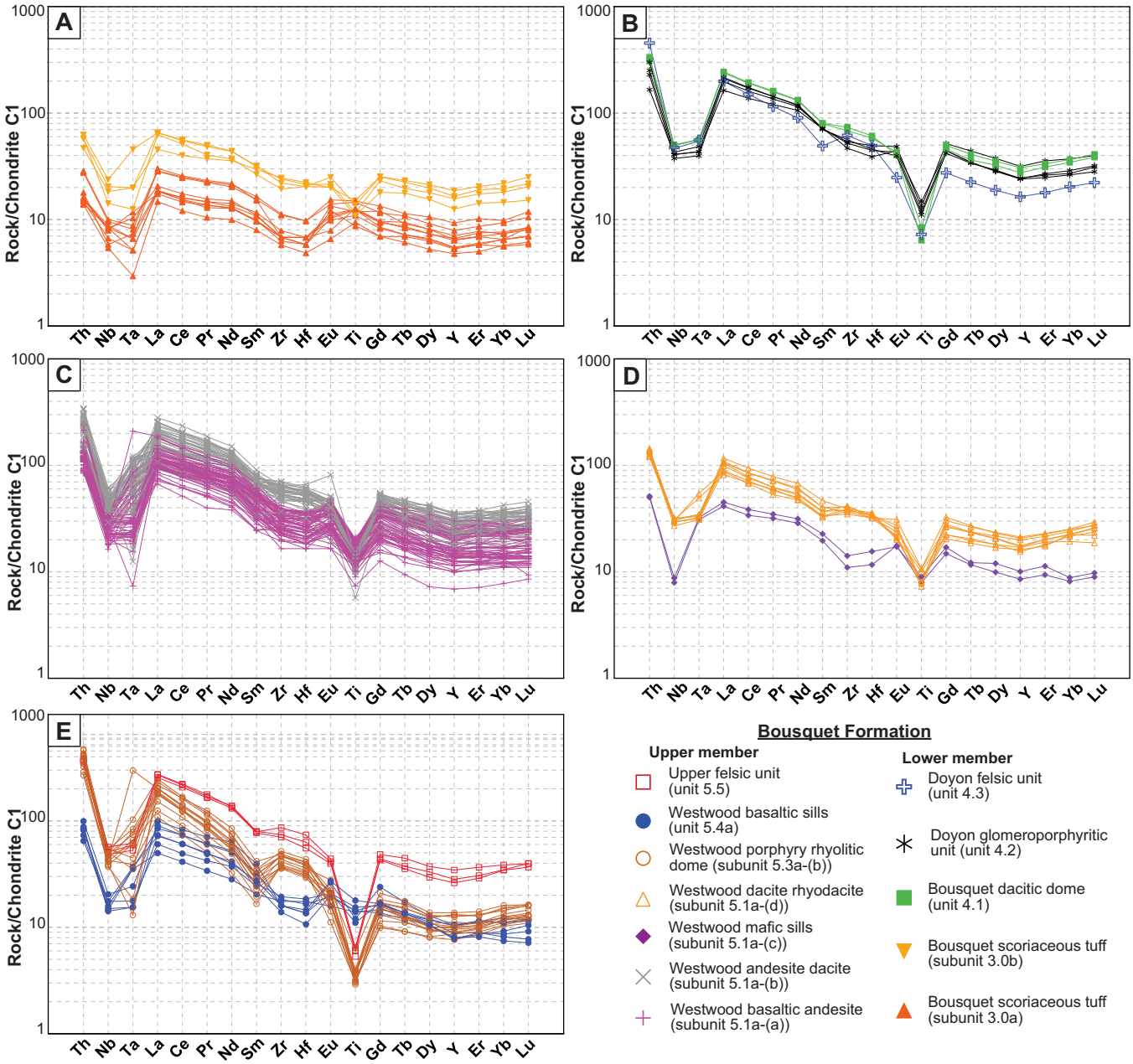

Figure 8. C1 chondrite-normalized (McDonough and Sun, 1995) multi-element patterns of **a)** units 3.0a and 3.0b; **b)** units 4.1, 4.2, and 4.3; **c)** units 5.1a-(a) and 5.1a-(b); **d)** units 5.1a-(c) and 5.1a-(d); and **e)** units 5.3a-(b), 5.4a, and 5.5.

basalt and andesite (Fig. 6a,b). Fresh samples are characterized by a SiO_2 content averaging 55.1 wt%, a TiO_2 content averaging 1.02 wt%, and a $Zr/(TiO_2*10{,}000)$ ratio averaging 0.01 (Fig. 6e, 7).

The Westwood andesite-dacite (subunit 5.1a-(b)) is composed mainly of massive volcanic rocks of intermediate to felsic composition, with a minor component of volcaniclastic rocks (Fig. 6a,b). This unit is also characterized by a high percentage of amygdules (up to 10 vol.%: Fig. 5b). Least altered samples from subunit 5.1a-(b) are characterized by higher SiO_2 content (63.5 wt% on average), lower TiO_2 content (0.9 wt% on average), and a higher $Zr/(TiO_2*10{,}000)$ ratio (0.02 on average: Fig. 6e, 7). This subunit is also characterized by high Zr and Y contents (207 ppm and 40 ppm, respectively: Fig. 6d, 7).

Rocks from the Westwood mafic sills (subunit 5.1a-(c)) consist of thin and discontinuous mafic dykes and slightly discordant sills. This unit is generally intersected by irregular networks of quartz veins that do not extend into the bounding units (Fig. 5f). This unit is of very limited extent and is generally strongly altered. All analyzed samples show evidence of major alteration (e.g. 10–12 wt% loss-on-ignition values). The composition of the protolith is difficult to establish, but appears to be mafic (Fig. 6e, 7).

The Westwood dacite-rhyodacite (subunit 5.1a-(d)) forms metric to decametric volcanic domes, cryptodomes, and lobes that are spatially and genetically associated with a significant succession of tuff, lapilli tuff, and tuff breccia (Yergeau, 2015). Least altered samples from this subunit are characterized by a high SiO_2 content of 68 wt% on average, a relatively low TiO_2 content of 0.7 wt%, and a $Zr/(TiO_2*10{,}000)$ ratio of 0.02 (Fig. 6e, 7). On a Winchester and Floyd (1977) volcanic rock classification diagram, the samples of the Westwood dacite-rhyodacite subunit plot between the field for andesite and rhyodacite/dacite (Fig. 6a,b).

The multi-element patterns of samples from the Westwood basaltic andesite and the Westwood andesite-dacite are characterized by strong enrichment in high field strength elements (HFSE) and LREE, pronounced negative anomalies in Nb and Ta, negative anomalies in Ti, and relatively flat heavy REE (HREE) patterns (Fig. 8c). The Westwood mafic sills are characterized by chondrite-normalized multi-element plots showing slight enrichment in HFSE and LREE, flat to negative HREE pattern, and a negative Nb anomaly (Fig. 8d). The Westwood mafic sills also show a weak positive Eu anomaly and a weak negative Ti anomaly (Fig. 8d). The Westwood dacite-rhyodacite shows strong enrichment in HFSE and LREE, pronounced negative anomalies in Nb and Ta, a negative anomaly in Ti, and relatively flat to U-shaped HREE patterns (Fig. 8d).

The Westwood basaltic sills (unit 5.4a) almost exclusively consist of massive basaltic intrusive rocks that do not have distinctive volcanic textures (Yergeau, 2015). The sills and dykes have variable thicknesses and occur at different stratigraphic positions (Yergeau, 2015). Westwood basaltic sill samples have high loss-on-ignition values. Consequently, a protolith composition based on a selection of least altered samples could not be obtained. Samples from this unit show, on average, a SiO_2 concentration of 51.6 wt%, a TiO_2 concentration of 1.3 wt%, and a $Zr/(TiO_2*10{,}000)$ ratio of 0.004 (Fig. 6e, 7). This unit is also characterized by negative Nb and Ta anomalies, slight LREE enrichment, a negative HREE pattern, as well as a weak positive Eu anomaly and a weak negative Ti anomaly (Fig. 8e).

The Ellison Zone B is located stratigraphically higher than the LZ5 zones 4, 4.1, and 5, whereas the Ellison Zone A is at a similar stratigraphic position as Zone 4 and could, therefore, represent the western extension of that zone on the Ellison property. The Ellison Zone A is hosted within the Westwood basaltic andesite (subunits 5.1a-(a)) and the Ellison Zone B is hosted within more deformed and altered rocks of the Westwood porphyritic rhyolite dome (subunit 5.3a-(b)). The footwall at Ellison consists almost exclusively of intermediate volcaniclastic rocks of the Doyon dacite-rhyodacite (subunit 5.1a-(d)), intercalated with a thin layer of felsic volcaniclastic rocks geochemically correlated to the upper felsic unit (unit 5.5).

The upper felsic unit is the uppermost unit of the Bousquet Formation and consists of massive to fragmental microporphyritic rhyodacitic to rhyolitic rocks. Least altered samples from this unit at LZ5 and Ellison show, on average, high SiO_2 content (66.8 wt%) and low TiO_2 (0.43 wt%) content, and a $Zr/(TiO_2*10{,}000)$ ratio of 0.03 (Fig. 6e, 9). The upper felsic unit is classified as calc-alkaline rhyodacitic to rhyolitic rocks using the Winchester and Floyd (1977) classification diagrams and the Ross and Bédard (2009) magmatic affinity diagram (Fig. 6a,b,c). On a chondrite-normalized multi-element plot, this unit shows strong enrichment in Th and LREE, flat HREE, strong negative Nb-Ta and Ti anomalies, and weak positive Zr-Hf anomalies (Fig. 8e).

Hanging-wall Units of the LZ5 and Ellison Mineralized Zones

The two main units comprising the Bousquet Formation upper member are present in the immediate hanging wall of the LZ5 mineralized corridors (Fig. 2, 7), i.e., the Westwood basaltic andesite (subunit 5.1a-(a)) and the Westwood andesite-dacite (subunit 5.1a-(b)). The hanging wall sequence of the Ellison zones A and B is composed of felsic volcaniclastic rocks of the Westwood porphyritic rhyolite dome (Fig. 5g,h, 6a,b) intercalated with felsic volcanic rocks of the upper felsic unit (Fig. 5h, 6a,b). The Westwood porphyritic rhyolite dome consists of felsic lapilli tuff and/or tuff breccia that has a distinct geochemical signature (Yergeau, 2015). On the Ellison property, least altered samples from the Westwood porphyritic rhyolite dome (Fig. 5h) have high SiO_2 content (73.5 wt% on average), very low TiO_2 content (0.25 wt%), and a high $Zr/(TiO_2*10{,}000)$ ratio (0.68: Fig. 6e). It is also characterized by a distinctively high Nb/Y ratio (0.73: Fig. 6b). This subunit is geochemically similar to the Westwood quartz porphyritic rhyolite (subunit 5.3a) but is visually distinct due to the absence of blue quartz phenocrysts (Yergeau, 2015). The Westwood porphyritic rhyolite dome consists of calc-alkaline rhyodacitic to rhyolitic rocks according to the Winchester and Floyd (1977) volcanic rock classification diagrams and the Ross and Bédard (2009) magmatic affinity diagram (Fig. 6a,b,c). This unit is characterized by chondrite-normalized multi-element plots showing strong enrichment in Th and LREE, flat HREE, strong negative Nb-Ta and Ti anomalies, and weak positive Zr-Hf anomalies (Fig. 8e).

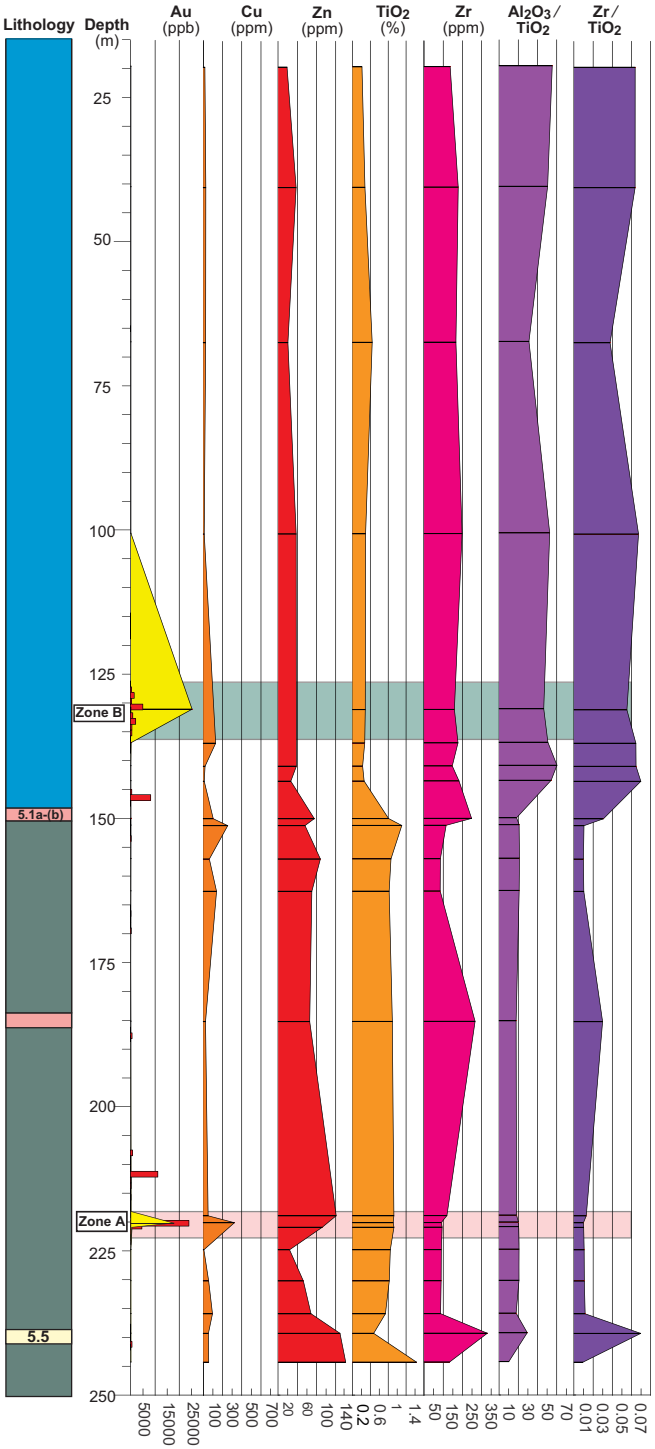

Figure 9. Geochemical profile of drillhole 121-06-11. Locations of samples and geochemical data are shown by short horizontal lines. Red bars in the Au column represent assays obtained from Agnico Eagle Mines Ltd.

DISCUSSION

Stratigraphic Setting of the LZ5 and Ellison Mineralized Zones

The LZ5 and the Ellison Zone A mineralized corridors where previously interpreted to be hosted within the Bousquet heterogeneous unit (unit 4.4) of the Bousquet Formation lower member, making them one of the lowermost ore zones in the DBL camp. Only the intrusion-associated vein systems of the Doyon and Westwood Zone 2 Extension deposits are currently considered to be hosted within the lower member of the Bousquet formation, associated with subvolcanic felsic units equivalent to the overlying upper member units (Yergeau et al., 2015). This study, however, indicates that the LZ5 mineralized corridors occur at the base of the upper member of the Bousquet Formation (Doyon dacite-rhyodacite; unit 5.1a; Fig. 2). The Bousquet heterogeneous unit has not been recognized in the stratigraphy of the LZ5 Project nor on the Ellison property. The uppermost part of the lower member of the Bousquet Formation could be missing in this part of the camp. This is in agreement with Yergeau (2015), who indicates that the Bousquet heterogeneous unit gradually thins east of the Westwood deposit. Also, the Doyon glomeroporphyritic unit (unit 4.2) and the Doyon felsic unit (unit 4.3) have not previously been recognized/mapped on the Bousquet property, despite their relationships with the formation of the intrusion-associated quartz-sulphide veins at Doyon and the Westwood mine (Yergeau, 2015). The Doyon glomeroporphyritic unit is present at surface in the Doyon mine area as a lobe-hyaloclastite complex, and as sills and dykes in the Westwood mine area. The Doyon felsic unit is present at Westwood, where it may thin out just east of the deposit (Yergeau, 2015). Anomalous Au values in the footwall of the LZ5 could represent the distal expression of the Zone 2 Extension of the Westwood deposit. These anomalous values are hosted within the Bousquet scoriaceous tuff (unit 3.0), at the base of the Westwood basaltic andesite (unit 5.1a-(a)) (Fig. 7).

The zones 4, 4.1, and 5 of the LZ5 project are hosted within the same unit as the Ellison Zone A, and approximately at the same stratigraphic position as the Westwood North Corridor ore zones, i.e., principally within the Doyon dacite-rhyodacite (unit 5.1a) (Fig. 2). This indicates that the LZ5 and the Ellison Zone A mineralized corridors are also spatially associated with the transition zone between the tholeiitic volcanism of the Bousquet Formation lower member and the calc-alkaline volcanism of the upper member. The transitional to calc-alkaline, intermediate to felsic volcanic and intrusive units of the upper member are an important metallotect in the area.

In terms of style, the LZ5 and the Ellison Zone A mineralized corridors are similar to some ore zones at the Westwood deposit. The Westwood North Corridor is characterized by replacement zones, disseminated sulphides, and centimetre to decimetre-thick veins of massive to semi-massive sulphides that are concordant to subconcordant. The Westwood North Corridor is hosted at the base of the upper member of the Bousquet

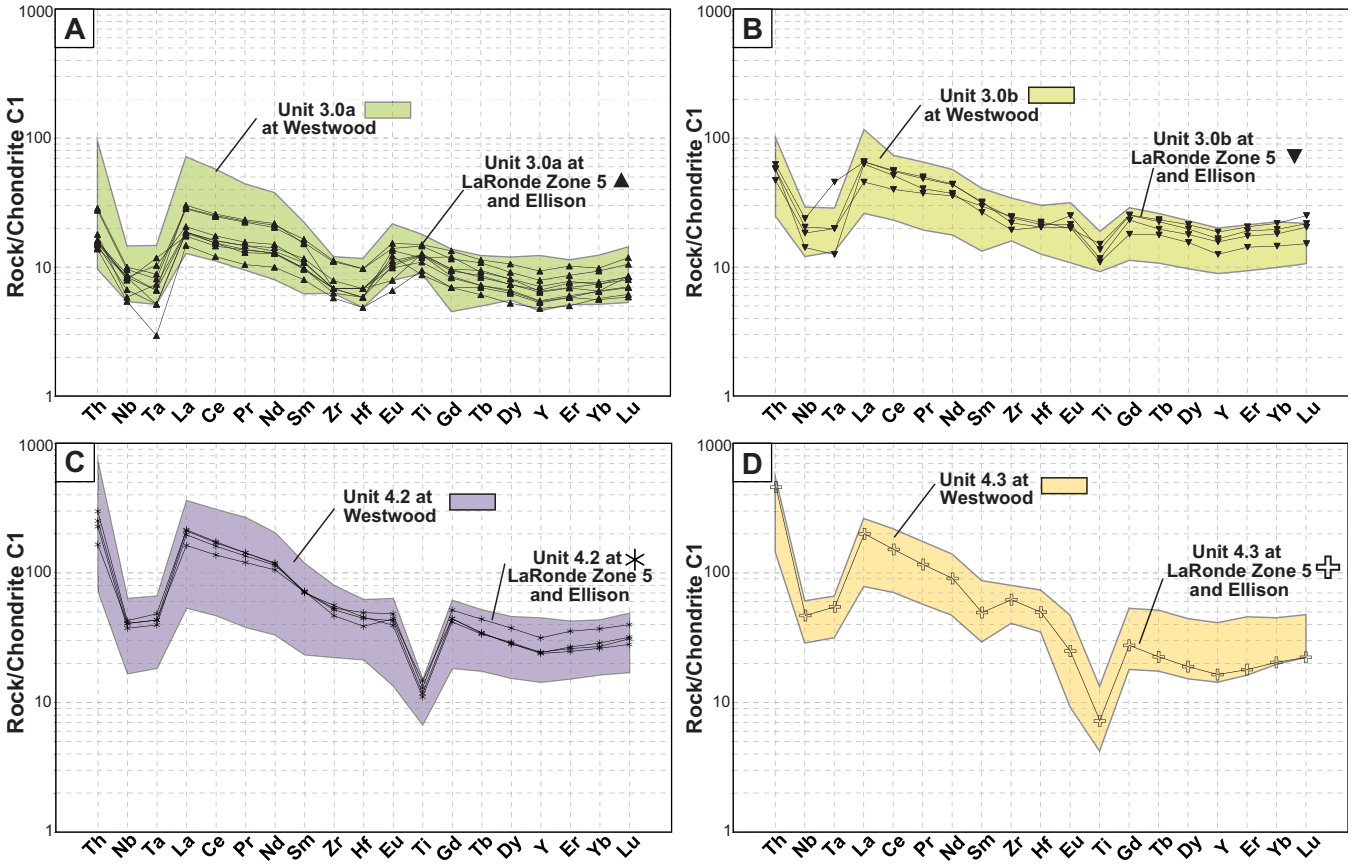

Figure 10. Geochemical comparison of the main units of the Bousquet Formation Upper and Lower members from the LaRonde Zone 5 project, and the Ellison property (samples from drillholes S10-04, S11-44, BZ-1805136-1, 121-06-11, 121-06-16, and 121-06-20) from the Westwood Property (Fig. 2, 3). The data from the Westwood deposits are from Yergeau (2015). The values are normalized to C1 chondrite from McDonough and Sun (1995). **a)** Comparative profile for unit 3.0a (Bousquet scoriaceous tuff). **b)** Comparative profile for unit 3.0b (Bousquet scoriaceous tuff). **c)** Comparative profile for unit 4.2 (Doyon glomeroporphyritic unit). **d)** Comparative profile for unit 4.3 (Doyon felsic unit). Figure is continued on the next page.

Formation in the Doyon dacite-rhyodacite (unit 5.1a) (Yergeau, 2015). These similarities and the stratigraphic position of the mineralization indicate that the LZ5, Ellison property, and Westwood North Corridor ore zones are time-stratigraphic equivalents. Ongoing work will help complete a thorough comparison between the Westwood deposit and LZ5-Ellison Zone A mineralized zones.

The footwall of the LZ5 mineralization consists of tholeiitic to transitional mafic rocks of the Bousquet scoriaceous tuff (unit 3.0), the lowermost unit of the Bousquet Formation. As at Westwood, unit 3.0 at LZ5 is intercalated with thin calc-alkaline intermediate to felsic sills or dykes that are part of units 4.2 and 4.3 (Doyon glomeroporphyritic unit and Doyon felsic unit, respectively). At the Westwood Zone 2 Extension, these two units are key factors in the formation of the Au-rich quartz-sulphide vein system (Yergeau, 2015), and suggest a potential for similar mineralization in the LZ5 area. The Bousquet dacitic dome (unit 4.1) does not occur at Westwood but is present within the Bousquet scoriaceous tuff on the Bousquet property and may also have influenced the development and location of the LZ5 ore zones.

At LZ5, the Doyon dacite-rhyodacite (subunits 5.1a-(a), 5.1a-(b), 5.1a-(c), and 5.1a-(d)), which constitute the immediate footwall succession to the Zone 5, are intercalated with thin discontinuous sills of the Westwood basaltic units (unit 5.4a). These units have compositions similar to those at the Westwood property (Fig. 10e,f,g,h, 11a). The Westwood basaltic sills are considered a marker unit in the immediate footwall and/or hanging wall of the Westwood Corridor and North Corridor ore zones. It also locally hosts some of the mineralization (Yergeau, 2015). In areas where the Westwood basaltic sills are not present, such as east of the Bousquet fault, mineralization is generally non-economic or absent. These observations suggest that there is a direct link between the presence of the Westwood basaltic sills and the fertility of the Westwood Corridor and the North Corridor (Yergeau, 2015), as recognized at the LaRonde Penna deposit (Dubé et al., 2007; Mercier-Langevin et al., 2007b). The Westwood basaltic sills are present in both the

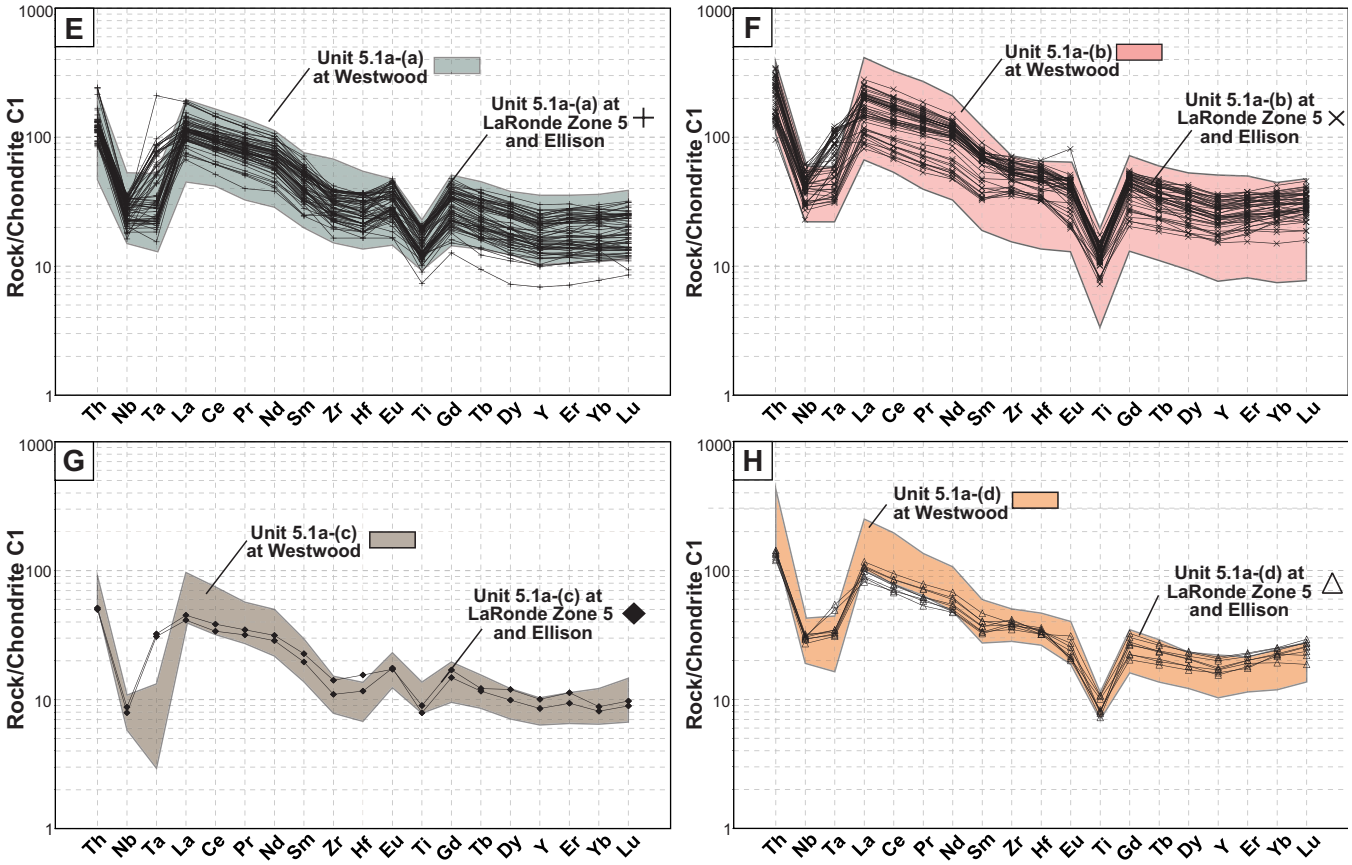

Figure 10 continued from the previous page. Geochemical comparison of the main units of the Bousquet Formation Upper and Lower members from the LaRonde Zone 5 project, and the Ellison property (samples from drillholes S10-04, S11-44, BZ-1805136-1, 121-06-11, 121-06-16, and 121-06-20) from the Westwood Property (Fig. 2, 3). The data from the Westwood deposits are from Yergeau (2015). The values are normalized to C1 chondrite from McDonough and Sun (1995). **e)** Comparative profile for unit 5.1a-(a) (Westwood basaltic andesite). **f)** Comparative profile for unit 5.1a-(b) (Westwood andesite-dacite). **g)** Comparative profile for unit 5.1a-(c) (Westwood mafic sills). **h)** Comparative profile for unit 5.1a-(d) (Westwood dacite rhyodacite).

footwall and hanging wall to the Zone 5 and could therefore also serve as an indicator for mineralization at the LZ5 project and on the Ellison property.

The immediate hanging wall to the LZ5 and Ellison mineralized corridors also consists of the Doyon dacite-rhyodacite (unit 5.1a). The hanging wall units of the LZ5 have not been studied since none of the available drill cores or underground development intersect this part of the stratigraphy. However, the units composing the LZ5 hanging wall are presumably similar to those found in the hanging wall of the Ellison Zone B. The Ellison Zone B hanging wall rocks consist of dacite, rhyodacite, and rhyolite of calc-alkaline magmatic affinity attributed to the Westwood porphyritic rhyolite dome (subunit 5.3a-(b)) and the upper felsic unit (unit 5.5). The chondrite-normalized multi-element patterns of the Westwood porphyritic rhyolite dome and the upper felsic unit present at Ellison are very similar to those present in the Westwood mine area (Fig. 11b,c). The Doyon rhyodacite-rhyolite (units 5.2a) and the Westwood quartz porphyritic rhyolite (unit 5.3a), which respectively forms the footwall and hanging wall of the 20 North massive sulphide lens at the LaRonde Penna mine, as well as the footwall of the Bousquet 2-Dumagami deposit mineralization (Fig. 2), are not present at LZ5 and Ellison. Both the LaRonde rhyodacite-rhyolite (unit 5.2) and the LaRonde quartz-rhyolite (unit 5.3) are considered as critical elements for the formation and location of the giant LaRonde Penna 20 North lens and the Bousquet-2-Dumagami exceptionally Au-rich VMS deposit. Their absence at LZ5 may explain the differences of mineralization style between the two areas, i.e., sulphide veins, stockworks, and disseminations versus Au-rich massive sulphide lenses.

CONCLUSION

The interim results of this ongoing study demonstrate that the LZ5 Project and Ellison property mineralized zones are located higher in the Bousquet Formation stratigraphy than previously interpreted. The mineralized corridors are hosted in the Bousquet Formation upper member rather than in the units of the lower member. The LZ5 zones 4, 4.1, and 5, as well as the

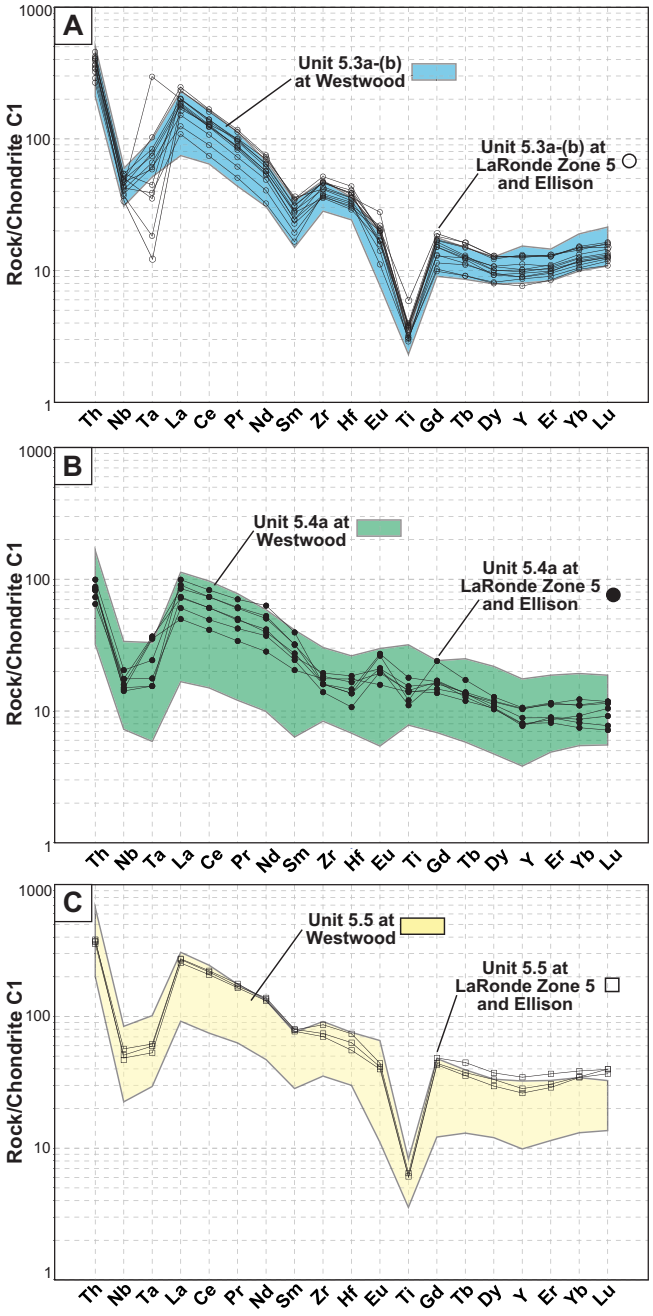

Figure 11. Geochemical comparison of the main units of the Bousquet Formation upper and lower members at the LZ5 Project and from the Ellison property with those found on the Westwood property (Fig. 2, 3). The data from the Westwood deposit are from Yergeau (2015). The values are normalized to C1 chondrite from McDonough and Sun (1995). **a)** Comparative profiles for unit 5.3a-(b) (Westwood porphyry rhyolitic dome). **b)** Comparative profiles for unit 5.4a (Westwood basal-tic sills). **c)** Comparative profiles for unit 5.5 (Upper felsic unit).

Ellison Zone A mineralized horizons are hosted within the Doyon dacite-rhyodacite (unit 5.1a) and associated subunits, whereas the Ellison Zone B is hosted slightly higher in the stratigraphy, within the Westwood porphyritic rhyolite dome (subunit 5.3a-(b)). This implies that the LZ5 ore is younger than unit 5.1a, which marks the onset of volcanism and magmatic activity associated with the upper member of the Bousquet Formation, i.e., the change from tholeiitic to transitional mafic to intermediate volcanism to transitional to calc-alkaline intermediate to felsic volcanic and magmatic activity. This change in the magmatic regime and the association with the ore-forming hydrothermal activity has been noted at camp scale but did not apply in the LZ5 area (former Bousquet 1 mine area) because of a previously erroneous interpretation about the exact stratigraphic position of the mineralized zones. This study provides further evidence for a direct association between magmatic evolution and Au-bearing, synvolcanic hydrothermal activity in the DBL mining camp. This study also strengthens the stratigraphic correlation with the Westwood deposit North Corridor ore zones. The LZ5 and Ellison Zone A are located at the same stratigraphic position as the Westwood mine North Corridor ore zones that similarly consist of strongly folded, partly transposed and boudinaged sulphide-rich veins and semi-massive sulphide bands. More work is needed to complete the characterization of the LZ5 and Ellison ore zones and to establish their significance in the metallogenic evolution of the DBL mining camp. This study represents a first step in the better understanding of the LaRonde Zone 5 project and Ellison property sulphide veins, stockworks, and disseminations, which represent an unusual style of Archean Au mineralization.

ACKNOWLEDGMENTS

This report is a contribution to NRCan's Targeted Geoscience Initiative Program (TGI-5) Gold Project. Support for this study was provided through Activity G-1.1: Gold through space and time at the Archean. This study is part of an ongoing M.Sc. project by E. Boily-Auclair. Agnico Eagle Mines Ltd. LaRonde Division and its personnel, in particular, D. Fortin, R. Dubuc, D. Lussier, and M. Bernier are sincerely thanked for access to the property, core and data, and for scientific support and numerous constructive discussions. We acknowledge E. Ambrose and V. Bécu for their editorial handling and review. This report benefited from constructive reviews by L. Ootes and S. Castonguay.

REFERENCES

Agnico Eagle Mines Limited, 2019a. LaRonde mine operations; Agnico Eagle Mines Limited. < https://www.agnicoeagle.com/English/operations-and-development-projects/operations/laronde/default.aspx> [accessed December 29, 2019]

Agnico Eagle Mines Limited, LaRonde Zone 5 survey division, 2019b. LaRonde Zone 5 underground development; Agnico Eagle Mines Limited, Map of level 18 of the LaRonde Zone 5 project, scale 1:200.

Barrett, T.J. and MacLean, W.H., 1994. Chemostratigraphy and hydrothermal alteration in exploration for VHMS deposits in

greenstones and younger volcanic rocks; *in* Alteration and Alteration Processes Associated with Ore-Forming Systems, (ed.) D.R. Lentz; Geological Association of Canada, Mineral Deposits Division, Short Course Notes, v. 11, p. 433–467.

Boily-Auclair, E., Mercier-Langevin, P., Ross, P.-S., and Pitre, D., 2019. Lithological and structural controls on the nature and distribution of gold at the LaRonde Zone 5 Project, Doyon-Bousquet-LaRonde gold camp, Abitibi, Quebec; *in* Targeted Geoscience Initiative: 2018 report of activities, (ed.) N. Rogers; Geological Survey of Canada, Open File 8549, p. 23–32.

Davis, D.W., 2002. U-Pb geochronology of Archean metasedimentary rocks in the Pontiac and Abitibi subprovinces, Quebec, constraints on timing, provenance and regional tectonics; Precambrian Research, v.115, p. 97–117.

Dubé, B., Mercier-Langevin, P., Hannington, M., Lafrance, B., Gosselin, G., and Gosselin, P., 2007. The LaRonde Penna world-class Au-rich volcanogenic massive sulphide deposit, Abitibi, Québec: mineralogy and geochemistry of alteration and implications for genesis and exploration; Economic Geology, v. 102, p. 633–666.

Galley, A.G. and LaFrance, B., 2014. Setting and evolution of the Archean synvolcanic Mooshla Intrusive Complex, Doyon-Bousquet-LaRonde mining camp, Abitibi greenstone belt: Emplacement history, petrogenesis, and implications for Au metallogenesis; Economic Geology, v. 109, p. 205–229.

Goutier, J., 1997. Géologie de la région de Destor (SNRC 32D/07); Ministère des Ressources naturelles du Québec, RG 1996-13, 37 p.

Ishikawa, Y., Sawaguchi, T., Iwaya, S., and Horiuchi, M., 1976. Delineation of prospecting targets for Kuroko deposits based on modes of volcanism of underlying dacite and alteration haloes; Mining Geology, v. 26, p. 105–117.

Lafrance, B., Moorhead, J., and David, D.W., 2003. Cadre géologique du camp minier Doyon-Bousquet-LaRonde; Ministère des Ressources naturelles, de la Faune et des Parcs du Québec, ET 2002-07, 45 p.

Lafrance, B., Davis, D.W., Goutier, J., Moorhead, J., Pilote, P., Mercier- Langevin, P., Dubé, B., Galley, A.G., Mueller, W.U., 2005. New isotopic ages in the Québec portion of the Blake River Group and adjacent units; Ministère des Ressources naturelles, de la Faune et des Parcs du Québec, RP2005-01 (A), 15 p.

Large, R. R., Gemmell, J. B., Paulick, H., and Huston, D. L., 2001. The alteration box plot: A simple approach to understanding the relationship between alteration mineralogy and lithogeochemistry associated with volcanic-hosted massive sulfide deposits; Economic Geology, v. 96, p. 957–971.

McDonough, W.F. and Sun, S.S., 1995. The composition of the Earth; Chemical Geology, v. 120, p. 223–253.

McNicoll, V., Goutier, J., Dubé, B., Mercier-Langevin, P., Ross, P.-S., Dion, C., Monecke, T., Legault, M., Percival, J., and Gibson, H., 2014. U-Pb Geochronology of the Blake River Group, Abitibi greenstone belt, Quebec, and implications for base metal exploration; Economic Geology, v. 109, p. 27–59.

Mercier-Langevin, P., Dubé, B., Hannington, M.D., Davis, D., Lafrance, B., and Gosselin, G., 2007a. The LaRonde Penna Au-rich volcanogenic massive sulphide deposit, Abitibi greenstone belt, Quebec: Part I. Geology and geochronology; Economic Geology, v. 102, p. 585–609.

Mercier-Langevin, P., Dubé, B., Hannington, M.D., Richer-Laflèche, M., and Gosselin, G., 2007b. The LaRonde Penna Au-rich volcanogenic massive sulphide deposit, Abitibi greenstone belt, Quebec: Part II. Lithogeochemistry and paleotectonic setting; Economic Geology, v. 102, p. 611–631.

Mercier-Langevin, P., Dubé, B., Lafrance, B., Hannington, M., Galley, A., Moorhead, J., and Gosselin, P., 2007c. Metallogeny of the Doyon-Bousquet-LaRonde mining camp, Abitibi greenstone belt, Quebec; *in* Mineral Deposits of Canada: A Synthesis of Major Deposit Types, District Metallogeny, the Evolution of Geological Provinces, and Exploration Methods, (ed.) W.D. Goodfellow; Geological Association of Canada, Mineral Deposits Division, Special Publication, No. 5, p. 673–701.

Mercier-Langevin, P., Ross, P.-S., Lafrance, B., and Dubé, B., 2008. Volcaniclastic rocks of the Bousquet scoriaceous tuff units north of the LaRonde Penna mine, Doyon-Bousquet-LaRonde mining camp, Abitibi greenstone belt, Quebec; Geological Survey of Canada, Current Research 2008-11, 19 p.

Mercier-Langevin, P., Wright-Holfeld, A., Dubé, B., Bernier, C., Houle, N., Savoie, A., and Simard, P., 2009. Stratigraphic setting of the Westwood-Warrenmac ore zones, Westwood Project, Doyon-Bousquet-LaRonde mining camp, Abitibi, Québec; Geological Survey of Canada, Current Research 2009-3, 20 p.

Mercier-Langevin, P., Dubé, B., Blanchet, F., Pitre, D., and Laberge, A., 2017. The LaRonde Penna Au-rich volcanic-hosted massive sulfide deposit; *in* Archean base and precious metal deposits, southern Abitibi greenstone belt, Canada, (ed.) T. Monecke, P. Mercier-Langevin and B. Dubé; Reviews in Economic Geology, v. 19, p. 225–245.

Monecke, T., Mercier-Langevin, P., Dubé, B., and Frieman, B.M., 2017. Geology of the Abitibi greenstone belt; Reviews in Economic Geology, v. 19, p. 7–49.

Ross, P.-S. and Bédard, J.H., 2009. Magmatic affinity of modern and ancient subalkaline volcanic rocks determined from trace-element discriminant diagrams; Canadian Journal of Earth Sciences, v. 46, p. 823–839.

Stone, W.E., 1990. Archean volcanism and sedimentation in the Bousquet gold district, Abitibi greenstone belt, Quebec: implications for stratigraphy and gold concentration; Geological Society of America Bulletin, v. 102, p.147–158.

Tourigny, G., Brown, A.C., Hubert, C., and Crépeau, R., 1989. Synvolcanic and syntectonic gold mineralization at the Bousquet mine, Abitibi greenstone belt, Quebec; Economic Geology, v. 84, p. 1875–1890.

Valliant, R.I., Mongeau, C., and Doucet, R., 1982. The Bousquet pyritic gold deposit, Bousquet region, Quebec: descriptive geology and preliminary interpretations on genesis; *in* Geology of Canadian Gold Deposits, (ed.) R.W. Hodder and W. Petruk; Canadian Institute of Mining, Metallurgy, and Petroleum, Special Volume 24, p. 41–49.

Williams, N.C. and Davidson, G.J., 2004. Possible submarine advanced argillic alteration at the Basin Lake prospect, western Tasmania, Australia; Economic Geology, v. 99, p. 987–1002.

Winchester, J.A. and Floyd, P.A., 1977. Geochemical discrimination of different magma series and their differentiation products using immobile elements; Chemical Geology, v. 20, p. 325–343.

Yergeau, D., 2015. Géologie du gisement synvolcanique aurifère atypique Westwood, Abitibi, Québec; Ph.D. thesis, Institut national de la recherche scientifique – Centre Eau Terre Environnement, Québec, Quebec, 643 p.

Interrogating the composition and genesis of argillite-hosted pyrite nodules at the LaRonde Penna gold-rich volcanogenic massive sulphide deposit, Abitibi, Quebec: Insights into metallogenic implications

Jean-Luc Pilote[1*], Patrick Mercier-Langevin[1], Simon E. Jackson[2], Benoît Dubé[1], Zhaoping Yang[2], Christopher J.M. Lawley[2], Duane C. Petts[2], Graham D. Layne[3], and Stephen J. Piercey[3]

[1]Geological Survey of Canada, 490 rue de la Couronne, Québec, Quebec G1K 9A9
[2]Geological Survey of Canada, 601 Booth Street, Ottawa, Ontario K1A 0E8
[3]Memorial University of Newfoundland, St. John's, Newfoundland A1B 3X5
[*]Corresponding author's e-mail: jean-luc.pilote@canada.ca

ABSTRACT

This study investigates pyrite nodules hosted in argillite horizons within (Zn-Ag-Au-Cu±Pb) massive sulphide ore of the 20N Zn zone at the LaRonde Penna Au-rich volcanogenic massive sulphide deposit, Abitibi greenstone belt, Quebec. Two pyrite nodules are examined in detail: LA-001 and LA-002. These nodules are spherical and oblate spheroidal in shape and display similar textures, including a core (zone 1) composed of fine, equigranular grains with variable amounts of silicate-carbonate inclusions; a rim (zones 2a to c) that varies from inclusion-poor to -rich and consists of equigranular to radially oriented, acicular pyrite grains; and a thin layer of idiomorphic pyrite overgrowth that surrounds the nodules (zone 3). Sulphide inclusions in nodule LA-001 consist predominantly of sphalerite, whereas sulphide inclusions in nodule LA-002 include an assemblage of sphalerite, Zn-bearing stannite ($Cu_2(Fe,Zn)SnS_4$), and galena, all of which occur also in the surrounding massive sulphide ore. In nodule LA-002, sphalerite is intimately associated with stannite, and together they are preferentially concentrated along both the concentric zones of the inclusion-rich section of the rim (zone 2b) and within the radially bladed rim (zone 2c), parallel to blade elongation. Whereas textures are similar in the two nodules, compositional maps generated by laser ablation-inductively coupled plasma-mass spectrometry (LA-ICP-MS) reveal important distinctions in element distribution patterns for inclusion-partitioned elements (Cu, Zn, Sn, Pb, Bi), which reflect the mineralogy and bulk abundances for lattice-bound elements (Ni, As, Au). Gold is mainly concentrated in the fine-grained cores, but in different amounts in LA-001 (average of 0.38 ppm Au; n = 6918) and LA-002 (average of 1.04 ppm Au; n = 10,539). Nickel and As values in LA-001 are respectively 10 and 3 times greater than in LA-002. In both nodules, Ni is enriched in the rim relative to the core. The pyrite nodules have in situ $\delta^{34}S$ values (secondary ion mass spectrometry analyses) that range from -0.8 to +5.0‰ (average +2.1‰, n = 50), with the core showing slightly lighter values than the rim. Based on these results, the nodules (zones 1 and 2) are interpreted to have formed by diagenetic processes and the presence of stannite, sphalerite, and galena (enrichment in Zn, Sn, Cu, and Pb) is likely the expression of a previously hydrothermally enriched sediment rather than a direct hydrothermal contribution during crystal growth. While more work is needed, the composition of pyrite nodules could potentially be used as vectors toward syngenetic mineralization.

INTRODUCTION

The LaRonde Penna deposit is an Au-rich volcanogenic massive sulphide (VMS; ~9 Moz Au) hosted in the upper part of the 2704–2695 Ma Blake River Group (Fig. 1) in the southern Abitibi greenstone belt (Mercier-Langevin et al., 2017). Thin argillite layers occur within the main sulphide orebody of the 20 North lens in the uppermost levels of the mine (≤1700 m below surface: Dubé et al., 2004; Mercier-Langevin et al., 2007b) and host centimetre-scale pyrite nodules that share textural similarities with diagenetic pyrite nodules reported in various ancient and modern sedimentary sequences around the world (e.g. Guy et al., 2010, 2014; Rickard, 2012; Gregory et al., 2019). In some areas (e.g. Timmins district) pyrite nodules can host significant amounts of Au (up to >10 ppm Au; Pilote et al., 2019, 2020). Over the past few decades, the origin of Au at LaRonde and other VMS deposits in the Doyon-Bousquet-LaRonde mining camp has been a source of much controversy. Various models have been

Pilote, J.-L., Mercier-Langevin, P., Jackson, S.E., Dubé, B., Yang, Z., Lawley, C.J.M., Petts, D.C., Layne, G.D., and Piercey, S.J., 2020. Interrogating the composition and genesis of argillite-hosted pyrite nodules at the LaRonde Penna gold-rich volcanogenic massive sulphide deposit, Abitibi, Quebec: Insights into metallogenic implications; *in* Targeted Geoscience Initiative 5: Contributions to the Understanding of Canadian Gold Systems, (ed.) P. Mercier-Langevin, C.J.M. Lawley, and S. Castonguay; Geological Survey of Canada, Open File 8712, p. 75–91. https://doi.org/10.4095/323666

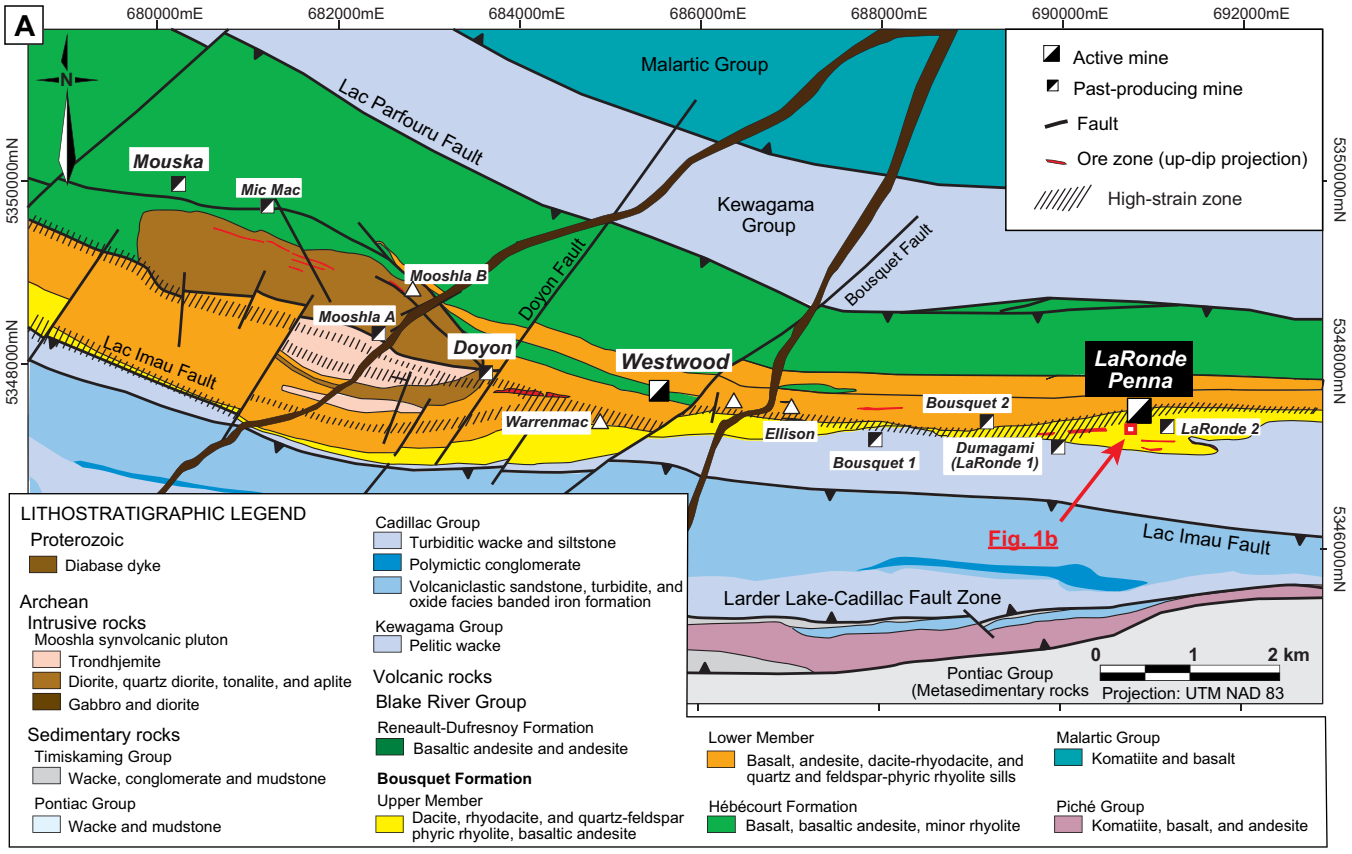

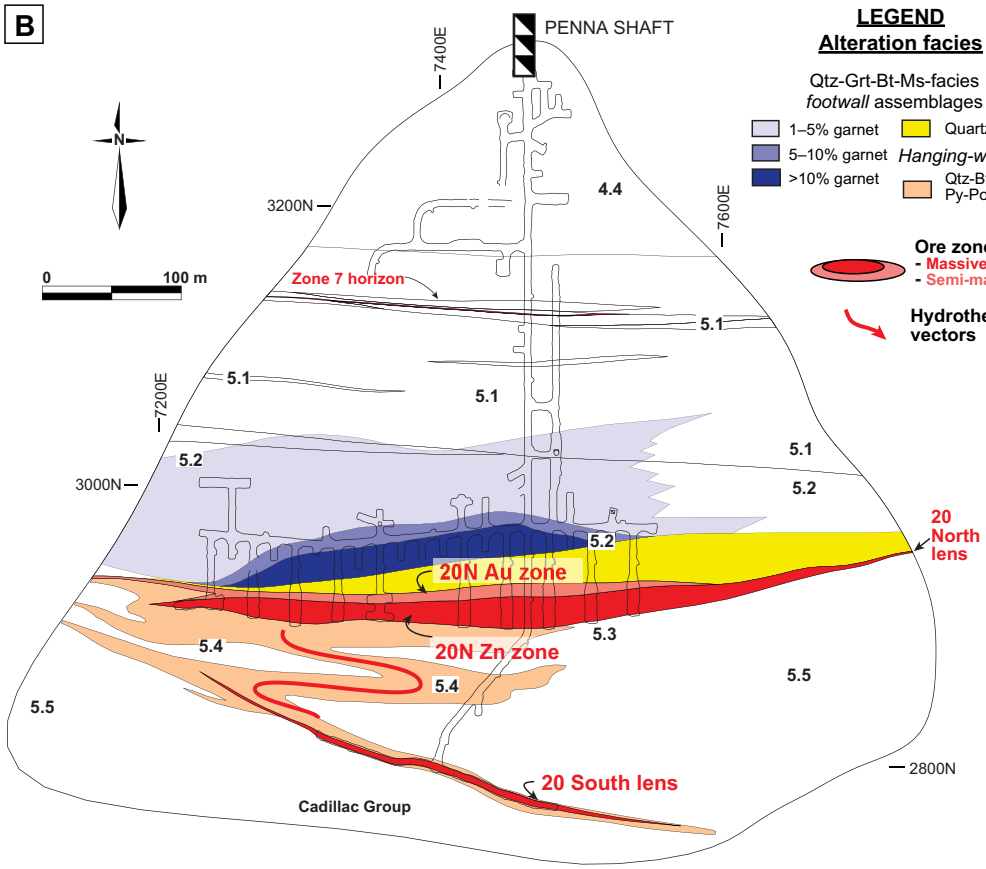

Figure 1. a) Simplified geology of the Doyon-Bousquet-LaRonde mining camp showing the location of the LaRonde Penna deposit. *Modified after* Mercier-Langevin et al. (2017). **b)** Map of level 146 (1460 m depth) of the LaRonde Penna mine showing the distribution of the upper units of the Bousquet Formation, ore zone 7, the 20 North and 20 South lenses, and the distribution of the main alteration assemblages. *Modified after* Mercier-Langevin et al. (2017). Abbreviations: Ab = albite; Bt = biotite, Grt = garnet, Ms = muscovite, Po = pyrrhotite, Py = pyrite, Qtz = quartz, Rt = rutile, Ttn= titanite.

proposed, including the following: 1) synvolcanic or syngenetic Au enrichment; 2) multi-stage Au enrichment with the Au being structurally introduced and/or remobilized into high-strain zones; and 3) epigenetic (syndeformation) Au enrichment (Mercier-Langevin et al., 2017, and references therein). An improved understanding of processes responsible for the genesis of deposits in modern systems, fossil hydrothermal systems and reconstruction of the Doyon-Bousquet-LaRonde mining camp geology have provided substantial insights into the synvolcanic and/or syngenetic model for the introduction of Au in the VMS deposits of the camp, including LaRonde (to cite only a few, Sillitoe et al., 1996; Hannington et al., 1999b, 2005; Dubé et al., 2007a,b, 2014; Mercier-Langevin et al., 2007b,c; Monecke et al., 2008, 2009). Given that nodules can incorporate significant amounts of Au, constraining the timing and factors controlling this enrichment could provide another line of evidence for the timing of Au introduction in VMS deposits, which can be helpful in understanding complex and/or understudied metamorphosed syngenetic systems elsewhere. Also, because nodules can host a number of trace elements (e.g. Zn, Cd, and Cu as inclusions; Co, Ni, Se, and Te as stoichiometric substitutions; and As, Tl, Au, Mo, Pb, Ag, Sb, Bi, and Mn as non-stoichiometric substitutions; Large et al., 2007, 2014) and can co-exist with the mineralization at LaRonde, understanding their compositions can provide further, independent constraints into the local paleoconditions (e.g. redox) of this world-class Au-rich VMS system.

Previous work concluded that part of the mineralization at LaRonde formed by sub-seafloor replacement rather than seafloor accumulation (Dubé et al., 2007b; Mercier-Langevin et al., 2007b) and, moreover, that the deposition of argillite was likely contemporaneous with the hydrothermal activity that formed the sulphide lens (Dubé et al., 2004, 2007b). Because of the seafloor and sub-seafloor replacement-style sulphide deposition, the formation of nodules in argillite lenses in the massive sulphide zones could have been contemporaneous with the hydrothermal activity. The ore lenses at the LaRonde Penna deposit vary in mineralogy, style, and metal composition, which relates to the protracted nature of the system and the compositionally evolving ore-forming fluids (Dubé et al., 2004, 2007a,b). Therefore, the nodules are a potential record of direct or indirect evidence of hydrothermal activity, and variations in mineralogical and chemical compositions may possibly record the evolving, Au-rich hydrothermal system. The objectives of this contribution, which forms part of a broader study on Archean sulphide nodules (*see* Pilote et al., 2020), involve characterization of the mineralogy, textures, and chemical and S-isotope compositions of the LaRonde Penna pyrite nodules, and discussion of their possible metallogenic and exploration implications.

GEOLOGICAL CONTEXT

Only a brief overview of the regional geological setting and deposit geology is presented here. Readers are encouraged to read Monecke et al. (2017), and references therein, for a geology review of the southern Abitibi greenstone belt and Dubé et al. (2007a,b) and Mercier-Langevin et al. (2007a,b,c) for details about the geology of the LaRonde Penna deposit.

The LaRonde Penna deposit is hosted by volcanic rocks of the eastern Blake River Group, which is structurally bounded to the north by the southeast-northwest-oriented Lac Parfouru fault zone (Fig. 1a). This fault separates the Blake River Group from the sedimentary rocks of the ≤2687 Ma (Davis, 2002) Kewagama Group. To the south, the Blake River Group is overlain by sedimentary rocks of the Cadillac Group (≤2689 Ma in the LaRonde deposit area: Mercier-Langevin et al., 2007b). Further to the south, the sedimentary rocks of the Cadillac Group are truncated by the east-west-striking Larder Lake-Cadillac fault zone.

The LaRonde deposit is hosted by the south-younging 2699–2697 Ma Bousquet Formation (Blake River Group: Lafrance et al., 2003; Mercier-Langevin et al., 2007b; McNicoll et al., 2014), which is divided into lower and upper members (Lafrance et al., 2003; Mercier-Langevin et al., 2007b). The 200 to 600 m thick lower member (unit 4.4 in Fig. 1b) is dominated by mafic to intermediate and tholeiitic to transitional rocks, whereas the upper member (units 5.1 to 5.5 in Fig. 1b) mostly comprises felsic volcanic and shallow intrusive rocks of transitional to calc-alkaline magmatic affinity (Lafrance et al., 2003; Mercier-Langevin et al., 2007b,c). The latter forms flows, lobes, flow-breccia deposits, and sill complexes of basalt and andesitic to rhyolitic compositions.

The ore lenses of the LaRonde deposit are hosted in the volcanic flows and volcaniclastic rocks of the upper member of the Bousquet Formation (Fig. 1b) and are characterized by semi-massive to massive sulphides or narrow intervals of transposed sulphide veins and veinlets. The lenses are spatially associated with several metamorphosed alteration assemblages developed in both the stratigraphic footwall and hanging-wall volcanic units (Dubé et al., 2007b). The stacked ore lenses represent different episodes of sulphide precipitation in a single protracted hydrothermal system (Dubé et al., 2007a; Mercier-Langevin et al., 2007b). In the upper stratigraphic part of the deposit, the 20 North lens comprises a transposed pyrite-chalcopyrite (Au-Cu) stockwork (20N Au zone), which is directly overlain by a pyrite-sphalerite-galena-chalcopyrite-pyrrhotite (Zn-Ag-Pb) massive sulphide lens (20N Zn zone).

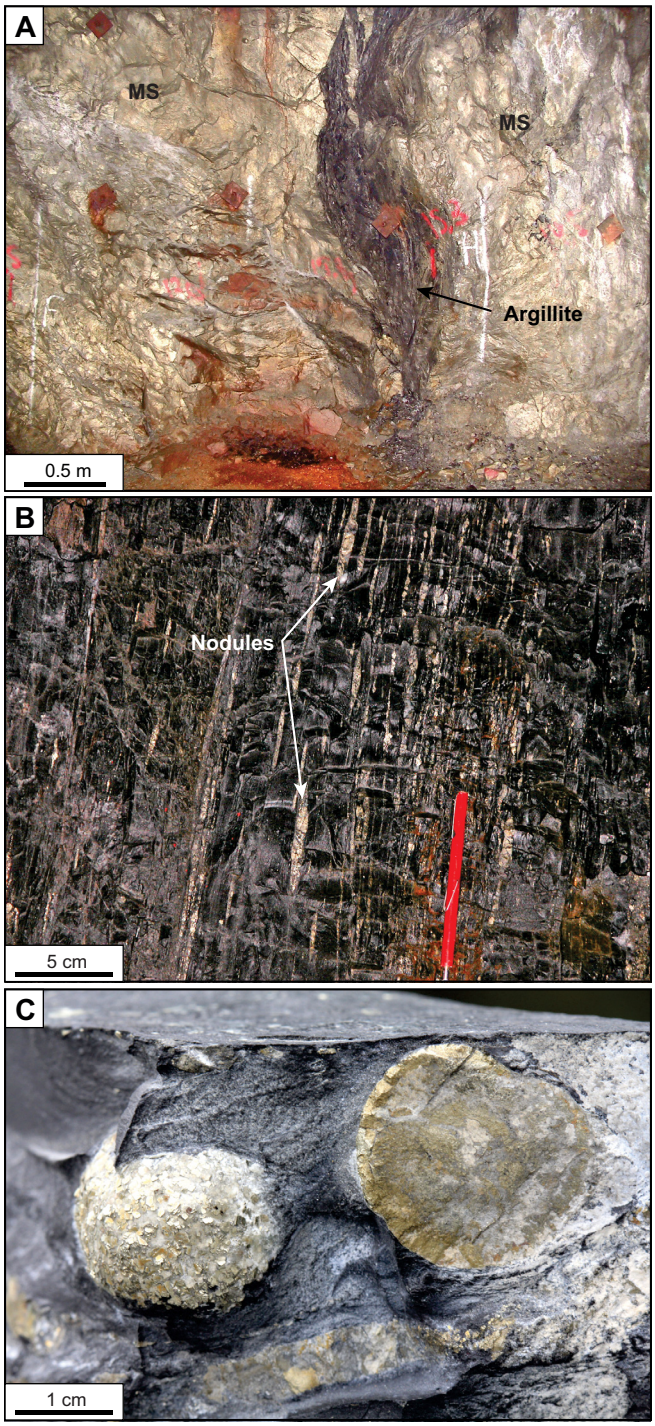

Figure 2. a) 20N Zn zone massive sulphide lens (pyrite, sphalerite±galena, chalcopyrite, pyrrhotite) enclosing a highly strained graphitic argillite lens (stope 152-20-66 west wall, 1520 m below surface). **b)** Strongly deformed (flattened ±stretched) pyrite nodules in siliceous graphitic argillite, stope 131-20-70 west wall, 1310 m below surface. **c)** Pyrite nodules in a graphitic argillite unit. The section view of the nodule to the right shows a perfectly preserved concentric zonation, whereas the nodule to the left is complete and shows a granoblastic outer rim (sample courtesy of D. Pitre). Abbreviation: MS = massive sulphide.

Discontinuous argillite layers are found within the massive sulphide lens of the 20N Zn zone that, because of their low competency relative to the sulphides, generally accommodate much of the tectonic strain (Fig. 2a: Mercier-Langevin et al., 2007b). Abundant centimetre-scale pyrite nodules are present in these sedimentary layers and are generally strongly deformed (Fig. 2b,c), although some remain locally unstrained. Late quartz-carbonate veins are also abundant in these argillitic units, crosscutting both the nodules and their enclosing sedimentary rock.

RESULTS

Nodule Mineralogy and Textures

Unstrained nodules from the argillite in the 20N Zn zone are round to slightly oblate and generally less than two centimetres in diameter (Fig. 2c, 3a,b). Pyrite forms most of the mass of the nodules, with inclusions that vary in abundance, distribution, and composition. The inclusions are composed of quartz, chlorite±mica, calcite, and other sulphide minerals. Two samples were studied in detail (LA-001 and LA-002) and both show concentric zones that are reflected by the distribution of inclusions or a change in the crystal habit of pyrite (Fig. 3a–c, 4a). Nodule LA-001 is spherical (Fig. 3a), whereas LA-002 is slightly elongated (Fig. 3b), forming an oblate spheroid with its flattening parallel to the main foliation in the argillite.

Based on their textures, three main growth zones can be distinguished (Fig. 4a). The innermost zone (or "core") is composed of very fine, polycrystalline pyrite with abundant calcite-silicate material (zone 1; Fig. 3a,b, 4a,b). While polishing the samples for SIMS analysis, a thin massive pyrite corona was revealed, which surrounds the inclusion-rich core in LA-001 (subdivided into zones 1b and a, respectively). Zone 2 forms most of the outer mass of the nodules (or "rim") and is subdivided into three parts (zones 2a–c; Fig. 4a,b), which consist of an equigranular assemblage of very fine decussate- or sheaf-like grains (zone 2a), inclusion-rich concentric features (zone 2b), and a radially oriented acicular outer region (zone 2c). An overgrowth of euhedral, inclusion-poor pyrite, such as the one shown in Figure 2c, forms the outer edge of nodule LA-002 (zone 3; Fig. 3d, 4f). A similar overgrowth is developed on nodule LA-001 but separated during mounting of the sample in epoxy. This overgrowth is likely metamorphogenic and parts of it are possibly synchronous with the development of a quartz vein that truncates the nodule (Fig. 3e,f).

Sphalerite constitutes the dominant sulphide inclusion phase in nodule LA-001 where it is largely concentrated around the core (Fig. 3c). Pyrite nodule LA-002 contains inclusions with an assemblage of galena<

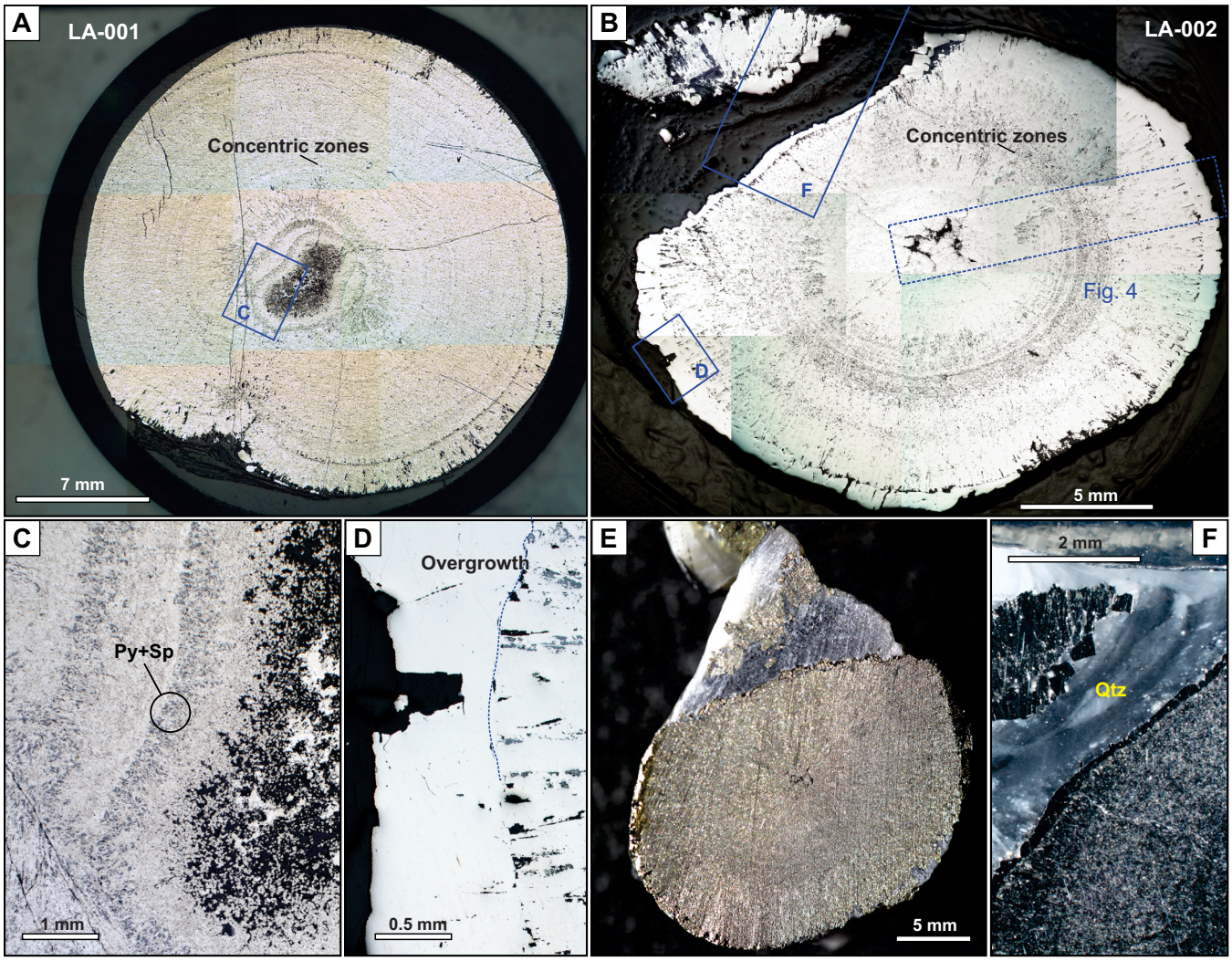

Figure 3. Representative photographs and photomicrographs of nodules LA-001 and LA-002 from the 20N Zn zone of the LaRonde Penna Au-rich VMS deposit. **a)** Nodule LA-001 in reflected light. **b)** Nodule LA-002 in reflected light. **c)** Close-up of (a) showing in the inclusion-rich core and concentric zones defined by abundant sphalerite (Sp) inclusions in the pyrite (Py) nodules. **d)** Close-up of (b) showing the idiomorphic nature of the overgrowth pyrite surrounding the nodule. **e)** Photograph of nodule LA-002 (unpolished) showing the crosscutting quartz veins. **f)** Close-up of (b) in natural light showing the dark grey quartz (Qtz) vein and the development of the inclusion-free pyrite overgrowth.

sphalerite≤stannite ($Cu_2(Fe,Zn)SnS_4$) (Fig. 4d,g–j) with most sulphide inclusions restricted to zones 1 and 2 as <40 µm sized grains (Fig. 4c-j); however, <500 µm sized galena grains are also found within overgrowth pyrite grain boundaries (Fig. 4f,j). The composition of stannite (semi-quantitative) was obtained by scanning electron microscope (SEM)-electron dispersive X-ray spectroscopy (EDS) and revealed Zn abundances averaging ~3 wt% Zn (Table 1). Sphalerite is typically in contact with stannite and together they concentrate along the main elongation of the nodules (and the acicular pyrite) and within the concentric, inclusion-rich zone (Fig. 4d–f,h–j). Galena is not spatially associated with the other two sulphides; however, galena is present outside the core and tends to be concentrated preferentially near the margin of the flattened nodule.

Geochemistry of Nodules

Methodology

Two-dimensional element content maps of the two nodules were generated by LA-ICP-MS (GSC-Ottawa) to allow quantitative determination of the distributions of Au and other major and trace elements (Fig. 5, 6). The areas mapped were sampled via tens of thousands of discrete edge-to-edge square ablation spots (with 3–5 "pre-ablation" laser pulses for surface cleaning, 1.5 s flush, and 2 s ablation). Quantification of the data from the multi-phase mineral assemblages was achieved via external calibration against United States Geological Survey synthetic basaltic glass reference material GSE-1G, coupled with ablation yield correction via normalization to 100% total element abundance (Halicz and Günther, 2004), performed on a spot-by-

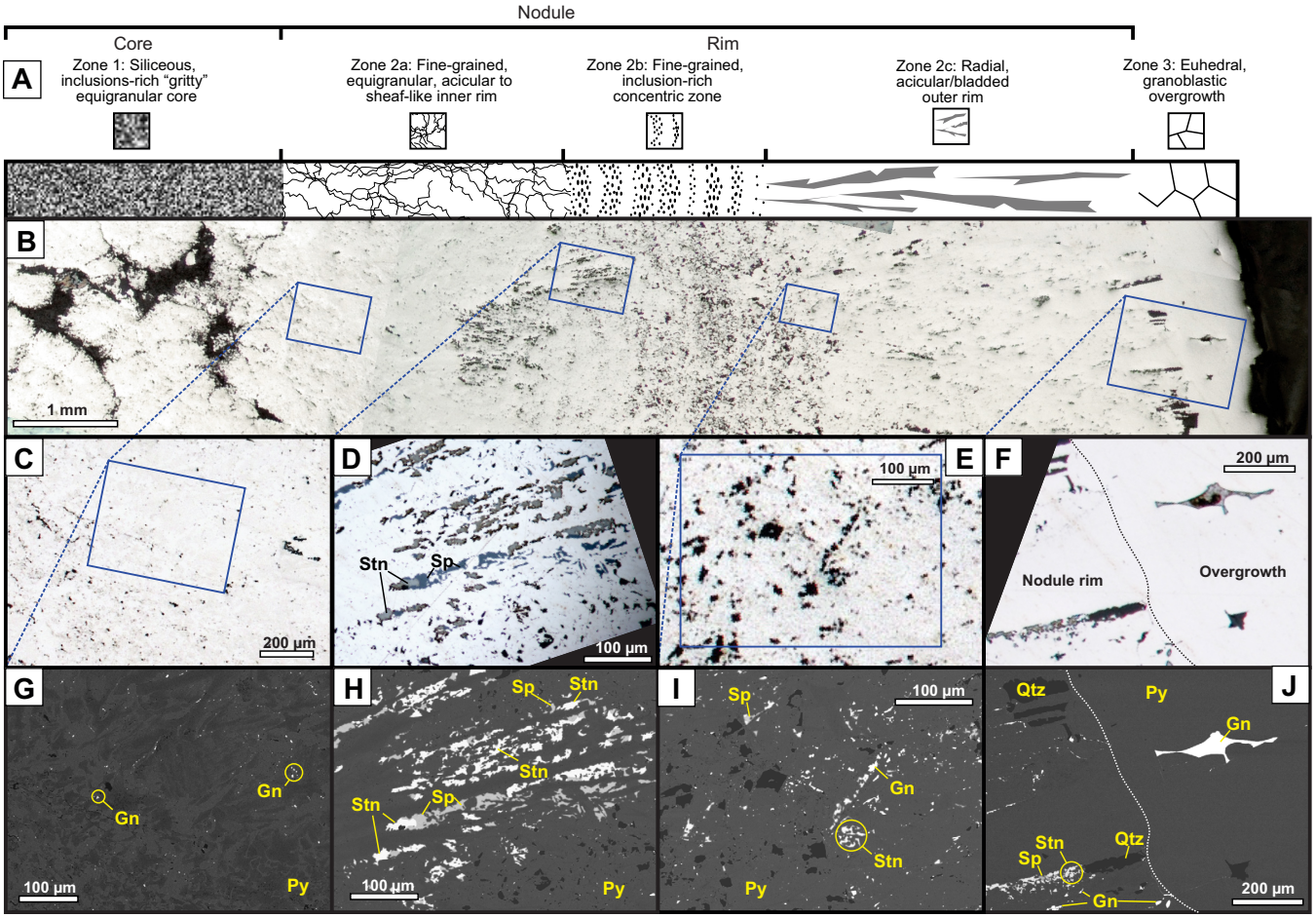

Figure 4. a) Schematic diagram showing the various zones composing pyrite nodule LA-002 based on textures. Note that zone 1b is absent in LA-002. **b)** Section close-up of Figure 3b. **c to f)** Episcopic images with respective regions shown in (b). **g to j)** Backscattered electron images (BSE) of (c) to (f). Abbreviations: Gn = galena, Py = pyrite, Qtz = quartz, Sp = sphalerite, Stn = stannite.

spot basis. To extend the calibration to S and C, which are not measurable in GSE-1G, surrogate calibration was applied using S/Fe and C/Ca sensitivity ratios determined by ablation of pure pyrrhotite and calcite, respectively. Data reduction was achieved using fully automated in-house spreadsheet software, LAMTrace, and its sister program, Convert (Jackson, 2008). Element contents for GSE-1G were GeoRem "preferred values" (http://georem.mpch-mainz.gwdg.de/). Another in-house spreadsheet program (PixeLAte) was used to generate element concentration maps by assembling and displaying element concentrations for each spot as coloured pixels using percentile or logarithmic scaling functions.

Trace element distribution

Element maps (Fig. 5, 6) show the general concentric zonation of the nodules, which are in agreement with petrographic observations. The presence of silicate inclusions in the cores and inside the rims is reflected by the abundance in Al_2O_3 (Fig. 5b, 6b). In nodule LA-001, Mn, Cu, Zn, Ag, Sn, Sb, Au, and Tl are most abun-

Table 1. Scanning electron microscopy analyses of stannite from LaRonde Penna Mine pyrite nodule LA-002.

Weight %						
S	31.34	31.85	32.64	31.16	30.66	31.38
Fe	11.17	10.72	11.60	10.34	10.61	10.82
Cu	27.37	26.21	26.12	26.84	27.07	25.84
Zn	2.28	2.67	2.43	3.19	3.60	3.54
Sn	27.85	28.55	27.21	28.48	28.06	28.41
Atomic %						
S	52.05	52.85	53.49	52.02	51.31	52.26
Fe	10.65	10.22	10.91	9.91	10.19	10.35
Cu	22.94	21.95	21.60	22.61	22.86	21.72
Zn	1.86	2.18	1.96	2.62	2.95	2.89
Sn	12.50	12.80	12.04	12.85	12.68	12.78

Analyses carried out at the Institut national de la recherche scientifique, Centre Eau Terre et Environnement in Québec City with an automated x-spectrometer Carl Zeiss EVO 50 Smart electron microprobe by energy dispersive X-ray spectrometry microanalysis system (EDS). Raw X-ray data were converted to elemental wt% by the Cameca PAP matrix correction program. Analyses done using a 20 kV accelerating voltage, 2 nA beam current, 5 µm electron beam with a counting time of 20 s.

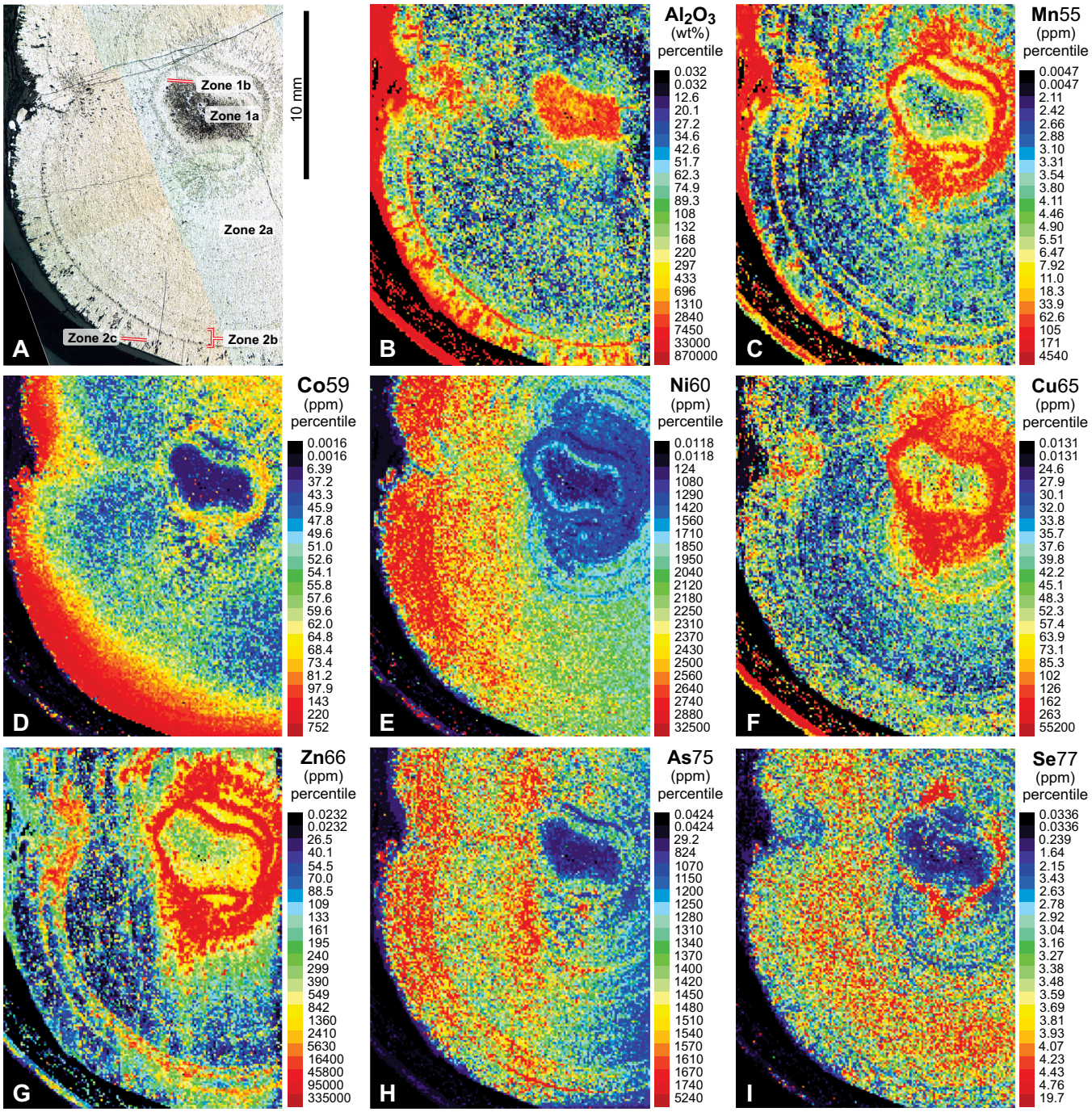

Figure 5. LA-ICP-MS element maps of pyrite nodule LA-001 from the 20N Zn zone of the LaRonde Penna Au-rich VMS deposit: **a)** episcopic image, **b)** Al_2O_3, **c)** Mn, **d)** Co, **e)** Ni, **f)** Cu, **g)** Zn, **h)** As, **i)** Se. All scales are in ppm, with the exception of Al_2O_3, which is in wt%. Figure is continued on the next page.

dant near or within the core, whereas As, Se, Te, Pb, and Bi are distributed more evenly across the nodule. Nickel and Co, however, are significantly enriched within and toward the outer rim (zones 2b and c).

In nodule LA-002, most elements decrease toward the rim except for Ni, Se, Pb, and Bi (Fig. 6); however, Mn, Co, Cu, Zn, Sn, Pb, and Bi also show localized concentrations that are either discordant to the concentric zones or follow them. High contents of Cu, Zn, and Sn correlate with the occurrence of sphalerite and stannite inclusions. High Pb and Bi contents correlate with galena inclusions. Although Au is concentrated in the core in both nodules, its highest content in nodule LA-001 overlaps areas that contain abundant sphalerite inclusions, whereas, in nodule LA-002, Au is evenly distributed within zones 1 and 2a.

The overgrowth envelope (zone 3) in nodule LA-002 is host to Co and Ni but contains lesser amounts of

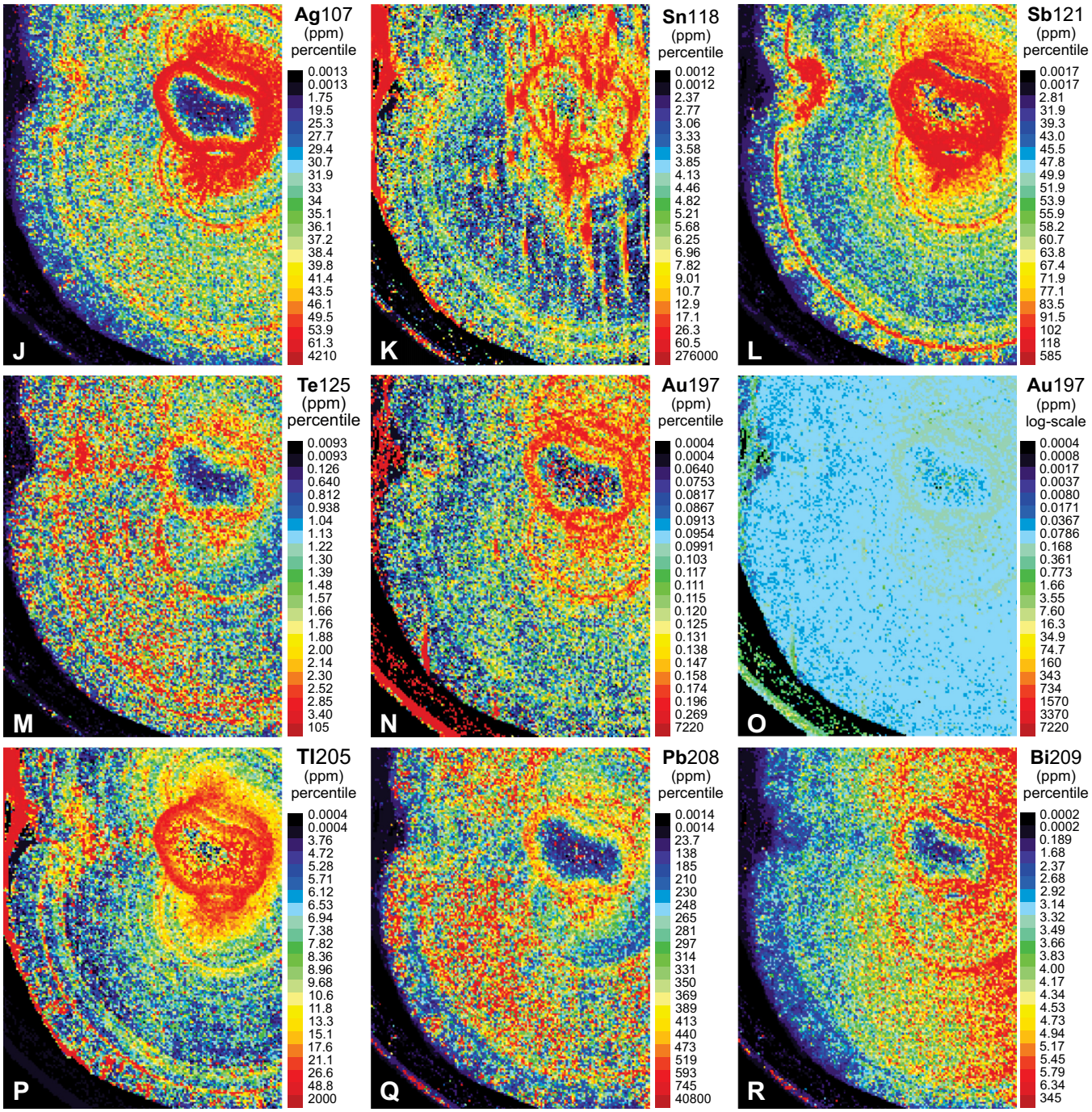

Figure 5 continued. LA-ICP-MS element maps of pyrite nodule LA-001 from the 20N Zn zone of the LaRonde Penna Au-rich VMS deposit: **j)** Ag, **k)** Sn, **l)** Sb, **m)** Te, **n)** Au (percentile scaling), **o)** Au (log scaling), **p)** Tl, **q)** Pb, **r)** Bi. All scales are in ppm.

other trace elements (Fig. 6d,e). Interestingly, whereas Co is enriched in most of the overgrowth pyrite grains, it is depleted in those formed along the quartz vein (Fig. 6d). Spotty, high concentrations of Pb and Bi in zone 3 can be explained by the presence of galena inclusions between overgrowth grain boundaries (Fig. 4f,j).

Comparison of Trace Element Abundance

Element concentrations derived from the LA-ICP-MS mapping are represented as violin plots in Figure 7. The two nodules show similar Mn, Co, Se, Ag, Sb, Te, and Tl values, whereas differences in mean values and/or highly variable concentrations of Ni, Cu, Zn, As, Sn, Au, Pb, and Bi were observed between nodules LA-001 and LA-002. For example, nodule LA-001 yielded Ni, Zn, As, and Bi concentrations that range from ~2 to 10 times greater than nodule LA-002. Apart from Zn (which preferably partitions into other sulphide phases over pyrite), the differences in Ni and As contents between the two nodules are noticeable (Fig.

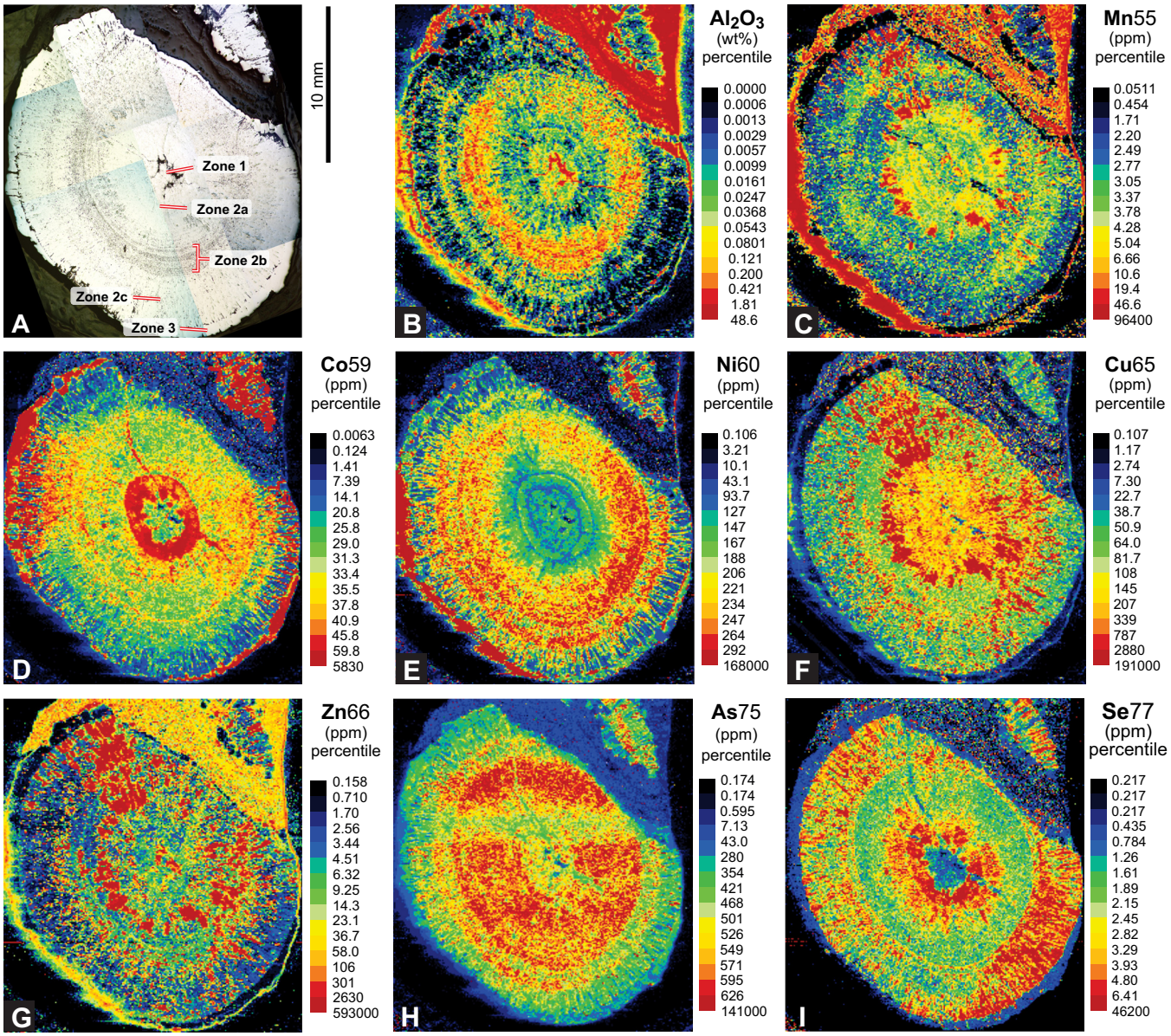

Figure 6. LA-ICP-MS element maps of pyrite nodule LA-002 from the 20N Zn zone of the LaRonde Penna Au-rich VMS deposit. **a)** episcopic image, **b)** Al_2O_3, **c)** Mn, **d)** Co, **e)** Ni, **f)** Cu, **g)** Zn, **h)** As, **i)** Se. All scales are in ppm, with the exception of Al_2O_3, which is in wt%. Figure is continued on the next page.

7c,f). Although Au is more abundant in nodule LA-002 by a factor of 2 to 3, both nodules have the highest Au concentrations in or near the core (Fig. 5n,o, 6n,o). Cores from nodules LA-001 and LA-002 average 0.38 ppm Au (n = 6918 pixels) and 1.04 ppm Au (n = 10,539 pixels), respectively. It is noteworthy that, although nodule LA-002 has more Au, it contains significantly less As than LA-001. This raises questions regarding the control of As on Au during trace element uptake and/or factors controlling the auriferous nature of the nodules (cf. Reich et al., 2005; Gregory et al., 2015), which is beyond the scope of this report but is an area currently being investigated by a broader study (Pilote et al., 2020).

Statistical analysis

Principal component analysis (PCA) is used to summarize the structure of the multivariate data set generated in this study (15 variables and 43,156 objects). Using the sulphide data from the LA-ICP-MS maps, principal components (PC) were computed in R software (R Core Team, 2019) after a log-transformation procedure to minimize any possible effects from closure and outliers (e.g. Filzmoser et al., 2009). For nodule LA-001 (Fig. 8a), most variance in the data is explained by the first PC (70.5%), which defines a strong separation between Zn and the rest of the trace elements. This can be explained by the presence of sphalerite inclusions, predominantly regulating Zn deportment. Similarly, the first PC also explains most of the variance (67.7%) in

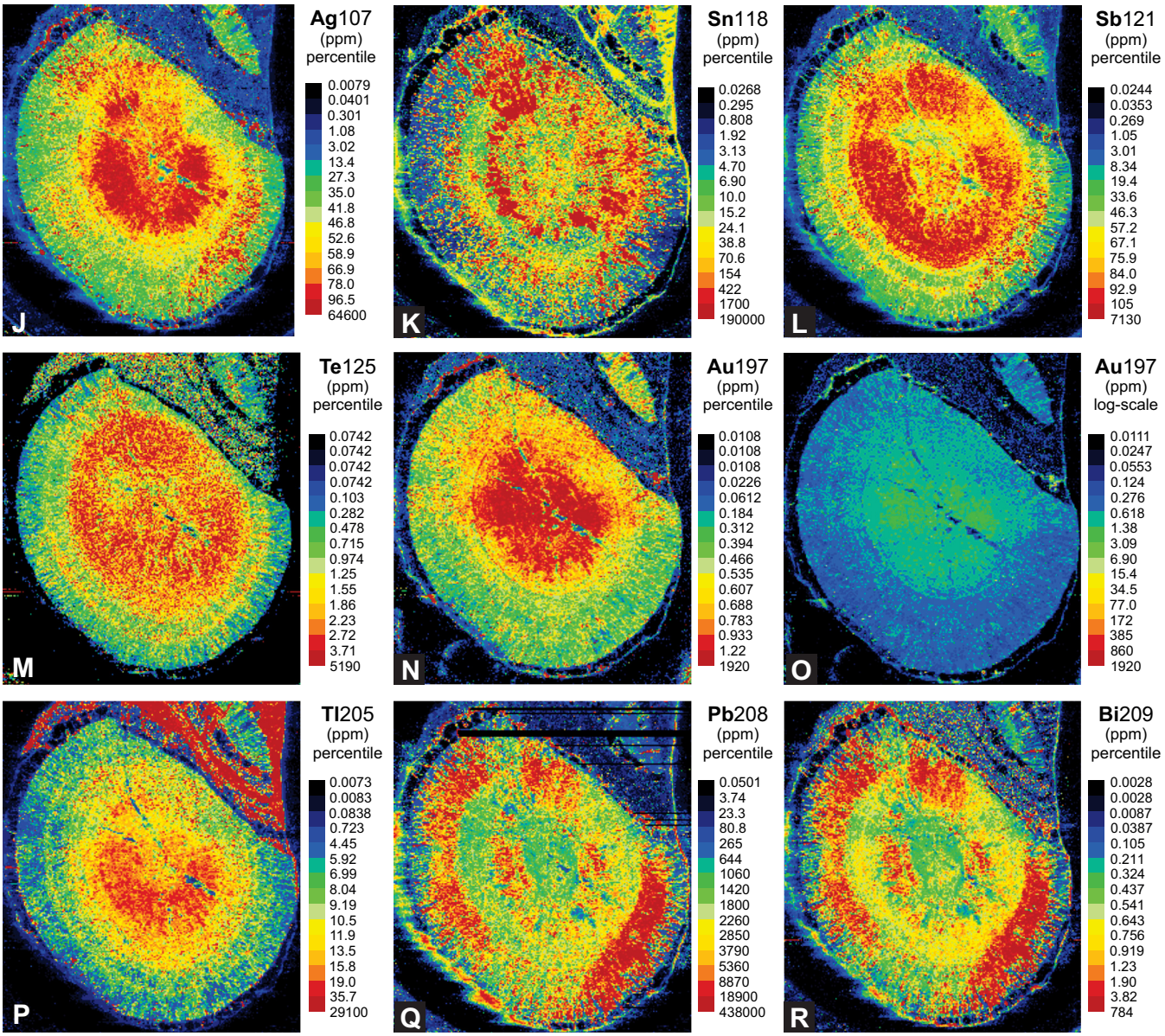

Figure 6 continued. LA-ICP-MS element maps of pyrite nodule LA-002 from the 20N Zn zone of the LaRonde Penna Au-rich VMS deposit: **j)** Ag, **k)** Sn, **l)** Sb, **m)** Te, **n)** Au (percentile scaling), **o)** Au (log scaling), **p)** Tl, **q)** Pb, **r)** Bi. All scales are in ppm.

nodule LA-002, with a strong separation of Zn, Sn, and Cu from the rest of the trace elements. The correlation between those three elements reflects the presence of sphalerite and Zn-bearing stannite ($Cu_2(Fe,Zn)SnS_4$) inclusions. Moreover, the strong correlation between Pb and Bi and their separation from the rest of the data in the second PC space (which explains 16.3% of the variance) concurs with the presence of galena in the nodule. The antithetic chemical relationship that exists between Zn-Cu-Sn and Bi-Pb from the PCA agrees with the lack of spatial association between sphalerite-stannite and galena, both from petrographic observations and from the distribution of the elements from the compositional maps. Elements that best mirror the overall Au distribution in nodule LA-001 (despite the low PC2 variance) are Co, Ni, Cu, As, Se, Sb, and Bi, and in LA-002, Te and Tl.

SULPHUR ISOTOPES

Methodology

Fifty sulphur isotope analyses were made on the nodules. Analyses were performed using the Cameca IMS 4f Secondary Ion Mass Spectrometer (SIMS) at the MAF-IIC Microanalysis Facility of Memorial University of Newfoundland. Samples were bombarded with a primary ion microbeam of 650–800 pA of Cs^+ accelerated through a nominal 10 keV potential, and focused into an 8–15 µm diameter spot following pre-sputtering for 120 s with a 25 μm^2 raster. Negatively charged sputtered secondary ions were

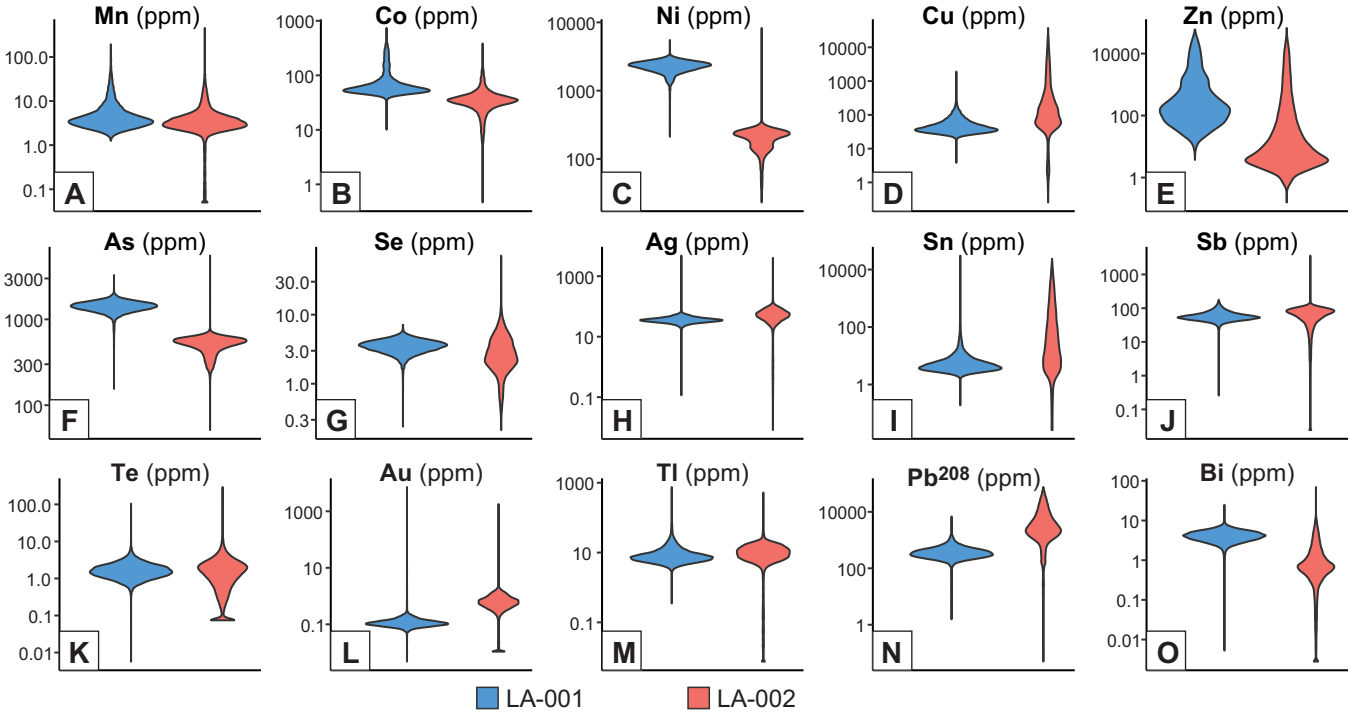

Figure 7. Violin plots of element abundances (ppm) in pyrite nodules LA-001 and LA-002: **a)** Mn, **b)** Co, **c)** Ni, **d)** Cu, **e)** Zn, **f)** As, **g)** Se, **h)** Ag, **i)** Sn, **j)** Sb, **k)** Te, **l)** Au, **m)** Tl, **n)** Pb, and **o)** Bi. The data are derived from the respective 13,494 and 29,662 analyses obtained by LA-ICP-MS. The thickness of each violin is proportional to the density of the values, and the length (including tails) represents the range of values:

accelerated into the mass spectrometer using a potential of 4.5 keV. The instrument was operated with a 150 µm diameter contrast aperture, and entrance and exit slits paired to give flat-topped peaks at a mass resolving power (MRP) of ≥2975 (10% peak height definition), which is sufficient to discriminate $^{33}SH^-$ (and $^{32}SH_2^-$) from $^{34}S^-$. A sample offset voltage of -60 eV and an energy window of 40 eV were also deployed. Overall reproducibility, based on replicate standard analyses, was typically better than ±0.4‰ (1σ). Complete details of the analytical methods, including the performance of in-house sulphide mineral stan-

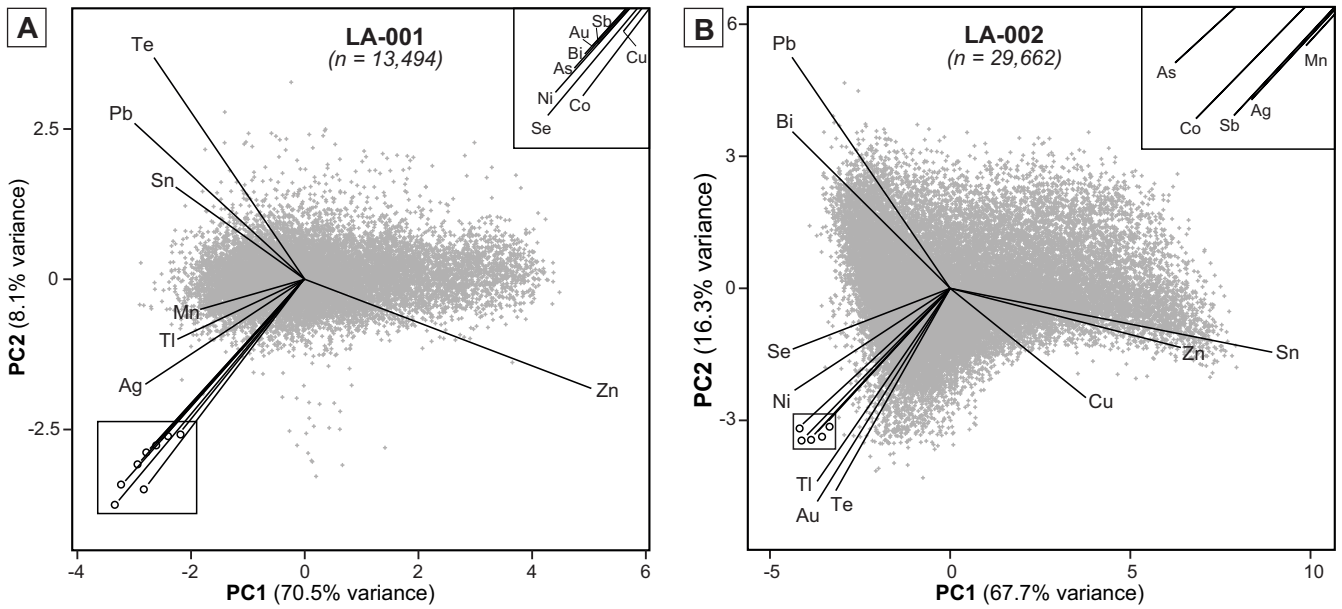

Figure 8. Bivariate plots of PC1 versus PC2 for **(a)** LA-001 and **(b)** LA-002 pyrite nodule data sets. In (a), PC1 and PC2 account for 70.5% and 8.1% of the variances, respectively. In (b), PC1 and PC2 account for 67.7% ad 16.3% of the variances, respectively.

Table 2. Secondary ion mass spectrometry in situ $\delta^{34}S$ stable isotopic data of pyrite nodules from the LaRonde Penna deposit.

Analysis	$\delta^{34}S$ VCDT (‰)	1s(SEM) (‰)	$^{34}S/^{32}S$ ratio	2SD ratio	SEM (%)	Poisson (%)	N cycles	Analyzed area
Nodule LA-001								
PML1 Py1	3.8	0.2	0.043919	0.000177	0.024	0.027	72	Zone 3: overgrowth
PML1 Py2	3.2	0.2	0.043895	0.000176	0.023	0.025	77	Zone 3: overgrowth
PML1 Py3	2.6	0.2	0.043866	0.000135	0.018	0.026	72	Zone 2c: Radial, bladded rim
PML1 Py4	1.9	0.2	0.043838	0.000147	0.019	0.025	76	Zone 2b: inclusion-rich concentric zone
PML1 Py5	1.8	0.2	0.043835	0.000158	0.021	0.026	76	Zone 2c: Radial, bladded rim
PML1 Py6	2.1	0.2	0.043846	0.000170	0.023	0.027	72	Zone 2b: inclusion-rich concentric zone
PML1 Py7	1.7	0.2	0.043828	0.000171	0.023	0.026	75	Zone 2b: inclusion-rich concentric zone
PML1 Py8	3.3	0.2	0.043900	0.000163	0.022	0.027	73	Zone 2b: inclusion-rich concentric zone
PML1 Py9	2.1	0.2	0.043845	0.000150	0.020	0.025	76	Zone 2b: inclusion-rich concentric zone
PML1 Py10	2.2	0.2	0.043849	0.000153	0.021	0.026	71	Zone 2a: Fine-grained inner rim
PML1 Py11	2.9	0.2	0.043882	0.000142	0.019	0.026	72	Zone 2a: Fine-grained inner rim
PML1 Py12	-0.6	0.2	0.043730	0.000167	0.022	0.026	76	Zone 1b: Recrystallized outer "clean" core
PML1 Py13	-0.8	0.2	0.043721	0.000180	0.023	0.026	77	Zone 1b: Recrystallized outer "clean" core
PML1 Py14	2.1	0.2	0.043846	0.000143	0.019	0.025	76	Zone 1a: Siliceous, inclusion-rich "gritty"core
PML1 Py15	1.8	0.2	0.043831	0.000134	0.017	0.025	77	Zone 1a: Siliceous, inclusion-rich "gritty"core
PML1 Py16	2.2	0.2	0.043851	0.000158	0.021	0.026	74	Zone 1a: Siliceous, inclusion-rich "gritty"core
PML1 Py17	1.9	0.2	0.043837	0.000144	0.019	0.026	76	Zone 1a: Siliceous, inclusion-rich "gritty"core
PML1 Py18	3.4	0.3	0.043902	0.000184	0.025	0.028	70	Zone 3: overgrowth
PML1 Py22	1.1	0.2	0.043802	0.000156	0.020	0.027	76	Zone 2b: inclusion-rich concentric zone
PML1 Py23	1.3	0.2	0.043812	0.000125	0.016	0.024	76	Zone 2a: Fine-grained inner rim
PML1 Py24	1.0	0.2	0.043797	0.000142	0.018	0.024	78	Zone 2a: Fine-grained inner rim
PML1 Py25	1.9	0.2	0.043836	0.000151	0.020	0.024	77	Zone 2a: Fine-grained inner rim
PML1 Py26	2.6	0.2	0.043866	0.000130	0.017	0.025	74	Zone 2a: Fine-grained inner rim
PML1 Py27	2.9	0.2	0.043879	0.000137	0.018	0.025	73	Zone 2c: Radial, bladded rim
PML1 Py28	2.2	0.2	0.043850	0.000157	0.021	0.024	75	Zone 2c: Radial, bladded rim
PML1 Py29	1.9	0.2	0.043837	0.000145	0.019	0.024	78	Zone 2b: inclusion-rich concentric zone
Nodule LA-002								
PML2 Py13	1.5	0.2	0.043819	0.000141	0.019	0.026	75	Zone 1: Siliceous, inclusion-rich "gritty" core
PML2 Py14	1.7	0.2	0.043827	0.000160	0.021	0.026	75	Zone 1: Siliceous, inclusion-rich "gritty" core
PML2 Py15	1.9	0.2	0.043838	0.000156	0.020	0.025	76	Zone 1: Siliceous, inclusion-rich "gritty" core
PML2 Py16	2.3	0.3	0.043853	0.000203	0.026	0.031	78	Zone 2c: Radial, bladded rim
PML2 Py17	0.0	0.2	0.043755	0.000175	0.023	0.028	77	Zone 2c: Radial, bladded rim
PML2 Py18	5.0	0.3	0.043974	0.000222	0.032	0.032	64	Zone 2c: Radial, bladded rim
PML2 Py19	3.2	0.3	0.043893	0.000218	0.030	0.031	68	Zone 3: overgrowth
PML2 Py20	1.5	0.3	0.043820	0.000210	0.028	0.029	73	Zone 2b: inclusion-rich concentric zone
PML2 Py21	0.1	0.2	0.043760	0.000185	0.024	0.029	76	Zone 2b: inclusion-rich concentric zone
PML2 Py22	1.6	0.2	0.043825	0.000169	0.022	0.029	75	Zone 2a: Fine-grained inner rim
PML2 Py23	2.2	0.2	0.043849	0.000176	0.024	0.030	72	Zone 2a: Fine-grained inner rim
PML2 Py1	1.7	0.2	0.043829	0.000163	0.022	0.027	73	Zone 3: overgrowth
PML2 Py2	3.5	0.3	0.043906	0.000200	0.027	0.028	73	Zone 2c: Radial, bladded rim
PML2 Py3	3.0	0.2	0.043884	0.000168	0.023	0.028	71	Zone 2c: Radial, bladded rim
PML2 Py4	3.9	0.3	0.043926	0.000188	0.025	0.025	71	Zone 2c: Radial, bladded rim
PML2 Py5	2.3	0.2	0.043855	0.000139	0.018	0.024	76	Zone 2c: Radial, bladded rim
PML2 Py6	2.2	0.2	0.043852	0.000115	0.015	0.024	72	Zone 2c: Radial, bladded rim
PML2 Py7	1.9	0.2	0.043836	0.000153	0.020	0.024	73	Zone 2b: inclusion-rich concentric zone
PML2 Py8	1.4	0.2	0.043813	0.000161	0.021	0.025	73	Zone 2b: inclusion-rich concentric zone
PML2 Py9	2.9	0.2	0.043881	0.000125	0.017	0.025	73	Zone 2a: Fine-grained inner rim
PML2 Py10	2.4	0.2	0.043861	0.000179	0.023	0.024	76	Zone 2a: Fine-grained inner rim
PML2 Py11	2.8	0.2	0.043877	0.000176	0.023	0.025	75	Zone 2a: Fine-grained inner rim
PML2 Py12	1.9	0.2	0.043836	0.000144	0.019	0.025	76	Zone 2a: Fine-grained inner rim

dards, their accepted $^{34}S/^{32}S$ ratios, and the calibration of instrument mass fractionation (IMF) factors, can be found in Brueckner et al. (2015).

Composition

Results for all the analyzed zones from both nodules are shown in Figure 9 and Table 2. From core to rim, including the overgrowth, the data average +2.1‰ (n = 50) and range between -0.8 and +5.0‰. In nodule LA-001, zone 1b (inclusion-free, equigranular pyrite that envelopes the gritty, inclusion-rich pyrite; Fig. 9b) shows the lowest $\delta^{34}S$ values (-0.8‰ and -0.6‰).

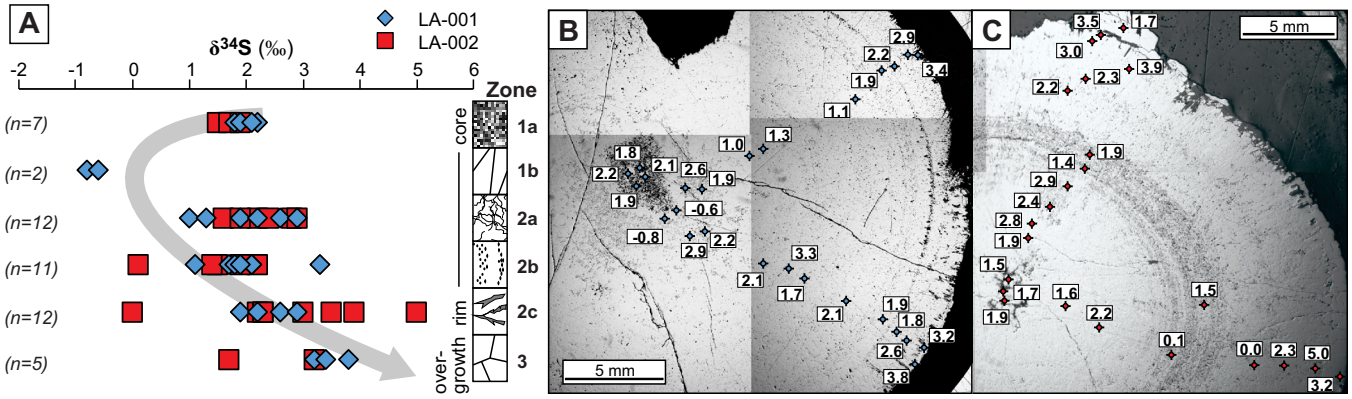

Figure 9. a) δ34S values of pyrite in each textural zone. **b and c**) Spot locations and δ34S values from SIMS analyses on pyrite nodules LA-001 and LA-002.

From the inner to the outer rim, despite some outliers, the isotopic values tend to become heavier (Fig. 9). The values for the overgrowth pyrite in nodule LA-001 are slightly higher than the rest of the nodule (+3.2 to +3.8‰), whereas the pyrite overgrowths from nodule LA-002 show values that overlap those of the outer rim (+1.7 and +3.2‰) (Table 2). Dubé et al. (2004) report $\delta^{34}S$ values (n = 6) from pyrite from the surrounding 20N Zn zone with an average of +2.2‰ and a range from +1.7 to +2.8‰. These are broadly consistent with the SIMS S-isotope data reported in the present study for nodules LA-001 and LA-002, which suggest a similar source of sulphur.

DISCUSSION

Pyrite nodules are common in many fine-grained sedimentary units (distal and proximal to mineralization) of the Abitibi greenstone belt and elsewhere in the Superior Province (Jonasson et al., 1999; Hannington et al., 2012; Pilote et al., 2019). Although many consider pyrite nodules diagenetic, certain aspects about their timing of formation and controls on their Au enrichment remain to be clarified, which constitute subjects of a larger study about nodules (Pilote et al., 2019, 2020). Here, the characteristics of nodule LA-001 and LA-002, which show a transition from a polycrystalline core to an envelope of radially oriented acicular grains of pyrite, are not unique to LaRonde, and appear to be similar to global examples from low-temperature-related diagenetic pyrite nodules from unmetamorphosed sequences (e.g. Rickard, 2012; Jeans et al., 2016).

Crystal growth is regulated by the degree of departure from equilibrium state (Sunagawa, 2005; Hu et al., 2019) and, for pyrite nodules in sedimentary rocks, the degree of supersaturation of the main reactant agents in hydrothermal or diagenetic fluids (i.e. Fe(II) and S(-II)) is the main driving factor. In sedimentary settings, concentrations of reduced Fe and S required to nucleate and form pyrite can be achieved in pore fluids without a hydrothermal contribution (Rickard, 2012). Pyrite growth will stop when the rate of supply of the reactant agents is less than the rate of crystal growth (i.e. equilibrium is reached). Some workers suggest that the transition from irregular-shaped, fine-grained crystals (core) to elongated, well defined crystal habits (rim) reflects a decrease in the degree of supersaturation (Murowchick and Barnes, 1987; Rickard, 2012; Hu et al., 2019), which also likely dictates the ability to concentrate trace elements (including Au). In pyrite nodules LA-001 and LA-002, Au is concentrated and controlled by the transition from fine-grained to bladed pyrite. The analytical approach used here does not allow us to recognize if Au occurs as a solid solution in pyrite lattices (e.g. Reich et al., 2005; Gregory et al., 2015) or as nanoparticles (Palenik et al., 2004; Fougerouse et al., 2016), but its core-restricted distribution suggests that the enrichment is related to the early formation of the nodules, possibly during a time of a high degree of supersaturation.

A similar core-to-rim decrease in Au abundance is common in pyrite nodules from the Timmins region (Pilote et al., 2019), and whereas most nodules from Timmins also show a decrease in trace elements, the LaRonde nodules exhibit some distinct patterns. Studies of Pilote et al. (2019, 2020) show that the contents of Ni and Tl (two relatively abundant trace elements that provide good discriminants for nodules (diagenetic) versus pyrite of epigenetic origins (e.g. porphyroblasts, granoblasts) within argillites) in the Timmins nodules decrease from core to rim, but with relatively less variability in Tl than Ni. This is expressed as a decrease in both Au and Ni/Tl on a bivariate plot (Fig. 10). In the LaRonde nodules, however, the opposite is observed (Fig. 10) and Ni/Tl increases at the expense of Au. Thallium bonds 'loosely' to pyrite crystal lattices (George et al., 2019), and Deditius and Reich (2016) suggested that its concentration in pyrite is controlled mainly by the abundances of trivalent Sb and As. The covariation

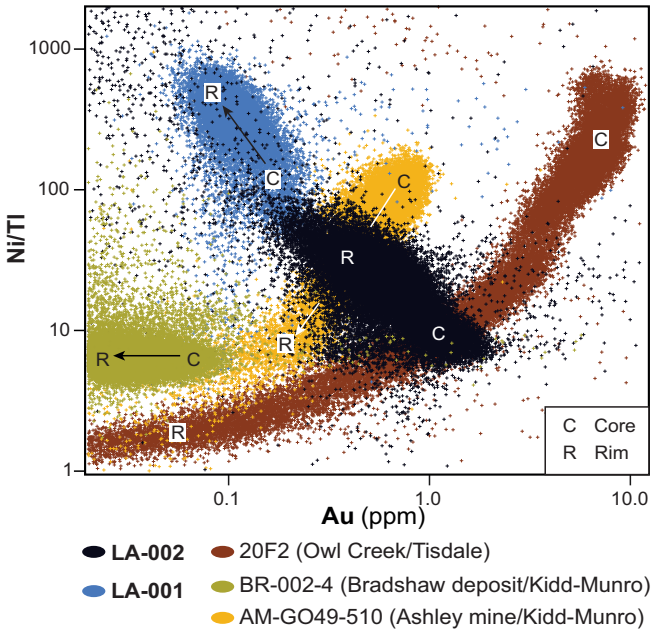

Figure 10. Gold (ppm) versus Ni/Tl from LA-ICP-MS element maps. Nodules LA-001 and LA-002 are compared to three representative nodules from the Timmins region (data from Pilote et al., unpublished): 1) nodule BR-002-4 from the Bradshaw deposit, 2) nodule AM-GO49-510 from the Ashley Mine, and 3) nodule 20F2 from the Owl Creek deposit.

observed for these three elements in the LaRonde pyrite nodules (Fig. 5h,l,p, 6h,l,p) concurs with this hypothesis. Moreover, Huston et al. (1995) suggest that the rate at which pyrite precipitates regulates the amount of Tl that it can accommodate. If correct, this would suggest that the cores precipitate at a faster rate than their surrounding rim. As for Ni, its enrichment in sediments is commonly suggested to be the result of hydrogenous adsorption onto metastable iron sulphides (e.g. mackinawite, although its presence in natural environments is debated; Rickard, 2012; Gregory et al., 2019) and/or of formation of organometallic complexes in reducing marine conditions (Tribovillard et al., 2006; Wilkin and Beak, 2017; Gadd et al., 2019). Diagenetic breakdown of the transporting agent would then release Ni (along with other trace elements) to be concentrated in the early formed pyrite (Tribovillard et al., 2006; Large et al., 2011). Given the relatively late Ni enrichment in the LaRonde nodules, this process is questionable, but more work is needed to substantiate this interpretation and test the mechanisms that led to Ni enrichment. The increase in Ni values in nodule LA-002 correlates with an increase in the abundance of stannite, sphalerite, and galena inclusions that is also reflected by an increase of Sn, Cu, Zn, Pb, and Bi. Similar minerals, in trace amounts, are present in the 20N Zn zone, although with evidence of recrystallization/replacement (Dubé et al., 2004). It would be reasonable to argue that a contribution from the ore-forming hydrothermal fluids during the growth of the nodule would explain the sudden appearance of these minerals in the nodules. However, this argument faces an important obstacle, and that is the type of hydrodynamic regime required to form large, concentrically zoned, nodular-shaped pyrite (Rickard, 2012). In order to maintain this texture, the supply of reactant agents (reduced Fe and S) has to be constant and the growth relatively rapid, with a gentle to nearly stagnant hydrodynamic regime (Rickard, 2012). These requirements can only be achieved in a closed or highly isolated system (Gregory et al., 2019) and a case for a direct hydrothermal contribution is difficult to support given the strong advective and open regime of a VMS system. Alternatively, instead of direct hydrothermal input, elements Sn, Cu, Zn, Pb, and Bi could have been enriched in the sediment (from nearby hydrothermal venting) at the time of deposition and partitioned into pyrite during diagenetic formation, before or after the formation of the 20 North lens.

The hourglass-shaped distribution of Cu, Zn, Sn, Pb and Bi observed in nodule LA-002 (Fig. 6f,g,k,q,r) from the sphalerite, stannite, and galena inclusions, which is parallel to the main elongation, is likely the product of deformation. Partial recrystallization of the rim in nodule LA-002 could have accommodated the liberation and/or reorganization of elements parallel to the plane of flattening.

We speculate that the strong variability in trace element abundances (e.g. Au, Ni, As; Fig. 7) in the nodules could be explained by differences in the host sediment composition, which are largely governed by its provenance (detrital versus hydrothermal). The possible compositional effects of the sediments (and source) on the pyrite compositions are currently being investigated in the Timmins region (Pilote et al., in prep). Lastly, an overall decrease in trace element abundance from the core to the rim, accompanied by an increase in $\delta^{34}S$ values, as in the LaRonde nodules, is also a common phenomenon. Gregory et al. (2019) report similar trends in nodules from Western Australia, the Urals, and Tasmania from sedimentary sequences of Neoarchean, Mesoproterozoic, and Cambrian ages, respectively. To explain the increase in $\delta^{34}S$ values observed in pyrite nodules LA-001 and LA-002, the authors suggest the progressive relative depletion of light S from bacterial sulphate reduction (BSR) activity in a closed or highly isolated system.

EXPLORATION IMPLICATIONS

Despite the limited number of samples, the presence of galena and stannite in close association with sphalerite inclusions in one of the pyrite nodules from an argillite lens within the 20N Zn orebody is interpreted as a signature of the hydrothermal activity that formed the enclosing mineralization. The preliminary results sug-

gest that a large portion of the enrichment in Sn, Zn, and Cu relates to a synsedimentary deposition process, prior to the nodule formation. Regardless, from an exploration perspective, the ore-like mineralogy and consequent chemical composition recorded by authigenic argillite-hosted pyrite nodules could potentially be used as a vector proxy for mineralization (contingent on a larger sample population from a wider distribution). While important questions remain, pyrite (and commonly pyrrhotite) nodules in argillitic sequences near VMS deposits are common in the Abitibi greenstone belt (e.g. pyrite nodules proximal to the main orebodies at Kidd Creek; Hannington et al., 1999a); however, detailed studies on their compositions in a well constrained metallogenic context are scarce. It should be noted that the presence of nodules alone should not be considered as a proxy for mineralization since they commonly form, as aforementioned, diagenetically and do not require hydrothermal fluids, which could be in fact an inhibiting factor if otherwise involved.

ONGOING AND FUTURE WORK

More robust comparisons are being made between nodules from LaRonde and the Timmins-Matheson gold corridor using multivariate statistical tools (i.e. PCA and linear discriminate analysis) to classify sedimentary pyrite generations as a function of their chemical assemblages ("clustering"). This approach will improve our understanding of the factors that control their genesis and auriferous nature. Gold enrichment in the core of nodules is very common but its genetic link with VMS systems remains poorly understood. Also, although the decrease in gold tenor from the core to the rim is likely related to the degree of supersaturation during pyrite growth, the cause of variability in gold content in the core from one nodule to another is still poorly understood.

ACKNOWLEDGMENTS

The authors wish to acknowledge Agnico Eagle Mines Ltd. and the LaRonde Penna mine personnel for having shared their knowledge of the LaRonde Penna deposit, for logistical and scientific support, and authorization to publish. A. de Coninck (INRS-ETE) helped with scanning electron microscope analyses. This contribution was reviewed by S. Paradis and D. Gregory.

REFERENCES

Brueckner, S.M., Piercey, S.J., Layne, G.D., Piercey, G., and Sylvester, P.J., 2015. Variations of sulphur isotope signatures in sulphides from the metamorphosed Ming Cu(-Au) volcanogenic massive sulphide deposit, Newfoundland Appalachians, Canada; Mineralium Deposita, v. 50, p. 619–640.

Davis, D.W., 2002. U-Pb geochronology of Archean metasedimentary rocks in the Pontiac and Abitibi Subprovinces, Quebec, constraints on timing, provenance and regional tectonics; Precambrian Research, v. 115, p. 97–117.

Deditius, A.P. and Reich, M., 2016. Constraints on the solid solubility of Hg, Tl, and Cd in arsenian pyrite; American Mineralogy, v. 101, p. 1451–1459.

Dubé, B., Mercier-Langevin, P., Hannington, M.D., Davis, D., and Lafrance, B., 2004. Le gisement de sulfures massifs aurifères volcanogènes LaRonde, Abitibi, Québec: altérations, minéralisations et implications pour l'exploration; Ministère des Ressources naturelles, de la Faune et des Parcs du Québec, MB 2004-03, 112 p.

Dubé, B., Gosselin, P., Mercier-Langevin, P., Hannington, M.D., and Galley, A., 2007a. Gold-rich volcanogenic massive sulphide deposits; *in* Mineral Deposits of Canada: A Synthesis of Major Deposit Types, District Metallogeny, the Evolution of Geological Provinces, and Exploration Methods, (ed.) W.D. Goodfellow; Geological Association of Canada, Mineral Deposits Division, Special Publication No. 5, p. 75–94.

Dubé, B., Mercier-Langevin, P., Hannington, M.D., Lafrance, B., Gosselin, G., and Gosselin, P., 2007b. The LaRonde Penna world-class Au-rich volcanogenic massive sulfide deposit, Abitibi, Québec: Mineralogy and geochemistry of alteration and implications for genesis and exploration; Economic Geology, v. 102, p. 633–666.

Dubé, B., Mercier-Langevin, P., Kjarsgaard, I., Hannington, M.D., Bécu, V., Côté, J., Moorhead, J., Legault, M., and Bédard, N., 2014. The Bousquet 2-Dumagami world-class Archean Au-rich volcanogenic massive sulfide deposit, Abitibi, Quebec: Metamorphosed submarine advanced argillic alteration footprint and genesis; Economic Geology, v. 109, p. 121–166.

Filzmoser, P., Hron, K., and Reimann, C., 2009. Principal component analysis for compositional data with outliers; Environmetrics, v. 20, p. 621–632.

Fougerouse, D., Reddy, S.M., Saxey, D.W., Rickard, W.D.A., van Riessen, A., and Micklethwaite, S., 2016. Nanoscale gold clusters in arsenopyrite controlled by growth rate not concentration: Evidence from atom microscopy; American Mineralogist, v.101, p. 1916–1919.

Gadd, M.G., Peter, J.M., Jackson, S.E., Yang, Z., and Petts, D., 2019. Platinum, Pd, Mo, Au and Re deportment in hyper-enriched black shale Ni-Zn-Mo-PGE mineralization, Peel River, Yukon, Canada; Ore Geology Reviews, v. 107, p. 600–614.

George, L.L., Biagioni, C., Orazio Lepore, G., Lacalamita, M., Agrosì, G., Carlo Capitani, G., Bonaccorsi, E. and d'Acapito, F., 2019. The speciation of thallium in (Tl,Sb,As)-rich pyrite; Ore Geology Reviews, v. 107, p. 364–380.

Gregory, D., Large, R.R., Halpin, J.A., Baturina, E.L., Lyons, T.W., Wu, S., Danyushevsky, L., Sack, P., Chappaz, A., Maslennikov, V.V., and Bull, S.W., 2015. Trace element content of sedimentary pyrite in black shales; Economic Geology, v. 110, p. 1389–1410.

Gregory, D., Mukherjee, I., Olson, S.L., Large, R.R., Danyushevsky, L.V., Stepanov, A.S., Avila, J.N., Cliff, J., Ireland, T.R., Raiswell, R., Olin, P.H., Maslennikov, V.V., and Lyons, T.W., 2019. The formation mechanisms of sedimentary pyrite nodules determined by trace element and sulfur isotope microanalysis; Geochimica et Cosmochimica Acta, v. 259, p. 53–68.

Guy, B.M., Beukes, N.J., and Gutzmer, J., 2010. Paleoenvironmental controls of pyrite from non-conglomeratic sedimentary rocks of the Mesoarchean Witwatersrand Supergroup, South Africa; South African Journal of Geology, v. 113, p. 195–228.

Guy, B.M., Ono, S., Gutzmer, J., Lin, Y., and Beukes, N.J., 2014. Sulfur sources of sedimentary "buckshot" pyrite in the Auriferous Conglomerates of the Mesoarchean Witwatersrand

and Ventersdorp Supergroups, Kaapvaal Craton, South Africa; Mineralium Deposita, v. 49, p. 751–775.

Halicz, L. and Günther, D., 2004. Quantitative analysis of silicates using LA-ICP-MS with liquid calibration; Journal of Analytical Atomic Spectrometry, v. 19, p. 1539–1545.

Hannington, M.D., Bleeker, W., and Kjarsgaard, I., 1999a. Sulfide mineralogy, geochemistry, and ore genesis of the Kidd Creek deposit: Part I. North, Central, and South Orebodies; *in* The Giant Kidd Creek Volcanogenic Massive Sulfide Deposit, western Abitibi Subprovince, Canada, (ed.) M.D. Hannington and C.T. Barrie; Society of Economic Geologists, Monograph 10, p. 163–224.

Hannington, M.D., Poulsen, K.H., Thompson, J.F.H., and Sillitoe, R.H., 1999b. Volcanogenic gold in the massive sulfide environment; Reviews in Economic Geology, v. 8, p. 325–356.

Hannington, M.D., de Ronde, C.E.J., and Petersen, S., 2005. Seafloor tectonics and submarine hydrothermal systems; *in* 100th Anniversary Volume (1905–2005), (ed.) J.W. Hedenquist, J.F.H. Thompson, R.J. Goldfarb, J.P. Richards; Society of Economic Geologists, p. 111–141.

Hannington, M.D., Coombs, A., van Hees, G., Duff, S., and Campos-Alvarez, N., 2012. Regional lithogeochemical study of the Kidd–Munro MEGATEM® survey areas, Timmins–Kirkland Lake, northern Ontario: Discover Abitibi Initiative; Ontario Geological Survey, Miscellaneous Release Data 291, 209 p.

Hu, S., Barnes, S.J., Glenn, A.M., Pagès, A., Parr, J., MacRae, C., and Binns, R., 2019. Growth history of sphalerite in a modern sea floor hydrothermal chimney revealed by electron backscattered diffraction; Economic Geology, v. 114, p. 165–176.

Huston, D.L., Sie, S.H., Suter, G.F., Cooke, D.R., and Both, R.A., 1995. Trace elements in sulfide minerals from eastern Australian volcanic-hosted massive sulfide deposits; Part I, Proton microprobe analyses of pyrite, chalcopyrite, and sphalerite, and Part II, Selenium levels in pyrite; comparison with delta ^{34}S values and implications for the source of sulfur in volcanogenic hydrothermal systems; Economic Geology, v. 90, p. 1167–1196.

Jackson, S.E., 2008. LAMTRACE data reduction software for LA-ICP-MS; *in* Laser ablation-ICP-mass spectrometry in the Earth sciences: Current practices and outstanding issues, (ed.) P. Sylvester; Mineralogical Association of Canada, Short Course Series, v. 40, p. 305–307.

Jeans, C.V., Turchyn, A.V., and Hu, X., 2016. Sulfur isotope patterns of iron sulfide and barite nodules in the Upper Cretaceous Chalk of England and their regional significance in the origin of coloured chalks; Acta Geologica Polonica, v. 66, p. 227–256.

Jonasson, I.R., Kingston, D.M., Watkinson, D.H., and Elliot, S.R., 1999. Role of pyrite in the formation and localisation of gold mineralization at the Owl Creek mine, Timmins, Ontario; *in* The Giant Kidd Creek Volcanogenic Massive Sulfide Deposit, western Abitibi Subprovince, Canada, (ed.) M.D. Hannington and C.T. Barrie; Society of Economic Geologists, Monograph 10, p. 627–660.

Lafrance, B., Moorhead, J., and Davis, D.W., 2003. Cadre géologique du camp minier de Doyon-Bousquet-LaRonde: Ministère des Ressources Naturelles, de la Faune et des Parcs du Québec, ET 2002-07, 45 p.

Large, R.R., Maslennikov, V.V., Robert, F., Danyushevsky, L.V., and Chang, Z., 2007. Multistage sedimentary and metamorphic origin of pyrite and gold in the Giant Sukhoi log deposit, Lena Gold Province, Russia; Economic Geology, v. 102, p. 1233–1267.

Large R.R., Bull S.W., and Maslennikov V.V., 2011. A carbonaceous sedimentary source-rock model for Carlin-type and orogenic gold deposits: Economic Geology, v. 106, p. 331–358.

Large, R.R., Halpin, J.A., Danyushevsky, L.V, Maslennikov, V.V., Bull, S.W., Long, J.A., Gregory, D., Lounejeva, E., Lyons, T.W., Sack, P., McGoldrick, P., and Calver, C.R., 2014. Trace element content of sedimentary pyrite as a new proxy for deep-time ocean-atmosphere evolution; Earth and Planetary Science Letters, v. 389, p. 209–220.

McNicoll, V., Goutier, J., Dubé, B., Mercier-Langevin, P., Ross, P.S., Dion, C., Monecke, T., Legault, M., Percival, J., and Gibson, H., 2014. U-Pb geochronology of the Blake River Group, Abitibi greenstone belt, Quebec, and implications for base metal exploration; Economic Geology, v. 109, p. 27–59.

Mercier-Langevin, P., Dubé, B., Lafrance, B., Hannington, M., Galley, A., Moorhead, J., and Gosselin, P., 2007a. Metallogeny of the Doyon-Bousquet-LaRonde mining camp, Abitibi greenstone belt, Quebec; *in* Mineral Deposits of Canada: A Synthesis of Major Deposit Types, District Metallogeny, the Evolution of Geological Provinces, and Exploration Methods, (ed.) W.D. Goodfellow; Geological Association of Canada, Mineral Deposits Division, Special Publication No. 5, p. 673–701.

Mercier-Langevin, P., Dubé, B., Hannington, M.D., Davis, D.W., Lafrance, B., and Gosselin, G., 2007b. The LaRonde Penna Au-rich volcanogenic massive sulfide deposit, Abitibi greenstone belt, Quebec: Part I. Geology and geochronology; Economic Geology, v. 102, p. 585–609.

Mercier-Langevin, P., Dubé, B., Hannington, M.D., Richer-Laflèche, M., and Gosselin, G., 2007c. The LaRonde Penna Au-rich volcanogenic massive sulfide deposit, Abitibi greenstone belt, Quebec: Part II. Lithogeochemistry and paleotectonic setting; Economic Geology, v. 102, p. 611–631.

Mercier-Langevin, P., Dubé, B., Blanchet, F., Pitre, D., and Laberge, A., 2017. The LaRonde Penna Au-rich volcanogenic massive sulfide deposit; *in* Reviews in Economic Geology; Society of Economic Geologists, v. 19, p. 225–245.

Monecke, T., Gibson, H., Dubé, B., Laurin, J., Hannington, M.D., and Martin, L., 2008. Geology and volcanic setting of the Horne deposit, Rouyn-Noranda, Quebec: Initial results of a new research project; Geological Survey of Canada, Current Research 2008-9, 16 p.

Monecke, T., Gibson, H., Huthmann, F., Dubé, B., Hannington, M.D., McNicoll, V., and Mercier-Langevin, P., 2009. Giant volcanogenic massive sulphide deposits of the Blake River Group: Current knowledge and implications for exploration Part II – Horne; Congrès Abitibi 2009 – Abitibi Cuivre, Rouyn-Noranda, September 28th, 2009, Excursion Guidebook, GM 64196, p. 51–60.

Monecke, T., Mercier-Langevin, P., Dubé, B., Frieman, B., and Goutier, J., 2017. Geology of the Abitibi greenstone belt; Reviews in Economic Geology, v. 19, p. 7–49.

Murowchick, J.B. and Barnes, H.L., 1987. Effects of temperature and degree of supersaturation on pyrite morphology; American Mineralogist, v. 72, p. 1241–1250.

Palenik, C.S., Utsunomiya, S., Reich, M., Kesler, S.E., Wang, L., and Ewing, R.C., 2004. "Invisible" Au revealed: Direct imaging of Au nanoparticles in a Carlin-type deposit; American Mineralogist, v. 89, p. 1359–1366.

Pilote, J.-L., Jackson, S.E., Mercier-Langevin, P., Dubé, B., and Rhys, D., 2019. Characteristics of diagenetic and epigenetic sulphides in deformed and metamorphosed Archean carbonaceous metasedimentary rocks of the Timmins-Matheson corridor: establishing a framework for fingerprinting ore-forming processes in shear zone-hosted orogenic gold systems; *in* Targeted Geoscience Initiative: 2018 report of activities, (ed.) N. Rogers; Geological Survey of Canada, Open File 8549, p. 33–41.

Pilote, J.-L., Jackson, S.E., Mercier-Langevin, P., Dubé, B., Lawley, C.J.M., Petts, D.C., Yang, Z., van Hees, E., and Rhys, D., 2020. Fingerprinting ore processes in orogenic auriferous systems: Insights into metallogenic and exploration implica-

tions from argillite-hosted iron sulphide nodules from the Timmins-Matheson gold corridor; *in* Targeted Geoscience Initiative 5: Contributions to the Understanding of Canadian Gold Systems, (ed.) P. Mercier-Langevin, C.J.M. Lawley, and S. Castonguay; Geological Survey of Canada, Open File 8712, p. 165–178. doi:10.4095/323675

R Core Team, 2019. R: A language and environment for statistical computing; R Foundation for Statistical Computing, Vienna, Austria. <https://www.R-project.org/>

Reich, M., Kesler, S.E., Utsunomiya, S., Palenik, C.S., Chryssoulis, S.L., and Ewing, R.C., 2005. Solubility of gold in arsenian pyrite; Geochimica et Cosmochimica Acta, v. 69, p. 2781–2796.

Rickard, D.T., 2012. Sulfidic sediments and sedimentary rocks: Developments in sedimentology; Amsterdam, Elsevier, 816 p.

Sillitoe, R.H., Hannington, M.D., and Thompson, J.F.H., 1996. High sulfidation deposits in the volcanogenic massive sulfide environment; Economic Geology, v. 91, p. 204–212.

Sunagawa, I., 2005. Crystals: growth, morphology, and perfection; Cambridge, Cambridge University Press, 295 p.

Tribovillard, N., Algeo, T.J., Lyons, T., and Riboulleau, A., 2006. Trace metals as paleoredox and paleoproductivity proxies: An update; Chemical Geology, v. 232, p. 12–32.

Wilkin, R.T. and Beak, D.G., 2017. Uptake of nickel by synthetic mackinawite; Chemical Geology, v. 462, p. 15–29.

The B26 Cu-Zn-Ag-Au project, Brouillan volcanic complex, Abitibi greenstone belt, part 1: Geological setting and geochronology

Quentin Fayard[1,2*], Patrick Mercier-Langevin[3], Natasha Wodicka[4], Réal Daigneault[1], and Serge Perreault[2]

[1]Université du Québec à Chicoutimi, 555 Boulevard de l'Université, Chicoutimi, Quebec G7H 2B1
[2]SOQUEM Inc., 1740 Chemin Sullivan, Val-d'Or, Quebec J9P 7H1
[3]Geological Survey of Canada, 490 rue de la Couronne, Québec, Quebec G1K 9A9
[4]Geological Survey of Canada, 601 Booth Street, Ottawa, Ontario K1A 0E8
[*]Corresponding author's e-mail: quentin.fayard@gmail.com

ABSTRACT

Archean synvolcanic base metal deposits vary greatly in style and metal budget through time and space. This variability is due to contrasting geological and magmatic settings, the influence of which remains a research topic with potential exploration implications. The B26 Cu-Zn-Ag-Au project, located in the Harricana-Turgeon belt of the northern Abitibi greenstone belt, is interpreted as a volcanogenic massive sulphide deposit formed in an evolving calc-alkaline (FII-type) intermediate to felsic centre (Brouillan volcanic complex). The B26 deposit is enriched in Ag and is part of a group of precious metal-enriched Archean volcanogenic massive sulphide deposits that are associated with calc-alkaline volcanic rocks, indicating that such successions are highly prospective.

The B26 host succession, informally divided into a lower intermediate member and an upper felsic member, is composed of an andesitic base intercalated with dacitic domes, onto which the felsic member was emplaced. The felsic member comprises three geochemically and texturally distinct rhyolite units that were emplaced as sills, domes, and/or flows with associated relatively voluminous fragmental facies. This felsic succession, dated at 2728 Ma, is coeval both with the host rhyolite of the nearby Selbaie polymetallic deposit and the Brouillan pluton. It is overlain by thin sedimentary strata and cut by andesitic sills and andesitic transposed dykes. This volcanic pile, undergoing extension and containing thick permeable strata, was favourable for the development of a high-temperature hydrothermal system characterized by extensive zones of Cu-rich stringers and sub-seafloor Zn-Ag-(Pb)-rich sulphide lenses in an evolving, possibly shallow-water, active volcanic centre.

INTRODUCTION

The Archean Abitibi greenstone belt is known for its mineral wealth, including volcanogenic massive sulphide (VMS) deposits and other pre-main regional deformation (synvolcanic) polymetallic deposits (e.g. Monecke et al., 2017 and references therein). A unique concentration of Archean precious metal-rich VMS deposits is found in the Abitibi, and such provinciality suggests specific underlying genetic relationships (e.g. Mercier-Langevin et al., 2015).

Although VMS deposits are present throughout the Abitibi belt, the overall endowment varies greatly among the different volcanic assemblages. The 2734–2724 Ma Deloro assemblage (Ayer et al., 2002) contains numerous VMS deposits, including those of the Matagami, Joutel, and Chibougamau districts. It also includes the Selbaie deposit in the Brouillan volcanic complex (part of the Harricana-Turgeon belt), which hosts the Cu-Zn-Ag-Au mineralized zones of the B26 mining property (Fig. 1). The past-producing Selbaie mine (56.9 Mt at 1.85% Zn, 0.87% Cu, 39 g/t Ag, and 0.55 g/t Au: Adam, 2004) has been interpreted as an epithermal system characterized by base and precious metal veins that overprint a mostly barren massive pyrite lens (Deptuck et al., 1982; Larson, 1987; Faure et al., 1990, 1996; Larson and Hutchinson, 1993; Taner, 2000). It represents the only example of this type of ore system in the Abitibi greenstone belt. A shallow subaqueous to subaerial caldera environment of formation is inferred (Deptuck et al., 1982; Larson and Hutchinson, 1993) and the age of the epithermal-like mineralization is constrained by a crosscutting synvolcanic felsic dyke (2726 ± 3 Ma: Barrie and Krogh, 1996). The 2729 ± 4 Ma Brouillan synvolcanic pluton (Barrie and Krogh, 1996), which underlies the mineral-

Fayard, Q., Mercier-Langevin, P., Wodicka, N., Daigneault, R., and Perreault, S., 2020. The B26 Cu-Zn-Ag-Au project, Brouillan volcanic complex, Abitibi greenstone belt, part 1: Geological setting and geochronology; *in* Targeted Geoscience Initiative 5: Contributions to the Understanding of Canadian Gold Systems, (ed.) P. Mercier-Langevin, C.J.M. Lawley, and S. Castonguay; Geological Survey of Canada, Open File 8712, p. 93–107. https://doi.org/10.4095/323668

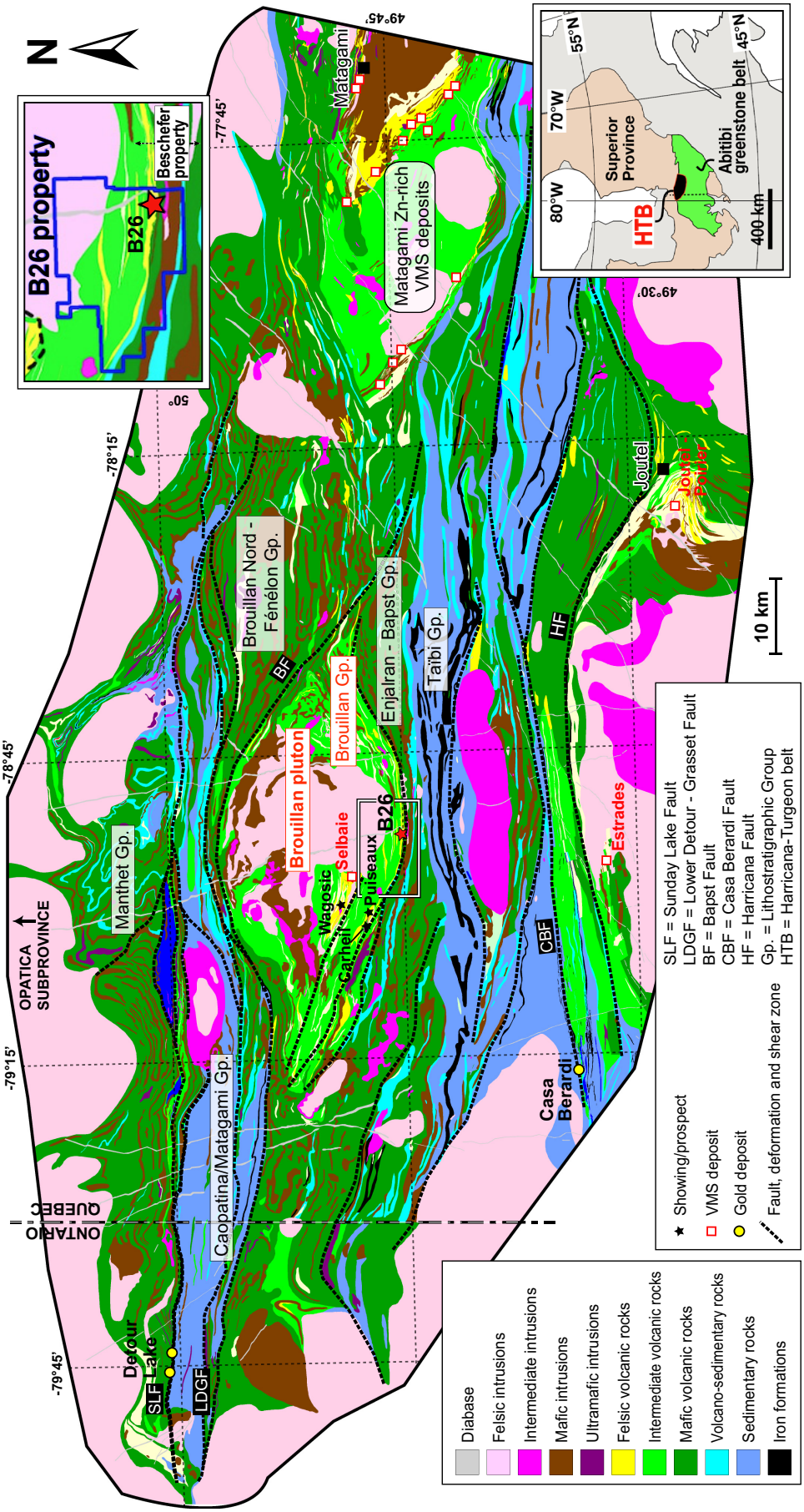

Figure 1. Regional geological map of the Harricana-Turgeon belt showing the location of the B26 project and other mineral occurrences. *Modified from* Faure (2015).

ized host succession at Selbaie, is considered as a potential driver for the hydrothermal activity associated with the base and precious metal-rich zones in the surrounding Brouillan volcanic complex (Larson and Hutchinson, 1993). One key characteristic of the Selbaie deposit is the presence of very high-grade Ag zones (i.e. up to 1–2 kg/t Ag: Taner, 2000). Such high-grade Ag intersections are also common at B26, as well as in other prospects of the area. This suggests the presence of regional controls on the precious metal-budget of some base metal deposits.

The age of the host succession at the B26 project and its potential relationship with the Selbaie deposit host rocks remain to be established. Copper-Au occurrences were discovered on the B26 property by Billiton Metals in 1997. The property was optioned in 1998 and then acquired by SOQUEM in 2009. Several drilling campaigns have been completed on the property in the last 20 years, providing a good understanding of the geological context and documentation of the B26 deposit host units (Adam, 1997; Beaudin, 2017). The "atypical" metallogenic characteristics of the Brouillan volcanic complex and the presence of locally very high Ag and Au grades (100–2000 ppm Ag, 0.5–50 ppm Au) at B26 and elsewhere in the area constitute a good opportunity to improve our understanding of precious metal enrichment processes in Archean base metal deposits.

This study is part of an M.Sc. thesis (Fayard, in prep) that aims at identifying the controls on the precious metal enrichment at B26, and this paper summarizes the geology, physical volcanology, geochemistry, and geochronology of the host volcanic succession of the B26 project. The description of the alteration and mineralized zones are presented in a companion paper (Fayard et al., 2020).

REGIONAL GEOLOGY

The Harricana-Turgeon belt in northwestern Quebec and northeastern Ontario is part of the northern Abitibi greenstone belt and extends for approximately 200 km from the Detour mine area to the Matagami district (Fig. 1). It is a volcano-sedimentary and plutonic belt mainly affected by regional greenschist-facies metamorphism, reaching the amphibolite-facies near the contact with the Opatica subprovince to the north (Lacroix, 1994). According to Lacroix et al. (1989) and Daigneault et al. (2004), the Harricana-Turgeon belt is affected by major phases of deformation, including a significant north-south shortening event (post-2710 Ma) that was responsible for the regional northwest-southeast- to east-west-trending subvertical foliation (generally referred to as S_2 at regional scale, but referred to as S_p in this study). The S_p foliation is associated with east-west-trending regional-scale folds, such as the Enjalran syncline and the Brouillan anticline. Major longitudinal faults and deformation corridors initiated during the north-south shortening were later accentuated or reactivated as dextral shears. A number of gold deposits (e.g. Detour Lake and Casa Berardi) and volcanogenic massive sulphide deposits (e.g. Matagami and Joutel districts) are present in the area (Fig. 1).

The Brouillan volcanic complex, located in the central portion of the Harricana-Turgeon belt, comprises the Brouillan Group and the Brouillan pluton. It is surrounded by the basaltic units of the Brouillan Nord-Fénélon Group to the north and Enjalran-Bapst Group to the south (Fig. 1). The Brouillan pluton is a polyphase intrusive complex composed of felsic (tonalite and granite) and intermediate (diorite) transitional to calc-alkaline phases and a mafic (gabbro) tholeiitic phase (Faure, 2012). The Brouillan Group is dominated by intermediate to felsic lapilli tuff, tuff breccia, and crystal-rich coarse tuff, intercalated with calc-alkaline to transitional andesitic flows and sills, and rhyolitic domes (Lacroix, 1994; Faure, 2012). All units dip moderately to steeply to the south (40–85º) and generally face south (Faure et al., 1996; Faure, 2012; Beaudin, 2017).

According to Lacroix (1994), Taner (2000), Beaudin (2017), and Fayard et al. (2018), strain intensity is moderate over the entire complex, except for narrow east-west-trending high-strain zones, especially in the vicinity of the Brouillan and Enjalran-Bapst contact.

The Brouillan tonalite and the Selbaie mine rhyolite have been dated at 2729 ± 4 Ma and 2729 +3/-2 Ma, respectively (Barrie and Krogh, 1996), and are considered coeval and co-magmatic. These ages were the only time constraints for the Brouillan volcanic complex prior to this study, and no age data are available for the Enjalran-Bapst Group.

MINERALIZED ZONES AT THE B26 PROJECT

The B26 mineralized system consists of stacked sulphide zones with a (transposed) discordant stringer-type Cu-rich zone at the base (Copper zone) overlain by Zn-(Pb)- and Ag-rich, concordant to stratabound, semi-massive to massive sulphide lens associated with peripheral disseminated and vein sulphides (Main and Upper Zinc zones; Fig. 2: Fayard et al., 2018). The Copper zone (indicated and inferred resources of 8.61 Mt at 1.94% Cu, 0.07% Zn, 0.97 g/t Au, and 6.84 g/t Ag: SOQUEM Inc., 2018; Camus and Valdnais-LeBlanc, 2018) consists of transposed millimetre- to decimetre-thick chalcopyrite stringers and veins that can locally contain up to 50 g/t Au. The chalcopyrite veins are associated with a large sub-concordant sericite-chlorite alteration halo and a proximal chlorite-

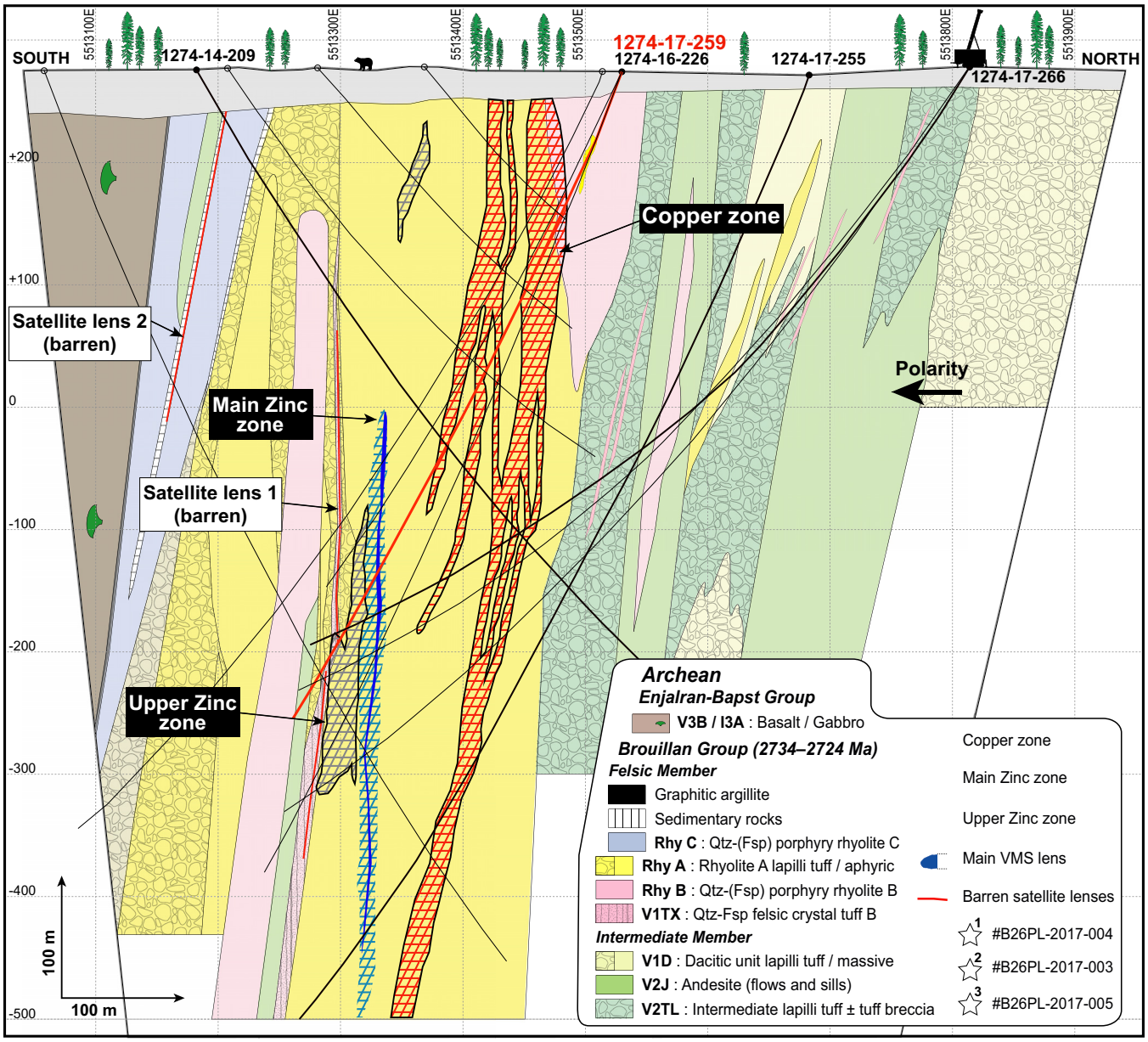

Figure 2. Simplified composite section (652950E ± 50 m) of the B26 deposit in which lithologies and mineralized zones are represented. The location (projected) of the dated U-Pb zircon geochronology samples is also shown. Abbreviations: Fsp = feldspar, Qtz = quartz.

dominated halo along the vein selvages developed in rhyolite A (*see below*). The Main and Upper Zinc zones are located in the upper part of rhyolite A (Fig. 2) and have total indicated and inferred resources of 2.77 Mt at 0.21% Cu, 4.66% Zn, 0.21 g/t Au, and 102.2 g/t Ag (SOQUEM Inc., 2018; Camus and Valdnais-LeBlanc, 2018). The Main Zinc zone consists mainly of a Zn-(Pb)-Ag semi-massive to massive sulphide lens and veins, whereas the Upper Zinc zone comprises Zn (sphalerite) disseminations, Zn-(Pb) veins, and Ag-rich (up to 2 kg/t) veins and veinlets. Mineralized zones have been metamorphosed, deformed, and transposed into the east-west-trending foliation and stretched parallel to a lineation that plunges 65°W.

VOLCANIC STRATIGRAPHY

The northwestern part of the Abitibi greenstone belt is known for its lack of outcrops, including the B26 area, which has up to a few 10s of metres of overburden. Consequently, the only available rock samples and direct observations come from drill core. In addition, most rock units are altered, deformed, and metamorphosed, which commonly hamper the recognition of protoliths and primary facies. Therefore, whole-rock lithogeochemistry was used extensively, together with the geological and petrographic drill core descriptions, to differentiate and map units at the deposit scale. From 2111 core rock samples collected from 85 drillholes, a subset of 49 least altered samples was selected to best

Table 1. Summary of the main features of the B26 deposit host volcanic rocks.

Lithology	Lithofacies	Composition and magmatic affinity	Inferred volcanic setting	Additional informations
Intermediate tuff (V2TL)	Lapilli tuff ±tuff breccia; 2–30% aphyric fragments; kilometric extent	Andesite, calc-alkaline	Autoclastic ? Pyroclastic ?	
Andesite (V2J)	Massive aphyric to locally amygdaloidal; variable thickness; kilometric extent	Andesite, calc-alkaline	Effusive (subaqueous flows), and intrusive (sills, dykes)	
Dacite (V1D)	Massive and aphyric (rare Qtz), to lapilli tuff facies; 30–120 m thick; limited extent	Dacite, calc-alkaline	Effusive, subaqueous flows and probably domes with peripheral autoclastic breccia	
Rhyolite A (Rhy A)	Massive aphyric, <3 vol.% 0.5–1.5 mm Qtz, locally relict spherulitic and flow banding textures, and lapilli tuff portions; 300 m thick; kilometric extent	Rhyolite calc-alkaline	Effusive, subaqueous flows, domes and lobes, autoclastic/talus breccia, and dykes in intermediate basement	FW: **2728.5 ± 0.8 Ma**; HW: **2727.9 ± 0.8 Ma**; Hosts Zn-Ag-(Pb) VMS lens and Cu-Au stringers; fragmental proportion probably under-estimated due to alteration/ deformation
Rhyolite B (Rhy B)	Dominant massive porphyritic facies with 10–15 vol.% of 0.5–5 mm bluish Qtz and 5–10 vol.% 0.5–5 mm Fsp (only preserved in hanging wall) in a microcrystalline matrix; minor peripheral volcaniclastic facies (Qtz-Fsp crystal-rich coarse tuff, and lapilli tuff to tuff breccia); maximum thickness 200 m in footwall and 70 m in hanging wall; kilometric extent	Rhyolite, calc-alkaline	Intrusive shallow subvolcanic sills	FW: **2728.2 ± 0.7 Ma**; The upper part of the footwall unit hosts the lower part of the Cu-Au stringers and the Qtz-Fsp crystal-rich tuff hosts the satellite barren semi-massive pyrite lens
Rhyolite C (Rhy C)	Massive porphyritic facies with 10–20 vol.% 0.5–4 mm Qtz with variable (2–10 vol.%) Fsp (usually altered); minor peripheral lapilli tuff facies; 10–50 m thick; kilometric extent	Rhyodacite/rhyolite, calc-alkaline	Intrusive as shallow subvolcanic sills and dykes (in part in the footwall), and partly effusive as flows/domes at the top of the B26 felsic member	Hosts a satellite barren massive pyrite-pyrrhotite (<1 m) lens; alternates with thin sedimentary rocks (thinly bedded argillite, siltstone, chert) and andesitic sills

Abbreviations: Fsp = feldspar, FW = footwall, HW = hanging wall, Qtz = quartz, VMS = volcanogenic massive sulphides.

characterize the initial composition of the different units present at B26. Readers are referred to Fayard (in prep) for more information about the criteria used in selecting the least altered samples.

Exploration work by Billiton Metals and SOQUEM documented six principal lithologies of the Brouillan Group at B26 (Adam, 1997; Beaudin, 2017); these lithologies have been further documented in this study: an intermediate lapilli tuff with lesser tuff breccia (V2TL), a massive andesite (V2J), a dacitic unit (V1D), an aphyric rhyolite (rhyolite A; Rhy A), a quartz- and feldspar-porphyritic rhyolite (rhyolite B; Rhy B), and a quartz±feldspar porphyritic rhyolite (rhyolite C; Rhy C; Fig. 2). The principal characteristics of these units are summarized in Table 1. Sedimentary rocks were also mapped but were not studied in detail.

The base of the host stratigraphy has only been locally intersected by drilling. It consists of a ≥500 m thick succession of andesitic to dacitic massive and volcaniclastic rocks that comprise the aforementioned intermediate lapilli tuff ± tuff breccia (V2TL), massive andesite (V2J), and dacitic unit (V1D), which are here collectively and informally referred to as the intermediate member. The mineralized zones are hosted higher in the stratigraphy in what is here informally referred to as the felsic member, which comprises rhyolite units A, B, and C. The felsic member has an approximate thickness of 400 m near the deposit (Fig. 2); the rhyolite units are intercalated with andesitic sills and dykes and minor sedimentary rocks, especially in the uppermost part. The lower intermediate member is not as well exposed as the upper felsic member because of the drilling pattern. Only a brief description of the units of the intermediate member is given here, but the rhyolite units of the felsic member are described in detail below as they host the mineralized zones and have been strongly affected by the associated hydrothermal alteration.

Intermediate Member Units

Intermediate lapilli tuff ± tuff breccia (V2TL)

This unit mostly consists of lapilli tuff with local occurrences of tuff breccia. It appears at several stratigraphic positions between the Brouillan pluton north of B26 (Fig. 1) to the base of the felsic member (Fig. 2). This

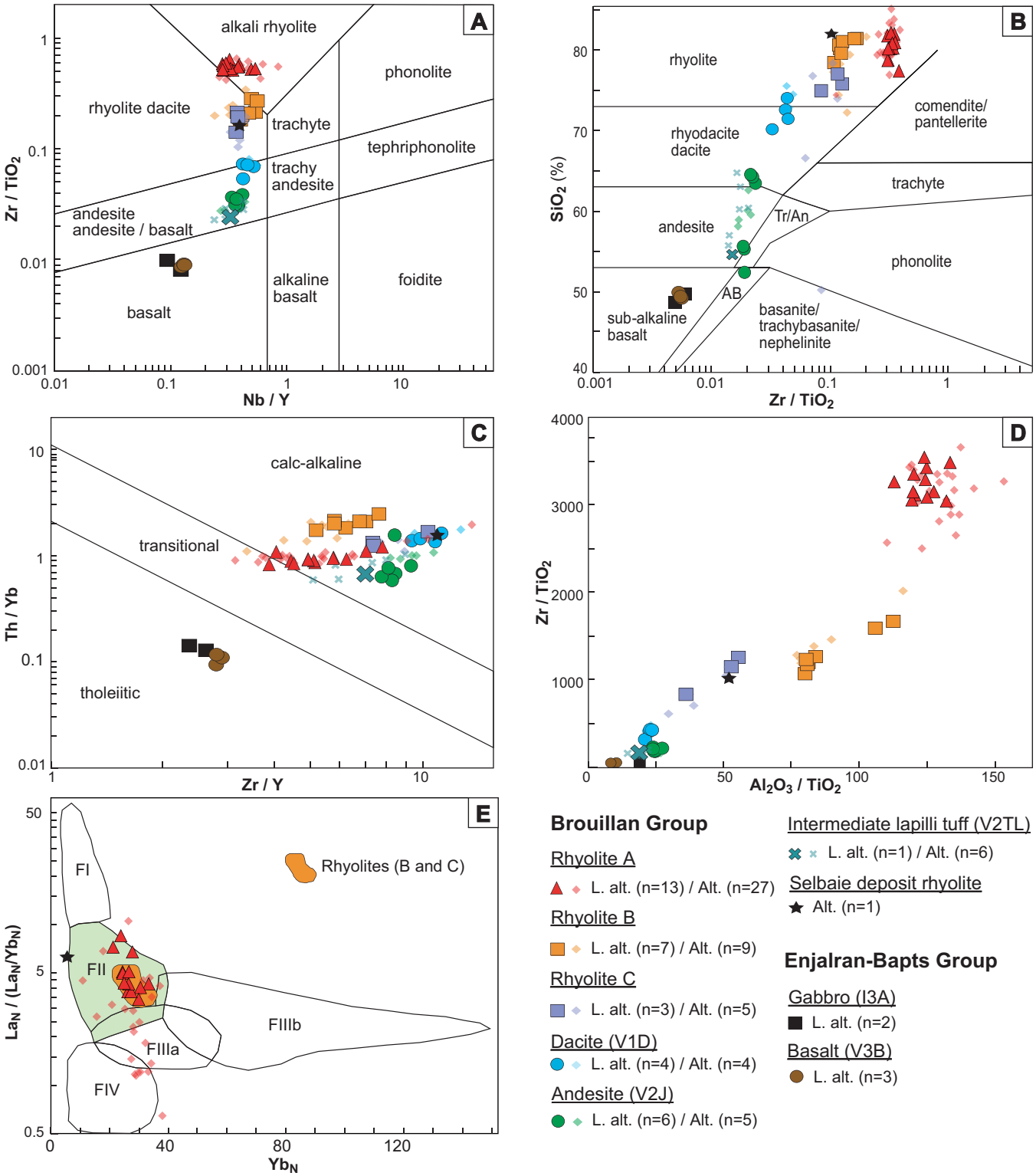

Figure 3. Diagrams illustrating the geochemical signature of the B26 volcanic rocks. **a)** (Zr ppm/10,000)/Ti (%) versus Nb/Y classification diagram of Pearce (1996). **b)** SiO_2 (%) versus (Zr ppm/10,000)/TiO_2 (%) classification diagram of Winchester and Floyd (1977). **c)** Magmatic affinity diagram of Ross and Bédard (2009). **d)** Zr/TiO_2 versus Al_2O_3/TiO_2 discrimination diagram. **e)** Rhyolite fertility diagram of Hart et al. (2004) applied to the felsic rocks only. Abbreviation: L. alt.= least altered.

unit has a basaltic-andesite to andesitic composition (Fig. 3a,b) and a calc-alkaline magmatic affinity (Fig. 3c). It is considered a fragmental facies of the andesite (V2J) unit (*see below*).

Andesite (V2J)

The andesite unit, which occurs as massive flows and sills, is a significant part of the intermediate member in the lowermost part of the stratigraphy at B26. It is also

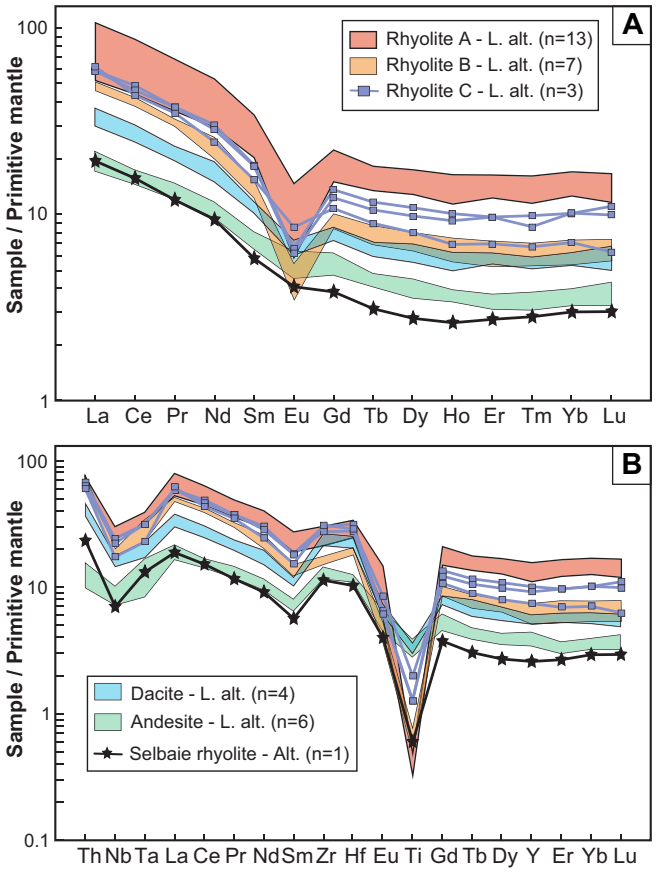

Figure 4. a) Rare earth element patterns and **(b)** multi-element patterns for the B26 host rocks. A rhyolite from Selbaie is shown for comparison. All elements are normalized to primitive mantle values of McDonough and Sun (1995).

present in the felsic member as narrow sills and thin flows in the uppermost part of the Brouillan Group stratigraphy (Fig. 2). The andesite is aphyric and has no distinctive characteristics except for some amygdales in some of the sills and uppermost flow. The composition of the andesite is andesitic with a calc-alkaline magmatic affinity (Fig. 3a,b,c). The Zr/TiO_2 and Al_2O_3/TiO_2 ratios are low at 200.9 and 24.9, respectively (Fig. 3d). The primitive mantle normalized rare earth element (REE) profile shows a moderate negative slope for the light REE ($[La/Sm]_n$ = 2.65) and an almost flat heavy REE pattern (Fig. 4a). The multi-element plot shows moderate negative Nb-(Ta) and positive Zr-Hf anomalies (Fig. 4b), typical of arc-style calc-alkaline rocks.

Dacite (V1D)

The dacite, which varies in thickness from 30 to 120 m, forms several domes with a massive core and peripheral volcaniclastic rocks (lapilli tuff and tuff breccia). The massive part is largely aphyric with a vitreous aspect but can very locally contain quartz phenocrysts (Fig. 5a). The least altered samples (n = 4) are andesitic to dacitic (Fig. 3a,b) and calc-alkaline (Fig. 3c), with relatively low Zr/TiO_2 and Al_2O_3/TiO_2 ratios at 400.8 and 22.6, respectively (Fig. 3d). The REE profile has a moderate slope for the light REEs (Fig. 4a). This unit is also characterized by moderate negative Nb-Ta and positive Zr-Hf anomalies (Fig. 4b).

Felsic Member Units

Rhyolite A (Rhy A)

Rhyolite A has a maximum thickness of 300 m in the deposit area. It hosts the Zn-mineralized zones and most of the Copper zone (Fig. 2). Although alteration and deformation hamper the recognition of primary textures in some parts of the succession, the lowermost two-thirds of the unit is dominated by massive and aphyric rocks (~70 vol.%), with local evidence of flow banding and spherulites (Fig. 5b,c). The upper third of the unit is mainly dominated by lapilli tuff (Fig. 2, 5d,e). The microcrystalline matrix of the aphyric rhyolite can locally contain 1–3 vol.% quartz phenocrysts (0.5–1.5 mm). The unit is strongly altered and deformed in the footwall of the Main and Upper Zinc zones (Fig. 5f,g). In the hanging wall, it has a slightly different, vitreous appearance (Fig. 5h). Dykes of rhyolite A are common in the intermediate member (Fig. 2).

Least altered samples (n = 13) indicate a rhyolitic composition (Fig. 3a,b). Rhyolite A is characterized by distinctly high Zr/TiO_2 and Al_2O_3/TiO_2 ratios (~3300 and ~125, respectively; Fig. 3d) due to its very low TiO_2 content (~0.08 wt%). The magmatic affinity is calc-alkaline to slightly transitional (Fig. 3c). Rhyolite A has an FII-type signature, which is typical of slightly transitional to calc-alkaline Archean rhyolite (cf. Lesher et al., 1986; Fig. 3e). The primitive mantle normalized REE profile (Fig. 4a) is characterized by a moderately negative light REE slope ($[La/Sm]_n$ = 2.74) and a flat heavy REE pattern ($[Gd/Lu]_n$ = 1.34). The entire REE pattern has a moderately negative slope ($[La/Yb]_n$ = 5.13) with a negative Eu anomaly ($[Eu/Eu^*]_n$ = 0.49). Rhyolite A is also characterized by a moderately negative Nb-Ta anomaly, a strongly negative Ti anomaly, and a very weakly positive Zr-Hf anomaly on the multi-element plot shown in Figure 4b.

Rhyolite B (Rhy B)

Rhyolite B occurs in both the footwall and hanging wall of the Main and Upper Zinc zones (Fig. 2). It forms two main masses, one at the base of rhyolite A (≤200 m thick), and the other in the uppermost part of rhyolite A (≤70 m thick; Fig. 2). Dykes and thin sills of rhyolite B also intrude the intermediate member. Rhyolite B is quartz- and feldspar-porphyritic with 10–15 vol.%, 0.5–5 mm, round to angular and commonly recrystallized (in subgrains) quartz phenocrysts in a microcrystalline quartz-feldspar matrix (Fig. 6a).

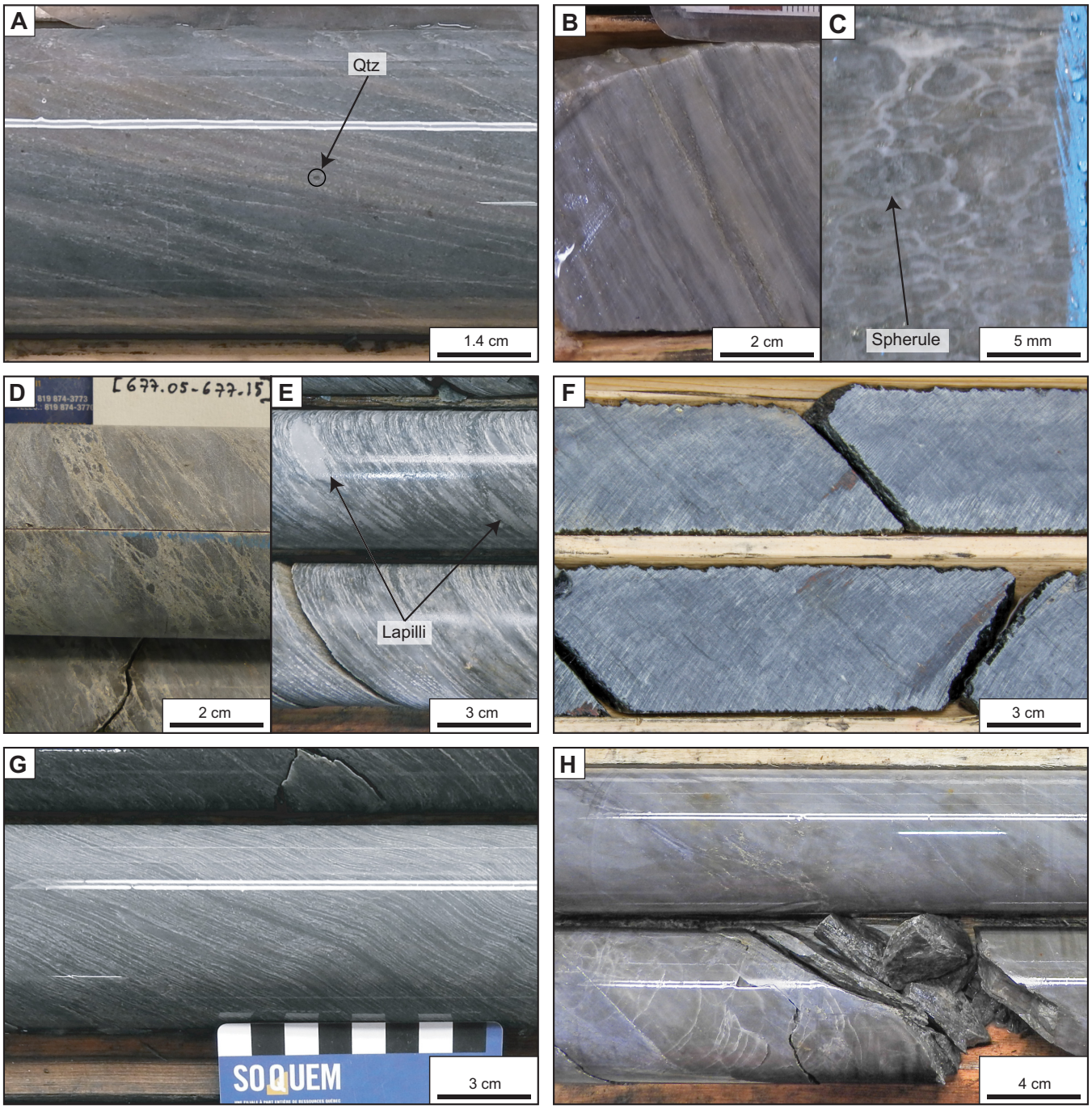

Figure 5. a) Massive dacite. **b)** Flow-banded massive aphyric rhyolite A. **c)** Spherulitic massive aphyric rhyolite A. **d-e)** Volcaniclastic facies of rhyolite A. **f)** Footwall sericite and chlorite-altered (massive) rhyolite A. **g)** Strongly foliated footwall sericite-quartz-(pyrite) altered rhyolite A. **h)** Hanging-wall aphyric and coherent rhyolite A with typical vitreous aspect. Abbreviation: Qtz = quartz.

Feldspar phenocrysts are locally preserved in the less altered hanging-wall rocks (Fig. 6b). The unit is massive for the most part (≥90 vol.%) with a minor proportion of volcaniclastic rocks including coarse tuff, lapilli tuff, and rare tuff breccia. The coarse, 2 to 4 m thick tuff bed is present in the lowermost part of the rhyolite B in the hanging wall of the Zinc zones. It contains up to 40 vol.% quartz and feldspar crystal fragments and locally some aphyric lapilli clasts (Fig. 6c,d). This tuff locally hosts a barren semi-massive pyrite lens (satellite lens 1; Fig. 2). The lapilli tuff and rare tuff breccia (Fig. 6e) are present along the margins of rhyolite B masses and can be up to a few metres thick.

Least altered samples (n = 7) indicate that rhyolite B is rhyodacitic to rhyolitic (Fig. 3a,b) and calc-alkaline (Fig. 3c) with an FII-type signature (Fig. 3e). There are some variations in the Zr/TiO_2 and Al_2O_3/TiO_2 ratios (Fig. 3d). Moderate negative slope of light REEs

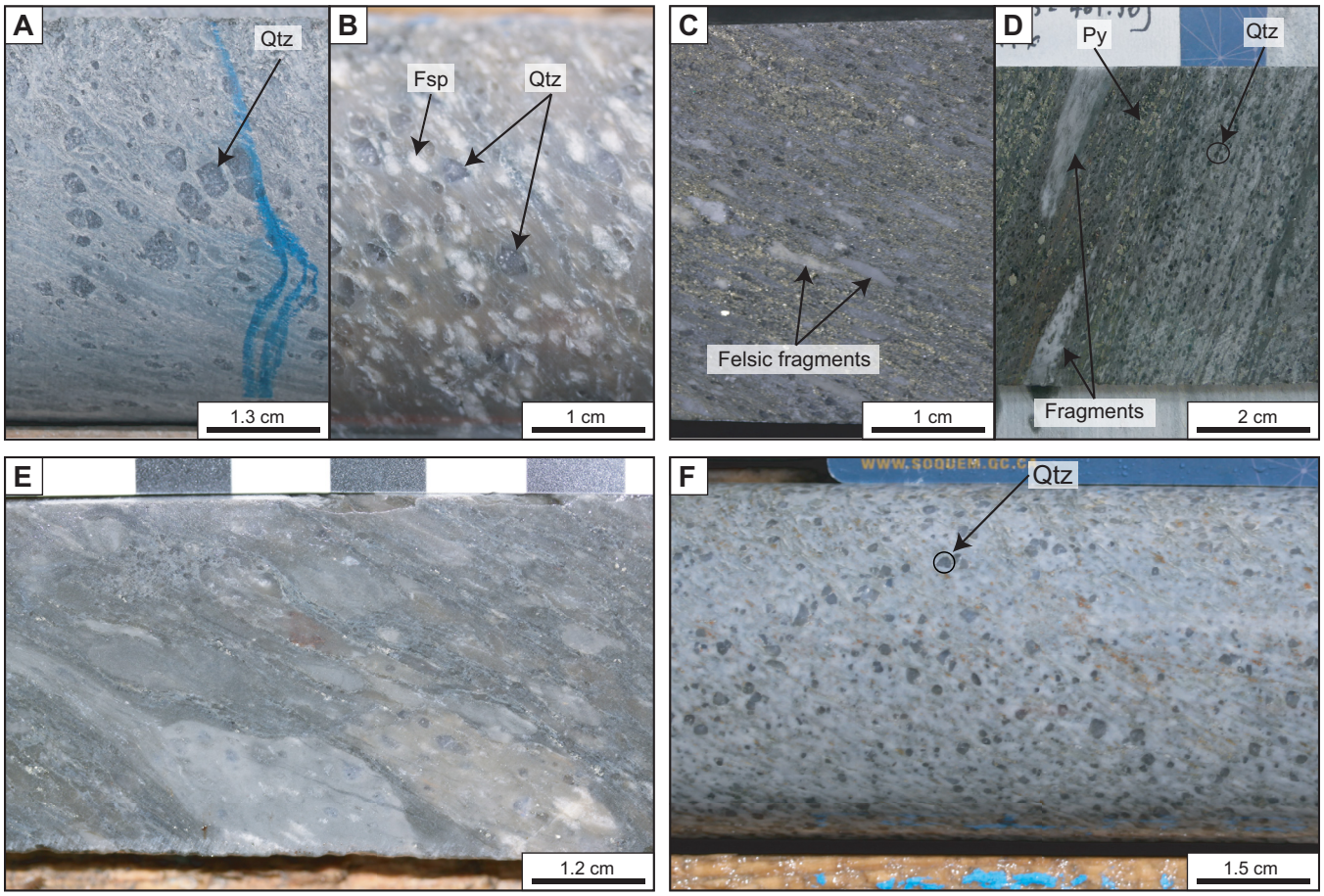

Figure 6. a) Footwall sericite and chlorite-altered quartz porphyritic rhyolite B. **b)** Hanging-wall quartz- and feldspar-phyric rhyolite B. **c)** Quartz and feldspar crystal-bearing coarse tuff facies of the hanging-wall rhyolite B. **d)** Lapilli tuff facies of the hanging-wall rhyolite B. **e)** Fragmental facies (lapilli tuff) of rhyolite B. **f)** Quartz-(feldspar) porphyritic rhyolite C. Abbreviations: Fsp = feldspar, Py = pyrite, Qtz = quartz.

($[La/Sm]_n = 3.37$), an almost flat heavy REE ($[Gd/Lu]_n = 1.42$) pattern, and a strong negative Eu anomaly ($[Eu/Eu^*]_n = 0.36$) characterize this unit (Fig. 4a). Rhyolite B is also characterized by negative anomalies in Nb-Ta and Ti (Fig. 4b).

Rhyolite C (Rhy C)

Rhyolite C is a 10 to 50 m thick, mostly massive unit that occurs in the uppermost part of the B26 host sequence (Fig. 2). It is spatially associated with andesitic sills. The unit stratigraphically overlies rhyolite A and the contact is locally brecciated. It is very locally associated with ankerite-altered sandstone and argillite hosting a 0.5 to 1 m thick barren pyrite-pyrrhotite semi-massive lens (satellite lens 2; Fig. 2).

Rhyolite C comprises 10–20 vol.% subangular to subrounded quartz phenocrysts (0.5–4 mm; Fig. 6f). The phenocrysts are commonly recrystallized in subgrains and have a bluish colour. Feldspar is rarely preserved and has undergone selective sericite alteration and stretching.

Least altered samples (n = 3) indicate a rhyodacitic to rhyolitic composition (Fig. 3a,b). Rhyolite C is geochemically distinguished from the other B26 rhyolites by its lower SiO_2 content and its relatively higher Zr, TiO_2, Al_2O_3, and Hf contents (Fayard, in prep). It is calc-alkaline (Fig. 3c) and shows a similar, but slightly more enriched heavy REE pattern compared to rhyolite B (Fig. 4a). Rhyolite C is differentiated from rhyolite units A and B by its positive Zr-Hf anomaly and a less developed negative anomaly in Ti (Fig. 4b).

Sedimentary Rocks

Sedimentary rocks gradually evolve, up-stratigraphy, from thinly bedded ±cherty siltstone to argillite. They overlie rhyolite A and are interlayered with rhyolite C and andesitic rocks at the top of the felsic member, close to the contact with the Enjalran-Bapst Group (Fig. 2).

Enjalran-Bapst Group Mafic Rocks

The Enjalran-Bapst Group is separated from the Brouillan Group (felsic member) by a thin graphitic argillite layer. The Enjalran-Bapst Group is composed of aphyric basalt and fine- to coarse-grained gabbro. These rocks have a basaltic composition (Fig. 3a,b) and

a tholeiitic affinity (Fig. 3c) that strongly contrasts with the calc-alkaline affinity of the Brouillan Group rocks. In the B26 project area, the regional deformation does not affect the Enjalran-Bapst rocks as much as the underlying Brouillan Group rocks. Fayard (in prep) provides more information about the relationship between the Enjalran-Bapst and Brouillan groups.

U-Pb ZIRCON GEOCHRONOLOGY

To better constrain the timing of formation of the B26 mineralized zones and to establish correlations with other ore deposits of the region, a series of three drill core samples from the felsic member was selected for U-Pb zircon geochronology. Two of the samples analyzed were from the Main Zinc zone footwall succession (samples B26PL-2017-003 and B26PL-2017-004 from rhyolite units A and B, respectively) and one from the hanging wall (B26PL-2017-005 from rhyolite A). Analysis was completed at the Geochronology Laboratory of the Geological Survey of Canada in Ottawa. Heavy minerals were concentrated from the samples using standard crushing, grinding, and separation on a Wilfley table and by heavy liquid techniques. Mineral separates were sorted by magnetic susceptibility using a FrantzTM isodynamic separator and hand-picked using a binocular microscope. Single zircon grains were chemically abraded following the techniques of Mattinson (2005), including annealing for 48 hours at 1000°C prior to leaching with hydrofluoric acid (HF) at 180°C for 12 hours. Details of zircon morphology, quality, and HF leaching times are summarized in Table 2. U-Pb isotope dilution-thermal ionization mass spectrometry (ID-TIMS) techniques utilized in this study—including the addition of a ^{205}Pb-^{233}U-^{235}U spike—dissolution, column chemistry, and analysis on a Triton thermal ionization mass spectrometer, are modified after Parrish et al. (1987). The treatment of analytical errors follows Roddick (1987), with regression analysis modified after York (1969). Procedural blank levels were generally less than 1.0 pg for Pb. U-Pb ID-TIMS analytical results are presented in Table 2 and displayed in concordia plots in Figure 7). All age uncertainties and error ellipses are presented at the 2σ level. The zircon grains that were analyzed were mostly euhedral to subhedral, equant to prismatic, and ranged in length from 50 to 150 µm. The three rhyolite samples, B26PL-003, -004, and -005, yielded concordant to slightly discordant analyses with similar weighted average ^{207}Pb/^{206}Pb ages of 2728.5 ± 0.8 Ma, 2728.2 ± 0.7 Ma, and 2727.9 ± 0.8 Ma, respectively, which are interpreted as the crystallization ages of the rhyolite units (Fig. 7).

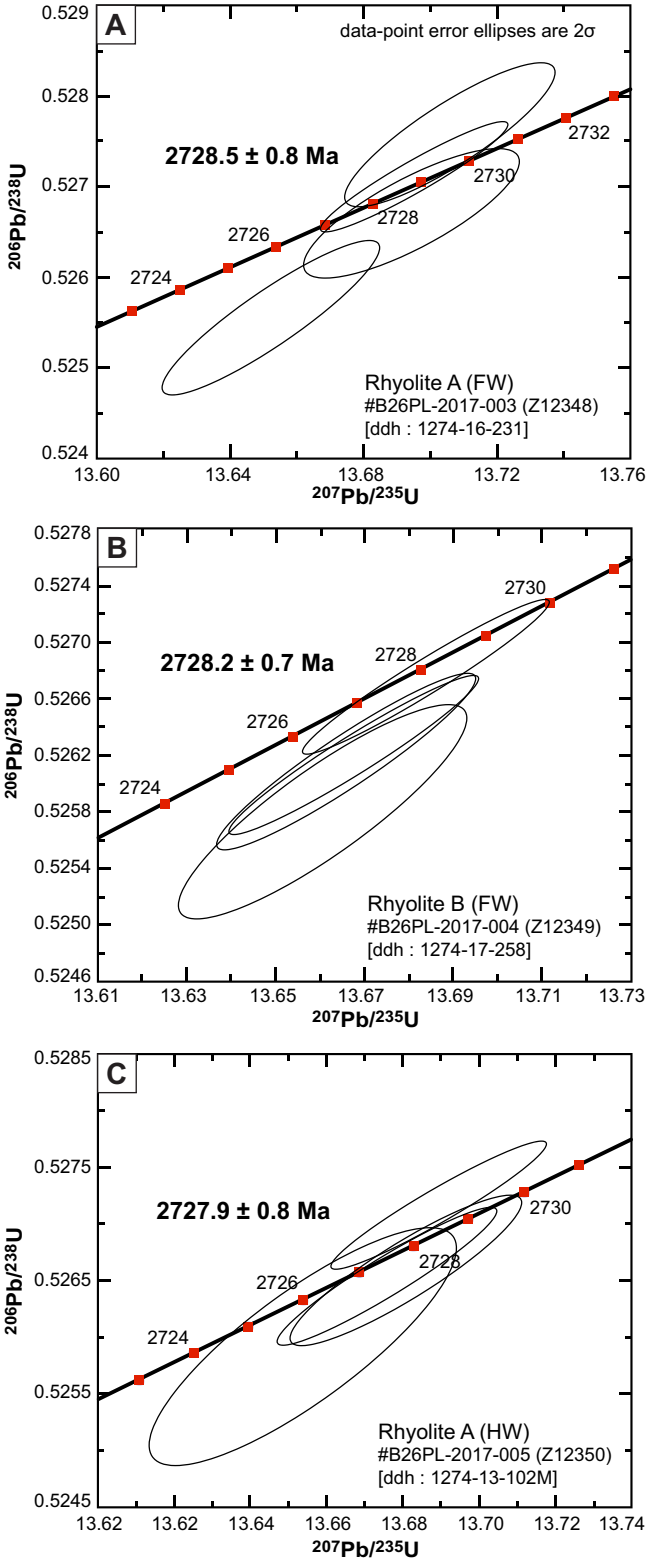

Figure 7. Concordia plots of U-Pb isotope dilution-thermal ionization mass spectrometry (ID-TIMS) analyses for the three dated samples. **a)** Footwall rhyolite A. **b)** Footwall rhyolite B. **c)** Hanging-wall rhyolite A. Error ellipses at 2σ. Abbreviations: ddh = diamond drillhole; FW = footwall; HW = hanging wall.

Table 2. U-Pb isotope dilution-thermal ionization mass spectrometry (ID-TIMS) analytical data from the host rhyolite units A and B of the B26 mineralized zones.

		Composition					Isotopic Ratios										Dates (Ma)							
Fraction[§]	Description[*]	Wt[a] (µg)	U (ppm)	$\frac{Th^b}{U}$	$\frac{Pb^{*c}}{Pb^d}$ (pg)	Pb[cd] (pg)	$\frac{Pb^{*e}}{Pb^c}$	$\frac{^{206}Pb^f}{^{204}Pb}$	$\frac{^{208}Pb^g}{^{206}Pb}$	$\frac{^{207}Pb^g}{^{235}U}$	±2σ (%)	$\frac{^{206}Pb^g}{^{238}U}$	±2σ (%)	Corr.[h] coeff.	$\frac{^{207}Pb^g}{^{206}Pb}$	±2σ (%)	$\frac{^{207}Pb^i}{^{235}U}$	±2σ (abs)	$\frac{^{206}Pb^i}{^{238}U}$	±2σ (abs)	$\frac{^{207}Pb^i}{^{206}Pb}$	±2σ (abs)	%[j] Disc.
B26PL-2017-003 (Rhyolite A): Z12348																								
A12-1 (1)	Co,Clr,Su,Pr,CA12	2.9	40	0.60	71	0.85	83.8	4494	0.16	13.650	0.201	0.52552	0.13574	0.905	0.18838	0.09186	2725.7	1.9	2722.6	3.0	2728.1	1.6	0.2
A12-2 (1)	Co,Clr,Su,Eq,rIn,CA12	3.3	37	0.57	74	1.82	40.8	2210	0.16	13.694	0.199	0.52670	0.11362	0.800	0.18856	0.12330	2728.7	1.9	2727.5	2.5	2729.6	2.1	0.1
A12-3 (1)	Co,Clr,Eu,Pr,rFr,CA12	2.6	52	0.63	84	0.42	198.5	10546	0.17	13.694	0.173	0.52711	0.09642	0.945	0.18842	0.08179	2728.8	1.6	2729.3	2.1	2728.4	1.4	0.0
A12-4 (1)	Co,Clr,Su,St,rFr,CA12	2.6	17	0.40	26	0.44	59.8	3347	0.11	13.705	0.194	0.52759	0.12565	0.866	0.18841	0.10081	2729.6	1.8	2731.3	2.8	2728.3	1.7	-0.1
B26PL-2017-004 (Rhyolite B): Z12349																								
A12-1 (1)	Co,Clr,Su,Pr,Frag,rIn,CA12	4.7	20	0.58	58	0.99	58.7	3170	0.16	13.660	0.194	0.52580	0.11949	0.873	0.18843	0.10220	2726.4	1.8	2723.7	2.7	2728.5	1.8	0.2
A12-2 (1)	Co,Clr,Eu,Pr,fFr,rIn,CA12	17	31	0.54	315	0.50	628.0	33957	0.15	13.684	0.166	0.52677	0.08587	0.966	0.18840	0.07992	2728.1	1.6	2727.8	1.9	2728.3	1.4	0.0
A12-3 (1)	Co,Clr,Su,Pr,fFr,rIn,CA12	4.2	35	0.38	87	0.46	189.9	10627	0.11	13.666	0.174	0.52616	0.09851	0.939	0.18837	0.08256	2726.8	1.7	2725.2	2.2	2728.0	1.5	0.1
A12-4 (1)	Co,Clr,Su,Pr,fFr,rIn,CA12	7.6	38	0.59	178	0.54	329.9	17685	0.16	13.667	0.168	0.52620	0.08883	0.960	0.18838	0.08042	2726.9	1.6	2725.4	2.0	2728.1	1.4	0.1
B26PL-2017-004 (Rhyolite A): Z12350																								
A12-1 (1)	Co,Clr,Su,Pr,rFr,CA12	1.2	40	0.63	29	0.54	54.2	2894	0.17	13.653	0.242	0.52591	0.16554	0.829	0.18829	0.13575	2726.0	2.3	2724.2	3.7	2727.3	2.3	0.1
A12-2 (1)	Co,Clr,Su,Pr,fFr,CA12	4.3	51	0.61	136	0.53	255.4	13628	0.17	13.676	0.172	0.52654	0.09566	0.945	0.18837	0.08132	2727.5	1.6	2726.9	2.1	2728.0	1.4	0.0
A12-3 (1)	Co,Clr,Su,Pr,Frag,fFr,rIn,CA12	1.8	43	0.55	47	0.59	80.0	4329	0.15	13.680	0.182	0.52659	0.10470	0.902	0.18842	0.09273	2727.8	1.7	2727.1	2.3	2728.4	1.6	0.0
A12-4 (1)	Co,Clr,Su,Pr,fFr,CA12	5.9	46	0.61	168	0.78	215.2	11478	0.17	13.689	0.169	0.52717	0.08907	0.954	0.18833	0.08191	2728.4	1.6	2729.5	2.0	2727.6	1.5	-0.1

Notes:

§ Number in bracket refers to the number of zircon grains in the analysis.

* Fraction descriptions: CA12 = chemically abraded for 12 hours, Clr = clear, Co = colourless, El = elongate, Eq = equant, Eu = euhedral, fFr = few fractures, Frag = fragment, In = inclusions, Pr = prismatic, rFr = rare fractures, rIn = rare inclusions, St = stubby prism, Su = subhedral,

[a] Weights estimated concentration uncertainty up to 50%.

[b] Th/U ratio calculated from the $^{208}Pb/^{206}Pb$ ratio and the $^{206}Pb/^{238}U$ date of the sample.

[c] Total radiogenic Pb.

[d] Total common Pb.

[e] Ratio of radiogenic Pb (including ^{208}Pb) to common Pb.

[f] Measured ratio corrected for fractionation and spike contribution only, reduced using GSC 535 spike calibration v. 2012.

[g] Measured ratios corrected for fractionation, spike, blank, and, where applicable, initial common Pb. Laboratory blanks were corrected using $^{206}Pb/^{204}Pb = 18.20 \pm 0.47$, $^{207}Pb/^{204}Pb = 15.37 \pm 0.14$, $^{208}Pb/^{204}Pb = 37.40 \pm 0.19$.

[h] Correlation coefficient of radiogenic $^{207}Pb^*/^{235}U$ and $^{206}Pb^*/^{238}U$.

[i] Dates (Ma) calculated using $^{238}U/^{235}U = 137.88$ (Steiger and Jäger, 1977), and decay constants of $^{238}U = 1.55125 \times 10^{-10}$ yr^{-1} and $^{235}U = 9.8485 \times 10^{-10}$ yr^{-1} (Jaffey et al., 1971).

[j] % discordance = 100 - (100 * ($^{206}Pb/^{238}U$ date) / ($^{207}Pb/^{206}Pb$ date)).

DISCUSSION

Stratigraphy of the B26 Host Volcanic Succession

The inferred primary volcanic architecture of the B26 project area is schematized in Figure 8. The interpreted relative and absolute timing of the emplacement of the different units is detailed below following four phases of an evolving volcanic centre. The focus of this paper is the timing of the events and the potential architecture in the study area. Petrogenetic considerations will be presented and discussed in detail elsewhere (Fayard, in prep).

First phase: Intermediate member volcanism

The intercalated andesite and intermediate lapilli tuff ± tuff breccia deposit have the same geochemical signature, which suggests a cogenetic relationship. The relative proportion of flows versus sills is, however, difficult to estimate as both facies are texturally similar (Fig. 8). The dacite was probably coeval with the andesite as it is located at different stratigraphic positions in the andesitic strata (Fig. 8). The textures and distribution of the dacite are in agreement with an emplacement as isolated domes. These domes may have been extrusive, but they could also have been partly emplaced in a sub-seafloor setting (i.e. cryptodomes). Dacitic volcanism probably marks the gradual transition towards more felsic volcanism in the upper part of the stratigraphy. The nature of the andesite and dacite (e.g. massive with surrounding unsorted, monogenic volcaniclastic deposits) does not confirm that they were emplaced in a subaqueous setting. However, the general context strongly suggests it, although the water depth at the time of emplacement remains unconstrained.

Second phase: Early volcanism of the felsic member

The onset of calc-alkaline felsic volcanism is established at about 2728 Ma, as indicated by the two ages (2727.9 ± 0.8 and 2728.5 ± 0.8 Ma) obtained from rhyolite A. The rhyolite A was most likely emplaced as coalescing flow-dome complexes at, or very near, the seafloor, forming isolated massive, flow-foliated aphyric rhyolites in a thick pile of associated fragmental deposits (Fig. 8). Dome growth might have been in part endogenous, as suggested by the vertical continuity of some of the massive rhyolites that seem to match the dome's lateral extension. Although the age and chemistry are identical to the underlying strata, the upper third of the unit may represent a secondary pulse of rhyolite A volcanism as it has a slightly different aspect (vitreous) with more abundant volcaniclastic rocks.

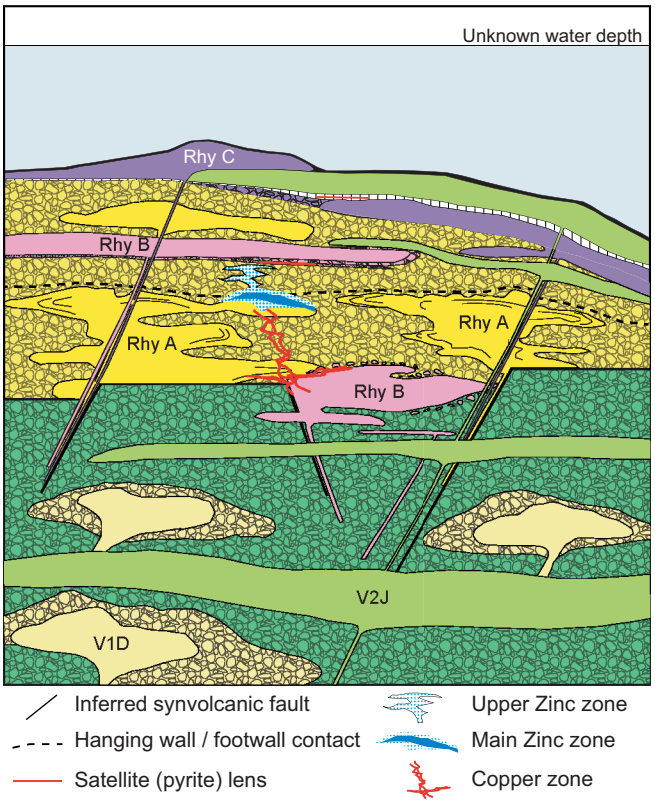

Figure 8. Schematic representation of the inferred primary architecture of the B26 host volcanic succession and the mineralized zones. Legend for the units is shown in Figure 2. Note that the colours of the volcaniclastic facies patterns have been slightly attenuated to highlight the mineralized zones.

Third phase: Rhyolite B

Volcanism related to rhyolite B is contemporaneous with that of rhyolite A as indicated by similar U-Pb crystallization ages (Fig. 7). However, both rhyolite units are distinct as indicated by their contrasting texture and slightly different chemistry. The facies and distribution of rhyolite B indicate that it was emplaced as shallow subvolcanic domes or sills at the interface between the intermediate and felsic members, and higher up in rhyolite A (Fig. 8). Such an interpretation is in agreement with the presence of common dykes and sills of rhyolite B intruding the volcanic succession.

Fourth phase: Waning volcanism and sedimentation

The age of rhyolite C is unconstrained, but its distribution and chemistry indicate that it is part of the same felsic magmatic system as the other intermediate to felsic volcanic rocks at B26. It was emplaced as a series of sills in the uppermost part of rhyolite A and extruded as flows and/or as domes on the paleo-seafloor, forming the top of the felsic member. Rhyolite C probably represents the waning stages of felsic volcanic activity

in the study area, which was succeeded by clastic sedimentation. Calc-alkaline andesitic volcanism covered the top of the volcanic edifice, forming amygdaloidal flows interlayered with rhyolite C and sediments. Finally, a thin layer of graphitic argillite covers the entire volcanic sequence.

Geological Controls on the Style and Geometry of Mineralized Zones

The volcanic architecture in the B26 project area comprises permeable volcaniclastic strata that were more favourable to hydrothermal fluid upflow and thus influenced the metal distribution. The transposed and slightly discordant Copper zone extends over at least 150 to 200 m of flattened stratigraphy, indicating that it was certainly significantly thicker prior to flattening. This suggests a significant vertical extension of the Cu mineralization that may have been accentuated by the permeable nature of the volcaniclastic strata. Though the Main and Upper Zinc zones are concordant, they are considered to have been formed largely by subseafloor replacement processes (*see* Fayard et al., 2020). More "diffuse-style" mineralization formed within the hanging-wall fragmental facies of rhyolite A.

The alteration is widespread and extends in the hanging-wall rocks, further supporting a sub-seafloor deposition. Although there are no constraints on the water depth at the time of volcanism, the extensive Copper zone suggests a deep setting that would have prevented fluid boiling, whereas the comparatively smaller, Pb-bearing, Ag-rich Zinc zones suggest a much lower temperature, and perhaps a shallower setting allowing fluids to boil (cf. Hannington et al., 1999). It is possible that the apparent lack of a significant hiatus (e.g. interlayered sedimentary strata) in the felsic volcanism associated with rhyolite A in the immediate B26 area could have hampered the development of a large sulphide lens. Such a hiatus seems to have only occurred during the emplacement of rhyolite C, much higher in the stratigraphy, perhaps during the waning stage or after the hydrothermal activity. This does not preclude the possibility that favourable local hiatuses in rhyolite A volcanism may have developed elsewhere in the Brouillan Group.

The volcanic succession in the Selbaie area, which occurs less than 10 km to the northwest, has the same age as that at B26. It has been interpreted as a shallow submarine to subaerial volcanic centre comprising epithermal polymetallic mineralization (e.g. Larson and Hutchinson, 1993). Thus, the B26 zones may represent an intermediate mineralization style between typical Archean Zn-Cu systems and epithermal systems. The presence of distinct intermediate to felsic units as coalescing domes and laterally restricted flows, dykes, and sills indicates that the area was undergoing extension. It also means that the area was the location of focused volcanic activity with a well developed thermal corridor (cf. Galley, 2003) in proximity to the Brouillan synvolcanic intrusion, explaining the presence of the B26 mineralized zones in that area.

Analogies between the Host Rocks of the B26 Zones and the Selbaie Deposit

The Selbaie and B26 rhyolite units are geochemically largely similar. They both have a strongly calc-alkaline magmatic affinity (Fig. 3c) and comparable extended primitive mantle-normalized trace element patterns (Fig. 4b). They have the same age (ca. 2729–2728 Ma) and are coeval with the 2729 ± 4 Ma Brouillan synvolcanic intrusion. Dissimilarities include the presence of shallow water to subaerial pyroclastic units at Selbaie, which are absent (or not preserved) at B26, perhaps explaining differences in ore styles (*see* Fayard et al., 2020 for further discussion). More work is underway to fully compare the B26 area with the Selbaie deposit.

IMPLICATIONS FOR EXPLORATION

This study presents preliminary volcanogenic, textural, geochemical, and geochronological information about the B26 Cu-Zn-Ag-Au project, which provides a better understanding of the key stratigraphic relationships between the volcanic units and the mineralization, and how these relate to the large past-producing Selbaie polymetallic deposit. B26 is a base metal (Zn-Cu) polymetallic mineralized system that contains significant Ag-rich zones. It is hosted in a ≥400 m thick sequence of predominantly felsic flows, domes, and sills that have a calc-alkaline magmatic affinity. It is also located very proximal to a large synvolcanic felsic calc-alkaline intrusion (Brouillan pluton), which is interpreted to have been the hydrothermal driver in the area (e.g. Selbaie deposit and Wagosic prospect). Archean calc-alkaline volcanic centres have traditionally been considered less prospective than tholeiitic successions. However, B26, Selbaie, and the Ag-rich mineralized zones of the Brouillan volcanic complex are similar to many of the Archean Au-rich VMS systems of the Superior province (e.g. Mercier-Langevin et al., 2015). They are associated with calc-alkaline rocks, indicating that such rocks (typical of very well metal-endowed younger arc settings) should not be neglected in exploring for Archean synvolcanic ore systems.

ACKNOWLEDGMENTS

This report is a contribution to the Targeted Geoscience Initiative Program of the Geological Survey of Canada. Support for this study was provided through the Gold Project, Activity G-1.1: Gold through space and time at

the Archean. Quentin Fayard is conducting a TGI-supported M.Sc. at the Université du Québec à Chicoutimi. The authors would like to thank SOQUEM Inc. for their support and collaboration in this study and access to data. Zircon mineral separates were prepared by R. Chung and G. Case at the Geological Survey of Canada. P. Hunt oversaw zircon imaging for in-situ SHRIMP analyses. SHRIMP data acquisition and data reduction were conducted with the help of T. Pestaj and N. Rayner. This report benefited from constructive comments by P-S. Ross and S. Castonguay.

REFERENCES

Adam, D., 1997. Rapport d'une campagne de forage, propriété B26, canton Brouillan, Québec, Canada; Les métaux Billiton Canada Inc., GM 57187, 14 p.

Adam, D., 2004. Les Mines Selbaie, final ore reserves statement as of January 22, 2004; Unpublished internal report to BHP Billiton, 25 p.

Ayer, J.A., Amelin, Y., Corfu, F., Kamo, S., Ketchum, J., Kwok, K., and Trowell, N., 2002. Evolution of the southern Abitibi greenstone belt based on U-Pb geochronology: autochthonous volcanic construction followed by plutonism, regional deformation and sedimentation; Precambrian Research, v. 115, p. 63–95.

Barrie, C.T. and Krogh, T.E., 1996. U-Pb zircon geochronology of the Selbaie Cu-Zn-Ag-Au mine, Abitibi Subprovince, Canada; Economic Geology, v. 91, p. 563–575.

Beaudin, A., 2017. Rapport de la campagne de sondages hiver-été 2014, propriété B26, canton Brouillan, Québec, Canada; SOQUEM Inc., GM 70058, 45p.

Camus, Y. and Valdnais-Leblanc, O., 2018. Rapport Technique NI 43-101 et estimation des ressources, Projet B26, Québec; Unpublished internal report to Soquem Inc, 136 p.

Daigneault, R., Mueller, W.U., and Chown, E.H., 2004. Abitibi greenstone belt plate tectonics: the diachronous history of arc development, accretion and collision; *in* The Precambrian Earth: Tempos and events, (ed.) P.G. Eriksson, W. Altermann, D.R. Nelson, W.U. Mueller, and O. Catuneanu; Developments in Precambrian Research, v. 12, p. 88–103.

Deptuck, R., Squair, H., and Wierzbicki, V., 1982. Geology of the Detour zinc-copper deposits, Brouillan Township, Quebec; *in* Precambrian sulfide deposits, H.S. Robinson Memorial Volume, (ed.) R.W. Hutchinson, C.D. Spence, and J.M. Franklin; Geological Association of Canada, Special Paper 25, p. 319–342.

Faure, S., Jébrak, M., and Bouillon, J.J., 1990. Géologie et minéralisations en Zn–Cu–Ag–Au de Les Mines Selbaie; *in* The northwestern Quebec polymetallic belt; a summary of 60 years of mining exploration. Proceedings of the Rouyn-Noranda 1990 symposium, (ed.) M. Rive, P. Verpaelst, Y. Gagnon, J.M. Lulin, G. Riverin, and A. Simard; Canadian Institute of Mining and Metallurgy, Special Volume 43, p. 363–372.

Faure, S., Jébrak, M., and Angelier, J., 1996. Structural evolution of Les Mines Selbaie, northern Abitibi, Québec, Canada; Exploration and Mining Geology, v. 5, p. 215–230.

Faure, S., 2012. Réévaluation paléo environnementale du complexe volcanique de Selbaie et de son potentiel métallogénique; CONSOREM project 2011-08, 26 p. <http://www.consorem.ca/production_scientifique/2011_08/Rapport%202011-08%20Selbaie.pdf> [accessed November 15, 2019]

Faure, S., 2015. Prolongement de la faille Sunday Lake (mine Detour Gold, Ont.) au Québec et son potentiel pour les minéralisations aurifères et en métaux de base; CONSOREM Project 2013-02, 41 p. < http://www.consorem.ca/production_scientifique/2013_02/Rapport%202013-02%20DETOUR_VF_20160401.pdf> [accessed November 15, 2019]

Fayard, Q., Mercier-Langevin, P., Daigneault, R., and Perreault, S., 2018. Volcanic, hydrothermal and structural controls on the nature and distribution of base and precious metals at the B26 project, Brouillan volcanic complex, Abitibi, Quebec; *in* Targeted Geoscience Initiative: 2017 report of activities, volume 1, (ed.) N. Rogers; Geological Survey of Canada, Open File 8358, p. 99–103.

Fayard, Q., Mercier-Langevin, P., Daigneault, R., and Perreault, S., 2020. The B26 Cu-Zn-Ag-Au project, Brouillan volcanic complex, Abitibi greenstone belt, part 2: Hydrothermal alteration and mineralization; *in* Targeted Geoscience Initiative 5: Contributions to the Understanding of Canadian Gold Systems, (ed.) P. Mercier-Langevin, C.J.M. Lawley, and S. Castonguay; Geological Survey of Canada, Open File 8712, p. 109–125. doi:10.4095/323669

Galley, A.G., 2003. Composite synvolcanic intrusions associated with Precambrian VMS-related hydrothermal systems; Mineralium Deposita, v. 38, p. 443–473.

Hannington, M.D., Poulsen, H.K., Thompson, J.F.H., and Sillitoe, R.H., 1999. Volcanogenic gold in the massive sulfide environment; *in* Volcanic-associated massive sulfide deposits: processes and examples in modern and ancient settings, (ed.) C.T. Barrie and M.D. Hannington; Reviews in Economic Geology, v. 8, p. 325–356.

Hart, T.R., Gibson, H. L., and Lesher, C.M., 2004. Trace element geochemistry and petrogenesis of felsic volcanic rocks associated with volcanogenic massive Cu-Zn-Pb sulfide deposits; Economic Geology, v. 99, p. 1003–1013.

Jaffey, A.H., Flynn, K.F., Glendenin, L.E., Bentley, W.C., and Essling, A.M., 1971. Precision measurements of half-lives and specific activities of ^{235}U and ^{238}U; Physical Review, v. 4, p. 1889–1906.

Lacroix, S., Simard, A., Pilote, P., and Dubé, L. M., 1989. Vers une image régionale du sillon Harricana-Turgeon (Matagami-Joutel-Casa-Berardi); Ministère de l'Énergie et des Ressources du Québec, PRO 89-04, 7 p.

Lacroix, S., 1994. Géologie de la partie ouest du sillon Harricana-Turgeon, Abitibi; Ministère des Ressources naturelles du Québec, MB 94-54, 26 p.

Larson, J.E., 1987. Geology, geochemistry and volcanic history of Les Mines Selbaie, Quebec, Canada: An Archean epithermal system; Ph.D. thesis, Colorado School Mines, Boulder, Colorado, 388 p.

Larson, J.E. and Hutchinson, R.W., 1993. The Selbaie Zn-Cu-Ag deposits, Quebec, Canada; an example of evolution from subaqueous to subaerial volcanism and mineralization in an Archean caldera environment; Economic Geology, v. 88, p. 1460–1482.

Lesher, C.M., Goodwin, A.M., Campbell, I.H., and Gorton, M.P., 1986. Trace-element geochemistry of ore-associated and barren, felsic metavolcanic rocks in the Superior province, Canada; Canadian Journal of Earth Sciences, v. 23, p. 222–237.

Mattinson, J.M., 2005. Zircon U–Pb chemical abrasion ("CA-TIMS") method; combined annealing and multi-step partial dissolution analysis for improved precision and accuracy of zircon ages; Chemical Geology, v. 220, p. 47–66.

McDonough, W.F. and Sun S-S., 1995. The composition of the Earth; Chemical Geology, v. 120, p. 223–253.

Mercier-Langevin, P., Hannington, M.D., Dubé, B., Piercey, S.J., Peter, J.M., and Pehrsson, S.J., 2015. Precious metal enrichment processes in volcanogenic massive sulphide deposits – a summary of key features, with an emphasis on TGI-4 research

contributions; *in* Targeted Geoscience Initiative 4: Contributions to the understanding of volcanogenic massive sulphide deposits genesis and exploration methods development, (ed.) J.M. Peter and P. Mercier-Langevin; Geological Survey of Canada Open File 7853, p. 117–130.

Monecke, T., Mercier-Langevin, P., Dubé, B., and Friemen, B., 2017. Geology of the Abitibi greenstone belt; *in* Archean base and precious metal deposits, southern Abitibi greenstone belt, Canada, (ed.) T. Monecke, P. Mercier-Langevin, and B. Dubé; Reviews in Economic Geology, v. 19, p. 7–49.

Parrish, R.R., Roddick, J.C., Loveridge, W.D., and Sullivan, R.W., 1987. Uranium-lead analytical techniques at the Geochronology Laboratory; Geological Survey of Canada, Paper 87-2, p. 3–7.

Pearce, J.A., 1996. A user's guide to basalt discrimination diagrams; *in* Trace Element Geochemistry of Volcanic Rocks: Applications for massive sulphide exploration, (ed.) D.A. Wyman, Geological Association of Canada, Short Course notes 12, p. 79–113.

Roddick, J.C., 1987. Generalized numerical error analysis with applications to geochronology and thermodynamics; Geochimica et Cosmochimica Acta, v. 51, p. 2129–2135.

Ross, P.-S. and Bédard, J.H., 2009. Magmatic affinity of modern and ancient subalkaline volcanic rocks determined from trace element discriminant diagrams; Canadian Journal of Earth Sciences, v. 46, p. 823–839.

SOQUEM Inc., 2018. SOQUEM divulgue une nouvelle estimation des ressources du gîte B26; Press release, 6 p. <https:// www.soquem.qc.ca/wp-content/uploads/com_soquem_fr_4_ mars_ final.pdf> [accessed November 15, 2019]

Steiger, R.H. and Jagger, E., 1977. Subcommission on geochronology: Convention on the use of decay constants in geo- and cosmochronology; Earth and Planetary Science Letters, v. 36, p. 359–362.

Taner, M.F., 2000. The Geology of the volcanic-associated polymetallic (Zn, Cu, Ag and Au) Selbaie deposits, Abitibi, Quebec, Canada; Exploration and Mining Geology, v. 9, p. 189–214.

Winchester, J.A. and Floyd, P.A., 1977. Geochemical discrimination of different magma series and their differentiation products using immobile elements; Chemical Geology, v. 20, p. 325–343.

York, D., 1969. Least squares fitting of a straight line with correlated errors; Earth and Planetary Science Letters, v. 5, p. 320–324.

The B26 Cu-Zn-Ag-Au project, Brouillan volcanic complex, Abitibi greenstone belt, part 2: Hydrothermal alteration and mineralization

Quentin Fayard[1,2*], Patrick Mercier-Langevin[3], Réal Daigneault[1], Serge Perreault[2], and Natasha Wodicka[4]

[1]Université du Québec à Chicoutimi, 555 Boulevard de l'Université, Chicoutimi, Quebec G7H 2B1
[2]SOQUEM Inc., 1740 Chemin Sullivan, Val-d'Or, Quebec J9P 7H1
[3]Geological Survey of Canada, 490 rue de la Couronne, Québec, Quebec G1K 9A9
[4]Geological Survey of Canada, 601 Booth Street, Ottawa, Ontario K1A 0E8
[*]Corresponding author's e-mail: quentin.fayard@gmail.com

The B26 project is located in the northern Abitibi greenstone belt a few kilometres south of the past-producing Zn-Cu-Ag-Au Selbaie mine. It consists of a transposed Au-rich chalcopyrite stringer zone (Copper zone) overlain by concordant Ag-rich Zn-(Pb) sulphide lenses (Main Zinc zone) and disseminated to discordant sulphide vein- and veinlet-rich zones (Upper Zinc zone). The footwall rocks are affected by a wide and intense semi-conformable alteration halo mainly composed of sericite, chlorite, and quartz assemblages. Fe-Mn carbonate and quartz are common as gangue minerals in the sulphide lenses. The hanging-wall rocks are affected by a proximal K-feldspar-quartz and a more distal albite alteration with Fe-(Mn)-carbonate veins and replacement zones. The mineralized zones and host rocks have undergone major shortening during the main phase of regional deformation, which is responsible for transposition of the Cu-rich footwall stringers, flattening and stretching of the concordant semi-massive to massive sulphide zones, and local remobilization of precious metal-bearing phases into the south-dipping foliation and along the associated southwest-plunging stretching lineation.

Gold is directly associated with Cu, and also with Bi, Se, and Sn in the Copper zone as native gold, and Au-rich electrum with native Bi, bismuthinite, laitakarite, ikunolite, stannite, and cassiterite. Silver is present in the Main and Upper Zinc zones as freibergite, native silver, allargentum, acanthite, and pyrargyrite. Deposit-scale metal distribution and primary sulphide assemblages indicate that precious metals introduction was primary, although later local (metre-scale) remobilization occurred in response to deformation and metamorphism. Copper and Zn are decoupled at B26 and result from a strong vertical zonation in the system, suggesting an evolving geological environment with potentially a gradually shallowing seawater level. Shallow-water to subaerial conditions have been documented at the nearby Selbaie deposit, where they are considered responsible for the epithermal-style characteristics of the ore.

INTRODUCTION

The B26 project is a recently discovered base and precious metals system hosted within the Brouillan volcanic complex in the northwestern Abitibi greenstone belt (Fig. 1). Total resources (indicated and inferred) are estimated at 11.4 Mt at 1.52% Cu, 1.19% Zn, 0.78 g/t Au, and 30 g/t Ag (Camus and Valdnais-LeBlanc, 2018). The Harricana-Turgeon belt, which comprises the Matagami and Joutel volcanogenic massive sulphide (VMS) camps (e.g. Legault et al., 2002; Debreil et al., 2018) and the Detour Lake orogenic gold deposit (e.g. Castonguay et al., 2020), have not been as extensively explored as other parts of the Abitibi belt, mostly due little surface exposure. The Brouillan volcanic complex has been studied because of its association with the Selbaie Zn-Cu-Ag-Au deposit that was mined between 1981 and 2004. The Selbaie deposit is distinctive amongst the polymetallic deposits of the Abitibi belt, as it has been interpreted as a possible Archean epithermal-like system formed in a shallow subaqueous to subaerial caldera environment (Deptuck et al., 1982; Larson, 1987; Faure et al., 1990, 1996; Larson and Hutchinson, 1993; Taner, 2000). Although some of the main features of the B26 mineralized zones are typical of precious metals-poor VMS deposits, they present some unusual characteristics. such as a strong decoupling of Cu and Zn, the association with calc-alkaline volcanic rocks, and anomalously high Ag contents (i.e. 100–2000 ppm Ag; Fayard et al., 2018). Selbaie and other mineralized zones of the Brouillan volcanic complex are also commonly characterized by high Ag grades and contents. This "provinciality"

Fayard, Q., Mercier-Langevin, P., Daigneault, R., Perreault, S., and Wodicka, N., 2020. The B26 Cu-Zn-Ag-Au project, Brouillan volcanic complex, Abitibi greenstone belt, part 2: Hydrothermal alteration and mineralization; *in* Targeted Geoscience Initiative 5: Contributions to the Understanding of Canadian Gold Systems, (ed.) P. Mercier-Langevin, C.J.M. Lawley, and S. Castonguay; Geological Survey of Canada, Open File 8712, p. 109–125. https://doi.org/10.4095/323669

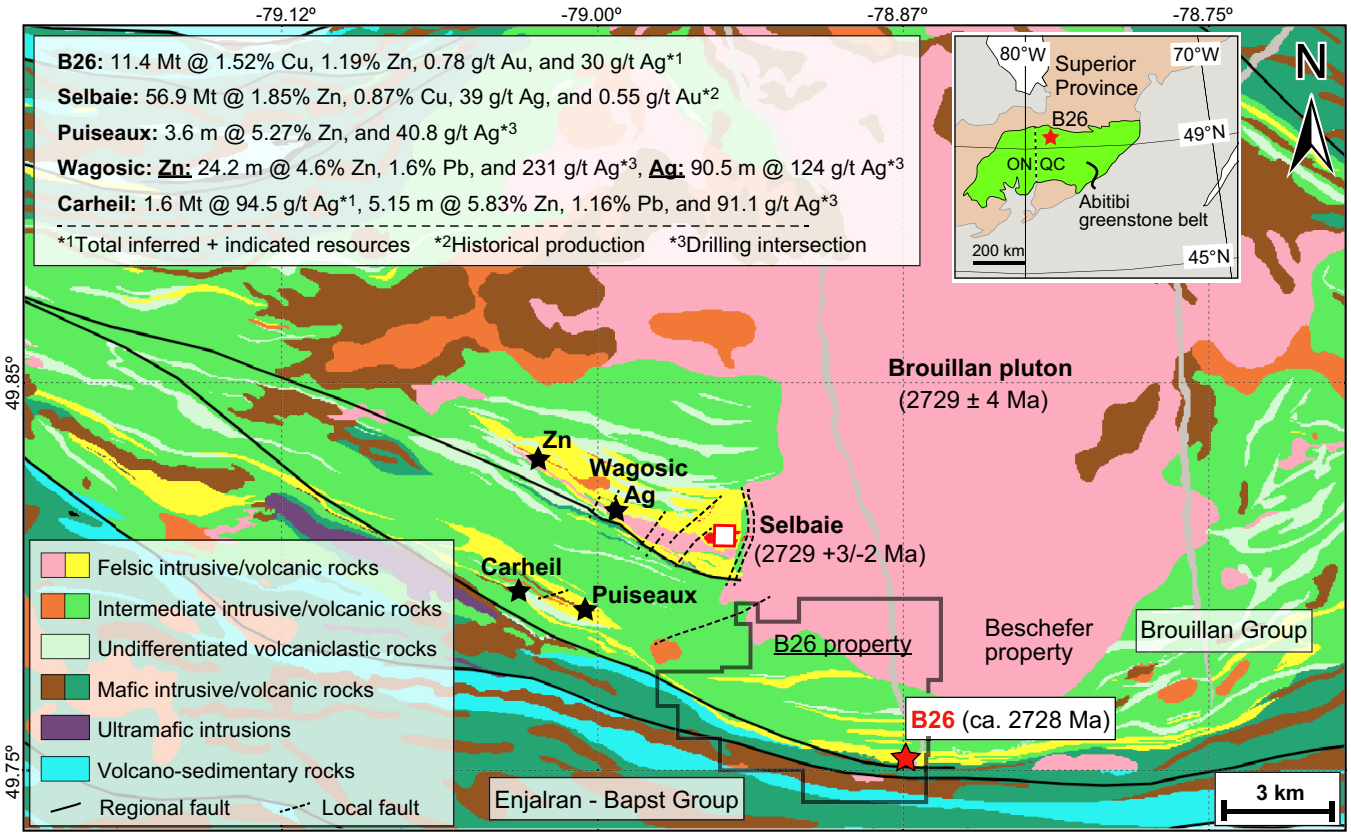

Figure 1. Geological map (*modified from* Faure, 2015) of the Brouillan volcanic complex showing the location of the B26 project and other significant deposits and prospects of the area. Ages are from Barrie and Krogh (1996) and Fayard et al. (2020).

regarding Ag and the presence of deposits with unusual styles of mineralization suggest that underlying factors may have controlled the precious metals budget (e.g. Mercier-Langevin et al., 2015).

This study is part of an ongoing M.Sc. project that aims at identifying the controls on the precious metal enrichment processes at B26. This report summarizes some of the main aspects of the metamorphosed and intensely deformed mineralized sulphide zones and hydrothermal alteration assemblages of the B26 project.

Geological Setting

The geological setting of the B26 project is given in Fayard et al. (2020) and only the main features are summarized here. The B26 mineralized zones are hosted in a ca. 2729–2727 Ma (Barrie and Krogh, 1996; Fayard et al., 2020) homoclinal succession of steeply dipping, south-facing, intermediate to felsic volcanic rocks (Fig. 2a) that are part of the Brouillan Group of the Harricana-Turgeon belt in the northern part of the Abitibi greenstone belt. (Fig. 1). The Brouillan Group is underlain by the synvolcanic Brouillan pluton (Barrie and Krogh, 1996), which together form the Brouillan volcanic complex, and is overlain by the mafic-dominated Enjalran-Bapst Group to the south. The B26 project area is highly strained, as part of major east-west-trending deformation corridors located north and south of the Brouillan pluton (Lacroix, 1994; Daigneault et al., 2004), separating the volcanic packages and marking the contacts with the Taibi and Coapatina Archean metasedimentary rocks to the south and north, respectively. The main regional deformation (D_p), which is responsible for the east-west-trending foliation (S_p), is associated with greenschist-facies metamorphism that affects the area and mineralized zones of the B26 project.

The host succession to B26 comprises andesitic and dacitic units at the base (intermediate member) overlain by three distinct rhyolite units (Rhy A, Rhy B, and Rhy C: Fig. 2a). The rhyolite units are intercalated with andesite and sedimentary rocks in the uppermost part of the stratigraphic sequence. The rhyolite units, the uppermost sedimentary rocks, and andesite form the felsic member, which hosts most of the mineralized rocks and associated alteration (Adam, 1997; Beaudin, 2017; Fayard et al., 2020).

The felsic member hosts three mineralized zones that form the B26 deposit: 1) The Copper zone at the base (north); 2) the Main Zinc zone, separated into two mineralized bodies (eastern and western parts) along the same stratigraphic level, including the semi-massive to massive main lens as part of the easternmost body; and 3) the Upper Zinc zone located above the Main Zinc zone (Fig. 2a).

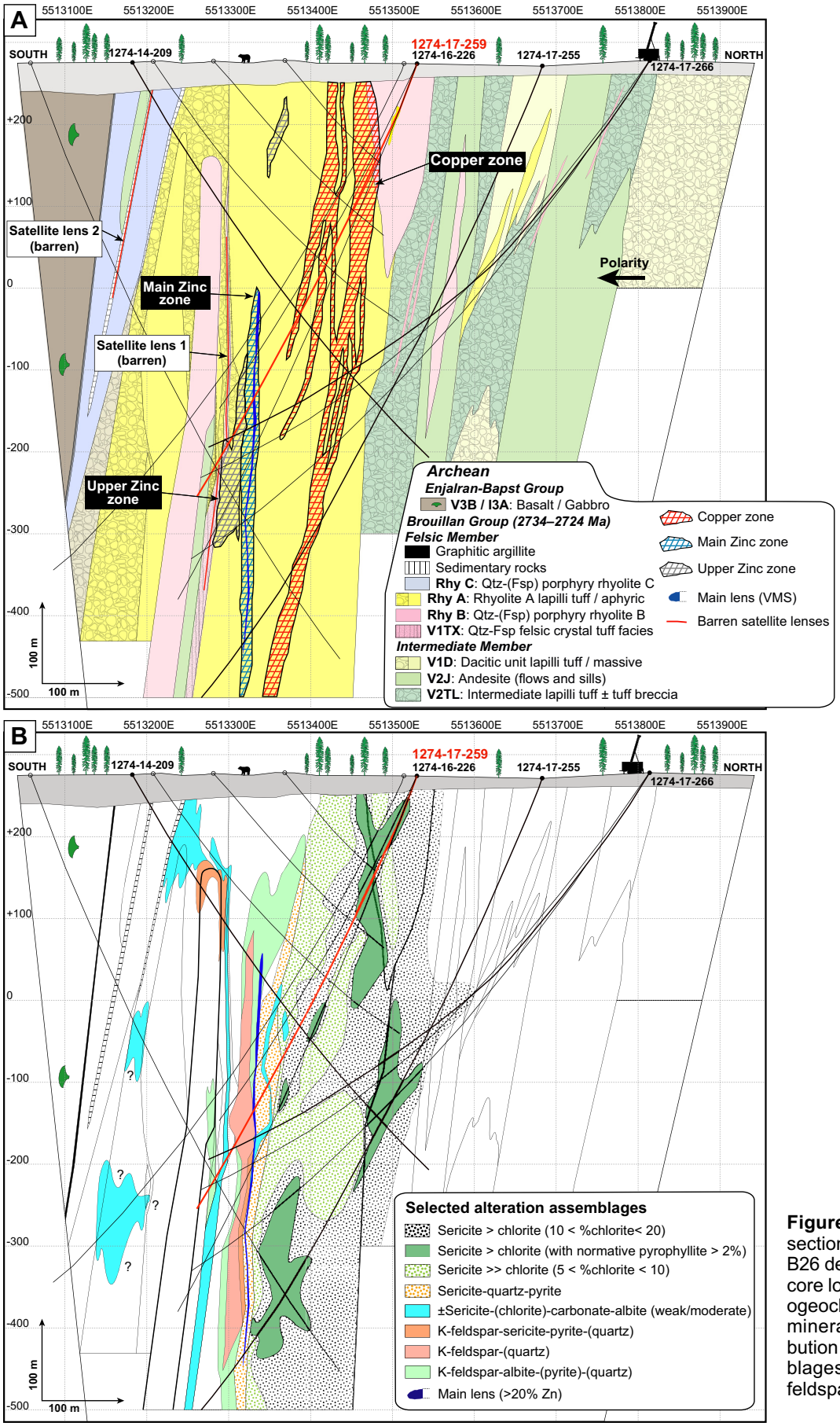

Figure 2. North-south cross-section (652950E ± 50 m) of the B26 deposit, established through core logging and whole-rock lithogeochemistry. **a)** Geology and mineralized zones. **b)** Distribution of the alteration assemblages. Abbreviations: Fsp = feldspar; Qtz = quartz.

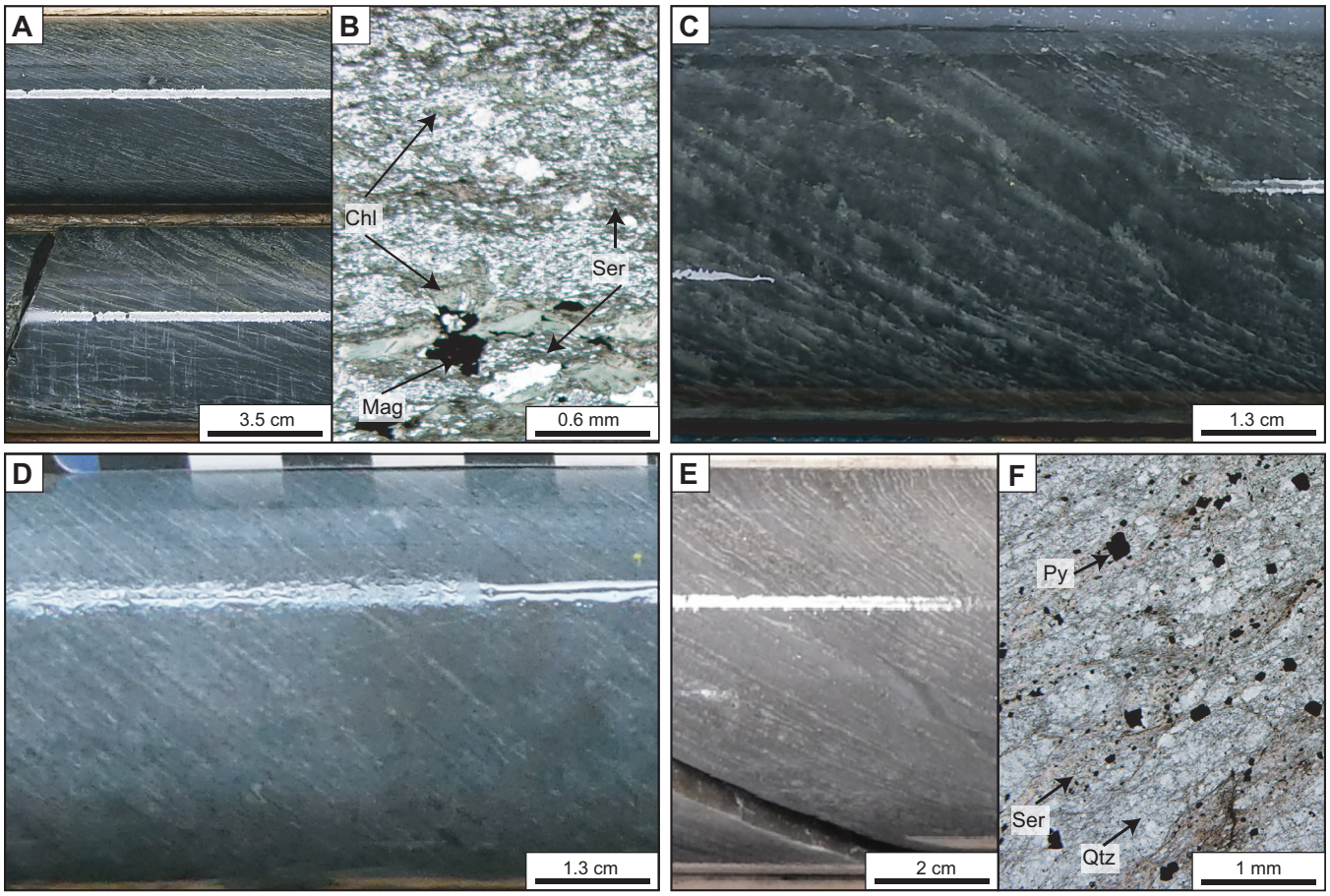

Figure 3. a) An example of the sericite ≥ chlorite alteration assemblage in rhyolite A. **b)** A photomicrograph (transmitted, natural light) of the sericite ≥ chlorite alteration assemblage. **c)** Chlorite > sericite alteration subassemblage. **d)** Sericite >> chlorite alteration subassemblage. **e)** An example of the sericite-quartz-pyrite alteration assemblage. **f)** A photomicrograph (transmitted, natural light) of the sericite-quartz-pyrite alteration assemblage. Abbreviations: Chl = chlorite, Mag = magnetite, Py = pyrite, Qtz = quartz, Ser = sericite.

HYDROTHERMAL ALTERATION

Six alteration assemblages (containing 11 subassemblages, Table 1) are defined at B26 on the basis of mineralogy, mineral chemistry, whole-rock lithogeochemistry, and spatial distribution relative to the mineralized zone: 1) sericite-chlorite, 2) sericite-quartz-pyrite, 3) sericite-(chlorite)-albite-carbonate, 4) K-feldspar, 5) albite, and, 6) carbonate.

The paragenetic assemblages are metamorphosed and form alteration zones that are affected by regional deformation. Although the primary shape of the alteration zones has been variously transposed by the main schistosity, the primary geochemical compositions of each of the assemblages are largely preserved despite metamorphism. Readers are referred to Fayard (in prep) for details on the data, analytical procedures, methods, and for an in-depth description of the B26 alteration assemblages, geochemistry, and distribution and zonation.

The most abundant metamorphosed alteration minerals are sericite, chlorite, quartz, albite, carbonate, K-feldspar, pyrite, and locally biotite. Sericite (used here to define foliated, fine-grained aggregates of white mica; cf. Rieder et al., 1999) occurs as millimetre-thick bands that are parallel to the S_p foliation and as fine (≤1 mm) porphyroblasts in the microcrystalline quartz±plagioclase matrix (Fig. 3e,f). Chlorite also occurs as millimetre thick bands that are parallel to the S_p foliation and as isolated clusters or grains disseminated in the matrix (Fig. 3b). Chlorite and sericite are usually mixed in variable relative abundance, with sericite commonly replacing chlorite. Albite and K-feldspar (orthoclase) occur with quartz as micro-grains disseminated in the microcrystalline matrix, especially in the hanging-wall rhyolite A (Fayard, in prep). The carbonate alteration minerals are mainly represented by manganiferous siderite/ankerite/dolomite as gangue minerals in the Zn-rich sulphide zones (*see below*), and as pervasive and fracture-controlled alteration in the hanging-wall rocks. The predominant and widespread sericite-chlorite and sericite-quartz-pyrite alteration assemblages affect most of the B26 host rocks; detailed descriptions are provided below. The remaining four

Table 1. Alteration assemblages of the B26 deposit.

Main assemblages	Subassemblages	Main minerals (vol.%)	Secondary minerals	Mass changes	Geometry
Sericite-chlorite	Chlorite > Sericite	15 < Chlorite < 25% 5 < Sericite < 20% (Rest = quartz)	pyrite, chalcopyrite	G: $Fe_2O_3^T$, MgO, SiO_2 L: Na_2O, K_2O, CaO, L-REE	stratabound and discordant
	Sericite ≥ chlorite	15 < Sericite < 20% 10 < Chlorite < 20% (Rest = quartz)	pyrite, chalcopyrite	G: $Fe_2O_3^T$, MgO L: Na_2O, K_2O, CaO, SiO_2, L-REE	discordant
	Sericite >> chlorite	20 < Sericite < 30% 5 < Chlorite < 10% (Rest = quartz)	pyrite, chalcopyrite, sphalerite	G: $Fe_2O_3^T$, MgO L: Na_2O, K_2O, CaO, SiO_2, L-REE	stratabound and discordant
Sericite-quartz-pyrite		20 < Sericite < 40% 2 < Pyrite < 5% (Rest quartz)	chlorite, carbonate, biotite, sphalerite	G: Fe_2O_{3T} L: Na_2O, K_2O, CaO, (SiO_2), L-REE	stratabound
Sericite-(chlorite)-albite-carbonate		5 < Sericite < 20% 2 < Chlorite < 5% 2 < Albite < 10% (Rest = quartz)	carbonate, pyrite, K-feldspar	G: CaO, ($Fe_2O_3^T$, MgO) L: Na_2O, K_2O, SiO_2,	stratabound and discordant
K-feldspar	K-feldspar	K-feldspar > 30% 0 < Albite < 10% (Rest = quartz)	pyrite, sphalerite, galena	G: SiO_2, K_2O L: Na_2O, $Fe_2O_3^T$, MgO, CaO	stratabound
	K-feldspar-sericite-pyrite	K-feldspar > 20% 5 < Sericite < 20% 0 < Albite < 5% 2 < Pyrite < 3% (Rest quartz)	pyrite, sphalerite	G: SiO_2, K_2O, $Fe_2O_3^T$ L: Na_2O, MgO, CaO	stratabound
	K-feldspar-Albite-Pyrite	20 < K-feldspar < 30% 10 < Albite < 20% 1 < Pyrite < 3% (Rest = quartz)	sphalerite, galena	G: SiO_2, K_2O, $Fe_2O_3^T$ L: Na_2O, MgO, CaO	stratabound
Albite	Albite dominated	20 < Albite < 50%	K-feldspar, carbonate		regional diffuse/pervasive
Carbonates	Carbonate-magnetite-(biotite)-pyrite veins and breccias	(Fe-Mg-Mn)-Carbonates (sideroplesite, pistomesite, ankerite, dolomite), Magnetite, Pyrite, (biotite)	sphalerite, pyrrhotite	G: SiO_2, $Fe_2O_3^T$, Cao, MgO, Na_2O L: K_2O	discordant
	Semi-massive to massive carbonates	(Fe-Mg-Mn)-Carbonates (sideroplesite, pistomesite, ankerite, dolomite), Magnetite	pyrite, pyrrhotite, stilpnomelane, chlorite	G: $Fe_2O_3^T$, SiO_2, CaO, MgO, Na_2O L: K_2O	stratabound

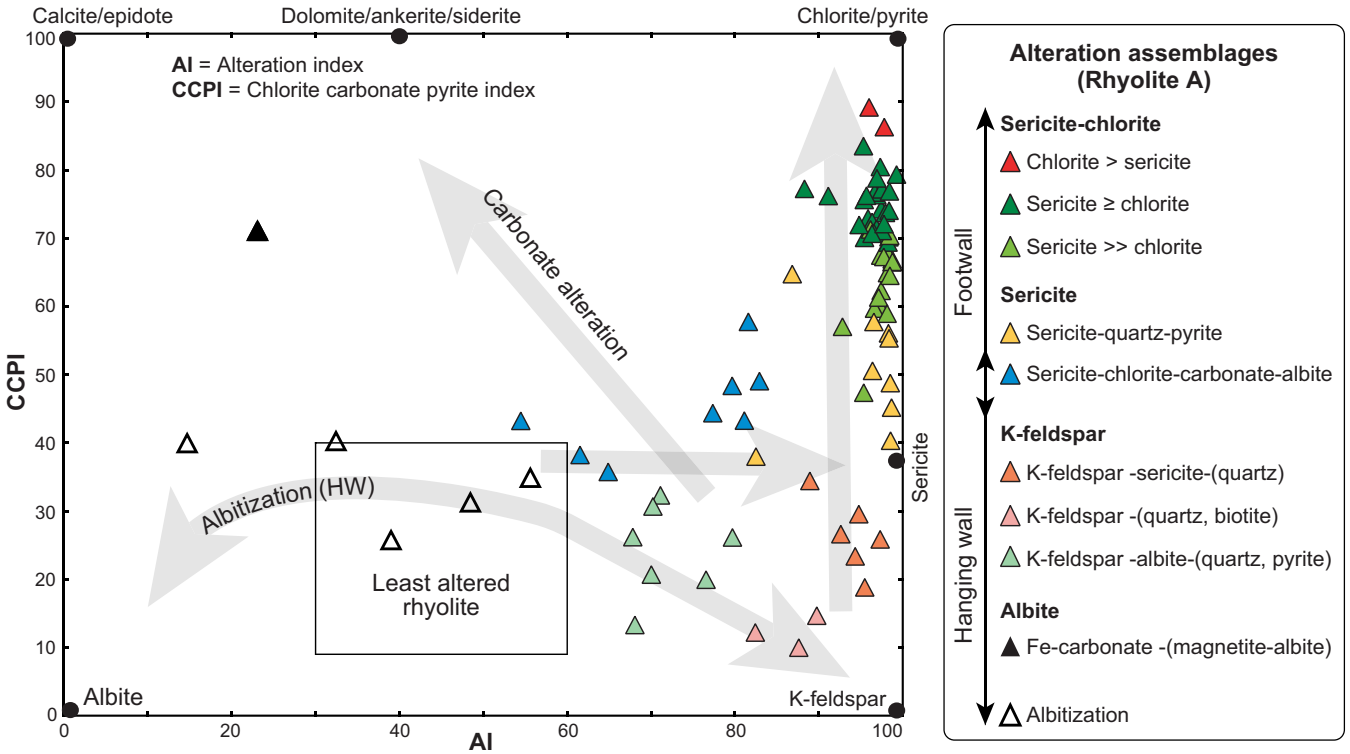

Figure 4. Alteration box plot of Large et al. (2001) of rhyolite A samples from the B26 project according to the alteration assemblages. AI = 100*[(MgO+K_2O)/(MgO+K_2O+Na_2O+CaO)] (Ishikawa et al., 1976), CCPI = 100*[(MgO+FeO)/(MgO+FeO+K_2O+Na_2O)] (Large et al., 2001).

assemblages are more localized; their principal characteristics are summarized in Table 1.

Sericite-Chlorite Alteration Assemblage

The sericite-chlorite alteration assemblage dominates in the footwall of the Main Zinc zone and around the Copper zone (Fig. 2b). It is discordant to locally stratabound and affects most of the footwall sequence in the study area, reaching a total thickness of up to 200 m (Fig. 2b). Although this alteration assemblage is pervasive, fine-grained and generally S_p-foliated, primary volcanic textures are commonly preserved. The Hashimoto alteration index (AI: Ishikawa et al., 1976) and chlorite-carbonate-pyrite alteration index (CCPI: Large et al., 2001) values vary from moderate to strong (Fig. 4, 5). Light rare earth elements (LREE) are variably leached (Fayard, in prep). Mass balance calculations indicate significant gains in $Fe_2O_3^T$ and MgO, and variable losses in Na_2O, K_2O, and CaO (±SiO_2) (Fig. 5, Table 1; Fayard, in prep). Although it was not identified visually, the normative calculation (i.e. CONSONORM_LG, performed using Lithomodeleur software: Trépanier et al., 2015) indicates the presence of pyrophyllite locally in this assemblage (Fig. 2b). Mineral chemistry indicates that the sericite varies in composition from muscovite to phengite, with high Al_2O_3 (30–35 wt%), low FeO (<3 wt%), and very low to low MgO (0.8–3 wt%) content. Chlorite consists of ripidolite and is FeO-poor (25–32 wt%) and MgO-rich (10–15 wt%). Chlorite, in the selvages of chalcopyrite veins in the Copper zone, is Fe-rich (34–38 wt% FeO) and Mg-poor (6–8 wt% MgO). Sericite is the principal alteration-related mineral at B26 but, depending on the relative abundance of chlorite, the sericite-chlorite alteration assemblage can be subdivided into subassemblages.

Chlorite > sericite

This subassemblage contains ≥20 vol.% chlorite and 5 to 20 vol.% sericite. It is present only locally, more commonly along chalcopyrite veins and locally at the contact with the main sulphide lens in the Main Zinc zone (e.g. diamond drillhole 1274-17-255: Fig. 2b). The zone comprising this subassemblage is discordant to stratigraphy, although transposed, except at the contact with the mineralized lens, where it is almost totally transposed. Chlorite dominates over sericite in this alteration facies (Fig. 3c), which represents some of the more geochemically altered rocks at B26 (Fig. 4). It is not mapped in Figure 2b as the sampling pattern was too widely spaced to allow a consistent representation in the section.

Sericite ≥ chlorite

This subassemblage contains between 10 and 20 vol.% chlorite and 15 to 20 vol.% sericite (Fig. 3a,b). It is particularly well developed in the lowermost part of rhyolite A (Fig. 2b). It is spatially related to the Copper

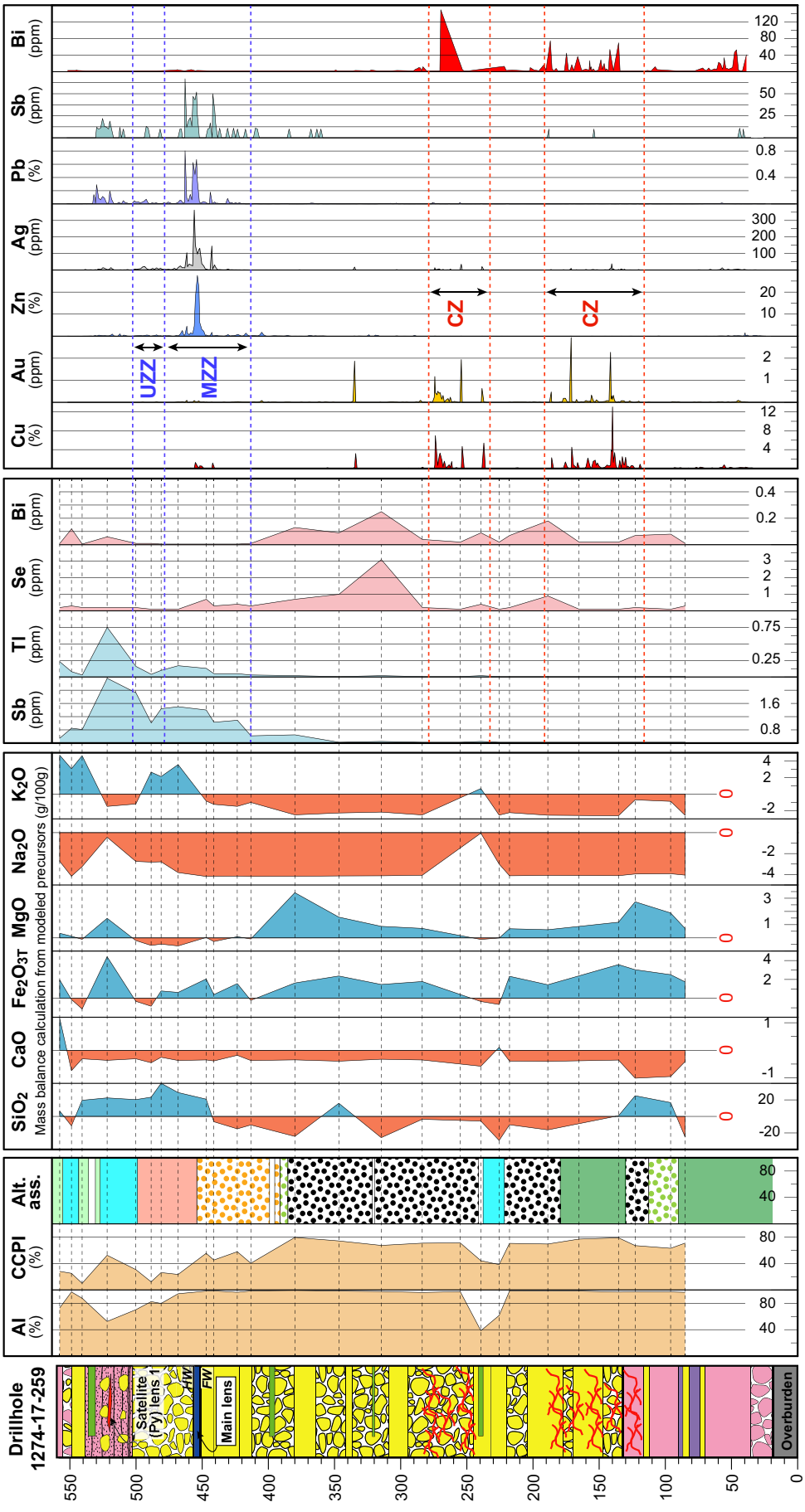

Figure 5. Simplified geology and geochemical profiles along drill core 1274-17-259 (see Fig. 2 for location, legend of lithological units, and formula for alteration indices). Alteration indices, mass balance calculations, and trace geochemistry are based on whole-rock geochemistry data and assays from SOQUEM. Mass balance calculations are based on the single precursor method of Trépanier et al. (2016). Abbreviations: AI = Hashimoto alteration index (Ishikawa et al., 1976), Alt. ass.= alteration assemblages, CCPI = chlorite-carbonate-pyrite alteration index (Large et al., 2001).

zone. Although strongly transposed, the geometry of this alteration seems to both be controlled by discordant structures and by the permeability of the volcaniclastic facies (Fig. 2b, Table 1). Rock units affected by this subassemblage alteration have high AI values and moderate CCPI values, in agreement with the dominant mineralogy (Fig. 4, 5).

Sericite >> chlorite

This subassemblage contains between 5 and 10 vol.% chlorite and 20 to 30 vol.% sericite (Fig. 3d). It affects the footwall rhyolite A and B units (Fig. 2a) and corresponds to a "distal" halo to the Copper zone (Fig. 2b). It is more diffuse than the previous subassemblage, and its distribution and intensity are probably controlled predominantly by the primary permeability and porosity of the volcanoclastic facies. Rock units altered by this subassemblage have high AI values and low to moderate CCPI values, in agreement with dominant sericite over chlorite values (Fig. 4, 5).

Sericite-Quartz-Pyrite Alteration Assemblage

This assemblage forms a stratiform band in the uppermost part of rhyolite A in the immediate footwall to the Main Zinc zone. It reaches its maximum thickness of about 30 m stratigraphically below the central part of the Main Zinc zone, and gradually decreases laterally (Fig. 2b). This concordant zone represents the proximal alteration assemblage underlying the massive main lens of the Main Zinc zone. It is composed of 20 to 40 vol.% sericite and 2 to 5 vol.% pyrite in a quartz± plagioclase groundmass (Fig. 3e,f). Pyrite abundance gradually increases towards the main lens. 1 to 2 vol.% of biotite porphyroblasts can be present a few metres under the main lens. Sericite occurs as closely spaced and strongly foliated millimetre thick bands (Fig. 3e,f).

The sericite-quartz-pyrite proximal footwall alteration assemblage has high alteration index values (AI >95: Fig. 4), with moderate CCPI values due to the absence of chlorite and generally low to moderate pyrite content. Rock units containing this assemblage show strong losses in Na_2O, limited K_2O and CaO losses, and moderate $Fe_2O_3^T$ gains (pyrite) (Table 1). Light REE are also leached in the alteration assemblage, although not as strongly as in the sericite-chlorite assemblage (Fayard, in prep).

Hanging-Wall Alteration Assemblages

Rock units in the hanging wall of the Main Zinc zone are weakly to locally moderately altered. Albite- and K-feldspar-bearing assemblages are usually of weak alteration intensity, except for the K-feldspar-sericite-pyrite subassemblage in which there can be up to 20 vol.% sericite. This latter subassemblage is proximal to the main lens, especially near its extremities, and generally transitional with the sericite-quartz-pyrite assemblage (Fig. 2b). The sericite (±chlorite)-carbonate-albite alteration assemblage occurs locally at the base of rhyolite B within the crystal tuff facies (Main Zinc zone hanging wall) and as discordant zones in the volcaniclastic facies of the uppermost part of rhyolite A (Fig. 2b). Although common at B26, carbonate alteration has not been systematically mapped since its footprint is diffuse. Carbonates (Fe-Mg-Mn-Ca) are present in veins, as matrix fill in rhyolite breccias, and as pervasive zones in the rhyolite C. The hanging-wall rock units are characterized by variable and heterogeneously distributed mass gains in SiO_2, $Fe_2O_3^T$ (due to Fe-carbonates) and locally in K_2O (Fig. 5, Table 1).

MINERALIZED ZONES

Several sulphidized intervals have been intersected by drilling on the B26 property (Adam, 1997; Beaudin, 2017). The Copper zone, the Main Zinc zone, and the Upper Zinc zone represent the most significant and continuous mineralized zones (Fig. 2a, 5, 6). Two thin, relatively continuous, but barren pyrite-(pyrrhotite) satellite lenses are located higher in the stratigraphic sequence. The latter are not discussed in this report; *see* Fayard (in prep) for details.

Copper Zone

The Copper zone is the largest mineralized zone at B26, both in total tonnage and extent. It consists of several juxtaposed mineralized intervals (Fig. 5, 6) that are discontinuous and transposed/flattened into the S_p foliation. It is located in the footwall of the Main Zinc zone, near the base of the felsic member, within rhyolite A and in the upper part of the lowermost rhyolite B unit (Fig. 2a). It can be up to 60 m thick and extends down to at least 1100 m below surface. It is interpreted to represent a strongly flattened or transposed feeder zone below the concordant Zn-rich zones (Fayard et al., 2018).

The Copper zone comprises stringer-style and disseminated Cu-bearing sulphide zones (Fig. 7a). The stringers locally form centimetre- to decimetre-thick semi-massive to massive sulphide veins (Fig. 7b) that contain variable amounts of quartz and carbonates. Durchbewegung structures (cf. Marshall and Gilligan, 1989) are common in the massive sulphide veins (Fig. 7b). Chalcopyrite is the main mineral and accounts for more than 95 vol.% of the sulphides. Pyrite generally constitutes 2 vol.% of the ore but can locally reach up to 20 vol.%. Pyrrhotite and sphalerite can be present in minor amounts, except very locally where they can reach up to 10 vol.%. Native gold is common in the chalcopyrite-rich stringers. Also, Bi-, Se-, and locally Sn-bearing trace minerals are present in chalcopyrite, as shown by whole-rock analyses (Table 2).

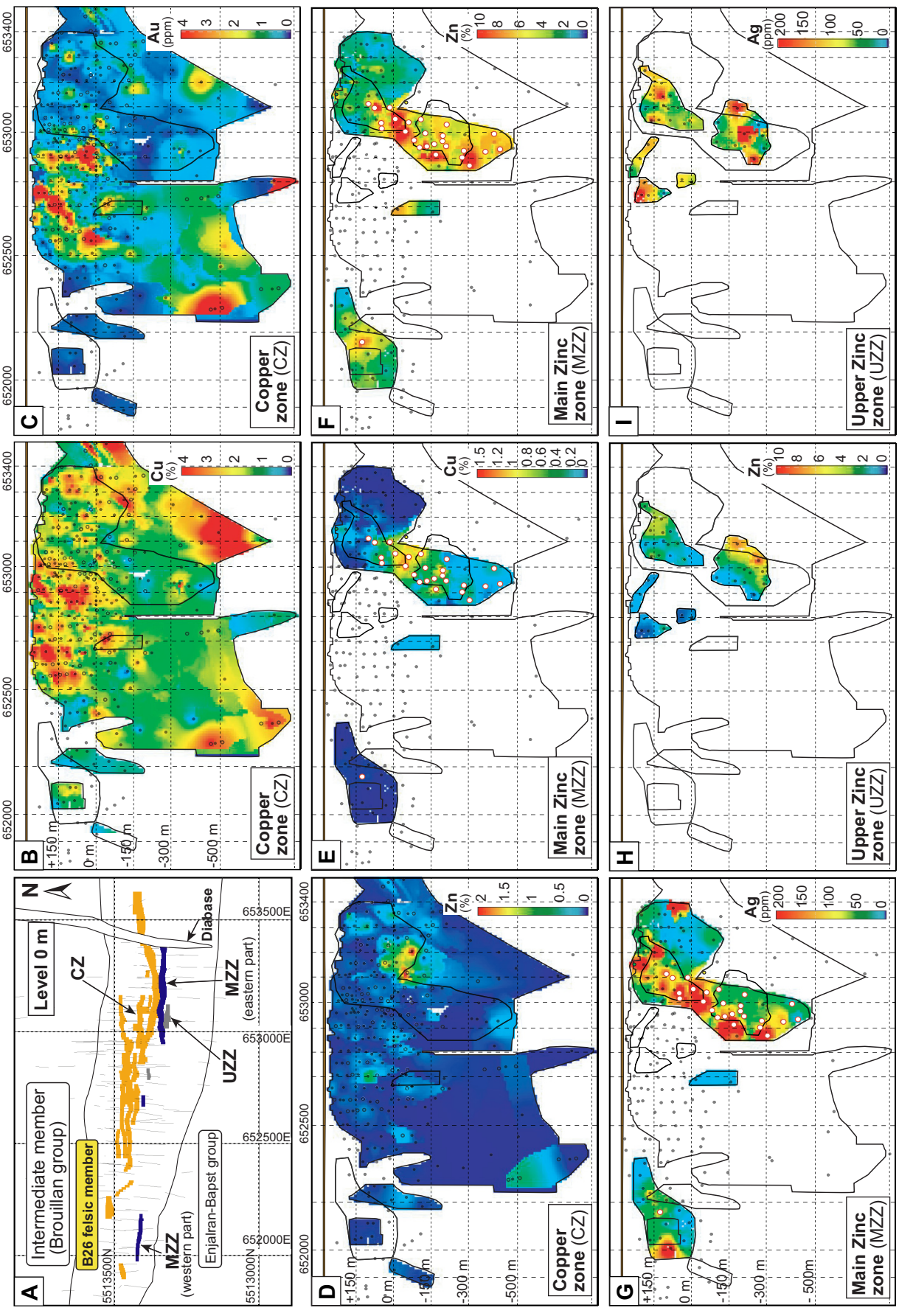

Figure 6. Interpolation (method given in Camus and Valdnais-Leblanc, 2018) of the Cu-Zn-Au-Ag values, showing the distribution of metals for each mineralized zone in an average longitudinal section: **a)** level 0 m plan view (± 50 m) of the mineralized zones; **b)** copper in CZ; **c)** gold in CZ; **d)** zinc in CZ; **e)** copper in MZZ; **f)** zinc in MZZ; **g)** silver in MZZ; **h)** zinc in UZZ; and **i)** silver in UZZ. Composite data are from Camus and Valdnais-Leblanc (2018). White circles with red contours represent semi-massive to massive sulphides in the MZZ. Abbreviations: CZ = Copper zone, MZZ = Main Zinc zone, UZZ = Upper Zinc zone.

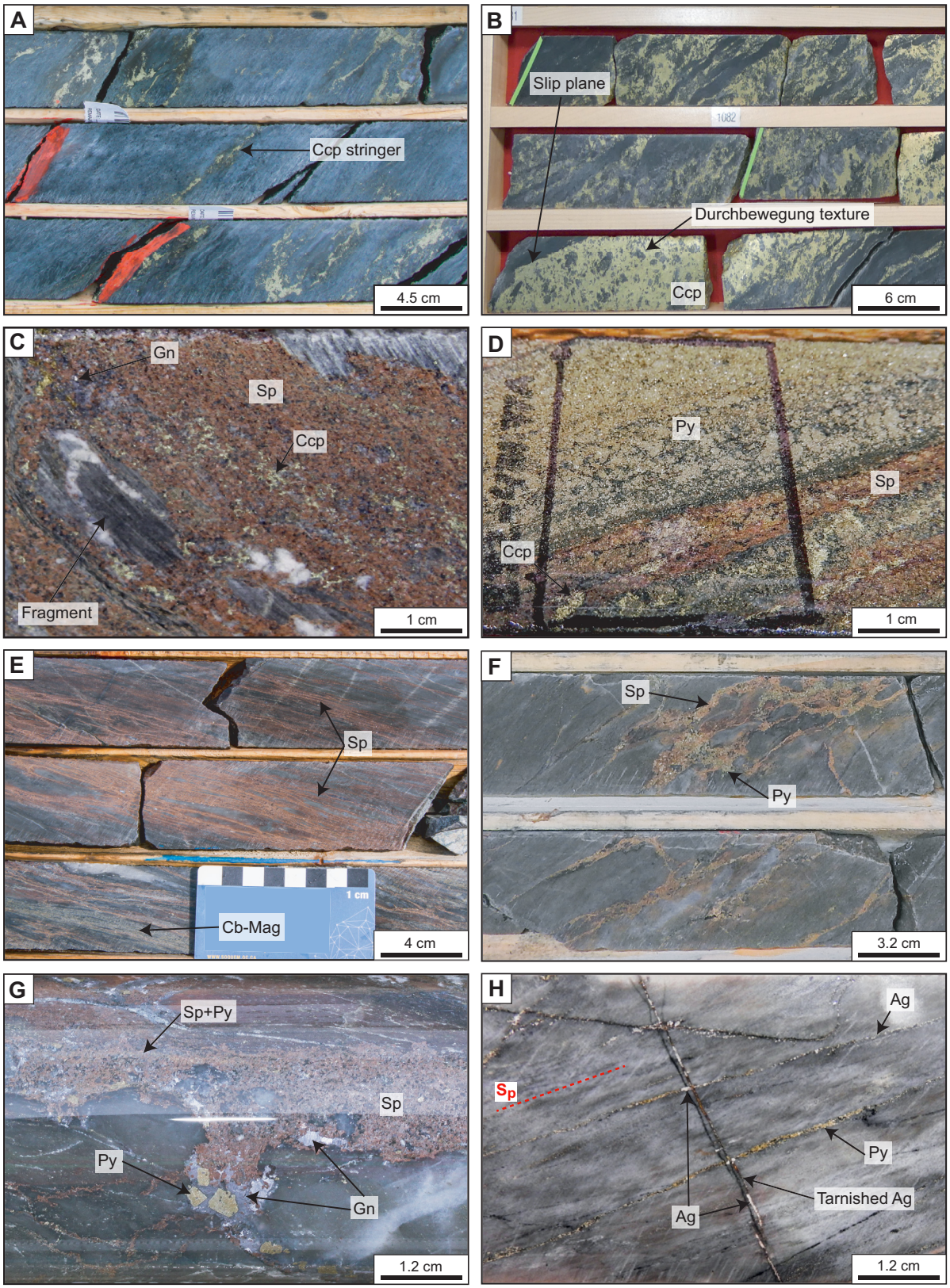

Figure 7. a and b) Semi-massive to massive chalcopyrite veins/stringers of the Copper zone, with sliding planes and durchbewegung texture. **c)** Massive sphalerite-rich ore of the Main Zinc zone (MZZ), with rounded rhyolite fragments. **d)** Massive pyrite-rich ore of the MZZ, with tectonometamorphic banding with sphalerite. **e)** Sphalerite-rich stratabound replacement mineralization of the Upper Zinc zone (UZZ) hosted in volcaniclastic rhyolite A. **f)** Sphalerite-pyrite veinlets/stringers hosted in MZZ hanging-wall rhyolite A. **g)** Polymetallic silver-rich piercement vein composed of sphalerite and galena with pyrite porphyroblasts. **h)** Native silver microveinlets of the UZZ that crosscut the main foliation (S_p). Abbreviations: Ag = silver, Cb = carbonate mineral, Ccp = chalcopyrite, Gn = galena, Mag = magnetite, Py = pyrite, Sp = sphalerite.

Table 2. Whole-rock geochemistry for selected elements of representative ore samples.

Zone	Copper Zone		Main Zinc Zone					
Type	SMS veins/stringers		MS			SMS		DS
Sample #	***23_144.1***	***245_860.6***	***266_666.7***	***259_451.9***	***250_294.4***	***259_454.5***	***238_605.7***	***259_455.9***
Cu (%)	14.35	12.6	0.28	0.74	0.22	1.04	0.36	2.12
Zn (%)	0.105	0.04	24.4	>30	16.85	12.4	7.44	1.605
Pb (ppm)	35.8	13.7	5440	650	13600	4610	1760	397
Au (ppm)	4.55	19.95	0.057	0.061	0.059	0.058	0.016	0.081
Ag (ppm)	37.8	23.1	191	149	419	171	122	388
Au/Ag	1 : 8.3	1 : 1.2	1 : 3350	1 : 2442	1 : 7101	1 : 2948	1 : 7625	1 : 4790
SiO_2 (%)	39	49	13.4	12.45	15.2	44.5	20.1	32.4
CaO (%)	0.31	0.02	0.98	0.77	5.22	0.51	3.56	5.86
Fe (%)	19.45	13.8	22.9	20.1	18.4	13.95	28.5	23.4
Mn (%)	0.37	0.03	0.19	0.15	0.17	0.3	0.46	0.96
S (%)	17	13.6	35	32.6	26.8	14.2	27.2	4.3
As (ppm)	12.7	3.3	178.5	195.5	1450	153.5	1190	633
Bi (ppm)	1205	602	20.9	1.67	0.93	1.55	2.05	0.21
Cd (ppm)	3.34	0.84	>1000	>1000	>1000	698	470	114
Sb (ppm)	4.5	2.04	47.6	12.2	333	33.6	15.25	12.35
Se (ppm)	143	114	44	29	5	2	12	1
Sn (ppm)	112	173	3.2	7.1	17.3	5.4	8	1.3
Tl (ppm)	0.05	0.25	0.54	1.21	1.92	4.12	1.24	3.18
Sum REE	26.48	74.78	15.47	22.14	237.15	26.38	12.16	37.72

Main and Upper Zinc Zones

The Main Zinc zone consists of two mineralized bodies that are divided into a western and eastern part and are located at the same stratigraphic level. The largest one is situated in the eastern part of the deposit (Fig. 2a, 6) and forms a subvertical panel that plunges 65° to the southwest with a thickness ranging from 40 m close to surface, to roughly 10 m at about 750 m below surface. It has a lateral extent of approximately 400 m. The easternmost mineralized body hosts the only occurrence of semi-massive to massive mineralization (white/red circles on Fig. 6e,f,g), named the main lens, which has the same geometry.

The Upper Zinc zone is less continuous and consists of small mineralized panels that are hosted in rhyolite A, in the hanging wall of the Main Zinc zone. The lateral extension can be up to 200 m long and the thickness varies from 3 to 25 m (Fig. 2a). The best intervals contain up to 10 wt% Zn.

The Main and Upper Zinc zones show four mineralization styles: 1) semi-massive to massive sulphides; 2) disseminated sulphides; 3) sulphide veins and stringers; and 4) silver-rich veins and veinlets. Whole-rock analyses of representative samples for each mineralization style are given in Table 2.

Semi-massive to massive sulphides

The semi-massive to massive Zn-bearing sulphide lens (i.e. main lens), which is up to 3.5 m thick, is more massive at the base (north) with ≥65 vol.% sulphides and becomes semi-massive (35–65 vol.% sulphides) towards the top of the lens. Sphalerite is the most abundant phase (20–60 vol.%: Fig. 7c), although pyrite can locally dominate (20–40 vol.%: Fig. 7d). Pyrite is generally recrystallized (granoblastic), although porous and/or nodular primary textures are locally partly preserved (Fayard, in prep). Chalcopyrite (1–5 vol.%) is mainly found at the base in the central part of the lens. Galena (≤2 vol.%) is present in association with sphalerite in the uppermost part of the lens. Native Ag and Ag-sulphosalts (e.g. freibergite) are common in the massive sulphides in the presence of galena. Magnetite is also present (1–3 vol.%) in the upper semi-massive part of the Main Zinc zone. Carbonate minerals are common as gangue in the massive sulphide zones. The sulphide assemblages are generally deformed and are largely recrystallized. Wall-rock fragments of host rhyolite A are common in the massive and semi-massive sulphides (Fig. 7c).

Disseminated sulphides

Zones of disseminated sulphides are present on both sides of the semi-massive to massive sulphides of the Main Zinc zone. Disseminated sulphides are also associated with the Upper Zinc zone. These zones mainly comprise finely disseminated pyrite and sphalerite. Total sulphide abundance generally varies between 2 to locally 10 vol.%, with pyrite more abundant than sphalerite.

The central part of the Upper Zinc zone is composed of 10-40 vol.% reddish sphalerite in very thin (0.2–1 mm) veinlets or stringers, and bands (Fig. 7e) that transition into a carbonate-pyrite-(magnetite) assemblage at the top of the zone. Laterally, this mineralization is more deformed and remobilized, forming semi-massive breccia zones with quartz and rhyolite clasts in a sphalerite matrix.

Sulphide veins and stringers

Zones of sulphide veins and stringers, strongly flattened into the S_p foliation, are common in the hanging wall to the Main and Upper Zinc zones in rhyolite A (Fig. 2a). Some of the veins appear to be late- to post-deformation as they cut across the S_p foliation.

A zone of sulphide veins and stringers is located within 5 m under (north) the main massive sulphide lens of the Main Zinc zone. These 0.2 to 5 cm thick veins and veinlets are partly to completely transposed into the S_p foliation. The veins consist of sphalerite ±pyrite-chalcopyrite.

A second zone of veinlets and veins is located in the upper part of the Main Zinc zone. This hanging-wall veining is better developed where the Main Zinc zone is devoid of massive sulphides (e.g. westernmost part, and easternmost part, close to surface: Fig. 6). These 0.2 to 2 cm thick veins mainly consist of reddish to orange sphalerite with pyrite and, very locally, galena. The veins appear as both tabular, parallel with the S_p foliation, and as a relatively weakly deformed anastomosing network in fragmental intervals (Fig. 7f). These sphalerite-rich vein and stringer zones are locally enriched in Ag in the presence of galena.

Silver-rich veins and veinlets

This type of mineralization consists of polymetallic piercement veins and Ag microveinlets. Piercement veins are common in the uppermost part of the massive sulphide lens in the Main Zinc zone, as well as in the Upper Zinc zone. Such veins are considered late as they cut across the S_p foliation and are not associated with a specific alteration. They are up to a few centimetres thick and contain variable amounts of sulphides and quartz. Sulphides typically consist of sphalerite and galena, with lesser amounts of other sulphides (Fig. 7g). Chalcopyrite is locally present, as well as some granoblastic pyrite. Piercement sulphide veins generally contain high Ag (typically 70–500 ppm) and Sb grades (≤300 ppm). The Ag-bearing accessory phases are mainly freibergite, allargentum, and less commonly, pyrargyrite and stephanite.

The Ag microveinlets are parallel and/or at a high sharp angle to the S_p foliation, forming a network pattern (Fig. 7h). They carry the highest Ag grades (commonly >1000 ppm) of the deposit. These veins are rectilinear, undeformed, and cut across the foliation, and are thus considered as late features that represent remobilized material in post-S_p fractures. Such Ag-rich microveinlets are common in the Upper Zinc zone where they contain abundant native silver with some micro-grains of automorphic pyrite. They are also locally present in the Main Zinc zone (under the main lens), where they contain acanthite instead of native Ag close to Fe-poor sphalerite veinlets.

Metal Distribution

Assay data from SOQUEM were used to illustrate the longitudinal metal distribution in the Copper, Main, and Upper Zinc zones, as shown in Figure 6. Interpolation methods, based on Camus and Valdnais-Leblanc (2018), are described in Fayard (in prep).

Copper distribution is represented on a composite longitudinal view because Cu-rich intervals are present at different stratigraphic positions in the footwall rhyolite A, where it occurs as several juxtaposed flattened bodies (Fig. 2a, 6a). Copper is unevenly distributed in the Copper zone. It is mainly concentrated close to surface and in several separate areas at depth (Fig. 6b), whereas Zn concentrations are very low except where the Copper zone converges with the Main Zinc zone (Fig. 6a,d). An area of lower Cu values in the Copper zone underlies the Main Zinc zone. Copper grades are low and much localized in the Main Zinc zone (Fig. 6e). The Main Zinc zone occurs as two separate mineralized bodies at the same stratigraphic horizon (Fig. 6a,f). Slightly higher in the stratigraphy is the Upper Zinc zone (Fig. 6a,h). Zinc in the Main Zinc zone occurs in a steeply southwest-plunging ore shoot that is parallel with the stretching lineation, which also parallels Cu distribution in the Copper zone. Gold is concentrated in the Copper zone and the distribution and geometry of the higher grade zones mimic those of Cu, although less laterally extensive (Fig. 6c). The high-grade zones are also parallel with the L_p stretching lineation, forming narrow shoots.

Silver grades are very low in the Copper zone (typically ≤20 ppm, 6.7 ppm on average). However, it is strongly enriched in the Main Zinc zone (average 100.4 ppm), where its distribution mimics that of Zn (Fig. 6g). Higher Ag grades (>200 ppm) occur mainly along the western edge of the massive sulphide lens of the Main Zinc zone. In the Upper Zinc zone, Ag is present in all the mineralized zones (average 138 ppm) with common intersections at 200 to >1000 ppm. These very high Ag values do not necessarily correlate with higher Zn grades (Fig. 6h,i). Moreover, although not illustrated in the longitudinal views shown in Figure 6, Pb is commonly associated with some of these high-Ag values (Fig. 5) but not the highest, which is a reflection of the complex mineralogy of Ag.

Despite significant syn-D_p transposition, flattening, and stretching in the direction of the L_p lineation, the deposit-scale metal distribution is still typical of many Archean VMS deposits with an Au-bearing stringer-style Cu-rich zone at the base and a stratiform Ag-bearing zinc lens in the upper part (Hannington, 2014). The Cu-rich part of the main lens at 653000 mE in the Main Zinc zone (Fig. 6e) probably represents the main upflow zone and corresponds to the area where the slightly discordant (transposed) Copper zone draws close to the Main Zinc zone at depth (Fig. 2a, 6a).

Precious metal-bearing phases

Gold occurs as ≤200 μm native gold grains in chalcopyrite, associated locally with sphalerite and pyrrhotite (Fig. 8a,b) or in quartz (Fig. 8c). Gold has a Ag content of 20 wt% on average with some electrum (i.e. Ag content >45 wt%) in the Main Zinc zone. Micron-size Bi- and Se-bearing sulphides are common in the Copper zone: bismuthinite (Bi_2S_3), laitakarite (Bi_4Se_2S), ikunolite ($Bi_4(S,Se)_3$), and native Bi have been identified (Fig. 8d,e). Traces amounts of stannite (Cu_2FeSnS_4) and cassiterite (SnO_2) are also present in the chalcopyrite of the Copper zone.

Silver-rich minerals and Ag-Sb sulphosalts are common in the Main and Upper Zinc zones. Freibergite ($(Cu,Ag)_{10}(Fe,Zn)_2Sb_4S_{13}$), which is generally associated with galena (Fig. 8f), is the main Ag-bearing mineral. It is also common in veinlets intergrown with anhedral native silver and allargentum ($Ag_{1-x}Sb_x$), chalcopyrite, and galena (Fig. 8g). Pyrargyrite (Ag_3SbS_3) and stephanite (Ag_5SbS_4) are locally present in freibergite masses and in galena-rich veins, where pyrargyrite replaces pyrrhotite, forming complex secondary textures associated with allargentum. Native silver is common and mainly appears in the late crosscutting microveinlets and disseminations in the Upper Zinc zone and in small complex clusters (associated with chalcopyrite-freibergite intergrowths) in galena.

DISCUSSION

Primary and Secondary Controls on Mineralization Styles and Geometry

Although the volcanic pile that hosts the B26 deposit has been tilted and strongly deformed (flattening, stretching, and transposition), primary features are partly preserved. The overall geometry of the mineralized system, comprising chalcopyrite stringers associated with a subconcordant to slightly discordant sericite-chlorite halo that lies underneath concordant Zn-rich sulphide lenses, is typical of many Archean and younger VMS deposits (Galley et al., 2007).

Although intensely transposed, the Cu-rich veins and proximal chlorite-sericite alteration assemblage of the Copper zone are still slightly discordant to the stratigraphic sequence and S_p foliation. The veins are both rooted in the rhyolite B and in the footwall andesites and are connected with the stratiform sulphide lens of the Main Zinc zone in the uppermost part of rhyolite A. Therefore, the Copper zone is interpreted as an extensive discordant stringer zone that has been flattened and transposed during the main (D_p) deformation event.

The Main Zinc zone overlies the Copper zone sulphide stringers and forms a stratabound to stratiform ore lens (main lens) hosted in rhyolite A in a large, semi-concordant sericite-dominated alteration halo. The Main Zinc zone probably formed between two separate flows of rhyolite A (Fayard et al., 2020). The presence of massive sulphides along a specific horizon suggests that part of the Main Zinc zone may have formed through exhalative activity on the seafloor. However, a large part of the mineralization was formed by subseafloor replacement, as indicated by the presence of partly preserved volcaniclastic rocks in the semi-massive, disseminated, and vein-style mineralization in both the footwall and hanging wall as well as in the massive sulphide intervals and by the stacking of mineralized zones in the stratigraphic sequence. Thus, it is suggested that the hanging-wall rhyolite A was emplaced soon after the beginning of the massive sulphide lens deposition at, or near the seafloor, making the calc-alkaline rhyolite A emplacement and hydrothermal activity broadly coeval at about 2728 Ma, the age of rhyolite A (Fayard et al., 2020). The thin (0.5–1.5 m thick) satellite semi-massive pyrite lens located above the Upper Zinc zone (in the rhyolite B felsic crystal tuff facies) and associated with moderate sericite-carbonate-albite alteration (Fig. 2a, 4) seems to be the product of late low-temperature and metal-poor fluids. These fluids were locally trapped due to an impermeable barrier formed by sills of rhyolite B in the volcanoclastic facies of rhyolite A, perhaps marking the waning stages of the B26 hydrothermal system.

Metal Zonation and Conditions of Deposition

Contrary to many Archean VMS deposits that show a gradual transition from Cu-rich basal to Zn-rich top parts (e.g. Noranda deposits: Galley et al., 2007), Cu and Zn are strongly decoupled at the deposit-scale at B26. The Copper, Main, and Upper Zinc zones are located at different stratigraphic levels and the mineralized system extends over a large part of the volcanic pile, i.e., ≥200 m after tectonic flattening. The original thickness of the host package and the vertical extent of the mineralized system can only be speculated, but using a conservative flattening ratio of 5-to-1 given by the volcanic clasts aspect ratio, the system might have had an original vertical extent of well over 500 m. As

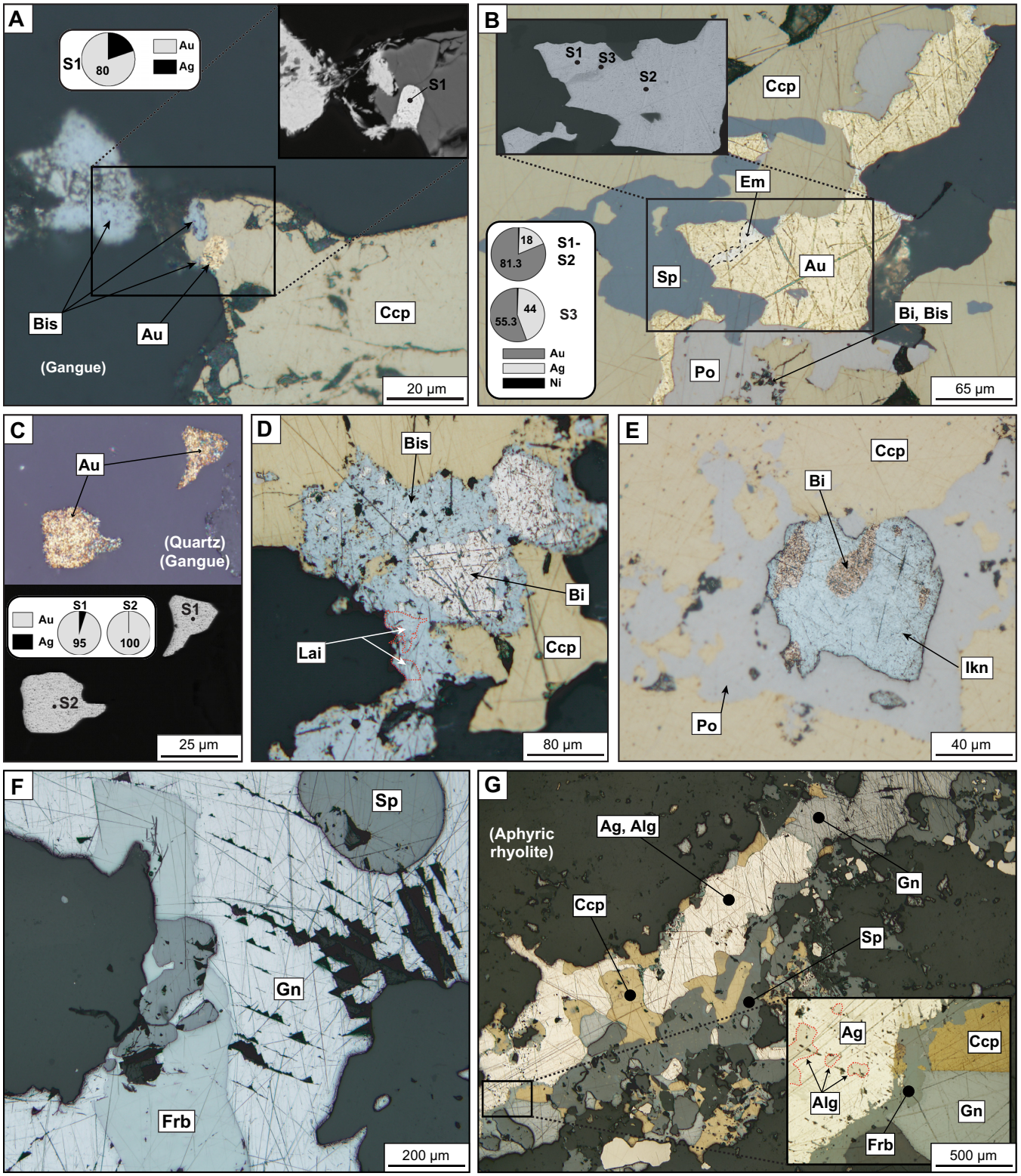

Figure 8. Reflected light microphotographs of ore assemblages. **a)** Gold-rich electrum and bismuthinite in chalcopyrite in the Copper zone. **b)** Native gold intergrown with minor Au-rich electrum and micrograins of native bismuth and bismuthinite in chalcopyrite, sphalerite, and pyrrhotite in the Copper zone. **c)** Free gold grains in the matrix of a chalcopyrite vein of the Copper zone. **d)** Bismuthinite, laitakarite, and native Bi in chalcopyrite, Copper zone. **e)** Native bismuth and ikunolite in pyrrhotite, Copper zone. **f)** Freibergite in galena in a piercement vein, Upper Zinc zone. **g)** Veinlet composed of complex intergrowths of native silver and allargentum, associated with freibergite, chalcopyrite, sphalerite, and galena within a polymetallic piercement vein, Upper Zinc zone. Abbreviations: Alg = allargentum, Au = gold, Bi = bismuth, Bis = bismuthinite, Em = electrum, Frb = freibergite, Ikn = ikunolite, Lai = laitakarite, Po = pyrrhotite, S_1 to S_3 = spot EDS semi-quantitative analyses.

in a classic VMS model, Cu at B26 was probably transported as a chloro-complex in high-temperature (325–375ºC), slightly acidic fluids, with conductive cooling over a significant vertical gradient as the main precipitating factor (Hannington, 2014). Zinc, Pb, and Ag were transported much higher up in the system as thio-complexes in lower temperature fluids that were destabilized through mixing with seawater (Galley et al., 2007). Such a geometry with such a strong decoupling of metals (Cu vs Zn-Pb) is tentatively interpreted as originating from a shallow water system in which metal transport and precipitation are largely controlled by the seawater boiling curve (e.g. Hannington, 2014).

Gold is mostly associated with Cu and the high-temperature assemblage (Bi, Se, Sn±In) at B26. Such an association is compatible with the transport of Au by chloro-complexes ($AuCl_2$) along with Cu (Huston, 2000).

Silver can precipitate at both high and low temperatures, depending on the redox state, pH, and Sb-Bi content of the fluid, and thus Ag can be incorporated in a wide range of host minerals (Huston et al., 1996). At B26, freibergite is the principal Ag-bearing mineral in the inferred low-temperature assemblage of the Main and Upper Zinc zones. According to Huston et al. (1996), this indicates that Ag has precipitated at low temperature from relatively oxidized fluids characterized by low ΣAs/ΣSb and ΣBi/ΣSb ratios. No micro-analyses of galena from B26 are available, but given the very low ΣBi/ΣSb ratio of bulk samples, galena is probably Sb-rich, in which case it can incorporate less Ag, and thus favours the precipitation of Ag-Sb sulphosalts. However, Huston et al. (1996) mention that there are exceptions to their model (e.g. Heath-Steele and Rosebery deposits) where Ag-Sb sulphosalts are stabilized under reduced conditions from low-temperature fluids. More work is underway to better constrain the possible nature of the Ag-transporting fluids at the B26 deposit.

Finally, the potassic feldspar-quartz microcrystalline alteration assemblage characterizing a part of the hanging-wall rhyolite A (Fig. 2b) could indicate low temperatures and near-neutral pH fluids buffered by mixing with ambient seawater at the margin of the hydrothermal system (e.g. Thalanga deposit: Paulick et al., 2001).

Source of Precious Metals and Possible Primary Enrichment Mechanisms

Silver and Pb are known to have been initially present in greater amounts in continental crust-derived rhyolites (Barrie and Hannington, 1999). However, Archean VMS deposits of the Abitibi greenstone belt are generally considered associated with oceanic-crust-derived rocks that have, in most cases, low Pb and Ag (Barrie and Hannington, 1999). Archean calc-alkaline felsic centres have empirically been associated with some of the largest synvolcanic Au deposits of the southern Superior Province (e.g. Doyon-Bousquet-LaRonde camp: Mercier-Langevin et al., 2015; Yergeau et al., 2015, Horne 5: Krushnisky et al., 2020, and Rainy River: Pelletier et al., 2015), suggesting an association between magmatic processes and precious metal-bearing volcanogenic hydrothermal systems in the southern Superior Province (e.g. Mercier-Langevin et al., 2015). Although more work is needed to determine the precise nature of the mineralizing fluid(s) and source(s) of metals at B26, some elements suggest the potential involvement of magmatic volatiles in the hydrothermal system (Fig. 9). This includes the presence of trace elements such as Bi, Se, Sn, and In (Table 2), a strong Au and Bi correlation (r = 0.75: Fayard, in prep), and the spatial and temporal association with the Brouillan synvolcanic pluton and the Selbaie epithermal-style (Larson and Hutchinson, 1993) Zn-Cu-Ag-Au deposit.

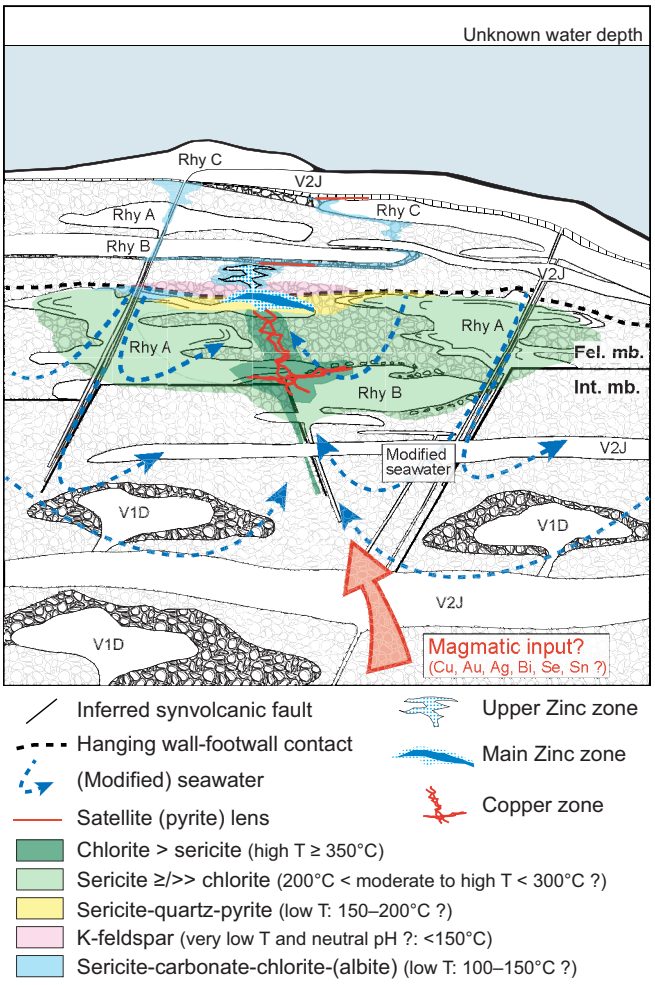

Figure 9. Inferred pre-deformation hydrothermal architecture of the B26 deposit. Lithological unit colours have been removed but codes and textural patterns are the same as in Figure 2a. Abbreviations: Fel. mb. = felsic member, Int. mb. = intermediate member, mod. = moderate, T = temperature.

Effect of Metamorphism and Deformation on Precious Metals Distribution

The general spatial correlation between Au and Cu distribution in the Copper zone and its association with other trace metals such as Bi are in agreement with a syngenetic introduction of Au in the system. However, the occurrence of higher grade Au zones as narrow shoots parallel to the stretching lineation suggests local (metre scale or less) remobilization during the main deformation.

Silver in the Main and Upper Zinc zones was locally remobilized due to metamorphism and deformation, but its overall association with the syngenetic sulphide zones also indicates a primary synvolcanic origin. Evidence of mechanical remobilization is given by the presence of post-S_p piercement veins with pyrite and sphalerite transitioning to chalcopyrite, galena, and sulphosalts in the tip of the veins due to the increasing ductility of these phases. Further remobilization, probably through chemical processes (solubilization), led to the crystallization of native Ag in very late fractures and the gradual increase in the Ag grade of piercement veins and fractures. Chemical remobilization is also supported by the presence of galena and sulphosalts at pyrite grain boundaries. The presence and solubility of Sb largely control Ag grades and distribution (remobilization) adjacent to the sulphide zones. Freibergite is the main Ag-bearing phase within and in proximity to the sulphide lenses. Therefore, the Sb:Ag ratio controls the nature of the Ag-bearing phases with a transition from freibergite (proximal to trace metal-bearing sulphide source) to allargentum to native Ag away from the sulphide zones.

Silver-rich mineralization is not unique to B26 and seems to be a recurring feature in the Brouillan volcanic complex area. The Selbaie deposit is known for very high-grade Ag intersections, commonly as native silver and freibergite (Larson and Hutchinson, 1993; Taner, 2000). Numerous prospects hosted in the Brouillan volcanic complex (e.g. Wagosic, Carheil, and Puiseaux: SIGÉOM, 2019 - Fig. 1) also contain significant Ag in both VMS-style and vein-style ore systems. This suggests the presence of some underlying, district-scale controls on the precious metal enrichment processes, which are the subject of ongoing research as part of this study.

ACKNOWLEDGMENTS

This report is a contribution to the Targeted Geoscience Initiative Program of the Geological Survey of Canada. Support for this study was provided through the Gold Project Activity G- 1.1: Gold through space and time at the Archean. Q. Fayard is conducting a TGI-supported M.Sc. at the Université du Québec à Chicoutimi. The authors would like to thank SOQUEM Inc. for their support and collaboration in this study and access to data. This report benefited from constructive comments by D. Yergeau and S. Castonguay.

REFERENCES

Adam, D., 1997. Rapport d'une campagne de forage, propriété B26, canton Brouillan, Québec, Canada; Les métaux Billiton Canada Inc., GM 57187, 14 p.

Barrie, C.T. and Hannington, M.D., 1999. Classification of volcanic-associated massive sulfide deposits based on host-rock composition; in Volcanic-associated massive sulfide deposits: Processes and examples in modern and ancient settings, (ed.) C.T. Barrie and M.D. Hannnington; Reviews in Economic Geology, v. 8, p. 1–11.

Barrie, C.T. and Krogh, T.E., 1996. U-Pb zircon geochronology of the Selbaie Cu-Zn-Ag-Au mine, Abitibi Subprovince, Canada; Economic Geology, v. 91, p. 563–575.

Beaudin, A., 2017. Rapport de la campagne de sondages hiver-été 2014, propriété B26, canton Brouillan, Québec, Canada; SOQUEM Inc., GM 70058, 45 p.

Camus, Y. and Valdnais-Leblanc, O., 2018. Rapport Technique NI 43-101 et estimation des ressources, Projet B26, Québec; Unpublished internal report to SOQUEM Inc., 136 p.

Castonguay, S., Dubé, B., Wodicka, N., and Mercier-Langevin, P., 2020. Geological setting and gold mineralization associated with the Sunday Lake and Lower Detour deformation zones, northwestern Abitibi greenstone belt, Ontario and Quebec; *in* Targeted Geoscience Initiative 5: Contribution to the Understanding of Canadian Gold Systems, (ed.) P. Mercier-Langevin, C.J.M. Lawley, and S. Castonguay; Geological Survey of Canada, Open File 8712, p. 127–1142. doi:10.4095/323670

Daigneault, R., Mueller, W.U., and Chown, E.H., 2004. Abitibi greenstone belt plate tectonics: the diachronous history of arc development, accretion and collision; in The Precambrian Earth: Tempos and events, (ed.) P.G. Eriksson, W. Altermann, D.R. Nelson, W.U. Mueller, and O. Catuneanu; Developments in Precambrian Geology 12, p. 88–103.

Debreil, J.-A., Ross, P.-S., and Mercier-Langevin, P., 2018. The Matagami district, Abitibi greenstone belt, Canada: Volcanic controls on Archean volcanogenic massive sulfide deposits associated with voluminous felsic volcanism; Economic Geology, v. 113, p. 891–910.

Deptuck, R., Squair, H., and Wierzbicki, V., 1982. Geology of the Detour zinc–copper deposits, Brouillan Township, Quebec; *in* Precambrian sulfide deposits, H.S. Robinson Memorial Volume, (ed.) R.W. Hutchinson, C.D. Spece, and J.M. Franklin; Geological Association of Canada, Special Paper 25, p. 319–342.

Faure, S., 2015. Prolongement de la faille Sunday Lake (mine Detour Gold, Ont.) au Québec et son potentiel pour les minéralisations aurifères et en métaux de base; CONSOREM Project 2013-02, 41 p. < http://www.consorem.ca/production_scientifique/2013_02/Rapport%202013-02%20DETOUR_VF_20160401.pdf> [accessed November 15, 2019]

Faure, S., Jébrak, M., and Bouillon, J.J., 1990. Géologie et minéralisations en Zn–Cu–Ag–Au de Les Mines Selbaie; *in* The northwestern Quebec polymetallic belt; A summary of 60 years of mining exploration; Proceedings of the Rouyn-Noranda 1990 symposium, (ed.) M. Rive, P. Verpaelst, Y. Gagnon, J.M. Lulin, G. Riverin, and A. Simard; Canadian Institute of Mining and Metallurgy, Special Volume 43, p. 363–372.

Faure, S., Jébrak, M., and Angelier, J., 1996. Structural evolution of Les Mines Selbaie, northern Abitibi, Québec, Canada; Exploration and Mining Geology, v. 5, p. 215–230.

Fayard, Q., Mercier-Langevin, P., Daigneault, R., and Perreault, S., 2018. Volcanic, hydrothermal and structural controls on the nature and distribution of base and precious metals at the B26 project, Brouillan volcanic complex, Abitibi, Quebec; *in* Targeted Geoscience Initiative: 2017 report of activities, volume 1, (ed.) N. Rogers; Geological Survey of Canada, Open File 8358, p. 99–103.

Fayard, Q., Mercier-Langevin, P., Wodicka, N., Daigneault, R., and Perreault, S., 2020. The B26 Cu-Zn-Ag-Au project, Brouillan volcanic complex, Abitibi, part 1: Geological setting and geochronology; *in* Targeted Geoscience Initiative 5: Contribution to the Understanding of Canadian Gold Systems, (ed.) P. Mercier-Langevin, C.J.M. Lawley, and S. Castonguay; Geological Survey of Canada, Open File 8712, p. 93–107. doi:10.4095/323668

Galley, A.G., Hannington, M.D., and Jonasson, I.R., 2007. Volcanogenic massive sulphide deposits; *in* Mineral deposits of Canada: A synthesis of major deposit-types, districts metallogeny, the evolution of geological provinces, and exploration methods, (ed.) W.D. Goodfellow; Geological Association of Canada, Mineral Deposits Division, Special Publication 5, p. 141–161.

Hannington, M.D., 2014. Volcanogenic massive sulfide deposits; *in* Treatise on Geochemistry (Second Edition), Volume 13: Geochemistry of Mineral Deposits, (ed.) S. Scott; Elsevier Science, Netherlands, p. 463–488.

Huston, D.L., 2000. Gold in volcanic-hosted massive sulphide deposits; distribution, genesis, and exploration; *in* Gold in 2000, (ed.) S.G. Hagemann and P.E. Brown; Reviews in Economic Geology, v. 13, p. 401–426.

Huston, D.L., Jablonski, W., and Sie, S.-H., 1996. The distribution and mineral hosts of silver in eastern Australian volcanogenic massive sulfide deposits; The Canadian Mineralogist, v. 34, p. 529–546.

Ishikawa, Y., Sawaguchi, T., Iwaya, S., and Horiuchi, M., 1976. Delineation of prospective targets for Kuroko deposits based on modes of volcanism of underlying dacites and alteration haloes; Mining Geology, v. 26, p. 105−117.

Krushnisky, A., Mercier-Langevin, P., Ross, P.-S., Goutier, J., Pilote, C., and Bernier, C., 2020. Geology and gold enrichment at the Horne 5 Archean volcanogenic massive sulphide deposit, Abitibi greenstone belt, Quebec: a synthesis; *in* Targeted Geoscience Initiative 5: Contribution to the Understanding of Canadian Gold Systems, (ed.) P. Mercier-Langevin, C.J.M. Lawley, and S. Castonguay; Geological Survey of Canada, Open File 8712, p. 31–44. doi:10.4095/323663

Lacroix, S., 1994. Géologie de la partie ouest du sillon Harricana-Turgeon, Abitibi; Ministère des Ressources naturelles du Québec, MB 94-54, 26 p.

Large, R.R., Gemmell, J.B., Paulick, H., and Huston, D.L., 2001. The alteration box plot: A simple approach to understanding the relationship between alteration mineralogy and lithogeochemistry associated with volcanic-hosted massive sulfide deposits; Economic geology, v. 96, p. 957–971.

Larson, J.E., 1987. Geology, geochemistry and volcanic history of Les Mines Selbaie, Quebec, Canada: An Archean epithermal system; Ph.D. thesis, Colorado School Mines, Golden, Colorado, 388 p.

Larson, J. E. and Hutchinson, R. W., 1993. The Selbaie Zn-Cu-Ag deposits, Quebec, Canada; an example of evolution from subaqueous to subaerial volcanism and mineralization in an Archean caldera environment; Economic Geology, v. 88, p. 1460−1482.

Legault, M., Gauthier, M., Jébrak, M., Davis, D., and Baillargeau, F., 2002. Evolution of the subaqueous to near-emergent Joutel volcanic complex, Northern Volcanic Zone, Abitibi Subprovince, Quebec, Canada; Precambrian Research, v. 115, p. 187−221.

Marshall, B. and Gilligan, L.B., 1989. Durchbewegung structure, piercement cusps, and piercement veins in massive sulfide deposits: formation and interpretation; Economic Geology, v. 84, p. 2311–2319.

Mercier-Langevin, P., Hannington, M.D., Dubé, B., Piercey, S.J., Peter, J.M., and Pehrsson, S.J., 2015. Precious metal enrichment processes in volcanogenic massive sulphide deposits – a summary of key features, with an emphasis on TGI-4 research contributions; *in* Targeted Geoscience Initiative 4: Contributions to the understanding of volcanogenic massive sulphide deposits genesis and exploration methods development, (ed.) J.M. Peter and P. Mercier-Langevin; Geological Survey of Canada Open File 7853, p. 117–130.

Paulick, H., Herrmann, W., and Gemmell, B., 2001. Alteration of felsic volcanics hosting the Thalanga massive sulfide deposit (Northern Queensland, Australia) and geochemical proximity indicators to ore; Economic Geology, v. 96, p. 1175–1200.

Pelletier, M., Mercier-Langevin, P., Dubé, B., Crick, D., Tolman, J., McNicoll, V.J., Jackson, S.E., and Beakhouse, G.P., 2015. The Rainy River "atypical" Archean Au deposit, western Wabigoon Subprovince, Ontario; *in* Targeted Geoscience Initiative 4: Contributions to the understanding of Precambrian lode gold deposits and implications for exploration, (ed.) B. Dubé and P. Mercier-Langevin; Geological Survey of Canada, Open File 7852, p. 193–207.

Rieder, M., Cavazzini, G., D'yakonov, Y.S., Frank-Kemenetskii, V.A., Gottardi, G., Guggenheim, S., Koval, P.V., Müller, G., Neiva, A.M.R., Radoslovich, E.W., Robert, J.-L., Sassi, F.P., Takeda, H., Weiss, Z., and Wones, D.R., 1999. Nomenclature of the micas; Mineralogical Magazine, v. 63, p. 267−279.

SIGÉOM, 2019. Système d'information géominière du Québec. Ministère de l'Énergie et des Ressources Naturelles. <http://sigeom.mines.gouv.qc.ca> [accessed November 15, 2019]

Taner, M. F., 2000; The Geology of the volcanic-associated polymetallic (Zn, Cu, Ag and Au) Selbaie deposits, Abitibi, Quebec, Canada; Exploration and Mining Geology, v. 9. p. 189−214.

Trépanier, S., Mathieu, L., and Daigneault, R., 2015. CONSONORM_LG: New normative minerals and alteration indexes for low-grade metamorphic rocks; Economic Geology, v. 110, p. 2127–2138.

Trépanier, S., Mathieu, L., Daigneault, R., and Faure, S., 2016. Precursors predicted by artificial neural networks for mass balance calculations: Quantifying hydrothermal alteration in volcanic rocks; Computers & Geosciences, v. 89, p. 32–43.

Yergeau, D., Mercier-Langevin, P., Dubé, B., Malo, M., McNicoll, V.J., Jackson, S.E., Savoie, A., and La Rochelle, F., 2015. The Archean Westwood Au deposit, southern Abitibi: Telescoped Au-rich VMS and intrusion-related Au systems; *in* Targeted Geoscience Initiative 4: Contributions to the understanding of Precambrian lode gold deposits and implications for exploration, (ed.) B. Dubé and P. Mercier-Langevin; Geological Survey of Canada, Open File 7852, p. 177−191.

Geological setting and gold mineralization associated with the Sunday Lake and Lower Detour deformation zones, northwestern Abitibi greenstone belt, Ontario and Quebec

Sébastien Castonguay[1*], Benoît Dubé[1], Natasha Wodicka[2], and Patrick Mercier-Langevin[1]

[1]Geological Survey of Canada, 490 rue de la Couronne, Québec, Quebec G1K 9A9
[2]Geological Survey of Canada, 601 Booth Street, Ottawa, Ontario K1A 0E8
[*]Corresponding author's e-mail: sebastien.castonguay@canada.ca

ABSTRACT

The Detour Lake gold mine (~25 Moz or 775 t Au) and Lower Detour zones (e.g. Zone 58N; 0.53 Moz or 16.6 t Au) are located in the northwestern part of the Abitibi greenstone belt in Ontario. They are spatially associated with the Sunday Lake and Lower Detour deformation zones, which extend eastward into Quebec where they host other auriferous zones (e.g. Vortex and Martiniere-Bug Lake deposits). Gold is associated with quartz-carbonate-pyrite-pyrrhotite±tourmaline veins and/or disseminated to very locally semi-massive sulphides in hydrothermally altered wall rocks. These structurally controlled auriferous zones are hosted in tholeiitic and calc-alkaline volcanic rocks of the 2734 to 2724 Ma Deloro assemblage and in ca. 2694 Ma subalkaline to locally alkaline porphyritic intrusive rocks near faulted contacts with the <2.70 Ga Caopatina clastic sedimentary assemblage. Panels or fault-bounded basin remnants of strained Timiskaming-like polymictic conglomerate locally delineate the regional-scale deformation zones and yield maximum depositional ages of between 2706 and 2692 Ma. These relationships are reminiscent of the prolific southern Abitibi greenstone belt in the Timmins-Porcupine and Val-d'Or gold districts. The revised regional geological setting, coupled with documentation of the key characteristics of gold deposits and their hydrothermally altered host rocks, provide a geological framework for improved mineral exploration strategies in a poorly exposed, but prospective region that includes the giant Detour Lake gold mine.

INTRODUCTION

The principal characteristics of orogenic gold deposits, such as the association with major fault zones, panels of polymictic conglomerate, felsic and locally alkaline intrusions, and various types of hydrothermal alteration (carbonate, biotite, sericite, albite) of tholeiitic and komatiitic basalt are present in the poorly exposed but prospective northwestern Abitibi greenstone belt (e.g. Ayer et al., 2009; Faure, 2015). In Ontario, the Detour Lake mine (~25 Moz or 775 tonnes Au) and Zone 58N (~534,000 oz or 16.6 t Au: Detour Gold Corporation, 2019) are spatially associated with the Sunday Lake and Lower Detour deformation zones, respectively (Fig. 1; Oliver et al., 2012; Castonguay et al., 2019). The latter deformation zones extend into Quebec and control the distribution of syndeformation auriferous zones comprising quartz-carbonate±tourmaline veins, silicified zones, and sulphides in hydrothermally altered wall rocks. This research aims to improve the knowledge of the geological setting, styles of gold mineralization, metallotects, and relative timing of events in the northwestern Abitibi region and draw analogies with that of mineralized corridors in the southern Abitibi greenstone belt. The present paper, which builds on previous reports (e.g. Castonguay et al., 2019), is a synthesis of observations of several gold deposits made through the examination of outcrops and drill core from numerous diamond drillholes and the analysis of new geochemical and geochronological data.

REGIONAL GEOLOGICAL SETTING

The northwestern portions of the Abitibi greenstone belt mostly comprise 2734 to 2724 Ma volcanic rocks of the Deloro assemblage (Fig. 1; Thurston et al., 2008; Ayer et al., 2009; Oliver et al., 2012). The <2707 to 2695 Ma Caopatina assemblage of turbiditic, volcaniclastic, and locally conglomeratic rocks unconformably overlies, or is in tectonic contact with the Deloro assemblage, forming an east-trending elongated sedimentary belt that is similar to those comprising the Porcupine/Cadillac assemblages in the southern Abitibi. To the east in Quebec, these assemblages correlate with the volcanic Manthet and Brouillan groups and the sedimentary Rivière Turgeon Formation, respectively (Lacroix, 1994; Faure, 2015). Synvolcanic (e.g. Brouillan pluton) and pre- to syntectonic (i.e. the main phase of shortening) tonalitic to granodioritic intrusions (e.g. Turgeon and Jeremie plutons) surround

Castonguay, S., Dubé, B., Wodicka, N., and Mercier-Langevin, P., 2020. Geological setting and gold mineralization associated with the Sunday Lake and Lower Detour deformation zones, northwestern Abitibi greenstone belt, Ontario and Quebec; *in* Targeted Geoscience Initiative 5: Contributions to the Understanding of Canadian Gold Systems, (ed.) P. Mercier-Langevin, C.J.M. Lawley, and S. Castonguay; Geological Survey of Canada, Open File 8712, p. 127–142. https://doi.org/10.4095/323670

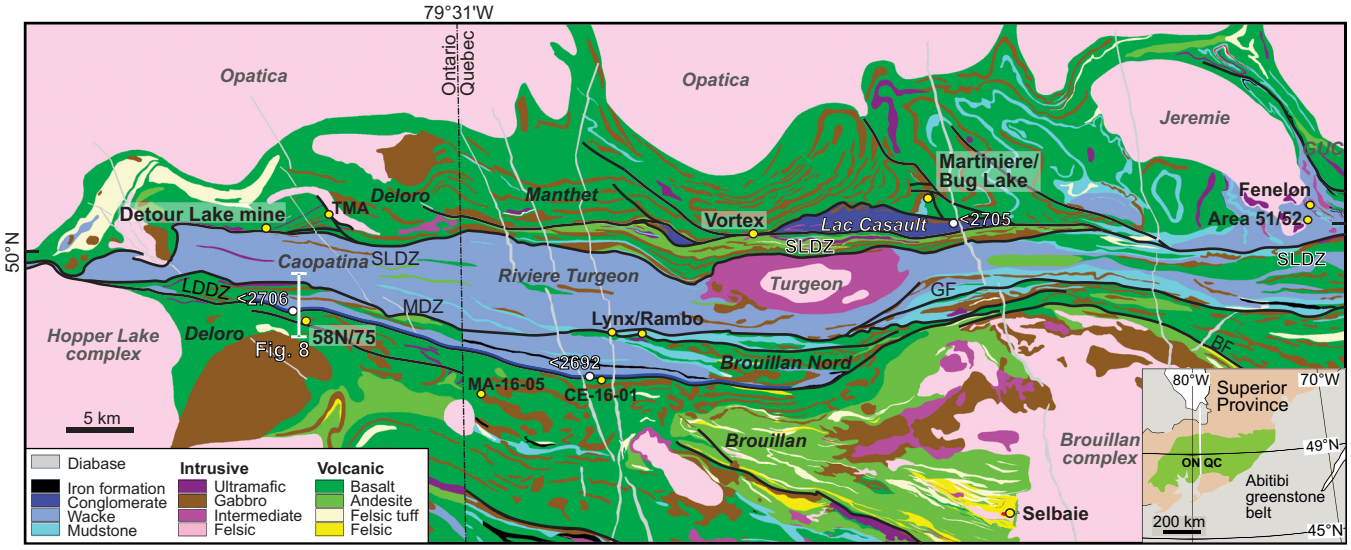

Figure 1. Simplified regional geological map of the northwestern Abitibi belt in the Sunday Lake and Lower Detour 'gold trends' area (*modified from* Faure, 2015) with identification of the main lithological assemblages and deformation/fault zones and the location of gold mines, mineralized zones, and cited exploration drillholes and preliminary U-Pb zircon geochronological data of polymictic conglomerate (maximum age in Ma). Abbreviations: BF = Bapst fault zone, GF = Grasset fault zone, GUC = Grasset ultramafic complex, LDDZ = Lower Detour deformation zone, MDZ = Massicotte deformation zone, SLDZ = Sunday Lake deformation zone.

and cut the volcanic and sedimentary assemblages. The Sunday Lake deformation zone (SLDZ) delineates the northern margin of the Caopatina assemblage, whereas the Lower Detour deformation zone (LDDZ) and its subsidiary Massicotte deformation zones (MDZ) mark its southern contact (Fig. 1). These deformation zones represent the main, first-order controlling structures for gold mineralization in the study area.

Rock units of the study area have been affected by polyphase deformation and greenschist to lower amphibolite facies metamorphism. In the Detour Lake mine area (Fig. 2), Oliver et al. (2012) recognized four

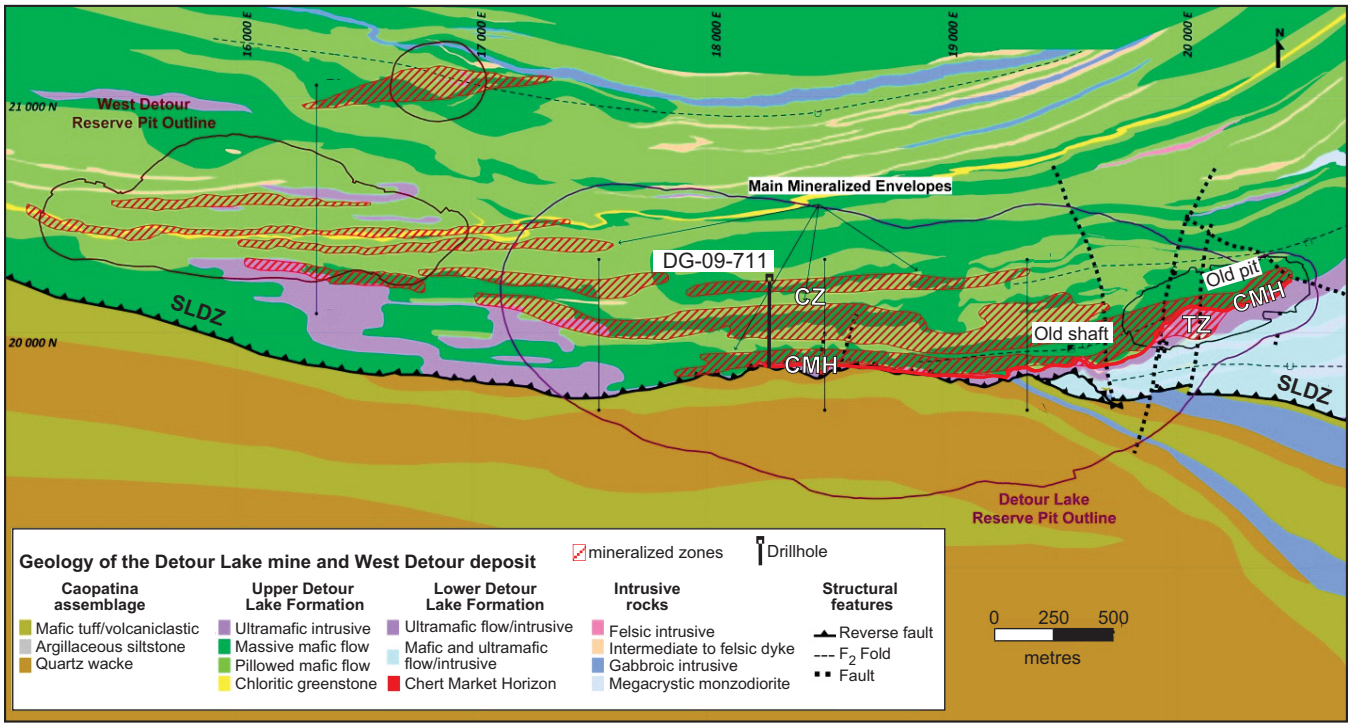

Figure 2. Simplified geological map of the Detour Lake deposit area, with the location of the main mineralized zones and historical and future pit locations outlined (*modified from* Oliver et al. (2012) and Detour Gold Corporation (2018)). Abbreviations: CMH = chert marker horizon, CZ = Calcite Zone, SLDZ = Sunday Lake deformation zone, TZ = Talc zone.

phases of deformation. The earliest phase, related to basin formation and deposition of the Caopatina sedimentary rocks, is not associated with any regional fabric. The main regional foliation (S_2) is generally steeply dipping and axial planar to west-trending tight to isoclinal F_2 folds. S_2 foliation varies from a spaced cleavage to a penetrative schistosity near high-strain or mylonitic zones, such as within the SLDZ (Fig. 1). Oliver et al. (2012) interpret the SLDZ as a south-directed D_2 reverse fault with late sinistral and dextral transpressive components. The steeply dipping S_2 foliation also affects units present within the southern part of the studied area where it is spatially associated with high-strain zones and L-tectonites within the LDDZ and its subsidiary splays. D_3 deformation is defined by broad, open, and southeast-trending F_3 folds that mostly occur north of the SLDZ (Fig. 1). The fourth phase of deformation, D_4, is characterized by a series of southeast-trending late faults that are locally intruded by Proterozoic diabase dykes.

In general, the regional metamorphic grade increases northward, reaching amphibolite facies toward the contact with the Opatica subprovince (Fig. 1). Mafic host rocks at the Detour Lake mine are metamorphosed to amphibolite facies, comprising biotite, actinolite, albite, and almandine garnet (Marmont, 1986; Oliver et al., 2012; Dubosq et al., 2019). Further south and eastward into Quebec, greenschist-facies assemblages predominate.

LITHOSTRATIGRAPHIC FRAMEWORK OF THE SUNDAY LAKE DEFORMATION ZONE

The lithostratigraphic framework of the SLDZ is best documented in the Detour Lake mine area (Fig. 2). Here, the Deloro assemblage has been assigned by Oliver et al. (2012) to the Detour Lake Formation, which these authors further subdivide into upper and lower subunits. The lower Detour Lake Formation comprises ultramafic-dominated flows, mostly komatiitic basalt, and sills or dykes that are intercalated with mafic flows of tholeiitic affinity (Fig. 3a) and gabbroic intrusions. The upper Detour Lake Formation mainly consists of massive to pillowed mafic volcanic flows of tholeiitic affinity and volcaniclastic rocks (Fig. 3a), with some interlayered subalkaline feldspar porphyritic units. The lower and upper members of the Detour Lake Formation are locally separated by the 2725.1 ± 1.4 Ma "chert marker horizon" (CMH; Oliver et al., 2012). The CMH is not a primary chert, but a fine-grained sulphidized and silicified band (2 m thick on average) of mafic volcanic or volcaniclastic rocks, intruded by subalkaline to locally alkaline (e.g. albitite) intermediate to felsic sills and/or dykes (Fig. 3b). In the eastern part of the Detour Lake mine area, felsic to intermediate calc-alkaline volcaniclastic rocks also occur along strike of the CMH. Massive to porphyritic, felsic, and gabbroic plutons and dykes (ca. 2722–2700 Ma) intrude the Detour Lake Formation (Marmont and Corfu, 1988; Oliver et al., 2012). South of the SLDZ, the Caopatina assemblage consists of younger than ca. 2697 Ma turbidite, volcaniclastic units, and local polymictic conglomerate (Oliver et al., 2012).

Eastward in Quebec, rocks of the Deloro assemblage north of the SLDZ are correlative with similar tholeiitic to calc-alkaline volcanic and volcaniclastic rocks, lesser ultramafic volcanic rocks, and carbonaceous mudstone, known locally as the Manthet Group (Fig. 1, 3a; Lacroix, 1994; Faure, 2015). Lesser gabbro-pyroxenite sills and intrusions, such as the Grasset ultramafic complex, intrude this sequence. Intermediate to felsic, subalkaline to alkaline, and porphyritic dykes (Fig. 3b) that also intrude the volcanic rocks are locally spatially related to gold mineralization (*see below*). The SLDZ becomes wider (up to 4 km) and splits into several splays that bound clastic, conglomerate-filled basins, such as the Lac Casault basin (Fig. 1; Faure, 2015). Sensitive high-resolution ion microprobe (SHRIMP) U-Pb analyses of detrital zircon from a polymictic conglomerate sample collected from the eastern part of the Lac Casault basin yielded a preliminary age of <2705 Ma (this study), which represents the best estimate for the maximum deposition age of the unit. South of the SLDZ, the Rivière Turgeon Formation (Lacroix, 1994) represents the eastern continuation of the Caopatina assemblage. The syntectonic Turgeon pluton, composed of quartz diorite with a core of quartz monzodiorite, intrudes the Rivière Turgeon Formation south of the SLDZ (Fig. 1; Lacroix, 1994). North of the SLDZ, the Jeremie pluton has a granitic to granodioritic composition and is interpreted as syntectonic, although its southern part may comprise an early synvolcanic phase (Lacroix, 1994; Faure, 2015).

SUNDAY LAKE 'GOLD TREND'

Gold deposits and mineralized zones occurring within the SLDZ and along second-order structures informally define the Sunday Lake 'gold trend'. The Detour Lake mine in Ontario and the Vortex Zone and the Martiniere-Bug Lake deposits in Quebec are three of the largest deposits within this trend (Fig. 1). Other gold deposits and occurrences, such as the Fenelon deposit and the recently discovered Area 51 (Wallbridge Mining Company, 2019) and Area 52 (Balmoral Resources, 2019) zones, also occur eastward along the Sunday Lake gold trend outside of the study area.

Detour Lake Gold Mine

Auriferous zones of the Detour Lake mine are commonly subvertical and oriented subparallel to a series

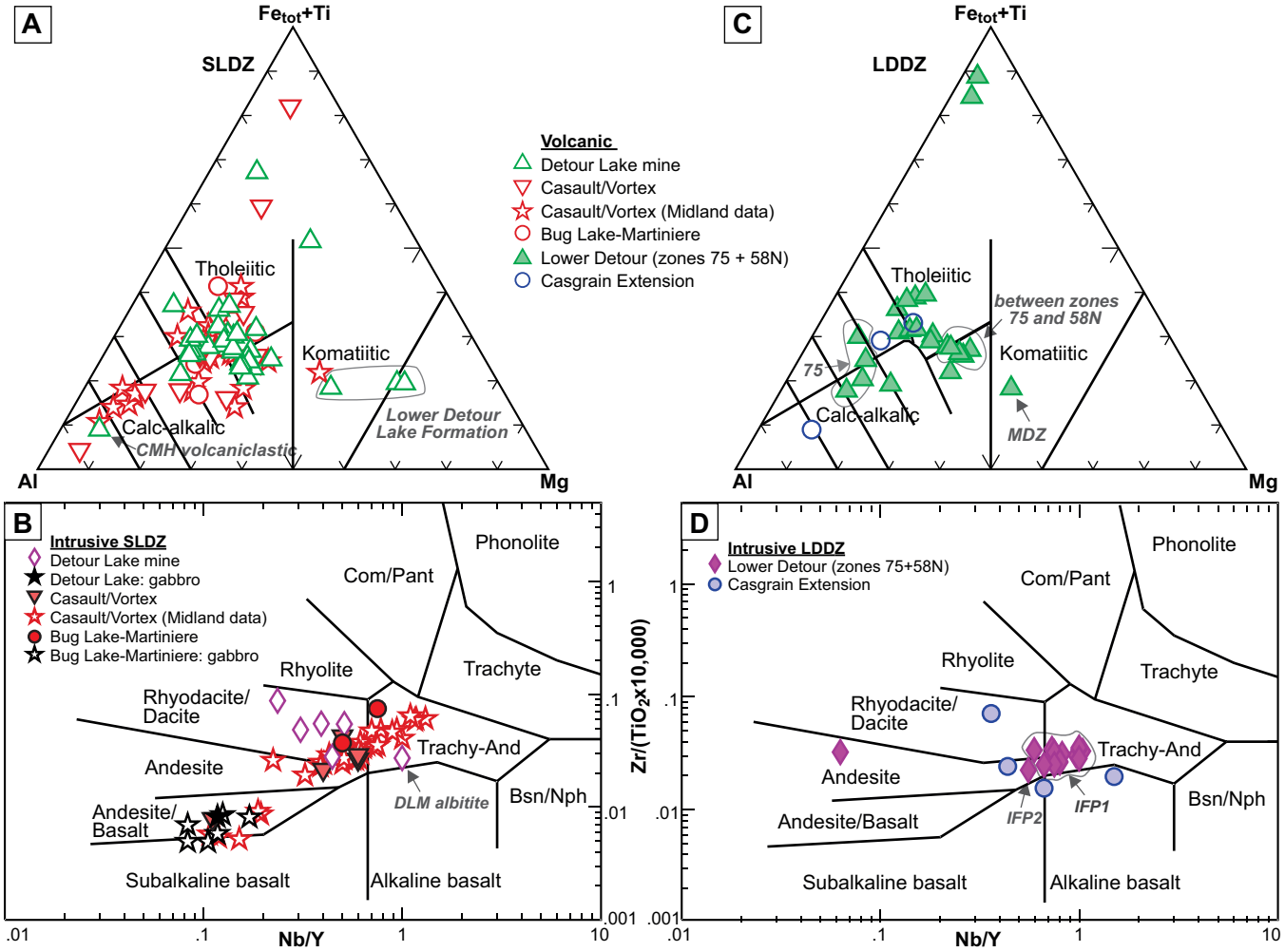

Figure 3. Geochemical classification diagrams of volcanic (a and c) and intrusive (b and d) rock samples taken from drill core collected at sites along the Sunday Lake (a and b) and Lower Detour deformation zones (c and d). **a, c**) Fe_{total}+Ti-Al-Mg ternary diagram of Jensen and Pyke (1982) for volcanic rocks. **b, d)** Zr/(TiO_2*10,000) versus Nb/Y diagram of Winchester and Floyd (1997) used here for intrusive rocks to minimize the effects of hydrothermal alteration. Abbreviations: Bsn/Nph = basanite nephelinite; CMH = chert marker horizon; Com/Pant = comendite pantellerite; DLM = Detour Lake mine; IFP = intermediate feldspar porphyry; LDDZ = Lower Detour deformation zone; MDZ = Massicotte deformation zone; Trachy-And = Trachyte-andesite.

of high-strain zones within the SLDZ (Fig. 2; Marmont, 1986; Oliver et al., 2012; Dubosq et al., 2018, 2019). Previously mined high-grade zones (i.e. the Main Zone) focused on the CMH and also included the hanging wall 'Q-Veins' and footwall 'Talc Zone', which preferentially occur at a structural bend in the orientation and dip of the SLDZ (historically called the "hanging-wall roll"). From 1987 to 1999, the total production (open pit and underground) of the Detour Lake mine is estimated to have been 1.76 Moz of gold from the milling of just over 14.3 Mt of rock at an average head grade of 3.8 g/t Au (Detour Gold Corporation, 2018). Open-pit production, between 2013 and 2019, has been approximately 2.36 Moz Au, leaving roughly 14.8 Moz Au of reserves at 2019 year-end (Detour Gold Corporation, 2019, 2020).

The mineralization associated with the CMH consists of 0.5 to 4 m zones with abundant quartz veins and stockwork veinlets, restricted zones of silicification (as replacement), and 3 to 7 vol.% pyrrhotite-pyrite (Fig. 4a,b; e.g. 15.8 g/t Au over 2.5 m: Oliver et al., 2012). It is hosted in altered volcanic or volcaniclastic units, which are intruded by altered subalkaline to locally alkaline, fine-grained intermediate intrusive rocks. Mineralization hosted within the "Q-Veins" (e.g. 8.6 g/t Au over 5.4 m: Oliver et al., 2012) consists of strongly deformed, centimetre-scale quartz±carbonate fault-fill and extensional veins and pyrrhotite-pyrite ±chalcopyrite stringers that cut biotite-rich, mafic volcanic rocks. Gold associated with pyrrhotite and pyrite also occurs in the Talc Zone (e.g. 9.4 g/t Au over 3.2 m: Oliver et al., 2012), which is located in the footwall of the CMH and is characterized by strongly foliated, serpentine-talc-chlorite-amphibole-altered ultramafic rocks adjacent to an intermediate intrusive body (Oliver et al., 2012; Detour Gold Corporation, 2018).

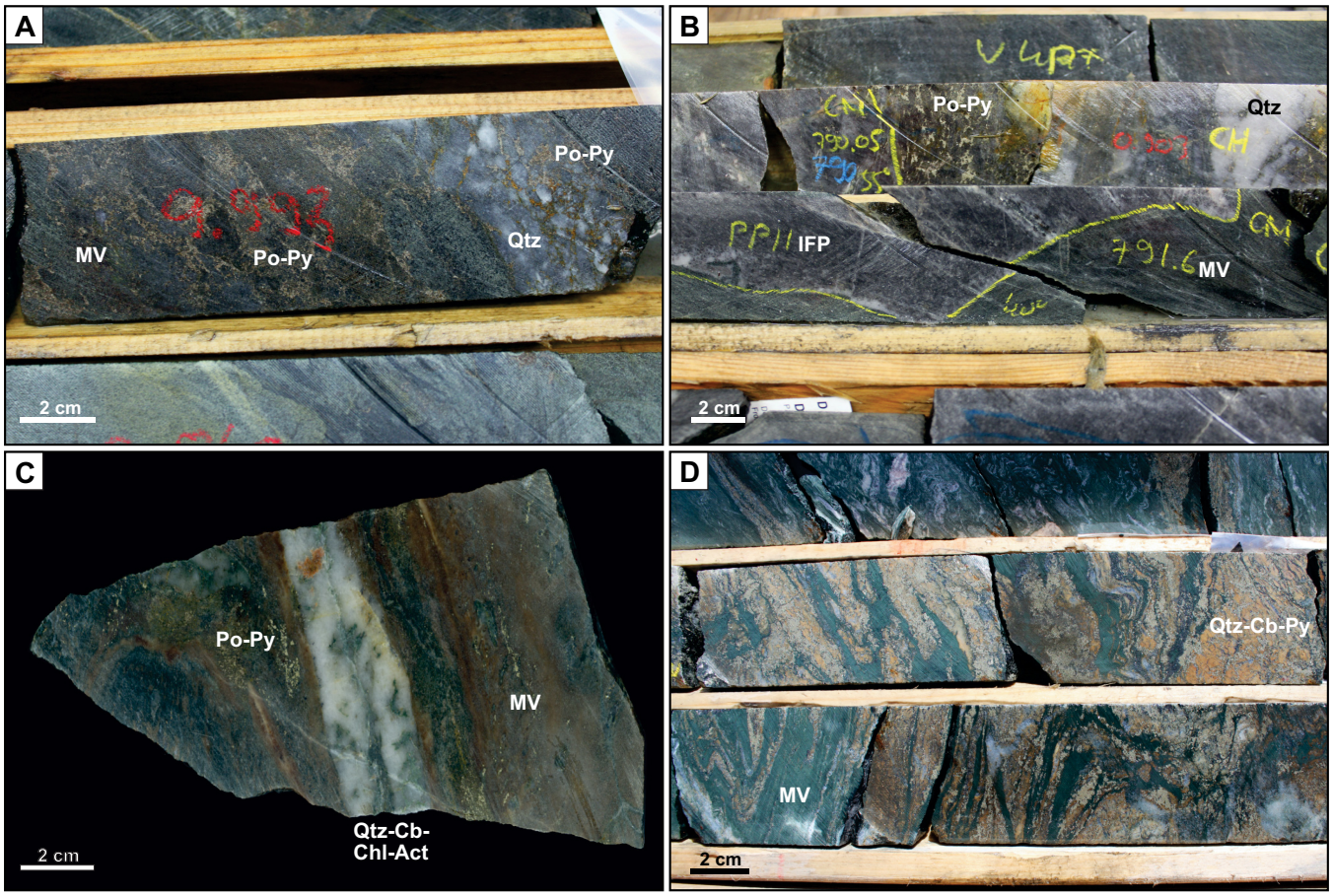

Figure 4. Photographs of representative mineralized zones along the Sunday Lake deformation zone. NQ core diameter is 47.6 mm. **a)** Detour Lake mine, chert marker horizon: quartz-biotite-chlorite-carbonate-altered basalt with 10 to 20 vol.% pyrrhotite-pyrite (interval is 9.9 g/t Au over 1.0 m). **b)** Detour Lake mine, chert marker horizon: albite±sericite±quartz-altered intermediate feldspar porphyry with 2 vol.% pyrrhotite-pyrite intruding a mafic volcanic unit with the contact marked by quartz veins and 5 vol.% pyrrhotite stringers (interval is 0.9 g/t Au over 0.5 m). **c)** Detour Lake mine, Calcite Zone ore: quartz-carbonate-chlorite-actinolite veins and disseminated pyrrhotite-pyrite (or as stringers) in biotite-altered mafic volcanic rocks. **d)** Vortex Zone 475: deformed quartz-carbonate-sulphide veins and stringers in sheared mafic blocky tuff, locally with 5 to 20 vol.% pyrite (2.7 g/t Au over 0.5 m). Abbreviations: Act = actinolite, Cb = carbonate, Chl = chlorite, IFP = intermediate feldspar porphyry, MV = mafic volcanic/volcaniclastic rock, Po = pyrrhotite, Py = pyrite, Qtz = quartz.

Since late 2012, open-pit mining has been concentrated in the low-grade (approximately 1 to 2 g/t Au average), high-tonnage Calcite Zone, which consists of steep, west-trending, and frequently boudinaged and folded, quartz-calcite veins with disseminated or stringers of pyrrhotite-pyrite hosted in biotite-altered massive and pillowed mafic volcanic rocks (Fig. 4c). Several veins types (early-, syn-, and post-D_2; Dubosq et al, 2018) occur in these hydrothermally altered domains, including sulphide-rich brecciated veins. Dubosq et al. (2018) interpret the latter vein-type to be associated with late brittle-ductile strain and gold remobilization.

Core from drillhole DG-09-711, which transects most of the ore zones at the Detour Lake mine including the Calcite Zone and the western extension of the Main Zone (Fig. 2; CMH and hanging-wall veins) was studied in detail and systematically sampled for whole-rock lithogeochemical analysis (Fig. 5a). Along this drillhole, the Calcite Zone comprises quartz-calcite veins, 1 to 8 vol.% pyrrhotite-pyrite within a biotite-quartz-actinolite-chlorite-albite±calcite and/or Fe-carbonate alteration envelope at the contact zone between massive and pillowed basalt. Mineralization within the Calcite Zone is relatively wide but low-grade (1.8 g/t Au over 82 m). Total sulphur and CO_2 contents and the $K_2O/(K_2O+Na_2O)$ ratios across the Calcite Zone are consistent with sulphide-carbonate-biotite alteration of the host rocks. The Main Zone (CMH and hanging-wall veins; 4.0 g/t Au over 46 m) lies roughly 200 m down this same drillhole below the Calcite Zone. In the hanging-wall of the CMH, mineralization is made up of strongly deformed quartz±carbonate veins with 2 to 5 vol.% pyrrhotite-pyrite±chalcopyrite stringers that cut altered massive mafic volcanic rocks. The mineralization associated with the CMH, which forms the southern part of the orebody, consists of quartz-sulphide veins (1–8 cm) and locally visible gold hosted in biotite-quartz-albite-carbonate-altered mafic volcanic

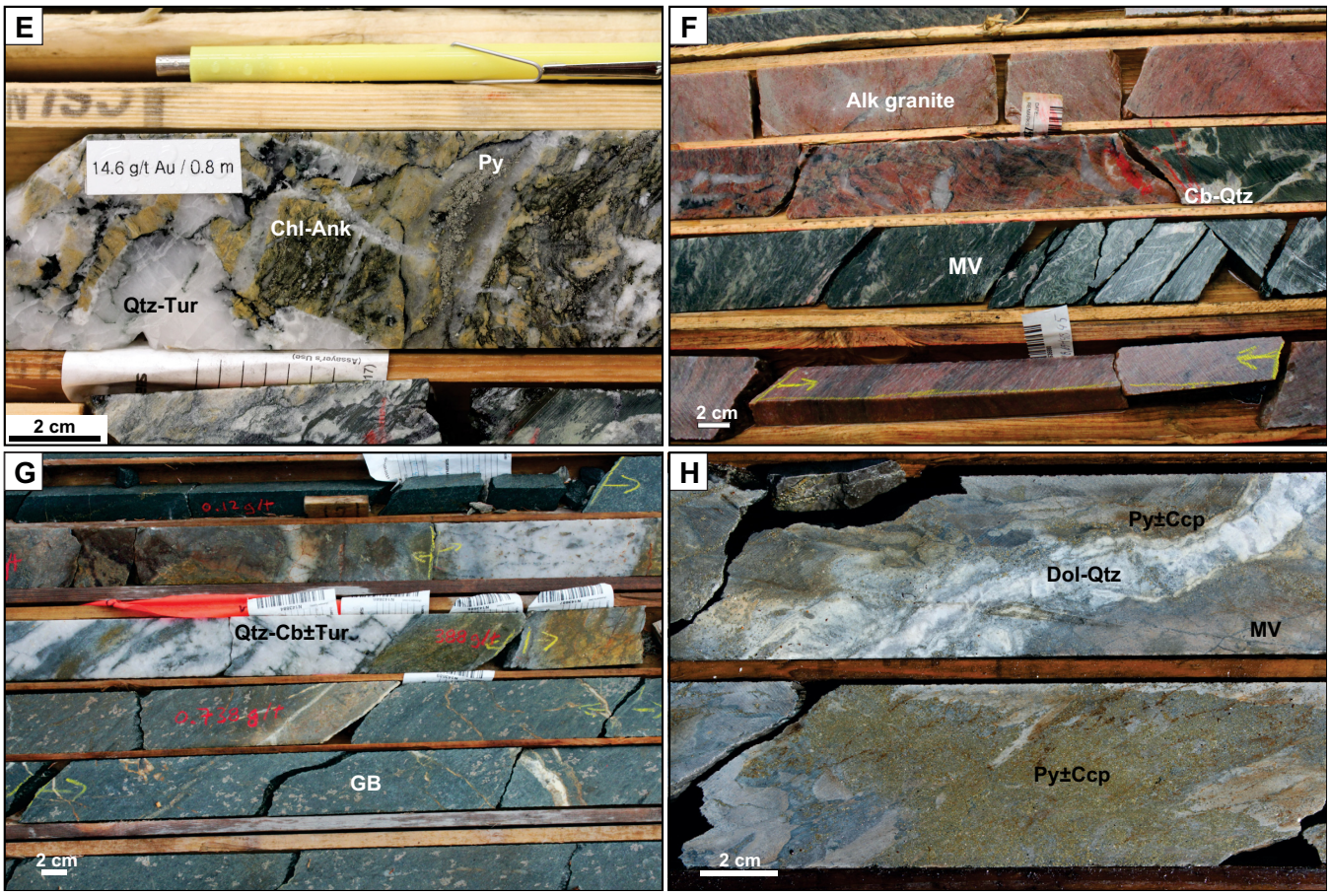

Figure 4 continued. Photographs of representative mineralized zones along the Sunday Lake deformation zone. NQ core diameter is 47.6 mm. **e)** Vortex Zone 450: quartz-carbonate±tourmaline veins, chlorite veinlets, and disseminated pyrite developed at the contact between an albite-ankerite-altered alkaline granitic dyke and mafic volcaniclastic rocks (14.6 g/t Au over 0.8 m; drillhole CAS-17-96). **f)** Reddish alkaline granitic dyke intruding mafic volcanic rocks in the footwall of Zone 450. Contacts are strongly foliated, brecciated, and marked by quartz-carbonate veins. **g)** Martiniere West: quartz-dolomite/ankerite-pyrite-tourmaline veins in a carbonate-quartz-sericite-altered, leucoxene-bearing quartz gabbro. **h)** Upper zone of Bug South: dolomite-quartz-pyrite veins and 5 to 10 vol.% pyrite±chalcopyrite stringer (5.8 g/t Au over 1.7 m) in sericitized pillowed basalt. Abbreviations: Alk = alkaline; Ank = ankerite, Cb = carbonate, Ccp = chalcopyrite, Chl = chlorite, Dol = dolomite, GB = gabbro, MV = mafic volcanic/volcaniclastic rock, Py = pyrite, Qtz = quartz, Tur = tourmaline.

rocks, talc-chlorite schist, and subalkaline intermediate albite-quartz-altered intrusive rocks. The CO_2 content and $K_2O/(K_2O+Na_2O)$ ratios (biotite alteration) are anomalous but significantly lower than in the Calcite zone.

Vortex Zone

The Vortex Zone, part of the Casault property (Midland Exploration, 2018) is located at the western tip of the Lac Casault conglomerate basin along a fault splay of the SLDZ, about 40 km east of the Detour Lake mine (Fig. 1). The auriferous, west-trending, high-strain Vortex Zone occurs at the contact between tholeiitic and calc-alkaline volcanic and volcaniclastic units of the Manthet Group (Fig. 3a, 6). Mineralized intervals within this zone are spatially associated with subalkaline to reddish albite-sericite-hematite-altered alkaline porphyritic dykes (Fig. 3b). Auriferous quartz veins are transposed, boudinaged, and folded, but some are locally oblique and cut the main foliation (likely the S_2 of Oliver et al., 2012), suggesting that the veins overlapped the main foliation forming event. Vein stockwork and hydrothermal breccia occur in the high-strain zones and locally comprise rotated foliated clasts, indicating that brecciation is syn- to late-main phase deformation. These hydrothermal breccia zones are spatially associated with a locally strongly developed crenulation cleavage that overprints the main deformation fabric near the mineralized zones. Mafic to intermediate volcaniclastic rocks of calc-alkaline affinity are likely correlative with the hydrothermally altered CMH, which occurs along strike of the SLDZ at the Detour Lake deposit (Faure, 2015).

The schematic and geochemical profile of drillhole CAS-17-094 (Fig. 5b, 6) illustrates the setting, distribution, and characteristics of the mineralized intervals and lithogeochemical signature of the Vortex Zone. Strain increases from north to south (i.e. down the drill-

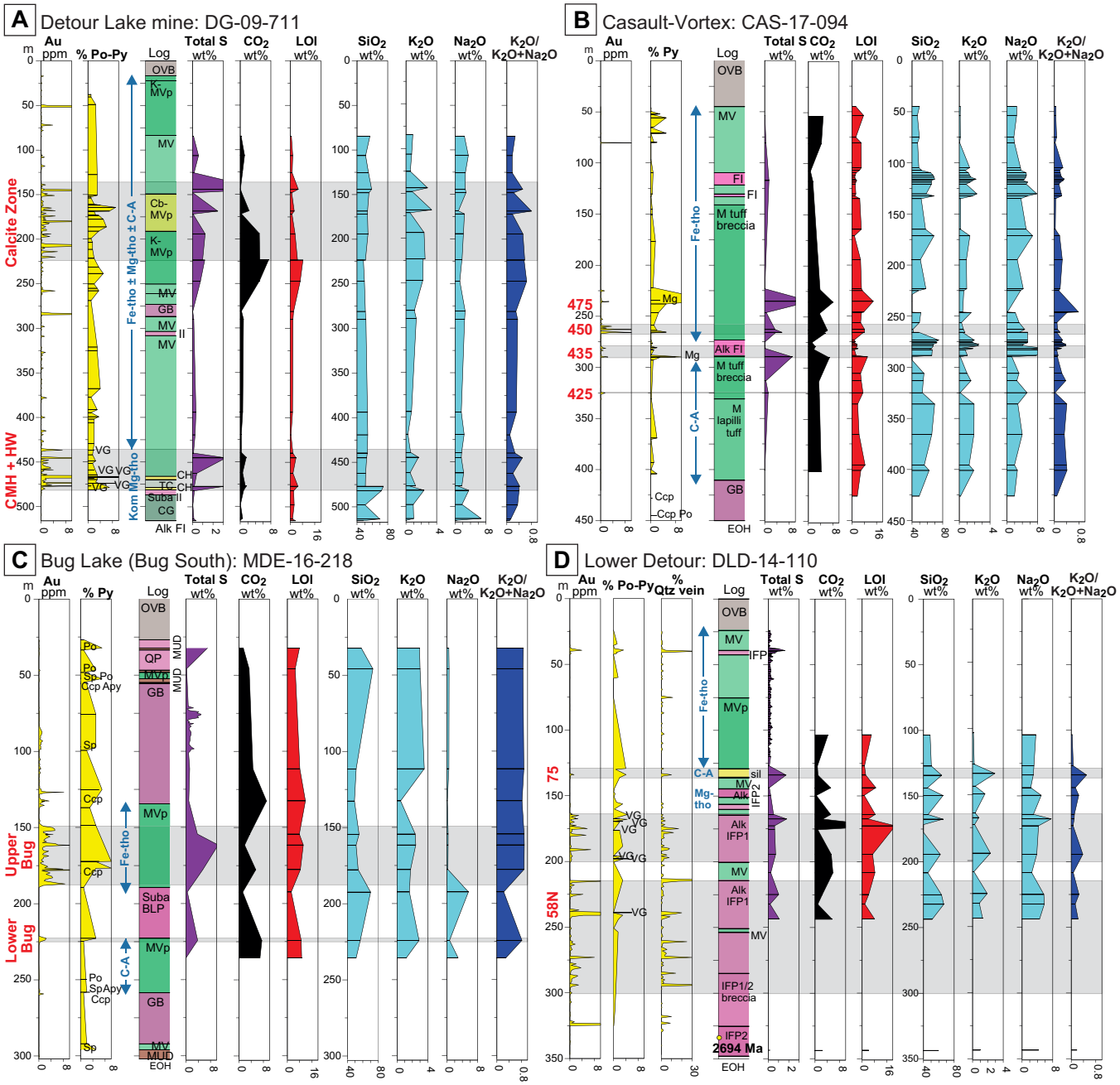

Figure 5. Drillhole profiles across the main mineralized zones showing the relationships between gold and vol.% of pyrite plus pyrrhotite (also showing number of specks of visible gold (VG) with other minerals (Apy = arsenopyrite, Ccp = chalcopyrite, Mg = magnetite, Po = pyrrhotite, Sp = sphalerite), other elements, and oxides (LOI= loss on ignition) in the logged rock types and their main geochemical affinities). The K_2O(/K_2O+Na_2O) ratio outlines the sericite and potassic alteration. **a)** Detour Lake mine, drillhole DG-09-711 with the chert marker horizon (CMH), hanging-wall zone, and the Calcite Zone labelled. **b)** Casault-Vortex Zone, drillhole CAS-17-094 with zones 425, 435, 450, and 475 labelled. **c)** Bug Lake-Bug South zone, drillhole MDE-16-218 with Upper and Lower Bug zones labelled. **d)** Lower Detour, drillhole DLD-14-110 with zones 75 and 58N labelled. Abbreviations for the log profile: Alk = alkaline, BLP = Bug Lake porphyry, C-A = calc-alkaline, Cb = carbonate-altered, CG = chloritic greenstone, CH and SIL = silicified zone, EOH = end of hole, Fe-tho = high-Fe tholeiite, FI = felsic intrusive, GB = gabbro, IFP = intermediate feldspar porphyry, II = intermediate intrusive, K = potassic-altered, Kom = komatiite, Mg-tho = high-Mg tholeiite, MUD = mudstone, MV = mafic volcanic, MVp = pillowed mafic volcanic, OVB = overburden, QP = quartz porphyry, Sil = silicified zone, Suba = subalkaline, TC = talc-chlorite schist.

hole), and several steeply north-dipping mineralized intervals were identified. Zone 475 consists of deformed quartz-carbonate-sulphide veins in sheared carbonate-chlorite-sericite-altered andesitic blocky tuff with 5 to 20 vol.% pyrite (locally semi-massive) and 3 to 5 vol.% magnetite (e.g. 0.4 g/t Au over 8 m, including 2.7 g/t Au over 0.5 m; Fig. 4d). Zone 450 comprises deformed quartz-carbonate (ankerite)±tourmaline veins

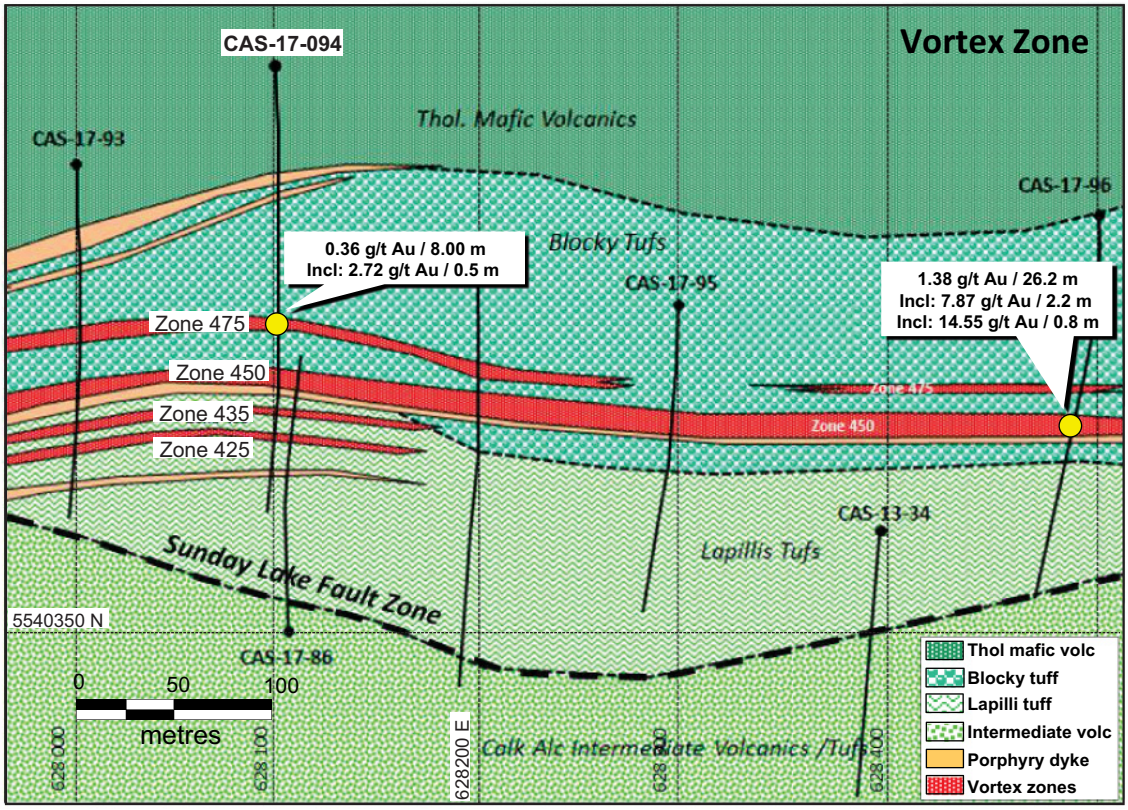

Figure 6. Simplified geological map of a part of the Vortex Zone (modified from Midland Exploration, 2018). Abbreviations: Calk Alc = calc-alkaline, Incl = including, Thol = tholeiitic, volc = volcanic rocks.

and disseminated pyrite (2–5 vol.%) associated with high-strain zones and hydrothermal breccia (e.g. 14.6 g/t Au over 0.8 m in drillhole CAS-17-096; Fig. 4e, 6) at the contact between strongly deformed carbonate-chlorite-altered basaltic volcaniclastic rocks and a more competent, albite-hematite-altered alkaline granitic dyke (Fig. 4f). At greater depths, secondary zones, such as zone 435, consist of quartz-carbonate veins and disseminated pyrite (3–10 vol.%, with ≤8 vol.% magnetite) in strongly deformed, hematite-sericite-altered andesitic lapilli tuff (e.g. Zone 435: 0.5 g/t Au over 4.6 m) in the footwall of the alkaline granite dyke. The higher Na_2O and $K_2O/(K_2O+Na_2O)$ index values of the dyke samples (Fig. 5b) is likely due to the original alkaline composition of the unit and/or overprinting albite-sericite alteration. In general, geochemical analyses within the mineralized zones yield anomalous S and CO_2 concentrations, which is consistent with the carbonate-pyrite alteration related to auriferous veins.

Martiniere West and Bug Lake Deposits

The Martiniere West and Bug Lake deposits (Fig. 7; Martiniere property; Voordouw and Jutras, 2018) are located about 50 km east of the Detour Lake mine, 12 km east of the Vortex Zone, and approximately 2 km from the interpreted northern splay of the SLDZ (Fig. 1).

The Martiniere West deposit comprises two northeast-trending mineralized brittle-ductile high-strain zones, which are approximately 10 to 20 m wide. Each zone is characterized by multiple generations of quartz-carbonate (dolomite/ankerite)-tourmaline veins and 1 to 5 vol.% pyrite±arsenopyrite±chalcopyrite (Fig. 4g). Intervals (10–40 cm wide) of breccia vein locally occur near the contact with carbonate-quartz-sericite±albite-altered wall rocks. The 400 m long West Main Zone (e.g. 10.6 g/t Au over 21.4 m: drillhole MDW13-88) is hosted in moderately foliated (likely S_2 foliation), leucoxene-bearing tholeiitic quartz gabbro (Fig. 3b), near and subparallel to the contact with mafic volcanic and sedimentary units. Away from mineralized high-strain zones, the host gabbro is massive to weakly foliated and contains chlorite and titanomagnetite.

The Bug Lake deposit consists of moderately to steeply eastward-dipping brittle-ductile high-strain zones with an en echelon (right-stepping) apparent geometry, delineating the North and South zones (Fig. 7). Both zones are hosted by mafic volcanic rocks and gabbro along both the upper and lower contacts (e.g. 'Upper Bug' and 'Lower Bug' subzones) of the north-northwest-trending Bug Lake porphyry, which lies almost perpendicular to the layering of host rocks. The dyke is a lenticular 10 to 30 m thick, massive to weakly foliated, fine-grained sericitized subalkaline quartz

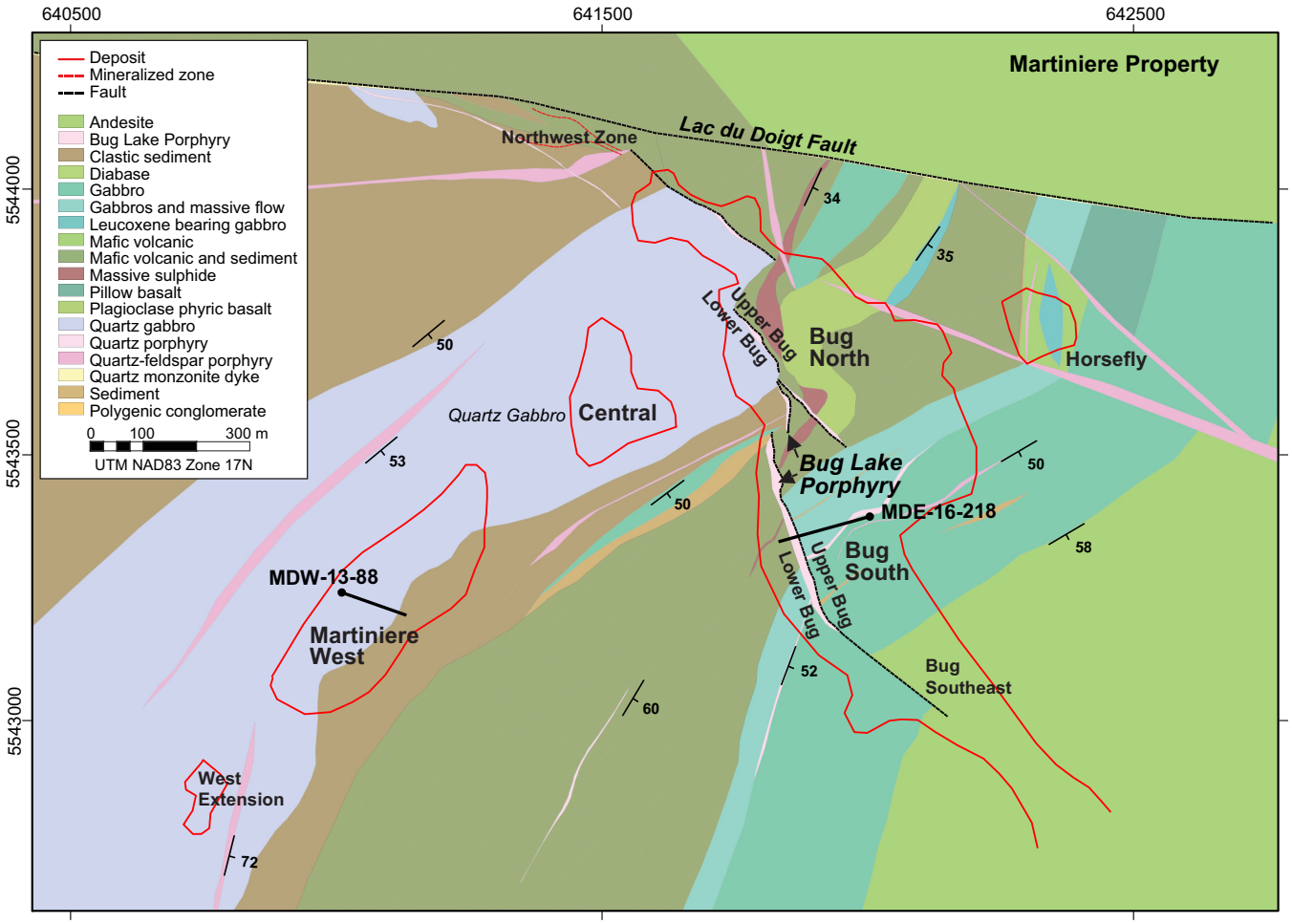

Figure 7. Geological map of the Martiniere West and Bug Lake deposits, Martiniere property (*modified from* Voordouw and Jutras, 2018).

porphyry (quartz diorite to granodiorite; rhyodacite/dacite field in Fig. 3b) with 1 to 2 vol.% disseminated pyrite, but with no significant (i.e. <25 ppb) gold values. The profile of drillhole MDE-16-218 (Fig. 5c, 7) shows that the auriferous intervals of Bug South occur as several discrete high-strain and hydrothermally altered (carbonate-sericite-quartz) zones overprinting pillow basalt and andesitic basalt of tholeiitic (Upper Bug) to calc-alkaline (Lower Bug) affinities (Fig. 3a). The Upper Bug subzone (e.g. 2.8 g/t Au over 40.3 m; Fig. 5c) is characterized by quartz-sericite veins, abundant crosscutting dolomite/ankerite-quartz±tourmaline veins (Fig. 4h) and breccia vein, locally showing a crustiform texture. Auriferous zones are associated with 5 to 10 vol.% pyrite±chalcopyrite, disseminated and within veinlets. Thin (2–3 m), secondary breccia zones with dolomite/ankerite-quartz-pyrite±chalcopyrite veins (0.5 to locally 8 g/t) occur in a ~50 m low-grade envelope (0.2–0.5 g/t Au) within massive basalt and leucoxene-bearing gabbro above the Upper Bug zone. The lower subzone at Bug South is a much thinner (~3 m) and lower grade (e.g. 2.2 g/t Au over 2.3 m) interval characterized by 2 to 5 vol.% pyrite stringers, with disseminated pyrrhotite, chalcopyrite, and arsenopyrite within the contact zone between the porphyry and sericite-altered pillow basalt (Fig. 5c).

LITHOSTRATIGRAPHIC FRAMEWORK OF THE LOWER DETOUR DEFORMATION ZONE

In Ontario, the LDDZ lies roughly 7 km south of the SLDZ, across the Caopatina assemblage (Fig. 1). Its geological setting is less defined than that of the SLDZ. However, active exploration by Detour Gold since 2011, including a fence of 28 diamond drillholes along a north-south cross-section (Detour Gold, 2018, unpub. data; Fig. 8), provides critical insights into the lithostratigraphic and structural settings of the Lower Detour mineralized zones. The section lies approximately 1.3 km west of the 58N and 75 zones (*see below*). Lithogeochemical data from Detour Gold and the present study are summarized here to better characterize the main host rocks.

The LDDZ juxtaposes volcanic units correlated with the Detour Lake Formation of the Deloro assemblage

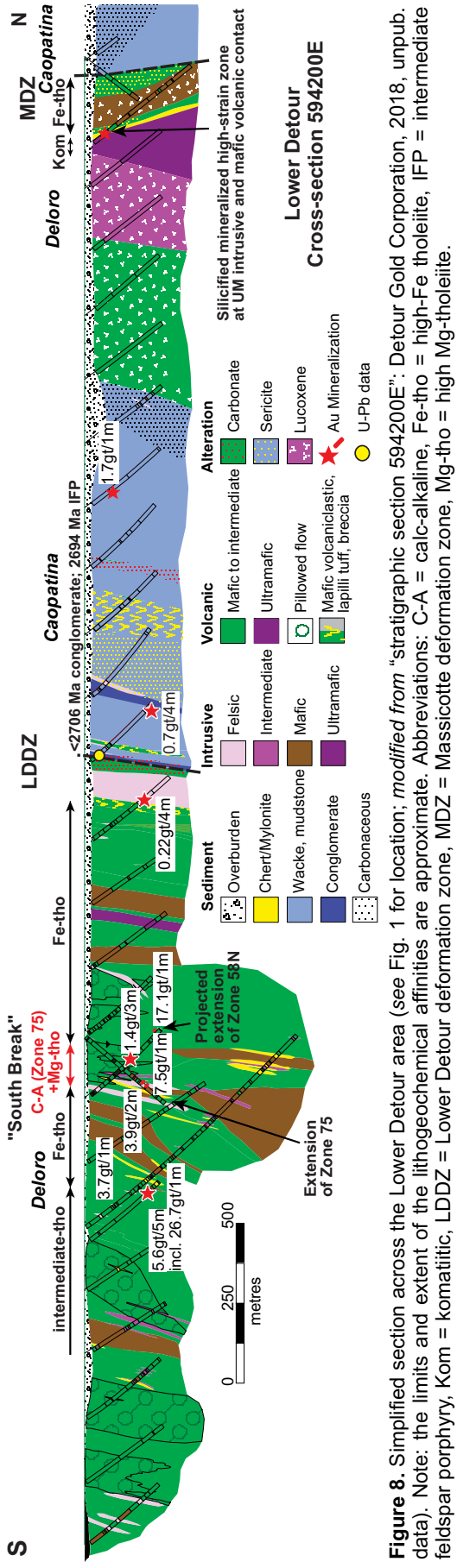

Figure 8. Simplified section across the Lower Detour area (*see* Fig. 1 for location; *modified from* "stratigraphic section 594200E": Detour Gold Corporation, 2018, unpub. data). Note: the limits and extent of the lithogeochemical affinities are approximate. Abbreviations: C-A = calc-alkaline, Fe-tho = high-Fe tholeiite, IFP = intermediate feldspar porphyry, Kom = komatiitic, LDDZ = Lower Detour deformation zone, MDZ = Massicotte deformation zone, Mg-tho = high Mg-tholeiite.

against sedimentary rocks of the Caopatina assemblage to the north (Fig. 1, 8). This inferred structural contact is repeated 2 km northward along the MDZ, where a locally mineralized silicified contact zone between ultramafic intrusive and mafic volcanic rocks, locally of calc-alkaline affinity, is similar to the CMH at the Detour Lake mine along the SLDZ. A strongly sheared and silicified deformation zone (informally termed the "South Break") occurring roughly 1 km south of the LDDZ is spatially associated with auriferous zones 75 and 58N and likely represents a second-order structure to the LDDZ.

The mafic to intermediate volcanic (pillow and massive) and volcaniclastic rocks occurring within and south of the LDDZ mostly have a Fe-rich tholeiitic affinity (Fig. 3c, 8). However, the thin panel of silicified intermediate volcanic rocks hosting Zone 75 within the South Break and the mafic units between zones 75 and 58N locally have distinctive calc-alkaline and high-Mg tholeiitic signatures, respectively. Again, this contact is similar to the CMH and the contact with the upper Detour Lake Formation at the Detour Lake mine.

The Caopatina sedimentary rocks located between the LDDZ and MDZ consist of interlayered polymictic conglomerate, wacke, mafic volcanoclastic and carbonaceous mudstone (Fig. 1, 8). The polymictic conglomerate along the LDDZ is frequently iron carbonate-altered, strongly deformed, and locally lineated, evolving into an L>S tectonite. U-Pb SHRIMP and thermal ionization mass spectrometry (TIMS) analyses of detrital zircon from a polymictic conglomerate sample from the immediate footwall of the LDDZ yielded a preliminary age of ≤2706 Ma (this study), which represents the maximum age for the deposition of the unit.

A swarm of feldspar porphyry dykes intrude the volcanic and sedimentary rocks within and south of the LDDZ. Two intrusive phases are interpreted (Malcolm et al., 2015): 1) intermediate feldspar porphyry 1 (IFP1) is leucocratic, plagioclase phenocryst-rich (30–50 vol.%) quartz monzonite, mainly of alkaline affinity (Fig. 3d); and 2) intermediate feldspar porphyry 2 (IFP2) is a melanocratic subalkaline quartz diorite consisting of less than 20 vol.% phenocrysts, which locally appear to intrude and brecciate IFP1, especially in Zone 58N where both phases occur in the hanging wall of an intermediate intrusion. U-Pb SHRIMP and TIMS zircon analyses from samples of IFP1 and IFP2 yielded identical (within error) preliminary crystallization ages of ca. 2694 Ma (this study).

The LDDZ, the MDZ, and the main lithological assemblages extend eastward into an extensively overburden-covered area of Quebec for which geological information is limited (Fig. 1; Faure, 2012, 2015). The

Rivière Turgeon Formation, which is the eastern continuation of the Caopatina assemblage, consists of turbiditic siltstone, sandstone, and locally mudstone (Lacroix, 1994). Layers of magnetite-bearing iron formation and polymictic conglomerate occur in the southern part of the sedimentary belt, in the immediate structural footwall (north) of the LDDZ. The volcanic rocks occurring south of the MDZ and LDDZ comprise the Brouillan Nord assemblage and the Brouillan Group (or volcanic complex; Lacroix, 1994; Faure, 2012), respectively. The Brouillan Group principally consists of calc-alkaline andesitic basalt and volcaniclastic rocks with lesser rhyolitic layers, which are surrounded by tholeiitic basalt, including that of the Brouillan Nord assemblage. The Brouillan Group extends southeastward in the Selbaie past-producing mine and B26 deposit area, where ca. 2729–2728 Ma felsic volcanic rocks (Barrie and Krogh, 1996; Fayard et al., 2020) are broadly coeval with the Deloro assemblage.

LOWER DETOUR 'GOLD TREND'

The Lower Detour gold trend comprises gold mineralization spatially associated with the Massicotte and Lower Detour deformation zones, including zones 58N and 75 (Zone 58N: 534,000 oz or 16.6 t Au; Detour Gold Corp., 2019) and lesser studied gold occurrences in Quebec. The MDZ and LDDZ correlate eastward with the Grasset fault zone (Fig. 1; Faure, 2015).

Zones 58N and 75

The steeply south-dipping zones 58N and 75 occur along an anticlockwise bend of the magnetic lineaments and structural grain within the South Break (Fig. 1, 5; Malcolm et al., 2015; Detour Gold Corporation, 2018). The profile of drillhole DLD-14-110 (Fig. 5d) illustrates that Zone 75 (1.4 g/t Au over 1.0 m) is hosted in silicified, sericite-biotite-altered tholeiitic andesite, calc-alkaline andesite, and dacite (Fig. 9a,b), and locally in a feldspar porphyry dyke. Zone 75 mineralization comprises 5 to 20 vol.% sulphide (i.e. mainly pyrite, chalcopyrite, sphalerite, and lesser pyrrhotite). Higher gold concentrations (e.g. 8.0 g/t Au over 6 m: drillhole DLD-16-203) generally correlates with increasing strain intensity and sulphide content. Below Zone 75, the much wider Zone 58N consists of discrete laminated quartz-tourmaline-carbonate ±visible gold veins and stockwork (e.g. 55.8 g/t Au over 6 m, including 308 g/t Au over 1 m; Fig. 5d, 9c) hosted in a swarm of leucocratic feldspar porphyry dykes, mostly of the IFP1 phase (Fig. 9d). The IFP2 is locally gold-bearing in high-strain zones. The highest gold grades within these zones are spatially associated with veining (Fig. 5d). The auriferous veins are associated with a decimetre-wide albite-sericite-quartz-carbonate (±hematite) alteration zone (Fig. 9c). Between 0.5 and 5 vol.% disseminated pyrite occurs within the veins or their immediate selvages, along with trace amounts of sphalerite and chalcopyrite. Based on the age of the host porphyry, the bulk of the mineralization is interpreted to be younger than 2694 Ma.

Lower Detour 'Gold Trend' in Quebec

Auriferous zones of the Lower Detour trend in Quebec include the Lynx and Rambo zones (Balmoral Resources) and those of Probe Metals-SOQUEM 'Detour Quebec' project. The Lynx (7.8 g/t Au over 7.2 m) and Rambo (6.3 g/t Au over 2.7 m) zones are east-trending, 0.4 to 13.4 m thick, and are characterized by quartz-carbonate-pyrite veins at the contact between andesitic and basaltic volcanic rocks within the MDZ (Fig. 1; Balmoral Resources, 2018). The Massicotte and Casgrain Extension properties cover a 74 km long corridor along the eastward extension of the LDDZ (Probe Metals, 2018). Sparse diamond drilling has intersected auriferous zones (e.g. 2.8 g/t Au over 0.7 m: drillhole CE-16-01; Fig. 1) along the LDDZ and second-order splays to the south. At Massicotte, a mineralized zone comprises pyrite±galena±sphalerite veins in a sericite schist (e.g. 5.3 g/t Au over 3.4 m, including 17.5 g/t Au over 1 m: drillhole MA-16-05; Fig. 1; Probe Metals, 2016). Mineralization at the Casgrain Extension comprises quartz-carbonate-tourmaline-pyrite veins at sheared contacts between chlorite-epidote-altered calc-alkaline andesitic basalt (Fig. 3c) and hematite-leucoxene-sericite-altered quartz-eye porphyry or rhyodacite (Fig. 3d, 9e), which are intruded by albite-hematite-sericite-altered alkaline porphyritic monzonite (alkaline basalt field in Fig. 3d).

Exploration drilling in the Casgrain Extension property has intersected several intervals of polymictic conglomerate. One, thick (~260 m) polymictic conglomerate interval occurs just north of the LDDZ, at the same structural position as that of the Lower Detour area to the west (blue line along LDDZ in Fig. 1). It consists of flattened subrounded to subangular clasts, principally of mafic volcanic origin with lesser felsic volcanic, porphyritic, and quartz vein clasts. The strongly deformed conglomerate is intruded by buff-coloured subalkaline to alkaline, porphyritic quartz diorite dykes (andesite to subalkaline basalt fields in Fig. 3d), at the contact of which occur strong albite, sericite and carbonate alteration, disseminated pyrite, and a thin (10 cm thick) quartz-tourmaline breccia vein (e.g. 1.3 g/t Au over 1.0 m; Fig. 9f). U-Pb SHRIMP detrital zircon analyses of this conglomeratic unit yielded a preliminary age of <2692 Ma (this study; Fig. 1), which represents a maximum deposition age that is significantly younger than the other age data for polygenic conglomerate obtained in this study.

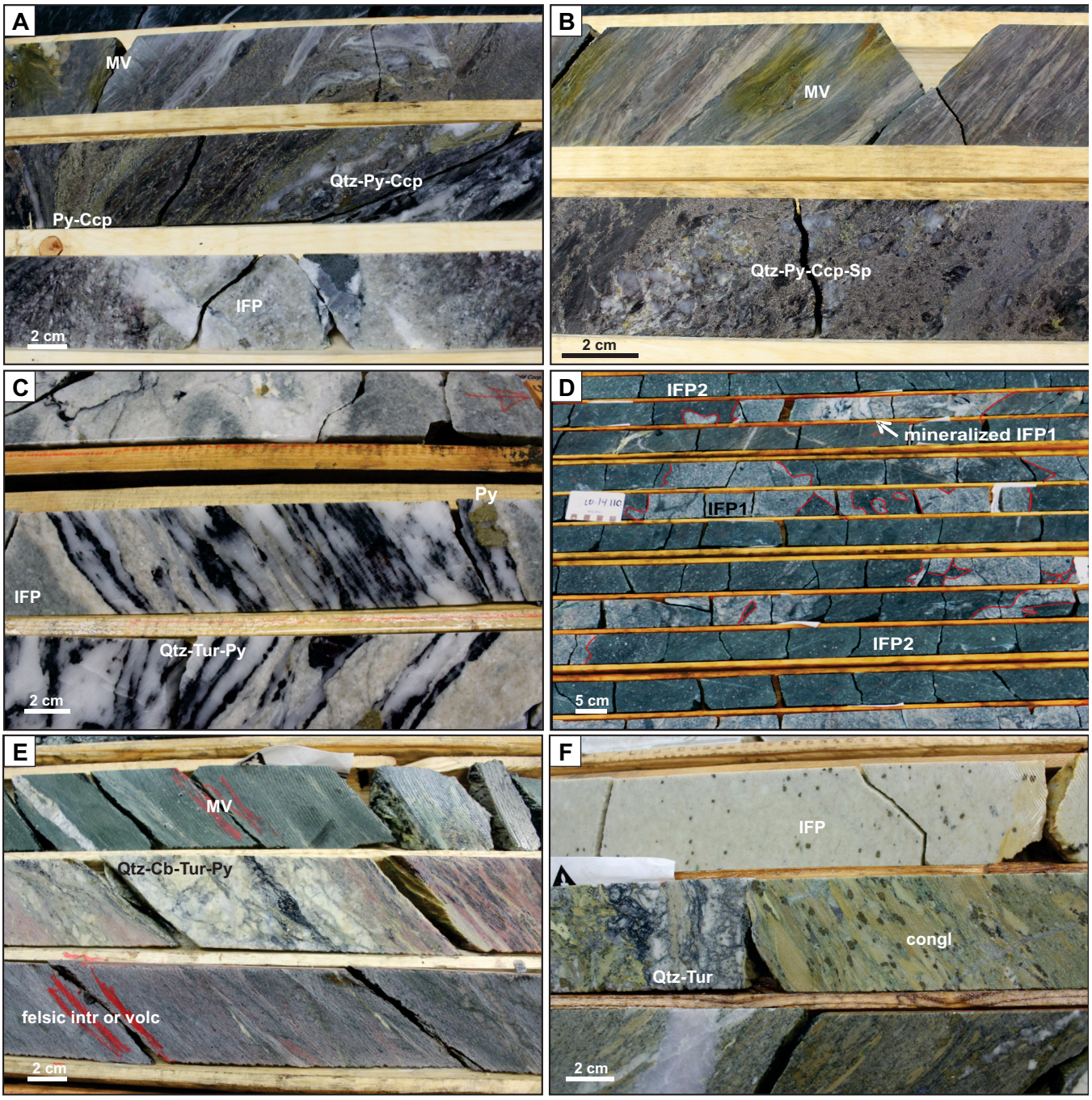

Figure 9. Photographs of representative mineralized zones related to the Lower Detour deformation zone. NQ core diameter is 47.6 mm. **a)** Zone 75: silicified, sulphidized, and biotite-sericite-albite-altered mafic volcanic units and feldspar-quartz porphyry. **b)** Zone 75: sulphide-rich zone (mainly pyrite with lesser pyrrhotite, chalcopyrite, and sphalerite) in highly strained and altered mafic volcanic rocks. **c)** Typical Zone 58N: laminated quartz-tourmaline veins in albite-sericite-quartz-altered feldspar porphyry with trace to 2 vol.% coarse pyrite along vein contacts with the feldspar porphyry (interval is 34.9 g/t Au over 1 m). **d)** Ore-hosting leucocratic porphyry (IFP1) brecciated by a melanocratic intermediate porphyry (IFP2; *modified from* Malcolm et al., 2015). Both units have the same preliminary crystallization age of ca. 2694 Ma. **e)** Casgrain Extension: quartz-tourmaline-pyrite vein (anomalous in gold) at sheared contact between hematite-sericite-altered felsic intrusive and chloritized mafic volcanic units. **f)** Casgrain Extension: contact marked by a quartz-tourmaline vein breccia between albite-sericite-pyrite-altered intermediate feldspar porphyry and sericitized polymictic conglomerate (1.27 g/t Au over 1 m interval). Abbreviations: Cb = carbonate, Ccp = chalcopyrite, congl = conglomerate, IFP = intermediate feldspar porphyry, intr = intrusive rock, MV = mafic volcanic, Po = pyrrhotite, Py = pyrite, Qtz = quartz, Sp = sphalerite, Tur = tourmaline, volc = volcanic rock.

DISCUSSION

The present study refines the geological setting of what we informally refer to as the Sunday Lake and Lower Detour gold trends. These gold trends follow regional deformation zones mainly affecting volcanic units of the Deloro assemblage and small fault-bounded basins of polymictic conglomerate. The most prolific deformation zones border the turbidite deposit of the Caopatina assemblage, which shares similarities with the deformed Porcupine/Cadillac basins of the southern Abitibi (Fig. 1). Preliminary dating of the polymictic conglomerate units yielded maximum detrital zircon ages of ≤2706 to ≤2692 Ma. Further work will determine if these conglomerate units are temporally distinct from the Caopatina assemblage. The somewhat older conglomerate (≤2706 Ma) may be part of the Caopatina assemblage and correlative to the <2703 Ma Stella Formation, such as in the Chapais-Chibougamau camp (e.g. Leclerc et al., 2012). However, the potentially younger conglomerate (≤2692 Ma) from the Casgrain Extension property may represent a different unit that unconformably or structurally overlies the Caopatina basin. If correct, some conglomerate horizons may be correlative with the Timiskaming-like Haüy Formation (<2691 Ma: David et al., 2007; Leclerc et al., 2012). Intermediate to felsic, typically reddish, subalkaline to alkaline porphyritic dykes (preliminary ages suggest that some of these dykes are ca. 2694 Ma) are also spatially related to the SLDZ and LDDZ. The preliminary dyke ages are similar to, but slightly older than, the ca. 2692 Ma alkaline syenitic intrusions occurring in the Chibougamau area (Leclerc et al., 2012).

The geological setting of the study area, including the lithostratigraphic characteristics and age relationships of the units, are reminiscent of the prolific gold camps of the southern Abitibi greenstone belt, such as the Timmins district (e.g. Robert et al., 2005; Dubé and Gosselin, 2007; Bleeker, 2015; Dubé et al., 2017). In these areas, major deformation zones (e.g. Destor-Porcupine fault zone) are thought to be inherited from extensional faults that delimit panels of "synorogenic" Timiskaming clastic rocks. These crustal-scale structures are interpreted to have facilitated mantle-derived alkaline magmatism and migration of gold-bearing fluids during later thrust inversion and regional tectonometamorphism (Cameron, 1993; Bleeker, 2015; Dubé et al., 2017).

The present study also outlines the main characteristics of the various deposits and prospects along the SLDZ and LDDZ, as summarized in Table 1. Gold along these major deformation zones is structurally controlled by second-order faults or high-strain zones that commonly coincide with structural flexures or bends. Auriferous zones occur along contact zones between Deloro volcanic units (and equivalent Manthet and Brouillan groups) of different compositions or signatures and intermediate porphyritic dykes or gabbroic intrusive rocks. Gold is associated with quartz-carbonate±tourmaline or sulphide-rich veins, stockwork, and breccia zones in hydrothermally altered (carbonate, sericite, biotite) wall rocks.

Along the SLDZ, a thin discontinuous band of volcaniclastic rocks occurs between the lower part of the Deloro assemblage (i.e. ultramafic komatiitic volcanic and intrusive units comprising the Lower Detour Lake Formation: Oliver et al., 2012) and the dominantly tholeiitic mafic volcanic rocks of the Upper Detour Lake Formation. Along strike, this thin band of volcaniclastic rocks is interpreted to correlate with the prolific CMH that hosts part of the higher grade mineralization at the Detour Lake mine (Fig. 1, 5a; Oliver et al., 2012). There, the strained horizon consists of a 0.5 to 2.0 m thick intermediate to felsic, calc-alkaline volcaniclastic unit, interlayered with silicified mafic volcanic rocks and albitite dykes. A similar lithological assemblage extends eastward in Quebec, such as across the Vortex Zone (Fig. 1). Here, the mineralization is subparallel to the SLDZ and likewise is located at the contact between tholeiitic mafic and calc-alkaline intermediate volcaniclastic units, adjacent to an alkaline granite or albitite dyke (Fig. 5b). Although the dyke is locally mineralized, most of the gold is hosted by the strongly deformed volcaniclastic units.

The settings of the Massicotte and Lower Detour deformation zones are also analogous to the CMH along the SLDZ (Fig. 1, 5, 8). A similar silicified and sulphidized (cherty) mineralized zone is present at the contact between komatiitic and tholeiitic volcanic and intrusive rocks just south of the MDZ. Further south, in the structural hanging wall of the LDDZ, the silicified and sulphidized rocks of Zone 75 locally have a calc-alkaline affinity and occur along a second-order deformation zone that juxtaposes Fe-rich with Mg-rich tholeiitic sequences. Gold in Zone 58N is almost exclusively hosted by the leucocratic alkaline intermediate feldspar porphyry (IPF1), which acted as a competent unit during deformation and formation of the gold-bearing quartz-carbonate-tourmaline vein network. The ca. 2694 Ma age of the dyke represents the maximum age of the mineralization. Some thin, higher grade zones occur near contacts with highly strained mafic volcanic rocks, which are mostly barren of gold.

The Bug Lake deposit may represent a different gold mineralization style. The auriferous, steeply dipping, high-strain zones are northwest- to north-northwest-trending and occur at the contacts of a porphyry dyke, most probably due to a strong competency contrast with the enveloping mafic volcanic rocks. These high-strain zones are subparallel to the Martiniere fault to

Table 1. Main characteristics of some of the gold mineralized deposits/zones associated with the Sunday Lake and Lower Detour deformation zones.

Locality	Geological setting	Main characteristics	Associated alteration	Timing versus main stage of deformation-metamorphism	Similar style
Detour Lake mine: Main Zone	Local bend/ramp in SLDZ: Contact between Deloro >2725 Ma komatiitic and <2725 Ma tholeiitic volcanic units, intruded by subalkaline to locally alkaline intermediate dykes/sills	Silicified/sulphidized zone (CMH) and hanging-wall fault-fill±extensional quartz-carbonate veins (Q veins) and late sulphide-rich breccia	Biotite-quartz-albite-carbonate; talc-chlorite in komatiitic basalt	Syn to late	
Detour Lake mine: Calcite Zone	Hanging wall of SLDZ: contacts between Deloro tholeiitic ±calc-alkaline massive and pillow basalt	High-strain zones with deformed quartz-calcite-sulphide veins, stockwork, and stringer	Biotite-quartz-actinolite-chlorite-albite±carbonate	Syn to late	
Vortex Zone 475	SLDZ: contacts between Manthet (Deloro) tholeiitic and calc-alkaline mafic±intermediate volcanic and volcaniclastic units (similar horizon as CMH)	High-strain zones with deformed quartz-carbonate-pyrite veins, locally with semi-massive pyrite	Carbonate-chlorite-sericite	Syn to late	Lower Detour Zone 75
Vortex Zone 450	SLDZ: contacts between Manthet tholeiitic and calc-alkaline volcanic and volcaniclastic units (similar horizon as CMH) in the hanging wall of alkaline granite dyke	High-strain zones with quartz-carbonate± tourmaline veins and disseminated pyrite-associated late breccia zones	Carbonate-chlorite-sericite in volcanic; albite-sericite-carbonate-hematite in dyke	Syn to late	CMH; Bug Lake
Martiniere West	Hanging wall of SLDZ: high-strain zones in tholeiitic leuco-xene-bearing quartz gabbro	Silicified high-strain and breccia zones with quartz-(dolomite/ankerite)-tourmaline veins and 1 to 5 vol.% pyrite±arsenopyrite±chalcopyrite	Carbonate-quartz-sericite	Syn to late	
Bug Lake	Hanging wall north of SLDZ: NW-trending high-strain zones in Manthet Fe-tholeiitic to calc-alkaline pillow basalt and gabbro along both contacts of a feldspar porphyry dyke	5 to 10 vol.% disseminated (±stringer) pyrite ±chalcopyrite with dolomite/ankerite-quartz ±tourmaline veins and breccia	Carbonate-sericite-quartz	Syn to late	Vortex 450; CMH
Lower Detour: Zone 75	Hanging-wall splay of the LDDZ (South Break): high-strain zone juxtaposing Deloro Fe-tholeitic basalt against calc-alkaline and high-Mg tholeiitic intermediate volcanic units	Silicified high-strain zone with 5 to 20 vol.% sulphides as mainly pyrite±pyrrhotite-chalcopyrite-sphalerite	Quartz-sericite-biotite	Syn	Vortex zone 475
Lower Detour: Zone 58N	Footwall of SouthBreak: in ca. 2694 Ma alkaline plagioclase-phyric quartz monzonite to tonalite	Discrete laminated quartz-tourmaline-carbonate±visible gold veins, stockwork, and pseudo-breccia; 0.5 to 5 vol.% sulphides	Albite-sericite-quartz-carbonate±hematite	Syn	Goldex
Lower Detour "trend" in Quebec	MDZ and LDDZ: high-strain zones at contacts between calc-alkaline andesite and tholeiitic basalt or at margins of sub-alkaline to alkaline, intermediate to felsic porphyritic intrusions	Quartz-carbonate±tourmaline veins with pyrite ±galena±sphalerite	Chlorite-epidote-carbonate in volcanic; albite (hematite)-sericite-chlorite in porphyry	Syn to late	Lower Detour zones

Abbreviations: CMH = chert marker horizon, LDDZ = Lower Detour deformation zone, MDZ = Massicotte deformation zone, SLDZ = Sunday Lake deformation zone.

the northeast (e.g. Faure, 2015) and may represent subsidiary structures of this fault. All structures related to this fault system extend southeastward where they are interpreted to merge into the SLDZ. At first glance, such overall lithological and structural settings are comparable to those of the Fenelon deposit (Wallbridge Mining Company, 2019), as well as the recently discovered auriferous high-strain zones at Area 51 (Wallbridge Mining Company, 2019), Area 52 (Balmoral Resources, 2019), and at the TMA area (Detour Gold Corporation, 2018), west of the Detour Lake mine (Fig. 1).

IMPLICATIONS FOR EXPLORATION

The geological setting and characteristics of gold mineralization along the SLDZ and LDDZ outline and refine the main critical metallotects for orogenic gold exploration in the northwestern Abitibi greenstone belt, which include (1) major long-lived deformation zones and second-order structures; (2) tholeiitic and komatiitic volcanic assemblages, locally separated by calc-alkaline volcaniclastic rocks; (3) Porcupine/Cadillac-like basins with turbidite deposits known locally as the Caopatina assemblage and deformed and altered Timiskaming-like polymictic conglomerate potentially correlative to the Haüy Formation; (4) intermediate to felsic, typically subalkaline to alkaline reddish-coloured dykes and small intrusions; (5) quartz-carbonate±tourmaline veins, stockwork and breccia zones, with varying amounts of sulphides and silicification; and (6) carbonate-sericite/biotite-albite-altered wall rocks. These key elements are analogous to parts of the prolific southern Abitibi gold belt, such as the Timmins-Porcupine and Val-d'Or gold districts. The revised geological and geochronological model for the SLDZ and LDDZ provides a framework to improve exploration strategies in a poorly exposed, but fertile region that includes the giant Detour Lake gold mine.

ACKNOWLEDGMENTS

This report is a contribution to NRCan's Targeted Geoscience Initiative Program (TGI-5). Support for this study was provided through Activity G-1.1: Gold through space and time at the Archean of the Gold Project. Detour Gold Corporation (A. DeLazzer, K. Malcolm, G. MacGillivray), Midland Exploration (M. Masson, S. Trépanier), Balmoral Resources (M. Tucker), Probe Metals (M. Gagnon, M. Guay), SOQUEM (O. Grondin), and their exploration staff are acknowledged for giving access to their property, sharing knowledge and data sets, including unpublished maps and sections and providing logistical support. This report greatly benefited from the constructive review of D. Rhys. We also acknowledge C. Lawley, V. Bécu, and E. Ambrose for their reviews and editorial handling.

REFERENCES

Ayer, J.A., Chartrand, J.E., Duguet, M., Rainsford, D.R.B., and Trowell, N.F., 2009. Geological compilation of the Burntbush-Detour lakes area, Abitibi greenstone belt; Ontario Geological Survey, preliminary maps P3609, scale 1:100 000.

Balmoral Resources, 2018. The Detour East Property; Balmoral Resources <http://www.balmoralresources.com/projects/detour-east/mineralization> [accessed November 14, 2019]

Balmoral Resources, 2019. Balmoral intersects 14.03 g/t gold over 3.29 metres in shallow, high-grade gold discovery, area 52, Detour gold trend project, Quebec <http://www.balmoralresources.com/assets/docs/nr/NR19-17-16-09-2019-BAR-Discovers-New-High-Grade-on-SLD.pdf> [accessed November 14, 2019]

Barrie, C.T. and Krogh, T.E., 1996. U-Pb zircon geochronology of the Selbaie Cu-Zn-Ag-Au Mine, Abitibi subprovince, Canada; Economic Geology, v. 91, p. 563–575.

Bleeker, W., 2015. Synorogenic gold mineralization in granite-greenstone terranes: The deep connection between extension, major faults, synorogenic clastic basins, magmatism, thrust inversion, and long-term preservation; *in* Targeted Geoscience Initiative 4: Contributions to the understanding of Precambrian lode gold deposits and implications for exploration, (ed.) B. Dubé and P. Mercier-Langevin; Geological Survey of Canada, Open File 7852, p. 25–47.

Cameron, E.M., 1993. Precambrian gold: Perspectives from the top and bottom of shear zones; The Canadian Mineralogist, v. 31, p. 917–944.

Castonguay, S., Dubé, B., Mercier-Langevin, P., and Wodicka, N., 2019. Geological setting and mineralization styles of the Sunday Lake and Lower Detour 'gold trends', northwestern Abitibi greenstone belt, Ontario and Quebec; *in* Targeted Geoscience Initiative: 2018 report of activities, (ed.) N. Rogers; Geological Survey of Canada, Open File 8549, p. 9–22.

David, J., Davis, D.W., Dion, C., Gautier, J., Legault, M., and Roy, P., 2007. Datations U-Pb effectuées dans la Sous-province de l'Abitibi en 2005–2006; Ministère des Ressources naturelles et de la Faune du Québec, RP 2007-01, 17 p.

Detour Gold Corporation, 2018. Detour Lake operation Ontario, Canada: NI 43-101 technical report; Detour Gold Corporation, 354 p. <https://www.detourgold.com/investors/news/press-release-details/2018/Detour-Gold-Files-Technical-Report-for-Detour-Lake/> [accessed November 14, 2019]

Detour Gold Corporation, 2019. Detour Gold Reports Fourth Quarter and Year-End 2018 Financial Results <https://www.detourgold.com/investors/news/press-release-details/2019/Detour-Gold-Reports-Fourth-Quarter-and-Year-End-2018-Financial-Results/> [accessed November 14, 2019]

Detour Gold Corporation, 2020. Detour Gold Reports Q4 and FY 2019 Production Results <https://www.detourgold.com/investors/news/press-release-details/2020/Detour-Gold-Reports-Q4-and-FY-2019-Production-Results> [accessed January 30, 2020]

Dubé, B. and Gosselin, P., 2007. Greenstone-hosted quartz-carbonate vein deposits; *in* Mineral Deposits of Canada: A synthesis of major deposit-types, district metallogeny, the evolution of geological provinces, and exploration methods, (ed.) W.D. Goodfellow; Geological Association of Canada, Mineral Deposits Division, Special Publication No. 5, p. 49–73.

Dubé, B., Mercier-Langevin, P., Ayer, J., Atkinson, B., and Monecke, T., 2017. Orogenic greenstone-hosted quartz-carbonate gold deposits of the Timmins-Porcupine camp; *in* Archean

Base and Precious Metal Deposits, southern Abitibi Greenstone Belt, Canada, (ed.) T. Monecke, P. Mercier-Langevin, and B. Dubé; Society of Economic Geologists, Reviews in Economic Geology, v. 19, p. 51–79.

Dubosq, R., Lawley, C.J.M., Rogowitz, A., Schneider, D., and Jackson, S.E., 2018. Pyrite deformation and connections to gold mobility: Insight from micro-structural analysis and trace element mapping; Lithos, v. 310–311, p. 86–104.

Dubosq, R., Schneider, D., Camacho, A., and Lawley, C.J.M., 2019. Geochemical and geochronological discrimination of biotite types at the Detour Lake gold deposit, Canada; Minerals, v. 9, 22 p.

Faure, S., 2012. Réévaluation paléo-environnementale du complexe volcanique de Selbaie et de son potentiel métallogénique; CONSOREM Project Report 2011-08, 26 p. <http://www.consorem.ca/production_scientifique/2011_08/Rapport%202011-08%20Selbaie.pdf> [accessed November 15, 2019]

Faure, S., 2015. Prolongement de la faille Sunday Lake (mine Detour Gold, Ont.) au Québec et son potentiel pour les minéralisations aurifères et en métaux de base; CONSOREM Project Report 2013-02, 41 p. <http://www.consorem.ca/production_scientifique/2013_02/Rapport%202013-02%20DETOUR_VF_20160401.pdf> [accessed November 15, 2019]

Fayard, Q., Mercier-Langevin, P., Wodicka, N., Daigneault, R., and Perreault, S., 2020. The B26 Cu-Zn-Ag-Au project, Brouillan volcanic complex, Abitibi greenstone belt, part 1: Geological setting and geochronology; *in* Targeted Geoscience Initiative 5: Contributions to the Understanding of Gold Deposit, (ed.) P. Mercier-Langevin, C.J.M. Lawley, and S. Castonguay; Geological Survey of Canada, Open File 8712, p. 98–107. doi:10.4095.323668

Jensen, L.S. and Pyke, D.R., 1982. Komatiites in the Ontario portion of the Abitibi belt; *in* Komatiites, (ed.) N.T. Arndt and E.G. Nisbet; George Allen and Unwin, London, p.147–157.

Lacroix, S., 1994. Géologie de la partie ouest du sillon Harricana-Turgeon, Abitibi; Ministère des Ressources naturelles du Québec, MB 94-54, 26 p.

Leclerc, F., Harris, L.B., Bédard, J.H., van Breemen, O., and Goulet, N., 2012. Structural and stratigraphic controls on magmatic, volcanogenic, and shear zone-hosted mineralization in the Chapais-Chibougamau mining camp, northeastern Abitibi, Canada; Economic Geology, v. 107, p. 963–989.

Malcolm, K.J., Kontak, D.J., Tinkham, D.K., Ayer, J.A., and MacGillivray, G., 2015. The Lower Detour Lake Au discovery, Ontario, Canada: A high-grade oxidized intrusion-related Au deposit; American Geophysical Union-Geological Association of Canada-Mineralogical Association of Canada-Canadian Geophysical Union Joint Assembly, Abstracts and Proceedings, p. 302–303.

Marmont, S., 1986. The geological setting of the Detour Lake gold mine, Ontario, Canada; *in* Gold '86: An International Symposium on the Geology of Gold Deposits, (ed.) A.J. Macdonald; Toronto, p. 3–22.

Marmont, S. and Corfu, F., 1988. Timing of gold introduction in the late Archean framework of the Canadian Shield: Evidence from U-Pb zircon geochronology of the Abitibi Subprovince; *in* The Geology of Gold Deposits: The perspective in 1988, (ed.) R.R. Keays, W.R.H., Ramsay, and D.I. Groves; Society of Economic Geologists, Monograph 6, p. 101–111.

Midland Exploration, 2018. Midland et SOQUEM découvrent un important système aurifère (zone Vortex) de type "syenite-associated" à l'est de Detour Lake; Midland Exploration <https://www.midlandexploration.com/fr/2018/01/17/midland-et-soquem-decouvrent-un-important-systeme-aurifere-zone-vortex-de-type-syenite-associateda-lest-de-detour-lake/> [accessed November 14, 2019]

Oliver, J., Ayer, J., Dubé, B., Aubertin, R., Burson, M., Panneton, G., Friedman, R., and Hamilton, M., 2012. Structure, stratigraphy, U-Pb geochronology, and alteration characteristics of gold mineralization at the Detour Lake gold deposit, Ontario, Canada; Exploration and Mining Geology, v. 20, p. 1–30.

Probe Metals, 2016. Probe Metals and SOQUEM drill 17.5 g/t Au over 1 metre along the Lower Detour gold trend and commence drilling on phase II program; Probe Metals <https://www.probemetals.com/site/assets/files/1069/2016-08-24_nr.pdf> [accessed November 14, 2019]

Probe Metals, 2018. Detour Quebec project overview Probe Metals <https://www.probemetals.com/projects/detour-quebec/overview/> [accessed November 14, 2019]

Robert, F., Poulsen, K.H., Cassidy, K.F., and Hodgson, C.J., 2005. Gold metallogeny of the Superior and Yilgarn Cratons; *in* Economic Geology 100th Anniversary Volume, (ed.) J.W. Hedenquist, J.F.H. Thompson, R.J. Goldfarb, and J.P. Richards; Society of Economic Geologists, p. 1001–1033.

Thurston, P.C., Ayer, J.A., Goutier, J., and Hamilton, M.A., 2008. Depositional gaps in Abitibi greenstone belt stratigraphy: A key to exploration for syngenetic mineralization; Economic Geology, v. 103, p. 1097–1134.

Voordouw, R. and Jutras, M., 2018. Technical (N.I. 43-101) Report on the Martiniere Property, March 27, 2018; Balmoral Resources, 113 p. <http://www.balmoralresources.com/assets/docs/Martiniere%202018%20NI%2043-101%20report%20redsize-20180329174245.pdf> [accessed November 14, 2019]

Wallbridge Mining Company, 2019. Fenelon Project <https://www.wallbridgemining.com/s/fenelon.asp> [accessed November 14, 2019]

Winchester, J.A. and Floyd, P.A., 1997. Geochemical discrimination of different magma series and their differentiation products using immobile elements; Chemical Geology, v. 20, p. 325–343.

Geology, structural evolution, and hydrothermal alteration of the Island gold deposit, Michipicoten greenstone belt, Ontario

Tyler J. Ciufo[1*], Katia Jellicoe[1†], Chris Yakymchuk[1], Shoufa Lin[1], Patrick Mercier-Langevin[2], and Natasha Wodicka[3]

[1]University of Waterloo, 200 University Avenue West, Waterloo, Ontario N2L 3G1
[2]Geological Survey of Canada, 490 rue de la Couronne, Québec, Quebec G1K 9A9
[3]Geological Survey of Canada, 601 Booth Street, Ottawa, Ontario K1A 0E8
*Corresponding author's e-mail: tjciufo@uwaterloo.ca
†Corresponding author's e-mail: k.jellicoe@gmail.com

ABSTRACT

The Archean Island Gold deposit is situated in the Michipicoten greenstone belt within the Abitibi-Wawa subprovince. Gold mineralization is hosted in dacitic volcanic and volcaniclastic rocks, gabbro, and a tonalite-trondhjemite body (Webb Lake stock) within the southern domain of the east-west-trending Goudreau Lake deformation zone. The area is highly prospective, however, the controls on high-grade mineralization and the timing of events in the Michipicoten belt remain to be firmly established and compared with major gold systems of the southern Abitibi belt.

Several phases of deformation have affected the host rocks. The first deformation (D_1) event produced regional-scale folds. The second deformation (D_2) event resulted in camp-scale folds (F_2), a steep axial planar foliation (S_2), regional greenschist-grade metamorphism, and the formation of the Goudreau Lake deformation zone. The third deformation (D_3) event is expressed by brittle reverse faults, camp- to outcrop-scale folds (F_3), and a weakly developed axial planar (S_3) cleavage.

Gold mineralization in the main Island Gold ore zones was emplaced along the Goudreau Lake deformation zone during the D_2 deformation event. The Goudreau Lake deformation zone is inferred to be the major conduit that focused the gold-bearing fluids. The main ore zones dip steeply towards the south and consist of shear-hosted laminated quartz veins (V_1) and associated extensional veinlets (V_2). This V_1-V_2 veining is sub-parallel to the S_2 foliation and concentrated in the strain shadow of the pre-mineralization Webb Lake stock during D_2 north-side-up, sinistral transpression. Shallowly dipping, extensional quartz veins (V_{GD}) also host economic gold mineralization in the Goudreau Zone, which is located north of the main zones. The V_{GD} and V_1-V_2 veins are cut by extensional quartz veins (V_3) that formed during the third deformation (D_3) event in areas of high competency contrast. Post-mineralization tourmaline-quartz veins (V_4) locally overprint the V_3 veins and pre-existing structures.

Alteration envelopes associated with auriferous veining at the Island Gold deposit range from the centimetre to metre scale and are enriched in Au, K_2O, Rb, S, and Te, and depleted in Na_2O. Alteration minerals associated with ore zones generally include biotite, Ca-Mg-Fe carbonates, chlorite, plagioclase, quartz, sulphides (pyrite±pyrrhotite±chalcopyrite), and white mica (muscovite±phengite). Weak alteration associated with the late V_3 non-auriferous veins is variable and local.

The upper and lower absolute limits on the timing of gold mineralization are constrained by the U-Pb zircon ages of the mineralized Webb Lake stock (2724.1 ± 4.3 Ma) and the post-mineralization silica-poor diorite-monzodiorite (I2M) dykes (2672.2 ± 3.5 Ma). The youngest detrital zircon ages from overlying Doré sedimentary rocks, which were affected by syn-D_2 greenschist-facies metamorphism, further constrain the maximum age limit for the timing of gold mineralization to 2680 ± 3 Ma. This timing (2680 ± 3 Ma to 2672.2 ± 3.5 Ma) falls within the typical age range for gold deposits in greenstone belts of the Superior Province.

INTRODUCTION

Island Gold is an operating underground gold mine located approximately 35 km north of Wawa, Ontario, near the town of Dubreuilville. At the end of 2016, indicated and measured resources were estimated at 0.48 Mt at 5.94 g/t Au (91,400 oz) with inferred resources estimated at 3.04 Mt at 10.18 g/t Au (995,700 oz: Adam et al., 2017). Additionally, proven and probable mineral reserves were estimated at 2.55 Mt at 9.17 g/t Au (752,200 oz: Adam et al., 2017).

The Island Gold deposit is part of the Wawa gold camp, which is located between the major mining

Ciufo, T.J., Jellicoe, K., Yakymchuk, C., Lin, S., Mercier-Langevin, P., and Wodicka, N., 2020. Geology, structural evolution, and hydrothermal alteration of the Island Gold deposit, Michipicoten greenstone belt, Ontario; *in* Targeted Geoscience Initiative 5: Contributions to the Understanding of Canadian Gold Systems, (ed.) P. Mercier-Langevin, C.J.M. Lawley, and S. Castonguay; Geological Survey of Canada, Open File 8712, p. 143–156. https://doi.org/10.4095/323671

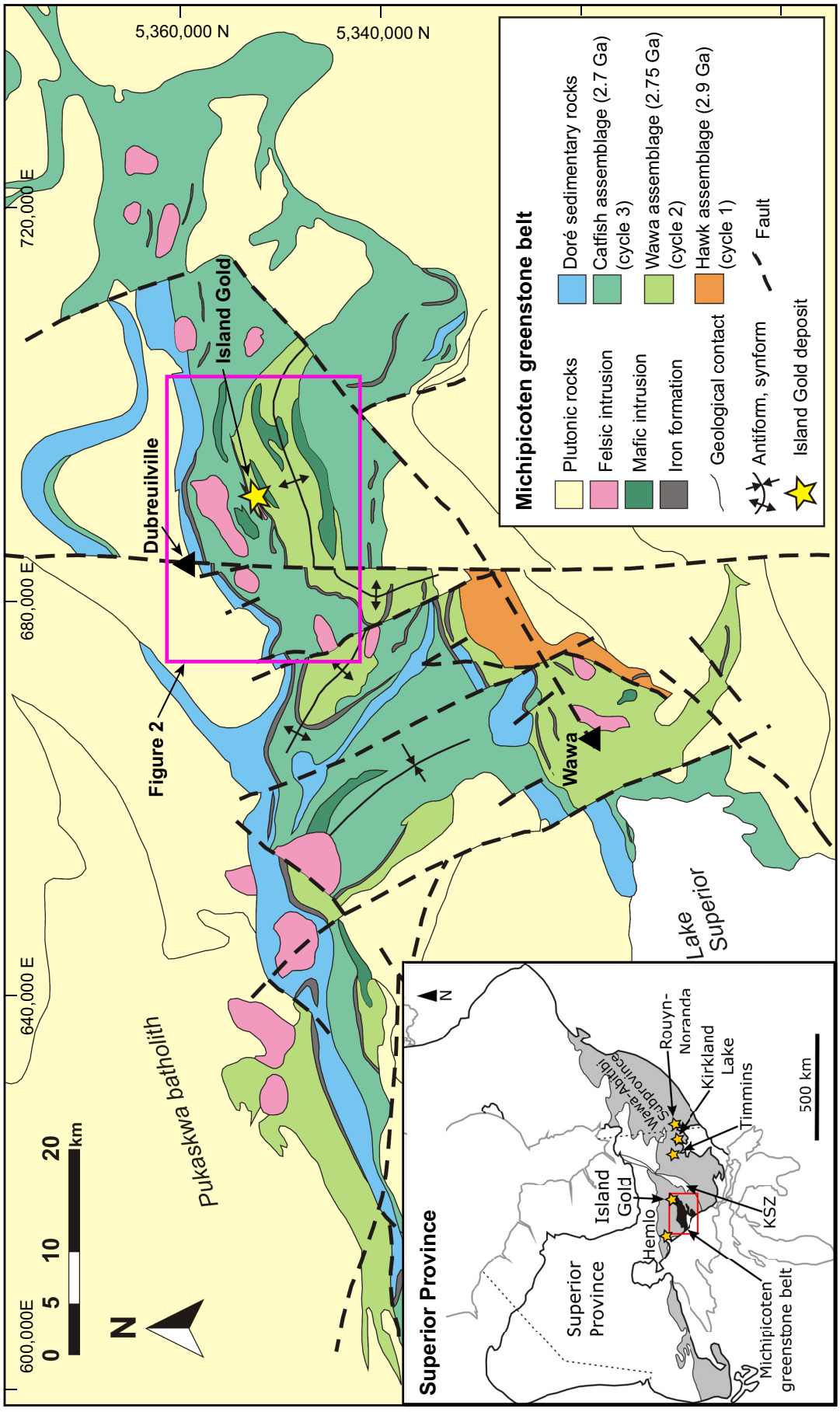

Figure 1. Geological map of the Michipicoten greenstone belt (*modified from* Arias and Heather, 1987; Williams et al., 1991; Jellicoe, 2019). The extent of Figure 2 is outlined by the purple rectangle. The inset delineates the location of the Michipicoten greenstone belt within the Abitibi-Wawa subprovince (*modified from* Card, 1990; Williams et al., 1991; Jellicoe, 2019). Abbreviation: KSZ = Kapuskasing structural zone.

camps of the Abitibi greenstone belt to the east (e.g. Kirkland Lake, Timmins, Val-d'Or, and Rouyn-Noranda), and the Hemlo gold camp to the west (Fig. 1). The deposit is hosted in the Goudreau Lake deformation zone (GLDZ), which has been compared with the gold-rich fault systems (specifically the Larder-Cadillac fault zone) that host numerous mining camps east of the Kapuskasing structural zone (Leclair et al., 1993; Fig. 1). The Wawa gold camp has not been as extensively studied as some of the other gold camps of the Abitibi-Wawa subprovince. The last study that included a detailed examination of the Island Gold deposit (Heather and Arias, 1992) predates the development of the Island Gold mine. Access to underground workings and drill core at Island Gold and in the vicinity allows access to a wealth of new information and data. This provides an opportunity to revisit the geology and metallogeny of a "re-emerging" district. Comparing the Island Gold deposit with other Archean gold deposits of the Abitibi greenstone belt will contribute to refining models for gold exploration in Archean terranes.

Two complementary M.Sc. research projects that focus on the structural and hydrothermal history of the Island Gold deposit commenced under the Gold Project of the Targeted Geoscience Initiative 5. The main findings of these projects are summarized here. Readers are referred to Jellicoe (2019) for detailed information about the deformation history, structural controls on ore, and the constraints on the timing of events, and to Ciufo (2019) for detailed information about the host lithologies, the nature and effects of hydrothermal alteration and metamorphism, and exploration vectors.

REGIONAL AND LOCAL GEOLOGY

The Island Gold deposit is located west of the Kapuskasing structural zone within the Abitibi-Wawa subprovince (Fig. 1). This subprovince consists mainly of east-west-trending supracrustal belts enveloped by larger granitoid-dominated areas. The volcanic and plutonic rocks mainly range in age from approximately 2.9 to 2.7 Ga and 2.9 to 2.6 Ga, respectively (Percival et al., 2012). The Michipicoten greenstone belt is located in the western part of the subprovince and hosts the Island Gold deposit. The Michipicoten greenstone belt is dominated by volcanic rocks that have been subdivided into three volcanic cycles: the ca. 2900 Ma Hawk assemblage, the ca. 2750 Ma Wawa assemblage, and the ca. 2700 Ma Catfish assemblage (Williams et al., 1991; Sage, 1994; Fig. 1). Each cycle has a mafic base and becomes more felsic towards the top. The first and second cycles are capped by unconformities separating the volcanic rocks from overlying iron formations. The volcanic and sedimentary rocks are cut by dioritic-gabbroic intrusions as well as granitic stocks of various ages (Sage et al., 1996). The Doré sedimentary rocks consist mainly of wacke and conglomerate that unconformably overlie the youngest volcanic cycle. The Doré sedimentary rocks are interpreted to be derived from the underlying volcanic rocks and their intrusive equivalents (Sage, 1994). Most rocks within the belt have been metamorphosed to greenschist facies, although contact aureoles of granitoid rocks at the outer margins of the belt can reach amphibolite grade (Rice and Donaldson, 1992). The granitoids proximal to the Michipicoten greenstone belt yield U-Pb ages mostly younger than, or equivalent to, the 2750 Ma Wawa cycle (Turek et al., 1982).

The Island Gold deposit is hosted by the GLDZ (Fig. 2) in the Goudreau-Lochalsh gold district of the Wawa gold camp. This 4.5 km wide regional structure is composed of multiple shear zones separating less strained domains. It has been traced along strike for >25 km (Arias and Heather, 1987). The Island Gold deposit is located in the southern domain of the GLDZ on the northern limb of the Goudreau anticline (Fig. 2). The southern domain is ~2 km wide, strikes N070°, and has been traced for ~8 km along strike (Arias and Heather, 1987). The Island Gold deposit is hosted mainly within the second cycle felsic-intermediate volcanic rocks of the Wawa assemblage (Arias and Helmstaedt, 1990) and, to a lesser extent, in mafic intrusive rocks (Fig. 3). The Michipicoten iron formation locally separates the cycle 2 felsic-intermediate volcanic rocks from the third cycle mafic volcanic rocks to the north. The Webb Lake stock, which hosts the Magino deposit a few kilometres west of the Island Gold mine (Fig. 3), forms an elongated intrusive body within the GLDZ. The Herman Lake nepheline-syenite intrusive complex (2671 +17/-10 Ma: Corfu and Sage, 1992) and the Maskinonge Lake granodiorite stock (2671 ± 2 Ma: Corfu and Sage, 1992) are large intrusive bodies located north of Island Gold (Fig. 2). Various pre- and post-ore dykes are also present in the Island Gold area.

HOST ROCKS, DEFORMATION, MINERALIZATION, AND ALTERATION

Field Relationships and Petrology

The main rock types present at the Island Gold mine include Wawa assemblage felsic-intermediate volcanic rocks, the Michipicoten iron formation, pre-ore mafic sills and dykes, the Webb Lake stock, and four sets of post-ore dykes (gabbro/lamprophyre, quartz diorite, I2M silica-poor diorite-monzodiorite, and diabase-quartz diabase). A summary of field relationships and petrological results is presented in this section for each of these lithologies. For more details, including methods and data, readers are referred to Ciufo (2019), Ciufo et al. (2019), and Jellicoe (2019).

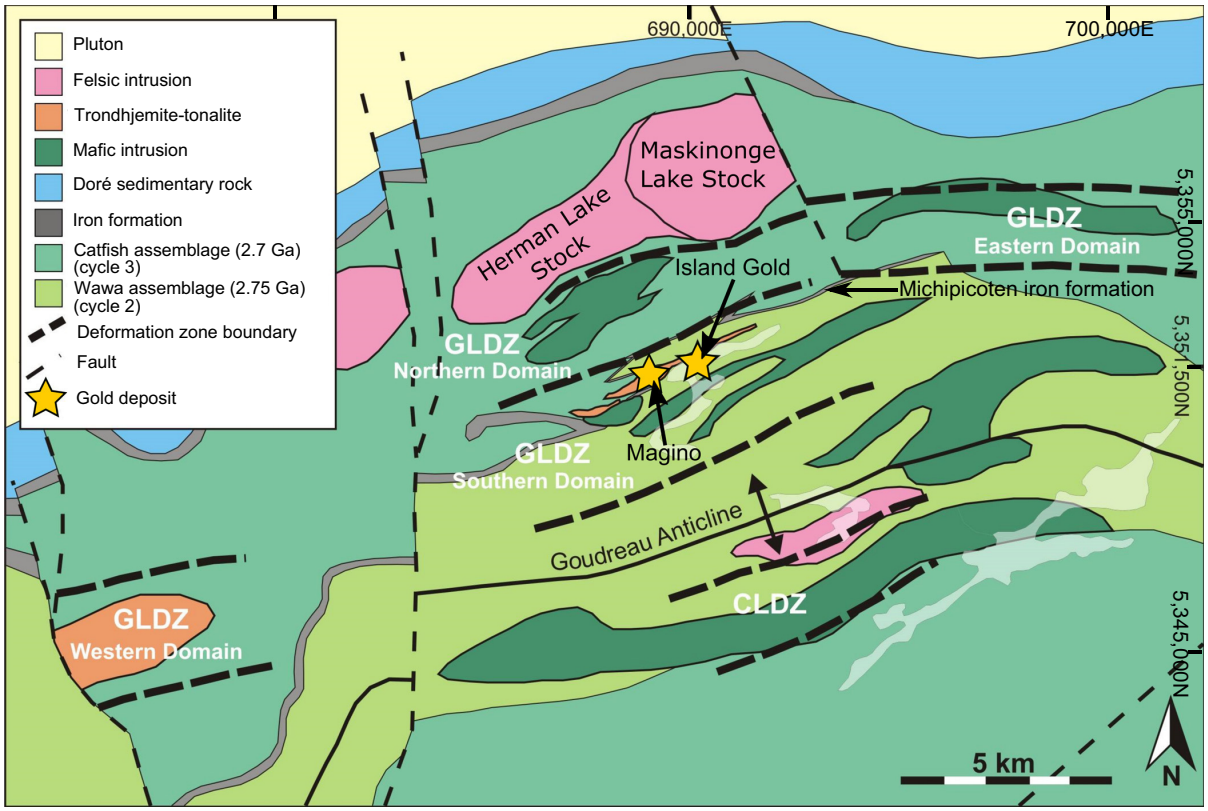

Figure 2. Geology of the Island Gold deposit and surrounding area (*modified from* Arias and Heather, 1987; Williams et al., 1991; and Jellicoe, 2019). Abbreviations: CLDZ = Cradle Lake deformation zone; GLDZ = Goudreau Lake deformation zone.

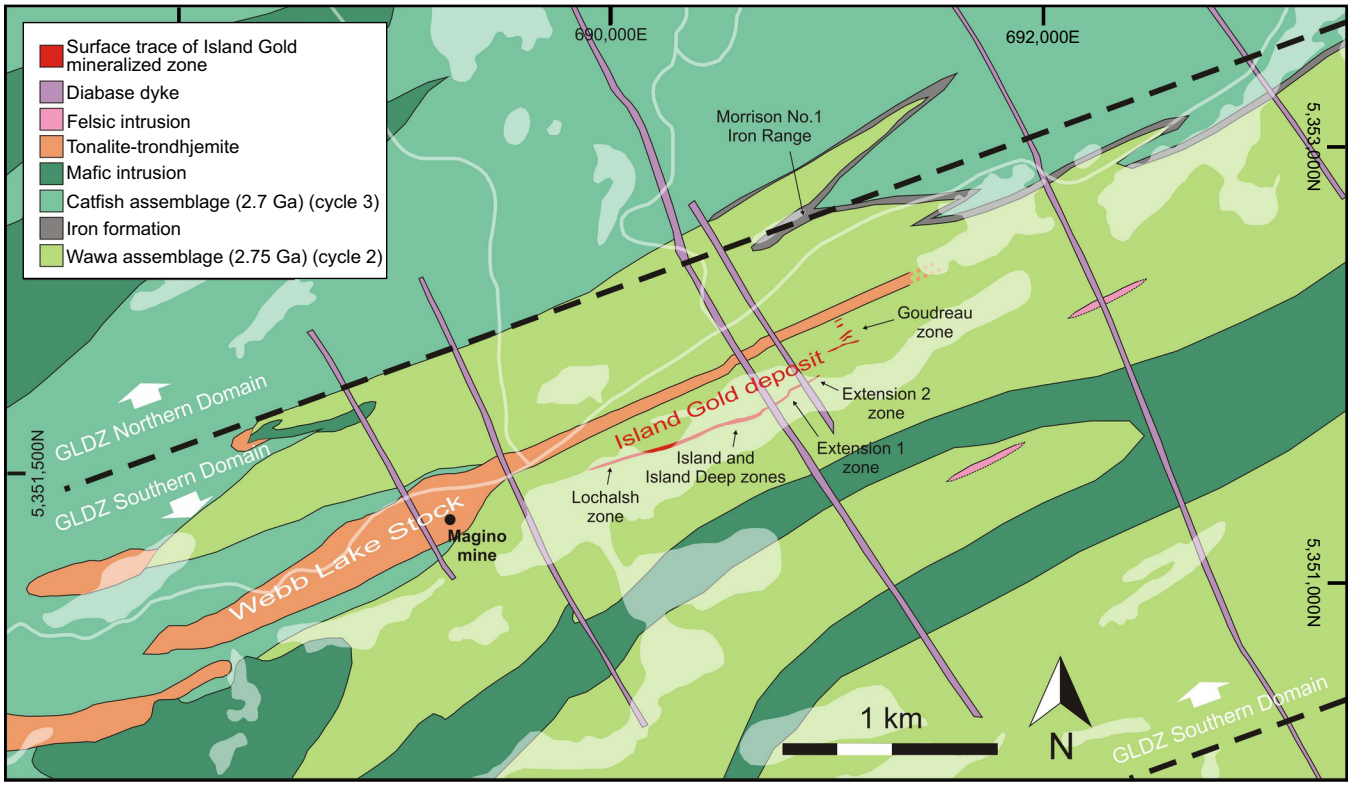

Figure 3. Geological map of the study area showing the southern Goudreau Lake deformation zone boundaries and the Island Gold deposit zones. Note the location of the Island Gold deposit relative to the Webb Lake stock. Partially transparent areas represent water bodies. *Modified from* Jellicoe (2019 and references therein).

The felsic-intermediate volcanic rocks (cycle 2, Wawa assemblage) are the most volumetrically significant lithologies at the Island Gold deposit (Fig. 3). They are also the oldest as they are stratigraphically overlain or crosscut by all other lithologies. They consist of tuff, lapilli tuff, tuff breccia, flows, and compositionally equivalent hypabyssal intrusive units. These rocks consist of plagioclase (andesine), quartz, calcite, biotite, chlorite, white mica (muscovite and illite), and epidote. Accessory minerals (typically <1 vol.%) include actinolite, apatite, chloritoid, grunerite, hematite, hornblende, ilmenite, magnetite, rutile, siderite, titanite, tourmaline, and zircon. These rocks are dacitic in composition (Ciufo, 2019), fine-grained (<1 mm), and often contain quartz and plagioclase phenocrysts (2–5 mm).

The Michipicoten iron formation stratigraphically overlies the dacitic volcanic rocks (Sage, 1994; Fig. 3), but thin iron formation beds are locally interlayered with the dacitic rocks as well. Sulphide and iron oxide-rich Algoma-type iron formation (cf. Gross, 1980) that can be massive or banded are present. Where banded, layers are composed of iron oxides (magnetite and hematite) and sulphides (mostly pyrite) alternating with chert, carbonate, and chlorite-rich layers. Accessory minerals include chloritoid, epidote, ilmenite, white mica, and tourmaline.

The pre-gold mineralization mafic intrusive rocks consist of gabbroic sills and dykes (Ciufo, 2019) and are cut by the auriferous veins in the ore zones. Their mineralogy consists of chlorite, quartz, epidote, carbonates (mostly calcite), actinolite, titanite, plagioclase (oligoclase–andesine), and hornblende. Accessory minerals include chloritoid, hematite, ilmenite, magnetite, clinopyroxene, rutile, tourmaline, and white mica (phengite). Most of the primary minerals in this lithology have been replaced with greenschist-facies minerals.

The Webb Lake stock is a relatively minor lithology at the Island Gold deposit, but it hosts the bulk of the ore at the Magino deposit to the west (Turcotte and Pelletier, 2008; Fig. 3). It is equigranular, medium- to coarse-grained, and intrudes the dacitic volcanic rocks, iron formation, and gabbro, and therefore post-dates these lithologies. It is composed of plagioclase (albite–oligoclase), quartz, chlorite, biotite, white mica (phengite±muscovite), epidote, and calcite. Accessory minerals include actinolite, apatite, chloritoid, hematite, hornblende, ilmenite, pyrite, pyroxene, rutile, titanite, tourmaline, and zircon. The Webb Lake stock is mainly tonalite with >10 vol.% ferromagnesian minerals (cf. Barker, 1979) but also has less abundant trondhjemitic phases composed of <10 vol.% ferromagnesian minerals (Ciufo, 2019).

Two distinct post-gold mineralization dyke sets commonly parallel and locally cut the V_1-V_2 ore zones (*see below* for vein nomenclature). One set consists of gabbro/lamprophyre composed of quartzo-feldspathic minerals (oligoclase-andesine and quartz), carbonate minerals, chlorite, and white mica. Accessory minerals include actinolite, epidote, hematite, rutile, titanite, tourmaline, and zircon. The other set consists of silica-poor diorite–monzodiorite (referred to as I2M by mine geologists), which is composed of plagioclase (oligoclase), carbonate minerals, biotite, chlorite, epidote, magnetite, and orthoclase. Accessory minerals include hematite, pyrite, quartz, rutile, titanite, tourmaline, white mica, and zircon. The silica-poor diorite-monzodiorite appears less deformed and metamorphosed than the gabbro/lamprophyre and therefore could be younger, although no clear crosscutting relationship between these two sets of dykes was observed. A minor quartz diorite dyke was exposed in one locality in the mine and as xenoliths within the silica-poor diorite-monzodiorite.

The lithologies discussed above in this section contain metamorphic assemblages that commonly include chlorite, actinolite, and epidote indicative of greenschist-facies metamorphism. Late diabase–quartz diabase dykes sharply cut all other lithologies and quartz veins, and are likely part of the Proterozoic Matachewan dyke swarm (Fig. 3).

Structural Geology

Three major deformation events (D_1 to D_3) affected the host rocks of the Island Gold deposit and surrounding rocks. The regional deformation event (D_1) is responsible for steepening of the volcanic and sedimentary rocks during regional- to camp-scale, northeast-southwest-striking upright folding (F_1) and formation of an axial-plane cleavage (S_1). The Goudreau anticline, the axial trace of which is located approximately two kilometres to the southeast of the Island Gold mine, is a regional F_1 fold (Fig. 2). The deposit is located on its northern limb in spatial association with a second-order parasitic synclinal fold to the Goudreau Anticline (Fig. 3). The Webb Lake stock tonalite-trondhjemite forms an elongate body along the axial plane of this parasitic fold, suggesting pre- or syn-D_1 deformation emplacement (Fig. 4).

The D_2 deformation event is a sinistral, north-side-up transpressional event. The GLDZ and associated S_2 foliation and L_2 stretching lineation formed during this event. Within the study area, the GLDZ strikes N070° with a gently sigmoidal trend (Heather and Arias, 1987) and follows the contact between the Wawa and Catfish assemblages (Fig. 3). The S_2 foliation is a penetrative foliation oriented subparallel to the strike of the GLDZ. It is expressed as schistosity in the volcanic rocks and the Webb Lake stock and displays a sinistral C-S fabric as well as sinistral offsets of veins along the

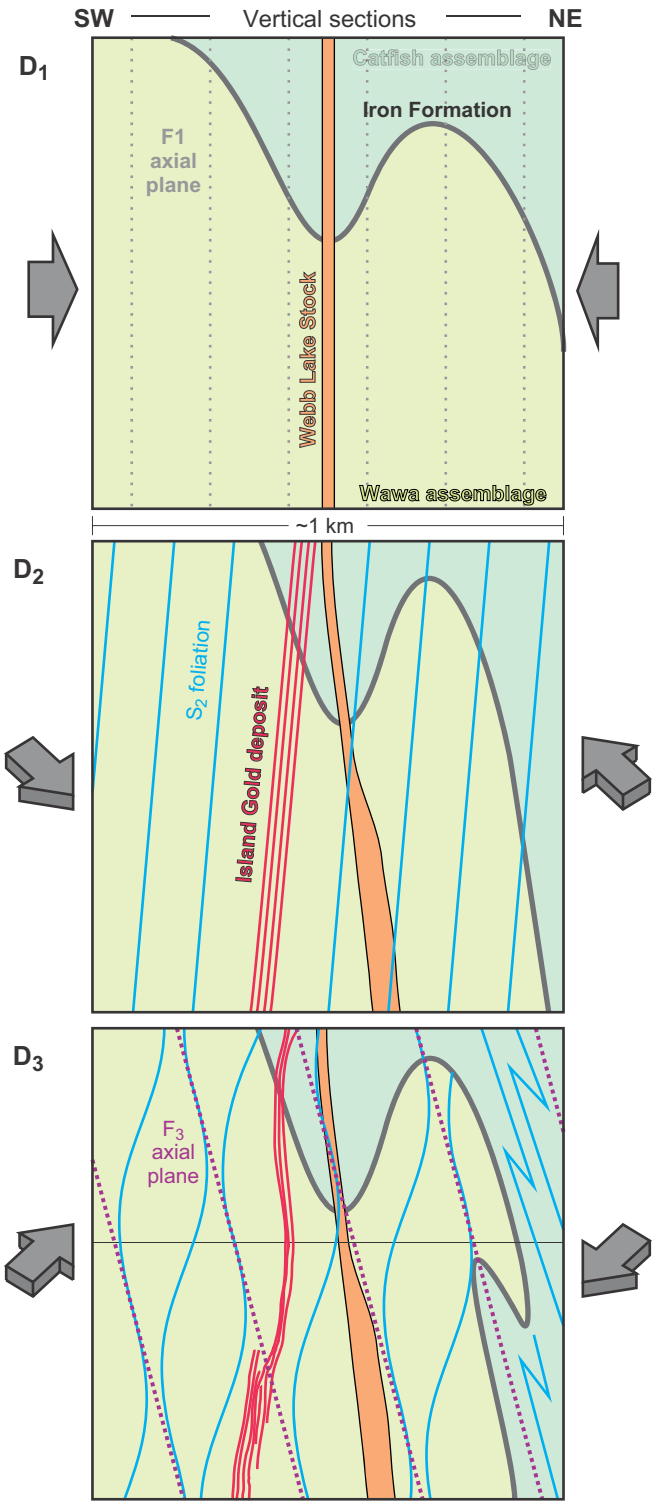

Figure 4. Schematic diagram showing the development of structures during $D_{1\text{-}3}$ deformation in the study area. Grey arrows represent principal shortening axes during progressive $D_{1\text{-}3}$ deformation. The horizontal grey line in the lowest block represents the current surficial expression.

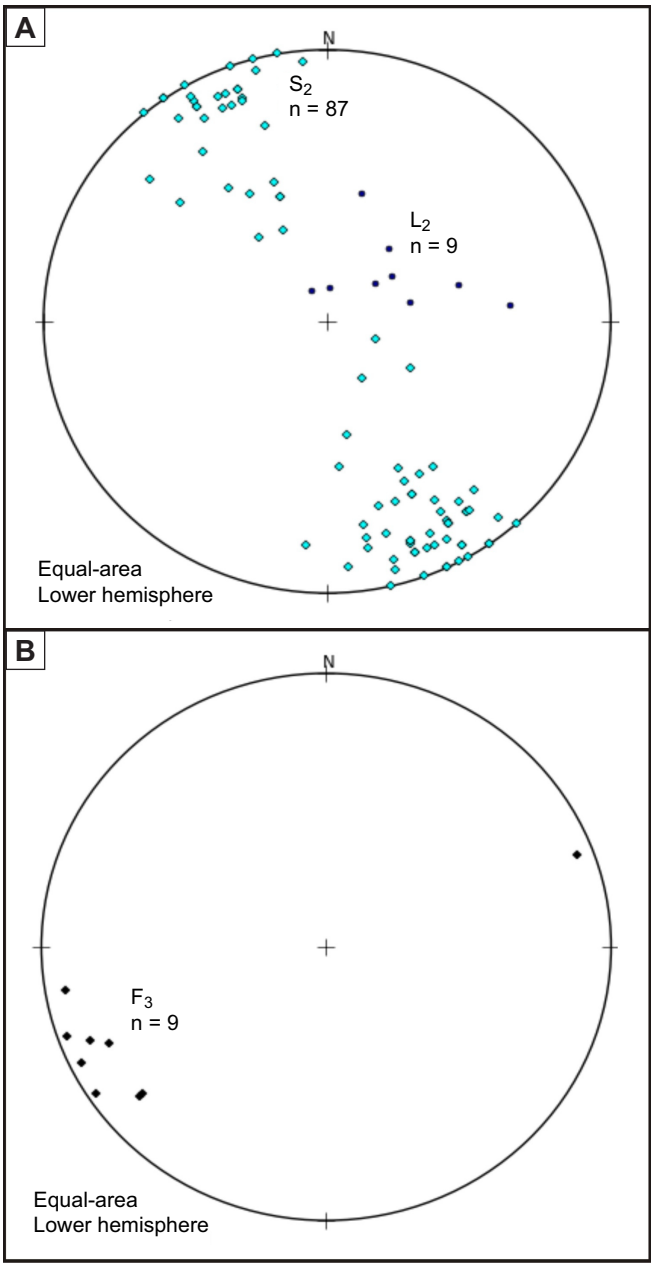

Figure 5. Stereographic projections: lower hemisphere equal area plots. **a)** Orientations of D_2 deformation fabrics in the study area. The light blue diamonds represent poles to S_2 foliation planes. The dark blue dots represent L_2 stretching lineations. **b)** Orientations of F_3 fold hinges (black diamonds) in the study area.

shear planes. The strike of the S_2 foliation is typically N070°, but ranges from N040° to N085°, with dips that vary from subhorizontal to subvertical (Fig. 5a). The L_2 stretching lineation, defined by stretched quartz and feldspar phenocrysts, plunges shallowly to steeply to the east along the S_2 foliation in the dacitic tuff. (Fig. 5a).

The D_3 deformation event produced camp- and outcrop-scale F_3 folds, an associated axial planar S_3 cleavage, and top-to-northwest reverse faults. The F_3 folds are open to tight, shallowly plunging, and Z-shaped. They occur at outcrop scale where they fold and transpose dykes and the S_2 foliation within the volcanic rocks and the Webb Lake stock, and at camp-scale

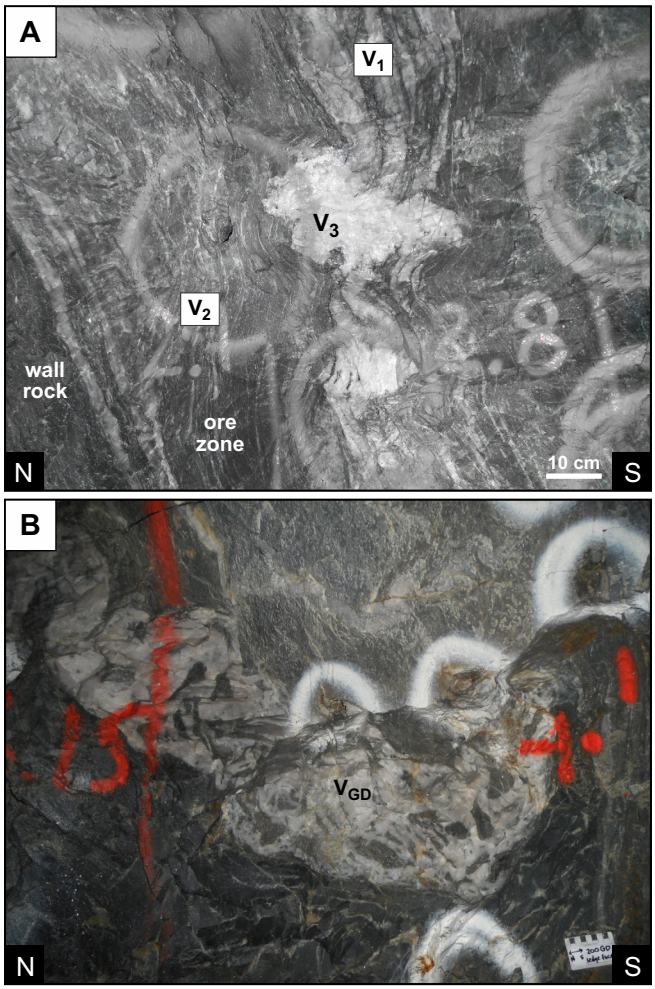

Figure 6. Photographs of vein sets found in the study area. **a)** An example showing the crosscutting relationships between V_1, V_2, and V_3 veins in the main Island zones. **b)** A typical example of a V_{GD} vein in the Goudreau Zone.

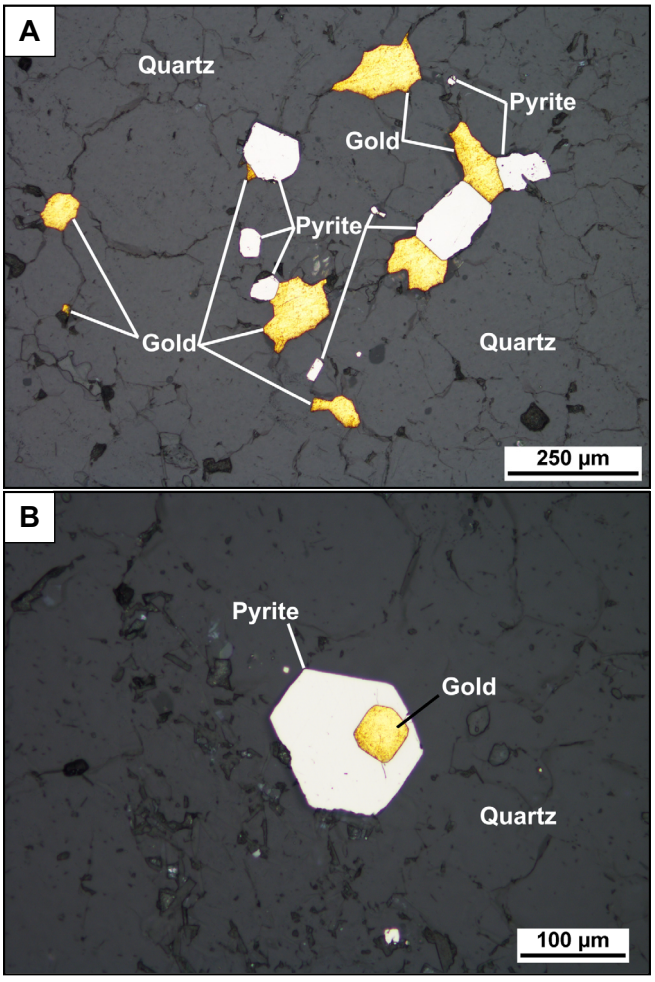

Figure 7. Reflected light photomicrographs of gold and sulphide minerals in quartz veins. **a)** Sulphides associated with gold. **b)** Gold inclusion in pyrite.

where they fold lithological contacts and the orebody. The poles to S_2 foliation form a girdle (Fig. 5a) that is sympathetic to F_3 fold axes (Fig. 5b), indicating that the variation in S_2 orientations is due to D_3 overprinting. The steeply north-dipping S_3 axial planar cleavage overprints the S_2 foliation and is weakly to moderately developed within folded felsic intrusions. In the northern part of the study area, the S_2 foliation is typically north-dipping and transposed subparallel to the S_3 axial planar cleavage.

Late brittle fractures, with minor (<1 m) offsets, overprint all previous structures. At the Island Gold deposit, mineralized zones (Extension 1 and 2 zones) show apparent sinistral offset of tens of metres along two diabase dykes, suggesting that the dykes were emplaced along brittle faults.

Vein Types and Gold Mineralization

Two types of veins are present in most of the ore zones throughout the Island Gold deposit: V_1 shear veins and V_2 extensional veins (Fig. 6a). Mutually crosscutting relationships and their close spatial association with each other suggest that the V_1 and V_2 veins (V_1-V_2) formed during the same gold mineralizing event. They also have overlapping alteration envelopes. White-coloured, semi-translucent, extensional quartz veins are present in the Goudreau Zone (V_{GD} veins) and these veins are folded and shallowly plunging (Fig. 6b). A shear zone hosting V_1-V_2 veins was observed offsetting a V_{GD} vein suggesting that V_1-V_2 veining postdates V_{GD} veining. The V_{GD}, V_1, and V_2 veins often crosscut and alter the dacite, gabbro, and Webb Lake stock, and commonly contain macroscopically visible gold. Envelopes of alteration progressively increase in intensity towards these veins, and although gold is present in these alteration envelopes, the highest concentrations are found within the veins.

Most of the gold within V_{GD}, V_1, and V_2 veins occurs as free gold along mineral grain boundaries in the form of micrometre- to millimetre-scale laminations, veinlets, or irregular masses (Fig. 7a). Occasionally, gold is present as inclusions within other

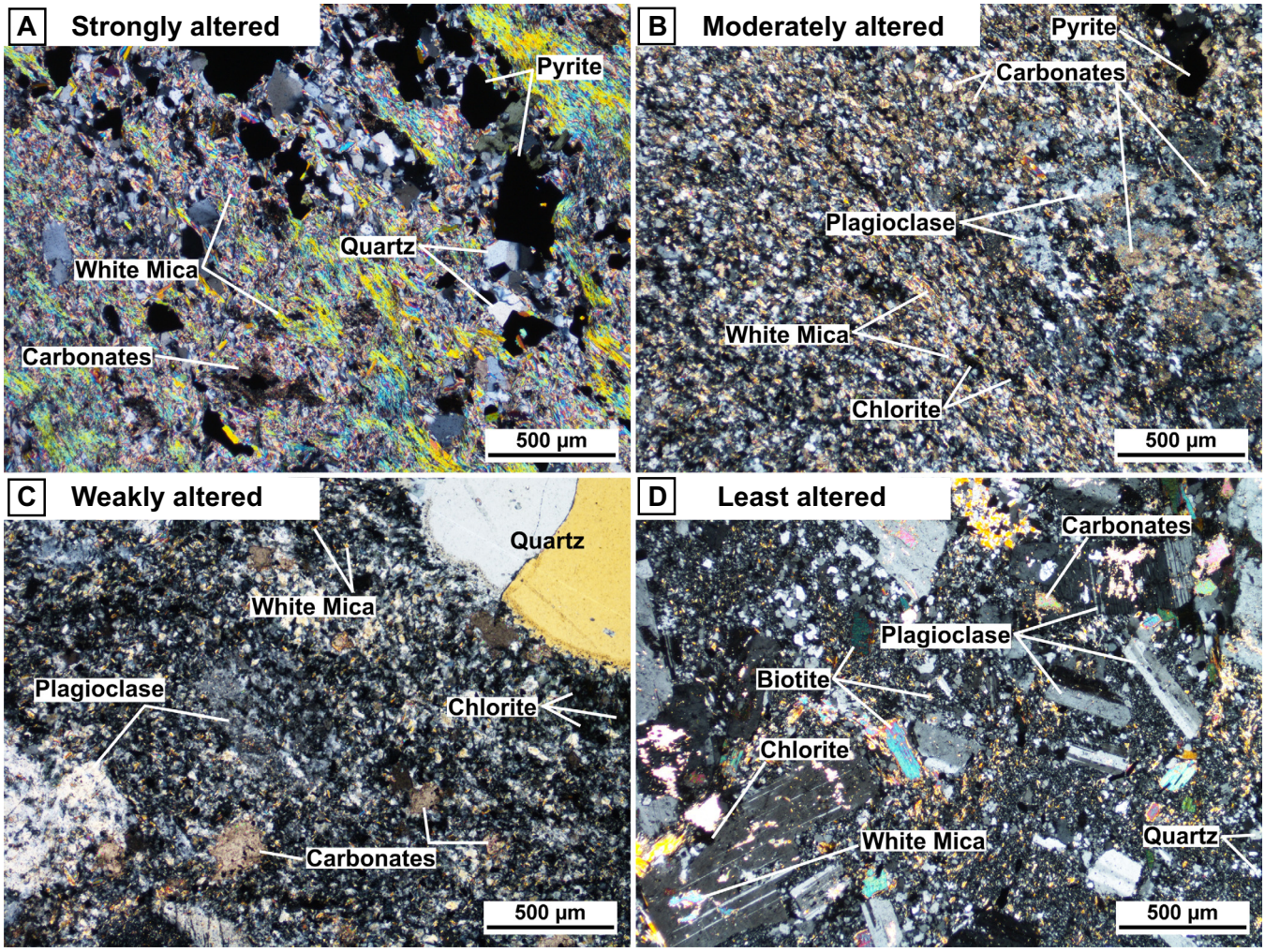

Figure 8. Cross-polarized transmitted light photomicrographs of dacitic samples that are variably altered by V_1-V_2 veins. The amount of pyrite, quartz, and white mica increase with increases alteration intensity. The proportions of plagioclase and primary biotite decrease with increasing alteration.

minerals such as quartz, carbonate, white mica, and pyrite grains (Fig. 7b). In all cases, gold is spatially associated with sulphide minerals within a few hundred micrometres. Less commonly, gold grains are present within the altered V_{GD}, V_1, and V_2 vein selvages. Gold grains in V_{GD}, V_1, and V_2 veins may also contain minor silver (<15 wt%).

A fourth vein-type (V_3) consists of barren, quartz-carbonate extensional veins that cut across all lithologies, with the exception of the diabase–quartz diabase, and also frequently cut across ore zones (Fig. 6a). Typically, V_{GD}, V_1, V_2, and V_3 quartz veins are composed of >90 % quartz and <10% carbonate minerals (calcite±dolomite±ankerite).

Tourmaline may be present as semi-planar ribbons (V_4 veins) or disseminated within various lithologies as well as within V_{GD}, V_1, V_2, and V_3 quartz veins. The tourmaline ribbons are commonly parallel to these veins, as well as various other contact surfaces. In addition to tourmaline, V_4 veins occasionally contain minor quartz and carbonate minerals. Tourmaline occurs within and postdates all lithologies and vein types, with the exception of the diabase-quartz diabase dykes.

Alteration and Vectors for Gold Mineralization

Isocon diagrams and mass balance calculations were used to determine consistent chemical mass gains and losses due to alteration based on the whole-rock geochemistry of multiple altered and less-altered sample pairs. Alteration strength groupings were initially outlined based on proximity to auriferous quartz veins and qualitative estimates of alteration intensity and later quantified on the basis of K_2O and S concentration. The methods used to determine immobile chemical species are outlined in Ciufo (2019). Alteration related to V_1-V_2 veining at the Island Gold deposit (e.g. Fig. 8a–d, 9) resulted in the enrichment of Au, K_2O, Rb, S, and Te, and typically depletion in Na_2O in alteration envelopes developed in dacite, gabbro, and the Webb

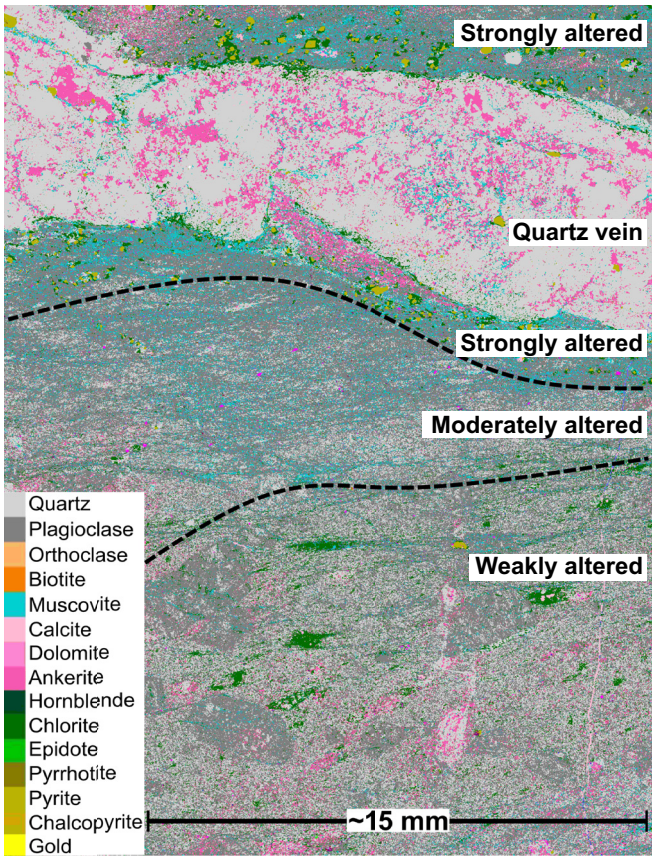

Figure 9. Scanning electron microscope mineral liberation analysis (SEM-MLA) image (using false colours to depict different minerals) of a V_2 quartz veinlet and an associated miniature dacite-hosted alteration envelope in a thin section. Approximate boundaries between alteration strength groupings are displayed.

Lake stock. Other common enrichments include As, Se, and W. Other consistent chemical gains and losses specific to dacite, gabbro, and the Webb Lake stock due to auriferous alteration are summarized in Figure 10.

Alteration minerals associated with V_1-V_2 auriferous quartz veining mainly consist of biotite, Ca-Mg-Fe carbonates, chlorite, plagioclase, quartz, sulphides (pyrite±pyrrhotite±chalcopyrite), and white mica (muscovite±phengite; e.g. Fig. 8a–c, 9). Changes in mineral proportions from strongly altered to least altered rock are depicted in Figure 11 for each of the three main host lithologies. The alteration mineral assemblage and mineral proportions vary depending on the host rock. In all lithologies, the volumetric proportion of potassic micas (sum of biotite and white mica) and sulphide minerals generally increases with increasing alteration intensity (Fig. 11). Based on the study of multiple alteration envelopes associated with V_1-V_2 veining at various locations throughout the deposit, the alteration minerals and major chemical gains remain relatively consistent. The mineralogical and chemical signature of alteration related to V_{GD} veins in the dacite is similar to that of alteration related to V_1-V_2

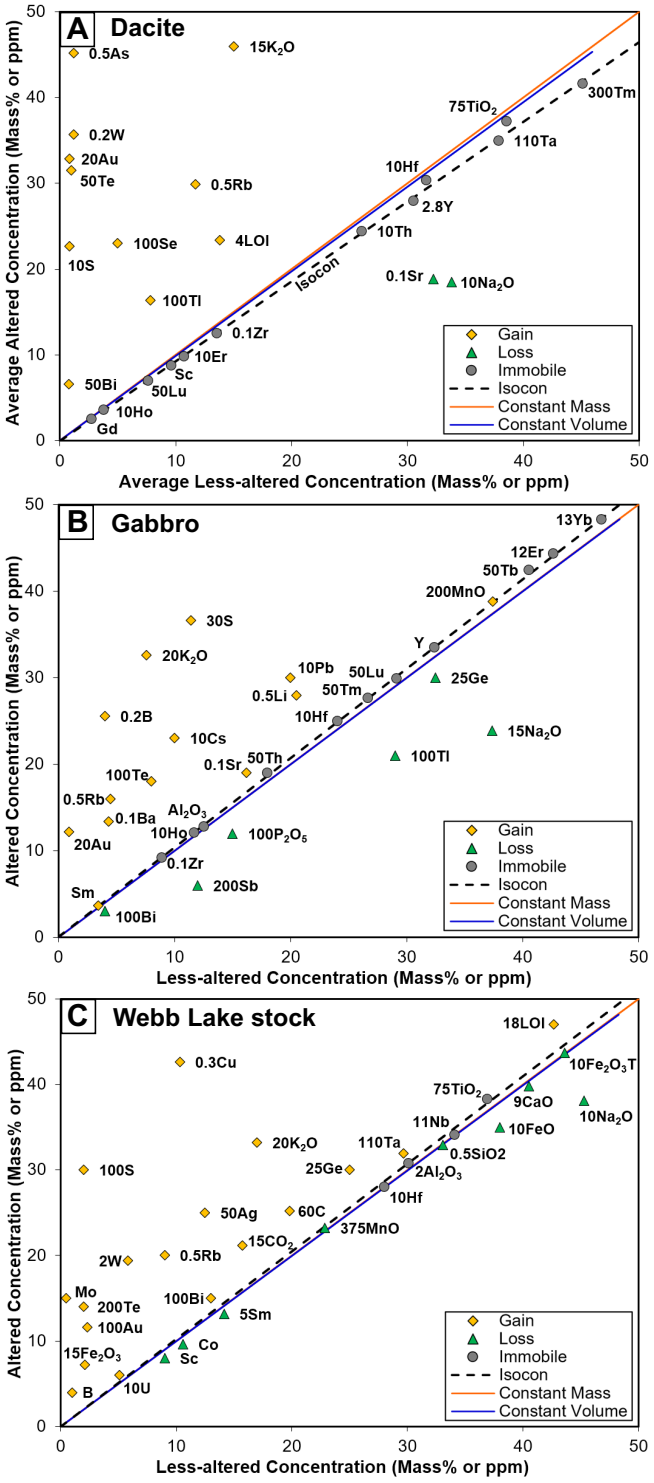

Figure 10. Isocon diagrams displaying the composition of samples of **(a)** dacite, **(b)** gabbro, and **(c)** the Webb Lake stock altered by V_1-V_2 veins plotted against the composition of corresponding less altered samples. In addition to relatively immobile chemical species, only chemical species that are consistently enriched or depleted due to alteration of that lithology are displayed. Concentrations of elements are arbitrarily scaled to avoid stacking/overlap and scale factors are displayed in front of each chemical species. Abbreviations: $Fe_2O_3^T$= total iron; LOI= loss on ignition. Methodology details are given in Ciufo (2019).

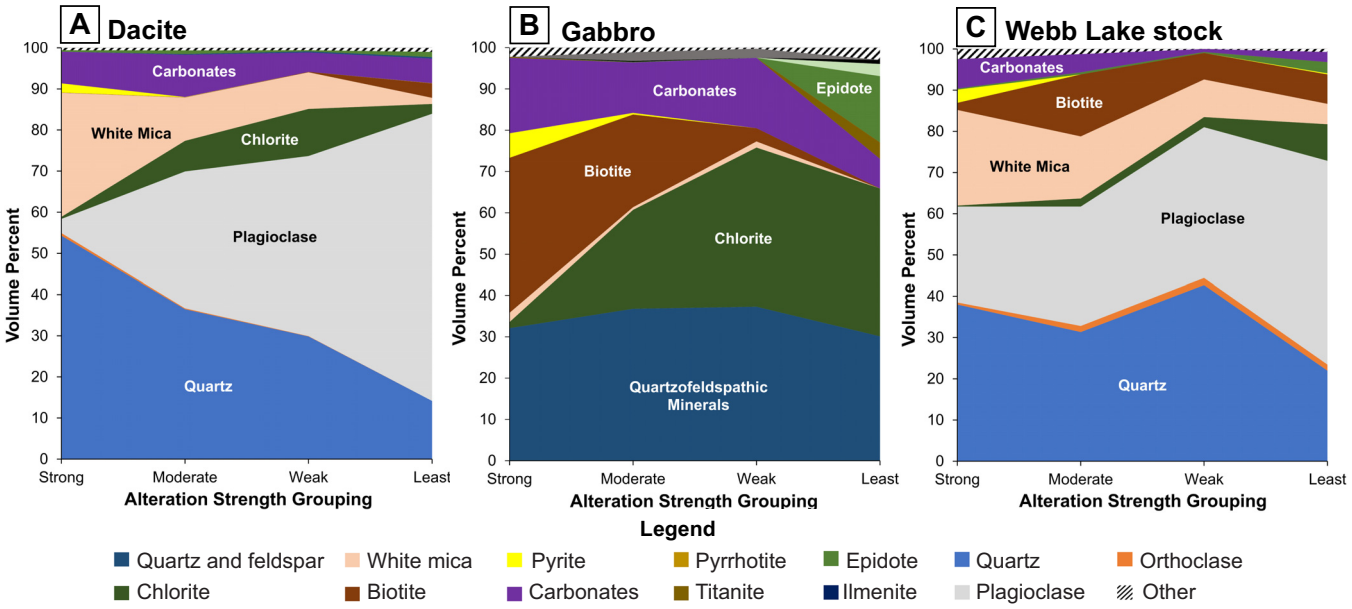

Figure 11. Mineral proportions in samples of **(a)** dacite, **(b)** gabbro, and **(c)** the Webb Lake stock variably altered by auriferous V_1-V_2 quartz veins. Mineral proportions were determined via scanning electron microscope mineral liberation analysis (SEM-MLA) for dacite and point-counting was used for gabbro and the Webb Lake stock.

veins in the same lithology (Ciufo, 2019). One side of an alteration envelope associated with auriferous quartz veining (V_1-V_2 and V_{GD}) can range in thickness from a few centimetres to 10 m or more perpendicularly outwards from a central vein to the outer margin of the alteration envelope.

The V_1, V_2, and V_{GD} quartz veins and their associated diffuse zones of silicification ("quartz flooding") are the most reliable indicators for gold grades that are >4 g/t at the Island Gold deposit. In low-grade samples (1–4 g/t Au), pyrite mode correlates well with gold grade. Samples with greater than 3 vol.% sulphide minerals (pyrite±pyrrhotite±chalcopyrite) typically have grades of >1 g/t Au. Proportions of alteration minerals, such as biotite, carbonates, chlorite, quartz, sericite, and sulphides, can be used as an approximate guide to determine the intensity of alteration (Fig. 11). Subsequently, this can be used to help estimate gold grade as gold concentrations that are >1 g/t are typically found in either strongly altered rock or auriferous quartz veins (Fig. 12). Increased proportions of chlorite and carbonate minerals relative to unaltered rock can be used to identify the weakly altered outer margins of alteration envelopes associated with auriferous quartz veins.

The V_3 veins have either no associated visible alteration or have local envelopes of weak alteration that typically do not extend more than 20 cm from the vein/wall-rock contact. Chemical mass gains and losses are minor, inconsistent, and vary depending on the host rock in which the veins formed (Ciufo, 2019).

Tourmalinization (V_4 veins) was probably unrelated to the main gold mineralizing events as least altered

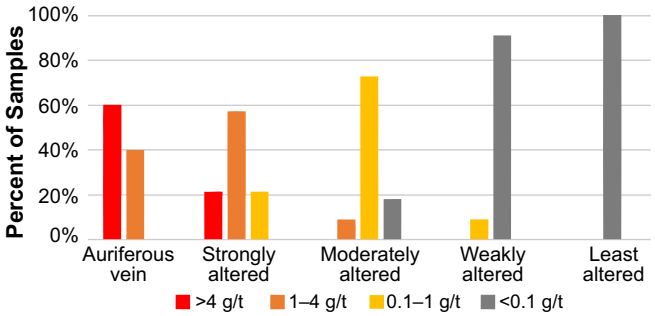

Figure 12. Samples of dacite, gabbro, the Webb Lake stock, as well as V_{GD} and V_1-V_2 auriferous quartz veins, are subdivided into five groupings: auriferous vein, strongly altered, moderately altered, weakly altered, and least altered (Ciufo, 2019). This histogram displays the proportion of these samples within each of the five groupings that fall into each of the gold-grade intervals outlined in the legend.

samples often contain tourmaline. Additionally, these least altered tourmaline-bearing samples have low gold grades, which are equivalent to least altered samples that are absent of tourmaline. In many cases, the tourmaline ribbons/veins have no visible alteration envelope.

U–Pb Zircon Geochronology

To better constrain the timing of events at the Island Gold deposit, two samples were analyzed for U-Pb zircon geochronology using a sensitive high-resolution ion microprobe. The zircons were analyzed at the J.C. Roddick Ion Microprobe Laboratory at the Geological Survey of Canada. Readers are referred to Jellicoe (2019) for analytical procedures and detailed results. Sample SH-3 is a drill core sample from a drillhole that intersected mineralized tonalite-trondhjemite of the

Webb Lake stock at a depth of 550 m below surface. Zircons from this sample yield a preliminary weighted mean $^{207}Pb/^{206}Pb$ age of 2724.1 ± 4.3 Ma (n = 23/24; mean square weighted deviation (MSWD = 1.5), which is inferred to be the crystallization age of the Webb Lake stock. It also provides a maximum age for gold mineralization (as discussed below).

Sample KJM095 is from a barren, silica-poor diorite-monzodiorite intrusion (I2M) that cuts across the Island ore zones at depth. The sample was collected from the 740 metre level underground workings of the Island Gold mine. The absence of pervasive fabric or alteration in the dyke suggests that it was emplaced late- or post-D_2 shearing and regional greenschist-grade metamorphism. The zircon grains from sample KJM095 define a preliminary weighted mean $^{207}Pb/^{206}Pb$ age of 2672.2 ± 3.5 Ma (n = 24/24, MSWD = 1.2), which is interpreted as the crystallization age of the silica-poor diorite-monzodiorite, and the minimum age for gold mineralization.

DISCUSSION

Structural History and Age of Gold Mineralization

The emplacement of the Webb Lake stock along an F_1 fold axial surface occurred before or during D_1 deformation. The Webb Lake stock acted as a more competent body during D_2 deformation. A large protrusion along the southwest edge of the Webb Lake stock (Fig. 3) passively created a strain shadow to the southeast. Dilation along the edge of this strain shadow allowed emplacement of V_1 and V_2 veins along the S_2 foliation, forming a mineralized corridor (Fig. 13). During D_3 deformation, the F_3 folds overprinted the S_2 foliation and the V_1 and V_2 veins, and the V_3 veins were emplaced in shallowly dipping extensional fractures (Fig. 4). The V_{GD} veins in the Goudreau Zone appear to be distinct from the V_1-V_2 veins of the main Island and Extension zones. V_{GD} veins are believed to represent an earlier, separate mineralizing event. Further investigation into the controls on this mineralizing event and its timing relative to the Island and Extension zones is necessary to confirm how the Goudreau Zone fits into the overall genetic model of the Island Gold deposit. Although the D_2-related V_1 shear veins and associated V_2 extensional veins represent the main mineralized features, hydrothermal activity in the area might have been protracted, or more than one mineralizing event may have affected the Island Gold deposit; this has potential implications for exploration at the camp scale.

U-Pb zircon ages from the mineralized Webb Lake stock (2724.1 ± 4.3 Ma) and the I2M post-mineralization dyke (2672.2 ± 3.5 Ma) define absolute constraints

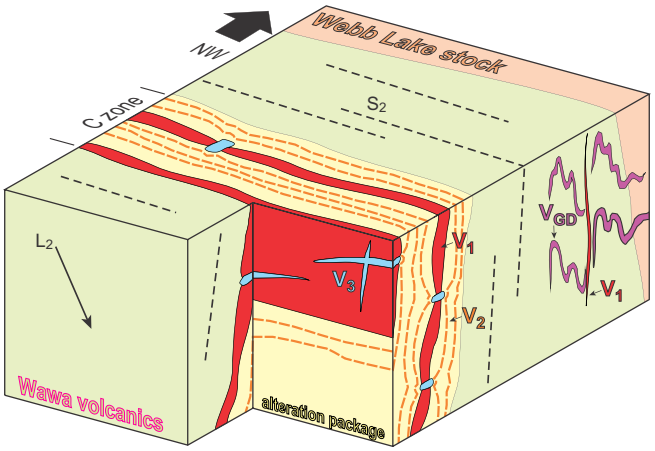

Figure 13. Schematic block diagram showing the geometry of D_2 deformation fabrics and the vein sets of the Island Gold deposit. The C zone is one of the main ore zones at the Island Gold deposit. Not to scale.

on the timing of gold mineralization at the Island Gold deposit. Like the Webb Lake stock and I2M, the overlying Doré sedimentary rocks were also affected by greenschist-facies metamorphism and the age of the youngest analyzed detrital zircon is 2680 ± 3 Ma (Corfu and Sage, 1992). D_2 deformation occurred during regional greenschist-facies metamorphism indicating that D_2 deformation began shortly after the deposition and subsequent rapid burial of the Doré sediments, and further constrains the timing of mineralization to post-2680 ± 3 Ma.

The likely age range for gold mineralization at the Island Gold deposit (between 2680 ± 3 Ma and 2672.2 ± 3.5 Ma) is consistent with the age of gold mineralization at the Hemlo deposit to the west (ca. 2677 Ma: Davis and Lin, 2003) that also took place during D_2 deformation (Lin, 2001) and during extensive ca. 2686–2677 Ma sanukitoid magmatism (Lin and Beakhouse, 2013 and references therein). Robert et al. (2005) and Dubé and Gosselin (2007) suggest that the peak of orogenic gold mineralization (greenstone-hosted quartz-carbonate vein systems) in the southern Abitibi greenstone belt occurred syn- to late-main deformation and late- to post-peak greenschist-facies metamorphism (i.e. <2670 Ma, the maximum age of the Timiskaming orogenic conglomerate, and postdates ca. 2680–2670 Ma alkaline magmatism±volcanism). However, there are post-volcanic, structurally controlled gold deposits that are slightly older in the Abitibi (e.g. the Kiena mine, which has a minimum age of gold mineralization of 2686 Ma: Morasse et al., 1995). More recently, Lin and Beakhouse (2013) suggested that gold mineralization, Timiskaming-type sedimentation and sanukitoid/alkaline magmatism were generally synchronous and probably related to the same tectonic process (synchronous vertical and horizontal tectonism) at the late stage of Archean cratoniza-

tion. In any case, the timing of gold mineralization at Island Gold falls within the age range of peak gold mineralization in the southern Abitibi greenstone belt. However, gold mineralization at Island Gold is perhaps slightly older than, or coeval with, the alkaline magmatism in the area based on the available U-Pb ages. More work is necessary to decipher the precise timing relationships between sedimentation, calc-alkaline to alkaline magmatism, and gold deposition at camp scale.

Although the GLDZ represents a major D_2 deformation corridor, it is not clear if it represents a first-order structure. Its nature, location in the district, and direct spatial association with gold suggest that it is perhaps rather a second- or third-order structure. If that is the case, it then raises the question about the location of what could be a first-order structure, or precursor major fault in the district, which is of crucial importance to understand gold metallogenesis and improve exploration models in the district.

Auriferous Alteration

Alteration associated with gold mineralization at the Island Gold deposit is similar to other orogenic gold deposits, including the presence of biotite, carbonates, chlorite, plagioclase, sericite, and sulphides in the auriferous alteration assemblage. Similar geochemical features include enrichments in As, Au, K, S, Te, and W in areas proximal to auriferous quartz veining (Groves et al., 1998).

The GLDZ, which hosts the Island Gold deposit, has been correlated with the large fault systems east of the Kapuskasing structural zone that host major orogenic gold deposits (Leclair et al., 1993). Studies of some of these gold deposits near Kirkland Lake (e.g. Kerr-Addison, Young-Davidson, Beattie), Rouyn-Noranda (e.g. Francoeur 3), and Timmins (e.g. Hoyle Pond, Dome) (Fig. 1) show similar geochemical alteration haloes. These deposits are typically characterized by enrichments in Au, K_2O, Rb, and S (Kishida and Kerrich, 1987; Moritz and Crocket, 1991; Couture and Pilote, 1993; Dinel et al., 2008; Bigot, 2012; Martin, 2012), which is consistent with the Island Gold deposit. Other common enrichments in these gold deposits east of the Kapuskasing structural zone include As, Ba, CO_2 (and/or volatiles/LOI), SiO_2, and W. These enrichments are also developed in auriferous vein-related alteration at the Island Gold deposit but do not consistently occur for all altered/less-altered pairs and each host lithology. In orogenic gold deposits east of the Kapuskasing structural zone, Na enrichment in the wall rock around auriferous quartz veins is common (e.g. Kishida and Kerrich, 1987; Couture and Pilote, 1993; Dinel et al., 2008; Martin, 2012). However, Na depletion occurs at the Island Gold deposit and also in some deposits east of the Kapuskasing structural zone, such as at the Beattie Gold deposit (Bigot, 2012).

In deposits that are located east of the Kapuskasing structural zone in the Abitibi-Wawa subprovince, gold-related alteration minerals typically include carbonate minerals, chlorite, sericite, and/or potassium feldspar, plagioclase, quartz, and sulphide minerals (Kishida and Kerrich, 1987; Smith et al., 1987; Moritz and Crocket, 1991; Couture and Pilote, 1993; Dinel et al., 2008; Bigot, 2012; Martin, 2012). Although biotite is not typically an alteration mineral at these deposits, it is an alteration mineral present in gabbro and in Webb Lake stock-hosted ore zones at the Island Gold deposit. In addition, although present in minor quantities, potassium feldspar is not a major alteration mineral in any lithologies at Island Gold. Similar to deposits east of the Kapuskasing structural zone, carbonate minerals, chlorite, sericite, plagioclase, quartz, and sulphides are all significant alteration minerals at the Island Gold deposit.

The overall consistency of the auriferous alteration at Island Gold deposit relative to these other deposits east of the Kapuskasing structural zone suggests a similar genetic history. However, the chemical and mineralogical footprint of gold-related hydrothermal alteration at each of these deposits is not identical. This is probably due to differences in the nature of host rocks, with Island Gold deposit being predominantly hosted in intermediate to felsic volcanic rocks, whereas many major orogenic gold deposits are hosted in mafic volcanic and sedimentary rocks, and in some cases, alkaline intrusions. This indicates that, although similar, both the composition of the auriferous fluids and the associated alteration mineral assemblages vary between deposits in response to local conditions.

IMPLICATIONS FOR EXPLORATION AND MINING

The results of this study provide improved guidelines for exploration. For example, exploration within the GLDZ should prioritize areas of high competency contrast within shear zones (e.g. intrusions and lithological contacts). The "lee-side" of intrusive bodies at the time of D_2 deformation should represent areas of particular interest as the Webb Lake stock acted more competently than the surrounding volcanic rocks in the GLDZ, thereby creating a strain shadow in which fluid circulation was facilitated and auriferous quartz veins preferentially formed. This exploration strategy can also be applied to other prospective deformation zones elsewhere.

The thorough documentation and classification of the types of auriferous veins and associated alteration envelopes will aid in identifying, tracking, and modelling the auriferous vein systems at the mine and in the

surrounding area and standardize mapping and core logging. In particular, alteration mineral assemblages and geochemistry can be used to identify subtle alteration and vector towards areas with an increased potential for gold.

The main orebody is oriented subparallel to S_2 foliation and the plunge of the L_2 lineation. The ability to explain and better anticipate the geometry of the ore zones in this structurally controlled deposit will help improve ore zone correlation, production drillhole targeting, mine planning, and reconciliation.

ACKNOWLEDGMENTS

This report is a contribution to NRCan's Targeted Geoscience Initiative Program (TGI-5) Gold Project. Support for this study was provided through Activity G-1.1: Gold through space and time at the Archean. We thank Alamos Gold Inc. and Richmont Mines Inc. for logistical, scientific, and financial support. We acknowledge funding from the Natural Sciences and Engineering Research Council of Canada. In addition, we thank the staff at the Island Gold mine, J. Richardson, B. Kendall, and other staff and students at the University of Waterloo for their assistance and recommendations. The scanning electron microscope mineral liberation analysis (SEM-MLA) laboratory work was conducted by D. Grant, D. Goudie, and Memorial University staff at the CREAIT Network's Micro Analysis Facility SEM/MLA Lab. Electron microprobe laboratory analyses were conducted with the help of M. Beauchamp at the Earth and Planetary Material Analysis Laboratory at Western University. Zircon mineral separates were prepared by R. Chung and G. Case at the Geological Survey of Canada. P. Hunt oversaw zircon imaging for in-situ SHRIMP analyses. SHRIMP data acquisition and data reduction were conducted with the help of T. Pestaj and N. Rayner. We also express our gratitude to E. Ambrose and V. Bécu (technical editors), S. Castonguay (scientific editor), and B. Lafrance (external reviewer) for their insightful revisions. For a complete version of this summary of acknowledgements, readers are referred to Ciufo (2019) and Jellicoe (2019).

REFERENCES

Adam, D., LeBlanc, L.G., Bélisle, M., Ramcharan, V.K., and Vincent, R., 2017. Island Gold mine technical report and expansion case preliminary economic assessment, Dubreuilville, Ontario, Canada, Technical report according to National Instrument 43-101 and Form 43-101F1; Richmont Mines Inc. <https://www.sedar.com> [accessed February 1, 2020]

Arias, Z.G. and Heather, K.B., 1987. Regional structural geology related to gold mineralization in the Goudreau-Lochalsh area, District of Algoma; *in* Summary of Field Work and Other Activities; Ontario Geological Survey, Miscellaneous Paper 137, p. 146–154.

Arias, Z.G. and Helmstaedt, H., 1990. Grant 343-Structural evolution of the Michipicoten (Wawa) greenstone belt, Superior Province: Evidence for an Archean fold and thrust belt; *in* Geoscience Research Grant Program Summary of Research 1989–1990, (ed.) V.G. Milne; Ontario Geological Survey, Miscellaneous Paper 150, p. 107–114.

Barker, F., 1979. Trondhjemite: Definition, environment and hypotheses of origin; *in* Trondhjemites, Dacites, and Related Rocks, (ed.) F. Barker; Elsevier, Developments in Petrology, Amsterdam, Vol. 4, p. 1–12.

Bigot, L., 2012. Gold mineralizations at the syenite-hosted Beattie gold deposit at Duparquet, Neoarchean Abitibi belt, Quebec, Canada; M.Sc. thesis, Université du Québec à Montréal, Montréal, Quebec, 136 p.

Card, K.D., 1990. A review of the Superior Province of the Canadian Shield, a product of Archean accretion; Precambrian Research, v. 48, p. 99–156.

Ciufo, T.J., 2019. Hydrothermal alteration and exploration vectors at the Island Gold deposit, Michipicoten greenstone belt, Wawa, Ontario; M.Sc. thesis, University of Waterloo, Waterloo, Ontario, 510 p.

Ciufo, T., Mercier-Langevin, P., Yakymchuk, C., Lin, S., Bécu, V., and Lauzière, K., 2019. Whole-rock lithogeochemistry of the Archean Island Gold deposit Ontario, Canada; Geological Survey of Canada, Open File 8524, 1 .zip file.

Corfu, F. and Sage, R.P., 1992. U-Pb age constraints for the deposition of clastic metasedimentary rocks and late-tectonic plutonism, Michipicoten Belt, Superior Province; Canadian Journal of Earth Sciences, v. 29, p. 1640–1651.

Couture, J.-F. and Pilote, P., 1993. The geology and alteration patterns of a disseminated, shear zone-hosted mesothermal gold deposit: The Francoeur 3 deposit, Rouyn-Noranda, Quebec; Economic Geology, v. 88, p. 1664–1684.

Davis, D.W. and Lin, S., 2003. Unravelling the geologic history of the Hemlo Archean gold deposit, Superior Province, Canada: A U-Pb geochronological study; Economic Geology, v. 98, p. 51–67.

Dinel, E., Fowler, A.D., Ayer, J., Still, A., Tylee, K., and Barr, E., 2008. Lithogeochemical and stratigraphic controls on gold mineralization within the metavolcanic rocks of the Hoyle Pond mine, Timmins, Ontario; Economic Geology, v. 103, p. 1341–1363.

Dubé, B. and Gosselin, P., 2007. Greenstone-hosted quartz-carbonate vein deposits in Mineral Deposits of Canada – A Synthesis of Major-Types, District Metallogeny, the Evolution of Geological Provinces, and Exploration Methods, (ed.) W.D. Goodfellow; Geological Association of Canada, Mineral Deposits Division, Special Publication No. 5, p. 49–73.

Gross, G.A., 1980. A classification of iron formations based on depositional environments; The Canadian Mineralogist, v. 18, p. 215–222.

Groves, D.I., Goldfarb, R.J., Gebre-Mariam, M., Hagemann, S.G., and Robert, F., 1998. Orogenic gold deposits: A proposed classification in the context of their crustal distribution and relationship to other gold deposit types; Ore Geology Reviews, v. 13, p. 7–27.

Heather, K.B. and Arias, Z.G., 1987. 024: Geological setting of gold mineralization in the Goudreau-Lochalsh area, district of Algoma; *in* Summary of Field Work and Other Activities 1987, (ed.) R.B. Barlow, M.E. Cherry, A.C. Colvine, B.O. Dressler, and O.L. White; Ontario Geological Survey, Miscellaneous Paper 137, p. 155–162.

Heather, K.B. and Arias, Z., 1992. Geological and structural setting of gold mineralization in the Goudreau-Lochalsh area, Wawa gold camp; Ontario Geological Survey, Open File Report 5832, 159 p.

Jellicoe, K.M., 2019. Structural controls and deformation history of the orogenic Island Gold deposit, Michipicoten greenstone belt, Ontario; M.Sc. thesis, University of Waterloo, Waterloo, Ontario, 84 p.

Kishida, A. and Kerrich, R., 1987. Hydrothermal alteration zoning and gold concentration at the Kerr-Addison Archean lode gold deposit, Kirkland Lake, Ontario; Economic Geology, v. 82, p. 649–690.

Leclair, A.D., Ernst, R.E., and Hattori, K., 1993. Crustal-scale auriferous shear zones in the central Superior Province, Canada; Geology, v. 21, p. 399–402.

Lin, S., 2001. Stratigraphic and structural setting of the Hemlo gold deposit, Ontario, Canada; Economic Geology, v. 96, p. 477–507.

Lin, S. and Beakhouse, G.P., 2013. Synchronous vertical and horizontal tectonism at late stages of Archean cratonization and genesis of Hemlo gold deposit, Superior craton, Ontario; Geology, v. 41, p. 359–362.

Martin, R.D., 2012. Syenite-hosted gold mineralization and hydrothermal alteration at the Young-Davidson deposit, Matachewan, Ontario; M.Sc. thesis, University of Waterloo, Waterloo, Ontario, 172 p.

Morasse, S., Wasteneys, H., Cormier, M., Helmstaed, H., and Mason, R., 1995. A pre-2686 Ma intrusion-related gold deposit at the Kiena mine, Val d'Or, Quebec, southern Abitibi subprovince; Economic Geology v. 90, p. 1310–1321.

Moritz, R.P. and Crocket, J.H., 1991. Hydrothermal wall-rock alteration and the formation of the gold-bearing quartz-fuchsite vein at the Dome mine, Timmins area, Ontario, Canada; Economic Geology, v. 86, p. 620–643.

Percival, J.A., Skulski, T., Sanborn-Barrie, M., Stott, G.M., Leclair, A.D., Corkery, M.T., and Boily, M., 2012. Geology and tectonic evolution of the Superior Province, Canada; Chapter 6 *in* Tectonic Styles in Canada: The LITHOPROBE Perspective, (ed.) J.A. Percival, F.A. Cook, and R.M. Clowes; Geological Association of Canada, Special Paper 49, p. 321–378.

Rice, R.J. and Donaldson, J.A., 1992. Sedimentology of the Archean Doré metasediments, Arliss Lake area, southern Michipicoten greenstone belt, Superior Province; Canadian Journal of Earth Sciences, v. 29, p. 2558–2570.

Robert, F., Poulsen, H.K., Cassidy, K.F., and Hodgson, C.J., 2005. Gold metallogeny of the Superior and Yilgarn cratons; *in* Economic Geology 100th Anniversary Volume, (ed.) J.W. Hedenquist, J.F.H. Thompson, R.J. Goldfarb, and J.P. Richards; Society of Economic Geologists, p. 1001–1033.

Sage, R.P., 1994. Geology of the Michipicoten greenstone belt; Ontario Geological Survey, Open File Report 5888, 592 p.

Sage, R.P., Lightfoot, P.C., and Doherty, W., 1996. Geochemical characteristics of granitoid rocks from within the Archean Michipicoten greenstone belt, Wawa Subprovince, Superior Province, Canada: implications for source regions and tectonic evolution; Precambrian Research, v. 76, p. 155-190.

Smith, E.J., Kesler, S.E., and Van Hees, E.H.P., 1987. Relationship of fluid inclusion geochemistry to wall-rock alteration and lithogeochemical zonation at the Hollinger-McIntyre gold deposit, Porcupine district, Canada; Journal of Geochemical Exploration, v. 29, p. 434.

Turcotte, B. and Pelletier, C., 2008. Technical report and mineral resource estimate for the Magino mine (according to Regulation 43-101 and Form 43-101F1); InnovExplo for Golden Goose Resources Inc. <https://www.sedar.com> [accessed February 1, 2020]

Turek, A., Smith. P.E., and Van Schmus, W.R., 1982. Rb-Sr and U-Pb ages of volcanics and granite emplacement in the Michipicoten belt-Wawa, Ontario; Canadian Journal of Earth Sciences, v. 19, p. 1608–1626.

Williams, H.R., Scott, G.M., Heather, K.B., Muir, T.L., and Sage, R.P., 1991. Wawa Subprovince; Chapter 12 *in* Geology of Ontario, (ed.) P.C. Thurston, H.R. Williams, R.H. Sutcliffe, and G.M. Stott; Ontario Geological Survey, Special Volume 4, Part 1, p. 485–539.

Bottom-up mineral exploration: Ore-element upgrading in the upper mantle and tools for its discovery

Christopher J.M. Lawley* and Bruce A. Kjarsgaard

Geological Survey of Canada, 601 Booth Street, Ottawa, Ontario K1A 0E8
*Corresponding author's e-mail: christopher.lawley@canada.ca

ABSTRACT

Mineral exploration targeting typically focuses on the critical pathways and depositional traps of ore systems. The role of pre-enriched source regions on ore deposit genesis is unclear, particularly for systems that involve significant transport of ore components (e.g. Au). Because Au is suggested to be derived from the mid- to lower-crust and/or upper mantle at orogenic deposits, it is not surprising that the deepest and most inaccessible parts of this ore system is also the least studied and understood. Herein we address that knowledge gap by studying the upper mantle directly, using examples of young ophiolitic mantle (Atlin, British Columbia) and ancient cratonic mantle (Superior craton, Ontario; Slave craton, Nunavut). Project results demonstrate two dominant mechanisms for Au upgrading in the lithospheric mantle: (1) base metal sulphide precipitated during melt:rock reactions between peridotitic residues and asthenospheric melts, and (2) hydrous, fluid-inclusions trapped after release from subducting slabs. The remelting of such pre-enriched metasomatized mantle has been previously proposed as a viable source for a variety of ore systems (e.g. mafic to ultramafic rock-hosted platinum-group element deposits). Mapping the architecture of these deep lithospheric metasomatized mantle domains and their association with rising asthenospheric melts is of significant interest for mineral exploration. New geochemical methods and data processing completed as part of the current study, coupled with advances in geophysical imaging, provide additional tools for mapping these pre-enriched lithospheric mantle domains at depth.

INTRODUCTION

Most ore systems are hosted in the crust and represent the focusing and upgrading of ore components (e.g. ore-forming elements and ligands) by fluids or melts along crustal pathways and at their depositional site (Begg et al., 2010; McCuaig et al., 2010; Hronsky et al., 2012; Huston et al., 2016). Multiple physical and/or chemical upgrading processes are required to produce the exceptional concentrations and tonnages of ore at individual deposits (i.e. often 100–10,000x enriched relative to the average continental crust: Boyle, 1979; Fyfe, 1987; Hedenquist and Lowenstern, 1994; Ulrich et al., 1999; Wilkinson et al., 2009; Heinrich and Zurich, 2014). The most important processes for upgrading are specific to each ore system (notwithstanding a number of similar processes across ore systems), but most are thought to occur during transport and/or during deposition (e.g. interaction between hydrothermal fluids and host rocks; crustal sulphur contamination and subsequent sulphide saturation during magmatic differentiation; separation of a magmatic volatile phase: McCuaig et al., 2010; Huston et al., 2016). However, upgrading processes that operate in the source regions of these systems, particularly for ore systems that involve significant transport of ore components (e.g. Au), are less well understood and their impact on metal endowment are more controversial (Richards, 2009; Hronsky et al., 2012; Arndt, 2013; Goldfarb and Groves, 2015).

The conventional view is that the source regions of most ore systems are rather unexceptional, which, if correct, would tend to focus most of the exploration effort on recognizing the critical pathways for ore components and the most favourable trapping environments for ore deposition (Fyfe, 1987; McCuaig et al., 2010; Richards, 2011; Barnes and Fiorentini, 2012; Wilkinson, 2013; Barnes et al., 2016; Huston et al., 2016). The world-class Sudbury Ni-Cu deposits provide perhaps one of the better examples of an ore system that did not involve a particularly Ni-, Cu- and/or PGE-rich source. Because the Sudbury impact structure is so large (≥200 km), the bulk composition of the resulting melt sheet is approximately the same as average and/or lower continental crust (Therriault et al., 2002; Mungall et al., 2004). The transfer and upgrading of ore components from the Ni-poor melt sheet to a Ni-rich sulphide liquid was the primary process responsible for one of the greatest concentrations of base metals on Earth (Therriault et al., 2002; Mungall et al., 2004; Laznicka, 2014). A source enriched in ore components

Lawley, C.J.M. and Kjarsgaard, B.A., 2020. Bottom-up mineral exploration: Ore-element upgrading in the upper mantle and tools for its discovery; *in* Targeted Geoscience Initiative 5: Contributions to the Understanding of Canadian Gold Systems, (ed.) P. Mercier-Langevin, C.J.M. Lawley, and S. Castonguay; Geological Survey of Canada, Open File 8712, p. 157–164. https://doi.org/10.4095/323674

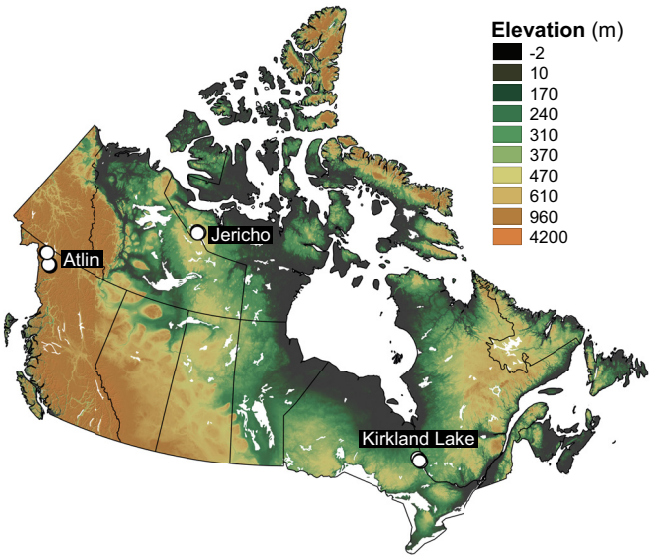

Figure 1. Map of Canada showing research activity locations and samples (white dots). Shuttle radar topography mission (SRTM) elevation data (m) is coloured coded using a percentile scaling.

is therefore not required for ore deposit genesis, at least in some cases.

Kimberlite-hosted diamond deposits, in contrast, require source regions that are pre-enriched in ore components (Richardson et al., 1984; Stachel and Harris, 2008; Griffin et al., 2013). Diamonds are carried to surface by ascending kimberlitic melts that sample diamondiferous lithospheric mantle underlying the continental crust (Fig. 1, 2). Intersecting diamond-bearing mantle lithosphere represents one of the critical controls on the diamond endowment of kimberlite-hosted deposits (Richardson et al., 1984). Accordingly, mineral exploration for diamonds often adopts a bottom-up approach during regional targeting. Advances in deep geophysical imaging of the mantle (e.g. seismic and magnetotelluric methods: Snyder et al., 2004), coupled with detailed petrology studies of kimberlite-derived mantle xenolith and xenocryst mantle cargo (Nimis, 1998; Grütter, 2009), are used to identify favourable lithospheric mantle domains that are prospective for diamond formation and preservation (Morgan, 1995). Crustal pathways (i.e. faults and rock contacts) overlying these fertile mantle source regions are considered more prospective environments for kimberlite ascent and diamond transport (Fig. 2). The bottom-up exploration approach is important because the footprint of fertile lithospheric mantle domains is significantly larger (10s to 100s of km) than the size of an individual kimberlite intrusion (100s of m), which means that the most prospective settings for finding diamond-bearing kimberlites can be prioritized and identified prior to detailed geophysical and surficial sediment discovery surveys and drilling.

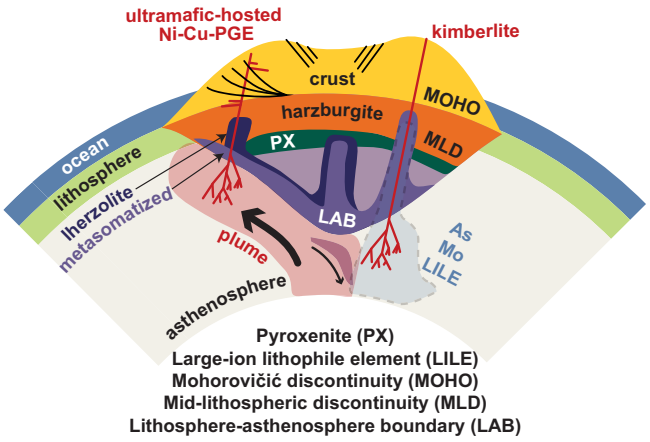

Figure 2. Sketch showing the inferred structure of the cratonic mantle. Fluid- and melt-rock reactions tend to precipitate base metal sulphide within the metasomatized mantle lithosphere. Re-melting of these pre-enriched mantle domains have previously been proposed as favourable source regions for generating ore-forming magmas.

The magmatic precursors of other mafic to ultramafic melts also interact with the lithospheric mantle during accent from their deeper asthenospheric mantle source regions (Fig. 2). Because samples of the lithospheric mantle can be up to 10x enriched in ore components relative to the convecting upper mantle (e.g. containing a few ppb, 10^9, platinum-group elements (PGE): Barnes et al., 2015; Lorand and Luguet, 2016; Saunders et al., 2018), interaction between rising ultramafic melts and refertilized lithospheric mantle provide a possible mechanism to explain the geochemical signature of some ore deposits (Begg et al., 2010; Hronsky et al., 2012; Arndt, 2013; Griffin et al., 2013). The giant Bushveld Complex provides one of the few recognized available examples of a magmatic ore system that owes its precious metal endowment, at least in part, to a pre-enriched lithospheric mantle source (Richardson and Shirey, 2008).

However, the role of a modified lithospheric mantle in the genesis of many other ore systems deposited in the crust remains controversial (McInnes et al., 1999; Richards, 2009; Hronsky et al., 2012; Arndt, 2013). Some of this uncertainty stems from the relatively poor understanding of how the deep mantle roots underlying the continents formed (Pearson et al., 2007; Griffin et al., 2009). The specific mechanisms for upgrading ore components in the lithospheric mantle also remain poorly understood, particularly for ore-forming elements other than PGE. These questions are important to address if bottom-up exploration is also to be applied to other ore-systems (Snyder et al., 2004; Begg et al., 2010; Griffin et al., 2013).

Research completed as part of the Targeted Geoscience Initiative-5 Mantle Metal Mobility activity provides new constraints on the mechanisms that drive

upgrading of ore components in the lithospheric mantle and new tools for recognizing where these processes may have occurred in the geological past. Research was focused on Au, but activity results also provided critical new constraints on the behaviour of a highly important suite of ore-forming elements during lithospheric mantle formation, melting, and metasomatism (i.e. Ni, Cu, Zn, As, Se, Mo, Ag, Sn, Sb, Te, W, Pb, and Bi). These results have potential applications to other ore systems (e.g. porphyry Cu, sedimentary-exhalative, volcanogenic massive sulphide, and magmatic Ni-Cu). The present activity was split into separate sub-activities, each studying different lithospheric mantle settings: 1) field- and laboratory-based research on young oceanic mantle as exposed in ophiolite belts from northern British Columbia; and 2) laboratory-based studies of ancient cratonic mantle, which were based on kimberlite-hosted mantle fragments (i.e. xenocrysts and xenoliths) from the Abitibi belt and Slave craton (Fig. 1). Research highlights from both sub-activities are described below.

MANTLE MECHANISMS FOR UPGRADING ORE COMPONENTS

Ophiolite belts preserve tracts of oceanic crust and its underling mantle. The excellent exposure of the upper mantle rocks at the Nahlin ophiolite (Atlin, British Columbia; Fig. 1) provide an opportunity to research the behaviour of ore-forming elements during mantle melting and metasomatism. However, the trace (low ppm) to ultratrace (low ppb) concentration of most elements within unmineralized mantle peridotite poses significant analytical challenges. To address that challenge, a new method was developed as part of the current study to analyze nanopowders by laser ablation - inductively coupled plasma - mass spectrometry (LA-ICP-MS: Lawley et al., 2020). The new wet-milling method was miniaturized to analyze very small sample volumes (1–2 g), which is required for the limited size typical of xenoliths from basaltic and/or kimberlitic volcanism. A research study applying this new approach has been successfully completed by Kroner (2019).

Whole-rock results acquired using the new nanopowders method, coupled with conventional lithogeochemistry and isotopic studies (Os and Pb), demonstrate that Nahlin ophiolite peridotite is the residue of extensive melt extraction, possibly in a suprasubduction zone setting (Lawley et al., 2020). Ore-forming elements are incompatible during partial melting and should, in principle, be transferred to the crust. However, many of the melt-depleted Nahlin ophiolite peridotite samples yield ore-forming element concentrations that approach (e.g. Cu, Se) and/or exceed (e.g. As, Ag, Mo, Te, Bi) the composition of the primitive upper mantle asthenosphere (i.e. mantle that is unaffected by melt extraction associated with crust formation). These unusual concentrations of the ore-forming elements are opposite to their expected behaviour during partial melting. Pyroxenite dykes and high-temperature, Si-metasomatized mantle peridotite (i.e. olivine websterite) also yield anomalous concentrations for these elements, suggesting that interaction between residual peridotite and passing melts (or fluids) re-fertilized Au and other ore components. Refertilized pyroxenite dykes share geochemical similarities with arc theoleiite and/or boninites (Edwards, 1995; Varfalvy et al., 1997), which, if correct, provide a genetic link of Au-upgrading in the lithospheric mantle to arc and back-arc magmatic processes. Anomalous ratios of ore-forming and other incompatible trace elements that are normally unfractionated by mantle melting further suggest that re-fertilization also involved hydrous fluids derived from the subducting plate. Such fluid- and melt-metasomatized mantle domains have previously been described as fertile source regions for generating magmas enriched in ore components, such as Au (Richards, 2011; Hronsky et al., 2012; Griffin et al., 2013). Our new work demonstrates that these same source regions are also enriched in other components associated with Au (e.g. As, Ag, Mo, Te, Bi; Fig. 2).

The refertilization of ore components to melt-depleted peridotite established by the nanopowders data is further recorded at the microscale. Documentation of the association between metasomatic clinopyroxene and base metal sulphide (BMS: pentlandite ±pyrrhotite±chalcopyrite) indicates metasomatic BMS precipitated during melt- and/or fluid-rock reactions (Fig. 3). Where present, BMS represent the dominant mineral host for base- and precious-metals, as demonstrated by high-resolution LA-ICP-MS mapping (Fig. 3: Lawley et al., 2019). Our results suggest that high-temperature mantle metasomatism is the dominant process for enriching melt-depleted peridotite, prior to serpentinization.

New, in situ LA-ICP-MS ore-element results from cratonic mantle olivine grains also point to trapped fluid and/or melt metasomatism that, for melt-depleted peridotite xenoliths devoid of metasomatic BMS, represent a significant host for the whole-rock budget of a subset of ore-forming elements. The composition of these olivine-hosted inclusions provide a new tool for tracing the upgrading of ore components at depth within the lithospheric mantle (*see discussion below*).

NEW TOOLS FOR DETECTING Au UPGRADING IN THE CRATONIC MANTLE

Most of what we know about the cratonic mantle comes from remotely acquired geophysical datasets and/or mantle fragments (1–10s cm; very rarely up to 1

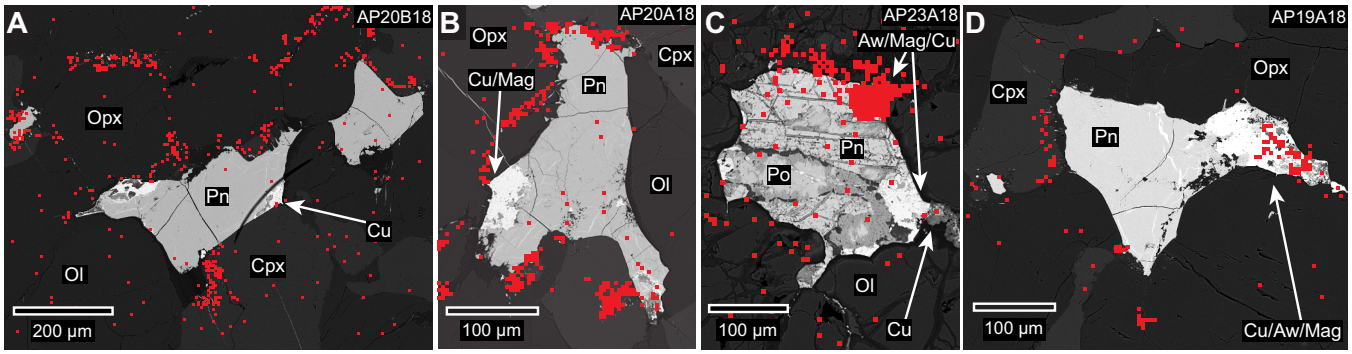

Figure 3. a–d) Scanning electron microscope (SEM) backscatter electron images (BSE) of base metal sulphide (BMS; Pn = pentlandite; Po = pyrrhotite) of the Nahlin ophiolite. Superimposed on the SEM-BSE images are laser alblation - inductively coupled plasma - mass spectrometry (LA-ICP-MS) mapping results (Lawley et al., 2019). Element map pixels with Au concentrations greater than the analytical detection limit (typically 0.5–1 ppm using a 4–6 µm spot) locally reflect trace element substitution into the S-poor mineral assemblage (Aw = awaruite; Cu = native Cu; Mag = magnetite) replacing the BMS **(c)**. Ultrafine electrum also occurs as inclusions within mantle silicates (Cpx = clinopyroxene; Ol = olivine; Opx = orthopyroxene) and fracture-hosted grains **(a, b, d)**. We suggest that ultrafine electrum may represent a significant host for the whole-rock Au budget, but, in this case, likely reflect microscale remobilization from BMS breakdown during serpentinization. Similar Au-rich inclusions have also been observed within fresh, unserpentinized mantle olivine from Kirkland Lake and Jericho.

m) transported to surface by kimberlites (i.e. xenoliths and xenocrysts: Snyder et al., 2004; Pearson et al., 2007; Pearson and Wittig, 2008; Stachel and Harris, 2008; Griffin et al., 2013). With the exception of PGE, very little research has been conducted on the concentration levels of other ore-forming components within the lithospheric mantle, precluding understanding the potential for upgrading processes. To address this knowledge gap, trace to ultratrace element studies using LA-ICP-MS analyses of mantle xenocrysts and xenoliths from the Superior and Slave cratons were studied as part of the Mantle Metal Mobility activity.

New results suggest that some ore-forming elements are readily substituted into the olivine crystal structure due to their size and charge (e.g. Ni, Zn, and to a lesser extent Cu). Other ore-forming element concentrations (including As, Se, Mo, Ag, Sn, Sb, Te, Pb, Bi, Au, Pt, and Pd) within olivine and clinopyroxene xenocrysts were anomalous and are interpreted to reflect trapped inclusions, which, if correct, likely represent the first direct sampling of precious metal modified cratonic mantle beneath the Abitibi greenstone belt (Lawley et al., 2018a,b). Although the concentrations of these ore-forming elements are extremely low (ppb), the association between Na-altered olivine xenocrysts with Au-, Pt-, and Pd-bearing inclusions likely reflect mantle metasomatism. Olivine xenocrysts also contain anomalous concentrations of As, Ag, Mo, Te, and Bi, possibly related to trapped, hydrous fluid-inclusions. A large proportion of the metasomatized mantle xenocrysts from the southern Superior craton were sampled at the base of the lithospheric mantle (~180 km), consistent with upgrading of ore components by rising asenthospheric melts (Fig. 2). Metasomatized mantle domains were also recognized in the mid-lithosphere (~100 km) by xenocrysts with anomalous high-field strength element-rich (HFSE) signatures. Modified mantle domains sampled at this depth correspond to relatively conductive lithosphere, suggesting re-fertilization of cratonic mantle may have also been associated with the crystallization of other metasomatic minerals (amphibole, phlogopite, etc.) in the mid-lithosphere (Fig. 2). Metasomatic clinopyroxene sampled at both of these depths yield variable Pb isotopic compositions and point to metasomatized domains that are up to one billion years older than the timing of kimberlite volcanism (Lawley et al., 2018a,b).

Similar ore-forming element inclusions were also recognized from olivine derived from Slave craton peridotite xenoliths and xenocrysts, indicating the findings are not restricted to the southern Superior craton (Fig. 1). Hence the trace to ultratrace element composition of mantle xenocrysts, coupled with isotopic studies and geophysical imaging, represent powerful tools for mapping the upgrading of ore-forming elements in the lithospheric mantle.

IMPLICATIONS FOR EXPLORATION

The lithospheric mantle represents the cold, melt-depleted residues leftover from the extraction of the continental crust (O'Reilly et al., 2001; Pearson et al., 2007; Griffin et al., 2009). Past melting events have depleted the lithospheric mantle in Fe, which makes it less dense relative to the convecting mantle (Jordan, 1975). The positive buoyancy of lithospheric mantle has played an important role in the stabilization of the continents and the preservation of ore systems hosted within the crust (Griffin et al., 2013). This is particularly critical for ancient cratons, which host a variety of ore systems that would likely have been destroyed and

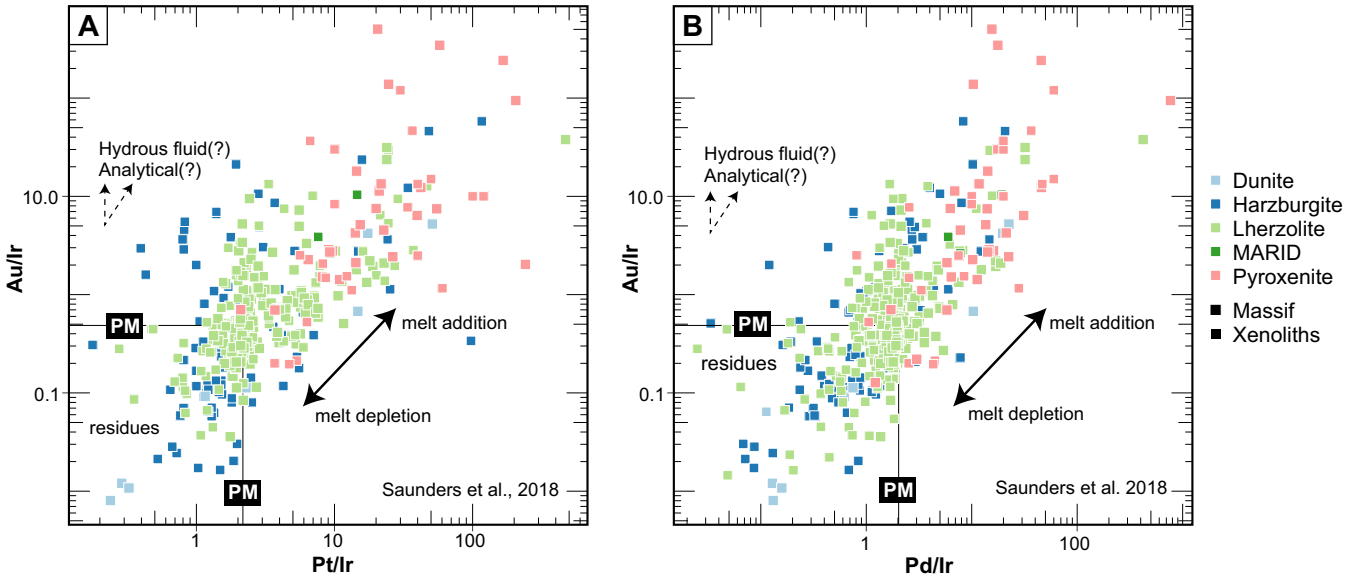

Figure 4. Global compilation of whole-rock platinum group elements (PGEs) and Au concentrations (Saunders et al., 2018). Melt-depleted peridotite samples yield Au/Ir, Pt/Ir, and Pd/Ir ratios that are lower than the primitive mantle (PM) due to their incompatibility during mantle melting. Increasing melt:rock interaction tends to increase incompatible element concentrations as demonstrated by the composition of pyroxenite dykes and melt-impregnated peridotite samples. Hydrous fluid metasomatism yields an Au/Ir ratio greater than the melt-rock array and may represent a second-order control for a smaller subset of mantle samples.

recycled into the mantle during subduction over geological time. The lithospheric architecture that formed during continent building also focuses magmas and their ore components during younger tectonic events (Begg et al., 2010; Mole et al., 2017). The concentration of numerous ore deposit types at the margins of cratonic blocks point to the important role that lithospheric architecture has on the genesis and preservation of ore systems (Begg et al., 2010; Hronsky et al., 2012; Griffin et al., 2013).

The precursors to ore-forming magmas likely interact with the lithospheric mantle during ascent (Fig. 2). Evidence for this process includes the precipitation of metasomatic BMS, which represents the primary mechanism for re-fertilizing melt-depleted mantle residues in precious metals and other ore components (Fig. 3). Because metasomatic BMS are typically enriched in Au, Pt, and Pd relative to other PGE (e.g. Ir), re-fertilized peridotite residues yield elevated Au/Ir, Pt/Ir, and Pd/Ir ratios (Fig. 4). Re-analysis of the global compilation of Au data for mantle rocks (Saunders et al., 2018), completed as part of the current study, suggests that a relatively large proportion of melt-depleted peridotite is re-fertilized (Fig. 4). At the Nahlin ophiolite, metasomatic BMS are also enriched in Ag, Bi, and Te and the BMS were likely precipitated during interaction between pyroxenite dykes with melt-depleted harzburgite in a suprasubduction zone setting. The precious metal signature of the Nahlin ophiolite pyroxenite dykes agrees with the trend towards elevated Au/Ir ratios defined by the global compilation, suggesting that passing melts play an important role in re-fertilizing the lithosphere through precipitation of BMS (Saunders et al., 2018).

New results further suggest that BMS alone are unable to explain the entire Au enrichment. Other Au-bearing phases are required to balance the whole-rock lithospheric budget in at least some cases (Luguet et al., 2004; Ferraris and Lorand, 2015). Olivine compositions and high-resolution LA-ICP-MS mapping suggests that some of this missing Au may be hosted by ultrafine native Au inclusions (Fig. 3). Similar inclusions have previously been reported (Ferraris and Lorand, 2015; Tassara et al., 2017; Zelenski et al., 2018) and were also identified in the current study due to the excellent sensitivity of the LA-ICP-MS mapping method (Fig. 3). Samples with a significant proportion of such Au-bearing inclusions would likely yield elevated whole-rock Au/Ir ratios (Fig. 4). A small subset of whole-rock analyses that deviate from the global trend defined by pyroxenite dykes and re-fertilized harzburgite may reflect the presence of such inclusions or possibly an analytical artefact due to the nugget effect (i.e. Au and other precious metals are heterogeneously distributed, which, coupled with the small sample volume used in some analytical methods, can yield spurious concentrations that are not representative of the rock as a whole; Fig. 4). We speculate that such inclusions, where present, reflect trapping of hydrous fluids, which has previously been suggested as a second important mechanism for upgrading Au within the lithospheric mantle (McInnes et al., 1999; Richards, 2009; Hronsky et al., 2012; Groves and Santosh, 2016). New results from the Nahlin ophiolite

demonstrate that such fluid-fluxed samples and their trapped inclusions also yield suprachondritic ratios for a range of ore-forming elements (e.g. Mo/Ce and As/Pb), providing additional tracers for identifying similar metasomatic mantle domains from the rock record (Lawley et al., 2020).

Overall, it would appear that re-fertilization has had a significant impact on some ore-forming element concentrations within the lithospheric mantle. For example, global compilations suggest that the lithospheric mantle contains 1.2 ppb Au (Saunders et al., 2018), which is essentially identical to the expected composition of the depleted mantle (1.0 ppb: Salters and Stracke, 2004) and primitive mantle (i.e. the expected composition of the mantle prior to crustal extraction, 1.7 ppb: Palme and O'Neill, 2014). The bulk continental crust also yields Au concentrations (1.3 ppb: Rudnick and Gao, 2003) that are similar to these mantle estimates. The agreement between all four reservoirs suggest that Au was not fractionated during the formation of the continents or, more likely, that Au was subsequently re-introduced into the lithospheric mantle after crust extraction.

One of the critical remaining questions is whether the metasomatized lithospheric mantle also supplies ore components to asthenospheric melts during ascent (Richards, 2009; Hronsky et al., 2012; Arndt, 2013). As an example of this process, assimilation of lithospheric mantle orthopyroxene by kimberlite melt is well documented (Sharygin et al., 2017). However, direct evidence for scavenging of ore components by rising asthenospheric melts and their interaction with previously metasomatized mantle lithosphere are comparatively scarce (Arndt, 2013). Peridotite xenoliths and corresponding volcanic arc lavas from Lihir Island (Papua New Guinea) provide one of the rare examples where a pre-enriched lithospheric mantle source could be linked directly to a gold deposit at surface (McInnes et al., 1999). The North China craton also represents one of the few examples of a major gold province (Yang et al., 2003) overlying lithospheric mantle that is systematically enriched in ore-forming elements relative to the global average (Saunders et al., 2018). Mesozoic gold deposits in the North China craton are hosted within previously metamorphosed Archean-Proterozoic basement, providing compelling evidence that fluids and ore components of metamorphic origin were not involved in deposit genesis (Yang et al., 2003; Li and Santosh, 2014; Groves and Santosh, 2016). Instead, these deposits have been linked to reworking of the lithospheric mantle underlying the North China craton with subcrustal sources of fluids and metals (Li and Santosh, 2014). Similar settings for Au have since been identified within Paleoproterozoic orogens superimposed on Archean basement in Canada and Tanzania (Lawley et al., 2013, 2015), although the source of gold at most Au ore systems and deposits remains equivocal. Most other studies that advocate for a mantle source region pre-enriched in ore components are based on indirect links, including distinct host rock compositions with a lithospheric mantle signature (Zhang et al., 2008), atypical ore-forming element ratios (Kepezhinskas and Defant, 2001), and/or isotopic evidence for interaction between ore-hosting rocks and an enriched mantle source (Richardson and Shirey, 2008).

Whether pre-enriched sources are required for ore deposit genesis is important because fertile source regions have the potential to significantly broaden the footprint of Au ore systems and provide a possible mechanism to explain the variable endowment observed between cratons (Sillitoe, 2008; Hronsky et al., 2012). Re-melting the kind of metasomatized, pre-enriched lithosphere documented herein, could, in principle, produce fertile melts that go on to form ore systems in the crust (McInnes et al., 1999; Sillitoe, 2008; Richards, 2009; Hronsky et al., 2012; Griffin et al., 2013). If correct, exploration should target lithospheric pathways that connect pre-enriched mantle with deep crustal fault networks. Unfortunately, the mechanisms for transferring ore components to rising asthenospheric melts remain very poorly understood and obvious examples of this process occurring are rare. Future research should focus on the composition of melts that have interacted with fertilized peridotite, particularly with ore-forming elements other than PGE. More research is also required on the interaction of lithospheric mantle-derived melts and their associated hydrothermal fluids once they reach the crust, since there is often very little evidence for such rocks at individual deposits. Finally, advances in geophysical and geochemical imaging technologies will continue to improve our understanding of the lithospheric mantle and its controls on ore systems.

ACKNOWLEDGMENTS

Thank you to all of the collaborators that contributed to this research activity, including Simon Jackson, Duane Petts, Alex Zagorevski, Graham Pearson, Pedro Waterton, Christian Veglio, Shuangquan Yang, Zhaoping Yang, Dany Savard, Donald Wright, Ryan Kroner, Sonja Aulbach, and Vicki Tschirhart. We also thank Norm Graham and Paula Vera of Discovery Helicopters (Atlin) for logistical support and transport during field work. Thanks to J.M. Gonzales-Jimenez for his comments on an earlier version of this report.

REFERENCES

Arndt, N., 2013. The lithospheric mantle plays no active role in the formation of orthomagmatic ore deposits; Economic Geology, v. 108, p. 1953–1970.

Barnes, S.J. and Fiorentini, M.L., 2012. Komatiite magmas and sulfide nickel deposits: A comparison of variably endowed archean terranes; Economic Geology, v. 107, p. 755–780.

Barnes, S.J., Mungall, J.E., and Maier, W.D., 2015. Platinum group elements in mantle melts and mantle samples; Lithos, v. 232, p. 395–417.

Barnes, S.J., Cruden, A.R., Arndt, N., and Saumur, B.M., 2016. The mineral system approach applied to magmatic Ni-Cu-PGE sulphide deposits; Ore Geology Reviews, v. 76, p. 296–316.

Begg, G., Hronsky, J., Arndt, N., Griffin, W., O'Reilly, S. Y., and Hayward, N., 2010. Lithospheric, cratonic, and geodynamic setting of Ni-Cu-PGE sulfide deposits; Economic Geology, v. 105, p. 1057–1070.

Boyle, R.W., 1979. The geochemistry of gold and its deposits; Geological Survey of Canada, Bulletin 280, p. 584.

Edwards, S.J., 1995. Boninitic and tholeiitic dykes in the Lewis Hills mantle section of the Bay of Islands ophiolite: Implications for magmatism adjacent to a fracture zone in a backarc spreading environment; Canadian Journal of Earth Sciences, v. 32, p. 2128–2146.

Ferraris, C. and Lorand, J., 2015. Novodneprite ($AuPb_3$), anyuiite [$Au(Pb, Sb)_2$] and gold micro- and nano-inclusions within plastically deformed mantle-derived olivine from the Lherz peridotite (Pyrenees, France): A HRTEM–AEM–EELS study; Physics and Chemistry of Minerals, v. 42, p. 143–150.

Fyfe, W., 1987. Tectonics, fluids, and ore deposits: Mobilization and remobilization; Ore Geology Reviews, v. 2, p. 21–36.

Goldfarb, R.J. and Groves, D.I., 2015. Orogenic gold: Common or evolving fluid and metal sources through time; Lithos, v. 233, p. 2–26.

Griffin, W.L., O'Reilly, S.Y., Afonso, J.C., and Begg, G.C., 2009. The composition and evolution of lithospheric mantle: A re-evaluation and its tectonic implications; Journal of Petrology, v. 50, p. 1185–1204.

Griffin, W.L., Begg, G.C., and O'Reilly, S.Y., 2013. Continental-root control on the genesis of magmatic ore deposits; Nature Geoscience, v. 6, p. 905–910.

Groves, D.I. and Santosh, M., 2016. The giant Jiaodong gold province: The key to a unified model for orogenic gold deposits?; Geoscience Frontiers, v. 7, p. 409–417.

Grütter, H.S., 2009. Pyroxene xenocryst geotherms: Techniques and application; Lithos, v. 112, p. 1167–1178.

Hedenquist, J.W. and Lowenstern, J.B., 1994. The role of magmas in the formation of hydrothermal ore deposits; Nature, v. 370, p. 519–527.

Heinrich, C. A. and Zurich, E.T.H., 2014. Fluids and ore formation in the Earth's crust; *in* Treatise on Geochemistry 2nd Edition, (ed.) H.D. Holland and K.K. Turekian; Elsevier Ltd., p. 1–28.

Hronsky, J.M.A., Groves, D.I., Loucks, R.R., and Begg, G.C., 2012. A unified model for gold mineralisation in accretionary orogens and implications for regional-scale exploration targeting methods; Mineralium Deposita, v. 47, p. 339–358.

Huston, D.L., Mernagh, T.P., Hagemann, S.G., Doublier, M.P., Fiorentini, M., Champion, D.C., Jaques, A.L., Czarnota, K., Cayley, R., Skirrow, R., and Bastrakov, E., 2016. Tectono-metallogenic systems—the place of mineral systems within tectonic evolution, with an emphasis on Australian examples; Ore Geology Reviews, v. 76, p. 168–210.

Jordan, T.H., 1975. The continental tectosphere; Reviews of Geophysics and Space Physics, v. 13, p. 1–12.

Kepezhinskas, P. and Defant, M.J., 2001. Nonchondritic Pt/Pd ratios in arc mantle xenoliths: Evidence for platinum enrichment in depleted island-arc mantle sources; Geology, v. 29, p. 851–854.

Kroner, R., 2019. The cordilleran lithosphere in south-central British Columbia: Insights from two xenolith suites; M.Sc. thesis, University of British Columbia, Vancouver, British Columbia, 110 p.

Lawley, C.J.M., Selby, D., and Imber, J., 2013. Re-Os molybdenite, pyrite and chalcopyrite geochronology, Lupa Goldfield, SW Tanzania: Implications for metallogenic time scales and shear zone reactivation; Economic Geology, v. 15, p. 1591–1613.

Lawley, C.J.M., Creaser, R.A., Jackson, S.E., Yang, Z., Davis, B., Pehrsson, S., Dubé, B., Mercier-Langevin, P., and Vaillancourt, D., 2015. Unravelling the western Churchill Province Paleoproterozoic gold metallotect: Constraints from Re-Os arsenopyrite and U-Pb xenotime geochronology and LA-ICP-MS arsenopyrite trace element chemistry at the BIF-hosted Meliadine Gold District, Nunavut, Canada; Economic Geology, v. 100, p. 1425–1454.

Lawley, C.J.M., Kjarsgaard, B., Jackson, S., Yang, Z., and Petts, D., 2018a. Olivine and clinopyroxene mantle xenocryst geochemistry from the Kirkland Lake kimberlite field, Ontario; Geological Survey of Canada, Open File 8376, 9 p.

Lawley, C.J.M., Kjarsgaard, B., Jackson, S., Yang, Z., Petts, D., and Roots, E., 2018b. Trace metal and isotopic depth profiles through the Abitibi cratonic mantle; Lithos, v. 314–315, p. 520–533.

Lawley, C.J.M., Petts, D.C., Jackson, S.E., Zagorevski, A., Pearson, D.G., Kjarsgaard, B.A., Savard, D., and Tschihart, V., 2019. Precious metal mobility during serpentinization and breakdown of base metal sulphide; Lithos.

Lawley, C.J.M., Pearson, D.G., Waterton, P., Zagorevski, A., Bédard, J.H., Jackson, S.E., Petts, D.C., Kjarsgaard, B.A., Zhang, S., and Wright, D., 2020. Ore-forming element and isotopic signature of re-fertilized mantle peridotite as determined by nanopowder and olivine LA-ICP-MS analyses; Chemical Geology.

Laznicka, P., 2014. Giant metallic deposits—A century of progress; Ore Geology Reviews, v. 62, p. 259–314.

Li, S. and Santosh, M., 2014. Metallogeny and craton destruction: Records from the North China Craton; Ore Geology Reviews, v. 56, p. 376–414.

Lorand, J. and Luguet, A., 2016. Chalcophile and siderophile elements in mantle rocks: Trace elements controlled by trace minerals; Reviews in Mineralogy and Geochemistry, v. 81, p. 441–488.

Luguet, A., Lorand, J., Alard, O., and Cottin, J., 2004. A multi-technique study of platinum group element systematic in some Ligurian ophiolitic peridotites, Italy; Chemical Geology, v. 208, p. 175–194.

McCuaig, T.C., Beresford, S., and Hronsky, J., 2010. Translating the mineral systems approach into an effective exploration targeting system; Ore Geology Reviews, v. 38, p. 128–138.

McInnes, B.I., McBride, J.S., Evans, N.J., Lambert, D.D., and Andrew, A.S., 1999. Osmium isotope constraints on ore metal recycling in subduction zones; Science, v. 286, p. 512–516.

Mole, D.R., Fiorentini, M.L., Cassidy, K.F., Kirkland, C.L., and Thebaud, N., 2017. Crustal evolution, intra-cratonic architecture and the metallogeny of an Archaean craton; *in* Ore Deposits in an Evolving Earth, (ed.) G.R.T. Jenkin, P.A.J. Lusty, I. McDonald, M.P. Smith, A.J. Boyce, and J.J. Wilkinson; Geological Society of London, Special Publication 393, p. 23–80.

Morgan, P., 1995. Diamond exploration from the bottom up: regional geophysical signatures of lithosphere conditions favorable for diamond exploration; Journal of Geochemical Exploration, v. 53, p. 145–165.

Mungall, J.E., Ames, D.E., and Hanley, J.J., 2004. Geochemical evidence from the Sudbury structure for crustal redistribution by large bolide impacts; Nature, v. 429, p. 3–5.

Nimis, P., 1998. Evaluation of diamond potential from the composition of peridotitic chromian diopside; European Journal of Mineralogy, v. 10, p. 505–519.

O'Reilly, S., Griffin, W.L., Djomani, Y.H.P., and Morgan, P., 2001. Are lithospheres forever? Tracking changes in subcontintental lithospheric mantle through time; GSA Today, p. 5–9.

Palme, H. and O'Neill, H. St. C., 2014. Cosmochemical estimates of mantle composition; *in* Treatise on Geochemistry 2nd Edition, (ed.) H.D. Holland and K.K. Turekian; Elsevier Ltd., p. 1–39.

Pearson, D.G. and Wittig, N., 2008. Formation of Archaean continental lithosphere and its diamonds: The root of the problem; Journal of the Geological Society, v. 165, p. 895–914.

Pearson, D.G., Parman, S.W., and Nowell, G.M., 2007. A link between large mantle melting events and continent growth seen in osmium isotopes; Nature, v. 449, p. 202–205.

Richards, J.P., 2009. Postsubduction porphyry Cu-Au and epithermal Au deposits: Products of remelting of subduction-modified lithosphere; Geology, v. 37, p. 247–250.

Richards, J.P., 2011. Magmatic to hydrothermal metal fluxes in convergent and collided margins; Ore Geology Reviews, v. 40, p. 1–26.

Richardson, S. and Shirey, S., 2008. Continental mantle signature of Bushveld magmas and coeval diamonds; Nature, v. 453, p. 10–13.

Richardson, S., Gurney, J., Erlank, A., and Harris, J., 1984. Origin of diamonds in old enriched mantle; Nature, v. 310, p. 198–202.

Rudnick, R. and Gao, S., 2003. Composition of the continental crust; *in* Treatise on Geochemistry, (ed.) H.D. Holland and K.K. Turekian; Elsevier Ltd., p. 1–64.

Salters, V.J.M. and Stracke, A., 2004. Composition of the depleted mantle; Geochemistry, Geophysics, Geosystems, v. 5, p. 27.

Saunders, J.E., Pearson, N.J., O'Reilly, S.Y., and Griffin, W.L., 2018. Gold in the mantle: A global assessment of abundance and redistribution processes; Lithos, v. 322, p. 376–391.

Sharygin, I.S., Litasov, K.D., Shatskiy, A., Safonov, O.G., Golovin, A.V, Ohtani, E., and Pokhilenko, N.P., 2017. Experimental constraints on orthopyroxene dissolution in alkali-carbonate melts in the lithospheric mantle: Implications for kimberlite melt composition and magma ascent; Chemical Geology, v. 455, p. 44–56.

Sillitoe, R., 2008. Major gold deposits and belts of the North and South American Cordillera: Distribution, tectonomagmatic settings, and metallogenic considerations; Economic Geology, v. 103, p. 663–687.

Snyder, D.B., Rondenay, S., Bostock, M.G., and Lockhart, G.D., 2004. Mapping the mantle lithosphere for diamond potential using teleseismic methods; Lithos, v. 77, p. 859–872.

Stachel, T. and Harris, J.W., 2008. The origin of cratonic diamonds—Constraints from mineral inclusions; v. 34, p. 5–32.

Tassara, S., González-jiménez, J.M., Reich, M., Schilling, M.E., Morata, D., Begg, G., Saunders, E., Grif, W.L., Reilly, S.Y.O., Grégoire, M., Barra, F., and Corgne, A., 2017. Plume-subduction interaction forms large auriferous provinces; Nature Communications, v. 8, p. 1–7.

Therriault, A., Fowler, A., and Grieve, R., 2002. The Sudbury igneous complex: A differentiated impact melt sheet; Economic Geology, v. 97, p. 1521–1540.

Ulrich, T., Günther, D., and Heinrich, C., 1999. Gold concentrations of magmatic brines and the metal budget of porphyry copper deposits; Nature, v. 399, p. 676–679.

Varfalvy, V., Hébert, R., Bédard, J., and Laflèche, M., 1997. Petrology and geochemistry of pyroxenite dykes in upper mantle peridotites of the North Arm mountain massif, Bay of Islands ophiolite, Newfoundland: Implications for the genesis of boninitic and related magmas; The Canadian Mineralogist, v. 35, p. 543–570.

Wilkinson, J.J., 2013. Triggers for the formation of porphyry ore deposits in magmatic arcs; Nature Geoscience, v. 6, p. 917–925.

Wilkinson, J.J., Stoffell, B., Wilkinson, C.C., Jeffries, T.E., and Appold, M.S., 2009. Anomalously metal-rich fluids form hydrothermal ore deposits; Science, v. 323, p. 764–768.

Yang, J., Wu, F., and Wilde, S.A., 2003. A review of the geodynamic setting of large-scale late Mesozoic gold mineralization in the North China Craton: An association with lithospheric thinning; Ore Geology Reviews, v. 23, p. 125–152.

Zelenski, M., Kamenetsky, V.S., Nekrylov, N., Abersteiner, A., Ehrig, K., and Khanin, D., 2018. Textural, morphological and compositional varieties of modern arc sulfides: A case study of the Tolbachik volcano, Kamchatka; Lithos, v. 319, p. 14–29.

Zhang, M., O'Reilly, S.Y., Wang, K., Hronsky, J., and Griffin, W.L., 2008. Flood basalts and metallogeny: The lithospheric mantle connection; Earth Science Reviews, v. 86, p. 145–174.

Fingerprinting ore processes in orogenic auriferous systems: Insights into metallogenic and exploration implications from argillite-hosted iron sulphide nodules from the Timmins-Matheson gold corridor

Jean-Luc Pilote[1*], Simon E. Jackson[2], Patrick Mercier-Langevin[1], Benoît Dubé[1], Christopher J.M. Lawley[2], Duane C. Petts[2], Zhaoping Yang[2], Ed van Hees[3], and Dave Rhys[4]

[1]Geological Survey of Canada, 490 rue de la Couronne, Québec, Quebec G1K 9A9
[2]Geological Survey of Canada, 601 Booth Street, Ottawa, Ontario K1A 0E8
[3]Ontario Geological Survey, 5520 Hwy 101 East, South Porcupine, Ontario, Canada P0N 1H0
[4]Panterra Geoservices Inc., 14180 Greencrest Drive, Surrey, British Columbia, Canada V4P 1L9
[*]Corresponding author's e-mail: jean-luc.pilote@canada.ca

ABSTRACT

Orogenic Au deposits of the world-class Timmins-Porcupine Au camp in Abitibi and its surroundings are commonly hosted by carbonaceous to non-carbonaceous argillite sequences, which contain Au-rich (≤10 ppm Au) nodules and concretions; two features widely considered to be diagenetic, but can be equivocal in some highly strained and hydrothermally altered zones. Hence, the goals of this research activity are to (1) fingerprint pyrite of diagenetic or epigenetic origin, (2) constrain factors that control Au uptake in diagenetic pyrite, and (3) determine if early Au enrichment fundamentally influences overprinting orogenic Au mineralization. Pyrite nodules and concretions are generally composed of two textural domains: a core and a rim. The pyrite rims exhibit much more textural complexity than the pyrite cores. Multivariate analysis of trace element data derived from laser ablation-inductively coupled plasma-mass spectrometry reveal a clear geochemical distinction between epigenetic textures (granoblasts, porphyroblasts, idiomorphic overgrowths) and nodules/concretions. In the Timmins-Matheson region, disparate pyrite textures can be discriminated simply by the abundance of thallium. Nodules and concretions also show geochemical attributes that are inherited from the composition of the rock assemblage in which they form. Regardless of their host rocks, the core and rim of the nodules possess different but systematic geochemical signatures, which were constrained with the help of multivariate statistics; Ni, As, Se, Ag, Sb, Au, Pb, and Bi tend to concentrate into the core, whereas Mo and Tl (±Mn) tend to concentrate into the rim. In situ Fe isotope analyses of three pyrite nodules reveal intra-grain variations in δ^{56}Fe values that range from -3.11 to 0.74‰, with 30% of the values <-2.5‰, which has, in the literature to date, been recorded only in Archean diagenetic pyrite in black shale. The results contribute to a framework that helps improving our interpretation of the genesis of pyrite nodules in deformed and metamorphosed sedimentary rocks, which will ultimately minimize uncertainties related to the interpretation of ore-forming processes.

INTRODUCTION

The Timmins-Matheson corridor of the Archean southern Abitibi greenstone belt encompasses one of the highest concentrations of Au deposits globally, with the Timmins-Porcupine camp alone having produced over 75 Moz (2125 metric tonnes) Au (Dubé et al., 2017). This ~60 km long, east-west-oriented corridor is characterized by volcanic and sedimentary assemblages that are host to numerous greenstone-hosted quartz-carbonate (orogenic) Au deposits, and is transected by the regional Destor-Porcupine and Pipestone fault zones (Fig. 1). Sulphide-bearing carbonaceous sedimentary units within the Timmins-Matheson area are common, although volumetrically a minor part of the sedimentary sequence, and many are spatially associated with orogenic Au deposits (Hannington et al., 2012; Dubé et al., 2017). Moreover, volcanogenic massive sulphide (VMS) and komatiite-hosted Ni-Cu-(PGE) deposits are also known to be hosted by, or closely associated with, such sedimentary units (Hannington et al., 1999; Mercier-Langevin et al., 2007; Houlé et al., 2010; Pilote et al., 2020). Common to these sedimentary rocks are sulphides that occur as individual or clusters of pyrite nodules (e.g. Jonasson et al., 1999; Gray and Hutchinson, 2001; Hannington et al., 2012).

Pilote, J.-L., Jackson, S.E., Mercier-Langevin, P., Dubé, B., Lawley, C.J.M., Petts, D.C., Yang, Z., van Hees, E., and Rhys, D., 2020. Fingerprinting ore processes in orogenic auriferous systems: Insights into metallogenic and exploration implications from argillite-hosted iron sulphide nodules from the Timmins-Matheson gold corridor; *in* Targeted Geoscience Initiative 5: Contributions to the Understanding of Canadian Gold Systems, (ed.) P. Mercier-Langevin, C.J.M. Lawley, and S. Castonguay; Geological Survey of Canada, Open File 8712, p. 165–178. https://doi.org/10.4095/323675

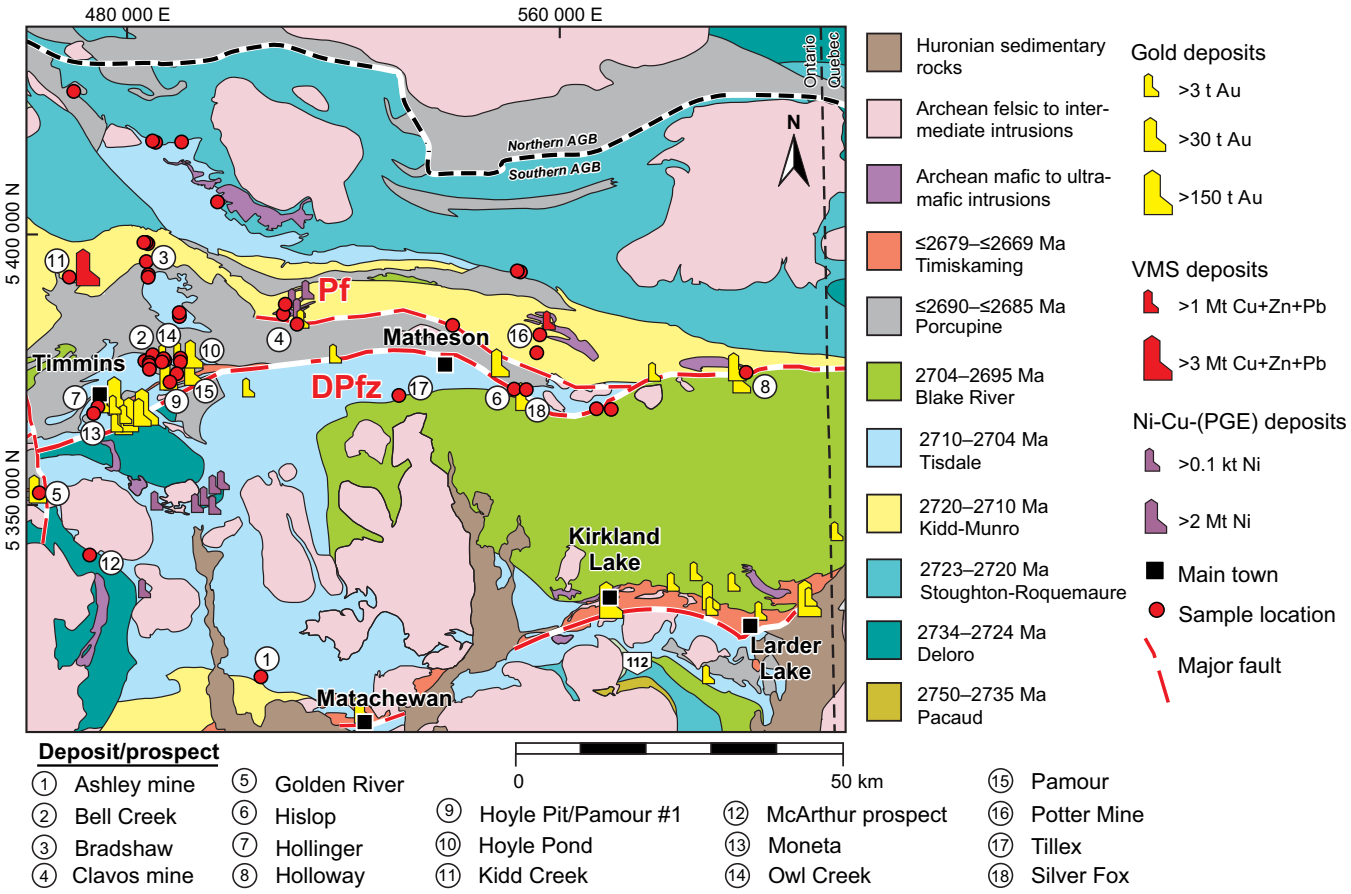

Figure 1. Simplified geological map of the western portion of the southern Abitibi greenstone belt (AGB) and location of samples collected (red circle). Map after Dubé et al. (2017). Abbreviations: DPfz = Destor-Porcupine fault zone, Pf = Pipestone fault.

Early work reported Au values in pyrite nodules ranging from a few ppb to >10 ppm Au (Jackson et al., 2017; Pilote et al., 2019), with the core typically enriched relative to its rim (Pilote et al., 2019). The factors controlling this enrichment are not fully understood. Pyrite nodules are widely accepted to be authigenic and diagenetic (e.g. Bonnell and Anderson, 1987; Guy et al., 2010, 2014; Rickard, 2012; Gregory et al., 2019). However, in high-strain zones and/or hydrothermally overprinted areas, their genesis is equivocal. For example, some could arguably be round, S-reactive lithic clasts, such as carbonaceous and/or Fe-rich argillite, that underwent partial or complete replacement by pyrite (i.e. hydrothermal pseudomorphs) resulting in a spherical or elliptical shape that could be misidentified as diagenetic (similar to what some have argued for the origin of rounded pyrite in the Witwatersrand basin: Barnicoat et al., 1997; Phillips and Law, 2000). The distinction between diagenetic versus epigenetic pyrite is important as these pyrites record different conditions, at different times with various metallogenic and exploration implications. For instance, Large et al. (2011) have proposed that a large part of the Au budget in auriferous systems is sourced from the metamorphic-induced liberation of Au from sedimentary pyrite. Although this model could be conceivable for certain areas, to our knowledge, it has yet to be demonstrated in the Timmins-Matheson region.

In part, this ongoing research aims to (1) characterize and classify diagenetic versus epigenetic iron sulphides based on textures and geochemical signatures (trace elements and isotopes), (2) improve our understanding of the factors controlling Au uptake in diagenetic pyrite, and (3) use isotope systems to constrain the source of metals from both ore-related and sedimentary pyrite grains. It should be noted that pyrrhotite nodules also occur in the sedimentary rocks of the Timmins-Matheson region but they only represent a small fraction (in abundance) relative to their pyritic counterpart in the study area and will be addressed in a separate publication.

This contribution provides a summary of the various textures observed in pyrite nodules, presents some of the key geochemical attributes of nodules and epigenetic textures (e.g. prophyroblasts, granoblasts, idiomorphic overgrowths) based on robust statistical analysis, describes the recently developed methodology and preliminary results from in situ Fe isotope work using the laser ablation-multi-collector-inductively coupled plasma-mass spectrometry (LA-MC-

ICP-MS), and discusses potential implications for exploration.

GEOLOGICAL SETTING

The study area is within the southwestern portion of the Neoarchean Abitibi greenstone belt, which is part of the Superior Province (Fig. 1). It encompasses seven volcano-sedimentary rock assemblages that range in age from 2734 to <2669 Ma, including (from oldest to youngest) the Deloro, Stoughton-Roquemaure, Kidd-Munro, Tisdale, Blake River, Porcupine, and Timiskaming assemblages (e.g. Ayer et al., 2002a,b, 2005; Bateman et al., 2008). The five oldest assemblages represent near continuous volcanism from 2734 to 2695 Ma with sequences consisting predominantly of komatiite and tholeiitic basalt to calc-alkalic mafic to felsic volcanic and volcaniclastic rocks (e.g. Ayer et al., 2002a, 2005; Bateman et al., 2008). Interflow sedimentary and iron formation units are present but represent only a small volume of the total rock package (e.g. Bateman et al., 2008). The Porcupine (<2690 to <2685 Ma) and Timiskaming (<2679 to <2669 Ma) assemblages, on the other hand, represent thick sedimentary packages with lesser volcanic sequences (Bleeker et al., 1999; Ayer et al., 2002b; Bateman et al., 2008). The base of the Porcupine assemblage is marked by polylithic and polygenic volcaniclastic successions and felsic lapilli tuff (i.e. the Krist Formation) that is overlain by and laterally transitions to carbonaceous argillite, mudstone, siltstone, and greywacke (i.e. Hoyle and Beatty formations). The unconformably overlying fluvial, alluvial, to deltaic Timiskaming assemblage consists of polylithic conglomerate at the base (including local sulphidic fragments; Gray and Hutchinson, 2001), overlain by successions of sandstone and siltstone, including greywacke (Born, 1995).

Two salient east-trending structural features, namely the Destor-Porcupine fault zone and the Pipestone fault, have played an integral role in the geological and metallogenic architecture of the Timmins-Matheson Au corridor (Fig. 1; e.g. Dubé et al., 2017). To the north, the Pipestone fault is interpreted to have developed soon after deposition of the Porcupine assemblage, which was thrust- and fold-imbricated with older volcanic rocks (e.g. the Tisdale assemblage) within major southwest-verging thrust slices (Bleeker, 2015). To the south, the Destor-Porcupine fault zone and associated structures record a complex history of basin subsidence and inversion, and north-directed thick-skinned thrusting, which occurred as a result of north-south shortening at <2669 Ma (Bateman et al., 2008; Dubé et al., 2017). The Timiskaming assemblage is exposed within close proximity of the Destor-Porcupine fault zone and the stratigraphic facies change from conglomerate to mudstone to conglomerate is likely the expression of the onset, deepening, and filling of a synorogenic basin (Bleeker, 2015). The bulk of the Au deposits are found along these fault zones and their splays (Fig. 1), which likely acted as important pathways to CO_2-rich metamorphic Au-bearing fluids (Bateman et al., 2008; Dubé et al., 2017).

PYRITE NODULES AND CONCRETIONS

Pyrite nodules are spherical to oblate and can range in size from a few millimetres to 5 centimetres in diameter. They are generally concentrically zoned, which is expressed by their textures that can be separated into two main domains: a core and a rim (Fig. 2a,b). The core exhibits two main types of textures: 1) an equigranular, polycrystalline, fined-grained, anhedral to subhedral pyrite (Fig. 2c,d), and 2) a massive pyrite cementing medium- to coarse-grained detrital inclusions ('cementing texture'), which typically include quartz+albitic to potassic feldspar+mica+Fe-Mg-carbonate±apatite±rutile (Fig. 2e,f, 3a). In low-strain areas, inclusions in nodules typically form layers concordant with bedding. The rims display a variety of textures; Figure 2g to p show the most common ones. Pyrite can develop acicular (Fig. 2g,h), tabular or stubby (Fig. 2i,j), braided (Fig. 2k,l), hexagonal/polygonal prisms (Fig. 2m,n), or skeletal (Fig. 2o,p) textures. The skeletal variety forms cross-hatched elongate crystals, commonly with co-existing sphalerite±chalcopyrite. The braided (or anastomosing) texture is defined by a network of inclusion-rich or 'dusty' pyrite that encloses prismatic, inclusion-poor, outward-oriented pyrite crystals (Fig. 2k,l). Whereas Au concentration is typically low in the rim relative to the core (e.g. Jackson et al., 2017; Pilote et al., 2020), the dusty pyrite in the braided texture can be enriched significantly relative to other common rim textures (Jackson et al., 2017).

Centimetre-scaled and irregular-shaped pyrite growths are also common in the sedimentary sequences. These are referred to as concretions and can be distinguished from nodules only by their shape, which is generally elongated and irregular, also zonation is parallel to bedding (S_0) rather than concentric. Concretions are typically formed of massive pyrite cementing coarse material developed in silty or sandy layers (Fig. 2b, 3a; Pilote et al., 2019) with a texture and mineralogy that resembles the cementing texture in some of the cores of the nodules (Fig. 2e,f). The rim of concretions can also develop similar textures to those of the nodules. Gold can reach multi-ppm levels in nodules and concretions (Jackson et al., 2017; Pilote et al., 2019) but it is invisible (as nano-inclusions and/or in solid-solution; Reich et al., 2005; Fougerouse et al., 2016). Where electrum (Ag-Au alloy) or native gold is

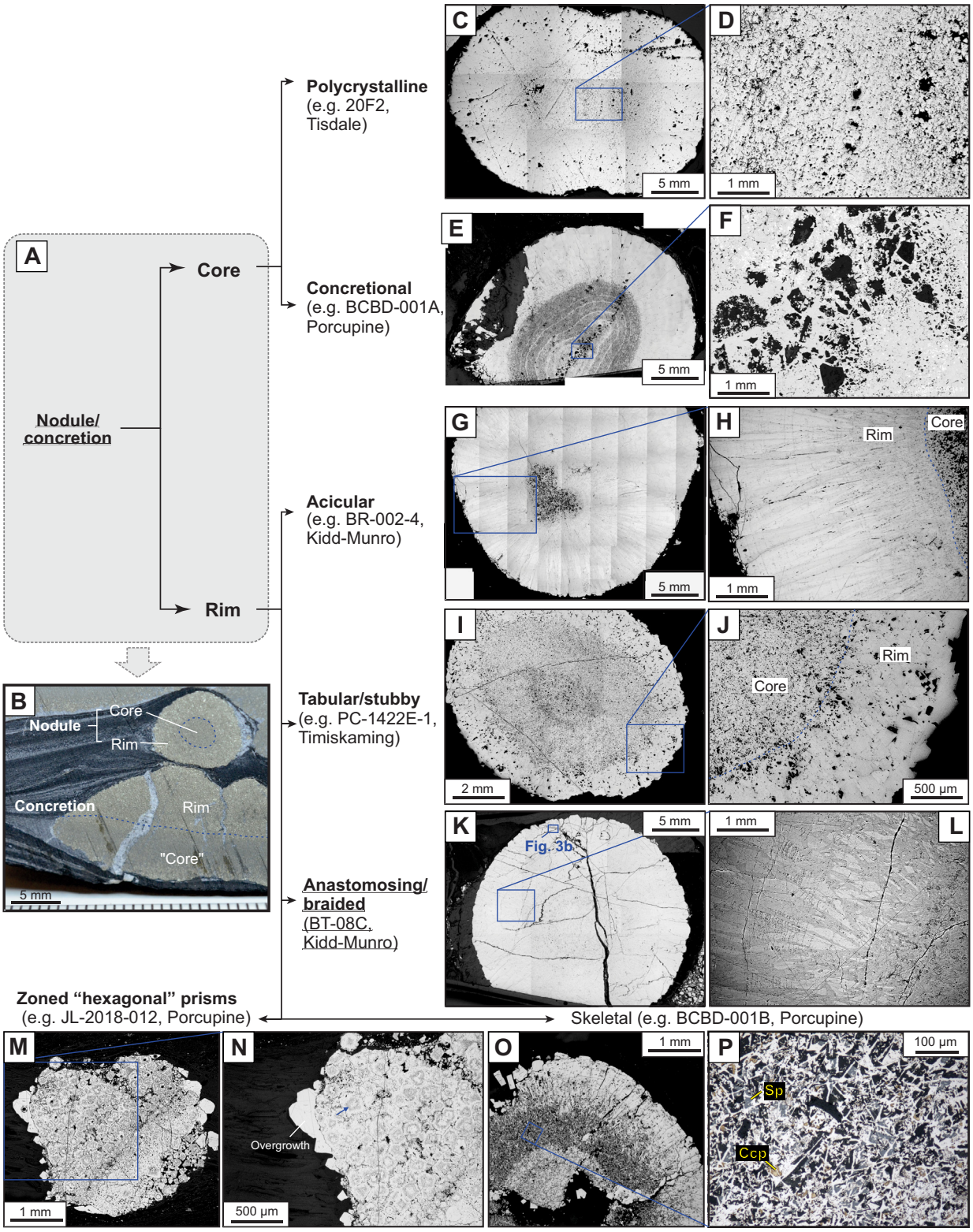

Figure 2. Photos and photomicrographs of representative textures in nodules and concretions from various assemblages of the Timmins-Matheson region. **a, b)** Main domains consisting of a core and rim (sample JL-2019-039, Bradshaw deposit, Kidd-Munro assemblage). **c, d)** Polycrystalline core texture (sample 20F2, Owl Creek deposit, Tisdale assemblage). **e, f)** Cementing texture in the core of a nodule composed of coarser detrital grains (sample BCBD-001A, Bell Creek deposit, Porcupine assemblage). **g, h)** Acicular texture pyrite (sample BR-002-4, Bradshaw deposit, Kidd-Munro assemblage). i**, j)** Tabular or stubby texture pyrite (sample PC-1422E-1, Pamour 1 and Hoyle deposit, Timiskaming assemblage). **k, l)** Braided texture composed of inclusion-poor prismatic crystals surrounded by a network of porous pyrite (sample BT-08C, Holloway deposit, Kidd-Munro assemblage). **m, n)** Agglomeration of zoned hexagonal pyrite (sample JL-2018-012, Bell Creek deposit, Porcupine). **o, p)** Skeletal texture with chalcopyrite (Ccp) and sphalerite (Sp) inclusions (sample BCBD-001B, Bell Creek deposit, Porcupine assemblage).

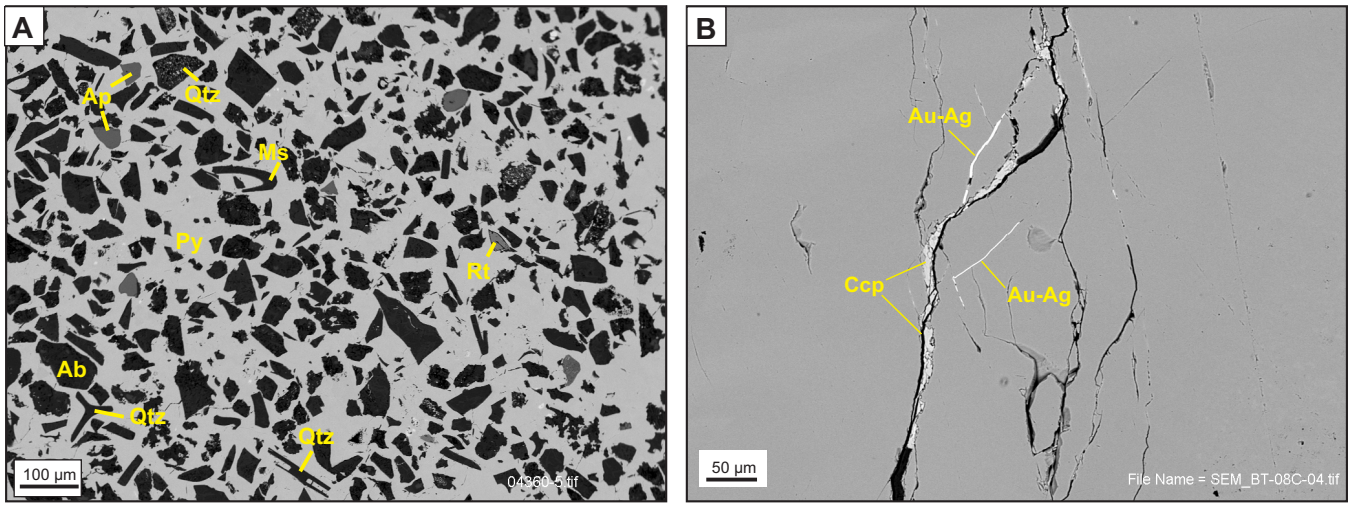

Figure 3. a) Backscattered-electron image of a concretional texture composed of albite (Ab), apatite (Ap), muscovite (Ms), pyrite (Py), quartz (Qtz), and rutile (Rt) (sample 04360, Bell Creek deposit, Tisdale assemblage). **b)** Backscattered-electron image of BT-08C (close-up of Fig. 2k) showing electrum (Au-Ag) and chalcopyrite (Ccp) developed within micro-fractures.

present, it occupies late (micro)fractures that also contain quartz+carbonate±sulphides (Fig. 3b).

METHODS

Trace Element Analysis

More than 1200 laser ablation-inductively coupled plasma-mass spectrometry (LA-ICP-MS) spot analyses were completed of 135 polished thick sections that were made from 122 rock samples from the Timmins-Matheson region. The analyses were performed in static (spot) mode at the Geological Survey of Canada, Ottawa, using an Agilent Technologies 7700 x ICP-MS coupled to a Photon Machines Analyte 193 nm excimer laser ablation system (Cabri and Jackson, 2011). Spot analyses (10–40 µm) were calibrated using USGS doped synthetic basaltic glass standard GSE-1G (Guillong et al., 2005) and doped synthetic pyrrhotite standard Po689 (Co, As, Ag, Sb, and Au; prepared at CANMET). Data reduction was done with the software Glitter™ (Griffin et al., 2008) using "GeoReM preferred values" (http://georem.mpch-mainz.gwdg.de/) for the elemental contents of GSE-1G. Sulphide reference material FeS-1 (LabMaTer, UQAC) was used as an external quality control standard to monitor instrument performance.

To highlight key geochemical features of pyrite in sedimentary rocks of the Timmins-Matheson Au corridor, principal component analysis (PCA) was used to investigate relationships among pyrite composition, textures, and host assemblages (Fig. 4–6). These were computed in the software *R* (R Development Core Team, 2019) after a log-ratio transformation of the data (Filzmoser et al., 2009). Variables included are Mn, Co, Ni, Cu, Zn, As, Se, Mo, Ag, Sb, Au, Tl, Pb, and Bi. Data below the lower detection limit were replaced by dividing the lower detection limit by the square root of two. Principal components (PC) point in the direction of the main variability of the bulk data. By ranking, the first PC (PC1) explains the maximum variability, the second PC (PC2) explains the second most variability, etc. Simply put, elements that correlate strongly together in a data set will cluster together on a PCA biplot and the further they are from the centre, the more significant they are in defining the structure of the data set. These elements are represented by their PCA loadings, which were rescaled for plotting purposes. The score (of each analysis) is calculated by using a covariance estimator (Filzmoser et al., 2009). Each analysis (or score) represented on the diagram is colour-coded by texture, domain, or host-rock assemblage. Complete data sets will be made available in separate contributions.

Iron Isotope Analysis

Iron isotopic analysis was performed on pyrite nodules from three samples (PC-1422E-1, Pamour Conglomerate in the Timiskaming assemblage; JL-2018-007, Stoughton-Roquemaure assemblage; 20F2, Tisdale assemblage) by laser ablation-multi-collector (MC)-ICP-MS at the Geological Survey of Canada, Ottawa. Two samples were prepared as polished, thick (~100 µm) sections. Analyses were performed in static (spot) analysis mode at intervals along quasi-linear transects from nodule core to rim, immediately adjacent to areas that had undergone prior LA-ICP-MS element mapping. One sample (20F2) was a polished section of a complete pyrite nodule mounted in a 25 mm diameter round epoxy mount. This nodule, which had previously undergone LA-ICP-MS element mapping of the whole nodule, was repolished prior to Fe isotope analysis. Several analyses were also made on narrow pyrite overgrowths on each nodule. Also analyzed were two pyrite

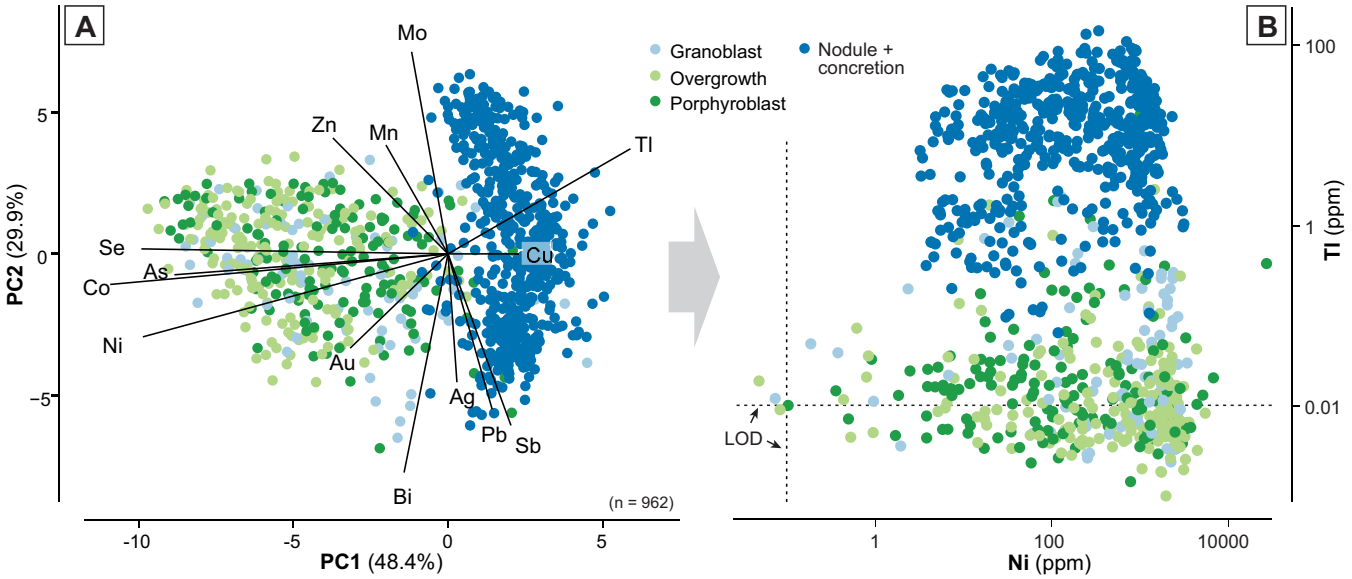

Figure 4. a) Principal component analysis (PCA) biplot of the first two principal components (PC1 and PC2) with their respective variation (in percentage). PCA scores are coloured by type of texture. **b)** Ni (ppm) versus Tl (ppm) of the data displayed in (a). Also shown are lines representing the average lower limits of detection (LOD).

Fe-isotope reference materials that were developed in-house to calibrate analyses and provide quality control: NMC12744 pyrite (Opasatica Lake, Timiskaming County, Quebec, Canada) and Tatlock Quarry pyrite (Lanark County, Ontario, Canada), respectively.

Iron isotopic analysis was performed using a Teledyne Photon Machines Analyte G1 excimer laser ablation system coupled to a Thermo Scientific™ Neptune Plus™ High Resolution MC-ICP-MS. Complete operating conditions are provided in Table 1. All analyses were performed using 43 µm spots and a low laser repetition rate (4 Hz) to minimize down-hole laser-induced isotopic fractionation. A plug of glass wool (~31 mg) in the sample delivery tubing was used to preferentially filter particles (>0.5 µm) too large to be quantitatively volatilized in the ICP, which can result in severe isotopic fractionation (Jackson and Günther, 2003). The Neptune was operated at medium resolution (mass resolving power of ~7700). In this mode, the Fe^+ peaks were resolved from major $^{40}Ar^{14}N^+$, $^{40}Ar^{16}O^+$, $^{40}Ar^{17}O^+/^{40}Ar^{16}O^1H^+$, and $^{40}Ar^{18}O^+$ argide interferences as "flat top" shoulders on the low-mass side of the polyatomic ion peaks (Weyer and Schwieters, 2003). Precise and accurate Fe isotope measurement were then achieved by positioning the centre mass slightly on the low-mass side (~0.001 amu) of the Fe peak (Dauphas et al., 2009). ^{53}Cr and ^{60}Ni were measured to allow correction of ^{54}Cr and ^{58}Ni isobaric interferences on ^{54}Fe and ^{58}Fe, respectively.

MC-ICP-MS signal intensity data were processed offline using an in-house Excel spreadsheet, which performed the following calculations: 1) integration of selected regions of the gas blank and ablation signals, 2) calculation of zero (gas blank) and then isobaric interference-corrected signal intensities and isotope ratios; 3) ±2 sigma outlier rejection; 4) calculation of mean ratios and their uncertainties (within-run precision; 5) application of a mass bias correction using data for pyrite calibration standard NMC12744 analyzed immediately before and after each sample analysis (standard-sample-standard bracketing); and 6) conversion of corrected Fe isotopic ratios and calculated uncertainties (external precision) to $\delta^{57}Fe_{IRMM014}$ and $\delta^{56}Fe_{IRMM014}$ values in per mil (‰), where

$$\delta^{57}Fe_{IRMM014} = ((^{57}Fe/^{54}Fe_{sample})/(^{57}Fe/^{54}Fe_{IRMM014}) - 1) \times 1000$$

and

$$\delta^{56}Fe_{IRMM014} = ((^{56}Fe/^{54}Fe_{sample})/(^{56}Fe/^{54}Fe_{IRMM014}) - 1) \times 1000.$$

Mean $\delta^{57}Fe_{IRMM014}$ and $\delta^{56}Fe_{IRMM014}$ values and external uncertainties for secondary Tatlock Quarry reference pyrite were 0.58 ± 0.23 and 0.39 ± 0.06‰ (2 sd, n = 18 over 3 days), which compare favourably with values of 0.56 ± 0.13 and 0.41 ± 0.09‰, (2 sd, n = 53 over 4 days), respectively, for solution nebulization MC-ICP-MS of digested separates of the same pyrite sample.

RESULTS

Fingerprinting Geochemical Signatures

Comparing nodules and concretions with epigenetic textures

In Figure 4a, calculated PC1 (explains 48.4% of the variance) for the LA-ICP-MS analyses on pyrite nodules/concretions, porphyroblasts, granoblasts, and

Table 1. Laser ablation-multicollector-inductively coupled plasma-mass spectrometry (LA-MC-ICP-MS) operating conditions.

Laser ablation (LA)	
Model	Analyte G1 (Teledyne Photon Machines Inc., USA)
Sample cell	"HelEx" 2-volume cell
Wavelength	193 nm
Pulse duration (FWHM)	4 ns
Repetition rate	4 Hz
Spot diameter	43 µm
Energy density	2.2 J/cm^2
Gas flows:	
Carrier (He) MFC-1 (cell cup)	0.50 Lmin^{-1}
Carrier (He) MFC-2 (cell base)	0.55-0.80 Lmin^{-1}
Make up (Ar)	1.040-1.080 Lmin^{-1}
Signal smoothing	50 mL aerosol mixing tube in sample delivery line
Particle filtering	Plug of glass wool (~31 mg) in sample delivery line
MC-ICP-MS	
Model	Neptune 2 (Thermo-Finnigan, Germany)
Cones	Standard (H) cones
Resolution	Medium resolution (a mass resolving power of ~7700)
Typical signals	8–18 V on ^{56}Fe
Data acquisition parameters	
Data acquisition protocol	Time resolved analysis (0.265 s per reading)
Detectors	Faraday cups equipped with 1011 Ohm resistors
Cup configuration	^{60}Ni (H4), ^{58}Cr (H2), ^{57}Fe (H1), ^{56}Fe (Ax), ^{54}Fe (L2), ^{53}Cr (L4)
Zero	On peak for 60 s prior to ablation
Ablation time	60 s
Calibration and data processing	
Mass bias correction	Standard-sample-standard bracketing
Calibration standard	NMC12744 (QC) in-house pyrite standard
Outlier rejection	± 2 sigma outlier rejection
Quality control standard	Tatlock Quarry (ON) in-house pyrite standard

overgrowths show two main controls: a strongly negative control from Co, Ni, As, and Se, and a strongly positive control from Tl. In PC2 space, which explains 29.9% of the variance, Mn, Zn, Mo, and Tl are positively contributing to the structure of the data set, whereas negative controls are shown for Ag, Sb, Au, Pb, and Bi. When samples (or PCA scores) are plotted in this PC1-PC2 space, a clear separation is shown between the nodules/concretions and the other three textures (Fig. 4a), which is mostly explained by Tl. This separation can also be demonstrated by a simple Ni versus Tl diagram (Fig. 4b) where nodules and concretions show abundances in Tl that are 100 to 10,000 times greater than values observed in epigenetic pyrite, which are generally close to detection limit (i.e. ~0.01 ppm). The data further suggest that elements with positive or negative loadings for PC2 are independent of pyrite texture (Fig. 4a).

Examining element correlations in nodules and concretions

PCA was also done exclusively on data from nodules and concretions to assess internal element correlations and examine features that explain best the structure of the data (Fig. 5; first two PCs only are shown). Figure 5a shows strong positive PC1 loadings for Mn, Zn, Mo, and Tl, and strongly negative loadings for Bi, Pb, Ag, Au, and Sb. In PC2 space, Bi contributed positively, whereas Sb, Au, Cu, Co, and Sb are closely associated with negative PC2 loadings (Fig. 5a). When PCA scores are classified by textural domain, the data from rims and cores largely overlap (Fig. 5a). However, when grouped by lithostratigraphic assemblage, nodules and concretions from the Kidd-Munro assemblage cluster distinctly from the rest of the data, regardless of textural domains (Fig. 5b). The close clustering of different assemblages suggests that intra-grain geochemical variations are less significant than the multivariate compositional differences between pyrite from different host successions. When PCA is done exclusively on cores or rims (Fig. 5c,d), the data also show a separation in PC1-PC2 space for the nodules and concretions from the Kidd-Munro assemblage, best explained by the antithetic contributions of Bi relative to the rest of elements. This is supported by the distinct trace element abundances in the nodules and concretions from the Kidd-Munro assemblage (not shown); for instance, the geometric mean of the Bi content (0.21 and 0.05 ppm Bi in core and rim, respectively) is 10 and 50 times less than for the other assemblages (Pilote et al., unpub. data).

Given the distinct geochemistry that the nodules and concretions have in the Kidd-Munro assemblage, core and rim data were further assessed by individual assemblage (Fig. 6). Only those with the most analyses are shown (i.e. Kidd-Munro, Tisdale, and Porcupine assemblages; Fig. 6a–c). By focusing on individual assemblages, this removes the effect of disparate pyrite compositions that occur between different host-rock assemblages. Nodules and concretions in the Kidd-Munro assemblage have strongly positive loadings for Mo, Zn, and Mn and strongly negative loadings for Sb and Bi in the PC1 space (Fig. 6a). In PC2 space, the strongest positive contributions are explained by Sb, Ag, Co, and Tl, whereas the most negative contributions are from Bi and Ni. In the Tisdale assemblage, Mn, Zn, Mo, and Tl have positive contribution in PC1, whereas they are negative for most elements except Co and Se (Fig. 6b). In PC2 space, Au and Co appear to explain most of the variability, displaying strongly negative contributions (Fig. 6b). As for the Porcupine assemblage, despite the different orientations of the main PCs, variability in the data is comparable to that in the Tisdale assemblage, such as the negative controls

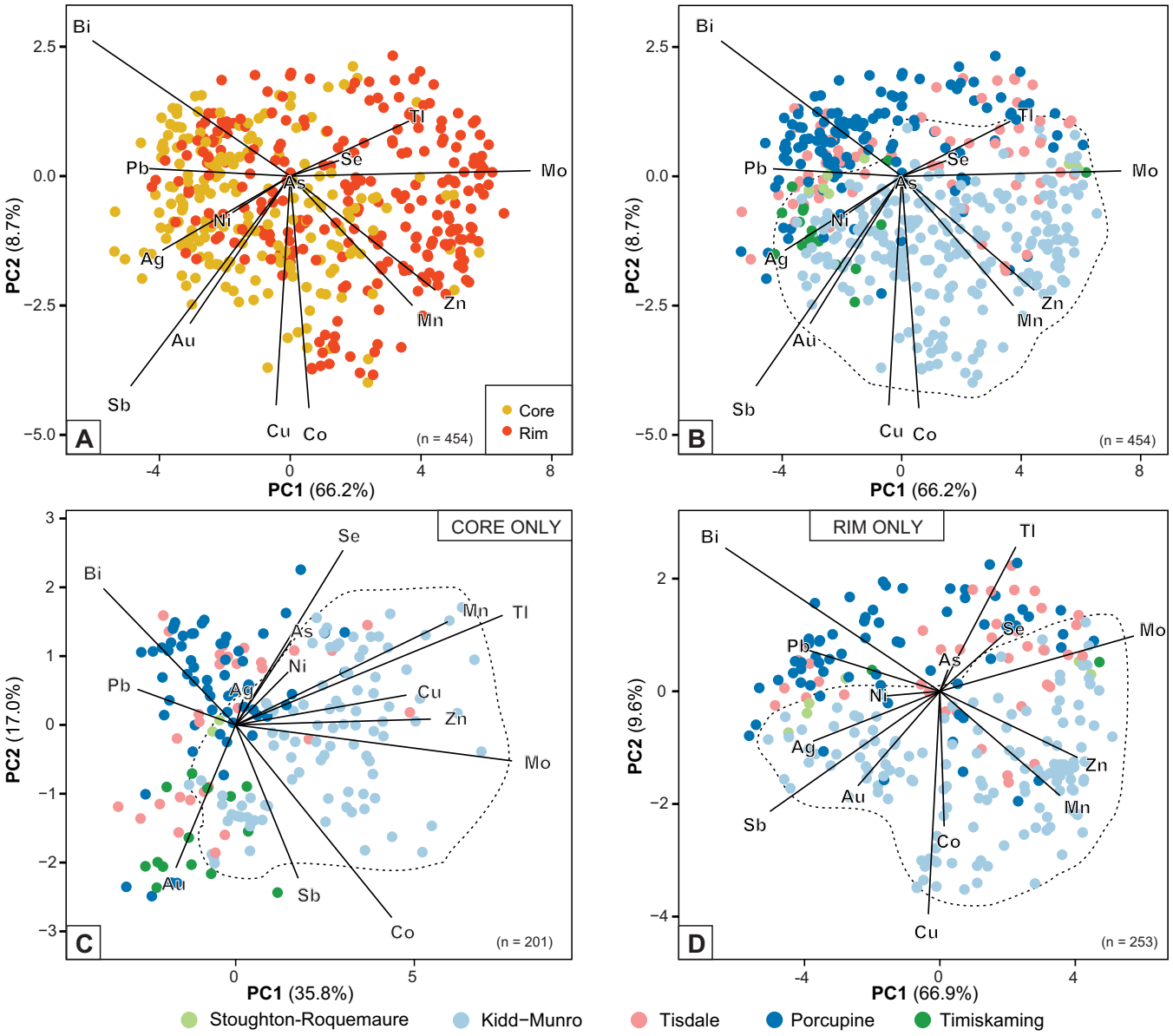

Figure 5. Principal component analysis (PCA) biplots of LA-ICP-MS data from nodules and concretions. Only the first two principal components are shown with their respective variation (in percentage). **a)** PCA of data from cores and rims with scores colour-coded by domain. **b)** Same as in (a), but scores are colour-coded by assemblage. **c)** PCA of cores only with scores colour-coded by assemblage. **d)** PCA of data from rims only with scores colour-coded by assemblage.

of Au and Co in PC2 space and the antithetic relationships between Mo and Tl and the rest of the elements in PC1 space (Fig. 6c). In all three assemblages, the variability in the rims are best explained by the behaviour of Mn, Zn, Mo, and Tl, while the cores, although less well defined, are best explained by the covariation of Ni, As, Se, Ag, Sb, Au, Pb, and Bi.

Iron Isotope Results

The three nodules show similar variations but different values in Fe isotope composition (Table 2, Fig. 7). For simplicity, given the linear relationship between $\delta^{56}Fe$ and $\delta^{57}Fe$ (Fig. 7g,h), only values for the former will be described here. The total range in $\delta^{56}Fe$ for all three samples is -3.11 ± 0.09‰ (2σ) to +0.97 ± 0.05‰ with lighter values in the nodules compared to the overgrowth pyrite grains (Table 2). Across the cores, the Fe isotope values tend to remain relatively constant (within 1‰; Fig. 7d–f). The cores in JL-2018-007 and 20F2 are similar with average values of -2.56 and -2.53‰, respectively, whereas the sample from the Pamour conglomerate (sample PC-1422E-1) shows a significantly heavier core, averaging -0.91‰. Most of the rim in the latter sample shows lighter values than its core, except for two analyses (+0.74 and +0.76‰), which overlap those of the overgrowth pyrite (Fig. 7g). The overgrowth pyrite grains developed around the nodules have significantly heavier values than the rest

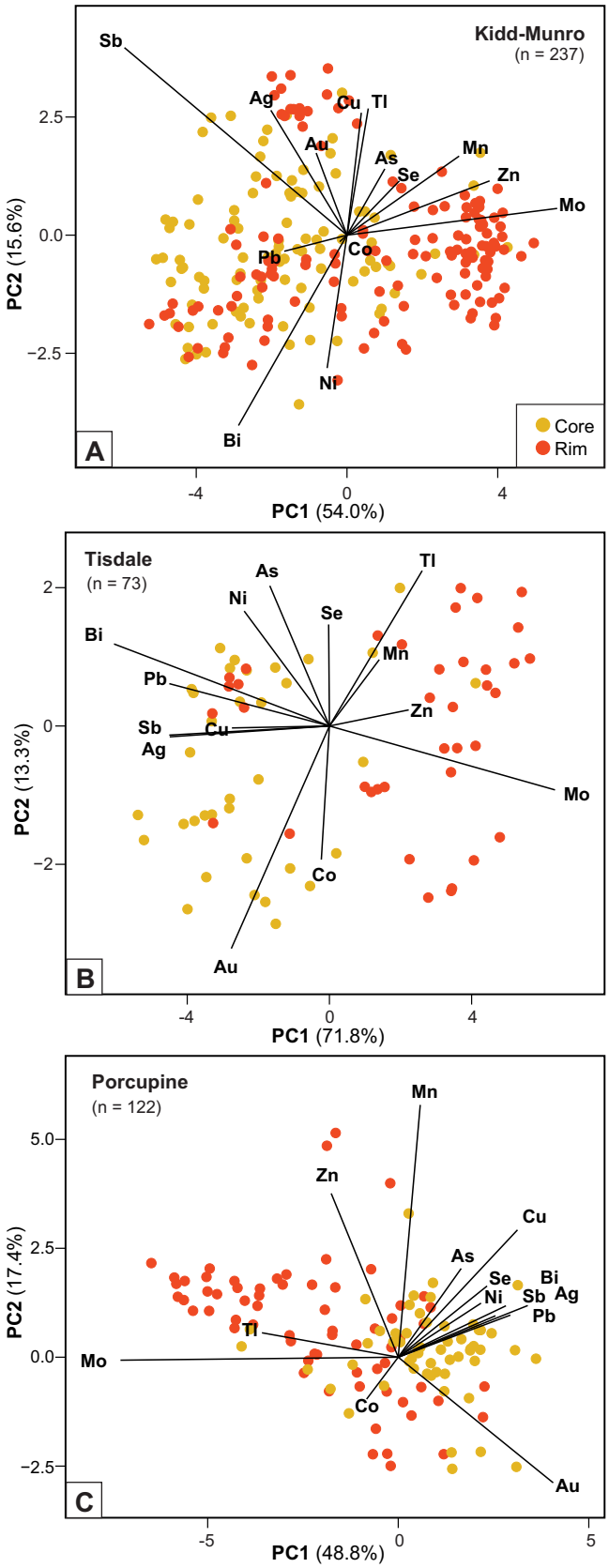

Figure 6. Principal component analysis (PCA) biplots of LA-ICP-MS data from nodules and concretions with scores colour-coded by domain (core or rim). **a)** Data from the Kidd-Munro assemblage. **b)** Data from the Tisdale assemblage. **c)** Data from the Porcupine assemblage.

Table 2. Summary of δ^{56}Fe values in per mil (‰) notation.

	PC-1422E-1			JL-2018-007			20F2		
	Mean	Min	Max	Mean	Min	Max	Mean	Min	Max
Core	-0.91	-1.97	-0.05	-2.53	-2.67	-2.40	-2.56	-2.72	-2.31
Rim	-1.21	-2.13	0.74	-2.45	-2.89	-1.61	-2.39	-3.11	-1.87
Overgrowth	0.45	-0.04	0.97						
Cataclast				-2.24	-2.68	-1.23			

of the analyzed grains, ranging from -0.04 ± 0.05‰ to +0.97 ± 0.05‰

Iron isotope values in the rim of sample JL-2018-007 overlap those of its core, ranging from -2.89 ± 0.07‰ to -1.61 ± 0.04‰, and display a lighter-to-heavier pattern toward the edge (Fig. 7e). The cataclastic fragments as seen in Figure 7b, show similar values as those of the rim, with a range from -2.68 ± 0.05‰ to -1.23 ± 0.09‰ (Table 2).

The rim of nodule 20F2 shows two distinct trends, which appear to reflect differences in textures. Much like nodule BT-08C (Fig. 2k,l), the rim of sample 20F2 is characterized by a braided network of dusty pyrite ("A" in Fig. 7c) enclosing massive, inclusion-poor, euhedral crystals ("B" in Fig. 7c). The progressive increase in δ^{56}Fe (and δ^{57}Fe) values from core to rim of the dusty pyrite correlate with the continuous textural transition observed in thin section (Fig. 7f). The clean euhedral crystals, however, show a distinctively lighter and flat pattern (Fig. 7f), which ranges between -2.6 and -2.4‰, as opposed to a range from -2.2 to -1.9‰ for the dusty pyrite.

DISCUSSION

Detailed field and petrographic observations reveal that despite textural complexities among argillite-hosted nodules and concretions (Fig. 2), commonalities exist across variably aged volcanic and sedimentary assemblages in the Timmins-Matheson Au corridor, regardless of the setting of the sediment deposition (e.g. volcanic interflows, deep-water basin-related), deformation, metamorphism, and/or alteration. Samples collected within 10 m of shear-hosted orogenic Au mineralization (e.g. Bradshaw, Bell Creek) showed no systematic textural differences to those sampled from 'greenfield' exploration drill cores (>10 km from any known ore-grade mineralization). Nodules that developed in the argillic sequences associated with the LaRonde Penna VMS deposit (Blake River Group; Mercier-Langevin et al., 2007) also display the same transition from a polycrystalline core to a crystalline rim (Pilote et al., 2020).

Multivariate statistical analysis of >1200 LA-ICP-MS spot analyses show that nodules and concretions from the Timmins-Matheson Au corridor have very distinct geochemical signatures compared to those with epigenetic textures (granoblastic, porphyroblastic, and

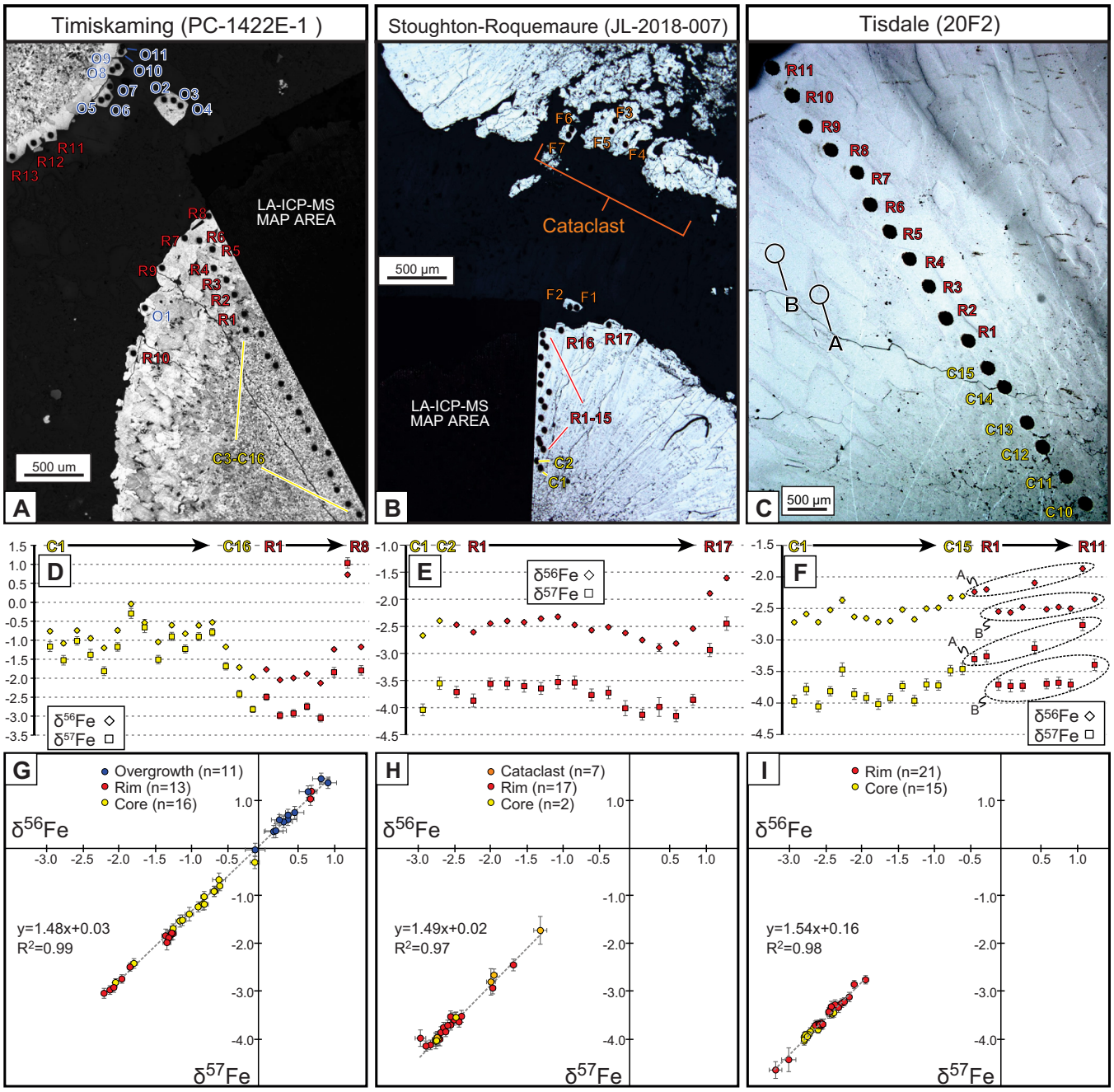

Figure 7. a to c) Photomicrographs (reflected light) of nodules with locations of Fe isotope analysis by LA-MC-ICP-MS. **d to f)** $\delta^{56}Fe$ and $\delta^{57}Fe$ values for transects across the nodules in a to c. **g to i)** Complete Fe isotope analyses represented on a $\delta^{56}Fe$ versus $\delta^{57}Fe$ biplot. The regression reflects the mass-dependent fractionation of the isotopes. Error bars represent ±2 standard deviations of the mean.

overgrowths in grains showing multiple growth zones and hosted in argillite, basaltic/ultramafic flows, mafic dykes, or quartz-carbonate veins). This is reflected mainly by the abundance of Tl in pyrite as seen in Figure 4b.

Geometric means of trace element abundances, including Au, in the nodules varies greatly from core to rim but also from the core of one nodule to another (Pilote et al., 2019). Despite this, systematic element patterns—shown here by PCA within the core and rim—suggest that, on the scale of a nodule, the evolving physical (e.g. permeability) and/or chemical (e.g. supersaturation of reactants, i.e., reduced Fe and S, redox) conditions controlling element uptake during crystal growth must be largely comparable, regardless of the host-rock composition. It is currently understood that the concentric zoning of a nodule reflects growth in closed or highly isolated conditions (Gregory et al., 2019) in a stagnant or gently advective hydrodynamic regime (Rickard, 2012) and that the textural transition

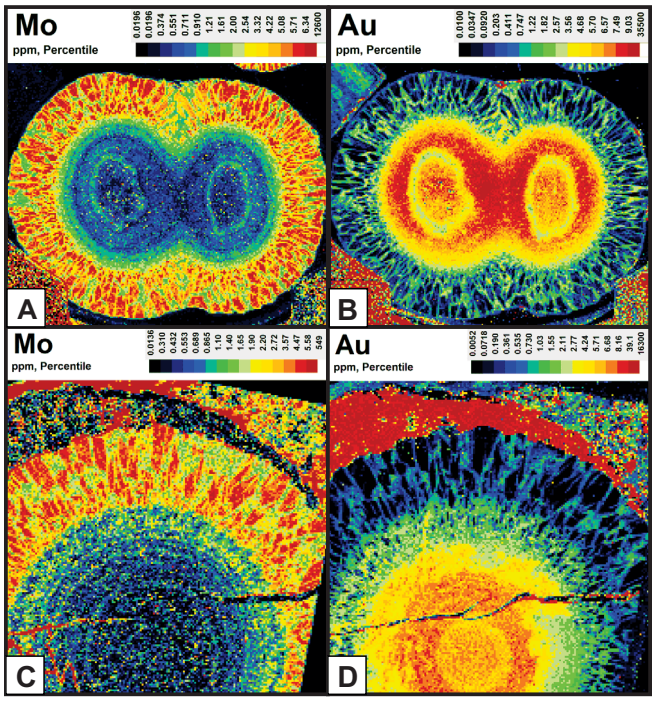

Figure 8. LA-ICP-MS element maps of nodules. **a)** Mo and **b)** Au in sample 20F2 (Owl Creek deposit, Tisdale assemblage; *see* Fig. 2c for photomicrograph). **c)** Mo and **d)** Au in sample BT-08C (Holloway deposit, Kidd-Munro assemblage; *see* Fig. 2k for photomicrograph). Note the distribution of Au in both samples and the high Au values along the fracture in BT-08C. The element maps use a percentile colour-scaling function.

from a fine polycrystalline core to a prismatic rim is the result of a decrease in the state of supersaturation (Murowchick and Barnes, 1987; Rickard, 2012; Hu et al., 2019). The cores are generally enriched in Ni, As, Se, Ag, Sb, Au, Pb, and Bi relative to the rims, which is validated by detailed LA-ICP-MS compositional mapping of more than 20 nodules from the Timmins region, which will be the subject of a separate contribution (preliminary results shown in Jackson et al., 2017 and Pilote et al., 2019). The rims are commonly strongly enriched in Mo, two examples of which are shown in Figure 8. This enrichment correlates with the development of prismatic pyrite and could be related to the change in pyrite crystallinity. Alternatively, the sudden enrichment in Mo could be related to a change in pH and/or redox in the sediment pore fluids, optimizing MoS_4^{2-} adsorption during crystal growth (Bostick et al., 2003). Because Mo and Au concentrations are antithetic in these two map examples on PCA biplots (Fig. 4), the process(es) controlling enrichment of accessory elements have important implications for Au fertility. Factors controlling the variability of Au (and other trace elements) from one nodule/concretion core to another are not fully understood but preliminary conclusions from this research activity suggest that Au abundance (multi-ppb versus -ppm levels) in cores could be predominantly linked to Au availability in the matrix sediments (Pilote et al., work in progress).

The interpretation of Fe-isotope signatures in Archean shale remains equivocal (e.g. Rouxel et al., 2005, 2006; Dauphas et al., 2017) because the processes giving rise to isotopic fractionation are incompletely understood. It is however recognized that the Fe isotopic ratio is largely regulated by (abiotic or biotic) redox reactions (Rouxel et al., 2005; Nishizawa et al., 2010; Yoshiya et al., 2012). The δ^{56}Fe range observed in the three pyrite nodules from Timmins overlaps with the values of the diagenetic pyrite grains in Neoarchean shale reported elsewhere (-3.5 to +0.5‰; *see* compilation in Dauphas et al., 2017). Moreover, many of the isotopically light pyrite values (<-2.5‰) observed in the Timmins samples (Fig. 7) are thought to only occur in diagenetic pyrite from pre-2.5 Ga black shale as a result of depletion of isotopically heavy Fe associated with partial Fe(II) oxidation and precipitation of Fe oxides from a globally anoxic, Fe-rich Neoarchean ocean (Dauphas et al., 2017). By contrast, sedimentary pyrite in post-2.5 Ga sedimentary sequences and pyrite of hydrothermal origin show smaller Fe isotopic ranges, with respective mean values that are close to modern oceanic values (i.e. dissolved δ^{56}Fe of ~0 to +0.5‰: Radic et al., 2011) and igneous rocks and hydrothermal sources (-0.8 to +0.2‰) (Dauphas et al., 2017).

At the intra-grain level, a study by Marin-Carbonne et al. (2014) on shale-hosted pyrite nodules from the ca. 2.7 Ga low-grade metamorphic rocks of the Bubi greenstone belt, Zimbabwe, reported in situ δ^{56}Fe values ranging from -2.1 to 0.7‰; a core displaying lighter values than its rim, correlating with an outward depletion in Ni and enrichment in Co. These values and patterns are strikingly similar to the three nodules from the Timmins region. Marin-Carbonne et al. (2014) interpret this relatively large negative excursion as the product of multiple Fe sources (metastable iron sulphides formed in seawater and the sediment) during complex early diagenetic processes.

EXPLORATION IMPLICATIONS

Careful examination is strongly encouraged before interpreting the genesis of pyrite in sedimentary rocks, particularly those in high-strain zones and/or medium- to high-grade metamorphic belts. The authigenic nodules and concretions described here show zoning and textural, chemical, and isotopic characteristics similar to those resulting from diagenetic processes reported elsewhere (e.g. Bonnell and Anderson, 1987; Rickard, 2012; Jeans et al., 2016; Gregory et al., 2019). However, 'nodular' pyrite composed entirely of medium- to coarse-grained, porous, idiomorphic pyrite and quartz enclosing visible Au grains near mineralized

zones have also been reported in carbonaceous argillite in the Timmins region. For example, Jonasson et al. (1999) described examples of such textures from the Owl Creek Au deposit and interpreted them to be the product of epigenetic hydrothermal processes (*see* Fig. 9e,f in Jonasson et al., 1999). Similar pyrite textures investigated in this study yield low Tl values (≤0.1 ppm), much like the other epigenetic textures studied in the Timmins region. Therefore, although interpreted to be epigenetic, their rounded nature could potentially be mistaken as diagenetic in the field.

The composition of diagenetic pyrite nodule cores can vary greatly and can contain up to >10 ppm Au; however, Au is refractory (or invisible), which is not optimal for metallurgical recovery. On a broader scale, if the amount of Au in diagenetic pyrite predisposes a region (among many other parameters; e.g. Hronsky et al., 2012) to be fertile and conducive for hosting orogenic-type mineralization as proposed by Large et al. (2011), then the spatial pairing that exists between the Au-enriched pyrite nodules and the Au endowment of the Timmins-Matheson Au corridor may be related. However, research on orogenic Au deposits has shown that many more elements are at play in forming world-class Au districts and equating sulphidic argillite and Au may be an oversimplification of a multi-parameter process. It is premature at this point to draw any conclusion about the potential role of the pyrite nodules (and other diagenetic pyrite) on the Au budget in a giant district such as the auriferous Timmins-Porcupine camp.

ONGOING WORK

Whereas significant progress has been made, many questions remain unanswered and important hypotheses remain untested in the Timmins-Matheson Au corridor. Ongoing work includes interrogation of multiple isotope systems (Fe, Pb, and S) by LA-MC-ICP-MS and ion microprobe on diagenetic and epigenetic iron sulphides, both proximal and distal to mineralization. Approximately 200 of the spots targeted for isotope analysis have also been analyzed by LA-ICP-MS for trace element abundances. A total of 31 LA-ICP-MS compositional maps have been generated (29 from the Timmins region and two from the LaRonde deposit; Pilote et al., 2020). The millions of data points derived from these maps have been classified via robust multivariate statistics and clustering methods to quantitatively define intra-grain pyrite generations and compare them within and between rock assemblages. Whole-rock geochemistry of the sedimentary host to the nodules and concretions is complete and the combination of in situ and whole-rock data will provide an opportunity to examine possible factors controlling and trace element uptake in pyrite by using, for example, various redox, provenance, and hydrothermal proxies. This multi-technique approach, combined with detailed field work, will provide, in part, a way to minimize the uncertainties related to the interpretation of the possible Au source(s).

ACKNOWLEDGMENTS

This report is a contribution to NRCan's Targeted Geoscience Initiative Program (TGI-5) Gold Project. Support for this study was provided through Activities G-1.1 (Gold through space and time at the Archean) and G-1.4 (Fingerprinting ore processes in auriferous systems). We thank the personnel at Pan American Silver (Bell Creek mine) and Gowest Gold Ltd. (Bradshaw mine) for providing access to their sites, data, and samples. Drs. Mark Hannington and Matthew Gray are acknowledged for providing samples from several localities in the district. We thank Lionel Bonhomme and Wayne Corstorphine of International Explorers and Prospectors Inc. for access to historical drill core from various exploration projects. David Diekrup and Ashley Abraham are thanked for sample preparation and description and SEM work. Valérie Bécu and Francis Aucoin are thanked for help with data and map compilation. This contribution received constructive reviews from B.M. Frieman and S. Castonguay.

REFERENCES

Ayer, J., Amelin, Y., Corfu, F., Kamo, S., Ketchum, J., Kwok, K., and Trowell, N., 2002a. Evolution of the southern Abitibi greenstone belt based on U-Pb geochronology: Autochthonous volcanic construction followed by plutonism, regional deformation and sedimentation; Precambrian Research, v. 115, p. 63–95.

Ayer, J.A., Ketchum, J.W.F., and Trowell, N.F., 2002b. New geochronological and neodymium isotopic results from the Abitibi greenstone belt, with emphasis on the timing and the tectonic implications of Neoarchean sedimentation and volcanism; Ontario Geological Survey, Open File Report 6100, p. 5-1–5-16.

Ayer, J.A., Thurston, P.C., Bateman, R., Dubé, B., Gibson, H.L., Hamilton, M.A., Hathway, B., Hocker, S.M., Houlé, M.G., Hudak, G., Ispolatov, V.O., Lafrance, B., Lesher, C.M., MacDonald, P.J., Péloquin, A.S., Piercey, S.J., Reed, L.E., and Thompson, P.H., 2005. Overview of results from the Greenstone Architecture Project: Discover Abitibi Initiative; Ontario Geological Survey. Open File Report 6154, 146 p.

Barnicoat, A.C., Henderson, I.H.C., Knipe, R.J., Yardley, B.W.D., Napier, R.W., Fox, N.P.C., Kenyon, A.K., Muntingh, D.J., Strydom, D., Winkler, K.S., Lawrence, S.R., and Cornford, C., 1997. Hydrothermal gold mineralisation in the Witwatersrand Basin; Nature, v. 386, p. 820–824.

Bateman, R., Ayer, J.A., and Dubé, B., 2008. The Timmins-Porcupine gold camp, Ontario: Anatomy of an Archean greenstone belt and ontogeny of gold mineralization; Economic Geology, v. 103, p. 1285–1308.

Bleeker, W., 2015. Synorogenic gold mineralization in granite-greenstone terranes: The deep connection between extension, major faults, synorogenic clastic basins, magmatism, thrust inversion, and long-term preservation; *in* Targeted Geoscience Initiative 4: Contributions to the Understanding of Precambrian

Lode Gold Deposits and Implications for Exploration, (ed.) B. Dubé, and P. Mercier-Langevin; Geological Survey of Canada, Open File 7852, p. 25–47.

Bleeker, W., Parrish, R.R., and Sager-Kinsman, A., 1999. High-precision U-Pb geochronology of the Late Archean Kidd Creek deposit and Kidd volcanic complex; *in* The Giant Kidd Creek Volcanogenic Massive Sulfide Deposit, western Abitibi Subprovince, Canada, (ed.) M.D. Hannington and C.T. Barrie; Society of Economic Geologists, Monograph 10, p. 43–70.

Bonnell, L. and Anderson, T.F., 1987. Sulfur isotopic variations in nodular and disseminated pyrite: hole 603B; *in* Initial Reports of the Deep Sea Drilling Project, (ed.) J.E. van Hinte et al.; U.S. Government Printing Office, Washington, p. 1257–1262.

Born, P., 1995. A sedimentary basin analysis of the Abitibi greenstone belt in the Timmins area, northern Ontario, Canada; Ph.D. thesis, Carleton University, Ottawa, Ontario, 489 p.

Bostick, B.C., Fendorf, S., and Helz, G.R., 2003. Differential adsorption of molybdate and tetrathiomolybdate on pyrite (FeS_2); Environmental Science and Technology, v. 37, p. 285–291.

Cabri, L. and Jackson, S., 2011. New developments in characterization of sulfide refractory Au ores; World Gold 2011, 50th Conference of Metallurgists, MetSoc, Montreal, Quebec, p. 51–62.

Dauphas, N., Pourmand, A., and Teng, F.-Z., 2009. Routine isotopic analysis of iron by HR-MC-ICPMS: How precise and how accurate?; Chemical Geology, v. 267, p. 175–184.

Dauphas, N., John, S.G., and Rouxel, O., 2017. Iron isotope systematics; Reviews in Mineralogy and Geochemistry, v. 82, p. 415–510.

Dubé, B., Mercier-Langevin, P., Ayer, J., Atkinson, B., and Monecke, T., 2017. Orogenic greenstone-hosted quartz-carbonate gold deposits of the Timmins-Porcupine camp; *in* Archean Base and Precious Metal Deposits, southern Abitibi Greenstone Belt, Canada, (ed.) T. Monecke, P. Mercier-Langevin, and B. Dubé; Reviews in Economic Geology, v. 19, p. 51–79.

Filzmoser, P., Hron, K., and Reimann, C., 2009. Principal component analysis for compositional data with outliers; Environmetrics, v. 20, p. 621–632.

Fougerouse, D., Reddy, S.M., Saxey, D.W., Rickard, W.D.A., van Riessen, A., and Micklethwaite, S., 2016. Nanoscale gold clusters in arsenopyrite controlled by growth rate not concentration: Evidence from atom microscopy; American Mineralogist, v. 101, p. 1916–1919.

Gray, M.D. and Hutchinson, R.W., 2001. New evidence for multiple periods of gold emplacement in the Porcupine mining district, Timmins area, Ontario, Canada; Economic Geology, v. 96, p. 453–475.

Gregory, D., Mukherjee, I., Olson, S.L., Large, R.R., Danyushevsky, L.V., Stepanov, A.S., Avila, J.N., Cliff, J., Ireland, T.R., Raiswell, R., Olin, P.H., Maslennikov, V.V., and Lyons, T.W., 2019. The formation mechanisms of sedimentary pyrite nodules determined by trace element and sulfur isotope microanalysis; Geochimica et Cosmochimica Acta, v. 259, p. 53–68.

Griffin, W., Powell, W., Pearson, N., and O'Reilly, S., 2008. GLITTER: Data reduction software for laser ablation ICP-MS; *in* Laser Ablation ICP-MS in the Earth Sciences; Current Practices and Outstanding Issues, (ed.) P.J. Sylvester; Mineralogical Association of Canada, Short Course 40, p. 308–311.

Guillong, M., Hametner, K., Reusser, E., Wilson, S.A., and Günther, D., 2005. Preliminary characterisation of new glass reference materials (GSA-1G, GSC-1G, GSD-1G and GSE-1G) by laser ablation-inductively coupled plasma-mass spectrometry using 193 nm, 213 nm and 266 nm wavelengths; Geostandards and Geoanalytical Research, v. 29, p. 315–331.

Guy, B.M., Beukes, N.J., and Gutzmer, J., 2010. Paleo-environmental controls of pyrite from non-conglomeratic sedimentary rocks of the Mesoarchean Witwatersrand Supergroup, South Africa; South African Journal of Geology, v. 113, p. 195–228.

Guy, B.M., Ono, S., Gutzmer, J., Lin, Y., and Beukes, N.J., 2014. Sulfur sources of sedimentary "buckshot" pyrite in the auriferous conglomerates of the Mesoarchean Witwatersrand and Ventersdorp Supergroups, Kaapvaal Craton, South Africa; Mineralium Deposita, v. 49, p. 751–775.

Hannington, M.D., Bleeker, W., and Kjarsgaard, I., 1999. Sulfide mineralogy, geochemistry, and ore genesis of the Kidd Creek deposit: Part I. North, Central, and South Orebodies; *in* The Giant Kidd Creek Volcanogenic Massive Sulfide Deposit, western Abitibi Subprovince, Canada, (ed.) M.D. Hannington and C.T. Barrie; Society of Economic Geologists, Monograph 10, p. 163–224.

Hannington, M.D., Coombs, A., van Hees, G., Duff, S., and Campos-Alvarez, N., 2012. Regional lithogeochemical study of the Kidd–Munro MEGATEM® survey areas, Timmins–Kirkland Lake, northern Ontario: Discover Abitibi Initiative; Ontario Geological Survey, Miscellaneous Release Data 291, 209 p.

Houlé, M.G., Lesher, C.M., Préfontaine, S., Ayer, J.A., Berger, B.R., Taranovic, V., Davis, P.C., and Atkinson, B. 2010. Stratigraphy and physical volcanology of komatiites and associated Ni-Cu-(PGE) mineralization in the western Abitibi greenstone belt, Timmins area, Ontario: a field trip for the 11th International Platinum Symposium; Ontario Geological Survey, Open File Report 6255, 99 p.

Hronsky, J.M.A., Groves, D.I., Loucks, R.R., and Begg, G.C., 2012. A unified model for gold mineralisation in accretionary orogens and implications for regional-scale exploration targeting methods; Mineralium Deposita, v. 47, p. 339–358.

Hu, S., Barnes, S.J., Glenn, A.M., Pagès, A., Parr, J., MacRae, C., and Binns, R., 2019. Growth history of sphalerite in a modern sea floor hydrothermal chimney revealed by electron backscattered diffraction; Economic Geology, v. 114, p. 165–176.

Jackson, S.E. and Günther, D., 2003. The nature and sources of laser induced isotopic fractionation in laser ablation-multi-collector-inductively coupled plasma-mass spectrometry; Journal of Analytical Atomic Spectrometry, v. 18, p. 205–212.

Jackson, S.E., Dubé, B., Mercier-Langevin, P., and Rhys, D., 2017. Fingerprinting ore processes in auriferous systems; *in* Targeted Geoscience Initiative – 2016 Report of Activities, (ed.) N. Rogers; Geological Survey of Canada, Open File 8199, p. 29–32.

Jeans, C.V., Turchyn, A.V., and Hu, X., 2016. Sulfur isotope patterns of iron sulfide and barite nodules in the Upper Cretaceous Chalk of England and their regional significance in the origin of coloured chalks; Acta Geologica Polonica, v. 66, p. 227–256.

Jonasson, I.R., Kingston, D.M., Watkinson, D.H., and Elliot, S.R., 1999. Role of pyrite in the formation and localization of gold mineralization at the Owl Creek mine, Timmins, Ontario; *in* The Giant Kidd Creek Volcanogenic Massive Sulfide Deposit, western Abitibi Subprovince, Canada, (ed.) M.D. Hannington and C.T. Barrie; Society of Economic Geologists, Monograph 10, p. 627–660.

Large, R.R., Bull, S.W., and Maslennikov, V.V., 2011. A carbonaceous sedimentary source rock model for Carlin-type and orogenic gold deposits; Economic Geology, v. 106, p. 331–358.

Marin-Carbonne, J., Rollion-Bard, C., Bekker, A., Rouxel, O., Agangi, A., Cavalazzi, B., Wohlgemuth-Ueberwasser, C.C., Hofmann, A., and McKeegan, K.D., 2014. Coupled Fe and S

isotope variations in pyrite nodules from Archean shale; Earth and Planetary Science Letters, v. 392, p. 67–79.

Mercier-Langevin, P., Dubé, B., Hannington, M.D., Davis, D.W., Lafrance, B., and Gosselin, G., 2007. The LaRonde Penna Au-rich volcanogenic massive sulfide deposit, Abitibi greenstone belt, Quebec: Part I. Geology and geochronology; Economic Geology, v. 102, p. 585–609.

Murowchick, J.B. and Barnes, H.L., 1987. Effects of temperature and degree of supersaturation on pyrite morphology; American Mineralogist, v. 72, p. 1241–1250.

Nishizawa M., Yamamoto, H., Ueno, Y., Tsuruoka, S., Shibuya, T., Sawaki, Y., Yamamoto, S., Kon, Y., Kitajima, K., and Komiya, T., 2010. Grain-scale iron isotopic distribution of pyrite from Precambrian shallow marine carbonate revealed by a femtosecond laser ablation multicollector ICP-MS technique: possible proxy for the redox state of ancient seawater; Geochimica et Cosmochimica Acta, v. 74, p. 2760–2778.

Phillips, G.N. and Law, J.D., 2000. Witwatersrand gold fields: geology, genesis, and exploration; *in* Gold in 2000, (ed.) S.G. Hagemann and P.E. Brown; Reviews in Economic Geology, v. 13, p. 439–500.

Pilote, J.-L., Jackson, S.E., Mercier-Langevin, P., Dubé, B., and Rhys, D., 2019. Characteristics of diagenetic and epigenetic sulphides in deformed and metamorphosed Archean carbonaceous metasedimentary rocks of the Timmins-Matheson corridor: establishing a framework for fingerprinting ore-forming processes in shear zone-hosted orogenic gold systems; *in* Targeted Geoscience Initiative: 2018 report of activities, (ed.) N. Rogers; Geological Survey of Canada, Open File 8549, p. 33–41.

Pilote, J.-L., Mercier-Langevin, P., Jackson, S.E., Dubé, B., Yang, Z., Lawley, C.J.M., Petts, D.C., Layne, G., and Piercey, S.J., 2020. Interrogating the composition and genesis of argillite-hosted pyrite nodules at the LaRonde Penna Au-rich volcanogenic massive sulphide deposit, Abitibi, Quebec: Insights into metallogenic implications; *in* Targeted Geoscience Initiative 5: Contributions to the Understanding of Canadian Gold Systems, (ed.) P. Mercier-Langevin, C.J.M. Lawley, and S. Castonguay; Geological Survey of Canada, Open File 8712, p. 75–91. doi10.4095/323666

R Development Core Team, 2019. R: A language and environment for statistical computing: R Foundation for Statistical Computing, Vienna, Austria. <https://www.R-project.org/>

Radic, A., Lacan, F., and Murray, J.W., 2011. Iron isotopes in the seawater of the equatorial Pacific Ocean: New constraints for the oceanic iron cycle; Earth and Planetary Science Letters, v. 306, p. 1–10.

Reich, M., Kesler, S.E., Utsunomiya, S., Palenik, C.S., Chryssoulis, S.L., and Ewing, R.C., 2005. Solubility of gold in arsenian pyrite; Geochimica et Cosmochimica Acta, v. 69, p. 2781–2796.

Rickard, D.T., 2012. Sulfidic sediments and sedimentary rocks: Developments in sedimentology; Amsterdam, Elsevier, 816 p.

Rouxel, O.J., Bekker, A., and Edwards, K.J., 2005. Iron isotope constraints on the Archean and Paleoproterozoic ocean redox state; Science, v. 307, p. 1088–1091.

Rouxel, O.J., Bekker, A., and Edwards, K.J., 2006. Response to comment on "Iron isotope constraints on the Archean and Paleoproterozoic ocean redox state"; Science, v. 311, p. 177.

Weyer, S. and Schwieter, J.B., 2003. High precision Fe isotope measurements with high mass resolution MC-ICPMS; International Journal of Mass Spectrometry, v. 226, p. 355–368.

Yoshiya, K., Nishizawa, M., Sawaki, Y., Ueno, Y., Komiya, T., Yamada, K., Yoshida, N., Hirata, T., Wada, H., and Maruyama, S., 2012. In situ iron isotope analyses of pyrite and organic carbon isotope ratios in the Fortescue Group: Metabolic variations of a Late Archean ecosystem; Precambrian Research, v. 212, p. 169–193.

Vein-hosted gold mineralization in the Wilding Lake area, central Newfoundland: Structural geology and vein evolution

Ian W. Honsberger[1]*, Wouter Bleeker[1], Hamish A.I. Sandeman[2], Dave T.W. Evans[3], and Sandra L. Kamo[4]

[1]Geological Survey of Canada, 601 Booth Street, Ottawa, Ontario K1A 0E8
[2]Geological Survey Division, Department of Natural Resources, Government of Newfoundland and Labrador, 50 Elizabeth Avenue, St John's, Newfoundland A1B 4J6
[3]Antler Gold Inc., 1969 Upper Water Street, Halifax, Nova Scotia B3J 3R7
[4]Jack Satterly Geochronology Laboratory, Department of Earth Sciences, University of Toronto, 22 Russell Street, Toronto, Ontario M5S 3B1
*Corresponding author's e-mail: ian.honsberger@canada.ca

ABSTRACT

Crustal-scale fault zones in central Newfoundland are being recognized as significant gold-mineralized structures. In particular, a northeast-trending structural corridor in the eastern Dunnage Zone (Exploits subzone), delineated by the Rogerson Lake Conglomerate, contains highly prospective vein-hosted gold deposits. Such mineralized vein systems, exposed near Valentine Lake (Marathon Gold Corp.) and Wilding Lake (Antler Gold Inc.), are products of progressive Paleozoic deformation and fluid-pressure cycling along crustal-scale faults that cut the Late Silurian to Early Devonian Rogerson Lake Conglomerate and underlying Neoproterozoic basement rocks. Well exposed, gold-bearing quartz-vein systems in the Wilding Lake area reveal a kinematic history that involved a main phase of reverse sinistral shearing and subsequent transient phases of horizontal extension, oblique compression, and, at least locally, components of late dextral strike-slip. High-grade gold mineralization is associated with siderite-ankerite-sericite alteration of the host rocks, structurally controlled quartz-vein emplacement, and supergene alteration of pyrite and chalcopyrite. Gold-bearing vein sets contain quartz, pyrite, chalcopyrite, tourmaline, native gold, Ag-poor electrum, bismuth-silver-gold tellurides, rutile, and secondary goethite, malachite, and acanthite. Prospective gold exploration targets in the Wilding Lake area are Late Silurian feldspar porphyry and felsic volcanic rocks overlying the Rogerson Lake Conglomerate, as well as, rheologically favourable Neoproterozoic basement granitoids that may provide a setting similar to that at Valentine Lake.

INTRODUCTION

The eastern Dunnage Zone of central Newfoundland is an area of active gold exploration because structurally controlled gold mineralization occurs predictably for more than 200 km along major northeast-trending fault structures (Fig. 1). The gold-bearing structural corridor includes the Cape Ray gold deposit in southwestern Newfoundland (Dubé and Lauzière, 1997), as well as the developing gold deposit at Valentine Lake in central Newfoundland (Lincoln et al., 2018). Numerous epigenetic gold showings and prospects along strike from Valentine Lake (*see* Evans, 1996), including the Wilding Lake gold prospect (this study), demonstrate the potential for additional structurally controlled gold deposits along trend of the Victoria Lake shear zone and in the vicinity of the Dunnage Zone – Gander Zone boundary in central Newfoundland (Fig. 1).

Structurally controlled gold mineralization in the Wilding Lake area is concentrated within quartz shear vein systems that cut Late Silurian to Early Devonian polymict conglomerate (Rogerson Lake Conglomerate) and associated Late Silurian felsic and mafic igneous rocks. Two exploration trenches that partially represent the Wilding Lake gold prospect (e.g. Honsberger et al., 2019a), the Alder and Elm zones, were mapped in detail during the summer of 2018 as part of Natural Resources Canada's Targeted Geoscience Initiative. This contribution and a supplementary Open File report (Honsberger et al., 2020a) present lithological and structural data from the Wilding Lake gold prospect to constrain the local structural geology and quartz vein evolution and provide a basis for future targeted exploration in the region. The results of this ongoing research demonstrate that the Paleozoic structural architecture of the emerging gold district in central Newfoundland bears strong similarity to world-class, orogenic Archean gold systems, such as in the Abitibi greenstone belt (e.g. Bleeker, 2015; Honsberger and Bleeker, 2018).

Honsberger, I.W., Bleeker, W., Sandeman, H.A.I., Evans, D.T.W., and Kamo, S.L., 2020. Vein-hosted gold mineralization in the Wilding Lake area, central Newfoundland: Structural geology and vein evolution; *in* Targeted Geoscience Initiative 5: Contributions to the Understanding of Canadian Gold Systems, (ed.) P. Mercier-Langevin, C.J.M. Lawley, and S. Castonguay; Geological Survey of Canada, Open File 8712, p. 179–191. https://doi.org/10.4095/326020

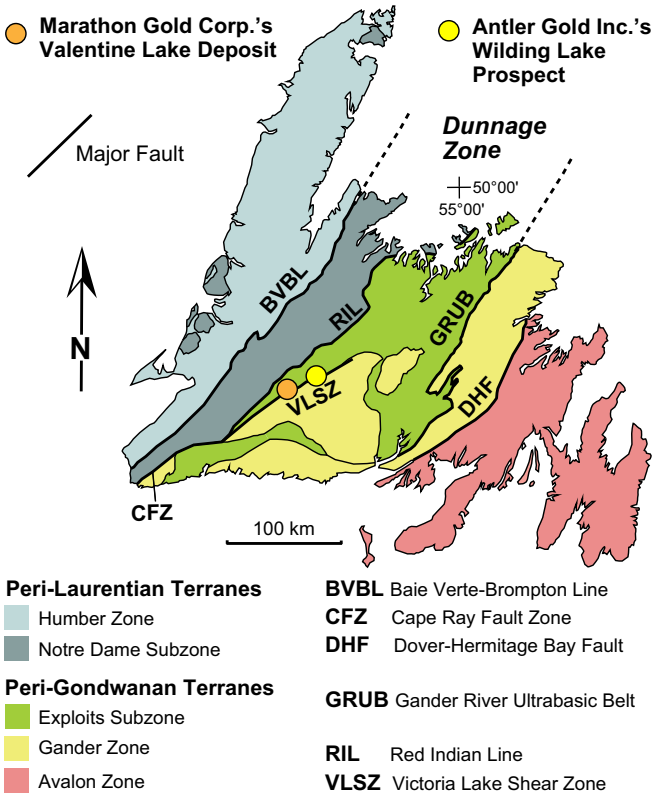

Figure 1. Generalized geological map of the Newfoundland Appalachians showing the distribution of pre-Silurian tectonostratigraphic zones and the locations of Marathon Gold Corp.'s Valentine Lake gold deposit and Antler Gold Inc.'s Wilding Lake gold prospect. Map *adapted from* Colman-Sadd et al. (1990) and Hibbard et al. (2006).

The supplementary Open File report (Honsberger et al., 2020a) that accompanies this Targeted Geoscience Initiative volume consists of two poster sheets that allow for enlargement and full viewing of the trench maps. Poster Sheet 1 of 2 presents a geological and structural overview of the Wilding Lake gold prospect and includes a detailed trench map and discussion of the smaller Alder Zone. Poster Sheet 2 of 2 presents a detailed trench map of the Elm Zone and summarizes the geological and structural features thereof. Readers are referred to the supplementary Open File report (Honsberger et al., 2020a) for a comprehensive lithological and structural synthesis of the Wilding Lake gold prospect in central Newfoundland.

GEOLOGICAL SETTING

The Island of Newfoundland (Fig. 1) occupies the northeastern portion of the northern Appalachian Orogen in Canada, which is subdivided into tectonostratigraphic zones based on geological, paleontological, and geochemical contrasts in pre-Silurian rocks (Williams, 1978). The Humber Zone underlies western Newfoundland and consists of basement and cover rocks of the early Paleozoic Laurentian margin. The Dunnage Zone spans central Newfoundland and consists of accreted peri-Laurentian (Notre Dame subzone) and peri-Gondwanan (Exploits subzone) arc terranes, juxtaposed along a major east-verging fault zone, the Red Indian Line (Williams et al., 1988). The Notre Dame subzone contains magmatic arc rocks that intruded the paleogeographically low-latitude microcontinent of Dashwoods (Waldron and van Staal, 2001). The Exploits subzone comprises Cambrian to Ordovician continental and oceanic arc- and back-arc complexes derived from Ganderia at higher latitudes on the opposite side of the Iapetus Ocean from the Dashwoods microcontinent and Laurentia (Williams et al., 1988; van Staal et al., 1998; Zagorevski et al., 2007). The Gander and Avalon zones represent peri-Gondwanan microcontinental fragments, accreted, respectively, to composite Laurentia during the Silurian to Early Devonian Salinic and Devonian Acadian orogenies (Dunning et al., 1990; van Staal and Barr, 2012; van Staal et al., 2014).

Structurally controlled, orogenic gold deposits in Newfoundland are associated with crustal-scale fault zones within, and along the boundaries of, the Dunnage Zone (Fig. 1). The major fault zones include, from west to east, Baie Verte-Brompton Line (Williams and St. Julien, 1982), Cape Ray fault zone (Dubé et al., 1996; van Staal et al., 1996), Red Indian Line (Williams et al., 1988), and Victoria Lake shear zone (Fig. 1; Valverde-Vaquero et al., 2006). The Cape Ray fault zone separates the Notre Dame subzone from the Exploits subzone in southwestern Newfoundland and, hence, correlates with the Red Indian Line farther to the northeast. The Victoria Lake shear zone is a splay of the Cape Ray/Red Indian Line fault system and separates Dunnage Zone from Gander Zone rocks in central Newfoundland (Fig. 1, 2a; Valverde-Vaquero and van Staal, 2001; Valverde-Vaquero et al., 2006). Key marker lithologies and gold exploration targets along the strike length of the Victoria Lake fault corridor are panels of Late Silurian to Early Devonian synorogenic Rogerson Lake Conglomerate and associated volcanic and plutonic rocks that nonconformably overlie and intrude faulted and imbricated basement terranes of Ganderia (e.g. Dubé et al., 1996; van Staal et al., 1996). The largest known gold deposit in Newfoundland is hosted by Neoproterozoic basement granitoid rocks at Valentine Lake (Valentine Lake pluton of the Crippleback Intrusive Suite: Evans et al., 1990; Rogers et al., 2006) that are juxtaposed against the Late Silurian to Early Devonian Rogerson Lake Conglomerate (Marathon Gold Corp., 2018).

WILDING LAKE GOLD PROSPECT

Exploration History

In 2015, prospecting along new logging roads in the Wilding Lake area (Fig. 2b) led to the discovery of vis-

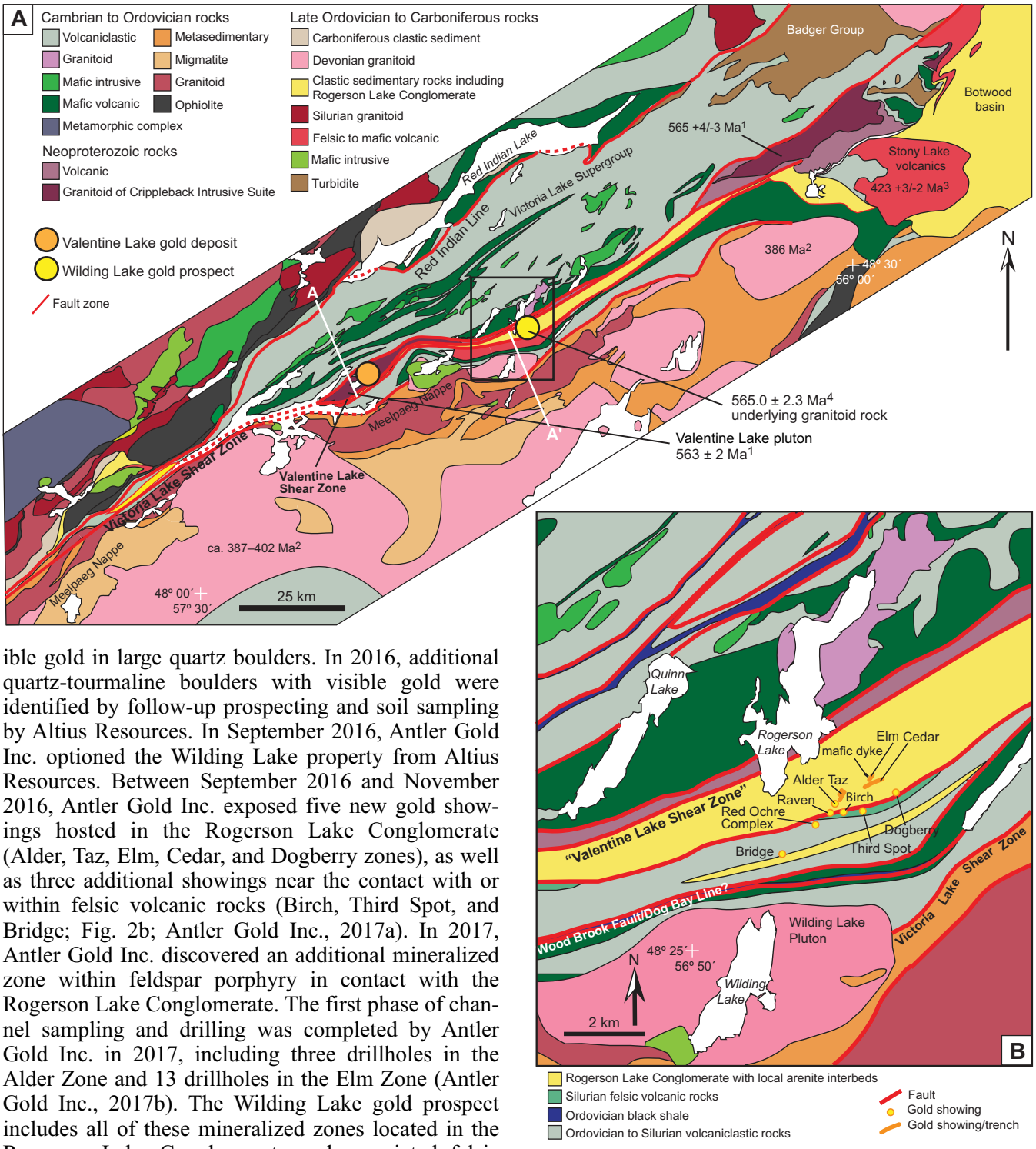

ible gold in large quartz boulders. In 2016, additional quartz-tourmaline boulders with visible gold were identified by follow-up prospecting and soil sampling by Altius Resources. In September 2016, Antler Gold Inc. optioned the Wilding Lake property from Altius Resources. Between September 2016 and November 2016, Antler Gold Inc. exposed five new gold showings hosted in the Rogerson Lake Conglomerate (Alder, Taz, Elm, Cedar, and Dogberry zones), as well as three additional showings near the contact with or within felsic volcanic rocks (Birch, Third Spot, and Bridge; Fig. 2b; Antler Gold Inc., 2017a). In 2017, Antler Gold Inc. discovered an additional mineralized zone within feldspar porphyry in contact with the Rogerson Lake Conglomerate. The first phase of channel sampling and drilling was completed by Antler Gold Inc. in 2017, including three drillholes in the Alder Zone and 13 drillholes in the Elm Zone (Antler Gold Inc., 2017b). The Wilding Lake gold prospect includes all of these mineralized zones located in the Rogerson Lake Conglomerate and associated felsic volcanic rocks.

Lithological and Structural Setting

The Wilding Lake gold prospect occurs within a gold-mineralized structural corridor that trends northeast from Cape Ray for more than 200 km across central Newfoundland and includes Marathon Gold Corp.'s Valentine Lake gold deposit (Fig. 1, 2a). The crustal-scale, regional thrust-fault architecture displays a

Figure 2. a) Generalized geological map of central Newfoundland, including the gold-mineralized Rogerson Lake Conglomerate belt (yellow sliver), correlative with rocks of the Botwood basin to the northeast. Fault zones are traced by red lines. The traces of the composite cross-section, A-A' (Fig. 3), are shown as white lines. Age data are from Evans et al. (1990)[1], Valverde-Vaquero et al. (2006)[2], Dunning et al. (1990)[3], and Honsberger et al. (2019b)[4]. **b)** Geological map of the Wilding Lake area, with locations and names of gold showings and trenches comprising Antler Gold Inc.'s Wilding Lake gold prospect. Faults are traced by red lines. Complete legend is shown in (a).

change in vergence from northwest directed to southeast directed across the Dunnage Zone (e.g. O'Brien, 2003), with economic gold mineralization preserved in the Rogerson Lake Conglomerate, felsic igneous rocks, and basement granitoids across the transition in vergence (Fig. 3). The steeply northwest-dipping "Valentine Lake shear zone" juxtaposes mineralized Neoproterozoic granitoids against panels of the Late Silurian to Early Devonian Rogerson Lake Conglomerate that occur in the overall footwall of the Victoria Lake shear zone (Fig. 3). The Victoria Lake shear zone forms the basal thrust of the Early Devonian Meelpaeg metamorphic nappe, which exhumes high-grade rocks of Ganderia and displaces them towards the northwest over lower grade rocks of the Dunnage Zone (Fig. 2, 3; Valverde-Vaquero et al., 2006). The nonconformable contact between basement granitoids and overlying Rogerson Lake Conglomerate at Valentine Lake (Fig. 3) has been referred to as the Valentine Lake thrust fault in previous publications (e.g. Lincoln et al., 2018), implying crustal-scale thrust motion along this contact. We prefer the term "Valentine Lake shear zone" (Fig. 3) because field relationships in the Valentine Lake area do not presently support major thrusting between basement granitoids and the Rogerson Lake Conglomerate (Honsberger et al., 2020b; S. Dunsworth, pers. comm., 2019).

Southeast of the Wilding Lake prospect, the Wood Brook Fault (Valverde-Vaquero et al., 2006) juxtaposes Late Silurian synorogenic sedimentary and volcanic rocks with older volcanic and volcaniclastic rocks of the eastern-most Dunnage Zone; hence, it correlates with the Dog Bay Line (Williams, 1993; Williams et al., 1993) in north-central Newfoundland (Fig. 3). The Dog Bay Line is interpreted to represent the terminal suture of the Iapetus Ocean and is considered to separate Silurian peri-Laurentian cover rocks from Silurian peri-Gondwanan cover rocks (Williams et al., 1993; Pollock et al., 2007). Farther south, the Late Silurian Wilding Lake pluton (*see* Honsberger et al., 2020b) intrudes, at depth, the contact between metasedimentary rocks and granitoids of the Gander Zone and overlying volcaniclastic rocks of the easternmost Dunnage Zone (Fig. 3). The entire panel of rocks, including the Wilding Lake pluton, is buried in the overall footwall of the Victoria Lake shear zone, the first-order structure that exhumed high-grade rocks towards the northwest following peak metamorphism in the earliest Devonian (Dunning et al., 1990; Dubé et al., 1996; Valverde-Vaquero et al., 2006). Northwest of the "Valentine Lake shear zone", metamorphosed and deformed mafic and felsic volcanic rocks (±sedimentary rocks) of the Neoproterozoic to Ordovician Victoria Lake Supergroup are imbricated along a steep, southeast-directed thrust system (Fig. 3; Rogers et al., 2005).

In the Wilding Lake area, Late Silurian to Early Devonian synorogenic sedimentary-volcanic rock sequences nonconformably overlie Neoproterozoic basement granitoids. These upper crustal sequences contain gold-mineralized Rogerson Lake Conglomerate and felsic volcanic rocks, and are spatially associated with altered mafic dykes and Late Silurian granitoid intrusions (e.g. Wilding Lake pluton, Fig. 2, 3). Primary sedimentary structures preserved within the Rogerson Lake Conglomerate sequence, including well bedded sandstone, are consistent with an overall stratigraphic younging direction towards the southeast; however, additional high-precision detrital zircon geochronology is required to determine if the contact between the Rogerson Lake Conglomerate and overlying felsic volcanic rocks is stratigraphic or tectonic (*see* "?" on Fig. 3). High-precision U-Pb chemical abrasion – thermal ionization mass spectrometry (CA-TIMS) zircon dating of tonalite from a drill core sample indicates that the underlying granitoid is 565.0 ± 2.3 Ma (Honsberger et al., 2019b), which correlates with the Neoproterozoic Crippleback Intrusive Suite at Valentine Lake (Valentine Lake pluton, 563.0 ± 2 Ma) and elsewhere in central Newfoundland (Evans et al., 1990; Rogers et al., 2006).

Structurally Controlled Vein Sets

High-grade gold mineralization of the Wilding Lake prospect is associated with at least four generations of structurally controlled vein sets that cut the Rogerson Lake Conglomerate, synorogenic volcanic and plutonic rocks, altered mafic dykes, and underlying granitoid rocks. The main quartz vein systems exposed by trenching, the Alder (Fig. 4, 5) and Elm zones (Fig. 6), are fault-fill (V_{1b}) and extensional (V_{1a}) vein systems that occur within moderately southeast-dipping reverse sinistral shear zones (Honsberger et al., 2019a). In the Elm Zone, the main fault-fill shear veins (V_{1b}) are up to two metres thick (Fig. 6a) and laminated, and accompanying southeast dipping extensional veins (V_{1a}) that emanate from the main shear veins are well exposed (Fig. 6b, 7). In the Alder Zone, the main shear vein comprises a network of discrete, thin, subparallel, interconnected quartz veins that together form a larger vein that is up to ~1 m thick (Fig. 5b). In both trenches, an early, generally east-west-striking foliation (S_1) in the Rogerson Lake Conglomerate displays sinistral kinematics, as it is rotated counter-clockwise into parallelism with the main fault-fill veins to form S_2 foliation (Fig. 4, 5a, 6a, 7). South-southwest- to south-southeast-plunging slickenlines are consistent with north-northeast- (Elm Zone) to north-directed (Alder Zone) hanging-wall motion along the main fault-fill shear veins (Fig. 5a,e,f, 7). Channel sampling reveals that gold concentrations peak across the main fault-fill

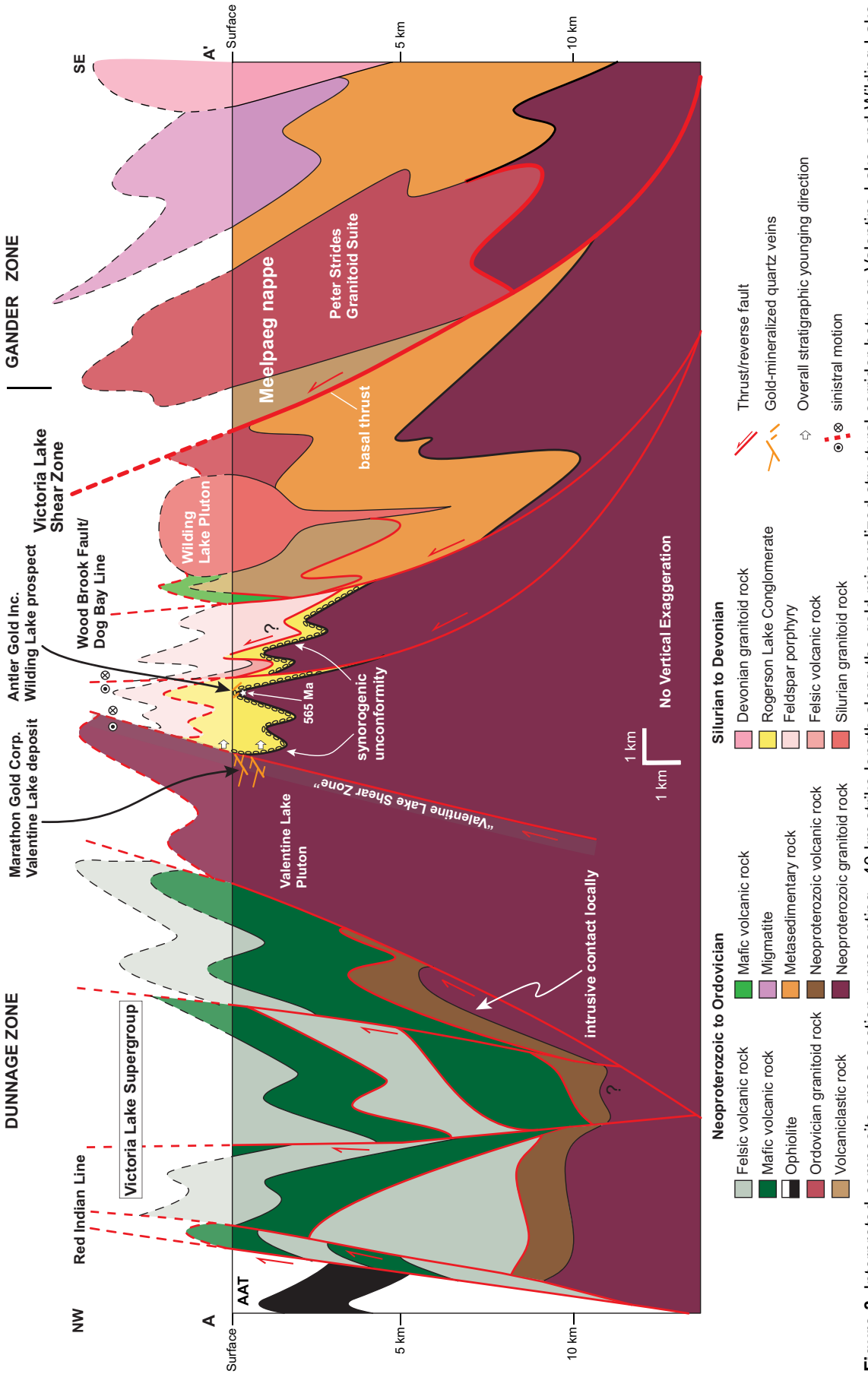

Figure 3. Interpreted composite cross-section representing ~40 km strike length along the gold-mineralized structural corridor between Valentine Lake and Wilding Lake (Fig. 2a), based on field work in the present study, the geological maps of Rogers et al. (2005), Valverde-Vaquero et al. (2005), and van Staal et al. (2005), and the geophysical-based cross-section presented in van Staal and Barr (2012). The section was drawn by "stitching" mineralized rocks of the Valentine Lake pluton with mineralized rocks of the Wilding Lake prospect along the "Valentine Lake shear zone" (thick, grey zone). Antler Gold's Inc.'s Alder and Elm zones (trenches indicated by orange lines) preserve shear vein-hosted gold mineralization in the Rogerson Lake Conglomerate. The underlying tonalite body was sampled between a depth of 296 and 290 m (white star) along a vertical drillhole. U-Pb zircon geochronology constrains the age of this body to 565 ± 2 Ma (Honsberger et al., 2019b). Gold mineralization at both Valentine Lake and Wilding Lake occurs in the overall footwall of the Victoria Lake shear zone, which is highlighted by a thicker red fault line. An overall southeast stratigraphic younging direction of the Rogerson Lake Conglomerate sequence is indicated by the white arrows. Abbreviation: AAT = Annieopsquotch Accretionary Tract

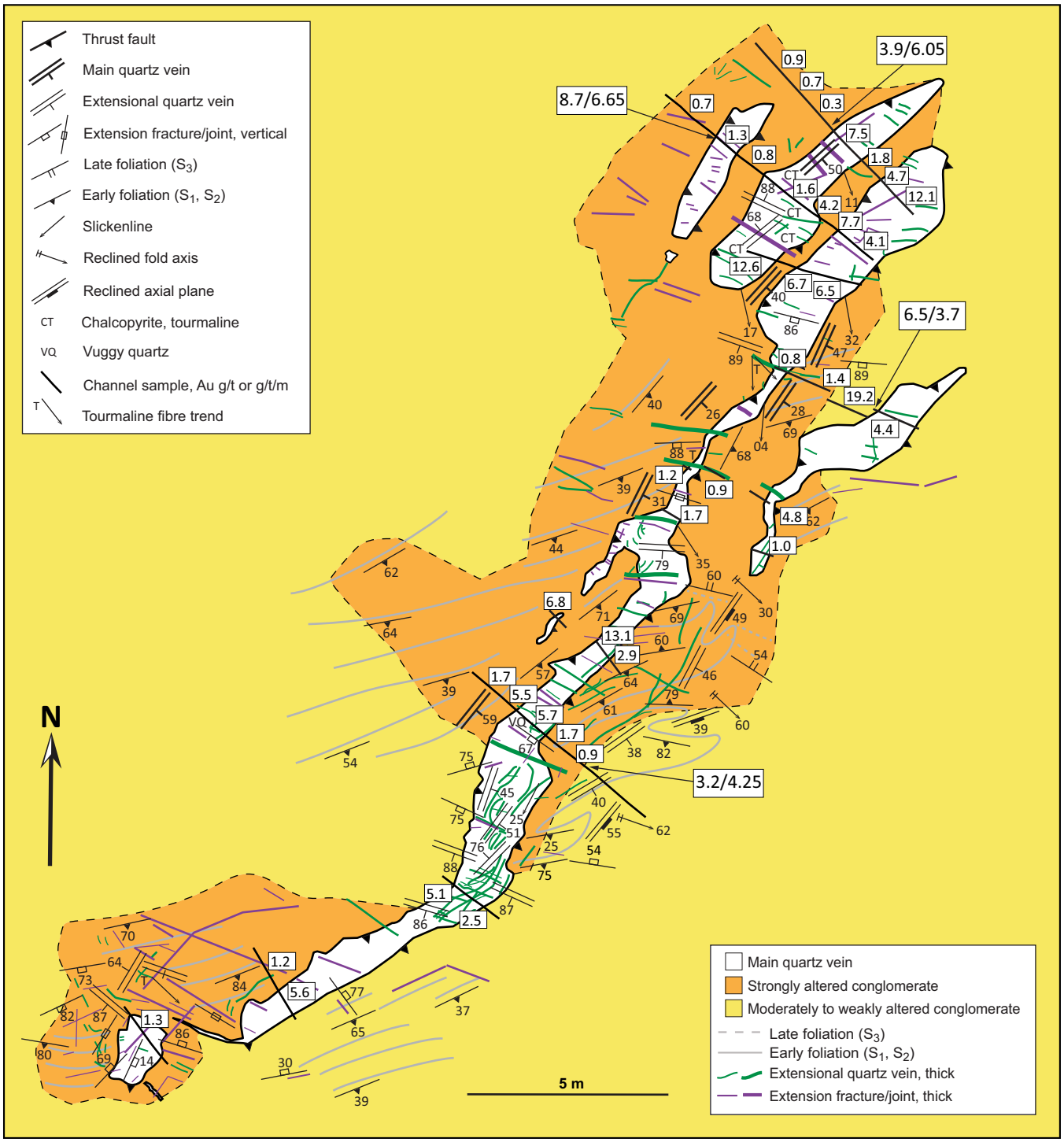

Figure 4. Detailed geological and structural map of the Alder Zone quartz shear vein system. Alteration of conglomerate host rock consists of ankerite-siderite-sericite assemblages. Gold values (grams/tonne/metre), in white rectangles, are from Antler Gold Inc.'s, press release of December 13, 2017.

veins and associated vein sets (Fig. 4), with gold values of up to 19.2 g/t over 0.9 m and 49.92 g/t over 0.98 m for the Alder and Elm zones, respectively (Antler Gold Inc., press release, Jan. 24, 2017).

The main shear vein systems (V_1) are overprinted by steep, generally east-west-striking, mineralized vein sets (V_2 and V_4) and moderately northwest-dipping vein and extension fracture/joint sets (V_3) (Fig. 5–7). In the Alder Zone, steeply south-dipping, tourmaline-bearing V_2 and V_4 vein sets are well developed across the main vein (V_{1b}) and contain less chalcopyrite than V_3 veins (Fig. 5d–f, 7). In the Elm Zone, vertical veins cutting the Rogerson Lake Conglomerate (V_2) contain tourmaline and are exceptionally rich in chalcopyrite

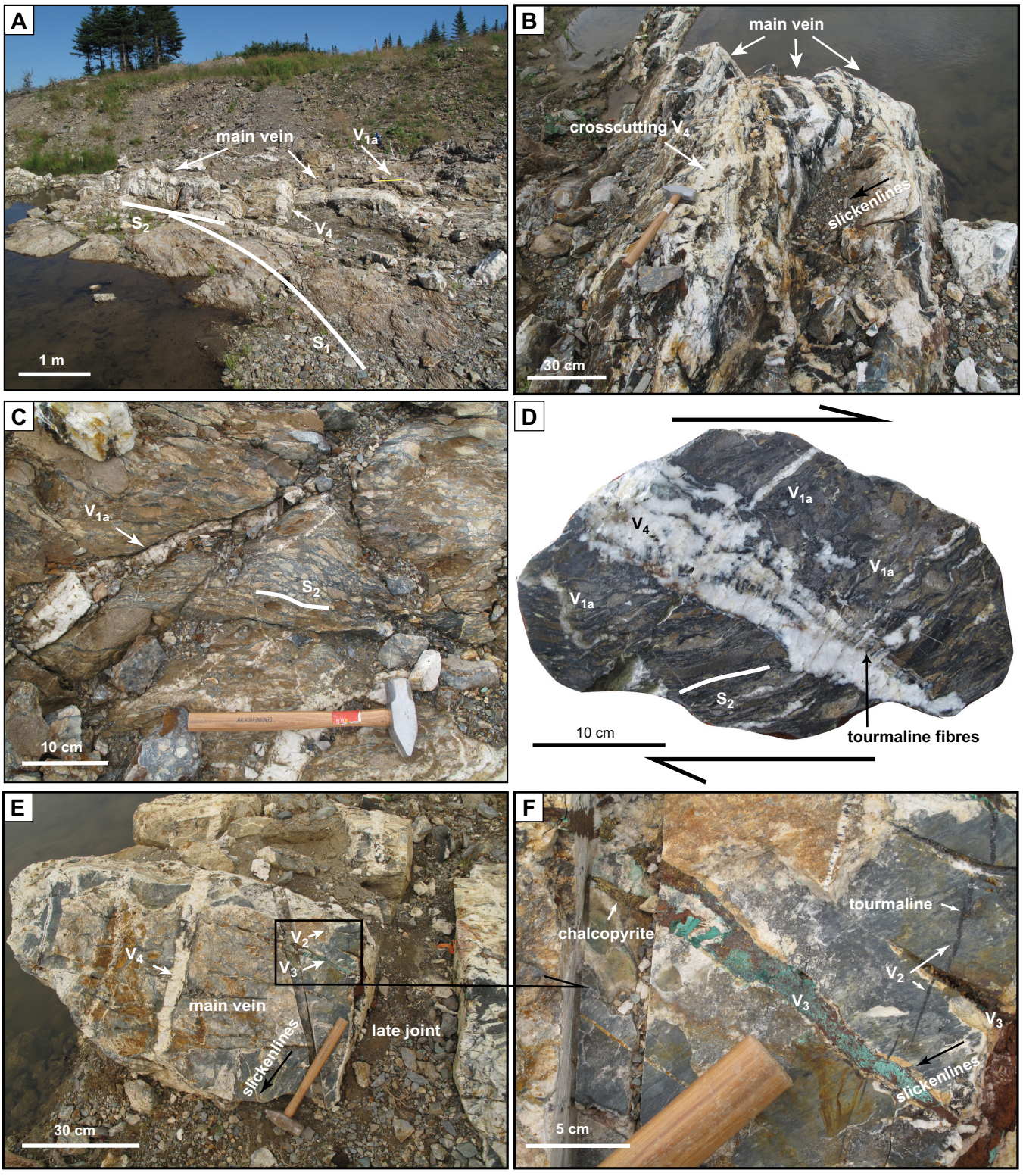

Figure 5. Field and rock photographs of the Alder Zone. *See* Table 1 for definitions of fabric elements (i.e. S_1, S_2, V_{1a}, and V_4) **a)** Main shear vein system, looking east. **b)** Network of fault-fill quartz veins ($V1_b$) comprising the main Alder Zone vein, looking southwest. **c)** Early extensional quartz vein (V_{1a}). **d)** Crosscutting quartz vein (V_4) consistent with dextral motion. **e)** Main Alder Zone vein cut by a chalcopyrite-bearing quartz vein (V_3) and a dextral quartz vein (V_4). **f)** Enlarged rectangular area outline in (e) showing tourmaline veinlets (V_2) cut by chalcopyrite-bearing quartz veins (V_3).

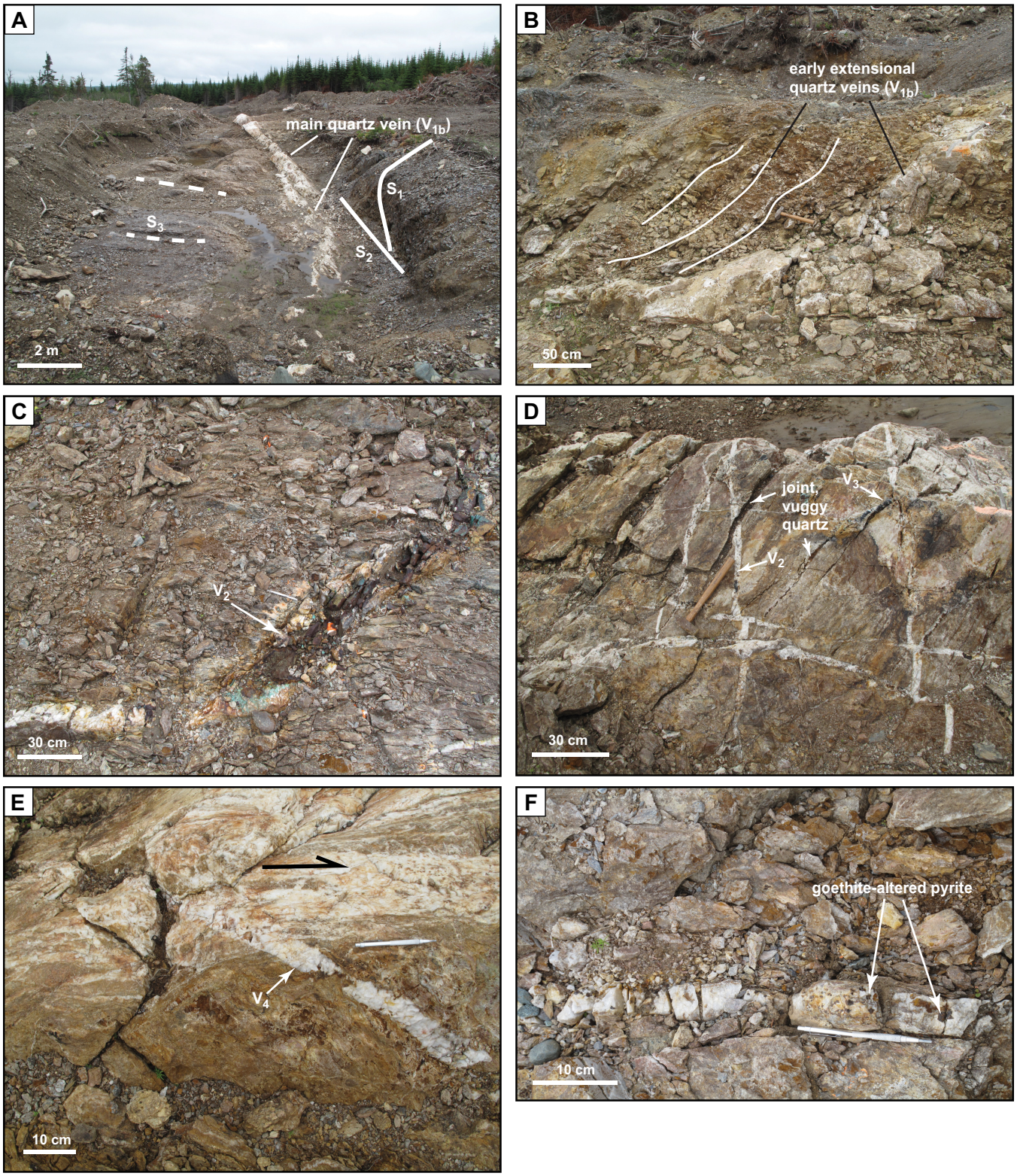

Figure 6. Field photographs from the Elm Zone. *See* Table 1 for definitions of fabric elements. **a)** Main fault-fill quartz vein (V_{1b}). **b)** Early extensional quartz veins (V_{1a}). **c)** Mineralized chalcopyrite-rich vein (V_2) cutting the Rogerson Lake conglomerate. **d)** Main vein cut by a tourmaline-bearing vein (V_2) and joints and V_3 veins filled with vuggy quartz. **e)** Late dextral quartz vein (V_4) cutting strongly altered conglomerate. **f)** Goethite after pyrite in rutile-bearing, dextral quartz vein (V_4). A preliminary U-Pb age of 407 ± 4 Ma has been obtained for rutile recovered from this vein (Honsberger et al., 2020b).

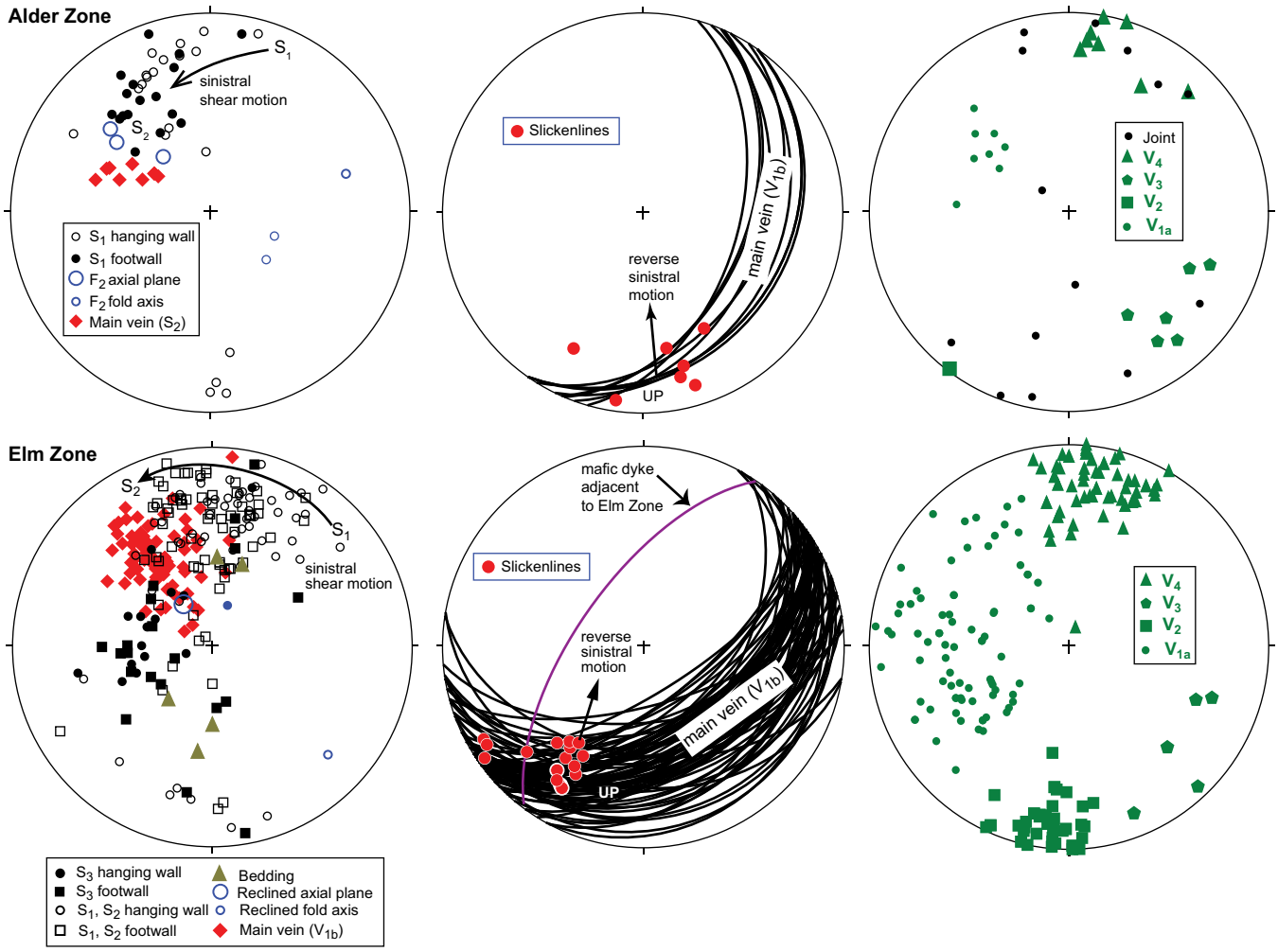

Figure 7. Lower hemisphere equal-area projections of structural elements of the Alder (top row) and Elm (bottom row) zones of the Wilding Lake gold prospect. Poles to planar features have been plotted, with the exception for great circles in the center of the diagrams. The great circles representing the main veins are the compilation of individual vein measurements along different sections of the main quartz veins (V_{1b}). *See* Table 1 for definitions of fabric elements.

Table 1. Summary of deformation phases and quartz vein evolution, Wilding Lake gold prospect, central Newfoundland.

Time	Deformation phase	Fabric element	Tectonic structure	Mechanism of formation
	D_1	S_1	East-west-striking early foliation in Rogerson Lake conglomerate	Folding of Rogerson Lake conglomerate and Ganderian basement
	D_2	S_2	Northeast-southwest-striking progressive foliation	Reverse sinistral shearing
		V_{1a}	Initial shallowly dipping extension veins	Reverse sinistral shearing
		V_{1b}	Main shear vein	Reverse sinistral shearing
	D_3	V_2	Northwest-southeast-striking vertical extension veins	Transient horizontal extension
	D_4	V_3	Southwest-northeast-striking extension veins, fracture/joints cutting main vein and mafic dyke	Oblique compression
	D_5	V_4	East-west-striking vertical extension veins	Local dextral strike-slip
↓	D_6	S_3	Shallowly dipping cleavage	Vertical compression and reclined to recumbent folding

(Fig. 6c), and coarse-grained vuggy quartz occurs with chalcopyrite in crosscutting V_3 vein and fracture sets (Fig. 6d). Adjacent to the Elm Zone, an altered mafic dyke (Fig. 2b) containing chloritoid is oriented subparallel to V_3 veins. Late, steep veins displaying dextral asymmetry (V_4) occur throughout the Alder Zone (Fig. 5d,e) and Elm Zone (Fig. 6e,f) trenches, and locally contain rutile crystals large enough for U-Pb dating (*see* Honsberger et al., 2020b). A shallowly dipping cleavage (S_3) defines the axial planes of locally developed, reclined to recumbent folds that overprint all the structures.

Structurally controlled, vein-hosted gold mineralization is associated with siderite-ankerite-sericite alteration of the Rogerson Lake Conglomerate, felsic volcanic rocks, and mafic dykes, and supergene alteration of pyrite and chalcopyrite in quartz veins. Gold-mineralized vein sets are composed of quartz, pyrite, chalcopyrite, tourmaline, native gold, Ag-poor electrum, bismuth-silver-gold-tellurides, rutile, and secondary goethite, malachite, and acanthite.

DISCUSSION

Evolution of Quartz Veins and Structures

The Wilding Lake gold prospect is characterized by at least six phases of deformation and four generations of structurally controlled quartz vein sets (Table 1). The first phase of deformation (D_1) involved regional folding and the development of an early, east-west-striking foliation (S_1) in the Rogerson Lake Conglomerate. Subsequently, progressive reverse sinistral shearing (D_2) of the Rogerson Lake Conglomerate resulted in the formation of northeast-southwest-striking S_2 foliation and crystallization of the main shear vein systems (V_{1a} and V_{1b}) exposed in the Alder and Elm zone trenches. Foliation attitudes (S_1 and S_2) of the Rogerson Lake Conglomerate exposed in the Alder and Elm zone trenches, combined with south-southwest- to south-southeast-plunging slickenlines on the main shear veins (V_{1b}), are consistent with overall north-directed motion of the hanging-wall conglomerate, with subparallel S_2 foliation and V_{1b} vein surfaces representing the main shear planes in both trenches (Fig. 8).

In this model, involving progressive shearing along a moderately dipping fault plane (Fig. 8), relatively flat-lying extensional veins (V_{1a}) form immediately prior to, and during, the formation of the main fault-fill veins (V_{1b}) (e.g. Robert and Brown, 1986). Numerous laminations in the main quartz shear vein (V_{1b}) of the Elm Zone and the composite nature of the main quartz vein (V_{1b}) of the Alder Zone (Fig. 6b) imply multiple fluid cycles and associated quartz crystallization. The fault-fill and extensional quartz vein systems of the Alder Zone (Fig. 4) and Elm Zone (*see* Honsberger et al., 2020a) trenches are consistent with a "fault-valve" model for orogenic gold mineralization, which attributes gold-bearing fluid transport and quartz vein formation to earthquake-induced fluid-pressure cycling across the brittle-ductile transition (Sibson et al., 1988).

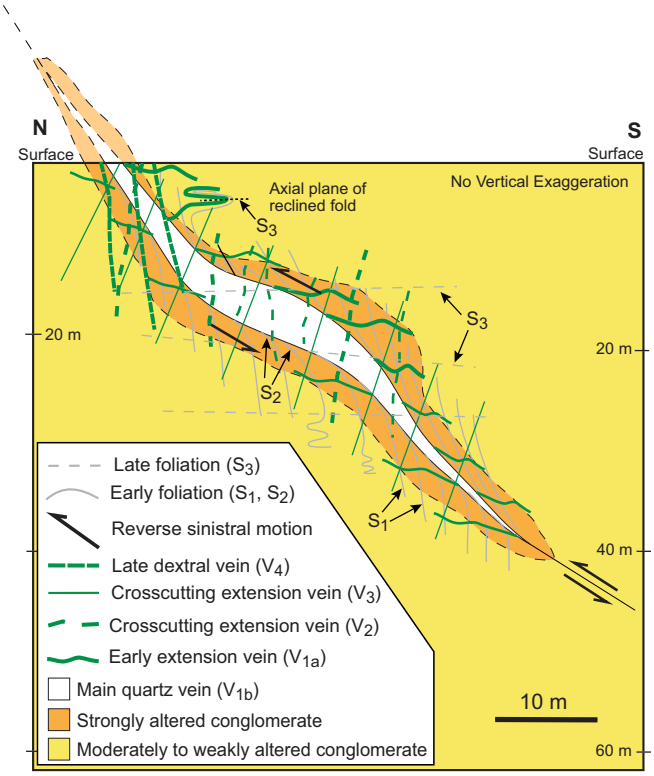

Figure 8. Synthesized, schematic cross-sectional slice through the main shear vein systems and overprinting vein sets, Wilding Lake gold prospect. The plane of the section is oriented subparallel to the overall average reverse sinistral slip vector (slickenlines) in the Alder Zone, which varies locally from south-southwest plunging to south-southeast plunging (Fig. 7). Reverse sinistral shear motion in the Elm Zone is directed towards the north-northeast.

Three distinct vein sets (V_2, V_3, and V_4), each corresponding to different phases of deformation, overprint the main vein systems (V_{1a} and V_{1b}) of the Wilding Lake gold prospect (Table 1). Steep, tourmaline- (Fig. 5e,f) and/or chalcopyrite-bearing veins (V_2, Fig. 6c) indicate transient phases of local horizontal extension (D_3), whereas younger, moderately to steeply dipping extensional veins (V_3, Fig. 5e,f, 6d) are consistent with local extension resulting from oblique compressional deformation (D_4). The attitude of an approximately 1.8 m wide, northeast-trending, altered mafic dyke that occurs northwest of the Elm Zone is subparallel to V_3 veins (Fig. 2b, 7); therefore, V_3 veins may have formed at the same time as intrusion of the mafic dyke. In both the Alder Zone and Elm Zone trenches, steeply south-dipping veins (V_4, Fig. 5d, 6e) display asymmetry that is consistent with local dextral strike-slip motion (D_5). Shallowly dipping, axial planar

cleavage (S_3), best developed in the most schistose rocks, implies a late phase of vertical compression and associated reclined to recumbent folding (D6, Table 1).

The deformation history and vein evolution of the Wilding Lake gold prospect in central Newfoundland are attributed to progressive tectonics during latest Silurian to Early Devonian orogenesis (*see* Honsberger et al., 2020b). The main phase of reverse sinistral shearing and quartz vein formation in the Alder Zone and Elm Zone trenches (D_2, Table 1) likely post-dates latest Silurian synorogenic magmatism in the eastern Dunnage Zone (*see* Honsberger et al., 2020b), as latest Silurian felsic volcanic rocks of the Wilding Lake prospect are displaced along Early Devonian thrust faults associated with exhumation of Gander Zone rocks (Valverde-Vaquero et al., 2006; Fig. 3). A preliminary U-Pb rutile age of 407 ± 4 Ma from a V_4 quartz vein in the Elm Zone trench (Fig. 6f) indicates that the last known stage of vein formation with gold mineralization in the Wilding Lake area is associated with Acadian (e.g. van Staal and Barr, 2012) orogenesis.

Implications for Exploration

The main fault-fill and extensional shear vein systems of the Alder Zone (Fig. 4) and Elm Zone (*see* Honsberger et al., 2020a) trenches may continue along trend towards the north-northeast and northeast, respectively, within the Rogerson Lake Conglomerate belt. However, additional quartz shear vein systems are likely to occur closer to the main fault planes bounding the Rogerson Lake Conglomerate belt (Fig. 2b, 3) because these were ultimately the local crustal-scale conduits for gold-bearing, silica-rich fluid flow. Accordingly, the bounding faults of the Rogerson Lake Conglomerate belt can be utilized to guide future exploration efforts farther northeast along strike, where additional gold prospects may be uncovered. Prospective gold exploration targets in the Wilding Lake area include Late Silurian feldspar porphyry and felsic volcanic and plutonic (Wilding Lake pluton) rocks overlying the Rogerson Lake Conglomerate, as well as rheologically favourable Neoproterozoic basement granitoids, which may provide a setting that is similar to that at Valentine Lake.

CONCLUSION

The Wilding Lake gold prospect in central Newfoundland preserves vein-hosted, structurally controlled gold mineralization within the Late Silurian to Early Devonian Rogerson Lake Conglomerate and associated felsic volcanic rocks. At depth, an unconformity preserved between Neoproterozoic basement granitoids of Ganderia and the overlying Rogerson Lake Conglomerate indicates Late Silurian to Early Devonian tectonism. The overall southeast younging-direction of the Rogerson Lake Conglomerate stratigraphy is consistent with truncation and tectonic burial of the upper crustal, synorogenic sequence by a northwest-verging master fault system, which ultimately controlled the formation and preservation of Late Silurian to Early Devonian orogenic gold mineralization.

The Paleozoic structural architecture and setting of the central Newfoundland gold district is remarkably similar to world-class, orogenic-style gold districts, such as the Archean Abitibi greenstone belt (e.g. Bleeker, 2015; Honsberger and Bleeker, 2018), implying that the progression of tectonic processes leading to gold mineralization and preservation in central Newfoundland was fundamentally similar to that of the Abitibi. The results of this focused study, therefore, help to unify age-independent models for structurally controlled, orogenic gold mineralization. Ongoing work involves a detailed step-by-step comparison of a number of features of the Abitibi systems, such as rates of tectonism, details of synorogenic magmatism, possible extensional processes, basin formation, basin collapse, and final thrust burial and preservation.

ACKNOWLEDGMENTS

This work is a contribution to NRCan's Targeted Geoscience Initiative (TGI) Program. Support for this study was provided through the TGI Gold Project's "Activity G-2.1: Deep faults, synorogenic clastic sequences, alkaline magmatism and gold deposits: testing and refining the Timmins-Kirkland Lake model in areas with high gold potential." Thanks to John Hinchey, Neil Rogers, and Cees van Staal for help and guidance at various times. This report has benefitted from reviews by Sébastien Castonguay and Stéphane De Souza.

REFERENCES

Antler Gold Inc., 2017a. Antler gold discovers new mineralized zones at the Wilding Lake gold project, Newfoundland; Antler Gold. <antlergold.com/files/PR_20170830_final_with_maps.pdf> [accessed December 2, 2018]

Antler Gold Inc., 2017b. Antler gold drills 10.01 grams per tonne gold over 5.35 metres at the Wilding Lake gold project, Newfoundland. <antlergold.com/files/PR_20171213_final_with_appendix_and_maps.pdf> [accessed December 2, 2018]

Bleeker, W., 2015. Synorogenic gold mineralization in granite-greenstone terranes: The deep connection between extension, major faults, synorogenic clastic basins, magmatism, thrust inversion, and long-term preservation; *in* Targeted Geoscience Initiative 4: Contributions to the Understanding of Precambrian Lode Gold Deposits and Implications for Exploration, (ed.) B. Dubé and P. Mercier-Langevin; Geological Survey of Canada, Open File 7852, p. 25–47.

Colman-Sadd, S., Hayes, J., and Knight, I., 1990. The geology of the Island of Newfoundland; map 90-01; Government of Newfoundland and Labrador, Department of Mines and

Energy, Geological Survey Branch, GS# NFLD/2192, scale: 1:1 000 000.

Dubé, B. and Lauzière, K., 1997. Gold metallogeny of the Cape Ray Fault Zone, southwest Newfoundland. Geological Survey of Canada, Bulletin 508, 100 p.

Dubé, B., Dunning, G.R., Lauzière, K., and Roddick, J.C., 1996. New insights into the Appalachian Orogen from geology and geochronology along the Cape Ray fault zone, southwest Newfoundland; Geological Society of America Bulletin, v. 108, p. 101–116.

Dunning, G.R., O'Brien, S.J., Colman-Sadd, S.P., Blackwood, R.F., Dickson, W.L., O'Neill, P.P., and Krogh, T.E., 1990. Silurian Orogeny in the Newfoundland Appalachians; Journal of Geology, v. 98, no. 6, p. 895–913.

Evans, D.T.W., 1996. Epigenetic gold occurrences, eastern and central Dunnage Zone, Newfoundland; Government of Newfoundland and Labrador, Department of Mines and Energy, Geological Survey, Mineral Resources Report 9, 135 p.

Evans, D.T.W., Kean, B.F., and Dunning, G.R., 1990. Geological studies, Victoria Lake Group, central Newfoundland; *in* Current Research, Government of Newfoundland and Labrador, Department of Mines and Energy, Geological Survey Branch, Report 90-1, p. 135–144.

Hibbard, J.P., van Staal, C.R., Rankin, D.W., and Williams, H., 2006. Lithotectonic map of the Appalachian Orogen, Canada-United States of America; Geological Survey of Canada, Map 2096A, scale 1:1 500 000.

Honsberger, I. and Bleeker, W., 2018. Orogenic comparison of structurally controlled gold systems of the Abitibi greenstone belt and central Newfoundland Appalachians: Implications for Newfoundland gold potential and recurring tectonic drivers of gold mineralization; *in* Targeted Geoscience Initiative: 2017 report of activities, volume 2, (ed.) N. Rogers; Geological Survey of Canada, Open File 8373, p. 65–70.

Honsberger, I.W., Bleeker, W., Sandeman, H.A.I., and Evans, D.T.W., 2019a. Structural geology of a gold-bearing quartz vein system, Wilding Lake region, central Newfoundland; *in* Current Research, Geological Survey of Newfoundland and Labrador. Department of Natural Resources, Geological Survey, Report 19-1, p. 23–38.

Honsberger, I.W., Bleeker, W., Kamo, S.L. Evans, D.T.W., and Sandeman, H.A.I., 2019b. A Neoproterozoic age for granodiorite underlying Rogerson Lake Conglomerate: confirmed Ganderian basement in the Wilding Lake area, central Newfoundland gold district; Government of Newfoundland and Labrador, Department of Natural Resources, Geological Survey, Open File 012A/07/1774, 12 p.

Honsberger, I.W., Bleeker, W., Sandeman, H.A.I., Evans, D.T.W., and Kamo, S.L., 2020a. The Wilding Lake gold prospect in central Newfoundland: A lithological and structural synthesis; Geological Survey of Canada, Open File 8658, 2 poster sheets.

Honsberger, I.W., Bleeker, W., Kamo, S.L., Sandeman, H.A.I., and Evans, D.T.W., 2020b. The emerging Paleozoic gold district of central Newfoundland: New insights on structural controls and tectonic drivers of gold mineralization and preservation; *in* Targeted Geoscience Initiative 5: Contributions to the Understanding of Canadian Gold Systems, (ed.) P. Mercier-Langevin, C.J.M. Lawley, and S. Castonguay; Geological Survey of Canada, Open File 8712, p. 193–210. doi:10.4095/326024

Lincoln, N., Farmer, R., Eccles, R., and Deering, P.D., 2018. Preliminary economic assessment of the Valentine Lake gold project Newfoundland, NL, Canada; Lycopodium Minerals Canada Ltd. for Marathon Gold Corp. < https://www.marathon-gold.com/site/assets/files/5047/2018-10-pea.pdf > [accessed December 2, 2018]

Marathon Gold Corp., 2018. Marathon Gold announces substantial improvements in updated PEA with 44% increase in recovered gold, at the Valentine Lake Gold Camp, Newfoundland. <https://www.marathon-gold.com/news/news-releases/2018//> [accessed December 2, 2018]

O'Brien, B.H., 2003. Geology of the central Notre Dame Bay region (parts of NTS areas 2E/3,6,11), northeastern Newfoundland; Government of Newfoundland and Labrador, Department of Mines and Energy, Geological Survey Branch, Report 03-03, 147 p.

Pollock, J.C., Wilton, D.H.C., van Staal, C.R., and Morrissey, K.D., 2007. U-Pb detrital zircon geochronological constraints on the Early Silurian collision of Ganderia and Laurentia along the Dog Bay Line: the terminal Iapetan suture in the Newfoundland Appalachians; American Journal of Science, v. 307, p. 399–433.

Robert, F. and Brown, A.C., 1986. Archean gold-bearing quartz veins at the Sigma Mine, Abitibi greenstone belt, Quebec: Part I. Geologic relations and formation of the vein system; Economic Geology, v. 81, p. 578–592.

Rogers, N., van Staal, C.R., McNicoll, V.J., Squires, G.C., Pollock, J., and Zagorevski, A., 2005. Geology, Lake Ambrose and part of Buchans, Newfoundland and Labrador; Geological Survey of Canada, Open File 4544, scale 1:50 000.

Rogers, N., van Staal, C.R., McNicoll, V.J., Pollock, J., Zagorevski, A., and Whalen, J., 2006. Neoproterozoic and Cambrian arc magmatism along the eastern margin of the Victoria Lake Supergroup: A remnant of Ganderian basement in central Newfoundland?; Precambrian Research, v. 147, p. 320–341.

Sibson, R.H., Robert, F., and Poulsen, K.H., 1988. High-angle reverse faults, fluid-pressure cycling, and mesothermal gold-quartz deposits; Geology, v. 16, p. 551–555.

Valverde-Vaquero, P. and van Staal, C.R., 2001. Relationships between the Dunnage – Gander Zones in the Victoria Lake – Peter Strides Pond Area; *in* Current Research, Newfoundland Department of Mines and Energy, Geological Survey, Report 2001-1, p. 1–9.

Valverde-Vaquero, P., van Staal, C.R., and Rogers, N., 2005. Geology, Snowshoe Pond, Newfoundland and Labrador; Geological Survey of Canada, Open File 4597, scale 1:50 000.

Valverde-Vaquero, P., van Staal, C.R., McNicoll, V., and Dunning, G.R., 2006. Mid – Late Ordovician magmatism and metamorphism along the Gander margin in central Newfoundland; Journal of the Geological Society of London, v. 163, p. 347–362.

van Staal, C.R. and Barr, S.M., 2012. Lithospheric architecture and tectonic evolution of the Canadian Appalachians and associated Atlantic margin; *in* Tectonic Styles in Canada Revisited: The LITHOPROBE Perspective, (ed.) J.A. Percival, F.A. Cook, and R.M. Clowes; Geological Association of Canada Special Paper 49, p. 41–95.

van Staal, C.R., Hall, L., Schofield, D., and Valverde, P., 1996. Geology, Port aux Basques, Newfoundland (part of NTS 11-O/11); Geological Survey of Canada, Open File 3165, scale 1: 25 000.

van Staal, C.R., Dewey, J.F., Mac Niocaill, C., and McKerrow, W.S., 1998. The Cambrian-Silurian tectonic evolution of the northern Appalachians and British Caledonides: history of a complex, west and southwest Pacific-type segment of Iapetus; *in* Lyell: The Past Is the Key to the Present, (ed.) D.J. Blundell and A.C. Scott; Geological Society of London, Special Publication 143, p. 199–242.

van Staal, C.R., Valverde-Vaquero, P., Zagorevski, A., Rogers, N., Lissenberg, C.J., and McNicoll, V.J., 2005. Geology, Victoria Lake, Newfoundland and Labrador; Geological Survey of Canada, Open File 1667, scale 1:50 000.

van Staal, C.R., Zagorevski, A., McNicoll, V.J., and Rogers, N., 2014. Time-transgressive Salinic and Acadian orogenesis, magmatism, and Old Red Sandstone sedimentation in Newfoundland; Geoscience Canada, v. 41, p. 138–164.

Waldron, J.W.F. and van Staal, C.R., 2001. Taconian orogeny and the accretion of the Dashwoods block: A peri-Laurentian microcontinent in the Iapetus Ocean; Geology, v. 29, p. 811–814.

Williams, H., 1978. Tectonic lithofacies map of the Appalachian Orogen; Memorial University of Newfoundland, St John's, Newfoundland and Labrador, scale 1:1 000 000.

Williams, H., 1993. Stratigraphy and structure of the Botwood Belt and definition of the Dog Bay Line in northeastern Newfoundland; *in* Current Research, Part D; Geological Survey of Canada, Paper 93-1D, p. 19–27.

Williams, H. and St. Julien, P., 1982. The Baie Verte-Brompton Line: Early Paleozoic continent ocean interface in the Canadian Appalachians; *in* Major structural zones and faults of the Northern Appalachians, (ed.) P. St-Julien and J. Béland; .Geological Association of Canada, Special Paper 24, p. 43–66.

Williams, H., Colman-Sadd, S.P. and Swinden, H.S., 1988. Tectonic-stratigraphic subdivisions of central Newfoundland; *in* Current Research, Part B; Geological Survey of Canada, Paper 88-1B, p. 91–98.

Williams, H., Currie, K.L., and Piasecki, M.A.J., 1993. The Dog Bay Line: a major Silurian tectonic boundary in northeast Newfoundland; Canadian Journal of Earth Sciences, v. 30, p. 2481–2494.

Zagorevski, A., van Staal, C.R., McNicoll, V., and Rogers, N., 2007. Tectonic architecture of an arc-arc collision zone, Newfoundland Appalachians; *in* Formation and Applications of the Sedimentary Record in Arc Collision Zones, (ed.) A. Draut, P.D. Clift, and D.W. Scholl; Geological Society of America, Special Paper 436, p. 1–26.

The emerging Paleozoic gold district of central Newfoundland: New insights on structural controls and tectonic drivers of gold mineralization and preservation

Ian W. Honsberger[1*], Wouter Bleeker[1], Sandra L. Kamo[2], Hamish A.I. Sandeman[3], and Dave T.W. Evans[4]

[1]Geological Survey of Canada, 601 Booth Street, Ottawa, Ontario K1A 0E8
[2]Jack Satterly Geochronology Laboratory, Department of Earth Sciences, University of Toronto, 22 Russell Street, Toronto, Ontario M5S 3B1
[3]Geological Survey Division, Department of Natural Resources, Government of Newfoundland and Labrador, 50 Elizabeth Avenue, St. John's, Newfoundland A1B 4J6
[4]Antler Gold Inc., 1969 Upper Water Street, Halifax, Nova Scotia B3J 3R7
[*]Corresponding author's e-mail: ian.honsberger@canada.ca

ABSTRACT

The formation and preservation of orogenic gold deposits are associated with a predictable set of magmatic, structural, and tectonic processes that have recurred throughout Earth's history. In world-class Archean gold districts, such as in the Superior Province of the Canadian Shield and the Yilgarn Craton of the West Australian Shield, the main gold-mineralized fault zones are characterized by early imbrication, lithospheric extension, synorogenic magmatism and sedimentation, thick-skinned re-imbrication, and late-stage strike-slip. Such an evolution results in the occurrence of gold-mineralized, upper crustal sequences of synorogenic magmatic and sedimentary rocks above terranes of granitoid rocks and/or older poly-deformed volcanic rocks. Targeted exploration for orogenic gold mineralization relies on remnant panels of synorogenic rocks (e.g. polymict conglomerate and bimodal magmatic rocks) as first-order field indicators of structurally controlled gold preservation along prospective crustal-scale fault zones.

Paleozoic crustal-scale fault zones in central Newfoundland have been known to host significant gold mineralization and recent major discoveries (e.g. Valentine Lake gold deposit) and associated exploration suggest the emergence of a new district centred on the footwall rocks of the Victoria Lake shear zone. Fieldwork, combined with structural analysis and high-precision U-Pb geochronology throughout central Newfoundland, demonstrates that the structurally controlled Paleozoic gold district is remarkably similar to the much older Archean Abitibi gold district in scale, geological setting, structural architecture, synorogenic magmatism and sedimentation, style of mineralization, tectonic evolution, and process rates. In central Newfoundland, orogenic gold occurs within footwall blocks of an overall northwest-directed fault system that juxtaposed and deformed Neoproterozoic basement granitoid rocks and Late Silurian to Early Devonian synorogenic rocks during the Acadian Orogeny. Preliminary high-precision U-Pb zircon and rutile geochronology demonstrates that the key tectonic interval driving gold mineralization and synorogenic sedimentation and magmatism, including syenogranite and monzonite intrusions, occurred between 424 and 407 Ma, approximately the same relative time interval (15–20 million years) as the Abitibi greenstone belt. The similarities between the gold systems of central Newfoundland and the Abitibi imply that a common predictable set of structural and tectonic processes throughout Earth's history, and thus independent of time, have led to the deposition and preservation of orogenic gold mineralization.

INTRODUCTION

Orogenic gold mineralization is known to occur within, and in proximity to, crustal-scale fault systems across the geological record (e.g. Poulsen et al., 1992, 2000; Groves, 1993; Hodgson, 1993; Groves et al., 1998; Goldfarb et al., 2001; Dubé and Gosselin, 2007; Percival, 2007). Similar geology and structural architecture in Archean gold systems world-wide, such as between the Abitibi greenstone belt of the Superior Province and the Yilgarn craton in West Australia, indicate a common sequence of structural and tectonic processes driving gold mineralization (e.g. Poulsen et al., 1992; Groves, 1993; Hodgson, 1993; Robert, 2001; Bleeker, 2012, 2015). The most productive gold mines in Canada have historically exploited structurally controlled Archean fault-vein systems (Hodgson, 1993),

Honsberger, I.W., Bleeker, W., Kamo, S.L., Sandeman, H.A.I., and Evans, D.T.W., 2020. The emerging Paleozoic gold distrct of central Newfoundland: New insights on structural controls and tectonic drivers of gold mineralization and preservation; *in* Targeted Geoscience Initiative 5: Contributions to the Understanding of Canadian Gold Systems, (ed.) P. Mercier-Langevin, C.J.M. Lawley, and S. Castonguay; Geological Survey of Canada, Open File 8712, p. 193–210. https://doi.org/10.4095/326024

where thin panels of upper crustal, synorogenic sequences of sedimentary and magmatic rocks overlie deformed and faulted basement terranes along major fault zones that structurally control mineralization. These remnant synorogenic sequences are crucial to understanding the dynamics and overall evolution of crustal-scale fault corridors and associated gold systems because they record the active phase of tectonics driving orogenic gold mineralization.

In the well studied, world-class Abitibi gold district (e.g. Robert and Brown, 1986a,b; Poulsen et al., 1992; Dubé and Gosselin, 2007), the key phase of gold-producing tectonics is characterized by a dynamic chain of processes (Bleeker, 2015): early thin-skinned fold-thrust belt development and imbrication of older volcanic rocks; uplift and erosion of the imbricated fold-thrust belt and development of synorogenic unconformity on this older basement; initiation of a master fault system during transient lithospheric extension; a flare-up in mantle-derived alkaline magmatism; an associated thermal pulse in lower crust; synorogenic sedimentation and volcanism; reactivation of faults as thick-skinned thrusts; development of gold-bearing vein sets; tectonic burial and preservation of mineralized rocks in footwall blocks; and late-stage degeneration to strike-slip deformation. To evaluate the applicability of process-oriented Archean models to younger orogenic gold districts, we are testing if an Abitibi prototype is valid in the emerging structurally controlled Paleozoic gold district of central Newfoundland, where panels of synorogenic magmatic and sedimentary (Rogerson Lake Conglomerate) rocks are preserved along the crustal-scale faults.

As the central Newfoundland gold district is still in the relatively early stages of exploration, the crustal-scale structural architecture and magmatic history of the prospective master fault system requires further study. The research herein integrates fieldwork throughout central Newfoundland with regional cross-sections, and new high-precision U-Pb geochronology to define and illustrate the lithological and structural setting of Paleozoic orogenic gold mineralization, the polarity of the master fault system, the magmatic and tectonic evolution, and key similarities with world-class Archean gold districts, such as those of the Abitibi greenstone belt.

GEOLOGICAL SETTING

The Island of Newfoundland in the northeastern Canadian Appalachians represents a Paleozoic accretionary system that formed along the ancient continental margin of Laurentia (Bird and Dewey, 1970; Williams, 1978; van Staal et al., 1998; van Staal and Barr, 2012). The geology of Newfoundland is subdivided into four broad tectonostratigraphic zones based on contrasting fossil assemblages, stratigraphy, structure, and geochemistry in pre-Silurian rocks (Fig. 1; Williams, 1978). The Humber Zone in western Newfoundland comprises rocks of the Laurentian margin, including strongly deformed metasedimentary rocks of the Taconic hinterland (Internal Humber Zone) and allochthonous, low-grade rocks transported towards the foreland (External Humber Zone). The core of the island spans the Dunnage Zone, historically referred to as the Central Mobile Belt (Williams, 1964), which includes peri-Laurentian (Notre Dame Subzone, Dashwoods) and peri-Gondwanan (Exploits Subzone) arc and back-arc complexes that were accreted to the Laurentian margin during Early Paleozoic orogenesis. The boundary between the Notre Dame and Exploits subzones, the Red Indian Line (Williams et al., 1988), is an overall southeast-directed, steep fault system that defines the fundamental suture between peri-Laurentian terranes in the west and peri-Gondwanan terranes in the east. The Red Indian Line suture zone was active in the Middle Ordovician as it buried volcanic and sedimentary cover rocks of Ganderia, along with allochthonous basement granitoid rocks, in its footwall (Zagorevski et al., 2007). Farther east, sedimentary and granitoid rocks of the main Ganderian and Avalonian microcontinents define the Gander and Avalon Zones (Fig. 1), respectively, which were accreted sequentially to composite Laurentia during the Silurian Salinic Orogeny and Devonian Acadian Orogeny.

The pre-Silurian tectonostratigraphy of the Dunnage Zone is conformable with overlying Middle Ordovician black shale and Late Ordovician to Early Silurian turbidite of the Badger Group (Fig. 2a). Unconformably above the Badger Group are Silurian synorogenic magmatic and terrestrial sedimentary rocks of the Topsails Suite (*see* Whalen et al., 2006; van Staal et al., 2014) in the Notre Dame Subzone, and Late Silurian to Early Devonian synorogenic magmatic and sedimentary rocks of the Rogerson Lake Conglomerate sequence and Botwood Group (Fig. 2; Williams, 1962; Colman-Sadd et al., 1990) in the Exploits Subzone. In north-central Newfoundland, the Botwood Group (Williams, 1962) is composed of a lower bimodal volcanic section (Lawrenceton Formation) and an upper section of interbedded green, grey, and red sandstones (Wigwam Formation), whereas farther southwest along strike it is dominated by panels of synorogenic polymict conglomerate (Rogerson Lake Conglomerate; Kean and Jayasinghe, 1980), felsic volcanic rocks, and mafic dykes (Fig. 2). The youngest rocks preserved in Newfoundland are Carboniferous clastic sedimentary rocks that occur along steep zones of late-stage strike-slip that overprint major faults (Colman-Sadd et al., 1990).

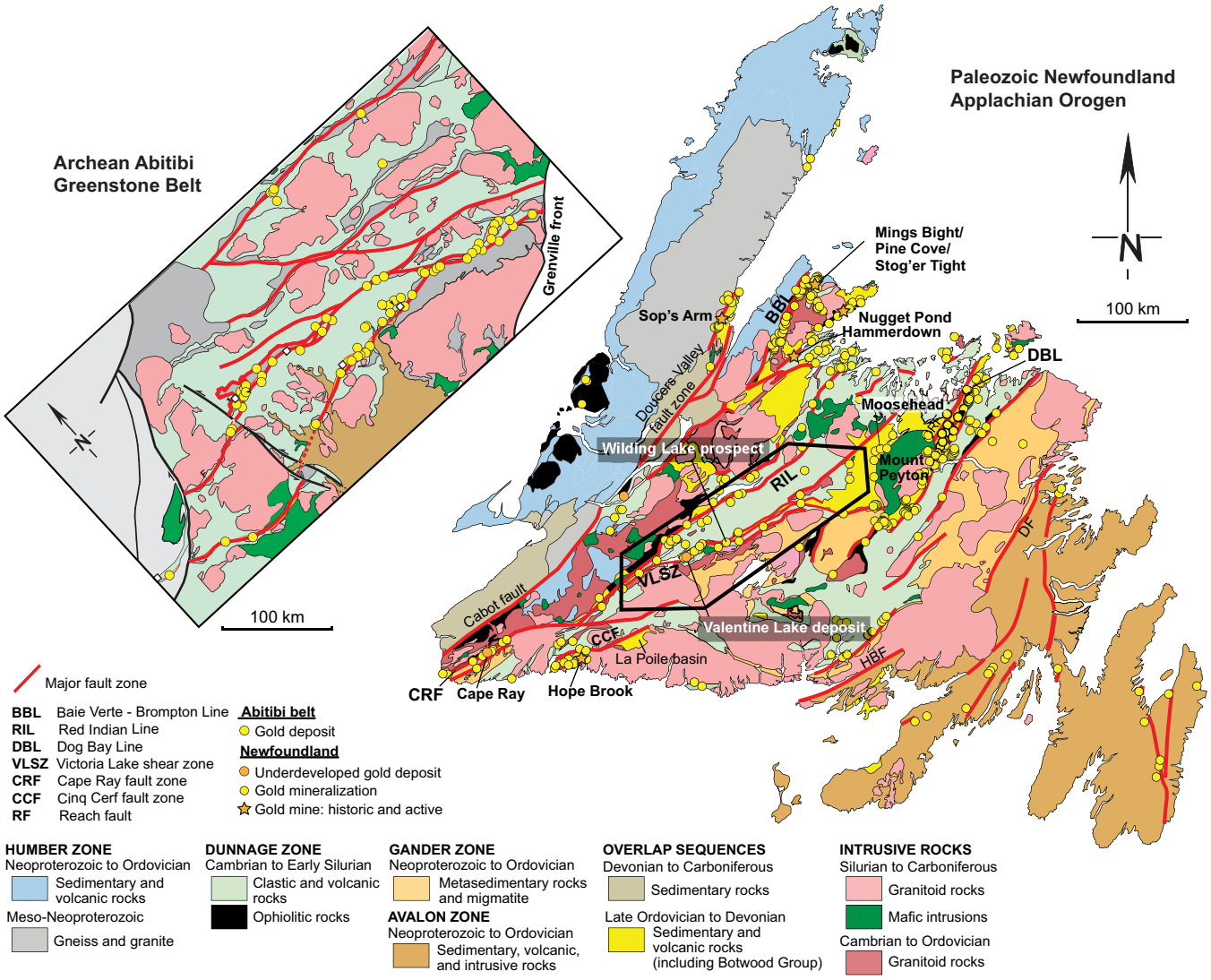

Figure 1. Comparison of the geology and gold-mineralized fault systems of the Archean Abitibi greenstone belt (left) and Paleozoic Newfoundland Appalachians (right), at the same scale. Map of the Abitibi *modified from* Poulsen et al. (2000), Dubé and Gosselin (2007), and Bleeker (2015). Newfoundland map was *adapted from* Colman-Sadd et al. (1990), with gold occurrences *compiled from* Evans (1996), O'Driscoll and Wilton (2005), Wardle (2005), and Sandeman et al. (2017).

GOLD-MINERALIZED FAULT ZONES, CENTRAL NEWFOUNDLAND

Late Silurian to Early Devonian panels of synorogenic, upper-crustal sequences overlying the Dunnage Zone and easternmost Humber Zone in central Newfoundland outline gold-mineralized, crustal-scale fault systems that are comparable in scale to the well endowed fault systems of the Archean Abitibi greenstone belt (Fig. 1; Honsberger and Bleeker, 2018). From west to east across central Newfoundland, the major northeast-trending, Paleozoic fault zones associated with orogenic gold mineralization include Doucers Valley fault zone (Smyth and Schillereff, 1982), Baie Verte – Brompton Line (Williams, 1978), Cape Ray fault zone (Dubé et al., 1996), and the Victoria Lake shear zone (Valverde-Vaquero and van Staal, 2001; Valverde-Vaquero et al., 2006). Table 1 summarizes the key attributes of these gold-mineralized fault zones, including notable gold showings/deposits, tonnages, and timing of synorogenic magmatism and gold mineralization. Although the Hope Brook gold mine is a Neoproterozoic high-sulphidation epithermal gold deposit (Dubé et al., 1995), it is included in Table 1 because it is was the first and most productive gold mine in Newfoundland and is associated with a crustal-scale fault system (Cinq Cerf fault zone) that preserves Silurian synorogenic sedimentary and volcanic rocks (Fig. 1; O'Brien et al., 1993; Dubé et al., 1995).

The focus of this study is the northeast-trending, gold-mineralized fault corridor that extends for more than 200 km between Cape Ray in southwestern Newfoundland and Mount Peyton in north-central Newfoundland, and includes the Cape Ray fault zone

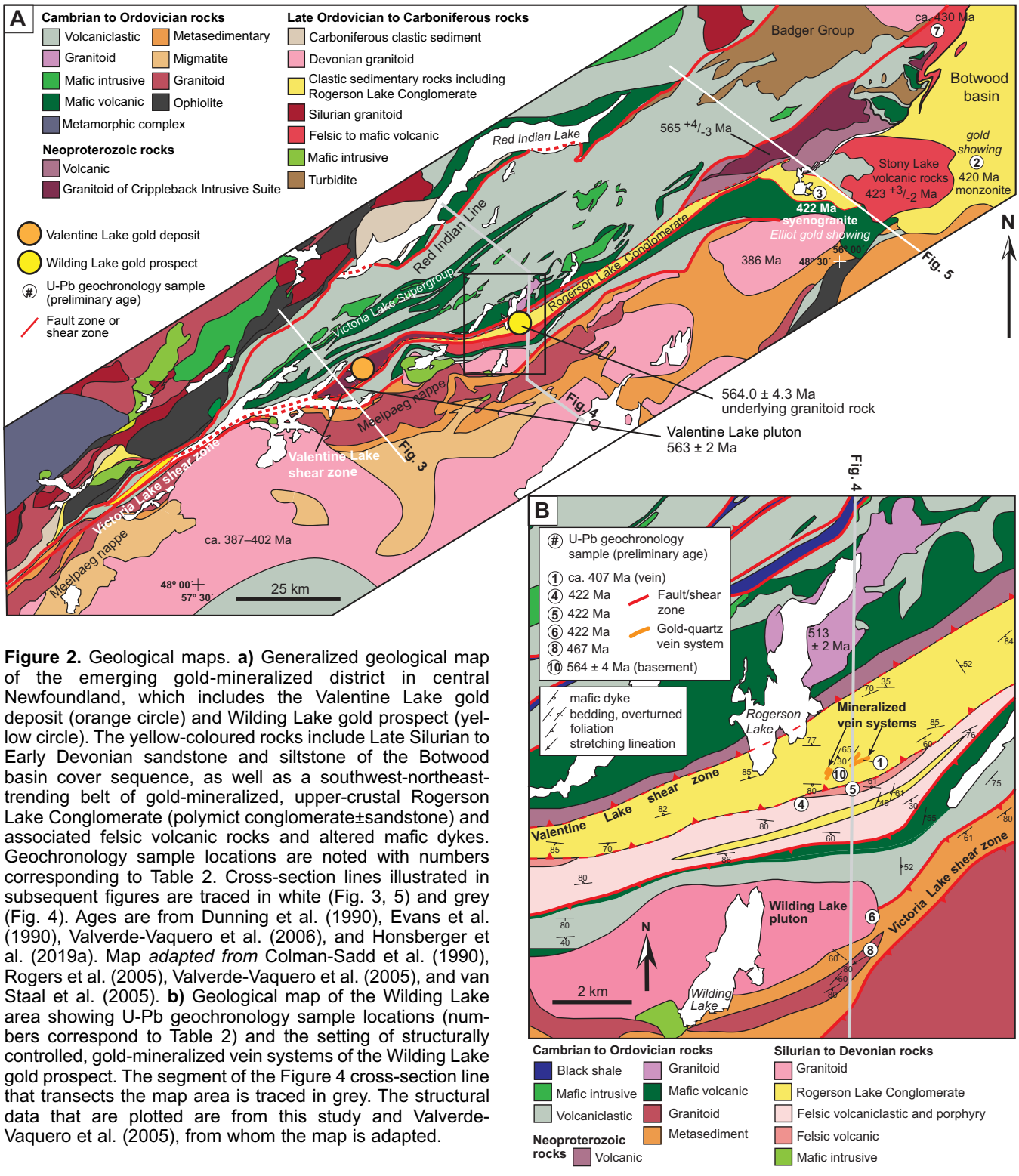

Figure 2. Geological maps. **a)** Generalized geological map of the emerging gold-mineralized district in central Newfoundland, which includes the Valentine Lake gold deposit (orange circle) and Wilding Lake gold prospect (yellow circle). The yellow-coloured rocks include Late Silurian to Early Devonian sandstone and siltstone of the Botwood basin cover sequence, as well as a southwest-northeast-trending belt of gold-mineralized, upper-crustal Rogerson Lake Conglomerate (polymict conglomerate±sandstone) and associated felsic volcanic rocks and altered mafic dykes. Geochronology sample locations are noted with numbers corresponding to Table 2. Cross-section lines illustrated in subsequent figures are traced in white (Fig. 3, 5) and grey (Fig. 4). Ages are from Dunning et al. (1990), Evans et al. (1990), Valverde-Vaquero et al. (2006), and Honsberger et al. (2019a). Map *adapted from* Colman-Sadd et al. (1990), Rogers et al. (2005), Valverde-Vaquero et al. (2005), and van Staal et al. (2005). **b)** Geological map of the Wilding Lake area showing U-Pb geochronology sample locations (numbers correspond to Table 2) and the setting of structurally controlled, gold-mineralized vein systems of the Wilding Lake gold prospect. The segment of the Figure 4 cross-section line that transects the map area is traced in grey. The structural data that are plotted are from this study and Valverde-Vaquero et al. (2005), from whom the map is adapted.

and Victoria Lake shear zone (Fig. 1). The Cape Ray fault zone is a steeply eastward-dipping, oblique reverse high-strain zone that is approximately 100 km long and several metres wide (Dubé and Lauzière, 1996, 1997; Dubé et al., 1996) and correlates with the Red Indian Line to the northeast (*see* Valverde-Vaquero et al., 2006). The Cape Ray fault zone is delineated by a panel of Ordovician bimodal volcanic rocks and gold-mineralized clastic sedimentary rocks of the Windsor Point Group, including mylonitized polymict conglomerate, greywacke, and siltstone (Dubé and Lauzière, 1996, 1997; Dubé et al., 1996). The northeastern extension of the Cape Ray fault zone splays into two major

Table 1. Summary of major gold-mineralized fault zones, central Newfoundland[1].

Terrane	Fault zone	Silurian synorogenic sequence	Notable gold showing/ deposit/mine	Historic/active (years in operation)	Gold resource estimate	Age of synorogenic magmatism (Ma)	Method	Age of gold mineralization (Ma)	Method	References
Humber Zone	Doucers Valley fault zone	Sop's Arm Group	Browning Mine	Historic (1903–1906)	150 oz	434.3 ± 1.1	U-Pb, zircon	374 ± 1	^{40}Ar-^{39}Ar, muscovite	Kerr (2006); Sandeman and Dunning (2016)
Dunnage Zone Notre Dame Subzone	Baie Verte Line	Topsails Suite	Ming's Bight, Goldenville Mine, first gold discovery in Newfoundland Pine Cove/ Stog'er Tight/Nugget Pond	Historic and active (1870s–present)	863,500 t at 2.07 g/t (indicated, Pine Cove)	ca. 433–425	U-Pb, zircon	420 ± 5 (Stog'er Tight); 375 ± 8 (Nugget Pond)	U-Pb, zircon; xenotime	Poulsen et al. (2000); Ramezani (2000); Sangster et al. (2007); van Staal et al. (2014)
Dunnage Zone Notre Dame/ Exploits Subzone	Cape Ray fault zone	Windsor Point Group[2]	Cape Ray deposit, under-developed	Active (1976–present)	450,000 t at 10.1 g/t (mineable reserve)	468.0 ± 1; 453 +5/-4	U-Pb, zircon	ca. 407–384	crosscutting relationships	This study; Dubé and Lauziere (1996, 1997) Dubé et al. (1996)
Dunnage Zone Exploits Subzone	Victoria Lake shear zone	Botwood Group Rogerson Lake Conglomerate	Valentine Lake deposit; Wilding Lake prospect	Active (1960s–present)	54.86 Mt at 1.75 g/t (measured and indicated)	424–418; 422 in Rogerson Lake Conglomerate corridor	U-Pb, zircon	407 ± 1.1	U-Pb, rutile	This study; Dunning et al. (1990); McNicoll et al. (2006); Sandeman et al. (2017)
Gander Zone	Cinq Cerf fault zone	La Poile Group	Hope Brook deposit[3]	Historic (1984–1997)	11.2 Mt at 4.54 g/t (indicated)	429 ± 2 to 418 +2/-1.5	U-Pb, zircon	578–574[3]	crosscutting relationships	Dubé et al. (1995); O'Brien (1989); O'Brien et al. (1993)

Notes: [1]Listed in order from northwest to southeast. [2]Ordovician synorogenic sequence. [3]High-sulphidation epithermal gold deposit.

fault zones, the Red Indian Line in the west and the Victoria Lake shear zone in the east (Fig. 1).

Structural Cross-Sections

For more than 200 km along strike, the gold-mineralized, crustal-scale fault corridor in central Newfoundland is delineated by deformed panels of polymict conglomerate—a distinctive synorogenic unit known as the Rogerson Lake Conglomerate—and magmatic rocks that non-conformably overlie Pan-African basement granitoid rocks (Valverde-Vaquero et al., 2005). To further understand the structural architecture of this prospective gold belt, field data from the Rogerson Lake Conglomerate corridor was utilized to construct regional cross-sections over an approximately 100 km tract between Valentine Lake in the southwest and the Botwood Group (basin) in the northeast (Fig. 3–5). Figure 4 is a detailed structural cross-section that transects the Wilding Lake gold prospect in the central part of the district, whereas figures 3 and 5 are more generalized geological cross-sections from the areas of the Valentine Lake gold deposit in the southwest and the Elliot gold showing in the northeast, respectively. The overarching master fault system controlling orogenic gold mineralization is interpreted to be a southeast-dipping, northwest-directed, listric fault zone that correlates with the Victoria Lake shear zone and splays thereof (Fig. 3–5).

The Neoproterozoic Valentine Lake pluton (Fig. 2a; Evans et al., 1990; trondhjemite, tonalite, gabbro, and mafic dykes), which hosts the Valentine Lake gold deposit (total measured and indicated resources of 54.86 million tonnes at 1.75 grams/tonne gold: Marathon Gold Corp., 2020), is juxtaposed against Late Silurian to Early Devonian Rogerson Lake Conglomerate in the overall structural footwall of the Victoria Lake shear zone (Fig. 2, 3). The northwest-directed Victoria Lake shear zone accommodated Early Devonian emplacement of the Meelpaeg nappe, composed dominantly of high-grade Cambrian to Ordovician metamorphosed sedimentary and granitoid rocks of the Gander Zone, including migmatite and the ca. 467 Ma Peter Strides granitoid suite (Fig. 3–5; Valverde-Vaquero et al., 2006). The structure separating Rogerson Lake Conglomerate from basement granitoid rocks is a steeply northwest-dipping, second-order reverse sinistral shear splay known as the Valentine Lake shear zone (Fig. 2–3; Lincoln et al., 2018). Structurally controlled, gold-bearing quartz-tourmaline-pyrite (QTP) vein systems along the Valentine Lake shear zone have been compared to orogenic quartz-carbonate-tourmaline veins at the Val-d'Or mining camp of the Abitibi greenstone belt (Dunsworth and Walford, 2018; Lincoln et al., 2018).

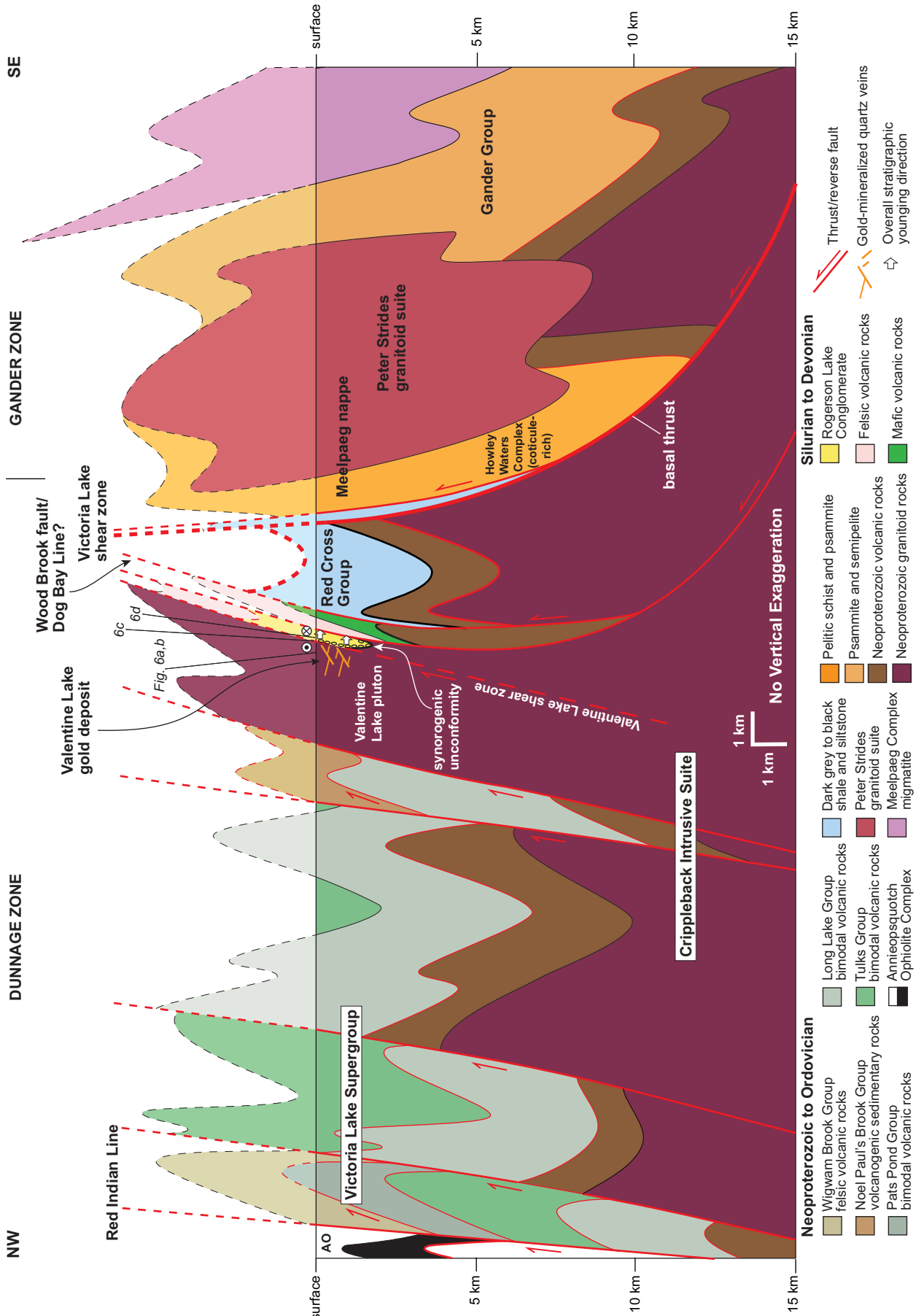

Figure 3. Generalized geological cross-section transecting the Valentine Lake gold deposit. The locations of the field photographs that are shown in Figure 6 are noted. A panel of synorogenic Rogerson Lake Conglomerate is coloured yellow.

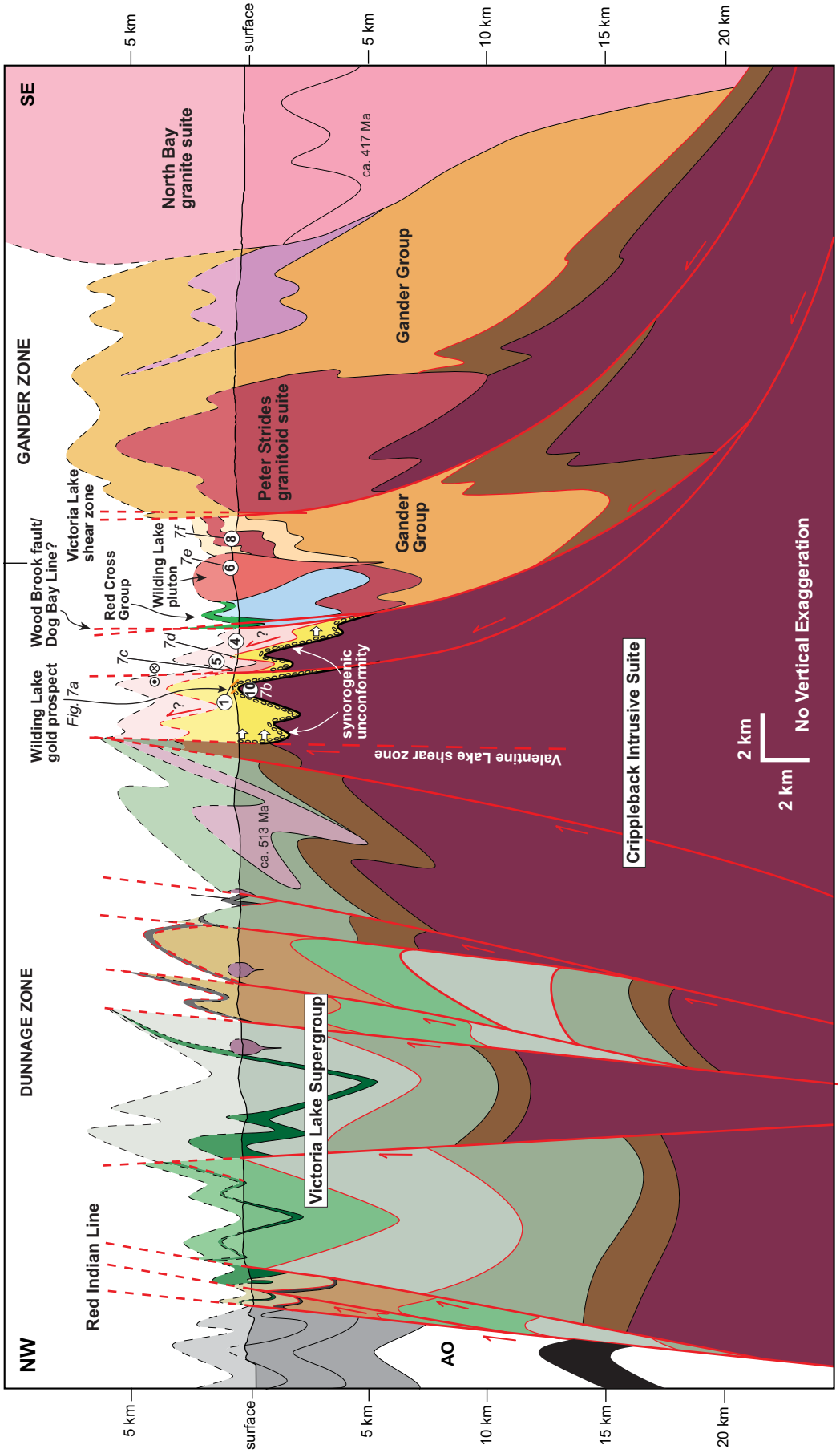

Figure 4. Detailed structural cross-section transecting the Wilding Lake gold prospect, with Rogerson Lake Conglomerate in yellow. The locations of the field and sample photographs that are shown in Figure 7 are noted. Ages are from Evans et al. (1990) and Valverde-Vaquero et al. (2005).

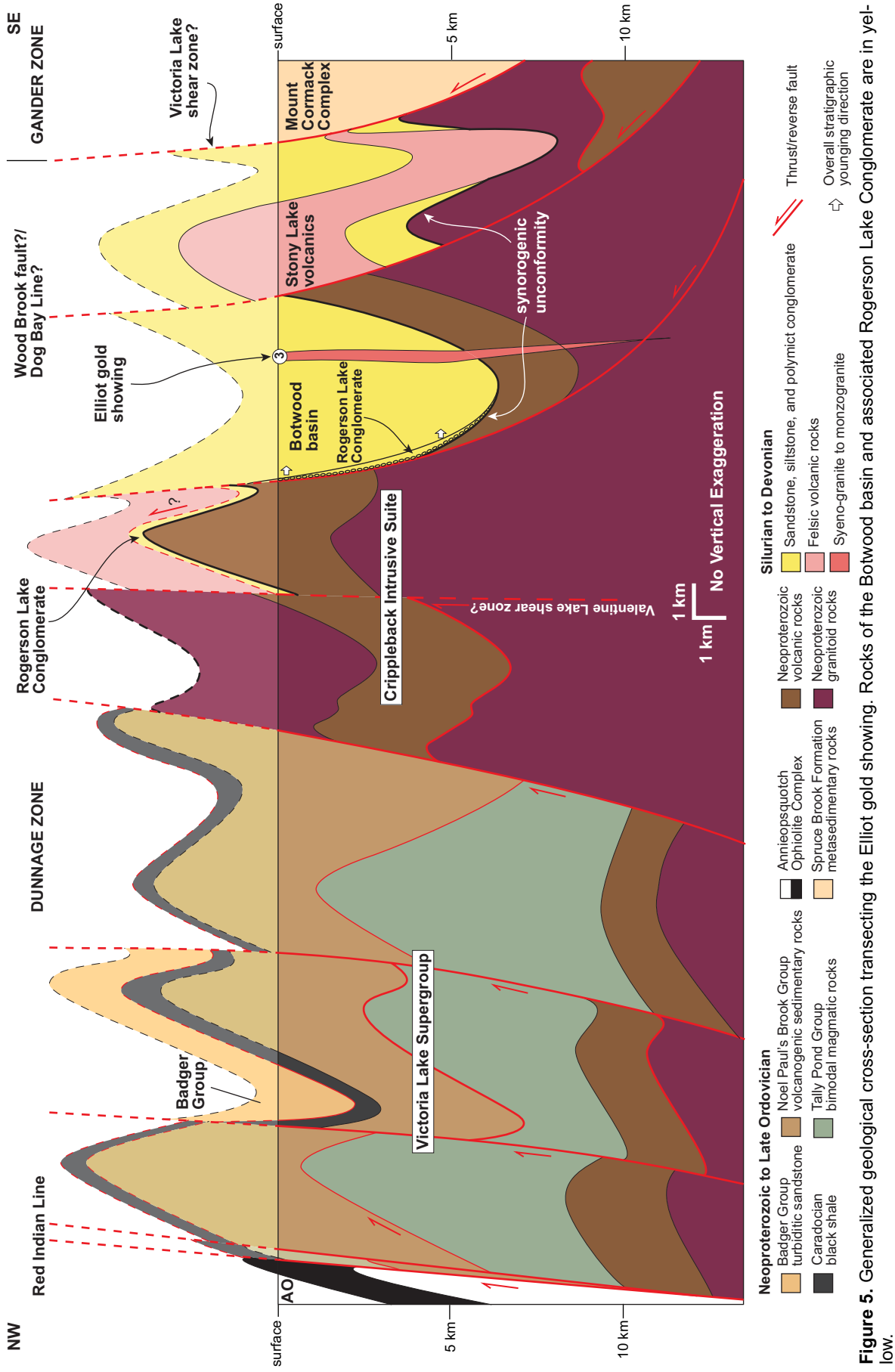

Figure 5. Generalized geological cross-section transecting the Elliot gold showing. Rocks of the Botwood basin and associated Rogerson Lake Conglomerate are in yellow.

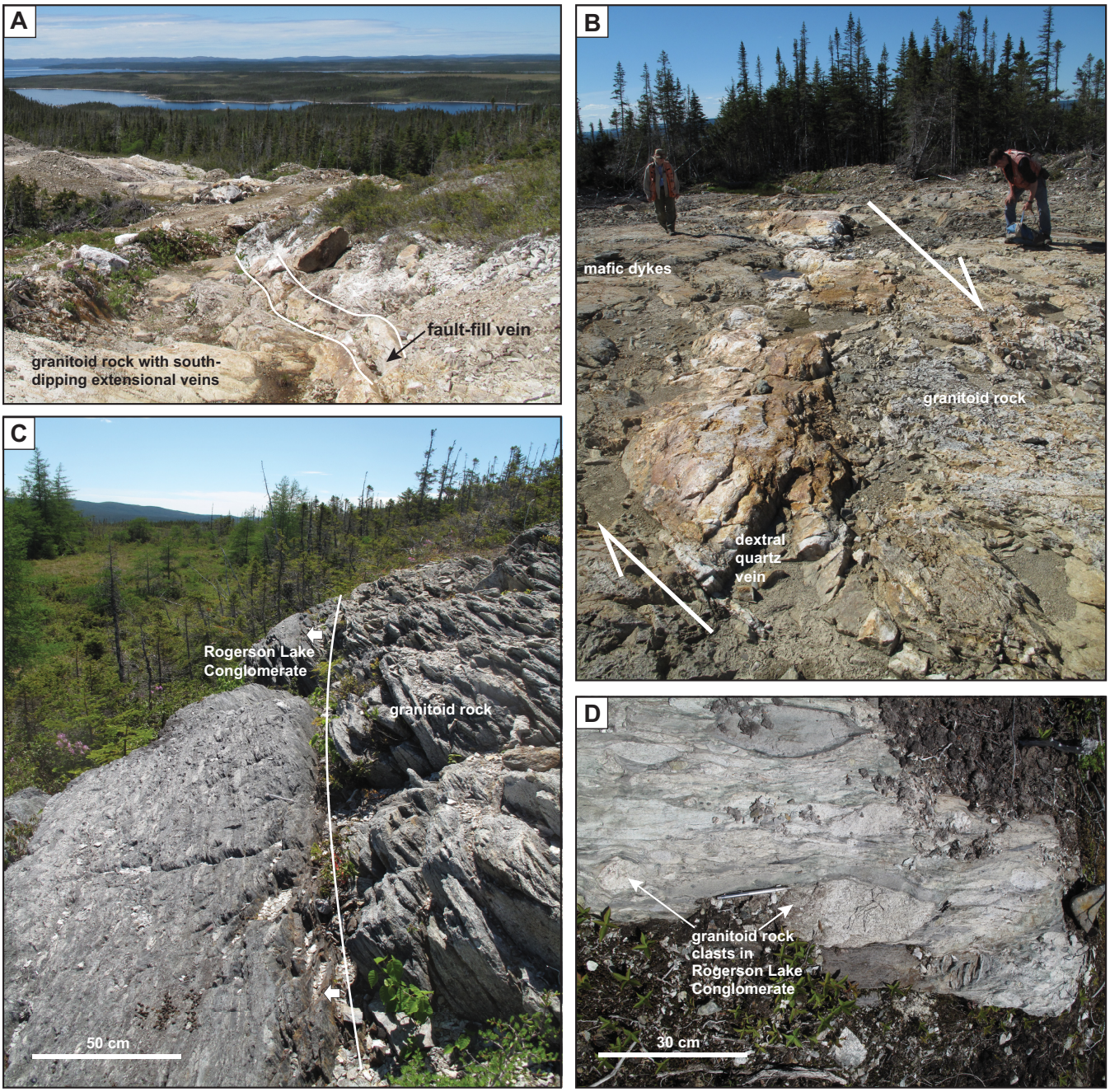

Figure 6. Field photographs from the Valentine Lake gold deposit. Refer to Figure 3 for photograph locations. **a)** A northwest-dipping fault-fill vein cutting gold-mineralized Neoproterozoic granitoid rock (Valentine Lake pluton, looking southwest). **b)** Quartz vein showing dextral motion and cutting the Valentine Lake pluton and mafic dykes (looking west). **c)** Contact between the Rogerson Lake Conglomerate (left, southeast) and the Valentine Lake pluton (right, northwest). **d)** Coarse-grained granitoid rock clasts in Rogerson Lake Conglomerate, shown near the contact with the Valentine Lake pluton.

The gold-mineralized Valentine Lake shear zone is a steeply northwest-dipping, reverse sinistral shear zone that cuts the Valentine Lake pluton and juxtaposes it against a panel of Late Silurian to Early Devonian Rogerson Lake Conglomerate and associated magmatic rocks (Fig. 3, 6; Lincoln et al., 2018). The Valentine Lake gold deposit is hosted within a network of fault-fill and extensional quartz vein sets along the Valentine Lake shear zone (Fig. 3, 6), with the bulk of gold mineralization hosted by the Valentine Lake pluton. Farther east from the Valentine Lake shear zone, northwest-directed, crustal-scale faults, including the Victoria Lake shear zone, imbricate Ordovician to Late Silurian sedimentary, volcanic, and volcaniclastic (Red Cross Group) rocks of the eastern-most Dunnage Zone. The fault zone marking the boundary between the Red Cross Group and the sedimentary-volcanic sequence immediately to the west correlates with the Wood Brook fault (Fig. 3; Valverde-Vaquero et al., 2006) in the southwest, and the Dog Bay Line (Williams et al.,

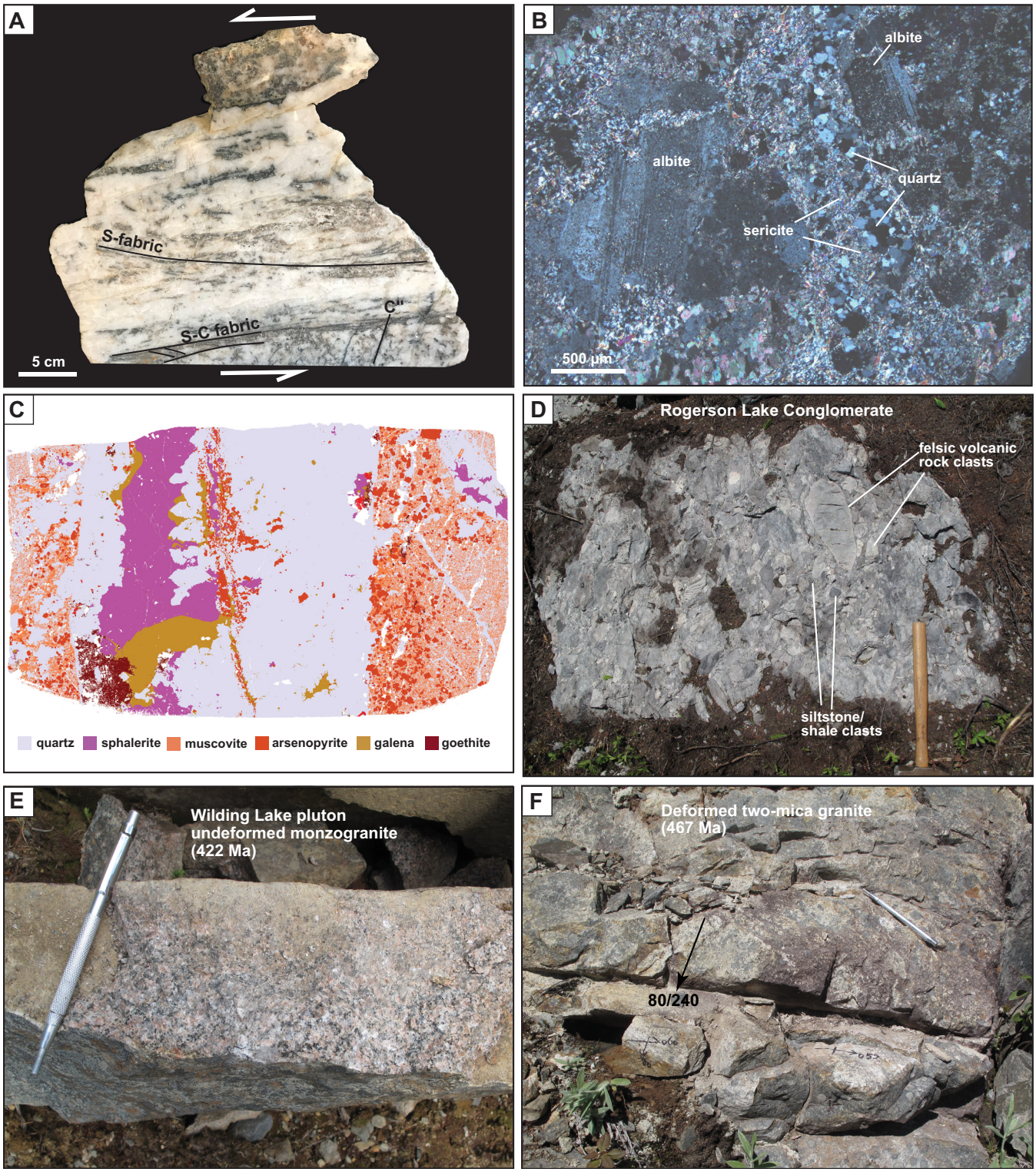

Figure 7. Field and sample photographs. Refer to Figure 4 for locations and Table 2 for descriptions and locations of the geochronology samples. **a)** A quartz vein sample from the Wilding Lake gold prospect displaying sinistral S-C fabrics. **b)** A microphotograph of altered Neoproterozoic basement tonalite (ca. 564 Ma) underlying the Wilding Lake gold prospect (geochronology sample #10). **c)** Scanning electron microscope-mineral liberation analyzer image of a mineralized vein cutting felsic volcanic rock (422 Ma), Wilding Lake gold prospect. The thin section image is ~46 mm long. **d)** Southern panel of Rogerson Lake Conglomerate near Wilding Lake containing coarse-grained clasts of felsic volcanic and sedimentary rocks. **e)** Undeformed two-mica monzogranite, Wilding Lake pluton (422 Ma: geochronology sample #6). **f)** Strongly deformed, two mica granite (467 Ma) displaying steeply southwest-dipping stretching lineations (black arrow), which is consistent with reverse motion towards the northeast (geochronology sample #8).

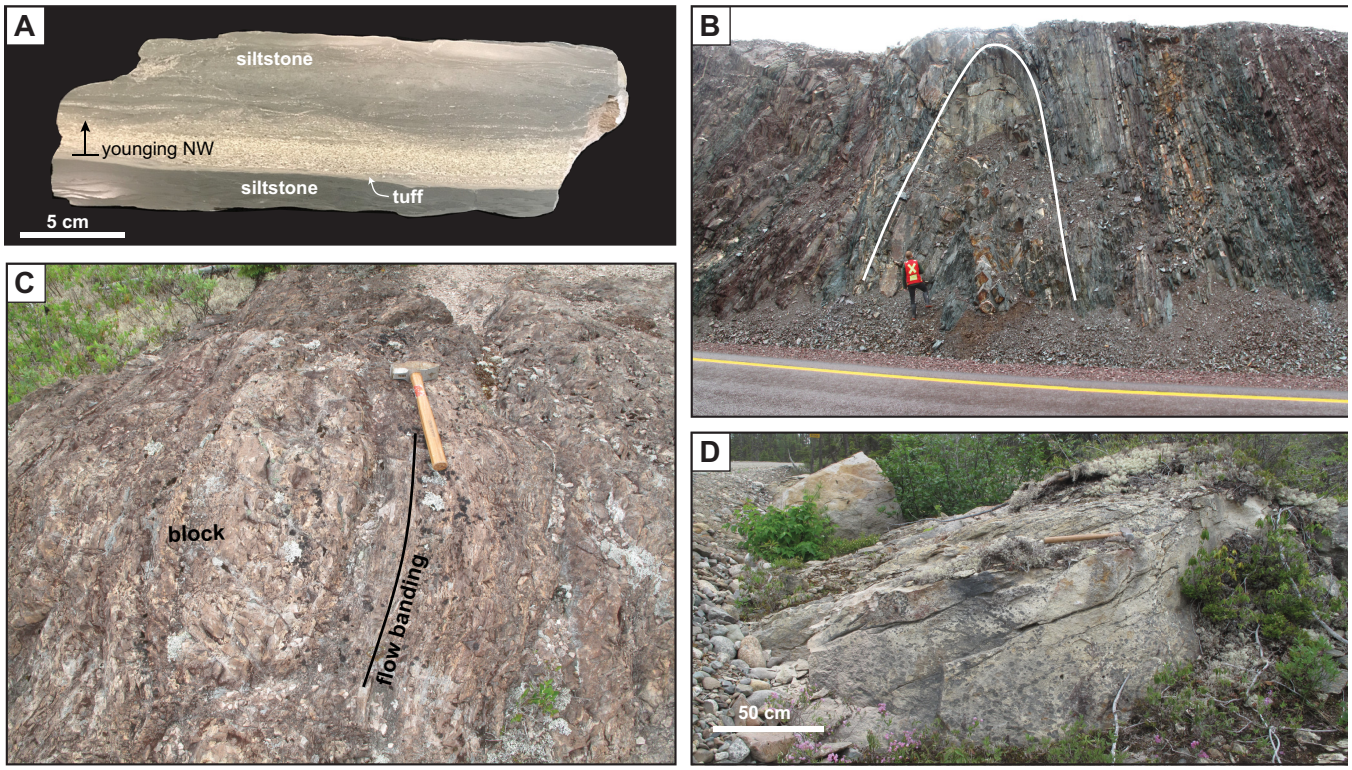

Figure 8. Field and sample photographs. *See* Figure 4 for locations and Table 2 for descriptions and locations of the geochronology samples. **a)** Sample of northwest-younging, stratified tuffite interlayered within siltstone of the Botwood basin (geochronology sample #11). **b)** Folded sequence of interlayered sandstone, siltstone, and tuffite from the Botwood basin. **c)** Autobrecciated, flow-banded rhyolite (ca. 430 Ma) dome of the Hodges Hill magmatic suite. **d)** Moderately deformed Late Silurian Stony Lake felsic volcanic rocks.

1993) in north-central Newfoundland. The Dog Bay Line is interpreted to represent the terminal suture of the Iapetus Ocean basin system (Williams et al., 1993; Pollock et al., 2007). West of the Valentine Lake pluton, Cambrian to Ordovician rocks of the Victoria Lake Supergroup (van Staal et al., 2005) are tectonically imbricated along steeply northwest-dipping, southeast-verging faults that record displacement before and during the Middle Ordovician (Zagorevski et al., 2007).

The structurally controlled Wilding Lake gold prospect (Honsberger et al., 2020a,b) occurs within a deformed panel of mineralized Rogerson Lake Conglomerate and associated felsic volcanic rocks and altered mafic dykes that unconformably overlie Neoproterozoic basement tonalite (Fig. 4, 7a–d; Honsberger et al., 2020b). It is yet to be determined if the contact between the overall southeast-younging Rogerson Lake Conglomerate sequence and overlying felsic volcanic rocks is a stratigraphic or structural boundary (*see* "?" in Fig. 4). The base of the Rogerson Lake Conglomerate sequence (western contact of syn-orogenic unconformity) is sheared along a vertical structural contact that correlates with the Valentine Lake shear zone to the southwest. This structure marks a transition from an overall northwest-verging thrust system in the southeast to an overall southeast-verging thrust system in the northwest, where subduction-related Cambrian arc volcanic rocks of the Tally Pond Group are preserved (Fig. 4). The Late Silurian Wilding Lake pluton (Fig. 7e) intrudes Ordovician and older, deformed sedimentary, volcanic, and plutonic (Fig. 7f) rocks of the Gander and Red Cross groups in the footwall of the Victoria Lake shear zone. Farther southeast, the Early Devonian North Bay granite suite (ca. 417 Ma: *see* Valverde-Vaquero et al., 2005) intrudes rocks of the Gander Group.

Northeast of the Wilding Lake section, mineralized syenogranite (422 Ma; *see below*) near Sandy Lake (a locality known as the "Elliot gold showing") intrudes deformed sandstone, siltstone, conglomerate, and associated tuffite of the Late Silurian – Early Devonian Botwood basin (Fig. 5, 8a,b). In this area and farther northeast, the panel of Rogerson Lake Conglomerate is not well preserved, interpreted to be related to deeper erosion of Neoproterozoic basement blocks composed of volcanic and granitoid rocks of the Sandy Brook Group (Rogers et al., 2006) and Crippleback Intrusive Suite (Evans et al., 1990), respectively. However, Silurian felsic magmatic rocks, including those of the Hodges Hill suite and the younger Mount Peyton/Fogo suite (van Staal et al, 2014; Sandeman et al., 2017), including the Stony Lake volcanic rocks, are well pre-

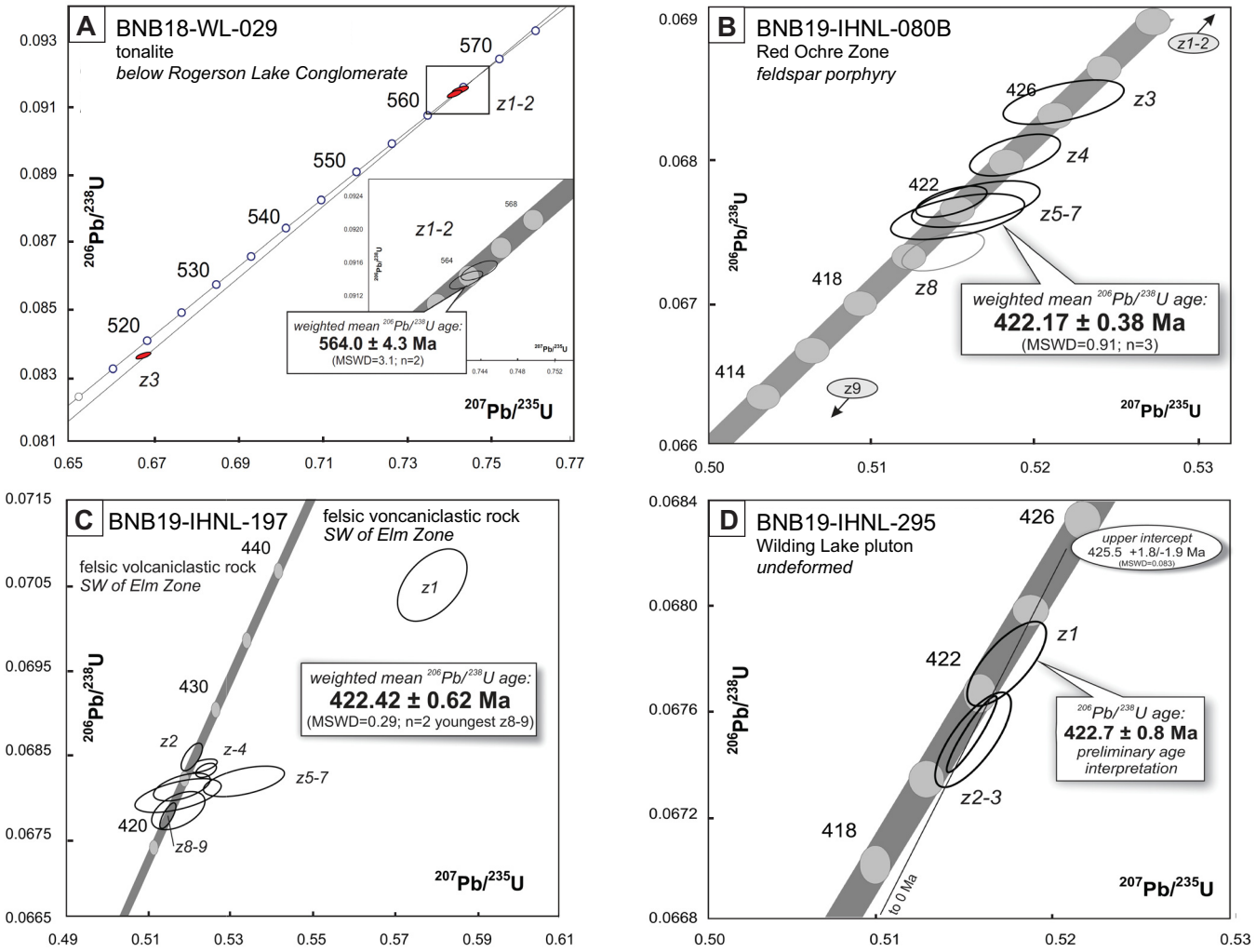

Figure 9. U-Pb Concordia diagrams for rocks from the Wilding Lake prospect and pluton: **a)** geochronology sample #10, **b)** geochronology sample #4, **c)** geochronology sample #5, and **d)** geochronology sample #6. *See* Figure 4 for locations and Table 2 for descriptions and locations of the geochronology samples.

served as structural domes (Fig. 5, 8c,d). Forthcoming high-precision U-Pb zircon geochronology on stratified, northwest-younging tuff layers within the sandstone and siltstone sequences of the Botwood basin (Fig. 8a) will help constrain the timing of synorogenic sedimentation and magmatism in north-central Newfoundland. High-grade metamorphic rocks of the Mount Cormack Complex (i.e. Ganderia; Fig. 5) tectonically bury rocks of the eastern Dunnage Zone along a northwest-directed thrust structure correlative with the Victoria Lake shear zone.

PRELIMINARY U-PB GEOCHRONOLOGY

Methods

Single zircon grains from 11 samples from central Newfoundland were dated by chemical abrasion – isotope dilution – thermal ionization mass spectrometry (CA-ID-TIMS) at the Jack Satterly Geochronology Laboratory, University of Toronto, following the methods described in Mattinson (2005). Age calculations were performed using ISOPLOT (Ludwig, 2008). Preliminary U-Pb geochronological data and analytical notes are presented in Table 2.

Results

Figure 9 shows a selection of four standard U-Pb concordia diagrams for the following units: Neoproterozoic basement tonalite, Late Silurian feldspar porphyry and felsic volcanic rocks of the Wilding Lake gold prospect, and Late Silurian monzonite of the Wilding Lake pluton. Results yield preliminary weighted mean $^{206}Pb/^{238}U$ zircon ages of 564.0 ± 4.3 Ma for basement tonalite (Table 2, sample #10), 422.17 ± 0.38 Ma for feldspar porphyry (sample #4), 422.42 ± 0.62 Ma for felsic volcanic rock (sample #5), and 422.7 ± 0.8 Ma for undeformed monzonite of the Wilding Lake pluton (sample #6). Other preliminary ages are listed in Table 2 and include monzonite (sample #2) and syenogranite (sample #3) intrusions in the Botwood basin, northeast of Wilding Lake, that yield preliminary zircon ages of

Table 2. Preliminary U-Pb zircon and rutile geochronological data.

#	Rock unit	Sample Number	Easting (m)	Northern (m)	Description	New U-Pb age (Ma)	Method[1]	Event	References
1	Mineralized quartz vein	BNB18-IHNL-180	518452	5368270	Goethite-altered pyrite-bearing (±Au) hydrothermal quartz vein cutting Rogerson Lake Conglomerate, Wilding Lake prospect	407.0 ± 4.0	U-Pb, rutile	Gold mineralization	This study
2	Paradise Lake monzonite	BNB18-IHNL-008	600796	5398557	Locally deformed and strongly altered, medium-grained monzonite at Paradise Lake, intrudes Botwood basin	420.0 ± 0.77	U-Pb, zircon	Mount Peyton felsic pulse	This study; s*ee also* Sandeman et al. (2017)
3	Elliot syenogranite	BNB19-IHNL-317	570646	5392646	Grey to pinkish grey, medium-grained, altered and mineralized syenogranite to monzogranite, Elliot gold showing	422.06 ± 0.47	U-Pb, zircon	Mount Peyton felsic pulse	This study; s*ee also* Sandeman et al. (2017)
4	Red Ochre feldspar porphyry	BNB19-IHNL-080B	516703	5367285	Mineralized feldspar porphyry, Wilding Lake prospect	422.17 ± 0.38	U-Pb, zircon	Felsic magmatism	This study
5	Third Spot felsic volcanic rock	BNB19-IHNL-197	518246	5367610	Fine-grained felsic volcanic, Wilding Lake prospect	422.42 ± 0.62	U-Pb, zircon	Felsic magmatism	This study
6	Wilding Lake pluton	BNB18-IHNL-295	519328	5363230	Light grey to pink, medium-grained, undeformed two mica monzogranite	422.7 ± 0.8	U-Pb, zircon	Felsic magmatism	This study
7	Red Cliffs rhyolite dome	BNB19-IHNL-092	591846	5423816	Flow-banded, fine-grained rhyolite dome, near quarry area in Grand Falls	429.5 ± 1.0	U-Pb, zircon	Hodges Hill felsic pulse	This study
8	Deformed granitoid rock	BNB19-IHNL-294	518837	5362019	Grey to grey-pink, medium-grained, foliated two mica granite along Granite Lake, south-side up shear indicators	467.41 ± 0.47	U-Pb, zircon	Peter Strides Granitoid Suite?	This study; *see also* Valverde-Vaquero et al. (2006)
9	Windsor Point felsic tuff	BNB19-IHNL-287	329506	5276517	Grey to tan, fine-grained, laminated, felsic to intermediate, pyroclastic tuff layer intercalated with pillow basalts younging to the northwest, Cape Ray	468.0 ± 1	U-Pb, zircon	Windsor Point extensional magmatism	This study; *see also* Dunning et al. (1990)
10	Basement tonalite	BNB18-WL-029 (drill core)	517453	5367934	Medium-grained, mineralized tonalite underlying Rogerson Lake Conglomerate, Wilding Lake prospect	564.0 ± 4.3	U-Pb, zircon	Cripplebacк intrusive suite	This study; *see also* Evans et al. (1990) and Honsberger et al. (2019b)
11	Felsic tuffite	BNB19-IHNL-291	612845	5431548	~3 cm wide, stratified tuffite layer, Wigwam Group, Botwood basin	in progress	U-Pb, zircon	Mount Peyton felsic pulse?	This study

Notes: [1]CA-ID-TIMS on single rutile and zircon grains, or small fragments thereof.

420.0 ± 0.77 Ma and 422.06 ± 0.47 Ma, respectively. An autobrecciated, flow-banded rhyolite dome west of the Botwood basin in Grand Falls (sample #7, Fig. 2a, 8c) records an older pulse of Silurian felsic magmatism at ca. 430 Ma (Table 2). A deformed granitoid rock that occurs immediately to the south of the Wilding Lake pluton is dated at 467 Ma (sample #8), which is the same age, within error, as felsic tuff (sample #9) interlayered with mafic volcanic rocks of the Windsor Point Group at Cape Ray. Hydrothermal rutile from an extensional quartz vein cutting Rogerson Lake Conglomerate from the Wilding Lake gold prospect yielded a preliminary $^{206}Pb/^{238}U$ age of 407 ± 4 Ma.

DISCUSSION

Orogenic gold mineralization in central Newfoundland occurs within footwall blocks along the length of an overall northwest-directed thrust system that exhumes high-grade rocks of Ganderia (Fig. 3–5). The Victoria Lake shear zone and correlative fault zones in central Newfoundland (Fig. 3–5) were, therefore, critical structures for controlling gold-bearing hydrothermal fluid flow, gold deposition, and tectonically burying and preserving gold mineralization in footwall blocks. The Valentine Lake gold deposit is preserved in an exhumed Neoproterozoic basement block (Valentine Lake pluton) where the northwest-directed fault system is steepened and overturned (Fig. 3). The Valentine Lake shear zone may be a secondary southeast-directed structure that was active during compression related to the overturning of the main fault system (Fig. 3).

Preliminary U-Pb zircon and rutile geochronology (Fig. 9, Table 2), combined with regional structural cross-sections (Fig. 3–5), constrain the critical phase of tectonism and associated hydrothermal fluid circulation for orogenic gold mineralization in central Newfoundland between ca. 424 and 407 Ma, with the main pulse of felsic magmatism in the southern Botwood basin and correlative Rogerson Lake Conglomerate sequence at ca. 422 Ma and hydrothermal gold mineralization between ca. 415 and 407 Ma. In addition to our samples, Late Silurian magmatic rocks of the Botwood basin sequence include the Stony Lake felsic volcanic rocks (Fig. 2a, 8d; 423 +3/-2: Dunning et al., 1990; 422 ± 2 Ma: McNicoll et al., 2008), mafic dykes, and mineralized bimodal rocks of the Mount Peyton Intrusive Suite (Fig. 1), which have been dated between 424 and 418 Ma (Sandeman et al., 2017). Field and structural relationships combined with geochronological results suggest that the magmatic pulse at ca. 422 Ma in central Newfoundland, as well as associated synorogenic sedimentation, are a result of transient lithospheric extension following the main phase of Salinic compressional deformation (433–426 Ma: van Staal et al., 2014), before emplacement of the Meelpaeg nappe during the Acadian Orogeny in the Early Devonian (e.g. Valverde-Vaquero et al., 2006; van Staal et al., 2014). Late Silurian magmatism in the gold-mineralized Ordovician Windsor Point Group along the southern coast at Cape Ray (Dubé et al., 1996) provides further evidence of an extension-related magmatic event. Metamorphic monazite in exhumed rocks of the Meelpaeg nappe in central Newfoundland and correlative rocks at Cape Ray are dated at ca. 420 Ma (Owen, 1992; Valverde-Vaquero et al., 2006) and ca. 415 Ma (Dubé et al., 1996), respectively, which places maximum age constraints on northwest-directed, Early Devonian thrust reactivation of faults that were initially extensional. This implies that the vein structures hosting gold mineralization in central Newfoundland formed during deformation associated with the Acadian Orogeny.

At Valentine Lake and Wilding Lake, orogenic gold mineralization is hosted within dominantly reverse sinistral shear vein systems characterized by fault-fill and extensional vein sets that cut Late Silurian to Early Devonian Rogerson Lake Conglomerate, Late Silurian volcanic rocks, and underlying Neoproterozoic basement granitoid rocks (Lincoln et al., 2018; Honsberger et al., 2020b). Furthermore, these main shear vein systems are in turn overprinted by at least three generations of younger gold-mineralized vein sets associated with subsequent local episodes of horizontal extension, oblique compression, and minor late dextral strike-slip (Honsberger et al., 2019b, 2020b). A preliminary age of ca. 407 ± 4 Ma (Table 2, this study) from hydro-thermal rutile in a crosscutting vein with overall dextral asymmetry on the Wilding Lake prospect provides a minimum age for the formation of the main auriferous shear vein system cutting Rogerson Lake Conglomerate. Assuming the initial phase of transient lithospheric extension terminated by 418 Ma (youngest Mount Peyton rocks: Sandeman et al., 2017) and that the youngest gold mineralization event occurred at ca. 407 Ma (U-Pb rutile), northwest-directed, Early Devonian progressive deformation related to quartz-gold vein development lasted for approximately 10 million years, between ca. 418 and 407 Ma. This is consistent with reverse sinistral and dextral shearing and associated orogenic gold mineralization that occured between 415 and 386 Ma along the Cape Ray fault zone (Dubé and Lauzière, 1996, 1997; Dubé et al., 1996) and Acadian Orogeny deformation between 415 and 410 Ma along the Dog Bay Line in north-central Newfoundland (McNicoll et al., 2006), which is slightly younger than the reverse sinistral inversion of the Silurian La Poile basin that occured between ca. 429 and 418 Ma along the Cinq Cerf fault zone in southwestern Newfoundland (Fig. 1; O'Brien et al., 1993).

The association of Ag, Cu, W, Mo, Sb, and B with Au in altered Late Silurian to Early Devonian Rogerson Lake Conglomerate, magmatic rocks, and structurally controlled vein sets in central Newfoundland may suggest Late Silurian magmatic fluid input to the surrounding rocks and encompassing fault system (e.g. Sandeman et al., 2017). Regardless, gold-bearing fluid circulation was structurally controlled by the crustal-scale, northwest-directed master fault system that may have reactivated Late Silurian extensional faults as thick-skinned thrusts in the Early Devonian. The undeformed Late Silurian Wilding Lake pluton (422 Ma) does not record Early Devonian deformation; potentially because of its competency and structural position in the centre of a fault block (Fig. 4). Nonetheless, the proposed evolution is explained by Late Silurian initiation of a southeast-dipping fault system, and associated synorogenic sedimentation and magmatism, resulting from transient lithospheric extension of the accreted Penobscot/Victoria/Popelogan arc during rollback and break-off of an underlying, subducted Ganderian slab (e.g. Whalen et al., 2006; Zagorevski et al., 2007; van Staal et al., 2014). Early Devonian, northwest-directed, thick-skinned inversion and thrust reactivation are attributed to Acadian orogenesis that resulted from the collision of Avalonia with the trailing margin of Ganderia (e.g. van Staal and Barr, 2012).

Comparison with the Abitibi Greenstone Belt

The emerging structurally controlled Paleozoic gold district of central Newfoundland is remarkably similar to the world-class Archean Abitibi orogenic gold system in scale (Fig. 1), synorogenic sedimentary and magmatic rocks, structural architecture, style of mineralization, tectonic evolution, and process rates (e.g. Bleeker, 2015; Honsberger and Bleeker, 2018). One key difference between the districts, other than the Abitibi systems being 2.2 billion years older, is that the Abitibi system is considerably more prolific, having produced 170 Moz (~5300 metric tonnes) of gold (Dubé and Mercier-Langevin, 2019).The detailed model presented in Bleeker (2015) for the Abitibi system was used as the main source of comparison in the following discussion.

First, the gold-mineralized crustal-scale fault systems in both areas extend continuously for ≥200 km along-strike and cut deformed and metamorphosed "granite-greenstone" basement terranes, with synorogenic unconformities separating uplifted basement blocks from younger, overlying upper-crustal synorogenic sequences of sedimentary (Rogerson Lake Conglomerate and Botwood basin, Newfoundland; Timiskaming conglomerate, Abitibi greenstone belt) and syenitic to monzonitic magmatic rocks (e.g. central Newfoundland: Sandeman et al., 2017), of overall low-grade metamorphic grade. Second, the synorogenic sequences of polymict conglomerate and cross-bedded sandstone occur as deformed and truncated synformal panels that display overall stratigraphic younging directions that point towards the master fault systems (Fig. 3–5; Victoria Lake shear zone and correlatives, Newfoundland: Destor-Porcupine and Larder Lake- Cadillac fault zones, Abitibi). Third, structurally controlled gold mineralization in both areas is preserved in the overall structural footwalls of the overarching crustal-scale fault zones. Fourth, orogenic-style gold mineralization (e.g. Groves et al., 1998) is hosted within laminated fault-fill and extensional shear vein networks (e.g. Dubé and Gosselin, 2007), as well as in brittle, crosscutting vein sets that indicate a period of extensive fluid cycling. Fifth, both gold systems record a process chain involving early imbrication of volcano-sedimentary terranes, transient lithospheric extension and uplift of basement blocks, synorogenic sedimentation and calc-alkaline to transitional alkaline magmatism, inversion and tectonic burial of the synorogenic basin during thick-skinned thrust re-imbrication, and degeneration to late-stage strike-slip deformation. Sixth, the time between transient lithospheric extension and subsequent tectonic burial of synorogenic basins in both areas spans approximately 15 to 20 million years. This implies comparable tectonic rates for Archean and Paleozoic lithospheric processes that produce and preserve structurally controlled gold deposits within crustal-scale fault systems.

Our study highlights that transient extension and synorogenic magmatism are critical ingredients for producing orogenic gold mineralization. Extension increases the geothermal gradient, generates deep-rooted magmas, and minimizes long-term post-orogenic uplift and erosion, whereas synorogenic magmatism further increases the geothermal gradient and may contribute fluids to the fault system (e.g. Bleeker, 2015). Additionally, inversion and tectonic burial of synorogenic clastic basins, followed by erosion of the overlying hanging-wall blocks, is essential for minimizing erosion of footwall blocks and preserving gold deposits. Ultimately, this research demonstrates that a common and predictable set of structural, magmatic, and tectonic processes leading to orogenic gold mineralization have recurred over more than 2 billion years of Earth's history (Goldfarb et al., 2005).

IMPLICATIONS FOR EXPLORATION

The present research has local, regional, and global implications for exploration for orogenic gold mineralization. On a local and regional scale in central Newfoundland, our study indicates that rocks in the footwall blocks of the Victoria Lake shear zone and associated splays, including Late Silurian to Early

Devonian Rogerson Lake Conglomerate, Late Silurian sub-alkaline to alkaline intermediate felsic magmatic rocks and altered mafic dykes, and Neoproterozoic basement granitoid rocks are highly prospective for orogenic gold mineralization for at least 200 km along-strike (Fig. 3–5). Accordingly, the occurrence of upper-crustal, altered Rogerson Lake Conglomerate with felsic magmatic rocks (±mafic dykes) is a key geological association within the gold-mineralized fault system of central Newfoundland. Future exploration may consider targeting Neoproterozoic basement granitoid rocks of the Crippleback Intrusive Suite along-strike of the fault corridor, as these rocks are presently underexplored (except the Valentine Lake pluton, the main host of the Valentine Lake deposit), occur in the overall footwall of the Victoria Lake shear zone and correlative structures, and are mechanically favourable, brittle host rocks; i.e., analogues to some of the granitoid and porphyry stocks along the major fault zones of the Abitibi greenstone belt.

The global implications of the present research include characterizing common geological settings and associated recurring processes for structurally controlled gold mineralization from the Archean to Paleozoic. Accordingly, the geological and structural relationships documented in our research can be utilized as first-order guides in gold exploration to target and explore prospective terranes of any age. More detailed comparisons of both Archean and these Paleozoic systems (e.g. magma associations and overall proportions; fluid inclusions; isotopic tracer studies) may contribute to more detailed process understanding.

ONGOING AND FUTURE WORK

Further high-precision U-Pb detrital zircon geochronology is required at a regional scale in central Newfoundland to determine if the contact between Late Silurian to Early Devonian synorogenic Rogerson Lake Conglomerate and overlying Late Silurian felsic volcanic rocks is a stratigraphic or structural boundary (*see* "?" in Fig. 3, 4). Furthermore, additional field-based structural studies of the Rogerson Lake Conglomerate and associated rocks in the Valentine Lake area will be important for testing and refining the overall architecture of the crustal-scale, gold-mineralized fault system. Considering the association of synorogenic magmatism with orogenic gold mineralization, an important next step in comparing and contrasting central Newfoundland with the Abitibi greenstone belt is to quantify the volume of synorogenic magmatism in both areas and assess how this may relate to differences in gold potential and endowment.

ACKNOWLEDGMENTS

This work represents a product of Natural Resources Canada's Targeted Geoscience Initiative 5, Gold Project. Thanks to Neil Rogers, Cees van Staal, Sherry Dunsworth of Marathon Gold Corp., Ryan Newman, Tyler Nickson, Tim Froude, and Lakeview Inn. This report benefitted from critical reviews by John Hinchey and Benoît Dubé.

REFERENCES

Bird, J.M. and Dewey, J.F., 1970. Lithosphere plate-continental margin tectonics and the evolution of the Appalachian Orogen; Geological Society of America Bulletin, v. 81, p. 1031–1060.

Bleeker, W., 2012. Targeted Geoscience Initiative (TGI-4) Lode Gold Deposits in Ancient Deformed and Metamorphosed Terranes: The role of extension in the formation of Timiskaming basins and large gold deposits, Abitibi greenstone belt—A discussion; *in* Summary of Field Work and Other Activities, 2012; Ontario Geological Survey, Open File Report 6280, p. 47-1 to 47-12.

Bleeker, W., 2015. Synorogenic gold mineralization in granite-greenstone terranes: The deep connection between extension, major faults, synorogenic clastic basins, magmatism, thrust inversion, and long-term preservation; *in* Targeted Geoscience Initiative 4: Contributions to the Understanding of Precambrian Lode Gold Deposits and Implications for Exploration, (ed.) B. Dubé and P. Mercier-Langevin; Geological Survey of Canada, Open File 7852, p. 25–47.

Colman-Sadd, S., Hayes, J., and Knight, I., 1990. The geology of the Island of Newfoundland. Government of Newfoundland and Labrador, Department of Mines and Energy, Geological Survey Branch, Map 90-01, GS# NFLD/2192, scale: 1:1 000 000.

Dubé, B., 1990. A preliminary report on contrasting structural styles of gold-only deposits in western Newfoundland; *in* Current Research, Part B; Geological Survey of Canada, Paper 90-1B, p. 77–90.

Dubé, B. and Gosselin, P., 2007. Greenstone-hosted quartz-carbonate vein deposits; *in* A Synthesis of Major Deposit Types, District Metallogeny, the Evolution of Geological Provinces, and Exploration Methods, (ed.) W.D. Goodfellow; Geological Association of Canada, Mineral Deposits Division, Special Publication No. 5, p. 49–73.

Dubé, B. and Lauzière, K., 1996. Structural evolution of a major fault zone: The Cape Ray Fault, SW Newfoundland; Canadian Journal of Earth Sciences, v. 33, p. 199–215.

Dubé, B. and Lauzière, K., 1997. Gold metallogeny of the Cape Ray Fault Zone, SW Newfoundland, Canada; Geological Survey of Canada, Bulletin 508, 90 p.

Dubé, B. and Mercier-Langevin, P., 2019. L'or dans la ceinture de roches vertes de l'Abitibi, Québec et Ontario, Canada: un aperçu géologique et historique; Ressources, Mines et Industrie, v. 6, no. 2, p. 2–29.

Dubé, B., Dunning, G., and Lauziére, K., 1995. Geology of the Hope Brook Mine, Newfoundland, Canada: A preserved Late Proterozoic high-sulfidation epithermal gold deposit and its implications for exploration; Economic Geology, v. 93, p. 405–436.

Dubé, B., Dunning, G.R., Lauzière, K., and Roddick, C., 1996. New insights into the Appalachian orogen from geology and geochronology along the Cape Ray Fault, SW Newfoundland; Geological Society of America Bulletin, v. 108, p. 101–116.

Dunning, G.R., O'Brien, S.J., Colman-Sadd, S.P., Blackwood, R.F., Dickson, W.L., O'Neil, P.P., and Krogh, T.E., 1990. Silurian

Orogeny in the Newfoundland Appalachians; The Journal of Geology, v. 98, p. 895–913.

Dunsworth, S. and Walford, P., 2018. Marathon's Valentine Lake Property – A developing multi-million ounce gold camp in central Newfoundland, Canada; Atlantic Geology, Abstracts, v. 54, p. 133–145.

Evans, D.T.W., 1996. Epigenetic gold occurrences, eastern and central Dunnage Zone, Newfoundland; Government of Newfoundland and Labrador, Department of Mines and Energy, Geological Survey, Mineral Resources Report 9, 135 p.

Evans, D.T.W., Kean, B.F., and Dunning, G.R., 1990. Geological studies, Victoria Lake Group, central Newfoundland; *in* Current Research; Government of Newfoundland and Labrador, Department of Mines and Energy, Geological Survey Branch, Report 90-1, p. 135–144.

Goldfarb, R.J., Groves, D.I., and Gardoll, S., 2001. Orogenic gold and geologic time: A global synthesis; Ore Geology Reviews, v. 18, p. 1–75.

Goldfarb, R.J., Baker, T., Dubé, B., Groves, D.I., Hart, C.J.R., Robert, F., and Gosselin, P., 2005. World distribution, productivity, character, and genesis of gold deposits in metamorphic terranes; *in* Economic Geology 100th Anniversary Volume, (ed.) J.W. Hedenquist, J.F.H. Thompson, R.J. Goldfarb, and J.P. Richards; Society of Economic Geologists, p. 407–450.

Groves, D.J., 1993. The crustal continuum model for late Archean lode-gold deposits of the Yilgarn Block, Western Australia; Mineralium Deposita, v. 28, p. 366–374.

Groves, D.J., Goldfarb, R.J., Gebre-Mariam, M., Hagemann, S.G., and Robert, F., 1998. Orogenic gold deposits: A proposed classification in the context of their crustal distribution and relationships to other gold deposit types; Ore Geology Reviews, v. 13, p. 7–27.

Hodgson, C.J., 1993. Mesothermal lode-gold deposits; *in* Mineral Deposit Modelling, (ed.) R.V. Kirkham, W.D. Sinclair., R.I. Thorpe, and J.M. Duke; Geological Association of Canada, Special Paper 40, p. 635–678.

Honsberger, I. and Bleeker, W., 2018. Orogenic comparison of structurally controlled gold systems of the Abitibi greenstone belt and central Newfoundland Appalachians: Implications for Newfoundland gold potential and recurring tectonic drivers of gold mineralization; *in* Targeted Geoscience Initiative: 2017 report of activities, Volume 2, (ed.) N. Rogers; Geological Survey of Canada, Open File 8373, p. 65–70.

Honsberger, I.W., Bleeker, W., Kamo, S.L. Evans, D.T.W., and Sandeman, H.A.I., 2019a. A Neoproterozoic age for granodiorite underlying Rogerson Lake Conglomerate: confirmed Ganderian basement in the Wilding Lake area, central Newfoundland gold district; Government of Newfoundland and Labrador, Department of Natural Resources, Geological Survey, Open File 012A/07/1774, 12 p.

Honsberger, I.W., Bleeker, W., Sandeman, H.A.I., and Evans, D.T.W., 2019b. Lithological and structural setting of structurally controlled gold mineralization in the Wilding Lake region, central Newfoundland; *in* Targeted Geoscience Initiative: 2018 report of activities, (ed.) N. Rogers; Geological Survey of Canada, Open File 8549, p. 59–69.

Honsberger, I.W., Bleeker, W., Sandeman, H.A.I., Kamo, S.L., and Evans, D.T.W., 2020a. The Wilding Lake gold prospect: A lithological and structural synthesis; Geological Survey of Canada, Open File 8658, 2 poster sheets.

Honsberger, I.W., Bleeker, W., Sandeman, H.A.I., Evans, D.T.W., and Kamo, S.L., 2020. Vein-hosted gold mineralization in the Wilding Lake area, central Newfoundland: Structural geology and vein evolution; *in* Targeted Geoscience Initiative 5: Contributions to the Understanding of Canadian Gold Systems, (ed.) P. Mercier-Langevin, C.J.M. Lawley, and S. Castonguay; Geological Survey of Canada, Open File 8712, p. 179–191. doi.10.4095/326020

Kean, B.F. and Jayasinghe, N.R., 1980. Geology of the Lake Ambrose (12A/10) and Noel Paul's Brook (12A/9) map areas; Newfoundland; Newfoundland Department of Mines and Energy, Report 88-1.

Kerr, A., 2006. Mesothermal gold mineralization in the Silurian Sops Arm group, western Newfoundland: A descriptive and historical overview; *in* Current Research; Newfoundland and Labrador Department of Natural Resources, Geological Survey, Report 06-1, p. 61–90.

Ludwig, K.R., 2008. User's Manual for ISOPLOT 3.60 – A Geochronological Toolkit for Microsoft Excel; Berkeley Geochronological Centre, Special Publication Number 4, 54 p.

Lincoln, N., Farmer, R., Eccles, R., and Deering, P.D., 2018. Preliminary economic assessment of the valentine lake gold project Newfoundland, NL, Canada; Lycopodium Minerals Canada Ltd. for Marathon Gold. <www.marathon gold.com/site/assets/files/5047/2018-10-pea.pdf> [accessed December 2, 2018]

Marathon Gold Corp., 2020. Marathon Gold reports commencement of 2020 exploration drill program at Valentine gold project. <marathon-gold.com> [accessed February 4, 2020]

Mattinson, J.M., 2005. Zircon U-Pb chemical abrasion ("CA-TIMS") method: combined annealing and multi-step partial dissolution analysis for improved precision and accuracy of zircon ages; Chemical Geology, v. 220, p. 47–66.

McNicoll, V., Squires, G.C., Kerr, A., and Moore, P.J., 2008. Geological and metallogenic implications of U-Pb zircon geochronological data from the Tally Pond area, central Newfoundland; *in* Current Research; Government of Newfoundland and Labrador, Department of Natural Resources, Geological Survey, Report 08-1, p. 173–192.

McNicoll, V.J., Squires, G.C., Wardle, R.J., Dunning, G.R., and O'Brien, B.H., 2006. U-Pb geochronological evidence for Devonian deformation and gold mineralization in the eastern Dunnage Zone, Newfoundland; *in* Current Research; Government of Newfoundland and Labrador, Department of Natural Resources, Geological Survey, Report 06-1, p. 45–60.

O'Brien, B.H., 1989. Summary of the Geology between La Poile Bay and Couteau Bay (11O/9 and 11O/16), southwestern Newfoundland; *in* Current Research; Newfoundland Department of Mines, Geological Survey of Newfoundland, Report 89-1, p. 105–119.

O'Brien, B.H., O'Brien, S.J., Dunning, G.R., and Tucker, R.D., 1993. Episodic reactivation of a Late Precambrian mylonite zone on the Gondwana margin of the Appalachians, southern Newfoundland; Tectonics, v. 12, p. 1043–1055.

O'Driscoll, J.M. and Wilton, D.H.C., 2005. Preliminary geochronological, geochemical, and isotopic studies of auriferous systems in the Botwood Basin and environs, central Newfoundland; *in* Current Research; Government of Newfoundland and Labrador, Department of Natural Resources, Geological Survey, Report 05-1, p. 207–222.

Owen, J.V., 1992. Comparative petrology of gneissic rocks in southwestern Newfoundland; Canadian Journal of Earth Sciences, v. 29, p. 2663–2676.

Percival, J.A., 2007. Geology and metallogeny of the Superior Province, Canada; *in* Mineral Deposits of Canada: A Synthesis of Major Deposit Types, District Metallogeny, the Evolution of Geological Provinces, and Exploration Methods, (ed.) W.D. Goodfellow; Geological Association of Canada, Mineral Deposits Division, Special Publication No. 5, p. 903–928.

Pollock, J.C., Wilton, D.H.C., van Staal, C.R., and Morrissey, K.D., 2007. U-Pb detrital zircon geochronological constraints on the Early Silurian collision of Ganderia and Laurentia along the

Dog Bay Line: The terminal Iapetan suture in the Newfoundland Appalachians; American Journal of Science, v. 307, p. 399–433.

Poulsen, K.H., Card, K.D., and Franklin, J.M., 1992. Archean tectonic and metallogenic evolution of the Superior Province of the Canadian Shield; Precambrian Research, v. 58, p. 25–54.

Poulsen, K.H., Robert, F., and Dubé, B., 2000. Geological classification of Canadian gold deposits; Geological Survey of Canada, Bulletin 540, 106 p.

Ramezani, J., Dunning, G.R., and Wilson, M.R., 2000. Geologic setting, geochemistry of alteration, and U-Pb age of hydrothermal zircon from the Silurian Stog'er Tight gold prospect, Newfoundland Appalachians, Canada; Exploration and Mining Geology, v. 9, p. 171–188.

Robert, F., 2001. Syenite-associated disseminated gold deposits in the Abitibi greenstone belt, Canada; Mineralium Deposita, v. 36, p. 503–516.

Robert. F. and Brown, A., 1986a. Archean gold-bearing quartz veins at the Sigma Mine, Abitibi greenstone belt, Quebec: Part I. Geologic relations and formation of the vein system; Economic Geology, v. 81, p. 578–592.

Robert. F. and Brown, A., 1986b. Archean gold-bearing quartz veins at the Sigma Mine, Abitibi greenstone belt, Quebec: Part II. Vein paragenesis and hydrothermal alteration; Economic Geology, v. 81, p. 593–616.

Rogers, N.,van Staal, C.R., McNicoll, V.J., Squires, G.C., Pollock, J., and Zagorevski, A., 2005. Geology, Lake Ambrose and part of Buchans, Newfoundland and Labrador; Geological Survey of Canada, Open File 4544, scale 1:50 000.

Rogers, N., van Staal, C.R., McNicoll, V.J., Pollock, J., Zagorevski, A. and Whalen, J., 2006. Neoproterozoic and Cambrian arc magmatism along the eastern margin of the Victoria Lake Supergroup: A remnant of Ganderian basement in central Newfoundland?; Precambrian Research, v. 147, p. 320–341.

Sandeman, H.A.I. and Dunning, G.R., 2016. Preliminary U-Pb geochronology and petrochemistry of volcanic rocks and felsic dykes of the Silurian Sops Arm Group, White Bay, western Newfoundland (NTS 12H/10 and 15); *in* Current Research; Newfoundland and Labrador Department of Natural Resources, Geological Survey, Report 16-1, p. 39–69.

Sandeman, H.A.I., Dunning, G.R., McCullough, C.K., and Peddle, C., 2017. U-Pb geochronology, petrogenetic relationships and intrusion-related precious-metal mineralization in the northern Mount Peyton Intrusive Suite: Implications for the origin of the Mount Peyton trend, central Newfoundland (NTS 2D/04); *in* Current Research; Government of Newfoundland and Labrador, Department of Natural Resources, Geological Survey, Report 17-1, p. 189–217.

Sangster, A.L., Douma, S.L., and Lavigne, L., 2007. Base metal and gold deposits of the Betts Cove Complex, Baie Verte Peninsula, Newfoundland; *in* Mineral Deposits of Canada: A Synthesis of Major Deposit Types, District Metallogeny, the Evolution of Geological Provinces, and Exploration Methods, (ed.) W.D. Goodfellow; Geological Survey of Canada, Mineral Deposits Division, Special Publication No. 5, p. 703–721.

Smyth, W.R. and Schillereff, H.S., 1982. Pre-Carboniferous geology of southwestern White Bay; *in* Report of Activities; Newfoundland Department of Mines and Energy, Mineral Development Division, Report 82-1, p. 78–98.

Tuach, J., Dean, P.L., Swinden, H.S., O'Driscoll, C.F., Kean, B.F., and Evans, D.T.W., 1988. Gold mineralization in Newfoundland: A 1988 review; *in* Current Research; Newfoundland Department of Mines and Energy, Report 88-1.

Valverde-Vaquero, P. and van Staal, C.R., 2001. Relationships between the Dunnage – Gander Zones in the Victoria Lake – Peter Strides Pond Area; *in* Current Research; Newfoundland Department of Mines and Energy, Geological Survey, Report 2001-1, p. 1–9.

Valverde-Vaquero, P., van Staal, C.R., and Rogers, N., 2005. Geology, Snowshoe Pond, Newfoundland and Labrador; Scale 1:50 000. Geological Survey of Canada, Open File 4597.

Valverde-Vaquero, P., van Staal, C.R., McNicoll, V., and Dunning, G.R., 2006. Mid – Late Ordovician magmatism and metamorphism along the Gander margin in central Newfoundland; Journal of the Geological Society of London, v. 163, p. 347–362.

van Staal, C.R. and Barr, S.M., 2012. Lithospheric architecture and tectonic evolution of the Canadian Appalachians and associated Atlantic margin; *in* Tectonic Styles in Canada Revisited: The LITHOPROBE Perspective, (ed.) J.A. Percival, F.A. Cook, and R.M. Clowes; Geological Association of Canada, Special Paper 49, p. 41–95.

van Staal, C.R., Dewey, J.F., Mac Niocaill, C., and McKerrow, W.S., 1998. The Cambrian-Silurian tectonic evolution of the northern Appalachians and British Caledonides: History of a complex, west and southwest Pacific-type segment of Iapetus; *in* Lyell: The Past is the Key to the Present, (ed.) D.J. Blundell and A.C. Scott; Geological Society of London, Special Publication 143, p. 199–242.

van Staal, C.R., Valverde-Vaquero, P., Zagorevski, A., Rogers, N., Lissenberg, C.J., and McNicoll, V.J., 2005. Geology, Victoria Lake, Newfoundland and Labrador; Geological Survey of Canada, Open File 1667, scale 1:50 000.

van Staal, C.R., Zagorevski, A., McNicoll, V.J., and Rogers, N., 2014. Time-transgressive Salinic and Acadian orogenesis, magmatism, and Old Red Sandstone sedimentation in Newfoundland; Geoscience Canada, v. 41, p. 138–164.

Wardle, R.J., 2005. Mineral Commodities of Newfoundland and Labrador: Gold; Geological Survey of Newfoundland and Labrador, Mineral Commodities Series, no. 4, 16 p.

Whalen, J.B., McNicoll, V.J., van Staal, C.R., Lissenberg, C.J., Longstaffe, F.J., Jenner, G.A., and van Breemen, O., 2006. Spatial, temporal and geochemical characteristics of Silurian collision zone magmatism, Newfoundland Appalachians: An example of a rapidly evolving magmatic system related to slab break-off; Lithos, v. 89, p. 377–404.

Williams, H., 1962. Botwood (West Half) Map-area, Newfoundland; Geological Survey of Canada, Paper 62-9, 16 p.

Williams, H., 1964. The Appalachians in northeastern Newfoundland-a two-sided symmetrical system; American Journal of Science, v. 262, p. 1137–1158.

Williams, H., 1978. Tectonic lithofacies map of the Appalachian Orogen; Memorial University of Newfoundland, St John's, Newfoundland and Labrador, scale 1:1 000 000.

Williams, H., Colman-Sadd, S.P., and Swinden, H.S., 1988. Tectonic-stratigraphic subdivisions of central Newfoundland; Geological Survey of Canada, Paper 88-1B, p. 91–98.

Williams, H., Currie, K.L., and Piasecki, M.A.J., 1993. The Dog Bay Line: A major Silurian tectonic boundary in northeast Newfoundland; Canadian Journal of Earth Sciences, v. 30, p. 2481–2494.

Zagorevski, A., van Staal, C.R., McNicoll, V., and Rogers, N., 2007. Tectonic architecture of an arc-arc collision zone, Newfoundland Appalachians; *in* Formation and Applications of the Sedimentary Record in Arc Collision Zones, (ed.) A. Draut, P.D. Clift, and D.W. Scholl; Geological Society of America, Special Paper 436, p. 1–26.

Paleoproterozoic gold and its tectonic triggers and traps: Implications from Re-Os sulphide and U-Pb detrital zircon geochronology, Lynn Lake, Manitoba

Christopher J.M. Lawley[1*], David Selby[2], William J. Davis[1], Eric Yang[3], Shuangquan Zhang[4], Simon E. Jackson[1], Duane C. Petts[1], A. Rhys O'Connor[5], and David A. Schneider[5]

[1]Geological Survey of Canada, 601 Booth Street, Ottawa, Ontario K1A 0E8
[2]Durham University, Science Labs, Lower Mountjoy, South Road, Durham DH1 3LE UK
[3]Manitoba Geological Survey, 365-1395 Ellice Avenue, Winnipeg, Manitoba R3G 3P2
[4]Carleton University, 1125 Colonel By Drive, Ottawa, Ontario K1S 5B6
[5]University of Ottawa, 120 University, Ottawa, Ontario K1N 6N5
[*]Corresponding author's e-mail: christopher.lawley@canada.ca

ABSTRACT

Orogenic Au deposits require a trigger to transport auriferous fluids from their deep-seated source regions to their depositional site in the mid- to upper-crust. Defining the tectonic trigger of Au ore systems requires precise age constraints. Herein we address that knowledge gap with new Re-Os sulphide (arsenopyrite and pyrite) and U-Pb detrital zircon geochronology results from the Lynn Lake greenstone belt of the Paleoproterozoic Trans-Hudson Orogen, Manitoba, Canada. We document an early-stage of Au-rich veins (ca. 1.82 Ga) that are coeval with syenitic magmatism (1.83–1.82 Ga) and immediately post-date new ages for the opening and closure of synorogenic basins (1.84–1.83 Ga) and late-stage arc magmatism (1.84–1.83 Ga). Together these data point to the importance of stalled subduction and upwelling asthenosphere as possible triggers for fluid release during the earliest stages of continental collision between the Hearne, Superior, and Sask cratons. New dating further documents a second, overprinting generation of auriferous fluids (ca. 1.78 Ga) that post-dates peak metamorphism (ca. 1.81 Ga). These late-stage fluids were driven by a second thermal pulse (ca. 1.78 Ga), which, based on the timing of coeval, crustally derived pegmatitic dykes, may be related to crustal thickening and/or another unrecognized subcrustal heat source. Mineral exploration should focus on the large-scale architecture that is required to focus multiple pulses of auriferous fluids to the same depositional trap over the lifespan of an orogen.

INTRODUCTION

Modern and ancient mountain belts are an important geological setting for giant Au deposits, as demonstrated by the large number of such deposits hosted within accreted terranes along the western Cordillera and older deposits in the Canadian shield (Goldfarb et al., 1998; Groves et al., 1998). The sources of auriferous fluids in accretionary orogens are generally considered to be metamorphic, possibly due to devolatilization of the mafic lower crust and/or sulphidic sediments during the active subduction of oceanic lithosphere (Goldfarb et al., 1998; Goldfarb and Groves, 2015). Because the duration of individual mineralization events is brief (≤0.1 m.y.) relative to the lifespan of an orogen (10–100 m.y.), a trigger is required to drive Au-bearing fluids, likely metamorphic in origin, from their upper mantle and/or crustal sources to their depositional sites in the mid- to upper-crust (Kerrich and Wyman, 1989; Goldfarb et al., 1991; Wyman et al., 2016).

The tectonic trigger(s) for Au-bearing fluid transport in modern accretionary settings include changes in subduction velocity, ridge subduction, slab roll-back, plate reorganization, and/or plume impingement (Goldfarb and Groves, 2015). Many of these triggers are also thought to be important to porphyry and epithermal deposits in modern arc and/or back-arc settings (Sillitoe, 2008; Goldfarb et al., 2014). Collisional orogens are also endowed with orogenic-style Au deposits (Goldfarb et al., 2001), but the tectonic trigger(s) in these settings is less clear because active subduction of oceanic lithosphere may not be directly involved and/or may be occurring 100s to 1000s km away from the Au deposits (Li et al., 2012; Li et al., 2015). Instead, the cessation of subduction, stalling of the subducting slab, lithospheric delamination, plume impingement, and/or far-field subduction effects may trigger the devolatilization of upper mantle to crustal sources in collisional to post-collisional settings (Richards, 2011; Groves and Santosh, 2016).

Lawley, C.J.M., Selby, D., Davis, W.J., Yang, E., Zhang, S., Jackson, S.E., Petts, D.C., O'Connor, A.R., and Schneider, D.A., 2020. Paleoproterozoic gold and its tectonic triggers and traps: Implications from Re-Os sulphide and U-Pb detrital zircon geochronology, Lynn Lake, Manitoba; *in* Targeted Geoscience Initiative 5: Contributions to the Understanding of Canadian Gold Systems, (ed.) P. Mercier-Langevin, C.J.M. Lawley, and S. Castonguay; Geological Survey of Canada, Open File 8712, p. 211–222. https://doi.org/10.4095/326033

Although the tectonic differences and the role active subducting oceanic lithosphere has between accretionary and collisional orogens are well described in the literature, the implications of differing orogenic styles on Au metallogeny are less well understood (Barley and Groves, 1991; Pehrsson et al., 2016). One of the factors contributing to this uncertainty is that Au deposits associated with the early accretionary orogenic stage, if present, were likely reworked and overprinted during later collisional orogenesis (Groves et al., 2016). The reworking of accretionary orogens is proposed as a possible explanation for the Au-rich signature of continent-continent collisions that incorporate early formed oceanic arcs (Leahy et al., 2005). The situation is even more complex along cratonic margins, which were typically reworked during multiple, overprinting orogens spanning billions of years (Carpenter et al., 2005; Davies et al., 2010; Lawley et al., 2013, 2015). Determining the timing of Au mineralization within this complex orogenic collage requires precise age constraints.

Herein we address that knowledge gap with new Re-Os arsenopyrite and pyrite, and U-Pb detrital zircon geochronology for the Paleoproterozoic Lynn Lake greenstone belt (LLGB of Manitoba; Fig. 1–3). These ages provide new constraints on the timing of Au mineralization, which, coupled with new U-Pb detrital zircon ages for synorogenic sedimentary basins, highlight the relationship between changes in tectonic style (e.g. accretionary versus collisional orogenesis) and its relationship to metallogenesis.

LOCAL GEOLOGY

The LLGB is hosted within the Paleoproterozoic Trans-Hudson Orogen (1.9–1.8 Ga: Ansdell, 2005; Corrigan et al., 2009). Rhyolitic flows are the oldest dated lithostratigraphic unit and were broadly coeval with mafic to intermediate volcanism (Baldwin et al., 1987; Beaumont-Smith and Böhm, 2002, 2004; Beaumont-Smith et al., 2006). The close structural intercalation of mafic volcanic rocks with disparate geochemical compositions suggests that the Wasekwan Group likely comprises rocks that initially formed in distinct environments but were juxtaposed during later structural reworking (Zwanzig, 1997, 2000; Zwanzig et al., 1999; Beaumont-Smith, 2008). Multiple volcanic rock packages are also demonstrated by distinct rhyolite ages within the northern and southern belts of the LLGB (Beaumont-Smith and Böhm, 2002, 2004). Based on the emplacement of the Pool Lake suite (1.89–1.87 Ga), which intrudes and stiches the different belts, some of these disparate mafic volcanic rock packages must have been structurally intercalated by ca. 1.87 Ga (Baldwin et al., 1987; Beaumont-Smith and Böhm, 2002, 2004; Beaumont-Smith et al., 2006). Mafic to ultramafic intrusions that host the Lynn Lake Ni mine were emplaced into the amalgamated Wasekwan-Pool Lake suite at 1871 ± 2 Ma (i.e. El gabbro: Turek et al., 2000). All three igneous assemblages were subsequently intruded by dykes and plutons of the 1.86–1.85 Ga Wathaman suite (Meyer et al., 1992), which marks the accretion of the LLGB and the Hearne craton to the north at ca. 1.85 Ga (Ansdell, 2005; Corrigan et al., 2005).

The Wasekwan Group is unconformably overlain by conglomerate (e.g. Hughes Lake unconformity; Fig. 3), psammite, arkose, and wacke comprising the Sickle Group (Anderson and Beaumont-Smith, 2001). A similar conglomerate separates the LLGB and large swaths of the Sickle Group and turbidite-like rocks comprising the Burntwood Group (i.e. Kisseynew Basin) to the south (Fig. 2). Previously reported ages suggest that the Burntwood Group extends to older maximum depositional ages than the structurally overlying coarse clastic sedimentary successions (Machado et al., 1999). However, both sedimentary packages are interstratified, suggesting that deposition of coarse clastic and deep-marine sedimentary facies were locally coeval (Zwanzig and Bailes, 2010).

RESULTS

Preliminary Re-Os Arsenopyrite and Pyrite Geochronology

Multiple pyrite and/or arsenopyrite mineral separates were prepared (n = 38) from different vein and alteration types collected at three deposits (MacLellan, Gordon, and Burnt Timber) as part of the current study (Fig. 4). Of these, only 19 samples yielded sufficient Re to attempt Re-Os dating (total analyses = 23) following the methods of Lawley et al. (2013).

Paleoproterozoic arsenopyrite and pyrite results scatter about a ca. 1.8 Ga errorchron (1794 ± 18 Ma; 2σ; MSWD = 159; n = 15; York model 3; initial $^{187}Os/^{188}Os = 1.0 \pm 0.9$). Reproducible replicate analysis of the sample, or multiple samples prepared from the same vein, strongly suggest that the excess data-point scatter is not an analytical artefact. Instead, excess data-point scatter is more likely a product of multiple sulphide generations of slightly to significantly different age.

Two replicate analyses of the two arsenopyrite samples with the highest $^{187}Re/^{187}Os$ ratios (6132–16564; n = 4) yield weighted average Re-model ages at 1824 ± 12 Ma and 1782 ± 16 Ma (n.b. model age uncertainties are reported at 2σ and include uncertainties in the ^{187}Re decay constant of 1.666×10^{-11} yr^{-1} and the initial Os composition = 0.5 ± 0.2; Smoliar et al., 1996). Model age calculations for these two samples is appropriate because nearly all of the measured ^{187}Os ($^{187}Os^{r}$

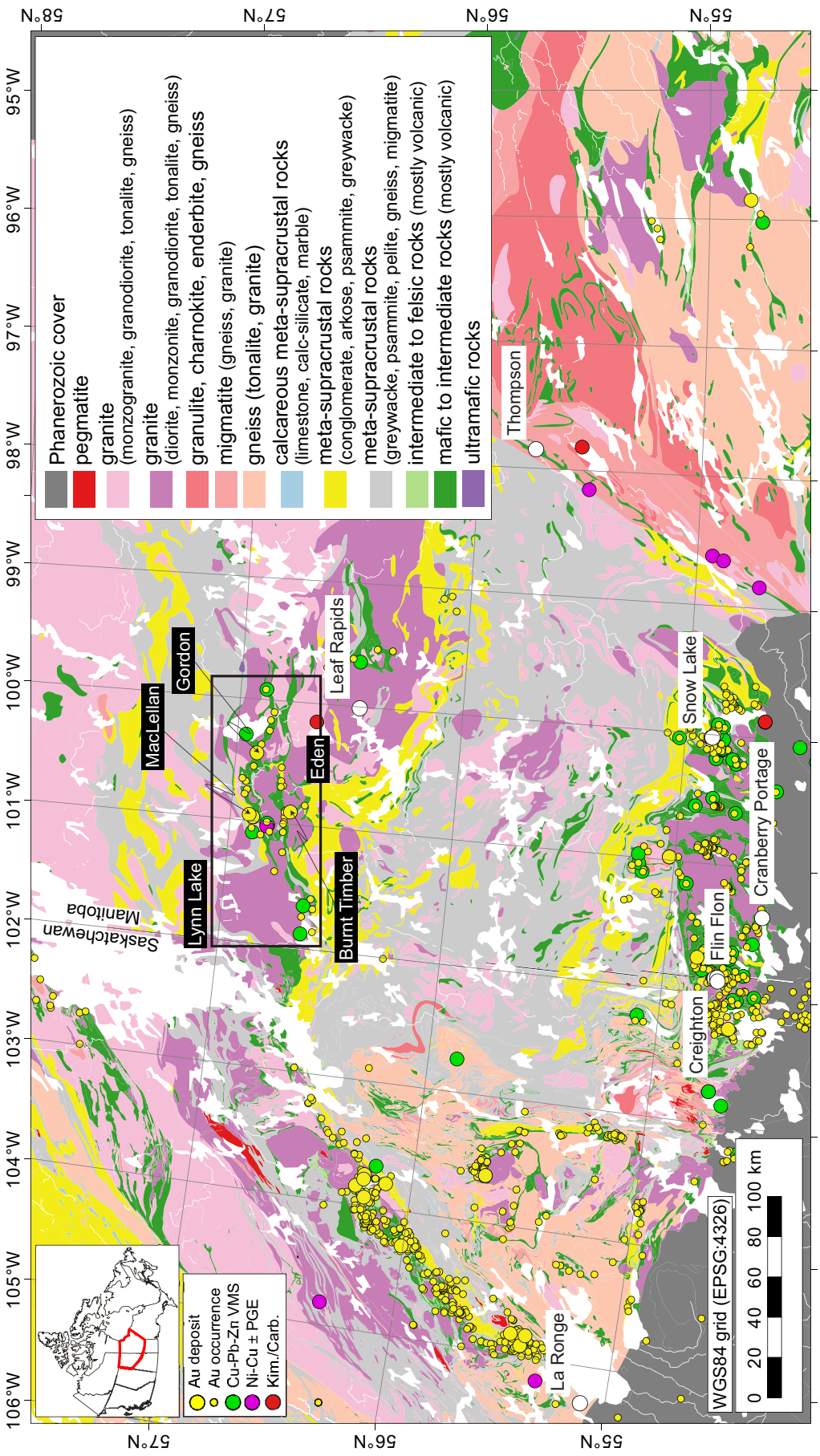

Figure 1. Regional geological map of Saskatchewan and Manitoba (Saskatchewan geological polygons from the Saskatchewan Mining and Petroleum GeoAtlas; Manitoba geological polygons from Manitoba Mineral Resources(2013)). Volcanogenic massive sulphide (VMS; Galley et al., 2007), nickel-platinum group element (Eckstrand and Hulbert, 2007), gold deposits (Dubé and Gosselin, 2007), kimberlite (Kim.; Faure, 2010) and carbonatite (Carb.; Woolley and Kjarsgaard, 2008) are shown for reference. Gold occurrences are also shown for reference (data are commodity-filtered from the provincial mineral occurrence databases).

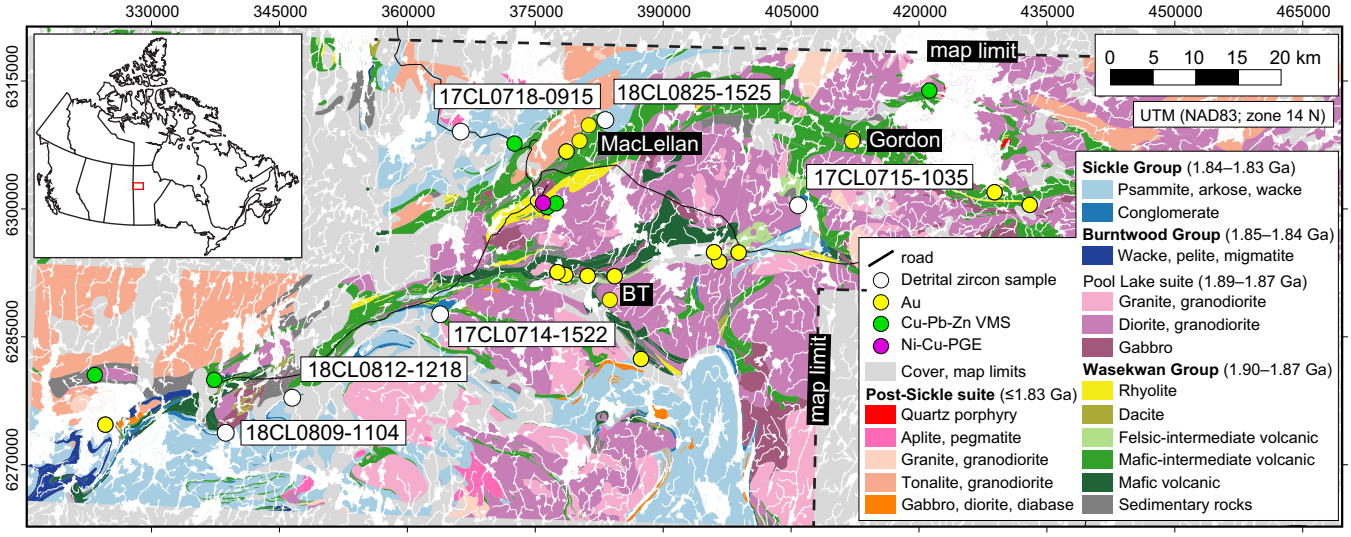

Figure 2. Local geology map of the Lynn Lake greenstone belt (Gilbert et al., 1980; Gilbert, 1993). Detrital zircon sample localities, volcanogenic massive sulphide (VMS; Galley et al., 2007), nickel-platinum group element (Eckstrand and Hulbert, 2007), and gold deposits (Dubé and Gosselin, 2007) are shown for reference.

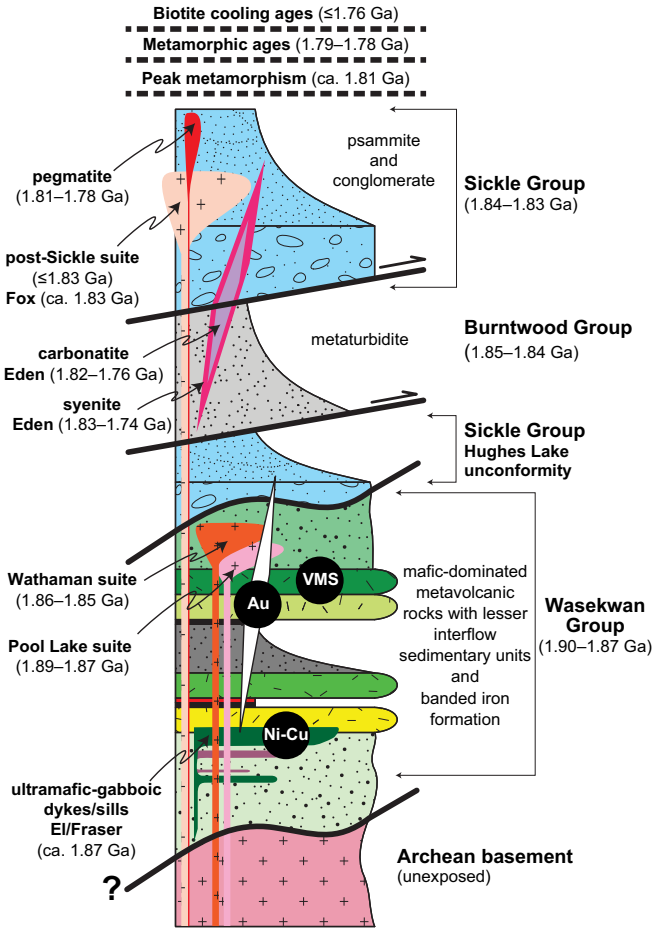

Figure 3. Schematic stratigraphic column summarizing the main supracrustal groups and plutonic suites comprising the Lynn Lake greenstone belt. Ages are summarized from several sources (*see* text for further details). Abbreviations: BIF = banded iron formation, VMS = volcanogenic massive sulphides.

= 99%) is due to radiogenic decay of ^{187}Re (Stein et al., 2000). The older ca. 1.82 Ga arsenopyrite sample was taken from a pre- to syn-D_2 vein at MacLellan; whereas the younger ca. 1.78 Ga arsenopyrite sample was collected from the sulphidized metavolcanic host rock at the same deposit. Two replicate analyses of one moderately radiogenic pyrite sample (^{187}Re/^{188}Os = 694–1005; ^{187}Os^{r} = 98%) represent the best available timing estimate for sulphide replacement at Gordon (1838 ± 28 Ma). A regression through a subset of reproducible arsenopyrite and pyrite samples from both deposits yield a York Model 1 Re-Os isochron age of 1827 ± 9 Ma (MSWD = 0.4; n = 5; initial ^{187}Os/^{188}Os = 0.46 ± 0.03).

The remaining arsenopyrite and pyrite analyses scatter to lower ^{187}Re/^{188}Os ratios (57–2418), but are still moderately radiogenic (^{187}Os^{r} = 57–99%) and yield a range of Re-Os model ages (1980–764 Ma). A subset of the older (≥1.83 Ga) pyrite vein analyses from MacLellan yield a York Model 1 Re-Os isochron age of 1865 ± 21 Ma (MSWD = 0.04; n = 4; initial ^{187}Os/^{188}Os = 0.48 ± 0.06). Two of these three samples were of pyritized biotite schist (Fig. 4e,f), which may suggest that the oldest Re-Os model ages reflect early sulphide deposition that predates regional metamorphism. However, the remaining pyrite sample within this potential group was sampled adjacent to vein pyrite samples that yield Re-Os model ages older than the host rock, suggesting that some of the older Re-Os model ages may also reflect isotopic disturbance. A subset of anomalously young samples, including the two samples from Burnt Timber, yield model ages that cluster around ca. 1.3 and 0.8 Ga. The scatter of anomalously young Re-Os results may reflect disturbance and/or variable resetting to produce geologically mean-

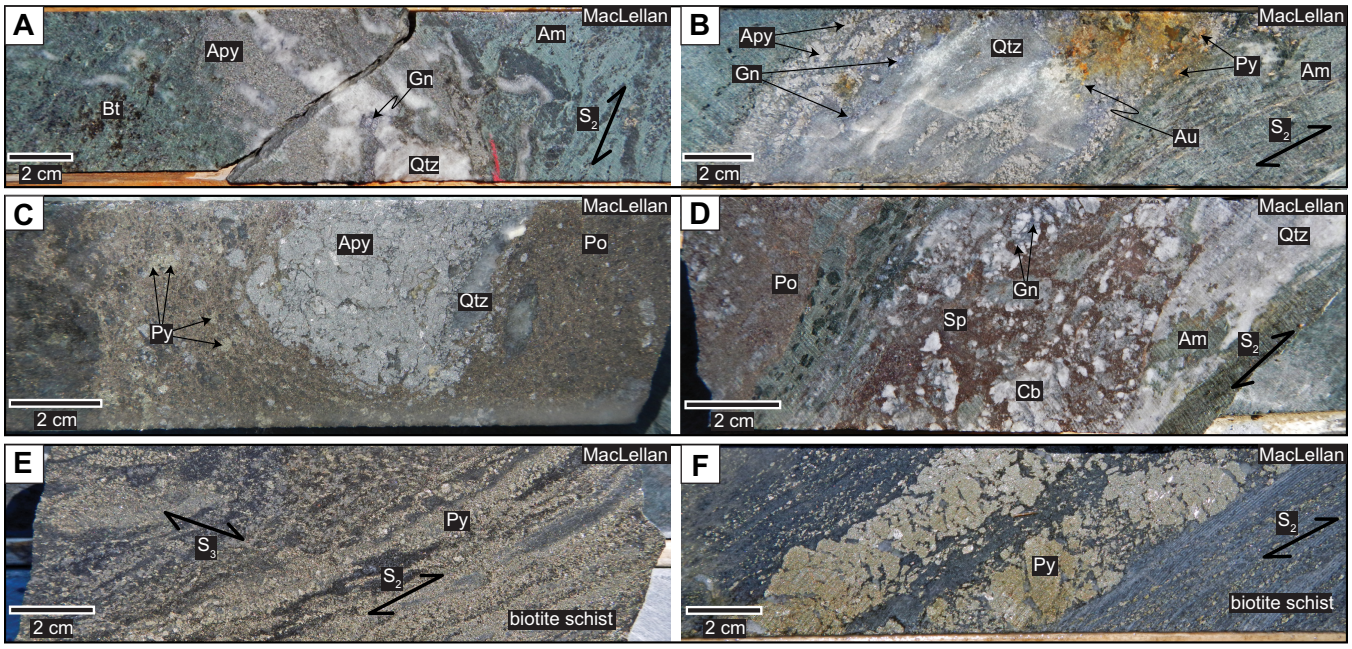

Figure 4. Photographs of drill core from ore zones of the MacLellan Au deposit: **a and b)** folded and/or transposed pre- to syn-D_2 quartz-arsenopyrite veins that cut metavolcanic rocks (amphibolite); **c)** sulphide replacement ore zone with coarse arsenopyrite; **d)** transposed and brecciated base metal vein cutting metavolcanic rocks (amphibolite); **e and f)** sulphide replacement with biotite schist. Pyrite defines S_2 and S_3 fabrics, suggesting post-D_2 fluids and/or remobilization (e). Coarsening of arsenopyrite (c) and pyrite (f) likely occurred during metamorphism. Abbreviations: Am = amphibole, Apy = arsenopyrite, Bt = biotite, Cb = carbonate, Gn = galena, Po = pyrrhotite, Py = pyrite, Qtz = quartz, and Sp = sphalerite.

ingless model ages, or possibly reflect reworking of the Trans-Hudson Orogen during the assembly and breakup of Rodinia (McDannell et al., 2018). As a result, the reproducible Re-Os model ages for the two highly radiogenic samples from MacLellan represent the preferred timing for sulphidation in the LLGB (ca. 1.82 and 1.78 Ga).

Preliminary U-Pb Detrital Zircon Geochronology

Six samples for detrital zircon analyses were collected across the LLGB as part of the current study (Fig. 2). Zircon mineral separates were prepared and analyzed using the sensitive high mass-resolution ion microprobe (SHRIMP) at the Geological Survey of Canada following the methods of Stern (1997).

Three of the samples represent Sickle Group conglomerate, which at the Hughes Lake area unconformably overlie the mafic volcanic host rocks (i.e. Wasekwan Group) of the Au deposits (Fig. 2, 3). Two samples, comprising psammite and pebble conglomerate, were collected from what is thought to be higher stratigraphic levels of the Sickle Group. One additional sample was collected from what was previously mapped as the Ralph Lake conglomerate. The youngest reproducible zircon grain from the entire data set is 1836 ± 15 Ma, which is interpreted to represent the maximum depositional age for the Sickle Group. The youngest detrital zircon grains from each of the other Sickle Group samples overlap within analytical uncertainty at 2σ (≤1.84 Ga); whereas the youngest grain from the Ralph Lake conglomerate is older at 1860 ± 5 Ma. The minimum depositional age for the Sickle Group is constrained by a suite of intermediate (i.e. tonalite, diorite, granodiorite, and quartz diorite) to felsic (i.e. granite) intrusions and plutons that are thought to intrude the Sickle Group (i.e. post-Sickle suite; Fig. 2, 3; Beaumont-Smith and Böhm, 2002, 2004). The Fox mine tonalite is thought to represent one of these suspected post-Sickle intrusions and is dated at 1831 ± 4 Ma (Turek et al., 2000). If correct, deposition of the Sickle Group therefore likely occurred during the earliest stage of the ca. 1.83 Ga collision between the composite Hearne-LLGB with the Superior craton to the southeast (Fig. 1, 5, 6). The implications of synorogenic basin closure to the Au endowment of the LLGB are discussed below.

DISCUSSION

New U-Pb detrital zircon geochronology from multiple quartzite and conglomerate localities, together with the age of the so-called post-Sickle intrusive suite (e.g. Fox mine Tonalite, 1831 ± 4 Ma: Turek et al., 2000; Dunphy Lakes tonalite 1829 ± 2 Ma: Beaumont-Smith, 2003), constrain the depositional timing of the Sickle Group to 1836–1831 Ma in the LLGB (Fig. 2, 3, 5, 6). The interpreted Sickle Group depositional age is coeval with similar siliciclastic rocks comprising the Missi

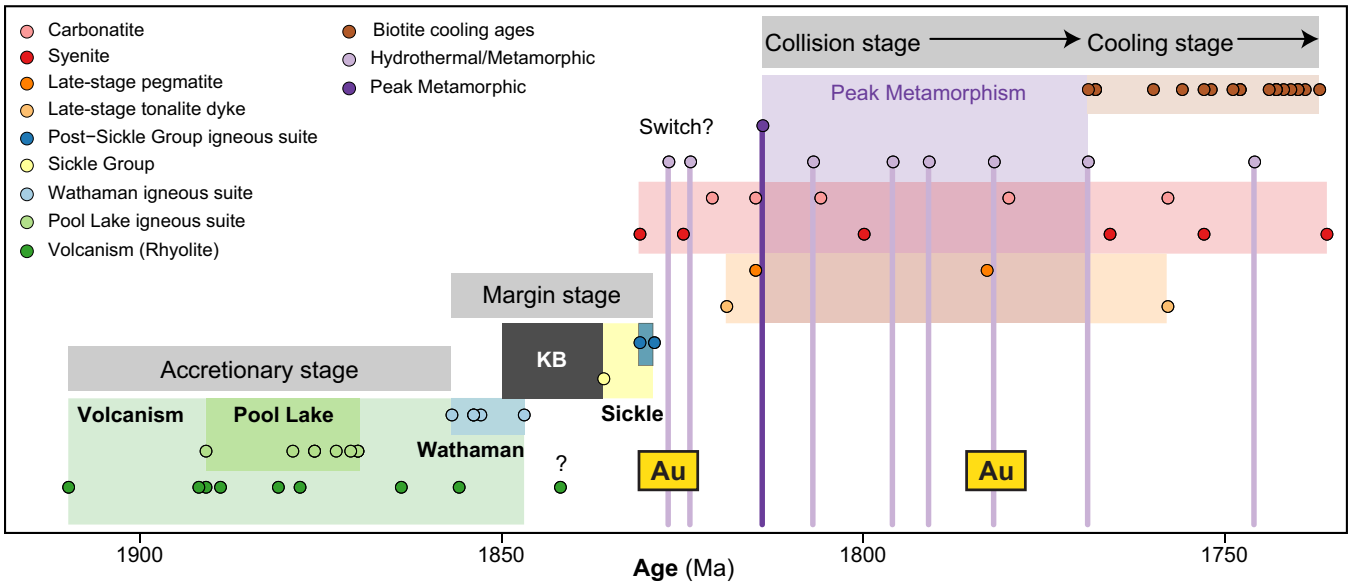

Figure 5. Compilation of previously reported and new ages for the Lynn Lake greenstone belt. Volcanic and plutonic U-Pb ages are from Baldwin et al. (1987), Turek et al. (2000), Beaumont-Smith and Böhm (2002, 2004), Beaumont-Smith et al. (2006), and Lawley et al. (2019). Inferred peak metamorphic zircon age from Beaumont-Smith and Böhm (2002, 2004). The scatter of syenite and carbonatite ages are from Elliott (2009) and may reflect a combination of crystallization ages and metamorphic resetting. Sickle Group (U-Pb detrital zircon maximum depositional age) and hydrothermal/metamorphic ages (Re-Os sulphide and U-Pb monazite and xenotime) were collected as part of the current study. Biotite cooling ages are from O'Connor et al. (2019).

and MacLellan groups south and west of Lynn Lake, respectively (Fig. 1; Ansdell et al., 1995; Machado et al., 1999; Maxeiner and Demmans, 2000; Zwanzig, 2000). South of the LLGB, synorogenic basins (i.e. Missi Group) share a similar tectonic evolution from rapid deposition, wide-spread intrusion of arc-like magmatism at 1.83–1.82 Ga (Ansdell and Norman, 1995; Norman et al., 1995; Connors et al., 1999; Machado et al., 1999; Zwanzig, 2000; Hollings and Ansdell, 2002), folding, burial, and peak metamorphism (ca. 1.81 Ga; Fig. 6). Ansdell and Norman (1995) suggested that the youngest of these intrusions (1.83–1.82 Ga) marks a period of intra-arc rifting prior to peak metamorphism. Extension and/or asthenospheric upwelling prior to the major phase of crustal thickening is partially supported by syenitic intrusions and mafic to ultramafic intrusions within the Kisseynew Basin (e.g. 1.83–1.82 Ga Touchbourne suite; Machado et al., 1999; Martins et al., 2011, 2012) and similar rocks east of Lynn Lake (ca. 1.83–1.82 Ga syenite within the Eden Lake complex; Fig. 1, 3, 5, 6; Chakhmouradian et al., 2008; Elliott, 2009). Potassic intrusions and volcanic rocks (i.e. Christopher Island Formation), which are exposed across much of the northern Trans-Hudson Orogen in Nunavut, occurred at broadly the same time (Ansdell, 2005). If correct, this brief synorogenic extensional period must have occurred immediately prior to crustal thickening, which ultimately led to the intrusion of crustally derived peraluminous granite at ca. 1816–1814 Ma (Kraus and Menard, 1997; Whalen et al. 1999; Zwanzig and Bailes, 2010) and pegmatite dykes (1815 ± 3 Ma; Fig. 5, 6; Beaumont-Smith and Böhm, 2002).

The timing of hydrothermal activity, metamorphism, and deformation are constrained by U-Pb monazite and xenotime ages (1.83–1.75 Ga; Lawley et al., 2019) and new Re-Os arsenopyrite ages reported herein (ca. 1.82 and 1.78 Ga; Fig. 5). The oldest, garnet-hosted xenotime provide a maximum age estimate for the peak metamorphic mineral assemblage at ≤1827 Ma, which is coeval with the oldest Re-Os model age of the highly radiogenic arsenopyrite sample at MacLellan (1824 ± 12 Ma). Both ages demonstrate that hydrothermal activity occurred within a few million years after deposition of the Sickle Group (1836–1831 Ma; Fig. 5, 6). One of the dated xenotime crystals occurs within the same veinlet as native Au (Lawley et al., 2019), which, coupled with close spatial association between arsenopyrite and ore zones at MacLellan, suggests that this earliest hydrothermal event was Au-bearing (Fig. 4a–c). The timing of early auriferous fluids marks an important transitional period in the development of the Trans-Hudson Orogen, which was triggered by the terminal collision between the composite Hearne-LLGB with the Superior and/or Sask cratons to the south (Fig. 5; Ansdell, 2005). Early-stage Au veins thus postdate the accretion of volcanic arcs (i.e. Wasekwan Group) to the Hearne cratonic margin by ca. 30 m.y. (Fig. 5). This early phase of auriferous fluids also predates most estimates for peak metamorphism within this part of the Trans-Hudson Orogen (ca. 1.81 Ga; Schneider et al., 2007), but are coeval with some estimates for an early-

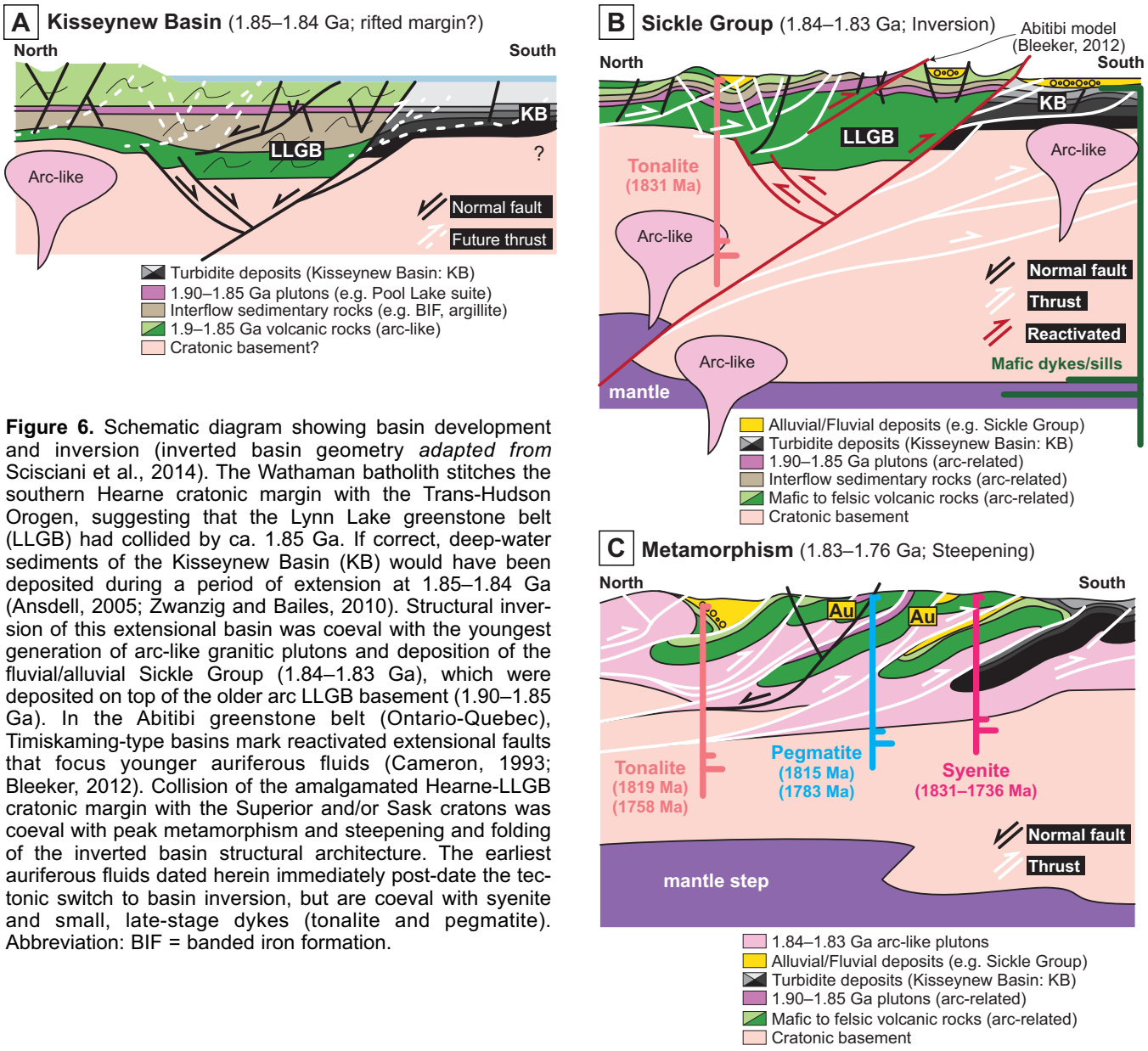

Figure 6. Schematic diagram showing basin development and inversion (inverted basin geometry *adapted from* Scisciani et al., 2014). The Wathaman batholith stitches the southern Hearne cratonic margin with the Trans-Hudson Orogen, suggesting that the Lynn Lake greenstone belt (LLGB) had collided by ca. 1.85 Ga. If correct, deep-water sediments of the Kisseynew Basin (KB) would have been deposited during a period of extension at 1.85–1.84 Ga (Ansdell, 2005; Zwanzig and Bailes, 2010). Structural inversion of this extensional basin was coeval with the youngest generation of arc-like granitic plutons and deposition of the fluvial/alluvial Sickle Group (1.84–1.83 Ga), which were deposited on top of the older arc LLGB basement (1.90–1.85 Ga). In the Abitibi greenstone belt (Ontario-Quebec), Timiskaming-type basins mark reactivated extensional faults that focus younger auriferous fluids (Cameron, 1993; Bleeker, 2012). Collision of the amalgamated Hearne-LLGB cratonic margin with the Superior and/or Sask cratons was coeval with peak metamorphism and steepening and folding of the inverted basin structural architecture. The earliest auriferous fluids dated herein immediately post-date the tectonic switch to basin inversion, but are coeval with syenite and small, late-stage dykes (tonalite and pegmatite). Abbreviation: BIF = banded iron formation.

stage of high-temperature, low-pressure metamorphism south of the LLGB, early folding and syenitic intrusions (e.g. 1.83–1.82 Ga; Fig. 5; Ansdell and Norman, 1995; Norman et al., 1995; Connors et al., 1999; Machado et al., 1999; Elliott, 2009; Martins et al., 2011).

Younger phosphate and sulphide ages suggest that hydrothermal activity and metamorphism continued for at least 80 m.y. after the onset of continent-continent collision (Fig. 5; Lawley et al., 2019). Arsenopyrite dated at 1782 ± 16 Ma based on the current study is broadly equivalent with individual hydrothermal monazite and xenotime ages that range from 1.81 to 1.77 Ga (Lawley et al., 2019). Monazite and xenotime at the margins of pyrite within the hydrothermal MacLellan host rocks, which, along with lesser sulphide-hosted phosphate inclusions, suggest that hydrothermal fluids overprinted auriferous veins during multiple tectonothermal events within this time interval (Fig. 4c,e,f). The punctuated hydrothermal history closely matches the clustering of metamorphic ages determined by monazite and titanite dating within unmineralized rocks peripheral to the LLGB (Schneider et al., 2007; Couëslan et al., 2013). Hydrothermal and/or metamorphic phosphate ages in the LLGB are also consistent with a broad period of high-temperature and low- to medium-pressure metamorphism across the Trans-Hudson Orogen, including peak metamorphic conditions during crustal thickening and on-going continent-continent collision at ca. 1.81 Ga (Beaumont-Smith and Böhm, 2002; Ansdell, 2005; Schneider et al., 2007; Couëslan et al., 2013). Ultimately, crustal thickening led to the production of pegmatite dykes (≤1.81 Ga) and other crustally derived

melts (e.g. 1816–1814 Ma peraluminous granite; Kraus and Menard, 1997; Whalen et al., 1999; Zwanzig and Bailes, 2010) during the same period (Fig. 6). Because sulphide replacement represents the dominant ore style in some parts of the MacLellan deposit, it is possible that hydrothermal fluids at ca. 1.78 Ga introduced new Au into the system (Fig. 5). The MacLellan deposit thus likely records multiple, overprinting Au-bearing events. A similar multi-stage genesis at this deposit was previously based on the relative chronology of veins and contrasting hydrothermal alteration assemblages (Samson and Gagnon, 1995; Samson et al., 1999; Hastie et al., 2018).

The youngest xenotime occurs with pyrite and is also aligned with the main, ductile deformation fabric (D_2) at the microscale, suggesting that deformation reactivated earlier structures at and/or after ca. 1746 Ma. Late-stage reactivation of early structures significantly postdates Re-Os arsenopyrite ages, which is consistent with folded and transposed auriferous veins at each of the studied deposits (Fig. 4). Metamorphism continued until approximately the same time based on new U-Pb apatite (1.75–1.70 Ga; O'Connor et al., 2019) and Ar-Ar biotite cooling ages (1.77–1.74 Ga; O'Connor et al., 2019). Continued cooling ultimately led to resetting of K-Ar biotite and muscovite ages to between 1.76 and 1.61 Ga (Fig. 5; Moore et al., 1960; Lowdon et al., 1963; Turek, 1967; O'Connor et al., 2019). It is possible that younger and undated hydrothermal events led to minor remobilization of Au into late-stage structures during cooling (Beaumont-Smith et al., 2000). However, pre- to syn-D_2 faults are the dominant structural control for Au mineralization across the LLGB (Anderson and Beaumont-Smith, 2001; Beaumont-Smith and Böhm, 2002). The ages and sequence of events described above are based on preliminary ages that will be refined in a future publication that is currently in preparation.

IMPLICATIONS FOR EXPLORATION

The timing of Au mineralization has important implication for ore system models and mineral exploration targeting. Giant orogenic Au deposits in the southern Abitibi greenstone belt (Ontario and Quebec) are interpreted to have formed late during the main deformational event (e.g. Canadian Malartic at 2664 ± 11 Ma: De Souza et al., 2015), which was coeval with or slightly pre-dating peak metamorphism (e.g. 2657.5 ± 4.4 Ma: Piette-Lauzière et al., 2019). This peak Abitibi Au event also occurred within a few million years after the closure of the synorogenic sedimentary basins (i.e. ca. 2669 Ma Timiskaming-type assemblage: Bleeker, 2012) and ca. 2680–2670 Ma alkaline magmatism. The spatial relationship between synorogenic basins and fertile fault segments have long been used as an exploration vector in the Abitibi (Cameron 1993, Hodgson, 1993; Robert et al., 2005; Bleeker, 2012).

The similar timing relationships between Au deposition, sedimentation, metamorphism, and alkaline magmatism documented for the LLGB herein points to a particular orogenic stage that is common to multiple Au districts through space and time (Fig. 5, 6; Kerrich and Wyman, 1989). Although the dated syenitic intrusions are not observed within the Au-deposit stratigraphy in the LLGB (Fig. 1) and are thus unlikely to represent the source of auriferous fluids, their timing, coupled with closure of the synorogenic basins, marks an important shift in the tectonic evolution of the Trans-Hudson Orogen (Fig. 5, 6). Ansdell (2005) suggested that alkalic, potassic, and carbonatitic magmatism and volcanism at this time was related to upwelling asthenosphere, which may have re-melted metasomatized portions of the lithospheric mantle after the termination of subduction. We demonstrate that the earliest auriferous fluids in the LLGB were coeval with this tectonic switch and were possibly driven by the heat from the upwelling asthenosphere (Fig. 5). In the Abitibi, upwelling asthenosphere was coeval with extensional basins as demonstrated by the deposition of deep-water sedimentary facies that are coeval with alkaline magmatism within the Timiskaming assemblage. Ansdell and Norman (1995) also attributed syenitic magmatism and synorogenic basins to a period of extension immediately predating continent-continent collision within the Trans-Hudson Orogen. Maximum depositional ages for deep-water facies within the Kisseynew Basin (≤1845 and ≤1842 Ga: Machado et al., 1999) are consistent with opening of synorogenic extensional basins at broadly the same time. However, deep-water facies are not recognized within the Sickle and Missi groups. Instead, these nominally younger synorogenic basins developed during an early phase of thrusting and folding (Fig. 6; Zwanzig, 1997), which obscures the link, if any, between extensional faulting and Au (cf. Bleeker, 2012). Sickle Group rocks also host very few Au occurrences and none of the major Au deposits in the LLGB (Fig. 2), which is unlike the mineralized Timiskaming-style basins in the Abitibi (e.g. Bleeker, 2012). In fact, synorogenic basins in the central Kisseynew Basin are almost entirely devoid of Au occurrences (Fig. 1). Because these basins were also metamorphosed and deformed by the same generations of faults that host Au in the LLGB, we speculate that their poor endowment is likely due to the scarcity of appropriate depositional traps and/or fluid focusing within the older greenstone belts. More fertile volcano-sedimentary panels may still underlie synorogenic basins in some cases, but such primary stratigraphic relationships have

since been reworked during multiple stages of folding and faulting (Fig. 6).

From an exploration perspective, the distribution of synorogenic basins and syenitic intrusions is likely to demarcate the large-scale, lithospheric architecture that may have been important for focusing auriferous fluids from their deep crustal and/or upper mantle source regions. Critically, this earliest phase of Au vein-hosted mineralization is overprinted by a later generation(s) of Au-rich veins, suggesting that this large-scale architecture was also important for focusing younger auriferous fluids within the evolving orogen (Fig. 5). The tectonic trigger for the younger, post-peak metamorphic fluids is less well understood, but is coeval with a second thermal pulse, as demonstrated by coeval prograde metamorphic monazite ages elsewhere in the Trans-Hudson Orogen (Schneider et al., 2007; Couëslan et al., 2013) and crustally derived pegmatitic dykes (Chiarenzelli et al., 1998; Bickford et al., 2005). The isotopic composition (Pb-Pb and Sm-Nd) of these pegmatitic dykes suggests that they may have remelted the Archean basement (Bickford et al., 2005). Crustal anatexis may have been triggered by significant crustal thickening (White, 2005) and/or some other as yet poorly defined subcrustal heat source. Together the data point to the importance of multiple thermal pulses (e.g. asthenospheric upwelling; crustal anatexis) as the main drivers of deep-seated fluids. The tectonic triggers for auriferous fluids were coeval with these thermal pulses, including the switch to the main collisional orogenic stage of the Trans-Hudson Orogen (Fig. 5). Ascending auriferous fluids were focused along large-scale structures before being deposited in a variety of geochemical and structural traps within the older accretionary arcs (Fig. 1, 2). Mineral exploration targeting should thus focus on identifying the large-scale architecture exploited by these fluids whilst also considering the most favourable depositional environments for Au within the host greenstone belts.

ACKNOWLEDGMENTS

This report is a contribution to NRCan's Targeted Geoscience Initiative Program (TGI-5). Support for this study was provided by Activity G-1.2: Paleoproterozoic Gold: Tectonic Triggers and Traps of the Gold Project. We thank Alamos Gold and the Manitoba Geological Survey for their continued support throughout the project. This report benefited from the review of Scott Anderson and Patrick Mercier-Langevin. We also acknowledge Elizabeth Ambrose for her editorial handling and review.

REFERENCES

Anderson, S.D. and Beaumont-Smith, C.J., 2001. Structural analysis of the Pool Lake-Boiley Lake area, Lynn Lake greenstone belt (NTS 64C/11); *in* Report of Activities 2001; Manitoba Industry, Trade and Mines, Manitoba Geological Survey, p. 76–85.

Ansdell, K. and Norman, A., 1995. U-Pb geochronology and tectonic development of the southern flank of the Kisseynew Domain, Trans-Hudson Orogen, Canada; Precambrian Research, v. 72, p. 147–167.

Ansdell, K.M., 2005. Tectonic evolution of the Manitoba–Saskatchewan segment of the Paleoproterozoic Trans-Hudson; Canadian Journal of Earth Science, v. 759, p. 741–759.

Ansdell, K.M., Sciences, G., Place, S., Sn, S., Lucas, S.B., Connors, K., and Stern, R.A., 1995. Kisseynew metasedimentary gneiss belt, Trans-Hudson orogen (Canada): Back-arc origin and collisional inversion; Geology, p. 1039–1043.

Baldwin, D.A., Syme, E.C., Zwanzig, H.V, Gordon, T.M., Hunt, P.A., and Stevens, R.D., 1987. U-Pb zircon ages from the Lynn Lake and Rusty Lake metavolcanic belts, Manitoba: two ages of Proterozoic magmatism; Canadian Journal of Earth Sciences, v. 24, p. 1053–1063.

Barley, M. and Groves, D., 1991. Supercontinent cycles and the distribution of metal deposits through time; Geology, v. 20, p. 291–294.

Beaumont-Smith, C., Machado, N., and Peck, D., 2006. New uranium-lead geochronology results from the Lynn Lake greenstone belt, Manitoba (NTS 64C11–16); Manitoba Science, Technology, Energy and Mines, Manitoba Geological Survey, Geoscientific Paper GP2006-1, 11 p.

Beaumont-Smith, C., 2003. Controls on gold mineralization associated with the Johnson shear zone and Agassiz metallotect, Lynn Lake greenstone belt: Summary of current activities (Parts of NTS 64C/10, /11, /12, /14, /15, /16); *in* Report of Activities 2000; Manitoba Industry, Trade and Mines, Manitoba Geological Survey, p. 49–50.

Beaumont-Smith, C., 2008. Geochemistry data for the Lynn Lake greenstone belt, Manitoba (NTS 64C11–16); Manitoba Science, Technology, Energy and Mines, Manitoba Geological Survey, Open File OF2007-1, 1 .zip file.

Beaumont-Smith, C. and Böhm, C., 2002. Structural analysis and geochronological studies in the Lynn Lake greenstone belt and its gold-bearing shear zones (NTS 64C10, 11, 12, 14, 15 and 16), Manitoba; *in* Report of Activities 2002; Manitoba Industry, Trade and Mines, Manitoba Geological Survey, p. 159–170.

Beaumont-Smith, C. and Böhm, C., 2004. Structural analysis of the Lynn Lake greenstone belt; *in* Report of Activities 2004; Manitoba Industry, Economic Development and Mines, Manitoba Geological Survey, p. 55–68.

Beaumont-Smith, C., Lentz, D., and Tweed, E., 2000. Structural analysis and gold metallogeny of the Farley Lake gold deposit, Lynn Lake greenstone belt; *in* Report of Activities 2000; Manitoba Industry, Trade and Mines, Manitoba Geological Survey, p. 73–81.

Bickford, M., Mock, T., Steinhart III, W., Collerson, K., and Lewry, J., 2005. Origin of the Archean Sask craton and its extent within the Trans-Hudson orogen: evidence from Pb and Nd isotopic compositions of basement rocks and post-orogenic intrusions; Canadian Journal of Earth Sciences, v. 42, p. 659–684.

Bleeker, W., 2012. Lode gold deposits in ancient deformed and metamorphosed terranes: The role of extension in the formation of Timiskaming basins and large gold deposits, Abitibi Greenstone Belt — A discussion; *in* Summary of Field Work and Other Activities 2012; Ontario Geological Survey, Open File Report 6280, p. 1–12.

Cameron, E.M., 1993. Precambrian gold: perspectives from the top and bottom of shear zones; The Canadian Mineralogist, v. 31, p. 917–944.

Carpenter, R.L., Duke, N.A., Sandeman, H.A., and Stern, R., 2005. Relative and absolute timing of gold mineralization along the

Meliadine trend, Nunavut, Canada: Evidence for Paleoproterozoic gold hosted in an Archean greenstone belt; Economic Geology, v. 100, p. 567–576.

Chakhmouradian, A.R., Mumin, A.H., Demény, A., and Elliott, B., 2008. Postorogenic carbonatites at Eden Lake, Trans-Hudson Orogen (northern Manitoba, Canada): Geological setting, mineralogy and geochemistry; Lithos, v. 103, p. 503–526.

Chiarenzelli, J., Aspler, L., Villeneuve, M., and Lewry, J., 1998. Early Proterozoic evolution of the Saskatchewan craton and its allochthonous cover, Trans-Hudson orogen; The Journal of Geology, v. 106, p. 247–267.

Connors, K.A., Ansdell, K.M., and Lucas, S.B., 1999. Coeval sedimentation, magmatism, and fold–thrust development in the Trans-Hudson Orogen: propagation of deformation into an active continental arc setting, Wekusko Lake; Canadian Journal of Earth Sciences, v. 291, p. 275–291.

Corrigan, D., Hajnal, Z., Németh, B., and Lucas, S.B., 2005. Tectonic framework of a Paleoproterozoic arc–continent to continent–continent collisional zone, Trans-Hudson Orogen, from geological and seismic reflection studies; Canadian Journal of Earth Sciences, v. 434, p. 421–434.

Corrigan, D., Pehrsson, S., Wodicka, N., and de Kemp, E., 2009. The Palaeoproterozoic Trans-Hudson Orogen: a prototype of modern accretionary processes; Geological Society, London, Special Publications, v. 327, p. 457–479.

Couëslan, C.G., Pattison, D.R.M., and Dufrane, S.A., 2013. Paleoproterozoic metamorphic and deformation history of the Thompson Nickel belt, Superior Boundary Zone , Canada, from in situ U-Pb analysis of monazite; Precambrian Research, v. 237, p. 13–35.

Davies, T., Richards, J.P., Creaser, R.A., Heaman, L.M., Chacko, T., Simonem, A., Williamson, J., and McDonald, D.W., 2010. Paleoproterozoic age relationships in the Three Bluffs archean iron formation-hosted gold deposit, Committee Bay greenstone belt, Nunavut, Canada; Exploration and Mining Geology, v. 19, p. 55–80.

De Souza, S., Dubé, B., McNicoll, V., Dupuis, C., Mercier-Langevin, P., Creaser, R., and Kjarsgaard, I., 2015. Geology, hydrothermal alteration, and genesis of the world-class Canadian Malartic stockwork-disseminated Archean gold deposit, Abitibi, Quebec; *in* Targeted Geoscience Initiative 4: Contributions to the Understanding of Precambrian Lode Gold Deposits and Implications for Exploration, (ed.) B. Dubé and P. Mercier-Langevin; Geological Survey of Canada, Open File 7852, p. 113–126.

Dubé, B. and Gosselin, P., 2007. Greenstone-hosted quartz-carbonate vein deposits; *in* Mineral Deposits of Canada: A Synthesis of Major Deposit-Types, District Metallogeny, the Evolution of Geological Provinces, and Exploration Methods, (ed.) W.D. Goodfellow; Geological Association of Canada, Mineral Deposits Division, Special Publication No. 5, p. 49–74.

Eckstrand, R. and Hulbert, L., 2007. Magmatic nickel-copper-platinum group element deposits; *in* Mineral Deposits of Canada: A Synthesis of Major Deposit-Types, District Metallogeny, the Evolution of Geological Provinces, and Exploration Methods, (ed.) W.D. Goodfellow; Geological Association of Canada, Mineral Deposits Division, Special Publication No. 5, p. 205–222.

Elliott, B.R., 2009. A mineralogical, geochemical and geochronological study of postorogenic carbonatites in the Eden Lake complex, northern Manitoba; M.Sc. thesis, University of Manitoba, Winnipeg, Manitoba, 200 p.

Faure, S., 2010. World Kimberlites CONSOREM Database (Version 3); Consortium de Recherche en Exploration Minérale CONSOREM, Université du Québec à Montréal. <www.consorem.com> [accessed 01/01/2019].

Galley, A.G., Hannington, M.D., and Jonasson, I.R., 2007. Volcanogenic massive sulphide deposits; *in* Mineral Deposits of Canada: A Synthesis of Major Deposit-Types, District Metallogeny, the Evolution of Geological Provinces, and Exploration Methods, (ed.) W.D. Goodfellow; Geological Association of Canada, Mineral Deposits Division, Special Publication No. 5, p. 141–161.

Gilbert, H., 1993. Geology of the Barrington Lake-Melvin Lake-Fraser Lake area; Manitoba Energy and Mines, Geological Services, Geological Services, GR87-3, p. 110.

Gilbert, H., Syme, E., and Zwanzig, H., 1980. Geology of the metavolcanic and volcaniclastic metasedimentary rocks in the Lynn Lake area; Manitoba Energy and Mines, Geological Services, GP80-1, p. 118.

Goldfarb, R., Snee, L., Miller, L., and Newberry, R., 1991. Rapid dewatering of the crust deduced from ages of mesothermal gold deposits; Nature, v. 354, p. 296–298.

Goldfarb, R., Phillips, G., and Nokleberg, W., 1998. Tectonic setting of synorogenic gold deposits of the Pacific Rim; Ore Geology Reviews, v. 13, p. 185–218.

Goldfarb, R.J. and Groves, D.I., 2015. Orogenic gold: Common or evolving fluid and metal sources through time; Lithos, v. 233, p. 2–26.

Goldfarb, R J., Groves, D.I., and Gardoll, S., 2001. Orogenic gold and geologic time: a global synthesis; Ore Geology Reviews, v. 18, p. 1–75.

Goldfarb, R.J., Taylor, R.D., Collins, G.S., Goryachev, N.A., and Felipe, O., 2014. Phanerozoic continental growth and gold metallogeny of Asia; Gondwana Research, v. 25, p. 48–102.

Groves, D., Goldfarb, R., Gebre-Mariam, M., Hagemann, S., and Robert, F., 1998. Orogenic gold deposits: A proposed classification in the context of their crustal distribution and relationship to other gold deposit types; Ore Geology Reviews, v. 13, p. 7–27.

Groves, D.I. and Santosh, M., 2016. The giant Jiaodong gold province: The key to a unified model for orogenic gold deposits?; Geoscience Frontiers, v. 7, p. 409–417.

Groves, D.I., Goldfarb, R.J., and Santosh, M., 2016. The conjunction of factors that lead to formation of giant gold provinces and deposits in non-arc settings; Geoscience Frontiers, v. 7, p. 303–314.

Hastie, E.C.G., Gagnon, J.E., Samson, I.M., and Lake, L., 2018. The Paleoproterozoic MacLellan deposit and related Au-Ag occurrences, Lynn Lake greenstone belt, Manitoba: An emerging, structurally-controlled gold camp; Ore Geology Reviews, v. 94, p. 24–45.

Hollings, P. and Ansdell, K., 2002. Paleoproterozoic arc magmatism imposed on an older backarc basin: Implications for the tectonic evolution of the Trans-Hudson orogen, Canada; Geological Society of America Bulletin, v. 114, p. 153–168.

Hodgson, C.J., 1993. Mesothermal lode-gold deposits; *in* Mineral deposits modeling, (ed.) R.V. Kirkham, W.D. Sinclair, R.I. Thorpe, and J.M. Duke; Geological Association of Canada, Special Paper 40, p. 635–678.

Kerrich, R. and Wyman, D., 1989. Geodynamic setting of mesothermal gold deposits: An association with accretionary tectonic regimes; Geology, v. 18, p. 882–885.

Kraus, J. and Menard, T., 1997. A thermal gradient at constant pressure: Implications for low- to medium-pressure metamorphism in a compressional tecotnic setting, Flin Flon and Kisseynew domains, Trans-Hudson, Orogen, Central Canada; The Canadian Mineralogist, v. 35, p. 1117–1136.

Lawley, C., Creaser, R.A., Jackson, S.E., Yang, Z., Davis, B., Pehrsson, S., Dubé, B., Mercier-Langevin, P., and Vaillancourt, D., 2015. Unravelling the western Churchill Province Paleoproterozoic gold metallotect: Constraints from Re-Os

arsenopyrite and U-Pb xenotime geochronology and LA-ICPMS arsenopyrite trace element chemistry at the BIF-hosted Meliadine Gold district, Nunavut, Canada; Economic Geology, p. 1425–1454.

Lawley, C., Davis, W., Jackson, S., Petts, D., Yang, E., Zhang, S., Selby, D., O'Connor, A., and Schneider, D., 2019. Paleoproterozoic gold and its tectonic triggers and traps; *in* Targeted Geoscience Initiative: 2018 report of activities, (ed.) N. Rogers; Geological Survey of Canada, Open File 8549, p. 71–75.

Lawley, C.J.M., Selby, D., Condon, D.J., Horstwood, M., Millar, I., Crowley, Q., and Imber, J., 2013. Lithogeochemistry, geochronology and geodynamic setting of the Lupa Terrane, Tanzania: Implications for the extent of the Archean Tanzanian Craton; Precambrian Research, v. 231, p. 174–193.

Leahy, K., Barnicoat, A., Foster, R., Lawrence, S., and Napier, R., 2005. Geodynamic processes that control the global distribution of giant gold deposits; *in* Mineral Deposits and Earth Evolution, (eds.) I. McDonald, A. Boyce, I. Butler, R. Herrington, and D. Polya; Geological Society, London, Special Publication, 248, p. 119–132.

Li, J., Bi, S., Selby, D., Chen, L., Vasconcelos, P., Thiede, D., Zhou, M., Zhao, X., Li, Z., and Qiu, H., 2012. Giant Mesozoic gold provinces related to the destruction of the North China craton; Earth and Planetary Science Letters, v. 350, p. 26–37.

Li, L., Santosh, M., and Li, S., 2015. The 'Jiaodong type' gold deposits: Characteristics, origin and prospecting; Ore Geology Reviews, v. 65, p. 589–611.

Lowdon, J., Stockwell, C., Tipper, H., and Wanless, R., 1963. Age determinations and geological studies; Geological Survey of Canada, Paper 62-17, p. 140.

Machado, N., Zwanzig, H., and Parent, M., 1999. U–Pb ages of plutonism, sedimentation, and metamorphism of the Paleoproterozoic Kisseynew metasedimentary belt, Trans-Hudson Orogen (Manitoba, Canada); Canadian Journal of Earth Sciences, v. 1842, p. 1829–1842.

Martins, T., Couëslan, C.G., and Böhm, C.O., 2011. GS-8 The Burntwood Lake alkali-feldspar syenite revisited, west-central Manitoba (part of NTS 63N8); *in* Report of Activities 2011; Manitoba Innovation, Energy and Mines, Manitoba Geological Survey, p. 79–85.

Martins, T., Couëslan, C.G., and Böhm, C.O., 2012. Rare metals scoping study of the Brezden Lake intrusive complex, western Manitoba (part of NTS 64C4); *in* Report of Activities 2012; Manitoba Innovation, Energy and Mines, Manitoba Geological Survey, p. 115–123.

Maxeiner, R. and Demmans, C.J., 2000. The final pieces of the "Bridge": Geology of the Southern Reindeer lake and Laurie lake areas; *in* Summary of Investigations 2000, Volume 2l; Saskatchewan Geological Survey, Saskatchewan Energy and Mines, Miscelaneous Report 2000-4.2, p. 30–50.

McDannell, K.T., Zeitler, P.K., and Schneider, D.A., 2018. Instability of the southern Canadian Shield during the late Proterozoic; Earth and Planetary Science Letters, v. 490, p. 100–109.

Meyer, M., Bickford, M., and Lewry, J., 1992. The Wathaman batholith: An Early Proterozoic continental arc in the Trans-Hudson orogenic belt, Canada; Geological Society of America Bulletin, v. 104, p. 1073–1085.

Moore, J., Hart, S., Barnett, C., and Hurley, P., 1960. Potassium-argon ages in Northern Manitoba; Bulletin of the Geological Society of America, v. 71, p. 225.

Norman, A., Williams, P., and Ansdell, K., 1995. Early Proterozoic deformation along the southern margin of the Kisseynew gneiss belt, Trans-Hudson Orogen: a 30 Ma progressive deformation cycle; Canadian Journal of Earth Sciences, v. 894, p. 875–894.

O'Connor, A.R., Lawley, C.J.M., and Schneider, D., 2019. Linking metamorphism and orogenic gold in the Proterozoic Lynn Lake greenstone belt, northern Manitoba; Geological Association of Canada-Mineralogical Association of Canada, Volume of Abstracts, v. 42, p. 153.

Pehrsson, S.J., Eglington, B.M., Evans, D.A.D., Huston, D., and Reddy, S.M., 2016. Metallogeny and its link to orogenic style during the Nuna supercontinent cycle; *in* Supercontinent Cycles Through Earth History, (ed.) Z. Li, D. Evans, and J. Murphy; Geological Society, London, Special Publication 424, p. 83–94.

Piette-Lauzière, N., Guilmette, C., Bouvier, A., Perrouty, S., Pilote, P., Gaillard, N., Lypaczewski, P., Linnen, R.L., and Olivo, G.R., 2019. The timing of prograde metamorphism in the Pontiac Subprovince, Superior craton; implications for Archean geodynamics and gold mineralization; Precambrian Research, v. 320, p. 111–136.

Richards, J.P., 2011. Magmatic to hydrothermal metal fluxes in convergent and collided margins; Ore Geology Reviews, v. 40, p. 1–26.

Robert, F., Poulsen, K.H., Cassidy, K.F., and Hodgson, C.J., 2005. Gold metallogeny of the Superior and Yilgarn Cratons; *in* Economic Geology 100th Anniversary Volume, (ed.) J.W. Hedenquist, J.F.H. Thompson, R.J. Goldfarb, and J.P. Richards; Society of Economic Geology, p. 1001–1033.

Samson, I. and Gagnon, J., 1995. Episodic fluid infiltration and genesis of the Proterozoic MacLellan Au-Ag deposit, Lynn Lake greenstone belt; Exploration and Mining Geology, v. 4, p. 33–50.

Samson, I.M., Blackburn, W.H., and Gagnon, J.E., 1999. Paragenesis and composition of amphibole and biotite in the MacLellan gold deposit, Lynn Lake greenstone belt, Manitoba, Canada; The Canadian Mineralogist, v. 37, p. 1405–1421.

Schneider, D.A., Heizler, M.T., Bickford, M.E., Wortman, G.L., Condie, K.C., and Perilli, S., 2007. Timing constraints of orogeny to cratonization: Thermochronology of the Paleoproterozoic Trans-Hudson orogen, Manitoba and Saskatchewan, Canada; Precambrian Research, v. 153, p. 65–95.

Scisciani, V., Agostini, S., Calamita, F., Pace, P., Cilli, A., Giori, I., and Paltrinieri, W., 2014. Positive inversion tectonics in foreland fold-and-thrust belts: A reappraisal of the Umbria–Marche Northern Apennines (Central Italy) by integrating geological and geophysical data; Tectonophysics, v. 637, p. 218–237.

Sillitoe, R., 2008. Major gold deposits and belts of the North and South American Cordillera: Distribution, tectonomagmatic settings, and metallogenic considerations; Economic Geology, v. 103, p. 663–687.

Smoliar, M., Walker, R., and Morgan, J., 1996. Re-Os ages of group IIA , IIIA , IVA , and IVB iron meteorites; Science, v. 271, p. 1099–1102.

Stein, H.J., Morgan, J.W., and Scherstén, A., 2000. Re-Os dating of low-level highly radiogenic (LLHR) sulfides: The Harnäs gold deposit, southwest Sweden, records continental-scale tectonic events; Economic Geology, v. 95, p. 1657–1672.

Stern, R.A., 1997. The GSC Sensitive High Resolution Ion Microprobe (SHRIMP): Analytical techniques of zircon U-Th-Pb age determinations and performance evaluation: Radiogenic Age and Isotopic Studies: Report 10; Geological Survey of Canada, Current Research 1997-F, p. 1–31.

Turek, A., 1967, Age of sulfide mineralization at Lynn Lake, Manitoba; Canadian Journal of Earth Sciences, v. 4, p. 572–574.

Turek, A., Woodhead, J., and Zwanzig, H., 2000. U-Pb Age of the gabbro and other plutons at Lynn Lake (Part of NTS 64C); *in*

Report of Activities 2000; Manitoba Industry, Trade and Mines, Manitoba Geological Survey, p. 97–104.

Whalen, J.B., Syme, E.C., and Stern, R.A., 1999. Geochemical and Nd isotopic evolution of Paleoproterozoic arc-type granitoid magmatism in the Flin Flon Belt, Trans-Hudson orogen, Canada; Canadian Journal of Earth Sciences, v. 36, p. 227–250.

White, D.J., 2005. High-temperature, low-pressure metamorphism in the Kisseynew domain, Trans-Hudson orogen: crustal anatexis due to tectonic thickening?; Canadian Journal of Earth Sciences, v. 721, p. 707–721.

Woolley, A. and Kjarsgaard, B., 2008. Carbonatite occurrences of the world: map and database; Geological Survey of Canada, Open File 5796, p. 28.

Wyman, D.A., Cassidy, K.F., and Hollings, P., 2016. Orogenic gold and the mineral systems approach: Resolving fact, fiction and fantasy; Ore Geology Reviews, v. 78, p. 322–335.

Zwanzig, H., 1997. Kisseynew metasedimentary gneiss belt, Trans-Hudson orogen (Canada): Back-arc origin and collisional inversion: Comment and Reply; Geology, p. 1995–1997.

Zwanzig, H., Syme, E., and Gilbert, H., 1999. Updated trace element geochemistry of ca. 1.9 Ga metavolcanic rocks in the Paleoproterozoic Lynn Lake belt; Manitoba Industry, Trade and Mines, Geological Services, Open File Report 99-13, p. 46.

Zwanzig, H.V, 2000. Structure and stratigraphy of the south flank of the Kisseynew Domain in the Trans-Hudson Orogen, Manitoba: implications for 1.845–1.77 Ga collision tectonics; Canadian Journal of Earth Sciences, v. 36, p. 1859–1880.

Zwanzig, H. and Bailes, A., 2010. Geology and geochemical evolution of the northern Flin Flon and southern Kisseynew domains, Kississing–File lakes area, Manitoba (parts of NTS 63K, N); Manitoba Innovation, Energy and Mines, Manitoba Geological Survey, Geoscientific Report GR2010-1, p. 135.

Superimposed Late Cretaceous and earliest Eocene gold mineralization and deformation events along the Llewellyn-Tally Ho deformation corridor in northwest British Columbia and southern Yukon

Sébastien Castonguay[1*], Luke Ootes[2], Fionnuala Devine[3], and Richard Friedman[4]

[1]Geological Survey of Canada, 490 rue de la Couronne, Québec, Quebec G1K 9A9
[2]British Columbia Geological Survey, Ministry of Energy, Mines and Petroleum Resources, Victoria, British Columbia V8W 9N3
[3]Merlin Geosciences Inc., Atlin, British Columbia V0W 1A0
[4]Pacific Centre for Geochemical and Isotopic Research, University of British Columbia, Vancouver, British Columbia V6T 1Z4
[*]Corresponding author's e-mail: sebastien.castonguay@canada.ca

ABSTRACT

A revised geological and metallogenic framework for the Llewellyn-Tally Ho deformation corridor in southern Yukon and northwest British Columbia is proposed. The long-lived fault zone generally demarcates the eastern and western limits of the Nisling (Yukon-Tanana) and Stikine terrane, respectively. Epithermal (e.g. Engineer mine), intrusion-related and 'mesothermal' (e.g. Bennett plateau - Middle Ridge areas and part of the Wheaton district and Wann River area) gold deposits and occurrences are spatially associated with the Llewellyn-Tally Ho deformation corridor.

The Llewellyn fault is a southeast-striking, steeply dipping, brittle and dextral strike-slip structure that overprints penetrative fabrics and ductile deformation. The Tally Ho shear zone, Yukon, represents a ductile deformation zone with a penetrative foliation and local mylonite zones. The Tally Ho shear zone is overprinted by late brittle faults, which likely correspond to the northern extension of the Llewellyn fault. Previous work and this study demonstrate that brittle strike-slip deformation along the Llewellyn fault occurred between ca. 56 and 50 Ma.

Two unfoliated ca. 75 Ma granodiorite intrusions crosscut the earlier ductile fabrics, which deform a ca. 98 Ma porphyry dyke in the Tally Ho shear zone and a ca. 98 Ma granodiorite pluton along its western limit, indicating that parts of the early ductile fabrics formed between ca. 98 and 75 Ma. At Bennett plateau, the Skarn Zone represents one of the "early" gold mineralization styles consisting of an amphibole-sulphide skarn with structurally controlled quartz-actinolite-carbonate veins within metasedimentary rocks of the Stuhini Group adjacent to Late (?) Cretaceous intrusions. A massive ca. 76 Ma dyke crosscuts the highly strained and hydrothermally altered host rock and hence provides a minimum age for the mineralization and ductile fabrics. To the south, the Engineer mine is a structurally controlled epithermal vein system related to second-order splays of the Llewellyn fault. A ca. 54 Ma dyke is cut and offset by the main-stage veins and related fractures locally providing a maximum age for mineralization. Vanadian-illite, dated at ca. 50 Ma and intergrown with gold from the Engineer vein constrains the timing of the main-stage veining and mineralization.

The ca. 20 Myr time-gap between the early and late deformation events and their respective gold mineralization not only confirms these occurred at different times and at different structural levels, but also suggest they are related to distinct tectonic events. The intrusion-related and 'mesothermal' gold mineralization along the Llewellyn-Tally Ho deformation corridor is associated with Late Cretaceous deformation and magmatism, and as such, is broadly coeval and analogous with some of the mineral occurrences of Dawson Range polymetallic belt in west-central Yukon. The epithermal mineralization and late brittle event are related to the earliest Eocene magmatism and the Llewellyn fault, and match the timing and tectonic framework of the Juneau gold camp in southeastern Alaska.

INTRODUCTION

Gold deposits of the Cordilleran Orogen range from ca. 180 to 50 Ma, occur at various crustal levels, and frequently result from changing kinematic regimes along major, long-lived fault zones (e.g. Goldfarb et al., 1998). In collaboration with the Yukon Geological

Castonguay, S., Ootes, L., Devine, F., and Friedman., R., 2020. Superimposed Late Cretaceous and earliest Eocene gold mineralization and deformation events along the Llewellyn-Tally Ho deformation corridor in northwest British Columbia and southern Yukon; *in* Targeted Geoscience Initiative 5: Contributions to the Understanding of Canadian Gold Systems, (ed.) P. Mercier-Langevin, C.J.M. Lawley, and S. Castonguay; Geological Survey of Canada, Open File 8712, p. 223–236. https://doi.org/10.4095/326039

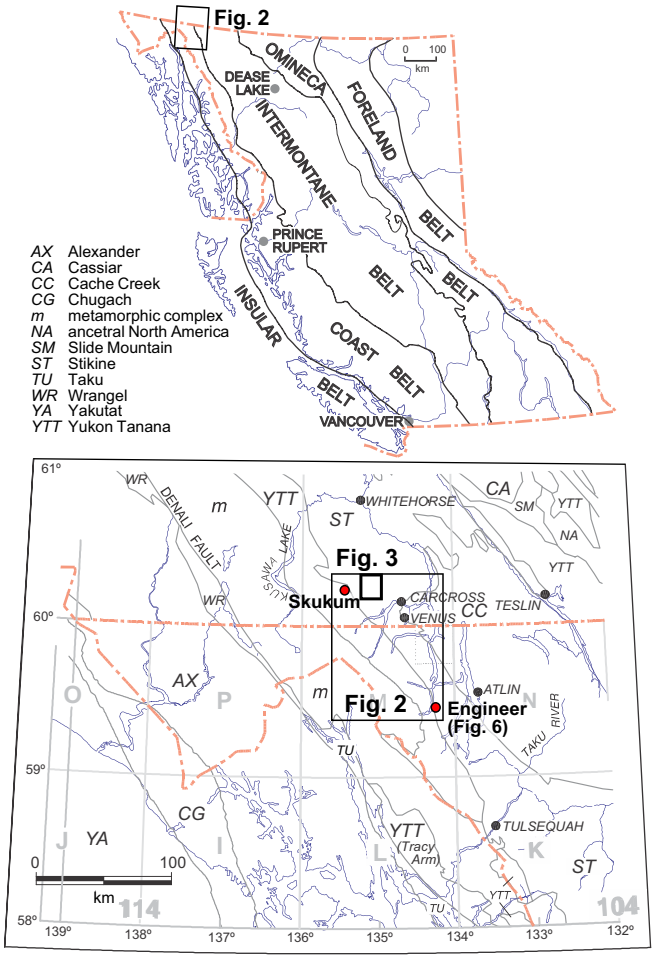

Figure 1. Location map with regional geography and terranes (*modified from* Mihalynuk et al., 1999).

Survey, this joint British Columbia Geological Survey (BCGS)-Geological Survey of Canada (GSC), Targeted Geoscience Initiative (TGI) supported study was designed to document the geological setting and controls on gold mineralization spatially associated with selected major fault zones of the Canadian Cordillera. The chosen field area extends from the Tagish Lake area of northwest British Columbia northward to the Wheaton River area in southern Yukon (Fig. 1, 2). This area is the locus of a series of structurally controlled, vein-hosted gold prospects and deposits, including past-producing mines (e.g. Engineer, Mount Skukum) that are spatially related to the Llewellyn fault and Tally Ho shear zone, which cut multiple lithotectonic suites (Fig. 2; e.g. Hart and Radloff, 1990; Mihalynuk et al., 1999; Tizzard et al., 2009). The Skarn Zone in the Bennett plateau - Middle Ridge area and the epithermal, low-sulphidation Engineer mine provide distinctive field laboratories to illustrate the two main types of gold mineralization along the Llewellyn - Tally Ho deformation corridor. Herein, we build on previous reports (Ootes et al., 2017, 2018, 2019; Castonguay et al., 2018) regarding the relationship between the Llewellyn fault and the Tally Ho shear zone and provide further constraints on the timing of ductile strain and associated gold mineralization that characterizes parts of this long-lived deformation corridor.

GEOLOGICAL SETTING

The Llewellyn fault, in northwest British Columbia, extends directly along strike from the Tally Ho shear zone in southwest Yukon (Fig. 1, 2). Herein both faults are considered as a composite structure and referred to as the Llewellyn-Tally Ho deformation zone or corridor. This northwest-striking deformation zone marks the boundary between the Nisling assemblage of the Yukon-Tanana terrane and the Stikine terrane to the west and east, respectively (Fig. 2; Hart and Radloff, 1990; Mihalynuk et al., 1999). Triassic-Jurassic and Early Cretaceous intrusive rocks, Late Cretaceous to Tertiary plutons (part of the Coast Plutonic Complex; Monger et al., 1982), and minor volcanic complexes occur on both sides of the Llewellyn-Tally Ho deformation zone, although predominantly to the west. Metamorphic grade within the deformation corridor is mostly greenschist facies (Hart and Radloff, 1990; Mihalynuk et al., 1999). A variety of gold prospects and minor past producers are spatially associated with this deformation zone (Fig. 2).

LLEWELLYN-TALLY HO DEFORMATION CORRIDOR

'Early' Deformation

In southern Yukon, the Tally Ho shear zone is defined by a 40 km long, kilometre-wide corridor of strongly deformed units of the Povoas Formation of the Lewes River Group (Upper Triassic; equivalent to Stuhini Group in British Columbia; Hart and Radloff, 1990). The shear zone comprises marble, mafic schist, and amphibolite that have a steep southwest-dipping penetrative foliation to mylonitic fabric, locally marked by a shallow southeast- or northwest-plunging mineral lineation (Hart and Radloff, 1990). Bedding is locally preserved in strongly deformed marble layers, but is folded and transposed into the foliation. The main foliation is locally folded, especially in less competent lithologies, such as the marble in the Tally Ho mountain area. The shear zone is bounded on either side by foliated Cretaceous intrusions, and by the Early Jurassic Bennett pluton to the southwest (Fig. 2, 3; Doherty and Hart, 1988; Hart and Radloff, 1990; Tizzard et al., 2009; Colpron et al., 2016). Brittle dextral fault zones are parallel to and overprint ductile fabrics, one of which occurs along the east side of the Tally Ho shear zone, and is considered part of the Llewellyn fault (Fig. 2, 3; Hart and Radloff, 1990).

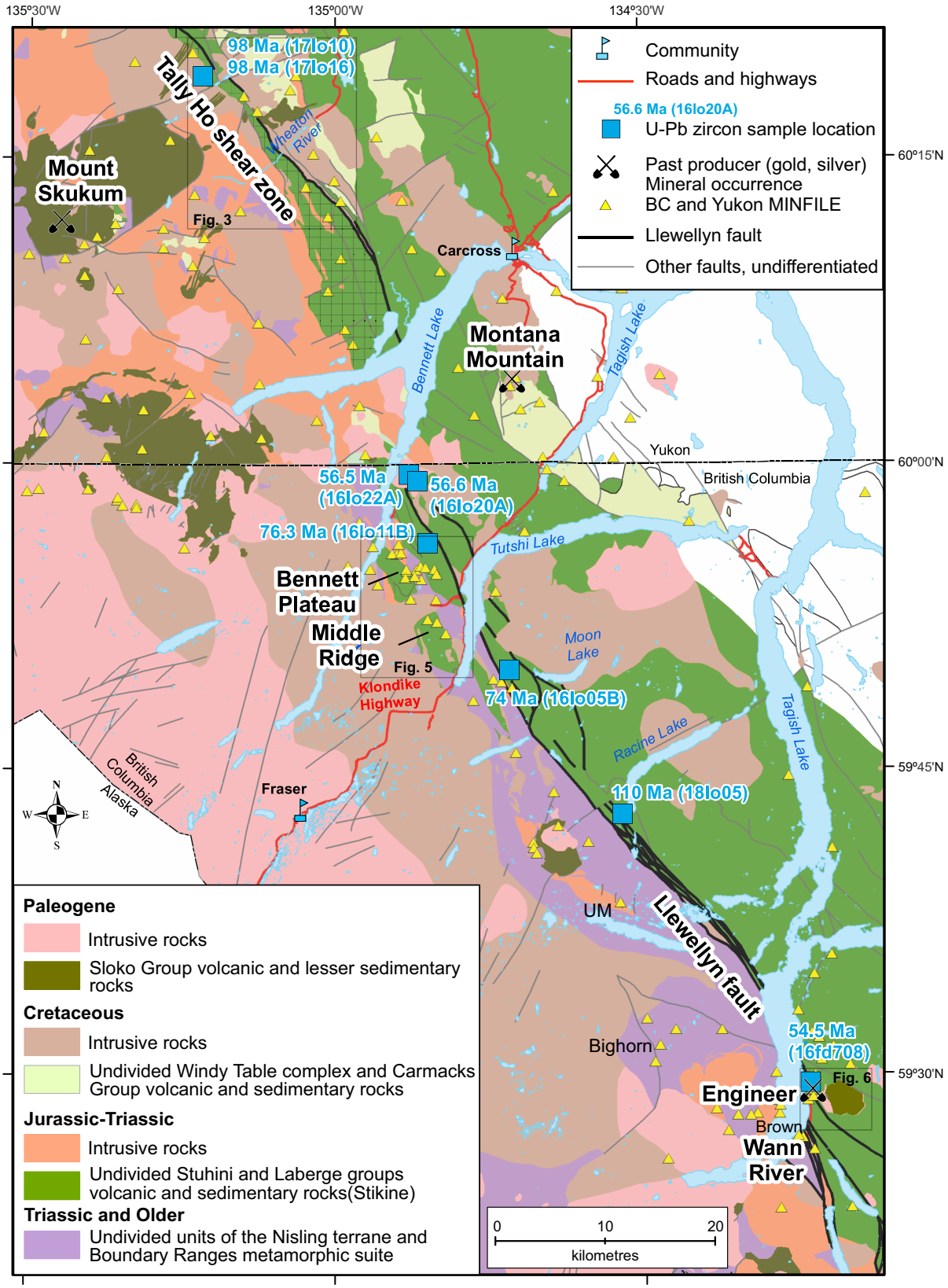

Figure 2. Generalized geology near the Llewellyn fault and Tally Ho shear zone (*modified from* Ootes et al., 2018, 2019). Geology is *after* Doherty and Hart (1988), Hart and Pelletier (1989), Hart and Radloff (1990), and Mihalynuk et al. (1999). Rocks of the Cache Creek assemblage (upper right) are unfilled. The square pattern outlines the Tally Ho shear zone in the Yukon as defined by Hart and Radloff (1990) and revisited by Tizzard et al. (2009). Although it is not formally delineated in British Columbia, Mihalynuk et al. (1999) recognized similar ductile high-strain zones along strike and within the Stuhini Group and Boundary Ranges metamorphic suite units.

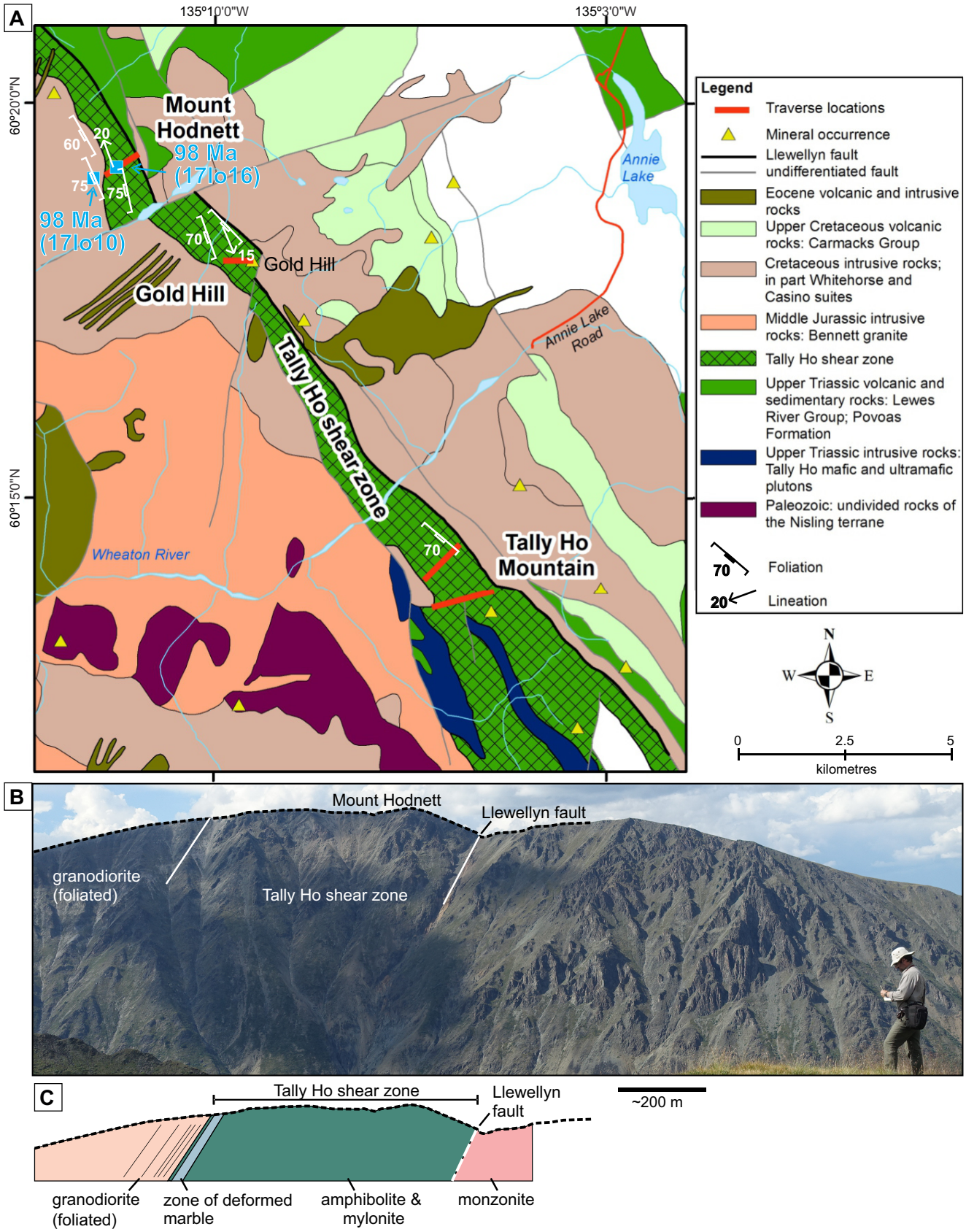

Figure 3. a) Generalized geology of the Tally Ho shear zone, southern Yukon (*modified after* Hart and Radloff, 1990). Foliations (line with pendants) and lineations (arrows) are from this study and Hart and Radloff (1990). **b)** View to the northwest of Mount Hodnett and the Tally Ho shear zone from Gold Hill. The trace of the Llewellyn fault is marked by a gossanous gully. **c)** Geological sketch of Mount Hodnett, in the upper left part of the photo; in part, *modified after* Tizzard et al. (2009).

Hart and Radloff (1990) interpreted the Tally Ho shear zone as a sinistral, terrane-bounding thrust fault that initially formed between 230 and 220 Ma. The lower age limit of deformation is based on a zircon U-Pb regressive intercept age of ca. 220 Ma (Doherty and Hart, 1988) for a sample of massive Bennett pluton collected roughly 3 km west of Tally Ho shear zone. Alternatively, Tizzard et al. (2009) considered that the shear zone represents a top-to-the-east crustal-scale thrust fault that juxtaposed foliated gabbro and pyroxenite (hanging wall) over Povoas Formation (shear zone and footwall). Faulted rocks were subsequently folded during the Nisling-Stikine collision. Tizzard et al. (2009) provided U-Pb zircon ages of ca. 208 Ma for a foliated leucogabbro in the hanging wall and ca. 173 Ma for a massive megacrystic granite sample (part of the Bennett granite; Fig. 3) west of the shear zone, which they interpreted as bracketing the timing of thrusting and subsequent folding. However, although the Bennett granite is not pervasively deformed, it contains xenoliths of foliated and unstrained Povoas Formation and is locally weakly foliated at its eastern margin and affected by the Tally Ho shear zone deformation, such as sinistral shear bands (Hart and Radloff, 1990). Consequently, there is evidence of a post-Early Jurassic ductile fabric, and the Tally Ho shear zone must have been active after ca. 173 Ma.

Traverses across the Tally Ho shear zone were conducted in the Tally Ho Mountain, Gold Hill, and Mount Hodnett areas of Yukon (Fig. 2, 3; Castonguay et al., 2018; Ootes et al., 2018, 2019). The best exposed section is at Mount Hodnett (Fig. 3) where units include (from west to east): weakly to moderately foliated granodiorite in sheared intrusive contact with steeply west-dipping amphibolite and marble; strongly sheared mafic volcaniclastic rocks (mylonite); and foliated metabasalt, locally intruded by massive to weakly foliated (at contacts) intermediate feldspar porphyry dykes. The steep southwest-dipping main foliation (S_{main}) occurs in most rocks but is best developed in mylonitic volcaniclastic beds. To the east, the shear zone mostly comprises strongly foliated amphibolite and metabasalt. Rare kinematic indicators include shear bands, sigmoidal clasts, and quartz vein boudins, which indicate apparent northeast-directed motion (Ootes et al., 2018). However, the shallowly southeast- or locally northwest-plunging stretching and/or mineral lineation on the S_{main} foliation and frequent L-S tectonites indicate a strike-slip component. Along the eastern side of the shear zone, the foliated amphibolite/metabasalt is structurally interlayered with moderately foliated monzonite of the Wheaton River pluton (part of the Late Cretaceous Casino suite; Colpron et al., 2016; Fig. 3). This juxtaposition is the result of a less than 10 m wide subvertical brittle high-strain zone, the Llewellyn fault (*see below*), which is marked by cataclasite and carbonate alteration that overprints the foliation in the metabasalt. All units are intruded by late, massive, intermediate to felsic feldspar-porphyritic dykes.

The granodiorite west of the shear zone (Fig. 3) is assigned to the Whitehorse plutonic suite (ca. 112–98 Ma; Hart and Radloff, 1990; Colpron et al., 2016). This granodiorite contains a steep southwest-dipping heterogeneously developed foliation (Fig. 4a), defined by chlorite-altered biotite and hornblende, which occurs in southeast-trending, high-strain corridors, and increases in intensity northeast toward the fault contact with the mylonitic metabasalt. This foliation in the granodiorite strikes south-southeast, dips west, and is subparallel to the S_{main} foliation in the shear zone (Ootes et al., 2018). In the contact zone, the foliated intrusion becomes progressively finer grained, more felsic, and interfingered with the mylonitic metabasalt. Basalt xenoliths also occur in strongly foliated granodiorite. The contact is overprinted by brittle fault and breccia zones and intruded by a late, massive, intermediate dyke. Based on these relationships, including the eastward-increasing heterogeneous strain gradient observed in the granodiorite and the occurrence of only one subparallel penetrative foliation across both units, the zone is interpreted as a sheared intrusive contact (Ootes et al., 2018, 2019). Ductile strain along this faulted contact was strongly partitioned in the metabasalt during the development of the Tally Ho shear zone. Two samples were analyzed for U-Pb zircon geochronology (Table 1; Ootes et al., 2018). The first sample comes from a moderately foliated granodiorite (sample 17lo10; Fig. 3) collected roughly 110 m west of the Tally Ho shear zone, which yielded a $^{206}Pb/^{238}U$ weighted mean zircon age of ca. 98.6 Ma (4 of 5 analyzed zircon grains), which is interpreted as the crystallization age of the granodiorite. The second sample (17lo16) is from the central part of an approximately 8 m thick feldspar porphyritic monzonite dyke intruding the metabasalt within the shear zone. The dyke is massive to locally weakly foliated (marked by the alignment of amphibole and biotite grains; Fig. 4b) and is probably folded. Five analyzed grains yielded ages between 98 and 99 Ma, and all are concordant. An older grouping of three results, at ca. 98.6 Ma, are interpreted as xenocrysts or possibly antecrysts, with two overlapping results at ca. 98.3 Ma, which is taken as the best age estimate for crystallization of the dyke. Ootes et al. (2019) previously incorrectly reported preliminary analytical results of this sample as having a maximum age of ca. 95 Ma.

‘Late’ Deformation

The Llewellyn fault is an over 100 km long, northwest-striking, steeply dipping, brittle dextral strike-slip

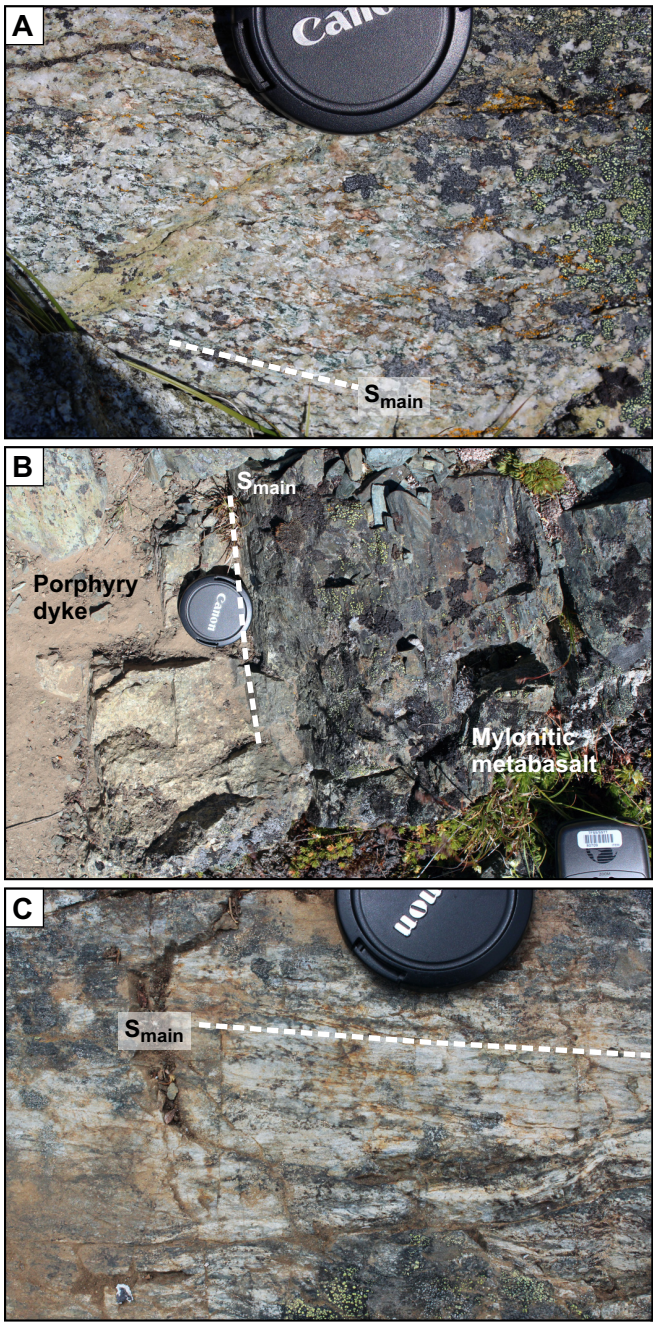

Figure 4. a) A foliated granodiorite near sample locality 17lo10, roughly 110 m west of the Tally Ho shear zone at Mount Hodnett, Yukon. **b)** A sheared intrusive contact, subparallel to the S_{main} schistosity, between a weakly foliated dyke and a mylonitic metabasalt within the Tally Ho shear zone at Mount Hodnett. **c)** A moderately foliated rhyolitic rock at sample locality 18lo05, along the Llewellyn fault zone, west of Racine Lake, British Columbia. For scale, the lens cap is 6 cm in diameter. *See* Figures 2 and 3 for location.

structure that extends from the Tulsequah region in the south to past the Mount Hodnett area in the Yukon (Fig. 1; Hart and Radloff, 1990; Mihalynuk et al., 1994, 1999). In northernmost British Columbia, it juxtaposes the Boundary Ranges metamorphic suite to the west (pre-Triassic; part of Nisling/Yukon Tanana terrane) against the volcano-sedimentary rocks of the Stuhini and Laberge groups to the east (Triassic-Jurassic; part of the Stikine Terrane; Fig. 2; Mihalynuk et al., 1999). The Llewellyn fault mostly consists of several anastomosed splays representing duplexes, marked by recessive zones of gouge comprising shear bands and slickensided surfaces, and locally developed L-S tectonites. As mentioned above, the Llewellyn fault overprints rocks affected by earlier south-southeast-trending penetrative fabrics, correlative with those of the Tally Ho shear zone (i.e. S_{main}). The S_{main} ductile fabric post-dates deposition of the Jurassic Laberge Group and is much better developed in the Boundary Ranges metamorphic suite (S_2 of Mihalynuk et al., 1999), where it is folded by northeast-verging folds, similar to those occurring at Tally Ho Mountain. Latest Cretaceous and Eocene plutons crosscut the ductile fabrics, providing a minimum age for the ductile deformation (Mihalynuk et al., 1999).

U-Pb geochronological data from key localities along the Llewellyn fault, south of the British Columbia-Yukon border, including the Bennett plateau area and a few others southeastward toward Tagish Lake, British Columbia (Fig. 2; Table 1; Ootes et al., 2017, 2018), provide constraints on the timing of structural and gold mineralization events. Two different granitic intrusions from east of Bennett Lake were dated (Fig. 2). A medium-grained unfoliated granite with K-feldspar phenocrysts (sample 16lo20A), mapped as middle Cretaceous to Tertiary (Mihalynuk et al., 1999), and intruding foliated Laberge Group metasedimentary rocks, yielded a weighted average $^{206}Pb/^{238}U$ concordant zircon age of 56.58 ± 0.07 Ma (2σ), which is interpreted as the crystallization age of the granite (Ootes et al., 2018). The second biotite-hornblende granite, mapped as the middle Cretaceous to Tertiary Pennington pluton (Hart and Radloff, 1990; Mihalynuk et al., 1999), crosscuts ductile fabrics but contains closely spaced (<30 cm), moderately east-dipping, brittle fractures that are subparallel and probably related to the Llewellyn fault (sample 16lo22A; Fig. 2). A $^{206}Pb/^{238}U$ weighted mean of four of the five concordant zircon analyses yields a crystallization age of 56.46 ± 0.06 Ma (Ootes et al., 2018).

A fine- to medium-grained, weakly porphyritic granodiorite pluton occurs within the trace of the Llewellyn fault, west of Moon Lake (Fig. 2), where it cuts the contact between the Stuhini Group and the Boundary Ranges metamorphic suite. The granodiorite is not foliated, but it contains moderate carbonate alteration and partially chloritized biotite and hornblende. The granodiorite post-dates the ductile deformation preserved in the host argillite, but is cut by a southeast-striking two metre wide gouge zone that is part of the Llewellyn fault (Ootes et al., 2017). A sample of the

Table 1. Geochronological data for the Llewellyn-Tally Ho deformation corridor area.

Sample	Location	Rock type	Field relationship	Method	Age (Ma)	Reference
	Engineer mine	quartz-vanadian mica vein	mineralized vein	$^{40}Ar/^{39}Ar$ V-illite	49.9 ± 0.25	Millonig et al. (2017)
16fd708	Engineer mine	monzodiorite dyke	cut by mineralized vein	U-Pb zircon	ca. 54.5	This report; preliminary
	Mt Skukum deposit	Au-quartz-calcite-adularia vein	mineralized vein	$^{40}Ar/^{39}Ar$ adularia	54.05 ± 0.31	Love et al. (1998)
16lo22A	Bennett Lake	biotite-hornblende granite	unfoliated	U-Pb zircon	56.46 ± 0.06	Ootes et al. (2018)
16lo20A	Bennett Lake	K-feldspar granite	unstrained	U-Pb zircon	56.58 ± 0.07	Ootes et al. (2018)
16lo05B	west of Moon Lake	biotite-hornblende granodiorite	unfoliated	U-Pb zircon	ca. 74	Ootes et al. (2018)
16lo11B	Bennett plateau	granodiorite porphyry	unfoliated	U-Pb zircon	76.30 ± 0.05	Ootes et al. (2018)
17lo16	Mount Hodnett	monzonite dyke	weakly foliated/folded	U-Pb zircon	ca. 98.3	This report; preliminary
17lo10	Mount Hodnett	biotite-hornblende granodiorite	foliated	U-Pb zircon	ca. 98.6	This report; preliminary
18lo05	SW of Racine Lake	rhyolitic unit	foliated	U-Pb zircon	ca. 110.2	This report; preliminary
	Middle Ridge	volcanic unit	openly folded	U-Pb zircon	124.9 ± 0.5	Mihalynuk et al. (2003)
	Tally Ho Mountain	megacrystic granite	massive	U-Pb zircon	172.9 ± 0.2	Tizzard et al. (2009)
	Tally Ho Mountain	Tally Ho leuco-gabbro	foliated	U-Pb zircon	208.4 ± 4.3	Tizzard et al. (2009)

least altered part of the granodiorite (sample 16lo05B) was collected near the contact with the host argillite, and yielded concordant to slightly discordant zircon analyses with a range of $^{206}Pb/^{238}U$ ages from ca. 92 to 74 Ma (Ootes et al., 2018), the youngest of which (i.e. 73.9 ± 0.3 Ma) gives the best estimate for the timing of crystallization.

Southwest of Racine Lake, along splays of the Llewellyn fault, is a zone of imbricated Stuhini and Laberge group rocks juxtaposed against the Boundary Ranges metamorphic suite (Mihalynuk et al., 1999). There, a penetrative moderate to strong foliation, potentially related to the regional S_{main} foliation, affects fault-bounded slices of carbonate-altered 'rhyolite' (Fig. 4c). The rhyolitic unit was sampled twice (samples 16lo18B and 18lo05) for geochronology. The first yielded two overlapping and concordant zircon results at ca. 121 Ma (reported in Ootes et al., 2018) and reinterpreted herein as xenocrysts or grains with older inheritance. The second gives a weighted $^{206}Pb/^{238}U$ crystallization age of ca. 110.2 Ma, based on the two youngest concordant and overlapping results.

GOLD MINERALIZATION

The Llewellyn-Tally Ho deformation corridor is spatially related to structurally controlled gold mineralization that has characteristics ranging from (1) 'mesothermal' (as per historically entrenched in the regional literature and assessments reports), such as the auriferous quartz veins (e.g. Bighorn, UM showings: Mihalynuk et al., 1999) and the polymetallic veins of the Wheaton district (e.g. Gold Hill: Hart and Radloff, 1990), the Wann River area south of the Engineer mine (e.g. Wann River project: Blind Creek Resources Limited, 2012; Engineer Gold Mines Limited, 2018), and part of the Montana Mountain mines (e.g. Venus vein; Fig. 2; Roots, 1981; Walton, 1986; Hart and Pelletier, 1989; Hart and Radloff, 1990); to (2) intrusion-related, such as the Bennett plateau and Middle Ridge prospects (Golden Eagle project: Mihalynuk et al., 2003; Wark, 2012); to (3) epithermal, such as the Engineer and Mount Skukum mines (Love, 1990, Love et al., 1998; Millonig et al., 2017; O'Brien et al., 2018).

Except for Montana Mountain mines, which are closer and probably related to reactivation of the Nahlin fault (Hart and Pelletier, 1989), the intrusion-related and 'mesothermal' gold mineralization is hosted in metamorphosed and moderately to strongly foliated units of Stuhini/Lewes River groups and Boundary Range metamorphic suite and predominantly occurs in the central part of the deformation corridor that is west of the Llewellyn fault (*sensu stricto*). The epithermal gold mineralization occurs on both sides of this deformation corridor and coincides both spatially and temporally with Eocene volcanic complexes and brittle faults (Love et al., 1998; Millonig et al., 2017; Ootes et al., 2018, 2019), suggesting a possible genetic relationship between large-scale deformation zones, gold mineralization, and Eocene magmatism in southwest Yukon and northwest British Columbia.

'Early' Intrusion-Related and 'Mesothermal' Gold

Some of the gold and base metal mineralization along the Llewellyn-Tally Ho deformation corridor predates, or is synchronous to late versus ductile deformation fabrics, and termed herein as 'early' mineralization. As mentioned above, some of this mineralization has been historically described in assessment or governmental reports as 'mesothermal' (as per Nesbitt et al., 1986). Although not studied in detail herein, these occurrences are likely analogs to deep epizonal to shallow mesozonal mineralization (as per Groves et al., 1998) to best match the depicted vein types and the deformation style of the host rocks.

A good and better documented example of 'early' mineralization are prospects named the Skarn Zone and Tannis (also known as Middle Ridge), which are part of a series of amalgamated mineral claims referred to as the Golden Eagle property (e.g. Rowins, 1997; Wark,

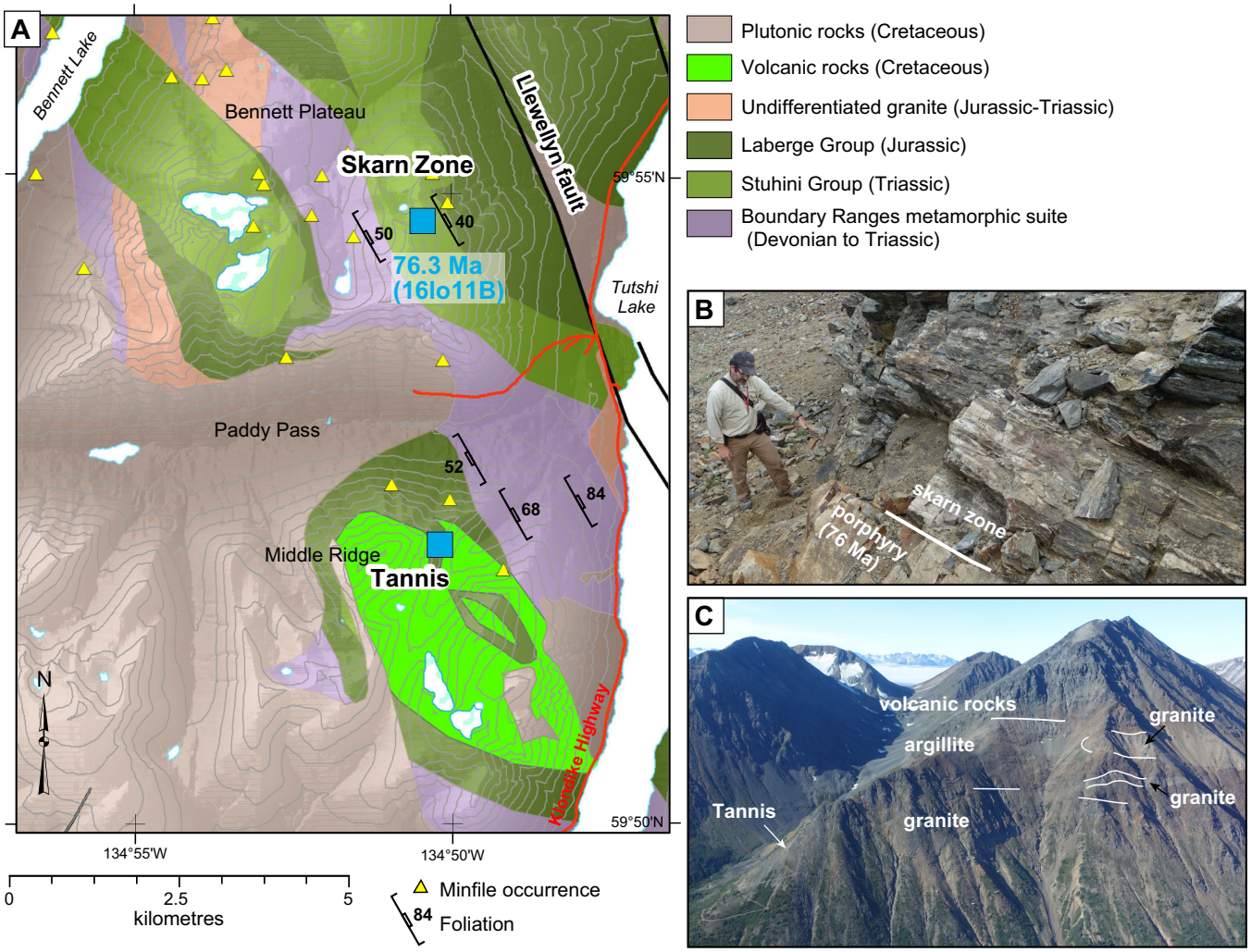

Figure 5. a) Generalized geology of the Bennett plateau - Middle Ridge area. Geology is *after* Mihalynuk et al. (1999). **b)** Typical exposure of the Skarn Zone near Bennett plateau, where an unfoliated porphyry intruded previously strongly deformed metasedimentary rocks of the Stuhini Group that host hydrothermal quartz-actinolite veins. The view is northeast. **c)** Aerial view of Middle ridge looking south-southwest.

2012). Both occurrences are west of Tutshi Lake and east of Bennett Lake on different mountains, separated by Paddy Pass (Fig. 2). In general, mineralization in this area was originally explored in the late 1800s and early 1900s, but, except for a few exploration adits and drillholes, there has been no development. Recent exploration drilling took place in the late 1980s to mid-2000s and in 2011, with varying results (e.g. Rowins, 1997).

The Skarn Zone (Fig. 5a,b) is a structurally controlled, amphibole-sulphide skarn that is thought to be related to felsic dykes and the sheared contact between the Stuhini Group and Boundary Range metamorphic suites (locally termed the "Paddy fault"; e.g. Rowins, 1997; Wark, 2012). Gold and base metal mineralization (disseminated pyrrhotite, chalcopyrite, and minor pyrite) is hosted within amphibole-albite-calcite-sulphide skarn and deformed (boudinaged and folded) quartz-actinolite-carbonate veins. Most of these veins cut metasedimentary rocks of the Stuhini Group and are adjacent (underlying) to Cretaceous intrusions (Rowins, 1997). The mineralization is erratic, with one historical sample reported to contain >185 g/t Au, with the vast majority of results indicating 1 g/t Au over 1 to 9 m and locally 100 g/t Au over narrow widths (Rowins, 1997 and references therein). More recent drilling on the Skarn Zone intersected 36.5 m grading 1.3 g/t Au, including a 4.1 g/t Ag over 15.5 m interval, in altered felsic volcanic units (Troymet Exploration Corporation, 2014). A two metre thick unfoliated granodiorite porphyry, which intruded the Skarn Zone subparallel to the host-rock fabrics (Fig. 5b), postdates the ductile deformation. Uranium-Pb zircon dating of this granodiorite porphyry (sample 16lo11B; Fig. 2) yielded a weighted mean age (four concordant zircon analyses) of 76.30 ± 0.05 Ma, which is interpreted as the crystallization age of the intrusion (Ootes et al., 2018). The age of the mineralization is unresolved, but the spatial

relationship with Cretaceous intrusions (undated) suggests that it occurred between ca. 98 and 76 Ma.

South of Bennett plateau, at Middle Ridge (Fig. 5a,c), a series of auriferous quartz-arsenopyrite veins are hosted in fine-grained granite and quartz porphyry, and along the contacts between the Laberge Group and Boundary Range metamorphic suite (Tannis prospect; Mihalynuk et al., 2003; Wark, 2012). Multiple sets of veins are present in the pervasively fractured host rock. The main mineralized vein set is discordant (N070/85) to the main regional fabric (north-northwest), but lesser north-northwest-striking veins are subparallel to the regional foliation. The highest gold values near the Tannis zone from surface sampling yielded between 1.0 and 13.8 g/t Au. Drill core assays range between 0.2 g/t Au over 13 m to 66 g/t Au over 0.6 m, and are typically around 1–3 g/t Au over 1.0 to 1.5 m (Wark, 2012). The intrusions crosscut ca. 124 Ma volcanic rocks (Mihalynuk et al., 2003), providing a local maximum age for mineralization. Mihalynuk et al. (2003) suggested that this mineralization was genetically related to underlying Late Cretaceous intrusions.

'Late' Epithermal Gold

The vein system at the Engineer mine is an important example of Eocene epithermal gold mineralization along the Llewellyn fault (Fig. 2; e.g. Mihalynuk et al., 1999; Millonig, et al., 2017; O'Brien et al., 2018). It is spatially associated to a roughly 20º-clockwise variation in the orientation of the Llewellyn fault at Tagish Lake. The vein system is related to a dextral fault zone referred to as 'Shear A', which is a southeastward splay of the Llewellyn fault where the main fault trends under the south end of Tagish Lake (Fig. 6a). The mine occurs adjacent to the Engineer Mountain volcanic complex (part of the Eocene Sloko Group; Mihalynuk et al., 1999), approximately 600 m vertically below the basal unconformity where Eocene volcanic rocks rest on Laberge Group sedimentary rocks.

Gold-bearing veins were discovered on the shore of Tagish Lake in 1899 by prospectors (e.g. O'Brien et al., 2018). This initial discovery led to significant mine development and continues to spur exploration interest in the region to this day. Over three kilometres of underground workings over eight levels (180 m vertical extent) were excavated from 1912 to 1927 during two main phases of mine development. The high-grade sections of the veins were targeted, with the Engineer and Double Decker veins being the highest producing (Fig. 6b). Reported production for 1925–1926 was over 10,000 ounces at an average grade of 26.4 g/t Au (O'Brien et al., 2018). Mining used stoping methods, creating a series of interconnected workings primarily following the main producing veins. The well exposed underground geology was mapped as part of an exploration program in 2008 (Fig. 6b; Devine, unpub. rep.). Recent drilling across the Double Decker vein revealed an interval of 22.3 g/t Au over 0.96 m (0.8 m true width; BCGE10-01; O'Brien et al., 2018).

The Engineer vein system includes a series of veins hosted in argillite and wacke of the Laberge Group and occurring on both sides of the Shear A fault (Fig. 6b). Veins include multistage vuggy and drusy quartz and carbonate (Fig. 6c) with gold-sulphide mineralization in multiple forms, namely as free gold in quartz, gold intergrown with vanadian illite, and gold associated with arsenopyrite (Millonig et al., 2017). On the southern side of the fault, the gold-rich Engineer and Double Decker vein systems are 5 cm to 2 m, locally up to 5 m thick, forming anastomosing sets of moderately to steeply southeast-dipping veins that pinch and swell along strike. Along with a series of more minor veins, these extensional veins outline a pattern correlative with dextral brittle deformation along the northeastern side of Shear A. Evidence of brittle shearing with identical relationships to the macro scale are mimicked in core (Fig. 6d). Sulphide (mainly pyrite)-cemented hydrothermal breccia along the northeastern side of the Shear A deformation zone was emplaced contemporaneous with this latest movement (Fig. 6e). Vanadian-illite intergrown with gold from the Engineer vein returns an age of 49.9 ± 0.25 Ma ($^{40}Ar/^{39}Ar$: Millonig et al., 2017). This age is interpreted to constrain the main-stage veining and mineralization and the most recent movement on Shear A.

The main-stage veining and youngest deformation events along the Shear A fault overprint several older features in the Engineer area. The foliation in the host Laberge Group sedimentary rocks progressively increases in intensity towards the south side of Shear A. This early, fault-parallel foliation is cut by a series of feldspar-porphyritic monzodiorite dykes (Fig. 6b). Many dykes are laterally and vertically continuous over 100s of metres, following fractures in orientations that suggest control by dextral brittle movement related to this earlier deformation along Shear A. A dyke sample from 63 m down drillhole BCGE08-05 (Fig. 6b) was dated as part of this study and returned a U-Pb zircon $^{206}Pb/^{238}U$ weighted mean age of ca. 54.5 Ma, based on five concordant and overlapping results. This concurs with field relationships, which demonstrate that the main-stage veins cut and occur along fractures that offset these dykes and suggests that the earliest movement along the Shear A fault occurred at least 4 Myr prior to the main veining event.

DISCUSSION

Timing of Deformation

Herein we define two spatially superimposed structural events along the Llewellyn-Tally Ho deformation cor-

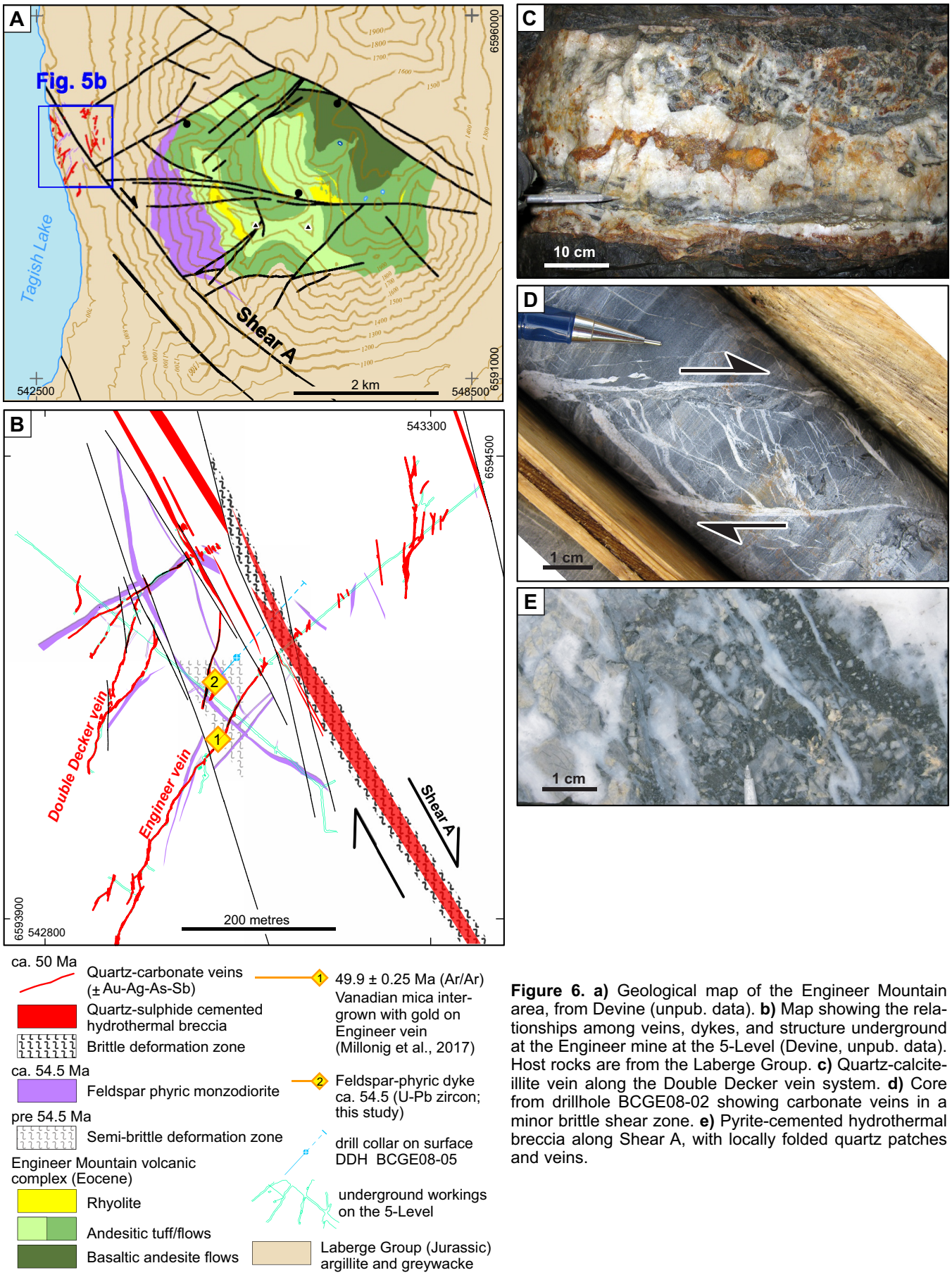

Figure 6. a) Geological map of the Engineer Mountain area, from Devine (unpub. data). **b)** Map showing the relationships among veins, dykes, and structure underground at the Engineer mine at the 5-Level (Devine, unpub. data). Host rocks are from the Laberge Group. **c)** Quartz-calcite-illite vein along the Double Decker vein system. **d)** Core from drillhole BCGE08-02 showing carbonate veins in a minor brittle shear zone. **e)** Pyrite-cemented hydrothermal breccia along Shear A, with locally folded quartz patches and veins.

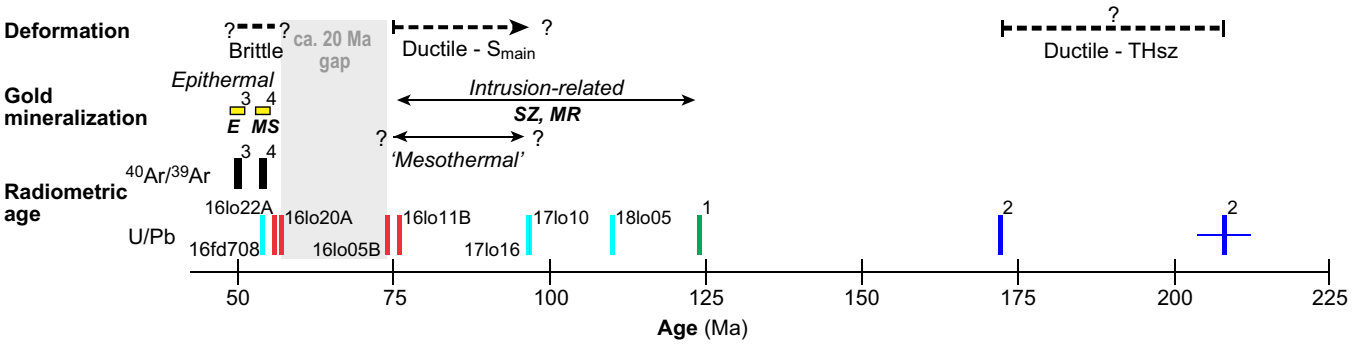

Figure 7. Timeline summary of the deformation and gold mineralization events in the Llewellyn-Tally Ho deformation corridor. The U-Pb zircon age data (labelled by sample number) from Ootes et al. (2018) are shown by a red bar, and preliminary data from this report are shown by a light blue bar. Label 1 data are from Mihalynuk et al. (2003; green bar) and label 2 are from Tizzard et al. (2009; blue bar). The $^{40}Ar/^{39}Ar$ mica results, labelled 3, are from Millonig et al. (2017) and those labelled 4 are from Love et al. (1998); these constrain the timing of epithermal gold mineralization at the Engineer mine (E) and Mount Skukum (MS), respectively. The suggested timing of intrusion-related mineralization at the Skarn Zone (SZ) is from this study and for Middle Ridge (MR), the suggested timing is from Mihalynuk et al. (2003). The tentative timing of 'mesothermal' mineralization is based on the relative relationship between S_{main} and auriferous quartz or polymetallic veins. Abbreviations: ? = uncertainty; S_{main} = main foliation along the Llewellyn-Tally Ho deformation corridor; THsz = Tally Ho shear zone timing of Tizzard et al. (2009). *See* the text for discussion.

ridor. An early ductile deformation phase exemplified by the Tally Ho shear zone in the Yukon, and its correlative, albeit lesser documented, ductile deformation zones in the Boundary Ranges metamorphic suite and Stuhini Group in British Columbia. Brittle fault zones related to the Llewellyn fault overprint these early ductile deformation zones. U-Pb geochronological data (Ootes et al., 2018, 2019, this study) provide new constraints on the timing of deformation of these superimposed structural events and associated gold mineralization (Fig. 7, Table 1).

Early ductile event

Although there is regional evidence for long-lived polyphase deformation and metamorphism (e.g. pre-Middle Jurassic; Hart and Radloff, 1990; Mihalynuk et al., 1999), only one penetrative ductile foliation (S_{main}) has been observed along the entire Llewellyn fault and Tally Ho shear zone corridor. In British Columbia, foliated and faulted rhyolite along the Llewellyn fault southwest of Racine Lake has a crystallization age of ca. 110 Ma, thus constraining the maximum age of ductile and brittle deformation. To further bracket the maximum age of the main foliation (S_{main}), we investigated the Tally Ho shear zone at Mount Hodnett, Yukon. There, the main foliation and related mylonitic fabric are parallel and probably formed at the same time as the locally penetrative foliation in the neighbouring granodiorite pluton to the west (part of the Whitehorse plutonic suite; Hart and Radloff, 1990). Tizzard et al. (2009) suggested that the foliation in the granodiorite is temporally distinct and related to a fault that juxtaposes the granodiorite and Tally Ho shear zone. Based on field relationships and geochronology at Tally Ho Mountain (Fig. 2), they interpreted that the S_{main} foliation and the development of the Tally Ho shear zone as coeval during the latest Triassic to Early Jurassic (i.e. 208–173 Ma). Instead, our field observations and U-Pb zircon data from the granodiorite at Mount Hodnett (ca. 98 Ma; sample 17lo10) suggest that the penetrative foliation (in the granodiorite pluton), the S_{main} foliation, and the consanguineous mylonitic fabric (in the shear zone) must have developed after ca. 98 Ma. Within the shear zone, the ca. 98 Ma dyke (sample 17lo16) contains a foliation in its margins that we interpret as equivalent to the S_{main} foliation, further constraining the maximum age of ductile deformation. In British Columbia, the ca. 74 Ma granodiorite pluton west of Moon Lake (sample 16lo05B) and the ca. 76 Ma granodiorite porphyry on Bennett plateau (sample 16lo11B) postdate ductile deformation in the Stuhini and Laberge groups and Boundary Ranges metamorphic suite. Therefore, ductile deformation fabrics along the Llewellyn-Tally Ho corridor developed between ca. 98 and 75 Ma.

Late brittle event

In British Columbia, the granodiorite west of Moon Lake (sample 16lo05B) is crosscut by the Llewellyn fault, constraining the brittle deformation to younger than ca. 74 Ma. The two granitic plutons sampled near the British Columbia-Yukon border along the Llewellyn fault (samples 16lo20A, 16lo22A; Fig. 2) both yield an indistinguishable age of ca. 56 Ma. Both intrusive phases postdate ductile deformation. However, the slightly younger equigranular granite pluton (sample 16lo20A) contains fractures that are along strike, and parallel to the Llewellyn fault, and is interpreted to have acted as a rigid body during brittle faulting (Ootes et al., 2018). The earliest phase of brit-

tle deformation may have started prior to ca. 56 Ma. However, new data from the Engineer mine (about 70 km to the southeast, Fig. 2, 5) suggest that brittle deformation and associated epithermal veining along the fault occurred between 54 and 50 Ma (Millonig et al., 2017; and sample 16fd708). This timing is coeval with epithermal mineralization at Mount Skukum (Love et al., 1998) and Cordilleran-scale brittle dextral strike-slip faulting (e.g. Gabrielse et al., 2006).

Gold Mineralization and Deformation

An important objective of this study was to test the apparent relationship between the various styles of gold mineralization and the structural and magmatic events along the Llewellyn-Tally Ho deformation corridor. One of the initial hypotheses was that the various gold mineralization styles were part of the same system in which gold mineralization occurs synchronously at various depths in the crust ("crustal continuum" model; e.g. Groves, 1993; Goldfarb et al., 2005). However, the field relationships and U-Pb zircon geochronology presented herein demonstrate a time gap of ca. 20 Myr between the mineralization associated with intrusions and "early" ductile fabrics and that related with the brittle deformation (Fig. 7). The ductile deformation is older than ca. 75 Ma and is defined by a regional foliation (S_{main}) in the Stikine terrane rocks (Stuhini, Lewes River, and Laberge groups) and possibly the Boundary Ranges metamorphic suite. Intrusion-related gold mineralization in the Skarn Zone at Bennett plateau is pre- to syn-(ductile) deformation and likely occurred between ca. 98 and 75 Ma. The polymetallic veins, such as at the Brown showing (Wann river area; Blind Creek Resources Limited, 2012), Tannis (Middle Ridge), Gold Hill (Hart and Radloff, 1990) and auriferous quartz vein occurrences hosted in metamorphic and intrusive rocks along the Llewellyn-Tally Ho corridor (e.g. Bighorn, UM; Mihalynuk et al., 1999), are locally strained and oriented subparallel to the S_{main} foliation, but most are discordant and thus are probably late relative to the associated ductile deformation. To the northeast, gold mineralization at Montana Mountain is related to late reactivation of the Nahlin fault, roughly constrained between ca. 88 and 59 Ma (Hart and Pelletier, 1989; Hart and Radloff, 1990). The epithermal gold mineralization, such as at Engineer mine and Mount Skukum, has been dated at ca. 55 to 50 Ma and is clearly related to brittle deformation and Eocene volcanism (Fig. 7; Love, 1990; Love et al., 1998; Millonig et al., 2017; Ootes et al., 2018). This epithermal mineralization is associated with Eocene dextral fault zones and is hosted in proximal second-order synthetic faults such as at Engineer (Fig. 6) or along distal antithetic faults, like at Mount Skukum (Love, 1990).

First-Order Comparison with an Archean Setting

The evolution of distinct structural and mineralization events related to the Llewellyn-Tally Ho deformation corridor is analogous to the Neoarchean southern Abitibi belt, where major deformation zones, such as the prolific Destor-Porcupine and Larder Lake-Cadillac deformation zones or "breaks" are spatially associated with numerous gold mineralization deposits of various styles (e.g. orogenic quartz-carbonate and intrusion-associated gold deposits; Monecke et al., 2017). These two Archean deformation zones have undergone a polyphase structural evolution, including early extension, syn-orogenic sedimentation and magmatism, inversion to ductile reverse faulting associated with metamorphism and gold mineralization (e.g. Bleeker, 2015). Late, brittle-ductile transpressional deformation subsequently reactivated parts of those deformation zones as strike-slip faults. However, neither the premetamorphic extensional faulting nor the late brittle-ductile structural event are associated with preserved epithermal gold deposits in the southern Abitibi, even for fault zones that demarcate conglomerate-filled syn-orogenic basin remnants with minor subsequent exhumation and erosion. Such first-order comparisons highlight similarities, but also differences in the tectonometamorphic and metallogenic evolution of these major structural corridors. Project results also highlight key differences between Phanerozoic versus Archean gold metallogenesis.

IMPLICATIONS FOR EXPLORATION

The Llewellyn fault and second-order brittle splays overprint early ductile fabrics in British Columbia and the Tally Ho shear zone in Yukon. Earliest Eocene epithermal gold mineralization is spatially associated with penecontemporaneous volcanic complexes, such as the past-producing Mount Skukum and Engineer mines, and occurs on both sides of the Llewellyn fault. This timeframe of late brittle deformation corresponds to that of major strike-slip Cordilleran faults (e.g. Gabrielse et al., 2006) and matches the timing and structural framework of orogenic gold in the Juneau camp in Alaska (e.g. Miller et al., 1994), suggesting a similar first-order tectonic or genetic process led to gold mineralization in both environments.

Previous work proposed that the Tally Ho shear zone developed between 208 and 173 Ma (Tizzard et al., 2009). Observations and U-Pb zircon data from this study indicate that some of the ductile deformation related to the Tally Ho shear zone and regional foliation occurred during the Late Cretaceous, between ca. 98 and 75 Ma. Structurally controlled intrusion-related and 'mesothermal' gold mineralization, for example at the Skarn Zone, is older than ca. 75 Ma and occurs in

foliated, metamorphosed units of the Stikine and Nisling assemblages, principally in the central part of the Llewellyn-Tally Ho deformation corridor. If this gold mineralization event developed between ca. 98 Ma and 75 Ma, then it is broadly coeval and analogous with some of the gold deposits and occurrences, plutonic suites, and regional structural controls (e.g. Big Creek fault zone) of the Dawson Range polymetallic belt in west-central Yukon (e.g. Allan et al., 2013).

The ca. 20 Myr time-gap between early and late deformation (Fig. 7) shows that intrusion-related/ 'mesothermal' and epithermal gold mineralization, respectively, associated with ductile and brittle fabrics and structures, not only formed at different times and tectonometamorphic levels, but are also related to distinct tectonic events. Disparate gold mineralization styles are thus the product of overprinting events, rather than a so-called 'crustal continuum' of mineralization (e.g. Groves, 1993) along the Llewellyn-Tally Ho deformation corridor.

ACKNOWLEDGMENTS

This joint British Columbia Geological Survey-TGI study is conducted in collaboration with the Yukon Geological Survey. We thank BC Gold Corp. (Engineer mine now owned by Engineer Gold Mines Limited), Troymet Exploration Corp. (now Bessor Minerals Inc.), and Terralogic Exploration Inc. for access to properties and data. Discovery Helicopters (Atlin, British Columbia) and Capital Helicopters (Whitehorse, Yukon) provided helicopter support. The study benefited from field assistants Jessica Elliott (in 2016) and Reid Simmonds (in 2017), both from the University of Victoria, and logistical support, field visits, and discussions with Scott Casselman and Craig Nicholson (Yukon Geological Survey), Stephen Rowins and Adrian Hickin (British Columbia Geological Survey), and Patrick Mercier-Langevin (GSC-Quebec). This report benefited from the reviews of Patrick Sack and Scott Casselman. We also acknowledge Christopher Lawley, Valérie Bécu, and Elizabeth Ambrose for their editorial handling and review.

REFERENCES

Allan, M.M., Mortensen, J.K, Hart, C.J.R, Bailey, L., Sanchez, M.G., Ciolkiewicz, W., and Creaser, R.A., 2013. Magmatic and metallogenic framework of west-central Yukon and eastern Alaska; *in* Tectonics, Metallogeny, and Discovery: The North American Cordillera and Similar Accredtionary Settings, (ed.) M. Colpron, T. Bissig, B.G. Rusk, and J.F.H. Thompson; Society of Economic Geologists, Special Publication 17, p. 111–168.

Bleeker, W., 2015. Synorogenic gold mineralization in granite-greenstone terranes: The deep connection between extension, major faults, synorogenic clastic basins, magmatism, thrust inversion, and long-term preservation; *in* Targeted Geoscience Initiative 4: Contributions to the Understanding of Precambrian Lode Gold Deposits and Implications for Exploration, (ed.) B. Dubé and P. Mercier-Langevin; Geological Survey of Canada, Open File 7852, p. 25–47.

Blind Creek Resources Limited, 2012. Wann River Project Within Blind Creek Resources Ltd Tagish Lake Group Claims Atlin Mining Division, British Columbia; British Columbia Ministry of Energy, Mines and Petroleum Resources, ARIS # 32004, 113 p.

Castonguay, S., Ootes, L., Mercier-Langevin, P., and Devine, F., 2018. Gold along Cordilleran faults: Key characteristics and analogies between Phanerozoic and Archean settings; *in* Targeted Geoscience Initiative: 2017 report of activities, volume 1, (ed.) N. Rogers; Geological Survey of Canada, Open File 8358, p. 139–145.

Colpron, M., Israel, S., and Friend, M. (comp.), 2016. Yukon Plutonic Suites; Yukon Geological Survey, Open File 2016-37, scale 1:750 000.

Doherty, R.A. and Hart, C.J.R., 1988. Preliminary geology of Fenwick Creek (105D/3) and Alligator Lake (105D/6) map areas; Yukon Geological Survey, Open File 1988-2, 2 maps, scale 1:50 000.

Gabrielse, H., Murphy, D.C., and Mortensen, J.K., 2006. Cretaceous and Cenozoic dextral orogen-parallel displacements, magmatism, and paleogeography, north-central Canadian Cordillera; *in* Paleogeography of the North American Cordillera: Evidence for and against large-scale displacements, (ed.) J.W. Haggart, R.J. Enkin, and J.W.H. Monger; Geological Association of Canada, Special Paper 46, p. 255–276.

Goldfarb, R.J., Phillips, G.N., and Nokleberg, W.J., 1998. Tectonic setting of synorogenic gold deposits of the Pacific Rim; Ore Geology Reviews, v. 13, p. 185–218.

Goldfarb, R.J., Baker, T., Dubé, B., Groves, D.I., Hart, C.J.R., and Gosselin, P., 2005. Distribution, character, and genesis of gold deposits in metamorphic terranes; *in* Economic Geology 100th Anniversary Volume, (ed.) J.W. Hedenquist, J.F.H. Thompson, R.J. Goldfarb, and J.P. Richards; Society of Economic Geologists, p. 407–450.

Groves, D.I., 1993. The crustal continuum model for late-Archean lode-gold deposits of the Yilgarn Block, Western Australia; Mineralium Deposita, v. 28, p.366–374.

Groves, D.I., Goldfarb, R.J., Gebre-Marian, M., Hagemann, S.G., and Robert, F., 1998. Orogenic gold deposits: A proposed classification in the context of their crustal distribution and relationship to other gold deposit types; Ore Geology Reviews, v. 13, p. 7–27.

Hart, C.J.R. and Pelletier, K.S., 1989. Geology of Carcross (105D/2) and Part of Robinson (105D/7) Map Areas; Indian and Northern Affairs Canada, Yukon Geological Survey, Open File 1989-1, 84 p.

Hart, C.J.R. and Radloff, J.K., 1990. Geology of Whitehorse, Alligator Lake, Fenwick Creek Carcross and part of Robinson map areas (105D/11, 6, 3, 2 & 7); Yukon Geological Survey, Open File 1990-4.

Love, D.A., 1990. Structural controls on veins of the Mount Skukum gold deposit, southwestern Yukon; *in* Current Research, Part E; Geological Survey of Canada, Paper 90-1E, p. 337–346.

Love, D.A., Clark, A.H., Hodgson, C.J., Mortensen, J.K., Archibald, D.A., and Farrar, E., 1998. The timing of adularia-sericite-type mineralization and alunite-kaolinite-type alteration, Mount Skukum epithermal gold deposit, Yukon Territory, Canada: ^{40}Ar-^{39}Ar and U-Pb geochronology; Economic Geology, v. 93, p. 437–462.

Mihalynuk, M.G., Smith, M., Hancock, K.D., Dudka, S.F., and Payne, J., 1994. Geology of the Tulsequah River and Glacier Creek Area (NTS 104K/12, 13); Ministry of Energy, Mines and

Petroleum Resources, British Columbia Geological Survey, Open File 1994-03, 3 sheets, scale 1:50 000.

Mihalynuk, M.G., Mountjoy, K.J., Currie, L.D., Smith, M.T., and Rouse, J.N., 1999. Geology and mineral resources of the Tagish Lake area (NTS 104M/8, 9, 10E, 15 and 104N/12W) northwestern British Columbia; British Columbia Geological Survey, Bulletin 105, 190 p.

Mihalynuk, M.G., Devine, F., and Friedman, R.M., 2003. Marksmen partnership: potential for shallow submarine VMS (Eskay-style) and intrusive-related gold mineralization, Tutshi Lake area; Ministry of Energy and Mines, British Columbia Geological Survey, Geofile 2003-09, 1 poster.

Miller, L.D., Goldfarb, R.J., Gehrels, G.E., and Snee, L.W., 1994. Genetic links among fluid cycling, vein formation, regional deformation, and plutonism in the Juneau gold belt, southeastern Alaska; Geology, v. 22, p. 203–206.

Millonig, L.J., Beinlich, A., Raudsepp, M., Devine, F., Archibald, D.A., Linnen, R.L., and Groat, L.A., 2017. The Engineer Mine, British Columbia: An example of epithermal Au-Ag mineralization with mixed alkaline and subalkaline characteristics; Ore Geology Reviews, v. 83, p. 235–257.

Monecke, T., Mercier-Langevin, P., Dubé, B., and Frieman, B.M., 2017. Geology of the Abitibi greenstone belt; *in* Archean Base and Precious Metal Deposits, southern Abitibi Greenstone Belt, Canada, (ed.) T. Monecke, P. Mercier-Langevin, and B. Dubé; Reviews in Economic Geology, v. 19, p. 7–49.

Monger, J.W.H., Price, R.A., and Tempelman-Kluit, D.J, 1982. Tectonic accretion and the origin of the two major metamorphic and plutonic welts in the Canadian Cordillera; Geology, v. 10, p. 70–75.

Nesbitt, B.E., Murowchick, J.B., and Muehlenbachs, K., 1986. Dual origins of lode gold deposits in the Canadian Cordillera; Geology, v. 14, p. 506–509.

O'Brien, D., Redfearn, M., and Dominy, S., 2018. Engineer Gold Mine, British Columbia, Canada – January 2018 (Amended and Restated); Blind Creek Resources Ltd. and Engineer Gold Mines Ltd., 152 p. <https://www.engineergoldmines.com/site/assets/files/5173/tech-report.pdf> [accessed November 26, 2019]

Ootes, L., Elliott, J.M., and Rowins, S.M., 2017. Testing the relationship between the Llewellyn fault, gold mineralization, and Eocene volcanism in northwest British Columbia: A preliminary report; *in* Geological Fieldwork 2016; British Columbia Ministry of Energy and Mines, British Columbia Geological Survey, Paper 2017-1, p. 49–59.

Ootes, L., Castonguay, S., Friedman, R., Devine, F., and Simmonds, R., 2018. Testing the relationship between the Llewellyn fault, Tally Ho shear zone, and gold mineralization in northwest British Columbia; *in* Geological Fieldwork 2017; British Columbia Ministry of Energy, Mines and Petroleum Resources, British Columbia Geological Survey, Paper 2018-1, p. 67–81.

Ootes, L., Castonguay, S., Friedman, R., and Devine, F., 2019. Superimposed auriferous structural events along the Llewellyn-Tally Ho deformation corridor in southern Yukon and northwest British Columbia; *in* Targeted Geoscience Initiative: 2018 report of activities, (ed.) N. Rogers; Geological Survey of Canada, Open File 8549, p. 49–58. https://doi.org/10.4095/313636

Roots, C.F., 1981. Geological setting of gold-silver veins on Montana Mountain; *in* Yukon Geology and Exploration 1979-80; Indian and Northern Affairs Canada, /Department of Indian and Northern Development, Exploration and Geological Services Division, p. 116–122.

Rowins, S., 1997. 1996 Assessment Report, Bennett Property; British Columbia Ministry of Energy, Mines and Petroleum Resources, ARIS # 24869.

Tizzard, A.M., Johnston, S.T., and Heaman, L.M., 2009. Arc imbrication during thick-skinned collision within the northern Cordilleran accretionary orogen, Yukon, Canada; *in* Earth Accretionary Systems in Space and Time, (ed.) P.A. Cawood and A. Kröner; Geological Society, London, Special Publications, v. 318, p. 309–327.

Troymet Exploration Corporation, 2014. Troymet Reports Significant Skarn Zone Prospecting Results. <https://www.bessorminerals.com/news/troymet-reports-significant-skarn-zone-prospecting-results> [accessed November 22, 2019]

Walton, L., 1986. Textural characteristics of the Venus vein and implications for ore shoot distribution; *in* Yukon Geology, Volume 1, (ed.) J.A. Morin and D.S. Emond; Exploration and Geological Services Division, Indian and Northern Affairs Canada, p. 67–71.

Wark, J.M., 2012. Technical Report, Golden Eagle Property, 43-101 Technical Report; Aurora Geosciences Ltd. for Troymet Exploration Corporation, 471 p. <https://www.troymet.com/assets/docs/projects/GE_TechRpt_Jul-12.pdf> [accessed December 27, 2018]

Structural controls and relative timing of gold mineralization of the banded iron formation-associated Tiriganiaq deposit, Meliadine district, Rankin Inlet greenstone belt, Nunavut

Brayden St.Pierre[1], Patrick Mercier-Langevin[2], Jean-Claude Blais[3], Guilhem Servelle[3], Marjorie Simard[4], Olivier Côté-Mantha[5], and Michel Malo[1]

[1]Institut national de la Recherche scientifique, Centre Eau Terre Environnement, 490 rue de la Couronne, Québec, Quebec G1K 9A9
[2]Geological Survey of Canada, 490 rue de la Couronne, Québec, Quebec G1K 9A9
[3]Agnico Eagle Mines Limited, Meliadine Division, Rankin Inlet, Nunavut X0C 0G0
[4]Agnico Eagle Mines Limited, Technical Services, 200 route de Preissac, Rouyn Noranda, Quebec J0Y 1C0
[5]Agnico Eagle Mines Limited, Exploration Division, 765 chemin de la mine Goldex, Val-d'Or, Quebec J9P 7G4
*Corresponding author's e-mail: braydenstpierre.geo@gmail.com

ABSTRACT

The Meliadine gold district is hosted within the Archean (ca. 2660 Ma) polydeformed Rankin Inlet greenstone belt, Nunavut. The district comprises numerous gold deposits and prospects that are spatially associated with the Pyke Fault and its splays. This includes the currently producing Tiriganiaq deposit, which is hosted within the turbidite-dominated structural hanging wall of the Lower Fault, a west-trending splay of the Pyke Fault.

The 1150 and 1250 "lode series" within the Tiriganiaq deposit are a series of ore zones with complex geometries. Before underground development, the knowledge of gold-grade distribution in these zones was based on surface drilling results and could therefore not take into account some of the small-scale structural features that control ore grade and ore zone geometry (e.g. <25 m wavelength folding).

New field relationships document the importance of horizontal to shallowly south-dipping ore-bearing extensional quartz±ankerite veins. These veins are associated with sulphide replacement zones that are preferentially developed in tightly folded banded iron formation (BIF) intervals. Folding and veining are associated with the main phase of deformation in the deposit area, which corresponds to the second phase (D_2) of regional deformation. The D_2 deformation at the Tiriganiaq deposit can be further subdivided into two main protracted phases: the first phase (D_2A), which is associated with northeast-southwest-oriented shortening and F_2A folding; and the second phase (D_2B), which is associated with north-south shortening, further folding (F_2B), and reverse shearing and veining (shallowly south-dipping extension veins and moderately north-dipping shear veins). The 1150 and 1250 lodes provide an excellent example of the complex geometry of the ore-bearing veins found within the shallowly west-plunging F_2B folded BIF successions. These zones provide some of the highest gold grades within the Tiriganiaq deposit and thus highlight the importance of fold hinges and their effect on the generation of favourable traps (thickened BIF intervals), the development of narrow shears (along the limbs), and the development of associated extensional veins in the competent BIF layers, forming structurally and lithologically controlled high-grade zones.

INTRODUCTION

Banded iron formation (BIF) represents an important host rock for a large number of world-class gold deposits, including the archetypical BIF-hosted Homestake mine, South Dakota, USA, which produced 40 million ounces (>1240 t) of gold (Bell, 2013). Other large BIF-hosted gold deposits include the Morro Velho mine in Minas Gerais, Brazil, which has produced over 15 million ounces (>465 t) of gold in almost 300 years of production (Vial et al., 2007) as well as past or currently producing Canadian mines such as Hardrock, Musselwhite, and Pickle Crow in Ontario and Lupin in Nunavut. The exceptional gold endowment of these deposits is due, at least in part, to the Fe-rich nature of the host rocks. Experimental geochemistry suggests that the solubility of gold within moderate-temperature hydrothermal fluids is favoured by S-ligands. These S-Au complexes are destabilized during fluid:rock interaction with Fe-rich rocks (Phillips et al., 1984), which is reflected in the rock record by the ubiquitous association between gold and sulphide-replacement zones (e.g. arsenopyrite, pyrite, and pyrrhotite) at most BIF-hosted deposits.

St.Pierre, B., Mercier-Langevin, P., Blais, J.-C., Servelle, G., Simard, M., Côté-Mantha, O., and Malo, M., 2020. Structural controls and relative timing of gold mineralization of the banded iron formation-associated Tiriganiaq deposit, Meliadine district, Rankin Inlet greenstone belt, Nunavut; *in* Targeted Geoscience Initiative 5: Contributions to the Understanding of Canadian Gold Systems, (ed.) P. Mercier-Langevin, C.J.M. Lawley, and S. Castonguay; Geological Survey of Canada, Open File 8712, p. 237–250. https://doi.org/10.4095/326041

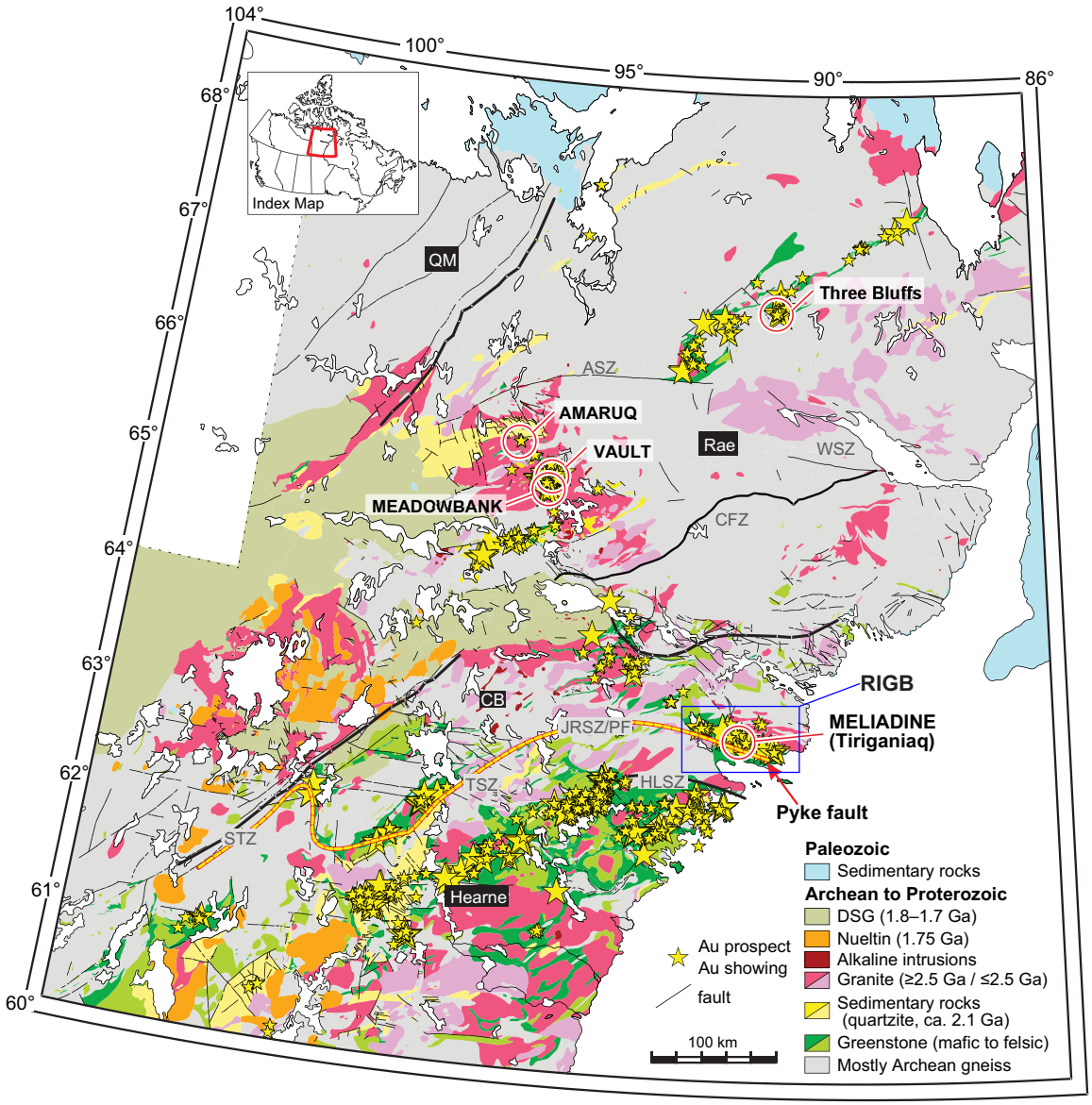

Figure 1. Western Churchill Province regional geology map showing the location of the Rankin Inlet greenstone belt (RIGB) and Meliadine gold district (MGD) and the distribution of other gold deposits, prospects, and showings of the region. Abbreviations: ASZ = Amer shear zone, CB = Chesterfield block, CFZ = Chesterfield Fault zone, DSG = Dubawant Super Group, HLSZ = Happy Lake shear zone, JRSZ = Josephine River shear zone, PF = Pyke Fault, QM = Queen Maud block, STZ = Snowbird Tectonic Zone, TSZ = Tyrrell shear zone, NWT = Northwest Territories, WSZ = Wager shear zone. *Modified from* Lawley et al. (2016).

Many of the so-called BIF-hosted gold deposits in the Western Churchill Province, including Meadowbank, Amuruq, and Tiriganiaq, are only partially BIF-hosted (i.e. BIF-associated: cf. Dubé et al., 2015). These major gold districts provide compelling evidence that a variety of depositional mechanisms control the distribution of gold, including structural and rheological lithological factors. Structural controls are commonly reflected in the close spatial relationship between gold ore zones and complexly deformed rocks at all scales, i.e., ranging from the distribution of the deposits to the internal textures and structures of the ore (Robert et al., 1994; Goldfarb et al., 2005). Layer anisotropy and/or competency contrasts between BIFs and the surrounding sedimentary or volcanic rocks create favourable structural and chemical traps for auriferous fluids, as suggested by the variety of ore-bearing vein styles at many deposits (Dubé et al., 2015 and references therein). However, the complete structural history and its controls on gold mineralization often remain equivocal at most BIF-hosted and BIF-associated gold deposits due to complex brittle-ductile fault-zone behaviour and/or multiple generations of folding and faulting.

The Meliadine gold district (MGD), located within the ca. 2660 Ma Rankin Inlet greenstone belt (RIGB), Nunavut (Fig. 1), is one of Canada's largest emerging

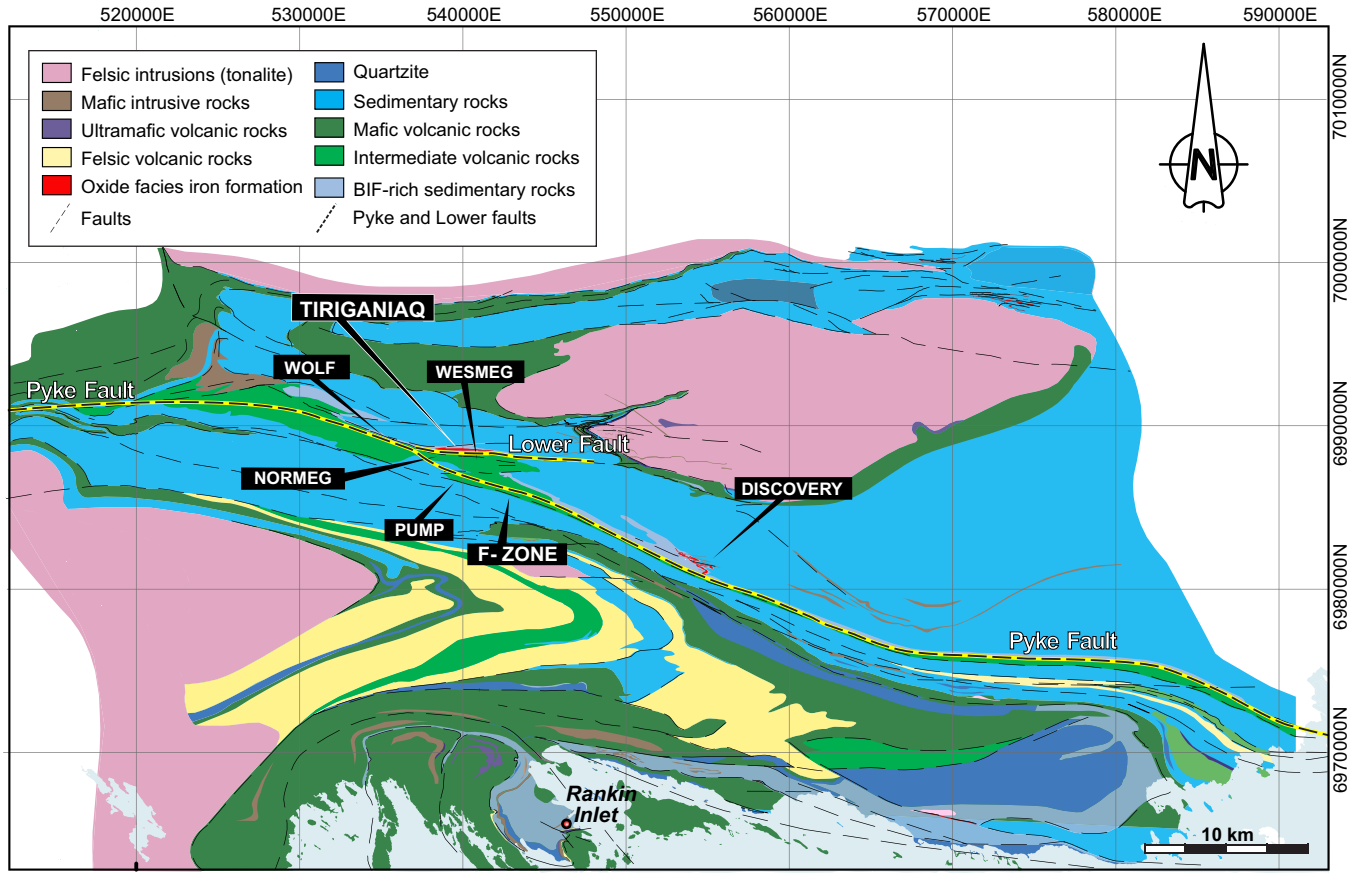

Figure 2. Geological map of the Meliadine gold district showing the location of the Tiriganiaq and other gold deposits and major prospects within the area. The alignment of gold deposits and occurrences in the district is defined by the northwest-trending major Pyke Fault zone. *Compiled from* Agnico Eagle Mines Limited (unpub. internal reports) and Comaplex Minerals Corporation legacy material (e.g. Barham, 2010 and references therein). Abbreviation: BIF = banded iron formation.

BIF-associated gold districts with 3.7 million ounces (115.1 t) of gold in proven and probable reserves, 3.1 million ounces (96.4 t) of gold in indicated resources, and 2.7 million ounces (84 t) of gold in inferred resources as of December 31, 2018 (Agnico Eagle Mines Limited, 2019). The MGD comprises numerous orogenic gold deposits and prospects that are spatially associated with the Pyke Fault and its splays (Fig. 2). Many of these gold deposits are BIF-associated, including Tiriganiaq, the largest deposit of the district. The Tiriganiaq deposit (Meliadine mine) entered into production in mid-May 2019 and is expected to produce 230,000 ounces (7.2 t) of gold in 2019 (including pre-commercial production), and 385,000 ounces (12 t) in 2020, its first full year of production (Agnico Eagle Mines Limited, 2019).

The timing of gold mineralization at the Tiriganiaq deposit and, more broadly across the Western Churchill Province, has yet to be precisely established. The uncertainty of the timing of the gold is due largely to the lack of bedrock exposure, the short timeframe of exploration and academic assessment relative to other major mining districts in Canada, and a protracted history of deformation and resultant geometric complexity. Nevertheless, the broad timing of gold introduction has been attributed to reworking and metamorphism during the Trans-Hudson Orogeny (1.9–1.8 Ga; Carpenter and Duke, 2004; Carpenter et al., 2005; Lawley et al., 2015a,b,c, 2016).

Exploration and previous research in the area in the last few decades led to a first-order understanding of the main ore zones at the Tiriganiaq deposit (e.g. Carpenter and Duke, 2004; Carpenter et al., 2005; Lawley et al., 2015a,b,c, 2016). The model was however challenged when underground development started of the 1150 and 1250 “lode series”, which highlighted structural complexities within the multiply folded BIF units. These multiply deformed ore horizons are challenging to model in 3-D, which impacts mine production and grade and tonnage estimations. Active mining has provided access to underground exposures of the 1150 and 1250 lode series. Detailed geological and structural mapping was carried out along newly developed drifts that exposed the footwall and extended beyond the 1150 lode series into the structural hanging wall.

This report summarizes the current status of the ongoing multidisciplinary research being conducted at

the Meliadine mine. In part, this project aims to constrain the structural and lithological controls on the formation and distribution of the BIF-hosted gold mineralization in the 1150 and 1250 lode series at the Tiriganiaq deposit. Most of the new results are based on underground drill-core observations, but also included are sampling for structural, petrographic, and geochemical analyses. This study builds on previous research in the MGD (e.g. Carpenter and Duke, 2004; Carpenter et al., 2005; Lawley et al., 2015a,b, 2016) to expand knowledge on the structural history and the relative timing of events in a complexly folded and sheared gold-rich BIF-associated ore zones. These new results provide a robust structural and geological framework for mineralization within the 1150 and 1250 ore zones and have led to a more precise geological model, stope design, and resource estimation.

REGIONAL GEOLOGICAL SETTING

The RIGB is located within the Western Churchill Province along the southern margin of the Chesterfield Block, near the boundary with the Hearne Craton (Fig. 1; Berman et al., 2007; Pehrsson et al., 2013; Lawley et al., 2015a,b,c, 2016). This boundary between the Chesterfield Block and the Hearne Craton is inferred to represent a crustal-scale feature but it is obscured by ca. 1800 Ma plutonism, multiple deformation stages, and by the lack of bedrock exposure. At surface it likely forms a broad, structurally imbricated zone rather than a discrete lineament (Lawley et al., 2015b) and may include part of the Tyrrell shear zone (MacLachlan et al., 2005) and/or Happy Lake shear zone (Fig. 1; Berman et al., 2002).

The RIGB is a polydeformed and metamorphosed sequence of intercalated ca. 2660 Ma mafic volcanic and turbiditic successions deposited on an unexposed Meso- to Neoarchean substrate (Lawley et al., 2016). Neoarchean rocks are intruded by undeformed and metamorphosed ≤1830 Ma lamprophyre dykes (Fig. 2; Tella, 1994; Carpenter and Duke, 2004; Carpenter et al., 2005; Lawley et al., 2015a,b,c, 2016). The RIGB has been subdivided into two volcanic cycles (Tella et al., 1986) or assemblages (Bannatyne, 1958): 1) Lower Volcanic Assemblage (LVA), and 2) Upper Volcanic Assemblage (UVA). Abundant mafic to ultramafic dykes and sills of unknown age crosscut the UVA and LVA (Lawley et al., 2015a,b,c, 2016).

The RIGB is interpreted as an east-dipping homocline that has been folded into a southeast-plunging upright F_2 synform (Tella et al., 1986; Tella, 1994; Carpenter and Duke, 2004; Carpenter et al., 2005). The MGD consists of multiple gold deposits and prospects that are spatially associated with the west- to west-northwest-trending and steeply north-dipping Pyke Fault and its subsidiary splays (Fig. 2; Tella et al., 1992, 1996; Carpenter and Duke, 2004). Carpenter and Duke (2004) have separated the deformation history of the RIGB into four increments. The oldest phase of deformation (D_1) lacks identifiable cleavage, but likely represents the initial juxtaposition of turbiditic and volcanic rock packages along an ancestral expression of what most probably now forms the Pyke Fault (Carpenter and Duke, 2004; Carpenter et al., 2005; Lawley et al., 2015a,b,c, 2016). This early phase of deformation has been inferred to explain the close intercalation of geochemically distinct mafic volcanic rocks (Lawley et al., 2016). The second phase of deformation (D_2) consisted of folding of the Archean successions by northeast-southwest shortening, which resulted in F_2 folds and an axial-planar S_2 cleavage. The third phase of deformation (D_3) consisted of a slight change of direction from northeast-southwest-directed to north-south-directed shortening (Carpenter and Duke, 2004), forming a west-trending fabric. At the Tiriganiaq deposit, there is one dominant fabric oriented at approximately N265/65, which has been interpreted by Miller et al. (1995) to represent the main regional S_2 foliation that was transposed into a west-trending orientation during D_3 deformation. The fourth deformation (D_4) fabrics consist of small-scale kink bands and a locally well developed north- to northwest-trending crenulation cleavage (Carpenter and Duke, 2004; Carpenter et al., 2005).

Deposit Stratigraphy

The Tiriganiaq deposit, located in the central part of the Meliadine district, is hosted in the overturned and dominantly turbidite-hosted structural hanging wall of the Lower Fault. The structural hanging wall comprises three distinct sedimentary formations stacked from south to north (Fig. 2–4): 1) the mineralized Tiriganiaq Formation, a package of laminated siltstone with graphitic argillite at its base, in contact with the Lower Fault; 2) the Upper Oxide Formation, a diverse package of iron-rich turbidite layers intercalated with complexly folded silicate-facies and oxide-facies BIF units, which host the majority of the ore at Tiriganiaq, including the 1150 and 1250 lode series (Fig. 3); and 3) the northern-most formation, the Sam Formation, which is a stacked package of laminated siltstone and greywacke.

South of the Lower Fault (i.e. structural footwall) the Wesmeg Formation comprises mafic volcanic rocks intercalated with interflow sedimentary rocks and oxide-facies BIF units. These rocks are cut by gabbro and lamprophyre dykes. The Normeg, Wesmeg, F-zone, and Pump orebodies are all hosted in the Wesmeg Formation (Fig. 2, 3).

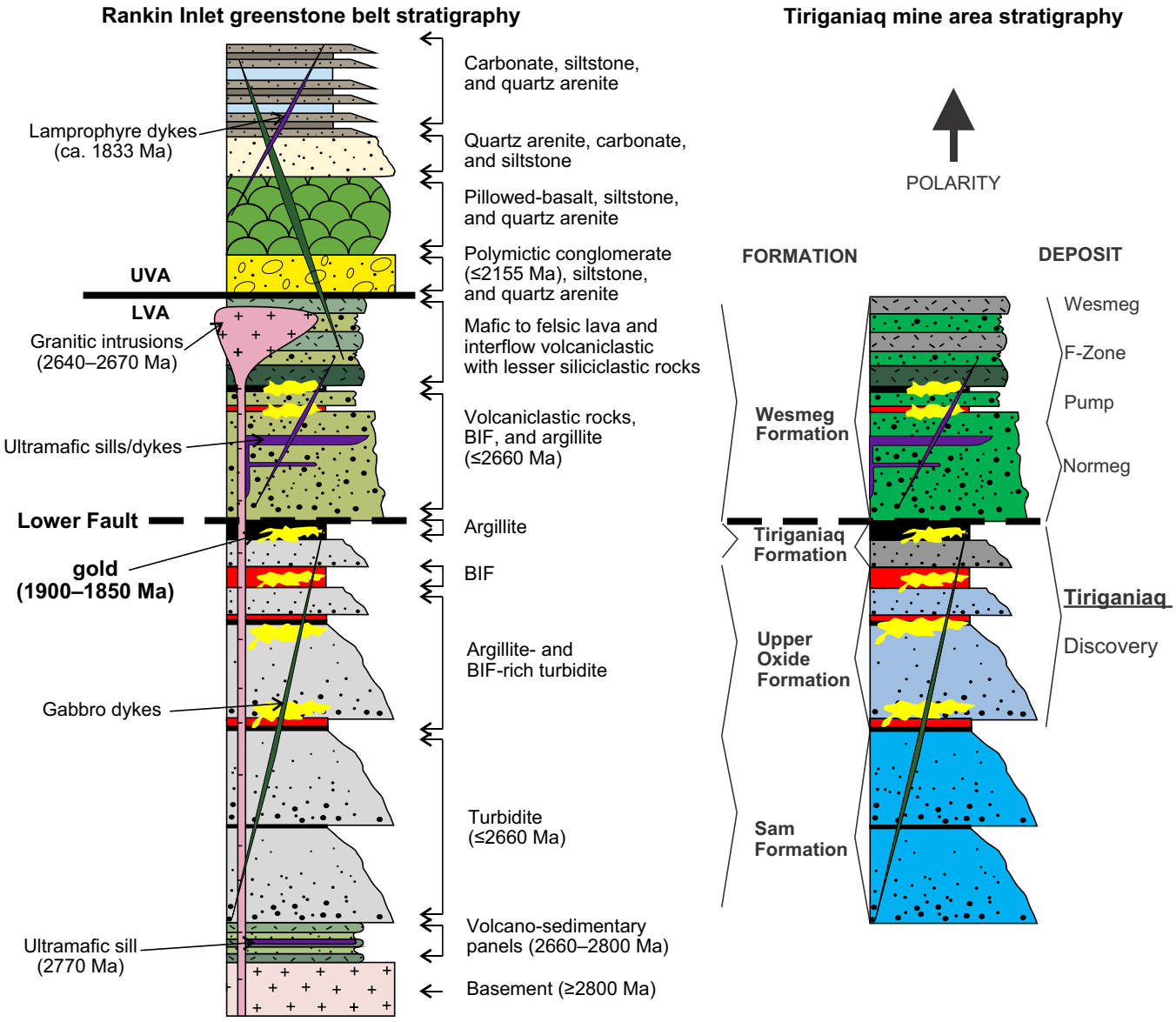

Figure 3. Lithostratigraphic columns of the Rankin Inlet greenstone belt (*modified from* Lawley et al., 2016) and the Tiriganiaq deposit area, displaying relative ages of the lithologies and the crosscutting relationships. The Tiriganiaq deposit area stratigraphic column colour scheme coincides with other diagrams in this contribution. Abbreviation: BIF = banded iron formation, LVA = Lower Volcanic Assemblage, UVA = Upper Volcanic Assemblage.

METHODOLOGY

Detailed underground geological and structural mapping was carried out in 2017 and 2018 along newly developed drifts that exposed the footwall and extended beyond the 1150 lode series into the structural hanging wall. Lithology, alteration, and structural measurements were recorded on georeferenced base maps of drift walls and backs that were surveyed by the Meliadine mine engineering team. Systematic logging and sampling of drill core were completed on a set of representative sections to link observations made from mapping with petrographic and whole-rock lithogeochemistry. Detailed underground mapping and observations are the focus of this contribution.

RESULTS

Structure

At the deposit scale, and based on the observations made in this study, the structural history can be subdivided into three deformation events (Table 1). The earliest deformation event (D_1) at Tiriganiaq, which is inferred from regional-scale observations, has resulted in sedimentary units being thrust on top of volcanic units by the north-dipping Lower Fault. The second deformation event (D_2) can be separated into three phases based on detailed underground observations of bedding, foliation, shear-plane development, and crosscutting relationships. The first phase of the second deformation event (D_2A) (D_2 deformation in Carpenter

Table 1. Summary table of the relative timing of events, including interpreted timing, cause, and characteristics of mineralization.

Age	Event	Description	Associated Structures	Associated Veins and Characteristics	Mineralization
Archean ?	**D_1?**	**D_1**- Initial juxtaposition of mafic volcanic package on top of turbiditic sequence	Ancestral north-verging thrust? S_0/S_1	Quartz along proto Pyke Fault/Lower Fault?	?
Paleoproterozoic (1.90–1.83 Ga)	**D_2**	**D_2A** - Onset of NE-SW shortening resulting in layer parallel folding	**S_2A** - Regional penetrative fabric **F_2A** - Isoclinal folds	Onset of main quartz-ankerite 1000 lode shear vein along Lower Fault	Arsenopyrite+gold precipitation in main shear within 1000 lode and septae
		D_2B - Progressive N-S shortening characterized by mixed brittle and ductile deformation	**S_2B** - Local EW cleavage development axial planar to regional asymmetric **F_2B** - Z-folds Shear plane development oblique to and dragging S_2A foliation indicating north over south motion within 1150 and 1250 lodes	Onset of quartz-ankerite shear veins and associated extensional veins within the 1150 and 1250 lode series Onset of extensional vein arrays north of the 1000 lode	Arsenopyrite+gold precipitation in main shear within 1000 lode and septae Stratabound arsenopyrite+gold along extensional vein selvages within BIF packages
		D_2C - Final stage of N-S shortening and associated reverse shearing, moving towards a more brittle regime	**S_2C** - N-NW crenulation cleavage and kink bands overprinting S_2A and S_2B	Some continuation of veining with same sigma orientation to D_2B Progressive deformation of extension vein arrays Continuation of 1000 lode formation	Arsenopyrite+gold within 1000 lode and septae Further gold mineralization within shear zones and associated extension

and Duke, 2004 and Carpenter et al., 2005; D_2A deformation in Miller et al., 1995) involved layer-parallel F_2A isoclinal folding of the host succession (e.g. Fig. 4) and the associated development of axial-planar, regionally penetrative S_2A cleavage, as well as reverse displacements along the Pyke and Lower faults. The second phase of the second deformation event (D_2B) (D_3 in Carpenter and Duke, 2004 and Carpenter et al., 2005; D_2B in Miller et al., 1995) marks a slight change of shortening orientation to north-south, creating west-trending regional F_2B asymmetric Z-folds (transposed F_2A folds at ore-zone scale) and a west-trending, moderately north-dipping (~45–70º) axial-planar S_2B cleavage that overprints the S_2A foliation. The S_2A foliation is commonly re-oriented into the S_2B fabric in narrow D_2B high-strain zones, forming a composite foliation. The S_2B shear fabric has a slightly shallower dip than the S_2A foliation and dragging of the west-trending S_2A foliation into the D_2B shears indicates a reverse (north-over-south) motion within west-trending decimetre- to metre-wide shear zones localized within chloritic-siltstone units intercalated within decimetre- to metre-wide F_2B folded BIF. The third phase of the second deformation event (D_2C) (D_4 in Carpenter and Duke 2004 and Carpenter et al., 2005; D_3 in Miller et al., 1995) consists of a S_2C crenulation cleavage and associated kink bands.

The D_3 deformation is characterized by box folds within well foliated rocks along the Lower Fault zone. Brittle fault gouges that overprint previous fabrics/structures (Fig. 5a) likely represent a phase of relaxation in a brittle regime immediately after major reverse motion (*see* Discussion *below*).

Mineralization and Structural Style

Tiriganiaq is a BIF-associated gold deposit (Dubé et al., 2015; Lawley et al., 2015a). At Tiriganiaq, gold mineralization largely consists of decimetre to metre thick laminated fault-fill and associated extensional veins with coarse arsenopyrite and minor pyrrhotite replacement of magnetite-rich layers in BIF units along vein selvages. Gold is paragenetically late and, at the micro-scale, occurs within low-strain micro-textural sites and clusters of inclusions within variably recrystallized and idioblastic arsenopyrite crystals (Carpenter et al., 2005; Lawley et al., 2015a,b,c, 2016).

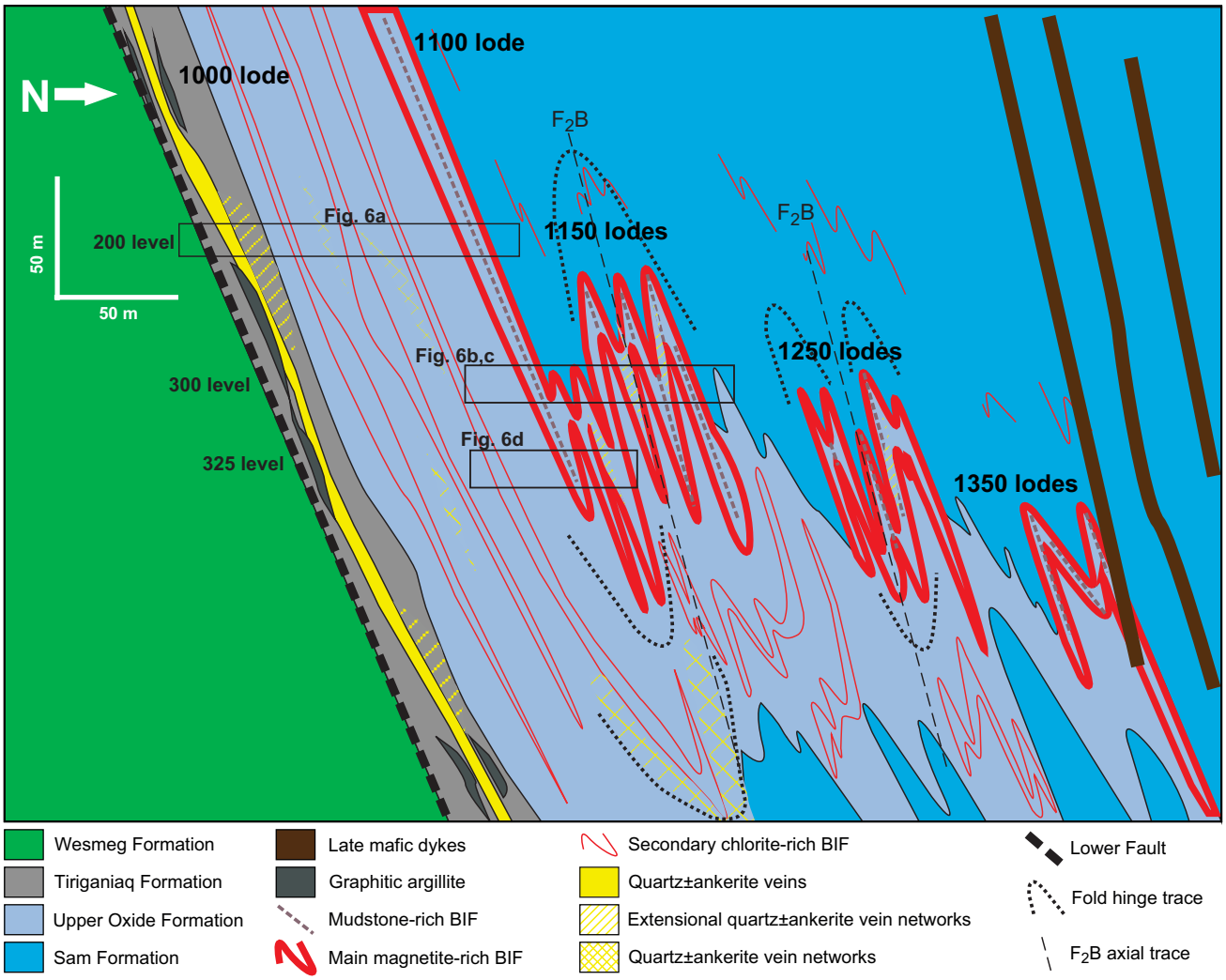

Figure 4. Schematic section of the Tiriganiaq deposit and its various ore zones (or "lodes"), looking west. The section shows the geometry of the different volcano-sedimentary formations, vein distribution, and the ore zone locations (*modified from* Agnico Eagles Mines Limited, unpubl. internal reports). Abbreviation: BIF = banded iron formation.

The 1000 lode vein (Fig. 4), hosted in the Tiriganiaq Formation, is a quartz±ankerite laminated shear vein (Fig. 5b,c) spatially associated with the Lower Fault. The syn-D_2 deformation 1000 lode vein is planar, but pinches and swells vertically and laterally and has an alteration halo comprising sericite±ankerite and coarse euhedral arsenopyrite, pyrrhotite, and minor galena (Lawley et al., 2015c). Sections of the 1000 lode that contain abundant deformed, horizontal to shallowly north-dipping, syn- to late-D_2B quartz±ankerite±gold extensional vein arrays (Fig. 5c) are part of a zone that is referred to as the "intervening lodes", which is located between the 1000 lode and the 1100 lode. These areas of intense veining contain significant concentrations of gold and are thus areas of great interest and the subject of an ongoing M.Sc. thesis at Université du Québec à Montréal, which aims to further the understanding of the controls on their development and to determine if they define ore shoots at the deposit scale.

Approximately 75–80% of the ore at the Tiriganiaq deposit is hosted within the Upper Oxide Formation, including the 1100 lode, which is associated with the transposed long limb of a F_2B fold that affects the BIF succession (Fig. 4, 6a). Gold mineralization comprises contact-parallel shear veins and horizontal to shallowly south-dipping quartz-ankerite extension veins that are preferentially developed in BIF units. Coarse arsenopyrite and minor pyrrhotite replacement of magnetite-rich layers in BIF units often occur along the selvages of these veins (Fig. 5d–g, 6b–d).

Detailed Underground Mapping of the 1150 and 1250 Lode Series

Figure 5 illustrates the main lithological and structural relationships observed in mapping the 1150 and 1250 lode series. In Figure 5d, D_2B mineralized reverse shear zones localized within chloritic siltstone contain mineralized quartz±ankerite veins along S_2B shear

planes that drag the S_2A foliation. Horizontal to shallowly south-dipping mineralized extensional veins, associated with the mineralized D_2B reverse shear zones, preferentially form within intercalated decimetre to metre wide F_2B-folded BIF (Fig. 5e-f). These horizontal to shallowly south-dipping extensional veins typically have coarse arsenopyrite and minor pyrrhotite replacement of magnetite-rich layers in BIF units occurring along the selvages of these veins (Fig. 5e-g). Figure 6 presents four detailed maps of underground exposures of the 1000, 1100, and 1150 lodes. These maps provide details about the host units, structural style, and distribution of the mineralized zones. The Upper Oxide Formation hosts the geometrically and structurally complex 1150 and 1250 lode series, which are controlled by narrow, syn- to late-D_2B deformation, Lower Fault-parallel and north-dipping reverse shear zones, which overprint the slightly steeper, north-dipping S_2A foliation (Fig. 5d, 6b–d). The earlier S_2A foliation is axial planar to tight F_2A folds (Fig. 4, 6).

Draw-point DP200-161

Draw-point DP200-161 (Fig. 6a) preserves the planar nature of the Lower Fault, the 1000 lode, and the 1100 lode. The Lower Fault is slightly less steep than the surrounding dominant S_2A fabric. The 1000 lode is defined by planar, laminated, composite quartz±ankerite shear veins spatially associated with Lower Fault. The 1100 lode, or ore zone, follows the planar geometry of the host stratigraphy and is further defined by contact-parallel shear veins and horizontal to shallowly south-dipping quartz±ankerite extensional veins.

Crosscut CC300-152

Crosscut CC300-152 (Fig. 6b) preserves shear zones that are localized within chloritic siltstone, between tightly folded BIF intervals in the 1150 lodes. Quartz±ankerite shear veins are coincident with D_2B shear planes (Fig. 5d). Shallowly, south-dipping quartz±ankerite extensional veins, associated with shear zones, occur in both the BIF and siltstone units (Fig. 5e,f). These extensional veins are up to 50 cm thick in the BIF but generally less than 10 cm thick in the siltstone. The extensional veins are refracted in the BIF intervals, and are weakly to strongly deformed in the intensely foliated siltstone. Stratabound arsenopyrite±pyrrhotite replaces magnetite-rich layers within the BIF intervals where quartz±ankerite vein selvages are present (Fig. 5g). In contrast, this pattern of alteration in largely absent in the siltstone intervals.

Crosscut CC300-153

Crosscut CC300-153 (Fig. 6c), which is located approximately 15 m east of crosscut CC300-152, exposes tighter folds, relative to those present in crosscut CC300-152. The 1150 lodes are well developed in this area, with shear veins that follow F_2A fold limbs in BIF intervals and associated shallowly south-dipping extension veins with distinctive arsenopyrite replacement halos. The S_2A fabric is axial planar to F_2A folds and slightly steeper than the D_2B shear zones.

Crosscut CC325-155

Crosscut CC325-155 (Fig. 6d) exposes a weakly deformed, subvertical, ore-bearing quartz±ankerite vein with a weak sericite-alteration halo that cuts BIF. Stratabound arsenopyrite and minor pyrrhotite replacement of magnetite-rich layers within the BIF are associated with the selvages of this vein.

Geometry of the 1150 zone

Horizontal to shallowly south-dipping extensional veins and related shear zones and fault-fill veins are preferentially developed in tightly F_2A/F_2B folded decimetre to metre thick BIF layers on both sides of the moderately north-dipping reverse shear zones (Fig. 6b–d; St.Pierre et al., 2018, 2019). Further investigation of the oriented samples revealed that there are distinct shear bands cutting the main deposit fabric. Kinematic indicators within the late shear bands are consistent with dextral shear localized within the chloritic siltstone. This indicates that the main deformation and its

Figure 5 opposite page. a) Photograph of the Lower Fault, looking west. The fault is characterized by overprinting fabrics and lineations with a late gouge zone. **b)** East wall of crosscut CC200-167 showing the shear-hosted 1000 lode main vein and the associated mineralization, alteration halo, and sulphidation. Photograph courtesy of Agnico Eagle Mines Limited. **c)** The West wall of crosscut CC200-157 showing the "interveining lodes" immediately north of the 1000 lode. The interveining lodes are represented by multiple generations of progressively deformed extensional vein arrays that are hosted by Tiriganiaq Formation sedimentary rocks. The extensional veins are predominantly subhorizontal to shallowly north-dipping and are intensely transposed and folded. **d)** Representative structures associated with D_2B shear zones and associated extensional veins within the 1150 zone in crosscut CC300-152 (East wall). D_2B shear planes cut and drag a steeper S_2A fabric forming a localized shear zone along a highly strained limb of an F_2A-folded BIF layer. **e)** Coarse, idioblastic arsenopyrite replacement in BIF along a quartz±ankerite vein selvage. **f)** Photograph of the 1150 zone in crosscut CC300-152 (East wall) showing a series of shallowly south-dipping D_2B quartz-arsenopyrite±ankerite-pyrrhotite veins and bedding-parallel BIF replacement (1). Veins that extend into siltstone tend to contain much less sulphide (2). Veins that cut the weaker (?) and intensely foliated sedimentary rocks also tend to be refracted and transposed. In some cases, the BIF-hosted veins do not extend into chloritic siltstone bands. **g)** Schematic drawing of photograph (f) showing the host rocks (blue and dark grey), barren and mineralized veins (white and yellow, respectively), and the associated arsenopyrite-rich alteration halos (light grey). Abbreviations: Ank = ankerite, Apy = arsenopyrite, BIF = banded iron formation, Qtz = quartz.

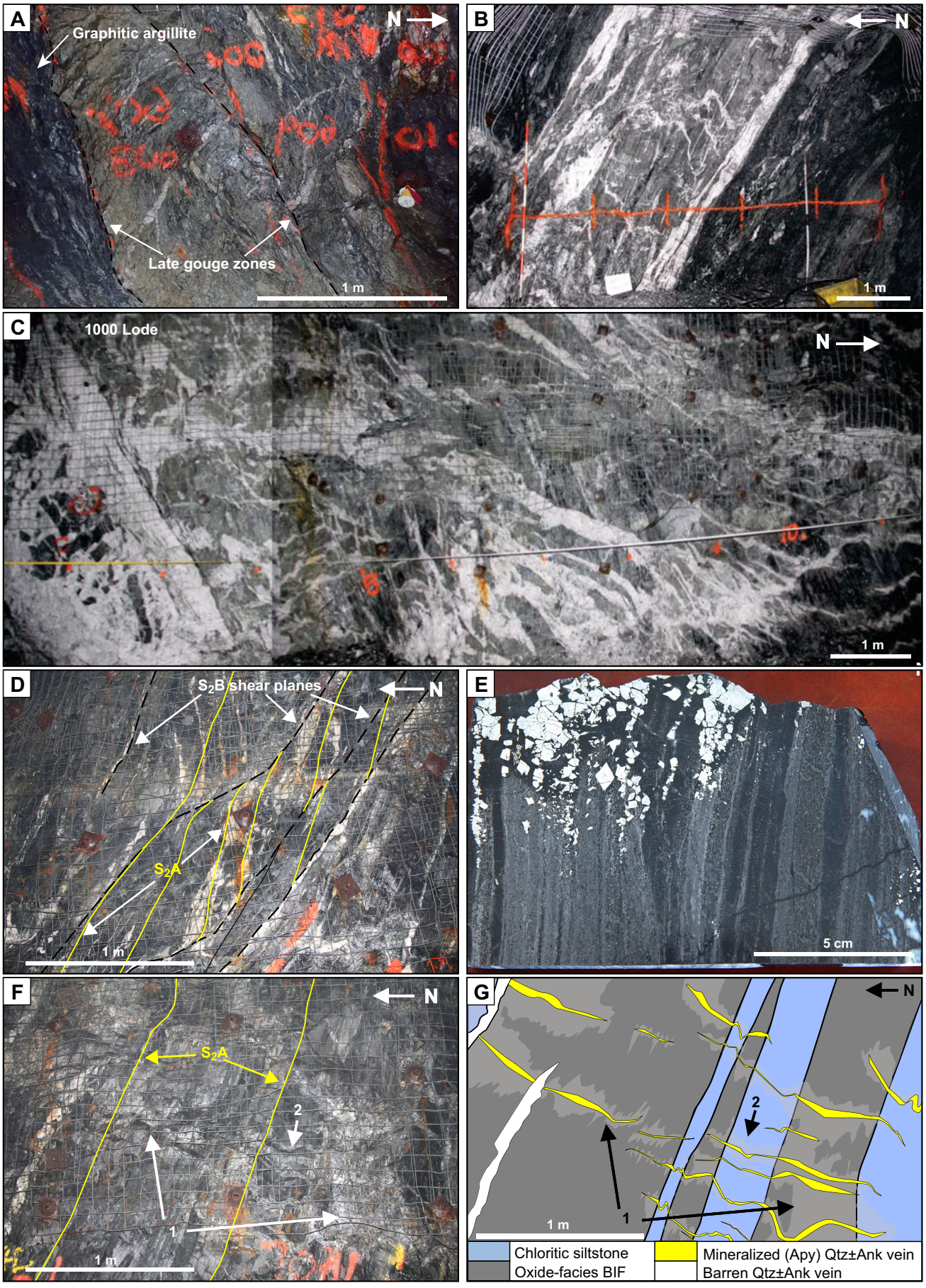
A
Graphitic argillite
N
Late gouge zones
1 m
B
N
1 m
C
1000 Lode
N
1 m
D
S2B shear planes
N
S2A
1 m
E
5 cm
F
N
S2A
2
1
1 m
G
N
2
1
1 m
Chloritic siltstone
Oxide-facies BIF
Mineralized (Apy) Qtz±Ank vein
Barren Qtz±Ank vein

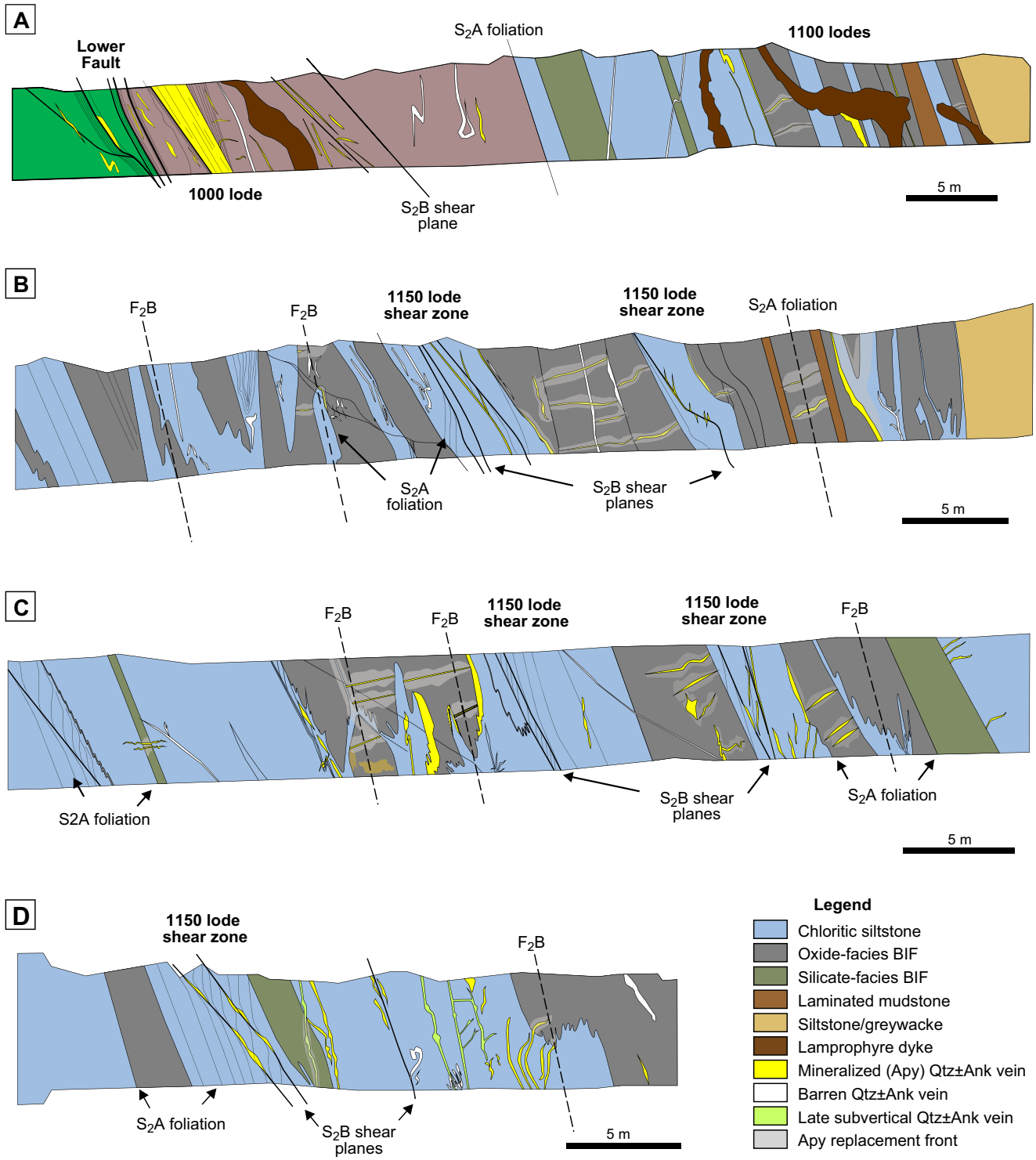

Figure 6. Detailed geological and structural maps of the underground workings of the 1000, 1100, and 1150 lodes at the Tiriganiaq deposit. **a)** The West wall of draw-point DP200-161 (level 200, 200 m below surface). The section exposes the Wesmeg Formation in the structural footwall of the Lower Fault, with the 1000 lode in the hanging wall of the fault. It also shows late lamprophyre dykes that cut across folded units. Further to the north is the 1150 lode corridor that consists of F_2A folded (long limbs exposed) and mineralized BIF units overprinted by moderately north-dipping S_2B shears. **b)** The West wall of crosscut CC300-152 (level 300, 300 m below surface). The section shows F_2A/F_2B folded BIF units (limbs and hinges are exposed) with narrow, weakly mineralized S_2B shear veins along the limbs and shallowly south-dipping extension veins. **c)** The West wall of stope CC300-153, 15 m east of crosscut CC300-152. The section displays well preserved F_2A/F_2B fold hinges and well developed S_2B shear-parallel veins with localized extension veins in the BIF units. **d)** The West wall of crosscut CC325-155 (level 325, 325 m below surface). The section shows weakly mineralized, narrow S_2B shear zones and a series of subvertical veins that are localized at the intersection with BIF units. Abbreviations: Ank = ankerite, Apy = arsenopyrite, BIF = banded iron formation, Qtz = quartz.

associated fabric have an oblique reverse dextral shear component, consistent with a major, syn-ore, reverse component of motion in the deposit area (St.Pierre et al., 2019).

In addition to the syn-D_2 ore-bearing shear veins and associated extensional veins, which are typical of the 1150 and 1250 lode series, there are also rare, relatively weakly deformed (transposed and boudinaged) subvertical quartz±ankerite veins (N270/88). Some of these veins carry gold where they intersect BIF and form stratabound replacement zones of coarse idioblastic arsenopyrite and minor pyrrhotite, which is typical of other BIF-hosted zones in the Upper Oxide Formation (Fig. 6d).

DISCUSSION

Relative Timing of Events

The best evidence for an early, pre-1900 Ma phase of deformation (D_1) comes from observed pre-F_2 mineral lineations, and stratigraphic and structural facing reversals within the upper volcanic cycle (Tella et al., 1986; Tella, 1994; Carpenter and Duke, 2004; Carpenter et al., 2005). However, Re-Os arsenopyrite model ages that range from 2270 to 1800 Ma provide evidence for a formerly unrecognized, pre-1860 Ma hydrothermal event(s) (Lawley et al., 2015b). Although these analyses may reflect isotopic disturbance and samples were gold-poor, there is still a possibility of an additional pre-1860 Ma hydrothermal event(s) (Lawley et al., 2015b). Deformed Paleoproterozoic conglomerate, which is folded with the Neoarchean stratigraphy, provided the most robust maximum age estimate for the main phase of deformation at ≤2155 Ma (Davis et al., 2008; Lawley et al., 2015b).

Gold mineralization at the Tiriganiaq deposit has previously been attributed to reworking and metamorphism during the Trans-Hudson Orogeny (1900–1800 Ma: Carpenter and Duke, 2004; Carpenter et al., 2005; Lawley et al., 2015a,b,c, 2016). This interpretation is favoured because D_2B mineralized reverse shear zones localized within chloritic siltstone contain mineralized quartz veins along S_2B shear planes that drag S_2A foliation. Also, associated horizontal to shallowly south-dipping mineralized extensional veins preferentially form within intercalated decimetre to metre wide F_2B-folded BIF. These and other observations, which are present at different scales, all agree with a major syn-ore incremental compressional deformation event (D_2). In this model, D_2 deformation starts with north-east-southwest shortening (D_2A) and a phase of layer-parallel F_2A isoclinal folding of the host successions and associated development of F_2A fold axial-planar and regionally penetrative S_2A cleavage. Thrusting and mineralized veining along the Pyke and Lower faults likely started at the onset of the D_2 deformation event (i.e. D_2A), as suggested in Miller et al. (1995). This was followed by, or transitioned to, a slight change in shortening orientation to north-south (D_2B) creating east-west regional asymmetric F_2B Z-folds and axial planar S_2B cleavage. The original boundary between the Chesterfield Block and Hearne Craton likely played a role in the timing and change in orientation of the developing penetrative fabrics (Berman et al., 2007). Progressive folding was associated with more brittle-ductile deformation (D_2B) until tightened folds could not accommodate further shortening. Preferential strain partitioning along fold hinges/limbs, relatively less competent units, and lithological contacts most likely led to the development of reverse shear zones. Ore-bearing shear veins were emplaced along shear planes that dragged the S_2A foliation. Mineralized localized shear zones and associated extensional veins were therefore emplaced during the D_2B deformation phase. The D_2C deformation consisted of S_2C crenulation cleavage development and associated kink-band development formed by continued shortening in the same orientation, which resulted in the emplacement of multiple generations of mineralized vein emplacement and progressive deformation. This is supported by variably deformed extensional vein arrays. However, this could also be explained by a mixture of fluid overpressure processes and/or changes in the strain rate, or temperature during deformation. Therefore, D_2 deformation can be constrained by the onset of the regional Trans-Hudsonian metamorphic event at ca. 1900–1850 Ma and by undeformed 1830 Ma lamprophyre dykes (Lawley et al., 2016).

Gold emplacement can be constrained further with U-Pb xenotime results that yield an upper intercept concordia age at 1862 ± 29 Ma on mineralized veins (Lawley et al., 2015b). This agrees with a $^{207}Pb/^{206}Pb$ monazite age of 1854 ± 6 Ma (Carpenter et al., 2005). Additionally, Re-Os dating suggest that ore-associated arsenopyrite-galena-ilmenite phases locally formed at ≥1860 Ma (Lawley et al., 2015a,b).

The D_3 deformation resulted in box folds within well foliated rocks along the Lower Fault zone, brittle fault gouges overprinting previous fabrics/structures, re-activation of the Lower Fault truncating post-D_2 deformation lamprophyre dykes, and subvertical relatively weakly deformed ore-bearing quartz±ankerite veins (N270/88) representing vertical compression and perhaps a phase of horizontal extension. Although considered a separate deformation event, the D_3 deformation could also represent the latest increment of the D_2 deformation. Ongoing work as part of this project should help resolve this question. The transition to brittle deformation and horizontal extension could hypothetically be linked with crustal relaxation after major compression, or it could be associated with the onset of

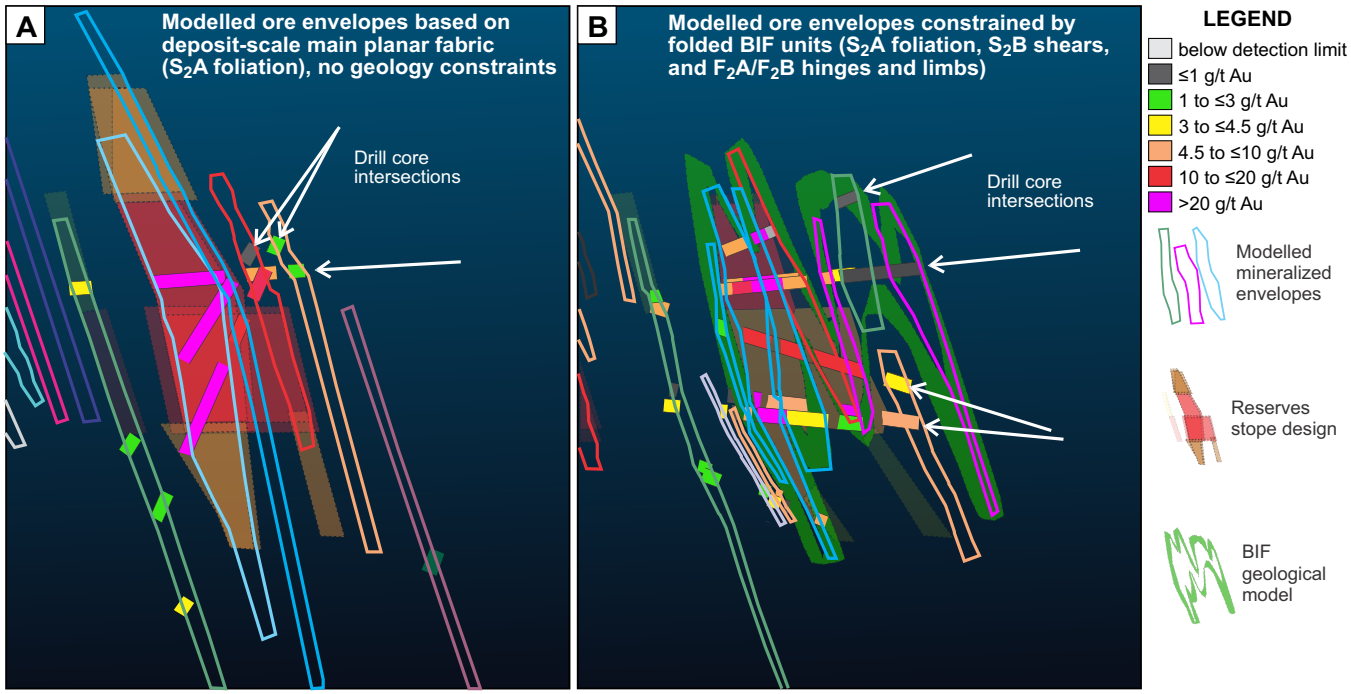

Figure 7. Sketch showing two models of the Tiriganiaq deposit, the first using knowledge before this study and the second using knowledge gained through this study. **a)** Modelling of typical ore zones based on drillhole intersections and the assumption that gold intersections are continuous and can be interpolated and extrapolated parallel to the main fabric. **b)** A revised model using information gained through this study and a better understanding of the combined structural and lithological controls on gold, which now integrates the folding and geometry of the BIF units and the presence of BIF-bound ore intervals, such as shallowly south-dipping extensional veins. Simplified from material provided by Agnico Eagle Mines Limited. Abbreviation: BIF = banded iron formation.

regional magmatism (e.g. Christopher Island Formation at 1830 Ma; Hudson granite suite at 1830 Ma; Nueltin granite suite at 1750 Ma; and the MacRae dyke swarm at 1750 Ma). Since D_3 deformation is associated with Lower Fault re-activation that truncates unfoliated lamprophyre dykes, it is likely that D_3 is younger than 1830 Ma. If regional magmatism played a role in deposit-scale horizontal extension and vertical compression, it would imply that D_3 could be constrained by the end of regional magmatism at ca. 1750 Ma and could potentially extend gold mineralization until ca. 1750 Ma. Further work planned at the Tiriganiaq deposit aims at clarifying the timing of events and should provide more insight into the timing and implications of the late deformation events.

IMPLICATIONS FOR MINE DEVELOPMENT AND EXPLORATION

New field relationships document the importance of horizontal to shallowly south-dipping ore-bearing D_2B/D_2C extensional quartz±ankerite veins. These veins and their associated sulphide replacement zones are preferentially developed in tightly F_2A/F_2B folded oxide-facies BIF intervals. The 1150 and 1250 lodes provide an excellent example of the type of geometric complexities of ore-bearing veins found within shallowly west-plunging F_2B folded BIF successions. These zones provide some of the highest gold grades and thickest gold intervals within the Tiriganiaq deposit and thus represent excellent exploration targets for both within the Tiriganiaq deposit as well as regionally within the RIGB. However, the orientation of these ore-bearing veins and their associated hydrothermal alteration zones were difficult to document in the absence of oriented drill core. Access to the 1150 lodes underground and their detailed documentation and study at drift scale as part of the current study helped understand the controls and geometry of these gold-rich zones.

This information significantly aided in stope design, 3-D modelling, and resource estimation. The revised understanding of the structural controls at play at the Tiriganiaq deposit that based on the results of this study provide excellent criteria for targeting near-mine and regional exploration by highlighting: 1) the importance of F_2A and F_2B fold hinge zones and their effect on the generation of favourable traps (thickened BIF intervals); and 2) the development of narrow shears along the limbs (S_2B) and the development of associated extensional veins in the BIF. Figure 7 illustrates how a better understanding of the geometry of the host BIF unit and the structural controls on the ore-bearing veins of the 1150 lodes could impact modelling results and grade and tonnage estimates. Updated modelling of

these ore zones now includes the folded geometry of the host BIF units (favourable host), the distribution of the veins along the sheared limbs (shear veins), and the development of shallowly dipping mineralized veins within the hinge zones of thickened BIF layers.

ONGOING AND FUTURE WORK

Results presented here are part of an ongoing M.Sc. research project, and current and future work includes analysis of the larger scale geometry of the ore zones and high-grade gold intercepts in 3-D. Whole rock geochemical analyses of the host rocks and mineralized zones will be applied to identify reliable stratigraphic markers within the complexly deformed stratigraphy and to define potential lithological control(s) on gold grade. Project results aim to improve stope design, reserve modelling, and exploration models by providing key information about the structural controls (conduits and traps) influencing the ore zones at various scales.

ACKNOWLEDGMENTS

This report is a contribution to the Targeted Geoscience Initiative Program (TGI-5) of the Geological Survey of Canada. Support for this study was provided through activity G-2.4 of the Gold project. B. St.Pierre is conducting a TGI-supported M.Sc. study at Institut national de la Recherche scientifique, Centre Eau, Terre, Environnement, Québec. This activity is conducted in close collaboration with the Meliadine Division and Technical Services divisions of Agnico Eagle Mines Limited that provided essential scientific and technical support as well as access to material and data. We are particularly grateful to M. Hjorth and G. Dyck from the Meliadine Division, and to B. Dubé and W. Bleeker for fruitful discussions of the geology of orogenic gold districts. Thanks to K. Lauzière and F. Aucoin for their help with Figure 7. This report benefited from thorough reviews by B. Frieman and C. Lawley. We also acknowledge E. Ambrose and V. Bécu for their editorial handling and review.

REFERENCES

Agnico Eagle Mines Limited, 2019. Agnico Eagle Mines Limited Detailed Mineral Reserves and Resources Data: As of December 31, 2017; Agnico Eagle Mines Limited. <https://www.agnico eagle.com/English/operations and development projects/ reserves and resources/default.aspx> [accessed January 23, 2019]

Bannatyne, M.J., 1958. The geology of the Rankin Inlet area and North Rankin Nickel Mines Limited, Northwest Territories; M.Sc. thesis, University of Manitoba, Winnipeg, Manitoba, 83 p.

Barham, B., 2010. Geological map of the Meliadine gold property, interpretation and compilation – Nov. 2009; Comaplex Minerals Corp. internal report.

Bell, C., 2013. Structural controls on gold mineralization at the Homestake mine and their implications for the geology of the Black Hills; Ph.D. thesis, James Cook University, Townsville, Queensland, Australia, 232 p.

Berman, R.G., Davis, W.J., Ryan, J.J., and Brown, N., 2002. In situ SHRIMP U-Pb geochronology of Barrovian facies-series metasedimentary rocks in the Happy Lake and Josephine River supracrustal belts: implications for the Paleoproterozoic architecture of the northern Hearne Domain, Nunavut; Geological Survey of Canada, Current Research 2002-F4, 14 p.

Berman, R., Davis, W., and Pehrsson, S., 2007. Collisional Snowbird tectonic zone resurrected: Growth of Laurentia during the 1.9 Ga accretionary phase of the Hudsonian orogeny; Geology, v. 35, p. 911–914.

Carpenter, R.L. and Duke, N.A., 2004. Geological setting of the West Meliadine gold deposits, Western Churchill Province, Nunavut, Canada; Exploration and Mining Geology Journal, v. 13, p. 49–65.

Carpenter, R.L., Duke, N.A., Sandeman, H.S., and Stern, R., 2005. Relative and absolute timing of gold mineralization along the Meliadine trend, Nunavut, Canada: evidence for Paleoproterozoic gold hosted in an Archean greenstone belt; Economic Geology, v. 100, p. 567−576.

Davis, W.J., Ryan, J.J., Sandeman, H.A., and Tella, S., 2008. A Paleoproterozoic detrital zircon age for a key conglomeratic horizon within the Rankin Inlet area, Kivalliq region, Nunavut: Implications for Archean and Proterozoic evolution of the area; Geological Survey of Canada, Current Research 2008-08, 8 p.

Dubé, B., Mercier Langevin, P., Castonguay, S., McNicoll, V.J., Bleeker, W., Lawley, C.J.M., De Souza, S., Jackson, S.E., Dupuis, C., Gao, J. F., Bécu, V., Pilote, P., Goutier, J., Beakhouse, G.P., Yergeau, D., Oswald, W., Janvier, V., Fontaine, A., Pelletier, M., Beauchamp, A. M., Katz, L.R., Kontak, D.J., Tóth, Z., Lafrance, B., Gourcerol, B., Thurston, P.C., Creaser, R.A., Enkin, R.J., El Goumi, N., Grunsky, E.C., Schneider, D.A., Kelly, C.J., and Lauzière, K., 2015. Precambrian lode gold deposits — a summary of TGI 4 contributions to the understanding of lode gold deposits, with an emphasis on implications for exploration; *in* Targeted Geoscience Initiative 4: Contributions to the understanding of Precambrian lode gold deposits and implications for exploration, (ed.) B. Dubé and P. Mercier Langevin; Geological Survey of Canada, Open File 7852, p. 1–24.

Goldfarb, R., Baker, T., Dubé, B., Groves, D., Hart, C., and Gosselin, P., 2005. Distribution, character and genesis of gold deposits in metamorphic terranes; *in* Economic Geology 100th Anniversary Volume, (ed.) J.W. Hedenquist, J.R.H. Thompson, R.J. Goldfarb, and J.P. Richards; Society of Economic Geologists, p. 407–450.

Lawley, C.J.M., Dubé, B., Mercier Langevin, P., McNicoll, V.J., Creaser, R.A., Pehrsson, S., Castonguay, S., Blais, J.-C., Simard, M., Davis, W.J., and Jackson, S.E., 2015a. Setting, age, and hydrothermal footprint of the emerging Meliadine gold district, Nunavut; *in* Targeted Geoscience Initiative 4: Contributions to the understanding of Precambrian lode gold deposits and implications for exploration, (ed.) B. Dubé and P. Mercier Langevin; Geological Survey of Canada, Open File 7852, p. 99–111.

Lawley, C.J.M., Creaser, R.A., Jackson, S., Yang, Z., Davis, B., Pehrsson, S., Dubé, B., Mercier Langevin, P., and Vaillancourt, D., 2015b. Unravelling the Western Churchill Province Paleoproterozoic gold metallotect: Constraints from Re-Os arsenopyrite and U-Pb xenotime geochronology and LA-ICP-MS arsenopyrite trace element chemistry at the BIF-hosted Meliadine gold district, Nunavut, Canada; Economic Geology, v. 110, p. 1425–1454.

Lawley, C.J.M., Dubé, B., Mercier Langevin, P., Kjarsgaard, B.A, Knight, R., and Vaillancourt, D., 2015c. Defining and mapping hydrothermal footprints at the BIF-hosted Meliadine gold district, Nunavut, Canada; Journal of Geochemical Exploration, v. 155, p. 33–55.

Lawley, C.J.M., McNicoll, V.J., Sandeman, H., Pehrsson, S., Simard, M., Castonguay, S., Mercier Langevin, P., and Dubé, B., 2016. Age and geological setting of the Rankin Inlet greenstone belt and its relationship to the gold endowment of the Meliadine gold district, Nunavut, Canada; Precambrian Research, v. 275, p. 471–795.

MacLachlan, K., Davis, W.J., and Relf, C., 2005. Paleoproterozoic reworking of an Archean thrust fault in the Hearne Domain, Western Churchill Province: U-Pb geochronological constraints; Canadian Journal of Earth Science, v. 42, p. 1313–1330.

Miller, A.R., Balog, M.J., and Tella, S., 1995. Oxide iron formation hosted lode gold, Meliadine Trend, Rankin Inlet Group, Churchill Province, Northwest Territories; Geological Survey of Canada, Current Research 1995-C, p. 163–174.

Pehrsson, S., Berman, R., and Davis, W., 2013. Paleoproterozoic orogenesis during Nuna aggregation: A case study of reworking of the Rae craton, Woodburn Lake, Nunavut; Precambrian Research, v. 232, p. 167–188.

Phillips, G.N., Groves, D.I., and Martyn, J.E., 1984. An epigenetic origin for Archean banded iron-formation-hosted gold deposits; Economic Geology, v. 79, p. 162–171.

Robert, F., Poulsen, K.H., and Dubé, B., 1994. Structural analysis of lode gold deposits in deformed terranes; Geological Survey of Canada, Open File 2850, p. 5–17.

St.Pierre, B., Mercier Langevin, P., Simard, M., Côté Mantha, O., Malo, M., and Servelle, G., 2018. Structural and lithologic controls on the nature and distribution of gold in the BIF associated 1150 and 1250 lode series at Tiriganiaq, Meliadine district, Rankin Inlet greenstone belt, Nunavut; *in* Targeted Geoscience Initiative: 2017 report of activities, volume 1, (ed.) N. Rogers; Geological Survey of Canada, Open File 8358, p. 157–161.

St.Pierre, B., Mercier Langevin, P., Simard, M., Côté Mantha, O., Malo, M., and Servelle, G., 2019. Structural and lithological controls on the nature and distribution of gold at the Tiriganiaq deposit, Meliadine district, Rankin Inlet greenstone belt, Nunavut; *in* Targeted Geoscience Initiative: 2018 report of activities, volume 1, (ed.) N. Rogers; Geological Survey of Canada, Open File 8549, p. 77–82.

Tella, S., 1994. Geology, Rankin Inlet (55K/16), Falstaff Island (55J/13) and Quartzite Island (55J/11), district of Keewatin, Northwest Territories; Geological Survey of Canada, Open File 2968, 2 sheets, 1 CD-ROM.

Tella, S., Annesley, I.R., Borradaile, G.J., and Henderson, J.R., 1986. Precambrian geology of parts of Tavani, Marble Island, and Chesterfield Inlet map areas, district of Keewatin: A progress report; Geological Survey of Canada, Paper 86-13, 20 p.

Tella, S., Mikkel, S., Armitage, A.E., Seemayer, B.E., and Lemkow, D., 1992. Precambrian geology and economic potential of the Meliadine Lake-Barbour Bay region, district of Keewatin, Northwest Territories; *in* Current Research, Part C; Geological Survey of Canada, Paper 92-1C, p. 1–11.

Tella, S., Roddick, J.C., and van Breemen, O., 1996. U-Pb zircon age for a volcanic suite in the Rankin Inlet Group, Rankin Inlet map area, district of Keewatin, Northwest Territories; *in* Radiogenic Age and Isotopic Studies, Report 9; Geological Survey of Canada, Current Research 1995-F, p. 11–15.

Vial, D.S., deWitt, E., Lobato, L.M., and Thorman, C.H., 2007. The geology of the Morro Velho gold deposit in the Archean Rio das Velhas greenstone belt, Quadrilátero Ferrífero, Brazil; Ore Geology Reviews, v. 32, p. 511–542.

Lithological and tectonic controls on banded iron formation-associated gold at the Amaruq deposit, Churchill Province, Nunavut, and implications for exploration

Manon Valette[1*], Stéphane De Souza[1], Patrick Mercier-Langevin[2], Olivier Côté-Mantha[3], Marjorie Simard[4], Natasha Wodicka[5], Vicki J. McNicoll[5], and Patrice Barbe[3]

[1]Université du Québec à Montréal, 201 Avenue du Président-Kennedy, Montréal, Quebec H2X 3Y7
[2]Geological Survey of Canada, 490 rue de la Couronne, Québec, Quebec G1K 9A9
[3]Agnico Eagle Mines Ltd., Exploration Division, 765 chemin de la mine Goldex, Val-d'Or, Quebec J9P 7G4
[4]Agnico Eagle Mines Ltd, Technical Services, 10 200 route de Preissac, Rouyn-Noranda, Quebec J0Y 1C0
[5]Geological Survey of Canada, 601 Booth Street, Ottawa, Ontario K1A 0E8
[*]Corresponding author's e-mail: valette.manon8331@gmail.com

ABSTRACT

The Amaruq gold deposit in Nunavut is underlain by the Neoarchean (ca. 2.73–2.63 Ga) supracrustal rocks of the Woodburn Lake group, within the Rae Craton of the Churchill Province. The mineralized zones are hosted in polydeformed, upper greenschist-facies banded iron formation and volcanic and sedimentary rocks of the Rumble assemblage. The assemblage includes rocks of contrasting rheology and geochemistry, such as greywacke, chert, graphitic argillite, komatiite, and komatiitic basalt, which have been deformed and metamorphosed in the Archean and during subsequent Paleoproterozoic orogenesis. In the Amaruq area, several generations of structures are recognized: 1) tight and isoclinal F_1 folds and D_1 shear zones; and 2) upright and isoclinal northeast-plunging F_2 folds and associated D_2 shear zones that host the bulk of gold mineralization. Progressive strain accommodation during D_2 deformation led to the development of northwest-verging overthrust and recumbent F_2 folds. Subsequent deformation consists of open to chevron-style, northeast- and southwest-plunging F_3 folds, and north- and east-striking D_4 and D_5 normal faults and shear zones, respectively. The two principal mineralized areas of the Amaruq deposit, the Whale Tail and IVR, comprise contrasting styles, geometry, and distribution of ore zones in distinct structural domains. The Whale Tail area is primarily characterized by stratabound and locally discordant disseminated to semi-massive pyrrhotite-arsenopyrite-gersdorffite replacement-style orebodies in chert-poor silicate-facies iron formation, and by "silica flooding" zones associated with arsenopyrite-löllingite-pyrrhotite in chert-rich silicate-facies iron formation. The IVR area occurs in an overturned F_2 fold-hinge zone and consists predominantly of shallowly southeast-dipping quartz±carbonate veins that cut the host volcano-sedimentary sequence. Proximal alteration is characterized by variable amounts of Ca-amphibole-feldspar-epidote-muscovite-biotite-carbonate. Petrographic relationships of metamorphic and auriferous sulphide minerals indicate that prograde upper greenschist metamorphism is coeval with D_2 deformation. Native gold was in part exsolved from prograde löllingite during retrograde metamorphism to lower greenschist facies associated with D_3 deformation. The crosscutting relationships between the contrasting ore styles suggest a protracted, multiphase hydrothermal history. The age and relative timing of the gold mineralization represent key issues that are being addressed to help in the development of improved exploration models for banded iron formation-hosted/associated gold deposits in the Churchill Province and other Archean terranes.

INTRODUCTION

The Amaruq deposit, which was discovered in 2013 (Côté-Mantha et al., 2017), is located 120 kilometres northwest of the community of Baker Lake in Nunavut (Fig. 1). It contains a total of 189.1 t of Au (6.08 Moz; reserves and resources) in 46.4 Mt of ore at a grade of 4.07 g/t Au (Agnico Eagle Mines Ltd., December 31, 2018). The deposit is part of a new emerging gold province comprising several mines and gold occurrences associated with Neoarchean supracrustal rocks (Fig. 1), such as (1) the Meadowbank mine hosted in the Woodburn Lake greenstone belt; (2) the Meliadine mine located in the Rankin Inlet greenstone belt; and (3) the Three Bluffs gold occurrences hosted in the Committee Bay belt, which were all deformed and metamorphosed during both the Archean and Proterozoic (Pehrsson et al., 2013a; Sanborn-Barrie et al., 2014; Lawley et al., 2016).

Valette, M., De Souza. S., Mercier-Langevin, P., Côté-Mantha, O., Simard, M., Wodicka, N., McNicoll, V.J., and Barbe, P., 2020. Lithological and tectonic controls on banded iron formation-associated gold at the Amaruq deposit, Churchill Province, Nunavut, and implications for exploration; *in* Targeted Geoscience Initiative 5: Contributions to the Understanding of Canadian Gold Systems, (ed.) P. Mercier-Langevin, C.J.M. Lawley, and S. Castonguay; Geological Survey of Canada, Open File 8712, p. 251–266. https://doi.org/10.4095/326042

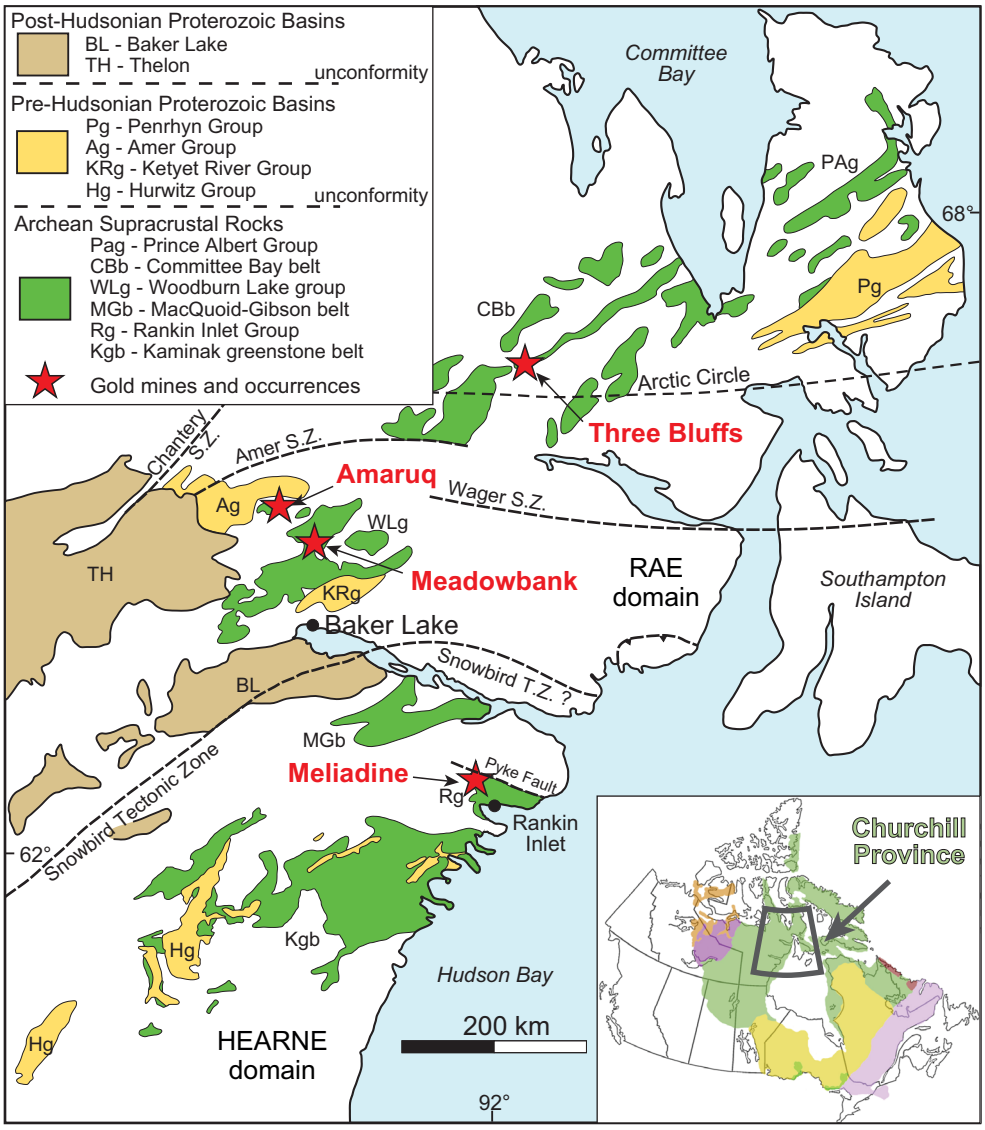

Figure 1. Simplified geological map of the Rae and Hearne cratons of the western Churchill Province showing the location of the Amaruq, Meadowbank and Meliadine mines and Three Bluffs gold occurrence in Nunavut. The white colour represents the undifferentiated Meso- to Neoarchean basement cut by widespread Neoarchean and Paleoproterozoic intrusive suites. The inset shows the distribution of the Churchill Province (*modified from* Valette et al., 2018). Abbreviation: S.Z. = shear zone.

The Amaruq deposit and other gold deposits and occurrences in the region are structurally and lithologically controlled. They are closely associated with crustal-scale faults, shear zones, and/or polydeformed banded iron formation (BIF) units (e.g. Sherlock et al., 2004; Davies et al., 2010; Sanborn-Barrie et al., 2014; Janvier et al., 2015; Lawley et al., 2015, 2016). Even though the bulk of the known gold occurrences in the region are hosted in Archean supracrustal rocks, Trans-Hudsonian orogenesis has controlled most of the structural style and part of the ore-forming events. Previous studies have presented field data, U-Pb monazite and xenotime ages (ca. 1.9–1.8 Ga), and Re-Os arsenopyrite ages from the Meadowbank, Meliadine, and Three Bluffs areas that confirm a Paleoproterozoic Trans-Hudsonian gold mineralizing event (Davies et al., 2010; Janvier, 2016; Lawley et al., 2016). However, 2.3 Ga Re-Os arsenopyrite ages are also obtained at Meliadine (Lawley et al., 2015) and preliminary data at Amaruq indicate that arsenopyrite is systematically older than 2.3 Ga, commonly yielding Archean ages (Mercier-Langevin et al., 2018). These data suggest a complex hydrothermal history, with indications that the mineralized zones are commonly deformed (e.g. boudinage, folding, transposition, and recrystallization) and that gold distribution was probably modified at various scales during deformation and metamorphism (Kerswill et al., 1998; Janvier, 2016; Lawley et al., 2016; Valette et al., 2018). This complexity in age, relative timing, and ore-controlling structures raises questions about the genesis of these deposits.

The working hypotheses are that some significant ore-forming event(s) possibly predate the Trans-Hudsonian Orogeny, and that hydrothermal activity was very long-lived, or, alternatively, the ore-forming event(s) was the result of an incremental process that involved distinct superimposed Archean to Paleoproterozoic gold events. This report summarizes interim results, which are part of an ongoing Ph.D. project that aims to (1) document the geology of the

Amaruq deposit and refine the stratigraphy of the Woodburn Lake group; (2) better constrain the tectonometamorphic evolution of the area; (3) identify the principal controls on gold mineralization; (4) understand how deformation and hydrothermal activity have affected the host rocks and influenced the style, geometry, and distribution of the ore zones; and (5) better constrain the age and relative timing of major ore-forming events.

REGIONAL GEOLOGY

The Amaruq gold deposit is hosted in the Woodburn Lake group of the Rae Craton of the western Churchill Province (Fig. 1). The Rae Craton is composed of a Meso- to Neoarchean (ca. 2.9–2.63 Ga) granodioritic to tonalitic gneissic basement and several Neoarchean greenstone belts (Fig. 1; Berman, 2010; Pehrsson et al., 2013b). The supracrustal rocks form extensive linear belts that are cut by widespread Neoarchean (ca. 2.63–2.58 Ga) granodioritic intrusive rocks of the Snow Island Suite (Berman et al., 2010; Pehrsson et al., 2013b). Paleoproterozoic (ca. 2.3–1.9 Ga) sedimentary basins of the Amer and Ketyet River groups commonly overlay the Archean rocks (Pehrsson et al., 2013a; Jefferson et al., 2015). The Rae Craton has been variably deformed and metamorphosed during several orogenic events: 1) the MacQuoid Orogeny (ca. 2.56–2.5 Ga) on its southeastern margin (Berman et al., 2000; Pehrsson et al., 2013a); 2) the Arrowsmith Orogeny (ca. 2.56–2.28 Ga) on the western edge (Berman, 2010; Pehrsson et al., 2013a); 3) the Taltson-Thelon Orogeny (ca. 1.98–1.91 Ga) on its western margin (McNicoll et al., 2000); and 4) the polyphased Trans-Hudson Orogeny (ca. 1.91–1.81 Ga) on the southeastern edge of the craton (Berman et al., 2005; Pehrsson et al., 2013b). The polyphased Trans-Hudsonian Orogeny coincides with the accretion of the Hearne Craton (ca. 1.9 Ga) and Meta Incognita – Sugluk block (ca. 1.88–1.865 Ga) to the southeastern margin of the Rae Craton, also known as the Snowbird phase, and with the collision of the Sask Craton and Superior Province (ca. 1.84–1.81 Ga) on the south margin of the Hearne Craton (Berman et al., 2013; Pehrsson et al., 2013b).

The Woodburn Lake group (ca. 2.73–2.63 Ga) is divided into six volcano-sedimentary rock assemblages that were affected by two Archean and five Paleoproterozoic deformation events (Pehrsson et al., 2013a). Paleoproterozoic deformation is attributed to the Trans-Hudson Orogeny and is associated with three metamorphic events (Pehrsson et al., 2013a). Following the nomenclature of Pehrsson et al. (2013a), where "A" and "P" represent Archean and Proterozoic deformation events, respectively, D_{A1} and D_{A2} deformation features are only locally and poorly preserved as a schistosity in clasts, and as an axial planar schistosity to small-scale isoclinal folds, respectively (Pehrsson et al., 2013a). D_{A1} fabrics predate 2.71 Ga, the maximum age of the sedimentary rocks comprising the clasts. The second Archean deformation event (D_{A2}) must post-date 2.71 Ga, the age of the rocks of the Woodburn Lake group that are affected by this fabric and may be attributed to the Arrowsmith Orogeny (Berman et al., 2005; Pehrsson et al., 2013a). The D_{P1} shortening event is characterized by tight to isoclinal F_{P1} folds plunging to the south, and by a subhorizontal to shallowly dipping axial planar S_{P1} schistosity. D_{P1} fabrics are affected by tight to isoclinal F_{P2} folds plunging towards the northeast, and by a northeast-trending axial planar S_{P2} schistosity developed during the D_{P2} compressional event. Additionally, northwest-verging thrust faults and shear zones were developed during the D_{P1} and D_{P2} deformation events and caused the repetition of the Archean stratigraphic succession and stacking of the older Archean rocks over younger Paleoproterozoic rocks (Pehrsson et al., 2013a; Calhoun, 2017). Collapse of the Trans-Hudson Orogen then lead to the development of a series of extensional events (Pehrsson et al., 2013a). D_{P3} deformation is characterized by the development of an axial planar S_{P3} crenulation cleavage, associated with shallowly plunging, open to closed, chevron-style F_{P3} folds that are overprinted by north- to northeast-trending, steeply dipping, open to tight F_{P4} folds. The latest structures, associated with the D_{P5} transtensional event comprise a network of east- to northeast-trending extensional shear zones and faults with south-side-down kinematics. These extensional structures are thought to reactivate D_{P2} thrusts, such as the Meadowbank River deformation zone situated between the Amaruq and Meadowbank areas (Pehrsson et al., 2013a; Jefferson et al., 2015; Calhoun, 2017).

The Rae Craton underwent multiple metamorphic events of varying intensity and regional imprint (e.g. Berman et al., 2005; Pehrsson et al., 2013a). In the Committee Bay belt, the first regional metamorphic event, dated at ca. 2.35 Ga, is attributed to the Arrowsmith Orogeny, and could also have affected the rocks of the Woodburn Lake group (Berman et al., 2005). In the Woodburn Lake group, M_{P1} metamorphism is defined by D_{P1} deformation fabrics that are attributed to the Snowbird phase (ca. 1.93–1.91 Ga; Pehrsson et al., 2013a). In both areas, D_{P2} deformation is associated with the main prograde M_{P2} regional metamorphic event (ca. 1.85–1.83 Ga), which is superimposed on the lower metamorphic grade mineral assemblages of the M_{P1} metamorphic event (Pehrsson et al., 2013a). Peak M_{P2} metamorphic conditions increase from lower greenschist facies in the southeast to upper amphibolite facies in the northwest (Berman et al., 2005; Pehrsson et al., 2013a). Retrograde meta-

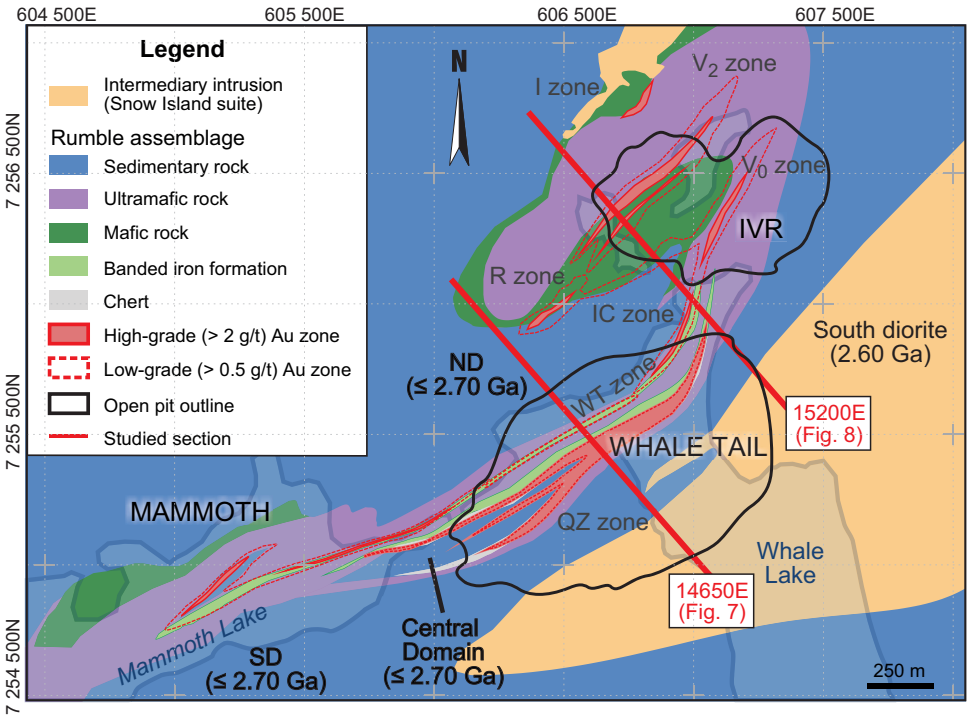

Figure 2. Simplified bedrock geological map of the Amaruq area, showing the location of the Whale Tail and IVR areas and the outlines of the open pits (*modified from* Agnico Eagle Mines Ltd., unpub. data). Abbreviations: ND = north domain, SD = south domain.

morphic conditions are related to M_{P3} metamorphism and are defined by neoblasts aligned in D_{P3} deformation fabrics (ca. 1.82 Ga; Armitage, 1996; Pehrsson et al., 2013a).

LOCAL GEOLOGY

Although the Meadowbank deposit area has been extensively studied over the past two decades (e.g. Pehrsson et al., 2000; Sherlock et al., 2004; Janvier, 2016), only a few regional-scale geological and structural maps are available for the Amaruq area (e.g. Annesley, 1990; Zaleski, 2005; Jefferson et al., 2015; Calhoun, 2017). The Amaruq deposit is hosted in the Rumble assemblage of the Neoarchean (ca. 2735–2630 Ma) Woodburn Lake group, which consists of ultramafic to intermediate igneous rocks, and siliciclastic to chemical sedimentary rocks, including chert and banded iron formation (BIF; Jefferson et al., 2015). The Turqavik-Meadowbank River composite deformation zone, situated 7 km south of the Amaruq deposit, marks the southern boundary of the Rumble assemblage, whereas the northern part is unconformably overlain by the Paleoproterozoic Amer Group (Jefferson et al., 2015).

Deposit Host Rocks and Domains

On the Amaruq property, the Rumble assemblage is characterized by three altered, deformed, and metamorphosed volcanic and/or sedimentary stratigraphic "packages" that are interlayered with silicate (±oxide) facies BIF (Fig. 2, 3). These packages are cut by intrusive diorite bodies (Fig. 2, 3), and by north- and east-striking lamprophyre and felsic dykes, respectively. Two main gold zones, the Whale Tail and IVR orebodies, are present on the Amaruq property (Fig. 2). They both exhibit contrasting ore and alteration styles related to distinct geochemical and structural traps. The Whale Tail area is associated with a laterally and vertically discontinuous central sedimentary domain (central domain: CD) that includes folded and faulted clastic and chemical units. The CD is structurally bounded by two distinct igneous and sedimentary rock packages defined as the south (SD) and north domains (ND) (Fig. 3). Rock units of the SD mainly outcrop south of the Whale Tail area but are also present east-northeast of the IVR area (Fig. 2) due to structural complexities (*see below*). The SD is mainly composed of tightly folded and structurally imbricated greywacke and transitional to calc-alkaline mafic-ultramafic volcanic rocks. The IVR area occurs 300 m northeast of the Whale Tail area (Fig. 2) and comprises the ND, which consists of tholeiitic mafic-ultramafic volcanic rocks and greywacke (Fig. 2). Faults, shear zones, and folds have imbricated and overturned the stratigraphic sequence of the ND, the inferred youngest units of which occur in the core of a recumbent fold hinge (Valette et al., 2018).

Preliminary sensitive high-resolution ion microprobe (SHRIMP) U-Pb geochronology of detrital zircons from the SD, CD, and ND greywackes indicates that these units are all younger than 2.7 Ga. The ND and SD both contain much older zircons (up to 3.15 Ga), whereas the ore-hosting CD has a generally younger zircon population varying between 2.73 and 2.65 Ga. The youngest zircons in the analyzed samples all show evidence of Pb loss and more work is under-

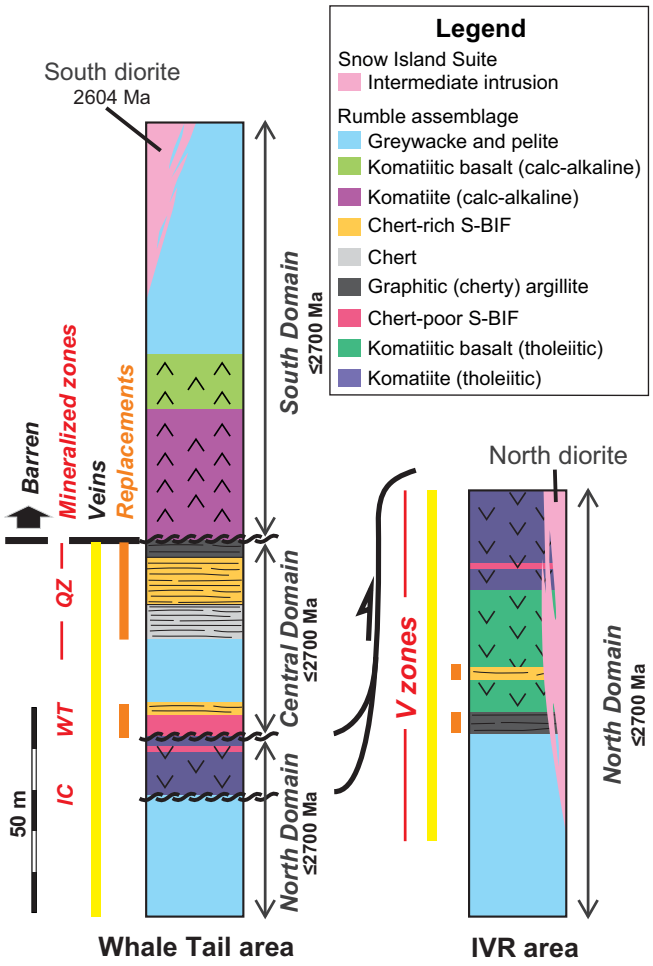

Figure 3. Simplified stratigraphic columns of the Whale Tail and IVR areas showing the location of the principal high-strain and mineralized zones. Abbreviation: S-BIF = silicate-facies banded iron formation.

way to refine the maximum age of the greywacke units of the three domains. A diorite intrusion crosscutting the SD yielded a 2604.9 ± 2.4 Ma age (this study) that falls in the Snow Island Suite age range. The stratigraphic and tectonic relationships between the IVR and Whale Tail orebodies and their host rocks are still under investigation, but structural mapping south of the IVR area suggests that a major shear zone separates the two areas. Thus, until stratigraphic relationships are clarified, two stratigraphic columns are necessary to illustrate the stratigraphy of the Rumble assemblage in the deposit area (Fig. 3).

Host-Rock Petrography

The SD consists of transitional to calc-alkaline mafic to ultramafic volcanic rocks structurally imbricated with greywacke. The volcanic portion comprises green, typically medium-grained, mafic rocks containing hornblende, plagioclase and biotite minerals, and typically dark grey, aphanitic komatiite and komatiitic basalt composed of tremolitic hornblende, phlogopite and albite/oligoclase (Fig. 4a). The mineralogy of the greywacke is homogeneous throughout the study area and mainly consists of millimetre-sized quartz, albite and K-feldspar in a matrix of fine-grained quartz, feldspar, biotite, and minor chlorite. However, the greywacke of the SD is devoid of iron formation and is more homogeneous and less laminated than those of the CD and ND.

Chemical sedimentary units with minor clastic sedimentary layers (i.e. greywacke and siltstone) dominate the CD. It mostly consists, from south to north of (1) a thin graphitic (±cherty) argillite unit (Fig. 4b); (2) mesobanded chert-rich silicate-facies BIF (S-BIF; Fig. 4c) and microbanded chert units; (3) a thicker central unit of greywacke and siltstone; and (4) an upper unit of mesobanded chert-rich S-BIF in contact with (5) chert-poor S-BIF (Fig. 4d). The chert-rich S-BIF is mainly composed of millimetre-thick alternating layers of chert with grunerite, ferrostilpnomelane, ripidolite, and magnetite (Fig. 4c), whereas the chert-poor BIF is a brownish dark green, locally laminated rock composed of hornblende, biotite, ferrostilpnomelane, ripidolite, and almandine garnet (Fig. 4d). In the ND, ultramafic rocks are alternating with chert-poor S-BIF, whereas mafic volcanic rocks and greywacke are intercalated with graphitic (±cherty) argillite and chert-rich S-BIF, respectively (Fig. 3).

The ND consists of tholeiitic mafic to ultramafic volcanic rocks structurally underlain by greywacke. The tholeiitic ultramafic rocks show local spinifex texture (Fig. 4e) and polyhedral jointing. These rocks consist predominantly of bluish gray and aphanitic komatiite and komatiitic basalt composed of tremolite, pycnochlorite, and talc with trace amounts of chromite, magnetite and Ni-Fe-sulphides such as nickeline and gersdorffite. The mafic portion consists of greenish and brownish, medium- to fine-grained volcaniclastic (Fig. 4f) and gabbroic rocks, which are mainly composed of actinolite or Mg-hornblende with ripidolite, clinozoisite, calcite, and minor titanite. A two metre-thick marker horizon of graphitic argillite outlines the contact between the mafic volcanic rocks and the greywacke of the ND (Fig. 3).

Host-Rock Geochemistry

Two geochemically distinct, mafic-ultramafic volcanic rock packages in the SD and ND were identified by whole-rock geochemistry and portable X-ray fluorescence (pXRF) analyses, which helped to reliably map the deposit geology throughout the exploration stages (Côté-Mantha et al., 2017). These two packages cannot be distinguished based on the Jensen (1976) classification diagram and mainly plot in the komatiite, komatiitic basalt, and high-Mg and high-Fe tholeiitic basalt fields (Fig. 5a). These can however easily be distin-

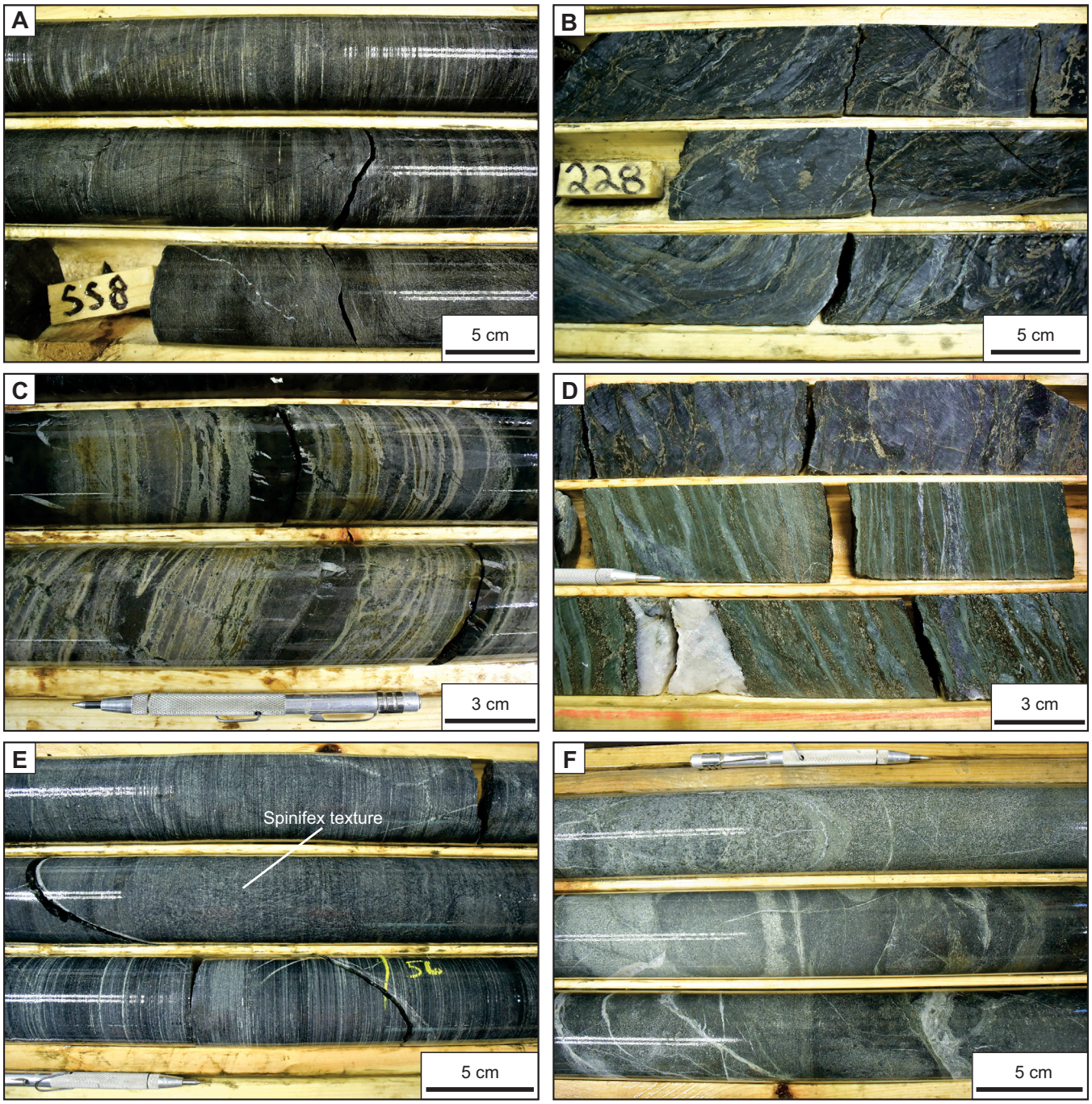

Figure 4. Photographs of the least altered lithologies present at Amaruq. **a)** The komatiite volcanic rock with a calc-alkaline magmatic affinity of the SD zone. **b)** The graphitic (cherty) argillite of the CD zone. **c)** The mesobanded chert-rich silicate-facies banded iron formation (S-BIF) of the CD zone. **d)** The mesobanded chert-poor S-BIF of the CD zone. **e)** The komatiite volcanic rock with a tholeiitic magmatic affinity of the ND zone. **f)** The mafic volcaniclastic rock of the ND zone.

guished on a Zr versus Y magmatic affinity diagram (Fig. 5b) and on a chondrite-normalized rare earth elements (REE) diagram (Fig. 5c). The mafic-ultramafic volcanic rocks of the ND have a typical tholeiitic signature, whereas those of the SD have transitional to calc-alkaline geochemical affinity.

The different sedimentary rocks at Amaruq can also be geochemically distinguished (Fig. 5d). The phyllosilicate-dominated chert-poor S-BIF has a higher Al-ratio and lower Fe-ratio, than the amphibole- and chert-rich S-BIF, which is interpreted to have a greater hydrothermal component (cf. Spry et al., 1998). The higher input of hydrothermal elements to the chert-rich S-BIF is supported by a positive Eu anomaly, which is generally interpreted as being associated with high-temperature and reduced hydrothermal fluids (Fig. 5c; Spry et al., 1998). The chert-poor S-BIF has a flat to slightly light-REE depleted signature, whereas the

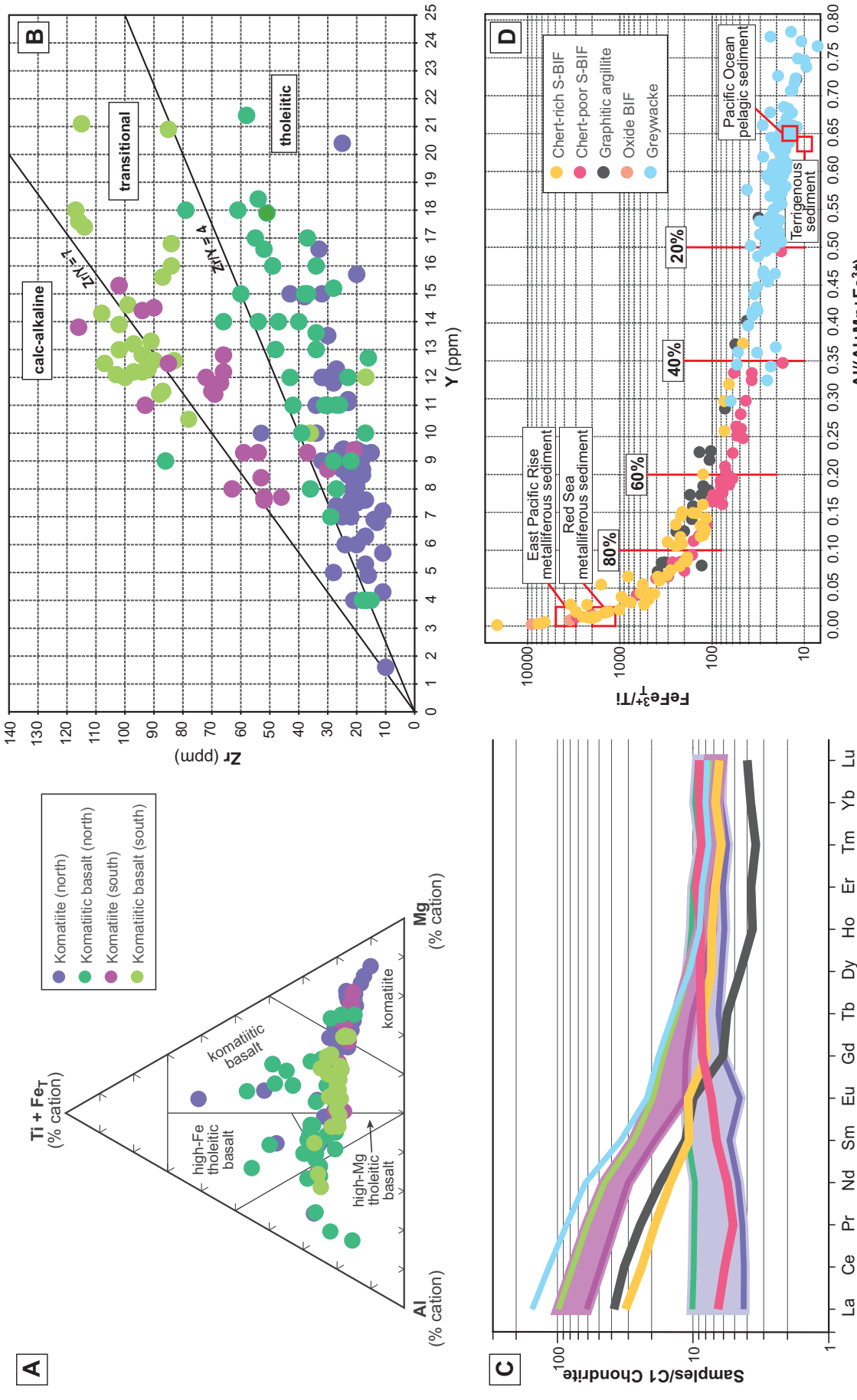

Figure 5. Geochemical diagrams for the classification and characterization of the protoliths of the Amaruq area. **a)** AFM ternary diagram of Jensen (1976), and **b)** Zr versus Y magmatic affinity diagram from MacLean and Barrett (1993) for igneous rocks. The legend is the same for plots (a) and (b). **c)** C1 chondrite normalized rare earth element profile envelops or average of the host rocks of the Amaruq deposit (McDonough and Sun, 1995). The legend is the same plots (c) and (d). For the igneous rocks, polygons represent the transition from komatiite to komatiitic basalts. **d)** Diagram of Fe^{3+}_T/Ti versus Al/(Al+Mn+Fe^{3+}_T) ratios to estimate the hydrothermal contribution to the sedimentary rocks with plots of the average of Pacific Ocean pelagic sediment, terrigenous sediment, as well as the Red Sea and East Pacific Rise metalliferous sediments (Boström, 1973).

chert-rich S-BIF is enriched in light-REE (Fig. 5c). The graphitic argillite has a strongly heavy-REE depleted signature. The SD, CD, and ND greywackes are strongly light-REE enriched and show fractionated REE patterns, as the chert-rich S-BIF and the graphitic argillite (Fig. 5c).

DEFORMATION AND METAMORPHISM

The structural geology of the Amaruq area is complex and, except for the IVR area, exposure is poor, hampering a complete documentation of the polyphase structural styles and geometric relationships among the strongly deformed ore zones. The different generations of fabrics in the Amaruq area are compared and correlated with the regional deformation phases of Pehrsson et al. (2013a) and summarized in Table 1.

The earliest recognized deformation event (D_1) at Amaruq is manifested by isoclinal to tight F_1 folds and the associated axial planar S_1 foliation defined by alignment of phyllosilicate minerals. D_1 fabrics were affected by tight to closed, gently to moderately, east- to northeast-plunging F_2 folds. The D_1 fabrics were variably transposed subparallel to the moderately (50°) southeast-dipping axial planar S_2 schistosity (Fig. 6a,b). Complete transposition of the S_1 foliation results in a composite $S_{1\text{-}2}$ schistosity on the F_2 folds limbs. S_2 schistosity is penetrative in all rock types, except in the chert-rich S-BIF where it is developed as a centimetre-spaced cleavage (Fig. 6a). A moderately to steeply southwest-plunging (45–70°) L_{m2} mineral lineation is defined by alignment of phyllosilicate minerals (e.g. chlorite).

Progressive strain accommodation led to the development of recumbent F_2 folds and south-dipping thrust faults and/or shear zones that are subparallel to the S_2 schistosity. Some faults may have been initiated during D_1 deformation and reactivated during D_2 deformation. One of these mineralized shear zones is well exposed between the Whale Tail and IVR areas and corresponds to the IC zone (Fig. 1, 6c). Compressive shearing fabrics (i.e. C/S fabrics) and quartz vein boudins indicate northwest-directed transport along these shear zones. Shearing and faulting observed in drill core along the overturned limbs of F_1 and/or F_2 folds in the most competent rocks (e.g. S-BIF) are interpreted to represent overthrusts that controlled the localization of the mineralized zones at smaller scale.

The D_2 deformation fabrics are folded by asymmetric, open to closed, chevron-style F_3 folds (Fig. 6d,e,f), which are associated with the development of shallow north- and south-dipping S_3 crenulations that define a conjugate cleavage set. The S_3 crenulations are poorly developed in chert-rich S-BIF but are preferentially developed near or within high-strain zones, as well as in fold-hinge zones affecting the volcanic and sedimentary rocks. The $L_{2\text{-}3}$ intersection lineation is shallowly plunging (0–20°) towards the northeast or southwest, and is subparallel to the F_2 and F_3 folds axes. The L_{m2} and the $L_{1\text{-}2}$ intersection lineation are only locally preserved on the long and south-dipping limbs of the asymmetric F_3 folds. Younger fabrics are characterized by northeast- to northwest-striking, steeply dipping, centimetre-spaced cleavage and normal faults (D_4 deformation), and steeply dipping, east-striking shear zones (D_5 deformation) preferentially developed in the less competent rocks (e.g. ultramafic volcanic rocks of the ND).

Petrographic and microstructural relationships between fabrics and metamorphic minerals, such as garnet porphyroblasts, provide evidence for syn- to late-D_2 peak metamorphism at upper greenschist facies (Fig. 6e). Peak metamorphic conditions overprint part of the ore-associated sulphides, which also show textural evidences of prograde and retrograde transformations, such as triple junctions and inclusion of löllingite in arsenopyrite (Lauzon et al., 2020). A retrograde greenschist-facies metamorphic event (M_3) is marked by andalusite crystals aligned along the S_3 crenulation cleavage in sedimentary rocks and pseudomorphs of M_2 metamorphic minerals (Fig. 6f).

ORE ZONES: STYLES, DISTRIBUTION, AND HYDROTHERMAL ALTERATION

At Amaruq, the high-grade gold zones are preferentially developed along lithological contacts between specific units, within structural traps such as brittle-ductile high strain zones, or F_2 fold hinges (Fig. 7, 8). The bulk of the gold is hosted in the BIF of the CD at Whale Tail (Fig. 3, 7), whereas a significant amount of gold in the IVR area occurs in quartz±calcite veins crosscutting the volcano-sedimentary sequence of the ND (Fig. 8). The mineral assemblage, intensity, and width of the hydrothermal alteration halo vary with the host rocks and style of mineralization. In general, the mineralized zones are characterized by a proximal Ca-enriched metasomatic alteration halo surrounded by a distal K- and/or Na-enriched envelope (Fig. 9a,b,c,d). The proximal alteration halo is characterized by a sulphidation front (pyrrhotite and arsenopyrite) locally associated with silicification of the chemical sedimentary rocks (Fig. 9a). Gold is present as inclusion in idioblastic arsenopyrite (Fig. 9e,f), pyrrhotite or gersdorffite, at sulphide crystal boundaries (Fig. 9e), as fracture-filling in sulphides, and as free grains (Fig. 9g) in quartz-rich rocks (i.e. veins, silicified zones, and chert).

Whale Tail Area

In the Whale Tail area, the chert-poor S-BIF is one of the principal hosts to ore, which consists of stratabound

Table 1. Summary of the main deformation events and fabrics present at Amaruq, and regionally in the Woodburn Lake group. Compiled from Pehrsson et al. (2013b), Jefferson et al. (2015), Janvier (2016), and Valette et al. (2018).

Events	**Orientation**	**Archean rocks of the Amaruq area** (this study)			**Events**	**Orientation**	**Archean rocks of Woodburn Lake** (Pehrsson et al., 2013)		
		Planar	**Linear**	**Fold geometry**			**Planar**	**Linear**	**Fold geometry**
Note: Archean fabrics are either not present at Amaruq, or more likely completely overprinted by Proterozoic fabrics		-	-	-	D_{A1} (pre-date 2.71 Ga)	-	Internal schistosity and foliation in lithic clasts	-	-
		-	-	-	D_{A2} (post-date 2.71 Ga) but pre-date KRg)	-	Axial planar schistosity	-	Outcrop-scale isoclinal folds
D_1	N-S or E-W compression?	Axial planar and folded penetrative schistosity Thrust faults/shear zones	L_{0-1} intersection lineation	Cylindrical Symmetric Tight to Isoclinal	D_{P1} (1.93–1.91 Ga)	NNE-SSW compression	Axial planar subhorizontal to shallowly dipping schistosity, slaty cleavage or clast flattening Grain shape fabric in plutonic rocks Subparallel to bedding or compositional layering D_{P1} thrusts that allow intercalated sequence (evident in ultramafic volcanic rocks)	-	At all scales Isoclinal Inclined to recumbent tight to isoclinal N-, NW-, or NE-dipping axial surfaces
D_2	WNW-ESE compression	Mostly subvertical ENE-WSW axial planar and penetrative schistosity or cleavage SE-dipping brittle-ductile reverse faults/shear zones	SW (or SE depending on D_3) moderately to steeply plunging mineral lineation that is locally subparallel to L_{1-2} intersection lineation	Cylindrical Symetric Upright to recumbent Isoclinal Tight to closed	D_{P2} (1.88–1.865 Ga)	NW-SE compression	The predominant map-scale structures NE-trending axial planar slaty to crenulation cleavage or schistosity, which is locally more intense (development of shear zone) on overturned limbs of F_{P2} folds Thinning and truncation of units and development of reverse fault on these limbs NW-vergent fold thrust belt with basement and cover thrust stacking (S or SE side up to the N or NW)	L_{P2} crenulation lineation or mineral elongation subparallel to F_{P2} fold hinges Strong downdip stretching lineation on S-dipping limbs affected by shear zone	At all scales NE-trending NW-vergent Close to isoclinal
D_3	NNW-SSE compression	Subhorizontal NE-SW axial planar crenulation cleavage (mm to dm)	Subhorizontal L_{2-3} intersection lineation that is subparallel to F_2 and F_3 fold axes	Non cylindrical Assymetric Open to closed Chevron-style	D_{P3} (1.82 Ga)	NW-SE compression	Axial planar crenulation cleavage Inhomogeneously distributed Moderately to shallowly N- and NE-dipping axial surfaces (40°) Rarely found north of the MRDZ Intensity increases to the south with discrete shallow-dipping shear zones parallel to axial surfaces	Subhorizontal plunging fold axis (20°) L_{P3} crenulation lineation parallel to F fold axes	SE vergence Open to closed Chevron to similar
D_4	NW-SE transtension/ extension	N-S subvertical centimetre-spaced cleavage and faults (E- and W-dipping) ± kink bands	-	-	D_{P4} (1.78–1.735 Ga)	NNW-SSE compression	NNE-trending and steeply dipping (>60°) axial surfaces A local crenulation cleavage Dome & basin (type-1) fold interference with F_{P3} folds	Coarse-spaced L_{P4} crenulation lineation Doubly plunging Plunge direction controlled by the limb dips of older F_{P2} and F_{P1} folds	Map- to outcrop-scale Open to tight Upright moderately to shallowly plunging angular to chevron style
D_5	NW-SE transtension/ extension	E-W shear zones	-	-	D_5 (1.76–1.75 Ga)	NW-SE transtension /extension	ENE-trending brittle-ductile extensional shear zones and faults with S- and N-sides down Reactivate DP_2 structures (e.g. MRDZ)	-	-

Abbreviations: KRg = Ketyet River group, MRDZ = Meadowbank River deformation zone.

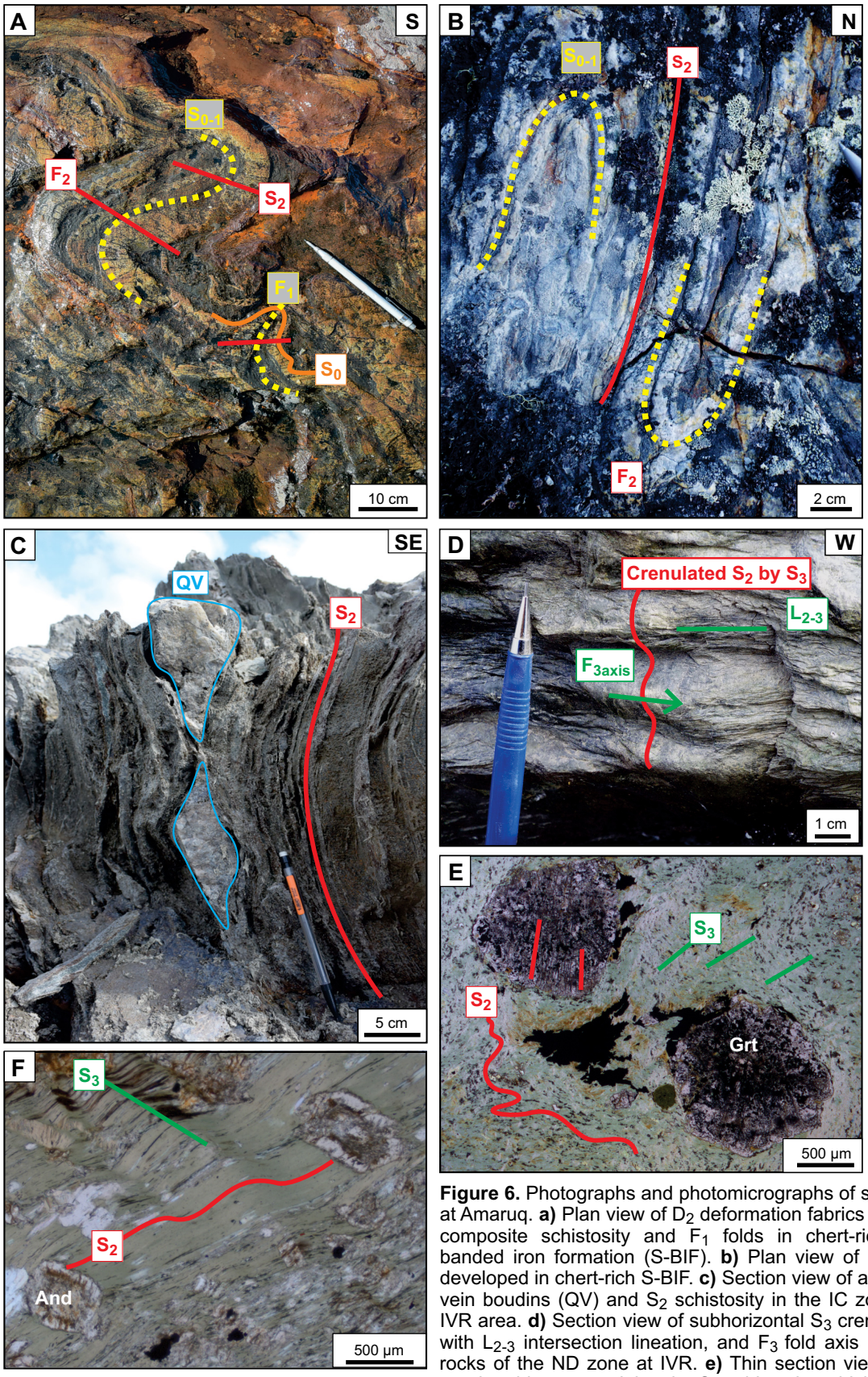

Figure 6. Photographs and photomicrographs of structures present at Amaruq. **a)** Plan view of D_2 deformation fabrics affecting the S_{0-1} composite schistosity and F_1 folds in chert-rich silicate-facies banded iron formation (S-BIF). **b)** Plan view of isoclinal F_2 folds developed in chert-rich S-BIF. **c)** Section view of asymmetric quartz vein boudins (QV) and S_2 schistosity in the IC zone, south of the IVR area. **d)** Section view of subhorizontal S_3 crenulation cleavage with L_{2-3} intersection lineation, and F_3 fold axis in mafic volcanic rocks of the ND zone at IVR. **e)** Thin section view of garnet (Grt) porphyroblasts containing the S_2 schistosity, which is crenulated by S_3 crenulation cleavage in chert-poor S-BIF. **f)** Plane-polarized thin section view of andalusite (And) crystals superimposed on S_2 schistosity and aligned along the S_3 crenulation cleavage in greywacke.

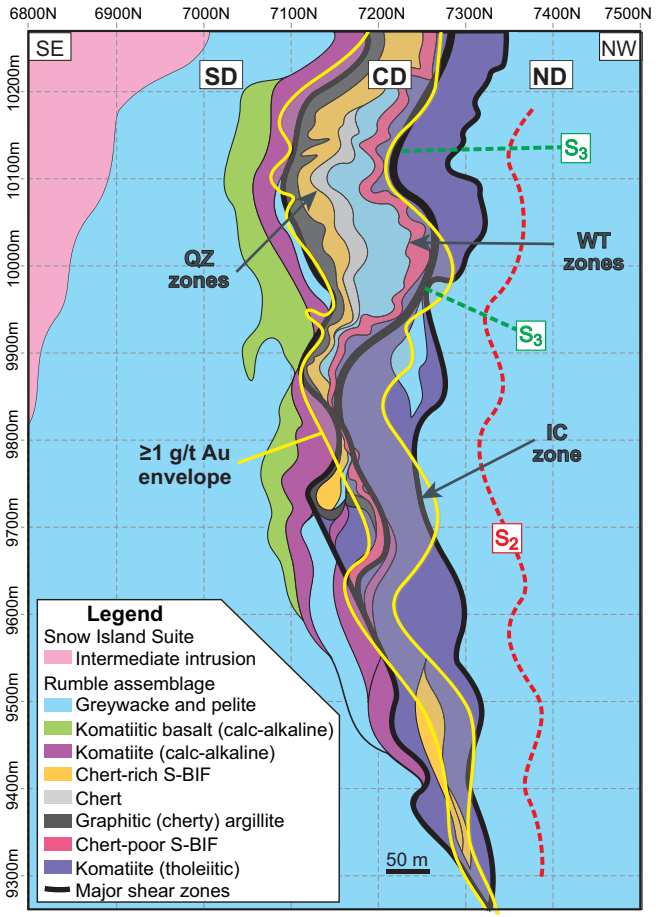

Figure 7. Interpretative cross-section of the Whale Tail (14600 E) area based on drill section. *See* Figure 2 for location of the section. Abbreviation: S-BIF = silicate-facies banded iron formation.

disseminated and replacement-style zones that are locally discordant (WT zones: Fig. 2, 6, 9b). The ore-bearing BIFs occur at the northern contact of the CD or intercalated within the tholeiitic komatiitic rocks of the ND (Fig. 7). It is mainly characterized by finely disseminated pyrrhotite-arsenopyrite±gersdorffite (Fig. 9f). Veins and veinlets are composed of actinolite-quartz±calcite, whereas the replacement zones comprise Ca-amphibole-siderophyllite-clinozoisite-garnet±apatite–titanite. This style of ore typically yields 5 to 7 g/t Au over 6 to 8 m intervals (Côté-Mantha et al., 2017). Ore in the southern part of the CD (QZ zones), consists of sharp to diffuse silicified zones (i.e. "silica flooding") within the chert-rich S-BIF (Fig. 7, 9a), and quartz veins in chert (Fig. 9c) and greywacke. Both styles of ore are mainly associated with coarse idioblastic arsenopyrite±löllingite as the main ore-related minerals. In the chert-rich S-BIF, the hydrothermal assemblage is composed of a distal zone of ripidolite-ferrostilpnomelane-siderophyllite-garnet, and a proximal ferroactinolite-calcite±apatite zone (Fig. 9a). The alteration of chert layers is characterized by a sequence of distal K-feldspar-biotite, outer proximal clinozoisite, and inner proximal actinolite-plagioclase-calcite±ilmenite/titanite zones (Fig. 9c). Mineralized intervals typically yield 4 to 5 g/t Au over 4 to 5 m intervals (Côté-Mantha et al., 2017).

The WT and QZ gold zones form a broad, steeply dipping to subvertical, F_2 and F_3 folded mineralized envelope (≥1 g/t Au; Fig. 7). Ore zones have an average thickness of 2 to 5 m, but they locally reach up to 18 m in thickness, especially in fold hinge zones. The miner-

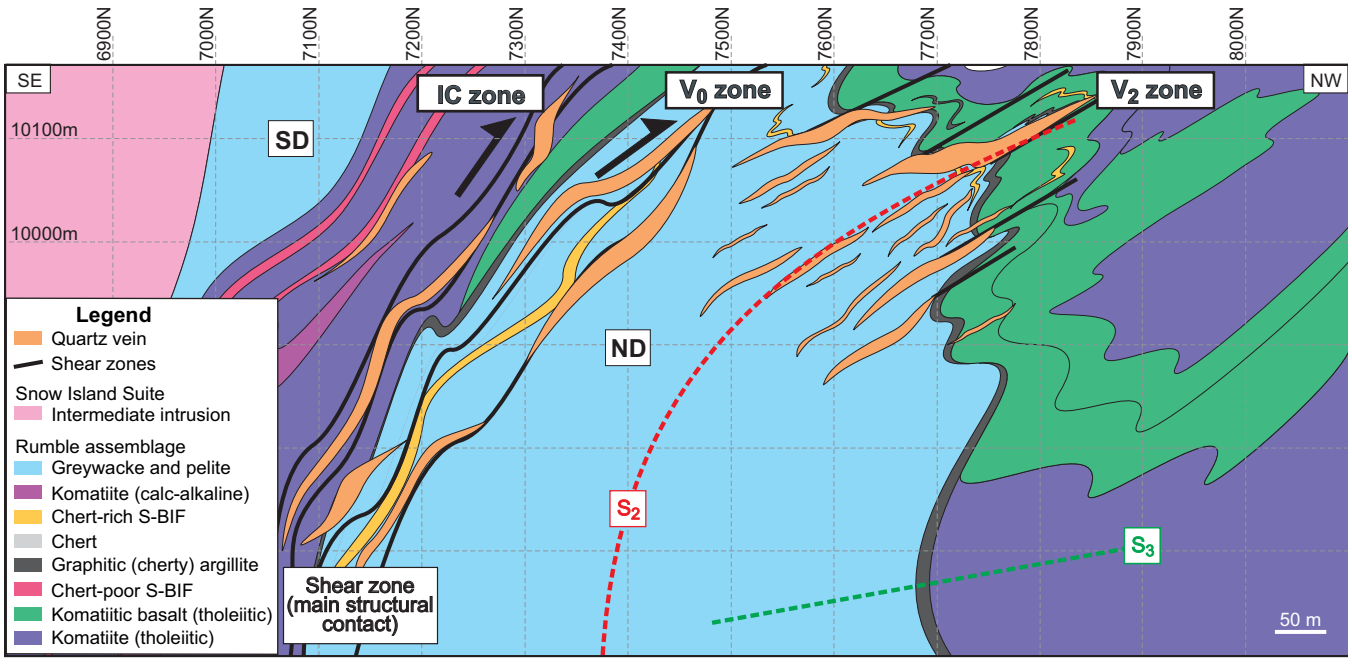

Figure 8. Interpretative cross-section of the IVR (15200 E) area based on drill section. *See* Figure 2 for the location of the section. Abbreviation: S-BIF = silicate-facies banded iron formation, SD = south domain.

alized envelope can extend for 800 m along strike, to 500 m below surface, and locally down to 730 m (Fig. 2, 7; Côté-Mantha et al., 2017). The southern and northern boundaries of the CD correspond to faults that delineate the contacts of the QZ and WT zones, respectively. To the south, the SD does not include any BIF nor gold zones. To the north and in the IVR area (Fig. 2), the contact between the komatiite and greywacke of the ND corresponds to the IC zones. The IC zones mainly consist of visible gold-bearing and sulphide-poor, shear-hosted and extensional quartz±calcite veins, which were folded, boudinaged, and recrystallized during D_2 deformation (Fig. 6c). These veins form an anastomosing network that is subparallel to the contact, which is now transposed parallel to S_2 schistosity. The komatiite is hydrothermally altered to a distal talcose and a proximal calcite-Mg-biotite-ripidolite-gersdorffite zone (Fig. 9d).

IVR Area

In the IVR area, the orebodies are mainly characterized by shallow to moderately (20–45°) southeast-dipping, auriferous quartz±calcite veins developed in high-strain corridors mostly affecting the tholeiitic mafic-ultramafic volcanic and sedimentary rocks (V zones; Fig. 8). These zones are transposed parallel to the S_2 schistosity and form a discontinuous anastomosing network of 3 to 15 m thick vein-rich corridors that extend for over 2000 m along strike, and down to at least 650 m depth (Fig. 8; Côté-Mantha et al., 2017). The alteration halo in the greywacke is characterized by proximal quartz-muscovite-calcite±apatite-tourmaline (Fig. 9g) and distal biotite-ripidolite assemblages. In the mafic volcaniclastic rocks, the distal and proximal assemblages are composed of ripidolite-clinozoisite-titanite and calcite-actinolite, respectively. The gold distribution in the V zones is usually less continuous and more erratic than the replacement-style orebodies, due to a strong nugget effect. The V zones typically yield intervals of 8 to 10 g/t Au over 4 to 5 m intervals (Côté-Mantha et al., 2017).

DISCUSSION

The presence of different styles of mineralization at Amaruq is considered a result of contrasting rheology and geochemistry of the host sequence. The main mechanisms of gold precipitation are attributed to fluid/pressure fluctuations (structural traps), and to fluid/rock interactions (lithological and geochemical traps; cf. Mikucki, 1998). The S-BIFs at Whale Tail, and to some extent at IVR, are the principal hosts of the disseminated-style orebodies, acting as a redox trap. The other lithologies are less favourable hosts for disseminated Au mineralization because of their low Fe-content, such as ultramafic volcanic rocks. In this less favourable lithology, the presence of carbonate facilitates the acidification of reacting fluid that promotes localized and sporadic precipitation of native gold ±arsenopyrite, instead of dissemination within the altered rocks (Fig. 9d; cf. Mikucki, 1998).

The study of the Amaruq area shows that two volcanic sequences are present with distinct petrographic, geochemical, and metallogenic features. The tholeiitic mafic-ultramafic rocks of the ND have a komatiitic affinity and are interlayered with chert-poor S-BIF. A large part of the auriferous quartz±carbonate auriferous veins of the V and IC zones are hosted in the ND volcanic rocks (Fig. 3, 4, 7, 8). In contrast, transitional to calc-alkaline mafic-ultramafic rocks of the SD are enriched in light REEs, and devoid of S-BIF and auriferous zones (Fig. 3, 4, 7). The structural nature of the contact between the barren SD and the ore-hosting CD, and the complete absence of mineralized and altered rocks in the SD, strongly suggest that this structural contact represents a major discontinuity. At Meadowbank, the bulk of the gold mineralization is also localized along an inferred major tectonic contact between two structurally juxtaposed volcano-sedimentary successions of slightly different ages (i.e. ca. 2717 and 2711 Ma) that may have acted as a major structure and hydrothermal fluid pathway (Janvier et al., 2015; Janvier, 2016).

Figure 9 (opposite page). a) Replacement-style zone of "silica flooding" in chert-rich silicate-facies banded iron formation (S-BIF) associated with granoblastic arsenopyrite±löllingite and textural characteristics of gold from the QZ zones. **b)** Stratabound and discordant disseminated Ca-amphibole-pyrrhotite and siderophyllite-arsenopyrite±Fe-gersdorffite and gold characterizing the replacement-style ore in chert-poor S-BIF of the WT zones. **c)** Quartz-Ca-amphibole-calcite veins with an albite-epidote proximal alteration zone, which are part of the QZ zones hosted in the chert (sample with 0.9 g/t Au). **d)** Shear zones and quartz-calcite vein hosted in the komatiite with biotite-talc proximal alteration characteristic of the IC zone (sample with 1.7 g/t Au). **e)** Backscatter photomicrograph of the replacement-style zone of "silica flooding" in chert-rich S-BIF showing the retrograde textural relationship between gold, löllingite, and arsenopyrite (sample with 18.1 g/t Au). **f)** Reflected light photomicrograph of the replacement-style ore and associated sulphide minerals in chert-poor S-BIF (sample with 4.7 g/t Au). **g)** Reflected light photomicrograph of native free gold and pyrrhotite in quartz-rich gangue characteristic of the quartz vein-style mineralization (88.9 g/t Au). **h)** Photograph of auriferous quartz±muscovite-arsenopyrite-pyrrhotite veins hosted in greywacke. Abbreviations: Ab = albite, Act = actinolite, Apy = arsenopyrite, Au = gold, Bt = biotite, Cal = calcite, Chl = chlorite, Czo = clinozoisite, Gers = gersdorffite, Grt = garnet, Lö = löllingite, Ms = muscovite, Oli = oligoclase, Po = pyrrhotite, Qtz = quartz, Rp = ripidolite, Sid = siderophyllite, Stp = stilpnomelane, Tc = talc, Ts = tschermakite.

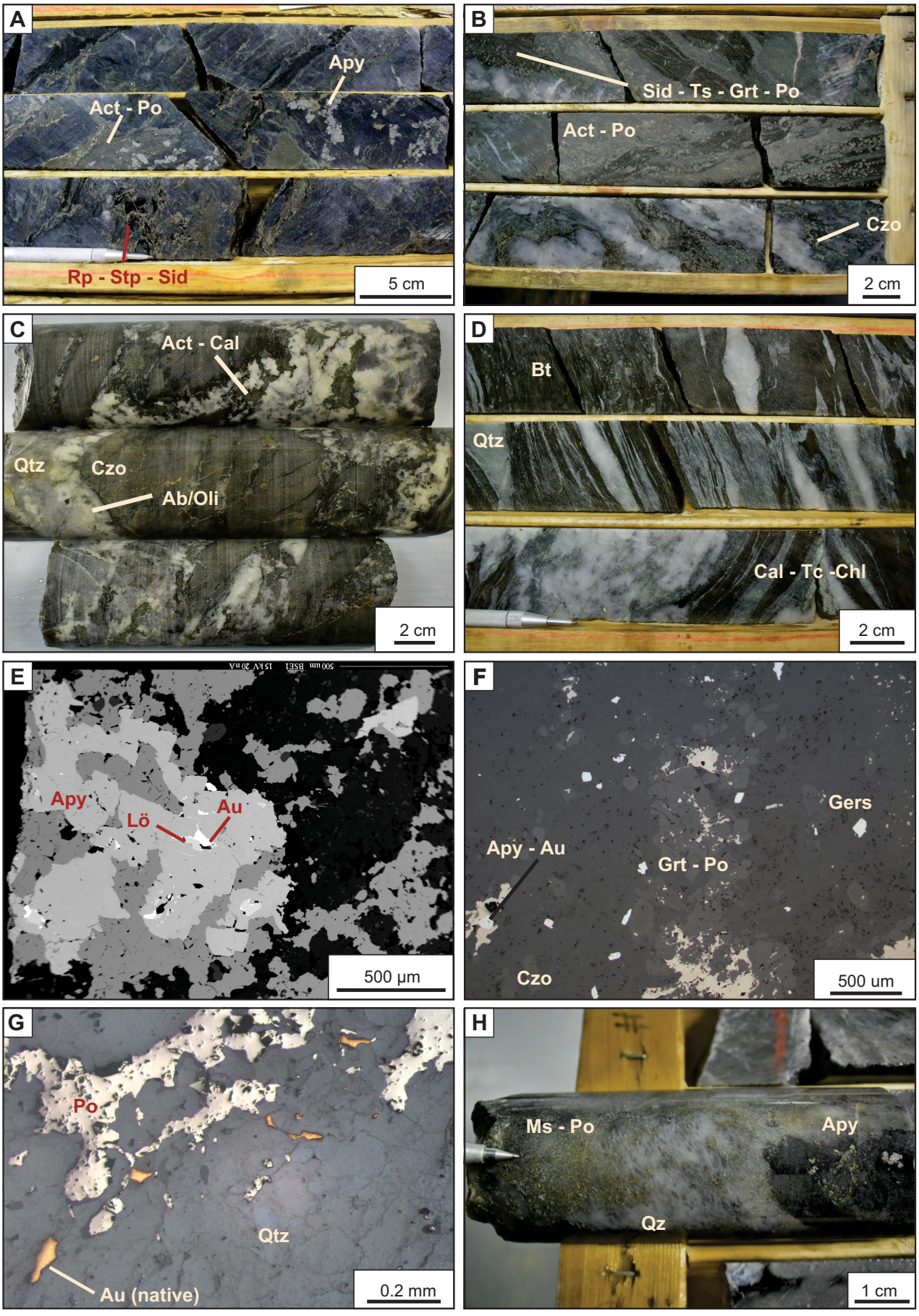
A
Apy
Act - Po
Rp - Stp - Sid
5 cm
B
Sid - Ts - Grt - Po
Act - Po
Czo
2 cm
C
Act - Cal
Qtz
Czo
Ab/Oli
2 cm
D
Bt
Qtz
Cal - Tc -Chl
2 cm
E
Apy
Lö
Au
500 µm
F
Gers
Apy - Au
Grt - Po
Czo
500 um
G
Po
Qtz
Au (native)
0.2 mm
H
Ms - Po
Apy
Qz
1 cm

Detailed studies of the Meadowbank, Amaruq, Meliadine, and Three Bluffs systems have documented the fundamental role of the Paleoproterozoic deformation in the localization of gold in the Woodburn Lake group and other greenstone belts of the western Churchill Province (Sanborn-Barrie et al., 2014; Janvier et al., 2015; Lawley et al., 2015, 2016; Janvier, 2016; Valette et al., 2018). Gold mineralization is associated with sulphidized BIF, and localized within hinge zones of F_2 folds and/or along D_1 (D_{P1}) and/or D_2 (D_{P2}) brittle-ductile shears zones, which were the key parameters in controlling the gold distribution (Sanborn-Barrie et al., 2014; Janvier et al., 2015; Lawley et al., 2015, 2016; Janvier, 2016; Valette et al., 2018). At Amaruq, the vein- and replacement-style orebodies are characterized by shallow (20°) east-plunging ore shoots subparallel to the colinear F_2 and F_3 fold axes, as well as $L_{2\text{-}3}$ intersection lineation. In the CD, moderately to steeply (65°) southwest-dipping ore shoots are locally present, especially on the south-dipping limbs of the asymmetric F_3 folds, which correspond to the stretching lineation developed during F_2 folding.

Although there is a recognized orogen-scale Trans-Hudsonian gold event in the western Churchill Province (e.g. Lawley et al., 2020), ongoing geochronology and field observations at Amaruq suggest a possible pre-Trans-Hudsonian epigenetic gold mineralizing event. Gold, or part of it, may have been initially introduced earlier, either during the Neoarchean and/or Paleoproterozoic, as suggested for the Meliadine district (Lawley et al., 2015, 2016). The Amaruq area may have preserved elements of deformation and metamorphism (and hydrothermal activity?) of the Arrowsmith Orogeny, as suggested by preliminary Re-Os ages of arsenopyrite, which are systematically older than 2.3 Ga (Mercier-Langevin et al., 2018).

IMPLICATIONS FOR EXPLORATION

Orogenic gold deposits in Precambrian greenstone belts are commonly located in the vicinity of first-order, deep-reaching crustal-scale fault zones, which allow fluid migration and vein filling of lower order shear zones and faults (e.g. Sibson et al., 1988; Groves et al., 1998; Dubé et Gosselin, 2007). Even if such a major structure has not yet been identified with confidence in the Amaruq area, lithological contacts are the locus of fertile conduits that are parallel to the northeast regional structural grain. Ore-forming hydrothermal fluids were focused along these contacts during regional deformation and metamorphism. D_2 (or D_1) high-strain brittle-ductile deformation zones, F_2 fold limbs, and/or fold hinge zones are the main structural parameters that can be used as gold metallotects in the Woodburn Lake greenstone belt. Chemical sedimentary and/or high-Fe units along with Ca-metasomatism and potassic±sodic alterations are also key lithological and geochemical parameters to consider. Identification of such key geological parameters and a better documentation of the absolute and relative timing of gold events in areas of superimposed deformation and metamorphism, are crucial for effective mineral exploration and targeting of BIF-hosted orogenic gold deposit in the Churchill Province and other Archean terranes affected by Paleoproterozoic orogenesis.

FUTURE/ONGOING WORK

Geochemical characteristics of the Amaruq deposit hydrothermal footprint are currently being studied and preliminary data are not presented in this report for conciseness. Other analytical work is still underway: 1) thermobarometry of silicate and sulphide minerals will allow estimation of the pressure and temperature conditions of the main metamorphic event(s), as well as fluid temperature during retrograde metamorphism and gold exsolution; 2) silicate and sulphide mineral chemistry analyses by scanning electron microscope (SEM) and laser ablation-inductively coupled plasma mass spectrometry (LA-ICP-MS) to constrain the composition of the ores and ore-forming conditions; 3) U-Pb and $^{40}Ar/^{39}Ar$ geochronology studies of zircon/titanite and amphibole/muscovite, respectively, to date the mafic(-ultramafic) volcanic rocks and cooling of the hydrothermal system; and 4) Re-Os dating of arsenopyrite and LA-ICP-MS elementary maps are being refined to improve the understanding of the timing of gold mineralization at different scales. All the field observations and analytical data will be integrated to develop a model for the formation of the BIF-hosted Amaruq gold deposit and to contribute to improved exploration models.

ACKNOWLEDGMENTS

This report is a contribution to NRCan's Targeted Geoscience Initiative Program (TGI-5). Support for this study was provided through the Gold Project and activity G-2.4: Lithologic and tectonic controls on Paleoproterozoic BIF-hosted/associated gold. This work is part of an ongoing MITACS supported Ph.D. study by M. Valette at the Université du Québec à Montréal (UQÀM). We thank Agnico Eagle Mines Ltd. for access to their property, drill core and databases, and for scientific, logistical, and financial support throughout the project. This report benefited from the reviews of Z. Toth and S. Castonguay. We also acknowledge E. Ambrose and V. Bécu for their editorial handling and technical reviews.

REFERENCES

Annesley, I.R., 1990. Petrochemistry of the Woodburn Lake group komatiitic suite, Amer Lake, N.W.T., Canada; Ph.D. thesis, University of Ottawa, Ottawa, Ontario, 523 p.

Armitage, A.E., 1996. Geology and petrology of gold-bearing banded iron formation Keewatin district, Northwest Territories; M.Sc. thesis, Laurentian University, Sudbury, Ontario, 161 p.

Berman, R.G., 2010. Metamorphic map of the western Churchill Province, Canada; Geological Survey of Canada, Open File 5279, 49 p., 3 sheets, scale 1:2 500 000.

Berman, R.G., Ryan, J.J., Tella, S., Sanborn-Barrie, M., Stern, R., Aspler, L., Hanmer, S., and Davis, W., 2000. The case of multiple metamorphic events in the Western Churchill Province: evidence from linked thermobarometric and in-situ SHRIMP data, and jury deliberations; GeoCanada 2000 Conference, Extended Abstracts, CD-ROM, Abstract 836.

Berman, R.G., Sanborn-Barrie, M., Stern, R.A., and Carson, C.J., 2005. Tectonometamorphism at ca. 2.35 and 1.85 Ga in the Rae domain, western Churchill Province, Nunavut, Canada: insights from structural, metamorphic and in situ geochronological analysis of the southwestern Committee Bay belt; The Canadian Mineralogist, v. 43, p. 409–442.

Berman, R.G., Davis, W.J., and Pehrsson, S., 2007. Collisional Snowbird tectonic zone resurrected: Growth of Laurentia during the 1.9 Ga accretionary phase of the Hudsonian orogeny; Geology, v. 35, p. 911–914.

Berman, R.G., Pehrsson, S., Davis, W.J., Ryan, J.J., Qui, H., and Ashton, K.E., 2013. The Arrowsmith orogeny: Geochronology and thermobarometric constraints on its extent and tectonic setting in the Rae craton, with implications for pre-Nuna supercontinent reconstruction; Precambrian Research, v. 232, p. 44–69.

Boström, K., 1973. The origin and fate of ferromanganoan active ridge sediments; Stockholm; Contributions in Geology, v. 27, p. 147–243.

Calhoun, L., 2017. Lithostratigraphy and structure of the eastern Amer Group, Nunavut: Using combined surface mapping and enhanced sub-surface geophysical data; M.Sc. thesis, University of New Brunswick, Fredericton, New Brunswick, 166 p.

Côté-Mantha, O., Gosselin, G., Vaillancourt, D., and Blackburn, A., 2017. The Amaruq deposit – Building a customized toolset and using a flexible geomodel: Optimization from discovery to mine development; *in* Proceedings of Exploration 17, (ed.) V. Tschirhart and M.D. Thomas; Sixth Decennial International Conference on Mineral Exploration, 2017, p. 553–567.

Davies, T., Richards, J.P., Creaser, R.A., Heaman, L.M., Chacko, T., Simonetti, A., Williamson, J., and McDonald, D.W., 2010. Paleoproterozoic age relationships in the Three Bluffs Archean iron formation-hosted gold deposit, Committee Bay greenstone belt, Nunavut, Canada; Exploration and Mining Geology Journal, v. 19, p. 55–80.

Dubé, B. and Gosselin, P., 2007. Greenstone-hosted quartz-carbonate vein deposits; *in* Mineral Deposits of Canada: A synthesis of Major Deposit-Types, District Metallogeny, the Evolution of Geological Provinces, and Exploration Methods, (ed.) W.D. Goodfellow; Geological Association of Canada, Mineral Deposits Division, Special Publication, No. 5, p. 49–73.

Groves, D.I., Goldfarb, R.J., Gebre-Mariam, M., Hagemann, S.G., and Robert, F., 1998. Orogenic gold deposits: A proposed classification in the context of their crustal distribution and relationship to other gold deposit types; Ore Geology Reviews, v. 13, p. 7–27.

Janvier, V., Castonguay, S., Mercier-Langevin, P., Dubé, B., Malo, M., McNicoll, V.J., Creaser, R.A., de Chavigny, B., and Pehrsson, S.J., 2015. Geology of the banded iron formation-hosted Meadowbank gold deposit, Churchill Province, Nunavut; *in* Targeted Geoscience Initiative 4: Contributions to the understanding of Precambrian lode gold deposits and implications for exploration, (ed.) B. Dubé and P. Mercier-Langevin; Geological Survey of Canada, Open File 7852, p. 255–269.

Janvier, V., 2016. Géologie du gisement d'or Meadowbank encaissé dans des formations de fer rubanées, Nunavut, Canada; Ph.D. thesis, Institut national de la recherche scientifique – Centre Eau Terre Environnement, Québec, Quebec, 472 p.

Jefferson, C.W., White, J.C., Young, G.M., Patterson, J., Tschirhart, V.L., Pehrsson, S.J., Calhoun, L., Rainbird, R.H., Peterson, T.D., Davis, W.J., Tella, S., Chorlton, L.B., Scott, J.M.J., Percival, J.A., Morris, W.A., Keating, P., Anand, A., Shelat, Y., and MacIsaac, D., 2015. Outcrop and remote predictive geology of the Amer Belt and basement beside and beneath the northeast Thelon Basin, in parts of NTS 66-A, B, C, F, G and H, Kivalliq Region, Nunavut; Geological Survey of Canada, Open File 7242, 1 sheet.

Jensen, L.S., 1976. A new cation plot for classifying subalkalic volcanic rocks; Ontario Ministry of Natural Resources, Miscellaneous Paper 66, 22 p.

Kerswill, J.A., Goff, S.P., Wilkinson, L., Jenner, G.A., Kjarsgaard, B.A., Bretzlaff, R., and Samaras, C., 1998. An update on the metallogeny of the Woodburn Lake group, western Churchill province, Northwest Territories; *in* Current Research 1998-C; Geological Survey of Canada, p. 29–41.

Lauzon, M.-C., Mercier-Langevin, P., Valette, M., Beaudoin, G., De Souza, S., Côté-Mantha, O., and Simard, M., 2020. Ore mineralogy and mineral chemistry of the Whale Tail zone, Amaruq gold deposit, Nunavut; *in* Targeted Geoscience Initiative 5: Contributions to the Understanding of Canadian Gold Systems, (ed.) P. Mercier-Langevin, C.J.M. Lawley, and S. Castonguay; Geological Survey of Canada, Open File 8712, p. 267–279. doi:10.4095/326044

Lawley, C.J.M., Creaser, R.A., Jackson, S.E., Yang, Z., Davis, B.J., Pehrsson, S.J., Dubé, B., Mercier-Langevin, P., and Vaillancourt, D., 2015. Unraveling the Western Churchill Province Paleoproterozoic gold metallotect: Constraints from Re-Os arsenopyrite and U-Pb xenotime geochronology and LA-ICP-MS arsenopyrite trace element chemistry at the BIF-hosted Meliadine gold district, Nunavut, Canada; Economic Geology, v. 110, p. 1425–1454.

Lawley, C.J.M., McNicoll, V., Sandeman, H., Pehrsson, S., Simard, M., Castonguay, S., Mercier- Langevin, P., and Dubé, B., 2016. Age and geological setting of the Rankin Inlet greenstone belt and its relationship to the gold endowment of the Meliadine gold district, Nunavut, Canada; Precambrian Research, v. 275, p. 471–795.

Lawley, C.J.M., Selby, D., Davis, W.J., Yang, E., Zhang, S., Jackson, S.E., Petts, D.C., O'Connor, A.R., and Schneider, D.A., 2020. Paleoproterozoic gold and its tectonic triggers and traps: Implications from Re-Os sulphide and U-Pb detrital zircon geochronology, Lynn Lake, Manitoba; *in* Targeted Geoscience Initiative 5: Contributions to the Understanding of Canadian Gold Systems, (ed.) P. Mercier-Langevin, C.J.M. Lawley, and S. Castonguay; Geological Survey of Canada, Open File 8712, p. 211–222. doi:10.4095/326033

MacLean, T.J. and Barrett W.H., 1993. Lithogeochemical techniques using immobile elements; Journal of Geochemical Exploration, v. 48, p. 109–133.

McDonough, W.F. and Sun, S.S., 1995. The composition of the Earth; Chemical Geology, v. 120, p. 223–253.

McNicoll, V., Thériault, R.J., and McDonough, M.R., 2000. Taltson basement gneissic rocks: U-Pb and ND isotopic constraints on the basement to the Paleoproterozoic Taltson magmatic zone, northeastern Alberta; Canadian Journal of Earth Sciences, v. 38, p. 1575–1596.

Mercier-Langevin, P., Valette, M., De Souza, S., Creaser, R.A., McNicoll, V., Grondin-Leblanc, P., St-Pierre, B., Lauzon, M.-

C., Malo, M., Côté-Mantha, O., and Simard, M., 2018. Lithologic controls on Paleoproterozoic BIF-hosted/associated gold: Overview of Re-Os geochronology and Pb isotopes preliminary results; *in* Targeted Geoscience Initiative: 2017 report of activities, volume 1, (ed.) N. Rogers; Geological Survey of Canada, Open File 8358, p. 147–152.

Mikucki, E.J., 1998. Hydrothermal transport and depositional processes in Archean lode-gold systems: A review; Ore Geology Reviews, v. 13, p. 307–321.

Pehrsson, S.J., Wilkinson, L., Zaleski, E., Kerswill, J., and Alexander, B., 2000. Structural geometry of the Meadowbank deposit area, Woodburn Lake Group – Implications for genesis of a major gold deposit in the Western Churchill Province; A Contribution to the Western Churchill NATMAP Project, Geological Survey of Canada, 4 p.

Pehrsson, S.J., Berman, R.G., and Davis, W.J., 2013a. Paleoproterozoic orogenesis during Nuna aggregation: A case study of reworking of the Rae craton, Woodburn Lake, Nunavut; Precambrian Research, v. 232, p. 167–188.

Pehrsson, S.J., Berman, R.G., Eglington, B., and Rainbird, R., 2013b. Two Neoarchean supercontinents revisited: The case for a Rae family of cratons; Precambrian Research, v. 232, p. 27–43.

Sanborn-Barrie, M., Davis, W.J., Berman, R.G., Rayner, N., Skulski, T., and Sandman, H., 2014. Neoarchean continental crust formation and Paleoproterozoic deformation of the central Rae craton, Committee Bay belt, Nunavut; Canadian Journal of Earth Sciences, v. 51, p. 635–667.

Sherlock, R., Pehrsson, S.J., Logan, A.V., Hrabi, R.B., and Davis, W.J., 2004. Geological setting of the Meadowbank gold deposits, Woodburn Lake group, Nunavut; Exploration and Mining Geology, v. 13, p. 67–107.

Sibson, R.H., Robert, F., and Poulsen, K.H., 1988. High-angle reverse faults, fluid-pressure cycling, and mesothermal gold-quartz deposits; Geology, v. 16, p. 551–555.

Spry, P.G., Peter, J.M., and Slack, J.F., 1998. Meta-exhalites as exploration guides to ore; *in* Metamorphosed and Metamorphogenic Ore Deposits, (ed.) P.G. Spry, B. Marshall, and F.M. Vokes; Reviews in Economic Geology, v. 11, p. 167–204.

Valette, M., De Souza, S., Mercier-Langevin, P., McNicoll, V.J., Grondin-LeBlanc, P., Côté-Mantha, O., Simard, M., and Malo, M., 2018. Lithological, hydrothermal, structural and metamorphic controls on the style, geometry and distribution of the auriferous zones at Amaruq, Churchill Province, Nunavut; *in* Targeted Geoscience Initiative: 2017 report of activities, volume 1, (ed.) N. Rogers; Geological Survey of Canada, Open File 8358, p. 153–156.

Zaleski, E., 2005. Geology, Meadowbank River area, Nunavut; Geological Survey of Canada, Map 2068A, scale 1:50 000.

Ore mineralogy and mineral chemistry of the Whale Tail zone, Amaruq gold deposit, Nunavut

Marie-Christine Lauzon[1], Patrick Mercier-Langevin[2*], Manon Valette[3], Georges Beaudoin[1], Stéphane De Souza[3], Olivier Côté-Mantha[4], and Marjorie Simard[5]

[1]Université Laval, 1065 Avenue de la Médecine, Québec, Quebec G1V 0A6
[2]Geological Survey of Canada, 490 rue de la Couronne, Québec, Quebec G1K 9A9
[3]Université du Québec à Montréal, 201 Avenue du Président-Kennedy, Montréal, Quebec H2X 3Y7
[4]Agnico Eagle Mines Limited, Exploration Division, 765 chemin de la mine Goldex, Val-d'Or, Quebec J9P 7G4
[5]Agnico Eagle Mines Limited, Technical Services, 10200 route de Preissac, Rouyn-Noranda, Quebec J0Y 1C0
[*]Corresponding author's e-mail: patrick.mercier-langevin@canada.ca

ABSTRACT

The 6 Moz Au (190 metric t Au) Amaruq deposit is hosted in a sequence of complexly deformed and metamorphosed chert, graphitic argillite, silicate-facies banded iron formation and mafic-ultramafic volcanic rocks of the Archean Woodburn Lake group in the Kivalliq region of Nunavut. The region was affected by Archean and Paleoproterozoic orogeneses and most Au occurrences are interpreted to be associated with the ca 1.91–1.81 Ga Trans-Hudson event. However, new work indicates that some of the Au may be Early Paleoproterozoic or perhaps even Archean, raising uncertainty about the timing of the Au ore-forming event(s) versus the tectonometamorphic evolution of the region.

The arsenopyrite- and pyrrhotite-dominant Au mineralization of the Whale Tail zone of the Amaruq deposit was sampled from representative drill core to determine the timing of Au introduction relative to the main deformation and associated metamorphism in the study area. Petrography and micro-analyses indicate that the sulphides underwent a complete prograde-retrograde metamorphic cycle, with pre-peak metamorphism Au-rich arsenopyrite being replaced by an assemblage of syn-peak prograde Au-rich löllingite and pyrrhotite. This was followed by retrogression of löllingite to Au-poor secondary arsenopyrite and native Au and electrum inclusions.

INTRODUCTION

Gold deposits of the Kivalliq region of Nunavut are commonly hosted in Neoarchean banded iron formation (BIF). These Au deposits generally consist of contrasting styles of mineralization that are partially to completely hosted in complexly deformed and metamorphosed BIF units (Kerswill, 1993; Dubé and Mercier-Langevin, 2015). This includes world-class Au deposits such as Meliadine (e.g. Lawley et al., 2015a,b; St.Pierre et al., 2020), Meadowbank (Janvier et al., 2015), and Amaruq (e.g. Côté-Mantha et al., 2015, 2017; Mercier-Langevin et al., 2018; Valette et al., 2020) (Fig. 1).

Gold is associated with a crustal-scale fault and its splays at Meliadine (Carpenter and Duke, 2004; Lawley et al., 2015b), with intensely poly-deformed BIF units at the Portage and Goose deposits of the Meadowbank mine (Sherlock et al., 2004; Janvier et al., 2015) and Three Bluffs prospect (Davies et al., 2010), with folded BIFs and steeply dipping high-strain zones and associated shallowly dipping vein systems at Amaruq (Valette et al., 2020). Although Au zones are geometrically controlled by Paleoproterozoic structures predominantly associated with ca. 1.91–1.81 Ga Trans-Hudson tectonometamorphism (e.g. Hrabi et al., 2003; Pehrsson et al., 2013), recent research reported Re-Os ages as old as 2.3 Ga at Meliadine (Lawley et al., 2015a) and ca. 2.65 Ga at Amaruq (Mercier-Langevin et al., 2018) indicates a more complex, or at least longer (older) hydrothermal history.

The timing of the Au ore-forming event(s) versus the tectonometamorphic evolution at the Whale Tail zone of the Amaruq deposit in eastern Nunavut is determined by documenting the mineralogy and mineral chemistry of the Au-associated sulphides in relation to the regional structural and metamorphic history (Fig. 1). This study provides preliminary constraints on the timing of Au mineralization at Amaruq, documenting that the ore-associated sulphides and Au were introduced before the peak of metamorphism and went through at least one entire prograde-retrograde metamorphic cycle.

Geological Context and Methodology

The Amaruq Au deposit is located in the Kivalliq region of Nunavut, 50 km north of the Meadowbank

Lauzon, M.-C., Mercier-Langevin, P., Valette, M., Beaudoin, G., De Souza, S., Côté-Mantha, O., and Simard, M., 2020. Ore mineralogy and mineral chemistry of the Whale Tail zone, Amaruq gold deposit, Nunavut; *in* Targeted Geoscience Initiative 5: Contributions to the Understanding of Canadian Gold Systems, (ed.) P. Mercier-Langevin, C.J.M. Lawley, and S. Castonguay; Geological Survey of Canada, Open File 8712, p. 267–279. https://doi.org/10.4095/326044

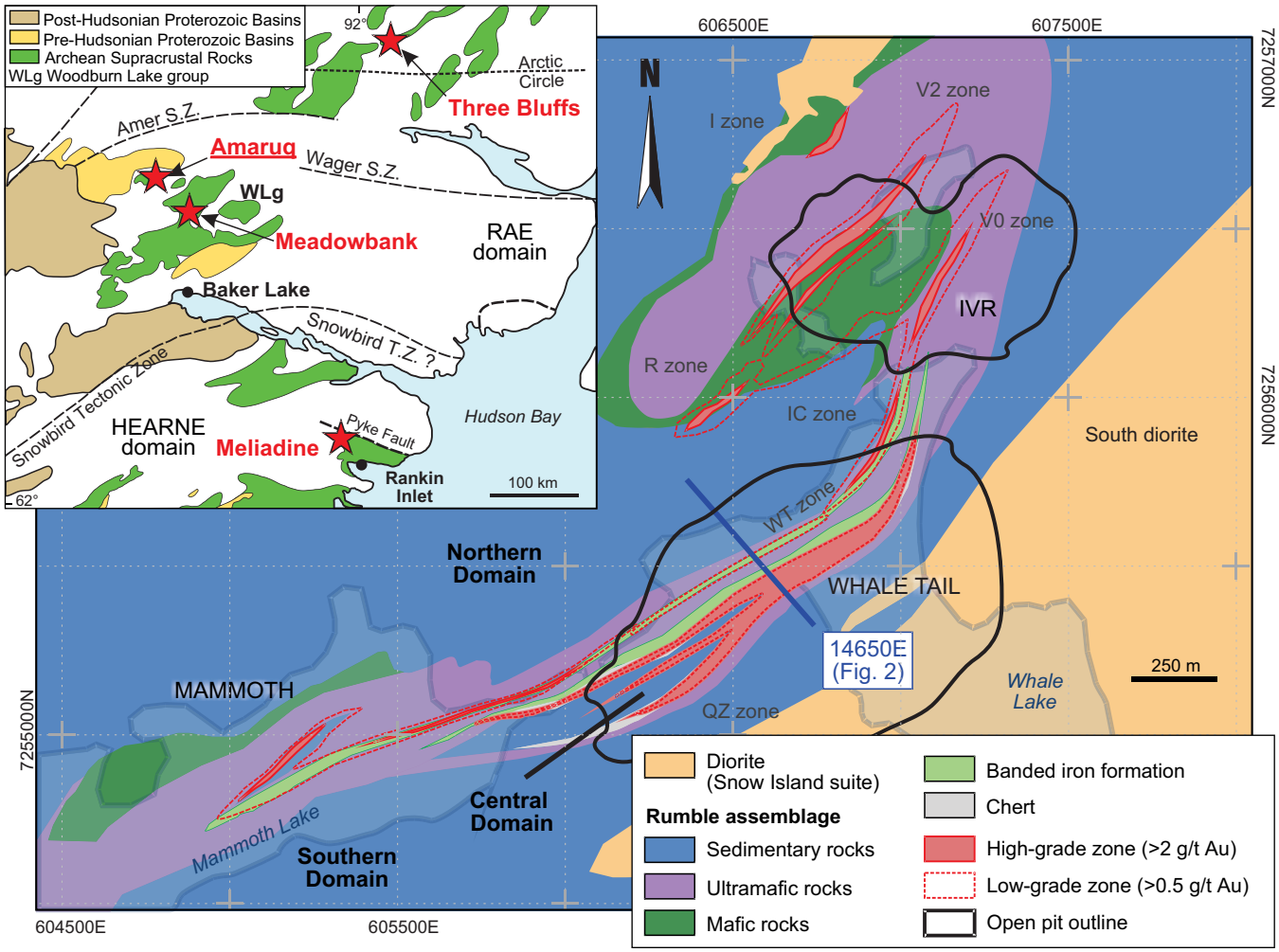

Figure 1. Simplified geological map showing the location and the Amaruq deposit (inset) and the geometry of the main ore zones (*modified from* Agnico Eagle Mines limited, and Valette et al., 2020). The location of section 14650E (Fig. 2) is also shown. Map coordinates are in UTM NAD83, Zone 14. Abbreviations: S.Z. = shear zone, T.Z. = tectonic zone.

mine (Fig. 1). It is hosted in the ca. 2.73–2.63 Ga metavolcanic and metasedimentary rocks of the Woodburn Lake group (Valette et al., 2020). Note that for conciseness, the prefix "meta" is omitted below. Three main mineralized zones (Whale Tail, IVR, and Mammoth: Fig. 1) have been delineated to date, with commercial production at the Whale Tail zone having officially started in September 2019. Total reserves (proven and probable) and resources (measured, indicated, and inferred) at Amaruq are estimated at 46.4 million metric tonnes of ore at an average grade of 4.08 g/t for a total gold content of 6.08 Moz (189.1 metric tonnes) of Au (Agnico Eagle Mines limited, 2019).

To characterize the ore mineralogy, mineral chemistry, and paragenetic evolution of the sulphide assemblage associated with the gold mineralization at Amaruq, targeted sampling of the altered and mineralized intervals in the Whale Tail zone was completed on core from drillhole IVR14-158. This drillhole has a total length of 303 metres, an azimuth of N146º with a plunge of 70º, and intersected several Au-rich intervals in the central part of the Whale Tail zone (e.g. 9.97 g/t Au over 6.4 m: Lauzon, 2017; Fig. 2). It is oriented approximately perpendicular to the trend of the units and dominant structural features, such as the principal penetrative planar fabric, but plunges subparallel to the dip of units in that area (Fig. 2). The drillhole intersects mineralized chert, graphitic argillite, and greywacke (Mercier-Langevin et al., 2020), which are part of the central sedimentary package that host most of the ore in the Whale Tail zone. It also intersects BIF and mafic-ultramafic volcanic rocks (Fig. 2).

Several orogenic events are recognized in the region, such as the 2.56–2.50 Ga MacQuoid Orogeny, the 2.56–2.28 Ga Arrowsmith Orogeny, the 1.98–1.91 Ga Taltson-Thelon Orogeny, and the polyphase 1.91–1.81 Ga Trans-Hudson Orogeny (Pehrsson et al., 2013). In the Meadowbank-Amaruq area (Fig. 1), the first phase of metamorphism (M_1), attributed to the Snowbird phase (D_1) of the Trans-Hudson Orogeny is overprinted by the main prograde metamorphic event (M_2) at ca. 1.85–1.83 Ga during the later phase of

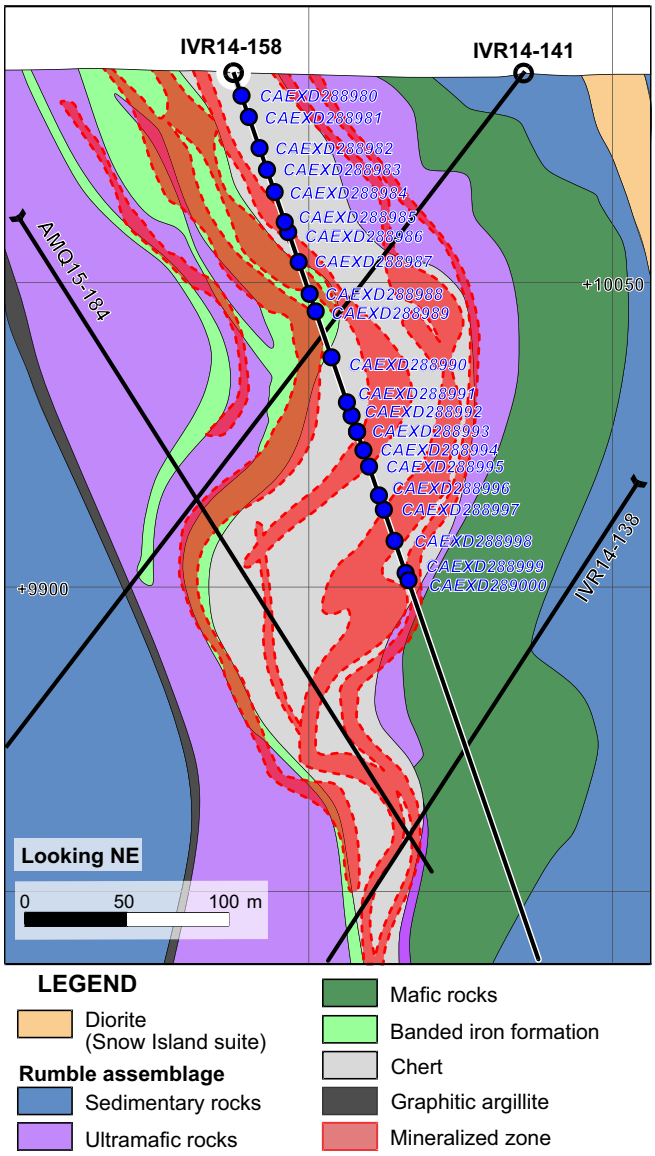

Figure 2. Simplified geological composite section (14,650E ± 50 m, looking northeast) of the central part of the Whale Tail zone showing the trace of drillhole IVR14-158 and the locations of studied samples. *Modified from* Agnico Eagles Mines limited.

Trans-Hudson deformation (D_2: Pehrsson et al., 2013 and references therein). Readers are referred to Valette et al. (2020) for more information about the structural and metamorphic evolution and potential correlation with regional tectonometamorphic events, nature of the host units, alteration assemblages, and ore zone geometry at Amaruq.

A series of representative samples of the different styles of mineralization was selected for petrographic (transmitted and reflected light microscopy) characterization, electron microprobe analyses, scanning electron microscopy (SEM) analyses (Lauzon, 2017), and whole-rock lithogeochemistry (Mercier-Langevin et al., 2020).

RESULTS

Gangue Mineralogy

The ore intervals in drillhole IVR14-158 are hosted in metasedimentary rocks such as chert (Fig. 3a,b), greywacke, siltstone (Fig. 3c) and mudstone (Fig. 3d), graphitic argillite (Fig. 3e), and silicate-facies iron formation (Fig. 3f). The chert units comprise fine Fe-rich laminae, which can complicate the classification of the units (e.g. chert-rich versus chert-poor BIF: Valette et al., 2020). Ore intervals mostly consist of stratabound to discordant silicification ("silica-flooding") zones and veins containing variable amounts of ore minerals (e.g. pyrrhotite, arsenopyrite, löllingite, and pyrite; Fig. 3g,h). Only some of the most common gangue minerals (quartz, chlorite, Fe- and Ca-amphiboles, biotite, stilpnomelane, garnet, and andalusite) are presented here, and readers are referred to Valette et al. (2020) for more information.

Quartz is the dominant gangue mineral, and occurs either as a primary component of the host rocks (e.g. detrital quartz in greywacke and microcrystalline quartz in chert) or as a secondary phase associated with alteration and/or veining (e.g. Fig. 3h). It is generally very fine-grained (0.05–2 mm) and shows evidence of recrystallization and deformation, such as undulose extinction. Quartz contains micron-sized silicate mineral inclusions. It is also present in the quartz-carbonate-chlorite veins in the mineralized intervals.

Chlorite is also a common constituent of the gangue. It occurs as bands, often associated with biotite and amphiboles, in both iron formation and chert units (Fig. 3a,b). Chlorite is Fe-rich (ripidolite ($(Mg,Fe,Al)_6(Si,Al)_4O_{10}(OH)_8$): Lauzon, 2017; Valette et al., 2020).

A range of Fe- and Ca-rich amphiboles is associated with the mineralized intervals (Valette et al., 2020). In BIF and in chert with Fe-rich laminae, grunerite has a prismatic to radial, acicular habit and is associated with biotite. Hornblende forms millimetre-sized isolated crystals, sometimes with biotite coronas. The amphiboles form porphyroblasts that overprint foliated white micas. According to Valette et al. (2020), white micas locally define the S_1 fabric at Amaruq, whereas amphiboles are associated with the M_2 peak metamorphism at upper greenschist facies.

Biotite (siderophyllite ($KFe^{2+}{}_2Al(Al_2Si_2O_{10})(OH)_2$): Lauzon, 2017; Valette et al., 2020) is the most common phyllosilicate in the samples studied from drillhole IVR14-158. It is locally present as inclusions in M_2 garnet cores and rims. It is locally aligned along a late crenulation cleavage. In chert units, biotite occurs as randomly oriented porphyroblasts in chlorite-rich bands. Stilpnomelane ($(K,Ca,Na)(Fe,Mg,Al)_8(Si,Al)_{12}(O,OH)_{36}\cdot nH_2O$) is also a common constituent of the gangue assemblage. It forms elongated, acicular crys-

tals in the granoblastic matrix of silicified and mineralized zones. It commonly fills the interstices between amphiboles.

Garnet porphyroblasts are present in BIF units. Garnet varies in size from 0.5 to 2 mm and is generally strongly fractured, poikiloblastic, and zoned, and contains micrometre-sized inclusions of magnetite, pyrrhotite, and silicates. Silicate inclusions define a pre-metamorphic peak fabric, whereas rims overprint that fabric, suggesting that garnet growth (and peak metamorphism) occurred syn- to late-D_2 deformation. Garnet varies in composition from the core to the rim. In samples from the IVR14-158 drillcore, the analyzed garnet cores are richer in Al and the rims are richer in Mn. In general, garnet has higher Mn content in BIF units and higher Al content in chert units (Lauzon, 2017).

Andalusite is locally present in the sedimentary rocks and is aligned parallel to a spaced cleavage that overprints the S_2 fabric, indicating a late metamorphic overprint (D_3 deformation: Valette et al., 2020). Post-D_2 retrogression is indicated by partial replacement of biotite by chlorite. Other gangue minerals (not described in detail in this study) such as epidote, tourmaline, titanite, albite, calcite, nickeline, and Cr-spinel are locally to commonly developed in the mineralized intervals, depending on the mineralization style and host rock.

Ore Mineralogy and Mineral Chemistry

Mineralized intervals at Amaruq, and especially in the Whale Tail zone, are directly associated with arsenopyrite and/or pyrrhotite-bearing intervals (e.g. Valette et al., 2020), and are considered very good visual indicators of potential high-grade Au mineralization (e.g. Fig. 3f,g,h). Therefore, the following section focusses on these two minerals and the most commonly associated phases, i.e., löllingite, pyrite, and electrum. Other phases commonly spatially associated with ore intervals, which can vary with host-rock composition, include chalcopyrite, gersdorffite, pentlandite, violarite, cobaltite, magnetite, ilmenite, scheelite, hessite, tourmaline, and titanite (Lauzon, 2017; Guillevic, 2019; Valette et al., 2020).

Arsenopyrite

Three types of arsenopyrite were documented, mostly based on textural relationships. Type 1 is fine grained (<0.5 mm) and occurs as isolated or disseminated idiomorphic grains (Fig. 4a,b). Type 2 consists of ≤2 mm, hypidiomorphic and idioblastic crystals often forming clusters in siliceous zones and quartz veins (Fig. 3h). Type 3 consists of relatively coarse (1–8 mm), heterogeneous grains or clusters with irregular edges and abundant pyrrhotite and löllingite inclusions (Fig. 3g, 4c). Arsenopyrite of the third type appears to be in equilibrium with the other two minerals as evidenced by triple junctions at the interface between grains (Lauzon, 2017). None of the three types of arsenopyrite appear to be zoned. Native Au (>75 wt% Au and <25 wt% Ag) and/or electrum (<75 wt% Au and >25 wt% Ag) grains commonly occur as inclusions along the margins of the arsenopyrite grains or in fractures. The contrasting arsenopyrite textures, the association with löllingite and pyrrhotite, and the presence of large idioblastic grains suggest recrystallization of arsenopyrite, which is in agreement with the complex element distribution discovered in some crystals by laser ablation inductively-coupled plasma mass spectrometry mapping (Mercier-Langevin et al., 2018).

Microprobe analyses by wavelength dispersive X-ray spectroscopy (WDS) show the presence of invisible Au in all three types of arsenopyrite, although results are commonly close to the detection limit (Table 1). Arsenopyrite types 1 and 2 contain higher Au values on average (101 and 257 ppm, respectively: Lauzon, 2017) than type 3, which is generally below the detection limit. Gold concentrations in type 1 arsenopyrite vary between 29 and 182 ppm (Table 1); although only one analysis is available for type 2 arsenopyrite, it is the highest Au concentration obtained in arsenopyrite from this study. Gold values in type 3 arsenopyrite vary

Figure 3 (opposite page). Photographs of the principal host lithologies and representative examples of mineralized rock intersections in drillhole IVR14-158. **a)** Sample CAEXD288990: barren (21 ppb Au), finely bedded chert with thin Fe-rich (amphiboles±oxides) laminae, with small amounts of disseminated pyrrhotite (from a 0.01 g/t Au over 1.5 m interval). **b)** Sample CAEXD288984: barren (59 ppb Au), finely bedded chert and amphibole-rich layers with small amounts of disseminated pyrrhotite and larger pyrrhotite grains (from a 0.28 g/t Au over 1.5 m interval). **c)** Sample CAEXD288992: barren (59 ppb Au), crudely bedded siltstone (from a 0.05 g/t Au interval). **d)** Sample CAEXD288995: barren (36 ppb Au), laminated mudstone with disseminated pyrrhotite (from a 0.07 g/t Au over 1.2 m interval). **e)** Sample CAEXD288998: barren (45 ppb Au), pyrrhotite-rich graphitic argillite (from a 0.11 g/t Au over 1.5 m interval). **f)** Sample CAEXD288989: mineralized (839 ppb Au), pyrrhotite-rich silicate-facies (amphibole-rich) banded iron formation with Mn-rich garnet porphyroblasts (from a 5.99 g/t Au over 0.9 m interval). **g)** Sample CAEXD288999: Au-rich (15,100 ppb Au), silicified chert with abundant pyrrhotite and granoblastic arsenopyrite (from a 5.97 g/t Au over 0.6 m interval). **h)** Sample CAEXD288985: Au-rich (27,200 ppb Au), massively silicified chert and/or diffuse quartz vein with abundant coarse-grained arsenopyrite (from a 25.5 g/t Au over 0.9 m interval). Gold concentrations (in ppb) from Mercier-Langevin et al. (2020). Assay values (in g/t) from Agnico Eagles Mines Limited. *See* Figure 2 for drillhole IVR14-158 and sample locations. Abbreviations: Am = Ca-Fe amphiboles, Apy = arsenopyrite, Grt = garnet, Gru = grunerite, Po = pyrrhotite, Qtz = quartz/chert, S_0 = bedding, S_2 = main foliation.

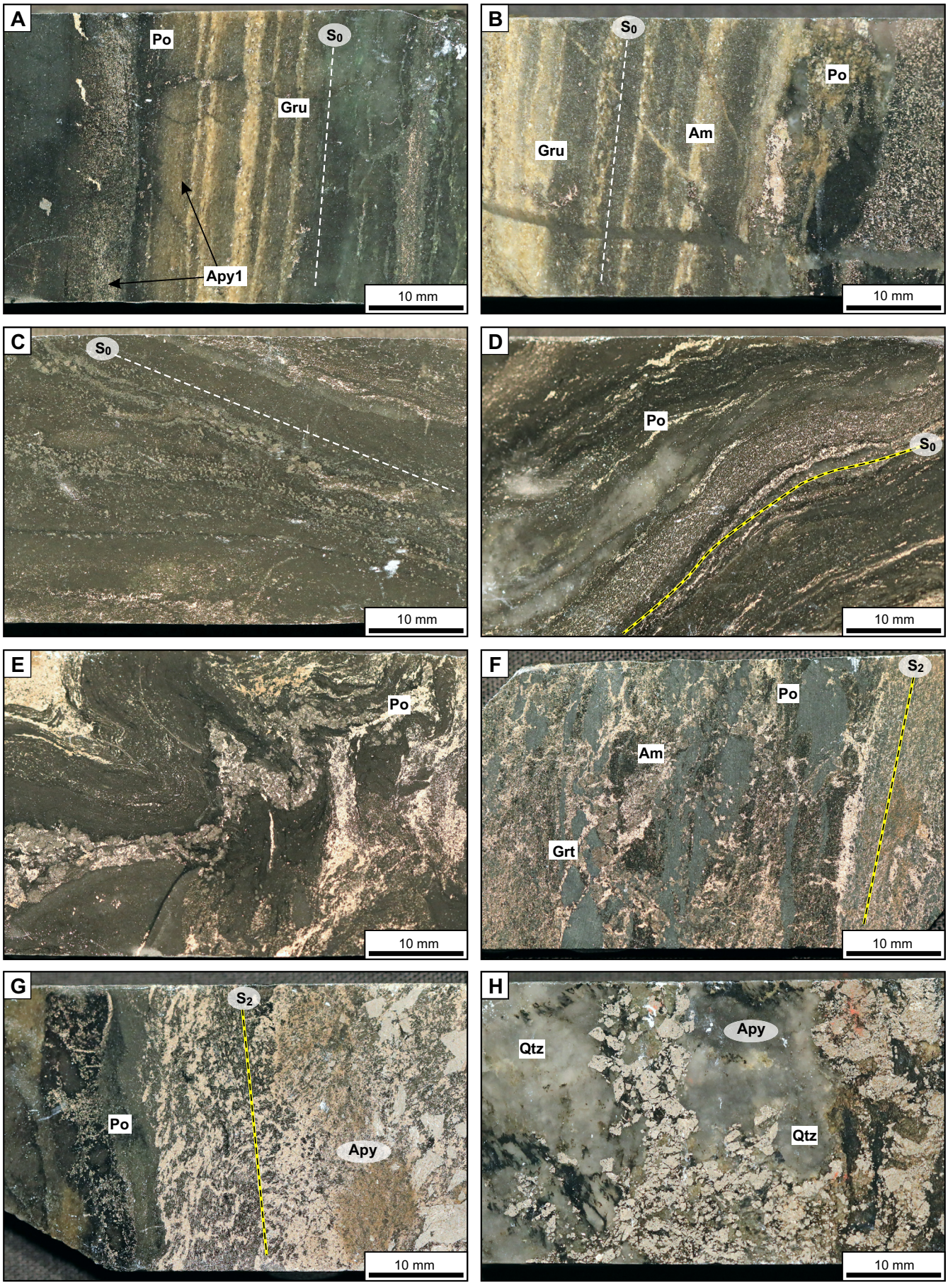
A
Po
S0
Gru
Apy1
10 mm
B
S0
Po
Am
Gru
10 mm
C
S0
10 mm
D
Po
S0
10 mm
E
Po
10 mm
F
S2
Po
Am
Grt
10 mm
G
S2
Po
Apy
10 mm
H
Apy
Qtz
Qtz
10 mm

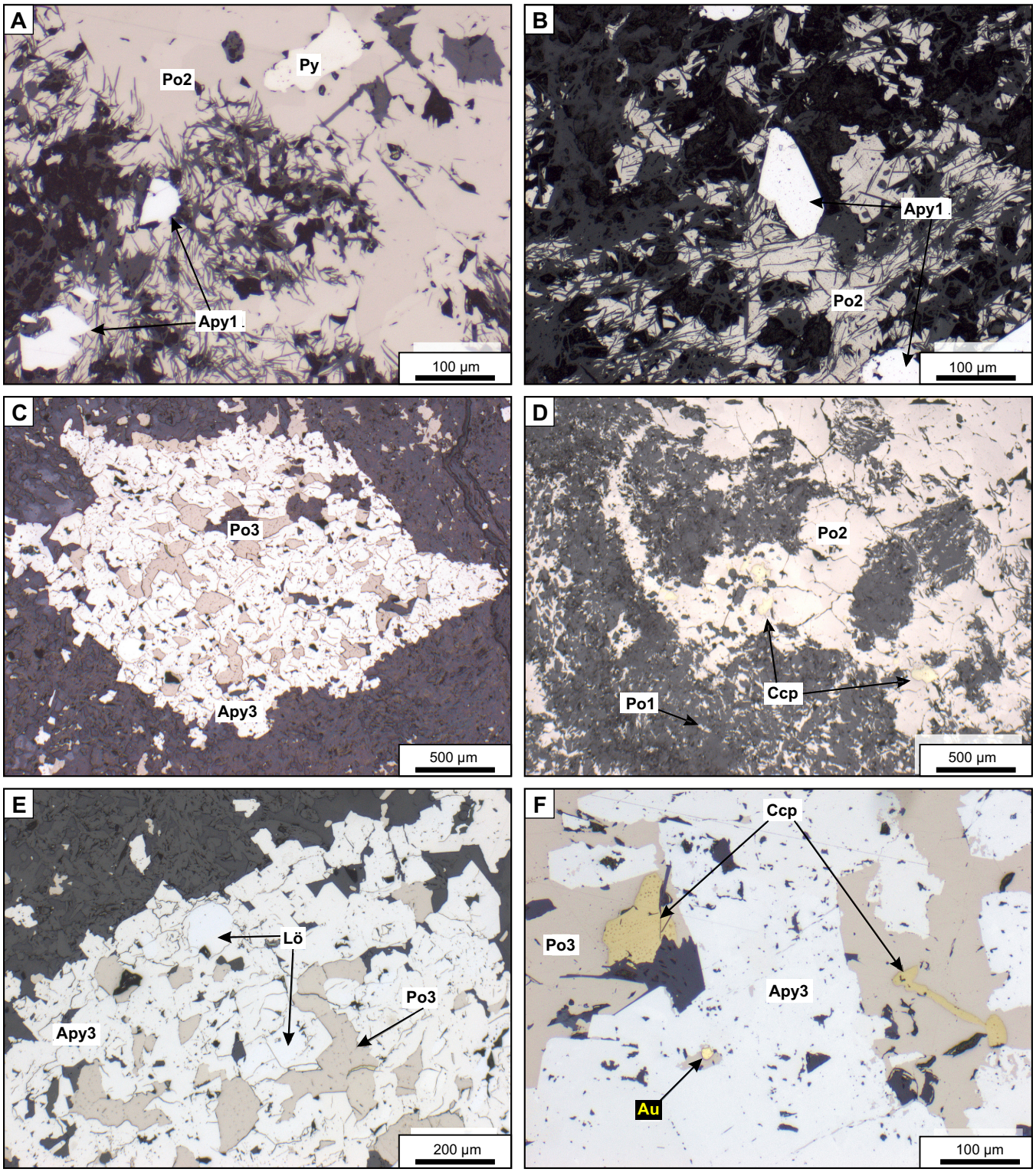

Figure 4. Photomicrographs (reflected light) of mineralized samples. **a)** Sample CAEXD288985: type 1 arsenopyrite crystals in a large mass of pyrrhotite (Po2). **b)** Sample CAEXD288985: type 1 arsenopyrite crystals in disseminated pyrrhotite. **c)** Sample CAEXD288991: aggregate (pseudomorph?) of type 3 arsenopyrite and type 3 pyrrhotite. **d)** Sample CAEXD288988: large, type 2 pyrrhotite mass close to disseminated, type 1 fine pyrrhotite. **e)** Sample CAEXD288991: aggregate (pseudomorph?) of type 3 arsenopyrite and type 3 pyrrhotite with small (<200 µm) löllingite. **f)** Sample CAEXD288985: type 3 arsenopyrite and type 3 pyrrhotite with chalcopyrite and small (<20 µm) free Au or electrum grains. Abbreviations: Apy = arsenopyrite, Au = gold, Ccp = chalcopyrite, Lö = löllingite, Po = pyrrhotite, Py = pyrite.

Table 1. Microprobe analyses of arsenopyrite from drillhole IVR14-158, Whale Tail zone, Amaruq deposit, Nunavut.

Phase	Sample Number	Type	Fe (wt%)	S (wt%)	As (wt%)	Ni (ppm)	Co (ppm)	Au (ppm)[1]
Arsenopyrite	CAEXD288984	type 1	34.7	19.1	47.1	338	1498	29 (bdl)
		type 1	34.0	18.8	47.2	530	4005	110
		type 1	34.4	19.6	46.0	71	1384	68
	CAEXD288985	type 1	33.5	19.2	45.5	344	bdl	98
		type 1	34.5	19.5	46.5	62	42	182
		type 3	34.6	18.9	47.1	153	30	8 (bdl)
		type 3	34.9	19.2	46.9	190	36	bdl
		type 3	35.2	19.6	46.5	bdl	bdl	159
		type 3	34.9	18.8	47.9	178	bdl	77
		type 3	34.9	18.8	47.5	229	17	8 (bdl)
	CAEXD288991	type 3	34.1	19.6	45.9	bdl	bdl	19 (bdl)
		type 3	34.2	18.6	47.2	197	bdl	41 (bdl)
		type 2	34.1	18.6	47.7	492	30	257
		type 1	34.4	18.5	47.7	19	bdl	114
		type 1	34.9	19.5	46.3	78	bdl	136

Abbreviations: bdl = below detection limit, wt = weight.

Analytical parameters: Majors (Fe, S, and As) at 15 kV accelerating voltage, 20 nA beam current, 5 µm electron beam, with a counting time of 20 seconds. Traces (Ni, Co, and Au) at 25 kV accelerating voltage, 100 nA beam current, 5 µm electron beam for 60 seconds (Ni and Co) and with a counting time of 100 seconds (Au). Automated five-spectrometer Cameca SX-100 wavelength dispersive X-ray electron microprobe, Université Laval.

[1]Detection limit calculated by the Cameca built-in software taking into account the standard known concentration, background and peak intentisities, and sample peak and background intensities, plus statistical parameters. Calculated detection limit for Au varied between 40 and 60 ppm. Values below 60 ppm are therefore considered unreliable.

greatly (from below the detection limit to 159 ppm: Table 1); with the exception of one 159 ppm outlier, all analyzed spots are below 80 ppm and therefore very close to the detection limit. This suggests each of these texturally distinct types of arsenopyrite grains has a different history. Nickel and Co concentrations vary greatly in all arsenopyrite types but seem to be lower on average in type 3 arsenopyrite. Cobalt concentration is markedly high in a few samples, perhaps due to host-rock effects (silicified chert with abundant amphiboles).

Pyrrhotite

Three types of pyrrhotite were also defined based on distinct textural and structural features. Type 1 consists of disseminated and stratiform, finely banded pyrrhotite. This pyrrhotite is fine-grained (Fig. 4d). Type 2 occurs as millimetre-sized discordant veinlets or irregular masses. Type 2 pyrrhotite varies in size and shape (Fig. 4d). Type 3 is texturally heterogeneous and coexists with arsenopyrite and löllingite (Fig. 4e). It occurs as inclusions in large crystals of type 3 arsenopyrite and seems to be in equilibrium with the adjacent löllingite and arsenopyrite.

Pyrrhotite is generally devoid of Au (except for a few analyses with a few tens of ppm Au that are too close to detection limit to be considered significant; Table 2). There is no correlation between the presence of Au and type of pyrrhotite or rock type. Nickel is systematically enriched in samples that come from a mineralized BIF interval. Cobalt is also significantly enriched in all pyrrhotite grains from these samples.

Löllingite

Löllingite is only locally present and is less abundant than arsenopyrite and pyrrhotite. It is systematically present as fine inclusions (0.02–0.5 mm) in type 3 arsenopyrite in silicified chert (Fig. 4e). Löllingite is irregular in shape and can be isolated in larger arsenopyrite grains or may be present as clusters of very tiny disseminated grains within arsenopyrite grains. As with arsenopyrite, native Au and/or electrum is commonly spatially associated with löllingite (*see below*).

Löllingite is significantly enriched in Au compared to the other sulphides analyzed in this study. Gold concentration varies between 69 and 452 ppm (Table 3), with an average of 185 ppm. There are no systematic variations among samples, which suggests that it is homogeneously rich in (invisible) Au. The overall low abundance of löllingite, however, means that it does not hold a significant part of the Au budget at ore-zone scale. It is also enriched in Ni relative to arsenopyrite and pyrrhotite.

Pyrite

Pyrite is more abundant in samples collected close to surface (within 50 m of the surface), where it can comprise up to 20 vol.% of the sulphide assemblage. It occurs as veinlets or as disseminated masses that are generally parallel with the foliation. It is sub-idiomorphic to idiomorphic. At greater depth (more than 50 m below the surface), the shape of the pyrite crystals mimics that of nearby pyrrhotite crystals (xenomor-

Table 2. Microprobe analyses of pyrrhotite from drillhole IVR14-158, Whale Tail zone, Amaruq deposit, Nunavut.

Phase	Sample Number	Type	Fe (wt%)	S (wt%)	As (wt%)	Ni (ppm)	Co (ppm)	Au (ppm)[1]
Pyrrhotite	CAEXD288984	Po2	59.4	39.6	bdl	150	3	bdl
		Po2	59.0	39.7	bdl	144	32	bdl
		Po1	59.1	39.7	bdl	49	2	bdl
		Po1	58.3	39.5	bdl	65	29	bdl
		Po1	59.5	39.7	bdl	119	bdl	bdl
	CAEXD288985	Po2	58.5	39.6	bdl	82	bdl	bdl
	CAEXD288988	Po2	58.4	39.4	bdl	1733	63	bdl
		Po2	58.7	39.4	bdl	1898	77	bdl
		Po1	59.0	39.6	bdl	1757	76	22 (bdl)
		Po2	58.5	39.4	bdl	1844	77	54 (bdl)
		Po2	58.5	39.6	bdl	1788	84	bdl
		Po2	59.1	39.2	bdl	1906	67	bdl
		Po2	59.0	39.2	bdl	1791	99	12 (bdl)
		Po2	58.6	39.6	bdl	1760	101	47 (bdl)
	CAEXD288991	Po3	58.8	39.5	bdl	78	bdl	bdl
		Po3	58.9	39.5	0.1	51	bdl	bdl
		Po3	58.4	39.4	bdl	74	bdl	25 (bdl)
		Po3	58.6	39.6	bdl	69	bdl	11 (bdl)
		Po2	58.8	39.4	bdl	50	bdl	bdl
		Po2	58.3	39.6	bdl	52	bdl	bdl
		Po1	59.0	39.4	bdl	15	bdl	16 (bdl)
		Po1	58.9	39.3	bdl	66	bdl	bdl
		Po1	58.6	39.6	bdl	56	bdl	bdl

Abbreviations: bdl = below detection limit, wt = weight.

[1]Detection limit calculated by the Cameca built-in software taking into account the standard known concentration, background and peak intentisities, and sample peak and background intensities, plus statistical parameters. Calculated detection limit for Au varied between 40 and 60 ppm. Values below 60 ppm are therefore considered unreliable.

phic), suggesting that this preserved pyrite occurred late in the paragenetic sequence. The grains range in size from 0.05 to 0.2 mm.

Pyrite contains little Au, based on the available microprobe analyses (Lauzon, 2017) and is only slightly enriched in Ni. Its trace element composition is very similar to that of pyrrhotite, to which it is generally spatially associated.

Native Au and electrum

Native Au and electrum are common in samples from drillhole IVR14-158, and more particularly in those containing arsenopyrite. It is spatially associated with pyrrhotite and arsenopyrite, most commonly as inclusions (Fig. 4f). Although some native Au and electrum grains are in fractures in sulphides, they are more commonly located at the löllingite-arsenopyrite interface (Fig. 5a,b). In some cases, it is in the gangue, but generally it is found in very close proximity to sulphides. Gold and electrum grains are rounded to angular in shape and range in size from <1 to 25 µm (Fig. 4f, 5a,b).

Scanning electron microscope (SEM) analyses of native Au and electrum grains show that Au concentration varies between 63.6 and 86.7 wt%, with Ag concentration varying between 13.3 and 36.4 wt% (Table 4). On average, the analyzed grains comprise 73.9 wt% Au and 26.1 wt% Ag (Lauzon, 2017). The Au/Ag ratio varies between 1.75 and 6.52; a range that is typical of orogenic Au deposits (cf. Boyle, 1979).

Table 3. Microprobe analyses of löllingite from drillhole IVR14-158, Whale Tail zone, Amaruq deposit, Nunavut.

Phase	Sample Number	Type	Fe (wt%)	S (wt%)	As (wt%)	Ni (ppm)	Co (ppm)	Au (ppm)[1]
Löllingite	CAEXD288985	Lö	26.1	1.2	71.1	11,669	479	89
		Lö	27.8	1.2	71.5	2310	26	452
		Lö	27.9	1.2	71.3	2701	40	77
		Lö	27.8	1.1	71.2	3814	17	69
	CAEXD288991	Lö	27.7	1.2	71.0	1370	28	147
		Lö	28.0	1.1	71.3	1440	22	160
		Lö	27.5	1.3	70.7	4395	bdl	233
		Lö	27.8	1.0	71.4	10,368	bdl	350
		Lö	27.0	1.2	71.2	10,503	79	89

Abbreviations: bdl = below detection limit; wt = weight.

[1]Detection limit for Au varied between 45 and 65 ppm.

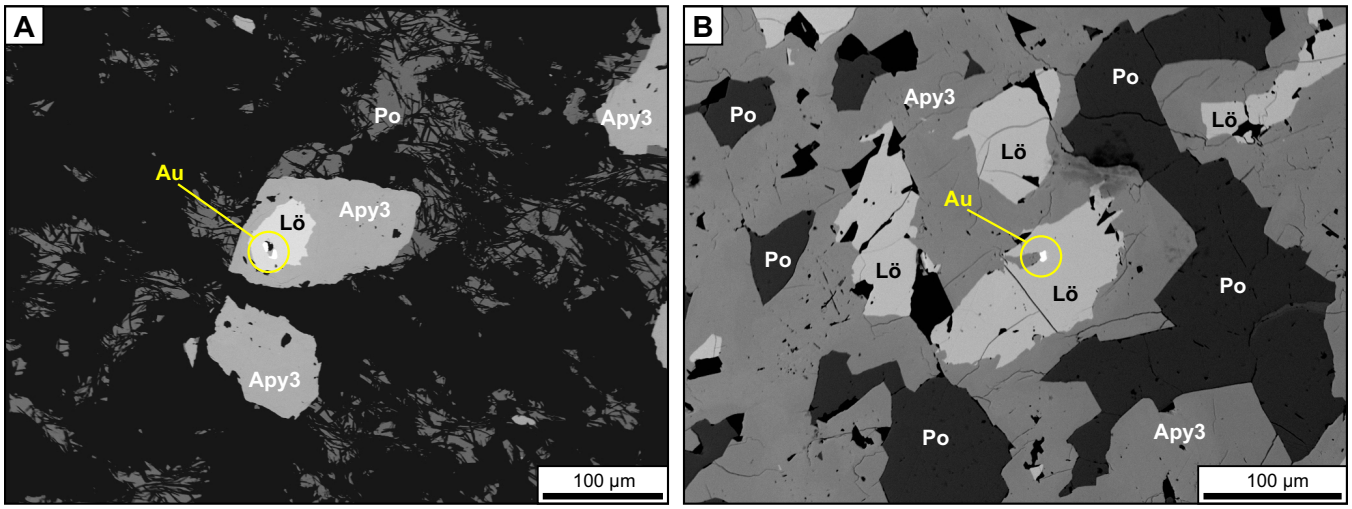

Figure 5. Backscattered electron images of type 3 arsenopyrite with löllingite, pyrrhotite and free gold or electrum. **a)** Sample CAEXD288985: isolated arsenopyrite with a löllingite core containing small Au grains. **b)** Sample CAEXD288991: a large type 3 arsenopyrite with remnant pyrrhotite and isolated löllingite. Free Au occurs at the contact between arsenopyrite and löllingite. Note that löllingite and pyrrhotite are not in contact. Abbreviations: Apy = arsenopyrite, Au = gold, Lö = löllingite, Po = pyrrhotite.

DISCUSSION

Different generations of fabrics related to at least three major deformation events (D_1 to D_3) affect the Amaruq deposit (Valette et al., 2020). The S_1 foliation, which is axial planar to F_1 folds, is affected by tight to closed, gently to moderately, east- to northeast-plunging F_2 folds and associated, moderately southeast-dipping axial planar S_2 schistosity (Valette et al., 2020). On the limbs of F_2 folds, S_1 folication and S_2 schistosity locally form a composite $S_{1\text{-}2}$ fabric. Progressive D_2 strain accommodation led to the development of shear zones that may have been initiated during D_1 deformation. According to Valette et al. (2020), the main fabric (S_2 schistosity) may correspond to the regional D_{p2} 1.91–1.81 Ga Trans-Hudsonian deformation event of Pehrsson et al. (2013). It is not excluded, however, that the main foliation at Amaruq may have originated from the regional S_1 fabric, or even from an earlier Archean foliation (S_{A2} of Pehrsson et al., 2013), which was subsequently transposed during D_2 deformation.

Petrographic and microstructural relationships between fabrics and metamorphic minerals, such as Mn-garnet porphyroblasts, provide evidence for syn- to late-D_2 peak metamorphism at upper greenschist facies (Valette et al., 2020). Retrogression during D_3 deformation (M_3 of Valette et al., 2020) is evidenced by late phases aligned along the S_3 cleavage in sedimentary rocks. Likewise, sulphide phases show evidence of deformation and metamorphic recrystallization, which indicates that metamorphism overprints and postdates at least part of the mineralizing system.

Type 3 arsenopyrite forms heterogeneous masses with löllingite and pyrrhotite. It contains a lower concentration of invisible Au than arsenopyrite types 1 and 2, which are generally more homogeneous and devoid of löllingite-pyrrhotite inclusions. This suggests that

Table 4. Scanning electron microscopy (SEM) analyses of electrum from drillhole IVR14-158, Whale Tail zone, Amaruq deposit, Nunavut.

Sample Number	Au (wt%)	Au (at%)	Ag (wt%)	Ag (at%)	Note
CAEXD288985	70.48	56.67	29.52	43.33	Contact Apy type 3 and Lö
	68.32	54.15	31.68	45.85	Along Apy type 3
	67.69	53.43	32.31	46.57	Contact Apy type 3 and Lö
	69.07	55.02	30.93	44.98	Inclusion in Apy type 3
CAEXD288991	69.36	55.35	30.64	44.65	Contact Apy type 3 and Lö
	63.56	48.86	36.44	51.14	Inclusion in Apy type 3
	82.20	71.66	17.80	28.34	Contact Apy type 3 and Lö
	76.60	64.19	23.40	35.81	Contact Apy type 3 and Lö
	78.81	67.07	21.19	32.93	Contact Apy type 3 and Lö
	86.73	78.16	13.27	21.84	Inclusion in Apy type 3
CAEXD288997	77.99	65.99	22.01	34.01	Inclusion in Apy type 1
	75.58	62.89	24.42	37.11	Contact Apy type 1 and Lö
	75.15	62.35	24.85	37.65	Contact Apy type 1 and Lö

Abbreviations: Apy = arsenopyrite, at = atomic, Lö = löllingite, wt = weight.

type 3 arsenopyrite formed, at least in part, at the expense of löllingite during retrograde metamorphism, which is in agreement with the laboratory experiments of Tomkins and Mavrogenes (2001) that showed that arsenopyrite resulting from Au-bearing löllingite retrogression contains low levels of invisible Au.

Several authors (e.g. Cathelineau et al., 1989; Morey et al., 2008) have suggested that the solubility of Au in arsenopyrite decreases with increasing temperature. Increasing temperature during prograde metamorphism results in the gradual expulsion of the Au contained in arsenopyrite. This agrees with the observations made of the different types of arsenopyrite and löllingite in samples from drillhole IVR14-158. Type 1 and type 2 arsenopyrites contain high concentrations of Au (120.62 ppm Au on average, n = 8), whereas recrystallized arsenopyrite (type 3), which result from retrogression of auriferous löllingite (185 ppm Au on average, n = 9), have significantly lower gold concentrations (below the detection limit in most cases).

Based on the progressive stages of evolution of arsenopyrite during metamorphism, as outlined by Tomkins and Mavrogenes (2001), retrograde metamorphism at Amaruq led to an increase in invisible Au concentration in the residual löllingite grains as it reverted to arsenopyrite (Fig. 6). The subsequent conversion of löllingite and pyrrhotite to arsenopyrite during cooling precluded Au to re-enter arsenopyrite structure, concentrating part of it (as electrum) at the löllingite-arsenopyrite interface (Fig. 6), with the rest continuing to diffuse into the remaining löllingite (Fig. 6). As temperature decreased and all the löllingite was consumed to form late, retrograde arsenopyrite, Au was largely expelled from the sulphides. Thus, the replacement of prograde löllingite by retrograde arsenopyrite, as seen in the samples from drillhole IVR14-158, is the main process that led to the presence of native Au and electrum.

The Amaruq Au system is the result of a polyphase tectonometamorphic evolution that may have comprised (1) a simple pre- to early peak metamorphism mineralizing event that was quickly overprinted by increasing metamorphic conditions in a "deep earlier context" (cf. Phillips and Powell, 2009) during Trans-Hudson orogenesis; or (2) a syn-D_2 Trans-Hudson event overprinting a separate and much older mineralizing event. The former interpretation is perhaps the simplest and fits the "Paleoproterozoic Au metallotect" concept of Miller et al. (1994). However, preliminary Re-Os geochronology results suggest a long, protracted hydrothermal history at Amaruq (Mercier-Langevin et al., 2018). This agrees with the work of Lawley et al. (2015a), which demonstrated that mineralization in the Meliadine district resulted from temporally distinct Au events. Ongoing work and analyses (Re-Os, $^{40}Ar/^{39}Ar$, U-Pb geochronology, Pb and isotopes, and laser ablation inductively coupled-plasma mass spectrometry element mapping) will help unravel the sequence of events at Amaruq.

In summary, syn-ore ("primary") Au-bearing arsenopyrite grains were converted to löllingite and pyrrhotite during prograde metamorphism. Gold diffused into löllingite during this process. It was later exsolved from löllingite during retrograde metamorphism, as illustrated in Figure 6. This agrees with the presence of native Au and/or electrum inclusions in the granoblastic gangue silicates that formed during peak metamorphism, which further support the interpretation that a gold mineralizing event predated the syn- to late-D_2 peak metamorphism at Amaruq.

CONCLUSION

Although the results presented here are preliminary, they provide clear evidence for a complex evolution of the Whale Tail gold mineralization, including pre-peak metamorphism, with significant modifications during prograde and retrograde metamorphism. Integrating the results of this study with the ongoing geochronology work and research done on the various aspects of the geology of the deposit will help elucidate the timing and mode of emplacement of the Amaruq Au deposit and help refine exploration models for Au in northern Canada.

FUTURE WORK

More detailed work is underway on the Amaruq ore minerals, including microprobe and scanning electron microscopy (SEM) analyses, laser ablation-inductively coupled plasma-mass spectrometry (LA-ICP-MS) spot analyses and element mapping, Pb and S isotopic analyses, and arsenopyrite Re-Os geochronology to better delineate the signature of the different ore zones and ore styles, and also to better constrain the relative and absolute timing of the ore-forming event(s) and the effects of deformation and metamorphism.

ACKNOWLEDGMENTS

This work results from a B.Sc. thesis by M.-C. Lauzon at Université Laval as part of the Gold Project's activity G-2.4: Lithological and tectonic controls on Paleoproterozoic BIF-hosted/associated gold. The authors want to thank E. Bédard, E. Rousseau, M. Sciuba, and J. Dubé for scientific and technical support. Thanks to M. Choquette and A. Ferland for their help with micro-analytical work. We thank Agnico Eagle Mines Ltd. for access to the property, drill core and database, and for scientific and logistical support. Thanks to A. Deschênes-Dénommé, G. Tremblay, and M. Boutin for their help with some of the figures. An earlier version of this report benefited from the reviews

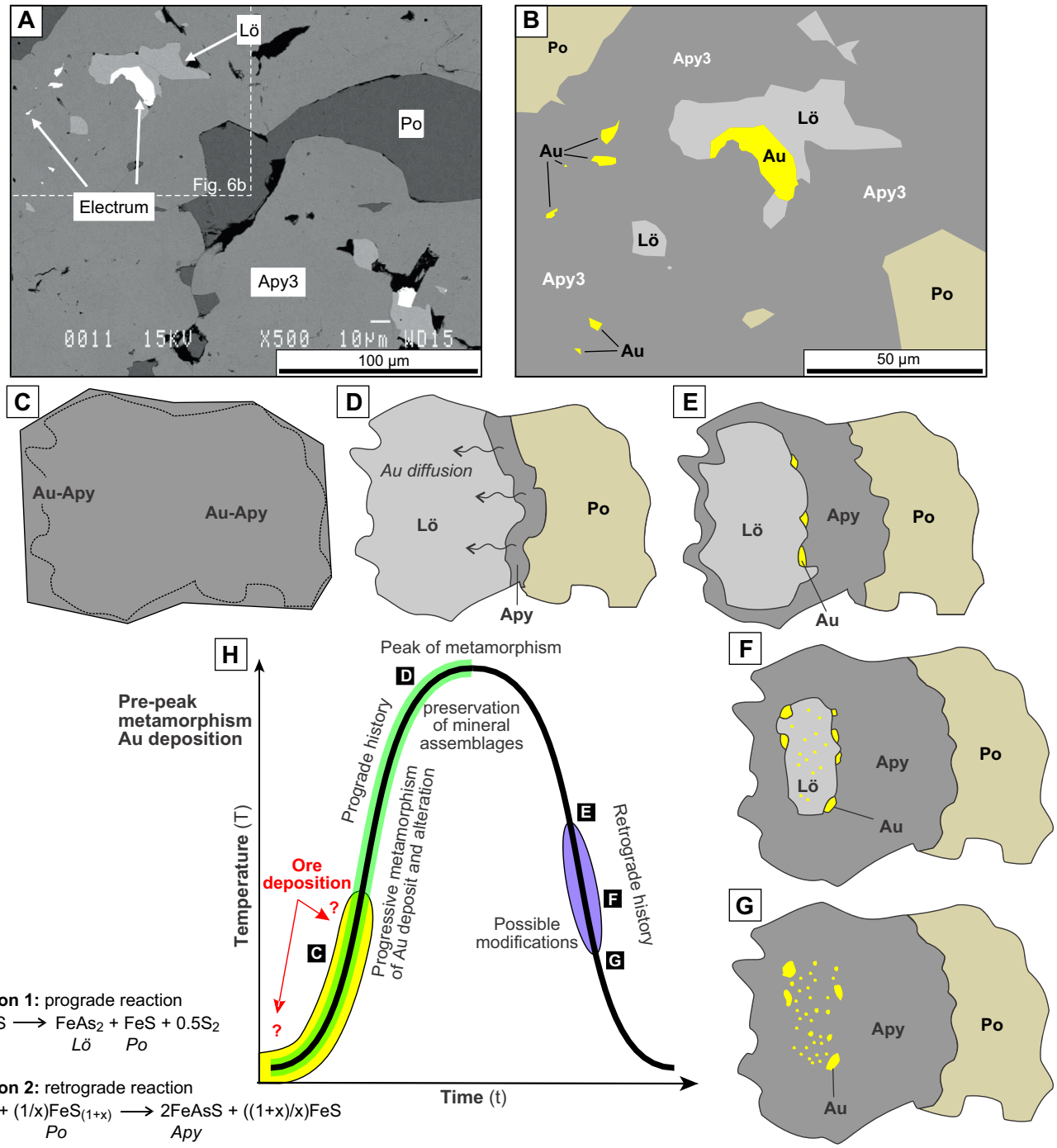

Figure 6. a) Backscattered electron image of type 3 arsenopyrite with löllingite, pyrrhotite, and electrum resulting from retrograde recrystallization of löllingite and liberation of Au. **b)** Close-up of (a), redrawn to show arsenopyrite, löllingite, electrum, and pyrrhotite relationships. **c, d, e, f, and g)** Theoretical sketches of the progressive stages of destruction of Au-bearing arsenopyrite and Au-rich löllingite showing how Au is redistributed during a prograde-retrograde metamorphic cycle (*modified from* Tomkins and Mavrogenes, 2001). **c)** Syn-ore "primary" Au-bearing arsenopyrite crystal(s). **d)** Prograde metamorphism of the primary arsenopyrite forming an assemblage of Au-rich löllingite (Au diffusion) and pyrrhotite with or without remnant Au-bearing primary arsenopyrite. **e)** Early phase of retrograde metamorphism with löllingite reverting to retrograde (Au-poor) arsenopyrite, liberating Au (electrum) that does not re-enter arsenopyrite. **f)** Advanced retrogression of löllingite, increasing Au concentration in the remaining löllingite and liberating more Au at the interface with retrograde arsenopyrite. This stage is equivalent to what is shown in (a) and (b). **g)** Complete retrogression of löllingite leaving a residue of native Au (electrum) in late (post-peak metamorphism) arsenopyrite. **h)** Schematic diagram showing the formation of a gold deposit prior to, or in the early stages of high-grade regional metamorphism and its possible evolution (*modified from* Phillips and Powell, 2009). Equation 1 is from Barnicoat et al. (1991) and equation 2 is from Neumayr et al. (1993). The prograde-retrograde evolution of Au-bearing arsenopyrite, löllingite, pyrrhotite, and gold is shown along the temperature-time (T-t) curve for reference. Abbreviations: Apy = arsenopyrite, Au = gold, Lö = löllingite, Po = pyrrhotite.

of C. Yakymchuk and S. Castonguay. We also acknowledge E. Ambrose and V. Bécu for their technical reviews and editorial handling.

REFERENCES

Agnico Eagle Mines Limited, 2019. <https://www.agnicoeagle.com/English/operations-and-development-projects/reserves-and-resources/default.aspx> [accessed December 15, 2019]

Barnicoat, A.C., Fare, R.J., Groves, D.I., and McNaughton, N.J., 1991. Synmetamorphic lode-gold deposits in high-grade Archaean settings; Geology, v. 19, p. 921–924.

Boyle, R.W., 1979. The geochemistry of gold and its deposits; Geological Survey of Canada, Bulletin 280, 584 p.

Carpenter, R.L. and Duke, N.A., 2004. Geologic setting of the West Meliadine gold deposits, Western Churchill Province, Nunavut, Canada; Exploration and Mining Geology, v. 13, p. 49–65.

Cathelineau, M., Boiron, M.-C., Holliger, P., Marion, P., and Denis, M., 1989. Gold in arsenopyrites: Crystal chemistry, location and state, physical and chemical conditions of deposition; *in* The Geology of Gold Deposits: The perspective in 1988, (ed.) R.R. Keys, W.R.H. Ramsay, and D.I. Groves; Society of Economic Geologists, Monograph 6, p. 328–341.

Côté-Mantha, O., Gosselin, G., Vaillancourt, D., and Blackburn, A., 2015. Amaruq: A new gold discovery in Nunavut, Canada; NewGenGold 2015 meeting, Extended Abstracts, p. 41–56.

Côté-Mantha, O., Gosselin, G., Vaillancourt, D., and Blackburn, A., 2017. The Amaruq deposits – Building a customized toolset and using a flexible geomodel: Optimization from discovery to mine development; *in* Proceedings of Exploration 17, (ed.) V. Tschirhart and M.D. Thomas; Sixth Decennial International Conference on Mineral Exploration, 2017, p. 553–567.

Davies, T., Richards, J.P., Creaser, R.A., Heaman, L.M., Chacko, T., Simonetti, A., Williamson, J., and McDonald, D.W., 2010. Paleoproterozoic age relationships in the Three Bluffs Archean iron formation-hosted gold deposit, Committee Bay greenstone belt, Nunavut, Canada; Exploration and Mining Geology Journal, v. 19, p. 55–80.

Dubé, B. and Mercier-Langevin, P. (ed.), 2015. Targeted Geoscience Initiative 4: Contributions to the Understanding of Precambrian Lode Gold Deposits and Implications for Exploration; Geological Survey of Canada, Open File 7852, 297 p.

Guillevic, F., 2019. Domaines géométallurgiques dans un gisement aurifère: le cas du dépôt Whale Tail, projet Amaruq, Nunavut; M.Sc. thesis, Université du Québec à Chicoutimi, Chicoutimi, Quebec, 192 p.

Hrabi, R.B., Barclay, W.A., Fleming, D., and Alexander, R.B., 2003. Structural evolution of the Woodburn Lake group in the area of the Meadowbank gold deposit, Nunavut: Geological Survey of Canada, Current Research 2003-C27, 10 p.

Janvier, V., Castonguay, S., Mercier-Langevin, P., Dubé, B., Malo, M., McNicoll, V.J., Creaser, R.A., De Chavigny, B., and Pehrsson, S.J., 2015. Geology of the banded iron formation-hosted Meadowbank gold deposit, Churchill Province, Nunavut; *in* Targeted Geoscience Initiative 4: Contributions to the understanding of Precambrian lode gold deposits and implications for exploration, (ed.) B. Dubé and P. Mercier-Langevin; Geological Survey of Canada, Open File 7852, p. 255–269.

Kerswill, J.A., 1993. Models for iron-formation-hosted gold deposits; *in* Mineral Deposits Modeling, (ed.) R.V. Kirkham, W.D. Sinclair, R.I. Thorpe, and J.M. Duke; Geological Association of Canada, Special Paper 40, p. 171–199.

Lauzon, M.-C., 2017. Empreinte minéralogique et géochimique des minéralisations aurifères de la zone Whale Tail du projet Amaruq; B.Sc. thesis, Université Laval, Québec, Quebec, 48 p.

Lawley, C.J.M., Creaser, R.A., Jackson, S., Yang, Z., Davis, B., Pehrsson, S., Dubé, B., Mercier-Langevin, P., and Vaillancourt, D., 2015a. Unravelling the Western Churchill Province Paleoproterozoic gold metallotect: constraints from Re-Os arsenopyrite and U-Pb xenotime geochronology and LA-ICP-MS arsenopyrite trace element chemistry at the BIF-hosted Meliadine gold district, Nunavut, Canada; Economic Geology, v. 110, p. 1425–1454.

Lawley, C.J.M., Dubé, B., Mercier-Langevin, P., Kjarsgaard, B., Knight, R., and Vaillancourt, D., 2015b. Defining and mapping hydrothermal footprints at the BIF-hosted Meliadine gold district, Nunavut, Canada; Journal of Geochemical Exploration, v. 155, p. 33–55.

Mercier-Langevin, P., Valette, M., De Souza, S., Creaser, R.A., McNicoll, V., Grondin-Leblanc, P., St-Pierre, B., Lauzon, M.-C., Malo, M., Côté-Mantha, O., and Simard, M., 2018. Lithologic controls on Paleoproterozoic BIF-hosted/associated gold: Overview of Re-Os geochronology and Pb isotopes preliminary results; *in* Targeted Geoscience Initiative: 2017 report of activities, volume 1, (ed.) N. Rogers; Geological Survey of Canada, Open File 8358, p. 147–152.

Mercier-Langevin, P., Lauzon, M.-C., Bécu, V., Lauzière, K., and Côté-Mantha, O., 2020. Whole-rock lithogeochemistry along drill core through the gold-bearing Whale Tail zone, Amaruq deposit, Churchill Province, Nunavut; Geological Survey of Canada, Open File 8708, 1 .zip file.

Miller, A.R., Balog, M.J., Barham, B.A., and Reading, K.L., 1994. Geology of the Early Proterozoic gold metallotect, Hurwitz Group in the Cullaton-Griffin lakes area, central Churchill structural province, Northwest Territories; Geological Survey of Canada, Current Research 1994-C, p. 135–146.

Morey, A.A., Tomkins, A.G., Bierlein, F.P., Weinberg, R.F., and Davidson, G.J., 2008. Bimodal distribution of gold in pyrite and arsenopyrite: Examples from the Archean Boorara and Bardoc shear systems, Yilgarn craton, Western Australia; Economic Geology, v. 103, p. 599–614.

Neumayr, P., Cabri, L.J., Groves, D.I., Mikucki, E.J., and Jackman, J.A., 1993. The mineralogical distribution of gold and relative timing of gold mineralization in two Archean settings of high metamorphic grade in Australia; The Canadian Mineralogist, v. 31, p. 711–725.

Pehrsson, S.J., Berman, R.G., and Davis, W.J., 2013. Paleoproterozoic orogenesis during Nuna aggregation: A case study of reworking of the Rae craton, Woodburn Lake, Nunavut; Precambrian Research, v. 232, p. 167–188.

Phillips, G.N. and Powell, R., 2009. Formation of gold deposits: Review and evaluation of the continuum model; Earth-Science Reviews, v. 94, p. 1–21.

Sherlock, R., Pehrsson, S., Logan, A.V., Hrabi, R.B., and Davis, W.J., 2004. Geological setting of the Meadowbank gold deposit, Woodburn Lake Group, Nunavut; Exploration and Mining Journal, v. 13, p. 67–107.

St.Pierre, B., Mercier-Langevin, P., Simard, M., Côté-Mantha, O., Blais, J.-C., Servelle, G., and Malo, M., 2020. Structural controls and relative timing of gold mineralization of the banded iron formation-associated Tiriganiaq deposit, Meliadine district, Ranking Inlet greenstone belt, Nunavut; *in* Contributions to the Understanding of Canadian Gold Systems, (ed.) P. Mercier-Langevin, C.J.M. Lawley, and S. Castonguay; Geological Survey of Canada, Open File 8712 p. 237–250. doi:10.4095/326041

Tomkins, A.G. and Mavrogenes, J.A., 2001. Redistribution of gold within arsenopyrite and löllingite during pro- and retrograde metamorphism: Applications to timing of mineralization; Economic Geology, v. 96, p. 525–534.

Valette, M., De Souza. S., Mercier-Langevin, P., Côté-Mantha, O., Simard, M., Wodicka, N., McNicoll, V.J., and Barbe, P., 2020. Lithological and tectonic controls on banded iron formation-associated gold at the Amaruq deposit, Churchill Province, Nunavut, and implications for exploration; *in* Targeted Geoscience Initiative 5: Contributions to the Understanding of Canadian Gold Systems, (ed.) P. Mercier-Langevin, C.J.M. Lawley, and S. Castonguay; Geological Survey of Canada, Open File 8712, p. 251–266. doi:10.4095/326042

Neoproterozoic-hosted Carlin-type mineralization in central Yukon, part 1: Regional- to prospect-scale geological controls

Nicolas Pinet[1]*, Patrick Sack[2], Patrick Mercier-Langevin[1], Maurice Colpron[2], Denis Lavoie[1], Benoît Dubé[1], and Virginia I. Brake[1]

[1]Geological Survey of Canada, 490 rue de la Couronne, Québec, Quebec G1K 9A9
[2]Yukon Geological Survey, 91807 Alaska Hwy, Whitehorse, Yukon Y1A 5B7
*Corresponding author's e-mail: nicolas.pinet@canada.ca

ABSTRACT

In central Yukon, sediment-hosted gold mineralized zones have similar characteristics to Carlin-type deposits in Nevada. However, it remains unclear if exploration models applied to the southwest United States similarly apply to the Canadian Cordillera. This contribution tackles that knowledge gap by reviewing the regional- to prospect-scale setting of mineralized zones found in the Nadaleen trend, Yukon. Carlin-type gold-bearing zones in central Yukon are located near the boundary between the Ogilvie platform to the northeast and the Selwyn Basin to the southwest. This shelf-to-basin transition is marked in part by the Dawson fault, which is likely a long-lived, deep-seated structure that influenced sedimentation and younger structural history. Gold-mineralized zones are mainly hosted in two Neoproterozoic limestone units (informally known as the Conrad and Osiris limestones of the Nadaleen and Gametrail formations, respectively) and in Paleozoic siltstones. In the Nadaleen trend, the structural style is complex; the strata generally dip more steeply than in classic fold-and-thrust belts and faults bear a significant strike-slip component. Neoproterozoic-hosted gold ore zones are mostly concordant with bedding in complexly shaped anticlines. Gold mineralization is significantly younger than the main intrusion-related gold mineralizing event in the northern Selwyn Basin.

INTRODUCTION

Globally, Carlin-type deposits represent a major source of gold and one of the principal exploration targets due to their potential to form districts with large gold content. The vast majority of known Carlin-type gold deposits are located in Nevada, where they are defined by their common tectono-sedimentary setting, geochemical/mineralogical signature, and timing (Table 1; Cline et al., 2005; Muntean, 2018a). In Nevada, the huge gold endowment (~255 Moz: Muntean, 2018a) within Carlin-type deposits resulted from (1) geological processes spanning hundreds of millions of years that led to an ideal crustal architecture at regional- to drill-target scales (ground preparation); and (2) a relatively short-lived geodynamic event that modified the thermal state and tectonic regime of the lithosphere, which resulted in a change from shortening to extension and renewed magmatism. Studies of the few Carlin-type occurrences found outside the Great Basin of the southwest United States are limited (Muntean, 2018b and references therein), and it remains unclear if the geological processes/geodynamic events documented in Nevada are absolute prerequisites to generate Carlin-type deposits. This is important for mineral exploration because it impacts whether geological and exploration models developed in Nevada can be applied elsewhere. In this study, we tackle this knowledge gap by reviewing geological parameters that may have been critical in forming Carlin-type gold mineralization in central Yukon at the lithospheric to prospect scales (100s of kms to 100s of ms). A companion study (Pinet et al., 2020) documents the critical ore-forming processes at the drill-target scale and below (≤100 m).

REGIONAL SETTING

Geological Framework

In Yukon and Northwest Territories, the foreland belt forms the easternmost geological domain of the Cordilleran orogen. The foreland belt consists of sedimentary rocks deposited on the Laurentian (North American) continental margin, which is tectonically juxtaposed to the west against a variety of allochthonous lithotectonic assemblages. Each of these lithotectonic terranes was accreted to ancestral North America during the Mesozoic (Nelson et al., 2013).

Northeast of the Tintina fault, a major strike-slip fault with 430 km of Eocene and a further 60 km of Late Cretaceous right lateral displacement (Gabrielse et al., 2006), the foreland belt exhibits an arcuate geometry with salients and recesses characterized by different tectonic styles (Fig. 1). In the Mackenzie

Pinet, N., Sack, P., Mercier-Langevin, P., Colpron, M., Lavoie, D., Dubé, B., and Brake, V.I., 2020. Neoproterozoic-hosted Carlin-type mineralization in central Yukon, part 1: Regional- to prospect-scale geological controls; *in* Targeted Geoscience Initiative 5: Contributions to the Understanding of Canadian Gold Systems, (ed.) P. Mercier-Langevin, C.J.M. Lawley, and S. Castonguay; Geological Survey of Canada, Open File 8712, p. 281–297. https://doi.org/10.4095/326045

Table 1. Selected geological characteristics of Carlin-type deposits in Nevada.

Tectono-sedimentary setting
Host rock characterized by significant carbonate content
Location in the lower plate of a pre-ore regional thrust
Association with extensional faults and pre-ore contractional structures
Depth of formation <3 km
Geochemical/mineralogical signature
Pathfinder elements Tl, As, Hg, Sb
Low Ag and base metal content
Alteration characterized by decarbonatization, silicification, and argillitization
'Invisible' gold in arsenian pyrite either as rims on pre-ore pyrite or as sub-micrometre particles
Minor open-space filling minerization
210 ± 30°C low-salinity main ore-stage fluids
Timing
Narrow age range between 42 and 34 Ma

Mountains (Fig. 1a), shortening (~50 km) was accommodated by east- and west-verging folds and thrusts that trend parallel to the north-trending deformation front (Gordey, 1981). This contrasts with the deformation style of the northern boundary of the most pronounced salient, where major faults trend west-northwest (Fig. 1b). Among these faults, the 250 km long Dawson fault was a first-order structure during the Mesozoic building of the Cordillera (Abbott, 1997). However, evidence suggests that the fault is a deep-seated structure originating from older tectonic events.

1. The present-day location of the Dawson fault roughly coincides with the northern boundary of the Selwyn Basin (Fig. 1b), a domain with Neoproterozoic to Permian sedimentary rocks mainly deposited in basinal settings and characterized by deeper water sediments than the surrounding platform domains. Paleogeographic reconstructions (Cecile, 1982) indicate that the Ogilvie Platform-Selwyn Basin transition was relatively stable from the Cambrian to the Silurian and located close to the inferred Neoproterozoic platform-basin boundary (Abbott, 1997).
2. Mass-transport deposits most likely associated with syndepositional tectonism are ubiquitous in the Neoproterozoic to mid-Paleozoic sedimentary successions that are present near the Ogilvie Platform-Selwyn Basin transition, reinforcing the idea of a long-lived structurally controlled, south-facing (present coordinates) slope.
3. Kilometre-scale ultramafic bodies, possibly linked with the transform fault transition from the upper plate to the lower plate segments along the continental margin, are present along the Dawson fault system (Colpron, 2012).
4. Several occurrences of Cambrian, Silurian, and Devonian Paleozoic igneous rocks, including basalt, rhyolite and gabbro, are documented in the northern part of the Selwyn Basin. These are particularly notable in the vicinity of the Dawson fault (Yukon Geological Survey, 2019).

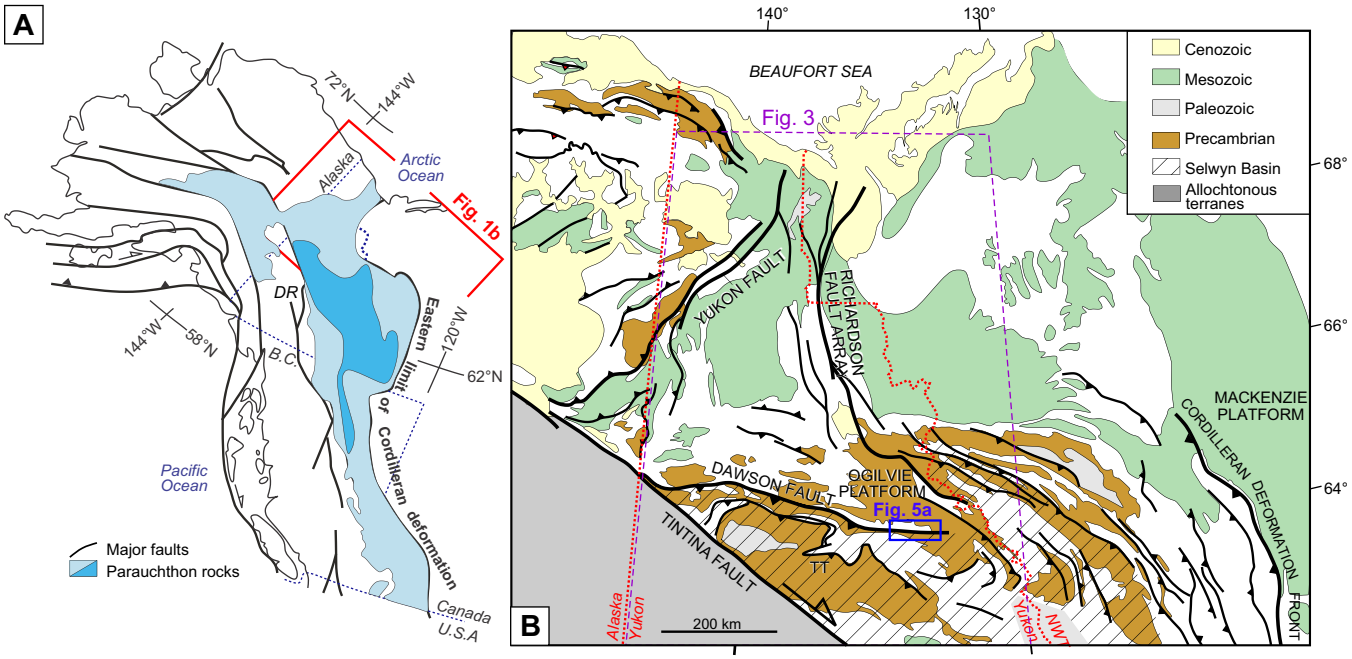

Figure 1. a) Simplified geological map of the northern Cordillera in Canada and Alaska. Parautochthonous rocks include basinal (darker blue) and platformal (lighter blue) strata. Abbreviations: DR = Dawson Range, MM = Mackenzie Mountains, OP = Olgilvie Platform, SB = Selwyn Basin. **b)** Geological map of the foreland belt in northern Yukon and Northwest Territories. Note the changes in strike of the major faults. Abbreviation: TT = Tombstone Thrust.

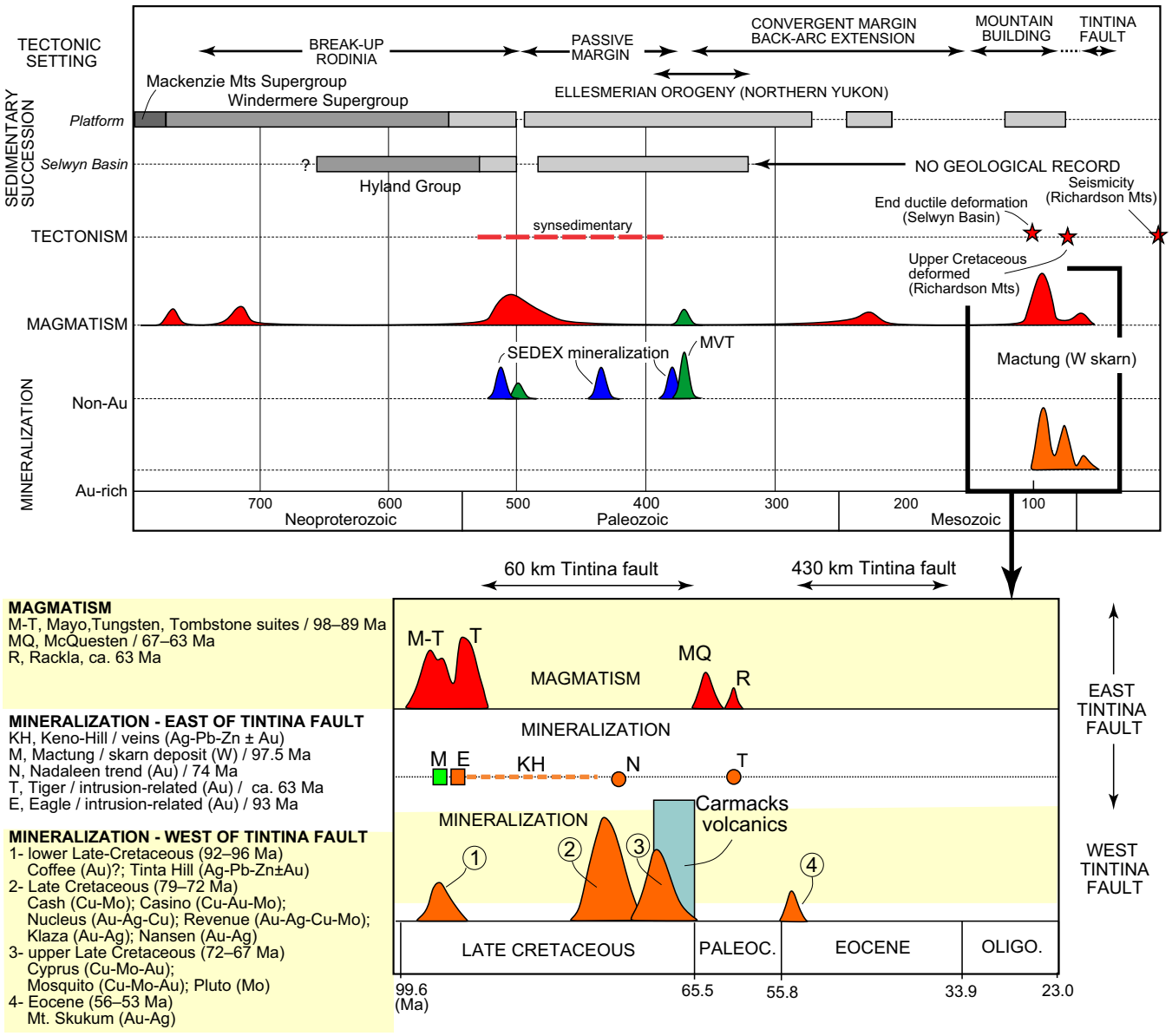

Figure 2. Schematic geological timeframe of north-central Yukon. For clarity, only the Windermere Supergroup and Hyland Group are distinguished (medium grey). Abbreviations: MVT = Mississippi Valley-type, SEDEX = sedimentary exhalative. Ages of magmatism from Murphy (1997), Hart et al. (2004a,b), Kingston et al. (2010), Rasmussen (2013), and Colpron et al. (2016). Ages of mineralization from Selby and Creaser (2001), Allan et al. (2013), Bineli Betsi et al. (2013), Nelson et al. (2013), Mortensen et al. (2016), and Davis et al. (2019).

Due to the lack of post-Permian rocks, the age and kinematics of Cordilleran deformation events that affected the Ogilvie Platform-Selwyn Basin boundary remain poorly constrained. In the western segment of the platform-basin boundary, ductile fabrics associated with the Tombstone thrust (Fig. 1b) are post-Jurassic, but pre-95 Ma, as they are intruded by Late Cretaceous plutons (Murphy, 1997). Brittle faults and open folds are superimposed on ductile fabrics, but their timing is poorly constrained. North of the Selwyn Basin, Cenozoic to Quaternary deformation is documented along the Yukon fault and the Richardson fault array (Fig. 1a; Jeletzky, 1961; Mazotti and Hyndman, 2002).

Most of the Mesozoic intrusive rocks in the northern Selwyn Basin belong to three early Late Cretaceous (98–89 Ma) magmatic suites (i.e. Mayo, Tungsten, and Tomstone suites, with dominantly metaluminous, peraluminous, and alkali characteristics, respectively; Hart et al., 2004a,b; Rasmussen, 2013) and to the volumetrically less important latest Cretaceous to earliest Paleocene (67–63 Ma) McQuesten suite (Fig. 2; Murphy, 1997; Rasmussen, 2013; Colpron et al., 2016).

Geophysical Framework

In northern Yukon and Northwest Territories, the residual total magnetic field is dominated by the high-

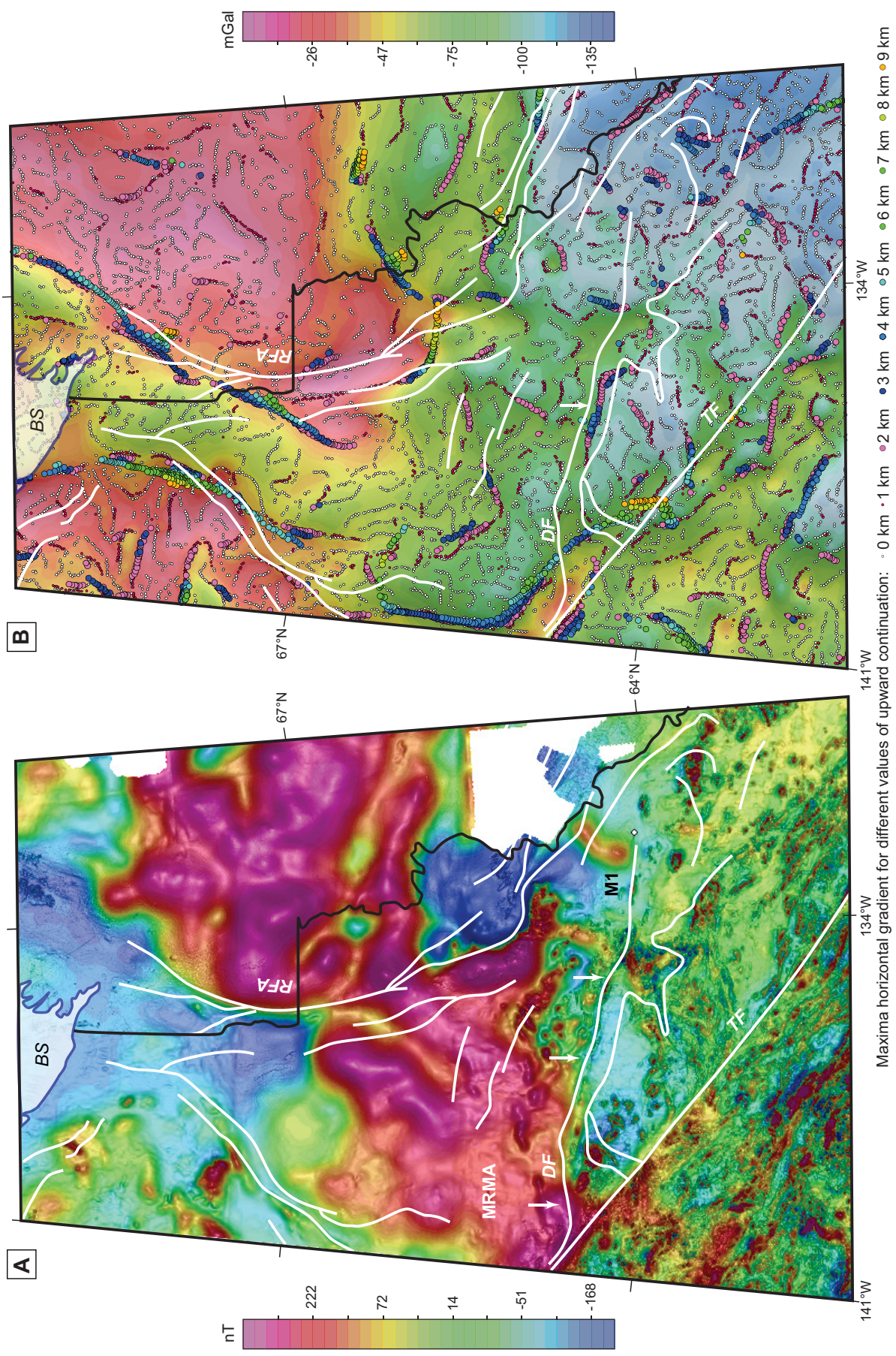

Figure 3. Residual total magnetic field **(a)** and Bouguer anomaly **(b)** over northern Yukon and Northwest Territories (*see* Fig. 1 for location). In (a), M1 is a magnetic anomaly that is discussed in the text. In (b), the points correspond to the maxima of the horizontal gradient for different values (0–9 km) of upward continuation and have been generated for this study. The maxima represent a way to automatically map the density contrast boundaries. White lines represent the regional faults. White arrows indicate major geophysical features associated with the Dawson fault. Abbreviation: BS = Beaufort Sea, DF = Dawson fault, MRMA = Mackenzie River magnetic anomaly, RFA = Richardson fault array, TF = Tintina fault.

amplitude, long-wavelength Mackenzie River magnetic anomaly (Fig. 3a) interpreted to be associated with Early Proterozoic magmatic arc crust at depth (Pilkington and Saltus, 2009). In Yukon, the southern boundary of the anomaly strikes west-northwest and is coincident with the western segment of the Dawson fault (Fig. 3). Regional seismic tomography models that map seismic velocity anomalies (dv/v; Fig. 4) is another tool to study the lithospheric architecture of the area. The low resolution of the regional tomographic image prevents the mapping of individual structures (such as the Dawson fault). However, the tomographic cross-section generated for this study and presented on Figure 4 clearly shows the juxtaposition of lithospheric domains with seismic waves propagating slightly faster (to the north) or slower (to the south) than average ambient mantle or crust, which correlate with density, temperature, and/or compositional variations (Kennett et al., 1995). This tomographic section substantiates the interpretation in which the northern boundary of the Selwyn Basin is a major structural break at the lithospheric scale.

Gravity stations in northern Yukon are typically located between 10 and 15 km apart, which prevents a detailed analysis of subtle gravity features. However, the western segment of the Dawson fault is marked by gravity gradients >1 mGal/km and is clearly defined by the linear distribution of maxima of the horizontal gravity gradient (white arrows on Fig. 3b). Similar to that of the magnetic data (Fig. 3a), the gravity signature of the eastern segment of the fault is more subtle, in agreement with geological evidence indicating that the fault splits into several branches to the east (*see below*).

Regional Metallogeny

In northern Yukon, the styles and ages of mineralization range from Proterozoic syngenetic deposits to Cenozoic epigenetic deposits (Nelson et al., 2013).

North of the Selwyn Basin-Ogilvie Platform boundary, mineralization is Precambrian and includes the following: 1) the Paleoproterozoic Cu-Au-U-Co-enriched Wernecke breccia (Thorkelson et al., 2001); 2) the Mesoproterozoic Hart River massive sulphide deposit; and 3) the Neoproterozoic Crest Fe deposit hosted by the glaciogenic strata of the Rapitan Group (Yeo, 1986).

In the northern Selwyn Basin, disparate mineralization styles broadly coincide with specific time periods (Fig. 2). Paleozoic mineralization consists largely of Zn-Pb±Ag sedimentary-exhalative-type occurrences that formed in mid-Cambrian (Anvil district: Pigage, 2004), early Silurian (Howards Pass district: Goodfellow and Jonasson, 1986) and Late Devonian (Macmillan Pass: Magnall et al., 2014). Although of lesser significance, Late Devonian–Mississippian poly-

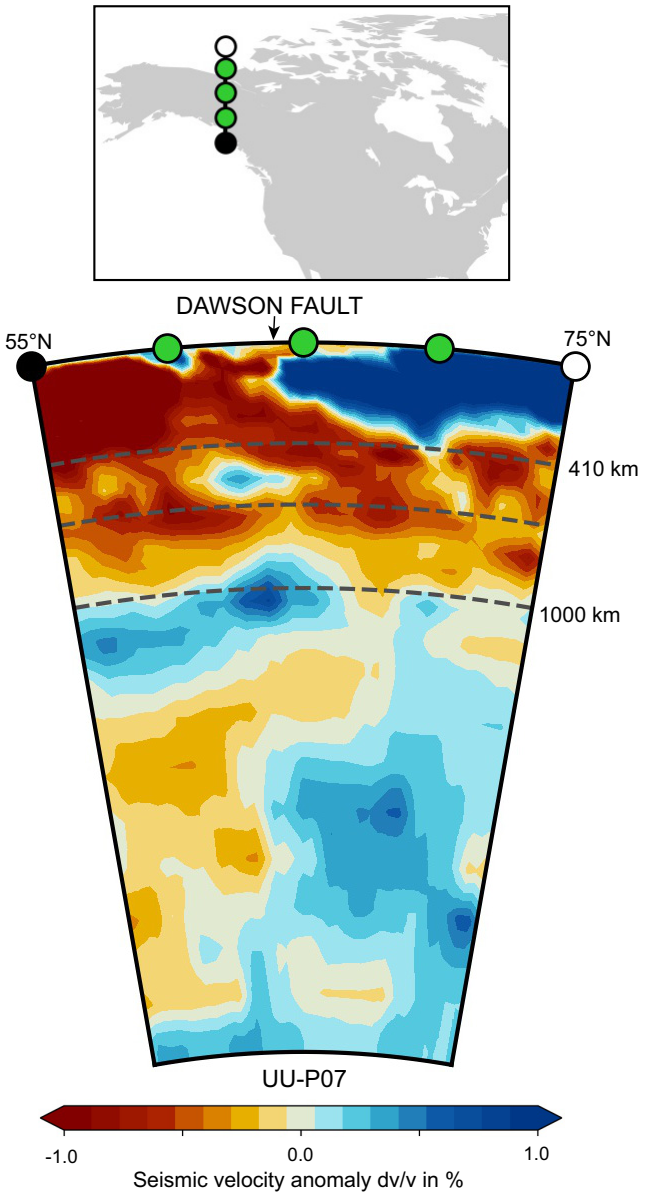

Figure 4. A tomographic image across the northern Cordillera, which has been generated for this contribution from the UU-P07 model (Amaru, 2007).

metallic, volcanogenic massive sulphide deposits also occur in Selwyn Basin and Mississippi Valley-type Zn-Pb occurrences in the Mackenzie Platform to the east are thought to be mainly mid-Paleozoic (Nelson et al., 2002).

Mesozoic mineralization in the northern Selwyn Basin region defines the eastern part of the Tintina gold province (Hart et al., 2004a,b), a regional belt of mineralization spatially and temporally associated with the early Late Cretaceous Tungsten (98–95 Ma), Mayo (98–93 Ma) and Tombstone (93–89 Ma) magmatic suites (Fig. 2). It includes the reduced intrusion-related Au deposits at Dublin Gulch, Clear Creek, Scheelite Dome, and Brewery Creek (Maloof et al., 2001; Marsh et al., 2003; Hart et al., 2004a,b; Lindsay, 2006; Mair et

al., 2011). Farther to the east, close to the boundary with Northwest Territories, the Mactung world-class W skarn deposit is also early Late Cretaceous. Quartzite-hosted polymetallic Ag-Pb-Zn veins of the Keno Hill district (Cathro, 2006) are classically associated with the Tombstone plutonic suite (e.g. Sinclair et al., 1980), but unpublished $^{40}Ar/^{39}Ar$ dating of mica suggests a possible Late Cretaceous age (Cragg, pers. comm., 2019), possibly related to nearby small intrusions of the McQuesten plutonic suite (ca. 67–63 Ma: Murphy, 1997; Colpron et al., 2016).

The youngest metallogenic event is upper Late Cretaceous to Eocene (?). East of the Tintina fault, it is documented only in the Rackla belt, a 5–15 km wide fold-and-fault belt bounded to the north by the Kathleen Lakes fault and to the south by the Dawson fault. The Rackla belt includes the Rau trend to the west and the Nadaleen trend to the east (Fig. 5a). The Rau trend consists of the Tiger deposit and a series of sediment-hosted occurrences that are still at an early stage of exploration. Sulphide replacement of Silurian carbonate rocks at the Tiger deposit (Thiessen et al., 2016) is linked to an intrusion that yielded Ar-Ar muscovite cooling ages between 62.3 and 59.1 Ma (Kingston et al., 2010). The Nadaleen trend consists of a series of Carlin-type gold mineralized zones (Arehart et al., 2013; Tucker et al., 2018) that are the focus of this study as well as auriferous quartz veins and sediment-hosted occurrences.

In the Nadaleen trend, U-Pb zircon dating from a locally gold-mineralized dyke indicates that the age of mineralization is <74 Ma (Tucker, 2015; Tucker et al., 2018). During the present study, late ore-stage calcite has been dated by U-Pb laser ablation inductively-coupled plasma mass spectrometry (LA-ICP-MS). Preliminary results reported in Davis et al. (2019) show variable degrees of complexity. Samples from the Conrad zone (n = 3) yield a relatively simple age distribution, including Tera-Wasserburg intercept ages between 72 and 75 Ma. Samples from the Osiris/Sunrise zone (n = 2) are significantly more complex and yield scattered U-Pb ages that may reflect several hydrothermal events, including one at ca. 73 Ma and one or several younger events. The relationship between these hydrothermal pulses and gold-mineralization is still under investigation.

DISTRICT-SCALE SETTING: THE EASTERN RACKLA BELT

Despite its remote location, our understanding of the geological setting of the eastern Rackla belt has been recently improved through active exploration in the area (e.g. Ristorcelli et al., 2018), a multiyear mapping project conducted by the Yukon Geological Survey (Fig. 5; Colpron et al., 2013; Moynihan, 2016) and the-

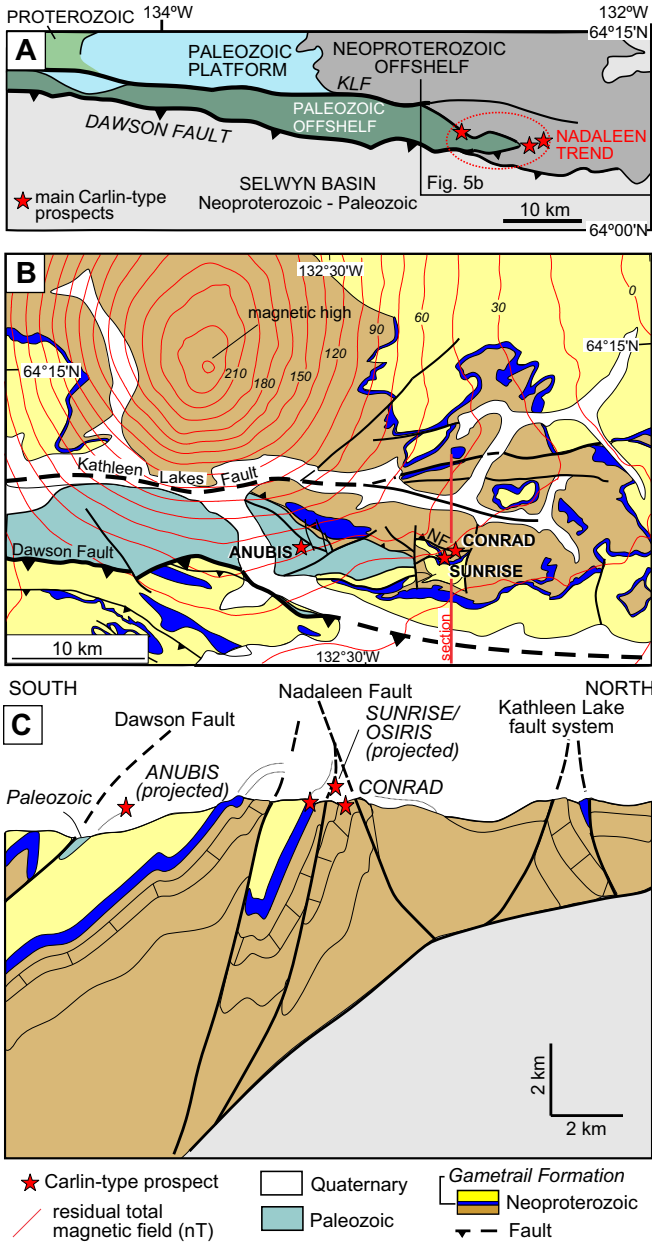

Figure 5. a) Simplified geological map of the eastern Rackla belt (*after* Colpron et al., 2013); abbreviation: KLF = Kathleen Lakes fault. **b)** Geological map (*modified from* Moynihan, 2016). Abbreviation: NF = Nadaleen fault. **c)** North-south cross-section, location of which is shown in (b).

matic research (e.g. Arehart et al., 2013; Beaton, 2015; Tucker, 2015; Palmer and Kuiper, 2016 Pinet et al., 2018; Steiner et al., 2018; Tucker et al., 2018; Pinet and Sack, 2019).

Stratigraphic Framework

The eastern Rackla belt comprises a lithologically diverse Neoproterozoic to Permian sedimentary succession (Fig. 6). The Neoproterozoic part of the succession belongs to the upper parts of the Windermere Supergroup (Moynihan et al., 2019). The oldest rocks in the eastern Rackla belt are latest Cryogenian and

consist of predominantly fine to coarse clastic strata with some silty to sandy limestone of the Twitya and Ice Brook formations (both belonging to the Hay Creek Group). The recently defined Rackla Group (Moynihan et al., 2019) conformably overlies the Ice Brook Formation and includes (1) fine-grained clastic rocks (Sheepbed Formation); (2) a heterogeneous mixed siliciclastic and carbonate succession (Nadaleen Formation); (3) distinctive, cliff-forming limestone and dolostone (Gametrail Formation) characterized by a large negative carbon isotope excursion that is correlated with the 579–551 Ma Shuram anomaly (Macdonald et al., 2013, 2017); (4) fine-grained siliciclastic rock (with some carbonate intervals) and sandstone (Blueflower Formation); and (5) cliff-forming limestone (Algae Formation). The Neoproterozoic-Cambrian contact is marked by an irregular erosional surface at the contact with overlying varicoloured mudstone and siltstone (Cambrian Narchilla Formation). A few kilometres southeast of the map area shown in Figure 5b, Cambrian-Ordovician rocks correspond to boulder conglomerate, mudstone, and siltstone of the Gull Lake Formation and mafic volcaniclastic and fragmental volcanic rocks of the Old Cabin Formation (Moynihan, 2013). In the Anubis area (Fig. 5b), Paleozoic rocks form a 2–7 km wide syncline with mainly fine-grained siliciclastic (black shale and siltstone) intervals alternating with three carbonate units. Within the syncline, fossil assemblages range from Middle Ordovician to Early Permian (Moynihan, 2016).

The entire Neoproterozoic succession was deposited below wave base in slope-to-basin settings, with the possible exception of some flat-pebble conglomerate layers in the Gametrail Formation that may indicate an outer ramp or shelf setting (Moynihan et al., 2019). Evidence of soft sediment deformation is present in almost all Neoproterozoic formations and in some Paleozoic units and include slump intervals with discontinuous folds and/or basal shears and flame structures.

Tectonic Framework

The Rackla belt is bounded by the Dawson fault to the south and the Kathleen Lakes fault to the north. Both faults split into several branches in the eastern Rackla belt. Some splays trend west-northwest, slightly oblique to the more east-west regional trend (Moynihan, 2016; Fig. 5b). As a result, displacements along individual faults tend to decrease toward the east and differences in the magnetic signature on both sides of faults are less apparent.

South of the Dawson fault, folds are generally tight and trend west-northwest- with a clear asymmetry to the north. In the Anubis area (Fig. 7a), the Dawson

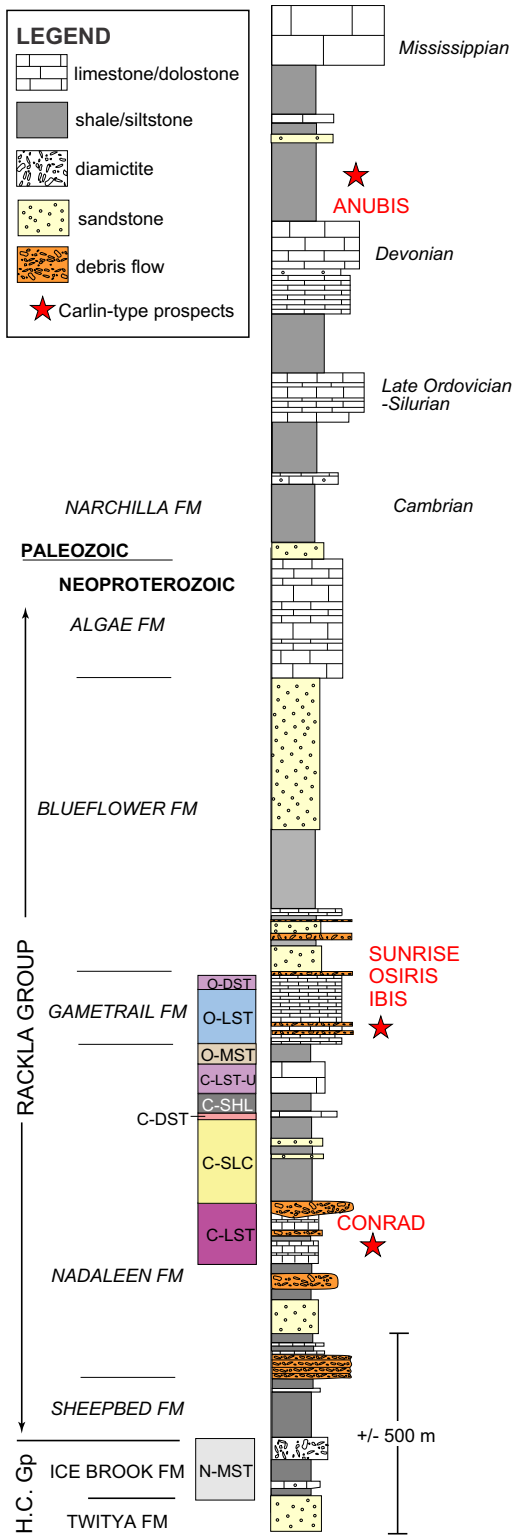

Figure 6. Sedimentary succession in the eastern Rackla belt, which has been *adapted from* Moynihan et al. (2019) for the Neoproterozoic. Informal sedimentary units are those cited in the text and are represented using the following abbreviations: C-DST = Conrad dolostone, C-CHL = Conrad shale, C-LST = Conrad limestone, C-LST-U = upper Conrad limestone, C-SLC = Conrad siliciclastic rock, H.C. Gp = Hay Creek Group, N-MST = NONAD mudstone, O-DST= Osiris dolostone, O-LST = Osiris limestone, O-MST = Osiris mudstone. Other abbreviation: FM = Formation.

fault is a moderately south-dipping structure that juxtaposes a >3 km succession of Neoproterozoic to Lower Cambrian rocks in its hanging wall upon Paleozoic strata in its footwall (Fig. 5, 7a).

North of the Dawson fault, fault dip direction and fold asymmetry vary. Fold interference is documented from regional (Moynihan, 2016) to outcrop scale (Steiner et al., 2018; this study). Regional west-northwest-trending folds predominate, some exhibiting an en échelon geometry relative to the Kathleen Lakes fault (Fig. 7a). Folds plunge either to the west-northwest or east-southeast and have a steeply dipping axial planar cleavage locally developed in fine-grained siliciclastic intervals. Faults trending obliquely to the east-west regional faults are common in the eastern Rackla belt (Fig. 7a). Northwest-striking faults are well developed throughout the area and generally exhibit a right-lateral component of displacement documented by the apparent offset of east-west-trending structures (including the Dawson fault) and magnetic markers on the high-resolution survey flown for ATAC Resources. A notable exception is the Osiris fault, which, despite trending east to east-northeast, is characterized by an apparent right-lateral sense of motion. It is likely that some of this apparent displacement reflects fault reactivation (*see below*). Some northeast-striking faults are also documented and exhibit a left-lateral component of displacement (Fig. 7a). Both northwest- and northeast-trending faults are compatible with a regime of left-lateral transpression (Fig. 7b). This regime is in agreement with the predominance of contractional structures and with the 10 km (northwest of Conrad) to 2.5 km (northeast of Conrad) left-lateral offset of steeply dipping contacts along the Kathleen Lakes fault (Fig. 7c,d; Moynihan, 2016). North of the Stewart River, regional mapping by Moynihan (2016) indicates that northeast-trending folds are also present in a restricted zone that includes the Osiris cluster. These anomalously trending folds are inconsistent with a model of left-lateral transpression and suggest that they formed in a distinct tectonic episode.

The structural complexity and polyphase structural history of the eastern Rackla belt are well exemplified by the scattering of bedding data on an equal-area lower-hemisphere stereodiagram (Fig. 7c), with a predominance of moderate to relatively steep dips (average 55°). Fault plane data collected during the course of this study are consistent with such structural complexity. Fault planes are generally steeply dipping and exhibit highly variable slickenline rakes attesting, in most cases, to mixed dip-slip (thrust or normal) and strike-slip (left- or right-lateral) components (Fig. 7d). In several cases, several generations (up to 3) of slickenlines are present on a single fault plane, demonstrating the polyphase structural history of the area. The relative timing of slickenlines is documented in a few cases only, preventing a detailed paleostress analysis.

LITHOSTRATIGRAPHY AND GEOMETRY OF THE NEOPROTEROZOIC-HOSTED GOLD MINERALIZED ZONES

The Nadaleen trend comprises several gold zones that are hosted in Neoproterozoic (Osiris cluster) and Paleozoic (Anubis cluster) rocks. This study focuses on the Conrad, Sunrise, and Osiris zones; the Ibis zone, also part of the Osiris cluster but located in the Osiris fault hanging wall (Fig. 8), has not been studied in detail.

Conrad Zone

The Neoproterozoic-hosted Conrad gold mineralized zone (Fig. 8) is the most intensively drilled (43,433 m in 108 holes) with inferred resources estimated at 9.7 Mt at 4.15 g/t (1.29 Moz Au: Ristorcelli et al., 2018). The Conrad area is poorly exposed. However, detailed mapping (Fig. 8) and drill data indicate that the main host unit (Conrad limestone, part of the Nadaleen Formation) forms the core of a doubly plunging anticline. The anticline is in fault-contact to the north and stratigraphic contact to the south with non-calcareous siliciclastic rocks with little evidence of paleofluid flow (veins), suggesting that siliciclastic rocks have low porosity and permeability. Mineralized intervals are documented for 800 m along strike and to a minimum vertical interval of 500 m (Ristorcelli et al., 2018).

The oldest sedimentary unit is found in the hanging wall of the Nadaleen fault, structurally overlying the Conrad mineralized zone (Fig. 8). It corresponds to varicoloured, thinly laminated mudstone and siltstone with quartz pebble conglomerate intervals. Evidence for soft-sediment deformation is common and pyrite (including locally cm-scale nodules) is disseminated throughout the unit. This unit, informally known as the NONAD mudstone, is regionally correlated with the Ice Brook Formation (Fig. 6; Moynihan et al., 2019).

In the footwall of the Nadaleen fault, the limestone unit is a medium grey lime mudstone/wackestone (Fig. 9a) with some intraclastic packstone (and minor grey to black siltstone). Limestone beds vary from a few millimetres to 20 cm (with a few beds >1 m) in thickness, and exhibit planar contacts. Cone-in-cone (Fig. 9b) and beef calcite are common and probably formed as hydraulic fractures through the degassing of biogenic methane during shallow burial (Meng et al., 2017), suggesting that the sediments were originally rich in organic matter. Calcium content of nonmineralized samples averages 28.9 wt% (i.e. approximately 72% calcite if all Ca is in calcite). At the surface, fabric-retentive dolomite is locally present with very irregular

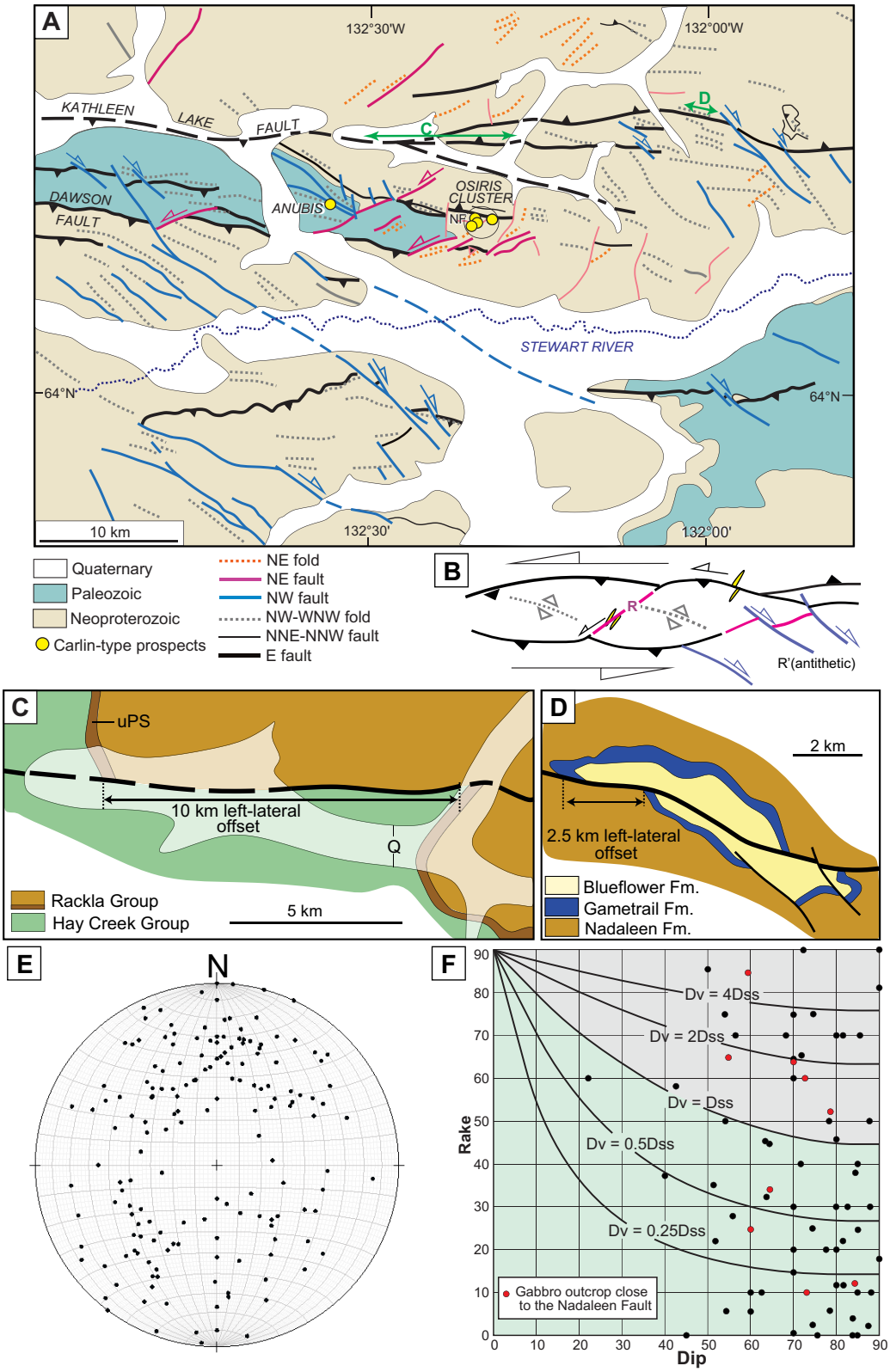

Figure 7. a) Structural framework of the eastern Rackla belt. The green arrows represent the apparent horizontal offsets along the Kathleen Lakes fault (*see* the discussion in the text). Abbreviation: NF = Nadaleen fault. **b)** Structural pattern expected in a left-lateral transpressional regime. **c and d)** Simplified geological maps showing the offsets of geological markers along the Kathleen Lakes fault system. The location is shown in Figure 7a (green arrows). *See* Moynihan (2016) for more detailed maps. Abbreviation: uPS= Sheepbed Formation. **e)** Schmidt equal-area lower-hemisphere projection of poles to bedding planes between the Kathleen Lakes fault and the Dawson Thrust/Stewart River (data are courtesy of D. Moynihan, Yukon Geological Survey). **f)** Fault-slip data were collected in the eastern Rackla belt. Abbreviations: Dss = strike-slip displacement, Dv = vertical displacement. The grey and green areas correspond to predominant down-dip and strike-slip motions, respectively.

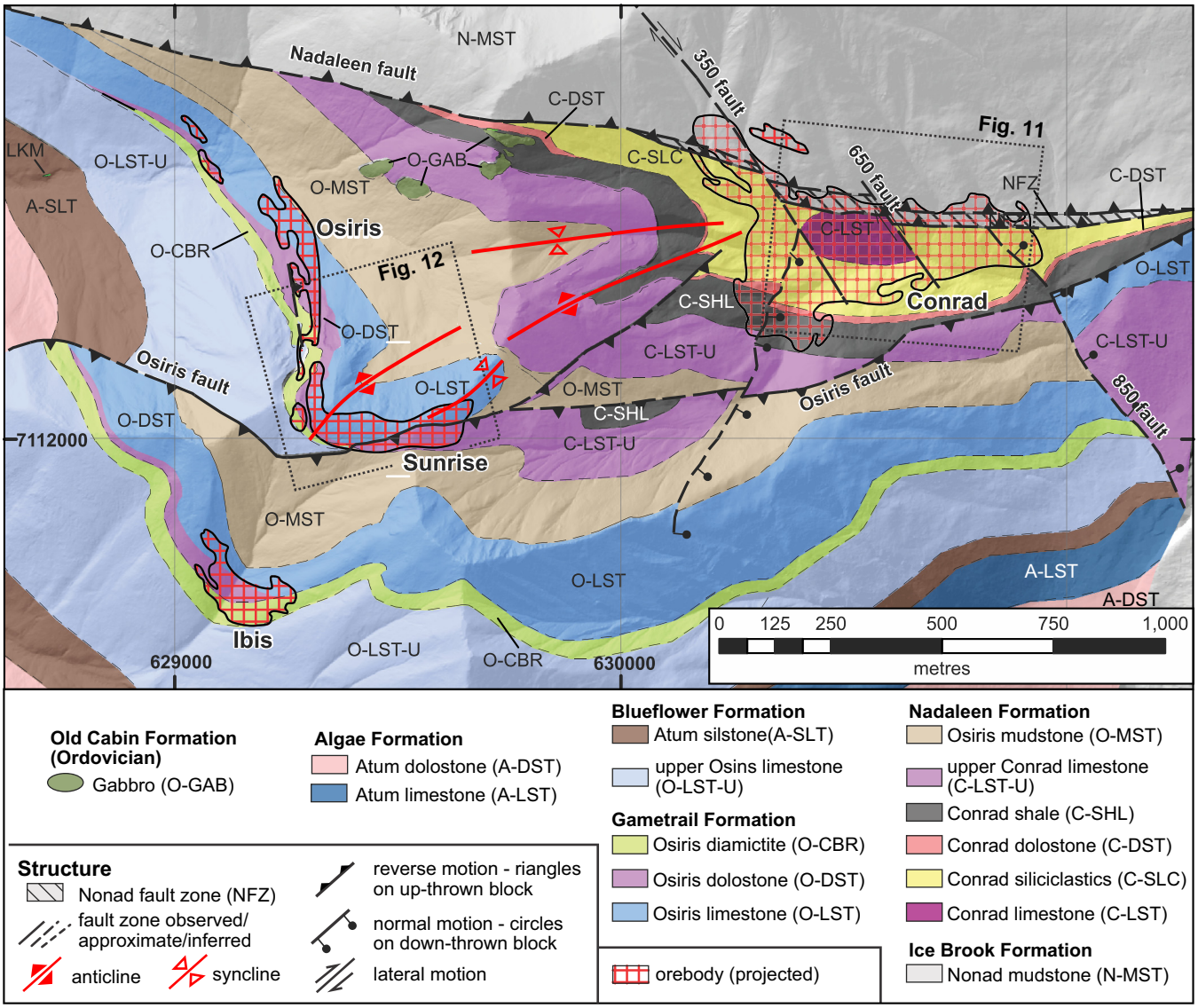

Figure 8. Geological map of the Osiris cluster area (*modified from* Steiner et al., 2018). Fold axes in the Conrad area are not shown for clarity.

dolomitization fronts. Analysis of the ATAC Resources geochemical database shows that >97% of Conrad limestone samples from the drilled area have less than 3 wt% Mg (<14% dolomite if all Mg is in dolomite), suggesting dolomitization was spatially restricted. Toward the top of the limestone unit, close to the contact with stratigraphically overlying siliciclastic rocks, the succession is more diverse. The upper part of the limestone unit is more finely laminated and includes light grey to black lime mudstone (Fig. 9e), intraclastic packstone, floatstone, and calcareous siltstone. Floatstone intervals (Fig. 9d) correspond to matrix-supported sedimentary breccia with angular fragments of lime mudstone, which are interpreted as debris flow deposits formed on a carbonate slope. The limestone unit is stratigraphically overlain by a siliciclastic unit locally known as the Conrad siliciclastics. It corresponds to grey-green siltstone and mudstone with some poorly sorted matrix-supported polymictic conglomerate with quartz pebbles (Fig. 9c) and a few weakly calcareous, centimetre-thick sandstone layers. Conglomeratic intervals up to 20 m thick are in gradational contacts with finer siliciclastic rocks and commonly exhibit synsedimentary deformation features. Pyrite (locally >2 vol.%) is disseminated throughout the unit. Both the Conrad limestone and the stratigraphically overlying Conrad siliciclastic rocks in the footwall of the fault are correlated with the Nadaleen Formation (Moynihan et al., 2019).

West of the Conrad mineralized zone, Neoproterozoic sedimentary units are cut by the Middle Ordovician Osiris gabbro that forms a 400 by 250 m intrusive body (Fig. 8; Tucker, 2015). Two 0.25–4 m thick dykes, also with gabbroic composition, are intersected in drill cores, in the footwall of the Nadaleen fault. These dykes, known as the Conrad dykes, are gabbroic and

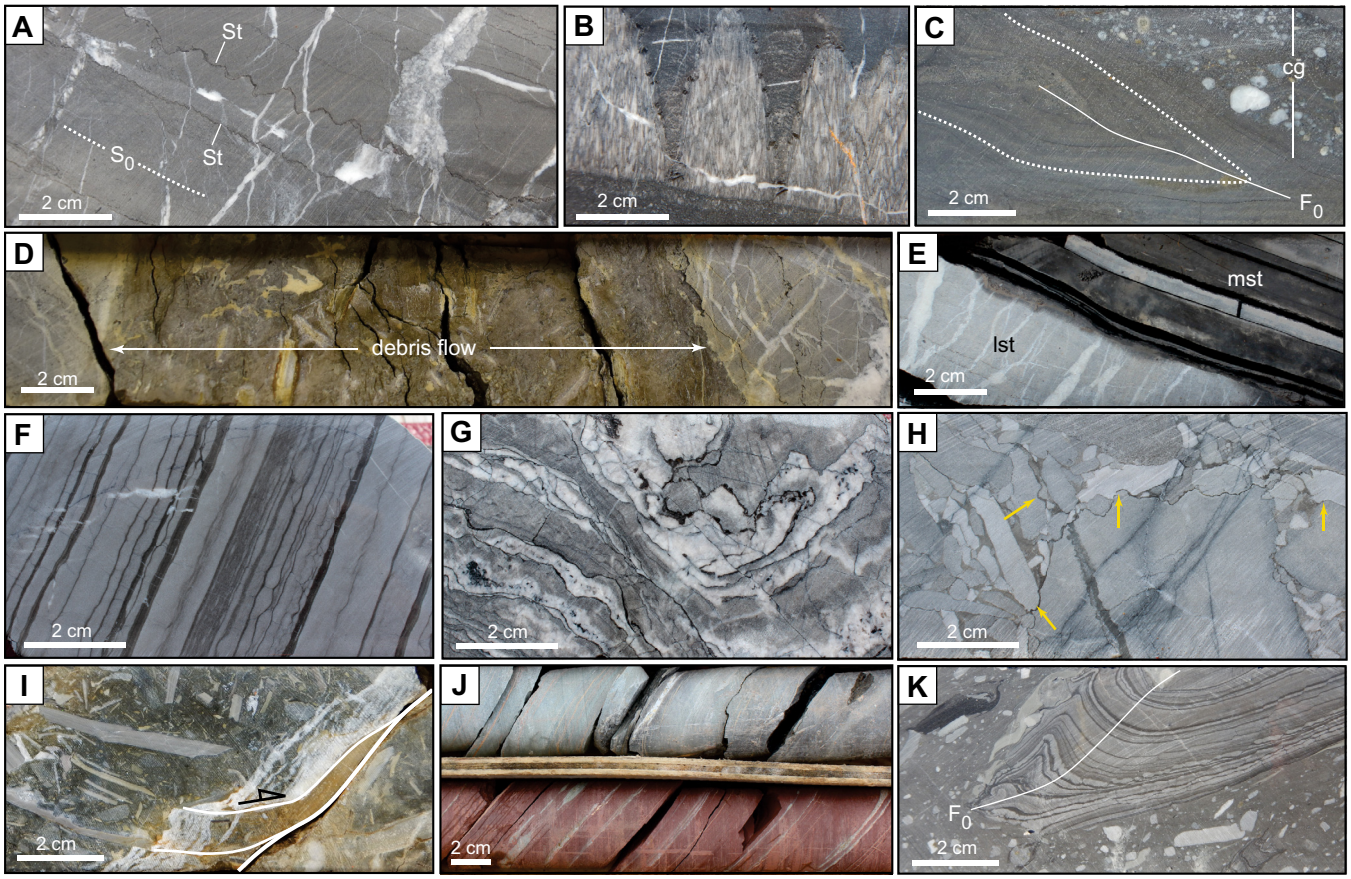

Figure 9. Photographs showing some of the lithological features of the Neoproterozoic succession in the eastern Rackla belt: a to e) Conrad area; f to k) Sunrise-Osiris area. **a)** Typical lime mudstone/packstone of the Nadaleen Formation (Conrad limestone). Abbreviations: S_0 = bedding, St = stylolite. **b)** Cone-in-cone calcite within lime mudstone of the Nadaleen Formation (Conrad limestone). **c)** Siltstone with synsedimentary folding (left part) and conglomerate with rounded to subrounded quartz clasts from the Nadaleen Formation (Conrad siliciclastic rocks). Abbreviations: cg = conglomerate, F_0 = synsedimentary fold. **d)** The floatstone interval is interpreted to have formed through debris flow within the limestone, close to the contact with the overlying siliciclastic rocks. **e)** Alternating veined lime packstone and mudstone within the Conrad limestone, close to the contact with overlying siliciclastic rocks. Abbreviations: lst = limestone, mst = mudstone. **f)** Typical lime-mudstone of the Gametrail Formation (Osiris limestone) with diagenetic stylonodular texture. **g)** Fabric-destructive dolomite within the Gametrail Formation. **h)** Clast-supported rudstone of the Gametrail Formation characterized by elongate clasts of lime mudstone. Note the indentation contacts between the clasts (yellow arrows). **i)** Floatstone interval within the Gametrail Formation. The basal contact is interpreted as a shear surface formed during debris flow emplacement. **j)** Typical varicoloured mudstone and siltstone from the Osiris mudstone. **k)** Matrix-supported polymictic conglomerate with a large clast exhibiting synsedimentary deformation.

composed of plagioclase, clinopyroxene, and secondary carbonate and pyrite. Tucker (2015) pooled five LA-ICP-MS U-Pb zircon analyses from two samples to calculate an emplacement age for the dykes of 74.1 ± 1.0 Ma. Dykes are commonly mineralized (Au >1 g/t) and contain realgar and fluorite. The inferred emplacement age of the dykes provides a maximum age limit for mineralization (Tucker et al. 2018; *see* discussion in Pinet et al., 2020).

The Nadaleen fault is the main structural feature in the Conrad area. It is an east-striking, steeply north-dipping (65º) fault with a damage zone that ranges from a few metres thick to up to several tens of metres between the north-northwest-trending 350 and 650 faults (Fig. 8). The Nadaleen fault zone records a polyphase structural history and is characterized by brittle to ductile fabrics (Fig. 10a) with kinematic indicators showing both strike-slip (predominantly left-lateral) and dip-slip (predominantly thrust) components. Most of the deformation predates mineralization, but in a few cases late- to post-mineralization displacement is documented by the offset of calcite veins with realgar and by minor fault planes with striated realgar coating. The Nadaleen fault is cut by a series of north-northwest-trending faults with apparent right-lateral displacement. Fault intersection zones show increased fracture density and mineralized intervals, but the timing of fracture permeability enhancement remains poorly constrained and both pre- and synmineralization fractures are possibly present (Pinet et al., 2020).

Though the limestone host unit is poorly exposed, there is evidence for complex folds and faults. In some cases, outcrop- to core-scale folds are a result of soft-sediment deformation (Fig. 9c). However, the radial

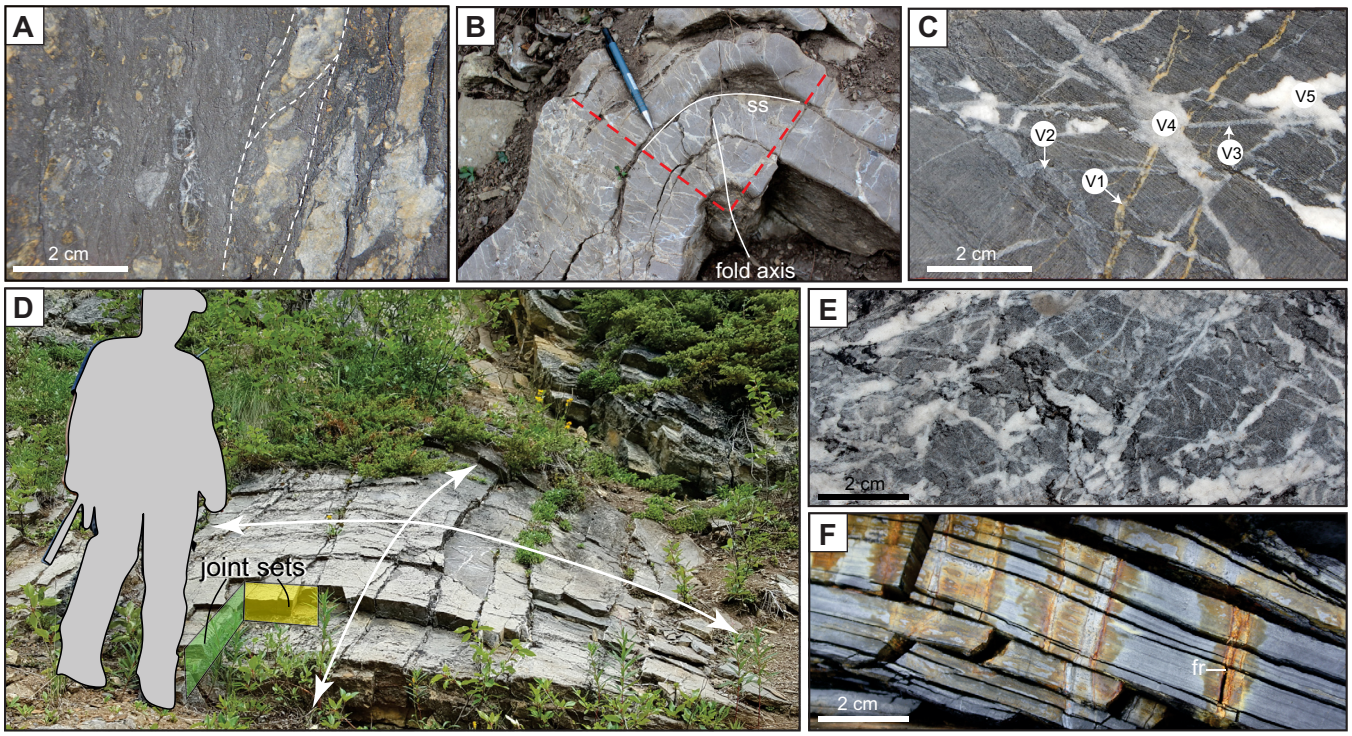

Figure 10. Photographs illustrating some tectonic features of the Neoproterozoic succession in the eastern Rackla belt. **a)** Typical brittle-ductile fabrics within the Nadaleen fault zone. Dashed lines show the main fabrics. **b)** Steeply plunging fold in the Conrad area. Note the fanning of veins (red dashed lines), suggesting that the veins are genetically associated with folding. Abbreviation: ss = slip surface. **c)** Multiple vein sets within the Conrad limestone. Crosscutting relationships allow identification of five vein generations (V_1 to V_5). **d)** Subperpendicular joint sets within the Conrad limestone. **e)** Irregular calcite veining within the Conrad limestone. **f)** A fracture that has developed perpendicular to the bedding. Note the oxidation halo around the fractures, suggesting fluid flow. Abbreviation: fr = fracture.

pattern of calcite veins in the hinge zones (Fig. 10b) clearly indicates a tectonic origin for at least some of the folds.

The deformation style at the Conrad zone varies with rock competency. In the more massive and competent intervals, multiple generations of calcite (± dolomite/quartz) veins locally represent up to 25 vol.% of the rock (Fig. 10e). Based on crosscutting relationships, up to four vein generations can be defined in hand samples (Fig. 10c), the latest generation is commonly characterized by coarse rhombohedral calcite crystals associated with realgar. Stylolites are locally well developed in thick-bedded limestone horizons (Fig. 9a). Early, bedding-parallel stylolites are the most common, but late stylolites crosscutting bedding are also present. In more thinly bedded and less competent intervals, shearing on bedding planes and bed-restricted joints predominate (Fig. 10f). Joint spacing varies from bed to bed and two well organized perpendicular joint sets are documented in outcrop (Fig. 10d).

Sunrise and Osiris Zones

The Sunrise and Osiris gold zones are located approximately 1.2 km west-southwest of the Conrad zone, on the east- and north-striking flanks of a complexly shaped anticline, respectively (Fig. 8; Steiner et al., 2018). The Sunrise and Osiris zones are in the footwall of the Osiris fault (Fig. 8). The Osiris fault is a steeply dipping (75º) fault with mixed right-lateral and reverse-sense of motion (*see* Pinet and Sack, 2019 for additional details).

Stratigraphic units in the Sunrise area (Fig. 8) have been described in Pinet and Sack (2019) and only a brief summary is given here. The oldest unit is limestone-dominated (alternating lime-mudstone and intraclastic packstone) and is locally known as the upper Conrad limestone. The upper Conrad limestone also includes a few weakly calcareous mudstone intervals and polymictic matrix-supported conglomerate with subrounded clasts. A finely (mm to a few cms) laminated varicoloured (brown, grey, green, purple) non-calcareous mudstone and siltstone unit (Fig. 9j; Osiris mudstone) stratigraphically overlies the upper Conrad limestone. This mudstone unit contains up to 3 vol.% of fine-grained pyrite and exhibits textures typical of soft-sediment deformation (Fig. 9k). Both the non-mineralized upper Conrad limestone and Osiris mudstone are part of the Nadaleen Formation (Moynihan et al., 2019). The unit that hosts the mineralization at Sunrise and Osiris corresponds to a 130 m thick limestone interval, locally known as the Osiris limestone, and has

been correlated with the Gametrail Formation of the Windermere Supergroup (Aitken, 1989; Moynihan et al., 2019). This unit is a medium grey lime-mudstone with bed thickness varying between 1 and 80 mm (average 8 mm). Some intervals show only a weak reaction to dilute (10 vol.%) HCl, indicating partial, fabric-retentive dolomitization.

The Osiris limestone also includes intraclastic rudstone and floatstone intervals interpreted as mass transport complexes resulting from different processes (short-distance translational sliding on a moderate slope and debris flows, respectively; Pinet and Sack, 2019). The rudstone intervals correspond to decimetre- to metre-thick clast-supported conglomerate with elongated lime-mudstone fragments showing stylolitic and indented contacts (flat-pebble conglomerate; Fig. 9h; Myrow et al., 2004). The floatstone intervals consist of poorly sorted polymictic, matrix-supported sedimentary breccia with variable matrix content and angular lime-mudstone clasts with variable colours and laminations (Fig. 9i). In the Osiris area (Fig. 8), a coarse-grained fabric-destructive dolostone with irregular dolomite veins (Fig. 9g; Beaton, 2015) overlies the Osiris limestone. In the Osiris limestone, multiple generations of calcite veins are documented, but they make up a smaller volume of the rock than in the Conrad limestone (Pinet and Sack, 2019).

DISCUSSION

At the regional scale, the Nadaleen trend exhibits two characteristics that have been identified as critical parameters for the formation of Carlin-type deposits in Nevada (Cline et al., 2005; Muntean, 2018a): 1) proximity to a long-lived, deep-seated tectonic feature (Dawson fault); and 2) a host sedimentary succession that includes carbonate and carbonaceous sedimentary rocks deposited in slope and base-of-slope settings. However, the spatial and temporal relationship of Carlin-type mineralized zones with magmatism (Muntean et al., 2011) remains equivocal in central Yukon because Late Cretaceous to Cenozoic igneous rocks is restricted to volumetrically minor stocks and dykes. A composite, positive magnetic anomaly with values up to 200 nT above the regional magnetic field is located 20 km west-northwest of the Conrad zone (M1 on Fig. 3) and may represent a large buried intrusion. Euler decomposition of the anomaly gives an estimate of 1.7 km for the depth of the uppermost part of the magnetic source and thus possibly the top of the intrusion. This interpretation is, however, not unique and the magnetic anomaly could also be associated with buried high magnetic susceptibility Paleoproterozoic to Mesoproterozoic sedimentary rocks. On high-resolution data flown for ATAC Resources, the residual total magnetic field also includes a low-amplitude (<50 nT) oval-shaped magnetic low centred 3.5 km southwest of the Sunrise zone. This anomaly could hypothetically be associated with a reduced (ilmenite series) intrusion.

In central Yukon, the sedimentary succession is complexly faulted and folded with several phases of deformation, but the ages of deformation are poorly constrained. Despite uncertainty about the timing and detailed kinematics of deformation phases, a regional-scale Late Cretaceous extensional event comparable to the Eocene-Miocene basin-and-range extension of the southwestern United States is not evident in the regional geology of east-central Yukon (Nelson et al., 2013). Importantly, synmineralization extension, if any, must have been kinematically linked with significant strike-slip motion along faults and not to a regional-scale episode of extension, for which no evidence has been found.

At the mineralized-zone scale, the dip (commonly >50º) of units hosting mineralization is significantly steeper than in most deposits of Nevada where shallowly dipping (<30º) favourable strata channelled mineralizing fluid out of high-angle faults contributing to the formation of tree-like mineralized envelopes (Rhys et al., 2015; Muntean, 2018a). Considering the remaining uncertainties about the exact timing of deformation and local evidence for late- to post-mineralization faults in the Osiris cluster area (fault planes with striated realgar, minor faults cutting calcite-realgar veins, and possibly brittle faults surrounding mineralized intervals in the Nadaleen fault zone), it is possible that folds may have been tightened after gold deposition and that the present-day geometry is not the same as during mineralization. However, the shape of gold-bearing mineralized bodies at Conrad strongly suggests that without the tight anticline geometry (Fig. 11) and the caprock integrity of siliciclastic intervals stratigraphically or structurally above limestone units hosting mineralization (Conrad siliciclastic units and NONAD mudstone), fluids would have escaped and may not have formed significant gold accumulations. In the Sunrise and Osiris zones, caprock units vary (Fig. 12) and correspond to the Osiris fault zone (including a 10 m thick Osiris mudstone interval) in the Sunrise area and to the Osiris dolostone in the Osiris area. In this latter case, irregular dolomite veins formed during sedimentary burial, with no evidence of younger hydrothermal fluid circulation, confirming that the dolostone, even if intensively veined, acted as an impermeable unit.

IMPLICATIONS FOR EXPLORATION

Maximum burial conditions recorded along the northern boundary of the Selwyn Basin decrease from greenschist facies in the west (Abbott, 1997) to the

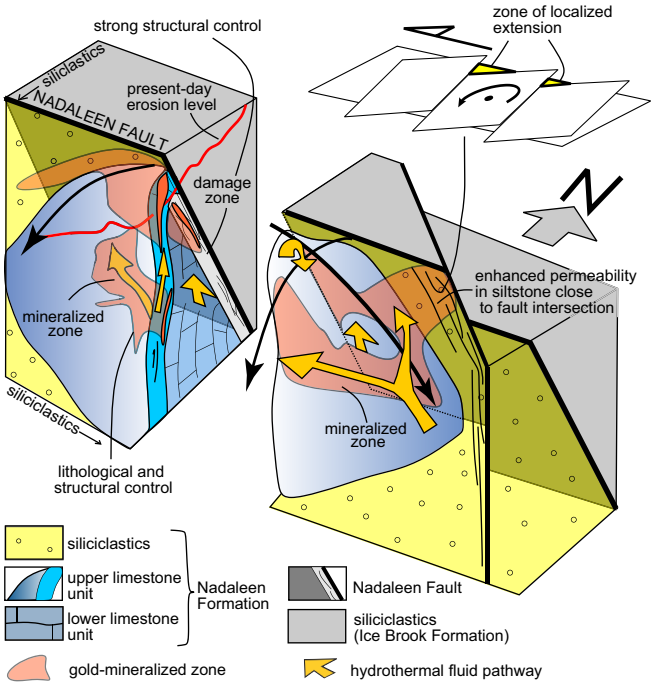

Figure 11. Schematic 3-D view of the Conrad zone.

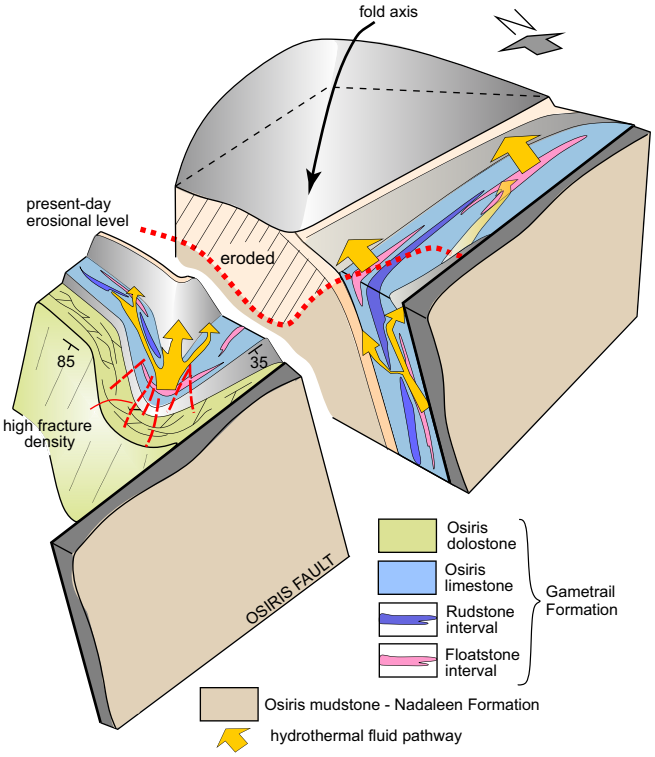

Figure 12. Schematic 3-D view of the Sunrise and Osiris zones.

anchizone in the eastern Rackla belt. In this latter area, Rock-Eval pyrolysis analyses done during this study (not shown) indicate that the kerogen present in organic-rich sedimentary rocks has lost almost all generative hydrocarbon potential (dry gas zone). The timing of differential exhumation is poorly constrained. However, if exhumation is syn- to post-mineralization, it may have resulted in the erosion of shallowly formed deposits, such as Carlin-type, in the western part of the Ogilvie platform-Selwyn Basin transition zone and their preservation in the eastern part.

The strike-slip component of motion along many of the structures that mark the northern boundary of the Selwyn Basin indicates that the detailed geometry in the map view of the main faults merits further consideration. In particular, areas characterized by a change in strike (bend) and/or step over (relay zones) may correspond to favourable zones of fluid flow and/or traps as they have the significant vertical connectivity necessary for tapping relatively deep fluid (and metal) reservoirs. Horsetail-style structures (i.e. fault that split into several branches) and fault intersections should also be considered as highly favourable zones due to the typical increase of second-order faults in these areas. Recognition of such zones may, however, be challenging, as the expression of intersecting small-displacement faults may be subtle on regional maps or regional magnetic surveys. The Conrad zone, where north-northwest-trending faults cut the Nadaleen fault is an example of such a highly favourable setting with enhanced permeability (increased density of pre- and/or synmineralization fractures and possibly localized zones of extension; Fig. 11; Pinet et al., 2020).

Several northeast-striking faults are present throughout the Nadaleen trend. Analysis of high-resolution aeromagnetic data suggests that most of these faults exhibit an apparent left-lateral sense of motion and offset more west-trending structures (Fig. 7). Interestingly, the spatial association between northeast-trending faults and latest Cretaceous mineralization (porphyry Mo and Cu systems, Ag-rich polymetallic veins, carbonate replacement, and skarn bodies) has been documented west of the Tintina fault, >350 km from the Nadaleen trend, where they exhibit left-lateral oblique extensional motion (Allan et al., 2013). East of the Tintina fault, mineralization of the Keno Hill district is also associated with northeast-trending faults with gently plunging slickenlines (D_3 of Craggs et al., 2010). Detailed structural analysis and better timing constraints should make it possible to test the potential relationship between motion on northeast-trending faults and a distinct, possibly short-duration, geodynamic event.

In the eastern Rackla belt, most of the first-order structures formed and/or have been reactivated in a regional left-lateral transpressional regime (Fig. 7b). However, the Nadaleen trend is characterized by 'anomalous' geological features that are not compatible with such a tectonic regime. These features include northeast-trending folds, the Osiris fault that exhibits

an apparent right-lateral component of motion, and the west- to northwest-trending Conrad dykes. It is presently unclear if northeast-trending folds, the motion of the Osiris fault, and intrusion of the Conrad dykes are contemporaneous. However, these structures are kinematically compatible with a west-southwest maximum principal compressive stress and there is a possibility that they represent a single 'late' structural event, hypothetically synchronous with mineralization. These late-stage structures, which post-date the main deformation event, may be significant for Carlin-type mineralization exploration in Yukon.

ACKNOWLEDGMENTS

This contribution is dedicated to Julia Lane who was instrumental in designing the project and conducting its various field and analytical components. Her help and enthusiasm are sincerely missed. Thanks to ATAC Resources for access to drill cores and data, and for logistical support and scientific input. This report beneficiated from discussions with A. Coulter, J. Ryan, and D. Moynihan (who shared the structural data presented in Fig. 7c). Y. Kuiper, C. Lawley, and R. Carne are acknowledged for their constructive reviews.

REFERENCES

Abbott, G., 1997. Geology of the upper Hart River area, eastern Ogilvie Mountains, Yukon Territory (116A/10, 116A/11); Yukon Geological Survey, Bulletin 9, 92 p.

Aitken, J.D., 1989. Uppermost Proterozoic formations in central Mackenzie Mountains, Northwest Territories; Geological Survey Canada, Bulletin 368, 26 p.

Allan, M.M., Mortensen, J.K., Hart, C.J.R., Bailey, L.A., Sanchez, M.G., Ciolkiewicz, W., McKenzie, G.G., and Creaser, R.A., 2013. Magmatic and metallogenic framework of west-central Yukon and eastern Alaska; *in* Tectonics, Metallogeny, and Discovery: The North American Cordillera and similar accretionary settings, (ed.) M. Colpron, T. Bissig, B.G. Rusk, and J.F.H. Thompson; Society of Economic Geologists, Special Publication 17, p. 111–168.

Amaru, M.L., 2007. Global travel time tomography with 3-D reference models; Ph.D. thesis, Utrecht University, Geologica Ultraiectina, v. 274, 174 p.

Arehart, G.B., Ressel, M., Carne, R., and Muntean, J., 2013. A comparison of Carlin-type deposits in Nevada and Yukon; *in* Tectonics, Metallogeny, and Discovery: The North American Cordillera and similar accretionary settings, (ed.) M. Colpron, T. Bissig, B.G. Rusk, and J.F.H. Thompson; Society of Economic Geologists, Special Publication 17, p. 389–401.

Beaton, N.I., 2015. Diagenetic controls on hydrothermal fluid flow in the Osiris, Isis and Isis East Carlin-type showings, Nadaleen trend, Yukon; M.Sc. thesis, University of Alberta, Edmonton, Alberta, 180 p.

Bineli Betsi, T., Lentz, D., Chiaradia, M., Kyser, K., and Creaser, R.A., 2013. Genesis of the Au-Bi-Cu-As, Cu-Mo±W, and base-metal Au-Ag mineralization at the Mountain Freegold (Yukon, Canada): constraints from Ar-Ar and Re-Os geochronology and Pb and stable isotope compositions; Mineralium Deposita, v. 48, p. 991–1017.

Cathro, R.J., 2006. Great mining camp of Canada- 1. The history and geology of the Keno Hill Silver camp, Yukon Territory; Geosciences Canada, v. 33, p. 103–134.

Cecile, M.P., 1982. The Lower Paleozoic Misty Creek Embayment, Selwyn Basin, Yukon and Northwest Territories; Geological Survey of Canada, Bulletin 335, 78 p.

Cline J.S., Hofstra A., H., Muntean J.L., Tosdal R.M., and Hickey K.A., 2005. Carlin-type gold deposits in Nevada: critical geologic characteristics and viable models; *in* Economic Geology 100th Anniversary Volume, (ed.) J.W. Hedenquist, J.F.H. Thompson, R.J. Goldfarb, and J.P Richards; Society of Economic Geologist, p. 541–484.

Colpron, M., 2012. Preliminary observations on the geology of the Rackla belt, Mount Ferell map area (NTS 106C/3), central Yukon; *in* Yukon Exploration and Geology 2011, (ed.) K.E. MacFarlane and P.J. Sack; Yukon Geological Survey, p. 27–43.

Colpron M., Moynihan D., Israel S., and Abbott G., 2013. Geologic map of the Rackla belt, east-central Yukon (NTS 106C/1-4, 106D/1); Yukon Geological Survey, Open File 2013-13, scale 1:50 000, 5 maps and legend.

Colpron, M., Israel, S., and Friend, M., 2016. Yukon plutonic suites; Yukon Geological Survey, Open File 2016-37, scale 1:750 000.

Craggs, S.D., Lentz, D.R., and White, J.C., 2010. Polyphase folding in the Keno Hill Ag-Pb-Zn mining district, Yukon, Canada; Expanded abstract, GeoCanada 2010, 4 p.

Davis, W.J., Pinet, N., Petts, D.C., Jackson, S.J., and Mercier-Langevin, P., 2019. U-Pb ages of hydrothermal calcite associated with Carlin-type mineralization, Nadaleen trend, north-central Yukon; Geological Association of Canada-Mineralogical Association of Canada, Volume of Abstracts, v. 42, p. 77.

Gabrielse, H., Murphy, D.C., and Mortensen, J.K., 2006. Cretaceous and Cenozoic dextral orogeny-parallel displacements, magmatism and paleogeography, north-central Canadian Cordillera; *in* Paleogeography of North American Cordillera: Evidence for and against large-scale displacements, (ed.) J.W., Haggart, R.J., Enkin, and J.W.H, Monger; Geological Association of Canada, Special Paper 46, p. 255–276.

Gordey, S.P., 1981. Structure section across south central Mackenzie Mountains, district of Mackenzie; Geological Survey of Canada, Open File 809, 1 plate.

Goodfellow, W.D. and Jonasson, I.R., 1986. Environment of formation of the Howards Pass (XY) Zn-Pb deposit, Selwyn Basin, Yukon; *in* Mineral Deposits of Northern Cordillera, (ed.) J.A., Morin; Canadian Institute of Mining and Metallurgy, Special volume 37, p. 19–50.

Hart, C.J.R., Goldfarb, R.J., Lewis, L.L., and Mair, J.L., 2004a. The northern Cordilleran Mid-Cretaceous plutonic province: Ilmenite/magnetite series granitoids and intrusion related mineralization; Resource Geology, v. 54, p. 253–280.

Hart, C.J.R., Mair, J.L., Goldfarb, R.J., and Groves, D.I., 2004b. Source and redox controls on metallogenic variations in intrusion-related ore systems, Tombstone-Tungsten belt, Yukon territory, Canada; Transactions of the Royal Society of Edinburgh, Earth Sciences, v. 95, p. 339–356.

Jeletzky, A., 1961. Eastern slope, Richardson Mountains: Cretaceous and Tertiary structural history and regional significance; *in* Geology of the Arctic, Proceedings of the first international symposium on Arctic geology, (ed) G.O., Raasch; Alberta Society of Petroleum Geologists, v. 1, p. 532–583.

Kennett, B.L.N., Engdahl, E.R., and Buland, R., 1995. Constraints on seismic velocities in the Earth from traveltimes; Geophysical Journal International, v. 122, p. 108–124.

Kingston, S., Mortensen, J.K., Gabites, J., and Dumala, M., 2010. Ar-Ar geochronology and Pb isotopic constraints on the origin

of the Rau gold-rich carbonate replacement deposit, central Yukon; *in* Yukon Exploration and Geology 2009, (ed.) K.E. MacFarlane, L.H. Weston, and L.R. Blackburn; Yukon Geological Survey, p. 213–222.

Lindsay, M.J., 2006. The structural and hydrothermal evolution of intrusion-related gold mineralization at the Brewery Creek mine, Yukon, Canada; Ph.D. Thesis, James Cook University, North Queensland, 348 p.

Macdonald, F.A., Strauss, J.V., Sperling, E.A., Halverson, G.P., Narbonne, G.M., Johnson, D.T., Kunzmann, M., Schrag, D.P., and Higgins, J.A., 2013. The stratigraphic relationship between the Shuram Carbon isotope excursion, the oxygenation of Neoproterozoic oceans, and first appearance of the Ediacara biota and bilaterian trace fossils in northwestern Canada June beds; Chemical Geology, v. 362, p. 250–272.

Macdonald, F.A., Schmitz, M.D., Strauss, J.V., Halverson, G.P., Gibson, T.M., Eyster, A., Cox, G., Mamrol, P., and Crowley, J.L., 2017. Cryogenian of Yukon; Precambrian Research, v. 319, p. 114–143.

Magnall, J.M., Gleeson, S.A., and Paradis, S., 2014. SEDEX mineralization, Macmillan Pass (Yukon): petrography, mineralogy and bulk geochemistry of the Tom and Nidd deposits; Geological Survey of Canada, Open File 7457, 37 p.

Mair, J.L., Farmer, G.L., Groves, D.I., Hart, C.J.R., and Goldfarb, R.J., 2011. Petrogenesis of postcollisional magmatism at Scheelite Dome, Yukon, Canada: evidence for a lithospheric mantle source for magmas associated with intrusion-related gold systems; Economic Geology, v. 106, p. 451–480.

Maloof, T.L., Baker, T., and Thompson, J.F.H., 2001. The Dublin Gulch intrusion-hosted gold deposit, Tombstone plutonic suite, Yukon Territory, Canada; Mineralium Deposita, v. 36, p. 583–593.

Marsh, E.E., Goldfarb, R.J., Hart, C.J.R., and Johnson, C.A., 2003. Geology and geochemistry of the Clear Creek intrusion-related gold occurrences, Tintina gold province, Yukon, Canada; Canadian Journal Earth Sciences, v. 40, p. 681–699.

Mazotti, S., and Hyndman, R.D., 2002. Yakutat collision and strain transfer across the northern Canadian Cordillera; Geology, v. 30, p. 495–498.

Meng, Q., Hooker, J., and Cartwrigth, J., 2017. Early overpressuring in organic-rich shales during burial: evidence from fibrous calcite veins in the Lower Jurassic shales with beef member in the Western Basin, UK; Journal of Geological Society, v. 174, p. 869–882.

Mortensen, J.K., Hart, C.J.R., Tarswell, J., and Allan, M.M., 2016. U-Pb zircon age and Pb isotopic constraints on the age and origin of porphyry and epithermal vein mineralization in the eastern Dawson Range, Yukon; *in* Yukon Exploration Geology 2015, (ed.) K.E. MacFarlane and M.G. Nordling; Yukon Geological Survey, p. 165–185.

Moynihan, D., 2013. Bedrock geology of NTS 106B/04, eastern Rackla belt; *in* Yukon Exploration and Geology 2017, (ed.) K.E. MacFarlane, M.G. Nording, and P.J. Sack; Yukon Geological Survey, p. 147–167.

Moynihan D., 2016. Bedrock geology compilation of the eastern Rackla belt, NTS 105N/15, 105N/16, 105O/13, 106B/4, 106C/1, 106C/2, east-central Yukon; Yukon Geological Survey, Open File 2016-2, scale 1:75 000.

Moynihan, D., Strauss, J.V., Padget, C.D., and Nelson, L.L., 2019. Upper Windermere Supergroup and the transition from rifting to continent-margin sedimentation, Nadaleen River area, northern Canadian Cordillera; Geological Society of America Bulletin, v. 131, p. 1673–1701.

Muntean, J.L., Cline, J.S., Simon, A.C., and Longo, A.A., 2011. Magmatic-hydrothermal origin of Nevada's Carlin-type gold deposits; Nature Geoscience, v. 4, p. 122–127.

Muntean, J., 2018a. The Carlin gold system: Applications to exploration in Nevada and beyond; *in* Diversity of Carlin-style Gold Deposits, (ed.) J. Muntean; Society of Economic Geologists, Reviews in Economic Geology, v. 20, p. 39–88.

Muntean, J. (ed.), 2018b. Diversity of Carlin-style gold deposits; Society of Economic Geologists, Reviews in Economic Geology, v. 20, 363 p.

Murphy, D.C., 1997. Geology of the McQuesten River region, northern McQuesten and Mayo map area, Yukon Territory (115P/14, 15, 16; 105M/13, 14); Exploration and Geological Services Division, Yukon, Indian and Northern Affairs Canada Bulletin 6, 122 p.

Myrow, P.M., Tice, L., Archuleta, B., Clark, B., Taylor, J.F., and Ripperdant, R.L., 2004. Flat-pebble conglomerate: its multiple origins and relationship to metre-scale depositional cycles; Sedimentology, v. 51, p. 973–996.

Nelson, J.L., Colpron, M., and Israel, S., 2013. The Cordillera of British Columbia, Yukon and Alaska: Tectonics and Metallogeny; *in* Tectonics, Metallogeny and Discovery: The North American Cordillera and Similar Accretionary Setttings, (ed.) M. Colpron, T. Bissig, B.G. Rusk, and J.F.H. Thompson; Society of Economic Geologists, Special Publication 17, p. 53–109.

Nelson, J.L., Paradis, S., Christensen, J., and Gabites, J., 2002. Canadian Cordillera Mississippi Valley-type deposits: A case for Devonian-Mississippian back-arc hydrothermal origin; Economic Geology, v. 97, p. 1013–1036.

Palmer, J.C. and Kuiper, Y.D., 2016. Structural geology of the eastern Nadaleen trend, Yukon Territory, Canada: Implications for recently discovered sedimentary rock-hosted gold; Ore Geology Reviews, v. 80, p. 48–60.

Pigage, L.C., 2004. Bedrock geology compilation of the Anvil district (parts of 105K/2, 3, 5, 6, 7, and 11), central Yukon; Yukon Geological Survey, Bulletin 15, 103 p.

Pilkington, M. and Saltus, R.W., 2009. The Mackenzie River magnetic anomaly, Yukon and Northwest Territories, Canada—Evidence for Early Proterozoic magmatic arc crust at the edge of the North American craton; Tectonophysics, v. 478, p. 78–86.

Pinet, N., Sack, P., Mercier-Langevin, P., Lavoie, D., Dubé, B., Lane, J., and Brake, V., 2018. Breccia styles and controls on carbonate replacement type ('Carlin type') gold zones, Rackla belt, east-central Yukon; *in* Targeted Geoscience Initiative – 2017 Report of Activities, (ed.) N. Rogers; Geological Survey of Canada, Open File 8358, p. 163–168.

Pinet, N. and Sack, P., 2019. Macroscopic control on Carlin-type gold mineralization in north-central Yukon; *in* Targeted Geoscience Initiative: 2018 report of activities, (ed.) N. Rogers; Geological Survey of Canada, Open File 8549, p. 89–103.

Pinet, N., Sack, P., Mercier-Langevin, P., Davis, W.J., Lavoie, D., Haeri-Ardakani, O., Komaromi, B.A., Dubé, B., Cline, J.S., Petts, D.C., Jautzy, J., Jackson, S.E., Percival. J.B., Savard, M.M., and Brake, V.I., 2020. Neoproterozoic-hosted Carlin-type mineralization in central Yukon, part 2: Mineralization; *in* Targeted Geoscience Initiative 5: Contributions to the Understanding of Canadian Gold Systems, (ed.) P. Mercier-Langevin, C.J.M. Lawley, and S. Castonguay; Geological Survey of Canada, Open File 8712, p. 299–314. doi:10.4095/326047

Rasmussen, K.L., 2013. The timing, composition, and petrogenesis of syn- to post- accretionary magmatism in the northern Cordilleran miogeocline, eastern Yukon and southwestern Northwest Territories; Ph.D. thesis, University of British Columbia, Vancouver, British Columbia, 788 p.

Rhys, D., Valli, F., Burgess, R., Heitt, D., Griesel, G., and Hart, K., 2015. Controls of fault and fold geometry on the distribution of

gold mineralization on the Carlin trend; Geological Society of Nevada, New Concepts and Discoveries: 2015 Symposium Proceedings, p. 333–389.

Ristorcelli, S., Ronning, P., Martin, C., and Christensen, O., 2018. Technical report and estimate of mineral resources for the Osiris project, Yukon, Canada, Mine Development Associates for ATAC Resources Ltd. <https://www.atacresources.com/assets/img/Osiris_Resource_Estimate_and_Technical_Report_2018.pdf> [accessed October 30, 2019]

Selby, D. and Creaser, R.A., 2001. Late and mid-Cretaceous mineralization in the northern Canadian Cordillera: Constraints from Re-Os molybdenite dates; Economic Geology, v. 96, p. 1461–1467.

Sinclair, A.J., Tessari, O.J., and Harakal, J.E., 1980. Age of Ag–Pb–Zn mineralization, Keno Hill – Galena Hill area, Yukon Territory; Canadian Journal of Earth Sciences, v. 17, p. 1100–1103.

Steiner, A., Hickey, K., and Coulter, A., 2018. The structural framework for Carlin-type gold mineralization in the Nadaleen trend, Yukon; *in* Yukon Exploration and Geology 2017, (ed.) K.E. MacFarlane; Yukon Geological Survey, p. 139–149.

Thiessen, E.J., Gleeson, S.A., Bennett, V., and Creaser, R.A., 2016. The Tiger deposit: a carbonate-hosted, magmatic-hydrothermal gold deposit, central Yukon, Canada; Economic Geology, v. 111, p. 421–446.

Thorkelson, D.J., Mortensen, J.K., Davidson, G.J., Creaser, R.A., Perez, W.A., and Abbott, J.G., 2001. Mesoproterozoic intrusive breccias in Yukon, Canada: the role of hydrothermal systems in reconstruction of North America and Australia; Precambrian Research, Special Volume 111, p. 31–56.

Tucker, M.J., 2015. Geology, mineralization and geochronology of the Conrad zone Carlin-type prospect, east-central Yukon Territory, Canada; M.Sc. thesis, University of British Columbia, Vancouver, British Columbia, 160 p.

Tucker, M.J., Lane, J.C., and Hart, C.J.R., 2018. Overview of Carlin-type prospects of the Nadaleen trend: A Yukon analogue to Carlin-type gold mineralization of the Great Basin; *in* Diversity of Carlin-style Gold Deposits, (ed) J. Muntean; Society of Economic Geologists, Reviews in Economic Geology, v. 20. p. 235–256.

Yeo, G.M., 1986. Iron formation in the late Proterozoic Rapitan Group, Yukon and Northwest Territories; *in* Mineral Deposits of the northern Cordillera, (ed.) J.A., Morin; Canadian Institute of Mining and Metallurgy, Special Volume 37, p. 142–153.

Yukon Geological Survey, 2019. Yukon Digital Bedrock Geology. Yukon Geological Survey. <http://data.geology.gov.yk.ca/Compilation/3> [accessed October, 2019]

Neoproterozoic-hosted Carlin-type mineralization in central Yukon, part 2: Mineralization

Nicolas Pinet[1]*, Patrick Sack[2], Patrick Mercier-Langevin[1], William J. Davis[3], Denis Lavoie[1], Omid Haeri-Ardakani[4], Bram A. Komaromi[4], Benoît Dubé[1], Jean S. Cline[5], Duane C. Petts[3], Josué Jautzy[1], Simon E. Jackson[3], Jeanne B. Percival[3], Martine M. Savard[1], and Virginia I. Brake[1]

[1]Geological Survey of Canada, 490 rue de la Couronne, Québec, Quebec G1K 9A9
[2]Yukon Geological Survey, 91807 Alaska Hwy, Whitehorse, Yukon Y1A 5B7
[3]Geological Survey of Canada, 601 Booth Street, Ottawa, Ontario K1A 0E9
[4]Geological Survey of Canada, 3303 33rd Street NW, Calgary, Alberta T2L 2A7
[5]University of Nevada, 4505 South Maryland Parkway, Las Vegas, Nevada 89154-4010
*Corresponding author's e-mail: nicolas.pinet@canada.ca

ABSTRACT

Gold-rich zones in the Nadaleen trend (central Yukon) exhibit several characteristics consistent with Carlin-type mineralization: 1) alteration zones with partial to complete decalcification of mineralized intervals and very fine-grained quartz associated with silicification; 2) the association of gold with certain pathfinder elements (Tl, As, Hg, and Sb) and minerals (realgar, orpiment, and fluorite); 3) the low base metal and Ag content of the mineralized intervals; and 4) the 'invisible' nature of gold, which occurs as rims of Au-bearing arsenian pyrite on pre-ore pyrite and/or as sub-micrometre particles. Mineralization styles vary significantly between intervals and even within an interval, attesting to the 'passive' or 'opportunistic' nature of the mineralizing fluids that exploited a variety of porous and permeable pathways regardless of their sedimentary and/or tectonic origin. Alternating finely laminated limestone and siltstone (Conrad zone) and floatstone intervals (Conrad, Sunrise, and Osiris zones) are the most favourable sedimentary units. Pre-mineralization fractures acted as feeders for selective bed replacement and pre-mineralization vein networks were preferentially dissolved by early acidic fluids and channelized later by gold-bearing fluids. With ongoing research, we hope to better constrain the occurrence of gold at the micron scale, the geochemical variations due to alteration, the temperature of the mineralizing fluids, and the timing of the gold mineralization.

INTRODUCTION

Carlin-type gold systems are the results of a number of critical geological processes acting at lithospheric to mineral scales (Cline et al., 2005; Muntean, 2018). The regional- to prospect-scale setting of Carlin-type gold zones in central Yukon (Nadaleen trend, Fig. 1) has been reviewed by Pinet et al. (2020). These zones are located close to the northern boundary of the Selwyn Basin, a domain characterized by sedimentary rocks deposited in deeper water settings than surrounding domains. The northern boundary of the basin is controlled by the Dawson fault, a long-lived deep-seated structure. In the Nadaleen trend, the sedimentary succession is Neoproterozoic to early Permian and includes fine- to coarse-grained clastic and carbonate rocks. The structural style of the Nadaleen trend is complex; strata generally dip steeper than in classical fold-and-thrust belts and faults include a significant component of strike-slip motion. Carlin-type mineralized zones are mainly hosted in two Neoproterozoic limestone units (informally known as the Conrad and Osiris limestones, and formally referred to as the Nadaleen and Gametrail formations, respectively; Moynihan et al., 2019) and in variably calcareous Paleozoic siltstone. In Neoproterozoic-hosted zones, mineralized intervals are grossly concordant with bedding in complexly shaped anticlines. This contribution complements Pinet et al. (2020) and focuses mainly on Neoproterozoic-hosted mineralized zones at the tens of metres to thin-section scale.

MINERALIZATION

History of Exploration

The Nadaleen trend was discovered in 2010 by ATAC Resources Ltd. during a follow-up investigation of arsenic anomalies detected in a regional stream sediment sampling program conducted by the Geological Survey of Canada (Goodfellow and Lynch, 1978). Subsequent analysis of arsenic in soil was a highly successful exploration tool with all known gold mineralization occurrences being spatially associated with a multi-element soil anomaly.

Pinet, N., Sack, P., Mercier-Langevin, P., Davis, W.J., Lavoie, D., Haeri-Ardakani, O., Komaromi, B.A., Dubé, B., Cline, J.S., Petts, D.C., Jautzy, J., Jackson, S.E., Percival. J.B., Savard, M.M., and Brake, V.I., 2020. Neoproterozoic-hosted Carlin-type mineralization in central Yukon part 2: Mineralization; *in* Targeted Geoscience Initiative 5: Contributions to the Understanding of Canadian Gold Systems, (ed.) P. Mercier-Langevin, C.J.M. Lawley, and S. Castonguay; Geological Survey of Canada, Open File 8712, p. 299–314. https://doi.org/10.4095/326047

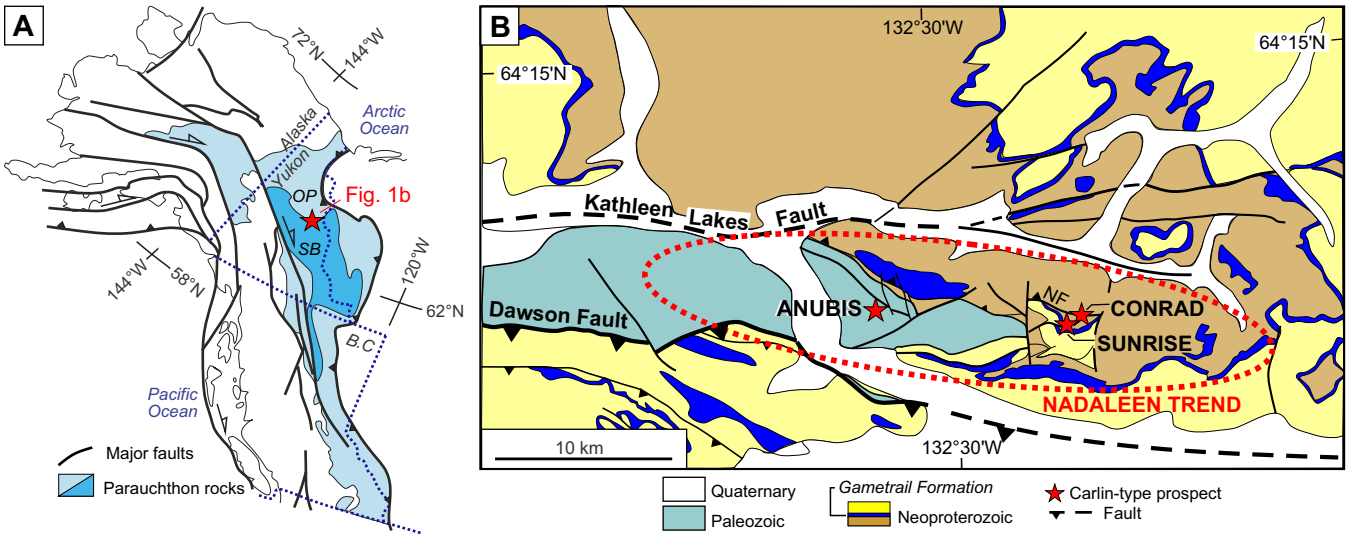

Figure 1. Geological map of the Nadaleen trend (*modified from* Moynihan, 2016). Abbreviations: B.C. = British Columbia, NF = Nadaleen fault, OP = Olgilvie Platform, SB = Selwyn Basin.

Drill targeting of the realgar-rich mineralized zones, which are locally exposed at surface, started in 2010. To date, more than 90 kms of drilling have been completed in five main zones. In June 2018, the first gold resource estimate for the Neoproterozoic-hosted Osiris cluster (Conrad, Ibis, Osiris, and Sunrise zones) was published by ATAC Resources at 8 Mt at 4.1 g/t amenable to open pit mining and 4.3 Mt at 4.52 g/t amenable to underground mining, for a total of about 1.7 Moz (52.3 metric t) (Ristorcelli et al., 2018). All gold-bearing zones have significant potential for additional resources, both along-strike and at depth.

Common Characteristics of Mineralization

Realgar and orpiment±fluorite are generally good visual guides for gold mineralization in Neoproterozoic-hosted Carlin-type mineralized zones. In some cases, realgar is found in calcite veins that clearly postdate the main stage of gold mineralization. However, the spatial association of realgar and orpiment with gold-rich intervals indicates that these minerals formed during the late stage of a single event, not during a later hydrothermal pulse unrelated to gold mineralization (Pinet et al., 2018; Tucker et al. 2018; Pinet and Sack, 2019).

At the macroscopic scale, mineralized zone contacts are generally sharp. Decalcification is the main alteration type associated with gold mineralization and resulted in a significant increase in the porosity of the host rocks. The intensity of decalcification varies strongly, with some decimetre-scale intervals reacting with HCl a few centimetres from totally decalcified mineralized segments. Silicification and argillization are more subtle to document visually, but may be significant alteration styles at the microscopic scale, as described below.

First-Order Lithological and Structural Controls on Mineralization

In the Conrad, Sunrise, and Osiris mineralized zones (Fig. 1), the geometry of the sedimentary units with permeability either higher or lower than the surrounding rocks exerted a first-order control on gold-bearing fluid flow (Pinet and Sack, 2019; Pinet et al., 2020). Figure 2 shows two nearly perpendicular sections of the Conrad zone and illustrates the tight domal geometry of the limestone unit. This geometry constitutes a four-way, dip-closure fold/fault trap for mineralizing fluids (Pinet et al., 2020). The mixed stratigraphic-structural trap is sealed by two low-permeability mudstone/siltstone units: the NONAD mudstone (Ice Brook Formation) that is in fault contact with the Conrad limestone to the north and the Conrad siliciclastic rocks (Nadaleen Formation) that stratigraphically overlie the limestone to the south. These siliciclastic units (including the Nadaleen fault damage zone) acted as prospect-scale aquitards. At the tens of metre scale, some relatively thick (>1 m) massive, and weakly fractured limestone beds also may have acted as discontinuous impermeable barriers. In the Conrad zone, gold mineralized bodies are mainly hosted in three settings (Fig. 3): 1) the steeply dipping upper part of the limestone unit, close to its contact with stratigraphically overlying siliciclastic rocks; 2) in fractured corridors associated with the north-northwest-trending faults, including the 350 and 850 faults; and 3) in the immediate footwall of the Nadaleen fault. Due to the closure of the main host units at the top of the Conrad limestone, and to increased fracture density in the hinge zone, the mineralization envelope is more continuous in map view close to surface (Fig. 3).

In the Sunrise and Osiris zones (Fig. 4), the location of the steeply dipping limestone host unit (Osiris lime-

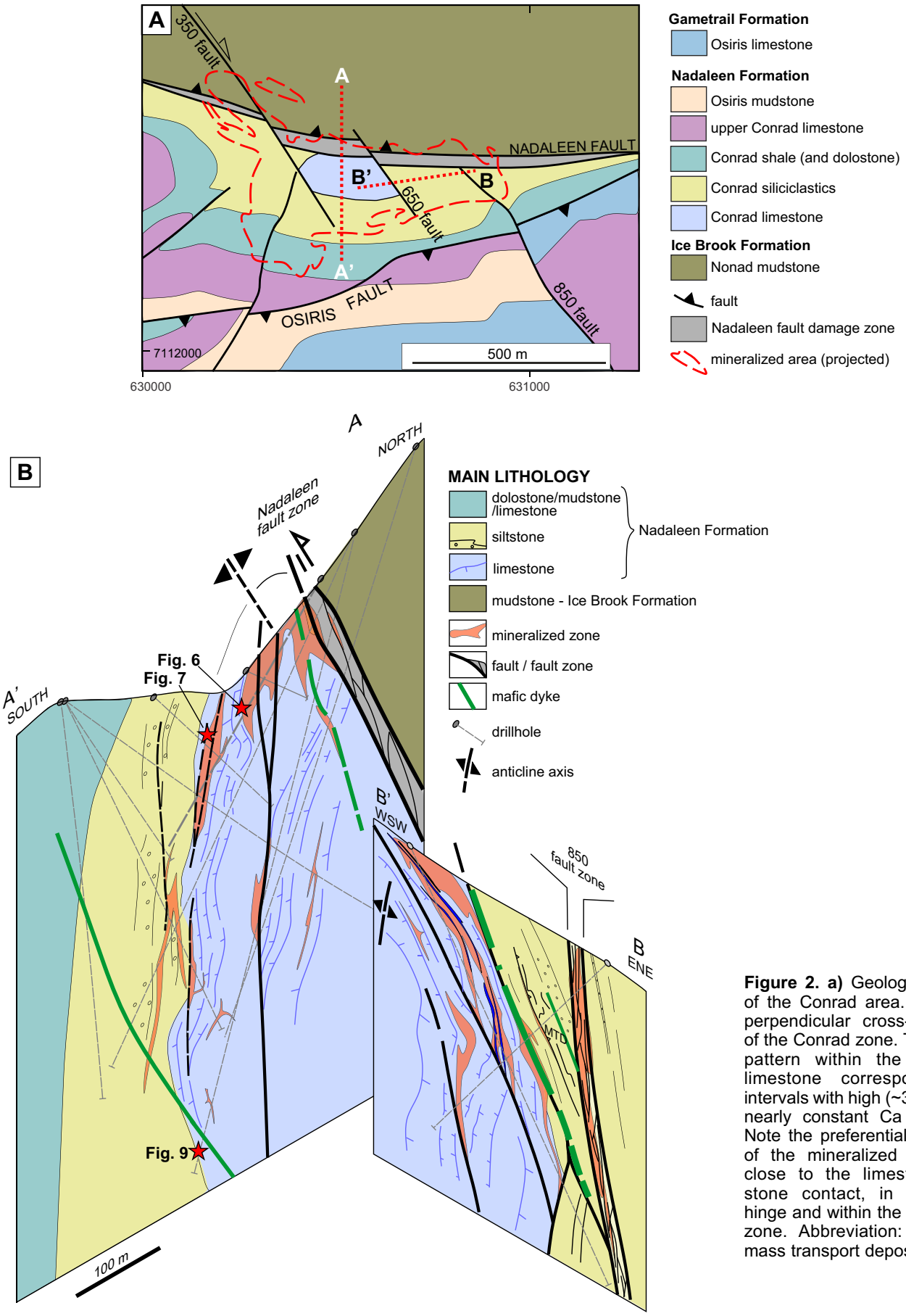

Figure 2. a) Geological map of the Conrad area. **b)** Sub-perpendicular cross-sections of the Conrad zone. The brick pattern within the Conrad limestone corresponds to intervals with high (~34%) and nearly constant Ca content. Note the preferential location of the mineralized intervals close to the limestone-siltstone contact, in the fold hinge and within the 850 fault zone. Abbreviation: MTD = mass transport deposit.

stone of the Gametrail Formation) between low-permeability intervals (Osiris mudstone and Osiris fault zone in the Sunrise area; Osiris mudstone and Osiris dolostone in the Osiris area) is a first-order control on fluid flow. At the scale of tens of metres, the location of the mineralized bodies in the Sunrise and Osiris zones were also controlled by tight, clast-supported rudstone intervals (flat-pebble conglomerate with lime mudstone fragments showing indented and stylolitic relationships) that are found in the Osiris limestone. These rudstone intervals acted as local discontinuous impermeable barriers (Pinet and Sack, 2019).

Second-Order Sedimentological and Structural Controls on Mineralization

Drill core indicates that sedimentological and structural parameters provided second-order controls that resulted in a complex geometry of gold zones and variable mineralization styles and breccia types. As documented in Pinet et al. (2018) and Pinet and Sack (2019), sedimentological and structural controls are not mutually exclusive and multiple mineralization styles are documented in the same interval.

Sedimentological control

At the macroscopic scale, several mineralization styles denote a predominant sedimentological control.

1. *Selective replacement of beds.* This mineralization style is documented in all Neoproterozoic-hosted mineralized zones and is mainly restricted to intervals including millimetre to centimetre thick limestone beds with a granular texture alternating with millimetre thick fine-grained beds (Fig. 5a). Drill core indicates that mineralized beds are connected to feeder veins at high angles to bedding (Fig. 5b). In a few cases, mineralization is confined to mudstone beds bounded by massive limestone beds (Fig. 5c).
2. *Mineralized floatstone (debris flow).* Matrix-supported, monomictic to polymictic, floatstone intervals are the most favourable host-rocks for gold mineralization at the Sunrise and Osiris zones (Fig. 5e,f; Pinet and Sack, 2019). Floatstone-hosted mineralization also represents a significant part of high-grade (>5 g/t Au) intervals in the Conrad zone (Fig. 5d, 6). Clasts are generally calcareous (lime mudstone to packstone with variable colours and laminations), represent between 40 and 90 vol.% of the rock, are angular to subangular, and show no clear preferential orientation, except close to the basal contact. Mineralization is confined to the generally silty matrix and to a few fractures within clasts. Realgar is ubiquitous in mineralized floatstone intervals within the Osiris limestone of the Gametrail Formation (Osiris, Sunrise, and Ibis

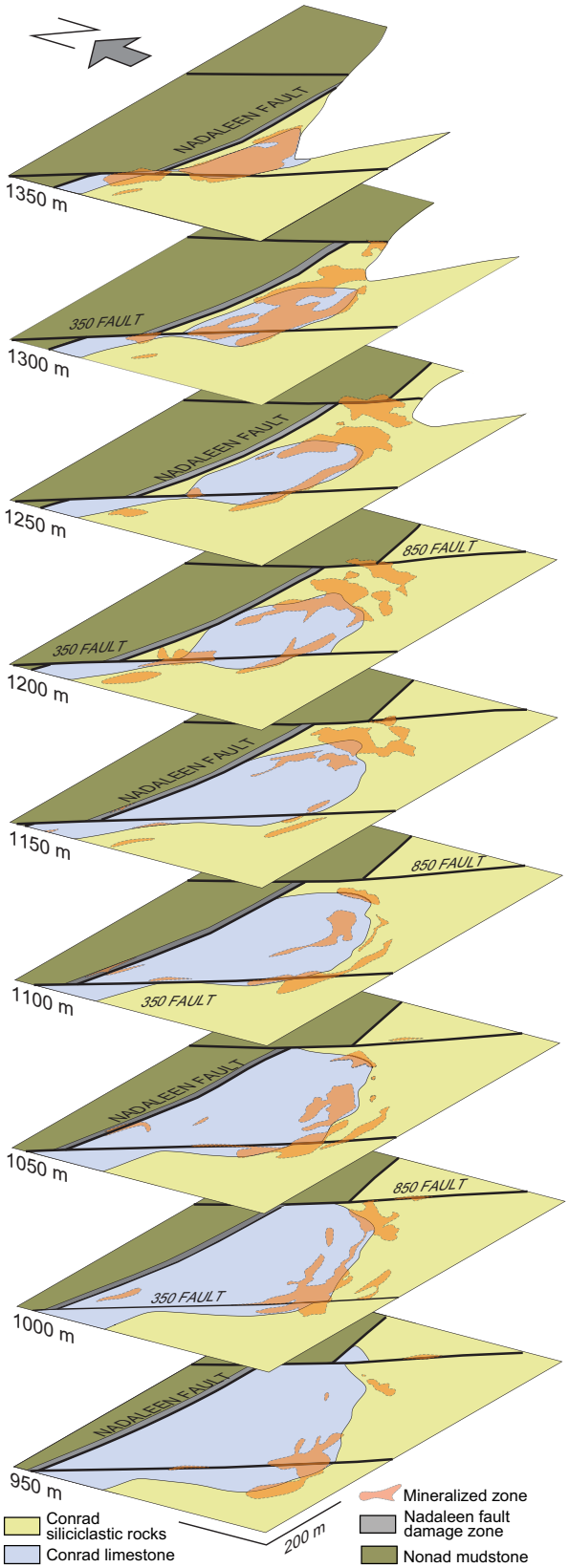

Figure 3. Map views of the Conrad zone showing the location of mineralized zones at several elevations. Same colour scheme as used in Figure 2. Note the preferential location of the mineralized intervals close to the limestone-siltstone contact, in the fold hinge (1300–1350 m elevation), and within/close to the 350 and 850 fault zones.

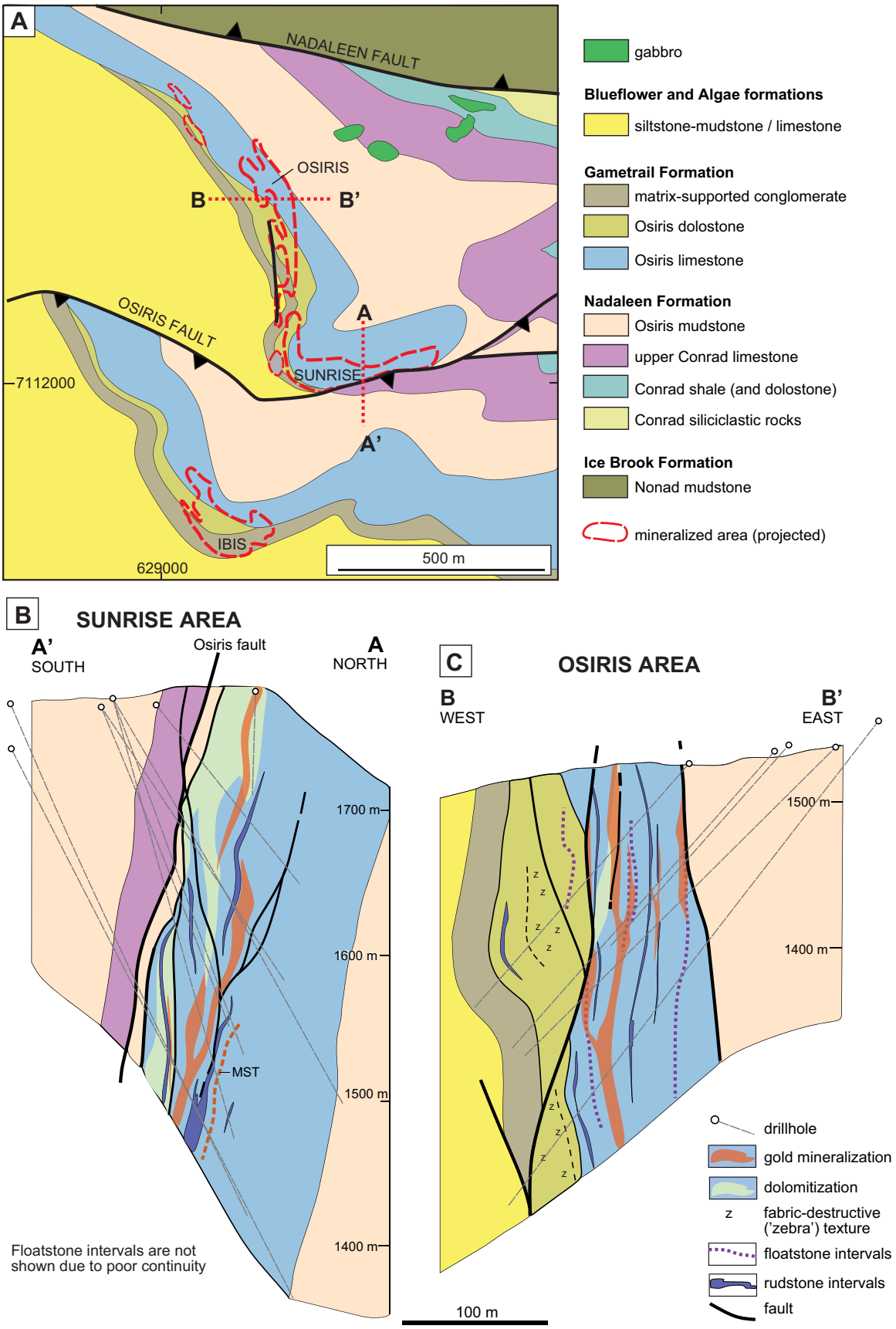

Figure 4. a) Geological map of the Osiris-Sunrise-Ibis area. **b and c)** Cross-sections of the Sunrise and Osiris gold-bearing zones, respectively. Note that mineralized intervals are mostly concordant with bedding. Abbreviation: MST = mudstone.

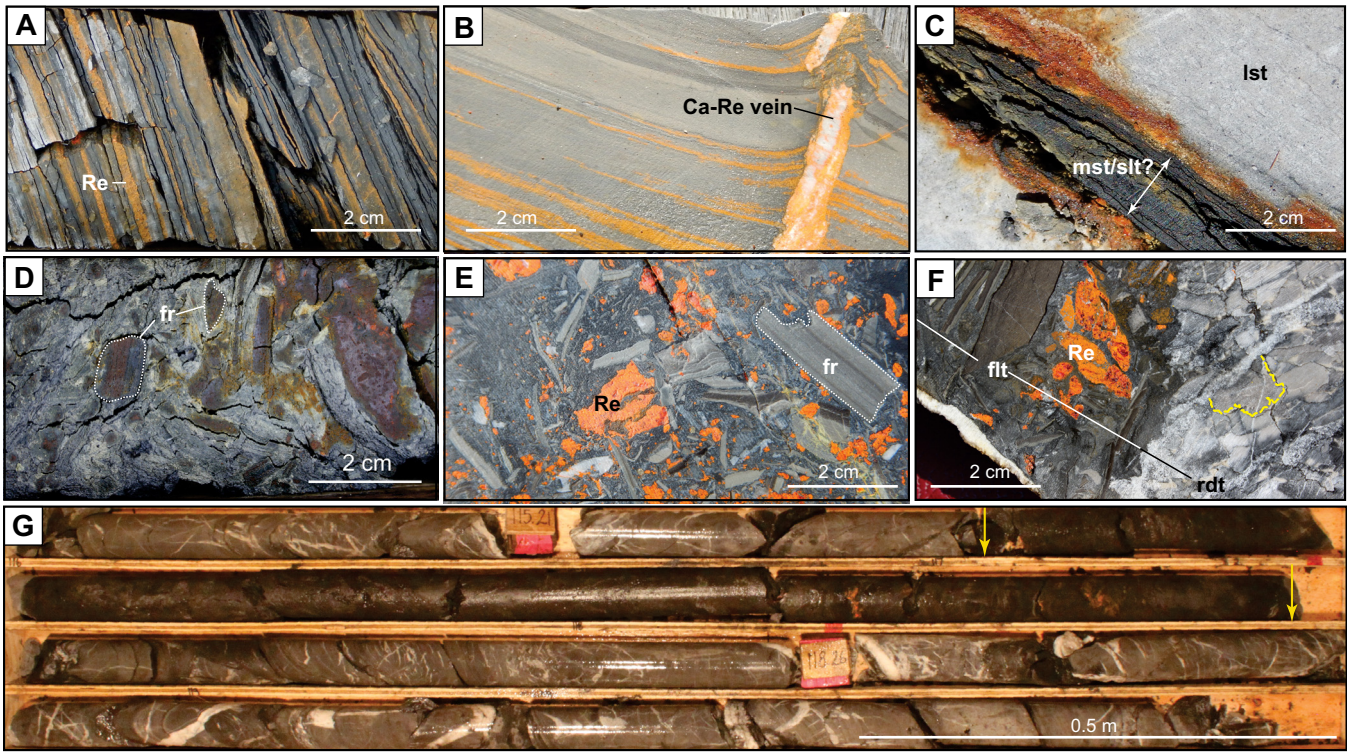

Figure 5. Photographs illustrating the sedimentological control on mineralization. Photographs (a), (b), (d), and (g) are from the Conrad zone. Photographs (b),(e), and (f) are from the Sunrise zone. **a)** Finely laminated limestone showing the selective replacement of 1–5 mm thick beds with realgar (Re). **b)** Selective replacement of 1–4 mm thick beds and bedding-perpendicular calcite-realgar feeder vein (Ca-Re vein). **c)** Mineralized fine-grained bed (originally calcareous mudstone/siltstone?: mst/slt?) bounded by barren thickly bedded massive limestones (lst). **d)** Mineralized floatstone interval with monomictic fragments (fr). **e)** Mineralized floatstone interval with angular fragments (fr) of various orientation. Note that realgar (Re) is found exclusively in the matrix. **f)** Contact between a mineralized matrix-supported floatstone (flt) and a barren clast-supported rudstone (rdt). Note the stylolitic relationship between the fragments (yellow dashed line) in the rudstone. **g)** A 1.82 m thick black, almost featureless decarbonatized interval (between the yellow arrows) yielding 9.88 g/t Au.

zones), but is rarely present within the Conrad limestone of the Nadaleen Formation (Conrad zone).

3. *Dark grey to black mineralized interval.* These decimetre to metre thick decarbonatized intervals (Fig. 5g) are visually featureless with only a few laminations preserved locally. Their boundaries are concordant with bedding and a few irregularly shaped fragments are observed, suggesting that these intervals were originally matrix-rich, floatstone intervals.

In the Conrad zone, all of the mineralization styles described above are developed in the upper part of the limestone unit that hosts a significant portion of the mineralization (Fig. 3). Figure 7 illustrates a high-grade mineralized interval located close to the limestone-siltstone contact that consists of interbedded and thinly bedded, lime mudstone, packstone, floatstone, and calcareous siltstone. In this interval, mineralization styles correspond mainly to the selective replacement of millimetre to centimetre beds and 0.5 to 3 m thick breccia zones with angular fragments. Mineralization along pre-ore tectonic joints and fractures also account for a minor part of the gold-bearing interval. Tectonic features in this interval include bedding-parallel faults that are notably absent in more thickly bedded successions.

Floatstone beds are interpreted to originate from debris flow events in which sediments are supported above the sediment-water interface by matrix strength and buoyancy, which allows larger clasts to float along in a mud-sand matrix (Moscardelli and Wood, 2008). In this interpretation, sedimentary breccias (floatstone) and clast-bearing mud limestone lithofacies (dark grey to black interval) may coexist over a short distance, reflecting different density flow mechanisms or different ratios of carbonate mud, sand and clasts. Intervals with a granular texture (intraclastic packstone) may also belong to 'mass-transport' deposits, as suggested by the presence of small (mm) angular clasts and may represent the upper and/or distal parts of floatstone intervals (Pinet and Sack, 2019).

Structural control

Fracture density and permeability also influenced mineralizing fluid flow. This general statement is substan-

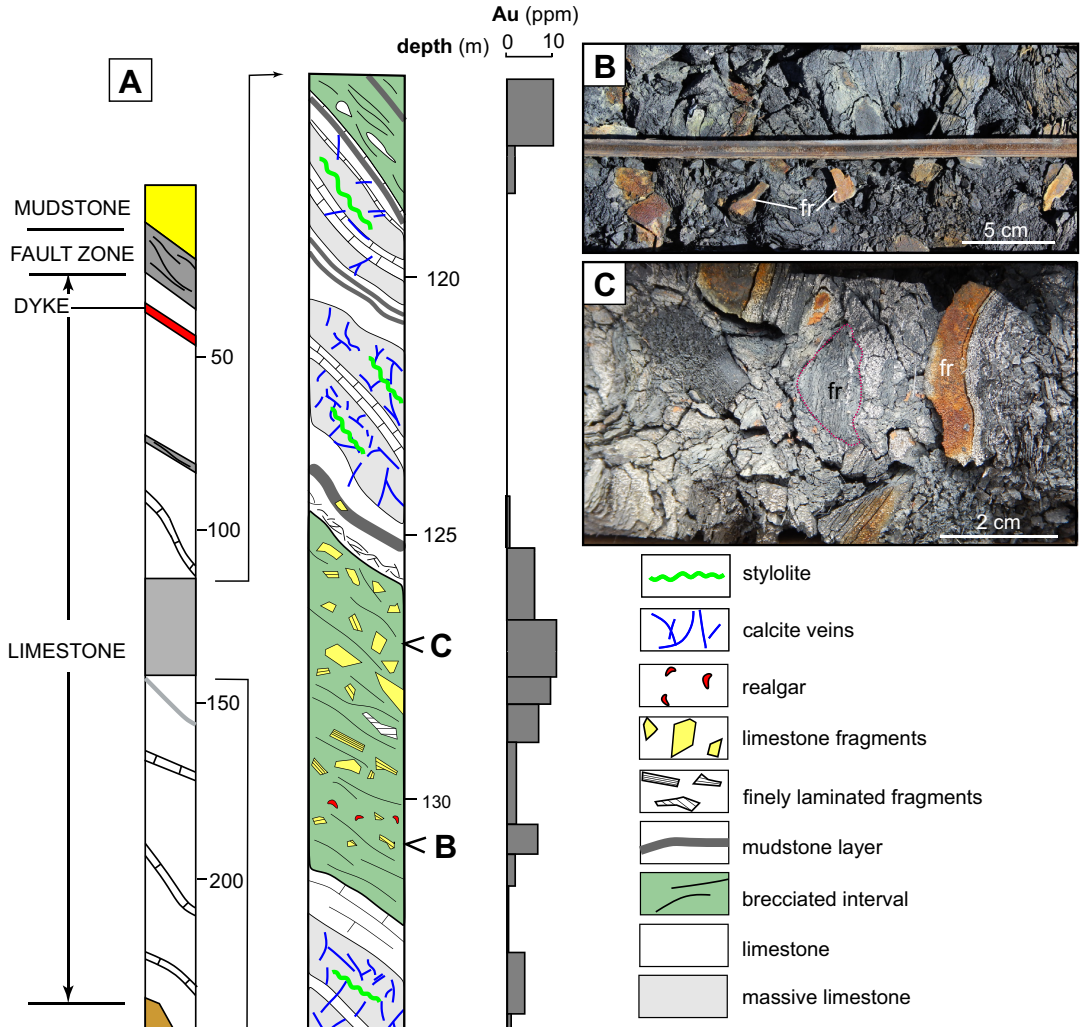

Figure 6. a) Mineralized zone preferentially associated with floatstone intervals formed through debris flows. **b and c)** Representative photographs illustrating the debris flow intervals. Note the polymictic nature of the fragments. Abbreviation: fr = fragment.

tiated by the highest-grade intervals being located in fold hinges with high fracture-density and by the close spatial relationship occurring between fractured rock intervals (i.e. domains with poor rock quality designation, RQD) and gold. Interestingly, intervals above mineralized zones are often characterized by higher than average RQD index values, suggesting that these intervals are less fractured and thus less permeable. Low-permeability domains likely acted as a cap rock for mineralizing fluids. At the tens of metres to hand-sample scales, several types of mineralized structural features can be distinguished.

1. *Mineralized joints.* Among the mineralized structures, some clearly formed as joints under low deviatoric stress, before the main deformation and mineralization events. The joints recorded almost no displacement (tensile-type fractures) and have limited calcite infill. They formed well organized joint sets perpendicular to bedding (Pinet et al., 2020) and contributed to enhance permeability in a way similar to fractured petroleum reservoirs in which there is a clear relationship between the spacing of joints and bed thickness, and in a less pronounced way, between joint spacing and lithology (Rustichelli et al., 2013; Afşar et al., 2014).
2. *Pre-mineralization veins and brecciated intervals.* Pre-mineralization breccias are the most common type of tectonic breccia. At Conrad, the selective replacement of irregular and often complex pre-mineralization vein sets is an important process. Comparison of barren and mineralized samples located a few metres apart (Fig. 8a,b) suggests that calcite between breccia fragments were preferentially dissolved by acidic, early stage mineralizing

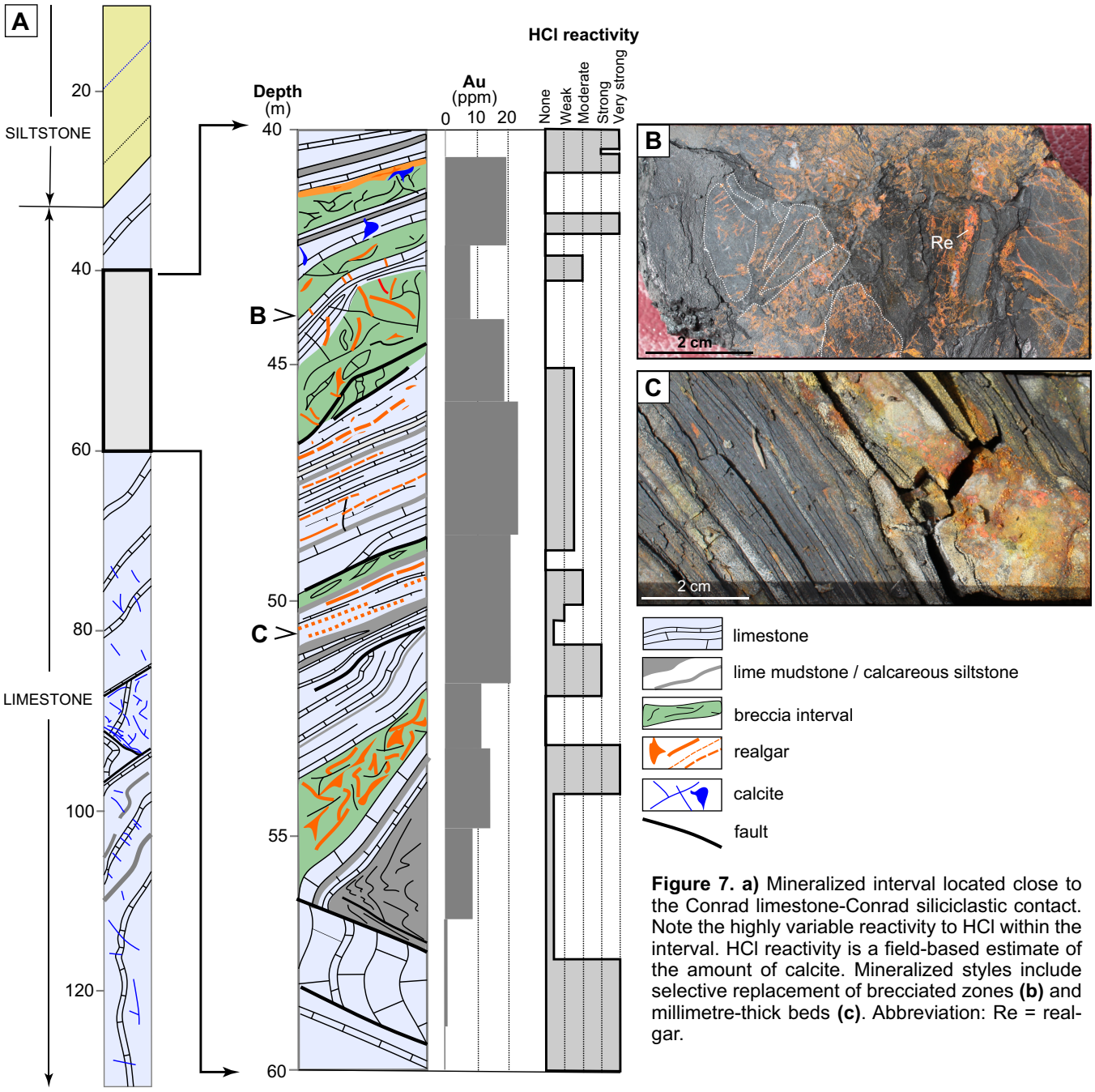

Figure 7. a) Mineralized interval located close to the Conrad limestone-Conrad siliciclastic contact. Note the highly variable reactivity to HCl within the interval. HCl reactivity is a field-based estimate of the amount of calcite. Mineralized styles include selective replacement of brecciated zones **(b)** and millimetre-thick beds **(c)**. Abbreviation: Re = realgar.

fluids, resulting in increased porosity and permeability that focused later gold-bearing fluids. Realgar, orpiment, and fluorite (Fig. 8c) are the most obvious late-mineralization stage minerals in brecciated intervals. Similar to the joints, the amount of pre-mineralization veins and fractures in the pre-mineralization breccia is linked with the structural position (increase in fold hinge zones and fault damaged zones), bed thickness, and lithology (Fig. 8g). Figure 8e and f show an example in which brecciation may be erroneously interpreted as postdating mineralization. In this case, realgar selectively replaces fractures that are mostly confined to the clasts, but closer inspection shows that, in a few cases, realgar-filled veins extend into the matrix, indicating that mineralization postdates fracture and breccia development. Comparison of pre-mineralization breccia intervals within the same drillhole shows a complete transition from barren to realgar-rich gold mineralized rocks (Fig. 8h to j).

3. *Late mineralization stage veins.* Veins associated with the late stage of mineralization are found within and adjacent to (<10 m) gold-bearing intervals. Late mineralization-stage veins are defined by the presence of realgar (±orpiment) and calcite

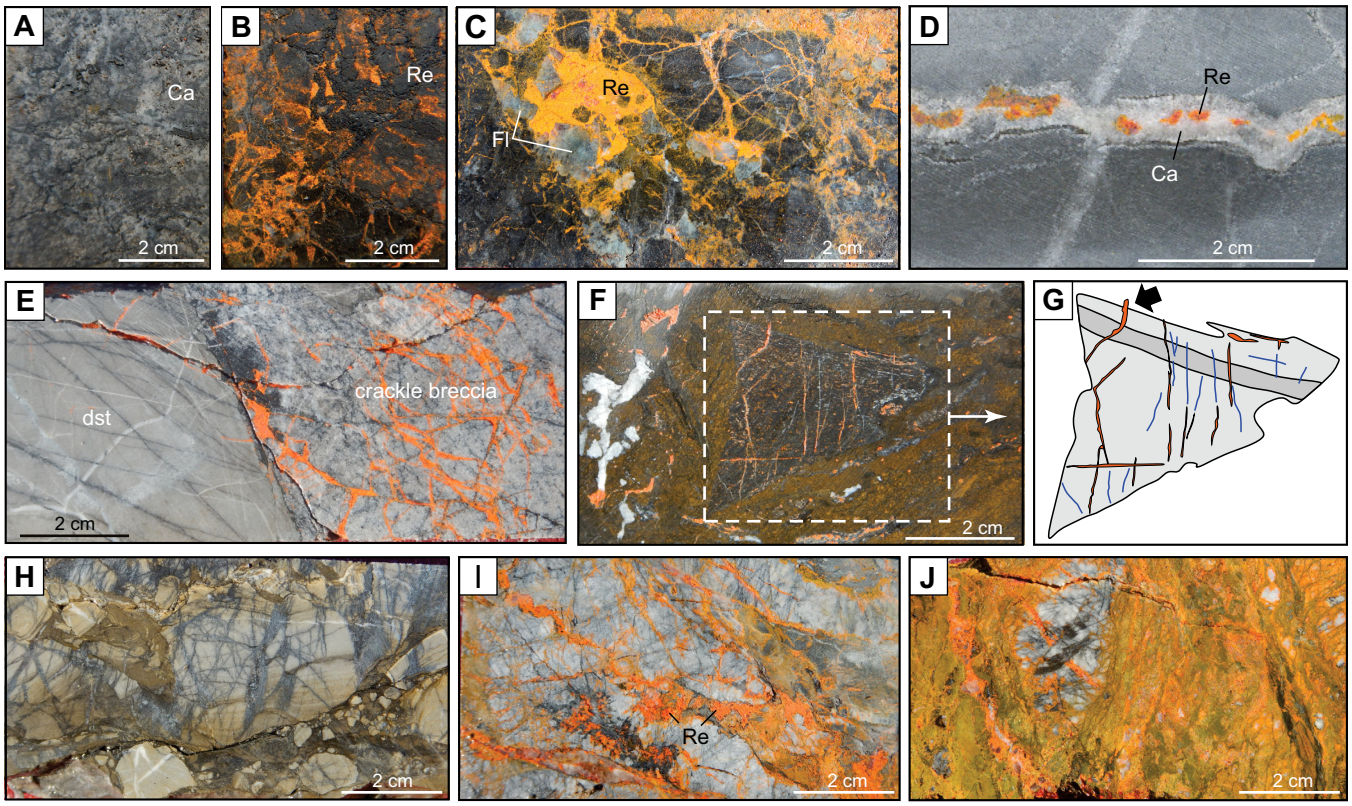

Figure 8. Photographs illustrating the tectonic control on mineralization. Photographs (a) to (f) are from the Conrad zone. Photograph (g) and photographs (h) to (j) are from the Osiris and Sunrise zones, respectively. **a and b)** Comparison of a barren sample (a) and a mineralized sample (b) suggesting that the preferential dissolution of calcite (Ca) between the breccia fragments by early acidic fluids created pathways used by gold-bearing fluids. Abbreviation: Re = realgar **c)** Typical mineralized breccia with fluorite (Fl) and realgar (Re). **d)** Late mineralization calcite (Ca)-realgar (Re) vein crosscutting an earlier calcite vein. **e)** Contact between a massive dolostone bed (dst, left) and a crackle breccia (right). Note that mineralization is almost entirely confined to the crackle breccia. **f and g)** Photograph and interpretation of fractures filled with realgar: most of fractures are confined to a fragment, but one mineralized fracture clearly extends in the matrix (black arrow) indicating that mineralization postdates fragmentation. **h, i, and j)** Photographs of core from within the same drillhole illustrating the transition between barren breccia (h) and realgar (Re)-rich zones in which the pre-existing breccia texture is only locally preserved.

(Fig. 8c). Realgar is found in the central part of the veins or along their margins, suggesting that it both pre- and postdates calcite. The late-stage veins commonly have centimetre-size calcite crystals and, in some cases, a central cavity. In mineralized intervals, these late-stage mineralization veins are visually distinct, but they most likely represent a very small part of the gold endowment. Minor faults cutting calcite-realgar veins attest to some post-veining deformation (Pinet and Sack, 2019).

4. *Hydrothermal breccia.* In some cases, fracture permeability increased during mineralization and fluid pressure was high enough to fracture rock fragments to form cement-supported breccia ('mosaic breccia'). The amount of cement is variable and locally represents more than 50 vol.% of the rock (Fig. 9d). Cement is typically realgar and/or calcite, but orpiment and, to a lesser extent, fluorite also occur. In the example shown on Figure 9, cement-supported hydrothermal breccia is found below one of the mineralized Conrad mafic dykes. In this case, the local increase in fluid pressure was probably due to the aquitard that was formed by the dyke.

5. *Synmineralization fractures and minor faults.* Synmineralization brittle faults, with or without cataclasite and gouge development, locally contributed to the development of pathways for mineralizing fluids. Fault planes with realgar slickenlines attest to such syn- to late-mineralization deformation (Pinet and Sack, 2019).

In Conrad, discontinuous gold zones are associated with steeply dipping, northwest-trending fault corridors. For the 350 fault, the zones are located close to the contact between the Conrad limestone and the Conrad siliciclastic rocks, whereas they are entirely hosted in the Conrad siliciclastic rocks in the case of the 850 fault (Fig. 2b, 3). In the latter case, drill core indicates that some deformation occurred during to post mineralization. Tectonic features also include early brittle structures with poorly constrained timing and it is presently unclear if the mineralizing fluids

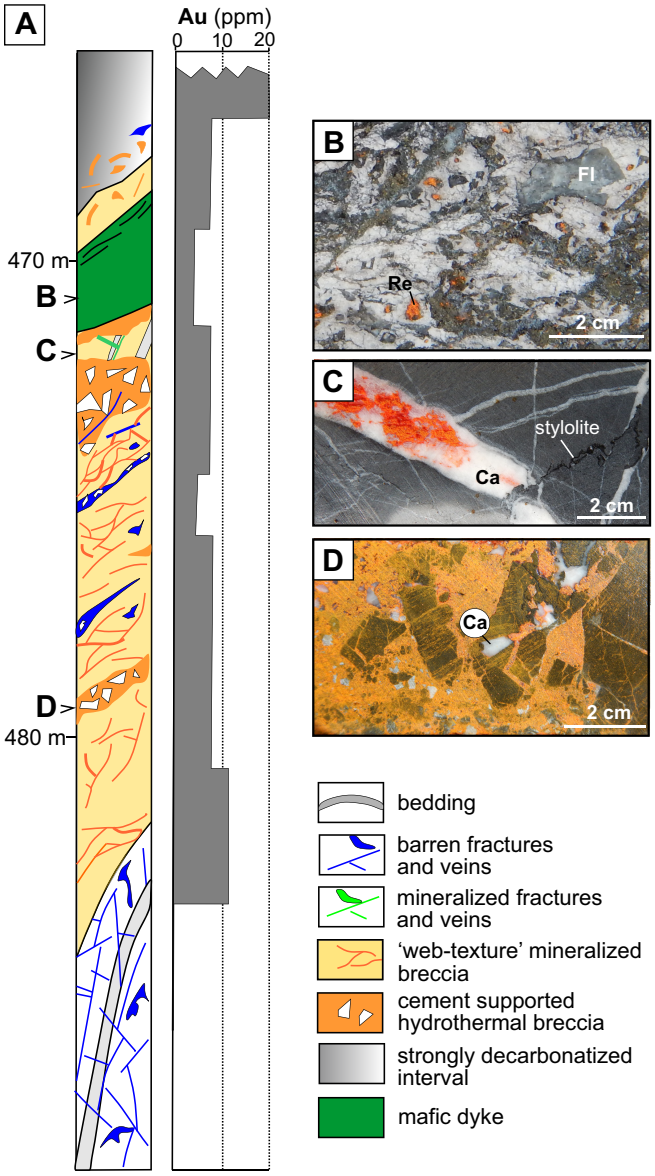

Figure 9. a) Mineralized zone with hydrothermal breccia. Note the location of the hydrothermal breccia below a mafic dyke, which probably acted as a local aquitard and contributed to the increase in the fluid pressure. **b)** Mineralized mafic dyke with realgar (Re) and fluorite (Fl). **c)** Late-stage calcite (Ca)-realgar vein. **d)** Hydrothermal breccia in which the chemical matrix represents approximatively 50 vol.% of the rock. Abbreviation: Ca = calcite.

used a pre-existing pathway or if they circulated in an active deformation corridor.

Variations in mineralization styles and feedback effects between sedimentological and tectonic factors

At the macroscopic scale, gold mineralization styles vary significantly, even in the same mineralized interval. Variations in mineralization styles attest to the opportunistic nature of gold-bearing fluids that exploit permeable pathways, regardless of their origin, including floatstone units and intervals characterized by a network of pre-existing fractures. The factors favouring gold mineralization should not be considered separately as sedimentological and tectonic parameters show feedback effects that have resulted in complex mineralized zone geometries. Figure 10 illustrates some of the feedback effects between sedimentological and tectonic controls: 1) due to their high matrix content, floatstone intervals were frequently used as bedding-parallel décollement; 2) fractures acted as feeder pathways for the selective replacement of beds; 3) pre-mineralization fracturing and veining was intimately linked with bed thickness and lithology; and 4) there is a continuum between tectonic and hydrothermal breccia, the only difference being the presumably higher fluid pressure during formation of hydrothermal breccia.

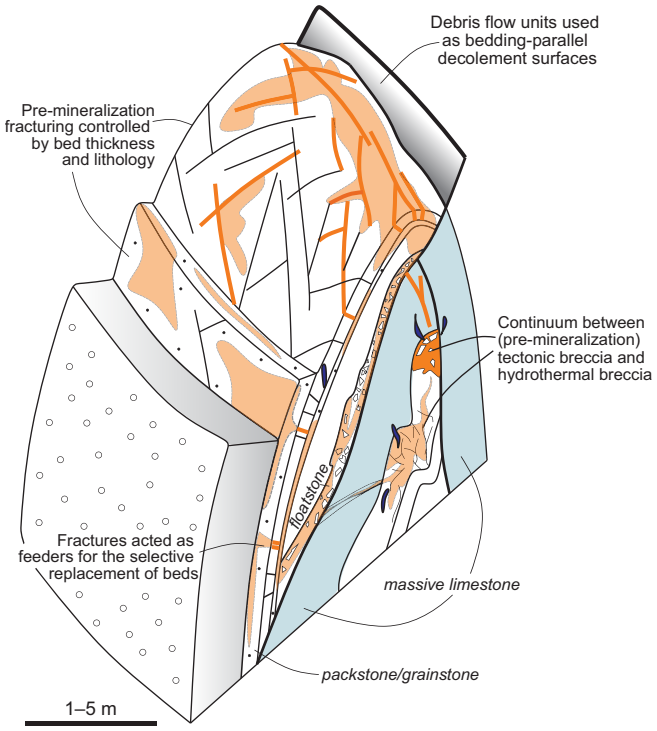

Figure 10. Sketch showing the feedback effects between sedimentological and structural features at the 1 to 5 m scale.

Factors that decrease the permeability also played a major role in focusing mineralizing fluid flow in the Osiris, Sunrise, and Conrad zones. Within the Osiris limestone (Osiris and Sunrise zones), clast-supported rudstone intervals with indented and stylolitic relationships between fragments are never mineralized, even if proximal to gold-bearing intervals (Pinet and Sack, 2019). These discontinuous rudstone intervals acted as impermeable barriers and contributed to the complexity of gold-bearing fluid pathways. A similar interpretation is also valid for thickly (>1 m) bedded limestone intervals at Conrad, which are generally not mineral-

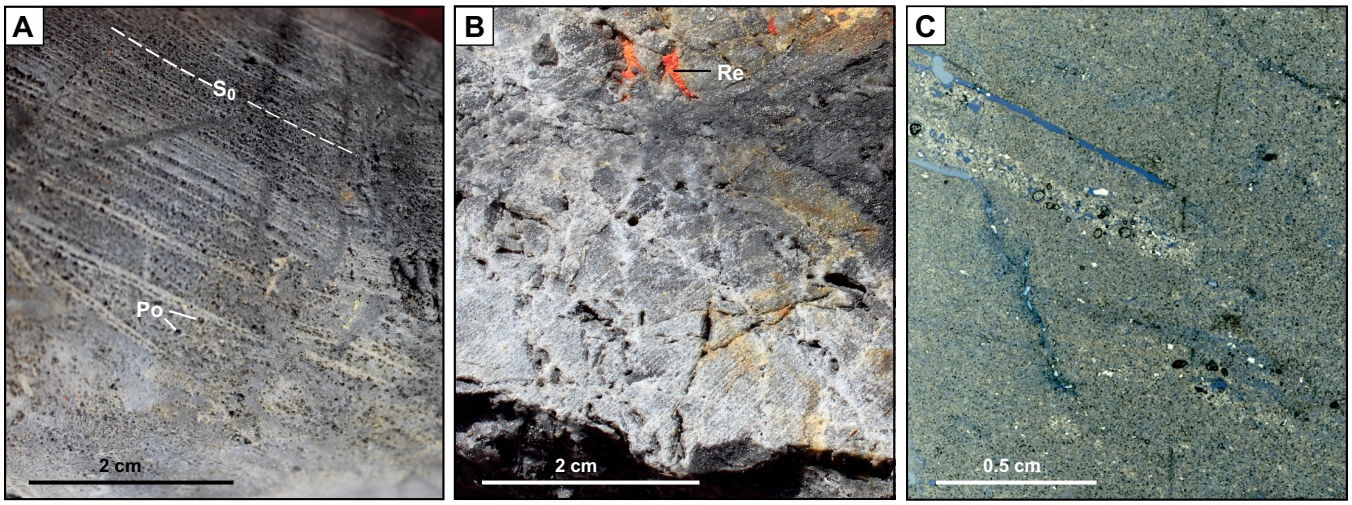

Figure 11. Photographs illustrating the various alteration styles. **a)** Porosity enhancement due to decarbonatization (Sunrise zone). Abbreviations: Po = pore, S_0 = bedding. **b)** Decarbonatization and silicification associated with mineralization (Conrad zone). Abbreviation: Re = realgar. **c)** Thin section showing porosity enhancement due to decarbonatization (Conrad zone). The blue colour corresponds to blue epoxy filling micropores.

ized, even though fractures at high-angle to bedding may have served as by-pass pathways.

Alteration and Gold Mineralization

In the Nadaleen trend, gold deposition resulted from the same processes documented in Nevada (Cline et al., 2005), including an early stage characterized by the dissolution of carbonate, a gold-bearing stage associated with very fine quartz, and a late stage characterized by the deposition of calcite, realgar, orpiment, and fluorite. Alteration associated with gold is restricted to the mineralized zones and immediately surrounding host rocks (generally <1 m).

Within mineralized intervals, decarbonatization (removal of both calcite and dolomite) is the most obvious alteration style. Alteration intensity is highly variable with some decimetre-scale core segments still reacting with HCl a few centimetres from totally decarbonatized core segments (Fig. 7). Decarbonatization is always associated with porosity enhancement. This porosity is sometimes visible at the sample scale (Fig. 11a,b), with some millimetre-wide voids or granular texture and is clear at thin-section scale (Fig. 11c).

Preliminary results of a detailed analysis of Au-bearing arsenian pyrite, here referred to as ore-pyrite, were reported in Sack et al. (2019). Gold-bearing pyrite progressed from early 'blocky' single-stage grains and rims to late 'fuzzy' single-stage grains and rims (Fig. 12). Early, 'blocky' ore-pyrite has low 'Carlin-type' trace element content. Late, 'fuzzy' ore-pyrite has high 'Carlin-type' trace element content. Both types of ore-pyrite are very fine grained. 'Blocky' ore-pyrite has relatively low As and may have precipitated from fluids saturated in Au, with gold partly deposited as nanoparticles. 'Fuzzy' ore-pyrite has higher As content and likely precipitated from an unsaturated fluid with Au incorporated in solid solution. Electron microprobe data suggest that As substitutes for S in both types of ore-pyrite, which is consistent with hydrothermal fluids that were reduced throughout both early and late stages of mineralization. Previous studies have shown that Au and As concentrations decrease in pyrite as temperature of formation increases (Deditius et al., 2014). This retrograde solubility of As (±Au) in ore-pyrite suggests early, 'blocky' pyrite was formed at higher temperatures than late, 'fuzzy' pyrite. Laser-ablation inductively-coupled plasma mass-spectrometry (LA-ICPMS) results show that between 10 and 80% of the gold is contained within very small (<2 µm) single-stage pyrite and the balance is contained in the rims on pre-ore pyrite.

Ore-pyrite is accompanied by variable amounts of silicification through carbonate replacement by fine-grained quartz ('jasperoid'; Lovering, 1972) and very fine quartz lining vugs. Almost all silicified rocks can be scratched, which makes the logging of alteration intensity challenging. No erosion-resistant outcrops of densely silicified rocks (jasperoids) that are locally associated with Carlin-type mineralization in Nevada (Cline et al., 2005) have been found in the Nadaleen trend.

Strong and obvious argillization is rare and reliable estimates of argillization could not be made, even under the microscope, because of their fine grain size and the uncertain genesis of most clay minerals (i.e. hydrothermal or detritic-diagenetic). As mentioned above, realgar, orpiment, and fluorite are ubiquitous in or close to gold-bearing intervals and constitute generally good visual guides for gold mineralization, even if these minerals postdate gold deposition and silicification.

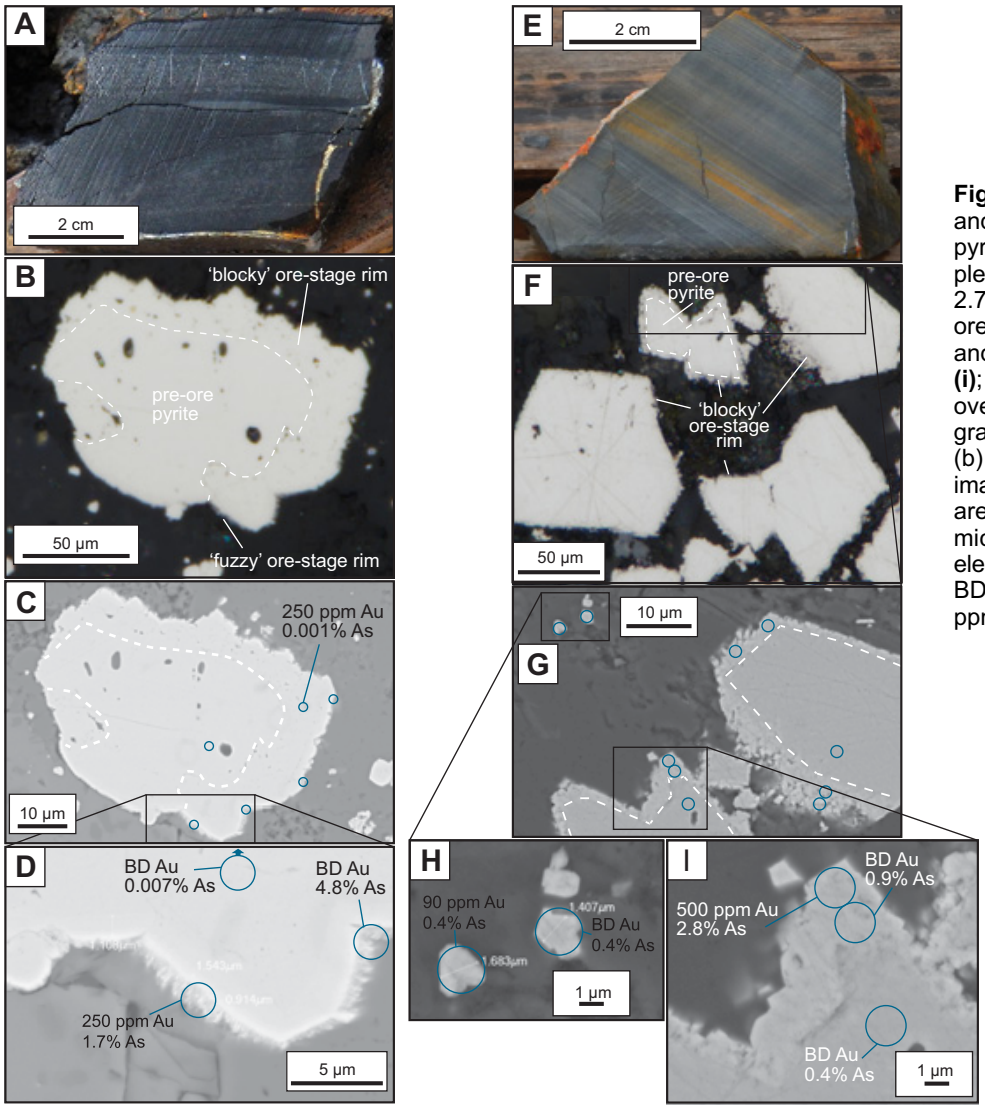

Figure 12. Ore-pyrite from Conrad and Osiris zones. **a to d)** 'Blocky' pyrite with a <1 µm 'fuzzy' rim; sample OS058, 182.8 m (4.5 g/t Au over 2.75 m), Conrad zone. **e to i)** 'Blocky' ore-pyrite as single-stage grains **(h)** and a rim overgrowing pre-ore pyrite **(i)**; sample OS244, 128.0 m (4.9 g/t over 3.04 m), Osiris deposit. Photographs (a) and (e) are of drill core; (b) and (f) are reflected light (50X) images; and (c), (d), (g), (h), and (i) are field emission scanning electron microscope (FE-SEM) backscatter electron (BSE) images. Abbreviation: BD = below detection, which is ~100 ppm Au.

Whole-Rock Geochemistry

The geochemical signature of the gold mineralizing event was investigated using ATAC Resources data. The ATAC Resources database comprises over 29 000 samples assayed for 50 elements, not including Si. The average length of the assayed interval is approximately 3 m. New whole-rock analyses from samples collected along transects from barren rocks to mineralized intervals will be presented in a separate contribution.

Figure 13 presents the correlation coefficients between gold and several elements for the Neoproterozoic-hosted Conrad, Osiris, and Sunrise zones. Thallium, Hg, and As present a high to moderate coefficient of correlation with gold in all three zones. Sulphur and Sb are also positively correlated with gold. Calcium is weakly negatively correlated with gold. However, this weak correlation is mainly due to the original variability of Ca in the host rocks and a clear decrease in Ca content in high-grade (>5 g/t Au) mineralized samples is obvious for the Conrad limestone (Fig. 14; *see* Pinet and Sack, 2019 for a similar plot for the Osiris limestone).

Figure 15 presents the Fe versus S diagram, normalized to Al, the least mobile element (with Ti) among those analyzed. For both the Conrad and Osiris limestone, gold mineralized samples show little or no Fe increase compared to barren samples but a significant enrichment in S. This suggests that S was added to the rock during mineralization but Fe was not, indicating that sulphidation was the dominant process rather than pyritization. Some barren samples have relatively high Fe content, but Fe is probably associated with pre-mineralization ferroan carbonate.

DISCUSSION

Initial Porosity and Permeability Enhancement

In the Nadaleen trend, the preferential occurrence of gold in some sedimentary intervals raises the question of what lithological or alteration features focused fluid flow. In particular, floatstone intervals formed through

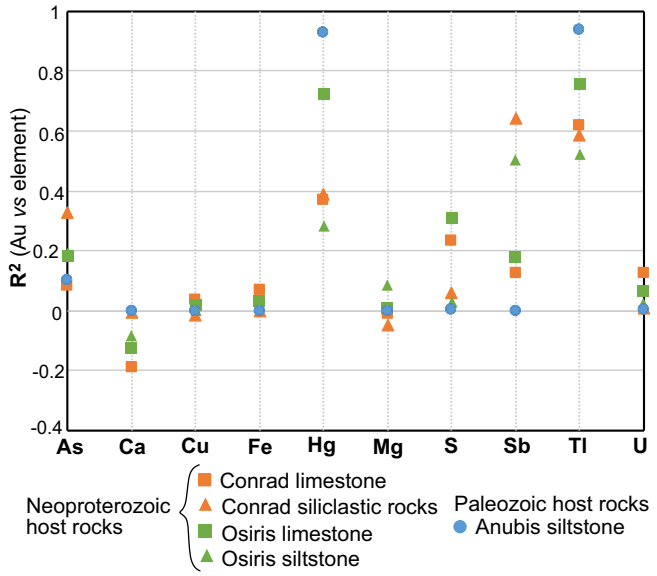

Figure 13. Plot of correlation coefficients between Au and As, Ca, Cu, Fe, Hg, Mg, S, Sb, Tl, and U for several mineralized zones and host rocks. High (>0.5) correlation coefficients are associated with quasi-linear relationships.

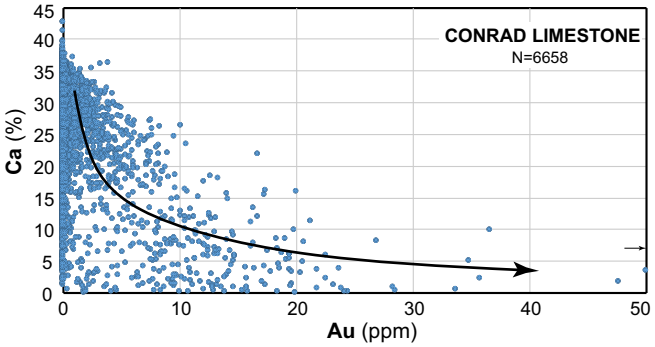

Figure 14. Plot of Au versus Ca for the Conrad limestone showing the decrease in calcium content from decarbonatization as the gold content of samples increases. Samples with low calcium content (Ca <15 wt%) generally indicate intense decarbonatization, however the possibility that the rocks were originally less calcareous than the average rock unit cannot be ruled out.

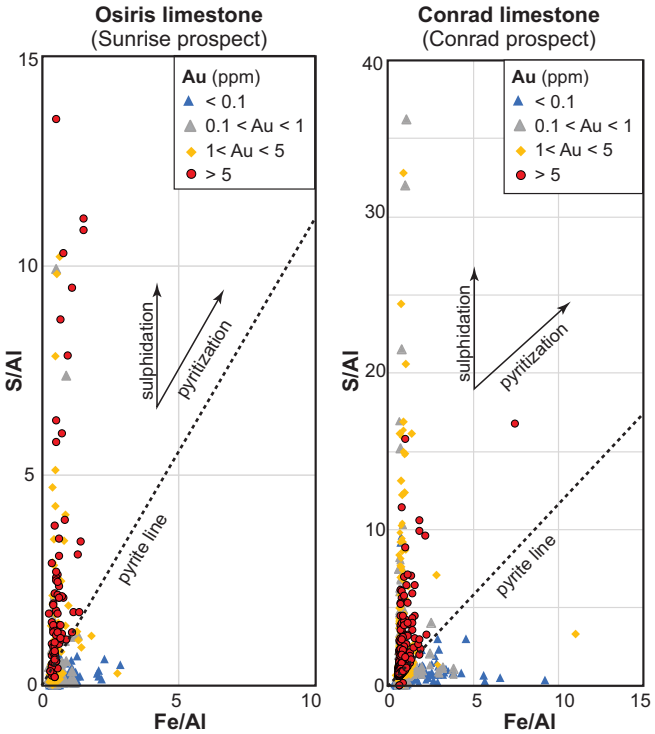

Figure 15. Plots of Fe versus S (normalized with Al) for the Osiris limestone and Conrad limestone. Note that different scales have been used for the two diagrams. In both zones, mineralized samples are characterized by an increase in sulphur.

debris flows are a major host for gold mineralization, suggesting that their original properties contrast with surrounding slope or base-of-slope sedimentary rocks not affected by mass-wasting processes. During debris flow events, clasts 'float' in a mud- to sand-dominated matrix above the sediment-water interface due to matrix strength and buoyancy (Loucks et al., 2010). This results in a slightly higher porosity after mass-wasting compared to the initial, undeformed micrite slope lithofacies. However, the porosity of most carbonate rocks, particularly dominantly mud-rich lithofacies such as those in the Conrad and Osiris limestones, is substantially reduced by early cementation and compaction during burial. Therefore, it seems unlikely that the early (primary) porosity was preserved for >450 Ma between the time of deposition and mineralization. Beaton (2015) proposed that post-depositional dissolution of lime mud and dolomitization of the matrix of the Osiris limestone (Osiris and Sunrise zones) may have contributed to enhance the primary porosity/permeability at the microscale. However, this hypothesis is difficult to consider in the case of the Conrad limestone, which is characterized by sparse and very irregular dolomitization zones at surface and low Mg content (average 0.86 wt%, <2% dolomite if all the Mg is in dolomite). Secondary porosity may also be created through the migration of carbonic acid associated with the generation of carbon dioxide during the maturation of organic matter to hydrocarbon and interaction with subsurface water, but this mechanism remains largely hypothetical in the Nadaleen trend. Whatever the mechanism, hydraulic efficiency of floatstone units was higher than surrounding units during mineralization and was acquired either through the preservation of a secondary porosity or the dissolution of secondary carbonate by early stage acidic hydrothermal fluids.

Pre-mineralization tectonic breccia zones were also probably characterized by a slightly higher fracture permeability than surrounding rocks during the early mineralizing stage. However, in this case, a comparison of barren and mineralized samples suggests that acidic fluids dissolve the calcite infill between fragments more efficiently than the original host rock,

enhancing the original porosity and permeability and making these zones effective pathways for late gold-bearing fluids.

Comparison with Paleozoic Rock-Hosted Gold Mineralization

The tight anticline geometry of the Neoproterozoic-hosted gold zones contrasts with the geometry documented for the Paleozoic-hosted zones (including the Anubis area; Fig. 1). The latter are preferentially located along the west-northwest-trending, north-northeast-dipping Anubis fault zone (Moynihan, 2016). The fault zone has a polyphase history with structural events recording predominantly dip-slip and predominantly strike-slip motions (Pinet, unpublished data). Second-order north-northeast-trending faults cut or merge with the Anubis fault.

Mineralization is hosted in a steeply dipping Devonian-Mississippian siliciclastic unit, close to the fault contact with a Middle Devonian dolostone unit. Mineralized intervals are generally highly fractured and are typically difficult to differentiate from the dark grey to black, moderately to non-calcareous, pyrite-rich siltstone and mudstone. In Anubis, the amount of calcite veins, realgar, and orpiment in or close to mineralized intervals is much lower than in Neoproterozoic-hosted zones. Association of gold mineralization with pathfinder elements classically associated with Carlin-type mineralization is also present in Paleozoic-hosted zones, even if some differences with Neoproterozoic zones exist (Fig. 13; absence of correlation with S and Sb, higher correlations with Hg and Tl).

In the absence of temporal constraints on the gold mineralizing event and detailed characterization of mineralizing fluids, Paleozoic gold-bearing zones are tentatively interpreted as a structural end-member (Teal and Jackson, 2002) of Carlin-type mineralization in the Nadaleen trend.

IMPLICATIONS FOR EXPLORATION

Classification of deposit types must be pragmatic and criteria used for defining the specific characteristics of each type should be factual, not interpretative. With this general statement in mind, gold mineralization in the eastern Rackla belt can be classified as a 'true' Carlin-type example.

The characteristics consistent with Carlin-type mineralization include the following: 1) host-sedimentary rocks deposited in slope to base-of-slope settings (Moynihan et al., 2019; Pinet et al., 2020); 2) ore-forming events that significantly post-date the ages of the host rocks (Tucker et al., 2018; Davis et al., 2019); 3) the 'passive' or 'opportunistic' nature of the mineralizing fluids that exploited a variety of porous and permeable pathways regardless of their sedimentary and/or tectonic origin (Pinet and Sack, 2019); 4) alteration that includes partial to complete decalcification of mineralized intervals, and very fine-grained quartz associated with silicification (Tucker et al., 2018); 5) the association of gold with pathfinder elements Tl, As, Hg and Sb, and with minerals such as realgar, orpiment and fluorite (even if the amount of realgar and orpiment is greater than most Carlin-type deposits of Nevada); 6) the low base metal and Ag content of the gold-bearing zones; and 7) the 'invisible' nature of gold, which occurs as rims of Au-bearing arsenian pyrite on pre-ore pyrite or as sub-micrometre particles (Sack et al., 2019).

The classification of Nadaleen gold mineralized zones as 'true' Carlin-type mineralized zones should not mask the need to refine interpretative models at the upper-crustal to lithospheric scales, which is the aim of ongoing work in the study area.

ONGOING WORK

A better understanding of gold prospects in central Yukon can be achieved only with better geochronological constraints for the age(s) of mineralization. A first step toward this objective was achieved with in situ U-Pb dating on late-stage calcite performed at the Geological Survey of Canada (Ottawa). Preliminary results reported in Davis et al. (2019) show that the U-Pb data from the calcite vein samples exhibit variable degrees of complexity. U-Pb data from three Conrad samples define Tera-Wasserburg intercept ages of between 75 and 72 Ma with relatively simple systematics. Two samples, one from the Osiris zone and one from the Sunrise zone, exhibit complex U-Pb systematics and the dispersion of ages is interpreted to reflect several hydrothermal events, including one at ca. 73 Ma and one or several younger events. The relationship between these hydrothermal pulses and gold mineralization is still under investigation. Ongoing research, including additional U-Pb calcite dating, will provide a tighter control on the age of the gold-mineralizing event and a sound basis to address a number of scientific questions: Is the Carlin-type mineralization event distinct from other metallogenic events documented in the Cordillera? Are other types of mineralization formed contemporaneously? Does the age of mineralization correspond to a change in the magmatic and/or tectonic setting?

Several geochemical methods were used for the characterization of various aspects of the mineralization and results will be reported in future contributions. Geochemical variations due to alteration are investigated through whole rock geochemistry of drillhole samples selected from visually unaltered rocks to

altered mineralized zones. The mineralogical content of a few samples was studied through X-ray diffraction to quantitatively study the fine-grained material that may be difficult to characterize with other methods. Hydrothermal fluids and their interaction with host rocks are also being investigated through stable isotope ($\delta^{13}C$ and $\delta^{18}O$) analyses of calcite from several generations of cement and veins, including calcite from late-mineralization veins.

The temperature of mineralizing fluids is being investigated through a fluid inclusion study and clumped isotopes analyses. Fluid inclusion characterization focusses on calcite and fluorite crystals associated with the late-mineralization event. Carbonate clumped-isotopes analysis is a relatively new method with good potential for contributing to hydrothermal fluid characterization (Ghosh et al., 2006). Importantly, thermometry using carbonate clumped-isotopes does not require knowing the isotopic signal of parent water to estimate the precipitation temperature. Analyses were acquired on calcite at the Delta-Lab facility (GSC Quebec) using a Thermo Fisher MAT253 IRMS coupled to a modified KIEL IV carbonate device. To obtain the most precise estimation of the formation temperature of calcite relevant to hydrothermal contexts, the temperature frame was extended to 250°C. This development benefitted from the acquisition of a pressure- and temperature- (T) controlled set-up allowing calcite to be precipitated at high T, linking T to the clumped-isotopic results (Δ_{47} in ‰). An exploratory organic matter study has also been carried out and included Rock-Eval analyses and organic petrography of a few samples to characterize the amount and type of organic matter in dark shale, to investigate the eventual role of organic matter/hydrocarbon in the mineralization processes as well as to qualitatively evaluate the maximum paleo-temperature experienced by the samples.

ACKNOWLEDGMENT

This study is dedicated to Julia Lane who provided tremendous support and scientific inputs. This report beneficiated from discussions with Adam Coulter, and careful analyses were done at the GSC-Quebec, GSC-Calgary, GSC-Ottawa, and University of Nevada laboratories. J. Muntean, C. Lawley, and R. Carne are acknowledged for constructive reviews.

REFERENCES

Afşar, F., Westphal, H., and Philipp, S.L., 2014. How facies and diagenesis affect fracturing of limestone beds and reservoir permeability in limestone-marl alternations; Marine and Petroleum Geology, v. 57, p. 418–432.

Beaton, N.I., 2015. Diagenetic controls on hydrothermal fluid flow in the Osiris, Isis and Isis East Carlin-type showings, Nadaleen Trend, Yukon; M.Sc. thesis, University of Alberta, Edmonton, 180 p.

Cline J.S., Hofstra A., H., Muntean J.L., Tosdal R.M., and Hickey K.A., 2005. Carlin-type gold deposits in Nevada: critical geologic characteristics and viable models; *in* Economic Geology 100th Anniversary volume (1905-2005), (ed.) J.W. Hedenquist, J.F.H. Thompson, R.J. Goldfarb, and J.P Richards; Society of Economic Geologist, p. 541–484.

Davis, W.J., Pinet, N., Petts, D.C., Jackson, S.J., and Mercier-Langevin, P., 2019. U-Pb ages of hydrothermal calcite associated with Carlin-type mineralization, Nadaleen trend, north-central Yukon. Abstract, Geological Association of Canada Annual Meeting. p. 77.

Deditius, A.P., Reich, M., Kesler, S.E., Utsunomiya, S., Chryssoulis, S.L., Walshe, J., and Ewing, R.C., 2014. The coupled geochemistry of Au and As in pyrite from hydrothermal ore deposits; Geochimica et Cosmochimica Acta, v. 140, p. 644–670.

Ghosh, P., Adkins, J., Affek, H., Balta, B., Guo, W., Schauble, E., Schrag, D., and Eiler, J., 2006. ^{13}C-^{18}O bonds in carbonate minerals: A new kind of paleothermometer; Geochimica et Cosmochimica Acta, v. 70, p. 1439–1456

Goodfellow W.D. and Lynch, J.J., 1978. Regional stream sediment and water geochemical reconnaissance data, central Yukon Territory (NTS 106D and parts of 106C, E and F); Geological Survey of Canada, Open File 518, 424 p. (15 sheets).

Loucks, R.G., Kerans, C., Janson, X., and Rajano, M.A.M, 2010. Lithofacies analysis and stratigraphic architecture of a deep-water carbonate debris apron: Lower Cretaceous (Latest Aptian to Latest Albian) Tamabra Formation, Poza Rica field area, Mexico; *in* Mass-Transport Deposits in Deepwater Settings, (ed.) C. Shipp, P. Weimer, and H.W. Posamentier; Society for Sedimentary Geology, Special Publication 95, p. 3367–390.

Lovering, T.G., 1972. Jasperoid in the United States—its characteristics origin and economic significance; U.S. Geological Survey, Professional Paper 710, 164 p.

Moscardelli, L. and Wood, L., 2008. New classification system for mass-transport complexes in offshore Trinidad; Basin Research, v. 20, p. 73–98.

Moynihan D., 2016. Bedrock geology compilation of the eastern Rackla Belt, NTS 105N/15, 105N/16, 105O/13, 106B/4, 106C/1, 106C/2, east-central Yukon; Yukon Geological Survey, Open File 2016-2, 1:75:000 scale.

Moynihan, D., Strauss, J.V., Padget, C.D., and Nelson, L.L., 2019. Upper Windermere Supergroup and the transition from rifting to continent-margin sedimentation, Nadaleen River area, northern Canadian Cordillera; Geological Society of America Bulletin, v. 131, p. 1673–1701.

Muntean, J.L., 2018. The Carlin gold system: Applications to exploration in Nevada and beyond; *in* Diversity of Carlin-Style Gold Deposits, (ed.) J. Muntean; Society of Economic Geologists, Reviews in Economic Geology, v. 20, p. 39–88.

Pinet, N., Sack, P., Mercier-Langevin, P., Lavoie, D., Dubé, B., Lane, J., and Brake, V., 2018. Breccia styles and controls on carbonate replacement-type ('Carlin-type') gold zones, Rackla belt, east-central Yukon; *in* Targetted Geoscience Initiative: 2017 Report of Activities, Volume 1, (ed) N. Rogers; Geological Survey of Canada, Open File 8358, p. 136–168.

Pinet, N. and Sack, P., 2019. Macroscopic control on Carlin-type gold mineralization in north-central Yukon; *in* Targeted Geoscience Initiative: 2018 Report of Activities, (ed.) N. Rogers; Geological Survey of Canada, Open File 8549, p. 89–103.

Pinet, N., Sack, P., Mercier-Langevin, P., Colpron, M., Lavoie, D., Dubé, B., and Brake, V.I., 2020. Neoproterozoic-hosted Carlin-type mineralization in central Yukon, part 1: Regional- to

prospect-scale geological controls; *in* Targeted Geoscience Initiative 5: Contributions to the Understanding of Canadian Gold Systems, (ed.) P. Mercier-Langevin, C.J.M. Lawley, and S. Castonguay; Geological Survey of Canada, Open File 8712, p. 281–297. doi:10.4095/326045

Ristorcelli, S., Ronning, P., Martin, C., and Christensen, O., 2018. Technical report and estimate of mineral resources for the Osiris project, Yukon, Canada; Technical report submitted to ATAC Resources Ltd.

Rustichelli, A., Agosta, F., Tondi, E., and Spina, V., 2013. Spacing and distribution of bed-perpendicular joints throughout layered, shallow-marine carbonates (Granada Basin, southern Spain); Tectonophysics, v. 582, p. 188–204.

Sack, P., Cline, J., Ren, M., Petts, D., and Pinet, N., 2019. Gold bearing pyrite in Carlin-type gold prospects of the Nadaleen trend, Yukon; Abstract, Geological Association of Canada, Annual Meeting. p. 169.

Teal, L. and Jackson, M., 2002. Geologic overview of the Carlin Trend gold deposits; *in* Gold Deposits of the Carlin Trend, (ed.) T.B. Thompson, L. Teal, and R.O. Meeuwig; Nevada Bureau of Mines and Geology, Bulletin 111, p. 9–19.

Tucker, M.J., Lane, J.C., and Hart, C.J.R., 2018. Overview of Carlin-type prospects of the Nadaleen trend: a Yukon analogue to Carlin-type gold mineralization of the Great Basin; *in* Diversity of Carlin-style gold deposits, (ed.) J.L. Muntean; Society of Economic Geologists, Reviews in Economic Geology, v. 20., p. 235–256.

Appendix 1
Peer-reviewed journal publications related to the TGI-4/TGI-5 gold projects (2015–2020)

Caté, A., Schetselaar, E., Mercier-Langevin, P., and Ross, P.-S., 2018. Classification of lithostratigraphic and alteration units from drillhole lithogeochemical data using machine learning: a case study from the Lalor volcanogenic massive sulphide deposit, Snow Lake, Manitoba, Canada; Journal of Geochemical Exploration, v. 188, p. 216–228. doi:10.1016/j.gexplo.2018.01.019

De Souza, S., Dubé, B., McNicoll, V., Dupuis, C., Mercier-Langevin, P., Creaser, R.A., and Kjarsgaard, I., 2017. Geology and Hydrothermal Alteration of the World-Class Canadian Malartic Gold Deposit: Genesis of an Archean Stockwork-Disseminated Gold Deposit in the Abitibi Greenstoone Belt; *in* Archean Base and Precious Metal Deposits, southern Abitibi Greenstone Belt, Canada, (ed.) T. Monecke, P. Mercier-Langevin, and B. Dubé; Reviews in Economic Geology, v. 19, p. 263–291.

De Souza, S., Dubé, B., Mercier-Langevin, P., McNicoll, V., Dupuis, C., and Kjarsgaard, I., 2019. Hydrothermal alteration mineralogy and geochemistry of the Archean world-class Canadian Malartic disseminated-stockwork gold deposit, southern Abitibi greenstone belt, Quebec, Canada; Economic Geology, v. 114, p. 1057–1094. doi: 10.5382/econgeo.4674

Debreil, J.-A., Ross, P.-S., and Mercier-Langevin, P., 2018. The Matagami district, Abitibi greenstone belt, Canada: Volcanic controls on Archean volcanogenic massive sulfide deposits associated with voluminous felsic volcanism; Economic Geology, v. 113, p. 891–910. doi:10.5382/econgeo.2018.4575

Dubé, B., Mercier-Langevin, P., Ayer, J., Atkinson, B., and Monecke, T., 2017. Orogenic Greenstone-Hosted Quartz-Carbonate Gold Deposits of the Timmins-Porcupine Camp; *in* Archean Base and Precious Metal Deposits, southern Abitibi Greenstone Belt, Canada, (ed.) T. Monecke, P. Mercier-Langevin, and B. Dubé; Reviews in Economic Geology, v. 19, p. 51–79.

Dubosq, R., Lawley, C.J.M., Rogowitz, A., Schneider, D.A., and Jackson, S., 2018. Pyrite deformation and connections to gold mobility: Insight from micro-structural analysis and trace element mapping; Lithos, v. 310-311, p. 86–104. doi:/10.1016/j.lithos.2018.03.024

Dubosq, R., Schneider, D.A., Camacho, A., and Lawley, C.J.M., 2019. Geochemical and geochronological discrimination of biotite types at the Detour Lake Gold Deposit, Canada; Minerals, v. 9., 22 p. doi:10.3390/min9100596

Harmon, R.S., Lawley, C.J.M., Watts, J., Harraden, C.L., Somers, A.M., and Hark, R.R., 2019. Laser-induced breakdown spectroscopy - an emerging analytical tool for mineral exploration; Minerals, v. 9., 45 p. doi:10.3390/min9120718

Lawley, C.J.M., 2016. Compositional symmetry between Earth's crustal building blocks; Geochemical Perspectives Letters, v. 2, p. 117–126. doi:10.7185/geochemlet.1612

Lawley, C.J.M., Creaser, R.A., Jackson, S., Yang, Z., Davis, B., Pehrsson, S., Dubé, B., Mercier-Langevin, P., and Vaillancourt, D., 2015. Unraveling the Western Churchill Province Paleoproterozoic gold metallotect: constraints from Re-Os arsenopyrite and U-Pb xenotime geochronology and LA-ICP-MS arsenopyrite trace element chemistry at the BIF-hosted Meliadine gold district, Nunavut, Canada; Economic Geology, v. 110, p. 1425–1454. doi:10.2113/econgeo.110.6.1425

Lawley, C.J.M., Dubé, B., Mercier-Langevin, P., Kjarsgaard, B., Knight, R., and Vaillancourt, D., 2015. Defining and mapping hydrothermal footprints at the BIF-hosted Meliadine gold district, Nunavut, Canada; Journal of Geochemical Exploration, v. 155, p. 33–55. doi:10.1016/j.gexplo.2015.04.001

Lawley, C.J.M., McNicoll, V., Sandeman, H., Pehrsson, S., Simard, M., Castonguay, S., Mercier-Langevin, P., and Dubé, B., 2016. Age and geological setting of the Rankin Inlet greenstone belt and its relationship to the gold endowment of the Meliadine gold district, Nunavut, Canada; Precambrian Research, v. 275, p. 471–495. doi:10.1016/j.precamres.2016.01.008

Lawley, C.J.M., Jackson, S., Yang, Z., Davis, W., and Eglington, B., 2017. Tracing the transition of gold from source to sponge to sink; Economic Geology, v. 112, p. 169–183. doi:10.2113/econgeo.112.1.169

Lawley, C.J.M., Kjarsgaard, B., Jackson, S.E, Yang, Z., Petts, D. and Roots, E., 2018. Trace metal element and isotopic depth profiles through the Abitibi cratonic mantle; Lithos, v. 314-315, p. 520–533. doi:10.1016/j.lithos.2018.06.026

Lawley, C.J.M., Petts, D.C., Jackson, S.E., Zagorevski, A., Pearson, D.G., Kjarsgaard, B.A., Savard, D., and Tschihart, V., 2019. Precious metal mobility during serpentinization and breakdown of base metal sulphide; Lithos. doi:10.1016/j.lithos.2019.105278

Appendix 1: Peer-reviewed journal publications related to the TGI-4/TGI-5 gold system projects (2015–2020); *in* Targeted Geoscience Initiative 5: Contributions to the Understanding of Canadian Gold Systems, (ed.) P. Mercier-Langevin, C.J.M. Lawley, and S. Castonguay; Geological Survey of Canada, Open File 8712, p. 315–316.

Lawley, C.J.M., Pearson, D.G., Waterton, P., Zagorevski, A., Bédard, J.H., Jackson, S.E., Petts, D.C., Kjarsgaard, B.A., Zhang, S., and Wright, D., 2020. Ore-forming element and isotopic signature of re-fertilized mantle peridotite as determined by nanopowder and olivine LA-ICP-MS analyses; Chemical Geology. doi:10.1016/j.chemgeo.2020.119464

McNicoll, V., Dubé, B., Castonguay, S., Oswald, W., Biczok, J., Mercier-Langevin, P., Skulski, T., and Malo, M., 2016. The world-class Musselwhite BIF-hosted gold deposit, Superior Province, Canada: New high-precision U-Pb geochronology and implications for the geological setting of the deposit and gold exploration; Precambrian Research, v. 272, p. 133–149. doi:10.1016/j.precamres.2015.09.029

Mercier-Langevin, P., Dubé, B., Blanchet, F., Pitre D., and Laberge, A., 2017. The LaRonde Penna Au-rich volcanogenic massive sulfide deposit; *in* Archean Base and Precious Metal Deposits, southern Abitibi greenstone belt, Canada, (ed.) T. Monecke, P. Mercier-Langevin, and B. Dubé; Reviews in Economic Geology, v. 19, p. 225–245.

Mercier-Langevin, P., Simard, M., Dubuc, R., Côté, J., Doucet, P., Daigneault, R., and Gaboury, D., 2017. Geology of the Lapa orogenic gold deposit; *in* Archean Base and Precious Metal Deposits, southern Abitibi Greenstone Belt, Canada, (ed.) T. Monecke, P. Mercier-Langevin, and B. Dubé; Reviews in Economic Geology, v. 19, p. 247–261.

Monecke, P., Mercier-Langevin, P., Dubé, B., and Frieman B.M., 2017. Geology of the Abitibi Greenstone Belt; *in* Archean Base and Precious Metal Deposits, southern Abitibi Greenstone Belt, Canada, (ed.) T. Monecke, P. Mercier-Langevin, and B. Dubé; Reviews in Economic Geology, v. 19, p. 7–49.

Monecke, P., Mercier-Langevin, P., Dubé, B., and Hannington, M., 2017. Archean base and precious metal deposits, southern Abitibi Greenstone Belt, Canada – introduction; *in* Archean Base and Precious Metal Deposits, southern Abitibi Greenstone Belt, Canada, (ed.) T. Monecke, P. Mercier-Langevin, and B. Dubé; Reviews in Economic Geology, v. 19, p. 1–5.

Pilote, J.-L. and Piercey, S.J., 2018. Petrogenesis of the Rambler rhyolite formation: Controls on the Ming VMS deposit and geodynamic implications for the Taconic seaway, Newfoundland Appalachians, Canada; American Journal of Science, v. 318, p. 640–683. doi:10.2475/06.2018.02

Pilote, J.-L., Piercey, S.J., Brueckner, S.M., and Grant, D., 2016. Resolving the relative timing of Au-enrichment in volcanogenic massive sulfide (VMS) deposits using scanning electron microscopy-mineral liberation analyzer: empirical evidence from the Ming deposit, Newfoundland, Canada; Economic Geology, v. 111, p. 1495–1508. doi:10.2113/econgeo.111.6.1495

Pilote, J.-L., Piercey, S., and Mercier-Langevin, P., 2017. Volcanic and structural reconstruction of the deformed and metamorphosed Ming volcanogenic massive sulfide deposit, Canada: implications for ore zone geometry and metal distribution; Economic Geology, v. 112, p. 1305–1332. doi:10.5382/econgeo.2017.4511

Pilote, J.-L., Piercey, S., and Mercier-Langevin, P., 2019. Hydrothermal alteration architecture of the Ming volcanogenic massive sulfide deposit, Baie Verte Peninsula, Newfoundland, Canada; Mineralium Deposita. doi:10.1007/s00126-019-00899-z

Pinet, N., Gloaguen, E., and Giroux, B., 2019. Introduction to this special issue on geophysics applied to mineral exploration: *in* Geophysics Applied to Mineral Exploration, (ed.) N., Pinet, E., Gloaguen, and B., Giroux; Canadian Journal of Earth Sciences, v. 56, p. 5–8. doi:10.1139/cjes-2018-0314

Ross, P.-S., Bourke, A., Mercier-Langevin, P., Lépine, S., Leclerc, F., and Boulerice, A., 2016. High-resolution physical properties, geochemistry and alteration mineralogy for the host rocks of the Archean Lemoine auriferous VMS deposit, Canada; Economic Geology, v. 111, p. 1561–1574. doi:10.2113/econgeo.111.7.1561

Ross, P.-S., Boulerice, A., Mercier-Langevin, P., and McNicoll, V., 2020. Volcanology, chemo-stratigraphy, geochronology, hydrothermal alteration and VMS potential of the Lemoine Member of the Waconichi Formation, Chibougamau district, Abitibi greenstone belt, Québec; Mineralium Deposita, v. 55, p. 21–46. doi:10.1007/s00126-019-00884-6

Schetselaar, E., Bellefleur, G., Craven, J., Roots, E., Cheraghi, S., Shamsipour, P., Caté, A., Mercier-Langevin, P., El Goumi, N., Enkin, R., and Salisbury, M, 2017. Geologically driven 3D modelling of physical rock properties in support of interpreting the seismic response of the Lalor volcanogenic massive sulphide deposit, Snow Lake, Manitoba, Canada; *in* Characterization of Ore-Forming Systems from Geological, Geochemical and Geophysical Studies, (ed.) K., Gessner, T.G., Blenkinsop, P., Sorjonen-Ward; Geological Society, Special Publication 453, p. 57–79. doi:10.1144/SP453.5

Appendix 2
Government publications related to the TGI-4/TGI-5 gold projects (2015–2020)

Beauchamp, A.-M., Dubé, B., Malo, M., McNicoll, V., Archer, P., Lavoie, J., and Chartrand, F., 2015. Geology, mineralization and alteration of the turbidite-hosted Mustang Au showing, Lower Eastmain greenstone belt, Superior Province, Quebec; *in* Targeted Geoscience Initiative 4: Contributions to the Understanding of Precambrian Lode Gold Deposits and Implications for Exploration, (ed.) B. Dubé and P. Mercier-Langevin; Geological Survey of Canada, Open File 7852, p. 227–243. doi:10.4095/296624

Bleeker, W., 2015. Syn-orogenic gold mineralization in granite-greenstone terranes: the deep connection between extension, major faults, syn-orogenic clastic basins, magmatism, thrust inversion and long-term preservation; *in* Targeted Geoscience Initiative 4: Contributions to the Understanding of Precambrian Lode Gold Deposits and Implications for Exploration, (ed.) B. Dubé and P. Mercier-Langevin; Geological Survey of Canada, Open File 7852, p. 25–47. doi:10.4095/296624

Boily-Auclair, É., Mercier-Langevin, P., Ross, P.-S., and Pitre, D., 2019. Lithological and structural controls on the nature and distribution of gold at the LaRonde Zone 5 project, Doyon-Bousquet-LaRonde gold camp, Abitibi, Quebec; *in* Targeted Geoscience Initiative: 2018 report of activities, (ed.) N. Rogers; Geological Survey of Canada, Open File 8549, p. 23–32. doi:10.4095/313631

Boily-Auclair, É., Mercier-Langevin, P., Ross, P.-S., and Pitre, D., 2020. Stratigraphic setting of the LZ5 and Ellison mineralized zones, LaRonde Zone 5 project, Doyon-Bousquet-LaRonde mining camp, Abitibi, Quebec; *in* Targeted Geoscience Initiative 5: Contributions to the Understanding of Canadian Gold Systems, (ed.) P. Mercier-Langevin, C.J.M. Lawley, and S. Castonguay; Geological Survey of Canada, Open File 8712, p. 57–73. doi.org/10.4095/323665

Boudreau, C., Mercier-Langevin, P., Krushnisky, A., and Goutier, J., 2020. Sulphide clast-bearing felsic volcaniclastic units of the Rouyn-Pelletier Formation: Comparison with similar units of the Horne Block, Rouyn-Noranda, Abitibi greenstone belt, Quebec; *in* Targeted Geoscience Initiative 5: Contributions to the Understanding of Canadian Gold Systems, (ed.) P. Mercier-Langevin, C.J.M. Lawley, and S. Castonguay; Geological Survey of Canada, Open File 8712, p. 45–56. doi:10.4095/323664

Boulerice, A.R., Ross, P.-S., and Mercier-Langevin, P., 2015. Geological and geochemical characteristics of the Waconichi Formation east of the Lemoine auriferous volcanogenic massive sulphide deposit, Abitibi greenstone belt, Quebec; *in* Targeted Geoscience Initiative 4: Contributions to the Understanding of Volcanogenic Massive Sulphide Deposit Genesis and Exploration Methods Development, (ed.) J.M. Peter and P. Mercier-Langevin; Geological Survey of Canada, Open File 7853, p. 171–182. doi:10.4095/296540

Castonguay, S., Ootes, L., Mercier-Langevin, P., Rowins, S., and Devine, F., 2017. Orogenic gold along Cordilleran faults: Key characteristics and analogies between Phanerozoic and Archean settings; *in* Targeted Geoscience Initiative: 2016 report of activities, (ed.) N. Rogers; Geological Survey of Canada, Open File 8199, p. 35–37. doi:10.4095/299585

Castonguay, S., Dubé, B., Mercier-Langevin, P., McNicoll, V.J., DeLazeer, A., and Malcolm, K., 2018. Nature and significance of deformation zones on gold mineralization in the Detour Lake area: Implications for exploration in Ontario and Quebec; *in* Targeted Geoscience Initiative: 2017 report of activities, volume 1, (ed.) N. Rogers; Geological Survey of Canada, Open File 8358, p. 105–111. doi:10.4095/306441

Castonguay, S., Ootes, L., Mercier-Langevin, P., and Devine, F., 2018. Gold along Cordilleran faults: Key characteristics and analogies between Phanerozoic and Archean settings; *in* Targeted Geoscience Initiative: 2017 report of activities, volume 1, (ed.) N. Rogers; Geological Survey of Canada, Open File 8358, p. 139–145. doi:10.4095/306460

Castonguay, S., Dubé, B., Mercier-Langevin, P., and Wodicka, N., 2019. Geological setting and mineralization styles of the Sunday Lake and Lower Detour 'gold trends', northwestern Abitibi greenstone belt, Ontario and Quebec; *in* Targeted Geoscience Initiative: 2018 report of activities, (ed.) N. Rogers; Geological Survey of Canada, Open File 8549, p. 9–22. doi:10.4095/313625

Castonguay, S., Dubé, B., Wodicka, N., and Mercier-Langevin, P., 2020. Geological setting and gold mineralization associated with the Sunday Lake and Lower Detour deformation zones, northwestern Abitibi greenstone belt, Ontario and Quebec; *in* Targeted Geoscience Initiative 5: Contributions to the Understanding of Canadian Gold Systems, (ed.) P. Mercier-Langevin,

Appendix 2: Government publications related to the TGI-4/TGI-5 gold system projects (2015–2020); *in* Targeted Geoscience Initiative 5: Contributions to the Understanding of Canadian Gold Systems, (ed.) P. Mercier-Langevin, C.J.M. Lawley, and S. Castonguay; Geological Survey of Canada, Open File 8712, p. 317–325.

C.J.M. Lawley, and S. Castonguay; Geological Survey of Canada, Open File 8712, p. 127–142. doi:10.4095/323670

Castonguay, S., Ootes, L., Devine, F., and Friedman., R., 2020. Superimposed Late Cretaceous and earliest Eocene gold mineralization and deformation events along the Llewellyn-Tally Ho deformation corridor in northwest British Columbia and southern Yukon; *in* Targeted Geoscience Initiative 5: Contributions to the Understanding of Canadian Gold Systems, (ed.) P. Mercier-Langevin, C.J.M. Lawley, and S. Castonguay; Geological Survey of Canada, Open File 8712, p. 223–236. doi:10.4095/326039

Caté, A., Mercier-Langevin, P., Ross, P.-S., Duff, S., Hannington, M.D., Dubé, B., and Gagné, S., 2015. Geology and Au enrichment processes at the Paleoproterozoic Lalor auriferous volcanogenic massive sulphide deposit, Snow Lake, Manitoba; *in* Targeted Geoscience Initiative 4: Contributions to the Understanding of Volcanogenic Massive Sulphide Deposit Genesis and Exploration Methods Development, (ed.) J.M. Peter and P. Mercier-Langevin; Geological Survey of Canada, Open File 7853, p. 131–145. doi:10.4095/296540

Caté, A., Mercier-Langevin, P., Ross, P.-S., Bécu, V., Lauzière, K., Hannington, M., Duff. S., Dubé, B., and Gagné, S., 2017. Whole-rock lithogeochemistry of the Lalor auriferous volcanogenic massive-sulfide deposit, Manitoba; Geological Survey of Canada, Open File 8107, 1 .zip file.

Ciufo, T.J., Yakymchuk, C., Lin, S., Jellicoe, K., and Mercier-Langevin, P., 2018. Hydrothermal alteration and vectors at the orogenic Island Gold deposit, Michipicoten greenstone belt, Wawa, Ontario; *in* Targeted Geoscience Initiative: 2017 report of activities, volume 1, (ed.) N. Rogers; Geological Survey of Canada, Open File 8358, p. 117–120. doi:10.4095/306443

Ciufo, T.J., Mercier-Langevin, P., Yakymchuk, C., Lin, S., Bécu, V., and Lauzière, K., 2019. Whole-rock lithogeochemistry of the Archean Islang Gold deposit, Ontario, Canada; Geological Survey of Canada, Open File 8524, 1 .zip file. doi:10.4095/314791

Ciufo, T.J., Jellicoe, K., Yakymchuk, C., Lin, S., Mercier-Langevin, P., and Wodicka, N., 2020. Geology, structural evolution, and hydrothermal alteration of the Island Gold deposit, Michipicoten greenstone belt, Ontario; *in* Targeted Geoscience Initiative 5: Contributions to the Understanding of Canadian Gold Systems, (ed.) P. Mercier-Langevin, C.J.M. Lawley, and S. Castonguay; Geological Survey of Canada, Open File 8712, p. 143–156. doi:10.4095/323671

Davis, W.J., McNicoll, V.J., Mercier-Langevin, P., Dubé, B., Rhys, D., Jackson, S.E., Lawley, C.J.M., and Hunt, P.A, 2017. New approaches to dating hydrothermal gold deposits; *in* Targeted Geoscience Initiative: 2016 report of activities, (ed.) N. Rogers; Geological Survey of Canada, Open File 8199, p. 27–28. doi:10.4095/299582

De Souza, S., Dubé, B., McNicoll, V., Dupuis, C., Mercier-Langevin, P., Creaser, R.A., and Kjarsgaard, I., 2015. Geology, hydrothermal alteration, and genesis of the world-class Canadian Malartic stockwork-disseminated Archean gold deposit, Abitibi, Quebec; *in* Targeted Geoscience Initiative 4: Contributions to the Understanding of Precambrian Lode Gold Deposits and Implications for Exploration, (ed.) B. Dubé and P. Mercier-Langevin; Geological Survey of Canada, Open File 7852, p. 113–126. doi:10.4095/296624

De Souza, S., Dubé, B., McNicol, V., Mercier-Langevin, P., Creaser, R.A., and Kjarsgaard, I., 2017. (Day 5 – Part I) Geology and disseminated-stockwork gold mineralization at the world-class Canadian Malartic mine, Abitibi greenstone belt, Canada; Chapter 8 *in* Precious- and Base-Metal Deposits of the southern Abitibi Greenstone Belt, Superior Province, Canada: A field trip to the 14th Biennial Society for Geology Applied to Mineral Deposits meeting, (ed.) P. Mercier-Langevin, J. Goutier, and B. Dubé; Geological Survey of Canada, Open File 8317, p. 55–64. doi:10.4095/306259

Dubé, B., Mercier-Langevin, P., Castonguay, S., McNicoll, V.J., Bleeker, W., Lawley, C.J.M., De Souza, S., Jackson, S.E., Dupuis, C., Gao, J.-F., Bécu, V., Pilote, P., Goutier, J., Beakhouse, G.P., Yergeau, D., Oswald, W., Janvier, V., Fontaine, A., Pelletier, M., Beauchamp, A.-M., Katz, L.R., Kontak, D.J., Tóth, Z., Lafrance, B., Gourcerol, B., Thurston, P.C., Creaser, R.A., Enkin, R.J., El Goumi, N., Grunsky, E.C., Schneider, D.A., Kelly, C.J., and Lauzière, K., 2015. Precambrian lode gold deposits — a summary of TGI-4 contributions to the understanding of lode gold deposits, with an emphasis on implications for exploration; *in* Targeted Geoscience Initiative 4: Contributions to the Understanding of Precambrian Lode Gold Deposits and Implications for Exploration, (ed.) B. Dubé and P. Mercier-Langevin; Geological Survey of Canada, Open File 7852, p. 1–24. doi:10.4095/296624.

Duff, S., Hannington, M., Caté, A., Mercier-Langevin, and Kjarsgaard, I.J., 2015. Major ore types of the Paleoproterozoic Lalor auriferous volcanogenic massive sulphide deposit, Snow Lake, Manitoba; in Targeted Geoscience Initiative 4: Contributions to the Understanding of Volcanogenic Massive Sulphide Deposit Genesis and Exploration Methods Development, (ed.) J.M. Peter and P. Mercier-Langevin; Geological Survey of Canada, Open File 7853, p. 147–170. doi:10.4095/296540

El Goumi, N., De Souza, S., Enkin, R.J., and Dubé, B., 2015. Petrophysical signature of gold mineralization and alteration assemblages at the Canadian Malartic deposit, Quebec, Canada; *in* Targeted Geoscience Initiative 4: Contributions to the Understanding of Precambrian Lode Gold Deposits and Implications for Exploration, (ed.) B. Dubé and P. Mercier-Langevin; Geological Survey of Canada, Open File 7852, p. 127–138. doi:10.4095/296624

Fayard, Q., Mercier-Langevin, P., Daigneault, R., and Perreault, S., 2018. Volcanic, hydrothermal and structural controls on the nature and distribution of base and precious metals at the B26 project, Brouillan volcanic complex, Abitibi, Quebec; *in* Targeted Geoscience Initiative: 2017 report of activities, volume 1, (ed.) N. Rogers; Geological Survey of Canada, Open File 8358, p. 99–103. doi:10.4095/306440

Fayard, Q., Mercier-Langevin, P., Wodicka, N., Daigneault, R., and Perreault, S., 2020. The B26 Cu-Zn-Ag-Au project, Brouillan volcanic complex, Abitibi greenstone belt, part 1: Geological setting and geochronology; *in* Targeted Geoscience Initiative 5: Contributions to the Understanding of Canadian Gold Systems, (ed.) P. Mercier-Langevin, C.J.M. Lawley, and S. Castonguay; Geological Survey of Canada, Open File 8712, p. 93–107. doi:10.4095/323668

Fayard, Q., Mercier-Langevin, P., Daigneault, R., Perreault, S., and Wodicka, N., 2020. The B26 Cu-Zn-Ag-Au project, Brouillan volcanic complex, Abitibi greenstone belt, part 2: Hydrothermal alteration and mineralization; *in* Targeted Geoscience Initiative 5: Contributions to the Understanding of Canadian Gold Systems, (ed.) P. Mercier-Langevin, C.J.M. Lawley, and S. Castonguay; Geological Survey of Canada, Open File 8712, p. 109–125. doi:10.4095/323669

Fontaine, A., Dubé, B., Malo, M., McNicoll, V., Brisson, T., and Doucet, D., 2015. Geology of the metamorphosed Roberto gold deposit (Éléonore Mine), Baie-James region, Québec: Diversity of mineralization styles in a polyphase tectono-metamorphic setting; *in* Targeted Geoscience Initiative 4: Contributions to the Understanding of Precambrian Lode Gold Deposits and Implications for Exploration, (ed.) B. Dubé and P. Mercier-Langevin; Geological Survey of Canada, Open file 7852, p. 209–225. doi:10.4095/296624

Fontaine, A., Dubé, B., Malo, M., McNicoll, V.J., Prud'homme, N., Beausoleil, C., and Goutier, J., 2018. Geology of the Éléonore gold mine and adjacent gold showings, Superior Province, northern Quebec; *in* Targeted Geoscience Initiative: 2017 report of activities, volume 1, (ed.) N. Rogers; Geological Survey of Canada, Open File 8358, p. 121–125. doi:10.4095/306444

Gao, J.-F., Jackson, S.E., Dubé, B., and De Souza, S., 2015. Genesis of the Canadian Malartic, Côté Gold, and Musselwhite gold deposits: Insights from LA-ICP-MS element mapping of pyrite; *in* Targeted Geoscience Initiative 4: Contributions to the Understanding of Precambrian Lode Gold Deposits and Implications for Exploration, (ed.) B. Dubé and P. Mercier-Langevin; Geological Survey of Canada, Open file 7852, p. 157–175. doi:10.4095/296624

Gill, S.B., Piercey, S.J., Layton-Matthews, D., Layne, G.D., and Piercey, G., 2015. Mineralogical, sulphur, and lead isotopic study of the Lemarchant Zn-Pb-Cu-Ag-Au-VMS deposit: Implications for precious-metal enrichment processes in the VMS environment; *in* Targeted Geoscience Initiative 4: Contributions to the Understanding of Volcanogenic Massive Sulphide Deposit Genesis and Exploration Methods Development, (ed.) J.M. Peter and P. Mercier-Langevin; Geological Survey of Canada, Open File 7853, p. 183–195. doi:10.4095/296540

Gosselin, P. and Dubé, B., 2015. World lode gold deposit database; Geological Survey of Canada, Open File 7930, 27 p. doi:10.4095/297322

Gourcerol, B., Thurston, P.C., Kontak, D.J., Côté-Mantha, O., and Biczok, J., 2015. Depositional setting of Algoma-type banded iron formation from the Meadowbank, Meliadine, and Musselwhite gold deposits; *in* Targeted Geoscience Initiative 4: Contributions to the Understanding of Precambrian Lode Gold Deposits and Implications for Exploration, (ed.) B. Dubé and P. Mercier-Langevin; Geological Survey of Canada, Open File 7852, p. 55–68. doi:10.4095/296624

Gourcerol, B., Thurston, P.C., Kontak, D.J., Côté-Mantha, O., and Biczok, J., 2015. Distinguishing primary and mineralization-related signatures of chert from the banded iron formation-type gold deposits at Musselwhite, Ontario and Meadowbank, Nunavut; Geological Survey of Canada, Current Research 2015-1, 21 p. doi:10.1095/295531

Grondin-LeBlanc, P., Mercier-Langevin, P., Malo, M., Côté-Mantha, O., Simard, M., Barbe, P., Valette, M., and De Souza, S., 2017. Structural controls on the nature and distribution of gold in polytectonized Precambrian volcano-sedimentary successions: An example from the Whale Tail Zone, Amaruq project, Nunavut; Geological Survey of Canada, Scientific Presentation 63, 1 sheet. doi:10.4095/300660

Grunsky, E.C., Brauhart, C.W., Hagemann, S., and Dubé, B., 2015. The magmato-hydrothermal space: a new metric for geochemical characterization of ore deposits; Geological Survey of Canada, Open File 7487, 1 sheet. doi:10.4095/295662

Grunsky, E.C., Dubé, B., Hagemann, S., and Brauhart, C., 2015. A Global Database of Gold Deposits: Quantification of Multi-element Ore Signatures; in Targeted Geoscience Initiative 4: Contributions to the Understanding of Precambrian Lode Gold Deposits and Implications for Exploration, (ed.) B. Dubé and P. Mercier-Langevin; Geological Survey of Canada, Open file 7852, p. 271–285. doi:10.4095/296624

Honsberger, I. and Bleeker, W., 2018. Orogenic comparison of structurally controlled gold systems of the Abitibi Greenstone Belt and central Newfoundland Appalachians: implications for Newfoundland gold potential and recurring tectonic drivers of gold mineralization; *in* Targeted Geoscience Initiative: 2017 report of activities, volume 2, (ed.) N. Rogers; Geological Survey of Canada, Open File 8373, p. 65–70. doi: 10.4095/306602

Honsberger, I.W., Bleeker, W., Kamo, S.L., Evans, D.T.W., and Sandeman, H.A.I., 2019. A Neoproterozoic age for granodiorite underlying Rogerson Lake Conglomerate:

Confirmed Ganderian basement in the Wilding Lake area, central Newfoundland gold district; Government of Newfoundland and Labrador, Department of Natural Resources, Geological Survey, Open File 012A/07/1774, 12 p.

Honsberger, I.W., Bleeker, W., Sandeman, H.A.I., and Evans, D.T.W., 2019. Lithological and structural setting of structurally controlled gold mineralization in the Wilding Lake region, central Newfoundland; *in* Targeted Geoscience Initiative: 2018 report of activities, (ed.) N. Rogers; Geological Survey of Canada, Open File 8549, p. 59–69. doi:10.4095/313640

Honsberger, I.W., Bleeker, W., Sandeman, H.A.I., and Evans, D.T.W., 2019. Structural geology of a gold-bearing quartz vein system, Wilding Lake region, central Newfoundland; *in* Current Research; Geological Survey of Newfoundland and Labrador, Department of Natural Resources,Geological Survey, Report 19-1, p. 23–28.

Honsberger, I.W., Bleeker, W., Sandeman, H.A.I., Evans, D.T.W., and Kamo, S.L., 2019. Structurally controlled gold system, Antler Gold Inc.'s Wilding Lake property, central Newfoundland; Government of Newfoundland and Labrador, Department of Natural Resources, Geological Survey, Open File 012A/1811, 12 p.

Honsberger, I.W., Bleeker, W., Kamo, S.L., Sandeman, H.A.I., and Evans, D.T.W., 2020. The emerging Paleozoic gold district of central Newfoundland: New insights on structural controls and tectonic drivers of gold mineralization and preservation; *in* Targeted Geoscience Initiative 5: Contributions to the Understanding of Canadian Gold Systems, (ed.) P. Mercier-Langevin, C.J.M. Lawley, and S. Castonguay; Geological Survey of Canada, Open File 8712, p. 193–210. doi:10.4095/326024

Honsberger, I.W., Bleeker, W., Sandeman, H.A.I., Evans, D.T.W., and Kamo, S.L., 2020. Vein-hosted gold mineralization in the Wilding Lake area, central Newfoundland: Structural geology and vein evolution; *in* Targeted Geoscience Initiative 5: Contributions to the Understanding of Canadian Gold Systems, (ed.) P. Mercier-Langevin, C.J.M. Lawley, and S. Castonguay; Geological Survey of Canada, Open File 8712, p. 179–191. doi:10.4095/326020

Honsberger, I.W., Bleeker, W., Sandeman, H.A.I., Evans, D.T.W., and Kamo, S.L., 2020. The Wilding Lake gold prospect in central Newfoundland: A lithological and structural synthesis; Geological Survey of Canada, Open File 8658, 2 sheet. doi:10.4095/321490

Janvier, V., Castonguay, S., Mercier-Langevin, P., Dubé, B., Malo, M., McNicoll, V., Creaser, R.A., de Chavigny, B., and Pehrsson, S., 2015. Geology of the banded iron formation-hosted Meadowbank gold deposit, Churchill Province, Nunavut; *in* Targeted Geoscience Initiative 4: Contributions to the Understanding of Precambrian Lode Gold Deposits and Implications for Exploration, (ed.) B. Dubé and P. Mercier-Langevin; Geological Survey of Canada, Open File 7852, p. 255–269. doi:10.4095/296624

Janvier, V., Castonguay, S., Mercier-Langevin, P., Dubé, B., McNicoll, V., Pehrsson, S., Malo, M., De Chavigny, B., and Côté-Mantha, O., 2015. Preliminary results of the geology of the Portage deposit, Meadowbank gold mine, Churchill Province, Nunavut; Geological Survey of Canada, Current Research 2015-2, 21 p. doi:10.4095/295532

Jellicoe, K.M., Lin, S., Ciufo, T.J., Yakymchuk, C., and Mercier-Langevin, P., 2018. Structural controls and relative timing of events at the orogenic Island Gold deposit, Michipicoten greenstone belt, Wawa, Ontario; *in* Targeted Geoscience Initiative: 2017 report of activities, volume 1, (ed.) N. Rogers; Geological Survey of Canada, Open File 8358, p. 113–116. doi:10.4095/306442

Katz, L.R., Kontak, D.J., Dubé, B., and McNicoll, V., 2015. The Archean Côté gold intrusion-related Au (-Cu) deposit, Ontario, Canada: A large-tonnage, low-grade deposit centred on a magmatic-hydrothermal breccia; *in* Targeted Geoscience Initiative 4: Contributions to the Understanding of Precambrian Lode Gold Deposits and Implications for Exploration, (ed.) B. Dubé and P. Mercier-Langevin; Geological Survey of Canada, Open File 7852, p. 139–155. doi:10.4095/296624

Katz, L.R., Kontak, D.J., Dubé, B., Mercier-Langevin, P., Bécu, V., and Lauzière, K., 2016. Whole-rock lithogeochemistry of the Archean intrusion-related Côté Gold Au(-Cu) deposit, Ontario, Canada; Geological Survey of Canada, Open File 8040, 5 p., 1 .zip file. doi:10.4095/299354

Kelly, C.J. and Schneider, D.A., 2015. Insights into the timing of mineralization and metamorphism in the North Caribou Greenstone Belt, Western Superior Province; *in* Targeted Geoscience Initiative 4: Contributions to the Understanding of Precambrian Lode Gold Deposits and Implications for Exploration, (ed.) B. Dubé and P. Mercier-Langevin; Geological Survey of Canada, Open File 7852, p. 245–253. doi:10.4095/296624

Krushnisky, A., Mercier-Langevin, P., Ross, P.-S., Bécu, V., Lauzière, K., and Goutier, J., 2017. Whole-rock lithogeochemistry of the gold-bearing mineralized zones of the Horne 5 deposit, Québec, Canada; Geological Survey of Canada, Open File 8501, 1 .zip file. doi:10.4095/314545

Krushnisky, A., Mercier-Langevin, P., Ross, P.-S., Goutier, J., Pilote, C., Bernier, C., and Moore, L., 2017. (Day 3 – Part II) The Horne 5 deposit; Chapter 6 *in* Precious- and Base-Metal Deposits of the southern Abitibi Greenstone Belt, Superior Province, Canada: A field trip to the 14th Biennial Society for Geology Applied to Mineral Deposits meeting, (ed.) P. Mercier-Langevin, J. Goutier, and B. Dubé; Geological Survey of Canada, Open File 8317, p. 41–47. doi:10.4095/306257

Krushnisky, A., Mercier-Langevin, P., Ross, P.-S., McNicoll, V., Goutier, J., Moore, L., Pilote, C., and Bernier, C., 2017. The Au-Ag-Cu-Zn-bearing mineralized zones at the Horne 5 deposit, Rouyn-Noranda, Quebec – New observations and preliminary results; Geological Survey of Canada, Scientific Presentation 62, 1 sheet. doi: 10.4095/300665

Krushnisky, A., Mercier-Langevin, P., Ross, P.-S., Goutier, J., McNicoll, V.J., Moore, L., Pilote, C., and Bernier, C., 2018. Controls on the distribution, style, composition and timing of the gold-bearing mineralized zones of the Horne 5 deposit, Abitibi greenstone belt, Quebec; *in* Targeted Geoscience Initiative: 2017 report of activities, volume 1, (ed.) N. Rogers; Geological Survey of Canada, Open File 8358, p. 95–98. doi:10.4095/306439

Krushnisky, A., Mercier-Langevin, P., Ross, P.-S., Goutier, J., Pilote, C., and Bernier, C., 2020. Geology and gold enrichment at the Horne 5 Archean volcanogenic massive sulphide deposit, Abitibi greenstone belt, Quebec: A synthesis; *in* Targeted Geoscience Initiative 5: Contributions to the Understanding of Canadian Gold Systems, (ed.) P. Mercier-Langevin, C.J.M. Lawley, and S. Castonguay; Geological Survey of Canada, Open File 8712, p. 31–44. doi:10.4095/323663

Lafrance, B., 2015. Structural and lithological controls on gold mineralization at the Cheminis mine: Implications for the formation of gold deposits along the Cadillac – Larder Lake deformation zone, Ontario; in Targeted Geoscience Initiative 4: Contributions to the Understanding of Precambrian Lode Gold Deposits and Implications for Exploration, (ed.) B. Dubé and P. Mercier-Langevin; Geological Survey of Canada, Open File 7852, p. 49–54. doi:10.4095/296624

Lauzon, M.-C., Mercier-Langevin, P., Beaudoin, G., Côté-Mantha, O., Simard, M., Valette, M., and De Souza, S., 2017. Mineralogy and geochemistry of the Whale Tail zone, Amaruq gold project, Nunavut; Geological Survey of Canada, Scientific Presentation 61, 1 sheet. doi: 10.4095/300659

Lauzon, M.-C., Mercier-Langevin, P., Valette, M., Beaudoin, G., De Souza, S., Côté-Mantha, O., and Simard, M., 2020. Ore mineralogy and mineral chemistry of the Whale Tail zone, Amaruq gold deposit, Nunavut; *in* Targeted Geoscience Initiative 5: Contributions to the Understanding of Canadian Gold Systems, (ed.) P. Mercier-Langevin, C.J.M. Lawley, and S. Castonguay; Geological Survey of Canada, Open File 8712, p. 267–279. doi:10.4095/326044

Lawley, C.J.M. and Kjarsgaard, B.A., 2020. Bottom-up mineral exploration: Ore-element upgrading in the upper mantle and tools for its discovery; *in* Targeted Geoscience Initiative 5: Contributions to the Understanding of Canadian Gold Systems, (ed.) P. Mercier-Langevin, C.J.M. Lawley, and S. Castonguay; Geological Survey of Canada, Open File 8712, p. 157–164. doi:10.4095/323674

Lawley, C.J.M., Creaser, R.A., Jackson, S., Yang, Z., Davis, B., Dubé, B., Mercier-Langevin, P., Pehrsson, S., and Vaillancourt, D., 2015. Protracted Paleoproterozoic gold history at the Archean BIF-hosted Meliadine Gold District, Nunavut; Geological Survey of Canada, Open File 7743, 23 p. doi:10.4095/295629

Lawley, C.J.M., Dubé, B., Mercier-Langevin, P., and Vaillancourt, D., 2015. Mapping hydrothermal footprints: case studies from the Meliadine Gold District, Nunavut; Geological Survey of Canada, Open File 7744, 22 p. doi:10.4095/295920

Lawley, C.J.M., Dubé, B., Mercier-Langevin, P., Kjarsgaard, B.A., and Knight, R.D., 2015. Whole-rock lithogeochemistry and pXRF data from the Meliadine gold district, Nunavut, Canada; Geological Survey of Canada, Open File 7711, 11 p. doi:10.4095/296223

Lawley, C.J.M., Dubé, B., Mercier-Langevin, P., McNicoll, V.J., Creaser, R.A., Pehrsson, S.J., Castonguay, S., Blais, J.-C., Simard, M., Davis, W.J., and Jackson, S.E., 2015. Setting, age, and hydrothermal footprint of the emerging Meliadine gold district, Nunavut; *in* Targeted Geoscience Initiative 4: Contributions to the Understanding of Precambrian Lode Gold Deposits and Implications for Exploration, (ed.) B. Dubé and P. Mercier-Langevin; Geological Survey of Canada, Open File 7852, p. 99–111. doi:10.4095/296624

Lawley, C.J.M., McNicoll, V.J., Creaser, R.A., Dubé, B., Mercier-Langevin, P., Pehrsson, S.J., and Vaillancourt, D., 2015. Unravelling the Archean to Proterozoic history at the Meliadine Gold District, Nunavut, Canada; Geological Survey of Canada, Open File 7884, 1 sheet. doi:10.4095/297045

Lawley, C.J.M., Jackson, S.E., Yang, Z., Davis, W.J., Creaser, R.A., Mercier-Langevin, P., and Dubé, B., 2017. Tracing gold mobility using in situ Pb isotope geochemistry of early and remobilized sulphide minerals, Meliadine gold district, Nunavut; Geological Survey of Canada, Scientific Presentation 51, 39 p., 1 .pptx file.

Lawley, C.J.M., Kjarsgaard, B.A., Zagorevski, A., Jackson, S.E., Yang, Z., and Mercier-Langevin, P., 2017. Mantle metal mobility; in Targeted Geoscience Initiative: 2016 report of activities, (ed.) N. Rogers; Geological Survey of Canada, Open File 8199, p. 23–25. doi:10.4095/299581

Lawley, C.J.M., McNicoll, V.J., Davis, W.J., Jackson, S.E., Yang, Z., and Mercier-Langevin, P., 2017. Paleoproterozoic gold and its tectonic triggers and traps; in Targeted Geoscience Initiative: 2016 report of activities, (ed.) N. Rogers; Geological Survey of Canada, Open File 8199, p. 33–34. doi:10.4095/299584

Lawley, C.J.M., Jackson, S.E., Petts, D.C., Savard, D., Zagorevski, A., Pearson, D.G., Tschirhart, V., and Kjarsgaard, B., 2018. Precious metal mobility during serpentinization-driven redox reactions; Geological Survey of Canada, Open File 8506, 1 sheet. doi:10.4095/315041

Lawley, C.J.M., Kjarsgaard, B.A., Jackson, S.E., Yang, Z., and Petts, D., 2018. Olivine and clinopyroxene mantle xenocryst geochemistry from the Kirkland Lake kimberlite field, Ontario; Geological Survey of Canada, Open File 8376, 9 p. doi:10.4095/308048

Lawley, C.J.M., Kjarsgaard, B.A., Jackson, S.E., Yang, Z., Petts, D.C., and Roots, E., 2018. Mapping the ore element signature of the Abitibi Greenstone Belt cratonic mantle, Ontario; Geological Survey of Canada, Open File 8387, 1 sheet. doi:10.4095/308417

Lawley, C.J.M., Kjarsgaard, B.A., Jackson, S.E, Yang, Z., Petts, D., and Roots, E., 2018. Olivine and clinopyroxene mantle xenocryst geochemistry from the Kirkland Lake kimberlite field, Ontario; Geological Survey of Canada, Open File 8387, 1 sheet. doi:10.4095/308417

Lawley, C.J.M., Kjarsgaard, B.A., Zagorevski, A., Pearson, G., Waterton, P., Savard, D., Jackson, S.E., Yang, Z., Zhang, S., and Tschirhart, V., 2018. Preliminary geochemical results on mantle metal mobility; *in* Targeted Geoscience Initiative: 2017 report of activities, volume 1, (ed.) N. Rogers; Geological Survey of Canada, Open File 8358, p. 127–131. doi:10.4095/306445

Lawley, C.J.M., Schneider, D., Yang, E., Davis, W.J., Jackson, S.E., Yang, Z., Zhang, S., and Selby, D., 2018. Age relationships and preliminary U-Pb zircon geochronology results from the Lynn Lake Greenstone Belt; *in* Targeted Geoscience Initiative: 2017 report of activities, volume I, (ed.) N. Rogers; Geological Survey of Canada, Open File 8358, p. 133–137. doi:10.4095/306459

Lawley, C.J.M., Davis, W.J., Jackson, S.E., Petts, D.C., Yang, E., Zhang, S., Selby, D., O'Connor, A.R., and Schneider, D.A., 2019. Paleoproterozoic gold and its tectonic triggers and traps; *in* Targeted Geoscience Initiative: 2018 report of activities, (ed.) N. Rogers; Geological Survey of Canada, Open File 8549, p. 71–75. doi:10.4095/313641

Lawley, C.J.M., Jackson, S.E., Petts, D.C., Savard, D., Pearson, D.G., Zhang, S., Zagorevski, A. and Kjarsgaard, B.A., 2019. Mantle metal mobility: preliminary gold and platinum group element geochemical results; *in* Targeted Geoscience Initiative: 2018 report of activities, (ed.) N. Rogers; Geological Survey of Canada, Open File 8549, p. 43–48. doi:10.4095/313635

Lawley, C.J.M., Selby, D., Davis, W.J., Yang, E., Zhang, S., Jackson, S.E., Petts, D.C., O'Connor, A.R., and Schneider, D.A., 2020. Paleoproterozoic gold and its tectonic triggers and traps: Implications from Re-Os sulphide and U-Pb detrital zircon geochronology, Lynn Lake, Manitoba; *in* Targeted Geoscience Initiative 5: Contributions to the Understanding of Canadian Gold Systems, (ed.) P. Mercier-Langevin, C.J.M. Lawley, and S. Castonguay; Geological Survey of Canada, Open File 8712, p. 211–222. doi:10.4095/326033

Mercier-Langevin, P., Hannington, M.D., Dubé, B., Piercey, S.J., Peter, J.M., and Pehrsson, S.J., 2015. Precious metal enrichment processes in volcanogenic massive sulphide deposits — A summary of key features, with an emphasis on TIGI-4 research contributions; *in* Targeted Geoscience Initiative 4: Contributions to the Understanding of Volcanogenic Massive Sulphide Deposit Genesis and Exploration Methods Development, (ed.) J.M. Peter and P. Mercier-Langevin; Geological Survey of Canada, Open File 7853, p. 117–130. doi:10.4095/296540

Mercier-Langevin, P., Dubé, B., Castonguay, S., McNicoll, V., Pinet, N., Lawley, C., Bleeker, W., Bécu, V., Jackson, S., Davis, B., Enkin, R., Goutier, J., Préfontaine, S., Robichaud, L., Pilote, P., and Roy, P., 2017. Gold through space and time at the Archean: *in* Targeted Geoscience Initiative: 2016 report of activities, (ed.) N. Rogers; Geological Survey of Canada, Open File 8199, p. 17–21. doi:10.4095/299575

Mercier-Langevin, P., Dubé, B., Pitre, D., Bégin, J.-F., Laberge, A., and Burke, L., 2017. (Day 4) Au-rich VMS deposits of the Doyon-Bousquet-LaRonde mining camp – The LaRonde Penna mine; Chapter 7 *in* Precious- and Base-Metal Deposits of the southern Abitibi Greenstone Belt, Superior Province, Canada: A field trip to the 14th Biennial Society for Geology Applied to Mineral Deposits meeting, (ed.) P. Mercier-Langevin, J. Goutier, and B. Dubé; Geological Survey of Canada, Open File 8317, p. 49–54. doi:10.4095/306258

Mercier-Langevin, P., Goutier, J., and Dubé, B. (ed.), 2017. Precious and base metal deposits of the southern Abitibi greenstone belt, Superior Province, Canada: A field trip to the 14th Biennial Society for Geology Applied to Mineral Deposits meeting; Geological Survey of Canada, Open File 8317, 86 p. doi:10.4095/306250

Mercier-Langevin, P., Janvier, V., McNicoll, V., Castonguay, S., Dupuis, C., Dubé, B., de Chavigny, B., and Côté-Mantha, O., 2017. Géologie du gisement d'or Vault et implications pour l'exploration aurifère dans les ceintures de roches vertes précambriennes; Geological Survey of Canada, Scientific Presentation 64, 1 sheet. doi:10.4095/300661

Mercier-Langevin, P., Rogers, N., Dubé, B., Bleeker, W., Castonguay, S., McNicoll, V.J., Chapman, J.B., Lawley, C.J.M., Bellefleur, G., Houlé, M.G., Pinet, N., Jackson, S., Davis, B., Bécu, V., Peter, J.M., Paradis, S., Potter, E.G., Bjerkelund, C., Villeneuve, M.E., and Evans, R., 2017, Targeted Geoscience Initiative: 2016 Report of Activities – an overview: *in* Targeted Geoscience Initiative: 2016 report of activities, (ed.) N. Rogers; Geological Survey of Canada, Open File 8199, p. 7–16. doi:10.4095/299574

Mercier-Langevin, P., Valette, M., De Souza, S., McNicoll, V.J., Grondin-LeBlanc, P., Creaser, R.A., Côté-Mantha, O., Simard, M., and Malo, M., 2017. Lithologic and tectonic controls on Paleoproterozoic BIF-hosted/associated gold; *in* Targeted Geoscience Initiative: 2016 report of activities, (ed.) N. Rogers; Geological Survey of Canada, Open File 8199, p. 39–42. doi:10.4095/299586

Mercier-Langevin, P., Valette, M., De Souza, S., Creaser, R.A., McNicoll, V.J., Grondin-Leblanc, P., St.Pierre, B., Lauzon, M.-C., Malo, M., Côté-Mantha, O., and Simard, M., 2018. Lithologic controls on Paleoproterozoic BIF-hosted/associated gold: Overview of Re-Os geochronology and Pb isotopes preliminary results; *in* Targeted Geoscience Initiative: 2017 report of activities, volume 1, (ed.) N. Rogers; Geological Survey of Canada, Open File 8358, p. 147–152. doi:10.4095/306466

Mercier-Langevin, P., Lawley, C.J.M., Castonguay, S., Dubé, B., Bleeker, W., Pinet, N., Bécu, B., Pilote, J.-L., Jackson, S.E., Wodicka, N., Honsberger, I.W., Davis, W.J., Petts, D.C., Yang, Z., Jautzy, J., and Lauzière, K., 2020. Targeted Geoscience Initiative 5, Gold Project: A summary of contributions to the understanding of Canadian gold systems; *in* Targeted Geoscience Initiative 5: Contributions to the Understanding of Canadian Gold Systems, (ed.) P. Mercier-Langevin, C.J.M. Lawley, and S. Castonguay; Geological Survey of Canada, Open File 8712, p. 1–30. doi:10.4095/ 323662

Ootes, L., Castonguay, S., Friedman, R., Devine, F., and Simmonds, R., 2017. Geological fieldwork 2017: A summary of field activities and current research; *in* Geological Fieldwork 2017; British Columbia Ministry of Energy, Mines and Petroleum Resources, British Columbia Geological Survey, Paper 2018-1, p. 67–81.

Ootes, L., Castonguay, S., Friedman, R., and Devine, F., 2019. Superimposed auriferous structural events along the Llewellyn-Tally Ho deformation corridor in southern Yukon and northwest British Columbia; *in* Targeted Geoscience Initiative: 2018 report of activities, (ed.) N. Rogers; Geological Survey of Canada, Open File 8549, p. 49–58. doi:10.4095/313636

Oswald, W., Castonguay, S., Dubé, B., Malo, M., Mercier-Langevin, P. and Biczok, J., 2015. New insights on the geological and structural settings of the Musselwhite banded iron formation-hosted gold deposit, North Caribou greenstone belt, Superior Province, Ontario; Geological Survey of Canada, Current Research 2015-3, 19 p. doi:10.4095/295570

Oswald, W., Castonguay, S., Dubé, B., McNicoll, V., Biczok, J., Malo, M., and Mercier-Langevin, P., 2015. Geological setting of the world-class Musselwhite gold Mine, Superior Province, northwestern Ontario, and implications for exploration; *in* Targeted Geoscience Initiative 4: Contributions to the Understanding of Precambrian Lode Gold Deposits and Implications for Exploration, (ed.) B. Dubé and P. Mercier-Langevin; Geological Survey of Canada, Open File 7852, p. 69–84. doi:10.4095/296624

Pelletier, M., Mercier-Langevin, P., Dubé, B., Crick, D., McNicoll, V., Jackson, S., and Beakhouse, G.P., 2015. The Rainy River "atypical" Archean Au deposit, western Wabigoon Subprovince, Ontario; *in* Targeted Geoscience Initiative 4: Contributions to the Understanding of Precambrian Lode Gold Deposits and Implications for Exploration, (ed.) B. Dubé and P. Mercier-Langevin; Geological Survey of Canada, Open File 7852, p. 193–207. doi:10.4095/296624

Pelletier, M., Mercier-Langevin, P., Dubé, B., Bécu, V., Lauzière, K., and Richer-Laflèche, M., 2016. Whole-rock lithogeochemistry of the Archean Rainy River gold deposit, western Wabigoon, Ontario; Geological Survey of Canada, Open File 8048, 1 .zip file. doi:10.4095/ 299356

Pilote, J.-L., Piercey, S.J., and Mercier-Langevin, P., 2015. Volcanic architecture and alteration assemblages of the Ming Cu-Au-(Zn-Ag) VMS deposit, Baie Verte, Newfoundland and Labrador: Implications for Au-enrichment processes and exploration; *in* Targeted Geoscience Initiative 4: Contributions to the Understanding of Volcanogenic Massive Sulphide Deposit Genesis and Exploration Methods Development, (ed.) J.M. Peter and P. Mercier-Langevin; Geological Survey of Canada, Open File 7853, p. 197–210. doi:10.4095/ 296540

Pilote, J.-L., Piercey, S.J., and Mercier-Langevin, P., 2016. Geological environment and formational controls of auriferous massive sulfide deposit: An example from the Cambro-Ordovician Cu-Au Ming VMS deposit in the Newfoundland Appalachians; Geological Survey of Canada, Open File 7731, 1 sheet. doi:10.4095/298770

Pilote, J.-L., Jackson, S.E., Mercier-Langevin, P., Dubé, B., and Rhys, D., 2019. Characteristics of diagenetic and epigenetic sulphides in deformed and metamorphosed Archean carbonaceous metasedimentary rocks of the Timmins-Matheson corridor: establishing a framework for fingerprinting ore-forming processes in shear zone-hosted orogenic gold systems; *in* Targeted Geoscience Initiative: 2018 report of activities, (ed.) N. Rogers; Geological Survey of Canada, Open File 8549, p. 33–41. doi:10.4095/313632

Pilote, J.-L., Jackson, W.E., Mercier-Langevin, P., Dubé, B., Lawley, C.J.M., Petts, D.C., Yang, Z., van Hees, E., and Rhys, D., 2020. Fingerprinting ore processes in orogenic auriferous systems: Insights into metallogenic and exploration implications from argillite-hosted iron sulphide nodules from the Timmins-Matheson gold corridor; *in* Targeted Geoscience Initiative 5: Contributions to the Understanding of Canadian Gold Systems, (ed.) P. Mercier-Langevin, C.J.M. Lawley, and S. Castonguay; Geological Survey of Canada, Open File 8712, p. 165–178. doi:10.4095/323675

Pilote, J.-L., Mercier-Langevin, P., Jackson, S.E., Dubé, B., Yang, Z., Lawley, C.J.M., Petts, D.C., Layne, G.D., and Piercey, S.J., 2020. Interrogating the composition and genesis of argillite-hosted pyrite nodules at the LaRonde Penna gold-rich volcanogenic massive sulphide deposit, Abitibi, Quebec: Insights into metallogenic implications; *in* Targeted Geoscience Initiative 5: Contributions to the Understanding of Canadian Gold Systems, (ed.) P. Mercier-Langevin, C.J.M. Lawley, and S. Castonguay; Geological Survey of Canada, Open File 8712, p. 75–91. doi:10.4095/323666

Pinet, N. and Sack, P.J., 2019. Macroscopic control on Carlin-type gold mineralization in north-central Yukon; *in* Targeted Geoscience Initiative: 2018 report of activities, (ed.) N. Rogers; Geological Survey of Canada, Open File 8549, p. 89–103. doi:10.4095/313644

Pinet, N., Mercier-Langevin, P., Dubé, B., Colpron, M., Lane, J., and Asselin, E., 2017. Lithotectonic controls on the genesis and distribution of carbonate replacement-type ("Carlin-type") gold zones, east-central, Yukon; *in* Targeted Geoscience Initiative: 2016 report of activities, (ed.) N. Rogers; Geological Survey of Canada, Open File 8199, p. 43–45. doi:10.4095/299587

Pinet, N., Sack, P.J., Mercier-Langevin, P., Lavoie, D., Dubé, B., Lane, J., and Brake, V., 2018. Breccia styles and controls on carbonate replacement-type ("Carlin-type") gold zones, Rackla belt, east-central Yukon; in Targeted Geoscience Initiative: 2017 report of activities, volume 1, (ed.) N. Rogers; Geological Survey of Canada, Open File 8358, p. 163–168. doi:10.4095/306469

Pinet, N., Sack, P., Mercier-Langevin, P., Colpron, M., Lavoie, D., Dubé, B., and Brake, V.I., 2020. Neoproterozoic-hosted Carlin-type mineralization in central Yukon, part 1: Regional- to prospect-scale geological controls; *in* Targeted Geoscience Initiative 5: Contributions to the Understanding of Canadian Gold Systems, (ed.) P. Mercier-Langevin, C.J.M. Lawley, and S. Castonguay; Geological Survey of Canada, Open File 8712, p. 281–297. doi:10.4095/326045

Pinet, N., Sack, P., Mercier-Langevin, P., Davis, W.J., Lavoie, D., Haeri-Ardakani, O., Komaromi, B.A., Dubé, B., Cline, J.S., Petts, D.C., Jautzy, J., Jackson, S.E., Percival. J.B., Savard, M.M., and Brake, V.I., 2020. Neoproterozoic-hosted Carlin-type mineralization in central Yukon part 2: Mineralization; *in* Targeted Geoscience Initiative 5: Contributions to the Understanding of Canadian Gold Systems, (ed.) P. Mercier-Langevin, C.J.M. Lawley, and S. Castonguay; Geological Survey of Canada, Open File 8712, p. 299–314. doi:10.4095/ 326047

St.Pierre, B., Mercier-Langevin, P., Simard, M., Côté-Mantha, O., Malo, M., and Servelle, G., 2018. Structural and lithologic controls on the nature and distribution of gold in the BIF-associated 1150 and 1250 lode series at Tiriganiaq, Meliadine district, Rankin Inlet greenstone belt, Nunavut; *in* Targeted Geoscience Initiative: 2017 report of activities, volume I, (ed.) N. Rogers; Geological Survey of Canada, Open File 8358, p. 157–161. doi:10.4095/306468

St.Pierre, B., Mercier-Langevin, P., Simard, M., Côté-Mantha, O., Malo, M., and Servelle, G., 2019. Structural and lithological controls on the nature and distribution of gold at the Tiriganiaq deposit, Meliadine district, Rankin Inlet greenstone belt, Nunavut; *in* Targeted Geoscience Initiative: 2018 report of activities, (ed.) N. Rogers; Geological Survey of Canada, Open File 8549, p. 77–82. doi:10.4095/313642

St.Pierre, B., Mercier-Langevin, P., Blais, J.-C., Servelle, G., Simard, M., Côté-Mantha, O., and Malo, M., 2020. Structural controls and relative timing of gold mineralization of the banded iron formation-associated Tiriganiaq deposit, Meliadine district, Rankin Inlet greenstone belt, Nunavut; *in* Targeted Geoscience Initiative 5: Contributions to the Understanding of Canadian Gold Systems, (ed.) P. Mercier-Langevin, C.J.M. Lawley, and S. Castonguay; Geological Survey of Canada, Open File 8712, p. 237–250. doi:10.4095/ 326041

Tóth, Z., Lafrance, B., Dubé, B., McNicoll, V., Mercier-langevin, P., and Creaser, R.A., 2015. Banded Iron formation-hosted gold mineralization in the Geraldton area, Northwestern Ontario: structural setting, mineralogical characteristics and geochronology; *in* Targeted Geoscience Initiative 4: Contributions to the Understanding of Precambrian Lode Gold Deposits and Implications for Exploration, (ed.) B. Dubé and P. Mercier-Langevin; Geological Survey of Canada, Open File 7852, p. 85–97. doi:10.4095/296624

Tóth, Z., Lafrance, B., Dubé, B., Mercier-Langevin, P., and McNicoll, V.J., 2015. Structural setting, mineralogical characteristics and geochemical footprints of banded-iron-formation-hosted gold mineralization in the Geraldton area, Ontario; Geological Survey of Canada, Open File 7667, 1 sheet. doi:10.4095/295526

Valette, M., De Souza, S., Mercier-Langevin, P., Côté-Mantha, O., Simard, M., McNicoll, V., and Barbe, P., 2017. Geology of the 130 t (4.2 Moz) Au, banded iron-formation-hosted Amaruq project, Nunavut; Geological Survey of Canada, Scientific Presentation 60, 1 sheet. doi:10.4095/300658

Valette, M., De Souza, S., Mercier-Langevin, P., McNicoll, V.J., Grondin-LeBlanc, P., Côté-Mantha, O., Simard, M., and Malo, M., 2018. Lithological, hydrothermal, structural and metamorphic controls on the style, geometry and distribution of the auriferous zones at Amaruq, Churchill Province, Nunavut; *in* Targeted Geoscience Initiative: 2017 report of activities, volume 1, (ed.) N. Rogers; Geological Survey of Canada, Open File 8358, p. 153–156. doi:10.4095/306467

Valette, M., De Souza, S., Mercier-Langevin, P., McNicoll, V.J., Wodicka, N., Creaser, R.A., Cote-Mantha, O., and Simard, M., 2019. Geological setting of the 5.2 Moz Au Amaruq banded iron formation-hosted gold deposit, Churchill Province, Nunavut; *in* Targeted Geoscience Initiative: 2018 report of activities, (ed.) N. Rogers; Geological Survey of Canada, Open File 8549, p. 83–87. doi:10.4095/313643

Valette, M., De Souza. S., Mercier-Langevin, P., Côté-Mantha, O., Simard, M., Wodicka, N., McNicoll, V.J., and Barbe, P., 2020. Lithological and tectonic controls on banded iron formation-associated gold at the Amaruq deposit, Churchill Province, Nunavut, and implications for exploration; *in* Targeted Geoscience Initiative 5: Contributions to the Understanding of Canadian Gold Systems, (ed.) P. Mercier-Langevin, C.J.M. Lawley, and

S. Castonguay; Geological Survey of Canada, Open File 8712, p. 251–266. doi:10.4095/ 326042

Yang, X.M. and Lawley, C.J.M., 2018. Tectonic setting of the Gordon gold deposit, Lynn Lake greenstone belt, northwestern Manitoba (parts of NTS 64C16): Evidence from lithogeochemistry, Nd isotopes and U-Pb geochronology; *in* Report of Activities 2018; Manitoba Growth, Enterprise and Trade, Manitoba Geological Survey, p. 89–109.

Yergeau, D., Mercier-Langevin, P., Dubé, B., Malo, M., McNicoll, V., Jackson, S., Savoie, A., and La Rochelle, F., 2015. The Archean Westwood Au deposit, southern Abitibi: telescoped Au-rich VMS and intrusion-related Au systems; *in* Targeted Geoscience Initiative 4: Contributions to the Understanding of Precambrian Lode Gold Deposits and Implications for Exploration, (ed.) B. Dubé and P. Mercier-Langevin; Geological Survey of Canada, Open File 7852, p. 177–191. doi:10.4095/296624

Yergeau, D., Mercier-Langevin, P., Dubé, B., Malo, M., Bécu, V., and Lauzière, K., 2019. Whole-rock lithogeochemistry of the Archean Westwood deposit, southern Abitibi, Québec; Geological Survey of Canada, Open File 8171, 1 .zip file. doi:10.4095/321380

Appendix 3
Theses related to the TGI-5 Gold Project (2015–2020) and legacies of the TGI-4 Lode Gold Project (2010–2015)

Beauchamp, A.-M., 2018. L'indice Mustang : géologie et altération d'une minéralisation aurifère mise en place dans les turbidites de la ceinture de la Basse-Eastmain, Eeyou Itschee Baie-James; M.Sc. thesis, Institut national de la recherche scientifique – Centre Eau Terre Environnement, Québec, Quebec, 360 p.

Boily-Auclair, E., 2017. Nature et style de l'altération hydrothermale associée aux minéralisations aurifères du projet LaRonde Zone 5 (LZ-5), Abitibi, Québec; B.Sc. thesis, Université Laval, Québec, Quebec, 69 p.

Boily-Auclair, E., in prep. Contrôles lithologiques et structuraux sur la nature, le style et la géométrie des zones aurifères de la Zone 5 du complexe minier LaRonde, Abitibi, Québec; M. Sc. thesis, Institut national de la recherche scientifique – Centre Eau Terre Environnement, Québec, Quebec.

Boulerice, A., 2016. Volcanology of the Lemoine Member of the Waconichi Formation, Abitibi Subprovince, Chibougamau, Quebec; M.Sc. thesis, Institut national de la recherche scientifique – Centre Eau Terre Environnement, Québec, Quebec, 193 p.

Caté, A., 2017. Geology of the Paleoproterozoic Zn-Cu-Au lalor volcanogenic massive sulphide deposit and its gold-rich lenses, Snow Lake, Manitoba; Ph.D. thesis, Institut national de la recherche scientifique – Centre Eau Terre Environnement, Québec, Quebec, 384 p.

Ciufo, T.J., 2019. Hydrothermal alteration and exploration vectors at the Island Gold deposit, Michipicoten greenstone belt, Wawa, Ontario; M.Sc. thesis, University of Waterloo, Waterloo, Ontario, 510 p.

Dubé, J., 2016. Caractérisation de la distribution de l'or à l'intérieur de la lentille 20 Nord dans le secteur LaRonde Extension à la mine LaRonde Penna, Abitibi, Québec; B.Sc. thesis, Université Laval, Québec, Quebec, 115 p.

Duff, S., 2016. Ore types of the auriferous Lalor VMS deposit, Snow Lake, Manitoba: implications for genesis and post-depositional processes; M.Sc. thesis, University of Ottawa, Ottawa, Ontario, 123 p.

Fayard, Q., in prep. Contrôles primaires et secondaires principaux sur la nature et la distribution de l'or et de l'argent dans les zones minéralisées du projet B26, complexe volcanique de Brouillan, Abitibi, Québec; M.Sc. thesis, Université du Québec à Chicoutimi, Chicoutimi, Quebec.

Fontaine, A., 2019. Géologie des minéralisations aurifères de la mine Éléonore, Eeyou Istchee Baie-James, province du Supérieur, Québec, Canada; Ph.D. thesis, Institut national de la recherche scientifique – Centre Eau Terre Environnement, Québec, Quebec, 526 p.

Gourcerol, B., 2016. Characterization of banded iron formations associated with gold mineralization primary geochemical signatures and exploration implications; Ph.D. thesis, Laurentian University, Sudbury, Ontario, 370 p.

Janvier, V. 2016. Géologie du gisement d'or encaissé dans des formations de fer rubanées Meadowbank, Nunavut, Canada; Ph.D. thesis, Institut national de la recherche scientifique – Centre Eau Terre Environnement, Québec, Quebec, 472 p.

Jellicoe, K.M., 2019. Structural controls and deformation history of the orogenic Island Gold deposit, Michipicoten greenstone belt, Ontario; M.Sc. thesis, University of Waterloo, Waterloo, Ontario, 84 p.

Katz, L.R., 2016. Geology of the Archean Côté Gold Au(-Cu) intrusion-related deposit, Swayze Greenstone Belt, Ontario; Ph.D. thesis, Laurentian University, Sudbury, Ontario, 347 p.

Krushnisky, A., 2018. Controls on gold enrichment at the Horne 5 Archean VMS deposit, Abitibi greenstone belt, Québec; M.Sc. thesis, Institut national de la recherche scientifique – Centre Eau Terre Environnement, Québec, Quebec, 198 p.

Lauzon, M.-C., 2017. Empreinte minéralogique et géochimique des minéralisations aurifères de la zone Whale Tail du projet Amaruq; B.Sc. thesis, Université Laval, Québec, Quebec, 48 p.

O'Connor, A.R., in prep. Thermochronology of the Lynn Lake greenstone belt, Manitoba; M.Sc. thesis, University of Ottawa, Ottawa, Ontario.

Oswald, W., 2018. Geology of the Musselwhite banded iron formation-hosted gold deposit, Superior Province, Ontario, Canada; Ph.D. thesis, Institut national de la recherche scientifique – Centre Eau Terre Environnement, Québec, Quebec, 475 p.

Pelletier, M., 2016. The Rainy River gold deposit, Wabigoon Subprovince, Western Ontario: style, geometry, timing and structural controls on ore distribution and grades; M.Sc. thesis, Institut national de la recherche scientifique – Centre Eau Terre Environnement, Québec, Quebec, 364 p.

Appendix 3: Theses related to the TGI-5 Gold Project (2015–2020) and legacies of the TGI-4 Lode Gold Project (2010–2015); *in* Targeted Geoscience Initiative 5: Contributions to the Understanding of Canadian Gold Systems, (ed.) P. Mercier-Langevin, C.J.M. Lawley, and S. Castonguay; Geological Survey of Canada, Open File 8712, p. 327–328.

Pilote, J.-L. 2018. Geology, structure, petrogenesis, and hydrothermal alteration reconstruction of the Ming volcanogenic massive sulphide deposit, Baie Verte Peninsula, Newfoundland, Canada; Ph.D. thesis, Memorial University of Newfoundland, St-John's, Newfoundland and Labrador, 496 p.

St.Pierre, B., in prep. Structural and lithological controls on the nature and distribution of gold in the BIF-associated 1150 and 1250 lode series at Tiriganiaq, Meliadine district, Rankin Inlet greenstone belt, Nunavut; M.Sc. thesis, Institut national de la recherche scientifique – Centre Eau Terre Environnement, Québec, Quebec.

Sterckx, S., 2018. Géochimie des roches volcaniques archéennes du Groupe de Blake River, ceinture de roches vertes de l'Abitibi, Québec; M.Sc. thesis, Institut national de la recherche scientifique – Centre Eau Terre Environnement, Québec, Quebec, 209 p.

Tóth, Z., 2019. The geology of the Beardmore-Geraldton belt, Ontario, Canada: geochronology, tectonic evolution and gold mineralization; Ph.D. thesis, Laurentian University, Sudbury, Ontario, 303 p.

Valette, M., in prep. Contexte géologique, évolution tectono-métamorphique et activité hydrothermale du secteur Amaruq: implications pour la genèse des minéralisations aurifères de l'ouest de la Province de Churchill, Nunavut; Ph.D. thesis, Université du Québec à Montréal, Montréal, Quebec.

Veglio, C., in prep. Ore-forming element signature of the Slave cratonic mantle; M.Sc. thesis, University of Alberta, Edmonton, Alberta.

Watts, J., in prep. Element mapping of gold veins and geochemical vectoring with handheld LIBS, Lynn Lake, Manitoba; M.Sc. thesis, University of Windsor, Windsor, Ontario.